

# PHYSICAL CHEMISTRY 2008

# **Proceedings**

of the 9th International Conference on Fundamental and Applied Aspects of Physical Chemistry

# Volume I

The Conference is dedicated to the 200th Anniversary of the University in Belgrade



September 24-26, 2008, Belgrade, Serbia



# PHYSICAL CHEMISTRY 2008

# **Proceedings**

of the 9<sup>th</sup> International Conference on Fundamental and Applied Aspects of Physical Chemistry

Volume I

ISBN 978-86-82475-16-3

Title: Physical Chemistry 2008. (Proceedings)

Editor: Prof. dr A. Antić-Jovanović

Published by: The Society of Physical Chemists of Serbia, Student-

ski trg 12-16, P.O.Box 47, 11158 Belgrade, 218,

Serbia

Publisher: Society of Physical Chemists of Serbia

For publisher: Prof. dr S. Anić, president of the Society of Physical

Chemists of Serbia

Printed by: "Jovan" Printing and Published Comp;

250 Copies; Number of Pages: x + 468; Format B5;

Printing finished in September 2008.

Text and Layout: Aleksandar Nikolić

250 – copy printing

# The Conference is organized by the Society of Physical Chemists of Serbia

in cooperation with Institute of Catalysis, Bulgarian Academy of Sciences

Boreskov Institute of Catalysis, Siberian Branch of the Russian Academy of Sciences

Faculty of Physical Chemistry, University of Belgrade

Institute of Chemistry, Technology and Metallurgy, Belgrade

Institute of General and Physical Chemistry, Belgrade

#### **International Organizing Committee**

Chairman: S. Anić (Serbia) Vice-chairman: A. Elias (Bulgaria)

> I. V. Koptyug (Russia) B. Adnadjević (Serbia)

#### Members:

M. Gabrovska (Bulgaria), T. Grozdić (Serbia), D. Jovanović (Serbia), P. M. Lalic (BiH),

Manojlović (Serbia), D. Marković (Serbia), B. Milosavljević (USA),

N. Miljević (Serbia), T. Nenadović (Serbia), N. Ostrovski (Serbia), C. Pona (Italy),

B. Simonović (Serbia), A. G. Stepanov (Russiaia), N. Vukelić (Serbia),

V. Vukojević (Sweden)

#### International Scientific Committee

Chairman: A. Antić-Jovanović (Serbia) V. N. Parmon (Russia) Vice-chairmans:

Ž. Čupić (Serbia)

S. Rakovsky (Bulgaria)

#### Members:

G. Bacic (Serbia), R. Cervellati (Italy), B. Cretin (France), V. Dondur (Serbia), V. Gaspar (Hungary), M. Jeremić (Serbia), A. L. Kawczyński (Poland), Lj. Kolar-Anić (Serbia), I. V. Koptyug (Russia),

S. Mentus (Serbia), S. Miloniić (Serbia), B. Minceva-Sukarova (R.Macedonia).

Lj. Morozova-Roche (Sweden), Z. Noszticzius (Hungary), M. Perić (Serbia), V. Petruševski (R.Macedonija), M. Plavšić (Serbia), I. Poulios (Greece), G. Schmitz (Belgium), I. Schreiber (Czech), P. Sevcik (Slovakia), N. Stepanov (Russia), M. Trtica (Serbia), D. Veselinović (Serbia),

#### **Local Executive Committee**

Chairman: B. Adnadjević Vice-chairmans: S. Blagojević

#### Members:

N. Begović, S. N. Blagojević, I. Cekić, N. Cvjetičanin, M. Daković,

Lj. Damjanović, A. Đerić, A. Ignjatović, Lj. Ignjatović, A. Ivanović, A. Jović, D. Lončarević, M. Mojović,

I. Pašti, N. Pejić, N. Potkonjak, D. Ranković, D. Stanisavljev, B. Šljukić

## **Honorary Committee**

Nikola Hajdin, President of Serbian Academy of Sciences and Arts

Branko Kovačević, Rector, University of Belgrade

Paula Putanov, Member of Serbian Academy of Sciences and Arts

Momčilo Ristić, Member of Serbian Academy of Sciences and Arts

Ivan Draganić, Honorary Member of Society of Physical Chemists of Serbia

Bratislav Đorđević, Ambassador, Ministry of Foreign Affairs of Republic of Serbia

## **SPONSORS**

Ministry of Science of the Republic of Serbia

The Faculty of Physical Chemistry, University of Belgrade

Institute for Chemistry, Technology and Metalurgy, University of Belgrade

NovoLab, Belgrade

Organisation for the Prohibition of Chemical Weapons

MOL, Belgrade

ENOLOŠKA STANICA dp, Society Company for Agricultural Products and Foodstuffs Control, Vršac

Gradski zavod za zaštitu zdravlja, Beograd

Following the tradition of the preceding Conferences on Fundamental and Applied Aspects of Physical Chemistry, the aim of the present Conference is again to allow researchers from different countries to enhance contacts and exchange information and experiences.

The program of the Conference includes invited plenary lectures, invited section lectures, oral contributions and poster sessions of 480 authors from twenty three countries.

Beside six Plenary Lectures, given by internationally recognized scientists, this book contains twenty two Invited Lectures and 184 contributions, given as ether oral or poster presentations, arranged in sessions corresponding to their scientific topics. All accepted papers are reviewed but without language revision, for which authors bear responsibility.

Organizers of the Conference "Physical Chemistry 2008" thank to all authors for the effort to provide us with their paper and take part in the Conference, our sponsors, as well as to the Ministry of Sciences of the Republic of Serbia for contribution to the success of Conference.

Belgrade, 2008

Editor

# **Contents**

Volume I		
Plenary Lectures (PL)	1	
General Physical Chemistry (A)		
Spectroscopy, Molecular Structures (B)	63	
Kinetics, Catalysis (C)	123	
Nonlinear Dynamics (D)	199	
Electrochemistry (E)	253	
Biophysical Chemistry, Photochemistry, Radiation Chemistry (F)	319	
Volume II		
Radiochemistry, Nuclear Chemistry (G)	457	
Material Science (H)	469	
Phase Boundaries (I)	539	
Macromolecular Physical Chemistry (J)	553	
Environmental Protection, Forensic Science (K)	607	
Complex Compounds (L)	689	
Education (M)	719	
Supplement	727	
Autor Index	738	
Participating Institutions	747	
Sunnlement 2	757	

# Plenary Lectures (PL)

# RECENT ADVANCES IN PHYSICAL CHEMISTRY IN ALZHEIMER'S DISEASE

#### R.M. Leblanc

University of Miami, Department of Chemistry, 1301 Memorial Drive, Cox Science Center, Coral Gables, FL. 33146. U.S.A.

Amyloid beta  $(A\beta)$  is a major peptide constituent found in the neuritic plaques involved in Alzheimer's disease.[1] Significant progress has been made in the characterization of  $(A\beta)$  peptides like  $A\beta$  (1-40, 1-42) and other truncated peptide fragments. Characterization of  $A\beta$  is of great importance in understanding the mechanistic pathways leading to Alzheimer's disease. On the other hand, there have been studies showing that the formation of amyloid fibrils is not restricted to  $A\beta$  peptides; various proteins like lysozyme,  $\beta$ -lactoglobulin, the prion protein  $PrP^c$ , the immunoglobulin light chain, the SH3 domain of bovine phosphatidylinositol 3-kinase, and  $\beta_2$ -microglobulin can also form fibrils at different conditions. For most proteins, the condition that leads to partial unfolding results in fibrillization.[2] These proteins can also serve as models for the study of Alzheimer's disease.

Amyloid fibrils contain bundles of β-sheets with backbone orthogonal to fiber axis in the cross- $\beta$  structure.[3] The combination of spectroscopic characterization methods provides a clear picture of fibril formation. The self-assembly of A<sub>β</sub> (16-20), a fragment of the amyloid beta peptide, has been studied in dilute aqueous solutions and dry films.[4] Fourier transform infrared (FTIR), cryo-transmission electron microscopy (cryo-TEM), and Xray diffraction reveal β- sheet structures in the spectra obtained from more concentrated solutions and dry films of AB (16-20). At lower concentrations, circular dichroism (CD) and UV spectroscopy suggest the absence of well-defined β-sheet conformation. Conformational analysis of Aβ (11-28) have been studied in membrane-mimicking environment using sodium dodecylsulphate via CD spectropolarimetry and NMR spectroscopy.[5] CD spectra of all the peptides studied show that there is no  $\alpha$ -helical conformation and that small amounts of  $\beta$ -sheet structures in solution could seed the aggregation process. One of the most important elements of information used in determining secondary structure of protein by NMR is the characteristic short range NOE<sub>s</sub>. The inspection of NOE pattern of Aβ (11-28) A21G molecule shows lack of diagonistic d<sub>qN</sub> (i,i+3) NOE effects and provides the evidence of unstructured conformation of the peptide. High quality NMR experiments have also been analyzed using molecular simulations to check the structural diversity of Aß (21-30).[6] From the results, it was interpreted that majority (60%) of the population of  $A\beta$  was of unstructured conformers, lacking persistent hydrogen bonding networks.

The effect of temperature, pH, and ionic strength on A $\beta$  (1-40) aggregation mechanism was investigated by CD spectropolarimetry, isothermal titration calorimeter (ITC), and hydrophobic fluorescence assay.[7] The results from the kinetic analysis showed that the nucleation was the rate determining step during A $\beta$  aggregation. The thermodynamic analysis demonstrated that the hydrophobic effect is the driving force in the nucleation process. Colloidal gold has been used to visualize positive charge clusters on A $\beta$  fibrils via electron microscopy.[8]

There has also been some work conducted on A<sub>β</sub> (1-40) adsorption at air-lipid interface, which mimics the neuronal membrane. The interactions are studied using infrared reflection absorption spectroscopy (IRRAS).[9] Structural details of Aß-membrane association have been elucidated using complementary X-ray (grazing-incidence X-ray diffraction) and neutron scattering techniques.[10] In this study in situ association of AB with the lipid monolayer at the air-buffer interface, composed of either the anionic lipid 1,2 dipalmitoyl-sn-glycero-3-[phospho-rac-(1-glycerol)] (DPPG), the zwitterionic lipid 1,2-dipalmitoyl-sn-glycero-3-phosphocholine (DPPC), or the cationic lipid 1,2-dipalmitoyl 3-trimethylammonium propane (DPTAP), has been analyzed. It was revealed that the anionic lipid DPPG uniquely induced crystalline ordering of AB at the membrane surface that closely mimicked the β-sheet structure in fibrils. The behavior of amyloid-like peptide such as LSFD, a 12 amino acid peptide was studied at air-water interface using Brewster angle microscopy (BAM) showing formation of large condensed domains on compression.[11] Fourier transform infrared spectroscopy (FTIR) of Langmuir Blodgett films of LSFD revealed β-sheet strucat air-water interface. The morphology of film was investigated through atomic force microscopy (AFM) that highlighted the heterogeneity of the film, showing densely packed nanodomains that aggregate in coexistence with thick disordered spots. AB (25-35) was modified with an aliphatic chain (C<sub>18</sub>) at the N- terminal of the peptide for the study of the Langmuir monolayer at air-water interface.[12] Surface pressure and surface potential-area isotherms were measured to examine the self-assembly of the peptide moiety in the subphase and hence the aggregation process. The topography of the domains of the peptidolipid was observed utilizing the real time-epifluorescence microscopy. Also, polarization modulation infrared spectroscopy (PM- IRRAS) was applied to investigate the structural features of the domains at air-water interface, and to complement conformational analysis, CD of Langmuir-Blodgett (LB) films was investigated.

Fibril formation and mechanistic pathways involving misfolding and aggregation have been studied using a variety of proteins. FTIR has been utilized to detect amyloid-like fibrils formed in vitro from natively folded or unfolded β<sub>2</sub>-microglobulin (protein associated with dialysis related amyloidosis).[13] β<sub>2</sub>-microglobulin adopts an identical β-sheet architecture, regardless if fibril formation in vitro occurs spontaneously or from seeded reactions. Also, the amide I band that is observed in the range 1600-1700 cm<sup>-1</sup> is similar when compared to the amyloid fibrils extracted from the patients with dialysis-related amyloidosis. β-lactoglobulin and insulin have also been used as models for understanding neurodegenerative diseases. The thermal dependence of formation and growth of spherulite structures, in the two model protein systems, β-lactoglobulin and insulin at low pH and high temperature conditions have been monitored with time lapse optical microscopy and quantified.[14] Deep-UV Raman (DUVR) spectroscopy has been shown to directly probe the fibrillation nucleus in lysozyme, quantitatively characterizing the kinetics of nucleus formation.[15] Among lysozymes EL (equine lysozyme) forms one of the most stable molten globules and shows the most uncooperative refolding kinetics. Its partially-folded states serve as precursors for calcium-dependent self-assembly, into ring-shaped and linear amyloids.[16]

Physical chemistry has an important role in the diagnosis of Alzheimer's disease. Detection of tau protein has been proposed at room temperature using multi-spot localized surface plasmon resonance (LSPR) based immunochip.[17] Recently, infrared spectroscopy has been manifested as a new diagnostic tool in Alzheimer's disease.[18] Cerebrospinal fluid (CSF) tau and A $\beta$  (1-42) have been investigated via FTIR spectroscopy. Since FTIR spectra reflect the entire pattern of the biochemical constituents in the examined probe rather than the analysis of single parameter, a correlation of FTIR spectra with proteomic pattern has been suggested to study the effect of different proteins in the individual spectra.

#### References

- [1] Sondag, C. M., Combs, C. K. J. Neurochemistry 2006, 97, 449-461
- [2] Hamley. I. W. Angew. Chem. Int. Ed. 2007, 46, 8128-8147
- [3] Makin, O. S., Serpell, L. C. FEBS J. 2005, **272**, 5950-5961
- [4] Krysmann, M. J., Castelletto, V., Kelarakis, A., Hamley, I. W., Hule, R. A., Pochan, D. J. Biochemistry 2008, 47, 4597-4605
- [5] Motowidlo, S. R., Juszczyc, P., Kolodziejczyc, A. S., Sikorska, E., Skweirawska, A., Oleszczuk, M., Grzonka, Z. Biopolymers 2007, 87, 23-39
- [6] Fawzi, N. J., Phillips, A. H., Ruscio, J. Z., Doucleff, D. E., Head-Gordon, T. J. Am. Chem. Soc. 2008, 130, 6145-6158

- [7] Lin, M. S., Chen, L. Y., Tsai, H. T., Wang, S. S. S., Chang, Y., Higuchi, A., Chen, W.Y. Langmuir 2008, 24, 5802-5808
- [8] Yoshiike, Y., Akagi, T., Takashima, A. Biochemistry 2007, 46, 9805-9812
- [9] Maltseva, E., Brezesinski, G., Chem. Phys. Chem. 2004, 5, 1185-1190
- [10] Chi, E.Y., Ege, C., Winans, A., Majewski, J., Wu, G., Kjaer, K., Lee, K. Y. C. Proteins, 2008. In press (DOI: 10.1002/prot.21887)
- [11] Lepere, M., Chevallard, C., Hernandez, J. F., Mitraki, A., Guenoun, P. Langmuir, 2007, 23, 8150-8155
- [12] Triulzi, R. C., Li, C., Naistat, D., Orbulescu, J., Leblanc, R. M. J. Phys. Chem. C. 2007, 111, 4661-4666
- [13] Jahn, T.R., Tennent, G. A., Radford, S. E. J. Bio. Chem. 2008, 283, 17279-17286
- [14] Domike, K.R., Donald, A. M. Biomacromolecules 2007, **8**, 3930-3937
- [15] Shasilov, V., Lednev, I. K. Biospectroscopy 2007, 87-90
- [16] Morozova-Roche, L. A. FEBS Lett. 2007, **581**, 2587-2582
- [17] Vestergaard, M., Kerman, K., Kim, D.K., Hiep, H.M., Tamiya, E. Talanta 2008, 74, 1038-1042
- [18] Griebe, M., Daffertshofer, M., Stroick, M., Syren, M., Ahmad-Nejad, P., Neumaier, M., Backhau, J., Hennerici, M.G., Fatar, M. Neurosci. Lett. 2007, 420, 29-33

## DESIGN, FABRICATION, CHARACTERISATION AND APPLICATION OF NANOELECTRODE ARRAYS

#### R.G. Compton

Chemistry Department, Physical and Theoretical Chemistry Laboratory, South Parks Road, Oxford, OX1 3QZ, United Kingdom

#### **Abstract**

The lecture will highlight recent work carried out in the author's laboratory on methods of fabricating and characterising arrays of micro- and nanoelectrodes, as recently reported in the invited Frontiers article by R G Compton, G G Wildgoose, I Streeter, N V Rees and R Baron in Chemical Physics Letters, 2008, 459, 1-17.

The following will be discussed: The template fabrication of random arrays of nanoband electrodes on highly ordered graphite surfaces and on carbon nanotubes, acoutic methods of fabricating random arrayst of metal nanoparticles on electrodes surfaces, and numerical methods of simulating and modelling the electrochemical processes that occur at sich arrays. Finally examples of electroanalytical applications of nanoparticle arrays will be given, including multi-metal nanoparticle arrays for combinatorial electrochemistry.

### WATER AS A SOLUTE IN ORGANIC SOLVENTS AS SEEN BY NMR

S. Macura, N. Juranić, B. Nedić and F.G. Prendergast

Department of Biochemistry, Mayo Graduate School, Mayo Clinic, Rochester, Minnesota, 55905, USA

While water has been studied intensively for many years[1], many of its properties remain scantily described. This lack of understanding can be ascribed to the tendency of water molecules to communicate with each other via hydrogen bonding and proton exchange. The ability of a water molecule to act simultaneously as a Hbond donor and acceptor leads toward formation of the hydrogen bonding network which is in constant rearrangement due to molecular motion. In addition, water molecules rearrange constantly due to proton jump between H-bonded molecules:  $O-H\cdots O \leftrightarrow -O\cdots H-O$ . The picture is further complicated by the cooperativity of Hbonding which makes the whole system behave like a huge molecular assembly whose properties cannot be described as a sum of properties of its components. This limits theoretical description to a cluster of three water molecules [2]. Experimental measurements, on the other hand, necessarily define water in terms of the particular experimental technique used. For example, nuclear magnetic resonance (NMR) was able to determine that the proton exchange rate constant in the reaction  $H_2O + H_3O^+ = H_3O^+ + H_2O$  is  $10.6 \times 10^9$  L M<sup>-1</sup> s<sup>-1</sup> [3]. This means that in pure water, where  $[H^{+}] = 10^{-7} \text{ M L}^{-1}$ , the lifetime of the water molecule is of the order of one millisecond.

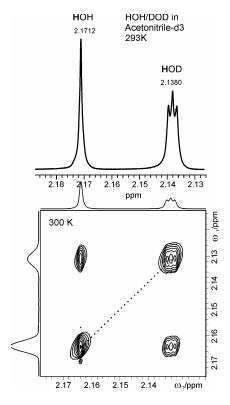
Main advantage of NMR spectroscopy is its extraordinary sensitivity to small perturbations of spin environment which makes it especially suitable for studies of weak interactions. On the other hand, compared to other spectroscopic techniques NMR is notoriously slow. If exchange processes are fast on the NMR time scale, the detected signal is then weighted average of all molecular species. Information content of NMR spectra considerably improves if the studied exchange is slowed down so that the signal from individual spin groups could be observed. In that respect, we resorted to water dilution with organic solvents. The added organic solvent breaks hydrogen bonds among water molecules and slows down proton exchange inasmuch that signature of individual molecules can be observed. For example, it is well known that, due to isotope effect, proton chemical shift in **HOH** and **HOD** are different. Yet, in the H<sub>2</sub>O/D<sub>2</sub>O mixture, under normal conditions, only one proton line is observed. Main reason for that is the fast chemical exchange between water isotopomers,

$$\mathbf{H}\mathbf{O}\mathbf{H} + \mathbf{D}\mathbf{O}\mathbf{D} = \mathbf{H}\mathbf{O}\mathbf{D} + \mathbf{H}\mathbf{O}\mathbf{D} \tag{1a}$$

$$\mathbf{H}\mathrm{OD} + \mathrm{HOH} = \mathrm{HOD} + \mathbf{H}\mathrm{OH} \tag{1b}$$

which averages chemical shifts, yielding single NMR line. However, if the water system is diluted enough, the proton spectrum shows two resonances separated by 0.0305 ppm [4], top figure. In addition, the proton resonance from HDO molecule

is split into triplet due to proton deuteron scalar coupling,  $J_{DH} = 1.1$  Hz. The proton exchange that takes place on the scale that is commensurate with the coupling constant and the chemical shift difference induces dynamical signal averaging that affects line shape of the HOD line and the linewidth of both lines. However, slower exchange processes do not affect 1D spectrum. A true dynamic character of the



system can be revealed from a double resonance experiments or, even better, from 2D exchange experiment (bottom figure). The main diagonal (dotted line) is equivalent to the 1D spectrum. Cross-peaks indicate magnetization transfer, here chemical exchange, between respective diagonal lines.

In this work we have studied H<sub>2</sub>O/D<sub>2</sub>O mixture in different organic solvents in an attempt to differentiate between various interactions of a water molecule with its surrounding. From a series of 2D experiments we were able to obtain proton exchange rate constants in Eqs. (1) under different conditions (solvent, temperature, water concentration). We found that the proton exchange is much slower in mildly polar solvents (acetone, acetonitrile, chloroform, dichloromethane) than in the strongly polar solvents (dimethylformamide, nitrobenzene, pyridine). Polar solvents are apparently able to generate traces of free H<sup>+</sup> or OH<sup>-</sup> ions which further catalyze the exchange reaction. From the analysis of the number of participating spins [5] we conclude

that the catalytic effect is partly due to the preferential hydration of polar centers.

#### References

- [1] D. Eisenberg, and W. Kauzmann, The Structure and Properties of Water, Clarendon, Oxford, 1969.
- [2] F.N. Keutsch, and R.J. Saykally, PNAS, 2001, 98, 10533-10540.
- [3] S. Meiboom, J. Chem. Phys., 1961, 34, 375-388.
- [4] J. R. Holmes, D. Kivelson, W. C. Drinkard, J.Chem. Phys., 1962, 37 150-152.
- [5] N. Juranic, Z. Zolnai, and S. Macura, J. Serbian Chem. Soc., 2000, 65 285-301.

#### RECENT ADVANCES IN FOOD ANALYSIS

### J. Hajslova and T. Cajka

Institute of Chemical Technology, Prague, Department of Food Chemistry and Analysis, Technicka 3, 16628 Prague 6, Czech Republic, jana.hajslova@vscht.cz; GSM: 00420602833424

The science of food analysis has been developed rapidly in the recent years. New analytical techniques have been developed and existing ones are continuously optimized. As a general trend, analysis systems have become fully automated including data processing. All this effort is aimed at obtaining more knowledge on a chemical composition of food since it is important to the health, well being and safety of the consumers. Besides of various sophisticated instrumental techniques, also a range of new technologies such as transcriptomics, proteomics and biosensors have been finding their place in food analysis. These new approaches are based on a rather new concept – the information about biological (toxic) effects rather than report on single target compound concentrations is delivered. The 'biomarker and fingerprinting' concept is the key to this strategy.

The 'food safety crises', examples of which include 'mad cow' disease, dioxin-contaminated feed, olive adulterated oil by mineral oils or Sudan dyes in curry powder and other spices, initiated a revision of food safety rules within the European Union. Rapid Alert System for Food and Food (RASFF) shows that monitoring of chemical contaminants in food and feed is a very relevant tool in European food safety. Also consumers placed chemical contaminants on top of the "worry-scale" of food-related risks.

Currently, modern trace analysis aims at implementation of broad scope, rapid, and cost-effective methods with performance characteristics (such as accuracy, limits of quantification, uncertainty of measurement, etc.) complying with particular purpose. Particularly, the hyphenation of mass spectrometry (MS) to capillary gas chromatography (GC) and liquid chromatography (LC) as well as the development of novel ionisation techniques caused an extensive spreading of this technique in this area. Both research and routine application have benefited from introduction of relatively inexpensive quadrupole and ion trap mass analysers and, at the end of the last century, the rediscovery of time-of-flight mass analysers (TOF MS) allowed further progress.

Referring to various pilot studies conducted in laboratories of Prague Institute of Chemical Technology, examples of challenges offered by selected advanced analytical techniques in identification / quantification of various contaminants, toxins and other biologically active food components, are illustrated in following paragraphs, the basic principles of are outlined:

#### ■ Comprehensive two-dimension gas chromatography, GC×GC-TOFMS

This technique offers an enormous potential in analysis of volatile and semivolatile compounds. When using conventional, one-dimensional GC coupled to unit resolution GC, for analysis of complex samples, co-elution sample components may

hamper their reliable identification/quantification. Fairly higher peak capacity and improved detectability is offered by recently introduced comprehensive twodimension (orthogonal) GC (GC×GC) technique. Two GC separations, both with different separation mechanisms, are applied for characterization of a particular sample. In most cases, separation of the sample components starts on a non-polar (narrow-bore) capillary GC column (typically 15-30 m, 0.25-0.32 mm internal diameter, 0.1-1 µm film thickness) where separation of analytes takes place according to their volatility. Slicing and refocusing of adjacent fractions of the firstcolumn eluate by an interfacing device called a modulator occurs continuously. These fractions are then released into a short microbore capillary column (typically 0.5-2 m, 0.1 mm internal diameter, 0.1 µm film thickness) employing specific interaction such as hydrogen bonding,  $\pi$ - $\pi$  interaction, steric effects, etc., for separation. On the latter, second dimension column, very fast separation occurs, resulting in extremely narrow peak widths of 50-500 ms. These second dimension peaks therefore require a detector with acquisition rate in a range of 40-400 Hz, which provides 20 data points across a peak. This criterion is partially met by, high-speed TOFMS, which, thanks to acquisition rates up to 500 spectra/s, which is sufficient for reconstruction of very narrow peaks typically produced by GC×GC.

In **Figure 1**, the example of 90 pesticide residues analysis in apple within 11 minutes is shown. The scope of method can be further expanded.

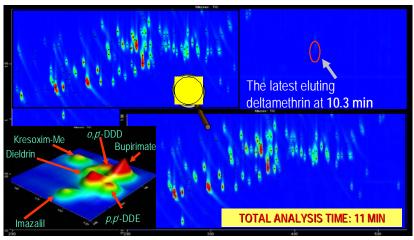


**Fig. 1.** Application of GC×GC–TOFMS in pesticide residue analysis

In **Figure 2**, the analysis of persistent halogenated pollutants (POPs) in fish, which is widely employed as indicator of water pollution is shown. Both major polychlorinated biphenyls (PCBs), brominated flame retardants and other compounds can be detected in a single run.

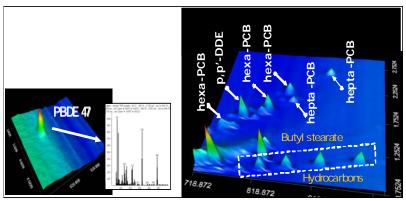


**Fig. 2.** Application of GC×GC–TOFMS in the analysis of persistent halogenated pollutants

### • Ultra pressure liquid chromatography (UPLC) coupled to TOF-MS.

This technique, applicable to a wide range of analytes, represents another challenge in food/quality safety control since it allows not only high throughput analysis, but also non-target screening (thanks to the use of high resolution TOFMS). Theoretically, there are several strategies to reduce analysis time, the main being: (i) an increase of mobile phase flow rate; (ii) the use of short columns with a low back pressures and, since recently, (iii) the use of normal size column filled with very small particles (<2µm). The latter approach represents obviously the best solution. In this way, both high peak capacity and fast separation of even complex mixtures can be obtained. However, due to a very high backpressures at typical LC–MS flow rates, such columns cannot be operated by common HPLC pumps. Current UPLC instruments are able to perform at operational pressures as high as 15,000 psi (1,025 bars). In our study, columns with porous 1.7 µm particles and common size parameters (100–150 mm, 2.1 mm) could be operated at high mobile phase flow rates without a loss of resolution. An example of substantial increase of the speed of multiple pesticide residues analysis is documented in Figure 3.

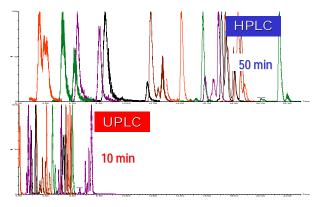


Fig. 3. Application of UPLC-TOFMS in pesticide residue analysis

Another example of UPLC-TOFMS potential in analysis of emerging toxins is shown in **Figure 4**. Although the analytical standards were not available, conjugates ("masked" forms) of deoxynivalenol (DON), the major trichothecene mycotoxin in cereal, were identified on the basis of accurate mass of adduct ion (HILIC chromatography, ESI- ionization).

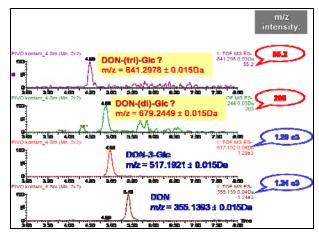
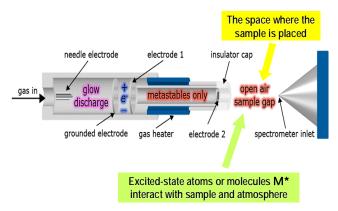


Fig. 4. Application of UPLC-TOFMS in mycotoxin analysis

# ■ Ambient mass spectrometry: "Direct Analysis in Real Time" (DART) interfaced with high-resolution time-of-flight mass spectrometry (TOF-MS)

As far as chromatographic separation of sample components is used prior to MS detection, less spectral interferences caused by matrix components are observed compared with direct measurement. However, the labour-intensity of sample preparation (which typically involves extraction, pre-concentration and/or clean-up steps), and the time required for the chromatographic run itself, can become a bottleneck in laboratory throughput. However, regardless of whether GC or LC is employed, the optimisation of the separation process for multiple analytes with different physicochemical properties is very challenging. The possibility of overcoming these difficulties has emerged with the introduction of three new ionisation techniques: direct analysis in real time (DART), desorption electrospray ionisation (DESI) and atmospheric pressure solids analysis probe (ASAP). These techniques allow a rapid, non-contact MS analysis of materials at ambient pressure and ground potential. Compared with GC-MS and LC-MS, ambient MS requires essentially no separation of Sample components employing chromatographic techniques. Additionally, these techniques allow direct access to the sample while mass spectra are being recorded. The outline of DART principle is shown in **Figure 5**.



**Fig. 5.** Principle of DART.

In **Figure 6**, identification of banned anabolic steroids in "natural" herbal supplements intended for musculature growth support is documented.

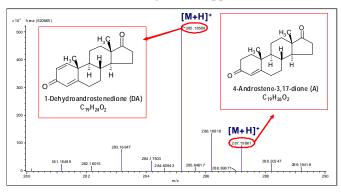


**Fig. 6.** Application of DART–TOFMS in the analysis of anabolic steroids.

## Recent ICT papers related to food quality/safety analysis:

- [1] Hajslova J., Cajka T.: Gas chromatography in food analysis. In: *Handbook of Food Analysis Instruments*. S. Ötleş (editor), ISBN: 9781420045666, CRC Press, Taylor & Francis Group (*in press*)
- [2] Cajka T., Hajslova J., Mastovska K.: Mass spectrometry and hyphenated instruments in food analysis. In: *Handbook of Food Analysis Instruments*. S. Ötleş (editor), ISBN: 9781420045666, CRC Press, Taylor & Francis Group (*in press*)
- [3] Cajka T., Vaclavik L., Riddellova K., Hajslova J.: GC–TOF-MS and DART–TOF-MS: Challenges in the Analysis of Soft Drinks. LC GC Eur. 21(5), 250–256 (2008).
- [4] Lancova K., Hajslova J., Poustka J., Krplova A., Zachariasova M., Dostalek P., Sachambula L.: Transfer of Fusarium mycotoxins and 'masked' deoxynivalenol (deoxynivalenol-3-glucoside) from field barley through malt to beer. Food Addit. Cont. 25(6), 732–744 (2008).
- [5] Kovalczuk T., Lacina O., Jech M., Poustka J., Hajšlová J.: Novel approach to fast determination of multiple pesticide residues using of ultraperformance liquid chromatog-

- raphy-tandem mass spectrometry (UPLC-MS/MS). Food Addit. Cont. 25(4), 444–457 (2008).
- [6] Čajka T., Hajšlová J.: Gas chromatography–time-of-flight mass spectrometry in food analysis. LC GC Eur. 20(1), 25–26, 28–31 (2007).
- [7] Hajšlová J., Pulkrabová J., Poustka J., Čajka T., Randák T.: Brominated flame retardants and related chlorinated persistent organic pollutants in fish from river Elbe and its main tributary Vltava. Chemosphere 69, 1195–1203 (2007).
- [8] Kovalczuk T., Jech M., Poustka J., Hajšlová J.: Ultra-performance liquid chromatography–tandem mass spectrometry: A novel challenge in multiresidue pesticide analysis in food. Anal. Chim. Acta 577, 8–17 (2006).
- [9] Hajšlová J., Čajka T.: Gas chromatography-mass spectrometry (GC–MS). In: Food Toxicants Analysis, Y. Picó (editor), ISBN-13: 978-0-444-52843-8, Elsevier, Oxford, UK, pp. 419–473 (2006).
- [10] Zrostlíková J., Hajšlová J., Čajka T.: Evaluation of two-dimensional gas chromatography-time- of-flight mass spectrometry for the determination of multiple pesticide residues in fruit. J. Chromatogr. A 1019, 173–186 (2003).

# EFFICIENCY OF THEORETICAL APPROACHES FOR DEVELOPMENT OF ADVANCED POLYMER MATERIALS

#### S.I. Kuchanov

Chair of Physics of Polymers & Crystals, Lomonosov Moscow State University, Vorobjevi Gory, 119992 Moscow, Russia, <u>kuchanov@polly.phys.msu.ru</u>

#### **Abstract**

A concise introduction to the statistical theory of polymers is presented in a popular manner. Special emphasis is made on specific peculiarities of quantitative description of polymer liquids.

#### Introduction

The physical chemistry of macromolecular compounds is a rapidly developing field of knowledge [1]. It is particularly remarkable that this branch of science is developing under the direct influence of technology which makes wide use of polymeric materials. Rubber, plastics, fibers such as cellulose, wool and silk, are high polymers. The very technological application of polymers is based principally on their special service properties. Essentially, polymeric substances differ from the majority of low-molecular weight substances of practical use in two key features.

Firstly, molecular weight of the former is normally several orders of magnitude higher than that of the latter. Macromolecules of linear polymers may be envisaged as a flexible string with threaded multicolored beads representing monomeric units of different types. Depending on whether number m of these types is equal to unity or  $m \ge 2$ , it is conventional to speak about homopolymer or heteropolymer, respectively.

Secondly, polymeric products synthesized in laboratories and in industry are a set of individual chemical compounds whose number is practically infinite. Macromolecules of such products can vary either in the set of numbers  $(l_1, ..., l_m)$  of monomeric units  $M_1, ..., M_m$  or in fashion of their mutual arrangement, i.e. configuration. For instance, the configuration of a linear heteropolymer macromolecule is defined by the sequence of types of its monomeric units. The number of different possible configurations of such a macromolecule equal to  $m^l$  exponentially grows with the increase of its chemical size  $l = l_1 + \cdots + l_m$ . Hence each particular specimen of a synthetic heteropolymer represents an ensemble of enormous number of macromolecules differing in chemical size, composition and configuration. Obviously, any quantitative description of such an ensemble is possible only on the basis of a statistical approach. Its elaboration is a subject matter of the statistical chemistry of polymers [2] whose major goal consists in establishing the dependence of statistical characteristics of the chemical structure of polymers on conditions of their synthesis.

Physicochemical and mechanical properties of a polymer specimen are essentially controlled by the above-mentioned structure characteristics. Revealing of this sort of dependencies for equilibrium macromolecular systems is the subject of the statistical physics of polymers [3],[4]. Among its major challenges is the finding of the free energy of polymer melts, solutions and blends predetermining their phase behavior. The solution of these problems rests on averaging over all possible configurations of macromolecules embedded in three dimensional space, that is over their conformations. The conformation of arbitrary polymer molecule is specified by a set of coordinates  $(\mathbf{r}_1,...,\mathbf{r}_m)$  of all l its units. Due to heat fluctuations a molecule drifts randomly in space changing simultaneously its conformation. Under thermodynamic equilibrium, the probability measure, over which conformational averaging is made, represents the Gibbs distribution. However in case of polymer systems, such an averaging differs fundamentally from that described in text-books on the statistical mechanics of low-molecular weight compounds. This distinction takes place because the probability distribution of different conformations of a macromolecule is controlled by its configuration. Therefore, when deriving the expression for the free energy of a polymer melt or solution one is supposed first to average over heat fluctuations in the ensemble of macromolecules with fixed configurations to average then the result obtained over the probabilities of these configurations.

A theoretical approach is mainly meant for predicting the dependence of the service properties of polymer products on the conditions of their synthesis. Such approaches, enabling to considerably reduce experimental research, play an ever increasing role in designing new industrial processes of polymer materials' manufacturing. The efficiency of this theoretical approach as applied to chemical engineering is predetermined to a great extend by an appropriate choice of the adequate kinetic model of a particular process, which is capable of taking into account its main physicochemical peculiarities on the basis of current concepts of polymer science. Only then the model chosen can be expected to provide right extrapolation and will allow thus a science-based application of the results of the laboratory research for the calculation of commercial processes of polymer production.

## Statistical chemistry of polymers

<u>Characterization of polymers</u>. A specimen of any synthetic polymer comprises so many different individual chemical compounds that evidently it makes no sense to speak about their concentrations since many of them are present in a single copy. That is why a description of a polymer specimen on the molecular level is normally performed in practice by virtue of some of its statistical characteristics defined as certain quantities found by averaging all over the set of macromolecules of the specimen under consideration.

There are two types of such characteristics. To the first of them there belong the distribution  $f(l_1,...,l_m)$  of polymer molecules in numbers  $\{l_\alpha\}$  of units of different types  $\alpha=1,...,m$ , as well as statistical momenta of such Size-

Composition Distribution (SCD). These characteristics are found experimentally by chromatographic techniques. Pertaining to the second type are the statistical characteristics carrying quantitative information on the fashion of arrangement of monomeric units, i.e., on the structure of macromolecules. Among such characteristics are fractions  $P(U_k)$  of k units long sequences  $U_k$ . Values of  $P(U_k)$  at k = 2,3,4 are often determined from the treatment of spectroscopic data obtained, for instance, by nuclear or proton magnetic resonance technique. Some important properties of heteropolymers are known to be governed by the sequence distribution  $P(U_k)$  in their macromolecules. In particular, some structure-additive physical characteristics of heteropolymers as well as their glass transition temperature are related by simple linear relationships with fractions of diads  $P(U_2)$ . An alternative way to describe the pattern of units' alternation in chains of linear heteropolymers implies introduction of the chemical correlators. The simplest among them, the two-point correlator  $Y_{\alpha\beta}(j)$ , is equal to the probability for a pair of randomly chosen units separated in a macromolecule by j arbitrary units to be of types  $\alpha$  and  $\beta$ . Analogously, *n*-point correlators  $Y_{\alpha_1 \cdots \alpha_n}(j_1, \dots, j_{n-1})$  are introduced having a sense of the probability that n units positioned at given distances  $j_1,\ldots,j_{n-1}$  one from another pertain to types  $\alpha_1,\ldots,\alpha_n$ . Generating functions of such correlators play a decisive role in the statistical thermodynamics of heteropolymer melts and solutions.

Kinetic models of macromolecular reactions. Polymer materials are generally obtained either by the synthesis of monomers or via chemical modification of macromolecules. Chain polymerization and step-growth polymerization belong to the first type processes, while polymeranalogous transformations, crosslinking and degradation belong to the second one. The processes of synthesis and transformation of polymer molecules proceed in consequence of chemical reactions of their active centers, such as functional groups, free valences in radicals, double bonds and so on. In many cases the reactivity of an active center in a polymer molecule may be taken to be independent of both its configuration and this center position in a molecule. This fundamental principle, bearing the name of Nobel prize winner Flory, permits considering as identical the rate constants of elementary reaction of any active centers of a particular type. In the framework of this approximation known as the "ideal model", the number of such elementary reactions in a typical polymer obtaining process is comparatively small and, thus, it can be characterized just by few kinetic parameters. The Flory principle makes it possible in a simple way to relate the rate constants of macromolecular reactions (whose number is virtually infinite) with corresponding rate constants of elementary reactions. Since in line with this principle all chemically identical active centers are kinetically indistinguishable, the rate constant of the reaction between any pair of molecules is proportional to the rate constant of elementary reaction between their active centers and the numbers of these centers in reacting molecules. Therefore, in the framework of the ideal kinetic model the rate constants of only elementary reactions enter as kinetic parameters in the material balance equations describing a reaction system.

The validity of the Flory principle is verified for a wide range of macromolecular reactions. It is a good approximation for the description of the kinetics of many processes of polymer obtaining. However, a considerable body of experimental data is available today, unambiguously testifying to the existence of polymerization systems in which this principle is certainly violated, and, consequently, the ideal model does not work. Possible reasons for the violation of the Flory principle may be due to either short-range or long-range effects.

To the first of them the so-called "substitution effects" should be attributed. They are caused by steric, induction, catalytic and some other types of the influence of reacted active centers on the reactivity of neighboring centers in a molecule. To take such short-range effects into account under a theoretical consideration the recourse has been suggested [5] to the extended Flory principle. According to this principle, the reactivity of any active center in a molecule is exclusively controlled by local chemical structure of neighboring fragments of this molecule. Essentially, the above-mentioned reactivity changes in the course of the process due to the change of this local structure induced by the entry in the reaction of neighboring active centers. In the framework of such models, one should to choose as kinetically independent elements the small fragments of molecules incorporating the active centers rather than the active centers themselves (like in case of the ideal model).

Specificity of polymer nature of the reagents is the most strongly pronounced in the long-range effects, where the reactivity of any active center in a macromolecule is acted upon by the fragments located in all its parts. Here intramolecular catalysis by functional groups should be mentioned. They, being spaced far apart from the active center in a macromolecule, fall nevertheless in vicinity of this center because of spatial conformation rearrangements of polymer chain. In the presence of such effects, the reactivity of its terminal active center can be controlled by the length of a macromolecule as well as by the distribution along this chain of units containing catalytic groups. For a rather fast reaction like recombination of macroradicals the dependence of its rate constant on their length is controlled by the diffusion factors.

Theoretical approaches. Under a theoretical consideration of polymer obtaining processes one faces with the problem of finding of SCD function. To have it solved the kinetic and statistical approaches are traditionally invoked. The first of them suggests the derivation and solution of the material balance equation for the concentration of molecules with fixed sets of numbers  $\{l_{\alpha}\}$  and  $\{a_i\}$  of different types of monomeric units and active centers, respectively. Summing this concentration over all sets  $\{a_i\}$  and dividing it by overall concentration of all molecules we will get the SCD function of macromolecules in a reaction system.

Under the statistical approach, each macromolecule is considered as a realization of particular stochastic process of conventional movement along heteropolymer chain. The probability of this realization equals, by definition, the fraction of corresponding macromolecules residing at the moment in the reaction system. The conventional movement along polymer chain may be considered as a succession of transitions from a monomeric unit to the next one. The type of unit at every step is determined therewith in accordance with the statistics of the stochastic process describing the heteropolymer specimen of interest. The most popular among the stochastic processes is the Markov chain, when the probability  $v_{\alpha\beta}$  to fall at any step in  $\beta$ -th type state depends only on type  $\alpha$  of the preceding state.

When the attempt to formulate the algorithm of finding the probability of any trajectory of the above-mentioned stochastic process meets with success, the task of exhaustive statistical description of a heteropolymer specimen may be considered as solved. For a specimen, in which the alternation of units is described by the Markov chain, this algorithm is trivial. It enables to find immediately any statistical characteristics of markovian heteropolymers in terms of elements  $v_{\alpha\beta}$  of the transition matrix. Specific peculiarities of particular processes of obtaining of such polymers are taken into account only for finding the dependence of these matrix elements on time of the synthesis as well as on stoichiometric and kinetic parameters of a reaction system.

Statistical and kinetic methods of calculation of the chemical structure of polymers both have advantages and shortcomings. Being introduced by Flory more than fifty years ago, the first of them found extensive application in quantitative description of the products formed in the course of many processes of synthesis and chemical modification of polymers [2], [5]. Principal merit of the statistical method is its ability to describe in rather simple manner the detailed structure of macromolecules in terms of just few probability parameters. However, the problem of the choice of a particular stochastic process for probabilistic description of polymeric products can not be solved in principle in the framework of the statistical approach. This task can be coped with only resorting to the kinetic approach, which also permits one to express the probability parameters of a stochastic process through the rate constants of elementary reactions and the reagents' concentrations.

## Statistical physics of polymers

<u>Dilute solutions.</u> Nowadays the most thoroughly theoretically studied among polymer systems are macromolecular solutions and melts. The simplest of such polymer liquids are dilute solutions of macromolecules, which being widely spaced almost do no interact one with another. That is why any of them can be considered as independent of other macromolecules.

The size of an individual macromolecule of given configuration is found by averaging its radius R over all conformations with allowance for their probabilities which are specified by the Gibbs distribution. For a linear homopolymer

chain the exponent  $\nu$  in asymptotic expression  $R_{a\nu} \sim l^{\nu}$  for the dependence of average radius of macromolecule  $R_{a\nu}$  on number l of it units can assume different values controlled by thermodynamic quality of the solvent. This is referred to as "good" or "poor" depending on with whom is more gainfully for monomeric units to contact, i.e. with the solvent molecules or one with another. As temperature decreases good solvent becomes poor one that happens at the so-called  $\theta$ -temperature. The theoretical analysis leads to values of exponent  $\nu$  equal to 3/5 and 1/3 for good and poor solvent, respectively. Therefore, the average density of units in a macromolecule decreases in limit  $l \to \infty$  as  $l^{-4/5}$  in good solvent and does not depend on the chain length l in poor one. In these two solutions, a macromolecule resides in conformational states of coil and globule, respectively. Transition from one of these states to another occurs at  $l \gg 1$  in narrow vicinity of the  $\theta$ -temperature whose width tends to zero at  $l \to \infty$ . For a flexible macromolecule such a change of its conformational state can be considered as the second order intramolecular phase transition.

The theory of homopolymer globules takes advantage of the possibility of the description of spatial position of a macromolecule in terms of a certain stochastic process. This is because the probability distribution of conformations of a linear macromolecule with l units residing in the globular state coincides with the probability distribution of l long trajectories of a particle walking randomly under the influence of external field  $\varphi(\mathbf{r})$  in the three-dimensional Euclidean space. Its role is played here by an effective field that at point  $\mathbf{r}$  acts upon the monomeric unit characterizing its interaction with other units and solvent molecules. At l>0 this field favors the swelling of a macromolecule in a good solvent, whereas at l>0 field l>0 being compressing in a poor solvent, tends to decrease the size of a polymer chain. In the framework of the self-consistent field approximation function l>0 depends on coordinate l>0 in an implicit way through function l>0 (l>0). This, in turn, is expressed through field l>0 (l>0). Hence the task of the quantitative description of a homopolymer globule is reduced to the solution of a set of equations for functions l>0 and l>0 a

When developing a theory of heteropolymer globules, macromolecules should be necessarily distinguished not only by their conformations but by configurations as well. In this case every polymer chain may be associated with the trajectory of random walk of a particle, which moving in space is also capable at every jump to change its "color"  $\alpha$  corresponding to the  $\alpha$ -th type unit. Statistics of alteration of units' types along a polymer chain completely predetermines the regularities of recoloring of a walking particle. The external field  $\varphi_{\alpha}(\mathbf{r})$  acting upon a particle is dependent on its color  $\alpha$ , so that in the self-consistent field approximation the globular state of a heteropolymer macromolecule with m types of units is

described by the solution of the set of 2m equations for densities  $\{\rho_{\alpha}(\mathbf{r})\}$  of  $\alpha$  - th type units and fields  $\{\varphi_{\alpha}(\mathbf{r})\}$ .

It is known that the rate of chemical reactions can be substantially increased by localization of reagents in minute volume microreactors. The role of them can be performed by polymer globules [6]. If the thermodynamic affinity of low-molecular weight reagents to polymer essentially exceeds that to solvent, their concentrations inside a globule will be considerably higher than those outside. Using globular solutions when conducting catalytic processes is especially efficient, provided macromolecules contain catalytic centers.

Concentrated solutions and melts of polymers. The phase behavior of such ensembles of macromolecules shows a number of qualitative peculiarities absent in low-molecular weight liquids. One of the most important among them is the formation of thermodynamically stable mesophases in which densities  $\{\rho_{\alpha}(\mathbf{r})\}$  of different type units change periodically in space with the period falling in nanoscale range. The spatial symmetry controlling the morphology of each of such mesophases corresponds to some type of crystal lattice. The most often encountered are lamellar, hexagonal and body-centered cubic mesophases.

Among fundamental problems arising in the statistical physics of polymers is revealing the dependence of the morphology of the mesophases formed and their period on temperature and chemical structure of macromolecules. The solution of this problem apart from crucial theoretical importance has as well a considerable applied value since many service properties of new heteropolymer-based polymeric materials are essentially controlled by the morphology of mesophases.

One of the main approaches commonly used for this purpose is the Weak Segregation Limit (WSL) theory [4], [7]. It rests on the ideas of the Landau theory of phase transitions extensively employed in theoretical physics of condensed matter under the description of magnetics, crystals and liquids. According to this theory, the nonequilibrium free energy F is written down as several first terms of the functional series in powers of order parameters  $\{\psi_{\alpha}(\mathbf{r})\}$  whose equilibrium values are found by minimization of functional F. The coefficients of such an expansion, referred to as the vertex functions, depend on the chemical structure of macromolecules of the specimen under consideration. The problem of finding this dependence from microscopic consideration constitutes the main challenge of the WSL theory of heteropolymer liquids.

Along with polydispersity there is another specific feature inherent to such liquids owing to which the Landau theory of phase transitions in polymer systems differs qualitatively from that traditionally employed in condensed matter physics. So, in the traditional Landau theory of low-molecular weight liquids the order parameter  $\psi_{\alpha}(\mathbf{r})$  is proportional to the deviation of local density  $\rho_{\alpha}(\mathbf{r})$  of  $\alpha$ -th type particles at point  $\mathbf{r}$  from its average value. When this theory is invoked to describe polymers, the role of particles is played by units. However, unlike parti-

cles, they are not true thermodynamic components because monomeric units are linked in a polymer chain by stable chemical bonds whose presence imposes some restrictions on mutual spatial arrangement of units.

In order to describe periodic mesophases it is more convenient to deal with the expression for functional F which is written down in momentum representation. This expression comprises the Fourier transforms  $\tilde{\psi}_{\alpha}(\mathbf{q})$  and

$$\tilde{\Gamma}_{\alpha_{1}\cdots\alpha_{n}}^{(n)}\left(\mathbf{q}_{1},\ldots,\mathbf{q}_{n}\right) \text{ of the order parameters } \psi_{\alpha}\left(\mathbf{r}\right) \text{ and } \Gamma_{\alpha_{1}\cdots\alpha_{n}}^{(n)}\left(\mathbf{r}_{1},\ldots,\mathbf{r}_{n}\right) \text{ descending the order parameters } \psi_{\alpha}\left(\mathbf{r}\right)$$

pending on wave vectors  $\mathbf{q}_1, \dots, \mathbf{q}_n$ . Coefficients  $\tilde{\Gamma}^{(n)}$  of the expansion of the Landau free energy F of polydisperse polymers exhibit at  $n \ge 4$  a remarkable peculiarity resulting from averaging over macromolecules' configurations. This peculiarity consists in the appearance in this expansion of the so-called "non-local" vertex functions. These, as distinct from the local ones, tend to infinity when momenta approach zero. The presence of such non-local contributions into the free energy is responsible for qualitative peculiarities in phase behavior of polydisperse polymer liquids that are absent in monodisperse specimens.

To have analytical expressions for the vertex functions it is convenient to resort to the diagram technique [4], [7] which allows the derivation of these general expressions in terms of the generating functions of the chemical correlators. The solution of this problem involves two stages. At the first of them the dependence of the vertex functions is found on the correlation functions of fluctuations of monomeric units' densities at different points. The connection of these physical correlators with chemical ones is established at the second stage.

The essentials of the statistical theory of synthetic polymers have been formulated. In my oral presentation I intend to provide examples illustrating the potentialities of this theory for the solution of some applied problems.

#### References

- S.Kuchanov, A.Khokhlov "Lectures on Physical Chemistry of Polymers", "MIR" Publ., Moscow, 2000.
- [2] S.Kuchanov, Adv.Polym.Sci., 2000, 152, 157-201.
- [3] A.Grosberg, A.Khokhlov "Statistical Physics of Macromolecules", Amer.Inst.Phys., New-York, 1994.
- [4] S.Kuchanov, S.Panyukov "Statistical Thermodynamics of Copolymers and Their Blends" in "Comprehensive Polymer Science", Second Suppl., Ed.G.Allen, Pergamon, 1996, ch.13, 441-496.
- [5] S.Kuchanov "Methods of Kinetic Calculations in Polymer Chemistry", "KHIMIA" Publ., Moscow, 1978.
- [6] S.Kuchanov et al., Macromolecules, 2008, 41, 2689-2693.
- [7] S.Kuchanov, Macromol.Symp., 2007, 252, 76-89.

# REVIEW OF PHOTOTHERMAL AND PHOTOACOUSTIC METHODS; APPLICATION TO SPECTROSCOPY

#### B. Cretin

FEMTO-ST Institute, department MN2S Université de Franche-Comté, CNRS, ENSMM, UTBM 32, avenue de l'observatoire, 25044 Besançon cedex France bcretin@femto-st.fr

#### **Abstract**

Reliable information on the thermophysical and thermochemical properties of materials is indispensable for engineers and scientists. Especially during the last decades, the need for data and the tentative detection of traces (even in environment applications and life science, e.g.) of specific components has been improved. This paper reviews different methods which have been developed in order to measure concentration, up to trace level of specific atoms, to monitor chemical reactions, ...

#### Introduction

Photothermal and photoacoustic methods have been first developed in the seventies and the early eighties [1-4]. They have been first used to image the thermal and thermoelastic properties of the materials and have enabled the detection of surface and subsurface defects [5-8]. But, at the same time, quantitative applications to physics and chemistry have been investigated. A new family of tools has been imagined, then built and tested [9, 10]. We review these methods, some of them being now quite unknown despite their potential advantages. Nevertheless, the techniques have progressed, principally in the field of optical sources and electronic circuits. A new glance at these techniques could be a way for developing very sensitive measurements.

The main advantage of photothermal techniques is the optical probing which is a powerful tool for non contact investigation of solids, liquids and gas, the main limitation being the transparency of the medium to analyse. In this paper we review the main physical principles and the applications of the photothermal and photoacoustic methods.

## Physical basis

Photothermal and photoacoustic methods are based on the absorption of an optical beam. The investigated material is heated with a modulated laser beam (the modulation is needed to obtained the highest signal to noise ratio because signal processing is easy at a given detection frequency). The different indirect detection methods are reminded in Fig. 1 for an opaque sample. The excitation beam heats the surface due to the absorption (a spectroscopic approach is possible by using selected wavelengths). A so-called "thermal wave" goes through the solid and interacts with it. By using one dimensional model, the investigation depth is expressed as

 $\mu_T = \sqrt{\frac{2a_T}{\omega}}$ , where  $\omega$  is the angular frequency and  $a_T$  the diffusivity. For instance, at 1 kHz excitation frequency and with the thermal constants of Al, the diffusion

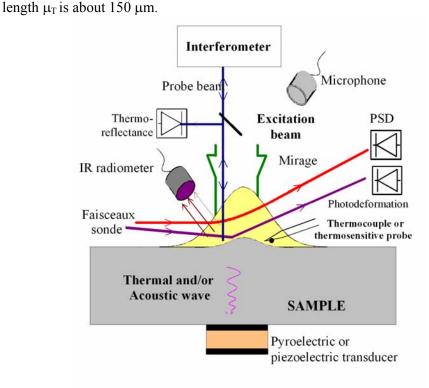


Fig. 1. Different methods for indirect detection of photothermal properties of solids

The thermal field is always indirectly detected. Different kinds of thermal sensors can be used in reflection mode (microthermocouple close to the excitation area, IR radiometer, e.g.) or in transmission mode (pyroelectric sensor). Some indirect measurements are uncommon: mirage effect, photoreflectance (measure of the variation of the reflectance depending on the temperature), thermo-deformation (effect of the surface gradient related to local thermal expansion). Another way to sense the temperature is to detect the thermal expansion effect (deformation of solids, pressure increase in gases, e.g.). Photoacoustic methods result from thermal to acoustic energy conversion. A simple microphone may detect the acoustic sound in the surrounding air and, on the other hand, an interferometer may measure the out-of-plane component of the surface motion related to dynamic thermal expansion (the excitation beam is modulated).

More generally, in photothermal experiments, the light of a laser beam is absorbed by the investigated medium. The temperature variation, or the physical effects resulting from photothermal excitation, give information about the required species.

### **Experimental techniques**

Basically, the excitation source is a laser (dye laser for spectroscopy or monochromatic one for the investigation at single wavelength). This source is usually modulated (direct modulation or use of modulation components: electro-optic or acousto-optic cell). The detection, as shown above, will depend on the applications. In this paper, we limit the presentation to some specific applications.

The spectroscopic approach for gas uses a modulated laser. The laser beam passes through a cell which contains the gas to be analyzed. Depending on the concentration of absorbing molecules, the generated heat is detected using the previously presented processes and the system is calibrated. Usually, this family of techniques is very sensitive and results are reproducible.

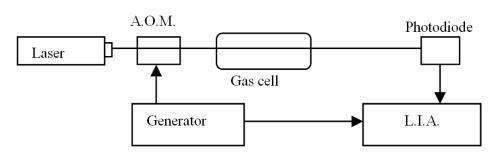


Fig. 2. Basic experiment of photothermal spectroscopy

A basic setup used to detect traces of specific traces in gas is shown in figure 2. The wavelength of the laser has to be chosen in the absorption bandwidth of the traces to detect. A low frequency generator drives, externally in this case, an acousto-optic modulator (A.O.M.) which enables to switch the beam at the output of the laser. The cell containing the gas is heated due to the presence of absorbing molecules. Basically, the photocurrent of the photodiode depends on the absorbed part of the light power following the Beer-Lambert relationship:

$$A_{t} = \log \left( \frac{I_{0}}{I} \right) = mlC_{0}$$

where  $A_t$  is the absorbance,  $I_0$  and I are the incident and transmitted light intensity respectively, m is the molar absorptivity, l the length of the gas cell, and  $C_0$  the concentration of the absorbing species.

A double phase lock-in amplifier (L.I.A.) gives the magnitude of the periodical signal detected by the photodiode. A second laser beam is often used to increase the detection capability and some original setups have been developed in order to optimize the detection. One of them is the photothermal lens spectroscopy which is an ultra-sensitive method using the thermal gradient inside the cell. It is applicable to trace analysis and studies involving photo-initiated reaction chemistries [11]. The cell is cylindrical and it is illuminated by the image of an excitation source (optical image obtained by focusing). The sample cell is illuminated with spatially

constant irradiance. Thermal diffusion results in the spatial anisotropic temperature change. This, in turn, produces the thermal lens element. In order to overpass classical problems associated with photothermal lens spectrometry, an apparatus using a two-laser photothermal lens apparatus can be built. Time-dependent photothermal signals are detected and enable to accurately measure the concentration of specific species. Focusing of the beam is an interesting effect, but simple deflection is also very sensitive. It is based on the same physics: photothermal deflection spectroscopy (PDS) is the measurement of the light absorptions by optical detection of the refractive index gradient resulting from temperature variations in or near the sample. The observed phenomenon is the "mirage effect" which was first reported by Boccara et al [12]. Uezima et al have demonstrated the high sensitivity of PDS to detect low concentration of Fe<sup>2+</sup> ions in a solution [13]. They have obtained a linear dependence showing the easy calibration of the technique.

The presented technique is closely related to photoacoustic spectroscopy (PAS) which also monitors the photothermal process and detects the expansion due to the generation of heat in the light absorbing material. Also called "Optoacoustic", an application of this method is given in [14] for the detection of organic molecules (Tinuvin-P and Rhodamine 6G) for laser applications. The basic configuration uses a photoacoustic cell with a microphone as a detector. The fluid sample resonates in the photoacoustic cell giving a strong signal for CW excitation at the resonant frequency. Pulsed excitation yields to a band limited strong signal which is superposed on the tail of the impulse response curve. Experimentally, this bandpass effect (second order) limits the measurement of the spectra at modulation frequencies higher than the resonant frequency. PAS has been widely used to investigate powder, gas traces and molecular dynamics [15-18]. Other more complex techniques have also been developed: photothermal-deflection spectrometry [19], e.g. Recent studies show that more investigation should be done in order to completely understand the experimental setups [20].

In order to complete this review, we should mention cross-techniques which enable to simultaneously give different properties of the same sample. An example is the SThEM (Scanning Thermo-Elastic Microscope) [7] which is a kind of multiacquisition microscope based on photothermoelastics. Its principle is given in figure 3. It uses an intensity modulated power laser (Ar+ or doubled NdYAG, but a tunable laser can also be used) as excitation source. The beam of a second laser at a different wavelength is split so that both optical, thermal (using photoreflectance) and thermoelastic images of the same area are simultaneously recorded. The two beams are focused with a microscope objective that enables a spatial resolution better than 1 micron. This microscope gives information on the physical properties of the surface and close subsurface (penetration depth up to about 20 µm). A set of 5 images are obtained simultaneously: optical image and amplitudes and phases of both thermal and thermoelastic signals. Two lock-in amplifiers are used to extract the required information for each point. The scanning is performed with two-axis translation stages with a total range above 5 mm and 0.1 µm resolution. Tested application concern physics and technology: thermal and thermoelastic properties of materials and non destructive testing: detection of defects (delamination of deposited layers, structure analysis, ...) and more generally subsurface observation and analysis. The main advantage of this technique is the absence of interference because thermal waves are evanescent and interferometric effect is very weak.

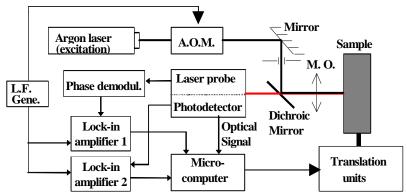


**Fig. 3.** Setup of the combined optical, photothermal and thermoelastic scanning microscope

### Conclusion

We have shown the interest of photothermal and photoacoustic techniques to investigate, analyze and accurately quantize traces and specific species, in either gas, liquid and solids. The presented techniques are, for some of them, industrialized. They can be applied in various fields related to high-technology industry (research and development) and academic laboratories. Innovative techniques have been developed to meet the new demands. The main advantage of photothermal and photoacoustic techniques is the non invasive way of the methods based on light probing (optical excitation and optical detection). In order to analyze traces, very sensitive techniques have been developed and tunable lasers are often used to enable a complete spectroscopy. Many kinds of sensors have been imagined and tested because the temperature can not be directly detected. The less invasive ways to sense the local temperature are based on beam deflection or thermal lens. The detection of the photoacoustic generated sound is also not invasive and without direct contact. The only potential limitation of the photoacoustic technique is the bandwidth which depends on the sensor itself. Finally, we have shown a multiphysic method which enables to simultaneously give optical, thermal and thermoelastic (or thermoacoustic) information. New developments can be expected in these fields because the cost of high tech optical sources and sensors is decreasing and the systems are more compact. Particularly, biomedical applications seem very promising.

### References

[1] A. Rosencwaig and A. Gersho, J. Appl. Phys., 1976, 47(1), 64-69.

- [2] W.B. Jackson, N.M. Amer, A.C. Boccara, and D. Fournier, Appl. Optics, 1981, 20(8), 1333-1344.
- [3] T. Baumann, F. Dacol, and R.L. Melcher, Appl. Phys. Lett., 1983, 43(1), 71-73.
- [4] R. Santos and L.C. Miranda, J. Appl. Phys. **52** (6), 4194-4198 (1981)
- [5] F. Lepoutre, D. Fournier and C. Boccara, J. Appl. Phys., 1985, **57**(4), 1009-1015.
- [6] B. Cretin and D. Hauden in Acoustical Imaging 14, Plenum Press, 1984, 653-655.
- [7] B. Cretin, J. Takadoum, A. Mahmoud, and D. Hauden, Thin Solid Films, 1992, 209, 127-131.
- [8] F. Lepoutre, P. Forget, F.C. Chen, and D. Balageas, La Recherche Aérospatiale, 1994, 1, 39-52.
- [9] A. Rosencwaig, Photoacoustics and Photoacoustic Spectroscopy, New York: Wiley, 1980
- [10] S.E. Bialkowski, Photothermal Spectroscopy Methods for Chemical Analysis, New York: Wiley, 1996.
- [11] A. Chartier and S. Bialkowski, Optical Engineering, 1997, 36, 303-311.
- [12] A. C. Boccara, D. Fournier, and J. Badoz, Appl. Phys. Lett., 1980, 36, 130-132.
- [13] A. Uejima, M. Habiro, F. Itoga, Y. Sugitani and K. Kato, Analytical Sciences, 1986, 2, 389-390.
- [14] S. Nonel, C. Martí, I. García-Moreno, A. Costela, and R. Sastre, Appl. Phys. B, 2001, 72, 355–360.
- [15] A. C. Tam and C. K. N. Patel, Appl. Phys. Lett., 1979, 35, 843–845.
- [16] I.G. Calasso, "Photoacoustic and Photothermal Laser Spectroscopy Applied to Trace Gas Detection and Molecular Dynamics", Series in Quantum Electronics, 11, Hartung-Gorre, Konstanz, 1999.
- [17] D. Costopoulos, A. Miklós, P. Hess, Appl. Phys. B, 2002, 75, 385-389.
- [18] R. Röhl and R.A. Palmer, "Photoacoustic Determination of Light Absorption by Aerosols", in Light Absorption by Aerosol Particles, H.E. Gerber and E.E. Hindman Ed., Spectrum Press, Hampton, Virginia, 1982.
- [19] J. Zhou, J. Zhao, J. Shen, and M. L. Baesso, J. Opt. Soc. Am. B, 2005, 22(11), 2409-2416.
- [20] D. K. Kobylińska, R. J. Bukowski, J. Bodzenia, S. Kochowski, and A. Kaźmierczak-Balata, Appl. Optics, 2008, 47(10), 1559-1566.

# General Physical Chemistry (A)

### DEPENDENCE OF ENTHALPY OF FORMATION OF ACYCLIC SATURATED KETONES ON MOLECULAR STRUCTURE

S. Marković, A. Despotović, D. Jovanović and I. Đurović Faculty of Science, University of Kragujevac, 34000 Kragujevac, Serbia

### **Abstract**

The dependences of enthalpy of formation ( $\Delta H_f$ ) of saturated acyclic ketones on the size of molecule, position of carbonyl group, and branching of molecule are examined. The major part of  $\Delta H_f$  is determined with the size and branching of molecule, whereas fine structure of  $\Delta H_f$  is determined with the position of carbonyl group.

### Introduction

Like many other properties, enthalpy of formation ( $\Delta H_f$ ) is dependent on molecular structure. To examine the dependence of  $\Delta H_f$  of ketones on molecular structure it is necessary to calculate the values for those ketones for which the experimental enthalpies are not available. The goal of this work is to investigate the dependence of the enthalpy of formation of ketones on molecular structure (i.e. the size of molecule, position of carbonyl group, and branching of molecule) using the Parametric Method 5 (PM5). In this method a new parameter set, called PM5, has been added [1]. Parameters are available for all non-radioactive main-group elements, Zn, Cd, and Hg. It is supposed that the average accuracy for enthalpies of formation over all parameterized elements is improved by approximately a factor of four, compared to the AM1 and PM3 parameterizations [1].

### **Results and Discussion**

Spartan'02 [2] is used to construct a series of low-energy conformers for each ketone molecule under investigation. The so obtained structures are used as input geometries for the program package CAChe 6.01 [3], which enables calculation of the enthalpies of formation employing PM5 Hamiltonian. Thus, a new series, consisting of the PM5 enthalpy values, is formed for each ketone. The enthalpies of formation for all investigated ketones are computed using Eqs (1) and (2) [4], at both PM3 and PM5 levels of theory.

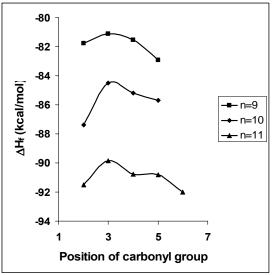
$$\Delta H_f = \sum_i N_i \left( \Delta H_f \right)_i \tag{1}$$

$$N_i + \sum_{j \neq i} \frac{N_i}{e^{\frac{\left(\Delta H_f\right)_j - \left(\Delta H_f\right)_i}{RT}}} = 1$$
 (2)

In Eqs (1) and (2)  $(\Delta H_f)_i$  and  $N_i$  represent the enthalpy of formation and mole fraction of the  $i^{th}$  conformer.

Following the above described procedure, the  $\Delta H_f$  values for 30 saturated acyclic ketones are calculated employing PM3 and PM5 Hamiltonians. This set embraces all ketones for which the experimental gas phase values for  $\Delta H_f$  are available in literature [5,6]. The average relative errors for the PM3 and PM5 approximations are equal to 3.5 and 2.5%, whereas the correlation coefficients amount to 0.96 and 0.990, respectively. PM5 reproduces enthalpies of formation of ketones better than PM3, but definitely not by a factor of four.

The dependences of  $\Delta H_f$  on the size of molecule  $\boldsymbol{n}$  (number of C atoms), position of carbonyl group, and branching of molecule are considered. For this purpose  $\Delta H_f$  values are calculated for all unbranched ketones up to  $\boldsymbol{n}$ =11. In agreement with the experimental results,  $\Delta H_f$  of ketones decreases with the increasing size of molecule by approximately 5 kcal/mol per methylene group. The dependence of  $\Delta H_f$  on  $\boldsymbol{n}$  is linear. The correlation coefficients for the homologous series of 2-, 3-, and 4-ketones are equal to -0.9993, -0.995, and -0.995, respectively.



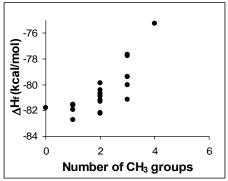


**Fig. 1.** Dependence of  $\Delta H_f$  of ketones on the position of carbonyl group (left) and number of  $CH_3$  groups (right).

The dependence of  $\Delta H_f$  on the position of carbonyl group is examined in the series of isomers where n=7-11. For example, when this dependence is investigated for n=8, then the  $\Delta H_f$  values of 2-, 3-, and 4-octanones are mutually compared. The influence of the position of carbonyl group is smaller than that of the size of molecule. For lower values of n (i.e.  $n \le 8$ ) the  $\Delta H_f$  values in a series of isomers differ by no more than 0.2 kcal/mol. For  $n \ge 9$  the differences among the  $\Delta H_f$  values of the members of isomeric ketones become more pronounced, but do not exceed 2 kcal/mol. Fig. 1 illustrates the influence of the position of carbonyl group upon  $\Delta H_f$  of higher isomeric ketones. In each examined series of isomeric

ketones the  $\Delta H_f$  value of 3-ketone is higher than that of 2-ketone. As the carbonyl group is further shifted towards the middle of a molecule, enthalpy of formation decreases. In case of decanones, where n is even number, 2-decanone exhibits the lowest  $\Delta H_f$  value. In case of nonanones and undecanones, where n is odd number, the lowest  $\Delta H_f$  values are associated with 5-nonanone and 6-undecanone, respectively, what can be a consequence of pronounced symmetry of these molecules.

To investigate the dependence of  $\Delta H_{\rm f}$  on the branching of molecule, all 2-ketones with n=9 (having 0-4 methyl substituents) are examined. The results of this investigation are presented in Fig. 1. The  $\Delta H_{\rm f}$  values of monosubstituted 2-oktanones are slightly lower than that of 2-nonanone. Enthalpy of formation further increases with increasing number of methyl substituents. The difference between the lowest (7-methyl-2-octanone) and highest (3,3,4,4-tetramethyl-2-pentanone)  $\Delta H_{\rm f}$  value exceeds 7 kcal/mol, implying that the influence of the branching of molecule is stronger than that of the size of molecule.

### Conclusion

Enthalpy of formation of acyclic saturated ketones decreases with the increasing size of molecule. This dependence is linear. The influence of the branching of molecule is even stronger than that of the size of molecule. Fine structure of  $\Delta H_f$  is determined with the position of carbonyl group.

### Acknowledgement

This work is supported by the Ministry of Science of the Republic of Serbia, project No 142025.

- [1] J.J.P. Stewart, MOPAC 2002, Fujitsu Limited, Tokyo, Japan (1999).
- [2] Spartan'02, Wavefunction, Inc., Irvine, CA.
- [3] CaChe 6.01, Fujitsu Limited, Tokyo, Japan.
- [4] W.J. Hehre, A.J. Shusterman and J.E. Nelson, The Molecular Modeling Workbook for Organic Chemistry, Wavefunction Inc., Irvine, 1998.
- [5] J.D. Cox and G. Pilcher, Thermochemistry of Organic and Organometallic Compounds, Academic Press, London, New York 1970.
- [6] J.D. Pedley, R.D. Naylor and S.P. Kirby, Thermochemical Data of Organic Compounds, 2nd ed. Chapman and Hall, London, 1986.

### APPLICATION OF ULTRA PERFORMANCE LIQUID CHROMATOGRAPHY (UPLC) FOR DETERMINATION OF Na<sup>+</sup>/K<sup>+</sup> ATPase ACTIVITY

J. Savić, K. Krinulović, T. Momić, M. Čolović and A. Vujačić Department of Physical Chemistry, Vinča Institute of Nuclear Sciences, P.O.Box 522, 11001 Belgrade, Serbia

### **Abstract**

An ion-pair ultra performance liquid chromatography (IP-UPLC) method was developed to obtain a sensitive and efficient means for quantification of ADP in order to follow the decrease of Na<sup>+</sup>/K<sup>+</sup> ATPase activity after its exposure to different inhibitors. The concentrations of ADP obtained after hydrolysis of ATP in the presence of enzyme depends on enzyme activity. Simultaneously with the chromatographic determination of ADP, the spectrophotometric determination of phosphates liberated after the hydrolysis of ATP was done.

### Introduction

Reversed-phase ion-pair chromatography (RP-IPC) is a popular separation technique [1]. The ultra performance liquid chromatography (UPLC) opens up new opportunities in liquid chromatography [2] because it offers the possibility of using bridged ethyl/siloxane silica (BEH) column packing with 1.7 µm particles, which increase the efficiency of chromatographic separation, reduce the time necessary for the analysis and also improve the resolution of chromatographic peaks.

Adenosinetriphosphatase (Na<sup>+</sup>/K<sup>+</sup>-ATPase) is an integral membrane protein found in most mammalian cells. It catalyze adenosinetriphosphate (ATP) hydrolysis and energy liberated in this process is used as the driving force for active electrogenic transport of monovalent cations (Na<sup>+</sup>,K<sup>+</sup>) through membrane [3]. The quantity of released inorganic orthophosphate (Pi) or adenosinetriphosphate (ADP) obtained during ATP hydrolysis corresponds to extent of enzyme activity.

The aim of this study was to develop IP-UPLC method for indirect determination of  $Na^+/K^+$ -ATPase activity based on the detection of ADP concentration liberated from the hydrolysis of ATP.

### **Experimental**

#### Instruments

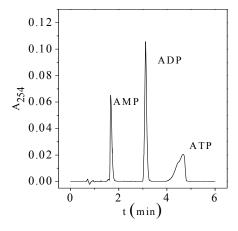
Waters ACQUITY Ultra Performance Liquid Chromatography (UPLC) system was used. Separations were performed on an ACQUITY UPLC BEH  $C_{18}$  100mm×2.1mm column (Waters), with 1.7 $\mu$ m particles, as a stationary phase. For spectrophotometric experiments Perkin Elmer Lambda 35 UV-Vis spectrophotometer was used.

### **Results and Disscusion**

Na<sup>+</sup>/K<sup>+</sup>-ATPase activity was determined in a standard incubation medium (200 μl), containing 50 mM Tris-HCl (pH 7.4), 100 mM NaCl, 20 mM KCl, 5 mM MgCl<sub>2</sub>, 2 mM ATP and 80-220 µg of protein. Incubation mixtures were preincubated for 15 min at 37 °C in the presence of inhibitor or distilled water (control). The reaction (in the presence or absence of inhibitor) was started by the addition of ATP, allowed to proceed for 15 min, and interrupted by the addition of 6M HCl and immediate cooling on ice. Afterwards, enzyme mixture was diluted to 2 ml and enzyme was excluded from working solution by centrifugation of samples at 13000×g for 10 min. After centrifugation an aliquot from the supernatant was taken and after dilution, solutions were divided into two portions. One portion was used for spectrophotometric determination of phosphates and the other was neutralized by adding of NaOH and used for UPLC experiments. The Pi liberated from the hydrolysis of ATP was measured using modified spectrophotometric procedure based on the stannous chloride method, by reading the absorbance at 690 nm [4]. The results are expressed as the mean percentage of enzyme activity relative to the corresponding control value, from at least three independent experiments performed in triplicate.

In order to develop the method for separation of adenine nucleotides, as initial condition, phosphate buffer with addition of ion-pairing reagent 4 mM tetrabutyl ammonium hydroxide (TBAH) in 4 mM phosphate buffer (phase A) and methanol (phase B) as organic modifier was used. The optimal chromatographic conditions for adenine nucleotide separation and quantification were determined and were as follows: the mobile phase was composed of solvents A and B in ratio A:B=75:25. Optimal flow rate was 0.25 mL/min. The autosampler was maintained at room temperature (20°C), and the column compartment at 40°C. Injection volume was 10  $\mu L$ . The chromatograms were obtained in single wavelength mode at 254 nm

A typical chromatogram with the separation of a mixed standard solution obtained by mixing of known adenine nucleotides concentrations (AMP, ADP and ATP), is shown on Fig. 1. The time necessary for recording of chromatogram was less than 6 min. The separation was clear and allowed easy identification of the peaks. For investigated adenine nucleotides, retention times were 1.66, 3.03 and 4.62 min for AMP, ADP and ATP, respectively. Afterwards, chromatograms of assayed Na<sup>+</sup>/K<sup>+</sup>-ATPase samples were recorded. Concentrations of ADP liberated by enzymatically catalyzed ATP hydrolysis were determined by comparing these chromatograms and standard curve. From these results enzyme activity was calculated. Comparison of enzyme activities obtained by UPLC and spectrophotometric method, showed very good agreement (Fig. 2).



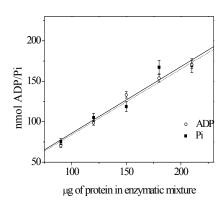


**Fig. 1.** Chromatogram obtained for the mixture adenine nucleotides by using of UPLC

**Fig. 2.** UPLC determination of amount of ADP and spectrophotometric determination of amount of P<sub>i</sub> both released from ATP by ATPase.

### **Conclusions**

IP-UPLC method for indirect determination of Na<sup>+</sup>/K<sup>+</sup>-ATPase activity based on the detection of ADP concentration liberated from the hydrolysis of ATP was developed. Results obtained by this method are in good accordance with spectrophotometric method for Na<sup>+</sup>/K<sup>+</sup>-ATPase activity detection, but more precise with lower experimental error, and simpler for experimentators.

### Acknowledgements

The authors gratefully acknowledge the financial support of the Ministry of Science of Republic Serbia (Project No. 142051).

- [1] Á. Bartha, J. Ståhlberg, Journal of Chromatography A, 1994, 668, 255-284.
- [2] D.T.-T. Nguyen, D. Guillarme, S. Rudaz, J.-L. Veuthey, J. Sep. Sci., 2006, 29, 1836-1848.
- [3] J.C.Skou, Methods Enzymol, 1988, **156**, 1-25.
- [4] V. Vasić, D. Jovanović, D. Krstić, G. Nikezić, A. Horvat, Lj. Vujisić, N. Nedeljković, Toxicology Letters, 1999, **110**, 95-104.

### APPLICATION OF HPLC TO DETERMINATION OF SELENIUM IN ROCKS AND SOILS

S. Khushvakhtova, V. Danilova and V. Ermakov

V. I. Vernadsky Institute of Geochemistry and Analytical Chemistry of the Russian Academy of Science, Moscow

### **Abstract**

The data by comparative determination of selenium in rocks and soils by means of a high effective liquid chromatography (HPLC) with spectrofluorimetric detection are presented. It is shown that spectrofluorimetric determination (SD) with HPLC is more comprehensible than SD alone.

### Introduction

Selenium is chalcophilous dispersed trace element included approximately in 40 microminerals. Taking into account, that the contents of the last in the basic rocks of an earth's crust is  $10^{-5}$  -  $10^{-6}$  per cent, special value has an increase in sensitivity and selectivity of the analysis by development of analytical methods of determination of selenium. It is connected not only to necessity of the analysis of trace amounts of this element, but also to the requirement of reduction of mass of investigated samples. Last circumstance is especially actual at the analysis of biogeochemical objects.

Now to determinate a ng quantities of selenium apply various physical and chemical methods. Most it is frequently used the spectrofluorimetric method with use 2.3-diaminonaphtalene (DAN) [1-3]. However, formation of complex of Se (IV) with DAN-piazselenol is accompanied by formation of some products of oxidation which have similar spectral characteristics that complicates quantitative determination of this trace element.

### Methods

With the purpose of more selective determination of selenium as a complex with DAN we used a method highly pressure (effective) liquid chromatography (HPLC). The chromatograph consisted from column "Diaspher"-110-C16 (150 x 4.0 mm, size of sorbent 5 microns), pumps "Knauer", the spectrofluorimetric detector RF-530 "Shimadzy" and injector with a loop in volume 20 mcl., liquid cell in volume 3 mcl. Excitation light was about a maximum at 376 nm, and a maximum of fluorescing light was at 570 nm. Eluent: a mix of ethanol and hexane 1:1 (on volume), a flow rate -0.5 ml/ min.

Tested objects were ore standards RUS-1, RUS-3, PS-1 and various types of soils. Samples decomposed by means of HNO<sub>3</sub>, HF and HClO<sub>4</sub> acids, and selenium (VI) was reduced up to Se (IV) by means of 6 M HCl. The objects with high contents of iron cleared on a column of catione exchange resin (hard acidic).

### **Results of Researches**

1. Structural formulas of basic derivatives of DAN are below, formed during reaction between selenite and DAN (fig. 1):

Fig. 1. Products of transformation of DAN.

2. It is achieved the clear resolution of a product of oxidation of DAN and a complex of selenium with DAN (fig. 2). Thus linear dependence between height (area) of peak of the basic Se-complex and intensity of its fluorescence (in mV) is observed.

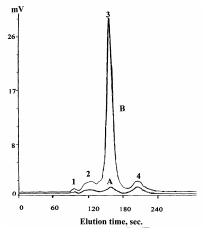


Fig. 2. The comprehensive chromatograms of HPLC-spectrofluorimetric method. 20 ng of piazselenol (B, peak 3) and control (blank) extract (A).

Peaks 1,2,4 – products of oxydation of DAN. The injected volume - 20 mcl.

A flow rate of eluent, (the mixture of hexane an ethanol 1:1 (on volume) -0.5 ml/min.

3. It is established the basic possibility of determination of selenium in the specified objects with application of HPLC (fig. 3). The method allows to estimate quantitatively the contents of pg amounts of selenium in natural materials after their decomposition by a mix of inorganic acids with the subsequent complex of Se

(IV) with 2,3-DAN and selective extraction of piazselenol. Detection of selenium in standard samples reaches about 100 per cent and differences in repeated determinations - within the limits of 3-6 per cent (table 1).

**Fig. 3.** The comprehensive chromatograms of HPLC-spectrofluorometric method. The first 2 peaks – a blank, standard - 2 ng of selenium (3,4), RUS-3 (10 mg)(5,6), RUS-1 (7,8), soils – chernozems of Transbaikalie (100 mg) (9-12). The injected volume of sample – 20 mcl. A flow rate – a mixture of hexane and ethanol, 1:1 – 0.5 ml/min.

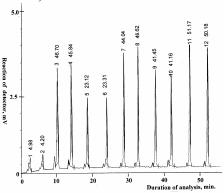


**Table 1.** Determination of selenium in ore samples and soils

			1		
Sample	Se, ng/20 mcl	Mass of sample, mg	Discovery of Se, ng/20 mcl	Se in standard, %	Se in sample, %
RUS-1	1.28	10	1.33±0.02 (n=5)	0.0032	0.0033
RUS-3	0.80	10	0.88±0.02 (n=5)	0.0020	0.0022
RUS-3	2.00	25	1.90±0.09 (n=5)	0.0020	0.0019
PS-1 Soil	2.40	10	2.58±0.18 (n=5)	0.0060	0.0064
15ч/2004-1 Soil	-	100	1.01±0.07 (n=3)	-	0.00025
3ч/2004-1	_	100	1.37±0.06 (n=3)	-	0.00034

- [1] P. Parker, L. Harvey. Luminescence of some Piazselenols// Analyst, 1962, 87, 558.
- [2] P. Whetter, D. Ullrey. Improved fluorometric method for determining selenium// J. Assoc. Off. Anal. Chem., 1978. 61, 927-930.
- [3] H. Yamada, T. Hattori, S. Matsuda, Y. Kang. Determination of selenium in soils by HPLC with fluorescence detection// Bunseki Kagaku (Jpn. Anal.), 1987, **36**, 542-546.

### MASS TRANSFER AND FLUID FLOW VISUALIZATION IN PAC-KED AND FLUIDIZED BEDS BY THE ADSORPTION METHOD

N. Bošković-Vragolović, R. Garić-Grulović, Ž. Grbavčić and R. Pjanović

<sup>1</sup>Faculty of Technology and Metallurgy, University of Belgrade, Belgrade, Serbia <sup>2</sup>Institute for Chemistry, Technology and Metallurgy, University of Belgrade, Belgrade, Serbia

### **Abstract**

Mass transfer coefficient between fluid and column wall in liquid packed and fluidized beds of spherical inert particle has been studied experimentally using adsorption method.

The adsorption method is based on the dynamic adsorption of an organic dye onto a surface covered with a thin layer of a porous adsorbent. This method is, also, suitable for fluid flow visualization

### Introduction

Research of transport phenomena in liquid – particles systems, in past years, had more theoretical then practical importance[1-3]. For industrial use, especially with fast development of bio and water cleaning processes, better knowing of these systems become more important. Industrial application of these systems requires determination of transfer characteristics, especially mass transfer.

### **Experimental**

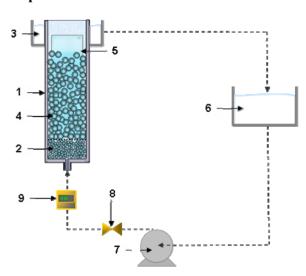


**Fig. 1.** Experimental system.

The experimental system was shown in Fig. 1. Experiments were conducted in column 40 mm in diameter (1), with liquid distributor (2) and water overflow (3). Very diluted solution of methylene blue ( $c_0$  =  $2.5 \cdot 10^{-3}$  g/dm<sup>3</sup>) was used as a fluid in the presence of inert glass particles 3.04 mm in diameter (4). The foils of silica gel (5) was used as adsorbent. ("Merck", DC-Alufolien Kieselgel). Concentration profiles of methylene blue were measured in the flow of water through packed and fluidized beds. Colour intensity of the

surface was determinated by "Sigma Scan Pro 5" software. The fluid flow was changed with valve (8) and measured by flowmetar (9).

### **Results and Discussion**

Average color intensity of silica gel surface varies with fluid flows. Higher color intensity means higher mass transfer coefficient as can be seen on Fig. 2. With increasing liquid velocity in packed beds mass transfer coefficient increases while in fluidized beds mass transfer coefficient decrease. The highest mass transfer coefficient was at minimum fluidization velocity because of high concentration of moving particles.

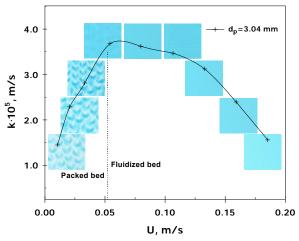
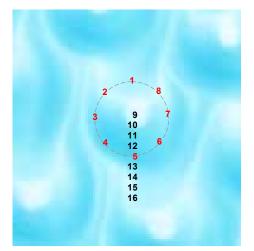


Fig. 2. Relationship between mass transfer coefficient and superficial liquid velocity

Adsorption method is also very useful for determination of local mass transfer coefficient and fluid flow visualization as can be seen on Fig. 3. Values of local mass transfer coefficients at a different points are shown in table on Fig. 3.



	$ \mathbf{k} \cdot 10^{\circ},  \mathrm{m/s} $
1	5,57
1 2 3 4 5 6 7 8	3,85
3	7,82 20.2 24.2 18.7
4	20.2
5	24.2
6	18.7
7	10
8	2.02
9	0.825
10	15.2
11 12 13	19.9 22.5 19.7
12	22.5
13	19.7
14	17.6
15	14.4
16	12.6
	1

Fig. 3. Fluid flow visualization around spherical particle in packed bed

Figure 4. presents the mass transfer factor as a function of Reynolds number in packed and fluidized beds for different experimental techniques. It could be

seen that there is no significant difference between mass transfer factors obtained by this two methods. [4, 5] Often used dissolution method is very reliable, and agreement of data shows that the adsorption method gives good results also. Adventage of this method is possibility to obtain local mass transfer coefficients.

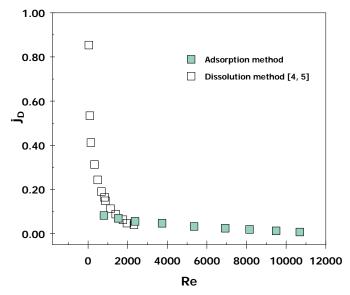


Fig. 4. The relationship between mass transfer factor and Reynolds number.

### Conclusion

The wall-to-liquid mass transfer in packed and fluidized beds, with the adsorption method of methylene blue was investigated. These method is suitable for fluid flow visualization.

The wall-to-liquid mass transfer factor in packed beds is higher then in fluidized beds for Reynolds number of column.

Result of adsorption method gives permanent picture of fluid flow and local and average mass transfer coefficients in packed and fluidized beds.

- [1] P.N. Dwivedi, S.N. Upadhyay, Ind. Eng. Chem. Proc. Des. Dev., 1977, 16, 157.
- [2] T. Chun, J.P. Couderc, Chem. Eng. Sci., 1980, 35 (8), 1707-1715.
- [3] J.P. Coudrec, Fluidization, 2nd Edition, Editors Academic Press, London, 1985, 1-46,..
- [4] N. Bošković-Vragolović, D. Brzić, Ž. Grbavčić, J. Serb. Chem. Soc., 2005, 70 (11), 1373-1379.
- [5] N. Bošković, R. Garić-Grulović, Ž. Grbavčić, J. Serb. Chem. Soc., 2007, 72 (11) 1103-1113.

### EXTRACTION OF GALLIUM USING DIFFERENT POLYMERIC FIBRE

A. Marinković, D. Tošković, M.B. Rajković and D. Stanojević

<sup>1</sup>Faculty of Technology and Metallurgy, University of Belgrade, Belgrade, Serbia <sup>2</sup>Faculty of Technology, Zvornik, University of East Saraevo, Bosna & Herzegovina <sup>3</sup>Faculty of Agriculture, University of Belgrade, Zemun, Serbia

### **Abstract**

In this paper the results of work on the synthesis of modified PAN fibres are given, and a certain number of experiments were done to establish the necessary molal surplus of reagent in relation to fibres, as well as the time and temperature in which the modification was done. Such received PAN fibres were used for adsorption and extraction of gallium from decomposed Bayer's alkaline. PAN fibres show the capacity from 16-28% adsorption of gallium in one pass which corresponds to the capacity of exchange 1.4-2.5 mg Ga/g of fibres.

### Introduction

Modification of poly acryl fibres was also done according to the literature practices (which were modified in accordance with co-polymers that could be found on the market) [1-4]. The conditions of syntheses were changed (temperature, time of reaction, module of the bath etc.) such as adequate amines that, according to literature, can react with selected poly acryl nitrile co-polymers and produce chelate fibres that adsorbed gallium from Bayer's solution.

### **Experimental**

Two fibres with following characteristics were used:

PAN-1 co-polymer acrylnitrile (92%), itaconic acid (5%) and methyl-acrylate (3%) PAN-2 co-polymer acrylnitrile and methyl-acrylate of unknown ratio.

The mechanism of polyacrylnitrile co-polymers modification is shown in the following scheme. In reaction with hydroxyl amine, derivates of amidoxim (A) and carbohydroxim (B) acids were received:

COOH 
$$\frac{\text{NH}_2\text{OH}}{\text{N}}$$
  $\frac{\text{NH}_2\text{OH}}{\text{N}}$   $\frac{\text{N}}{\text{N}}$   $\frac{\text{N}}$ 

where, due to reaction medium of water, hydrolysis of amidoxim derivates of acids could arise according to the following reaction:

Transformation of poly acrylnitrile co-polymers with hydrazine occurs according to the following chemism and hydrazone derivates of acids are obtained:

COOH 
$$H_2NNH_2$$
 $H_2NNH_2$ 
 $H_2NHN$ 
 $H$ 

where is also possible to obtain hydrolysis of originated derivates according to equitation:

The chemism of reactions which arise is highly complicated and all acids derivates that arise are not stable so, due to the successive treatments with solutions during the process, there comes to transformations that lower the capacity of change. The number of cycles during which the defined synthesised chelate resin – PAN fibre could give the satisfactory capacity of change represent the part of future researches.

During the experimental work on the synthesis of modified PAN fibres a certain number of experiments was done in order to make the necessary molal surplus of reagent in relation to fibres, as well as time and temperature in which the modification was done. In those experiments three types of ion changeable PAN modified fibres were chosen and those are:

- **B1** modified fibre received by the reaction of PAN-1 fibre with hydroxyl amine on 90-95°C during 90 min;
- **B2** modified fibre received by the reaction of PAN-1 fibre with mixture hydroxylamine/hydrazine (1:1) during 90 min;
- **B3** modified fibre received by the reaction of PAN-2 fibre with mixture hydroxylamine/hydrazine (1:1) during 90 min;

The addition of work represents the modification of different poly acryl nitrile copolymers with different ratio of functional groups (nitrile, carboxylic, halogenide etc.) under different conditions (pre treatment with attenuate alkali and treatment with different basis (ammonia, hydroxyl amine, hydrazine, diethylentriamine or any other combination).

### **Results and Discussion**

According to so far results of gallium extraction from Bayer's solution, the results are received showing that present chelate resin does the extraction of gallium from alkali aluminates solutions [5].

Modified resin based on LEWATIT TP 207 has better kinetic characteristics while modified PAN fibres have larger capacity of change. Analytic method "VAMI" Sankt Peterburg which has been used for determination of gallium oxide in bauxite and red sludge was also used for quantitative determination of gallium in solution after its extraction by acids from chelate resin.

Synthesized resin on the LEWATIT TP 207 basis showed the capacity from 12-21% adsorption of gallium in one pass or what correspond to the capacity of change 1.1-1.9 mg Ga/g of resin. More significant capacity of change shows the resins which are modified PAN fibres and moves in ratio 16-28% of extracted gallium in one pass or 1.4-2.5 mg Ga/g of fibres (Table 1).

**Table 1.** The results of the analysis of acid water solution after the extraction of Ga

PAN	Extraction of Ga (in %)	Capacity of exchange (mg Ga/g PAN)
<b>B</b> 1	22	2,0
<b>B2</b>	28	2,5
В3	16	1,4

### Conclusion

In this paper the results of work on modified PAN fibres synthesis are given, a certain number of experiments were done in order to establish the necessary molal surplus of reagent in relation to fibres, such as time and temperature in which modification was done. Synthesized modified PAN fibres were used for adsorption and extraction of gallium from decomposed Bayer's alkaline.

According to the results of gallium extraction from Bayer's solution, the received results show that modified PAN fibres do the extraction of gallium from alkali aluminates solutions.

Modified PAN fibres show the capacity from 16-28 % adsorption of gallium in one pass that correspond to capacity of change of 1.4-2.5 mg Ga/g fibres.

- [1] Y.Kato, M.Matsuda, US 4999171, Sumitomo Chemical Co., 1991.
- [2] L.A.Volf, "Volokna s osoimi svojstvami", Himiya, Moskva, 1980.
- [3] M.Matsuda, K.Ochi, K.Yamada, M.Yoshihara, H.Kato, EP 206081, Sumitomo Chemical Co., 1986.
- [4] O.V.Dubov, P.S.Vlasov, A.V.Pimenov, S.D.L'vovich, RU 2262557 (2005) Akvafor.
- [5] D.V. Tošković, D.D. Stanojević, M.B. Rajković, A. Marinković, Lj. C. Vasiljević, Č.M. Lačnjevac, Zaštita materijala, 2007, 48(3), 59-63.

### THE PREDICTION OF MINERAL SOLUBILITIES IN THE SYSTEM NaCl+MgCl<sub>2</sub>+H<sub>2</sub>O AT T = 298.15 K

J. Miladinović, M. Todorović and R. Ninković

Faculty of Technology and Metallurgy, University of Belgrade, Karnegijeva 4, 11000 Belgrade, Serbia

### **Abstract**

Mineral solubilities in ternary electrolyte solution NaCl+MgCl<sub>2</sub>+H<sub>2</sub>O at T = 298.15 K are calculated using available thermodynamic data for solids and for aqueous electrolyte solutions. Activity and osmotic coefficients are derived from the extended ion-interaction model of Pitzer and co-workers, the parameters of which are evaluated from experimentally determined solution properties in binary and ternary mixtures. The parameters of NaCl(aq) valid up to  $m \le 11 \text{ mol} \cdot \text{kg}^{-1}$  were obtained by treatment of osmotic coefficients in unsaturated region and estimated values in supersaturated solution. The calculated solubilities of halite NaCl(c) and bischofite MgCl<sub>2</sub>·6H<sub>2</sub>O(c) are shown to be in agreement with experimental data indicating that the model can be successfully used to predict mineral-solution equilibria at temperature 298.15 K.

### Introduction

Equilibrium considerations based on experimental data and thermodynamic calculations provide an important basis for understanding rock-fluid interactions in natural systems. The problems associated with experimental work, particularly in complex and concentrated electrolyte mixtures, underscore the need for a predictive model for calculating mineral-solution equilibria in brine systems. The objective of this study was to investigate the applicability of the extended ion-interaction model originally developed by Pitzer[1] to solubility equlibria. In this study, solubilities of halite NaCl(c) and bischofite MgCl<sub>2</sub>·6H<sub>2</sub>O(c) in the system NaCl+MgCl<sub>2</sub>+H<sub>2</sub>O at T = 298.15 K were calculated using available thermodynamic properties of the solids[2] and of aqueous electrolyte solutions[3-7] and were compared with experimentally determined values[8]. Model parameters of NaCl(aq) that are valid beyond solubility limit were obtained by treatment of data for osmotic coefficients in unsaturated and estimated values[3] in supersaturated solution.

### **Results and Discussion**

Ion-interaction parameters necessary to calculate osmotic and activity coefficients of binary mixtures NaCl(aq) and MgCl<sub>2</sub>(aq) at T = 298.15 K are given in Table 1. Interaction coefficients  $\theta_{\text{Na,Mg}}$  and  $\psi_{\text{Na,Mg,Cl}}$  complete the parameterization necessary to describe the thermodynamic properties of investigated electrolyte mixture.

In order to obtain these mixing parameters of the extended ion-interaction model for the system NaCl+MgCl<sub>2</sub>+H<sub>2</sub>O the treatment of available osmotic coeffi-

cients data[6-8] included the correction of values according to newly published parameters of the binary solutions used as reference standards in isopiestic measurements. Thus obtained mixing parameters were:  $\theta_{\text{Na,Mg}} = 0.07 \text{ kg} \cdot \text{mol}^{-1}$  and  $\psi_{\text{Na,Mg,Cl}} = 0.0092574 \text{ kg}^2 \cdot \text{mol}^{-2}$  valid up to ionic strength of the mixed solution  $I \le 8.4945 \text{ mol} \cdot \text{kg}^{-1}$  with standard deviation of the fit s = 0.0043.

**Table 1.** Parameters of the extended ion-interaction model of Pitzer for binary mixtures NaCl(aq) and MgCl<sub>2</sub>(aq) at T = 298.15 K valid up to max. molality (Max. m).

	$\beta_{ ext{MX}}^{(0)}$	$\beta_{\mathrm{MX}}^{(1)}$	$\alpha_{ m MX}$	$C_{ m MX}^{(0)}$	C <sub>MX</sub> <sup>(1)</sup>	$\omega_{ m MX}$	Max.m (mol/kg)
NaCl(aq)	0.10157	0.31851	2.0	-	-	2.5	11.0
				0.0012643	0.17456		
$MgCl_2(aq)[4]$	0.68723	1.56760	3.0	-0.007594	-	1.0	4.0251
- , 2					0.35497		

Mineral solubilities in concentrated electrolyte solutions can be calculated from thermodynamic consideration provided that equilibrium constants[2] (including appropriate chemical potentials) for the solubility reactions are known:

$$lnK = lnK^{o}(m_1, m_2) + R(m_1, m_2)\theta + T(m_1, m_2)\psi$$

where  $m_1$  and  $m_2$  are the molalities of the NaCl and MgCl<sub>2</sub>,  $\ln K^{\rm o}(m_1,m_2)$  is equilibrium constant based only on binary mixtures terms and  $R(m_1,m_2)$ ,  $T(m_1,m_2)$  are collection of terms contributing to equilibrium constant involving  $\theta$  and  $\psi$  mixing parameters.

Comparison of the calculated results for the solubilities in the system NaCl+MgCl<sub>2</sub>+H<sub>2</sub>O with experimental data[8] shows good qualitative agreement. For the halite solubility limit, calculations yield  $m_{\text{NaCl,calc}} = 6.0952 \text{ mol·kg}^{-1}$ , while experimental value is  $m_{\text{NaCl,exp}} = 6.1628 \text{ mol·kg}^{-1}$ , which is of sufficient accuracy with respect that parameters for NaCl(aq) at T = 298.15 K are valid up to  $m \le 11 \text{ mol·kg}^{-1}$ . Calculated solubility limit of MgCl<sub>2</sub>(aq) was  $m_{\text{MgCl}_2,\text{calc}} = 5.7632 \text{ mol·kg}^{-1}$  with parameters applicable up to  $m \le 4 \text{ mol·kg}^{-1}$ , while experimental value is  $m_{\text{MgCl}_2,\text{exp}} = 5.8721 \text{ mol·kg}^{-1}$ .

The advantage of application of this ion-interaction model is that it can be used not only for satisfactory prediction of mineral solubilites but also for precise calculations of activity coefficients of the system  $NaCl+MgCl_2+H_2O$  at T=298.15 K in unsaturated region of the mixed solution.

In Figure 1. are presented calculated values of halite and bischofite solubilities using extended ion-interaction model of Pitzer with parameters from Table 1. and mixing parameters  $\theta_{\text{Na,Mg}} = 0.07 \text{ kg} \cdot \text{mol}^{-1}$  and  $\psi_{\text{Na,Mg,Cl}} = 0.0092574 \text{ kg}^2 \cdot \text{mol}^{-2}$ , together with experimental data[8].

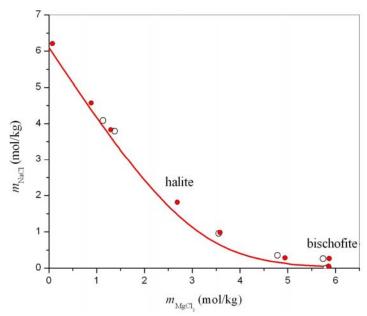


**Fig. 1.** Solubilities in the system NaCl+MgCl<sub>2</sub>+H<sub>2</sub>O at T = 298.15 K:

• - experimental data[8], curves - calculated values using extended ion-interaction model of Pitzer parameters from Table 1. and mixing parameters  $\theta_{\text{Na,Mg}} = 0.07$  and  $\psi_{\text{Na Mo Cl}} = 0.0092574$  with standard deviation of the fit s = 0.0043.

### Conclusion

Comparison of calculated versus experimentally determined solubilities of halite and bischofite in the system NaCl+MgCl<sub>2</sub>+H<sub>2</sub>O at T = 298.15 K show that ion-interaction model of Pitzer can be used to calculate brine-mineral equilibria at this temperature.

- [1] K. S. Pitzer, J. J. Kim, J. Amer. Chem. Soc., 1974, 96, 5701-5707.
- [2] C. E. Harvie, J. H. Weare, Geochim. et Cosmochim. Acta, 1980, 44, 981-997.
- [3] D. T. An, T. T. Teng, J. M. Sangster, Can. J. Chem., 1978, 56, 1853-1855.
- [4] J. Miladinovic, R. Ninkovic, M. Todorovic and J. A. Rard, J. Solution Chem., 2008, 37, 307-329.
- [5] R. F. Platford, J. Phys. Chem., 1968, 72, 4053-4057.
- [6] J.A. Rard, D. G. Miller, J. Chem. Eng. Data, 1987, 32, 85-92.
- [7] Y. C. Wu, R. M. Rush and G. Scatchard, J. Phys. Chem., 1968, 72, 4048-4053.
- [8] W. F. Linke, Solubilities of Inorganic and Metal-Organic Compounds, Am. Chem. Soc., Washington D. C., 1965.

## GEOCHEMICAL SYSTEMS WATER-ROCK-ORE AND GENESIS OF TWO FE-SULFATE MINERAL WATERS AT WESTERN BALKAN

### A. Dangić and J. Dangić

<sup>1</sup>Faculty of Mining & Geology, University of Belgrade, Đušina 7, Belgrade, Serbia, adangic@EUnet.yu

### **Abstract**

Two mineral water springs at Western Balkan: Crni Guber (CG), in Bosnia, and Djavolja Varoš (DV), in Serbia, are characterized by acid (pH  $\sim$ 3.5) iron-sulfate waters rich in several trace elements. The water composition appear is forming in ground water-rock-ore interactions. The geochemical models of mineral water genesis based on phase relations in  $K_2O-Na_2O-CaO-MgO-FeO-Fe_2O_3-Al_2O_3-SiO_2-H_2O$  and Fe sulfides-M sulfides- $H_2O$  systems were established and discussed.

### Introduction

At Western Balkan (SE Europe), in the Serbo-Macedonian (SM) Tertiary petrologic calco-alkaline and Pb-Zn geochemical and metallogenic province there are numerous mineral waters. The SM province extends through Serbia and parts of Bosnia and Macedonia and is characterized by numerous large massifs of dacito-andesites and hydrothermal Pb-Zn-polimetalic ore deposits [1-3]. Two mineral waters (MW) in the province: Crni Guber (CG), in Bosnia, well known iron-arsenic medical water, and Djavolja Varoš (DV), in Serbia, are geochemically interesting due their low pH and Fe-sulfatic composition [4-6]. The paper presents and discusses geochemical systems and models of genesis of these mineral waters.

### **Mineral Water Geochemical Systems and Models**

The CG water spring is situated in NW part of the SM province, in NE Bosnia, in central part of the volcanic and Pb-Zn ore area of Srebrenica, which is built up mostly by volcanic rocks of dacite and quartz latite composition and contains several quartz-sulfide Pb-Zn ore veins [1-3]. The CG water appears from an old mining tunnel [4, 5]. The spring capacity is 0.05 L/s, water temperature 13° C, Eh 0,460 V, and composition as in Table 1.

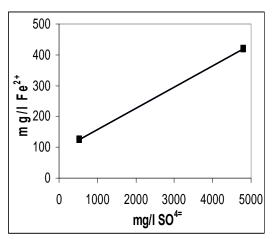
The DV water spring is situated in NW part of the SM province, in central-south Serbia, in the dacito-andesite and Pb-Zn ore area of Lece, at the world famous geomorphological locality of Djavolja Varoš (Infernal Town). It appears in an paleovolcanic caldera, built up by andesites and their pyroclastics and containing some poor Pb-Zn and Cu sulfide minarizations [4]. The spring capacity is 0.05 L/s, water temperature is 13° C, Eh 0,460 V, and composition as in Table 1.

<sup>&</sup>lt;sup>2</sup>Faculty for Physical Chemistry, University of Belgrade, Studentski trg 12, Belgrade, Serbia

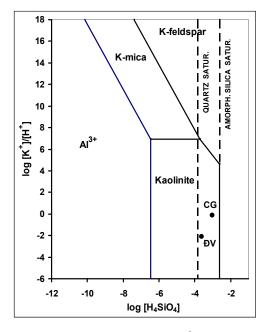
Table 1.	Geochemical characteristics
of the	studied mineral waters.

	2			
Mineral water		$CG^1$	$\mathrm{DV}^2$	
Mineral. (g/L)		0,77	9,09	
рН		3,6	3,5	
	Na <sup>+</sup>	1,9 7,5 6,4	1,8	
	K <sup>+</sup>	7,5	0,1	
	$Ca^{2+}$ $Mg^{2+}$ $Fe^{2+}$	6,4	50,0	
	$Mg^{2+}$	3,9	61,0	
	Fe <sup>2+</sup>	125	$419^{3}$	
mg/L	$SO_4^=$	525	4800	
	Cl <sup>-</sup>	0,5	3590	
	HCO <sub>3</sub>	0,0	0,0	
	$CO_3^=$	0,0	0,0	
	SiO <sub>2</sub>	55,9	15,0	
	$Al^{3+}$	41,9	$52,9^3$	
	Cu <sup>2+</sup>	0,07	52,9 <sup>3</sup> 5,0	
	$\begin{aligned} & \text{HCO}_3 \\ & \text{CO}_3^{=} \\ & \text{SiO}_2 \\ & \text{Al}^{3+} \\ & \text{Cu}^{2+} \\ & \text{Zn}^{2+} \end{aligned}$	8,0	5,0	
	$HAsO_4^{=}$	8,0	0,03	
1 Enom [2] 2 Enom [4] 3 Decelerated				

<sup>&</sup>lt;sup>1</sup>- From [3]. <sup>2</sup>-From [4]. <sup>3</sup>-Recalculated from Fe<sub>2</sub>O<sub>3</sub>, Al<sub>2</sub>O<sub>3</sub>.



**Fig. 1.** The relationship between sulfate and Fe<sup>2+</sup> contents in CG and DV mineral waters.



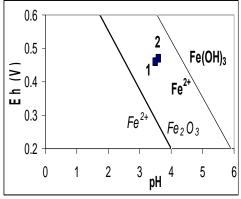


**Fig. 2.** A part of the pH-Eh diagram for the system FeO-Fe<sub>2</sub>O<sub>3</sub>-H<sub>2</sub>O. (Phase relations at 25°C, 1 atm, [Fe<sup>2+</sup>]=10<sup>-2.90</sup>, after [5]). 1=CG, 2=DV.

**Fig. 3.** The diagram showing stability fields of some phases in the  $K_2O-Al_2O_3$ -

SiO<sub>2</sub>-H<sub>2</sub>O system at 25°C, 1 atm, as a function of K<sup>+</sup>/H<sup>+</sup> and H<sub>4</sub>SiO<sub>4</sub>. (Phase boundaries for activity Al<sup>3+</sup>=10<sup>-3,29</sup> and pH=3,6, after [5]).

### **Discussion and Conclusions**

The geochemical water-rock-ore systems of the both MW are near symilar. The rocks generaly consist of feldspars and Fe-Mg silicates. The predominate feldspars in DV- and CG-systems are plagioclase (CaNa-Al silicate) and K-feldspar (K-Al silicate), respectively. In CG-system quartz (SiO<sub>2</sub>) also appears. In the ores, most abundant are Fe-sulfides (pyrrhottite FeS and/or pyrite FeS<sub>2</sub>) predominate, and they are accompained in CG-system by galena (PbS), sphalerite (ZnS) and arsenopyrite (FeAsS) and in DV-system by Cu-sulfides.

In water-ore interaction, the processes of oxidation/disolution of Fesulfides produce  $SO_4^-$  and  $Fe^2$ + ions and a strong pH water decrease (equation 1) which support dissolution of other sulfide minerals (equation 2):

$$2FeS_2 + 2H_2O + 7O_2 = 2Fe^{2+} + 4SO_4^{-} + 4H^{+} \qquad (1)$$

$$7nS + 2O_2 = 7n^{2+} + SO_4^{-} \qquad (2)$$

The iron content in water depend also on redox conditions, i.e. phase relation in the system FeO-Fe<sub>2</sub>O<sub>3</sub>-H<sub>2</sub>O (Fig. 2).

In water-rock interaction, processes of feldspar transformation and quartz dissolution, appearing in the system K<sub>2</sub>O-Na<sub>2</sub>O-CaO-Al<sub>2</sub>O<sub>3</sub>-SiO<sub>2</sub>-H<sub>2</sub>O<sub>3</sub> as for transformation of K-feldspar into kaolinite (equation 3):

$$2KAlSi_3O_8 + 3H_2O = 2K^+ + \bar{A}l_2Si_2O_5(OH)_4 + 4SiO_2 + 2OH^-$$
.....(3) and in corresponding reactions in the other parts of the systems:  $K_2O-Na_2O-CaO-MgO-FeO-Fe_2O_3-Al_2O_3-SiO_2-H_2O$ . The phase relations are modelized in Fig. 3.

The established geochemical models indicate the following:

- (1) Contents of Fe<sup>2+</sup> and sulfate in both waters are connected with oxidation of Fesulfides and, accordingly, express a good positive correlation (Fig. 1).
- (2) Contents of Fe<sup>2+</sup> depend on both water pH and Eh, i.e. stability of hematite and Fe(OH)<sub>3</sub> (ferrihydrite): in the related pH-Eh diagram (Fig. 2) both CG and ĐV are in the hematite stability field but are unsaturated to respect Fe(OH)<sub>3</sub>.
- (3) The mineral waters differ significantly in contents of base cations. However, in both of them base cations are in equilibrium with kaolinite and silica is saturated to quartz and unsaturated to non-crystalline (amorphous) SiO<sub>2</sub> (Fig. 3).
- (4) The differences in K<sup>+</sup>, Na<sup>+</sup> и Ca<sup>2+</sup> contents in water depend on diversities of feldspar i.e. rock types (quartz latite, dacite, andesite) in the water-rock systems; the differences in Mg<sup>2+</sup> contents depend on Fe-Mg silicate types.
- (5) The differences in Cu, Zn and As contents in CG and ĐV depend on differences in ore composition in the related water-ore-rock systems.

- [1] A. Dangić, A., Annales Geol. Penins. Balk., 1979/80, 48-49, 305-509.
- [2] A. Dangić, Annales Geol. Penins. Balk., 1993, 57/1, 257-285.
- [3] S. Janković, Ore deposits of Serbia, 1990, RGF, Belgrade.
- [4] A. Dangić, J. Dangić, 27th. Int. Geol. Congr., Moscow, 1984, VII, 379-380.
- [5] A. Dangić, A., J. Dangić, Annales Geol. Penins. Balk., 1989, 53, 445-458.
- [6] D. Protić, Special editions of Geoinstitute, Belgrade, 1995, 17.

### VANADIUM IN ANCIENT SEDIMENTARY ROCKS OF MARINE ORIGIN: ZVONCE BLACK SHALE

B.S. Ilić, N.S. Krstić, P.I. Premović and M.S. Pavlović

Laboratory for Geochemistry, Cosmochemistry and Astrochemistry, University of Niš, P.O. Box 224, 18000 Niš, Serbia and Institute of Nuclear Sciences, Vinča, Belgrade, Serbia

### **Abstract**

Vanadium in the Zvonce black shale was determined by atomic absorption spectrometry (100 ppm). To obtain an indication of the chemical nature of the vanadium, a sample was analysed for vanadium at various stages of demineralization. It is suggested that a likely source of vanadium in the Zvonce black shale was normal seawater and that most of the vanadium was adsorbed in the shale iron oxides.

### Introduction

The East Serbian Silurian sequence, which is wholly marine, includes well-dated strata of the early Llandovery age to early Devonian [1]. The Zvonce (Middle and Upper) Silurian sedimentary deposits belong to the E. Serbia Silurian units. They are calcerous and carbonaceous black shales with graptolitic faunal associations. Although Silurian graptolitic black shale occurs throughout E. Serbia, our investigations have centered on an outcrop area near the village of the Zvonce.

Extensive work has been done on the geology and paleobiology of the Zvonce black shale and related geological materials; the reader is referred to Petković [1], Veselinović [2], Veselinović and Krstić [3]. Despite this interest in the Zvonce no modern detailed geochemical analysis of this rocks is available in the literature. A sample of the Zvonce shale was investigated in order to establish the geochemical distribution of vanadium (V).

### **Results and Discussion**

The distribution of V in the various fractions of shaly rock is shown in Table 1. This table reveals that the levels of total V in the rock sample, determined by atomic absorption spectrometry (AAS) and the sum of V in the various rock fractions, are in good agreement with one another within experimental error.

In order to try to understand the overall source of V in the Zvonce graptolitic shale, the metal content of seawater (2 ppb) [4], ordinary shale (130 ppm) [5] and Black Sea sediments (175 ppm) [6] were compared to the Zvonce shale, Table 1. Relative to sea water the Zvonce black shale is enriched (*ca.* 10<sup>5</sup> times) in V but similar to ordinary shale and recent Black Sea sediments in V abundance. Holland [7] showed by calculation for several black shales of marine origin that 10<sup>5</sup> metal enrichments including V could be obtained by removing these metals from normal seawater. Thus, we suggest that V in Zvonce black shale is syngenetic and extracted from sea water.

Fraction	Shale (wt. %)	V (ppm)	Total V (wt. %)
Extractable or- ganic	≤ 1	≥ 1000	≤10
Cold HCI	55	70	40
Boiling HCI	8	375	30
HF-Soluble	31	30	10
Kerogen	5	170	10
Shale	100	100	100

**Table 1.** Concentration and distribution of V in the Zvonce black shale:

HCl-soluble V may represent: V associated with shale iron oxides, V adsorbed on clay minerals of V precipitated in limestone. However, Krauskopf has shown that hydrated Fe<sub>2</sub>O<sub>3</sub> is the most effective adsorbent for V in solution and the association of V with sedimentary iron oxides (mainly geothites) is well known. Thus, the content of HCl-soluble V may reasonably be explained in terms of adsorption on shale iron oxides. Our analysis indicates that the Zvonce shale contains a relatively high content of iron oxides: 2.43%.

Finally, it can be seen from Table 1. that the extractable organic fraction of the Zvonce black shale contains a relatively high concentration of V ( $\geq 1000$  ppm). This indicates that the organic matter was also the control for the V abundance in the shale. The organic matter usually has functional groups that are able to ion-exchange V, probably before it reaches the sediment.

### **Conclusions**

The geochemical analyses of the Zvonce black shale shows that the most of V is located in HCl fractions.

Most of these V is located in iron-oxides.

- [1] K. Petković, N. Milojević, Die Geologische Beschaffenheit und Tektonik in der Umgebung zum Zvonačka Banja mit Besonderder Rucksicht auf der Erscheinung der Thermolquellen, Naučna knjiga, Beograd 1956.
- [2] M. Veselinović, Geološki anali Balkanskog poluostrva, Vol. XXXI (1964).
- [3] M. Veselinović, B. Krstić, Carp. Balk. Geol. Assoc. VII Congr., Report Part, Vol. 1.-Sofia 1965.
- [4] J. D. Saxby, Chem. Geol., 1970, 6, 173.
- [5] J. D. Saxsby, in Oil Shale, T. F. Yen and G. V. Chilingarian Eds., Elsevier, Amsterdam 1976.
- [6] D. M. Hirst, Geochemistry of Sediments from Black Sea, in The Black Sea, D. A. Ross and E. T. Degens Eds., Am. Ass. Petrol. Geol., Tulsa 1974.
- [7] H. D. Holland, Econ. Geol., 1979, 74, 1976.

# FAST SYNTHESIS OF NOVEL COUMARIN DERIVATIVES BY THE KNOEVENAGEL CONDENSATION UNDER MICROWAVE IRRADIATION

N. Vuković, S. Sukdolak and S. Solujić

Department of Chemistry, Faculty of Science, University of Kragujevac, P.O.Box 12, Serbia, nvukovic@kg.ac.yu

### **Abstract**

Knoevenagel condensation of 3-acetyl-4-hydroxy-chromene-2-one in the presence of catalytically amount of piperidine leads to the effective synthesis of coumarin derivatives (**2b-8b**) by a solvent free reaction under microwave irradiation.

### Introduction

Coumarins are nowadays an important group of organic compounds that are used as additives to food and cosmetics [1], optical brightening agents [2], and dispersed fluorescent and laser dyes [3]. The derivatives of coumarin usually occur as secondary metabolites present in seeds, root, and leaves of many plant species. Their function is far from clear, though suggestions include waste products, plant growth regulators, fungistats and bacteriostats [4]. It is therefore of utmost importance that the synthesis of coumarin and its derivatives should be achieved by a simple and effective method.

The solvent-free condition under microwave irradiation offers several advantages [5]: solvents are often expensive, toxic, difficult to remove in the case of aprotic dipolar solvents with high boiling point, and are environment polluting agents. Moreover, liquid-liquid extraction is avoided for the isolation of reaction products, and the absence of solvent prevents from the risk of hazardous explosions when the reaction takes place in a microwave oven. From the other side, the workup procedure is simply reduced to the recrystallization of product from an appropriate solvent.

The aim of the present paper is to show that under the microwave irradiation the Knoevenagel condensation can be successfully applied to the synthesis of a number of coumarin derivatives starting from 3-acetyl-4-hydroxy-chromene-2-one.

### **Experimental**

The reactions were carried out under atmospheric pressure in an open teflon vessel adapted to microwave monomode reactor. All the compounds were identified by IR and 1H NMR spectroscopy, GC/MS and elemental analysis. Microanalysis of carbon, hydrogen and nitrogen was carried out with a Carlo Erba 1106 microanalyser. The IR spectra were run on a Perkin-Elmer Grating Spectrophotometers Model 137 and Model 337,  $\bf v$  in cm-1. The NMR spectra were recorded on a Varian Gemini 200 spectrometer (1H at 200 MHz), in solvent CDCl3, using TMS (SiMe4) as the internal standard. GC/MS were carried out in a Agilent 6890N/5975B gas chromatograph.

Diethyl 2-(1-(4-hydroxy-2-oxo-2H-chromen-3-yl)ethylidene)malonate **2b**. Anal. for C18H18O7 (346.33). M+ 346 m/z. Calc. C: 62.42, H: 5.24. Found C: 62.44, H:

5.23. IR (KBr disc) 3434 v(OH), 2949 and 2841 v(CH3 and CH2), 1731 v(lactone and ester C=O), 1611, 1546 and 1496 v(C=C)ar, 1368 and 1032 v(C-O-C) cm-1. 1H NMR (CDCl3): □1.23 (m, 6H, CH3, mixture of Z and E isomers), 4.21 (q, 4H, 4CH2), 7.31-7.83 (m, 4H, H-5, H-6, H-7, H-8), 16.73 (bs, 1H, OH-4). Yield: 96 %.

Methyl 2-acetyl-3-(4-hydroxy-2-oxo-2H-chromen-3-yl)but-2-enoate **3b**. Anal. for C16H14O6 (302.28). M+ 302 m/z. Calc. C: 63.57, H: 4.67. Found C: 63.55, H: 4.71. IR (KBr disc) 3433 v(OH), 2948, 2930 and 2856 v(CH3), 1730 v(lactone and ester C=O), 1700 v(C=O), 1610, 1545 and 1495 v(C=C)ar, 1369, 1032 and 1024 v(C-O-C) cm-1. 1H NMR (CDCl3): □2.20 (s, 3H, CH3), 2.26 (s, 3H, CO-CH3), 3.81 (s, 3H, COO-CH3), 7.29-7.83 (m, 4H, H-5, H-6, H-7, H-8), 17.01 (bs, 1H, OH-4). Yield: 97%.

Methyl 3-(4-hydroxy-2-oxo-2H-chromen-3-yl)but-2-enoate **4b**. Anal. for C14H12O5 (260.24). M+ 260 m/z. Calc. C: 64.61, H: 4.65. Found C: 64.63, H: 4.69. IR (KBr disc) 3422 v(OH), 2949, 2930 and 2841 v(CH3), 1729 v(lactone and ester C=O), 1609, 1542 and 1491 v(C=C)ar, 1364, 1033 and 1023 v(C-O-C) cm-1. 1H NMR (CDCl3): □2.22 (s, 3H, CH3), 3.86 (s, 3H, COO-CH3), 5.76 (s, 1H, C=C-H), 7.29-7.82 (m, 4H, H-5, H-6, H-7, H-8), 17.11 (bs, 1H, OH-4). Yield: 96%.

Methyl 2-cyano-3-(4-hydroxy-2-oxo-2H-chromen-3-yl)but-2-enoate **5b**. Anal. for C15H11NO5 (285.06). M+ 285 m/z. Calc. C: 63.16, H: 3.89, N: 4.91. Found C: 63.18, H: 3.84, N: 4.95. IR (KBr disc) 3434 v(OH), 2949, 2929 and 2854 v(CH3), 2231 v(C≡N), 1731 v(lactone and ester C=O), 1611, 1546 and 1497 v(C=C)ar, 1368, 1032 and 1025 v(C-O-C) cm-1. 1H NMR (CDCl3): □2.23 (s, 3H, CH3), 3.80 (s, 3H, COO-CH3), 7.29-7.83 (m, 4H, H-5, H-6, H-7, H-8), 17.06 (bs, 1H, OH-4). Yield: 94%.

3-(1-(4-Hydroxy-2-oxo-2H-chromen-3-yl)ethylidene)pentane-2,4-dione **6b**. Anal. for C16H14O5 (286.28). M+ 286 m/z. Calc. C: 67.13, H: 4.93. Found C: 67.15, H: 4.87. IR (KBr disc) 3434 v(OH), 2949 and 2929 v(CH3), 1731 v(lactone C=O), 1697 and 1686 v v(C=O) 1610, 1544 and 1496 v(C=C)ar, 1371 and 1032 v(C-O-C) cm-1. 1H NMR (CDCl3): □2.23 (s, 3H, CH3), 2.29 (s, 3H, CO-CH3), 7.31-7.83 (m, 4H, H-5, H-6, H-7, H-8), 17.01 (bs, 1H, OH-4). Yield: 94%.

2-Cyano-3-(4-hydroxy-2-oxo-2H-chromen-3-yl)but-2-enoic acid **7b**. Anal. for C14H9NO5 (271.22). M+ 271 m/z. Calc. C: 62.00, H: 3.34, N: 5.16. Found C: 62.05, H: 5.11, N: 5.21. IR (KBr disc) 3433 v(coumarine OH), 3100 v(OH from COOH), 2947 and 2927 v(CH3), 1731 v(lactone C=O), 1699 v(C=O from COOH) 1611, 1543 and 1495 v(C=C)ar, 1371 and 1032 v(C-O-C) cm-1. 1H NMR (CDCl3): □2.24 (s, 3H, CH3), 7.31-7.83 (m, 4H, H-5, H-6, H-7, H-8), 12.37 (bs, 1H, COOH), 17.13 (bs, 1H, OH-4). Yield: 84%.

2-Acetyl-3-(4-hydroxy-2-oxo-2H-chromen-3-yl)but-2-enoic acid **8b**. Anal. for C15H12O6 (271.22). M+ 288 m/z. Calc. C: 62.50, H: 4.20. Found C: 62.55, H: 4.21. IR (KBr disc) 3437 v(coumarine OH), 3111 v(OH from COOH), 2991 v(CH3), 1727 v(lactone C=O), 1699 and 1689 v(C=O from COOH and keto group) 1601, 1541 and 1491 v(C=C)ar, 1369 and 1031 v(C-O-C) cm-1. 1H NMR (CDCl3): □2.21 (s, 3H, CH3), 2.28 (s, 3H, CO-CH3), 7.31-7.83 (m, 4H, H-5, H-6, H-7, H-8), 12.65 (bs, 1H, COOH), 17.17 (bs, 1H, OH-4). Yield: 87%.

### **General Procedure**

A mixture of a 3-acetyl-4-hydroxy-chromene-2-one (1) (2.5 mmol), carbonyl compound (2a-8a) (2.8 mmol), and piperidine (catalytically amount) was irradiated and heated the microwave reactor with power and by the time indicated in Scheme 1. At the end of exposure to microwave, the reaction mixture was cooled to room temperature, and the crude product was recrystallised from methanol to effort the coumarin derivatives (2b-8b) (Scheme 1).

### **Results and Discussion**

<sup>a</sup>Final temperature reached by the reaction mixture

Scheme 1. Reaction conditions of Knoevenagel reaction

### Conclusion

In summary, the method describes a noticeable improvement in reactions conditions for the synthesis of coumarin derivatives by the Knoevenagel condensation and takes advantage of both solvent free conditions reaction and microwave activation. As it is shown in Scheme 1, the reaction time is reduced to only a few seconds by using microwave dielectric heating. The reactions can be run safely in good yields, and the work-up procedure is reduced to the recrystallization of desired products.

### Acknowledgement

This study was financially supported by a Grant No 142025 from the Serbian Ministry of Science.

- [1] R. O'Kennedy, R. D. Thornes, Coumarins: Biology, Applications and Mode of Action, Wiley and Sons, Chichester, 1977
- [2] M. Zahradnik, The Producton and Application of Fluorescent Brightening Agents, Wiley and Sons, 1992.
- [3] M. Maeda, Laser Dyes, Academic Press, New York, 1994.
- [4] R. D. H. Murray, J. Mendes, S. A. Brown, The Natural Coumarins: Occurance, Chemistry and Biochemistry, Wiley and Sons, New York, 1982.
- [5] G. Bram, A. Loupy, D. Villemin, Solid Supports and Catalysts in Organic Chemistry, Ellis Harwood, London, 1992

### CHEMOMETRY AS TOOL FOR INVESTIGATION AND CLASSI-FICATION OF ANCIENT CERAMICS

<u>I. Pašti</u>, I. Holclajtner-Antunović, Lj. Damjanović and U.B. Mioč Faculty of Physical Chemistry, Studentski trg 12-16, 11158 Belgrade 118, PAC:105305, Serbia, \*igor@ffh.bg.ac.yu

### **Abstract**

Artifacts found at the archaeological sites which are produced at high temperatures provide information about manufacturing techniques. Well-preserved ceramic objects are therefore excellent chronological markers and general markers of society development. In this work Fourier transform infrared (FTIR) spectra of ceramic body of 57 shards found at three excavation sites (Ras, Reljina Gradina and Novo Brdo) were analyzed by unsupervised (hierarchical cluster analysis-HCA and principal component analysis-PCA) and supervised (linear discriminant analysis-LDA) statistical methods in order to establish reference groups for the purpose of assigning future samples according to their origin, mineralogical composition and firing temperature.

### Introduction

The study of pottery objects is relevant because, once produced, they are practically indestructible and found in quantity at the majority of archaeological sites dating from the Neolithic period onwards. Very often, pottery represents the only available marker of provenance and dating. Thus it is of great importance to combine archaeological findings with detailed knowledge of chemical and structural features of pottery samples. The scarcity of analysis on Byzantine pottery still strongly limits the classification and technology information of this important material which represents a missing link between Roman and Ottoman production. Therefore, the subject of our work is systematic investigation of archaeological pottery samples, mainly shards of bowls, plates and pitchers from Ras, Reljina Gradina and Novo Brdo by a multianalytical approach.

Because of the variability in chemical and mineralogical compositions within an individual clay or temper source as well as within an individual production group, provenance studies based on compositional fingerprint involve the analysis of a large number of samples. Although FTIR spectroscopy is simple, fast, almost nondestructive and reliable technique, complete analysis of spectral data in such complex systems is a demanding task [2]. In order to establish reference groups among investigated samples for the purpose of assigning future samples according to the their origin, mineralogical composition or firing temperature we have performed chemometric analysis of FTIR spectra. The objective of our work is to explore suitability of FTIR data in statistical analysis instead of the chemical composition traditionally used for this purpose in provenance studies of pottery.

### Methodology

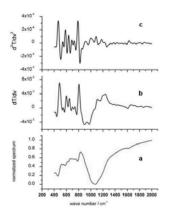
The FTIR spectra were recorded on a FTIR Nicolet 6700 spectrometer using KBr pellets technique, in the wavenumber range from 2000 cm<sup>-1</sup> to 400 cm<sup>-1</sup> and submitted to chemometric analysis. Employed chemometric techniques were: principal component analysis (PCA), hierarchical cluster analysis (HCA), and linear discriminant analysis (LDA). The first two techniques belong to unsupervised methods while LDA belongs to class of supervised methods. Prior to chemometric analysis, FTIR spectra acquired on 57 shards were all normalized to values between 0 and 1 and smoothed using Savitzky-Golay method with a 25 points third order polynomial filter. Numerical differentiation was additionally performed in order to remove baseline and emphasize small peaks and shoulders (Fig.1). Chemometric techniques were applied on normalized FTIR spectra as well as on their first and the second derivatives. As a measure of distance between samples for HCA, squared Euclidean distance was used, while Ward's method was used for aggregation. Model obtained by LDA was tested by cross-validation procedure. For all calculations SPSS 12 software was used.

### Results and discussion

The results of PCA on 57 investigated pottery samples have shown that total variance explained by first two PCs were 74.8 %, 47.6 % and 37.3 % for spectra, 1<sup>st</sup> derivative and 2<sup>nd</sup> derivative, respectively. This confirmed that numerical differentiation emphasized small variations between samples. By inspection of score plots three main groups of samples have been observed, although there was large variability within these groups. HCA has also shown that there was certain grouping between samples. If one assume that there are three clusters, which is equal to number of possible different sources of samples, percentage of correctly classified (%CC) samples was: 66.6 (spectra), 58.8 (1<sup>st</sup> derivative) and 78.4 % (2<sup>nd</sup> derivative).

Prior to LDA, samples were separated in three groups (NB, RAS, RG). This assumption was based on their archeological origin and supported by the results of unsupervised methods (PCA and HCA). Analysis has showed (Fig. 2) that reliable model can be built on this categorization (%CC for samples from training set was over 90% in all cases). After cross-validation procedure, %CC was less by few percents but still over 90%, which assures that obtained model can be characterized as very good.

The described results suggest that the obtained groups could be reliably used for the purpose of assigning further new unknown samples.



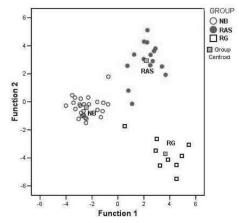


**Fig. 1.** Representative sample RAS-9: normalized FTIR spectrum (a), 1<sup>st</sup> derivative (b) and 2<sup>nd</sup> derivative spectrum (c)

**Fig. 2.** Combined-group plot obtained by LDA on the second derivatives (stepwise algorithm based on Fisher method was employed)

#### Conclusion

The results of this work have shown that chemometric analysis of FTIR data could be applied with success for classification of ceramic. The obtained results are also in good accordance with chemometric analysis of chemical composition obtained by ICP/MS technique for samples from sites Ras and Reljina Gradina [1]. Obtained results have unquestionably confirmed that pottery samples, classified by archaeologists to the same excavation site – Ras belong to two different sites: Ras and Reljina Gradina. Future work will include other types of experimental data (for example XRPD, XRF) for the purpose of chemometric analysis and more sophisticated chemometric techniques such as SIMCA.

# Acknowledgement

This work was supported by Serbian Ministry of Science within the project No. 142047.

- [1] Lj. Damjanović, U. Mioč, I. Holclajtner-Antunović, V. Andrić, Spectroscopic Studies of Medieval Serbian Ceramics from Ras and Novo Brdo, The Eight Biennial Conference of the Infrared and Raman Users Group, March 26-29, 2008, Book of Abstracts, 58.
- [2] G.E. De Benedetto, B. Fabbri, S. Gualtieri, L. Sabbatini, P.G. Zambonin, J. Cult. Herit. 2005, 6, 205.

# Spectroscopy Molecular Structures

(B)

#### SOME CHARACTERISTICS OF THE FULLERENE IONS

#### A.R. Tančić

VINCA Institute for Nuclear Sciences, 11001 Beograd, P.O.Box 522, Serbia

#### **Abstract**

In this paper we investigated characteristics of the fullerene  $C_{60}^+$  which are connected with the photoionization process. We calculated the photoionization cross section (PCS) and demonstrated that the giant plasmon resonance in the photoionization spectrum of  $C_{60}^+$  is much stronger and narrower that for  $C_{60}$ . There is a slight shift of the position of that resonance in  $C_{60}^+$  spectrum. We obtained that the giant resonance in the photoionization cross section for  $C_{60}^+$  arises due to the correlations between transition from  $\sigma$ - orbitals. Our calculations are based on the consistent many-body theory accounting for many-electron correlations ( the Random Phase Approximation-RPA). We have used a simple self-consistent spherical jellium model to treat the delocalized electron structure of the fullerenes. Our improved RPA (ImRPA) calculations are in agreement with earlier calculations.

#### Introduction

The fullerenes  $C_{60}$  and  $C_{60}^+$  has received a lot of attention during the last few years. An interest to these objects is connected with its exotic hollow, but highly stable structure caused by a significant delocalization of a large number of valence electrons in this molecule. The many interesting physical phenomena occurring in the collision processes involving fullerenes. For example, the surface plasmon oscillations in  $C_{60}$  can be excited and they manifest themselves as giant resonances in the spectrum (centered at the photon energy about 20eV) [1,2,3,4]. According to that we investigated the corresponding characteristics of  $C_{60}^+$ , i.e. we calculated the plasmon oscillations in the photon energy range: (ionization threshold  $C_{60}^+$ ;  $\approx 40eV$ ) [4]. The atomic system of units is used throughout the paper,  $m_e = |e| = \hbar = 1$ .

# Theory and Discussion

The total photoionization cross section may be presented as the sum of the partial cross sections for the ion orbitals. We calculated the amplitude of the each orbital in the one-electron approximation (where we use the frozen core model and the local density approximation LDA) and taking into account the many-electron cor-

relations in the RPA model. From The RPA equations we obtained the amplitudes of photoionization  $D_{\nu,\nu_2}(\omega)$  (in matrix form) [5]:

$$D_{v,v_2}(\omega) = f(d_{v,v_2}; \quad \chi_{v,v_2}(\omega), V_{v,v_2,v_3,v_2})$$
 (1)

where the matrix elements of D are expressed via single-electron amplitudes d, virtual electron-hole excitations  $\chi(\omega)$  and the interelectron interaction V [5]. Single-electron states of the fullerene ion have been calculated within simple spherical jellium model [6]. We assumed that four 2s2p electrons of C atoms are delocalized in the  $C_{60}^+$  (the ionic core is formed by positive  $C^{4+}$  ions with the electronic configuration  $1s^2$ ). We also use that the charges of the C ions are averaged over the radius of the fullerene ions  $R(C_{60}^+) \approx 6.69a.u.$  [9].

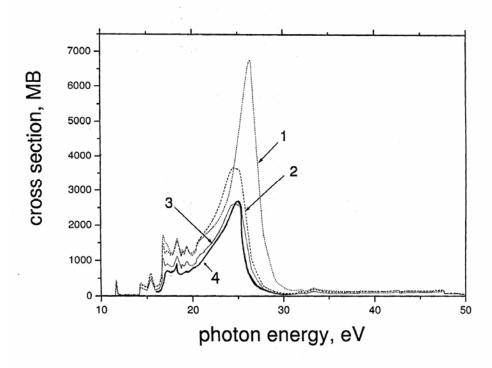


**Fig.1**. Photoionization cross section of the  $C_{60}^+$  ion. Results 1, 2, 3 [4,7] are obtained with averaged term, with coefficients, and RPA (respectively); 4-our result.

Our system has the open electronic shell  $((L_{tot},S_{tot})\neq 0)$ . In order to avoid this complicated problem (to obtain the system which like to the closed shell system), in recently published work [4,7] are introduced some approximation: 1. with averaged terms; 2. with numerical coefficients in one-electron approximation and 3. with the numerical coefficients in RPA [7]- they have been determined from the

sum rule analysis of the partial photoionization cross sections of the open fullerene shells. We have obtained our results using the third method with the improved RPA (imRPA) (Fig.1.- number 4) [5].

In fig. 1 we present the photoionization cross section of the ion  $C_{60}^+$ . We see that the giant resonance pattern is not much depend by the choice of the coefficients, but the maximum of the cross section depends very much of their choice. The comparison between theoretical [7] and experimental cross sections [2] for the  $C_{60}$  /  $C_{60}^+$ , one can see that the plasmon resonance for both fullerenes are close and the resonance profile is much higher for  $C_{60}^+$  than for  $C_{60}$ . We obtain that the resonance of the fullerene ion is placed at the photon energy  $\approx 26eV$ . This resonance arises from the correlation between transitions from  $\sigma$ -orbitals [4]. The giant resonances may be explained by the influence of the Coulomb core potential on the ground and excited states of valence electrons (ionic target).

#### Conclusion

In this paper we presented our calculations for prediction the plasmon resonance in photoionization cross section of the fullerene ion  $C_{60}^+$ . Our results are in agreement with earlier calculations. The method presented here may be generalized for the calculation of the photoionization cross sections for many different (positive) negative ions of  $C_{60}$  (with larger multiplicity) which are of great interest for experimental [10] and theoretical and experimental investigations [10, 11].

- [1] N. Ju, A. Bugac and J. Keller, Phys. Rev. B., 1993, 48, 9071.
- [2] I. V. Hertel, H. Steger, J. de Vries and al., Phys. Rev. Lett., 1992, 68, 784.
- [3] T. Libsch, O. Plotzk and F. Heiser, Phys. Rev. A., 1995, **52**, 457.
- [4] V. K. Ivanov, G. Kashenock, R. Polozkov and A. V. Solovyov, J.Phys.B., 2001, 34, L669.
- [5] M. Ya. Amusia M and L. V. Chernisheva, Automatic System of Investigation of Atoms, Nauka ,1983, 180 pp.( in Russian).
- [6] K. Yabana and G. Bertsch, Phys. Scripta, 1993, 48, 633.
- [7] V. K. Ivanov, G. Kashenock, R. Polozkov and A. V. Solovyov, J. of Exp. And Theor. Phys. (JETP), 2003, 96, 658.
- [8] O. Gunnarsson and B. Lundqvist, Phys. Rev. B.,1976, 13, 4274.
- [9] R. C. Haddon, L. E. Brus and K. Ragh., Chem. Phys. Lett., 1986, 125, 459.
- [10] Hertel I., Steger H., et al., Phys. Rev. Lett. 1992, 68, 784.
- [11] NATO Adv.St. Inst., Sess.LXXIII, Summ. School "At. Clusters and Nanopart.", eds C. Guet et al, Les Houshes, 2000, Paris.

# MICRO-RAMAN SPECTROSCOPY FOR ANALYSIS OF MEDIEVAL PIGMENTS AND GLAZED CERAMICS – CASE STUDIES

B. Minčeva-Šukarova, V. Tanevska and O. Grupče

Institute of Chemistry, Faculty of Natural Sciences & Mathematics, University "Ss Cyril & Methodius", Arhimedova 5, 1000 Skopje, Republic of Macedonia, <a href="mailto:biljanam@iunona.pmf.ukim.edu.mk">biljanam@iunona.pmf.ukim.edu.mk</a>

#### Abstract

Micro-Raman spectroscopy was used for non-destructive identification of pigments in fragments of wall paintings found in a sacral building, built in the 14<sup>th</sup> century, on the archaeological site of *Skopsko Kale* (Skopje Fortress). The identified pigments in some of the wall paintings at *Skopsko Kale* could support the assumption of the art historians that the sacral building was repainted over the period of four centuries. Micro-Raman spectroscopy was also employed to characterize the materials and technological process used in manufacturing the glazed Byzantine ceramics found at two different archaeological sites in Republic of Macedonia: *Skopsko Kale* in Skopje and *Markovi Kuli* and *Sv. Atanas* church in Prilep. The study of the glazes and the ceramic body of 12 Byzantine glazed ceramics enlightened the technological process, i.e. firing temperature of the glazes and the mineralogical composition of the clays used for manufacturing the Byzantine glazed ceramics.

#### Introduction

Raman spectroscopy is an experimental technique for identification and analysis of molecular species. It enables the identification of both inorganic as well as organic compounds. By introducing the microscope to focus the laser on the sample, micro-Raman spectroscopy could be used to analyze a very small spot, with the diameter of 1 to 10  $\mu$ m, depending on a selected laser wavelength and the focal length of the objective. This enables obtaining molecular information from a small particle, such as a pigment grain or a microcrystal of a mineral, but also a single fiber, gems, etc.

Nowadays, micro-Raman spectroscopy has been widely applied in analysis of numerous archaeological objects and has become an important analytical tool in conservation sciences and archaeometry. The number of scientific and professional papers dealing with micro-Raman spectroscopic analysis of various materials used in art and archaeology objects has increased enormously in the last decade [1, 2].

In this work, we present two examples (case studies) of application of micro-Raman spectroscopy on different artefacts from the Byzantine and post-Byzantine period, found in the archaeological excavations in Republic of Macedonia: (a) Micro-Raman pigment analyzes of wall paintings from a sacral building unearthed in *Skopsko Kale* and (b) micro-Raman studies of glazed ceramics finds from Skopje and Prilep.

# **Experimental**

#### Micro-Raman spectrometer:

Micro-Raman measurements were performed with LabRam 300 (Horiba Jobin-Yvon) Raman spectrometer equipped with two lasers: He-Ne laser operating at 17 mW and 633 nm and frequency doubled Nd:YAG laser operating at 50 mW and 532 nm. An Olympus MPlanN microscope with x10, x50 and x100 magnification was used to focus the laser on the samples. The microscope was equipped with color video camera, allowing positioning the samples to a selected region of investigation. The backscattered light was dispersed by using the 1800 lines/mm grating and is detected on a multi-channel air cooled CCD detector. This allows recording the spectra with the spectral resolution of 3–4 cm<sup>-1</sup>. The LabSpec software was used for data acquisition and GRAMS software was used for data manipulation.

# Samples:

<u>Pigments</u> from wall paintings were provided by the archaeologists from the Museum of Macedonia and the Museum of the City of Skopje, directly involved in the 2007 excavations at the *Skopsko Kale* site. The small fresco fragments were placed directly under the microscope, while from some of the larger ones, the samples were collected with cotton buds. The obtained Raman spectra were compared to the reference data base of pigments [3]. Most of the pigments were analyzed with the 633 nm He-Ne laser and an average power of the laser on the sample of 13.7 mW.

<u>Ceramic samples</u>: The glazes and the ceramics body were analyzed using 532 nm laser line with the average power on the sample of 7 mW. The Raman spectra of the ceramics body were recorded from the pellets prepared from 250 mg scratched powder from the body of each fragment which were then placed under the microscope (fx100) and recorded on a mapping stage (10 x 10 point-to-point) on a 0.03 x 0.03 mm area.

#### **Results and Discussion**

#### Pigment Analysis

In the year 2007, an extensive excavation has been carried out on several sectors in the *Skopsko Kale* (Skopje Fortress), Republic of Macedonia (Fig. 1). The site is known to be inhabited since Neolithic times. In several layers, mostly dating from the Middle Ages, 1500 different archaeological objects were excavated. Remains of sacral and profane buildings were also unearthed, among them at least one church. According to the archaeological finds, it originated from the middle or the second half of the 14<sup>th</sup> century, with evidences of reconstructions dateable to the 16<sup>th</sup> century, and more recent ones, from the 19<sup>th</sup> century, both of them made during the Ottoman rule in this region. Fragments of wall painting were uncovered in its vicinity [4] and their micro-Raman spectra were recorded [5].



**Fig. 1.** The foundation of the Medieval church – *Skopsko Kale* (Skopje Fortress) – Skopje Republic of Macedonia

On Fig. 2.a, a detail of a conserved wall painting of a profane figure, most probably from the middle of 14<sup>th</sup> century, according to the stylistic features [4], is presented. The recorded micro-Raman spectra of some pigments from this wall painting and a fragment from the later redecorations are shown on Fig. 2.b and 2.c.

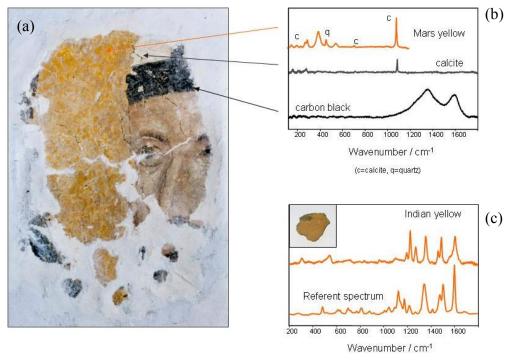


**Fig. 2.** (a) Fragment of conserved wall painting of a profane figure from the sacral building at *Skopsko Kale*, (b) Raman spectra of the pigments and (c) Raman spectra of a fragment from the later redecorated wall paintings.

All pigments identified by micro-Raman analyses are listed in Table 1. As it can be noticed, the palette is limited since most of the pigments are natural, mineral based, in use since Antiquity. However, in some fragments of the wall paintings,

few pigments, dated from the 16<sup>th</sup> and 19<sup>th</sup> century were observed. The identification of pigments was made by comparison of their Raman spectra to the reference database of pigments [3]. As seen from Table 1, the red pigments were identified as vermilion, red earth and litharge and one of the red pigments was identified as Mars red (in use since 19th century) [3]. The blue pigments were detected as lazurite and smalt, black as carbon black and white as calcite (chalk). Two yellow/ochre pigments were identified as Indian yellow (in use from 15<sup>th</sup> until 19<sup>th</sup> century) [3] and Mars yellow (in use since 19<sup>th</sup> century) [3]. This could support the tentative dating of the redecoration of some parts of the wall paintings: it could have been made not earlier than beginning of the 15<sup>th</sup> century when Indian yellow was introduced as a pigment [3], most probably during the 16<sup>th</sup> century. Further evidence for this suggestion is the recorded Raman spectrum of the blue pigment, identified as smalt, in use since 16<sup>th</sup> century [3].

**Table 1.** Pigments identified in the fragments of the wall paintings from the sacral building at *Skopsko Kale*.

Colour	Minerals / Antiquity	Other pigments
red	red ochre, vermilion, hematite, litharge	Mars red (since 19 <sup>th</sup> c.)
yellow / ochre		Indian yellow (15 <sup>th</sup> –19 <sup>th</sup> c.) Mars yellow (since 19 <sup>th</sup> c)
blue	lazurite	smalt (since 16 <sup>th</sup> c.)
black	magnetite, carbon black	
white	calcite	

The variety of pigments found and their allocation to different time periods confirms the assumption of the archaeologists that the sacral building has been most probably reconstructed/redecorated both in the 16<sup>th</sup> and 19<sup>th</sup> century [5].

#### **Ceramics**

Twelve shreds of Byzantine glazed ceramic finds excavated in archaeological sites in Skopje and Prilep, Republic of Macedonia, all dated from the  $12^{th}$  — $14^{th}$  century were analyzed using micro-Raman spectroscopy. They are characterized with an under glaze engobe and sgraffito slip decoration. Although the glazes are coloured, the pigments gave no significant Raman signature, possibly, due to the dissolution of the metal oxides in the glass matrix. One of the Byzantine glazed ceramic shreds and its microscopic cross section is shown on Fig. 3.a and 3.b. Its corresponding Raman spectra of the glaze and under glaze engobe are shown on Fig. 3.c. The two broad bands, the strong one, at ~1000 cm<sup>-1</sup> and the less intense one, at ~500 cm<sup>-1</sup> (Fig. 3.c.) are characteristic for Si—O stretching and Si—O—Si bending modes from SiO<sub>4</sub>, observed in any glassy network containing a large amount of fluxing PbO [6, 7].

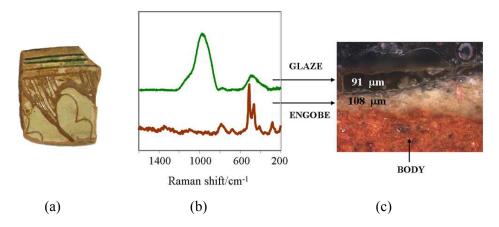


**Fig. 3.** (a) Glazed ceramic shred from *Markovi Kuli* (Prilep); (b) its corresponding Raman spectra of the glaze and the engobe and (c) its cross section (from Ref. 2). The polished cross sections photographs were taken with a reflected light optical microscope - Leica MEF4 (magnification x100).

The recorded Raman spectra of the glazes were used for determining the ratio of the integrated areas of the Raman band envelopes, i.e. the polymerization index  $(I_p)$  [6–8]. The glazes of the twelve ceramic shreds have already been studied extensively with micro-Raman spectroscopy [2, 9–11]. They were classified according to their indexes of polymerization calculated from the ratio of the Raman band areas of the Si–O–Si bending and Si–O stretching modes  $(A_{500}/A_{1000})$  [6–8]. Hence, the majority of the studied Byzantine ceramic glazes could be classified as lead-rich and fired below 700 °C, while only two samples are classified as lead-based and fired at around 800 °C [2, 10, 11].

Point-to-point micro-Raman spectroscopy [12] was used in assessment of the mineralogical composition of the ceramic bodies of the analyzed ceramic shreds. The pellets from the body of each ceramic shred were placed under the microscope (fx100) on a mapping stage covering an area of  $0.03 \times 0.03$  mm (Fig. 4.), acquiring approximately 100 Raman spectra. Depending of the surface that has been recorded, some of the spectra represent a pure mineral (Fig. 4.a – 4.c), while others are mixtures of minerals (Fig. 4.d and 4.e). The results from the recorded point-to-point micro-Raman spectra of all studied ceramics bodies are summarized in Table 2. As presented on Table 2, fifteen different minerals were identified. According to the recorded Raman spectra, quartz, hematite, magnetite and feldspars have been detected in all the studied samples of the ceramics body. Four different feldspars could be identified: microcline, albite, sanidine and andradite and three different polymorphic forms of TiO<sub>2</sub>: anatase, rutile and brukite could be distinguished from

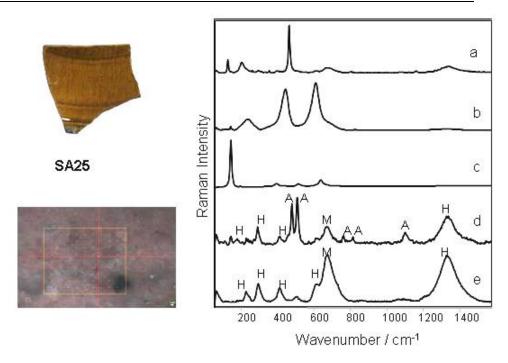


**Fig. 4.** Raman spectra of the obtained minerals from the mapping area (given on the left hand side). Spectrum **a** corresponds to Quartz; **b** to Rutile; **c** to Anatase; **d** to mixture of minerals: Albite(A)+Hematite(H)+Magnetite(M) and **e** to mixture of minerals: Hematite(H)+Magnetite(M).

**Table 2.** List of the obtained minerals by point-to-point micro-Raman spectroscopy from the ceramic samples. (F = Feldspars)

MINERALS	SA25	SA27	SA29	SK31	MK2	MK9	MK10	MK14	MK22
Quartz	<b>V</b>	<b>√</b>		<b>√</b>		V	<b>V</b>	<b>V</b>	V
Hematite	√	√	<b>V</b>	<b>√</b>	<b>√</b>	√	√	<b>√</b>	<b>√</b>
Magnetite	√	$\checkmark$	$\checkmark$	$\checkmark$	$\checkmark$	√	√	√	
TiO <sub>2</sub> (rutil)	√		$\checkmark$						$\checkmark$
TiO <sub>2</sub> (anatase)	√		$\checkmark$	$\checkmark$			√	√	
TiO <sub>2</sub> (brukite)			<b>√</b>						
F (microcline)		$\checkmark$	$\sqrt{}$	$\checkmark$		√	√	√	$\sqrt{}$
F (albite)	√						√		
F (sanidine)					√				
F (andradite)						√			
Calcite					$\checkmark$			√	
Apatite		<b>√</b>			√		√		
Forsterite							√	√	$\sqrt{}$
Enstatite		$\checkmark$				√			
Maghemite		$\checkmark$							

the Raman spectra in most of the samples studied. Calcite, apatite, forsterite (as olivine) and enstatite (as pyroxene) were also easily identified by micro-Raman spectroscopy in some of the samples. The Raman signature of maghemite from lepidocrocite has been observed in sample SA27.

A comparative study of the mineralogical composition of the ceramic shreds was made, using the well established techniques in this field, as XRD [12] and XRF [9, 10]. The obtained results from the three applied techniques are in good agreement, although in some cases Raman spectroscopy is more informative.

#### Conclusions

A spectroscopic analysis by micro-Raman spectroscopy on medieval pigments and glazed ceramics provides information on (a) the type of pigments used in wall paintings and (b) the technology of manufacturing of ceramics, i.e. the firing temperature of the ceramics glazes as well as the mineralogical composition of the ceramics body.

- (a) The characterization and identification of the pigments used in the wall paintings remains one of the most important analytical tasks in characterization of the art objects. It provides artistic, historical and technological information and enables correct and appropriate approach during conservation and restorations procedures.
- (b) Non-destructive Raman analysis offers considerable data and information about the technological and manufacturing processes of medieval glazed ceramics. The data recaptured from the polymerization indexes ( $I_p$ ) of the studied glazes provide information on their manufacturing processes, such as firing temperatures. On the other hand, the mineralogical composition of the ceramics body can be easily studied by point-to-point micro-Raman spectroscopy, by mapping the ceramics body in a chosen area, which leads to identification of numerous minerals in ceramics. The mineralogical data obtained by XRD [12] and XRF [9, 10] techniques on the same samples were compared with the data obtained by micro-Raman spectroscopy. Although time consuming, micro-Raman spectroscopy was proven to be accurate and precise and could be used in mineralogical assessment of ceramics.

# Acknowledgments

The authors would like to thank Ms Ljubinka Dzidrova from the Museum of Macedonia for providing the samples for pigment analysis and Dr. Branislav Ristevski, from the Institute of Old Slavonic Studies in Prilep for providing the samples of Byzantine glazed ceramics. The micro-Raman spectrometer LabRam 300 has been obtained through the FP6 project *Reinforcement of the Research Capacities of the Spectroscopy Laboratory for Archaeometry* (ForcaSpeclab) financed by the EU Commission.

#### References

[1] P. Vandenabeele, H. G. M. Edwards, L. Moens, Chem. Reviews, 2007, 675–686.

- [2] B. Minčeva-Šukarova, O. Grupče, V. Tanevska, L. Robeva-Čukovska, S. Mamučevska-Miljković, *Maced. J. Chem. Chem. Eng.*, 2007, **26**, 103–110.
- [3] I. M. Bell, R.J.H. Clark, P.J. Gibbs, Raman Spectroscopic Library of Natural and Synthetic Pigments (pre-~1850), *Spectrochim. Acta*, 1997, **A 53**, 2159–2179.
- [4] *Skopje Fortress Archaeological Excavations 2007 and exhibition*, Museum of the City of Skopje, Skopje, 2007.
- [5] B. Minčeva-Šukarova, V. Tanevska, Lj. Džidrova, O. Grupče, K. Ristov, *IRUG 8, The Eighth Biennial Conference of the Infrared and Raman Users Group*, March 2008, Vienna, Austria, Book of Abstracts, **Poster 14**, p.80.
- [6] Ph. Colomban, J. Non-Cryst. Solids, 2003, 323, 248–258.
- [7] Ph. Colomban, in *Raman Spectroscopy in Archaeology and Art History*, Eds. E.HGM Edwards and JM Chalmers, Royal Soc. Chem. London, 2005, pp. 192–206.
- [8] Ph. Colomban, A. Tournie, L. Bellot-Gurlet, J. Raman Spectrosc., 37, 841–852 (2006).
- [9] V. Tanevska, P. Colomban, B. Minčeva-Šukarova, O. Grupče, V. Andrić, A. Tourrnie, ICOSECS 5, Book of Abstracts, Vol.1, ACH-47, p. 93, September 2006, Ohrid, Republic of Macedonia.
- [10] V. Tanevska, P. Colomban, V. Andrić, O. Grupče, B. Minčeva-Šukarova, A. Tournie, Cultural heritage and Science: An Interdisciplinary Approach for the Conservation of Museum Objects, Programme and abstracts, p. 87, Ghent, Belgium, December 2006.
- [11] V. Tanevska, P. Piccardo, Ph. Colomban, O. Grupče, B. Minčeva-Šukarova, *EMAC'07 9<sup>th</sup> European meeting on Ancient ceramics*, October 24–27, 2007, Budapest, Hungary, Program and Abstracts, **P-51**, p. 121.
- [12] B. Minčeva-Šukarova, V. Tanevska, O. Grupče, Lj. Damjanović, GeoRaman '08 8<sup>th</sup> International Conference on Raman Spectroscopy Applied to the Earth Sciences Sensu Latu, June 2008, Ghent, Belgium, Book of Abstracts, p. 102.

# EVIDENCE FOT THE EXISTANCE OF INTERACTIONS BETWEEN WATER MOLECULE AND ARYL RINGS IN MUTUAL PARALLEL ALIGNMENT

G.V. Janjić, B.D. Ostojić and S.D. Zarić

<sup>1</sup>IHTM, University of Belgrade, Njegoševa 12, P. O. Box 473, 11001 Belgrade, Serbia
<sup>2</sup>Faculty of Chemistry, University of Belgrade, Studentski trg 16, P.O. Box 158, 11001 Belgrade,
Serbia

#### **Abstract**

An analysis of crystal structures from the Cambridge Structural Database (CSD) was performed in order to study interactions of water molecule with C<sub>6</sub> aromatic group. The interactions of water molecule where whole molecule or one of the O-H bonds is parallel to the C<sub>6</sub> aromatic rings were recognized. The number of observed interactions was 720. The observed normal distances between the OH bond and the plane of the aryl ring are in the range of the distances previously found to be typical for the stacking interactions of two aromatic rings. *Ab initio* calculations were performed on the model systems and the energies were calculated at the CCSD(T) complete basis set limit.

#### Introduction

The  $OH/\pi$  interactions of water molecule with the  $\pi$ -electron cloud of aromatic groups can play important role enabling interactions of nonpolar groups with polar solvent. These interactions were observed in various molecular systems [1-5]. The study of  $OH/\pi$  interactions between water molecule and aromatic groups of amino acids in proteins confirmed the relatively frequent occurrence of aromatic  $OH/\pi$  hydrogen bonding in protein crystal structures [2,3].

Besides XH/ $\pi$  aromatic interactions, there are abundant aromatic interactions such as  $\pi$ - $\pi$  stacking that also play important role for protein structure and protein-ligand recognition. The Protein Data Bank studies revealed that the NH/ $\pi$  interactions are outnumbered by the aromatic-amide stacked structures [6].

In this paper we present the intermolecular interactions of water molecule where whole molecule or one the O-H bonds is parallel to the  $C_6$  aromatic rings. The results were obtained by analyzing the interactions in crystal structures from the CSD and by *ab initio* calculations of the benzene-water dimer model systems including the CCSD(T) level of electron correlation correction.

#### **Results and Discussion**

The crystal structures involving non coordinated water molecule and C<sub>6</sub>-aromatic group were screened for intermolecular contacts. A survey of crystal structures revealed that the total number of parallel contacts is 720. We found the parallel alignments of the whole water molecule (79 contacts, A set) and parallel alignments of one of the O-H bonds (B and C sets). When one of the O-H bonds is in

parallel alignment another O-H bond can be in positions ranging from the upward orientation from the aromatic ring and the parallel alignment to the orientation toward the  $\pi$ -system of the aromatic ring. In the last case the dominant interaction is  $OH/\pi$  interaction. The number of intermolecular contacts where the contribution of parallel alignment of one O-H bond is dominant is 391 contacts (B set).

The analysis of the geometries of the sets A and B pointed out that most water molecules are positioned close to the edge of the aromatic ring or outside of the ring - above the region of the C-H bonds. The normal distances of the O-H bonds in parallel alignment are between 3.0 and 4.0 Å. They cover the range typical for stacking interactions of two aromatic rings, 3.3 - 3.8 Å.

Ab initio calculations were done on the model systems based on the geometries observed in the crystal structures. The calculation of the intermolecular interaction potentials were performed at the MP2 and CCSD(T) levels using the Dunning's correlation consistent basis sets (cc-pVTZ, cc-pVTZ, cc-pVQZ, aug-cc-pVDZ, aug-cc-pVDZ, aug-cc-pVDZ). The basis set superposition error (BSSE) was calculated using the standard Boys-Bernardi counterpoise procedure. The method of Helgaker et al. for the estimation of MP2 and CCSD(T) interacting energies at the basis set limit was used. The Gaussian98 series of programs were employed.

The model systems of the water-benzene dimers were made based on the geometries observed in crystal structures. The ab initio calculations were done on a number of model systems with the parallel alignment of the whole water molecule and with one of the the O-H bonds parallel to the ring plane. The most stable structure with the parallel alignment of the whole water molecule  $(A_1)$  has the calculated CCSD(T) basis set limit energy  $E_{CCSD(T)limit} = -1.45$  kcal/mol. The calculated model systems with the water molecule above the ring have smaller interacting energy. The interacting energy of the  $A_2$  dimer is  $E_{CCSD(T)limit} = -0.90$  kcal/mol. The most stable model system of all considered has one O-H bond parallel to the C-H bond of the benzene with the oxygen atom above the hydrogen atom of the benzene (B<sub>1</sub>) with the interacting energy  $E_{CCSD(T)limit} = -1.60$  kcal/mol. Similar to the model systems A, the B structures with the water molecule above the ring have smaller interacting energy, the  $B_2$  structure has interactions energy  $E_{CCSD(T)limit} = -0.78$  kcal/mol. In all model systems the calculated normal distances are shorter for the water molecule above the C-H region (3.0 - 3.3 Å) than above the ring (3.4 - 3.6 Å). The calculated normal distances are in agreement with the distances observed in the similar interactions in the crystal structures.

The calculated energy for the  $OH/\pi$  interaction is  $E_{CCSD(T)limit} = -3.29$  kcal/mol, showing that the  $OH/\pi$  interactions [7] are significantly stronger than the parallel-alignment interactions. In spite of that, in the crystal structures parallel alignments occur quite frequently. The explanation can be additional stabilization achieved since in the parallel alignment all atoms of the water molecule can form classical hydrogen bonds simultaneously. Such hydrogen bonds were observed in the crystal structures.

#### Conclusion

The observed parallel-alignment interactions in crystal structures confirm that this kind of interaction like other weak interactions coexists or is in competition with much stronger interactions. The *ab initio* calculations at the CCSD(T) complete basis set limit support the assumption that observed parallel alignments are consequence of attractive interactions of the water and aryl rings. The results indicate that the water molecule could be involved in parallel-alignment interactions with other aromatic systems that are part of various systems, including biomolecules.

- [1] D. Braga, F. Grepioni, and E. Tadesco, Organometallics, 1998, 17, 2669.
- [2] T. Steiner and G. Kolelner, J.Mol.Biol., 2001, 305, 535.
- [3] T. Steiner, Biophys. Chem., 2002, 95, 195.
- [4] M. Milčić and S. D. Zarić, Eur. J. Inorg. Chem., 2001, 2143.
- [5] M. K. Milcic, Z. D. Tomic, and S. D. Zaric, Inorg. Chimica Acta, 2004, 357, 4327.
- [6] J. B. O. Mitchell, C. L. Nandi, I. K. McDonald, and J. M. Thornton, J.Mol. Biol., 1994, 239, 315.
- [7] S. Tsuzuki, K. Honda, T. Uchimaru, M. Mikami, K. Tanabe, J.Am.Chem.Soc., 2000, 122, 11450.

## INTERMOLECULAR INTERACTIONS BETWEEN EFFLUX PUMP SUBSTRATES AND MDR MODULATORS

#### M. Zloh and S. Gibbons

School of Pharmacy, 29-39 Brunswick Square, London, WC1N 1AX, United Kingdom.

#### Abstract

In this paper we describe the use of molecular modelling, NMR spectroscopy and mass spectrometry to investigate small molecule-small molecule interactions between substrates of multidrug-resistance (MDR) and inhibitors (modulators) of MDR pumps. These MDR pumps confer resistance to many cells including bacteria, plasmodia and cancer cells leading to resistance to certain drugs.

We show that computationally, substrates of efflux processes and modulators have the capacity to form complexes and this can be supported by NMR and mass spectral data. The formation of such complexes may facilitate entry of drugs into the cell and may also make the drug 'opaque' to efflux once inside the cell. The complex could then dissociate to yield the drug and modulator.

#### Introduction

MDR (multidrug resistance) causes many forms of resistance in human malignancies. One prominent MDR mechanism in tumours involves membrane-bound efflux pumps, which actively export anticancer agents from the cell resulting in a low ineffective concentration of the therapeutic. It is still not fully known how modulators of these MDR pumps function since many modulators are structurally unrelated and from different chemical classes.

Our previous studies have indicated that there is a relationship between MDR modulation and the molecular properties of complexes between MDR modulators and drugs which are substrates of efflux pumpss [1,2].

We therefore proposed a novel mechanism of MDR modulation, where small molecule – small molecule interactions could play an important role. Here we examine experimentally the possibility of complex formation between some MDR substrates (e.g. the drugs doxorubicin and vinblastine) and efflux pumps modulators (verapamil, theanine and reserpine) shown in Scheme 1.

#### Methods

Molecular modelling studies were carried out using the Schrodinger suite with integrated Maestro and MacroModel software. All molecules were prepared using

the Ligprep module. The conformational search was carried out on all complexes using 5000 steps of Monte Carlo multiple minimum (MCMM) conformational search analysis. The MMFFs force field was employed with the implicitly represented aqueous environment using the GB/SA solvation method.

1D <sup>1</sup>H NMR spectra were acquired on a BRUKER AVANCE 500 MHz spectrometer at 298K. Samples were dissolved in D<sub>2</sub>O and spectra were referenced using the internal standard TSP.

ESI-MS spectra were acquired using a Navigator LC-MS system in the positive mode.

#### **Results and Discussion**

Verapamil is known to restore the efficacy of vinblastine against MDR cancer cells [3]. The complexation is predicted by molecular modelling (Figure 1a), which was confirmed by NMR spectroscopy. The change of chemical shifts of vinblastine aromatic hydrogen atoms was observed after verapamil addition. This change was most prominent for atoms that are surrounded by verapamil in the molecular model (Figure 1b). The complex formation was also confirmed at lower concentrations using ESI-MS spectrometry with a peak at 1264.5 *m/z* in the ESI spectrum (Figure 1c).

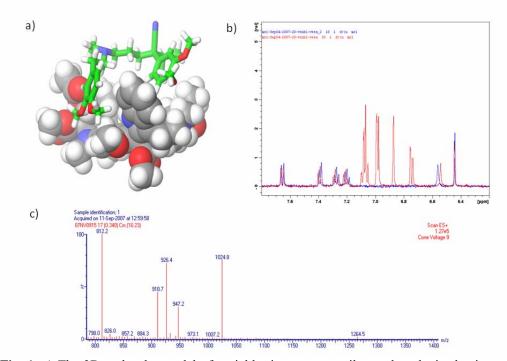


**Fig. 1**. **a)** The 3D molecular model of a vinblastine – verapamil complex obtained using conformational search analysis (vinblastine in CPK representation, verapamil is depicted as sticks with carbon atoms in green). **b)** The expansion of a 1D <sup>1</sup>H NMR spectrum of vinblastine (blue) and the mixture of vinblastine and verapamil (1:1) in red at 298K and 500 MHz. **c)** ESI-MS spectrum of a vinblastine-verapamil mixture.

Reserpine is a natural product that has exhibited modulatory activity for a range of efflux pump substrates [3]. The molecular model of the complex is predicted by molecular modelling (Figure 2a). The evidence of complex formation was found in the NMR spectrum, where the change of chemical shifts of vinblastine aromatic protons was observed, in a similar fashion to that found in the vinblastine – verapamil complex (Figure 2b). The complex between vinblastine, a reserpine fragment,  $SO_4^-$  and  $Na^+$  was observed at lower concentrations using ESI-MS spectrometry with a peak at 1328.8 m/z (Figure 2c).

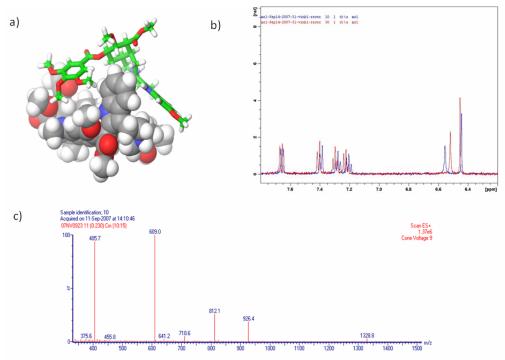


**Fig. 2. a)** The 3D molecular model of a vinblastine – reserpine complex obtained using conformational search analysis (vinblastine in CPK representation, reserpine is depicted as sticks with carbon atoms in green). **b)** The expansion of a 1D <sup>1</sup>H NMR spectra of vinblastine (blue) and a mixture of vinblastine and reserpine (1:1) in red at 298K and 500 MHz. **c)** ESI-MS spectrum of a vinblastine-reserpine mixture.

Theanine, a green tea constituent, potentiates the activity of doxorubicin [4] even though it is a relatively small molecule to occupy a broad binding site of efflux pumps. Although molecular modelling predicts complex formation (Figure 3a) and the presence of theanine induces chemical shifts changes of doxorubicin (Figure 3b), we could not prove existence of complexes by MS. It is notable that chemical shift changes are more prominent in a solution of 1:0.5 doxorubicin to theanine. The MS spectra of doxorubicin-theanine were possibly not observed due to the fragmentation of the doxorubicin in the ESI-MS conditions. Further work is need to be conducted to optimize the experimental conditions.

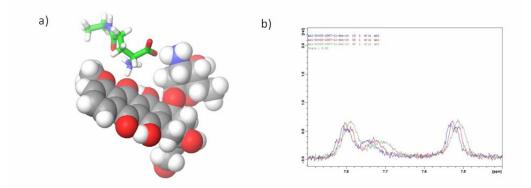


**Fig. 3**. **a)** The 3D molecular model of a doxorubicin – theanine complex obtained using conformational search analysis (doxorubicin in CPK representation, theanine is depicted as sticks with carbon atoms in green). **b)** The expansion of 1D <sup>1</sup>H NMR spectra of doxorubicin (blue), mixture of doxorubicin and theanine (1:0.5) in green and mixture of doxorubicin and theanine (1:1) in red at 298K and 500 MHz.

The interactions between small molecules are evident in solutions, although at concentrations higher than the biologically active concentrations. These interactions might not fully explain modulation and replace the current views on the mechanisms of MDR modulation, but it may account for some effects of modulation that are still not fully understood. The search for novel modulators could benefit from considerations of possible small molecule – small molecule interactions particularly in the area of anti cancer drugs and modulators.

#### **Conclusions**

MS and NMR experiments have confirmed that formation of non-covalent complexes between these small molecules is possible *in vitro*. We are proposing that these inhibitors could function as 'escorts' by binding therapeutics outside the cell and facilitating their entry into the cell and protecting them from efflux. Further work is underway to confirm the complex formation in cells and *in vivo*.

- [1] M. Zloh, G. W. Kaatz, S. Gibbons Bioorg. Med. Chem Lett., 2004, 14, 881-885.
- [2] M. Zloh, S. Gibbons, Theor. Chem. Acc. 2007, 117, 231-238.
- [3] T.-c. Chou et al. Proc. Natl. Acad. Sci. USA, 1998, 95, 8369–8374
- [4] T. Sugiyama, Y. Sadzuka, Biochim Biophys Acta., 2003, **1653**, 47-59.

# A SPECTROSCOPIC INVESTIGATION OF STABILIZED DC ARGON ARC BY POWER MODULATION TECHNIQUE

J.J. Savović, D.P. Ranković, M. Stoiljković and M.M. Kuzmanović

<sup>1</sup>Laboratory of Physical Chemistry, Institute Vinča, P.O. Box 522, 11001 Belgrade, Serbia <sup>2</sup>Faculty of Physical Chemistry, University of Belgrade, P.O. Box 137, 11000 Belgrade, Serbia

#### **Abstract**

Spatial distribution of delayed responses of argon and hydrogen spectral line and continuum intensity to square power modulation was investigated in order to get better insight into the processes occurring in argon dc arc plasma. The power was abruptly changed between stationary values, 9 and 3.5 A. For these currents steady state radial distributions of electron number density, temperature and emission intensity were measured. On part of the discharge, radial profiles the power drop and the power jump are both accompanied by intensity peaks which may be explained by displacement of the arc core axis and change in the arc core diameter during the power modulation.

#### Introduction

In spite of the fact that direct current argon arcs have various applications in different fields, and are intensively studied, a complete understanding of excitation mechanisms and transport processes in some types of plasma is not yet accomplished. In addition to well known plasma diagnostic techniques, these processes could be studied by monitoring the plasma behavior (spectral emission responses) during and after the interruption or modulation of plasma power. A square modulation of plasma power permits a variety of combinations of low and high current duration times thus making it convenient for studying slow processes in plasmas. The method of power modulation has often been used for studying inductively coupled plasmas [1].

This work deals mainly with delayed responses of argon and hydrogen line and background intensities, to square modulation of the arc current, in order to get better understanding of the processes in the arc column of argon dc plasma. For the above purpose, we have measured the radial distribution of electron number density, temperature and emission intensity in the plasma arc column for the arc currents of 9 and 3.5 A, between which the power was alternately switched. Electron number densities were evaluated from measured  $H_{\beta}$  line profiles, and corresponding temperatures were evaluated from measured absolute emissivity of argon line.

# **Experimental**

A detailed description of the U-shaped dc argon arc with combined gas vortex and wall stabilization, operating at atmospheric pressure was described in reference [2].

In order to differentiate between the two sides of arc column we labeled the displacements from the arc axis with the plus (+) and minus (-) signs. The plus side is the one from which argon gas carrying aerosol is introduced into plasma. The modulation period was 250 ms with variable low current interval up to 50 ms. These modulation parameters prevent the superposition of effects coming from subsequent disturbances which means that discharge has enough time to return to stationary state before the next disturbance occurs. The time constant for a current change was better than 5  $\mu s$ .

#### **Results and Discussion**

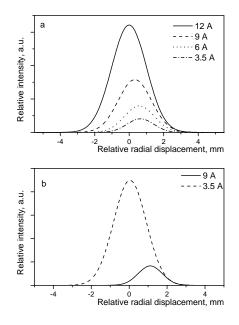


**Fig. 1.** Radial distribution of Ar I 696.54 nm line intensity for different arc current. Argon flow a) 2.7 L/min. b) 2.0 L/min.

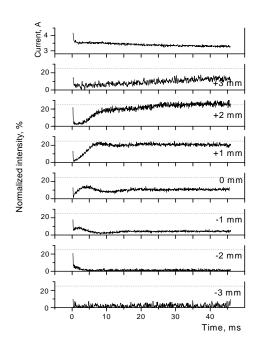


**Fig. 2.** Temporal evolution of the Ar I 696.54 nm spectral line after the current drop.

Radial distribution of Ar I 696.54 nm line intensity for different arc currents and 2.7 L/min argon flow is shown in Fig. 1a. The arc axis for the arc current of 12 A is represented as zero position on the x-axis. As it may be seen in Fig. 1a, by lowering the arc current the arc axis is displaced toward the (+) side while the radial dimension of the arc core is decreased simultaneously. Displacement that is even more evident is observed with lower argon flow (2 L/min), Fig. 1b. So, transition of the arc column (displacement and width change) between two stationary regimes, that correspond to upper and lower current, must be taken in considerations when we elucidate the line intensity evolution, caused by power modulation.

For elements with high ionization potential like Ar and H, and for continuum radiation there is a pronounced asymmetry in radial distribution of delayed responses to power modulation. The observed asymmetry can not be explained by asymmetry in radial distribution of plasma parameters. On part of the radial profiles, both a current jump and a current drop are accompanied by line intensity increase. As these are the same parts of radial profiles where displacement of the discharge axis takes place, it is obvious that delayed responses are actually a consequence of this displacement. To support this assumption we have varied experimental conditions that are related to the arc axis position and the arc column diameter such as carrier gas flow and arc current.

#### Conclusion

The obtained results were in accordance with previous conclusions: intensity peak increase and asymmetry were more pronounced for larger displacements of the arc axis. Displacement of the arc column after the power modulation must be a consequence of asymmetrical introduction of a carrier gas flow. Delayed responses of analyte line intensity (metal atoms with ionization potential usually lower than 8 eV) show completely different evolutions [2, 3] and for their interpretation, it is essential to understand the evolutions of a carrier gas and continuum, i.e. to take the arc column displacement in consideration.

# Acknowledgments

This work has been financially supported by Ministry of Science of the Republic of Serbia under Project No. 142065.

- [1] C. E. Hensman, L. R. Drake and G. D. Rayson, Spectrochim. Acta, 1997, **52B**, 503-515.
- [2] M. M. Kuzmanović, M. S. Pavlović, J. J. Savović, M. Marinković, Spectrochim. Acta, 2003, 58B, 239-248.
- [3] M. Kuzmanović, J. Savović, M. Pavlović, M. Stoiljković, A. Antic-Jovanovic and M. Marinkovic, J. Serb. Chem. Soc., 2005, **70**, 1033-1040.

# THEORY AND PRACTICE IN THE ANALYSIS OF POLARIZED IR REFLECTANCE SPECTRA OF LOW SYMMETRY SINGLE CRYSTALS

#### V. Ivanovski

Institute of Chemistry, Faculty of Natural Sciences and Mathematics, University of Sts. Cyril and Methodius, Arhimedova 5, 1000 Skopje, Republic of Macedonia

#### Abstract

An overview on the theoretical and experimental conditions in the investigation of single crystals, with emphasis on crystals crystallizing in the monoclinic crystal system is presented. The main idea is to explain in short how the complexity of the theories applied and the demands in the experimental conditions increases on lowering the crystal symmetry. The procedure of dispersion analysis (DA) employed on the IR polarized spectra of monoclinic Tutton salts single crystals, is explained. The results of the performed DA in these investigations are discussed in the course of the importance of such kind of analysis in the obtainment of the vibrational properties of low symmetry crystals.

#### Introduction

The interest towards the investigation of single crystals using IR reflectance spectroscopy follows from several reasons: it is in some cases (when polishing of the crystal plane can be avoided) a non-destructive technique; reflection is more easily applied than transmittance (for transmittance technique, samples with thickness around 10 µm are required [1]); investigation of low symmetry crystals using sand p-polarized light give insight into the mixed modes [2, 3]. Optical, dielectric and vibrational characteristics of the investigated material can be obtained in this way [4]. By optical characteristic we recognize the values of the complex index of refraction, i.e. its real and imaginary part [5, 6]. The dielectric characteristics of the sample are described through the real and the imaginary part of the dielectric function. Vibrational characteristics of materials can be characterized by the frequencies, oscillator strengths, damping constants, and orientation of the transition dipole moments of the oscillators in space.

The way in which the experiment is set, depends on the crystal system in which the crystal crystallizes and theories developed for the light propagation and reflection in those crystal systems [7]. The experiment is most easily performed on crystals crystallizing with cubic symmetry and is most complicated for triclinic crystals. In case of cubic crystals a complete optical isotropy exists, thus a care has to be taken only concerning the angle of incidence. If the angle of incidence is quite different from normal incidence (> 10°), then, reflectance function will depend on the polarization state of the radiation [7]. The results of the experiment though, will not depend on the crystal face of reflection. In optically uniaxial crystals, reflectance of the mixed ordinary and extraordinary ray will exist if the polari-

zation is neither s- nor p-polarized [8]. Optically biaxial crystals are characterized with two optical axes. Nevertheless, dielectric properties of the crystal will depend on the crystal system. For an arbitrary angle of incidence and face of the crystal, the task in acquiring the optical properties is quite difficult. Nevertheless there is a simplification in the theory as will be explained further in the text. In the most complicated case (the triclinic), to the knowledge of the author, only one paper concerned with the obtainment of vibrational parameters in  $CuSO_4 \cdot 5H_2O$  has been reported so far [9].

The intention of this work is to give an overview on the ways that single crystals of symmetries lower than cubic can be treated in order for the optical, dielectric and vibrational properties using specular IR reflected radiation to be obtained. The method of dispersion analysis (DA) and the results of the spectral treatment is presented on two Tutton salts single crystals  $K_2Ni(SO_4)_2 \cdot 6H_2O$  and  $(NH_4)_2Ni(SO_4)_2 \cdot 6H_2O$ , in the  $v_3(SO_4^{2-})$  spectral region [10, 11]. Tutton salts represent a large family of isomorphous compounds with a common formula  $M'_2M''(XY_4)_2 \cdot 6H_2O$  where M' stands for univalent ions like:  $K^+$ ,  $NH_4^+$ ,  $Rb^+$ ,  $Cs^+$ ; M'' for:  $Ni^{2+}$ ,  $Co^{2+}$ ,  $Mg^{2+}$ ,  $Cu^{2+}$ ,  $Zn^{2+}$ ,  $Fe^{2+}$ ,  $Cr^{2+}$ . X = S or Se when Y = O, but X = Se when Y = F. More on the structure and vibrational properties of these crystals can be found in refs. [12, 13] and [14, 15].

### Crystal optics – background

The Fresnel expression for the EM wave propagating in crystal with principal dielectric axes values  $\varepsilon_x$ ,  $\varepsilon_y$ ,  $\varepsilon_z$  and projections of the unit wave vector  $\mathbf{k}/k$  on these axes  $(s_x, s_y, s_z)$  is derived out of the Maxwell equations and can be written in the following form [16]:

$$\varepsilon_{x}(\varepsilon_{y}-n^{2})(\varepsilon_{z}-n^{2})s_{x}^{2}+\varepsilon_{y}(\varepsilon_{x}-n^{2})(\varepsilon_{z}-n^{2})s_{y}^{2}+$$

$$+\varepsilon_{z}(\varepsilon_{y}-n^{2})(\varepsilon_{y}-n^{2})s_{z}^{2}=0$$
(1)

where n is the complex index of refraction in the direction of propagation of the wave. In cubic crystals, due to the isotropy, the solutions of Eq. (1) are three waves (two transversal and one longitudinal) with same index of refraction. In optically uniaxial crystals the two solutions for the index of refraction of the two transversal waves are,

$$n_o^2 = \varepsilon_x$$
,  $n_{eo}^2 = \frac{\varepsilon_x \varepsilon_z}{\varepsilon_x \sin^2 \theta + \varepsilon_z \cos^2 \theta}$  (2)

where angle  $\theta$  is the angle formed between the z axis and the direction of **k**. The polarization of the radiation of the "ordinary" ray  $(n_o)$  is perpendicular, while that of the "extraordinary"  $(n_{eo})$  parallel to the plane formed by the z axis (c crystallographic) and the direction of **k**. In optically biaxial crystals, two independent waves

exist for every direction of the **k** vector being linearly polarized for non-absorbing and elliptically polarized for absorbing [5, 7]. In orthorhombic crystals, when the wave vector **k** is in the yz, ( $s_x = 0$ ), Eq.(1) give solutions for n similar as for uni-axial crystal, [Eq.(2)]. When **k** is along one of the principal axes (z axis), then  $s_x = s_y = 0$  and the two transversal waves will have complex indexes of refraction given by,

$$n_{x}^{2} = \varepsilon_{x}; n_{y}^{2} = \varepsilon_{y} \tag{3}$$

In monoclinic crystals this further complicates because the eigenvectors of the  $\varepsilon_{x,z}$  dielectric tensor are different for different frequencies, meaning that Eq. (1) can not be used, since it is expressed employing principal dielectric vectors. Since the y axis is symmetry fixed and if in the experiment the condition  $s_y = 0$  is satisfied, the solution for the index of refraction having polarization of the wave along the y axis is

$$n^2 = \varepsilon_{v} \tag{4}$$

### Reflectance function and dispersion analysis

From the previously said a conclusion can be derived that for crystals with symmetry as low as orthorhombic, IR active vibrations can always be separately investigated using normal incidence of the radiation on a principal dielectric plane with polarization along one of the principal axes (actually near-normal incidence is what can be physically attained in the experiments). This is possible since the direction of the radiation determined by the vector  $\mathbf{k}$ , does not change on entering the crystal. Reflectance function for the normal incidence is then,

$$R = \left| \frac{1 - n}{1 + n} \right|^2 \tag{5}$$

In optically uniaxial crystals the reflectance function will also depend on the crystal's reflecting plane. When the incidence radiation is perpendicular but the plane is not the principal dielectric one, the reflectance will be a mixture of ordinary and extraordinary ray. The case of non-normal incidence on a principal plane is explained in ref. [17], while the non-normal incidence on a non-principal plane can be found in ref. [18].

In monoclinic crystals, recording the spectra of IR active modes with transition dipole along the *b* crystallographic axis can be easily performed under experimental condition of normal incidence on the plane containing the axis, with polarization along the axis, so that Eqs.(4 and 5) are valid. For modes with transi-

tion dipole moments in the ac crystal plane, though, it is not possible to separately observe the corresponding bands in the spectra. This is due to the presence of the non-diagonal terms  $\varepsilon_{xz}$  in the dielectric tensor, meaning that every mode contribute more or less to the dielectric function and by that to every band, for arbitrary angle of polarization. The way to analyze IR active modes with transition dipole moments appearing in the ac crystal plane is to record at least three reflectance spectra with different polarization directions (cf. fig. 1; usually  $\phi = 0$ °, 45° and 90°) under normal incidence of the radiation. Afterwards, a least square non-linear fitting for the reflectance model function in Eq. (6) is performed in order to find the vibrational parameters [19, 20].

$$R_{x} = |r_{xx}|^{2} + |r_{xz}|^{2} \tag{6}$$

In the Eq. (6), the subscripts refer to the external XYZ coordinate system (cf. fig. 1) [4, 10, 11]. The dielectric tensor, characterizing the crystal ac plane, is written in internal xyz coordinates (fixed to the crystal) and given by:

$$\begin{pmatrix}
\varepsilon_{xx} & \varepsilon_{xz} \\
\varepsilon_{xz} & \varepsilon_{zz}
\end{pmatrix} = \begin{pmatrix}
\varepsilon_{xx}^{\infty} & \varepsilon_{xz}^{\infty} \\
\varepsilon_{xz}^{\infty} & \varepsilon_{zz}^{\infty}
\end{pmatrix} + \\
+ \sum_{k=1}^{N} \frac{S_{k}^{2}}{\omega_{tk}^{2} - \omega^{2} - i\omega\gamma_{tk}} \begin{pmatrix}
\cos^{2}\theta_{k} & \sin\theta_{k}\cos\theta_{k} \\
\sin\theta_{k}\cos\theta_{k} & \sin^{2}\theta_{k}
\end{pmatrix}$$
(7)

The  $S_k^2$  is the oscillator strength,  $\omega_{tk}$  – the transversal phonon frequency,  $\gamma_{tk}$  – the transversal attenuation constant of the k–th oscillator, while  $\varepsilon^{\circ}_{ij}$  is the background permittivity.

#### Results and discussion

In order for the DA of Tutton salt single crystals to be performed, the experiment was set as follows. The polished ac crystal face was rotated clockwise, meaning that the polarization vector was rotated counter clockwise (fig. 1) when recording spectra for a particular angle of polarization  $\phi$ .

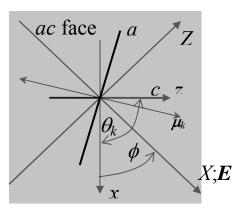


**Fig. 1.** xyz – internal right-handed crystal-fixed orthogonal system; XYZ – external right-handed orthogonal system. a and c – crystallographic axes (b axis is perpendicular to the view),  $\beta$  – crystallographic angle, E – external electric field vector,  $\mu_k$  – transition dipole moment vector of the k-th mode,  $\phi$  - angle of polarization.

The incidence angle of 5 ° was employed in the experiment, so that Eqs. (6, 7) were applicable. In order for the Eq. (7) to be used in conjunction with Eq. (6), a similarity transformation, converting the permittivity tensor from internal xyz into external XYZ coordinate system had to be performed [4, 10, 11]

$$\varepsilon_{XZ} = \begin{pmatrix} \cos \phi & \sin \phi \\ -\sin \phi & \cos \phi \end{pmatrix} \varepsilon_{xz} \begin{pmatrix} \cos \phi & -\sin \phi \\ \sin \phi & \cos \phi \end{pmatrix}$$
(8)

The investigations performed on eight Tutton salt single crystals (cf. ref. [11]) proved that the biggest change in the polarized spectra occurs when the univalent cation is changed (whether  $K^+$  or  $NH_4^+$ ). The  $v_3(SO_4^{2-})$  spectral region of Tutton salt representatives is given in fig. 2. For the salts containing  $K^+$ , a singlet band appeared for the angle  $\phi = 90^{\circ}$ , which is not a feature for the spectra of the  $NH_4^+$  containing salts. Due to the local symmetry of the sulfate ( $C_1$ ) and the factor group of the crystals ( $P2_1/a$  or  $C_{2h}^{5}$ ), three  $v_3(SO_4^{2-})$  mode components of  $A_u$  and the same number of  $B_u$  symmetry type are expected, which should lead to the appearance of three bands in the spectra for each symmetry type [14, 15]. As mentioned, pure  $B_u$  modes will be activated if the polarization direction is in the ac crystal plane, while the three of  $A_u$  type, if the polarization direction is along the b crystal axis.

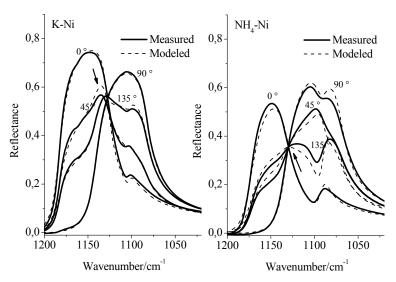


**Fig. 2.** Measured (solid line) and modeled (dashed line) polarized spectra for  $\phi = 0^{\circ}$ ,  $45^{\circ}$ ,  $90^{\circ}$ ,  $135^{\circ}$  of the  $v_3(SO_4^{2-})$   $B_u$  symmetry type mode components in  $K_2Ni(SO_4)_2 \cdot 6H_2O$  and  $(NH_4)_2Ni(SO_4)_2 \cdot 6H_2O$  single crystals. Extra bands in the spectra are indicated with arrows.

Just from the observation of the reflectance spectra, a conclusion on the number and frequencies of the bands is not possible without a DA performed. The results obtained from the performed DA on reflectance spectra of representative Tutton salts, given in Table 1, explain the peculiarity of the singlet band in K<sup>+</sup> containing samples. The orientation of the transition dipole moments for the three  $B_u$  symmetry type modes expressed through the angle  $\theta_k$  indicate two transition dipoles oriented close to the direction perpendicular to the c crystallographic axis ( $\phi = 0$ °), and one almost along the c axis ( $\phi = 90$ °). This is not the case for NH<sub>4</sub><sup>+</sup> Tutton salts (cf. Table 1). Thus, in K<sup>+</sup> containing salts, when the radiation has polarization along the c crystallographic axis, only one mode will be triggered and a singlet band will appear in the spectrum. Another gain from the performed DA is the correct obtainment of the transversal phonon frequencies, which is difficult for the spectra with an overlap between the bands. After the lifting of the degeneracy of the triply degenerated  $v_3(SO_4^{2-})$  mode, component frequencies are still close, producing overlap of the reflectance bands.

**Table 1.** Best fit parameters for the transversal and longitudinal modes in the two Tutton salts. The complete data can be found in ref. [11]

	$\omega_{\rm l}/{\rm cm}^{-1}$	$S_1$ /cm <sup>-1</sup>	$ heta_{ m l}$ /°	$\omega_2$ /cm <sup>-1</sup>	$S_2$ /cm <sup>-1</sup>	$\theta_2$ /°	$\omega_3$ /cm <sup>-1</sup>	$S_3$ /cm <sup>-1</sup>	$\theta_3$ /°
K-Ni	1128.6	514.5	8.1	1101.6	124.7	21.0	1083.3	507.8	103.5
NH4-Ni	1131.6	438.6	176.0	1089.8	255.5	32.6	1070.9	514.9	92.8

$\omega_{l1}/\text{cm}^{-1}$	$\theta_{l_1}$ /° $\omega_{l_2}$ /cm <sup>-1</sup>	$\theta_{l_2}$ /° $\omega_{l_3}$ /cm <sup>-1</sup>	$ heta_{l_3}$ / $^{\circ}$
K-Ni 1187.7	2.3 1102.6	175.9 1142.6	96.8
NH <sub>4</sub> -Ni 1179.5	177.6 1092.7	145.8 1138.7	86.4

By calculating  $S_k^2$  (Table 1), one can conclude that phonons in the ac plane consist of two strong and one weak mode. The bands of the two strong modes seem to be partially overlapped due to the appearance of the third, resultant band in the spectra. As explained elsewhere [2, 3, 21] it is just an artifact originating from the summation of the bands in the overlapping region and not a distinct band originating from a particular vibration. The band of the weakest mode seems to be completely overlapped by one of the strong modes. The width of the overlap region can be judged by the LO-TO splitting, that is if the longitudinal frequencies are known. Transition dipole moments of the longitudinal phonons, apart from being frequency dependent, have different orientation from the transition moments of the corresponding transversal phonons. Pavinich and Belousov [22] have proposed a method that can be used in the evaluation of their longitudinal frequencies and the directions of the transition moments in monoclinic crystals under approximation of  $\gamma_k = 0$ . Similar calculations where performed in ref. [11]. There, the  $S_k$  values were firstly found from the non-linear fitting. Afterwards, these were used in acquiring the longitudinal frequencies from the condition that the determinant of the dielectric tensor at the longitudinal frequency  $\omega_{lk}$  should obtain zero value. After frequencies were found, the corresponding angles were obtained with the aid of Eq (9),

$$\tan \theta_{lk} = -\frac{\varepsilon_{xz}}{\varepsilon_{zz}}\bigg|_{\omega = \omega_{lk}} \tag{9}$$

In Table 1 are given the obtained values for the longitudinal frequencies in the two Tutton salts. The frequencies of the longitudinal and transversal phonons in Table 1 prove the abovementioned presumption about the existing overlap type between the bands of the three  $B_{\rm u}$  symmetry type modes [11].

#### Conclusion

The theoretical bases for the practical analysis of single crystals using polarized IR specular reflectance differ on the symmetry of the crystals to be investigated. In

monoclinic crystals the theory is the simplest if the polarized radiation is perpendicularly reflected from the ac crystal plane. Then, in order to perform DA and obtain the knowledge on the vibrational, dielectric and optical characteristics, at least three spectra at different polarization angles  $\phi$  are needed (four were used in this work). By performing a DA the orientations of the transition moments in the ac crystal plane can be obtained, something that is impossible to perform just by visual or Kramers-Krönig analysis of the polarized spectra.

- [1] J. Herranz, J.M. Delgado, Spectrochim. Acta, 1975, 31A, 1255.
- [2] V. Ivanovski, V.M. Petruševski, J. Mol. Struct., 2003, 650, 165.
- [3] V. Ivanovski, V.M. Petruševski, Spectrochim. Acta, 2004, A60, 1601.
- [4] V. Ivanovski, T. G. Mayerhöfer, J. Popp, V. M. Petruševski, Spectrochim. Acta, 2008, 69A, 629.
- [5] P. Yeh, Optical Waves in Layered Media, Wiley, New York, 1988.
- [6] J.C. Decius, R.M. Hexter, Molecular Vibrations in Crystals, McGraw-Hill, 1977.
- [7] M. Born and E. Wolf, Principles of Optics, Pergamon, Oxford, 1968.
- [8] M. Ishigame, T. Satō, T. Sakurai, Phys. Rev., 1971, 3, 4388.
- [9] J.R. Aronson, A.G. Emslie, P.F. Strong, Appl. Opt., 1985, 24, 1200.
- [10] V. Ivanovski, T.G. Mayerhöfer, J. Popp, Vibrat. Spectrosc., 2007, 44, 369.
- [11] V. Ivanovski, T.G. Mayerhöfer, J. Popp, Vibrat. Spectrosc., 2008, doi:10.1016/j.vibspec.2008.02.010
- [12] E.N. Maslen, S.C. Ridout, K.J. Watson, Acta Cryst., 1988, C44, 409.
- [13] E.N. Maslen, S.C. Ridout, K.J. Watson, Acta Cryst., 1988, C44, 412.
- [14] V. Ananthanarayanan, J. Chem. Phys., 1968, 48, 573.
- [15] R.G. Brown, S.D. Ross, Spectrochim. Acta, 1970, **26A**, 945.
- [16] R. Claus, Phys. Stat. Sol., 1978, 88B, 683.
- [17] L.P. Mosteller, Jr., F. Wooten, J. Opt. Soc. Am., 1968, 58, 511.
- [18] Th.G. Mayerhöfer, H.H. Dunken, Vibrat. Spectrosc., 2001, 25, 185.
- [19] M.V. Belousov, M.F. Pavinich, Opt. Spektrosc., 1978, 45, 771.
- [20] J.R. Aronson, A.G. Emslie, E.V. Miseo, E.M. Smith, P.F. Strong, Appl. Opt., 1983, 22, 4093.
- [21] V. Ivanovski, V.M. Petruševski, Marta K. Gunde, Spectrochim. Acta., 2005, 61A, 67.
- [22] V.F. Pavinich, M.V. Belousov, Opt. Spectrosc., 1978, 45, 881.

# STUDY OF THE SPATIAL REDISTRIBUTION OF THE ANALYTE SPECTRAL EMISSION IN DC ARC PLASMA INDUCED BY EXTERNAL OSCILLATING MAGNETIC FIELD

M.M. Stoiljković, M.S. Pavlović, M. Momčilović and J.J. Savović

<sup>1</sup> The Vinča Institute, Laboratory of Physical Chemistry, P. O. Box 522, 11001, Belgrade, Serbia <sup>2</sup> Faculty of Physical Chemistry, P. O. Box 137, 11001, Belgrade, Serbia

#### Abstract

Monochromatic digital imaging technique was developed for studying the spatial emission intensity distribution of atmospheric pressure dc arc plasma with aerosol supply. Arc plasma was imposed to external oscillating magnetic fields of strengths up to 12 mT and frequency of 50 Hz. This plasma was studied in a laterally resolved manner and at selected observation heights. The intensity enhancement and spatial redistribution of the analyte emission was evaluated and compared to the steady state plasma. The intensity enhancements were correlated with the attained speeds of plasma core movement. Spatial regions in the arc plasma with maximal emission enhancement are identified and clarified. The effect of the electrode polarity was also investigated.

#### Introduction

Several diffusion-driven processes lead to partial separation of chemical elements of different ionization energy in steady state dc arc plasma at atmospheric pressure [1]. This causes spatial (lateral-axial) non homogeneity in composition of analyte/carrying-gas (argon) mixture in plasma followed by the limited analyte emission. Finally, this limits the power of detection for some chemical elements in analytical application of dc arc plasma.

The applied oscillating magnetic field forces the hot arc core to hasty penetrate into the plasma periphery enriched with analyte vapor resulting in considerable emission enhancement of spectral lines of the most chemical species.

# Experimental

Description of the device for generation the stabilized dc arc argon plasma at atmospheric pressure with aerosol supply, as well as the entire experimental set-up for coupling arc plasma with external magnetic field are given elsewhere [1, 2, 3] A slit-less monochromator assembled with a Canon Power Shot G5 digital camera as detector were used for instantaneous tracing of monochromatic emission (at single wavelength) of the whole plasma volume.

A 50 Hz sine wave external magnetic field was oriented orthogonally to the axial electric field of the arc plasma. Such configuration generates lateral drifts of the current carrying arc core with appropriate speeds relatively to the surrounding gas.

#### Results

A series of images of steady-state arc plasma and plasma exposed to the magnetic field of progressive strengths are captured and relative enhancements of the analyte emission on characteristic spatial plasma regions are evaluated.

In steady state arc plasma several demixing processes governed by both axial and radial electric fields induce typical spatial distribution of analyte emission which is controlled by the partial depletion of element species with medium ionization energy in the hot arc core. This fact is demonstrated by the spatial distribution of emission intensity of barium ion line in the steady state arc plasma **Fig. 1.** (left). All along the plasma axial distance the lateral distribution of the line emission exhibits two peaks separated by a deep minimum at lateral distance belonging to the arc core itself, i.e. to the hottest plasma region.

When the plasma core was compelled to oscillatory drifts with appropriate amplitudes a considerable changing in spatial redistributions of emission intensity occurs. On distinctive axial distances (closer to the cathode plasma region; axial electric field is upward oriented) the most remarkable emission enhancement was recorded, **Fig. 2.** (right). Supposing the periodical path of the arc core is sine wave, the maximum enhancement corresponds the moment of reaching the maximum speed.

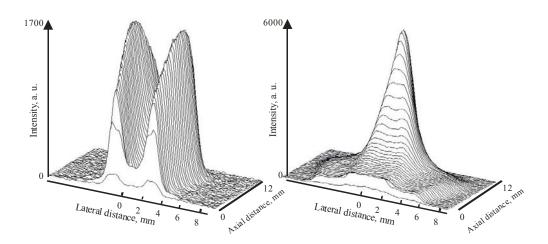


**Fig. 1** Spatial distribution (lateral-axial) of intensity on captured images of steady state arc plasma (left) and plasma exposed to the magnetic field strength of 7,5 mT (right) at wavelength Ba II 493, 409 nm

Correlation of laterally integrated emission with attained amplitudes (or maximal speeds) at distinctive axial positions show that emission enhancements at all positions linearly depends on maximal speed. But the biggest and nonlinearly

dependant correlation is obtained at axial distance of about 8,5 mm. This result was unexpected knowing that at all axial positions between 0 mm and about 8 mm the arc core reaches about the same amplitude.

In the case of the reverse electrode polarity (axial electric field is downward oriented) spatial distribution of barium ion emission intensity essentially differs in comparison to the plasma with regular electrode polarity. However, plasma core still stays depleted of barium ions. When the magnetic field of the same magnitude is applied (7,5 mT) the emission enhancement also occurs but now mostly at the lower axial distances (maximal at axial distance of about 3 mm). Moreover, lateral distribution of emission at that axial distance shows that maximum emission do not corresponds to the maximal speed of the arc core. Maximum emission is obtained for somewhat lower speed.

#### Conclusion

This study demonstrated the ability to overcome and to make clear the problem with inefficient introduction of the analyte into the hot dc arc plasma region. The effect of the fast periodical lateral shifts of the hot arc plasma core induced by the external magnetic field on the analyte emission enhancement was estimated. The emission intensity enhancement strongly depends on speed, i.e. on amplitude of the plasma core movement. Even that the emission enhancement is dissimilar on different axial plasma regions which may be contributed to the initial distribution of the analyte species in the steady state plasma. This fact is confirmed in the case of the reverse electrode polarity. Non conventional spectroscopic technique was successfully applied for studying the described effects.

- [1] A.B. Murphy, J. Phys. D:Appl. Phys., 2001, 34, R151-R173.
- [2] M. Stoiljković, M.S. Pavlović, J.J. Savović, M.M. Kuzmanović, M. Marinković, Spectrochimica Acta, 2005, **60B**, 1450-1457.
- [3] M. Stoiljković, M. Pavlović, J.J. Savović, M. Kuzmanović, Contrib. Plasma Phys., 2007, 47, 670-676.
- [4] M. Stoiljković, I. Holclajtner-Antunović, Contrib. Plasma Phys., 1997, 37, 459-468.

## THEORETICAL AND EXPERIMENTAL STUDIES OF THE ALL GAS-PHASE IODINE LASER (AGIL)

M. Endo, T. Nakamura, T. Masuda and T. Uchiyama

<sup>1</sup>Department of Physics, School of Science, Tokai University, 1117 Kitakaname, Hiratsuka 259-1292, Japan. <sup>2</sup>Department of System Design Engineering, Faculty of Science and Engineering, Keio University, 3-14-1 Hiyoshi, Kohokuku, Yokohama 223-8522, Japan

#### **Abstract**

All gas-phase iodine laser (AGIL) powered by the decomposition of nitrogen trichloride (NCl3) is studied. This reaction scheme uses commonly available reagents and reaction paths are milder than the previously studied azide-based AGIL. Theoretical studies revealed the necessary operational conditions for achieving positive gain. An apparatus is made based on the results of the theoretical works. Positive gain at iodine I(2P1/2)– I(2P3/2) transition is observed for the first time.

#### Introduction

The chemical oxygen-iodine laser (COIL) is a continuous-wave, near-infrared chemical laser. It offers excellent properties for applications that require highpower laser output from a mobile platform. The best-known example of a COIL system may be the "Airborne Laser" ballistic missile defense weapon system[1], which uses a multi-megawatt laser with good beam quality. For very-high-power applications, chemical lasers are still advantageous over solid-state and fiber lasers, in terms of its scalability and beam quality. Therefore, intensive studies are being conducted not only in the U. S., but also in other countries, including Japan. A typical COIL depends on the energy transfer from singlet oxygen  $O2(^1\Delta)$  to the iodine atom, which is the lasing species. The  $O2(^1\Delta)$  is typically generated by the following chemical reaction:

$$H2O2 + 2KOH + C12 \rightarrow 2H2O + 2KC1 + O2(^{1}\Delta).$$
 (1)

This reaction illustrates an inherent drawback for the mobile laser systems: the reactant, basic hydrogen peroxide (BHP) aqueous solution is bulky to carry and it decomposes over time, which limits both long-term storage of BHP and applications in remote places.

Because iodine is an ideal for the lasing species, scientists have sought an alternative donor that is compatible with singlet oxygen but does not depend on wet chemistry. In 2000, Henshaw et al. succeeded in operating an all-gas-phase iodine laser (AGIL)[2]. The energy donor of AGIL is an excited NCl molecule in the singlet state. Generating NCl( $^{1}\Delta$ ) is achieved by the following chain of gas-phase reactions:

$$F + DCl \rightarrow DF + Cl \tag{2}$$

$$Cl + HN_3 \rightarrow HCl + N_3 \tag{3}$$

$$C1 + N_3 \rightarrow NC1(^1\Delta) + N_2. \tag{4}$$

While this reaction avoids BHP, it still requires highly toxic and explosive hydrogen azide, highly corrosive fluorine, and expensive DCl. In search of a more friendly reaction, Exton et al. demonstrated that decomposition of nitrogen trichloride (NCl3) produces  $NCl(^{1}\Delta)$  with high yield by the following reactions,

$$NCl_3 + H \rightarrow NCl_2 + HCl \tag{5}$$

$$NCl_2 + H \rightarrow NCl(^1\Delta) + HCl$$
 (6)

and this could be used as an energy source of the AGIL[3]. To distinguish this concept from the previously demonstrated AGIL, the former is often called "azide-AGIL", and the later is called "amine-AGIL". Since then, studies have conducted in line of this scheme, and in 1993, energy transfer from the chemically generated NCl3 to the iodine atom is demonstrated[4]. In 2005, breaching-out of the absorption loss at the I(2P1/2)– I(2P3/2) transition is reported by Bauer et al.[5]. Nevertheless, positive gain at this transition has not been reported yet to date.

#### **Theoretical Work**

We have started the study of amine-AGIL with the numerical simulations. Based on the successful CFD / chemistry hybrid simulation[6]. we modeled the chemical reaction of amine-AGIL by a onedimensional multiple leaky stream tube model. Figure 1 illustrates the description of the model. The flow

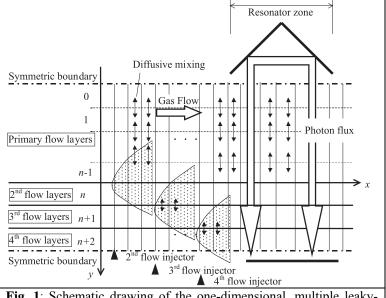


Fig. 1: Schematic drawing of the one-dimensional, multiple leaky-stream-tube kinetics model.

field is divided into n stream tubes of primary flow layers, and second, third, fourth flow layers those contain different species. The main-flow direction is defined as x

and the perpendicular axis is defined as y. The flows of adjacent layers are not mixed until the predefined injector position is reached. Downstream of the each injector, diffusive mixing of adjacent layers is assumed. A rooftop optical resonator is placed where the interaction of iodine atoms and photon flux is calculated. Since top and bottom boundaries are assumed to be symmetric, layer 0 represents the center of the duct, while the boundary of (n+2)th layer represents the top and bottom walls of the flow duct if a wall injection scheme is assumed.

The partial differential equation governing the flow field is as follows:

$$\frac{\partial M^{i}(x,y,t)}{\partial t} = \sum_{g} C_{g}^{2} [T(x,y,t)] M^{j}(x,y,t) M^{k}(x,y,t) 
+ \sum_{h} C_{h}^{3} [T(x,y,t)] M^{o}(x,y,t) M^{p}(x,y,t) M^{q}(x,y,t) 
- \frac{\partial}{\partial x} \{ M^{i}(x,y,t) H(x) v(x) \} / H(x) 
- D_{a} \frac{\partial^{2} M^{i}(x,y,t)}{\partial v^{2}} - \delta \frac{\partial n_{p}(x,t)}{\partial t}.$$
(7)

Here,  $M^{i}(x, y, t)$  is the number density of the *i*th species  $[1/\text{cm}^{3}]$ ,  $C_{g}^{2}[T]$  is the rate

constant of the gth reaction of 2nd order [cm3/s],  $C_h^3[T]$  is the rate constant of the hth reaction of 3rd order [cm6/s], T is the gas temperature [K], H(x) is the height of the duct [cm], v(x) is the gas velocity at position x [cm/s], Da is the artificial diffusion constant, and np is the photon density [1/cm3].  $\delta$ =-1 if i represents the upper state of the iodine atom,  $\delta$ =1 if i represents the ground state of the iodine atom, and  $\delta$ =0 for the other cases.

The differential equation is discretized by the upwind finite difference method. The upstream boundary condition is given by the set of equations,

$$M^{i}(0,t) = M_{0}^{i}. (8)$$

The difference equation is explicitly integrated in the time domain with first-order accuracy. The rate equation set used in this work is not shown here, but readers would find the complete description of the model in Ref. 7. The numbered reaction constants hereafter is in consistent with those appears in Ref. 7.

Soon after the initial calculations, we realized there are two key factors of the amine-AGIL reaction system that strongly affects the small signal gain. The primary one is the self annihilation reactions of  $NCl(^1\Delta)$ . Unlike the  $O2(^1\Delta)$ , the reaction constants of self annihilation reactions

$$NCl(^{1}\Delta) + NCl(^{1}\Delta) \xrightarrow{k26, k27, k28} \text{ products}$$
 (9)

are on the order of  $10^{-12}$  [cm<sup>3</sup>/s]. Since the reaction occurs at the rate of [NCl( $^{1}\Delta$ )]<sup>2</sup>, local high concentration of NCl( $^{1}\Delta$ ) should be avoided. The second important fac-

tor is the Cl atom accumulation. Cl atom is inherently generated as a by-product of amine-AGIL reaction system, for example, by

$$NCl(^{1}\Delta) + NCl(^{1}\Delta) \xrightarrow{k28} N2 + 2Cl,$$
(10)

where  $k_{28}$  is  $7.02 \times 10^{-12}$  [cm<sup>3</sup>/s]. Since it is a strong quencher of the I<sup>\*</sup> as

$$I^* + CI \xrightarrow{k40} I^* + CI, \tag{11}$$

where  $k_{40}$  is  $1.5 \times 10^{-11}$  [cm<sup>3</sup>/s], the accumulation of Cl atom affects the laser performance considerably. We found that changing the order of injectors is effective for both avoiding local high concentration of NCl( $^{1}\Delta$ ) and rapid gain build-up before accumulation of Cl atom. Figure 2 shows the comparison of the injector ar-

rangements. The "Conventional" arrangement was that of the first amine-AGIL setup[5]. We changed the order so that the NCl<sub>3</sub> is contained in the main flow, and HI is injected at the same position as H atoms.

Figure 3 shows the NCl( $^1\Delta$ ) concentration contours in the flow field with the conventional arrangement and the new arrangement. It is seen that NCl( $^1\Delta$ ) is generated locally and in a high density when conventional arrangement is used. On the other hand, the concentration of NCl( $^1\Delta$ ) is more uniformly distributed when the new arrangement is used. Figure 4 shows the concentrations of Cl atom and population inversion, namely,  $\Delta N$ =[ $^*$ ]-1/2[I], with the conventional arrangement and the new arrangement.

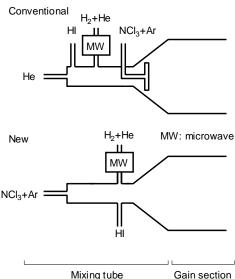


**Fig. 2:** Comparison of the injector arrangements. Conventional: Ref. [5], New: this work.

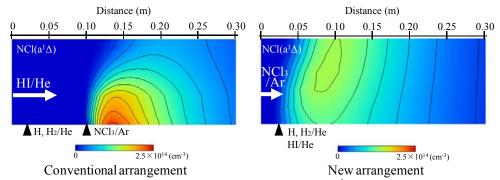


**Fig. 3:** Comparison of two injector arrangements:  $NCl(^{1}\Delta)$  density contour.

Population inversion is directly connected to the small signal gain  $g_0$  of the laser medium as

$$g_0 = \sigma \Delta N , \qquad (12)$$

where  $\sigma$  is the stimulated emission cross section, and therefore the most important parameter of any laser. The factor 1/2 applied to the ground state [I] comes from the quantum state degeneracy of the iodine atom. It is seen that the inversion evolution of the new arrangement is much faster than that of the conventional case, and its peak is reached before Cl atom accumulation. Therefore, I\* suffers less deactivation by Cl atom.

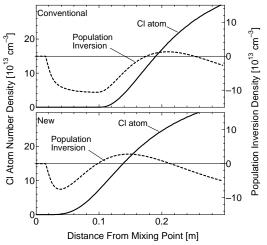


**Fig. 4:** Comparison of two injector arrangements: Cl<sub>2</sub> atom density and population inversion.

As a result, a higher peak population inversion (and gain) by a factor of two is seen in this figure.

Also, flow rates of the species, operating pressure, and the position of the optical axis are the parameters to be optimized. Numerical model was useful to find an optimum set from the vast parameter space. After a numerous runs of various boundary conditions, we found a recommended operational condition of the amine-AGIL as Table I.

**Table I:** Recommended flow conditions of the

amine-AGIL						
Species	Mole fraction	Pressure [Pa]				
НІ	0.13%	0.86				
$NCl_3$	0.32%	2.15				
$H_2$	1.61%	10.76				
Н	1.61%	10.76				
He (NCl <sub>3</sub> carrier)	48.17%	322.74				
He (H <sub>2</sub> carrier)	24.08%	161.37				
He (HI carrier)	24.08%	161.37				
total	100%	670				

## **Experimental setup**

Figure 5 shows the schematic drawing of the experimental setup. Amine-AGIL is composed of a simple mixing tube and a flow duct equipped with transparent windows. The mixing tube is made of a 25.4 mm Pyrex glass tube. Three injectors are devised as branches, namely, a 12.7 mm NCl<sub>3</sub> injector carried by Ar, a 12.7 mm H atom injector passing through a microwave resonator, and a 6.35mm HI tube. H atom branch is made of silica glass for better thermal durability.

Microwave is generated with a commercial magnetron (Panasonic) of 600 W output originally designed for microwave oven. A microwave resonator having a pair of holes is connected to the magnetron through a waveguide and the  $H_2$  tube is passing through it.  $H_2$  is carried by He to help easier production of discharge plasma. Pressure of the

mixing section is measured by a capacitance manometer (MKS Baratron). In the typical operational conditions, the pressure is 1000 Pa. The upstream end of the flow duct is 50 mm wide, 10 mm high, and it is directly connected to the mixing section. The duct can be set to diverging at an angle of 4 degrees or straight. Straight condition gave better result since we operated the laser at the subsonic flow condi-

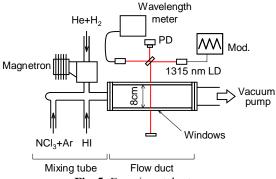


Fig. 5: Experimental setup

tions. Duct width at the intermediate section is 80 mm (enlarged from 50 mm to gain the optical path). A vacuum pump of 1,000 L/s capacity is driving the flowing gas, however, the capacity is greatly reduced by the variable restrictor devised at the inlet. The pressure at the center of the flow duct is monitored by a capacitance manometer (MKS Baratron) and the pressure is controlled to match the condition tabulated in Table I.

Small signal gain is measured by a distributed feedback laser diode (NTT Electronics NLK1B5EAAA) operated at 1.315  $\mu$ m, and its wavelength is modulated at 1,200 Hz near the 3-4 hyperfine level of the iodine transition,  $I(^2P_{1/2})-I(^2P_{3/2})$ . The absolute wavelength is assured by a wavelength meter (Advantest TQ8325).

#### **Results and Discussion**

Figure 6 shows the results. The traces show the intensity of the beam passed through the laser media, as a function of the LD frequency. Due to the vibration coming from the vacuum system and very small (on the order of 0.1%) round trip gain/loss, the sig-

nal to noise ratio of the traces were not good. Nevertheless, we could see the clear difference between two traces

As we use the microwave generator originally mounted on the commercial microwave oven, it works only the half cycle of the alternate current. The blue line (dip) shows the absorption of the 3-4 hyperfine level of the  $I(^2P_{1/2})$ –  $I(^2P_{3/2})$  transition when the microwave is off. Iodine atom is present probably by the following reaction,

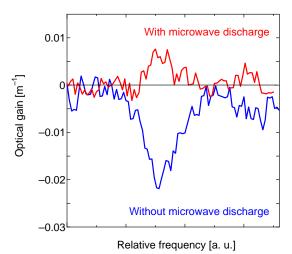


Fig. 6: Result of the gain measurement experiment.

$$HI + CI \rightarrow I + HCI$$
 (13)

but not pumped. When the microwave is "on" cycle, the trace turns to negative to positive and that is the proof of the following energy transition,

$$NCl(^{1}\Delta) + I \rightarrow NCl + I^{*}. \tag{14}$$

The round-trip small signal gain is not yet enough to achieve lasing and lower than what we expected from the theoretical works. The reason is presumably that the performance of the hydrogen discharge chamber is limited by the poor coupling of the microwave power to the flowing gas. In addition, During the process of  $NCl_3$  synthesis[5], notable amount of  $Cl_2$  is also trapped in the reservoir, and that is admixed to the supplied  $NCl_3$ . Since  $Cl_2$  molecule is a strong quencher of  $NCl(^1\Delta)$  as

$$NCl(^{1}\Delta) + Cl2 \xrightarrow{k18} NCl + Cl2, \tag{15}$$

where  $k_{18}$  is  $2.9 \times 10^{-11}$  [cm³/s], it should cause a serious influence to the laser performance. Simulation result predicted that a 20% Cl<sub>2</sub> admixture in the NCl<sub>3</sub> supplied is sufficient to extinguish the positive gain observed when Cl<sub>2</sub> was absent. We have not quantified the purity of the NCl<sub>3</sub> we have synthesized yet, however, an applicable contamination is suspected since the color of the trapped yellow liquid differed day-by-day in accordance with the change of synthesis conditions, indicating the existence of Cl<sub>2</sub> molecule. Reduction of the residual Cl<sub>2</sub> in the NCl<sub>3</sub> supplied is one of the keys to achieve higher gain.

## **Summary**

An amine-based all gas-phase iodine laser (AGIL) was studied theoretically and experimentally. The numerical simulation code was developed to find the optimum operational conditions of the amine-AGIL. It was found that the arrangement of the injectors was the key for both avoiding a local high-concentration of  $NCl(^1\Delta)$  atoms, and rapid gain build-up before excited iodine atoms were quenched by Cl atoms. Based on the knowledge obtained by the theoretical works, we fabricated an experimental setup and conducted gain measurement experiments. As a result, a positive gain at iodine  $I(^2P_{1/2})-I(^2P_{3/2})$  transition was observed for the first time. Currently, the absolute gain magnitude is limited by the low hydrogen concentration due to the insufficient  $H_2$  atom decomposition, and/or by the admixed  $Cl_2$  molecule in the supplied  $NCl_3$ .

We are very grateful to Dr. Steven J. Davis of Physical Sciences Inc. for his useful advices. We are also grateful to Kawasaki Heavy Industries Ltd, for the lease of their vacuum system and measurement devices. This work is partly supported by the Society of Iodine Science.

#### References

[1] S. Lamberson, H. Schall and P. Shattuck, "The airborne laser," Proc. SPIE 2007, 6346, 63461M.

- [2] T. L. Henshaw, G. C. Manke II, T. J. Madden, M. R. Berman1 and G. D. Hager, "A new energy transfer chemical laser at 1.315 µm", *Chem. Phys. Lett.* 2000, **325**, 537-544,
- [3] D. B. Exton, J. V. Gilbert, and R. D. Coombe, "Generation of Excited NCl by the Reaction of Hydrogen Atoms with NCl<sub>3</sub>," J. Phys. Chem. 1991, 91, 2692-2696.
- [4] R. W. Schwenz, J. V. Gilbert and R. D. Coombe, "NCl(a¹Δ) and I(<sup>5</sup>2P<sub>1/2</sub>) production in a D/NCl<sub>3</sub>/HI transverse flow," *Chem. Phys. Lett.* 1993, 207, 526-530.
- [5] J. R. Bauer, S. Lee, D. Vu, K. L. Galbaly, W. J. Kessler, and S. J. Davis, "Studies of an Advanced Iodine Laser Concept," in AIAA2005-5040, AIAA 36th Plasmadynamics and Lasers Conference, Toronto, Ontario, Canada, 2005.
- [6] M. Endo, T. Masuda, and T. Uchiyama, "Development of Hybrid Simulation for Supersonic Chemical Oxygen-Iodine Laser," AIAA Journal 2007, 45, 90-97.
- [7] T. Masuda, M. Endo and T. Uchiyama, "Numerical simulation of an all gas-phase iodine laser based on NCl<sub>3</sub> reaction system," J. Phys. D: Appl. Phys. 2008, 41 055101.

## ISOTOPE EFFECTS ON BAND INTENSITIES IN THE $B^2\Sigma^+$ – $X^2\Sigma^+$ SYSTEM OF GaO ISOTOPOMERS

M. Kuzmanović, V. Bojović and A. Antić-Jovanović

Faculty of Physical Chemistry, University of Belgrade, P.O.Box 47, 11158 Belgrade 118, Serbia (ankica@ffh.bg.ac.yu)

#### **Abstract**

Relative intensities of twenty-eight vibronic bands, belonging to the  $\Delta \nu$  = -2 sequence of the  $B^2 \Sigma^+ - X^2 \Sigma^+$  transition of four GaO isotopomers, have been measured and interpreted in terms of possible isotope effects on the parameters governing the band-intensity. Obtained results indicated that the observed intensity ratio of the corresponding isotopic bands can be related to the abundance <sup>69</sup>Ga and <sup>71</sup>Ga isotopes in natural gallium.

#### Introduction

The analysis of the relative intensities in emission bands is based upon expression for the intensity of the  $v' \rightarrow v''$  transition [1]:

$$I_{v'v''} \propto N_{v'} \, v_{v'v''}^4 \, q_{v'v''} R_e^2(r) \tag{1}$$

where  $I_{v'v''}$  is the measured signal produced by the  $v' \rightarrow v''$  transition,  $N_{v'}$  is the relative number density in vibrational level of the upper electronic state,  $v_{v'v''}$  is the transition wavenumber, approximated often by the band head position, and  $R_e(r)$  is the electronic transition moment function.

The isotope effects on band intensities may thus be due: (i) to differences in relative population of  $\upsilon'$  level; (ii) to the obvious effect of the change in frequency, which is usually very small; (iii) to the effect on Franck-Condon factors (FCFs), and (iv) to isotope effects on the electronic transition moment (ETM), which is the most difficult to predict. Any isotope effect on the ETM most be reflected either by an isotope effect on the r-centroid (average internuclear separation for a given transition,  $r_{\upsilon'\upsilon''}$ ), or on the parameters a, b, c ...in expression:

$$R_e(r) = a + br + cr^2 + \dots$$
 (2)

which describes the dependence of ETM on internuclear distance.

This paper contains the results of analysis of measured band-head intensity ratios of the B-X isotopic bands of two pairs of GaO isotopomners,  $I(^{69}\text{Ga}^{16}\text{O})/I$  ( $^{71}\text{Ga}^{16}\text{O}$ ) and  $I(^{69}\text{Ga}^{18}\text{O})/I(^{71}\text{Ga}^{18}\text{O})$ . Attention was focused on the bands of  $\Delta v = -2$  sequence (407-418 nm) due to well resolved isotopic heads. Until the present work, any data concerning the intensity measurements for the B-X bands of GaO have not been available.

## **Experiment and Calculation**

Intensity measurements were performed on emission bands produced in discharge of low-pressure arc in the atmosphere of both the oxygen-16 and oxygen-18 (enriched to 90%), as reported earlier[2,3]. Since the natural gallium is a mixture of two isotopes, <sup>69</sup>Ga (60.2%) and <sup>71</sup>Ga (39.8%), in both cases the bands of two corresponding isotopomers, <sup>69</sup>Ga <sup>16</sup>O and <sup>71</sup>Ga <sup>16</sup>O, as well as <sup>69</sup>Ga <sup>18</sup>O and <sup>71</sup>Ga <sup>18</sup>O, were recorded. From a densitometer tracing of the recorded spectrum we measured the peak height at the positions of R-heads above the corresponding background for each isotope species. Uncertainty of the measurements was determined to be not more than 10%.

To analyze observed data, we computed FCFs and r-centroids for the isotopic bands involving  $\upsilon$ ' and  $\upsilon$ '' levels up to 10. Computations were performed by using Morse potential functions and suitable modified Felenbok's computer program[4]. The molecular constants needed for these computations were taken from Ref. [2,3 and 5] and partly calculated by known isotopic relations[1]. Reduced masses of four isotopic gallium oxides were calculated from atomic masses of the  $^{69}$ Ga and  $^{71}$ Ga atoms and atomic masses of the  $^{16}$ O and  $^{18}$ O atoms.

#### **Results and Discussion**

For economy of space, Table 1 contains only a set of FCFs and r-centroids for the isotopic bands of the  $\Delta v = -1$  and -2 sequences, isotope ratios of FCFs and the observed relative band-head intensity ratios for the bands of  $\Delta v = -2$  sequence. Due to different molecular constants used in present computation, obtained FCFs for  $^{69}$ Ga $^{16}$ O differ somewhat from those reported earlier. FCFs for the bands of other three isotopomers are given in this work for the first time.

Data listed in Table 1 clearly show very small isotope effect on FCFs and almost the same (very close to unity) ratio  $q(^{69}\text{Ga}^{16}\text{O})/q(^{71}\text{Ga}^{16}\text{O})$ , and  $q(^{69}\text{Ga}^{18}\text{O})/q(^{71}\text{Ga}^{18}\text{O})$  for all bands. Isotope effect on *r*-centroids is negligible. Due to this fact, and due to impossibility to determine any possible isotope effect on the parameters a, b,... in Eq. (2) from the intensity measurements, the assumption of equal transition probabilities was thus reasonable for the analysis of intensity data listed in two last columns of Table 1. These data revealed almost the same observed band-head intensity ratios for all isotopic bands amounting approximately 1.5.

Returning to Eq. (1), it was possible to discuss observed intensity ratios by using the evaluated FCFs and quoted transition wavenumbers in Ref. [2] and those presently determined for the new bands. In spite of noticeable isotope effect on band- head positions (about 4 cm<sup>-1</sup>), the ratio of fourth power of wavenumbers of isotopic bands, resulting in the same  $\upsilon' \rightarrow \upsilon''$  transition, was found to be 0.9993 for all sequence bands. Both, these data, and the fact that natural  $^{69}$ Ga/ $^{71}$ Ga ratio is 1.507 [6], indicated that the intensity ratios of measured isotopic bands can be related to the ratio of number density of isotopic species in  $\upsilon'$  levels.

**Table 1**. Franck-Condon factors (q), r-centroids (r) and observed relative band-head intensity ratios for selective B-X bands of GaO isotopomers

υ',υ''	$q_{(1)}$	$q_{(2)}$	$q_{(1)}/q_{(2)}$	$q_{(3)}$	$q_{(4)}$	$q_{(3)}/q_{(4)}$	$r_{(1)}$	$r_{(2)}$	$I_{(1)}/I_{(2)}$	$I_{(3)}/I_{(4)}$
0,1	3.031-1	3.035-1	0.999	3.111-1	3.116-1	0.998	1.8194	1.8193		_
0,2	3.072-1	3.092-1	0.994	3.553-2	3.562-2	0.992	1.9374	1.9366	1.507	1.500
1,2	4.549-1	4.549-1	1.000	4.546-1	4.545-1	1.000	1.8220	1.8218		
1,3	6.160-1	6.212-1	0.992	7.186-2	7.248-2	0.992	1.9683	1.9672	1.514	1.501
2,3	5.464-1	5.457-1	1.001	5.331-1	5.522-1	1.002	1.8225	1.8224		
2,4	8.984-2	9.055-2	0.992	1.046-1	1.054-1	0.992	1.9910	1.9898		
3,4	5.779-1	5.769-1	1.002	5.561-1	5.548-1	1.002	1.8280	1.8279		
3,5	1.316-1	1.325-1	0.993	1.500-1	1.509-1	0.994	1.9844	1.9836	1.505	1.500
4,5	5.360-1	5.349-1	1.002	5.104-1	5.090-1	1.003	1.8453	1.8451		
4,6	1.929-1	1.939-1	0.995	2.167-1	2.180-1	0.994	1.9615	1.9608	1.506	1.507
5,6	4.659-1	4.646-1	1.003	4.344-1	4.328-1	1.003	1.8731	1.8728		
5,7	2.454-1	2.469-1	0.994	2.796-1	2.812-1	0.994	1.9505	1.9498	1.510	1.509
6,7	4.314-1	4.297-1	1.004	3.901-1	3.885-1	1.004	1.8989	1.8987		
6,8	2.567-1	2.586-1	0.993	3.016-1	3.037-1	0.993	1.9614	1.9605	1.504	1.517
7,8	4.443-1	4.423-1	1.004	3.942-1	3.927-1	1.004	1.9147	1.9145		
7,9	2.380-1	2.400-1	0.992	2.890-1	2.914-1	0.992	1.9849	1.9839	1.509	1.511

Numbers in parentheses 1, 2, 3 and 4 denote <sup>69</sup>Ga<sup>16</sup>O, <sup>71</sup>Ga<sup>16</sup>O, <sup>69</sup>Ga<sup>18</sup>O and <sup>71</sup>Ga<sup>18</sup>O, respectively. The negative entry in each listing indicates the decimal exponent.

Bands (5,7), (6,8) and (7,9) are reported for the first time.

#### Conclusion

Experimental and theoretical study of the isotope effect on band intensity of GaO B-X bands of  $\Delta v = -2$  sequence, showed very small isotope effect on FCFs and r-centroids and indicated difference in relative population of levels by isotopic species as main parameter governing the band intensity ratio of investigated isotopic bands.

## Acknowledgment.

This work was supported by the Ministry of Science of the Republic of Serbia, Project No 142065

- $[1]~G.~Herzberg, "\textit{Spectra of Diatomic Molecules"}, 2^{nd}~ed, 1951, Van~Nostrand, Princeton.$
- [2] V.Bojovic, D.S.Pesic and A. Antic-Jovanovic, J. Serb.Chem.Soc., 1993, 58, 109-115.
- [3] A. Antic-Jovanovic, V. Bojovic and D. S. Pesic, Spectrosc. Letters, 1994, 27, 247-256
- [4] P. Felenbok, C. R. Acad. Sc., 1963, 256, 2334 -2347
- [5] B. R. Yadav, S. B. Rai and D. K. Rai., Canad. J. Phys. 1979, 57, 496-504.
- [6] M. Vaygues Pelaes, J. M. Costa Fernandez and A.Sauz-Medel, AAS, 2002, 17, 950-957.

## STUDY ON FISETIN-ALUMINIUM (III) INTERACTION IN AQUEOUS BUFFERED SOLUTIONS BY SPECTROSCOPY AND MOLECULAR MODELING

J.M. Dimitrić-Marković, Z.S. Marković, Z.P. Nedić and M.S. Petrović

<sup>1,4</sup>Faculty of Physical Chemistry University of Belgrade Studentski trg 12-16, 11158 Belgrade 118, Serbia, markovich@ffh.bg.ac.yu

<sup>2</sup>Faculty of Agronomy, University of Čačak, Cara Dušana 34, 32000 Čačak, Serbia, <sup>3</sup>Institute of Chemisty, Technology and Metallurgy - Department of Catalysis and Chemical Engineering, Njegoseva 12, 11000 Belgrade, Serbia

#### **Abstract**

The spectroscopic (UV/VIS and IR) and theoretical studies were used to assess relevant interaction of fisetin, tetrahydroxylated flavone's molecule, and trivalent aluminium in a wide range of buffered aqueous solutions. The chelation sites, stoichiometry, stability and the dependence of the complexes structures from pH and aluminium/fisetin mole ratios were defined. Obtained results implicated successive formation of several complexes of stoichiometry aluminium (III) –fisetin 1:1, 2:1 and 1:2. Considering the fisetin molecular structure, the results of vibrational analysis and the theoretical calculations it is possible to implicate 3-hydroxyl-4-carbonyl and 3'4'-dihydroxyl groups as those with the chelating power. The equilibrium geometries are optimized in vacuum at the B3LYP/6-31G(d) level of theory. Structural modifications have been observed between the ligand molecule in free state and in the complex structure. The theoretical model has been validated by both vibrational and electronic spectroscopies.

#### Introduction

Flavonoid family is the vast, highly diverse, one with more than 8000 known compounds. The basic flavonoid structure consists of 15 carbon atoms arranged in three rings, benzo-ring referred to as ring A, the pyrone-ring as ring C, and the phenyl-ring as ring B,  $(C_6H_5(A)-C_3-C_6H_5(B))$ . A great number of flavonoids, especially flavones, can efficiently chelate metals like Al (III), Fe (II), Fe (III), Cu (II) or Zn (II). Metal complexation reactions play important and multiple roles in biological systems. They are sensitive colour stabilization mechanism developed in higher plants under in vivo [1, 2]. They are also one of the mechanisms which enable accumulation of metals in peripheral tissues limiting their bioavailability and the possibility of their migration to eco systems suppressing metal toxicity and at the same time enhancing protection of plants from pathogens and plant eaters. Aluminium is the most abundant metal in the earth's crust. It is a trivalent cation found in its ionic form in most kinds of animal and plant tissues and in natural waters everywhere [3]. Its presence has beneficial and harmful effects depending of the conditions. Fisetin is an active biological ligand which can act as a chelator of aluminium (III) reducing its overload in the diet. It can also be a heavy metal chelator in the case of their deficiency caused by irradiation, since the use of heavy metal salts is not recommended because of highly pronounced toxicity. A detailed study of the influence of the medium on the chelation process between fisetin and aluminium (III) could be of use in unraveling the nature of its interaction in the processes of biological relevance under *in vivo*.

#### **Results and Discussion**

In the investigated solutions (pH 2-8) aluminium (III) bonded well with ligand molecule fisetin. The pH value of the medium has a considerable impact on complex stability and stoichiometry since the fisetin, as all other flavonoids, is a weak polybasic acid which tend to protonate. Depending on pH and metal/ligand mole ration the addition of aluminium to fisetin solutions resulted in successive formation of three complexes of different stoichiometries (Fig. 1). As all the spectra, at pH≥5, cross at least one of two isosbestic points the simultaneous presence of free and two forms of the complex is not observed. This fact indicates that the formation of the second complex begins at the moment when all fisetin molecules are already involved in first complex. The first complex (complex I) is formed at low molar ratios of the components and the second one (complex II) is formed at higher molar ratios. The stoichiometric composition of the first complex (aluin the buffered solutions pH 2-4 is 1:1 and in buffered minium:fisetin) formed solutions pH 6 and pH 7 is 1:2. The stoichiometric composition (aluminium:fisetin) of the second complex (complex II) in the buffered solutions pH 5-9 is 2:1.

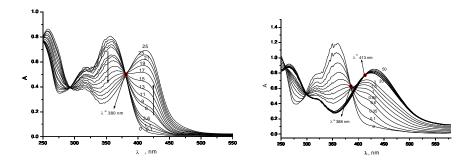


**Fig.1** Electronic spectra of equilibrated solutions of fisetin in pH 3 and pH 6 at different aluminium–fisetin mole ratios (indicated on spectra)

Chelating properties of flavonoids towards metal ions could be generally attributed to the presence of the 3-hydroxy-4-carbonyl groups or 5-hydroxy 4-carbonyl groups and *ortho*-hydroxyl groups in the B ring.

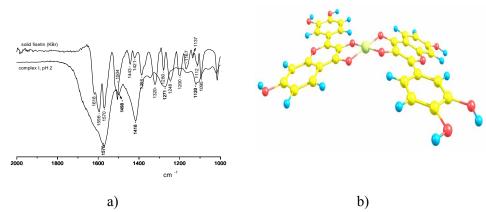


**Fig.2** IR spectra of solid fisetin and complex formed at pH 2 (a) and geometry optimized structure of the complex I in 1:2 stoichiometry (aluminium:fisetin) (b)

Much information on complex structures has been provided by infrared spectroscopy. According to previous IR data [4] the presence of hydroxyl group in C-3 position generally lowers the wavenumbers of carbonyl as well as C2=C3 stretching modes. The bands in the 1600-1400 cm<sup>-1</sup> region can be associated with aromatic in plane skeletal vibrations, aromatic character of the pyrone ring and double bond character of the carbonyl group (Fig. 2a). The comparative analysis of the IR spectra of solid fisetin and complexes confirmed the assumption of possible involvement of 3-OH-4- carbonyl and catechol structural units in chelation of aluminium. The theoretical treatment performed also fairly reproduces the experimental results. Fig 2b presents geometry optimized structure of the complex I in 1:2 stoichiometry formed at lower components molar ratios.

#### Conclusion

Although the results obtained *in vitro* can not be simply extrapolated to the conditions *in vivo* it is possible to get some insights into the conditions of chelation in acidic medium, which may be important in some pathological conditions, and the conditions of chelation in neutral or slightly basic media, which may be of relevance in interactions with biological targets, e.g. membranes, at the molecular level.

- [1] B. Harborne, R. Grayer, The Flavonoids Advances In Research since 1980, Chapman and Hall: London, 1988, 1-20.
- [2] J. B. Harborne, H. Baxter, Handbook of Natural Flavonoids, Wiley, Chichester, 1999.
- [3] E. Pilon-Smits, M. Pilon, Critical Reviews in Plant Sciences 2002, 21 (5), 439-446.
- [4] J. P.Cornard, J. C. Merlin, Polyhedron 2002, 21, 2801-2810.

### ANALYSIS OF FLUORESCENT SPECTRA OF DIFFERENT LIGNIN MODEL COMPOUNDS

D. Đikanović, A. Kalauzi, M. Jeremić and K. Radotić

<sup>1</sup>Institute for Multidisciplinary Research, University of Belgrade, Knesla Viseslava 1, 11000 Belgrade, Serbia

<sup>2</sup>Faculty of Physical Chemistry, University of Belgrade, 11000 Belgrade, Serbia

#### **Abstract**

Variation in the structure of different lignin model compounds can be observed through characteristics of their fluorescent spectra. We explored differences in fluorescence emission spectra of lignin model compounds (DHP) synthesized from coniferyl alcohol and ferulic acid (CF) or coniferyl alcohol and p-cumaric acid (CP) in different proportions. The obtained results indicate that differences in the emission spectra can be related to the variation in polymer composition.

#### Introduction

Lignin, as a major structural polymer in the plant cell walls, is the second most abundant polymer on Earth. Lignin is highly branched and random polymer composed of cross-linked phenyl propanoid units derived from coniferyl, sinapyl and p-coumaryl alcohols as precursors. In plants, it is intertwined and cross-linked with other macromolecules in the cell walls [1]. Various types of inter-unit bonds are possible in lignin, leading to different types of substructures. Fluorescence is an intrinsic property of lignin [2]. The structural complexity of lignin makes its fluorescence spectra difficult to interpret. In order to interpret the results, fluorescence spectra of a variety of lignin model compounds were examined [3].

We performed deconvolution of fluorescence spectra of different DHP samples using appropriate mathematical model. The aim of the study was to use the results of deconvolution to get a more detailed insight into the structure of these polymers.

#### **Materials and Methods**

Lignin model compounds (DHPs) were synthesized from coniferyl alcohol and ferulic acid (CF) in proportion 1:1, 2:1, 5:1, 10:1, 20:1 (w/w), coniferyl alcohol and p-cumaric acid (CP) in proportion 10:1 (w/w) and pure coniferyl alcohol (CA), according to the procedure of Freudenberg [4].

Fluorescence spectra were collected using a Fluorolog-3 spectrofluorimeter (Jobin Yvon Horiba, Paris, France) equipped with a 450 W xenon lamp and a photomultiplier tube. The lignin model compounds were dissolved in dioxan/water (9:1, v/v) and placed in a 1-cm optical path length quartz cuvette for spectral recording. Solution contained 0.5 mg/mL lignin model compound. The slits on the excitation and emission beams were fixed at 4 and 2 nm, respectively. The spectra were corrected for the dark counts. In each measurement, five scans were averaged.

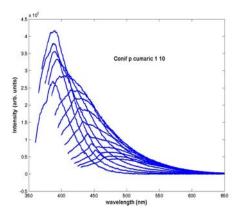
The emission spectrum of the solvent (dioxan/water) was subtracted. All measurements were performed at 25 °C controlled by a Peltier element.

Emission spectrum of each sample was collected by exciting at different wavelengths, starting from excitation maximum at 340 up to 460 nm, with a 5 nm-step (Fig. 1, left panel). Nonlinear fitting of each obtained spectrum was performed using the Nelder–Mead algorithm implemented in Matlab, version 6.5. Spectra were deconvoluted into one Gaussian and four Lorenzian components. We calculated approximate probability distribution (APD) for positions of component maxima by weighed averaging histogram values for a set of histograms.

#### **Results and Discussion**

Differences in the emission spectra (Fig.1, right panel) of studied polymer samples reflect the influence of structural characteristics on the spectral properties.

Synthetic polymer containing ferulic acid shows high energy shift of emission component positions (Fig.2). In contrast, presence of p-cumaric acid causes low energy shift. This indicates that DHP containing p-cumaric acid has longer system of conjugated bonds than the polymer obtained from pure conifervl alcohol. The extension of conjugated system of bonds leads to the decreasing of energy gap between excited and ground states, which shifts emission to longer wavelengths. Contrary to that, the blue shift of component positions in the presence of ferulic acid in DHP is caused by increasing of energy gap between excited and ground states. This is a consequence of different structural arrangements in the polymer. Ferulic acid has been shown to participate in forming transversal connection between lignin and the other cell walls polymers. Structural variations of lignin containing p-coumaric and ferulic acid are found in native cell walls. Since lignin is major polymer providing mechanical strength in plants, it is reasonable to assume that structures containing p-coumaric acid and ferulic acid have different roles. Structures containing p-coumaric acid have extended system of conjugated bonds that prevents rotational movement, while those containing ferulic acid provides lateral strength. This interpretation is consistent with findings of p-coumaric structures in compressed wood.



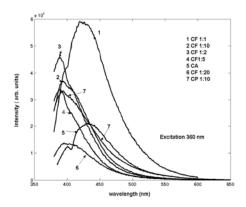


**Fig. 1.** Figure 1. Left panel: Emission spectra of CP- DHP dissolved in dioxane/water (9:1, v/v), for excitation wavelengths in the range 340 - 460 nm with 5 nm step. Right panel: Overlaid spectra of all samples.

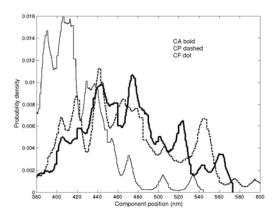


**Fig. 2.** Approximate probability distribution for three samples (CA, CF, CP).

- [1] N. Lewis, E. Yamamoto, Lignin: occurrence, biogenesis and biodegradation, Annu. Rev. Plant Physiol. Plant Mol. Biol. 1990, **41**, 455–496.
- [2] K. Lundquist, B. Josefsson, G. Nyquist, Analysis of lignin products by fluorescence spectroscopy, Holzforschung, 1978, **32**, 27–32.
- [3] H. Konschin, F. Sundholm, G. Sundholm, Fluorescence characteristics of lignin model compounds, Acta Chem. Scand. 1976, **B 30**, 262–266.
- [4]K. Freudenberg, Lignin im rahmen der polymeren neturstoffe, Angew. Chem. 1956, **68**, 84–92.

### DETERMINATION OF THE SIZE OF QUANTUM DOTS BY FLUORESCENCE SPECTROSCOPY

D. Mutavdžić, K. Radotić, J. Xu, A. Kalauzi, M. Jeremić and R. Leblanc

<sup>1</sup>Institute for Multidisciplinary Research, Kneza Višeslava 1, 11000 Beograd, Serbia <sup>2</sup>Department of Chemistry, University of Miami, Coral Gables, FL 33124, USA

#### **Abstract**

We studied dependence of the fluorescence maximum position (FMP) on the size of CdSe quantum dots (QD). It was found a linear correlation between QD size and FMP. We also examined possibility of using dependence of the FMP on the QD size as a means to check homogeneity of the QD solution. Deconvolution of the QD emission spectra obtained by excitation with different wavelengths reveals the number of QD groups having different diameter. The size of QD in particular group is defined by FMP of corresponding component in the deconvoluted spectrum. The size and homogeneity of the QDs in one given solution are two essential parameters for their application as fluorescent markers in biology.

#### Introduction

Quantum dots (QD) are semiconductor nanoparticles with increasing application as fluorescent markers in biology. Their physical, electronic and optical properties are strongly dependent on their size [1]. Therefore, special attention has been paid to accurate measurements of the size distributions using different methods, such as transmission electron microscopy (TEM), small-angle X-ray scattering, Raman scattering, UV-Vis absorption spectroscopy, laser-induced breakdown detection. Fluorescence spectrosopy is used for detection of QDs alone or complexed to a molecule/structure of interest, but it has not been used, to our knowledge, for QDs size determination. Subtle differences in preparation can lead to batch-to-batch variation in QDs' basic spectroscopic properties. The commercial dots are neither spectroscopically standardized, nor are they characterized completely enough to be used without further evaluation [2].

In this work we explored applicability of fluorescence spectroscopy in QD size determination. More precisely, the aim of this study was to explore if it is possible to correlate the fluorescence maximum position (FMP) with the QD size (diameter). This would have importance in further practical application. We also examined possibility of using dependence of the FMP on the QD size as a means to check homogeneity of the QD's solution. This is also an essential parameter for QD application.

#### **Materials and Methods**

CdSe QDs were prepared by following procedure. The cadmium oxide (CdO) and tetradecylphosphonic acid (TDPA) were used as Cd precursor, and the trioctylphosphine selenide as Se precursor. The CdSe QDs were formed by pyrolysis of

Cd and Se precursors in a coordinating solvent, trioctylphosphine oxide (TOPO), at high temperature (270 - 320°C). The QDs were collected as powders using size-selective precipitation with methanol and dried in vacuum.

Fluorescence spectra were collected using a Fluorolog-3 spectrofluorimeter (Jobin Yvon Horiba, Paris, France) equipped with a 450 W xenon lamp and a photomultiplier tube. The CdSe QDs were dissolved in chloroform, in a 1-cm optical path length quartz cuvette. The slits on the excitation and emission beams were fixed at 4 and 2 nm, respectively. The spectra were corrected for the dark counts. Integration time for one spectrum measurement was 1 s. The emission spectrum of the solvent (chloroform/methanol) was subtracted. All measurements were performed at controlled temperature of 25 °C by means of a Peltier element.

#### **Results and Discussion**

In Figure 1, absorption spectra and corresponding emission spectra, for two CdSe particles of different diameters (sizes), are shown as an example. The size of the particles was determined from the QD's absorption spectra [3]. The dependence of FMP on the QD size can be modelled using a linear regression model (Fig. 2). The coefficient of determination is 0.89, which shows a strong linear dependence of the emission maximum position on the particle size. This is important since determination of the size of QDs smaller than 10 nm is difficult [4]. Our results show that this fluorescence method is applicable and sensitive for size (diameter) determination of such small QDs.

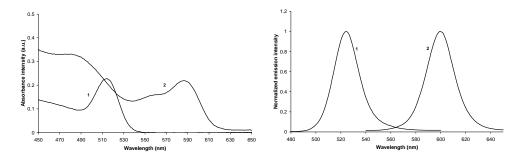


**Fig. 1.** UV-Vis absorption spectra of two sizes of CdSe QDs: 2. 7 nm (1) and 4.4 nm (2) (left), and related emission spectra obtained by excitation at 435 nm and 520 nm, respectively

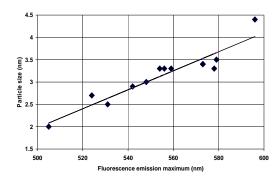


**Fig. 2.** Emission maximum position versus CdSe QDs versus their size

Advantage of fluorescence in comparison with absorption method is in higher linearity, smaller quantity of substance necessary for analysis, and in particular, fluorescence method can be readily applied to solid samples. Analysis of QD's emission spectra obtained by excitation with different wavelengths can give information about homogeneity of the QD's particle sizes. Shifting of the FMP, upon excitation by different wavelengths with a 5 nm-step (Fig. 3), means that there are more than one size of QDs, although the absorption spectra did not show that. The absorption spectra are not reliable regarding the size distribution because of band asymmetry caused by strong UV absorption.

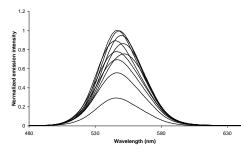


**Fig. 3.** Emission spectra of CdSe QD dissolved in chloroform, for excitation wavelengths in the 400 - 460 nm range with 5 nm step. The absorption spectra indicated presence of only one size (3 nm) of QDs in the solution.

Further deconvolution of the obtained emission spectra can show how many and which QD sizes are present in the solution. This method is also good for screening of the (in)homogeneity of the solution during purification of QDs, in the process of their synthesis, but also in the exploration of stability of a given QD. The fact that in some cases, the sizes of CdSe nanocrystals with the same absorption peak position are different in size [4] illustrates how useful can be our method for homogeneity checking of a QD's solution.

- [1] X. Michalet, F.F. Pinaud, L.A. Bentolila et al., Science, 2005, 28, 538-544.
- [2] D. Tonti, F. van Mourik, M. Chergui, Nano Lett., 2004, 4, 2483-2487.
- [3] W. Yu, L. Qu, W. Guo, X. Peng, Chem. Mater., 2003, 15, 2854-2860.
- [4] C.B. Murray, C.R. Kagan, M.G. Bawendi, Annu. Rev. Mater. Sci., 2000, 545-548.

## ATR-FT INFRARED MICROSPECTROSCOPY OF Cu(II) COMPLEXES WITH REDUCED DEXTRAN DERIVATIVES

G.S. Nikolić, M. Cakić, Ž. Mitić, B. Ilić and P. Premović

<sup>1</sup>Faculty of Technology, Bulevar Oslobođenja 124, 16000 Leskovac, Serbia (goranchem\_yu@yahoo.com)

<sup>2</sup>Faculty of Medicine, Department of Pharmacy, Bul. dr Zorana Đinđića 81, 18000 Niš, Serbia (<u>zak\_chem2001@yahoo.com</u>)

<sup>3</sup>Laboratory for Geochemistry, Cosmochemistry and Astrochemistry, University of Niš, 18000 Niš, Serbia

#### **Abstract**

Synthesized copper(II) complexes with reduced low-molar dextran (RLMD), of average molar mass  $M_w = 5000$  g/mol were investigated by Attenuated total reflectance-Fourier transform infrared (ATR-FTIR) spectroscopy and FTIR imaging microscopy. The changes in intensity and width of the IR bands in region 1500–1000 cm<sup>-1</sup> were related to changes in conformation and short-range interactions of the ligand dextran. The aim of this work is to use ATR-FTIR spectroscopy, and FTIR imaging microscopy as the main tools to verify the conformation and structure of this type of ligand around the copper(II) ions.

#### Introduction

Dextran is extracellular polysaccharide described as a  $\alpha$ –(1 $\rightarrow$ 6) linked polymer of  $\alpha$ –D–glucopyranose units. The numerous investigations have indicated that the polysaccharide dextran and its derivatives have the extraordinary power to forming the water–soluble complexes with various biometals [1,2]. It has been established that the degree of Cu(II) ion binding within the complex depends primarily on the pH of the solution, as well as on the participation both of the OH groups and the H<sub>2</sub>O molecules in the first coordination sphere of Cu(II) ion. ATR–FTIR microspectroscopic data of synthesized complexes are rare in literature The emergence of modern structural chemical methods such as Attenuated total reflectance–Fourier transform infrared (ATR–FTIR) spectroscopy and FTIR microscopy made it possible to assign the binding OH or other groups, and also to characterize the metal ion coordination of polysaccharides, monitoring the ligand conformation or/and configuration changes forced by the complexation processes [3–6].

## **Experimental**

Copper(II) ion complex synthesis with RLMD have been described in detail by Mitić et al. [4]. FTIR microspectroscopy system, ATR-FTIR spectrometer Bruker Hyperion Tensor-27 in conjunction with a FTIR Bruker Hyperion-1000/2000 microscopy attachment equipped with a 15× objective and a 250-µm liquid nitrogen cooled a narrow-band mercury-cadmium-telluride (MCT) detector (ATR objective GMBH, Germany) with the range of the IR spectrum from 4000 to 400 cm<sup>-1</sup>,

was used in this work. The spectra were measured with 4 cm<sup>-1</sup> resolution and 50 scans co–addition. The measurements were conducted in transmission mode.

#### **Results and Discussion**

ATR–FTIR spectrum of the polysaccharide dextran consists following bands:

$\overline{V}$ (cm <sup>-1</sup> )	Band assignation	Comment			
3600 – 3400	ν(O–H)	CH-OH glucopyranose units,			
3000 – 3 <del>1</del> 00	3000 – 3400 V(O-II)	$\mathrm{H_{2}O}$			
~2950	ν(C–H)	СН			
~1640	δ(ΗΟΗ)	$\mathrm{H_{2}O}$			
1450 - 1345	δ(C–H)	СН			
~1420	δ(O–H)	ОН			
1150 - 1010	$v_{as}(C-O), v_{as}(C-C)$	glucopyranose units			
1000-700	$\gamma$ (C–H)	configuration			

The ATR-FTIR spectra of Cu(II)-dextran complexes synthesized at different pH (pH 7–8, pH 8–10 and pH 10–12) recorded at 298 K and related FTIR microscopy images (250 µm × 300 µm) are presented on Fig. 1. The differences of the number. frequencies, intensity and shape of the bands (3600–3100 cm<sup>-1</sup>) implies that in the complexes there is displacement of H<sub>2</sub>O molecules by the OH groups in the first coordination sphere of Cu(II) ion. These results agree with a structural studies of the investigated complexes have been based on other spectroscopic techniques. [4,5]. The changes in number, frequencies, intensity, and width of the IR bands in the particular region of v(O-H) vibrations (3400 cm<sup>-1</sup>), δ(C-H) vibrations (1500-1300 cm<sup>-1</sup>) and v(C-O) vibrations (1200–1000 cm<sup>-1</sup>) were related to changes in the conformation and short-range interactions of the polysaccharide dextran. Very important changes can be observed in the range 1500-1300 cm<sup>-1</sup> by detailed empirical analysis. Otherwise, the IR range is specific of bending vibrations of CH-OH groups. Namely, exchange position and intensity of complex bands can be registered in this range, where C-H and O-H bending vibrations from the CH-OH groups take part. An approximate effect exists in the stretching of the IR range of C-H vibrations (3000–2800 cm<sup>-1</sup>). The appearance of bands at about 1460 cm<sup>-1</sup> and 1370 cm<sup>-1</sup> from  $\delta$ (C–H) vibrations and the band at about 1420 cm<sup>-1</sup> from  $\delta$ (O– H) vibrations are characteristic for one of more possible positions of the CH–OH group, rotating around the C2–C3 and C3–C4 bond of the glucopyranose unit. The Cu(II) ions in solution have a possible influence on the rotation of CH–OH groups in the complexes. The band at 1080 cm<sup>-1</sup> in the spectra of RLMD is attributed to the antisymmetric stretching vibration of C(6)–O–C(1) glycosidic bridge. The band at 1080 cm<sup>-1</sup> in the spectra of Cu(II) complex with RLMD is more pronounced than in the spectra of RLMD. In the case of dextran, all C(6) atoms participate in the formation of the C(6)–O–C(1) linkages; as a result, the band intensity at 1080 cm<sup>-1</sup> for dextran is reduced. The similarities of the  $\gamma$ (C–H) range indicate that there is no difference in the conformation of the glucopyranose unit in the dextran and complex molecules and they probably exhibit C1 chair conformation (916 and 850 cm<sup>-1</sup>).

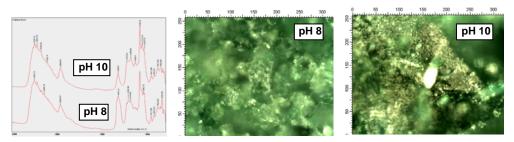


**Fig. 1.** Typical attenuated total reflectance Fourier transform infrared spectra of Cu(II)–dextran complexes synthesized at different pH, and related FTIR microscopy images (250  $\mu$ m × 300  $\mu$ m)

#### Conclusion

ATR-FTIR spectra of polysaccharide dextran and its complexes with Cu(II) ion, recorded at room temperature, were analyzed in order to obtain the information about the structure and the conformation of these compounds. The similarities of the  $\gamma(C-H)$  range indicate that there is no difference in the conformation of the glucopyranose unit in the dextran and the complex molecule, and they probably exhibit C1 chair conformation of  $\alpha$ -D-glucopyranose units. The differences in the region 3600–3100 cm<sup>-1</sup>, indicate that complexes originate from the displacement of H<sub>2</sub>O molecules by ligand O-H groups in the first coordination sphere of Cu(II) ion.

- [1] G. Nikolić, M. Cakić, Ž. Mitić, R. Nikolić, Lj. Ilić, Chemical Industry, 2005, **59**(1–2), 9–14.
- [2] Ž.J. Mitić, M.D. Cakić, G.S. Nikolić, R.S. Nikolić, Lj.A. Ilić, Chemical Industry, 2007, 61(5), 257–262.
- [3] G.S. Nikolić, M. Cakić, Ž. Mitić, Lj. Ilić, Russ. J. Coord. Chem., 2008, 34(5), 322–328.
- [4] Ž. Mitić, G.S. Nikolić, M. Cakić, R. Nikolić, Lj. Ilić, Russ. J. Phys. Chem. 2007, 81(9), 1433–1437.
- [5] M. Cakić, Ž. Mitić, G.S. Nikolić, Lj. Ilić, G.M. Nikolić, Spectrosc.—Int. J., 2008, <u>22(2–3)</u>, 177–185.
- [6] Ž. Mitić, G. Nikolić, M. Cakić, R. Nikolić, Lj. Ilić, XII European Conference on the Spectroscopy of Biological Molecules, Paris France, 2007, 319.

# INTERPRETATION OF ELECTRONIC ABSORPTION SPECTRA OF SOME ANTHRAQUINONES USING ZINDO/S METHOD

### Z. Marković and N. Manojlović

<sup>1</sup>Faculty of Agronomy, University of Kragujevac, Čačak 32000, Serbia, <sup>2</sup>Department of Pharmacy, Medical Faculty, University of Kragujevac, 34000 Kragujevac, Serbia, e-mail: ntm@kg.ac.yu

Anthraquinones physcion (1,8-dihydroxy-3-methoxy-6-methylanthracene-9,10-dione), aloeemodin (1,8-dihydroxy-3-(hydroxyl-methyl) anthracene-9,10-dione) and chrysophanol (1,8-dihydroxy-3-methylanthracene-9,10-dione) were isolated from lichen *Xanthoria parietina* and medical plant *Casia tora* and their UV/VIS spectra were recorded. Electronic absorption spectra of above-mentioned anthraquinone were investigated. Molecular geometries of the substituted anthraquinones in the ground state were optimized using semiempirical AM1 method without imposing any symmetry constrains. The ground state geometries of all the molecular systems were found to be planar. For interpretation of the spectra, ZINDO/S-CI investigation employing singly excited configuration using the completely optimized geometries was carried out. Such calculations on the electronic spectra of aloeemodin, chrysophanol, physcion and emodin were carried out for the first time. On the basis of these investigations, the assignments of the spectra were successfully made.

#### Introduction

The anthraquinones and their hydroxy and amino derivatives posses a wide ranging potential for application in pharmaceutical, food and dye industries. [1-3] As part of our investigations on the spectroscopy of substituted anthraquinones, we carried out the detailed theoretical and experimental studies on the electronic absorption spectra of physcion, emodin, chrysophanol and aloeemodin (Figure 1). For the interpretation of the electronic absorption spectra of these substituted anthraquinones, we performed the calculations of their electronic transition energies intensities using the Zerner's Intermediates Neglect of Differential Overlap/Spectroscopy (ZINDO/S) [4] semiempirical method. This method has been successfully tested for the calculations of the ground and excited state properties for a wide rang of organic compounds [5].

#### **Results and Discussion**

The experimental data on the geometries of the anthraquinones under investigation are not available. It is well known, that the ZINDO/1 and AM1 methods reproduce structural/geometrical parameters of the parent molecules 1,4-dihydroxy-9,10-anthraquinone, 1,5-dihydroxy-9,10-anthraquinone, and 1,8-dihydroxy-9,10-anthraquinone [6]. Our investigation by means of the AM1 method showed that planar structures had the deepest local minima in all molecules considered (Figure 1).

**Fig. 1.** Molecular structure of anthraquinones under investigation.

*Physcion.* We studied the electronic spectrum of this molecule in methanol. In the ultraviolet region, we observed four strong absorptions at 224, 253, 265 and 286 nm. The UV band at 224 nm was accompanied with two shoulders at 219 and 217 nm. In the visible region, a broad absorption band was observed at 433 nm. The results of the ZINDO/S calculation performed on the AM1 geometry showed very good matching with these bands: 239, 264, 305 and 406 nm. Chrysophanol. The UV-visible spectrum of chrysophanol measured in methanol at 298 K is depicted in Figure 2. This experiment revealed three bands located at 287, 277 and 256 nm in the UV region. The broad band at 428 nm was found to have a dominant charge transfer character. The ZINDO/S calculations showed the electronic bands at 236, 264, 302 and 397 nm. Aloeemodin. The electronic absorption spectrum of aloeemodin was measured in methanol at 298 K. The analysis of the electronic spectrum revealed four prominent bands with the maxima at 428, 286, 277 and 255 nm. The optimized geometry predicted that the most stable ground state structure of the molecule allowed the formation of the two intramolecular hydrogen bonds. The calculation by ZINDO/S method predicted four bands with the maxima at 394, 299, 263 and 236 nm. The ZINDO/S results are in good agreement with the experimental results.

The overall agreement between the calculated and experimental results is quite satisfactory. We will investigate biological activities of these compounds in the future.

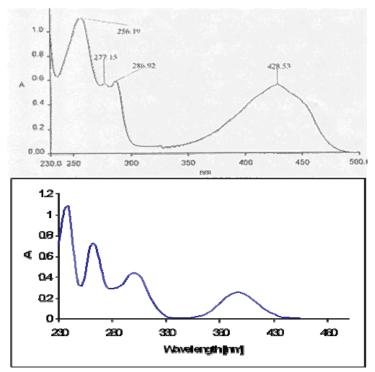


**Fig. 2.** Electronic absorption spectrum of chrysophanol measured in methanol and calculated by means of the ZINDO/S method.

## Acknowledgements

The authors acknowledge financial support by the Ministry of Science of the Republic of Serbia (Grant No. 142025) and Medical Faculty University of Kragujevac, Serbia (Grant No. 01-1362).

- [1] Fain V., 1970. Tabeles of Electronic Spectra of Anthraquinone and its Derivatives, Khimiya
- [2] Tomson R., 1971. Natural occurring Quinone, Academic Press, New York
- [3] Patai S., 1974. The Chemistry of the Quinonoid Compounds, Wiley, New York
- [4] Lipkowitz K. at all 1990. Reviews in computational chemistry, VCH Publisher, New York
- [5] Kubo Y. et all J. Am. Chem. Soc. 1991, **113**, 2868-2873.
- [6] Khan M. et all *Spectrochemica Acta* Part A 2003, **59**, 1409-1426.

Kinetics Catalysis

(C)

## STUDY ON THE DEACTIVATION REASONS OF Fe-Mo INDUSTRIAL CATALYST FOR PARTIAL OXIDATION OF METHANOL TO FORMALDEHYDE

Z. Cherkezova-Zheleva, D. Dimitrov, D. Paneva, K. Ivanov, H. Kolev and I. Mitov

<sup>1</sup>Institute of Catalysis, Bulgarian Academy of Sciences, 1113 Sofia, Bulgaria <sup>2</sup>Agricultural University, 4000 Plovdiv, Bulgaria

#### Abstract

An industrial iron-molybdenum catalyst for methanol to formaldehyde oxidation, produced by NEOCHIM SA, was investigated to study the work conditions and the reasons of its deactivation in the course of its long-term use. The phase composition and structural properties of the catalyst samples were investigated by X-ray diffraction, Moessbauer spectroscopy and X-ray photoelectron spectroscopy.

#### Introduction

Formaldehyde is a raw material for many industrial processes in chemical industry and cosmetics production. It is produced industrially by methanol oxidation, catalyzed either by supported silver or by bulk-phase iron molybdate catalysts. Nowadays, there are many studies concerning the optimal work conditions of iron oxide – molybdenum oxide catalyst, but the question of increase of catalyst lifetime has been not still established [1-2]. The main deactivation reasons are poisoning, chemical and mechanical deactivation of the catalyst. Therefore, more knowledge on the mechanism of deactivation is required.

The aim of this investigation was to study the work conditions of industrial iron-molybdenum catalyst and the reasons of its deactivation in the course of its long-term use.

## **Experimental**

An industrial catalyst, produced by NEOCHIM SA according to BG patent Ne 60779 B<sub>1</sub>, was used [3]. A fifteen months' industrial experiment was carried out. The industrial installation monitored consists of two pseudo-isothermal reactors. Both reactors were fed with 14600 Nm³ of gas mixture (6.0  $\pm$  0.2 % methanol and 11 $\pm$  0.5 % oxygen) at the start and 12000 Nm³ at the end of the experiment. The outlet gas mixture it is analyzed for CO, dimethyl ether, dimethoxymethane and CO<sub>2</sub> content.

Catalyst samples taken from four different sites of the reactors (at different height) were analyzed. The Moessbauer spectroscopy and XRD were used to determine their phase composition and structure characterization of the used catalyst samples. The phase composition and structure of the samples was determined by XRD using TUR M62 diffractometer with Co  $K_{\alpha}$  radiation. The transmission Moessbauer spectra were obtained at RT with a Wissel

electromechanical Moessbauer spectrometer (Wissenschaftliche Elektronik GmbH, Germany) working at a constant acceleration mode ( $^{57}$ Co/Cr, 10 mCi,  $\alpha$ -Fe standard). XPS measurements were carried out in the UHV electron spectrometer ESCALAB-MkII (VG Scientific) by using AlK $_{\alpha}$  radiation. The Fe2p spectra were decomposed into two components: Fe $^{2+}$  and Fe $^{3+}$  components taken from the appropriate standards.

#### **Results and Discussion**

The X-Ray diffraction patterns (Fig. 1) registered two main crystalline phases -  $Fe_2(MoO_4)_3$  (monoclinic structure) and  $MoO_3$  (orthorhombic structure) with additional carbon phase used as a solid lubricant. The ratio of mentioned Mocontaining phases was determined to be different at different points. The analysis of the obtained results showed that the major differences are observable between the fresh catalyst, those from the "hot spot"(spent catalyst) zone and "20 cm after hot spot" zone sample. The spent catalyst sample showed also some low degree of crystallographic transformation from monoclinic to orthorhombic  $Fe_2(MoO_4)_3$ .

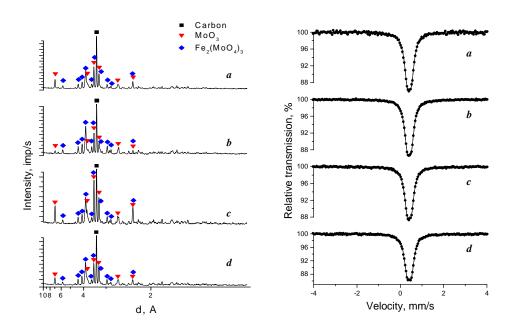


**Fig. 1.** Powder XRD patterns of selected samples.

**Fig. 2.** Moessbauer spectra of selected samples.

a) fresh; b) "hot spot" zone; c) "20 cm after hot spot" zone; d) "40 cm after hot spot" zone catalyst.

The Moessbauer analysis (Fig. 2) showed one component spectra of high spin ferric ions (Fe<sup>3+</sup>) in octahedral coordination. The obtained hyperfine parameters are characteristic of Fe<sup>3+</sup> ions, included in Fe<sub>2</sub>(MoO<sub>4</sub>)<sub>3</sub>. There is no

registered change in the phase composition of the iron-molybdenum oxide phase in the studied samples.

Two samples were studied by XPS, fresh and spent catalyst (from the "hot spot" zone) with ratio between Fe/Mo =1:3 for the bulk and 1:5(4) for the surface, respectively. The measured spectra from the surface and bulk (Fig. 3) showed that the catalyst surface has MoO<sub>3</sub> excess in comparison to the respective bulk sample. It was established different ratio between the Fe<sup>2+</sup> and Fe<sup>3+</sup> ions on the surface and in the bulk of both samples, respectively.

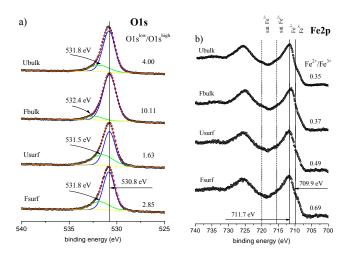


**Fig. 3.** XPS spectra of **a)** O1s and **b)** Fe2p for fresh (Fbulk for bulk and Fsurf for surface) and spent catalyst Ubulk for bulk and Usurf for surface). The ratio between O1s low and high energy peeks as well as for Fe<sup>2+</sup> and Fe<sup>3+</sup> are noted above the spectra in each case.

#### **Conclusions**

The obtained data allow us to conclude that the probable reason of deactivation is the loss of molybdena from the catalyst surface in the "hot spot" zone. This is probably due to MoO<sub>3</sub> sublimation from the "hot spot" zone and its deposition in the "20 cm after hot spot" zone.

## Acknowledgments

The authors are grateful to the Bulgarian National Science Fund at the Ministry of Education and Science for the financial support under Project VU X-305/2007.

- [1] A. P. Vieira Soares, M. F. Portela, A. Kiennemann, L. Hilaire, Chem. Eng. Sci., 2003, 58, 1315-1322.
- [2] Yi Ding, Shu-Hong Yu, Chen Liu, Zheng-An Zang, Europ. J. Chem., 2007, 13(3), 746-753.
- [3] BG patent № 60779 B1, 1993.

## IN SITU NMR SPECTROSCOPY IN THE STUDIES OF HYDROCARBON CONVERSION ON SOLID ACID CATALYSTS

#### A.G. Stepanov

Boreskov Institute of Catalysis, Siberian Branch of Russian Academy of Sciences, Prospekt Akademika Lavrentieva 5, Novosibirsk 630090, Russia.

#### **Abstract**

The paper demonstrates the possibilities of in situ <sup>1</sup>H and <sup>13</sup>C high resolution solid state NMR spectroscopy for characterization of chemical reactions on solid acid catalysts in a wide temperature range, from room temperature to 300 °C.

#### Introduction

High resolution solid state NMR spectroscopy (MAS NMR) has been used for more than two decades for the study of hydrocarbon conversion on solid acid catalysts. The progress in the development of in situ NMR technique allowed one to obtain a valuable information, which was indispensable for the development of modern concepts of catalysis science. New results were obtained on the products and intermediates formed on the catalyst surface and never earlier detected at the reactor outlet, the nature and the structure of some important intermediates were established. Many processes which are of importance for hydrocarbon activation and transformation, but «invisible» by conventional ex situ techniques were identified.

In this paper we provide the basic principles of using solid-state NMR in situ for the analysis of adsorbed hydrocarbons and offer some particular examples of application of MAS NMR for characterization of chemical reactions on solid acidic catalysts.

## **Experimental**

Preparation of the samples and performance of in situ NMR experiments are realized in a following manner. The powder of the catalyst is placed in axially highly symmetrical glass tube of 5.5 or 2.5 mm o.d. The tube is further connected to a vacuum line. After the catalyst activation under vacuum at temperature 400-450 °C, the reactant alkane is adsorbed on the catalyst and the glass tube is sealed off the vacuum line. So the reaction occurs in a closed batch microreactor of 0.03-0.1 cm<sup>3</sup>. Glass microreactor is further placed in zirconia NMR rotor and closed with zirconia cap. Then the rotor with sample is transferred to the NMR probe. Increase of the temperature of the reactor inside the probe initiates the chemical reaction. Magic angle spinning of the sample at 20-300 °C makes the signals from adsorbed organic species narrow, which allow us both to perform the analysis of hydrocarbons on the catalysis surface and follow the reaction kinetics by monitoring the variation of NMR spectrum with time.

#### **Results and Discussion**

Capability of solid state NMR to perform in situ analysis of reaction products and intermediate based on their <sup>1</sup>H and <sup>13</sup>C chemical shifts allows characterization of chemical reaction directly on the surface of solid catalysts. This makes possible to discover in situ with NMR of occurrence of the novel reactions; to unravel the mechanisms of the reactions, based on: (a) identified intermediates; (b) monitoring the peculiarities of redistribition of the selective <sup>13</sup>C or <sup>1</sup>H labels in the course of the reaction; (c) monitoring the kinetics of the reaction.

Some examples, demonstarting the possibilities of NMR in situ for characterization of chemical reactions on solid acid catalysts are provided. They include a disclosure by NMR of occurrence of the reactions of small olefin and alkane carbonylation with CO on zeolite H-SZM-5 and sulfated zirconia under mild conditions [1], identification of key reaction intermediate, N-alkyl-nitrilium cation in the Ritter reaction [2], clarifying the mechanisms of ethane aromatization and methane and propane co-aromatization on Zn-modified zeolite BEA [3].

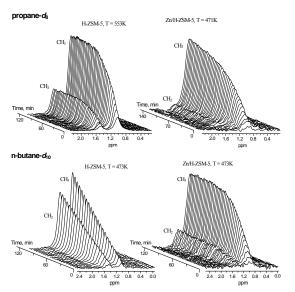


**Figure 1.** Regioselectivity of H/D exchange for propane and n-butane on Zn/H-ZSM-5.

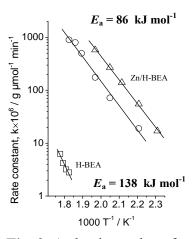


Fig. 2. Arrhenius plot for the rate of H/D exchange for methane  $(\Box,8)$  and ethane  $(\circ)$  on zeolites H-BEA and Zn/H-BEA.

Importance of the kinetics measurements for clarifyindg the mechanisms of alkane activation is illustrated with the particular examples of the study of the reactions of hydrogen exchange, <sup>13</sup>C-labeled carbon scrambling on solid acidic catalysts and Zn-loaded zeolites. Particular attention is drawn to the significance of simultaneous monitoring the kinetics of the transformation of different fragments

of hydrocarbon molecules. This is crucial for evaluation of the different pathways of the hydrocarbon activation and conversion.

Particular example of evaluation of difference in small alkane activation by acidic and Zn-modified zeolite by means of monitoring the reaction kinetics of hydrogen exchange shows, that propane and n-butane exhibit regioselectivity of H/D hydrogen exchange. Only methyl groups of these alkanes are involved in the exchange. H MAS NMR spectra reveal increase of the intensities of only methyl groups at 1.0 ppm with reaction time for Zn/H-ZSM-5, whereas intensities of signals at 1.0 and 1.5 ppm from both methyl and methylene groups increase with time for propane and n-butane on pure acidic zeolite H-ZSM-5(see Fig. 1).

For methane and ethane, the rate of exchange is about three order of magnitude higher and apparent activation energies are lower for Zn-modified zeolites ZSM-5 and BEA (see Fig. 2).

Strong promoting effect of Zn on H/D exchange reaction and the activation of C-H bonds of small alkanes by the zeolite Brønsted sites is rationalized by involvement in the exchange of Zn-alkyl species, which formation from alkane precedes its further involvement in interaction with Brønsted acid sites (See Scheme 1).

Scheme 1. Potential routes for the H/D exchange and dehydrogenation for C<sub>2</sub>-C<sub>4</sub> alkanes on Zn-modified zeolites.

- [1] A.G. Stepanov, M.V. Luzgin, V.N. Romannikov, K.I. Zamaraev, J.Am.Chem.Soc. 1995, 115, 3615-3616; A.G. Stepanov, M.V. Luzgin, A.V. Krasnoslobodtsev, V.P. Shmachkova, N.S. Kotsarenko, Angew.Chem. Int.Ed., 2000, 39, 3658-3660; M.V. Luzgin, V.A. Rogov, V.P. Shmachkova, N.S. Kotsarenko, A.G. Stepanov, J. Phys. Chem. C, 2007, 111, 10624-10629.
- [2] A.G. Stepanov, M.V. Luzgin, *Chem.-Eur.J.* 1997, **3**, 47-56.
- [3] M.V. Luzgin, V.A. Rogov, S.S. Arzumanov, A.V. Toktarev, A.G. Stepanov, V.N. Parmon, Angew. Chem. Int.Ed., 2008, 47, 4559-4562.

## NEW KINETIC METHOD FOR DETERMINATION HERBICIDE DIFENZOOUAT-METHYLSULPHATE

Z.M. Grahovac, S.S. Mitić, T.G. Pecev and E.T. Pecev

Faculty of Mathematics and Natural Sciences, Department of Chemistry, University of Niš, Višegradska 33, 18000 Niš

#### **Abstract**

A new kinetic method is described for determination of herbicide Difenzoquat (DFQ). The reaction of sulphanile acid (SA) and  $H_2O_2$ , catalysed by Cu(II) in phosphate buffer (pH=7.9), was used as the indicatory reaction in this study [1]. It was noted that small amounts of DFQ inhibit the reaction, which was used for its kinetic determination. Detection limit that experimentally determined is 0.36  $\mu$ g/ml. The relative error ranges between 3,61 and 1.0% for the concentration interval 0.36 to 1.80  $\mu$ g/ml. Kinetic equations are proposed for the investigated process.

#### Introduction

Difenzoquat (DFQ) is widely used in agricultural applications and it is on a priority list of herbicides of potential concern established for the Mediterranean Countries by the European Union (EU) [2]. The determination of this pesticide at ppb levels requires the development of a preconcentration step such as solid phase extraction (SPE) which is frequently employed nowadays [3,4]. HPLC is the most effective technique for its determination [5,6]. The aim of this work was to develop a kinetic method for DFQ determination.

#### **Results and Discussion**

The investigated reaction rate was followed spectrophotometrically. The absorbance of the solution was measured at the wavelength of 370 nm which corresponds to the maximum absorption of SA in phosphate buffer at pH 7.9. The dependence of the apsorbance (A) on time (t) was measured by Perkin-Elmer Lambda 15 spectrophotometer, connected to a thermochirculating bath.

A tangent method was used for the processing of the kinetic data, because of the existing linear correlation between the  $\Delta A/\Delta t$ . [7]

Under the optimal reaction condition: pH=7.9;  $c_{H_2O_2}$ =0.16 mol/l;  $c_{SA}$ =6·10<sup>-4</sup> mol/l; c(Cu(II))=3·10<sup>-6</sup> mol/l; t=25°C, the concentration of DFQ, as the inhibitor, was varied from 0.36 to 1.80 µg/ml. Figure 1. show the calibration line, at the temperature 25±0,1°C, which can be used for the determination of DFQ concentration in the interval mentioned.

The following kinetic equations were deduced on the basis of the graphic correlations obtained for the investigated process. For the indicatory reaction (1), and for inhibited reaction (2):

$$\frac{dc}{dt} = k_0 \cdot c_{H_2O_2} \cdot c_{H^+}^{-1} \cdot c_{SA} \cdot c_{Cu(II)}$$
 (1)

$$\frac{dc}{dt} = k_1 \cdot c_{H_2O_2} \cdot c_{H^+}^{-1} \cdot c_{SA} \cdot c_{Cu(II)} \cdot c_{DFQ}^{-1}$$
 (2)

 $k_0$  – constant proportional to the rate constant of the indicatory reaction  $k_1$  – constant proportional to the rate constant of the inhibited reaction

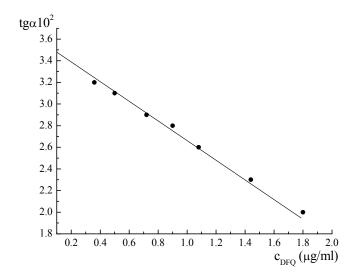


**Fig. 1.** Dependence of tgα on the DFQ for the inhibited reaction (calibration line)

The accuracy and precision of the measurements presented in Table 1. It can be seen that the relative error ranges from 3,61 to 1.0 % for the concentration of DFQ in the range from 0.36 to  $1.80 \,\mu\text{g/ml}$ .

Chemical structure of Difenzoguat

Table 1. Accuracy and precision of the DrQ determination							
Taken (μg/ml)	Found $x$ (µg/ml)	n	S (µg/ml)	G (%)	$\frac{\overline{x} - \mu}{\mu} \cdot 100  (\%)$		
0.36	0.38		0.0112	3.61	6.16		
0.90	0.87	5	0.0178	2.55	3.11		
1.80	1.83		0.0134	1.00	2.00		

Table 1. Accuracy and precision of the DFQ determination

x - mean value;  $\mu$ -true value; n-number of determinations; S-standard deviation; G-relative error (=100·t·s/x  $\sqrt{n}$ , where n=5 and t is Student's for 95% confidence)

#### Conclusion

In this paper, the new kinetic method is proposed for determination of herbicide Difenzoquat. Under the optimal reaction condition a calibration line is constructed, it can be used for determination of DFQ in the interval from 0.36 to 1.80  $\mu g/ml$ . Kinetic equations are calculated.

- [1] A. A. Alexiev, P. R. Bontchev, and S. Grantcheva, Microchimica Acta 1976 (II), 487-495.
- [2] D. Barceló, in "Environmental Analysis Tehniques, Applications and Quality Assurance", D. Barceló, ed., Elsevier, Amsterdam, p. 149, 1993.
- [3] I. Liska, J. Chromatography A, 1993, **655**, 163.
- [4] J. M. Huen, R. Guillard, A. G. Mayer, B. Baltensperger, H. Kern, Fresenius J. Anal. Chem., 1994, 348, 606.
- [5] O. Huschens, Wasser Abwasser 134 (10), 620, 1993.
- [6] M. C. Carneiro, L. Puignou, M. T. Galceran, J. Chromatography A, 1994., 665, 295.
- [7] H. Müler, M. Otto, G. Werner, Katalytische methoden in der spuren analyse, Leipzig, 1980.

# CATALYST COKING – FROM A DAMAGE TO NANO - TECHNOLOGY

## N.M. Ostrovskii HIPOL a.d., 25250 Odžaci, Serbia

The formation of carbonaceous deposits on the catalyst surface is the major cause for the degradation of catalyst performance in many industrial processes.

In catalytic cracking,  $\sim 3-6\%$  of a raw material is converted into coke and burnt off during catalyst regeneration. In the United States alone, this makes up 15–18 million tons of vacuum gas oil a year and is nearly identical to the capacity of all cracking units in Russia [1].

In the steam-methane-reforming process, the formation of carbon filaments over metallic catalysts is treated up to now as a serious problem due to the catalyst deactivation and possible damages in the reactor walls.

The catalyst coking is the main obstacle in developing of catalysts for "dry reforming" and for fuel cells [2].

The industrial application of solid acid catalysts in isobutane alkylation with butenes is hampered by a very rapid deactivation owing to deposition of highly unsaturated products on the catalyst [3].

Generally, the formation of coke-like deposits on catalysts becomes the key problem in modern catalysis, the main goal of which is not yet the higher activity, but the higher stability and selectivity. That is why a numerous techniques are used for identification and characterization of carbonaceous deposits [4], such as TPO, EM, EELS, FTIR, LRS, NMR, AES, XRD, XPS, EPR, etc.

On the other hand, the long-term investigations of the coke structure create a base for purposeful synthesis of different carbon materials (filaments, fibers, like-onion carbon, nanofoams, nanotubes, etc.) using solid catalysts. In such a manner, the catalyst coking (a danger of industrial catalysis) gives birth to its "daughter" – that is a nano-technology of carbon materials. Thus, it can be considered as an "illegitimate child" of catalyst coking, born due to "extramarital relationships" with physical methods.

# **Structure of Coke Deposits**

Carbonaceous deposits grow like children – affected by "parents" (catalyst and reaction) and by "street" (temperature, pressure and concentrations).

Generally, coke deposits differ in chemical composition (H/C ratio); in molecular structure (aliphatic, aromatic, graphitic); in morphology (2D-patches, 3D-blocks, filaments, tubes, shells); in localization (on metal crystallite, on support, inside or outside of zeolite crystallites). The variety of cokes is manifested, for example, through different curves of temperature-programmed oxidation (TPO) of coked catalysts (Fig. 1).

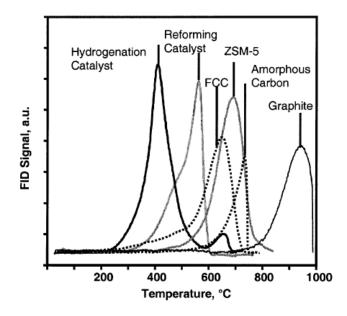


**Fig. 1.**TPO profiles of several coked catalysts [4].

With this information, the general formula CHx of coke can be obtained. The H/C ratio is determined by measuring the total amount of H2O and CO2 released during TPO. It was found in butane isomerization on ferrierite [5], that this ratio decreases in time, and that during the TPO analysis, the H/C ratio varied from as high as 4 at 300°C to as low as 0 at 600°C.

In n-heptane dehydrogenation, "...coke deposited on various aluminasupported Pt–Re catalysts revealed a tri-dimensional stacking of aromatic ring structures less than 1 nm in size which may further form larger porous carbon particles as coking increased" [6].

Nickel and iron catalysts are well known for their ability to form whisker (or filamentous) carbon. In butane steam reforming on Ni/Al2O3 and Ni/MgO catalysts, using high resolution electron microscopy, the three kinds of carbon deposits were found: true filaments, tubes, and shells [7]. The deposits produced at low temperatures (below 500-600°C) consist of true filaments. At higher temperatures (600-680°C) tubes with carbon layers nearly parallel to the tube axis are formed. The close carbon shells occurred only on large metal particles of 100 nm approximately.

Certain types of these carbon fibers, also known as "nanotubes", have been discovered as far as at beginning of 50-th by Radushkevich and Lukianovich [8,9], and are extensively characterized last fifteen years [9]. The nanotubes have the graphite planes parallel to the cross-section of the fiber; whereas the whisker carbon has the graphite planes parallel to the axis.

In carbon nanotubes (CNT) history, single-walled nanotubes (SWCNT) should be distinguished from multi-walled nanotubes (MWCNT) [9]. The formation of SWCNTs was first reported in 1993 [10,11], but MWCNTs are widely investigated and used during at least sixty years [9,12].

#### **Mechanisms and Models**

Voorhies [13] was the first to quantitatively describe catalyst coking for catalytic cracking based on the theory of topochemical reactions:

$$a = a_o - \gamma C_c, \quad C_c = A t^n \tag{1}$$

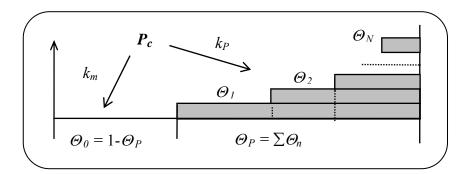
where  $\gamma$ , A, and n are the formal parameters.

Linear and exponential dependencies of catalyst activity vs. coke concentration [14] are the simplest and widely used in theoretical and engineering calculations:

$$a=1-\gamma C_c$$
,  $a=\exp(-\gamma C_c)$  (2)

The linear dependency is related with the monolayer (or monomolecular) deposition of coke; and the exponential one corresponds to the case when the rate of coke formation remains unchanged and independent of the catalyst activity [15].

The follows scheme presents the mechanism of multilayer coke formation:



Corresponding equations that relate the a and  $C_c$  parameters have two forms [15]:

a) infinite coke formation: 
$$\frac{C_c}{C_m} = (1 - \varphi) (1 - a) - \varphi \ln a$$
 (3)

b) finite number of layers: 
$$\frac{C_c}{C_{\text{max}}} = 1 - \frac{C_m}{C_{\text{max}}} a - \left(1 - \frac{C_m}{C_{\text{max}}}\right) a^{\varphi}$$
 (4)

These equations and their combinations are applicable to solid acid catalysts [15] and some zeolites [17]. Fig. 2 presents the plots corresponding to Eq. (4) at various values of  $\varphi = k_p / k_m$ . The curves between the straight lines  $\varphi = 0$  and  $\varphi = 1$  are similar to those within the framework of the model of infinite coke formation.

The relations at  $\varphi > 1$  correspond to the case of substantial coke deposition  $(C_c)$  at an insignificant decrease in the activity (a). Nevertheless, the long period of slight deactivation is followed by its avalanche decrease or by so-called "critical deactivation". Such a deactivation is often observed in practice and may be caused by blockage of pores or zeolite channels during coke deposition.

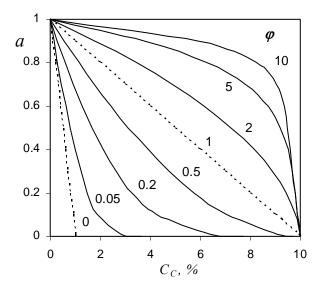
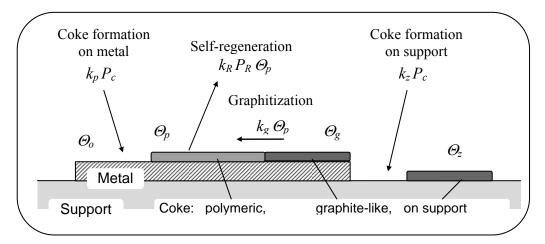


Fig. 2.

Relative catalytic activity as a function of the coke concentration calculated by Eq.(4).

The coking of metal supported catalysts has a number of specific features that influence its kinetics and the dependence of catalyst activity on coke concentration. This is most clearly seen for the low percentage platinum catalysts used in naphtha reforming (Pt, Pt–Re, Pt–Sn on  $Al_2O_3$ ). The corresponding mechanism and models are proposed in [16]:



The main peculiarities are: the formation of several types of coke; the self-regeneration of metal crystallites by hydrogen; and the coke graphitization.

Therefore, different equations for relationships between activity and coke concentration should be derived for each type of active centers. For the metallic active centers (hydrogenation-dehydrogenation reactions) such an equation has the following form [16]:

$$\frac{a - a_s}{1 - a_s} = \left(1 - \frac{C_c}{C_{\text{max}}}\right)^{\frac{\varphi_1}{1 - a_s}} \tag{5}$$

The model of dynamics of "polymeric"  $(C_p)$  and total coke deposition  $(C_c)$  is also derived in [16]:

$$C_p = \frac{C_s}{1 - \alpha/\beta} \left( e^{-\alpha t} - e^{-\beta t} \right) \tag{6}$$

$$C_c = \frac{C_m}{1 - \gamma/\beta} \left( e^{-\gamma t} - e^{-\beta t} \right) + \gamma C_{\text{max}} \left( 1 - e^{-\gamma t} \right)$$
 (7)

Here  $C_s$  corresponds to  $a_s$ , and parameters  $\alpha$ ,  $\beta$  and  $\gamma$  are proportional to rates of graphitization ( $\alpha \sim k_g$ ), coking of metal ( $\beta \sim k_p P_c$ ), and of support ( $\gamma \sim k_z P_c$ ).

Even more complicated is the filament carbon formation on supported Fe, Ni, and Co metal catalysts [18-22] in according to so called "mechanism of carbide cycle" [18]. It is generally accepted that it involves the formation of adsorbed surface carbon, dissolution/segregation, diffusion of carbon through metal particles and precipitation of filaments [20]. Snoeck et al. [20] have proposed that the global driving force for carbon filament formation is the difference in chemical potential between the gas phase and the carbon filament.

It is interesting that metal crystallites reshape its structure under process condition [21] due to the carbon formation on the crystal face (111), Fig. 3.

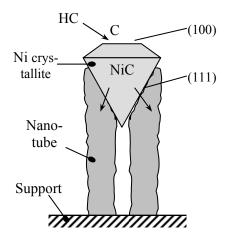


Fig. 3.

Schematic representation of the mechanism of filamentous carbon formation.

C – carbon; HC – hydrocarbon; NiC – nickel carbide.

Thus, tacking into account Fig. 3, the equation of carbon diffusion

through the nickel crystallite, which is proposed in [20], can be written in the form:

$$r_{Dc} = \frac{a_{Ni}}{d_{Ni}} D_c \left( C_{c(100)} - C_{c(111)} \right), \tag{8}$$

and should be supplemented with kinetic model of hydrocarbon conversion over such a catalyst [22].

## **Applications**

Before the age of carbon nanotubes, the application of coke deposits was limited by combustion of coke during catalyst regeneration. For example, in catalytic cracking (FCC) the catalyst coking continually adjusts itself to stay in heat balance. The unit produces and burns enough coke to provide energy to:

- (i) increase the temperature of the fresh feed, recycle, and atomizing steam from their preheated states to the reactor temperature;
- (ii) provide the endothermic heat of cracking.

Therefore, FCC units in USA, Russia, and Serbia burn respectively about 42000, 2500 and 150 t/day of coke, producing 4800, 280, and 17 MW of energy.

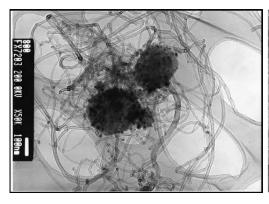
The specific feature of carbon deposits on platinum catalyst is that carbon can incorporates into active sites of certain reactions [23, 24]. In other words, carbon participates in active site formation under the action of the reaction mixture.

The mechanism shown in Fig. 3 indicates that filamentous coke formed the structure of metal crystallite, and can even increase its activity [25], while encapsulating coke promoted deactivation. In such a manner, the catalyst coking becomes an effective method of the synthesis of new catalysts Ni-Me/C for different reactions, such as hydrogenation, CO conversion etc. [26].

Naturally, the main attention is paid in the literature to the synthesis of different carbon materials using hydrocarbons decomposition on the catalyst. The variation of catalysts, feeds and reaction conditions provide the production of carbons with different morphology – from filaments (Fig. 4) to "flowers" (Fig. 5).

Many fields of application of such a new allotropic carbon structures arise each month, especially in a popular scientific literature. Some of them, such as catalyst supports, special adsorbents, or composites are successfully used. Others, especially single-walled nanotubes, are at the beginning of application.

Carbon paper, carbon wool, and carbon felt are well-known materials applied in adsorption technique, in fuel cells, and in medicine.



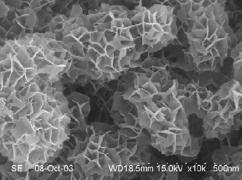


Fig. 4. Carbon nanotubes [22].

Fig. 5. Carbon nanoflowers [28].

Many special adsorbents are developed, such as N-contained filamentous carbon [27]; macro-porous carbon nanotubules, with diameters greater than 30 nm; and micro-porous carbon with three-dimensional nanoarray structure, which has a 3600 m2/g surface area [29], etc.

Carbon nanotubes have already been used as composite fibers in polymers to improve the mechanical, thermal and electrical properties of the bulk product [30].

#### **Problems**

In spite of significant progress, the most interesting are numerous practical and theoretical problems of catalyst coking and formation of carbon deposits. From the practical point of view, two contrary problems still remain:

- 1. In catalysis: The maximal suppression of coke formation;
- 2. In carbon materials: The maximal increasing of carbon deposition.

There are also many scientific problems, having interdisciplinary character. Probably the most complicated is the problem of application of some usual lows, theories, and equations (like diffusion (8)) to the processes in nano-scale.

The new approach is necessary in kinetics of topochemical reactions that can be applicable to the growing of nanotubes.

The application of thermodynamic functions (based on critical parameters) to nano-materials probably should be revised.

It would be very useful to obtain the new simple equation of adsorption on(in) nano-materials instead of Dubinin equation for micro-porous structure.

Note that new ideas in physics of solid state have already arisen during investigation of carbon allotropes (fullerene, graphene, nanotubes, nanobud etc.).

It shouldn't be wonder if some new ideas and results will have presented at this conference.

#### Nomenclature

 $a = r / r^{\circ}$  – relative catalyst activity;

 $a_s$  – residual or stationary catalyst activity;

 $C_c$ ,  $C_p$  – coke concentration and polymeric coke on supported metal;

 $C_{m}$ ,  $C_{\text{max}}$  – monolayer and maximal coke concentration;

 $D_c$  – carbon diffusivity in metal;

 $k_m$ ,  $k_p$  – constants of the formation of the first (monolayer) and next coke layers;

t – time:

r,  $r^{o}$  – current and initial reaction rate;

 $\Theta_n$  – surface fraction occupied by n coke layers;

 $\Theta_0$ ,  $\Theta_P$  – overall fractions of the free and coked surfaces, respectively;

- [1] N.M. Ostrovskii Catalyst deactivation kinetics, Moscow, Nauka, 2001, 334 p. (Rus.)
- [2] De Chen, R. Lodeng, et al. Chem. Eng. Sci., 2001, **56**, 1371-1379.
- [3] J.M. Martinis, G.F. Froment Ind. Eng. Chem. Res., 2006, 45, 940-953.
- [4] C.A. Querini "Coke Characterization", In Catalysis, vol. 17, The Royal Society of Chemistry, 2004, 166-209.
- [5] W.Q. Xu, Y.G. Yin, S.L. Suib, C.L. O'Young, J. Phys. Chem., 1995, 99, 758-765.
- [6] C.A. Querini, S.C. Fung Catalysis Today, 1997, 37, 277-283.
- [7] E. Tracz, R. Scholz, T. Borowiecki Appl. Catal., 1990, 66, 133-147.
- [8] L.V. Radushkevich, V.M. Lukianovich J. Phys. Chem., 1952, 26, 88-95 (Rus.)
- [9] M. Monthioux, V.L. Kuznetsov Carbon, 2006, 44, 1621-1623.
- [10] S. Iijima, T. Ichihashi Nature, 1993, **363**, 603-605.
- [11] D.S. Bethune, C.H. Kiang, et al. Nature, 1993, **363**, 605-607.
- [12] H.P. Boehm Carbon, 1997, **35**, 581-584.
- [13] A. Voorhies Ind. Eng. Chem., Prod. Res. Dev., 1945, 37, 318-322.
- [14] G.F. Froment, K.B. Bischoff Chem. Eng. Sci., 1962, 17, 105-114.
- [15] N.M. Ostrovskii Kinetics & Catalysis, 2001, 42, 317-325.
- [16] N.M. Ostrovskii Kinetics & Catalysis, 2001, 42, 326-333.
- [17] N.M. Ostrovski, S.A. Rovenskaja, G.V. Echevski Chem. Ind. & Chem. Eng. Quarterly, 2007, 13, 51-54.
- [18] R.A. Buyanov Coking of the Catalysts, Novosibirsk, Nauka, 1983, 208 p. (Rus.)
- [19] J.R. Rostrup-Nielsen, D.L. Trimm J. Catal., 1977, 48, 155-165.
- [20] J.W. Snoeck, G.F. Froment, M.J. Fowles J. Catal., 1997, **169**, 240-249.
- [21] V.V. Chesnokov, R.A. Buyanov, V.I. Zaikovskii Eurasian ChemTech Journal, 2003, **5**, 253-260.
- [22] M. Perez-Cabero, E. Romeo, et al. J. Catal., 2004, **224**, 197-205.
- [23] S.M. Davis, F. Zaera, G.A. Somorjai J. Catal., 1982, 77, 439-459.
- [24] M.J. Sterba, V. Haensel Ind. Eng. Chem., Prod. Res. Dev., 1976, 15, 3-17.
- [25] A.L. Alberton, M. Souza, M. Schmal Catal. Today, 2007, 123, 257-264.
- [26] V.V. Molchanov, V.V. Chesnokov, R.A. Buyanov 5-th. Russian Conf. on Catalyst Preparation and Technology, Omsk, 2004, p. 18.
- [27] G.N. Il'inich, R.I. Kvon et al. Ibid, p. 72.
- [28] Jimin Du, Zhimin Liu et al. Materials Letters., 2005, 59, 456-458.
- [29] B. Sakintuna, Y. Yurum Ind. Eng. Chem. Res., 2005, 44, 2893-2902.
- [30] Yu Min-Feng Science, 2000, **287**, 637-640.

# STUDY OF REDUCED Pd-NiMg/SiO<sub>2</sub> SYSTEM BY MEANS OF X-RAY DIFFRACTION TECHNIQUE

M. Gabrovska, P. Tzvetkov, D. Lončarević and M. Stanković

<sup>1</sup>Institute of Catalysis, Bulgarian Academy of Sciences, Sofia 1113, Bulgaria (margarita.gabrovska@abv.bg)

<sup>2</sup>Institute of General and Inorganic Chemistry, Bulgarian Academy of Sciences, Sofia 1113, Bulgaria <sup>3</sup>ICTM, Department of Catalysis and Chemical Engineering, Belgrade 11000, Serbia

#### **Abstract**

Two series of palladium modified Ni-Mg materials with close composition are synthesized on  $SiO_2$  support derived from two silica sources: diatomite activated at  $800^{\circ}$ C (Series **a**; Mg/Ni = 0.1 and  $SiO_2/Ni = 1.07$ ) and synthetic water glass (Series **b**; Mg/Ni = 0.1 and  $SiO_2/Ni = 1.15$ ). The palladium content corresponds to the molar ratios of Pd/Ni = 0.0025, 0.025 and 0.1.

The effect of the support origin and the amount of palladium modifier on the metallic nickel dispersion in reduced-passivated Pd-NiMg/SiO<sub>2</sub> samples has been established by X-ray diffraction technique. It has been elucidated that the usage of diatomite as silica precursor provokes better metallic nickel phase crystallization than the water glass one. The modification of NiMg/SiO<sub>2</sub> samples with palladium increases the degree of nickel phyllosilicate reduction accompanied by formation of relative smaller metallic nickel particles more pronounced in the water glass supported samples. The highest content of the palladium modifier causes the highest dispersion of the metallic nickel phase on both supports, more remarkable in the water glass supported sample.

#### Introduction

X-ray diffraction (XRD) is a well-consolidated technique, which continues to maintain its relevance in the catalyst characterization. Though in heterogeneous catalysis the active sites are usually located on the solid surface, the bulk structure plays an important role, because many of the catalyst characteristics depend on it. Traditionally, the information contained in a powder diffraction pattern has been used essentially as a fingerprint, for crystal phase identification purposes [1].

The most widely used catalyst in the hydrogenation of vegetable oils consists of small Ni clusters (nm range) dispersed on oxidic carriers like SiO<sub>2</sub> or Al<sub>2</sub>O<sub>3</sub> [2]. Despite of the intensive research activity in this field there are only scarce attempts to investigate the role of additives or modifiers on the phase composition, formation and dispersion of the metallic nickel phase of these catalysts.

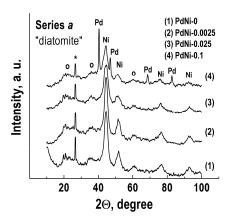
In the present work Pd-modified  $NiMg/SiO_2$  materials are investigated as potential precursors of vegetable oil hydrogenation catalysts. The effect of the source of the support and the palladium content on the metallic nickel dispersion establish by XRD technique in reduced-passivated Pd-Ni-Mg/SiO<sub>2</sub> samples is the object of this study.

## **Experimental**

Pd-Ni-Mg materials are synthesized on SiO<sub>2</sub> support derived from two silica sources: activated at 800°C diatomite (Series a) and synthetic water glass (Series b). Co-precipitation of metal nitrates with Na<sub>2</sub>CO<sub>3</sub> at 90°C and pH=10.00±0.05 is applied. All samples are prepared with composition (Mg/Ni = 0.1 and SiO<sub>2</sub>/Ni = 1.07 (Series a) and Mg/Ni = 0.1 and SiO<sub>2</sub>/Ni = 1.15 (Series b), while the molar ratios of Pd/Ni are 0.0025, 0.025 and 0.1. The designation of the materials corresponds to the Pd/Ni molar ratio, i.e. Ni-0 (Pd free), PdNi-0.0025, PdNi-0.025 and PdNi-0.1. The studied samples are reduced at 430°C for 5 h with a gas mixture of H<sub>2</sub>/Ar (1/1) followed by passivation at room temperature with a mixture of 350 ppm O<sub>2</sub> in nitrogen in order to diminish the exceptional pyrophority of the metallic nickel. XRD measurements of the reduced samples are performed on a Bruker D8 Advance powder diffractometer employing  $CuK_{\alpha}$  radiation ( $\lambda = 0.15418$  nm). The crystalline phases are identified using Joint Committee on Powder Diffraction Standards (JCPDS). The estimation of the mean metallic nickel crystallite size is done by "A curve fitting and data analysis program Fityk 0.8.6" using the Scherer equation.

#### **Results and Discussion**

XRD patterns of the reduced-passivated materials from Series **a** (Fig. 1) demonstrate very narrow diffraction line at  $2\theta = 26.7^{\circ}$ , due to the presence of quartz phase (\*) (JCPDS file #03-0444) from the diatomite used as a source of support.



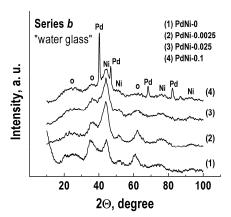


Fig. 1. XRD patterns of reducedpassivated samples from Series a

**Fig. 2**. XRD patterns of reduced-passivated samples from Series **b** 

The diffractograms of all samples show low intensity lines located at  $2\theta = 21.6$ , 36 and  $60^{\circ}$  characteristics of unreduced remainder of nickel phyllosilicate phase (o) formed during that the preparation procedure (Figs. 1 and 2). This phase

is in a higher amount in the materials from Series **b**, particularly in the case of unmodified material (Fig. 2, PdNi-0 sample). Obviously, the reduction of phyllosilicate phase is more completed in the supported on diatomite samples.

The XRD patterns of unmodified solids from both Series (Figs. 1 and 2, PdNi-0 samples) are characterized by four peaks situated at  $2\theta = 44.5$ , 51.7, 76.6 and  $92.9^{\circ}$  which may be related to the metallic nickel phase in a cubic symmetry (JCPDS file #4-0850), better organized in the material from Series **a.** This result reflects on the Ni<sup>0</sup> particle size, namely 4 nm of the sample supported on diatomite and 2 nm of the corresponding material supported on water glass.

The addition of palladium to  $NiMg/SiO_2$  sample from Series **b** leads to decrease of the amount of nickel phyllosilicate phase depending on Pd/Ni ratio in lesser extent than the samples from Series **a**.

The palladium presence in the samples from both Series causes appearance of a phase, located at  $2\theta = 40.3$ , 47, 68.6, 82.2 and  $86.7^{\circ}$  corresponding to the cubic metallic palladium phase (JCPDS file #46-1043). It should be noted that well-organized Pd<sup>0</sup> phase appears only in the materials with the highest loading of modifier (Figs. 1 and 2, PdNi-0.1 samples). Absence of any reflections from Pd<sup>0</sup> phases in PdNi-0.0025 and PdNi-0.025 samples due to the lower palladium concentration.

The broadening of the  $\mathrm{Ni^0}$  diffraction lines demonstrates the presence of small crystallites particularly on the water glass supported samples. These results are confirmed by H<sub>2</sub>-chemisorption data revealing that the usage of water glass as silica precursor ensures higher total metal dispersion in all palladium containing samples than the analogues supported on diatomite applied as a source of silica.

#### Conclusions

XRD reveals that the usage of diatomite as silica precursor provokes better crystallization of the metallic nickel phase than water glass does.

The modification of  $NiMg/SiO_2$  samples with palladium increases the degree of nickel phyllosilicate reduction accompanied by formation of relative smaller metallic nickel particles more pronounced in the water glass supported samples.

The highest content of the palladium modifier causes the highest dispersion of the metallic nickel phase on both supports, more remarkable in the water glass supported sample.

# Acknowledgements

The authors are grateful to the National Science Fund at the Ministry of Education and Science of Bulgaria, for the partial financial support (Project X-1411) and to the Serbian Ministry of Science through the Project 166001B.

- [1] G. Perego, Catal. Today, 1998, 41, 251-259.
- [2] J. Veldsink, M. Bouma and N. Schoon, Catal. Rev. Sci. Eng., 1997, 39, 253-318.

# INFLUENCE OF MICROWAVE FIELD ON THE KINETIC OF SUCROSE'S ISOTHERMAL HYDROLYSES WITH ION EXCHANGE RESIN

B. Adnađević, J. Jovanović and D. Milovanović Faculty of Physical Chemistry, Studentski trg 12-16, 11001 Belgrade, Serbia

#### **Abstract**

Kinetics of isothermal sucrose's hydrolyses with strong acid type ion exchange resin in microwave field was investigated. It was established that kinetic of isothermal sucrose's hydrolyses in the microwave field with strong acid type ion exchange resin may be modeled with kinetics model of pseudo-first order chemical reaction. The determined specific hydrolyses rate constants are higher for 5-12 times for microwave heated reaction system then for conventionally process at same temperature. Under the influence of microwave heating, both activation energy and pre-exponential factor of the process was decreased 2.4 times compared to the same process under conventional conditions.

#### Introduction

Bucheman [1] and Pitar [2] have been investigated kinetics of isothermal sucrose's hydrolyses with strong acid type ion exchange resin. Khan [3] has been investigated kinetics of sucrose's inversion on the fixed layer of strongly acidic carbon exchanger resin, while Siegers[4] has been examined influence of the exchange resin type (gel or macroporous) on the kinetics of sucrose hydrolyses. Bearing in mind that there are not any publications dealing with the influence of microwave field on the mechanism and kinetics of sucrose hydrolyses, we investigated in this work influence of microwave irradiation on the kinetics of sucrose hydrolyses with strongly acidic exchanger resin.

# **Experimental**

In reaction round bottom vessel, 50 mL sucrose solution (c=57g/L) was putted and thermostated at predetermined temperature. Then, in this solution 15 mL of strongly ion exchang resin IRA-120 was added. That reaction mixture was stirred with a mechanic stirrer with glass-propeller mixer, with 200 rpm. Investigation of kinetics of sucrose hydrolyses in microwave field were performed in a focused microwave reactor (Discover, CEM Corporation, Matthews, North Carolina, US). At predetermined time intervals, samples were withdrawn from the reaction mixtures and glucose content was determined. Miler's spectrometric method was used to determine glucose concentration [5].

Degree of sucrose hydrolyses was determined as: 
$$\alpha = \frac{C_i}{C_{\text{max}}}$$
 (1)

Where:  $C_i$  is glucose concentration at reaction time (t) and  $C_{max}$  is maximal achieved glucose concentration in reaction mixture at certain temperature.

#### **Results and Discussion**

Conversion curves of isothermal sucrose hydrolyse with acidic exchanger resin under the conventional and microwave heating are present in Figures 1a and 1b.

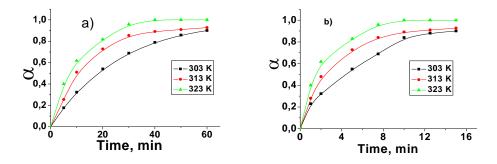


**Fig. 1.** Conversion curves of isothermal sucrose hydrolyse under a) conventional and b) microwave heating

The increase of temperature of the reaction system, for both conventional and microwave heating, leads to decrease of duration of the linear changes of the degrees of hydrolyses with reaction time.

By applying the so-called" model-fitting method" it was found that kinetic of isothermal sucrose's hydrolyses with strong acid type ion exchange resin that may be modeled with kinetics model of pseudo-first order chemical reaction.

The isothermal dependences of  $[-\ln(1-\alpha)]$  vs. reaction time for sucrose hydrolyses at different temperatures are shown in Figures 2a and 2b for the microwave and conventional heating, respectively.

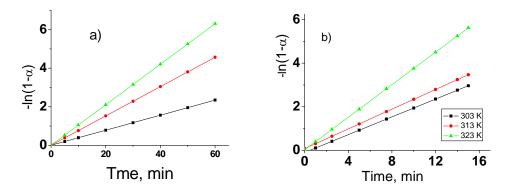


**Fig. 2.** The isothermal dependences of  $[-\ln(1-\alpha)]$  vs. reaction time

Rate constants of isothermal sucrose's hydrolyses and the kinetics parameters (activation energy (Ea) and – pre-exponential factor (lnA) for conventional and microwave heated processes are given in Table 1.

<b>Table 1.</b> Rate constants and the kinetics parameters	eters of sucrose's hydrolyses
------------------------------------------------------------	-------------------------------

T, K		conventional	l	microwave		
	k,min <sup>-1</sup> Ea,		lnA/min <sup>-1</sup>	k,min <sup>-1</sup>	Ea,	lnA/min <sup>-1</sup>
		kJ/mol			kJ/mol	
303	0.017	61±1	20,1±0.2	0.204	24±1	8.3±0.2
313	0.030			0.279		
323	0.079			0.373		

Based on the obtained results, it may conclude that microwave field, at same temperature, leads to the significant increase of the rate constants (from 5 to 12 times) and to important decrees of the kinetics parameters of sucrose's hydrolyses.

Under the influence of microwave heating, both activation energy and preexponential factor of the process was decreased 2.44 times compared to the same process under conventional conditions. Influence of various factors on the rate of sucrose hydrolyses under the microwave field was evaluated. It was found that microwave irradiation leads to the change of the mode of activation and to the specific value of the inner activation energy of the reacting species. That has a consequence the decrease of activation energy and the increase of the reaction rate.

#### **Conclusions**

Action of the microwave field at same temperature as conventional heating leads to the significant increase of the sucrose's hydrolyze rate. The increase of sucrose's hydrolyses in the microwave field is a consequence of the decrease of effective activation energy of hydrolyses process which are caused by the changes of the mode of the activation and with the inner energy of the reactive species under the influence of microwave field.

# Acknowledgement

The investigation was supported by the Ministry of Science of the Serbia, through project G 142025.

- [1] S. Buchman, G.Kubler, C.Meigs, M.Ovens, A.Tallman, Int. Chem. Kinet., 1983, **15**, 1229.
- [2] A. Pinter, J.Batista, J.Levec, Analyst, 2002, 127, 1535-1540.
- [3] S.khan, K.Rahman, Chem.Eng.J.\$Biovhem.Eng., 1996, 61, 7-12.
- [4] G.Siegers, F.Mantinola, Int.Sugar J. 1985, 87, 23-27.
- [5] G.Miller, Anal.Chem, 1959, 31, 426-428.
- [6] M. Brown, D.Dollimore, A.Galwey, Reactions in the Solid State, Comprehensive Chemical kinetics, Elsevier, 1980, 22, 87-91.

# STRUCTURAL AND TEXTURAL PROPERTIES OF Fe-CONTAINING PILLARED CLAY CATALYSTS

P. Banković, A. Milutinović-Nikolić, A. Rosić, N. Jović-Jovičić and J. Dostanić

<sup>1</sup>IChTM-Department of Catalysis and Chemical Engineering, Njegoševa 12, Beograd, Serbia <sup>2</sup> Faculty of Mining and Geology, Đušina 7, Belgrade, Serbia

#### **Abstract**

Metal oxide pillared interlayered clays (PILCs) represent a new class of materials that have found a wide range of potential applications including catalytic oxidative degradation of organic pollutants in water. Synthesized Fe pillared bentonite clays with different Fe content for possible catalytic application were characterized. Phase composition and textural properties of the starting clay and synthesized PILCs were determined using X-ray diffraction and physisorption of nitrogen.

#### Introduction

Catalytic wet peroxide oxidation (CWPO) of organic pollutants in water is a promising technique for the purification of industrial waste streams. Pillared clays (PILCs) can be employed as efficient catalysts in the CWPO, and Fe containing ones have been widely reported as catalysts for the degradation of phenol and phenolic monomers [1–3].

First step that follows the synthesis of a catalyst is its characterization. Certain physical-chemical properties of catalysts, including texture, directly determine their catalytic efficiency. It is known [4] that the indication of successful pillaring – the incorporation of pillars in the clay structure – is the change in basal spacing and its fixation, as well as the increase of the specific surface area of clay. Therefore, the characterization methods chosen in this work were X-ray diffraction and physisorption of nitrogen.

#### **Materials and Methods**

Starting material was a 2  $\mu$ m fraction of characterized domestic clay from Bogovina [5, 6]. The PILCs were obtained according to a common procedure comprising the following steps: grinding, sieving, Na exchange, pillaring, drying and calcination [7]. Pillaring solutions were adjusted to have the atomic ratio Fe<sup>3+</sup>/(Al<sup>3+</sup>+Fe<sup>3+</sup>) of either 10 or 15 %. Corresponding PILCs were denoted as AlFe10 PILC and AlFe15 PILC.

X-ray diffraction (XRD) patterns for powders of raw and pillared clays were obtained using a Philips PW 1710 X-ray powder diffractometer with a Cu anticathode ( $\lambda$ =0.154178 nm).

Nitrogen adsorption-desorption isotherms were determined on Sorptomatic 1990 Thermo Finningen at -196 °C.

#### **Results and Discussion**

According to X-ray diffraction patterns (Fig. 1) the following phases were identified in the investigated samples: smectite, quartz, feldspar and a small amount of amorphous phase [8].

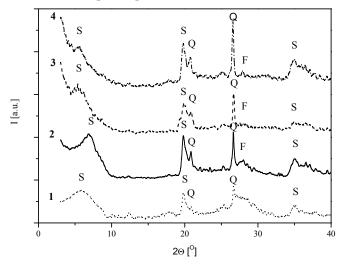


**Fig. 1**. X-ray diffraction patterns of 1) raw clay, 2) Naexchanged clay, 3) AlFe10 PILC and 4) AlFe15 PILC where S=smectite, Q=quartz and F=feldspar

The Na-exchange process lowered  $d_{001}$ from 1.53 nm  $(2\theta =$ 5.78) for starting clay to  $1.28 \text{ nm} (2\theta = 6.92)$ , but the clay retained its swelling properties. The pillaring process increased and fixed the basal spacing of the clay. This resulted in the shift of the (001) smectite neak  $2\theta = 5.40 (d_{001} = 1.64 \text{ nm})$ for AlFe10 PILC and  $2\theta = 5.66 (d_{001} = 1.56 \text{ nm})$ AlFe15 PILC for Apart from smectite, other phases remained unaffected.

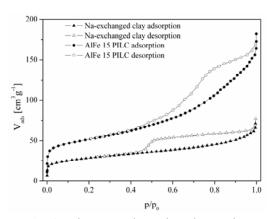


**Fig. 2**. Nitrogen adsorption-desorption isotherms

Figure 2 shows nitrogen adsorption-desorption isotherms registered for AlFe15 PILC (representing similar behavior of both obtained PILCs) and Na-exchanged clay. The curves correspond to the Type II isotherms according to IUPAC classification [9]. All the isotherms have reversible part at low relative pressures and hysteresis loops at higher relative pressures corresponding to the H3 type of hysteresis cycle characteristic to aggregated plane particles forming slit shape pores [6, 9].

Relevant data for all three samples obtained using WinADP software are presented in Table 1.

				1	
Sample	$S_{BET}$ [m <sup>2</sup> /g]	$ \begin{array}{c} V_{0.98} \\ [\text{cm}^3/\text{g}] \end{array}$	$V_{\text{mic}}$ [cm <sup>3</sup> /g]	$\begin{array}{c} D_{max} \\ [nm] \end{array}$	$D_{med}$ [nm]
Na-exchanged	99	0.094	0.041	3.9	3.9
AlFe10 PILC	172	0.229	0.072	5.3	7.3
AlFe15 PILC	175	0.236	0.075	5.7	6.5

**Table 1**. Selected textural properties of investigated samples

Where:  $S_{BET}$  - specific surface area;  $V_{0.98}$  - total pore volume,  $V_{mic}$  - micropore volume,  $D_{max}$  - the pore diameter where the maximum of derivative cumulative volume curves is reached;  $D_{med}$  - median value of pore diameter.

Table 2 shows expected increase in the specific surface area, total pore volume and volume of micropores for pillared samples comparing to the non-pillared one. From  $D_{max}$  and  $D_{med}$  values can be concluded that the pillaring process lead to the shift of mesopore fractions toward grater mesopore diameters.

#### Conclusion

Two Fe pillared clays with different Fe contents were synthesized from domestic clay. Their phase composition and textural properties were investigated. The pillaring process increased and fixed the basal spacing of the clay proving incorporation of pillars into the clay structure. The increase in the specific surface area from approximately 100 m²/g for Na exchanged clay to around 170 m²/g for both pillared clays was registered. Similarity in the textural properties of the two synthesized PILCs indicates that possible difference in their catalytic performance should be ascribed to the difference in the Fe content.

## Acknowledgements

This work was supported by the Ministry of Science of Republic of Serbia (Projects TR 6712B and ON 142019B)

- [1] J.G. Carriazo, E. Guelou, J. Barrault, J.M. Tatibouet, S. Moreno, Appl. Clay Sci., 2003, 22, 303–308
- [2] C. Catrinescu, C. Teodosiu, M. Macoveanu, J. Miehe-Brendle, R. Le Dred, Water Res., 2003, 37, 1154-1160
- [3] S. Caudo, G. Centi, C. Genovese, S. Perathoner, Appl. Catal., 2007, B, 70, 437-446
- [4] Gil, L. M. Gandia, M. A. Vicente, Cat. Rev. Sci. Eng., 2000, 42(1&2), 145–212
- [5] Z.Vuković, A. Milutinović-Nikolić, J. Krstić, A. Abu-Rabi, T. Novaković, D. Jovanović, Mater. Sci. Forum, 2005, 494, 339-344
- [6] Z. Vuković, A. Milutinović-Nikolić, L. Rožić, A. Rosić, Z. Nedić, J. Dušan, Clays Clay Miner., 2006, 6, 697-702
- [7] V. Kaloidas, C.A.Koufopanos, N.H. Gangas, N.G. Papayannakos, Microporous Mater. 1995, 5, 97-106
- [8] International Center for Diffraction Data, Joint Committee on Powder Diffraction Standards (JCPDS) 1990, Swarthmore, USA.
- [9] F. Rouquerol, J. Rouquerol, K. Sing, Adsorption by powders and porous solids, Academic Press, London, 1999

## CHARACTERISATION OF DOUBLE OXIDE SYSTEM Cu-Cr-O SUPPORTED ON γ-Al<sub>2</sub>O<sub>3</sub>

H. Kolev, Z. Cherkezova-Zheleva, J. Krstić, D. Dimitrov, D. Paneva, K. Ivanov and I. Mitov

<sup>1</sup>Institute of Catalysis, Bulgarian Academy of Sciences, 1113 Sofia, Bulgaria, hgkolev@ic.bas.bg <sup>2</sup>IChTM - Center of Catalysis and Chemical Engineering, Njegoševa 12, Belgrade,Serbia <sup>3</sup>Agricultural University, 4000 Ploydiv, Bulgaria

#### **Abstract**

Series of alumina supported chromium–copper catalysts were prepared by coimpregnation method. The samples were characterized by X-ray photoelectron spectroscopy and X-ray diffraction. Dispersion and porosity was also obtained. The experimental and catalytic test results have drawn a conclusion that an interaction between copper and chromium ions takes place. This interaction is responsible for the catalytic activity of the copper-chromium catalysts in reaction of total oxidation of industrial formaldehyde production exhaust gases.

#### Introduction

The industrial formaldehyde production all over the world produce huge amount of dusts and exhaust gases. Their complete oxidation is of high importance. In catalytic studies, much attention is paid to systems containing two different oxide phases deposited on the support [1]. The interaction between two oxide phases may lead to changes in the surface structure and modification of their catalytic properties in comparison to the systems containing such oxides separately. The type of interaction between supported oxides and the structure of the material formed depend on the chemical and crystallochemical properties of each component.

Thus, we considered it interesting to follow the changes in the surface structure of the system containing CuO and  $Cr_2O_3$  supported on  $\gamma$ -Al<sub>2</sub>O<sub>3</sub> and make an attempt to correlate the appearing surface species with catalytic activity [2].

# **Experimental**

Series of copper-chromium oxide catalysts were prepared by co-impregnation method. The samples were obtained by mixing of support  $\gamma$ -Al<sub>2</sub>O<sub>3</sub> with an aqueous solution of chromium anhydride and copper nitrate. The amount of solution taken was sufficient for incipient wetness to be observed. The samples were calcinated at different temperatures: sample  $1-300\,^{\circ}\text{C}$ ; sample  $2-500\,^{\circ}\text{C}$ ; sample  $3-700\,^{\circ}\text{C}$ ; sample  $4-800\,^{\circ}\text{C}$ ; sample  $5-500\,^{\circ}\text{C}$  (triple impregnated).

A Sorptomatic 1990 (Thermo Finningen) was used to determined nitrogen physisorption isotherms at 77K. Appropriate software-WinADP 5.1 was used to determinate textural parameters: Specific surface area ( $S_{BET}$ ), micropore volume ( $V_{mic}$ ) and mesopore volume ( $V_{mes}$ ). The phase composition and structure of the

samples was determined by XRD using TUR M62 diffractometer with Co  $K_{\alpha}$  radiation. Data interpretation was carried out using JCPDS database. XPS measurements were carried out in the UHV electron spectrometer ESCALAB-MkII (VG Scientific) with a base pressure of  $\sim 5 \times 10^{-10}$  mbar by using AlK<sub> $\alpha$ </sub> radiation.

#### **Results and Discussion**

Results of N<sub>2</sub> physisorption measurements indicated that applied procedure of coimpregnation caused significant changes of textural parameters. The corresponding

**Table 1.** Textural propreties of  $\gamma$ -Al<sub>2</sub>O<sub>3</sub> and samples 2 and 5

Sample	S <sub>BET</sub> ,	$V_{mic}$	$V_{mes}$ ,
Sumple	$m^2/g$	nm	nm
γ-Al <sub>2</sub> O <sub>3</sub>	305.7	0.119	0.370
Sample 2	102.2	0.038	0.282
Sample 3	92.8	0.035	0.346

calculated values  $S_{BET}$ ,  $V_{mic}$  and  $V_{mes}$  of some samples and the used support are presented in Table 1. Decrease of specific surface area for any of two chosen samples is adequate to decrease of  $V_{mic}$  (1/3 of beginning value of carrier), showing that  $S_{BET}$  value indubitable originates form partial blocking of micropores

system. Change of mesopore volume indicates that deposition of added copper-chromium species is present in this pore segment. Higher temperature of calcinations opened system of mesopores giving of  $V_{\text{mes}}$  similar to starting alumina values.

The XRD patterns of all studied samples showed broadened low intensity diffraction lines. The pattern of the support is exposed on Fig. 1-a. It was registered aluminum hydroxide phase -  $\alpha$ -AlOOH beside of main crystalline phase -  $\gamma$ -Al<sub>2</sub>O<sub>3</sub>. The registered spectra of double oxide samples Cu–Cr–O supported on  $\gamma$ -Al<sub>2</sub>O<sub>3</sub> (Fig. 1b-d) include mainly the characteristic pattern of the support, as well as broadened lines of low intensity, belonging to highly dispersed supported phases. The reason of this is the small crystallite size of supported phases, which complicated the exact analysis. The aluminum hydroxide phase was not registered in the XRD patterns after thermal treatment. The supported phases are Cu oxide and Cr oxide in sample 1 - CuO and Cr<sub>2</sub>O<sub>3</sub> (Fig. 1b). The crystallynity of the supported phases slowly increased and mixed Cu-Cr oxide phases (as CuCr<sub>2</sub>O<sub>4</sub>, CuCrO<sub>2</sub> and CuCrO<sub>4</sub>) are obtained with an increase of thermal treatment (Fig. 1c-d). There are no evidences of supported Cu-Cr oxides and alumina support interaction.

The samples were characterized also by XPS. The obtained spectra (Fig. 3a)) showed that the intensity of the satellite of the Cu2p peek increases from samples 1 to 5. This means that copper change from  $Cu^{1+}$  to mixture of  $Cu^{1+}$  and  $Cu^{2+}$ . The established  $Cu^{1+}/(Cu^{1+}+Cu^{2+})$  ratio is as follow: for sample 1-1; sample 2-0.85; sample 3-0.67; sample 4-0.25 and sample 5-0.47. The result of these values is in very good agreement with XRD analysis. The peek form and FWHM of Cr2p show that the chromium exists in two forms of different chromium oxides.

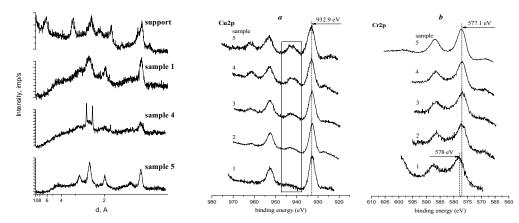


**Fig. 1.** Powder XRD patterns of studied samples.

**Fig. 2.** XPS spectra of **a)** Cu2p and **b)** Cr2p for investigated samples.

#### **Conclusions**

Complex copper-chromium oxide catalysts supported on  $\gamma$ -Al<sub>2</sub>O<sub>3</sub> have been prepared by co-impregnation method. The experimental methods have shown a high-dispersed and low crystalline supported copper-chromium oxide phases. With an increase of the treatment temperature the crystallynity of the supported phases increases and mixed Cu-Cr oxide phases (as CuCr<sub>2</sub>O<sub>4</sub>, CuCrO<sub>2</sub> and CuCrO<sub>4</sub>) are obtained. This result is supported by the obtained change of Cu<sup>1+</sup> to mixture of Cu<sup>1+</sup> and Cu<sup>2+</sup> in samples, respectively. All this explains the observed high catalytic activity of the samples.

# Acknowledgments

The authors are grateful to the Bulgarian National Science Fund at the Ministry of Education and Science (Project VU X-305/2007) and to the Ministry of Science of Serbia for the financial support.

- [1] M. Wojciechowska, J. Haber, S. Łomnicki, J. Stoch, Journal of Molecular Catalysis A: Chemical, 1999, **141**, 155–170.
- [2] D. Dimitrov, Ph Thesis, 2008, Sofia.

# THE CHEMICAL REACTIONS IN THE SYSTEM MoS<sub>2</sub>-CaCl<sub>2</sub>-O<sub>2</sub>

#### D. Zlatanović

Faculty of Mathematics and Natural Science, University of Priština, Serbia

#### **Abstract**

The influence if the temperature on the oxidation of  $MoS_2/CaCl_2$  mixture was investigated. It was corroborated origination of  $CaSO_4$ ,  $CaMoO_4$  and  $MoO_3$  as main solid products at temperatures of  $510^{\circ}C$  and  $610^{\circ}C$ . Thermodynamic calculations of standard enthalpy and standard Gibbs energy confirmed that two chemical reaction of  $CaMoO_4$  origination could proceed spontaneously. In the presence of oxygen this compound formed more probably via reaction of  $CaCl_2$  and  $MoO_2Cl_2$  than  $MoO_3$ .

#### Introduction

The main products of  $MoS_2$  oxidation are  $MoO_3$  and  $SO_2$ . In the mixture of NaCl and  $MoS_2$  those products react with NaCl producing  $Na_2Mo_2O_7$  and some of polymolibdates [1]. Oxidation of  $MoS_2$  begins at temperature above  $375^{\circ}C$  independently on the presence of NaCl. This reaction is always first step of the very complex chemical process. The  $Cl_2$  or molybdenum compound containing chlorine generates at temperature above  $400^{\circ}C$ . Scanning electron microscopy was confirmed melted layer on the surface on NaCl grain at the temperatures above  $425^{\circ}C$ , and EXD-analysis was confirmed the presence of molybdenum on the surface of them. By x-ray analysis was also confirmed  $Na_2S_2O_7$  generation, which melts at the temperature of  $425^{\circ}C$  [2]. It suggests the melting of  $Na_2S_2S_7$  is the main reason for law temperature melting.

In the system metal sulfide/ $CaCl_2$  chlorination also take place and the main products of the reactions are metal chloride and  $CaSO_4$  [3]. Metal chlorides generates by the reaction of gaseous chlorine and metal oxides originated by oxidation of metal sulfide. In the system  $MoS_2$ - $CaCl_2$ - $O_2$  both  $SO_2$  and  $MoO_3$  can react with  $CaCl_2$ . It was the reason for beginning the study of this system.

# Experimental

The equimolar mixture of MoS<sub>2</sub>/CaCl<sub>2</sub> was oxidized in air atmosphere during 30 min at the temperatures of 510 and 610 °C. X-ray diffraction analyze was used to investigate the composition of solid rest. The Siemens D-500 diffractometer, with Ni-filtered CuK<sub> $\alpha$ </sub> radiation and Scanning speed of 0,02 °2 $\Theta$ /s was used.

#### **Results and Discussion**

Following products was identified in the sample after oxidation: CaMoO<sub>4</sub>, CaSO<sub>4</sub>, and MoO<sub>3</sub>. Some of the x-ray reflections of CaMoO<sub>4</sub> and MoO<sub>3</sub> overlap. The Fig.1

shows the parts of the x-ray diffractogrames of the samples oxidized at  $510^{\circ}\text{C}$  and  $610^{\circ}\text{C}$ , respectively, and table 1 represents the results of the comparison of the intensities of the three most intensive reflections of each compound. The main product at  $510^{\circ}\text{C}$  is CaMoO<sub>4</sub>, and at  $610^{\circ}\text{C}$  is CaSO<sub>4</sub>. It is represented on the Fig.1. Comparing the intensity ratio,  $I_{610}/I_{510}$ , (Table 1) for all compounds, it can be seen that the temperature influence positively on the formation of MoO<sub>3</sub>, and CaSO<sub>4</sub>, and negatively on the formation of CaMoO<sub>4</sub>.

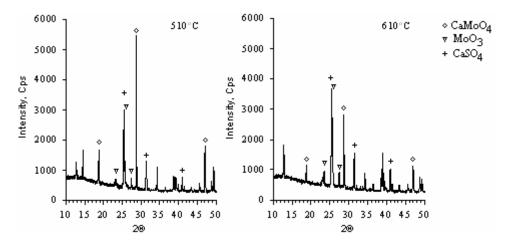


**Fig.1** X-diffractogram of the sample oxidized at 510°C

**Table 1** Intensity ratio,  $I_{610}/I_{510}$ 

14610 1 11110	Angle	<u>d</u>	Intensity	Angle	d	Intensity	
Compound	$2\Theta$	Å	Cps,	$2\Theta$	Å	Cps,	$I_{610}/I_{510}$
		510°C			610°C		
MoO <sub>3</sub>	23,380	3,80177	704	23,352	3,80621	944	1,34
	25,779	3,45317	1283	25,779	3,45317	2698	2,10
	27,395	3,25301	750	27,363	3,25670	915	1,22
CaMoO <sub>4</sub>	18,692	4,74332	1647	18,664	4,75045	1110	0,67
	28,802	3,09720	5457	28,796	3,09780	2805	0,51
	47,172	1,92516	1614	47,136	1,92652	1102	0,68
CaSO <sub>4</sub>	25,528	3,48652	2985	25,511	3,48883	3660	1,23
	31,377	2,84863	1283	31,384	2,84807	1481	1,15
	40,893	2,20505	763	40,897	2,20485	1007	1,32

It is well known that the MoO<sub>2</sub>Cl<sub>2</sub> is the main product of the reaction of MoO<sub>3</sub> and Cl<sub>2</sub>. This compound is stable to 500°C, but in oxygen atmosphere it decomposes to MoO<sub>3</sub> and Cl<sub>2</sub>. [4] At temperature of 553°C the vapor pressure of MoO<sub>3</sub> is only 0,1333Pa [5]. It is too little for significant transport of MoO<sub>3</sub> to the surface of CaCl<sub>2</sub> and reaction with it. Because we suppose that CaMoO<sub>4</sub> forms at 510°C in the reaction of MoO<sub>2</sub>Cl<sub>2</sub> with CaCl<sub>2</sub> or CaSO<sub>4</sub>:

$$CaSO_4 + MoO_2Cl_2 = CaMoO_4 + SO_2 + Cl_2$$
 (1)

$$CaCl_2 + MoO_2Cl_2 + O_2 = CaMoO_4 + 2Cl_2$$
 (2)

Thermodynamic calculations of standard enthalpy and standard Gibbs energy confirmed that both chemical reactions could proceed spontaneously. Table 2 represents values of standard enthalpy and standard Gibbs energy for all reactions, calculated for  $510^{\circ}$ C and  $610^{\circ}$ C.

**Table 2.** Calculated standard reaction enthalpy and standard Gibbs energy for reactions (1) and (2).

Reaction	(	1)	(2)		
Temperature	$\Delta H_{r,T}^{0}$ ,	$\Delta G_{r,T}^{0}$	$\Delta H_{r,T}^0$	$\Delta G_{r,T}^{0}$	
	kJmol <sup>-1</sup>				
783K (510°C)	399,29	-15,77	-42,85	-115,25	
883K (610°C)	413,77	-69,68	-46,55	-124,29	

At temperatures near  $500^{\circ}\text{C MoO}_2\text{Cl}_2$  is still stable and both reactions could occur. The temperature of  $610^{\circ}\text{C}$  is too high and  $\text{MoO}_2\text{Cl}_2$  decompose because no reactions with  $\text{CaSO}_4$  or  $\text{CaCl}_2$  occur.

#### Conclusion

During oxidation of MoS<sub>2</sub> in a mixture with alkali or earth-alkali chlorides chlorination of molybdenum does occur. Both products of oxidation, MoO<sub>3</sub> and SO<sub>2</sub>, can react with chlorides. In the case of CaCl<sub>2</sub> two solid products originate, CaSO<sub>4</sub> and CaMoO<sub>4</sub>. We corroborate origination of these products at 510°C and 610°C by x-ray analysis and confirm that the growing temperature favors CaSO<sub>4</sub> formation

# Acknowledgement

Financial support was provided by the Ministry of Science of the Republic of Serbia (Proj. No. 141049).

- [1] D.Zlatanović, Disertacija, Niš, 1999.
- [2] W.L.Fielder, C.A.Stearns, F.J.Kohl, J.Electrochim.Soc., 1984, 131, 2414-2417.
- [3] K.P.Perović, Ispitivanje kinetike hlorovanja odabranih sulfida metala kalcijumhloridom, Magistarska teza, Beograd, 1995.
- [4] A.A.Furman, Neorganičeskie hloridi, Himia, Moskva, 1980.
- [5] A.I.Efimov, Svoistva neorganičeskih soedinenii-Spravočnik, Leningrad, Himia, 1983.

## KINETICS OF DEEP OXIDATION OF DIMETHYLAMINE OVER Pt/Al<sub>2</sub>O<sub>3</sub> CATALYSTS

N. Radić, B. Grbić, Z. Arsenijević, R. Garić-Grulović and Z. Grbavčić

<sup>1</sup>Institute for Chemistry, Technology and Metallurgy, Department of Catalysis and Chemical Engineering, Njegoseva 12, Belgrade, Serbia <sup>2</sup>Faculty of Technology and Metallurgy, University of Belgrade, Karnegijeva 4, Belgrade, Serbia

#### **Abstract**

The dimethylamine deep oxidation has been studied over Pt/Al<sub>2</sub>O<sub>3</sub> catalysts with mean Pt crystallite sizes of 1.0 and 15.5 nm. The turnover frequency is for order of magnitude higher on the large Pt crystallites than for small Pt crystallites, indicating that the reaction is structure sensitive. The observed changes in dimethylamine reaction orders from 1 to 0 are interpreted on the basis of two kinetic mechanisms, Mars van Krevelen and model based on non equilibrium adsorption of oxygen and strong adsorption of dimethylamine on different active sites.

#### Introduction

Catalytic combustion of volatile organic compounds (VOCs) on noble metals is a widely used method to remove VOCs from industrial waste gases, especially in processes with high flow rates of waste gases and low concentrations of VOCs [1]. Typical catalysts for deep oxidation of VOCs are based on precious metal. For supported noble metal catalysts, any reaction whose rate is affected by the change in particle size is said to be structure sensitive [2]. Most studies have reported that the specific activity of supported noble metal is known to depend on metal crystallite size [3,4]. The aim of this work is to conducting kinetic investigations of the dimethylamine (DMA) deep oxidation over the Pt/Al<sub>2</sub>O<sub>3</sub> catalyst with platinum mean crystallite size of 1.0 and 15.5 nm, in order to determine whether the investigated reactions were structure sensitive.

# **Experimental**

Catalysts preparation- Catalysts were synthesized by impregnation of a  $(\gamma + \theta)$  Al<sub>2</sub>O<sub>3</sub> support by an aqueous solution of hexachloroplatinic acid. After the adsorption of hexachloroplatinic acid the catalyst was filtered, rinsed with distilled water, air-dried and reduced. The average Pt crystallite size of the sample prepared by the above procedure was 1.0 nm. In order to affect the Pt particle size the catalyst synthesized in the previous procedure was calcinated in air at 700 °C for 48 h. The sintered catalyst had a crystallite size of 15.5 nm.

*Catalysts characterization*- The platinum dispersion measurements were performed by CO chemisorption at a temperature of 24  $\pm$  0.2 °C using a pulse gas chromatographic method, home-made apparatus.

*Kinetic measurements*- The kinetics experiments of DMA oxidation were performed in a fixed bed catalytic reactor, made of a stainless steel tube having 6 mm

o.d., 4 mm i.d. and 115 mm in length. Catalytic reactor was situated within gas chromatograph Shimadzu 14-A in the oven that is originally designed for commercial on-column injector OCI–14. Reactor was loaded with 0.100 g of crushed Pt/Al<sub>2</sub>O<sub>3</sub> catalysts, which is near to a volume of 0.135 cm<sup>3</sup>. Applied air flow rates through the catalyst bed corresponded to the space velocity of 17500 h<sup>-1</sup>. The kinetics measurements were performed under steady state conditions and at conversion of DMA below 10%, to ensure the validity of a differential reactor assumption. The reaction rates were expressed as a turnover frequency (TOF), defined as the number of the molecules reacting per second per one exposed Pt atom.

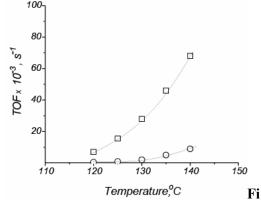
#### **Results and Discussion**

The TOF values for DMA oxidation is presented as a function of temperature in Fig. 1. TOF values was calculated from conversion data in kinetic region and at constant

DMA concentration of 1700 ppm.

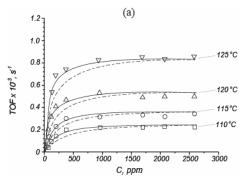
The turnover frequencies for DMA oxidation are for order of magnitude higher on the 15.5 nm Pt crystallites than those for 1.0 nm Pt crystallites size. This suggests that DMA deep oxidation is structure sensitive reactions.

The comparison of the experimentally determined rates (TOF) of deep oxidation of DMA with the values predicted by two kinetics models, which received the widest experimental support, are presented in Fig. 2.



g. 1. The dependence of TOF values in kinetic region on temperature

Symbols:□- d<sub>Pt</sub>-15.5 nm, ○- d<sub>Pt</sub>-1.0 nm.



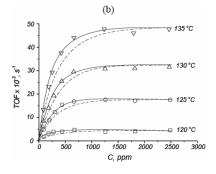


**Fig. 2.** TOF of DMA oxidation on Pt/Al<sub>2</sub>O<sub>3</sub> catalysts with (a)  $d_{Pt}$ -1.0 nm and (b)  $d_{Pt}$ -15.5 nm as function of DMA concentration; Symbols: experimental data. Dashed lines: Mars van Krevelen model; Filled lines: Model based on adsorption of reactants on different active sites.

The two classical kinetic models, Mars van Krevelen and model based on adsorption of reactants on different active sites, were used to fits and interpret the obtained results.

The values of apparent activation energies and the pre-exponential factors for the surface reactions rate constant  $k_i$  and the oxygen adsorption rate constant  $k_0$ , evaluated from Mars van Krevelen model, are summarized in Table 1.

**Table 1.** The kinetic parameters for DMA oxidation according to Mars Van Krevelen kinetic model

d <sub>Pt</sub> (nm)	k <sub>o</sub> (s <sup>-1</sup> )	k <sub>i</sub> (s <sup>-1</sup> )
1.0	$2.5 \times 10^{14} \exp[-123000/RT]$	5.1 x 10 <sup>15</sup> exp[-117500/RT]
15.5	$1.3 \times 10^{14} \exp[-108000/RT]$	$1.1 \times 10^{17} \exp[-117000/RT]$

According to Mars van Krevelen mechanism, the activation energy for oxygen chemisorption rate constant  $(k_0)$  decreases with the increase of the Pt crystallite size and the apparent activation energy for the surface reaction rate constant  $(k_1)$  is independent on the Pt crystallite size.

The values for  $k_o$  and  $k_i$  obtained from model based on adsorption of reactants on different active sites were equal to those obtained in Mars van Krevelen mechanism. This kinetic model suggest that adsorption of DMA play a significant role in overall reaction mechanism.

#### Conclusion

The calculated kinetics parameters from Mars van Krevelen mechanism fit fairly good experimentally measured TOF values. Rate equation based on adsorption of oxygen and DMA on the different active sites fit the kinetic data better than the Mars van Krevelen model.

A observed correlation between kinetic parameters and oxygen reactivity, suggesting that on large Pt crystallites oxygen involved in surface reaction is loosely held, enhancing the reactivity in complete oxidation of DMA. The changes in the reactivity of oxygen with the Pt crystallite size can explain the structure sensitivity found for DMA deep oxidation.

## Acknowledgements

This study was supported by the Ministry of Science of the Republic of Serbia (Proj. No. 142019B and No. 142014G).

- [1] J. Spivey, Ind. Eng. Chem. Res. 1987, **26**, 2165
- [2] M. Boudart, Advances in Catalysis 1969, **20**, 153
- [3] T.F. Garetto, C.R. Apesteguia, Catal. Today 2000, 62, 189
- [4] N. Radic, B. Grbic, A. Terlecki-Baricevic, Appl. Catal. B: Env. 2004, 50, 153

# ROLE OF THE PREPARATION METHOD ON THE ACTIVITY OF Cu-Mn SPINEL OXIDE CATALYSTS FOR LOW-TEMPERATURE WGS REACTION

T. Tabakova, V. Idakiev, G. Avgouropoulos, J. Papavasiliou and T. Ioannides

<sup>1</sup>Institute of Catalysis, Bulgarian Academy of Sciences, 1113 Sofia, Bulgaria
<sup>2</sup>Foundation for Research and Technology-Hellas (FORTH), Institute of Chemical Engineering and
High Temperature Chemical Processes (ICE-HT),
P.O. Box 1414, Patras, Greece

#### **Abstract**

The effect of the preparation method on the activity of Cu-Mn spinel oxide catalysts for low-temperature water-gas shift reaction (WGSR) was studied. Single-step urea-combustion and coprecipitation procedures were used for synthesis of the catalysts. The catalytic activity tests in idealized and realistic reformate demonstrated the superior performance of combustion-prepared catalyst. The comparison of WGS activity of these catalysts with that of commercial CuO-ZnO-Al<sub>2</sub>O<sub>3</sub> pointed out the potential application of Cu-Mn catalysts in low-temperature-WGSR. The results revealed that combustion synthesis leads to the preparation of very active and stable Cu-Mn catalysts.

#### Introduction

The WGSR is well established industrial process for hydrogen generation by conversion of CO in hydrogen-rich gas streams. The need of high-purity hydrogen for fuel cell application stimulates a great activity in the design of novel, highly active and stable WGS catalysts. Copper is often used as an active component in LT-WGS catalysts. The problem with the tendency of Cu to deactivate could be tackled by applying novel preparation methods. Different synthesis procedures have been employed for preparation of Cu-Mn spinel oxide catalysts [1]. To date, measurements of the WGS activity on combustion-prepared Cu-Mn catalysts in idealized and realistic reformate have not been reported. Recently, some of us have demonstrated that the urea-nitrates combustion method is an attractive technique for preparation of Cu-Mn catalysts with favorable characteristics and catalytic properties for steam reforming of methanol [2]. The aim of this study was to examine the role of the preparation method on the activity of Cu-Mn spinel oxides in the WGSR at low temperature.

# **Experimental**

Two different routes were used for the preparation of  $Cu_{0.30}Mn_{0.70}$  catalysts - single-step urea-combustion synthesis (CuMn-CB) and coprecipitation (CuMn-CP). The combustion method (CB) involved autoignition of mixed solution of urea with manganese nitrate and copper nitrate (75% excess of urea) in an open muffle furnace (preheated at 400–500 °C). The powder was further heated at 550 °C for 1

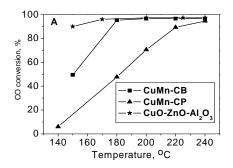
h in order to obtain pure, well-crystallized Cu–Mn catalyst. The coprecipitation (CP) took place by mixing aqueous solutions of manganese and copper nitrate with Na<sub>2</sub>CO<sub>3</sub> at 80 °C, keeping a constant pH value of 8.2 and aging the resulting precipitate at 80 °C for 6 h. After aging, the precipitate was filtered and washed. Further, the precipitate was dried at 100 °C and calcined at 700 °C for 7 h. The catalysts were characterized by N<sub>2</sub> physisorption, XRD, CO-TPR and TPD after CO adsorption. The WGS activity was evaluated in a conventional flow reactor. The following conditions were applied: catalyst bed volume 0.5 cm<sup>3</sup> (0.63-0.80 mm pellets), space velocity 4000 h<sup>-1</sup>, and partial pressure of water vapor – 31.1 kPa. The activity tests were performed after slow reduction up to 250 °C in the reaction gas mixture (CO/Ar + H<sub>2</sub>O). The influence of reaction gas mixture, including idealized reformate (4.492 vol.% CO/Ar) and realistic reformate (15 vol.% CO, 10 vol.% CO<sub>2</sub>, 63 vol.% H<sub>2</sub>, 12 vol. % Ar) were investigated.

#### **Results and Discussion**

The BET surface area of both Cu-Mn spinel oxide catalysts is quite low ( $S_{BET} = 5.8$  and  $5.9 \text{ m}^2/\text{g}$  for CB- and CP-prepared samples, respectively). XRD patterns of fresh catalysts correspond to the spinel phase  $Cu_{1.5}Mn_{1.5}O_4$  and  $Mn_2O_3$ . No detectable diffractions of copper oxide crystallites can be distinguished in both catalysts most probably due to incorporation of the copper ions in the spinel lattice. XRD analysis of used Cu-Mn catalysts showed that the spinel phase has not been completely decomposed after testing under WGSR conditions up to 240 °C and various  $Cu_xMn_yO_z$  spinel phases are still present and co-exist with  $MnO_x$  and copper oxide phases. The exact phases are hardly distinguishable due to the presence of many overlapping peaks.

The reduction profiles of Cu–Mn catalysts are very similar and are characterized by a single peak centered at about 450 °C. The amount of CO consumed during TPR is the same for both samples and corresponds to reduction of both CuO (to Cu $^0$ ) and Mn<sub>2</sub>O<sub>3</sub> (to MnO). The comparison with the TPR profiles of pure CuO (peak maximum at 330 °C) and of pure Mn<sub>2</sub>O<sub>3</sub> (broad low-temperature shoulder at 300–500 °C with a peak maximum at 520 °C) indicates that manganese ions are reduced at lower temperatures compared with pure Mn<sub>2</sub>O<sub>3</sub>. This behavior is due to the promoting effect of copper on the reduction of manganese ions in the spinel. TPD runs after CO adsorption at room temperature showed that: i) no CO adsorbs on pre-oxidized samples; ii) very low amounts of CO are adsorbed on pre-reduced CuMn-CB, while no CO or CO<sub>2</sub> were detected during TPD over CuMn-CP.

The WGS activity of both samples in idealized and realistic reformate (Fig. 1A and B) revealed the superior catalytic performance of combustion-prepared catalyst. This sample reached 95 %CO conversion at 180 °C in idealized reformate and 90 %CO conversion at 220 °C in realistic reformate.



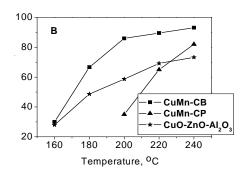


**Fig. 1.** Temperature dependence of CO conversion during WGSR in: A - idealized reformate; B - realistic reformate.

A favorable advantage of Cu-Mn catalyst is its stability. It is known the problem with commercial low temperature shift catalysts composed of CuO/ZnO/Al<sub>2</sub>O<sub>3</sub>, that degrade quickly after exposure to oxygen-containing stream. In order to simulate a shutdown step in the reaction process, the effect of decrease in reaction temperature was explored. The same WGS activity in the whole temperature range was observed after cooling in a wet gas mixture. The stability of Cu-Mn catalysts may be attributed to stabilization of metallic copper particles formed under reaction conditions due to interaction with the host oxide MnO. The catalytic performance of Cu-Mn oxide catalysts was compared to commercial low-temperature CuO-ZnO-Al<sub>2</sub>O<sub>3</sub>. The results indicated that CuMn-CB is more active than commercial sample in realistic conditions.

### **Conclusions**

The results of comparative study of two preparation method demonstrated that combustion synthesis is very suitable method for preparation of active and stable Cu-Mn spinel oxide catalysts for low-temperature WGSR. The comparison with commercial CuO-ZnO-Al $_2$ O $_3$  revealed the potential applicability of combustion synthesized Cu-Mn spinel oxide catalysts in LT-WGSR.

# Acknowledgement

The authors gratefully acknowledge the Ministry of Development, General Secretariat for Research and Technology – Greece and Ministry of Education and Science, National Science Fund –Bulgaria (Project BG-7/2005) for the financial support in common project.

- [1] Y. Tanaka, T. Takeguchi 1, R. Kikuchi and K. Eguchi, Appl. Catal. A, 2005, 279, 59-66.
- [2] J. Papavasiliou, G. Avgouropoulos and T. Ioannides, Catal. Commun., 2005, 6, 497-501.

# PROMOTED SULFUR-RESISTANT Re/γ-Al<sub>2</sub>O<sub>3</sub> SYSTEMS AS WATER-GAS SHIFT REACTION CATALYSTS: SYNERGISM IN CATALYTIC PERFORMANCE

D. Nikolova, T. Grozeva, R. Edreva-Kardjieva and E. Serwicka

<sup>1</sup>Institute of Catalysis, Bulgarian Academy of Sciences, Sofia, 1113, Bulgaria dimi nik@abv.bg

<sup>2</sup>Institute of Catalysis and Surface Chemistry, Polish Academy of Sciences, Krakow30-239, Poland

#### **Abstract**

The series of  $Re_2O_7/\gamma$ - $Al_2O_3$  catalysts (15.3 wt.%  $Re_2O_7$ ) promoted with Ni, Co and K additives were prepared by incipient wet impregnation. The in situ pre-sulfided catalysts were tested in water-gas shift reaction (WGSR) in sulfur-containing feed. The synergistic effect is observed in  $CoRe/\gamma$ - $Al_2O_3$  catalyst. The KCoRe system is a promising catalyst for WGSR with sulfur-containing feed reaching the equilibrium conversion degree still at 270°C.

#### Introduction

The water-gas shift reaction (WGSR) as well as the steam reforming of methane is the most economical processes for hydrogen production. A revival of the interest in the WGSR is observed because of the hydrogen consumption increase, coming from the fuel-cell power system development [1-4].

The development of sulfur-resistant catalysts is expected to help to increase the versatility of the syn-fuel process. A number of papers have appeared studying predominantly sulfided unpromoted and promoted CoMo and NiMo systems [5-8].

Alumina-supported Re-based catalysts have been used in various reactions as hydrogenation, metathesis, reforming. Some recent publications appeared about their application in the hydrodesulfurization and hydrodenitrogenation process [9, 10]. According to our knowledge, these catalysts have not yet been investigated in WGSR conditions. This prompted us to study the activity of Re<sub>2</sub>O<sub>7</sub>/γ-Al<sub>2</sub>O<sub>3</sub> system, with Ni, Co and K as additives, for the H<sub>2</sub> production from sulfur-containing feed via the WGSR.

# **Experimental**

The single-component Re (15.3 wt.% Re<sub>2</sub>O<sub>7</sub>), Ni (3 wt.% NiO), Co (3 wt.% CoO) and K (5 wt.% K<sub>2</sub>O) samples were prepared by incipient wet impregnation of the  $\gamma$ -Al<sub>2</sub>O<sub>3</sub> support (BASF D10-10) with aqueous solutions of the corresponding metal salts followed by drying at 105°C and calcination at 450°C. The nickel and cobalt was added as second component and the potassium was introduced either as a second or a third component to single-component Re sample, following the same preparation procedure of drying and calcination. The synthesized bi- and tri-component samples were denoted as KRe, NiRe, CoRe, KNiRe and KCoRe. The

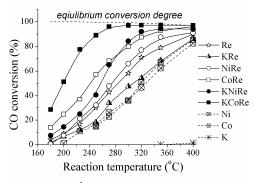
weight content of the Re<sub>2</sub>O<sub>7</sub> corresponded to a surface density of 2 atoms Re/nm<sup>2</sup> support.

The calcined samples were pre-sulfided *in situ* (6 vol.%  $H_2S$  in  $H_2$  at 400°C for 2 h) in continuous-flow reactor. The WGSR was carried out with gaseous mixture of 2 vol.%  $H_2S$ , 7.8 vol.% CO, 90 vol.% Ar. The returning to the initial reaction conditions (400°C and 4000 h<sup>-1</sup>) at the end of each temperature cycle is applied in order to verify if the deactivation has taken place.

#### **Results and Discussion**

Figure 1 illustrates that the CO conversion of the studied samples decreases in the following order:

 $KCoRe > CoRe \ge KNiRe > NiRe \cong Re > KRe > Ni = Co >> K$ .



GHSV 4000 h<sup>-1</sup>, steam/gas ratio 0.3, pressure 1 bar

**Fig. 1.** Catalytic activity of the pre-sulfided Re-containing and one-component Ni, Co, K samples.

Potassium deposition (KRe sample) decreases the activity of Re sample, while nickel addition has no significant influence. The cobalt additive (CoRe) raises the conversion in the whole temperature range of 180–400°C, showing, at higher temperature, activity comparable to that of KNiRe.

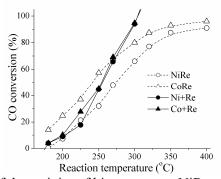


**Fig. 2.** Comparison of the activity of bi-component NiRe and CoRe samples with the sum of conversion degrees of one-component samples.

The best performance is given by the tri-component KCoRe sample, for which CO conversion comparable to the equilibrium conversion degree is reached already at  $270^{\circ}$ C. No deactivation has taken place at the return to the initial reaction conditions ( $400^{\circ}$ C and  $4000 \, h^{-1}$ ).

Fig.2 compares the activities of the bi-component NiRe and CoRe catalysts with the added activities of the one-component Ni, Co and Re samples. It may be seen that in the temperature range of 180–250°C the activity of CoRe catalyst shows a synergetic effect as compared to the sum activity of its single components, while an opposite phenomenon is observed for NiRe catalyst.

#### **Conclusions**

KCoRe system has been identified as a promising catalyst for WGSR with sulfurcontaining feed in the 250–400 °C temperature range.

- A. Tonkovich, J. Zilka, M. La Mont, Y. Wang, R. Wegeng, Chem. Eng. Sci., 1999, 54, 2947-2951.
- [2] Ch. Song, Catal. Today, 2002, 77, 17-49.
- [3] Wolfgang Ruettinger, Oleg Ilinich, Robert J. Farrauto, Journal of Power Sources, 2003, 118, 61–65.
- [4] Gary J. Stiegel, Massood Ramezan, International Journal of Coal Geology, 2006, 65, 173-190.
- [5] D.S. Newsome, Catal. Rev. -Sci. Eng., (1980), 21, 275-318.
- [6] Jin-Nam Park, Jae-Hyun Kim, Ho-In Lee, Bull. Korean Chem. Soc., 2000, 21, 1239-1244.
- [7] D. Nikolova, R. Edreva-Kardjieva, G. Gouliev, T. Grozeva, P. Tzvetkov, Appl. Catal., A: General, 2006, 297, 135-144.
- [8] M. Laniecki, M. Ignacik, Catalysis Today, 2006, 116, 400-407.
- [9] Jarkko Räty, Tapani A. Pakkanen, Catal. Lett., 2000, 65, 175-180.
- [10] N. Escalona, J. Ojeda, R. Cid, G. Alves, A. López Agudo, J.L.G. Fierro, F.J. Gil Llambías, Applied Catalysis A: General, 2002, **234**, 45-54.

# EFFECTS OF MICROWAVE TREATED SUBSTRATE ON PEPSIN REACTION KINETICS

V.M. Pavelkić<sup>1</sup>, D.R. Stanisavljev<sup>2</sup>, K.R. Gopčević<sup>3</sup> and M.V. Beljanski<sup>4</sup>

<sup>1</sup>Institute of Nuclear Sciences Vinča, Vinča, Belgrade, Serbia, vesnap@vin.bg.ac.yu

<sup>2</sup>Faculty of Physical Chemistry, Belgrade University, Belgrade, Serbia

<sup>3</sup>School of Medicine, University of Belgrade, Belgrade, Serbia

<sup>4</sup>Institute of General and Physical Chemistry, Belgrade, Serbia

#### Abstract

Microwave (MW) irradiated bovine serum albumin (BSA) and bromphenol blue (BPB) complex was used as substrate for the assay of pepsin by kinetic method. Decreased reaction velocity under absorbed MW energy and constant temperature was observed.

#### Introduction

Identifying and evaluating the biological effects of microwave (MW) have been complex and controversial. Because of the paucity of information on the mechanism of interaction between MW and biological systems, there has been a persistent view that MW fields are incapable of inducing bioeffects other than by heating. Using microwaves to promote reaction rates of chemical reactions become routine [1, 2]. Their application in enzyme-catalyzed reactions is relatively limited [3]. In general, it is believed that the reactions are accelerated since the molecules absorb energy by two modes: dipole rotation and ionic movement. There is evidence that microwaves cause different biological effects depending upon field strength, frequencies, waveforms, modulation and duration of exposure [4].

# **Experimental**

Bovine serum albumin (BSA), Brom-phenol blue sodium salt (BPB) and Porcine pepsin A were purchased from Sigma Aldrich and used without further purification. MW irradiation was performed in a single mode focused CEM reactor (Model Discover, CEM Co., Matthew, NC) working at 2.45 GHz. External cooling the reaction mixture provided the constant temperature and irradiation power of 0.45 W/g. Enzyme assay was performed in Gly-HCl buffer solution at pH 2 and 37° C using BSA-BPB as a substrate [6]. Lineweaver-Burk double reciprocal plots were used to analyze the effects of MW treated substrate on reaction kinetics.

#### **Results and Discussion**

The water solution of BSA (10 g/ 100 ml) was used for further substrate development. The appropriate amount of dye (BPB) was dissolved in the minimum amount of ethanol, diluted with glycine buffer pH 2.0 to the concentration of 1 mM. 1.80 ml of BSA solution was added to 3.0 ml of BPB solution, mixed well

and make up to 20 ml with glycine buffer pH 2.0. The final concentration of substrate solution was 150  $\mu$ M [6]. Albumin combines with BPB at pH 2.0 to give a product having a different color from the original dye (Figure 1).

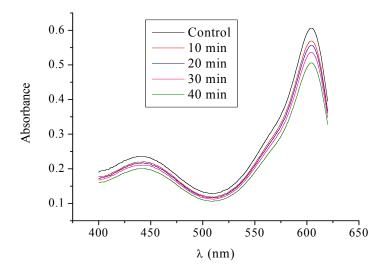


**Fig. 1.** Changes in absorption spectra of BSA-BPB complex under different MW exposure time at 37°C and pH 2.

The composition of BSA-BPB complex was determined by application of the low of mass action to the assumed equilibrium:

$$mBSA + nBPB \Leftrightarrow BSA_m - BPB_n$$

where *m* and *n* represents of molecule reacting. We also determined that albumin and bromphenol blue react in one-to-one molar ratio. There are two absorption peaks, at 445 nm and 605 nm. Induced MW irradiation did not degrade formed complex, but influence on its protein part, probably causing conformational changes in BSA, which manifests in decreased absorbance at characteristic maximum. Pepsin acting on this complex appears to break it up and regenerate the free BPB (the characteristic absorption maximum at 445 nm increased with release of free dye, while maximum at 605 nm decrease implying degradation of BSA-BPB complex). The change in absorbance during enzymatic reaction was followed at 605 nm.

To evaluate kinetic parameters of induced inhibition effects by microwave irradiated substrate, Lineweaver – Burk linearization of Michaelis equation was used. The Michaelis Menten constant ( $K_m$ ) and maximum reaction rate ( $V_{max}$ ) as well as apparent values for  $K_{mapp}$  and  $V_{maxapp}$  in a presence of inhibition effects of microwave irradiated substrate were derive from double reciprocal Lineweavre-Burk plot (Table 1). Catalytic constant  $k_{cat}$  and catalytic effectiveness  $k_{cat}$   $K_m^{-1}$  in a presence of MW treated substrate were also calculated.

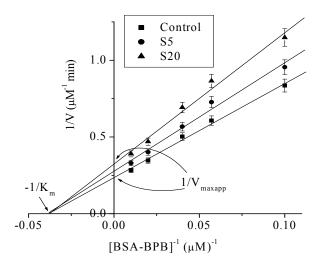


**Fig. 2.** Lineweaver-Burk plot of pepsin inhibition caused by MW treated substrate. ! - control reaction under conventional heating in water bath at 37°C; , - reaction with irradiated BSA-BPB solution for 5 minutes; 7 - reaction with irradiated BSA-BPB solution for 20 minutes.

**Tabe 1.** Kinetic parameters evaluated from double reciprocal Lineweaver-Burk

	V <sub>maxapp</sub> (μM min <sup>-1</sup> )	plots K <sub>mapp</sub> (μM)	k <sub>cat</sub> (min <sup>-1</sup> )	$k_{cat} K_m^{-1}$ (min <sup>-1</sup> $\mu$ M <sup>-1</sup> )
Control	3.51	19.28	2.34	0.121
S5	3.03	18.02	2.02	0.112
S20	2.56	18.23	1.71	0.094

#### Conclusion

The MW irradiation causes conformational changes in protein part of substrate complex and consequently a decrease of enzymatic activity as a function of the absorbed MW irradiation dose of substrate.

- [1] S. Caddick, Tetrahedron, 1995, **51**, 10403-10432.
- [2] V. Sridar, Current Science, 1998, 74, 446-450.
- [3] I. Roy, M. N. Gupta, Tetrahedron, 2003, 59, 5431-5436.
- [4] D.I. De Pomeari, B. Smith, A. Dawe, K. North, T. Smith, D.B. Archer, I.R. Duce, D. Jones, E.P.M. Candido, FEBS Letters, 2003, **543**, 93-97.
- [5] S.P. Gray, J.A. Billings, Clin. Chem, 1983, **29**, 447-451.

## LIPASE-CATALYZED TRANSESTERIFICATION IN SOLVENT FREE SYSTEM

L. Izrael-Živković and I. Karadžić

School of Medicine, Department of Chemistry, University of Belgrade, Visegradska 26, 11000 Belgrade, Serbia

#### **Abstract**

An extracellular lipase from *Pseudomonas aeruginosa* ATCC 27853 is active in a solvent free system where organic solvent (methanol) represent nucleophyle so the reaction of hydrolysis is replaced with reaction of transesterification. Gas chromatography analysis confirmed the formation of methyl-esters (methyl palmitate and methyl laurate) as products of enzyme reaction in methanol.

Kinetic parameters for the lipase reaction in solvent free media were determined showing that the enzyme affinity for p-NP caprylate is the highest. On the other side ratio Vmax/Km decreases in order: p-NP palmitate, p-NP caprylate, p-NP laurate, p-NP butyrate, suggesting that specificity for p-NP palmitate is significantly higher than for p-NP caprylate and butyrate.

#### Introduction

The use of enzymes in organic media has been one of the most exciting challenges of enzymology in recent times. Namely, it was found that there were numerous advantages of using enzymes in organic solvents or aqueous solutions containing organic solvents compared with water, such as increased solubility of nonpolar substrates, shifting thermodynamic equilibria in favor of synthesis over hydrolysis, avoiding side reactions, elimination of microbial contamination in reaction mixtures [1,2]. For non-aqueous enzymatic reaction, different solvent systems have been employed: cosolvent systems, two-phase systems, nearly anhydrous systems, ionic liquids and solvent free systems [3]. Lipases, besides proteases, are enzymes which continue to dominate in applications in the nonaqueous media.

Lipases (triacylglycerol acylhydrolases, EC 3.1.1.3) are ubiquitous in nature, catalyzing the hydrolysis of water insoluble triglycerides to di and mono acylglicerides, free fatty acids and glycerol. Lipases have been utilized for esterification, transesterification and the resolutions of chiral substrates. Lipases act on water insoluble compounds in an emulsion system that is favorable for its activation. Generaly enzymes are not stable in organic solvents and have tendency to denature, but lipases usually remain stable and active in organic solvents without any stabilizer. The stability in organic solvents has been reported for lipases from different microorganisms but it appears that the most widely and extensively used lipases in organosynthetic reactions in biotechnology originate from *Pseudomonas* [3-6]. Obviosly genus *Pseudomonas* is attractive and promising because of its enantiospecific biocatalytic efficiency and high organic solvent tolerance [7]. Between many potential biotechnological applications of lipases, the production of

biodiesel, an alternative diesel fuel (methyl esters of long fatty acids) attracts particular attention of scientific community nowadays offering several advantages over the chemical routes [8,9].

#### **Results and Discussion**

The solvent free media are preferred over nearly anhydrous solvent media because the use of solvent free media allows avoiding the unnecessary expenditure on the solvents and obviates the need for evaporating the solvent for recovery of the product [10].

As it was previously found that lipase from *P. a*eruginosa ATCC is stable in different organic solvents in concentracion 30 %, 50 %, 70 %, and active in cosolvent system methanol/water, it was assumed that the lipase could be active in a solvent free system where organic solvent would be utilized as nucleophyle so the reaction of hydrolysis would be replaced with reaction of transesterification. Enzymatic reaction was carried out in methanol as a nucleophile, by lipase powder using of *p*-NP-esters, as substrate. Gas chromatography analysis confirmed the formation of methyl-esters (methyl palmitate and methyl laurate) as products of enzyme reaction in methanol. This is suggesting that lipase from *P. aeruginosa* ATCC 27853, represents a new opportunity in the area of applied enzyme catalysis, in non water media particularly in methanolysis of vegetable oils using lipase, for the production of biodiesel.

The optimum temperature for the lipase reaction in solvent free system is 45 °C. ATCC lipase is stable at 45 °C for 50 min with remaining activity of 70 %. After the incubation at the temperature of 50 °C and 55 °C lipase activity in solvent free system is reduced to 50 % after 10 and 5 minutes respectively.

Kinetic parameters for lipase reaction in solvent free media were determined and it is shown in table 1.

Table 1.	Kinetic	parameters	of $I$	Ρ.	aeruginosa	ATCC	27853	lipase	ın
methanol									
Substrate		$V_{\text{max}} \times 10^{-3}$	.3		Km x 10 <sup>-3</sup>		V <sub>max</sub> \K	Im	

Substrate	$V_{\text{max}} \times 10^{-3}$	Km x 10 <sup>-3</sup>	$V_{max}\backslash Km$
	(mol/L min)	(mol/L)	(1/min)
<i>p</i> -NP-palmitate	0.169	5.2	0.0325
<i>p</i> -NP-laurate	0.127	7	0.0181
<i>p</i> -NP-caprylate	0.053	2.105	0.0251
<i>p</i> -NP-butyrate	0.104	17.86	0.0058

Obviously Km decreases in the following order: p-NP butyrate, p-NP laurate, p-NP palmitate p-NP caprylate, meaning that the affinity of enzyme for p-NP caprylate is the highest. On the other side ratio Vmax/Km decreases in order: p-NP palmitate, p-NP caprylate, p-NP laurate, p-NP butyrate, suggesting that specificity for p-NP palmitate is significantly higher than for p-NP caprylate and butyrate.

#### Conclusion

The study has shown that extracellular lipase from *P. aeruginosa* ATCC 27853 successfully catalyses transesterification in methanol. It seems as quite possible that many enzymes can function in organic solvent but the challenge is finding the appropriate conditions, what could create new opportunities in the area of applied enzyme catalysis, particularly in methanolysis of vegetable oils using lipase, for the production of biodiesel.

- [1] M. Gupta, I. Roy, Eur. J. Biochem., 2004, 271, 2575.
- [2] V. Gotor-Fernandez, R. Brieva, V.Gotor, J. Mol. Catal. B: Enzym., 2006, 40 111.
- [3] H. Ogino, H. Ishikawa, J. Biosci. Bioeng., 2001, 91, 109.
- [4] L. Kanwar, P. Goswami, Enz. Microb. Technol., 2002, 31, 727.
- [5] U. Jinwal, U. Roy, A. Chowdhury, A. Bhaduri, P.K. Roy, Bioorg. Med. Chem., 2003, 11, 1041.
- [6] I. Karadzic, A. Masui, L. Izrael Zivkovic, N. Fujiwara, J. Biosci. Bioeng., 2006, 102, 309.
- [7] S. Singh, U.C. Banerjee, Process Biochem., 2007, 42, 1063.
- [8] S. Shah, S. Sharma, M. N. Gupta, Indian Journal of Biochemistry and Biophysics, 2003, 40, 392.
- [9] A. Pandey, A. Benjamin, C. Soccol, P. Nigam, N. Krieger, V. Soccol, Biotechnol. Appl. Biochem., 1999, 29, 119.
- [10] S. Shah, M. Gupta, Process Biochem., 2007, 42, 409.

# SPECTROPHOTOMETRIC AND UPLC STUDY OF REACTION BETWEEN [AuCl<sub>4</sub>] AND QUERCETIN

J. Savić, T. Momić, A. Milenković, A. Vujačić and V. Vasić Vinča Institute of Nuclear Sciences, Department of Physical Chemistry, POB 522, 11001 Belgrade, Serbia

#### **Abstract**

The equilibrium and kinetics of the reaction between tetrachloroaurate(III) ion  $(AuCl_4)$  and quercetin in 0.1 M  $HClO_4$  were studied spectrophotometrically. The fast and the slow reaction steps were distinguished in the reaction mechanism, depending on the ratio of  $AuCl_4$  and quercetin concentration. The stoichiometry of reaction, determined by molar ratio and Jobb's methods, was 1:1. The kinetics of complex formation was followed under the pseudo-first order conditions by measuring the absorbance at 294 nm vs. time as the function of quercetin concentration in 5-15 fold excess.

#### Introduction

The interaction of flavonoids with metal ions may change the antioxidant activity and biological effects of flavonoids [1]. Quercetin (Q) is of a great importance for the potential biological and clinical use, because it is a potent inhibitor of some enzymes (myeloperoxidase, reductase) and has the antioxidant properties due to free radical scavenging. Au(III) is a strong oxidizing agent and is, therefore, highly toxic. One of the most investigated complexes of Au(III) with halogens is the tetrachloroaurate ion. The reaction between Au(III) and different flavonoids as the analytical method for the determination of gold in cosmetic preparates was investigated previously [2]. The aim of this work was to investigate the reaction between Q and [AuCl<sub>4</sub>].

#### Experimental

All chemicals were of reagent grade quality. Absorption spectra and kinetic experiments were performed on the Perkin Elmer Lambda 35 UV-Vis spectrophotometer fitted to the universal rapid kinetic accessory HI-TECH model SFA 12. The chromatographic experiments were performed on Waters ACQUITY Ultra Performance Liquid Chromatography (UPLC) system, using an ACQUITY UPLC<sup>TM</sup> BEH  $C_{18}$ ,  $1.7\mu m$ ,  $50mm \times 2.1mm$  column as a stationary phase. The mobile phase was composed of 0.5 vol %  $H_3PO_4$  in water (A) and acetonitrile (B) (A:B=70:30) at a constant flow rate of 0.4 mL/min.

#### **Results and Discussion**

#### Absorption spectra and chromatograms

The reaction between [AuCl<sub>4</sub>] and Q was studied spectrophotometrically in 0.05M HClO<sub>4</sub> 1:1 water/methanol solution. The absorption spectra of solution containing equimolar concentrations of Q and [AuCl<sub>4</sub>] (2.5×10<sup>-6</sup>M) in 0.05M HClO<sub>4</sub> as the function of time are presented in Fig. 1A. Quercetin has the absorption spectra with the maxima at 250 and 370 nm. The decrease of the intensity of these bands and the simultaneous rising of the absorption band at 294 nm indicates the formation of the typical oxidation product due to the Q oxidation by Au(III). The spectral

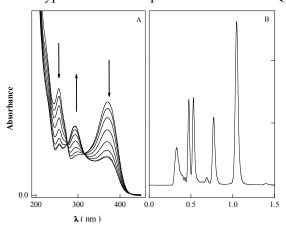


**Fig. 1.** Time dependence of A) absorption spectra of  $2.5 \times 10^{-6} M$  Q and  $[AuCl_4]^-$  in 0.05 M HClO<sub>4</sub> 1:1 water/methanol solution; B) chromatogram of the same solution obtained at 294 nm (injection volume  $10 \mu L$ ).

changes were followed by two quite well defined isobestic points at 273 and 323 nm. The reaction was almost completed after 35 min under the given experimental conditions.

The analysis of chromatogram (Fig. 1 B) indicates clearly, that at least three oxidation products and neutral quercetin form detectable in solution. These products were identified according the literature data [3] and are given in Table 1. They resulted from solvent addition (methanol or/and water) to pquinonemethide, formed by twoelectron oxidation of Q [3].

#### Kinetic studies

It is reasonable to assume that oxidation of Q proceeded as the consequence of the formation of the short time living intermediate formed between  $[AuCl_4]^-$  ion and Q. The absorption band with low molar absorptivity, in the wavelength range from 400 to 550 nm (data not shown) can be ascribed to the short living complex between  $[AuCl_4]^-$  and Q.

**Table 1**. Spectrophotometric and UPLC data for Q,  $[AuCl_4]$  and their reaction products in 0.05M  $HClO_4$  1:1 water/methanol solution

species	$t_{r}(s)$	$\lambda_{max}(nm)$
QH <sub>2</sub> O	28.3	294
QH <sub>2</sub> OMeOH	31.6	294
QMeOH	45.7	294
$QH_2$	61.6	254, 370
[AuCl <sub>4</sub> ]	213.2	225, 315

The complex formation was followed at 450 nm, in the excess of Q, under the pseudo first order conditions. The concentration of [AuCl<sub>4</sub>]<sup>-</sup> was 2.5×10<sup>-6</sup> M, since Q concentration was between 1.25×10<sup>-5</sup> M and 5×10<sup>-5</sup> M. The rise and fall of the absorbance at 450 nm as a function of time (Fig. 2) is characteristic for a reaction

(1) that involves an intermediate C in the overall process during which Q and  $AuCl_4$  react to give the oxidation product, QX:

$$Q + AuCl_4^- \xrightarrow{fast} C \xrightarrow{slow} QX \tag{1}$$

QX represents all possible reaction products obtained due to the oxidation of quercetin [3] and C represents the complex between [AuCl<sub>4</sub>] and quercetin. The dependence of concentration on time can be presented as:

$$[c] = \frac{k_1}{k_2 - k_1} [c]_{\infty} (e^{-k_1 t} - e^{-k_2 t})$$
(2)

where  $k_I$  and  $k_2$  are pseudo first order rate constants for complex formation and oxidation process, respectively, and  $[c]_{\infty}$  is the concentration on the plateau of c vs. t curve. Using Eq. 2, the rate constants  $k_1$ =0.030 s<sup>-1</sup> and  $k_2$ =0.002 s<sup>-1</sup> for the solution containing  $[AuCl_4]^-$  = 2.5×10<sup>-6</sup> M and  $[Q] = 1.25 \times 10^{-5}$  M were obtained. The recalculated results by using these constants are in good agreement with the experimental data. These finding supports the proposed reaction model.

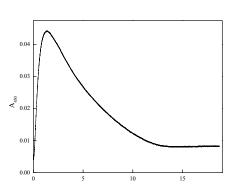


**Fig. 2.** Kinetic curve for formation of complex between Q and [AuCl<sub>4</sub>]<sup>-</sup> recorded at 450 nm ( $C_Q$ = 1.25×10<sup>-5</sup> M;  $C_{AuCl4}$ -=2.5×10<sup>-6</sup> M)

#### **Conclusions**

The reaction between quercetin and [AuCl<sub>4</sub>] in 0.05M HClO<sub>4</sub> 1:1 water/methanol solution leads to the oxidation of quercetin, which resulted in the formation at least three oxidation products. The proposed reaction mechanism involves the complex formation between Q and [AuCl<sub>4</sub>]. For investigation conditions kinetics of reaction between Q and [AuCl<sub>4</sub>] was followed under the pseudo-first order consecutive reaction.

#### Acknowledgements

The authors gratefully acknowledge the financial support of the Ministry of Science the Republic of Serbia (Project No. 142051).

- [1] L.Mira, M.T.Fernandez, M.Santos, R.Rocha, M.H.Florencio, K.R.Jennings, Free Radic. Biol. Med., 2002, **36**, 1199-1208.
- [2] M.Balcerzak, M.Kopacz, A.Kosiorek, E.Swiecicka, S.Kus, Analytical Sciences, 2004, **20**, 1333-1337.
- [3] H.E.Hajji, E.Nkhili, V.Tomao, O.Dangles, Free Radic Res, 2006, 40, 303-320.

# XPS STUDY OF THE NICKEL OXIDATION STATE IN THE REDUCED (Ag)NiMg/SiO<sub>2</sub> VEGETABLE OIL HYDROGENATION CATALYSTS

D. Nikolova<sup>1</sup>, M. Stanković<sup>2</sup>, S. Simić<sup>2</sup>, M. Gabrovska<sup>1</sup>, Pl. Stefanov<sup>3</sup> and R. Edreva-Kardjieva<sup>1</sup>

<sup>1</sup>Institute of Catalysis, BAS, 1113 Sofia, Bulgaria, dimi\_nik@abv.bg

<sup>2</sup>ICTM, Department of Catalysis and Chemical Engineering, 11000 Belgrade, Serbia

<sup>3</sup>Institute of General and Inorganic Chemistry, Bulgarian Academy of Sciences, Acad. G. Bonchev str., bl. 11, 1113 Sofia, Bulgaria

#### **Abstract**

Two series of  $(Ag)NiMg/SiO_2$  catalysts are synthesized on  $SiO_2$  support derived from two silica sources: diatomite activated at  $800^{\circ}C$  (Series **a**; Mg/Ni=0.1 and  $SiO_2/Ni=1.07$ ) and synthetic water glass (Series **b**; Mg/Ni=0.1 and  $SiO_2/Ni=1.15$ ). The modification with silver is made at three molar Ag/Ni ratios, namely 0.0025, 0.025 and 0.1.

The effect of the source of SiO<sub>2</sub> support as well as of the Ag presence and content on the nickel oxidation state in the co-precipitated (Ag)NiMg/SiO<sub>2</sub> catalysts after reduction-passivation procedure are studied by XPS.

The peak-fitting of the composite Ni2p level confirms that nickel on the surface is presented in  $Ni^0$  and  $Ni^{2+}$  oxidation states. The higher content of  $Ni^0$  on the surface of the diatomite supported catalysts shows that the metallic nickel is more stable to oxidation in comparison of the water glass supported ones.

#### Introduction

Nickel supported on a SiO<sub>2</sub> carrier is the most commonly used catalyst for hydrogenation of vegetable oils. It has been published that Ni-Mg catalysts, supported on SiO<sub>2</sub> derived from two siliceous sources, either diatomite or water glass, demonstrate both high soybean oil hydrogenation activity and high quantity of detrimental *trans* fatty acids (TFAs) production [1]. According to our data, the addition of Ag to the nickel/diatomite catalyst suppresses the TFAs formation in the hydrogenated products [2].

It is known that the metallic Ni is the active component in the vegetable oil hydrogenation catalysts. The X-ray photoelectron spectroscopy (XPS) supply useful information about the changes in the oxidation state of the components on the catalyst surface.

It presents some interest to study the effect of the source of  $SiO_2$  support as well as of the silver presence and content on the nickel oxidation state in  $(Ag)NiMg/SiO_2$  catalysts after reduction-passivation procedure. The last procedure is applied with purpose to monitor the stability of surface metallic Ni to oxidation.

#### **Experimental**

#### Sample preparation

(Ag)NiMg samples were synthesized on two silica sources of SiO<sub>2</sub> support: diatomite activated at 800°C (Series a; Mg/Ni=0.1 and SiO<sub>2</sub>/Ni=1.07) and synthetic water glass (Series b; Mg/Ni=0.1 and SiO<sub>2</sub>/Ni=1.15). Co-precipitation of corresponding metal nitrates with Na<sub>2</sub>CO<sub>3</sub> at 90°C and pH=10.00±0.05 was applied. The modification with silver is made at three molar Ag/Ni ratios, namely 0.0025, 0.025 and 0.1. These ratios are noted as a number at the sample denotation. The both Ag free samples are marked by zero (AgNiD-0 and AgNiWG-0).

The reduction-passivation procedure was performed by: (i) dry reduction at 430°C for 5 h with a H<sub>2</sub>:Ar (1:1) gas mixture; (ii) cooling down to room temperature in the same gas mixture; (iii) passivation of the reduced precursors with a mixture of 350 ppm  $O_2/N_2$  at room temperature.

#### Sample Characterization

The electronic properties of the reduced precursors were investigated by X-ray photoelectron spectroscopy (XPS). The measurements were performed in a VG ESCALAB II electron spectrometer using AlK<sub>a</sub> radiation with energy of 1486.6 eV. The binding energies (BE) were determined with an accuracy of  $\pm$  0.1 eV utilizing the C1s line at 285.0 eV (from an adventitious carbon) as a reference. The composition and chemical surrounding of the films were investigated on the basis of the areas and binding energies of C1s, O1s, Ni2p<sub>3/2</sub>, Ag3d, Mg2p and Si2p photoelectron peaks (after linear subtraction of the background) and Scofield's photoionization cross-sections.

#### **Results and Discussion**

The general view of the Ni2p level evidences two types of the nickel oxidation states. The binding energy (BE) values Ni2p<sub>3/2</sub> peak reveal that nickel is present as Ni<sup>2+</sup> oxidation state in all reduced samples in the range of 855.4–857.1 eV for Series **a** and 855.4–856.7 eV for Series **b**. These values characterize Ni<sup>2+</sup> state in Ni-O species. The asymmetry of the main Ni2p<sub>3/2</sub> peak towards lower binding energy values presumes the presence of Ni<sup>0</sup> oxidation state (BE=853 eV). This oxidation state is supported by X-ray diffraction and magnetic susceptibility data.

Sample		binding y (eV)	state con	oxidation ntribution %)	
	$N_i^0$	$Ni^{2+}$	$N_i^0$	$Ni^{2+}$	

**Table 1.** XPS data of the (Ag)NiMg/D samples (Series a)

The peak-fitting of the composite Ni2p level (Tables 1, 2) confirms that nickel on the surface is presented in Ni<sup>0</sup> and Ni<sup>2+</sup> oxidation states. The obtained data manifest that Ni<sup>0</sup> contribution of the samples on diatomite support (Table 1) changes within a wider range of 5.6–13.9 %, while its contribution in the samples on water glass support varies in the 3.6–6.3 % range (Table 2). The silver presence and content increase the Ni<sup>0</sup> oxidation state contribution on the (Ag)NiMg/D samples. On contrary, this effect is not clearly pronounced in the (Ag)NiMg/WG samples.

**Table 2.** XPS data of the (Ag)NiMg/WG samples (Series b)

Sample		Ni2p <sub>3/2</sub> binding energy (eV)		dation state ition (%)	Ni <sup>0</sup> /Ni <sup>2+</sup> ratio
1	Ni <sup>0</sup>	Ni <sup>2+</sup>	Ni <sup>0</sup>	Ni <sup>2+</sup>	
AgNiWG-0	853.6	856.6	3.6	96.4	0.037
AgNiWG-0.0025	852.5	855.0	6.1	93.9	0.065
AgNiWG-0.025	852.8	856.0	4.5	95.5	0.047
AgNiWG-0.1	852.3	854.9	6.3	93.7	0.067

The higher content of  $\mathrm{Ni}^0$  on the surface has been demonstrated by diatomite supported samples, where the metallic Ni crystallites possess larger size (chemisorption data). Obviously, the lower dispersed  $\mathrm{Ni}^0$  particles are more stable to oxidation. On contrary, the higher dispersed  $\mathrm{Ni}^0$  particles on water glass are more susceptible to oxidation.

#### **Conclusions**

In conclusion, the source of  $SiO_2$  support as well as of the silver presence and content affect the nickel oxidation state. The surface metallic Ni on  $(Ag)NiMg/diatomite\ catalysts\ is\ more\ stable\ to\ oxidation.$ 

#### Acknowledgements

The authors are grateful to the National Science Fund at the Ministry of Education and Science of Bulgaria, for the partial financial support (Project X-1411) and to the Serbian Ministry of Science through the Project 166001B.

- [1] M. Gabrovska, J. Krstić, R. Edreva-Kardjieva, M. Stanković, D. Jovanović, Appl. Catal. A: General, 2006, **299**, 73-83.
- [2]M. Stanković, J. Krstić, M. Gabrovska, P. Banković, D. Jovanović, XIII Workshop über die Charakterisierung von feinteiligen und porösen Festkörpern, Germany, Bad Soden, (2006).

### STUDY OF Ag-NiMg/SiO<sub>2</sub> SYSTEM BY MEANS OF TEMPERATURE PROGRAMMED REDUCTION

M. Gabrovska<sup>1\*</sup>, I. Shtereva<sup>1</sup>, J. Krstić<sup>2</sup>, M. Stanković<sup>2</sup>, R. Edreva-Kardjieva<sup>1</sup> and D.M. Jovanović<sup>2</sup>

<sup>1</sup>Institute of Catalysis, BAS, 1113 Sofia, Bulgaria (\*margarita.gabrovska@abv.bg) <sup>2</sup>Institute of Chemistry, Technology and Metallurgy, Department of Catalysis and Chemical Engineering, 11000 Belgrade, Serbia

#### Abstract

Two series of silver modified Ni-Mg materials with close composition are synthesized on  $SiO_2$  support derived from two silica sources: diatomite activated at  $800^{\circ}$ C (Series **a**; Mg/Ni = 0.1 and  $SiO_2/Ni = 1.07$ ) and synthetic water glass (series **b**; Mg/Ni = 0.1 and  $SiO_2/Ni = 1.15$ ). The silver content corresponds to the molar ratios of Ag/Ni = 0.0025, 0.025 and 0.1.

The effect of the support nature and the amount of silver modifier on the reducibility of Ni<sup>2+</sup> ions in Ag-NiMg/SiO<sub>2</sub> materials is established by temperature-programmed reduction. The enhanced nickel reducibility due to the silver addition depends on the source and the preliminary thermal treatment of both SiO<sub>2</sub>-containing carriers. This fact may be related to the formation of Ni<sup>2+</sup> species of different strengths as a result of the metal-support interaction phenomenon. It has been elucidated that the usage of water glass as silica precursor causes reduction of Ni<sup>2+</sup> species in all modified samples at temperatures significantly lower than in their analogues prepared on silica derivates from diatomite.

#### Introduction

Temperature-programmed reduction (TPR) technique has been widely used in studying the reduction behavior of supported and unsupported catalysts. The main feature of the method is its capability of continuously monitoring the consecutive reactions of reducible species at increasing temperatures.

Hydrogenation of vegetable oils is an important practice in the modification of fats and oils. Currently, the most applied commercial catalyst is active nickel supported on inert carriers as SiO2 or Al2O3.

Recently, it has been published that Ni-Mg catalysts, supported on SiO2 derived from two siliceous sources, either diatomite or water glass, demonstrate both high soybean oil hydrogenation activity and high quantity of detrimental trans-fatty acids (TFAs) production [1]. In order to suppress the TFAs formation, NiMg/SiO2 materials are modified by addition of different amounts of silver, based on the pioneer investigation of Lefèbvre and Baltes [2]. The authors reported the beneficial role of silver on the diminution of TFAs formation.

The aim of present study is to elucidate the effects of the source of support and the amount of silver on the reducibility of  $\mathrm{Ni}^{2^+}$  species in Ag-NiMg/SiO<sub>2</sub> precursors of vegetable oil hydrogenation catalysts by means of TPR technique.

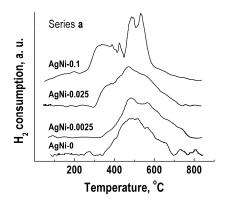
#### **Experimental**

Ag-Ni-Mg materials are synthesized on  $SiO_2$  support derived from two silica sources: diatomite activated at  $800^{\circ}$ C (Series **a**) and synthetic water glass (Series **b**). Co-precipitation of metal nitrates with  $Na_2CO_3$  at  $90^{\circ}$ C and  $pH=10.00\pm0.05$  is applied. All samples are prepared with the composition (Mg/Ni = 0.1 and  $SiO_2/Ni$  = 1.07 (Series **a**) and Mg/Ni = 0.1 and  $SiO_2/Ni$  = 1.15 (Series **b**), while the molar ratios of Ag/Ni are 0.0025, 0.025 and 0.1. The designation of the studied materials from both series corresponds to the Ag/Ni molar ratio, i.e. AgNi-0 (silver free), AgNi-0.0025, AgNi-0.025 and AgNi-0.1.

TPR behavior of the uncalcined samples ( $\sim 0.025$  g) is evaluated with a laboratory set-up using thermal conductivity detector from 50 to 850°C. The temperature is linearly raised at a rate of 10oC min-1. The samples are reduced with H<sub>2</sub>/Ar stream (10% H<sub>2</sub>) at a flow rate of 25 cm<sup>3</sup> min-1. The selected conditions are in agreement with the criteria proposed by Monti and Baiker [3] to avoid the mass transfer and temperature control limitations.

#### **Results and Discussion**

The unmodified precursors from both Series designated as AgNi-0 demonstrate broad asymmetric TPR profiles spreading throughout 340–800°C range (Figs. 1 and 2). TPR profile of the sample from Series **a** represents variety of different in intensity peaks situated at 270, 490, 520, 560, 730 and 810°C, also shoulders at 400 and 660°C. Their presence is due to the reduction of nickel phyllosilicate-type compounds formed during the precursor's preparation procedure. TPR profile of Ag-free sample from Series **b** discloses similar feature, however, only one broad peak at 615°C is clearly distinguished. The reduction in one step means whole precursor reduced simultaneously. This increases the future catalyst longevity.



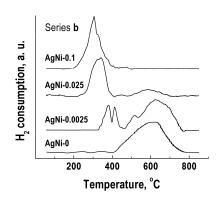


**Fig. 1.** TPR profiles of the samples from Series **a** ("diatomite" support)

**Fig. 2.** TPR profiles of the samples from series **b** ("water glass" support)

Series a: The modification of Ni-Mg material with the smallest silver content (Fig. 1, AgNi-0.0025) does not significantly change the position of the maximum in  $H_2$  consumption ( $T_{max}$ ). It may be seen disappearance of high temperature (HT)

peaks and formation of a shoulder at  $740^{\circ}$ C. The addition of higher quantity of silver (AgNi-0.025 sample) causes appearance of low-temperature (LT) shoulder at  $370^{\circ}$ C and shifting of HT shoulder at  $740^{\circ}$ C to  $550^{\circ}$ C. The introduction of the highest amount of modifier leads to splitting of  $T_{max}$  in two peaks (at 470 and  $530^{\circ}$ C), formation of broad peak at  $350^{\circ}$ C and small one at  $430^{\circ}$ C (AgNi-0.1 sample).

Series b: The well-pronounced LT peaks, namely 380 and 410oC, betterformed Tmax at 620oC and shoulders at 520 and 700°C may be observed on TPR profile of AgNi-0.0025 sample (Fig. 2). The modification of NiMg/SiO2 material with higher quantity of silver (AgNi-0.025 sample) provokes shifting of  $T_{max}$  towards lower temperature (340oC), appearance of low intensity peaks at 450 and 580°C and disappearance of the observed shoulders. It is clearly shown that Tmax of the sample with the highest silver loading (AgNi-0.1) is situated at the lowest temperature of 300°C.

It may be summarized that the presence of silver vastly affects reduction behavior of the materials supported on SiO2 obtained from water glass. The gradual decreases of the high-temperature peaks intensity and shifting to lower temperatures with increase of the silver concentration are visible. Consequently, the highest quantity of modifier pretty promotes the reduction of Ni<sup>2+</sup> ions. Moreover, the latter are completely reduced below 400°C.

#### **Conclusions**

The silver modification of MgNi/SiO2 samples from both series results in diminution of Ni<sup>2+</sup> ions reduction temperature by comparison with unmodified materials. The enhanced nickel reducibility due to the silver addition depends on the source and the preliminary thermal treatment of both studied carriers. This fact may be attributed to the formation of Ni<sup>2+</sup> species of different strengths of the metal–support interaction phenomenon.

The usage of water glass as silica precursor ensures reduction of Ni<sup>2+</sup> species in all modified samples at temperatures lower than in their analogues prepared on silica derivates from diatomite. The highest silver presence in the water glass supported sample leads to complete reduction of Ni<sup>2+</sup> ions below 400°C.

#### Acknowledgements

The authors are grateful to the National Science Fund at the Ministry of Education and Science of Bulgaria, for the partial financial support (Project X-1411) and to the Serbian Ministry of Science through the Project-TR 6712 B.

- [1] M. Gabrovska, J. Krstić, R. Edreva-Kardjieva, M. Stanković, D. Jovanović, Appl. Catal. A: General, 2006, **299**, 73-83.
- [2] Van J. Lefèbvre, J. Baltes, Fette Seifen Anstrichmittel, 1975, 77, 125-131.
- [3] D. Monti, A. Baiker, J. Catal., 1983, 83, 323-335.

#### CARBOXYLATION REACTION OF SODIUM 2-NAPHTHOXIDE

S. Marković<sup>1</sup>, I. Đurović<sup>1</sup> and Z. Marković<sup>2</sup>

<sup>1</sup>Faculty of Science, University of Kragujevac, Serbia <sup>2</sup>Faculty of Agronomy, University of Kragujevac, Serbia

#### Abstract

The carboxylation reaction of sodium 2-naphthoxide in the positions 1, 3, and 6 is examined by means of the B3LYP/CEP-31+G(d) method. After the initial formation of sodium 2-naphthoxide-CO2 complex, the carbon of the CO2 moiety can perform an electrophilic attack on the naphthalene ring in the position 1. Further transformation leads to the formation of 2-hydroxy-1-naphthoate. Sodium 3-hydroxy-2-naphthoate is obtained by a 1,3-rearrangement, whereas sodium 6-hydroxy-2-naphthoate is a result of a series of consecutive rearrangements. Our findings are in accord with the experimental results on the carboxylation reaction of sodium 2-naphthoxide.

#### Introduction

The Kolbe-Schmitt reaction is a carboxylation reaction of alkali and alkaline earth metal phenoxides or naphthoxides, where aromatic hydroxy acids are formed [1,2]. The carboxylation reaction of alkali metal phenoxides has been a subject of numerous experimental and theoretical investigations [1-9]. Carboxylations of various alkali and alkaline earth metal 2-naphthoxides were examined by Kosugi et al. [4]. It was shown that at moderate temperatures the only product of the reaction of sodium 2-naphthoxide (1) was 2-hydroxy-1-naphthoic acid. At temperatures above 200°C, a mixture of 2-hydroxy-1-naphthoic, and 3- and 6-hydroxy-2-naphthoic acids was produced.

Recent Density Functional Theory (DFT) studies, performed at the B3LYP/LANL2DZ level, explained the mechanism of carboxylation at enhanced temperatures [10,11]. The proposed mechanism required some high activation energies, thus it was not applicable to lower temperatures.

This provokes us to reinvestigate the mechanism of the carboxylation reaction of sodium 2-naphthoxide. The goal of this work is to explain the formation of 2-hydroxy-1-naphthoic acid at lower temperature, and the formation of a mixture consisting of three acids at higher temperatures. For this purpose different basis set is used.

#### **Results and Discussion**

Geometrical parameters of all stationary points and transition states are optimized in vacuum, at the B3LYP/CEP-31+G(d) level of theory, using GAUSSIAN 03 program package [12]. CEP-31+G(d) uses Stevens/Basch/Krauss ECP split-valence basis set and includes a set of polarization functions [13].

The scheme of the mechanism and energetic diagram of the reaction are presented in Figs 1 and 2. Our calculations reveal that the carboxylation reaction in the position 1 of 1 (i.e. the formation of 5) proceeds via three intermediates and three transition states. The reaction in the position 3 (i.e. the formation of 12) is a result of a rearrangement from C1 to C3, thus it includes six intermediates and six transition states. Similarly, the reaction in the position 6 (i.e. the formation of 10) is a result of a series of consecutive rearrangements, and includes the formation of a free radical 9.

Fig. 1. Intermediates in the carboxylation reaction of sodium 2-naphthoxide.

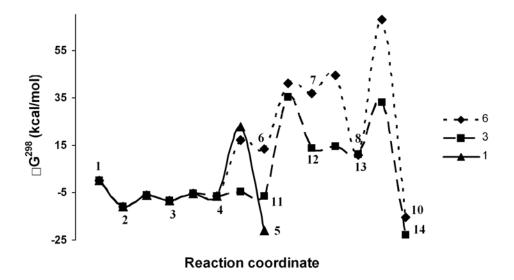


**Fig. 2.** Energy profile for the carboxylation reaction of sodium 2-naphthoxide.

Fig. 2 shows that all reaction paths for the carboxylation reaction of 1 are exothermic. Using free energies, the activation energies for all steps of the reaction are calculated. The activation barrier for the transformation  $4\rightarrow 5$  is relatively low: 29.7 kcal/mol, and allows the formation of 5 at moderate temperatures. The formation of 10 and 14 requires significantly higher activation energies (e.g. 11  $\rightarrow$ 12 41.7 kcal/mol;  $8\rightarrow$ 10 57.7 kcal/mol). These high activation energies are in agreement with the experiments which show that the reaction mixture needs to be heated above 200°C to produce a mixture of 5 and 14 (major products) and 10 (low concentration) [4,5].

#### Conclusion

There are three ways for 4 to transform.  $4\rightarrow 11$  and  $4\rightarrow 6$  are energetically more favorable, but these steps are followed with transformations that require significantly higher energy barriers. Thus, only 5 can be expected as a product at lower temperatures. At high temperatures 5 and 14 can be expected as major products, and 10 as a minor product.

#### Acknowledgement

This work is supported by the Ministry of Science of the Republic of Serbia, project N° 142025.

- [1] H. Kolbe, Liebigs Ann. 1860, **113**, 125-127.
- [2] R. Schmitt, J. Prakt. Chem. 1985, **31**, 397.
- [3] M. Kunert, E. Dinjus, M. Nauck, J. Sieler, Chem. Ber./Recueil 1997, **130**, 1461-1465.
- [4] M. A. Rahim, Y. Matsui, Y. Kosugi, Bul.l Chem. Soc. Jpn. 2002, 75, 619-622.
- [5] Y. Kosugi, Y. Imaoka, F. Gotoh, M. A. Rahim, Y. Matsui, K. Sakanishi, Org. Biomol. Chem. 2003, 1, 817-821.
- [5] Z. Marković, J. P. Engelbrecht, S. Z. Marković, Naturforsch. 2002, 57a, 812-818.
- [6] Z. Marković, S. Marković, N. J. Begović, Chem. Inf. Model. 2006, 46, 1957-1964.
- [7] I. Stanescu, R. R. Gupta, L. E. K. Achenie, Mol. Sim. 2006, 32, 279-290.
- [8] I. Stanescu, L.E.K. Achenie, Chem. Eng. Sci. 2006, 61, 6199-6212.
- [9] Z. Marković, S. Marković, N. Manojlović, J. Predojević-Simović, J. Chem. Inf. Model. 2007, 47, 1520-1525.
- [10] Z. Marković, S. Marković, I. Đurović, Monats. Chem. 2008, 139, 329-335.
- [11] S. Marković, I. Đurović, Z. Marković, Monats. Chem. accepted for publication.
- [12] Gaussian 03, Revision-E.01-SMP; Gaussian, Inc.: Pittsburgh, PA, 2003.
- [13] W.J. Stivens, H. Bach, and J. Krauss, J. Chem. Phys. 1984, 81, 6026.

#### KINETIC INVESTIGATION OF THE TETRACYCLINE REACTION WITH FENTON-LIKE REAGENT AT PHYSIOLOGICAL pH

S.M. Sunarić<sup>1</sup> and S.S. Mitić<sup>2</sup>

<sup>1</sup>Faculty of Medicine, Department of Pharmacy, University of Niš, Bulevar dr Zorana Djindjica 81, 18000 Niš, Serbia, (ssunaric@medfak.ni.ac.yu)

<sup>2</sup>Faculty of Natural Sciences and Mathematics, Department of Chemistry, University of Niš, Višegradska 33, P.O.Box 224, 18000 Niš, Serbia

#### **Abstract**

The reaction between tetracycline and Cu(II)/H<sub>2</sub>O<sub>2</sub> reagent in the presence of phosphate buffer is described. It was found that in aqueous solution at physiological pH degradation of antibiotic occurred. The influences of pH and temperature on the reaction were studied. The relative rate constant at 293K, 298K, 303K, 308K and activation parameters of the transition state at 308K were calculated.

#### Introduction

Tetracycline is a "broad-spectrum" antibiotic which is used to treat bacterial infections. Because of the development of resistant strains of microorganisms, this antibiotic has lost some of its usefulness. However, tetracycline is often an alternative drug for people who are allergic to penicillin.

The aim of our study was investigation of the reaction between tetracycline, hydrogen peroxide and Cu(II) ions at physiological pH.

The reaction of catalytic decomposition of  $H_2O_2$  in the presence of transition metal ions was studied by many authors. Although the mechanism of this reaction is not completely clear, it is known that numerous reactive oxygen species, including OH radicals are generated. This reaction is well-known as Fenton reaction and if occurs in the presence of Cu(II) ions the reaction is Fenton-like. The reagent  $Cu(II)/H_2O_2$  is Fenton-like reagent. The production of reactive oxygen species is the process which is permanently happened in human cells. Therefore, it was interesting to investigate the reaction between tetracycline and Fenton-like reagent at physiological pH.

#### **Experimental**

The stock solution of tetracycline  $(1.00 \times 10^{-4} \text{ mol/dm}^3)$  was freshly prepared by dissolving the required amount of tetracycline-hydrochloride (Sigma-Aldrich), p.a.  $C_{22}H_{24}N_2O_8$ ·HCl in deionised water. The solution of Cu(II)  $(1.00 \times 10^{-4} \text{ mol/dm}^3)$  was prepared by dissolving CuCl<sub>2</sub>·2H<sub>2</sub>O (Merck) in deionised water. Hydrogen peroxide solution  $(1.00 \text{ mol/dm}^3)$  was prepared just before use from a 35% commercial reagent (Merck). The phosphate buffer was obtained by mixing solutions of 0.5 mol/dm<sup>3</sup> KH<sub>2</sub>PO<sub>4</sub> and 0.5 mol/dm<sup>3</sup> Na<sub>2</sub>HPO<sub>4</sub>.

The reaction rate was followed spectrophotometrically by Perkin-Elmer Lambda 15 UV/VIS spectrophotometer, connected to a thermocirculating bath.

#### **Results and Discussion**

We have found that degradation of tetracycline occurs when the solution of antibiotic is mixed with Cu(II),  $H_2O_2$  and phosphate buffer. The degradation product has absorption maximum at 376 nm which decreases during first 6 minutes of the reaction. The rates of the reaction were calculated as the slopes of the initial tangents to the absorbance-time curves, dA/dt.

Investigating the reaction kinetics we have found at 20°C the reaction rate has maximal value for the next reactant concentrations:  $C_{buffer} = 0.2 \text{ mol/dm}^3$ ,  $C_{Cu(II)} = 3.33 \times 10^{-5} \text{ mol/dm}^3$ ,  $C_{H_2O_2} = 2.00 \times 10^{-2} \text{ mol/dm}^3$ . In the range of tetracycline concentration from  $0.67 \cdot 10^{-6} \text{ mol/dm}^3$  to  $6.67 \cdot 10^{-6} \text{ mol/dm}^3$  the pseudo-first order kinetics was found (respect to the tetracycline).

The dependence of the reaction rate on pH at 20°C (Fig. 1) shows that at physiological pH 7.4 reaction has significant progress.

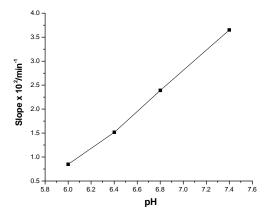


**Fig. 1.** Dependence of the reaction rate on pH. Concentrations in measured solutions:  $C_{Tetracycline}$ ,  $5.33 \cdot 10^{-6}$  mol/dm<sup>3</sup>;  $C_{H_2O_2}$ ,  $2.00 \cdot 10^{-2}$  mol/dm<sup>3</sup>;  $C_{Cu(II)}$ ,  $3.33 \cdot 10^{-5}$  mol/dm<sup>3</sup>;  $C_{buffer}$ , 0.2 mol/dm<sup>3</sup>;  $t = 20^{\circ}$ C.

The dependence of reaction rate at pH 7.4 on temperature shown progress of the reaction with the temperature increase. On the basis of first order reaction kinetics, the equation (1) was used for the calculation of the relative rate constant at 293K, 298K, 303K and 308K (Table 1.):

$$dA/dt = k_r \cdot C_{\text{Tetracycline}} \tag{1}$$

	- 1
T/ K	$(k_r \pm SD^a) \ x \ 10^{4} \ / \ dm^3 mol^{1}  min^{1}$
293	$0.92 \pm 0.052$
298	$1.16 \pm 0.017$
303	$1.33 \pm 0.010$
308	$1.52 \pm 0.031$

**Table 1.** The relative rate constant  $k_r$  at pH 7.4.

a. SD, standard deviation of the 3 different tetracycline concentrations.

From the dependence of the relative rate constant on temperature, using the Eyring equation, activation enthalpy ( $\Delta H^{\ddagger}$ ), activation entropy ( $\Delta S^{\ddagger}$ ), free activation enthalpy ( $\Delta G^{\ddagger}$ -Gibb's free energy) and the appearent activation energy  $E_a$  at 308K were calculated (Table 2.).

**Table 2.** Thermodynamic parameters of the activated complex for the tetracycline reaction with Fenton-like reagent at pH 7.4 and 308 K.

T (K)	E <sub>a</sub> kJ mol <sup>-1</sup>	ΔH <sup>‡</sup> kJ mol <sup>-1</sup>	$\Delta S^{\ddagger}$ J mol <sup>-1</sup> K <sup>-1</sup>	ΔG <sup>‡</sup> kJ mol <sup>-1</sup>
308	24.8	22.3	- 93	50.9

The reaction is characterized with low value of apperent (activation energy) but relatively large negative value of activation entropy. This shows that the activated complex in the transition state has a very ordered structure and points to a complex reaction mechanism.

#### Acknowledgement

This research was supported by grant 142015 from the Ministry of Science of the Republic of Serbia.

- [1] J. N. Delgado and W. A. Remers, *Wilson and Gisvold's Textbook of Organic Medicinal and Pharmaceutical Chemistry*, 10<sup>th</sup> ed., Lippincott Williams&Wilkins, 1998.
- [2] R. Kellner, J. M. Mermet, M. Otto, M. Valcarcel and H. M. Widmer, Eds., *Analytical Chemistry*, 2nd ed., Wiley-VCH, 2004, Chap. 17.

#### MECHANISM OF THE PREACTIVATION PROCESS OF TRANS-[PdCl<sub>2</sub>(DEA)<sub>2</sub>] IN PHOSPHINE-FREE HECK REACTIONS

S. Marković, Z.D. Petrović, V. Petrović and D. Simijonović Faculty of Science, University of Kragujevac, 34000 Kragujevac, Serbia

#### **Abstract**

The use of *trans*-[PdCl<sub>2</sub>(DEA)<sub>2</sub>]) as a precatalyst is examined. The mechanism of the formation of Pd(0) complex is investigated using density functional theory.

#### Introduction

In the past decade phosphine-free Pd complexes [1] have been introduced in the palladium-catalyzed arylation of olefins, known as the Heck reaction [2]. Recently synthetized [3] trans-dichlorobis (diethanolamine-N)palladium(II) complex (1) contains both diethanolamine (DEA) and Pd(II). For this reason we assume that it can be used as a precatalyst in phosphine-free Heck reactions in the presence of strong and weaker bases [4]. Thus, we investigate possible intramolecular reduction of Pd(II) to Pd(0) using computational methods.

#### **Results and Discussion**

It is reasonable to expect, for a reaction performed in the presence of a strong base, that a proton from OH group can be abstracted from 1 (Fig. 1). In this way the anion 2 would be formed. We assume that a hydrogen bonded to the carbinol C atom can be coordinated to Pd(II) [5], thus forming 4 via transition state 3 (Fig. 1). This transformation can be followed with reductive elimination of HCl, where 5 is produced. Complex 5 contains Pd(0), thus it is catalytically active species in the Heck reaction.

To confirm our assumptions we perform DFT investigation of the preactivation process of *trans*-[PdCl<sub>2</sub>(DEA)<sub>2</sub>]. All calculations are conducted using Gaussian03 [6] with the B3LYP hybrid functional. The 6-31G(d) basis set is used for C, H, O, N, and Cl, and LANL2DZ+ECP is employed for the Pd center. The optimized geometry of 3 is presented in Fig. 2, whereas some crucial bond distances for structures 1 - 5 are given in Table 1.

Our calculation of **1** yields the structure with bond distances and angles consistent with the crystallographic experimental data (Table 1) [3]. Following the above presented consideration (Fig. 1), H1 is removed from **1** as a proton, and the so-obtained structure is optimized (structure **2**). The atomic polar tensors (APT) charge distribution of **2** shows that positive charge is distributed among palladium (0.765), carbons, and some hydrogens, whereas negative charge is distributed among all other atoms. The C1-H2 and C1-H3 bonds become particularly polarized, with the ATP charges on C1, H2, and H3 of 0.700, -0.127, and -0.231, respectively. A nucleophilic attack of H2 on palladium leads to the formation of transition state **3** (Fig. 2) with an energy barrier of 83.0 kJ/mol. Here, the C1-H2

and Pd-N1 bonds are being broken, whereas the Pd-H2 bond is being formed (Table 1). The negative charge on H2 is slightly increased (-0.167). In the further course of the reaction H2 coordinates with palladium as a hydride ion (4 in Fig.1 and Table 1). The Pd-N1 and C1-H2 bonds are completely broken, implying that dehydrogenated DEA is eliminated. In the basic environment 4 undergoes reductive elimination, thus forming 5.

**Fig. 1.** Supposed mechanism of the preactivation process of trans-[PdCl2(DEA)2] precatalyst. R = -CH2CH2OH.

Table 1. S	Selected	bond distances	s in nm for	the species i	ınder consid	eration (1 -	- 6).
Distance	1	2	3	4	5	6	

Distance	1	2	3	4	5	6
Pd-Cl1	0.2376	0.2405	0.2396	0.2392	0.2385	0.2379
Pd-Cl2	0.2376	0.2408	0.2396	0.2408	-	0.2338
Pd-N1	0.2116	0.2111	0.2453	-	-	0.3871
Pd-N2	0.2116	0.2123	0.2247	0.2325	0.2191	0.2083
C1-H2	0.1098	0.1117	0.1201	-	-	0.1146
Pd-H2	0.2866	0.2603	0.2056	0.1536	-	0.1841

When a strong base is not present in the reaction mixture, the initial abstraction of a proton from an alcoholic OH group does not occur. Our calculations show that a transformation of 1 to 4 takes place via a transition state 6, which requires significantly higher activation energy of 117.0 kJ/mol. The results on the optimization of 6 are given in Table 1 and Fig. 2. In 6 the C1-H2 bond is being broken, whereas the Pd-H2 bond is being formed. The APT charges on H2 and Pd amount -0.461 and 0.852, respectively. In the further course of the reaction H2 is transferred to palladium as a hydride ion, thus yielding 4 and releasing OH-CH<sub>2</sub>-CH<sub>2</sub>-NH-CH-CH<sub>2</sub>-OH.

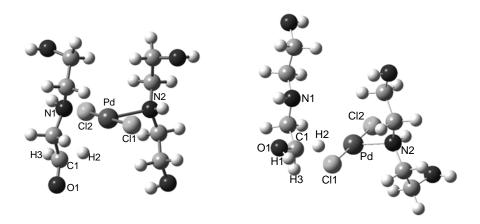


**Fig. 2.** Optimized geometries of transition states obtained in the presence of a strong base (left) and weaker base (right).

#### Conclusion

Our investigation shows that in *trans*-[PdCl<sub>2</sub>(DEA)<sub>2</sub>] carbinol hydrogen can coordinate with palladium in the presence of a strong or weaker base. Our predictions, obtained by means of DFT calculations, are confirmed by performing Heck reactions catalyzed with 1 in the presence of a weak and strong base.

#### Acknowledgements

This work is supported by the Ministry of Science of the Republic of Serbia, project N° 142025.

- [1] R. Heck, Acc. Chem. Res. 1979, 12, 146.
- [2] J. G. De Vries, Can. J. Chem. 2001, 79, 1086.
- [3] Z. D. Petrović, M. I. Đuran, F. W. Heinemann, S. Rajković, S. Trifunović, Bioorg. Chem. 2006, **34**, 225.
- [4] J. L. Hong, L. Wang, Eur. J. Org. Chem. 2006, 22, 5099.
- [5] D. R. Jensen, M. J. Schultz, J. A. Mueller, M. S. Sigman, Angew. Chem. Int. Ed. 2003, 42, 3810.
- [6] Gaussian 03, Revision E.01-SMP, Gaussian Inc., Pittsburgh.

## OXIDATION KINETICS OF SUNFLOWER OIL STUDIED BY DIFFERENTIAL SCANNING CALORIMETRY

S. Ostojić, S. Zlatanović and M. Kićanović

Holding Institute of General and Physical Chemistry Studenski trg 12/V P.O. Box 551 11000 Belgrade, Serbia

#### **Abstract**

The oxidation kinetic of cold pressed sunflower oils, obtained from two sunflower hybrides NSH2075 and NSH2034 with genetically defined unsatutrated fatty acid contempt, was studied by differential scanning calorimetry (DSC). Samples were heated at different heating rates (2.5, 5.0, 7.0, 10.0 and 12.5 K/min) and oxidation kinetic parameters from Arrhenius equation, apparent activation energy (Ea), pre-exponential factor (A), and oxidation rate constant (k) were calculated usig the Ozawa-Flynn-Wall method [1].

#### Introduction

Lipid oxidation is responsible for chemical changes in fats and oils that lead to food spoilage and flavor deterioration [1-5]. A good understanding of lipid oxidation kinetics in vegetable oils can improve our abilities to formulate food products that maintain the existing oil quality in food system and minimize production of undesirable breakdown components. Kinetic data are essential for predicting oxidative stability of vegetable oils under various heat processing, storage and distribution conditions. The oxidation of vegetable oils can be treated as an apparent first order reaction [1-4] because of the high concentration of oxygen compared to the amount of oil in the sample. The transfer of an oxygen molecule to an unsaturated fatty acid requires energy. This process can easily bee determined by differential scanning calorimetry (DSC).

The purpose of this work was to evaluate the effect of fatty acid composition on the oxidation kinetics of oils from different sunflower hybrids with defined amount of saturated and unsaturated fatty acid and tockopherol.

#### **Experimental**

Two cold pressed sunflower oils, obtained from two sunflower hybrides NSH2075 and NSH2034 (Institute of Field and Vegetable Crops, Novi Sad) with geneticlly defined palmitic, stearic, oleic, linolic and tocopherol compozition were heated at different heating rates (β): 2.5, 5.0, 7.0, 10.0 and 12.5 K/min, in temperature interval from 231.15K to 623.15K. Samples were heated in open aluminum pans with an oxygen purge flow of 50ml/min, using DSC Q1000 TA Instruments (Delaware USA). NSH2075 is highly unsaturated oil with 50% of linolic acid, while oil NSH2034 consists 17% of linolic acid. The onset temperature T<sub>o</sub> was determined from these runs by TA Instruments Universal analysis 2000 software. T<sub>o</sub> was defined as the temperature at which the heat flow significantly deviates from the baseline, when rapid increase in the rate of oxidation is observed. This temperature

is obtained from extrapolating the tangent drawn on the steepest slope of reaction exotherm. The first process at  $T_0$  is oxidation, and the second one at  $T_p$ , temperature maximum of first peak, could indicate the start of the oil thermal decoposition [1]

Arrhenius rate constant (k), activation energies  $(E_a)$  and preexponential factors (Z) were calculated using the Ozawa-Flynn-Wall method [1]. Assuming an overall first order process, the heat evolved (H) at time t is proportional to the amount of reacted substrate [1].

#### **Results and Discussion**

The oxidation profiles obtained by DSC for the oils NSH2034 at different heatig rates ( $\beta$ : 2.5, 5.0, 7.0, 10.0 and 12.5 K/min) are showen in Fig. 1.a). Generally, two peak can be observed: the first one is wide and small while the second one is sharper. The effect of heatig rate ( $\beta$ ) on the position and shape of these peaks can be also observed. As heating rate increases, the second peak becomes sharper while first one tends to disappear, or to move towards higher temperatures.

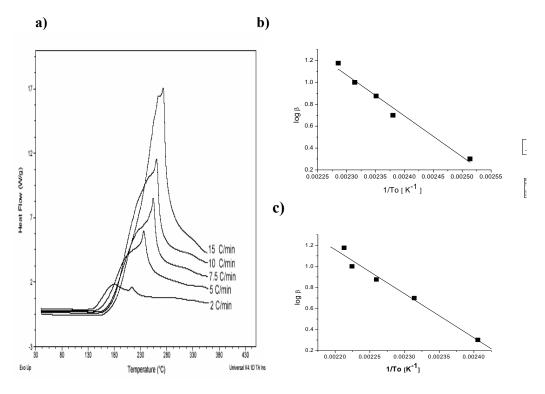


**Fig. 1 a)** DSC oxidative curves of cold pressed sunflower oil from hybrid NSH2034 as a function of the heating rate; **b)** Relationship between the heating rate and  $T_0$  for oil from NSH 2075 and **c)** Relationship between the heating rate and  $T_0$  for oil from NSH2034

Onset temperature  $T_o$  is the temperature used to calculate the kinetic parameters of oxidation. The activation energies  $E_{a,}$ , pre-exponential factors (Z), rate constant (k) at 298K for the oxidation reaction are shown in **Table 1.** 

**Table 1.** Kinetic parameters from the Arrhenius equation obtained from plotting log $\beta$  1/T<sub>o</sub>; Linear regressions parameters (y = b + ax) obtained from plotting log  $\beta$  1/T<sub>o</sub>;

Sample	b	a	Ea	Z	k <sub>298</sub>
	(intercept)	(slope)	[kJ/mol]	[min <sup>-1</sup> ]	[min <sup>-1</sup> ]
NSH2034	10.4	-4180	76±8	$5.49 \times 10^8$	$4.01x10^4$
NSH2075	9.6	-3733	67±7	$1.2x10^{8}$	$1.49 \times 10^{-4}$

**Table 2**. Kinetic parameters from the Arrhenius equation obtained from plotting log $\beta$  1/Tp; Linear regressions parameters (y = b + ax) obtained from plotting log  $\beta$  1/Tp

Sample	b	a	Ea	Z	k <sub>298</sub>
	(intercept)	(slope)	[kJ/mol]	[min <sup>-1</sup> ]	[min <sup>-1</sup> ]
NSH2034	5.0	-2082	38±4	$5.01 \times 10^4$	1.1x10 <sup>-2</sup>
NSH2075	8.8	-3669	67±7	$5.01 \times 10^8$	5.11x10 <sup>-11</sup>

Oxidation rate constant values k obtained with either  $T_o$  and  $T_p$  increased as the percentage of unsaturated fatty acids increased (NSH2075 is highly unsaturated oil with 50% of linolic acid, while oil NSH2034 consists 17% of linolic acid) what is in agreement to literature [1] As values for k calculated by Tp were lower than ones found with  $T_o$  suggestig that two different reactions are taking place at the  $T_o$  and  $T_p$  of the DSC curve. The first process at  $T_o$  is oxidation, and the second process at  $T_p$  could indicate the start of the oil thermal deconposition [1]. The activation energies  $E_a$ , pre-exponential factors (Z), are in the range comparable to literature [1].

#### Conclusion

Oxidation rate in lipids increases with the degree of unsaturation of the fatty acides present in the oil. This paper provides kinetics parameters that can be used to predict the oxidation behavior of cold pressed sunflower oils.

- [1] J. Thurgod, R. Ward, S. Martini, Food Res. International, 2007, 40, 1030-1037
- [2] T.C. Tan, Y.B. Man, J. Selmat M.S.A. Jusoff, JAOCS, 2001, 78, 1133-1138
- [3] A. Adhvary, S.Z. Erhan, Z.S.Liu, J.M. Perez, Thermochimica Acta, 2000, 364, 87-9
- [4] A. Kamal-Eldin, Eur.J.Lipid Sci. Technol.2006, 58, 1051-1061.
- [5] S. Sathivel, J. Huang, W. Prinyawiwatkul, Journal of Food Engineering, 2008, 84, 187-193

#### OXIDATION KINETICS OF SUNFLOWER OIL STUDIED BY DIF-FERENTIAL SCANNING CALORIMETRY- ISOTHERMAL OXI-DATIVE INDUCTION TIME METHOD

S. Ostojić, S. Zlatanović, M. Kićanović and B.R. Simonović Holding Institute of General and Physical Chemistry Studentski trg 12/V P.O. Box 551 11000 Belgrade, Serbia

#### **Abstract**

Cold pressed sunflower oils, obtained from sunflower hybrides NSH2075 and NSH2035 with geneticlly defined amount of saturated and unsaturated faty acid and tocopherol were isothermaly oxidized at eight different temperatures (from 358K to 393K) by DSC method. Oxidation induction time (OIT) was determined. The rates of lipid oxidation were highly correlated with temperature. Based on Arrhenius equation and activated complex theory [1] reaction rate constants (k), activation energies ( $E_a$ ), activation enthalpies ( $\Delta H$ ) and activation entropies ( $\Delta S$ ) for oxidation of oils were calculated

#### Introduction

Oxidative stability is an inportant property of edible oils in food science. It is represented by the time in which an oil sample resists to oxidation and it can be used to evaluate when an oil reaches an oxidation level inadequate for ingestion or for its utilization in frying processes. This time, called oxidative induction time (OIT) or induction period, has been determined by heating the sample (in oxygen) to a constant temperature and measuring a physical or chemical parameter (evolved heat in DSC experiment) [1-5] A good understanding of lipid oxidation kinetics in vegetable oils, especially genetically modified, where is possible to illustrate the effect of unsaturated fatty acids on the thermal and oxidative behavior, can improve our abilities to formulate food products that maintain the existing oil quality and minimize production of undesirable breakdown components. Kinetic data are essential for predicting oxidative stability of vegetable oils under various heat processing, storage and distribution conditions. The oxidation of vegetable oils can be treated as an apparent first order reaction [1-4] because of the high concentration of oxygen compared to the amount of fatty acids in the sample. The transfer of an oxygen molecule to an unsaturated fatty acid requires energy. This energy can easily be determined by differential scanning calorimetry (DSC).

The aim of this work is to compare the oxidative stability of two sunflower oils from different sunflower hybrids with genetically defined amount of saturated and unsaturated fatty acides and tocopherol, to illustrate the effect of high linolic acid content on the oil thermal and oxidative behavior.

#### **Experimental**

Two cold pressed sunflower oils, obtained from two sunflower hybrides NSH2075 and NSH2034 (Institute of Field and Vegetable Crops, Novi Sad) with geneticlly defined palmitic, stearic, oleic, linolic acids and tocopherol content were isothermaly oxidized in oxygen atmosphere (purge flow 50ml/min) at eight different temperatures (358K, 363K, 368K, 373K, 378K 383K, 388K and 393K) by DSC, using oxidative induction time (OIT) method, on DSC Q1000 TA Instruments (Delaware USA). An oil sample of 5.0-5.5 mg was weighed in the open aluminum pan. The opened aluminum pan was used as the reference. NSH2075 is highly unsaturated oil with 50% of linolic acid, while oil NSH2034 consists 17% of linolic acid. A rapid increase in evolved heat was observed with an exothermic heat flow appearing during initiation of the oxidation reaction. From resulting exotherm oxidation induction time (OIT) was determined (software TA Instruments Universal analysis 2000).

#### Results and Discussion

From results obtained it is obvious that the rate of lipid oxidation was highly correlated with temperature. Linear relationships were determined by extrapolation of the ln OIT against isothermal temperature. Based on Arrhenius equation and activated complex theory [1], reaction rate constants (k), activation energies (Ea), enthalpies of formation of the activated complex ( $\Delta$ H) and entropies of formation of the activated complex ( $\Delta$ S) for oxidation of edible oils were calculated. Estimated (Ea), ( $\Delta$ H) and ( $\Delta$ S) for lipid oxidation in oils are summarized in **Table 1**.

**Table 1** Kinetic and thermodynamic values for lipid oxidation of cold pressed sunflower oils: k-reaction rate constant at 393.15K; Ea-activation energy;  $\Delta$ H-enthalpy of formation of the activated complex;  $\Delta$ S- entropy of formation of the activated complex

Oil	E <sub>a</sub> (kJmol <sup>-1</sup> )	ΔH (kJmol <sup>-1</sup> )	ΔS (kJmol <sup>-1</sup> )	k (x10 <sup>3</sup> min <sup>-1</sup> )
NSH2034	77±5	74±5	-25±2	69±4
NSH2075	88±6	84±6	-20±2	$128\pm10$

Generally, oils with higher proportions of unsaturated fatty acids are more prone to oxidation than those containing lesser amounts.

 $\Delta H$  and  $\Delta S$  were greater for highly unsaturated oil NSH2075, than for oil with lesser amounts of unsaturated fatty acids NSH2034 what is in agreement with literature [1]. Greater negative  $\Delta S$  value for NSH2034 indicates fever numbers of species in the activated complex state. Therefore, the activated complex for lipid oxidation in NSH2034 is less probable and rate is slower [1]. DSC isotherms for oils NSH2034 and NSH2075 are presented on **Figure 1**.

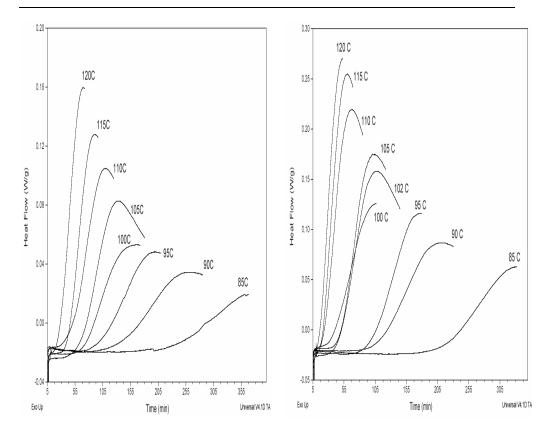


**Fig. 1.** DSC–OIT isotherms obtained for oils **a)** NSH 2034 in temerature range from 358K, to 393K; and **b)** NSH 2075 in temerature range from 358K to 393K.

#### Conclusion

Kinetic and thermodinynamic oxidation parameters: (k,  $E_a$ ,  $\Delta H$  and  $\Delta S$ ), for the cold pressed oils, from sunflower hybrids NSH 2034 and NSH 2075, have been determined. From results obtained it is clear that oil from hybrid NSH2075 with highly unsaturated fatty acid content (50% of linolic acid), was less oxidative stabile, then oil from hybrid NSH2034 which consists 17% of linolic acid

- [1] T.C. Tan, Y.B. Man, J. Selmat M.S.A. Jusoff, JAOCS, 2001, 78, 1133-1138
- [2] J. Thurgod, R. Ward, S. Martini, Food Res. International, 2007, 40, 1030-1037.
- [3] J. Velasco, M.L Andersen, L.H Skibsted, Food Chemistry, 2004, 85, 623-632
- [4] A. Kamal-Eldin, Eur.J.Lipid Sci. Technol.2006, 58, 1051-1061.
- [5] S. Sathivel, J. Huang, W. Prinyawiwatkul, Journal of Food Engineering, 2008, 84, 187-193

# KINETIC ANALYSIS OF EXPERIMENTAL INTENSITY CURVES OBTAINED DURING ZEOLITE A SYNTHESIS USING *IN SITU* <sup>27</sup>AI NMR SPECTROSCOPY

#### Z. Miladinović and J. Zakrzewska

Institute of General and Physical Chemistry, Studentski trg 12-16, 11000 Belgrade, Serbia

#### Abstract

Intensity curves obtained by *in situ* <sup>27</sup>Al NMR spectroscopy during zeolite A synthesis has been used as a method for comparative kinetic investigation of zeolite crystallization. Kinetic analysis was performed using inflection point analysis. Obtained time values for starting and finishing points of intensity decay during crystallization, shows increase dependency with decrease in absolute concentration of Na<sub>2</sub>O into reaction solution and increasing of batch SiO<sub>2</sub>/Al<sub>2</sub>O<sub>3</sub> molar ratio.

#### Introduction

Kinetic investigations play significant role in understanding the mechanism of zeolite formation. Different kinetic investigations of zeolite crystallization are performed using mostly diffraction techniques [1], particularly their *in situ* applications, could provides satisfied number of experimental data points necessary for further kinetics analysis [2]. Crystallization curves, obtained from such experiments are therefore used for evaluation of kinetic parameters. Typically, for this purpose is exploited model based on Avrami-Erofe'ev equation [2], consequently providing rate constant k and Avrami coeficient n.

In our previous work we have used Sharp-Hancock method for determination of kinetic parameters using for this purpose experimental intensity curves obtained from <sup>27</sup>Al NMR spectra, corresponding to the changes of aluminum in solution phase [3]. Here, will be presented using of inflection point analysis of intensity curves to provide a comparative kinetic analysis and consequently influence of chemical batch composition of synthesis to the crystallization kinetics.

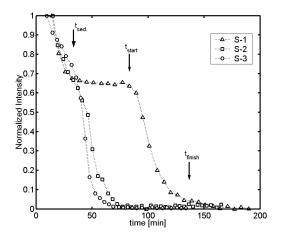
#### **Experimental**

All intensity curves were obtained from  $^{27}$ Al NMR spectra during zeolite crystallization in static condition inside Bruker MSL 400 NMR spectrometer, using experimental procedure described earlier [4]. The batch composition was Al<sub>2</sub>O<sub>3</sub>: xSiO<sub>2</sub>: yNa<sub>2</sub>O: zH<sub>2</sub>O, where x was 1.7, 2.0 and 2.5; y is ranged between 2.64 and 6.54; and z takes values from 84.30 to 130.53. Reaction temperature during synthesis was 82  $^{0}$ C for all synthesis.

#### Results

In situ <sup>27</sup>Al NMR spectroscopy was used to obtain experimental curves reflecting the changes of aluminum presented in the solution phase. Figure 1 shows changes of intensity of <sup>27</sup>Al NMR narrow line at 79 ppm from aluminum in solution phase for different

molar  $SiO_2/Al_2O_3$  compositions and different absolute  $Na_2O$  concentrations during the synthesis.



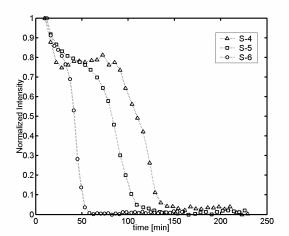


**Fig. 1.** Changes of normalized intensity of  $^{27}$ Al NMR line at 79 ppm during reaction time of zeolite synthesis for molar ratios:  $SiO_2/Al_2O_3 = 1.7$  (left),  $SiO_2/Al_2O_3 = 2.0$  (right); and for different absolute concentration of  $Na_2O$ . Arrows indicate time periods denoted as  $t_{sed.}$ ,  $t_{start}$  and  $t_{finsh}$  given in Table 1.

All presented curves in Fig 1 show similar shape with three clearly distinctive steps, corresponding to the processes occurring during synthesis in an *in situ* NMR experimental condition. During crystallization, intensity of the line at 79 ppm decreases for several reasons. Rapid drop of normalized intensity during first 15–30 min. is associated to the process of sedimentation of aluminum-silicate gel in NMR tube [3]. The induction period is represented with relatively flat part of intensity curve, succeeding with crystallization process which is manifested as fast drop in intensity of NMR signal, indicating rapid depletion of free alumina in solution phase and their incorporation into the solid crystalline phase [3]. Inflection points, evaluated from presented S-shaped intensity curves denoted as t<sub>sed</sub>, t<sub>start</sub> and t<sub>finish</sub> for sedimentation, beginning and ending of intensity decay respectively, are used for kinetic comparison of processes occurred during zeolite crystallization, and are given in Table 1. According to the obtained values in Table 1, kinetic analysis of zeolite crystallization could be performed.

All data presented in Table 1, are placed in increasing ordered of absolute  $Na_2O$  batch concentration and grouped with equal molar ratios  $SiO_2/Al_2O_3$ . It can be seen from Table 1 that with increasing  $Na_2O$  concentration, values of  $t_{start}$  and  $t_{finish}$  decrease for any particular values of  $SiO_2/Al_2O_3$ . Furthermore, comparing synthesis with similar  $Na_2O$  concentrations, general increasing trend of  $t_{start}$  and  $t_{finish}$  is consistent with increasing molar ratio  $SiO_2/Al_2O_3$  in order 1.7>2.0>2.5 (for example synthesis S-1, S-4, and S-7 respectively to the value of  $t_{finish}$ ). Overall

above trends indicate obvious connection between initial batch composition and rates of processes responsible for crystal growth.

Induction period also could be determined as difference between  $t_{\text{start}}$  and  $t_{\text{sed.}}$  (Table 1). As well as in the previous analysis, similar dependency of induction period from absolute concentration of Na<sub>2</sub>O and molar ratio SiO<sub>2</sub>/Al<sub>2</sub>O<sub>3</sub> could be observed, indicating that rate of nucleus formation, occurring during this stage of synthesis, is also batch concentration controlled process.

Changes in observed rate of sedimentation ( $t_{sed}$ ), depend on sample volume in NMR tube used for particular synthesis, coefficient of diffusion and viscosity of solution phase, middle radius of gel particles [5], but no significant dependency on batch concentration was observed (Table 1).

No. of Samp.	SiO <sub>2</sub> /Al <sub>2</sub> O <sub>3</sub>	t <sub>sed.</sub> [min]	t <sub>start</sub> [min]	$t_{\text{finish}}[\text{min}]$	t <sub>start</sub> -t <sub>sed</sub> [min]	Na <sub>2</sub> O [mol/dm <sup>3</sup> ]
S-1	1.7	25	88	117	63	1.685
S-2	1.7	19	45	62	26	2.671
S-3	1.82	16	38	51	22	2.858
S-4	2.0	28	88	145	60	1.681
S-5	2.0	24	70	107	46	1.711
S-6	2.0	17	36	52	19	2.683
S-7	2.5	22	110	150	88	1.700
S-8	2.5	31	85	134	54	1.713
S-9	2.5	19	34	46	15	2.702

**Table 1.** Different values of times of sedimentation, start and finishing obtained from normalized intensity curves during zeolite synthesis for different absolute Na<sub>2</sub>O concentration and molar batch composition.

#### Conclusion

The use of intensity curves obtained from  $^{27}$ Al NMR spectra during synthesis enable simplest method for comparing influence of different synthesis parameters on the rate of processes occurred during zeolite crystallization. On the base of this analysis, increasing of rate of crystallization with increase of Na<sub>2</sub>O concentration and decrease of SiO<sub>2</sub>/Al<sub>2</sub>O<sub>3</sub> molar ratio are observed.

- [1] R. J.Francis, D. O'Hare, J. Chem. Soc., Dalton Trans., 1998, 19, 3133-3148.
- [2] R. I. Walton, F. Millange, D. O'Hare, A. T. Davies, G. Sankar and, R.A. Catlow, J. Phys. Chem. B, 2001, **105**, 83-90.
- [3] Z. Miladinović, J.Zakrzewska, B.Kovačević, G.Bačić, Mater. Chem. Phys., 2007, 104, 384-389.
- [4] Z. Miladinović, J. Zakrzewska, Proceedings of the 8<sup>th</sup> International Conference on Fundamental and Applied Aspects of Physical Chemistry, Belgrade, Serbia, 2006, 561-563.
- [5] M. Mason, W. Weaver, Phys. Rev., 1924, 23, 412-426

# Nonlinear Dynamics (D)

# ELECTROHYDRODYNAMICS OF DEVELOPED LIQUID/LIQUID INTERFACES: FRACTIONAL ORDER TIME DELAY SYSTEMS

#### A.M. Spasić

Institute for Technology of Nuclear and Other Mineral Raw Materials 86 F. d'Esperey St. 11000 Belgrade, Serbia

#### Abstract/Introduction

The electroviscoelastic behavior of e.g., liquid/liquid interfaces (emulsions and double emulsions) is based on three forms of "instabilities"; these are rigid, elastic, and plastic. The events are understood as interactions between the internal (immanent) and external (incident) periodical physical fields. Since the events at the interfaces of finely dispersed systems have to be considered at the molecular, atomic, and/or entities level it is inevitable to introduce the electron transfer phenomenon beside the classical heat, mass, and momentum transfer phenomena commonly used in chemical engineering. Three possible mathematical formalisms have been derived and discussed related to this physical formalism, i.e. to the developed theory of electroviscoelasticity [1-7].

#### Stretching tensor model

It is assumed that the surface forces are, for the general case that includes the electroviscoelastic fluids, composed of interaction terms expressed by

$$dF_s^i = T^{ij} dA_j \tag{1}$$

where the tensor T<sup>ij</sup> is given by

$$T^{ij} = -\alpha_0 \delta^{ij} + \alpha_1 \delta^{ij} + \alpha_2 \zeta^{ij} + \alpha_3 \zeta_k^i \zeta^{kj}$$
 (2)

and  $T^{ij}$  is composed of two tensors,  $\delta^{ij}$  is Kronecker symbol, and  $\zeta^{ij}$  is the stretching tensor. In the first and second isotropic tensors the  $\alpha_0 = \alpha_0(\rho, U)$  and  $\alpha_1(\rho, U)$  are the potentiostatic pressures, where U represents hydrostatic or electrostatic potential. Now, the general equilibrium condition may be derived from Eq. (2), and may be expressed by

$$\tau = \frac{-\alpha_0 + \alpha_1 + \alpha_2 \left(\frac{\sigma}{d}\right) + \alpha_3 \left(\frac{\sigma}{d}\right)}{2(\alpha_2 + \alpha_3)} \tag{3}$$

where  $\tau$  is the tangential stress [2]. Note that for dispersed systems consisting of, or behaving as Newtonian fluids,  $\alpha_3 = \alpha_3(\rho, U)$  is equal to zero. The processes of formation/destruction of the droplet or droplet-film structure are non-linear. Furthermore, the viscosity coefficients  $\mu_i$  (i = 0, 1, 2), where each consists of bulk, shear, and tensile components, when correlated to the tangential tensions of mechanical origin  $\tau_v$  can be written as

$$\tau_{v} = \mu_{0} \frac{du}{dx} + \mu_{1} \frac{d^{2}u}{dx^{2}} + \mu_{2} \left(\frac{du}{dx}\right)^{2}$$
 (4)

where u is the velocity and x is one of the space coordinates. Using the electrical analog, the impedance coefficients  $Z_i$  (i = 0, 1, 2), where each consists of ohm, capacitive, and inductive components, will be correlated with the tangential tensions of electrical origin  $\tau_e$ , as follows:

$$\tau_e = Z_0 \frac{d\varphi_e}{dt} + Z_1 \frac{d^2\varphi_e}{dt^2} + Z_2 \left(\frac{d\varphi_e}{dt}\right)^2 \tag{5}$$

where  $\phi_e$  is the electron flux density, and t is the time coordinate.

#### Van der Pol integer order derivative model

Postulated assumptions for an Electrical Analogue [1] are: 1. The droplet is a macro system (collective of particles) consisting of structural elements that may be considered as electro-mechanical oscillators; 2. Droplets as micro collectives undergo tuning or coupling processes, and so build the droplet as a macro collective; 3. The external physical fields (temperature, ultrasonic, electromagnetic, or any other periodic) cause the excitation of a macro system through the excitation of micro-systems at the resonant/characteristic frequency, where elastic and/or plastic deformations may occur. Now, a nonlinear integral-differential equation of the van der Pol type represents the initial electromagnetic oscillation, homogeneous solution may be obtained beginning from

$$C\frac{dU}{dt} + \left(\frac{U}{R} - \alpha U\right) + \gamma U^3 + \frac{1}{L} \int U dt = 0$$
 (6)

where U is the overall potential difference at the junction point of the spherical capacitor C and the plate, L is the inductance caused by potential difference, and R is the ohm resistance (resistance of the energy transformation, electromagnetic into the mechanical or damping resistance), t is the time;  $\alpha$  and  $\gamma$  are constants determining the linear and nonlinear parts of the characteristic current and potential curves. A nonhomogeneous solution may be obtained considering the particular equation, where  $\omega$  is the frequency of the incident oscillation

$$C\frac{dU}{dt} + \left(\frac{1}{R} - \alpha\right)U + \gamma U^3 + \frac{1}{L}\int Udt = -2A_n \cos \omega t \tag{7}$$

Finally, considering the droplet or droplet-film structure formation, "breathing" and/or destruction processes, and taking into account all the noise frequency components equation is

$$C\frac{dU}{dt} + \left(\frac{1}{R} - \alpha\right)U + \frac{1}{L}\int Udt + \gamma U^{3} = i(t) = \frac{1}{2\pi}\int_{-\infty}^{\infty} \exp(j\omega t)A_{n}(\omega)d\omega$$

were i(t) is the noise current and  $A_n(\omega)$  is the spectral distribution of the noise current as a function of frequency [1, 4].

#### Van der Pol fractional order derivative model - linearized

In an effort to generalize equations (6 and 7) the ordinary time derivatives and integrals are now replaced with corresponding fractional-order time derivatives and integrals [1, 2]. Here, the capacitive and inductive elements, using fractional-order

p<2 (p = n -  $\delta$ , n = 1, 2,  $\delta$  << 1) enable formation of the fractional differential equation, i.e. more flexible or general model of liquid-liquid interfaces behaviour. Now, a differ-integral form using Riemann-Liouville definition is given by

$${}_{0}D_{t}^{p}[U(t)] = \frac{d^{p}U}{dt^{p}} = \frac{1}{\Gamma(1-p)} \frac{d}{dt} \int_{0}^{t} \frac{U(\tau)}{(t-\tau)^{p}} d\tau , \quad {}_{0}D_{t}^{-p}[U(t)] = \frac{1}{\Gamma(p)} \int_{0}^{t} \frac{U(\tau)}{(t-\tau)^{1-p}} d\tau , \text{ Further}$$

$$0 0$$

on, a linear fractional differential equation with zeros initial conditions is obtained

$$C_0 D_t^p [U(t)] + \left(\frac{1}{R} - \alpha\right) U + \frac{1}{L} {}_0 D_t^{-p} [U(t)] = i(t)$$
 (10)

#### Van der Pol fractional order derivative model - nonlinear case

Here, both cases, a nonlinear homogenous (i(t) = 0) and nonhomogeneous ( $i(t) \neq 0$ ) are considered. Equivalent nonlinear problem applying differentiation of Eq. (6) is presented

$$C\frac{d^2U}{dt^2} + \left(\frac{1}{R} - \alpha + 3\gamma U^2\right)\frac{dU}{dt} + \frac{1}{L}U = 0 \tag{11}$$

In an effort to generalize the previous equation fractional order van der Pol equation become

$${}_{0}^{c}D_{t}^{2p}U(t) = -\frac{1}{C}\left(\frac{1}{R} - \alpha\right){}_{0}^{c}D_{t}^{p}U(t) - \frac{3\gamma}{C}U(t)^{2}{}_{0}^{c}D_{t}^{p}U(t) - \frac{1}{CL}U(t)$$
(12)

#### **Experimental confirmation/Conclusion**

Presented theoretical predictions including both physical and mathematical formalisms have been experimentally corroborated by means of the electrical interfacial potential (EIP) measurements, and by means of the nuclear magnetic resonance spectroscopy (NMR) [1-7].

#### Acknowledgement

Financial support MSDFR-Serbia, grant 142034.

- [1] A.M. Spasic, M.P. Lazarevic, M.V. Mitrovic and D.N. Krstic In A.M. Spasic and J.P. Hsu (Eds.) *Finely Dispersed Particles: Micro-, Nano-, and Atto-Engineering,* CRC Press/Taylor and Francis, Boca Raton London New York, 2005/2006, 3-23 & 371-394.
- [2] A.M. Spasic, M.P. Lazarevic, J.Coll.Interf.Sci., 2005, 282, 223-230.
- [3] A.M. Spasic, M.P. Lazarevic, J. Coll.Interf.Sci., 2007 316/2, 984-995.
- [4] A.M. Spasic, V. Jokanovic and D.N. Krstic, J.Coll.Interf.Sci. 1997, 186, 434-446.
- [5] A.M. Spasic, N.N. Djokovic, M.D. Babic, M.M. Marinko and G.N. Jovanovic, Chem.Eng.Sci., 1997, 52, 657-675.
- [6] A.M. Spasic, Chem. Eng. Sci. 1992, 47, 3949-3957.
- [7] A.M. Spasic In A.V. Delgado (Ed.) *Interfacial Electrokinetics & Electrophoresis*, Marcel Dekker, New York, 2001/2002, 837-868.

#### BUFFERS CATALYSIS OF THE IODINE(+1) REDUCTION BY HYDROGEN PEROXIDE

#### G. Schmitz

Faculté des Sciences Appliquées, Université Libre de Bruxelles, CP165, Av.F.Roosevelt 50, 1050 Bruxelles, Belgium, E-mail: gschmitz@ulb.ac.be

#### **Abstract**

The iodine(+1) reduction by hydrogen peroxide is catalyzed by different buffers and its rate is a complicated function of the acidity and of the iodide concentration. The seemingly inconsistent published experimental results are reanalyzed and a new kinetic model is proposed. A key step is the catalysis by the buffers of the formation of the intermediate compound IOOH. This model reconciles the previous works.

#### Introduction

Although the reduction of iodine(+1) by hydrogen peroxide has been studied during more than eighty years, there is no consensus in the literature about its kinetics. The first investigations [1-3] dealt with the catalytic decomposition of hydrogen peroxide by iodine. The mechanism (1-5) was postulated in neutral or dilute acidic solutions.

$$I_2 + H_2O \rightleftharpoons IOH + I^- + H^+ \tag{1}$$

$$I_2 + I^- \rightleftharpoons I_3^- \tag{2}$$

$$IOH \rightleftharpoons IO^- + H^+ \tag{3}$$

$$IO^{-} + H_2O_2 \rightarrow I^{-} + H_2O + O_2 \tag{4}$$

$$I^- + H_2O_2 \rightarrow IO^- + H_2O \tag{5}$$

In more acidic solutions, the mechanism includes also reactions (6) and (7).

$$IOH + H_2O_2 \rightarrow I^- + H^+ + H_2O + O_2$$
 (6)

$$I^{-} + H^{+} + H_{2}O_{2} \rightarrow IOH + H_{2}O \tag{7}$$

The sum of reactions (4) and (5) or (6) and (7) gives the decomposition (8).

$$2 H_2O_2 \rightarrow 2 H_2O + O_2$$
 (8)

The reduction of iodine(+1) by hydrogen peroxide is also important as a part of the Bray-Liebhafsky oscillating reaction, that is the decomposition (8) catalyzed by iodate and iodine in acidic solutions [4-9]. This decomposition is the result of the global reactions (9) and (10).

$$2 \text{ IO}_3^- + 2 \text{ H}^+ + 5 \text{ H}_2\text{O}_2 \rightarrow \text{I}_2 + 5 \text{ O}_2 + 6 \text{ H}_2\text{O}$$
 (9)

$$I_2 + 5 H_2O_2 \rightarrow 2 IO_3^- + 2 H^+ + 4 H_2O$$
 (10)

In reaction (9), hydrogen peroxide acts as a reducing agent but its direct reaction with iodate is much too slow to explain the observed rates. The mechanism is complicated and the reducing action of hydrogen peroxide is mainly the result of reac-

tion (6). Liebhafsky [3, 10] and Furrow [11] have tried to isolate this reaction and to measure its rate constant but their values differ by a factor ten.

A third group of investigations deals with the importance of the iodine(+1) reduction by hydrogen peroxide in analyzing the iodine behavior after a nuclear reactor accident. <sup>131</sup>I is one of the most toxic fission products that would be released in the atmosphere and the behavior of iodine has been the subject of extensive studies for the nuclear industry [12-16]. An important part of these studies were devoted to the iodine reactions in solution controlling the distribution of iodine between volatile compounds (I<sub>2</sub> and organic compounds) and non-volatile compounds (mainly I<sup>-</sup> and IO<sub>3</sub><sup>-</sup>). Hydrogen peroxide being one of the products of the water radiolysis, the reactions of iodine(+1) with hydrogen peroxide producing iodide or iodate are important processes that would influence the release of <sup>131</sup>I in the atmosphere.

$$H_2O \xrightarrow{\gamma} e^-, H^+, H^-, OH^-, H_2, H_2O_2$$

The present state of our knowledge about the reduction of iodine(+1) by hydrogen peroxide is mainly the result of the works of Liebhafsky [2, 3], of Shiraishi *et al.* [12, 13] and of Ball and Hnatiw [16, 17].

# Liebhafsky (1932)

Liebhafsky has studied the catalytic decomposition (8) in an acetate buffers between pH = 4 and 6 and in a phosphate buffers between pH = 6 and 8 [2]. He has concluded that, under his experimental conditions, the rate of iodide oxidation (5) is nearly equal to the rate of the iodine(+1) reduction (4). From the observed rates of hydrogen peroxide decomposition and the well-known rate constant  $k_5$  [18], he has calculated  $k_4 = 6 \times 10^9$  mol<sup>-1</sup> dm<sup>3</sup> s<sup>-1</sup>. The obtained values were independent on the acidity, the nature of the buffer and the iodide concentration. In another work [3] he has measured the rate of oxygen production by reaction (4) far from the steady state and has obtained  $k_4 = 3.3 \times 10^9$  mol<sup>-1</sup> dm<sup>3</sup> s<sup>-1</sup> in satisfactory agreement with the above value. Both works suggest that the rate is proportional to [IO<sup>-</sup>] and is independent on the acidity, the phosphate concentration and the iodide concentration. It is this simplicity that led Liebhafsky to think that (4) was the rate determining step but further measurements have shown that it was an illusion.

# Shiraishi et al. (1991)

These authors have discovered that phosphate buffers catalyze the iodine(+1) reduction by hydrogen peroxide while citrate buffers do not [12]. For this reason they have performed a new kinetic study in a citrate buffer between pH = 5.5 and 7 [13] and found a new term in the rate law, proportional to [ $\Gamma$ ]. To explain this term, they have added reactions (11) and (12) to the mechanism proposed by Liehhafsky. Their value  $k_4 = 7 \times 10^7 \text{ mol}^{-1} \text{ dm}^3 \text{ s}^{-1}$  is much lower than Liebhafsky value.

$$IOH + I^- \rightleftharpoons I_2OH^- \tag{11}$$

$$I_2OH^- + H_2O_2 \rightarrow 2I^- + H^+ + H_2O + O_2$$
 (12)

## Ball and Hnatiw (2001)

Ball *et al.* [16] have observed deviations from the rate law of Shiraishi *et al.* and have decided to perform a more complete kinetic study as a function of acid, hydrogen peroxide, iodide and buffer concentration in three different buffers [17]. On the basis of this very important experimental work they have proposed the mechanism (11), (13-15) where B<sup>-</sup> denotes the anion of the buffer.

$$I_2OH^2 + H_2O_2 \rightleftharpoons I^2 + IOOH + H_2O$$
 (13)

$$IOOH + OH^{-} \rightarrow I^{-} + H_2O + O_2$$
 (14)

$$IOOH + B^- \rightarrow I^- + BH + O_2 \tag{15}$$

This mechanism explains their experimental results but we will see that it is inconsistent with the former works. We can reject proposed mechanisms but we cannot ignore published experimental results without a good reason. Thus, we have analyzed the published rate measurements, found that they are compatible and that a modification of the Ball and Hnatiw mechanism can explain them all.

## **Analysis of the Experimental Results**

The observed evolutions of the iodine concentration discussed in this work are the result of two reactions, the reduction of iodine(+1) by hydrogen peroxide and the oxidation of iodide to iodine by reaction (5). Denoting by  $[I_2]_t$  the total iodine(+1) concentration,  $[I_2]_t = [I_2] + [I_3^-] + [IO^-] + [IOH] + [I_2OH^-]$ , and by  $k_{obs}$   $[I_2]_t$  the global rate of iodine(+1) reduction, the expression of the observed rates is (16) where  $r_5 = k_5[I^-][H_2O_2]$  [18].

$$- d[I_2]_{t}/dt = k_{obs} [I_2]_{t} - r_5$$
 (16)

During the reduction of iodine(+1),  $k_{obs}$  [I<sub>2</sub>]<sub>t</sub> decreases and r<sub>5</sub> increases until  $k_{obs}$  [I<sub>2</sub>]<sub>t</sub> = r<sub>5</sub>. Then, the system has reached the steady state of the catalytic decomposition studied by Liebhafsky.

The different authors have presented their experimental results differently. In order to compare them it is necessary to define and calculate the same function of all the reported rates. The following function Z (mol<sup>2</sup> dm<sup>-6</sup> s<sup>-1</sup>) is especially convenient.

$$Z = \frac{[I^{-}][H^{+}]^{2}}{[H_{2}O_{2}]} \frac{[I_{2}]_{t}}{[I_{2}]} k_{obs} \times 10^{14}$$

Under the conditions of all the studied works the reactions (1-3) are quasi at equilibrium and the concentrations [IO<sup>-</sup>] and [I<sub>2</sub>OH<sup>-</sup>] can be neglected in the iodine mass balance. This gives the following relations.

$$\begin{split} &[IOH][I^{-}][H^{+}] = K_{1} \ [I_{2}] \\ &[I_{3}^{-}] = K_{2} \ [I_{2}][I^{-}] \\ &[IO^{-}][H^{+}] = K_{3} \ [IOH] \\ &[I_{2}]_{t} = [I_{2}] \ (1 + K_{2} \ [I^{-}] + K_{1}/[I^{-}][H^{+}]) \end{split}$$

The mechanism proposed by Liebhafsky assumes that  $k_{obs}$  [I<sub>2</sub>]<sub>t</sub> =  $k_4$ [IO<sup>-</sup>][H<sub>2</sub>O<sub>2</sub>]. As [IO<sup>-</sup>] =  $K_1K_3$ [I<sub>2</sub>]/[I<sup>-</sup>][H<sup>+</sup>]<sup>2</sup>, Z would be constant and equal to  $k_4K_1K_3\times 10^{14}$ . The changes of Z with the buffers, the acidity and the iodide concentration result from the complications revealed by further works.

# Kinetics in citrate buffers

Shiraishi *et al.* as well as Ball and Hnatiw have concluded that citrate buffers do not catalyze significantly the iodine(+1) reduction by hydrogen peroxide. On the other hand, Shiraishi *et al.* have observed a marked effect of the iodide ions, not observed by Ball and Hnatiw. The values given in their figures lead to

$$Z = 0.2 + 1.8 \times 10^8 \,[\text{H}^+][\text{I}^-] \tag{17}$$

A careful analysis of the results of Ball and Hnatiw reveals why they have not observed this effect: in the rate expression (16)  $d[I_2]_t/dt$  is proportional to  $[I_2]_t$  only if  $r_5$  can be neglected. Shiraishi *et al.* have analyzed their results using the complete expression (16) but Ball and Hnatiw have calculated  $k_{obs}$  assuming a simple first order rate law. This approximation was correct for nearly all their measurements but not for their study of the  $[\Gamma]$  effect in citrate buffers. At high iodide concentrations the  $r_5$  term is important and their  $k_{obs}$  values are too low. They did not publish the details of their measurements but the available information suggests that their values corrected for the  $r_5$  term would be similar to Shiraishi *et al.* values.

# Kinetics in phosphate buffers

Ball and Hnatiw have measured  $k_{obs}$  between pH = 6.2 and 7.7 with phosphate total concentrations equal to 0.02 or 0.05 mol dm<sup>-3</sup> and iodide concentrations equal to  $5 \times 10^{-4}$  or  $1 \times 10^{-3}$  mol dm<sup>-3</sup>. Figure 1 shows the increase of their reaction rates with [H<sup>+</sup>][B<sup>-</sup>]. Iodide has a much smaller effect than the buffer. Figure 1 shows also the Z values calculated from the Liebhafsky measurements between pH = 5.8 and 7.2 in 0.2 mol dm<sup>-3</sup> phosphate buffer with [I<sup>-</sup>] between 0.001 and 0.1 mol dm<sup>-3</sup>. The scatter is important but these values are in qualitative agreement with Ball values. They are higher because the phosphate buffer concentration is higher and they seem independent on [I<sup>-</sup>]. Liebhafsky values suggest that Z reaches a limiting value at high buffers concentrations. For comparison, figure 1 shows also the Z value calculated from the measurements by Shiraishi *et al.* for the reaction not catalyzed without effect of iodide (Z = 0.2 mol<sup>2</sup> dm<sup>-6</sup> s<sup>-1</sup>). The experimental results of these different works are in good agreement and the kinetic model must explain them all.

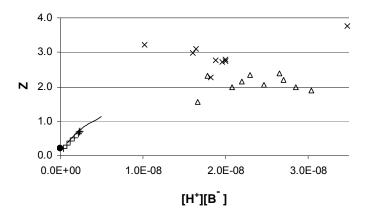


**Fig. 1.** Z values calculated from Ball and Hnatiw measurements in phosphate buffers 0.02 M (++) and 0.05 M (——) [17] and from Liebhafsky measurements in phosphate buffers 0.20 M (×) [2] or ( $\Delta$ ) [3]; Z value for the non-catalyzed reaction ( $\bullet$ ) [13].

## Kinetics in barbital buffers

Most of the Ball and Hnatiw results were obtained in barbital buffers. The authors have explained the observed effects of the buffer and of the iodide concentrations by the mechanism (13-15) giving the rate law

$$\mathbf{k}_{obs}[I_2]_t = \mathbf{k}_{13}[I_2 \mathrm{OH}^-][H_2 \mathrm{O}_2] \frac{\mathbf{k}_{14}[\mathrm{OH}^-] + \mathbf{k}_{15}[\mathrm{B}^-]}{\mathbf{k}_{-13}[I^-] + \mathbf{k}_{14}[\mathrm{OH}^-] + \mathbf{k}_{15}[\mathrm{B}^-]}$$

With the quasi-equilibrium (11) and  $K_w = [H^+][OH^-] = 10^{-14}$ , the corresponding expression of Z is (18).

$$Z = \frac{k_{13}K_{1}K_{11} \times 10^{14}[I^{-}][H^{+}](k_{14}K_{w} + k_{15}[B^{-}][H^{+}])}{k_{-13}[I^{-}][H^{+}] + k_{14}K_{w} + k_{15}[B^{-}][H^{+}]}$$
(18)

This expression can be fitted to the author's experimental values but is inconsistent with the other works. In citrate buffers the catalytic term  $k_{15}[B^{\text{-}}][H^{\text{+}}]$  can be neglected, the rate constants obtained by Ball and Hnatiw give  $k_{14}K_w/k_{-13}=2\times10^{-12}$  mol<sup>2</sup> dm<sup>-6</sup> and the expression of Z reduces to

$$Z = \frac{K_{13}K_1K_{11}k_{14}[I^-][H^+]}{[I^-][H^+] + 2 \times 10^{-12}}$$

The range of [ $\Gamma$ ][H<sup>+</sup>] values is  $5\times10^{-11}$  to  $6\times10^{-10}$  for the Ball and Hnatiw experiments and  $5\times10^{-11}$  to  $8\times10^{-9}$  for the Shiraishi *et al.* experiments. In both cases [ $\Gamma$ ][H<sup>+</sup>] is larger than  $2\times10^{-12}$  and Z should be independent on [ $\Gamma$ ][H<sup>+</sup>]. This is in contradiction with Shiraishi *et al.* results and also with Ball and Hnatiw  $k_{obs}$  values if they are corrected for the effect of reaction (5) as indicated above. The expression (18) is also inconsistent with the results of Liebhafsky in phosphate and ace-

tate buffers. The experimental Z values at high acetate or phosphate concentrations shown in figure 1 are independent on  $[\Gamma]$ . However, the expression (18) predicts the opposite: when the term  $k_{15}[B^-][H^+]$  becomes so large that Z becomes independent on the buffer concentration, Z should become proportional to  $[\Gamma][H^+]$ . Liebhafsky has mentioned in a footnote [ref.2, p.1798] results obtained at a lower phosphate concentration showing "a positive trend with increasing  $[\Gamma]$ ". Unfortunately he has discarded these results but this footnote confirms that the effect of  $[\Gamma]$  on Z decreases when the buffer concentration increases. In summary, Ball and Hnatiw mechanism is inconsistent with Shiraishi *et al.* measurements, with Ball and Hnatiw  $k_{obs}$  values in citrate buffers corrected for the effect of reaction (5) and with Liebhafsky measurements.

## **Proposed Mechanism**

The above contradictions can be resolved considering the following mechanism where reactions (3) and (11) are quasi at equilibrium.

$$IOH \rightleftharpoons IO^- + H^+ \tag{3}$$

$$IOH + I^- \rightleftharpoons I_2OH^- \tag{11}$$

$$IO^{-} + H_2O_2 \rightleftharpoons IOOH + OH^{-}$$
 (19)

$$IOH + B^{-} + H_{2}O_{2} \rightleftharpoons IOOH + BH + OH^{-}$$
(20)

$$I_2OH^- + H_2O_2 \rightleftharpoons IOOH + I^- + H_2O$$
 (13)

$$IOOH + OH^{-} \rightarrow I^{-} + H_2O + O_2$$
 (14)

$$IOH + H_2O_2 \rightleftharpoons IOOH + H_2O \tag{21}$$

This mechanism is similar to the one proposed by Ball and Hnatiw but the catalysis of the IOOH decomposition (15) is replaced with the catalysis of its formation (20). The non-catalyzed reaction (21) can be neglected under the experimental conditions of the studies discussed here but is probably important in non-buffered acidic solutions. The reactions (19), (20) and (13) are kinetically equivalent to its catalysis by OH, B and I gives respectively. This mechanism gives the rate law

$$k_{obs}[I_{2}]_{t} = k_{14}[H_{2}O_{2}] \frac{k_{19}[IO^{-}] + k_{20}[IOH][B^{-}] + k_{13}[I_{2}OH^{-}]}{k_{14} + k_{-19} + k_{-20}[BH] + k_{-13}[I^{-}][H^{+}] / K_{w}}$$

The rate constants are related by the condition of internal consistency of reaction mechanisms [19]. As (11) + (13) = (21) we must have  $K_{11}$   $K_{13}$  =  $K_{21}$  or  $K_{11}$   $k_{13}/k_{-13}$  =  $K_{21}$ . Similar relations for reactions (19) and (20) lead to

$$K_{21} = K_{11} \frac{k_{13}}{k_{-13}} = \frac{K_3}{K_w} \frac{k_{19}}{k_{-19}} = \frac{K_B}{K_w} \frac{k_{20}}{k_{-20}}$$

where  $K_B = [H^+][B^-]/[HB]$ . With these relations, the rate law gives

$$Z = k_{14}K_{21}K_1 \frac{k_{19}K_3 + k_{13}K_{11}[I^-][H^+] + k_{20}[B^-][H^+]}{k_{14}K_{21}K_w + k_{19}K_3 + k_{13}K_{11}[I^-][H^+] + k_{20}[B^-][H^+]}$$
(22)

Let us assume as a first approximation that  $k_{14}K_{21}K_w$  is much larger than  $k_{19}K_3 + k_{13}K_{11}[I^-][H^+]$ .

$$Z \sim k_{14} K_{21} K_1 \frac{k_{19} K_3 + k_{13} K_{11} [I^-] [H^+] + k_{20} [B^-] [H^+]}{k_{14} K_{21} K_w + k_{20} [B^-] [H^+]}$$
(23)

In citrate buffers the catalytic term  $k_{20}[B^-][H^+]$  can be neglected and this expression reduces to  $Z = K_1 (k_{19}K_3 + k_{13}K_{11}[\Gamma][H^+])K_w$  in accordance with equation (17) obtained by Shiraishi et al. The expression (23) explains also the maximum value of Z observed by Liebhafsky in concentrated buffers. When  $k_{20}[B^{-}][H^{+}]$  is very large Z approaches  $k_{14}K_{21}K_1$  and [I] has no effect. When  $k_{20}[B][H^+]$  is smaller, the term  $k_{13}K_{11}[I][H^+]$ explains the small effect of [I] observed. Thus, the simplified equation (23) explains qualitatively all the observations. To show that the agreement is also quantitative, we have estimated the rate constants using the complete equation (22). For numerical reasons, this was performed in two steps. A first analysis of all the different works shows that  $k_{14}K_{21}K_1$  must be equal to about 4 s<sup>-1</sup>. Then, keeping this value, the adjustment of the other rate constants to Shiraishi et al. results gives  $k_{19}K_3K_1/K_w = 0.20$ ,  $k_{13}K_{11}K_1/K_w$ =  $2.3 \times 10^8$  and  $k_{20} \sim 0$  as expected in citrate buffers. Finally, the adjustment of the other rate constants to Ball and Hnatiw results in barbital buffers gives  $k_{19}K_3K_1/K_w = 0.11$ ,  $k_{13}K_{11}K_1/K_w = 2.8 \times 10^8$ , in fair agreement with Shiraishi et al. values, and  $k_{20}K_1/K_w =$  $9\times10^8$ . These values depend somewhat on the chosen  $K_B$  value and we have used p $K_B$ = 7.5 for 0.2 mol dm<sup>-3</sup> ionic strength. Figure 2 shows the agreement between the experimental and calculated values. The equilibrium constants K<sub>1</sub>, K<sub>3</sub> and K<sub>11</sub> are well known at zero ionic strength [20] and, taking the approximate value 0.8 for the activity coefficients, the Ball and Hnatiw results give  $k_{13} = 1.3 \times 10^4$  mol dm<sup>-3</sup> s<sup>-1</sup> and  $k_{19} =$  $5.5 \times 10^7 \text{ mol dm}^{-3} \text{ s}^{-1}$ 

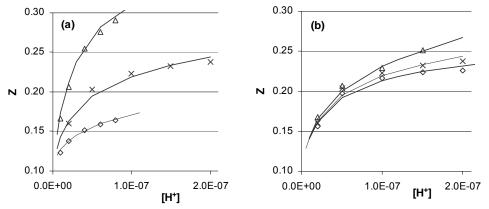


**Fig. 2.** Comparison of the calculated Z values (—) with Ball and Hnatiw experimental values in barbital buffers [17]. (a)  $[\Gamma] = 5 \times 10^{-4}$ ,  $[Barbital] = 1 \times 10^{-2}$  ( $\Delta$ ),  $5 \times 10^{-3}$  ( $\times$ ) and  $2.5 \times 10^{-3}$  ( $\Delta$ ); (b)  $[Barbital] = 5 \times 10^{-3}$ ,  $[\Gamma] = 1 \times 10^{-3}$  ( $\Delta$ ),  $5 \times 10^{-4}$  ( $\Delta$ ) and  $2.5 \times 10^{-4}$  ( $\Delta$ ).

#### Conclusions

Liebhafsky had used two different methods in different acetate and phosphate buffers and had obtained about the same value of Z. This let him to conclude logically that reaction (4) was the rate determining step. Actually, he had observed a new interesting kind of homogeneous catalysis, a catalytic reaction whose rate can be independent on the nature and on the concentration of the catalyst. The proposed model explains this phenomenon. When the action of the buffer is very effective, reaction (20) is quasi at equilibrium and the rate determining step is (14) giving  $Z = k_{14}K_{21}K_1$ . The work of Liebhafsky is instructive for another reason. He had observed that at low phosphate concentrations the values of Z were lower but had discarded these results because they seemed abnormal. Actually, they were an indication that the kinetics of the iodine(+1) reduction by hydrogen peroxide is not simple. Seemingly abnormal experimental results can be sometimes the most informative results. It is only sixty years later that Shiraishi et al. have discovered the catalytic effect of the buffers used by Liebhafsky and the complicated effect of the iodide concentration. Recently, Ball and Hnatiw have measured more precisely these effects but their mechanism does not explain all the former observations. The mechanism we propose explains all the well established experimental facts but we do not pretend that this is the end of the story.

- [1] E.Z. Abel, Z. physik. Chem., 1920, 96, 1; idem 1928, 136, 16.
- [2] H.A. Liebhafsky, J. Amer. Chem. Soc., 1932, 54, 1792.
- [3] H.A. Liebhafsky, J. Amer. Chem. Soc.., 1932, 54, 3499.
- [4] G. Schmitz, J. chim. phys. 1987, **84**, 957.
- [5] Lj. Kolar-Anić and G. Schmitz, J. Chem. Soc., Faraday Trans. 1992, 88, 2343.
- [6] Lj. Kolar-Anić, Ž. Čupić, S. Anić and G. Schmitz. J. Chem. Soc., Faraday Trans. 1997, 93, 2147.
- [7] G. Schmitz, Phys. Chem. Chem. Phys. 1999, 1, 4605.
- [8] G. Schmitz, Phys. Chem. Chem. Phys. 2001, 3, 4741.
- [9] G. Schmitz, Lj. Kolar-Anić, S. Anić, T. Grozdić and V.J. Vukojević, Phys. Chem. A 2006, 110, 10361.
- [10] I. Matsuzaki, R. Simic and H.A. Liebhafsky, Bull. Chem. Soc. Japan, 1972, 45, 3367.
- [11] S. Furrow, J. Phys. Chem., 1987, 91, 2129.
- [12] K. Ishigure, H. Shiraishi, H. Okuda and N. Fujita, Radiat. Phys. Chem. 1986, 28, 601.
- [13] H.Shiraishi, H. Okuda, Y.Morinaga and K. Ishigure in *Proc. 3rd CSNI Workshop Io-dine Chem. Reactor Safety*, 1991, JAERI-M-92-012, Japan, 1992, p.152.
- [14] J.C. Wren and J. M. Ball, Radiat. Phys. Chem. 2001, **60**, 577.
- [15] B. Clément, L. Cantrel, G. Ducros, F. Funke, L. Herranz, A. Rydl, G. Weber and C. Wren, State of the Art Report on Iodine Chemistry, Nuclear Energy Agency, NEA/CNSI/R(2007)1.
- [16] J.M. Ball, J.B. Hnatiw and H.E. Sims in *Proc. 4th CSNI Workshop Iodine Chem. Reactor Safety*, 1996, Edited by S.Guntay. Switzerland, 1997, p.169.
- [17] J.M. Ball and J.B. Hnatiw, Can.J.Chem; 2001, 79, 304.
- [18] H.A. Liebhafsky and A. Mohammad, J. Amer. Chem. Soc., 1933, 55, 3977.
- [19] G. Schmitz, J. Chem. Phys. 2000, 112, 10714.
- [20] G. Schmitz, Int. J. Chem. Kinet. 2004, **36**, 480.

# INVESTIGATION OF MICROWAVE EFFECTS ON THE OSCIL-LATORY BELOUSOV-ZHABOTINSKY REACTION

T. Grdanović, J. Brankov and D. Stanisavljev

Faculty of Physical Chemistry, Studentski trg 12-16. P.O. Box 137, 11001 Belgrade, Serbia

#### **Abstract**

The influence of the microwave (MW) field was examined on the Belousov-Zhabotinsky (BZ) oscillatory reaction, generated in a batch reactor. It was found that MW field reacted inhibitory on the decomposition of malonic acid contained in the BZ system.

#### Introduction

Experimental investigation of the influence of MW field on the reaction is followed by series of tehnical difficulties, primary caused by nature and effects of MW field. From these reasons there is a small number of scientific papers related with direct examination of process in the MW field [1,2]. Oscillatory chemical reactions represent an interesting model systems for testing in microwaves, because of the possible MW effects on the reaction dynamics. In this work is analised the BZ oscillatory reaction in which malonic acid decomposes trough alternative domination of two reaction pathways: one is caracterised by reduction of bromate to  $Br_2$  and the other by its backward oxidation to bromate.

# **Experimental**

As a source of MW radiation (2.45GHz), "single-mode" microwave CEM reactor with adjustable output power DISCOVER is used troughout. The temperature inside the reaction mixture is measured with a CEM-designed FIBER OPTIC sensor (enabling accuracy of the temperature reading within 1 °C), which do not react with MW radiation. Examination of the dynamics of the oscillatory BZ reaction was conducted in the batch reactor without mechanical mixing. The raction vessel was cylindrical glass vessel (inner diameter d  $\approx 21$  mm), created especially for operatig in MW field. The reaction is followed potentiometrically recording the potential of a platinum (Pt) electrode ( $5 \times 0.5$  mm glass-sealed Pt wire immersed in solution) versus a double-junction Ag/AgCl reference electrode (METROHM AG: Serial No.6.0726.100) with a saturated K<sub>2</sub>SO<sub>4</sub> electrolyte bridge. All sensors were shielded from MW, with a well grounded copper tube covered with Teflon. Because there is the possibility of a small penetration of radiation into the shielding tube, all electrical signals from the electrodes were additionally filtered to remove possible MW interference from registering instruments. The potential changes of Pt electrode during the experiment were followed and written down using data collector (Collecting system for electrochemical measuring EH-"Measuring instruments Miljkovic Budimir and others" O.D.). To provide constant MW irradiation and

constant temperature (measured in the vessel centre), the excessive heat during MW heating is removed by conventional thermostating (Thermostat-PolyScience 9106).

The volume of the BZ reaction mixture in the cylindrical glass vessel was V=6.09 ml. The initial composition in all experiments was (in mol/dm³):  $6\times10^{-1}$  H<sub>2</sub>SO<sub>4</sub> (Fluka),  $5.02\times10^{-2}$  KBrO<sub>3</sub> (Merck),  $1.27\times10^{-2}$  C<sub>3</sub>H<sub>4</sub>O<sub>4</sub> (Merck),  $1.48\times10^{-5}$  KBr (Zorka Sabac),  $2.45\times10^{-3}$  Ce<sub>2</sub>(SO<sub>4</sub>)<sub>3</sub> (97% purity, Sigma-Aldrich). All chemicals were of analytic grade and used without further purification. Deionized water of specific resistance  $\rho$ =18 M $\Omega$ cm was used throughout. The experiments are performed at T=53 °C and emitted MW power by CEM reactor of 20W, 40W and 60W.

#### **Results and Discussion**

In the MW field the BZ system retains same evolution with one pre-oscillatory and one oscillatory periods as it is for P=0 W (Fig. 1). But, the oscillations are much more irregular in respect to the oscillations recorded without microwaves. By increasing MW power, the oscillations have generally smaller amplitudes, but the oscillograms show extended duration of oscillatory evolution and irregular period between oscillations.

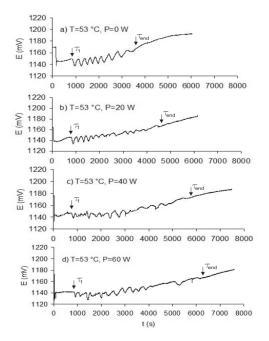


**Fig. 1.** Microwave effects on BZ reaction under different emitted MW powers (P).

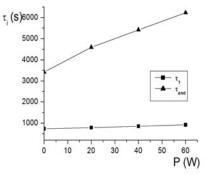


**Fig. 2.** Pre-oscillatory  $(\tau_1)$  and oscillatory period  $(\tau_{end})$  versus emitted microwave power (P).

It is known that pre-oscillatory ( $\tau_1$ ) and oscillatory period ( $\tau_{end}$ ) are kinetic parameters of the BZ reaction [3,4]. The pre-oscillatory period ( $\tau_1$ ) reflects on duration of reduction pathway which preceded oscillatory evolution, while oscilla-

tory period  $(\tau_{end})$  reflects the time in which reduction and oxidation pathways interchange. Figure 2. shows that MW have more expressive influence over the oscillatory period  $(\tau_{end})$  because corresponding curve is of the higher slope. Since the influence of MW on reduction processes  $(\tau_1)$  is considerably smaller, it can be concluded that the inhibitory influence is greater on oxidation processes in the BZ reaction.

In the reference [5], it was shown that on the recording signals of Pt-reference electrode, MW effects do not exist for actual cell geometry. Since the system is thermostated, and tested the influence of temperature have showed opposite effects of microwaves, the existence of thermal effects was ruled out as well. Considering that the effective MW heating of reaction mixture is enabled by the dipolar and conduction processes associated with breaking and reforming hydrogen bonds of water molecules, it can be assumed that detected MW effects are associated with their influence on the dynamics of hydrogen-bonded water network.

#### Conclusion

The dynamics of the Belousov-Zhabotinsky (BZ) oscillatory reaction is investigated in the presence of the microwave (MW) field. Conducting the reaction in isothermal conditions with MW heating, it is revealed that MW influence on the BZ system could significantly modify the reaction mechanism. The oscillograms are prolonged with increasing emitted MW power and at the same time poorly defined oscillations are generated with irregular period of appearing. The whole reaction is slowed by the microwaves, and the results show more expressive effects on oxidation processes in the overall reaction mechanism.

# Acknowledgement

The Ministry of Science of the Republic of Serbia, under the project number 142025, supported this work.

- [1] F. Marken, U.K. Sur, B.A. Coles, R.G. Compton, Electrochimica Acta, 2006, 51, 2195.
- [2] D.R. Stanisavljev, A.R. Đorđević, V.D. Likar Smiljanić, Chemical Physiscs Letters, 2006, **423**, 59.
- [3] E. Kőrös, Nature, 1974, **251**, 703.
- [4] S. Anić, Lj. Kolar-Anić, E. Kőrös, React. Kinet. Catal. Lett., 1997, 61, 111.
- [5] J. Brankov and T. Grdanović, The applicability of the platinum electrode for tracking the dynamics of the Belousov-Zhabotinsky oscillatory reaction in the microwave field, Physical Chemistry 2008, A. Antić-Jovanović (ed.), SFCS Belgrade 2007 p, xxx.

# DYNAMICS IN INTERACTING MASS-COUPLED CHEMICAL REACTORS

O. Pešek, L. Schreiberová and I. Schreiber

Institute of Chemical Technology Prague, Department of Chemical Engineering and Center for Nonlinear Dynamics of Chemical and Biological Systems, Technická 5,166 28 Praha 6, Czech Republic; e-mail: Igor.Schreiber@yscht.cz

#### **Abstract**

We present results of the experiments with two reaction cells coupled by diffusion-like mass transfer. The hydrogen peroxide-thiosulfate reaction catalyzed by Cu<sup>2+</sup> in the solution of H<sub>2</sub>SO<sub>4</sub> (HPTCu) was employed. We studied effects of the flow rate and intensity of coupling on autonomous dynamics of the system.

#### Introduction

Reaction between hydrogen peroxide and thiosulfate catalyzed by  $Cu^{2^+}$  ions (HPTCu) in an isothermal stirred flow-through reactor is an autocatalytic chemical oscillator with large amplitude pH variations. In these pH–regulated reactions the concentration of hydrogen ions plays a critical kinetic governing role in the dynamical behaviour of system [1]. The oxidation–reduction reaction between  $H_2O_2$  and  $S_2O_3^{2^-}$  in the presence of catalytic amount of  $Cu^{2^+}$  has been shown to exhibit a rich variety of dynamical behavior if it is carried out in a continuos-flow stirred tank reactor (CSTR)[2,3].

# **Experimental setup**

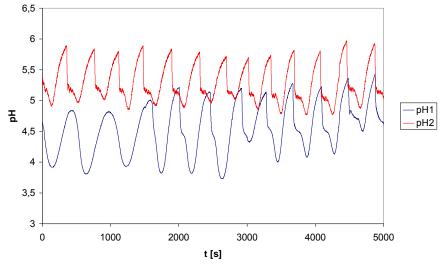
Experiments were carried out in a cascade of two reaction cells made of plexiglass covered on top by a teflon cap and coupled via an opening for mass transfer. A porous teflon grid was placed in the opening between both reaction cells so as to minimize convection flow caused by stirring. Each cell of volume 19 ml was stirred with a magnetic stirrer. Feed solutions were delivered with the use of a peristaltic pump (Ismatech). The solutions were prepared daily from standard commercially available chemicals. Required temperature of 25°C was maintained via a thermostat (Haake). The cells have a metal bottom to ensure rapid heat exchange with the coolant. Temperature and pH in the reactors were monitored during experiments by means of platinum thermocouples (Pt100) and glass combined pHelectrodes, respectively. The signals were amplified, digitized, processed and stored in a computer. The whole experiment, variation of the flow rate and data processing was controlled by a special programme designed in the LabVIEW programming environment. Feed concentrations were chosen as follows:  $c(H_2O_2) =$ 0.1 mol/l,  $c(S_2O_3^{2-}) = 0.008$  mol/l,  $c(Cu^{2+}) = 2.5 \cdot 10^{-5}$  mol/l,  $c(H_2SO_4) =$ 0.001 mol/l.

At the start of an experiment the selected coupling strength and initial flow rate were set. After an initial transient period the measurement started. The control program set a flow rate delivered by the peristaltic pump feeding the first reactor and successively varied the flow after a chosen time interval. The flow was varied stepwise from minimal to maximal value and then backward again so as to detect any possible hysteresis. The period of changes had to be long enough so that a sustained dynamical regime is obtained. The flow rate of the peristaltic pump feeding the second reactor is kept constant at the value, where single reactor would oscillate.

#### Results

Variation of the system's dynamics as the constraints are varied was examined by Orbán and Epstein [2]. They found that pH of the system corresponds to: steady state I (SSI) - pH  $\sim$  7-9, steady state II (SSII) - pH  $\sim$  5, steady state III (SSIII) - pH  $\sim$  3,5 and oscillations. In addition, the steady states may coexist and the system will operate at one of the alternative attractors depending on its history. In our earlier work we found that there are also parameter regions, where the system is excitable to pulsed addition of selected chemical species [4].

In the present experiments in coupled cells we study synchronization between two oscillators. An example of a measured time series is shown in Fig. 1, where the change of dynamical behaviour is monitored in time as the flow rate  $k_0$  is stepwise varied. For further analysis of the dynamics the recorded time series are used to construct one-parameter diagrams where the dependence of pH in both reactors on the flow rate (reciprocal residence time) in the first reactor  $k_{01}$  is represented (Figs. 2-3).



 $\begin{array}{l} \textbf{Fig. 1} \ \text{Measured time series}, \ [H_2O_2]_{01} = [H_2O_2]_{02} = 0.1 \ \text{mol/l}; \ [S_2O_3^{2^-}]_{01} = [S_2O_3^{2^-}]_{01} = 0.008 \ \text{mol/l}; \ [H_2SO_4]_{01} = [H_2SO_4]_{02} = 0.001 \ \text{mol/l}; \ [Cu^{2^+}]_{01} = [Cu^{2^+}]_{01} = 2.5 \cdot 10^{-5} \ \text{mol/l}; \ k_{01} = 0.0005, \ 0.001, \ 0.0015, \ 0.002 \ \text{s}^{\text{-1}}(\text{varied every } 1500 \ \text{s}); \ k_{02} = 0.003 \ \text{s}^{\text{-1}}; \ K = 0.00015 \ \text{s}^{\text{-1}} \end{array}$ 

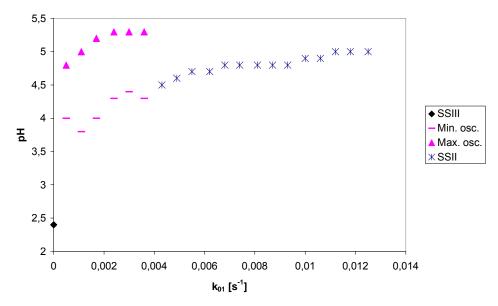


**Fig. 2** One-parameter diagram for the first reactor **w**ith increased flow rate,  $[H_2O_2]_{01} = [H_2O_2]_{02} = 0.1 \text{ mol/l}; <math>[S_2O_3^{-2}]_{01} = [S_2O_3^{-2}]_{01} = 0.008 \text{ mol/l}; [H_2SO_4]_{01} = [H_2SO_4]_{02} = 0.001 \text{ mol/l}; [Cu^{2+}]_{01} = [Cu^{2+}]_{01} = 2.5 \cdot 10^{-5} \text{ mol/l}; k_{02} = 0.003 \text{ s}^{-1}; K = 0.00015 \text{ s}^{-1}$ 

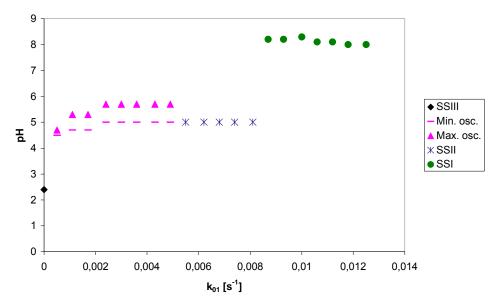


**Fig. 3** One-parameter diagram for the first reactor with decreased flow rate,  $[H_2O_2]_{01} = [H_2O_2]_{02} = 0.1$  mol/l;  $[S_2O_3^{2-}]_{01} = [S_2O_3^{2-}]_{01} = 0.008$  mol/l;  $[H_2SO_4]_{01} = [H_2SO_4]_{02} = 0.001$  mol/l;  $[Cu^{2+}]_{01} = [Cu^{2+}]_{01} = 2.5 \cdot 10^{-5}$  mol/l;  $k_{02} = 0.003$  s<sup>-1</sup>; K = 0.00015 s<sup>-1</sup>

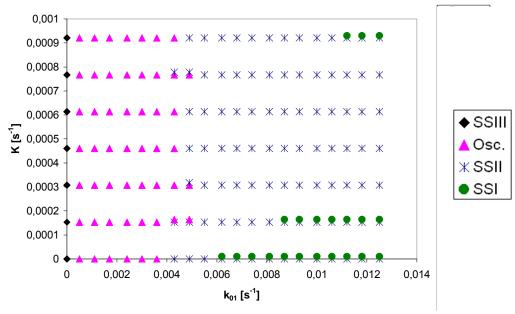


**Fig. 4** Bifurcation diagram for the first reactor,  $[H_2O_2]_{01} = [H_2O_2]_{02} = 0.1$  mol/l;  $[S_2O_3^{2-}]_{01} = [S_2O_3^{2-}]_{01} = 0.008$  mol/l;  $[H_2SO_4]_{01} = [H_2SO_4]_{02} = 0.001$  mol/l;  $[Cu^{2+}]_{01} = [Cu^{2+}]_{01} = 2.5 \cdot 10^{-5}$  mol/l;  $k_{02} = 0.003$  s<sup>-1</sup>

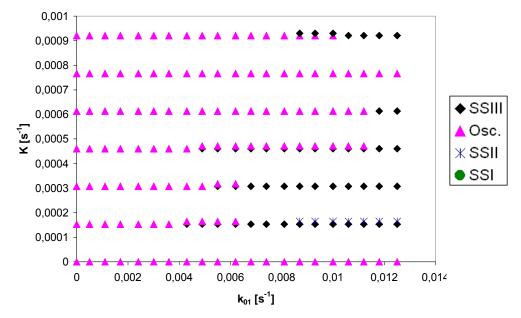


**Fig. 5** Bifurcation diagram for the second reactor,  $[H_2O_2]_{01} = [H_2O_2]_{02} = 0.1 \text{ mol/l};$   $[S_2O_3^{2^-}]_{01} = [S_2O_3^{2^-}]_{01} = 0.008 \text{ mol/l};$   $[H_2SO_4]_{01} = [H_2SO_4]_{02} = 0.001 \text{ mol/l};$   $[Cu^{2^+}]_{01} = [Cu^{2^+}]_{01} = 2.5 \cdot 10^{-5} \text{ mol/l};$   $k_{02} = 0.003 \text{ s}^{-1}$ 

The system can be found in a combination of the four aforementioned dynamical regimes, the state of system depends on direction of changes of flow rate thus its history and the reactors influence each other.

Series of experiments for various coupling strength are summarized in bifurcation diagrams, which are plotted in the parameter plane of the flow rate (reciprocal residence time)  $k_0$  and mass transfer coefficient K (Figs. 4-5). The figures show, that the coupling caused a disappearance of bistability between SS II and SS I in the first reactor and an extinction of oscillations in the second reactor, where oscillations are replaced by SS III.

#### **Discussion and Conclusions**

Due to its complex mechanism, the  $H_2O_2$ - $S_2O_3^2$ - $H_2SO_4$ - $Cu^{2+}$  system displays a rich variety of dynamical regimes including multiple steady states and periodic oscillations in a single CSTR. We found that by coupling two nonidentical reactors, dynamical behaviour becomes more complex than each of the two reactors separately. We measured time series of pH in a cascade of two mutually connected reaction cells with various intensity of mass transfer and flow rate in the first reactor. Data were processed and represented in terms of evolution (one-parameter) diagrams and then bifurcation diagrams were constructed in the plane  $k_0$ -K. These diagrams display parameter regions corresponding to various dynamical regimes. We focused mainly on the effects of coupling on the dynamical behavior. The studied system serves as a representative model for more complex biochemical and biological systems that are frequently pH-sensitive and can be represented as coupled subsystems.

# Acknowledgement

This work was supported by the project MSM 6046137306 from Ministry of Education of the Czech Republic and by the grant GAČR 203/06/1269 from the Czech Science Foundation.

- [1] Luo, Y.; Epstein, I. R.; J. Am. Chem. Soc., 1991, 113, 1518.
- [2] Orbán, M.; Epstein, I. R.; J. Am. Chem. Soc., 1987, 109, 101.
- [3] Kurin-Csörgei K., Orbán M., Rábai G. and Epstein I.R., J. Chem. Soc., Faraday Trans., 1996, 92, 2851.
- [4] Pešek O.; Kofránková V.; Schreiberová L.; Schreiber I., J. Phys. Chem. A, 2008, 112, 826.

# APPLICABILITY OF THE PLATINUM ELECTRODE FOR TRACKING DYNAMICS OF THE BELOUSOV - ZHABOTINSKY OSCILLATORY REACTION IN THE MICROWAVE FIELD

#### J. Brankov and T. Grdanović

Faculty of Physical Chemistry, Studentski trg 12-16, P.O. Box 137, 11001 Belgrade, Serbia

#### **Abstract**

It is carried out testing the applicability of platinum (Pt) electrode to follow evolution of Belousov - Zhabotinsky (BZ) oscillatory reaction in the microwave (MW) field. The Pt electrode potentials in a series of experiments without microwaves, as well as in the experiments in the presence of MW radiation are recorded. It has been found that using the carefully designed experimental setup, responses of Pt electrode agree within experimental error.

#### Introduction

One of the often-applicable ways to track evolution of chemical oscillators is continuously tracking the potential of the Pt electrode. Measuring the Pt electrode potential in the MW field is difficult to achieve because there are certain dangers, for the experimenter himself, measuring equipment and misinterpretation of obtained results:

- 1) In the MW field, arcing of the metal electrode can be reached as a consequence of induced high electrical potential, introducing undesirable new processes in the reaction mixture and possible damaging of the MW source;
- 2) Any metal wires which are parts of the sensors, act as antennas transmitting high voltages to the measuring apparatus and causes way out the harmful MW radiation outside the MW cavity, which represents a direct danger for experimenter himself. Also, induced electric voltage in metal conductors can lead to damage a delicate measuring instruments which, in the case of electrochemical measurements, are not constructed to measure voltage over 5 V;
- 3) As a consequence of using thin electrodes to follow electrode potentials, a local overheating of the reaction mixture and incorrect interpretation of the experimental results [1,2] can appear.

Despite of the existing problems, careful experimental design allows electrochemical measurements in presence of the MW field.

# Experimental

In Figure 1 is schematically shown the investigated experimental setup: 1-shielding copper tube, 2- temperature sensor; 3-Pt electrode, 4- reference electrode (METROHM AG. 6.0726.100), 5 - reaction vessel, 6-reaction mixture.

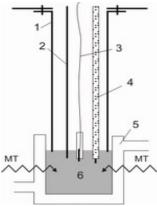


Fig. 1. Experimental setup

Experimental work has been performed by recording potential of the Pt electrode for various prepared Ce<sup>4+</sup>/Ce<sup>3+</sup> ratios [3], in a closed reaction vessel with double walls, which enabled thermostating tested mixture. The thermostating is necessary because according to Nernst equation electrode reading is temperature dependent. Changes in potential of the Pt electrode during the experiment were recorded using data collector (EH-"Measuring instruments Miljkovic Budimir and others" O.D.). As a source of MW radiation, single-mode 2.45 GHz MW CEM reactor with adjustable output power (Discover) is used. Reaction vessel was cylindrical glass vessel with the inner diameter of d≈21 mm. In

the reaction vessel was introduced: Pt electrode (5x0.5 mm glass-sealed Pt wire), electrolytic bridge Ag/AgCl reference electrodes and temperature sensor. Electrodes and temperature sensor were protected from microwaves by a well-grounded copper tube, which was coated with Teflon. That preserves chemical inertness in touch with solution and its vapor. The electrical signal from the electrodes is additionally filtered to remove possible high voltage 2.45 GHz alternating signal resulting from the MW field (induced electric voltage in metal conductors can lead to damage delicate measuring instruments) [4].

All chemicals are of p.a. grade:  $H_2SO_4$  from Fluka, KBrO<sub>3</sub> and  $C_3H_4O_4$  from Merck, KBr from Zorka Sabac,  $Ce_2(SO_4)_3$  97 % from Sigma-Aldrich and  $Ce(SO_4)_2$  99 % from Acros. Deionised water of resistivity ,  $\rho$ =18 M $\Omega$ cm was used.

The total volume of the BZ reaction mixture was V=6.09 ml. The initial composition in all experiments was:  $[H_2SO_4]=0.6$  mol/dm<sup>3</sup>,  $[KBrO_3]=5.02x10^{-2}$  mol/dm<sup>3</sup>,  $[C_3H_4O_4]=1.27x10^{-2}$  mol/dm<sup>3</sup>,  $[KBr]=1.48x10^{-5}$  mol/dm<sup>3</sup>. The ratio concentrations of the redox couple  $Ce^{4+}/Ce^{3+}$  has varied from 1:1000 to 100:1 for determining electrode responce. For those experiments, the reaction mixtures are made with  $H_2SO_4$  (0.6 mol/dm<sup>3</sup>) to simulate oscillatory BZ reaction environment.

#### **Results and Discussion**

Electrode potentials of the Pt electrode were obtained in a series of experiments performed at 53 °C, maintained constant with conventional thermostating. It is done in the absence of MW radiation, as well as during MW irradiating mixture with 20 W, 40 and 60 W.

**Table 1.** Slopes and intercepts of the Nernst lines

MW radiation emitted power / W	Slope / mV	Intercept /mV
0	$68 \pm 3$	$1172 \pm 5$
20	$69 \pm 3$	$1168 \pm 5$
40	$69 \pm 3$	$1168 \pm 5$
60	$69 \pm 3$	$1168 \pm 5$

Comparing the slopes and intercepts of the Nernst curves, E=f(log [Ce<sup>4+</sup>/Ce<sup>3+</sup>]) for different conditions we conclude that their values agree within experimental error. It means that Pt electrode shows the same response in experiments without MW, and in the presence of MW field (Table 1.).

This is important because it proves that near the working electrode there is no local overheating of the reaction mixture. In other words, it means that applied experimental configuration can be used for electrochemical measuring directly in the microwave field.

#### Conclusion

The electrode readings in the absence of MW field, as well as electrode readings in presence of MW radiation

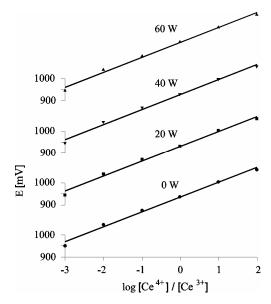


**Fig. 2.** Calibrating lines - electrode potentials in function of logarithm of the ratio concentrations redox couple Ce<sup>4+</sup>/Ce<sup>3+</sup> with MW power 0W, 20W, 40W, 60W, T=53 °C

readings in presence of MW radiation of 20 W, 40 W i 60 W is followed. It has been found that responses of Pt electrode within experimental error were agreeable in both cases, indicating that examined experimental configuration can be used for direct electrochemical tracking of the BZ oscillatory reaction in the MW field.

Obtained results are of wider significance because they open a way for a more detailed electrochemical investigation of different complex processes under microwave irradiation.

# Acknowledgement

This work is done under the leadership of professor D. Stanisavljev as part of the project 142025, supported by Ministry of Science of the Republic of Serbia.

- [1] R.G. Compton, B.A. Coles, F. Marken, Chem. Commun. (1998) 2595.
- [2] F. Marken, U. K. Sur, B. A. Coles, R. G. Compton, Electrochim. Acta 2005, 51, 2195.
- [3] S. Mentus, Elektrohemija, Faculty of Physical Chemistry, University in Belgrade, 2001.
- [4] D.R. Stanisavljev, A.R. Djordjevic, V.D. Likar-Smiljanic, Chem. Phys. Lett. 2005, 412, 420.

# LARGE DEVIATION SPECTRA OF CHAOTIC TIME SERIES FROM BRAY-LIEBHAFSKY REACTION

A.Z. Ivanović<sup>1</sup>, Ž.D. Čupić<sup>1</sup>, Lj.Z. Kolar-Anić<sup>2</sup> and S.R. Anić<sup>2</sup>

 IChTM, Department of Catalysis and Chemical Engineering, Njegoševa 12, 1100 Belgrade, Serbia (anaivanovic@nanosys.ihtm.bg.ac.yu)
 Faculty of Physical Chemistry, University of Belgrade, Studentski trg 12-16, 11000 Belgrade, Serbia

#### **Abstract**

In this paper, we applied multifractal analysis on time series obtained by deterministic simulation of the Bray-Liebhafsky oscillatory reaction. Large Deviation Spectrum was used to represent multifractal spectrum. We obtained spectrums with two peaks, one in region of low and the other in region of high values of Hölder exponent. Their intensity depends on flow rate.

#### Introduction

The Bray-Liebhafsky (BL) reaction is the decomposition of hydrogen peroxide into the water and oxygen in the presence of iodate and hydrogen ions:

$$2H_2O_2 \xrightarrow{H^+,IO_3^-} O_2 + 2H_2O$$
. **(D)**

Oscillatory dynamics of the BL reaction in CSTR can be simulated with the model consisted of eight reactions where three of them are reversible and the reactions due to flow of hydrogen peroxide through the system and outflow of all species from the reaction vessel. With increasing flow rate  $j_0$ , in numerical simulations based on model, various simple, complex and chaotic oscillations were observed. [1]

For detailed comparison of various chaotic states, multifractal analysis is used here, rather than local fractal dimension evaluation, since it may yield additional insight into the complex nature of the chaotic dynamical state. [2] The multifractal spectrum is graph, where abscissa represents the Hölder exponent in the signal and the ordinate is the fractal co-dimension which measures the extent by which a given singularity is encountered. One of the ways to represent multifractal spectrum is Large Deviation Spectrum since it yields information about the statistical behavior of the probability of finding a point with a given Hölder exponent in the signal under changes of resolution. [3]

#### Methods

Deterministic simulations were performed using the MATLAB program package using the ode15s solver. For the numerical calculation of the Large Deviation Spectrum, the FRACLAB toolbox has been used. [4]

#### **Results and Discussion**

Generally, large deviation spectrum is the method for examination of time series with highly irregular oscillation periods and their amplitudes.

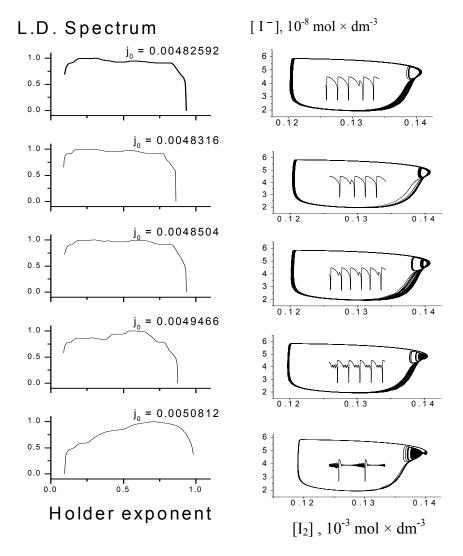


**Fig. 1.** Large Deviation Spectrum (left) and corresponding attractors (right) with their time series at the insets. The j<sub>0</sub> is given in min<sup>-1</sup>.

Here, the time series are also irregular, but with two types of oscillations with significantly different periods and amplitudes. Moreover, the amplitudes of large oscillations are almost same whereas the amplitudes of small oscillations are different between themselves.

By application of large deviation spectrum on these chaotic time series obtained at different flow rates we have found one kind of bimodal distribution which depends on fraction of large and small amplitude oscillations. In Figure 1, the five chaotic states obtained at different flow rates, are presented. For the flow rate  $0.0048504~\text{min}^{-1}$  contribution of small and large amplitude oscillations are similar. In that case large deviation spectrum has the same values for both corresponding Hölder exponents. At lower flow rates ( $j_0 = 0.00482592~\text{min}^{-1}$  and  $j_0 = 0.0048316~\text{min}^{-1}$ ) large deviation spectrum is higher for lower Hölder exponents that correspond to situation when fraction of large amplitude oscillations is higher. The situation is opposite at higher flow rates ( $j_0 = 0.0049466~\text{min}^{-1}$  and  $j_0 = 0.0050812~\text{min}^{-1}$ ).

#### Conclusion

Time series were obtained by numerical integration of the ordinary differential equations for the Bray-Liebhafsky oscillatory reaction model in the CSTR reactor under the conditions of the deterministic chaos and mixed mode periodic oscillations. The applicability of the multifractal analysis in comparison of various chaotic states was demonstrated. For the low flow rate value, smaller Hölder exponents dominate, indicating appearance of signal fractality, while for the increased flow rate values higher Hölder exponents are more pronounced.

# Acknowledgment

The authors thank the partial support of the Fund for Science and Technologies and Development of Serbia. Proj. 142019 and 142025.

- G. Schmitz, Lj. Kolar-Anić, T. Grozdić, V. Vukojević, J. Phys. Chem. A, 2006, 110, 10361-10368.
- [2] R. C. Hilborn, Chaos and Nonlinear Dynamics, 2nd edition, Oxford University Press, Oxford, 2000.
- [3] M. Meyer and O. Stiedl, Eur. J. Appl. Physiol., 2003, 90, 305–316.
- [4] Available at http://apis.saclay.inria.fr/FracLab/download.html

# STOICHIOMETRIC NETWORK ANALYSIS OF PHOTOCHEMICAL PROCESSES WITHIN MESOPAUSE REGION

O. Hadač, M. Kohout, I. Schreiber, V. Nevoral and M. Marek

Institute of Chemical Technology, Prague, Department of Chemical Engineering and Center for Nonlinear Dynamics of Chemical and Biological Systems,

Technická 5, 166 28 Prague 6, Czech Republic; e-mail: Otto.Hadac@yscht.cz

#### **Abstract**

The photochemistry of the mesopause region entails a chemical oscillator forced by solar short-wave radiation. Lumped periodically forced model produces nonlinear behaviour such as period-doublings cascades and chaos. Methods of stoichiometric network analysis are used to decompose the entire network into irreducible subnetworks and then apply linear stability analysis. Comparison of phase shifts of essential species indicated by linear stability analysis with simulations identifies subnetworks giving rise to oscillatory behaviour.

#### Introduction

The mesopause is the boundary region between the mesosphere and thermosphere. It can be located as a region of having the lowest temperature occurring between 80 and 90 km above the surface of the Earth [1]. This region is one of the most sensitive and least explored regions of the atmosphere. The atmosphere is essentially vertically stratified, hence the description by 1D-model, which combines reaction and transport (convection, diffusion, etc.), is a frequently used approximation.

The photochemistry of the mesopause region involves a nonlinear chemical system forced by solar short-wave radiation. The diurnal variation of the solar radiation permanently shifts the photochemical system out of equilibrium because of sunrise and sunset. The system also generates subharmonic oscillations and deterministic chaos [1, 2].

A photochemical mechanism consisting of eighteen chemical reactions can be found in literature [3, 4]. The systems or subsystems of the atmosphere are connected with each other and characterized by internal feedbacks, therefore the use of stoichiometric networks analysis is the appropriate technique.

#### The model

The model of the mesopause region [3] examined here can be expressed as a system of ordinary differential equations (lumped system) representing mass balance equations for O<sub>2</sub>, O<sub>3</sub>, OH, H and HO<sub>2</sub>:

$$\frac{dx_i(t)}{dt} = \sum_{j=1}^J V_{i,j} R_j , \qquad (1)$$

where  $x_i$  represents concentration of the species i, R is the reaction rate, v denotes the stoichiometric coefficient. This model involves the hydrogen/oxygen kinetics

of the mesosphere appropriate to an altitude of 81 km [3]. Photolysis of oxygen, water and ozone depends on the photon intensity  $\Phi$  that varies between 'day' and 'night'. For simplicity, the light variation is modelled by a square function:  $\Phi = 0$  for t < 0.25 and t > 0.75,  $\Phi = 1$  for  $0.25 \le t \le 0.75$ , where t = mod (time/day). This time-dependence of the photon intensity causes a periodic forcing on the system, with a forcing period of one day. The simplest response of the system is a periodic oscillation with one-day period. The concentrations of the major species  $O_2$  and M (any particle) are assumed constant, with  $[O_2] = 6.5 \times 10^{13}$  molecule cm<sup>-3</sup> and  $[M] = 3.4 \times 10^{14}$  molecule cm<sup>-3</sup>. The concentration of another component -  $H_2O$ , is fixed in any given computation, but regarded as the main bifurcation parameter.

# Stoichiometric network analysis (SNA)

The SNA [5] provides a method of estimating stability of steady states of Eq. (1) by expressing the set of all possible reaction rate vectors (R<sub>1</sub>,..., R<sub>J</sub>) as a linear combination of major (or extreme) subnetworks obtained from stoichiometric constraints imposed on the steady states. Any steady state reaction rate vector in the network is a linear combination of the rate vectors of the extreme subnetworks, which form a basis of elementary pathways defining characteristic modes available in the network. In geometrical terms, the space of all admissible (i.e., non-negative) rate vectors is an open cone with the extreme subnetworks forming its edges (1D-faces). Certain pairs of edges span 2D-faces, etc. The edges and the faces constitute a natural hierarchy of increasingly complex subnetworks whose stability is examined to reveal potential sources of oscillatory behaviour by determining conditions for a Hopf bifurcation.

Stability of a steady state (sub)network (not necessarily an edge or an n-face) is given in terms of principal minors of a matrix closely related to the Jacobian matrix [5]. The sign of the relevant minor determines whether the (sub)network is stable for any choice of kinetic parameters or may become unstable. The species associated with the negative minor play a decisive role in the instability if their steady state values are sufficiently small. By choosing the steady state values accordingly, the full Jacobian matrix is obtained. If there is a pair of pure imaginary eigenvalues of the Jacobian, the instability gives rise to periodic oscillatory dynamics via a Hopf bifurcation. At the Hopf bifurcation, a classification and determination of the role of species in oscillations [6] can be done, for example, by calculating mutual phase shifts of oscillating species [7], or by other methods [8, 9].

In terms of graphical interpretation of reaction networks, each reaction is represented as a multi-tail/multi-head arrow, where the number of feathers/barbs determines the stoichiometric coefficients of reactants/products and the number of left feathers determines the reaction order. In the present case, the reaction network can be decomposed into 35 extreme currents, where 13 out of those are unstable.

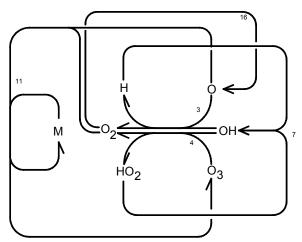


**Fig. 1:** Unstable subnetwork responsible for excitability of 'day' stationary state

The subnetwork in Figure 1 satisfies phase shifts of the full model (1) in the best way. The autocatalytic cycle involves reactions 4 and 7 and the species OH and HO<sub>2</sub> (*autocatalytic species*). An oscillatory instability

is achieved by combining this cyclic reaction path with reaction 3 involving O (*exit species*). The autocatalytic and the exit species are indicated by the negative minor as those, having small steady state concentrations. Finally, the oscillatory instability is made possible by the presence of O<sub>3</sub>. There is a negative feedback exerted by O<sub>3</sub> (*negative feedback species*) upon itself via the path through OH and HO<sub>2</sub> implying that the autocatalysis depletes the supply of O<sub>3</sub>, which must be replenished by the feed or by other transport processes (eddy diffusion, etc.) at a later time leading thus to oscillations. In the simulations [1-4] the 'day' stationary state is excitable, not oscillatory, but conclusions presented here apply also to this case, since excitability and oscillations are intimately connected.

# Acknowledgements

This work was supported by the Grants GAČR 104/06/P301, GAČR 203/06/1269, GAČR 104/08/H055 of the Czech Science Foundation and by the project MSM 6046137306 from the Ministry of Education of Czech Republic.

- [1] G. Sonnemann and A. M. Feigin, Phys. Rev. E, 1999, **59**, 1719.
- [2] G. Sonnemann and B. Fichtelmann, J. Geophys. Res., 1997, 102, 1193.
- [3] B.R. Johnson et al., J. Chem. Soc., Faraday Trans., 1998, 94, 2709.
- [4] S.K. Scott et al., Chem. Eng. Sci., 2000, 55, 209.
- [5] B.L. Clarke, Adv. Chem. Phys., 1980, 43, 1.
- [6] Eiswirth, M., A. Freund and J. Ross, Adv. Chem. Phys., 1991, 80, 127.
- [7] T. Chevalier et al., J. Phys. Chem., 1993, **97**, 6776.
- [8] J.D. Stemwedel et al., Adv. Chem. Phys., 1995, 89, 327.
- [9] J. Ross, I. Schreiber and M.O. Vlad, Determination of Complex Reaction Mechanisms, Oxford University Press, New York, 2006.

#### OSCILLATIONS AND HYSTERESIS IN THE HPTS REACTION

T. Veber, D. Bakeš, L. Schreiberová and I. Schreiber

Institute of Chemical Technology Prague, Department of Chemical Engineering and Center for Nonlinear Dynamics of Chemical and Biological Systems, Technická 5, 166 28 Prague 6, Czech Republic; tomas.veber@vscht.cz;

#### **Abstract**

We study oscillatory and steady state regimes in the hydrogen peroxide – thiosulfate – sulfite reaction carried out in a flow-through stirred reactor. We find a large region of regular oscillations when the inlet sulfite concentration and the flow rate are varied, separating two steady state regions at low and high flow rates. In the border zone between the two main dynamical modes complex transients are found, indicating a narrow zone of hysteresis.

#### Introduction

The reaction of hydrogen peroxide with thiosulfate and sulfite in acidic solution (HPTS reaction) is chemical system providing nonlinear behaviour in a continuous-flow stirred tank reactor (CSTR). The experimentally observed dynamical regimes of HPTS reaction are various steady states, periodic and aperiodic oscillations in the CSTR under isothermal conditions. HPTS reaction belongs to the family of pH oscillators where concentration of hydrogen ions exhibits large amplitude periodic changes in time, typically in the pH range between 4.5 and 7. HPTS reaction exhibits complex periodic changes of pH in time and the reaction is also temperature sensitive [1].

# **Experimental section**

The experiments were carried out in cylindrical-shaped plexiglass cell with the volume liquid of 17.6 mL, see Fig. 1. Inlet ports, outlet port and port for pH electrode are found in the reactor cap. Two reactant solutions were pumped into the reactor through inlet tubes by a peristaltic pump. One solution contained diluted hydrogen peroxide and the other contained mixture of thiosulfate with sulfite and sulfuric acid. Input concentrations of the reactants were:  $[H_2O_2]_0$ =0.0135 mol/L,  $[Na_2SO_3.5H_2O]_0$ =0.005 mol/L,  $[H_2SO_4]_0$ =5.10<sup>-4</sup> mol/L; the inflow concentration of sulfite  $[Na_2SO_3]_0$  was varied from 0.002 mol/L to 0.004 mol/L. All solutions were prepared daily from fresh demineralized water and bubbled with  $N_2$  for at least 12 hours for elimination of  $CO_2$ . The reactor was thermostated on required temperature at  $26 \pm 0.2$ °C. Throughout the experiments stock solutions were bubbled with  $N_2$ .

#### Results

Measurements were carried out under constant operating conditions (inlet concentrations and temperature) with the flow rate (reciprocal mean residence

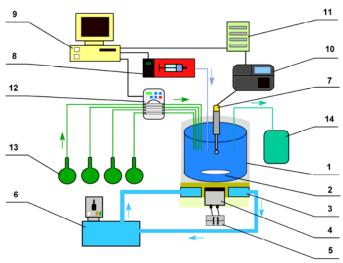
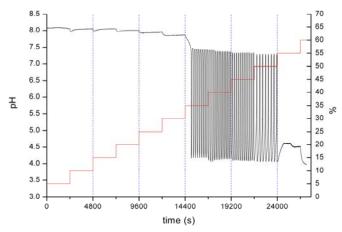


Fig. 1. Experimental setup: 1 - reactor, 2 - magnetic stirrer, 3 - heat exchanger, 4 - electromotor with magnet, 5 - voltage regulator, 6 - thermostat, 7 - pH-electrode, 8 - syringe pump (for the study of excitability), 9 - computer, 10 - pH-meter, 11 - A/D converter, 12 - peristaltic pump, 13 - stock solutions.

time)  $k_0$  being systematically varied in a step-wise manner up and then down to indicate possible hysteresis. Such experiments were systematically repeated for various inlet concentrations of the sulfite. Results for a particular inlet concentration are shown in Fig. 2. At the lowest value of  $k_0$  ( $k_0=0.000349 \text{ s}^{-1}$ ) the system is in the high steady-state. The pH value of this state is about 7.5. The flow rate is gradually increased in small steps while the system remains in high steady state up to  $k_0$ =0.00104 s<sup>-1</sup>. When  $k_0$  is greater than 0.00138 s<sup>-1</sup> the system occurs in a hysteresis region where the stable steady state coexists with simple oscillations. The system starts to regularly oscillate above  $k_0=0.00172$  s<sup>-1</sup>. For the flow rate  $k_0$ =0.00373 s<sup>-1</sup> the periodic oscillations are replaced by a long transient regime. Finally for  $k_0$ =0.00406 s<sup>-1</sup> the system entirely ceases to oscillate and the low steady state with pH value 4.0 is reached. If the flow rate is systematically decreased no hysteresis is observed. In the oscillatory region, the system displays stable simple regular large amplitude oscillations. When the experiments for different levels of the inlet sulfite concentration are put together, bifurcation diagram in Fig. 4 is obtained. It shows that the hysteresis is observed only at the lowest inlet sulfite concentrations and for large enough inlet concentrations of the sulfite oscillations disappears but no multiple steady states are observed. Transition between oscillations and steady states indicate a subcritical Hopf bifurcation.

#### **Conclusions**

Experiments have shown the existence of oscillatory behaviour in the system as well as strong sensitivity to the presence of carbon dioxide in the ambient air. The



**Fig. 2.** pH dynamics (black line) in the reactor with the flow rate step-wise increased at regular time intervals of 2400 s,  $[Na_2SO_3]_0 = 0.002$  mol/L. The step-wise line indicates the flow rate (5% corresponds to a step of  $k_0$ =0.000349 s<sup>-1</sup>).

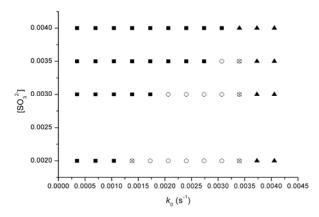


**Fig. 4.** Bifurcation diagram obtained by sequential increase of  $k_0$ ; square – high steady state, triangle – low steady state, circle – oscillations, shaded squares – transient dynamics.

results of dynamical measurements were summarized in bifurcation diagrams indicating steady states, periodic oscillations and a weak hysteresis. No irregular sustained oscillations were found.

# Acknowledgements

This work was supported by grants GACR 203/06/1269 and MSM 6046137306.

#### References

[1] Rabai G., Hanazaki I.: Chaotic pH Oscillations in the Hydrogen Peroxide-Thiosulfate-Sulfite Flow System, J. Phys. Chem. A, 1999, 103 7268-7273.

# PULSE PERTURBATION TECHNIQUE FOR DETERMINATION OF THIAMIN IN PHARMACEUTICALS USING AN OSCILLATORY REACTION SYSTEM

J. Maksimović<sup>1</sup>, N. Pejić<sup>2</sup>, D. Ribič<sup>1</sup> and Lj. Kolar-Anić<sup>1</sup>

<sup>1</sup>Faculty of Physical Chemistry, University of Belgrade, Studentski trg 12-16,

P.O. Box 137, 11001 Belgrade, Serbia

<sup>2</sup>Faculty of Pharmacy, University of Belgrade, Vojvode Stepe 450,

11000 Belgrade, Serbia, bimesel@eunet.yu

#### **Abstract**

A novel procedure for kinetic determination of thiamin (VB<sub>1</sub>) is proposed and validated. The method uses a Pt electrode for potentiometric monitoring of the concentration perturbations of the Bray-Liebhafsky (BL) matrix in a stable non-equilibrium stationary state close to the bifurcation point. The proposed method relies on the linear relationship between maximal potential shift,  $\Delta E_m$ , and the logarithm of VB<sub>1</sub> concentration. Under optimum conditions, linearity was obtained over the range of 0.01–1.0  $\mu$ mol with the limits of detection of 0.01  $\mu$ mol, as well as analytical throughput of 30 determinations per hour. The technique provides simple, effective and convenient method to assay the pharmaceutical samples.

#### Introduction

Oscillatory chemical systems in states far from equilibrium may be used as suitable matrices for analytical determinations by means of pulse perturbation technique (PPT). Applicability of oscillatory reactions to this goal originates from their nonlinear kinetics as well as from the inherent extreme sensitivity to various perturbations [1–3]. Here, the Bray-Liebhafsky oscillatory reaction [4], *i.e.* the reaction of catalytic decomposition of H<sub>2</sub>O<sub>2</sub> into H<sub>2</sub>O and O<sub>2</sub> in the presence of IO<sup>-</sup><sub>3</sub> and H<sup>+</sup>, is used as the matrix for quantitative determination of thiamin.

Numerous methods have been reported for analysis of  $VB_1$  in pharmaceuticals, (spectrofluorimetric, polarographic etc.). The wide linear range and low detection limit of the above-mentioned methods satisfy the requirements of most determinations. However, the determination of water-soluble vitamins has always been a peculiar problem largely due to instability of these compounds and complexity of the matrices in which they usually exist. Also, most of the proposed methods are laborious, time-consuming or not accurate enough. Therefore, new methods based on a relatively simple, fast and cheap device are desirable. Based on our previous experience [2,3] we have developed the PPT to this purpose and in particular, for quantitative determination of  $VB_1$  in bulk drugs and pharmaceuticals.

# **Experimental**

The oscillating assembly is composed of a 50 mL glass Continuosly fed well Stirred Tank Reactor (CSTR). Peristaltic pumps controlled the flows (inflow and outflow) of

reactants (KIO<sub>3</sub>, H<sub>2</sub>SO<sub>4</sub> and H<sub>2</sub>O<sub>2</sub>). Inflow concentration of H<sub>2</sub>SO<sub>4</sub> was the control parameter. Sensitivity of the method was tested at three non-equilibrium stationary states: [KIO<sub>3</sub>]<sub>o</sub> =  $5.9 \times 10^{-2}$  M, [H<sub>2</sub>O<sub>2</sub>]<sub>o</sub> =  $1.5 \times 10^{-1}$  M, specific flow rate, j<sub>o</sub> =  $2.95 \times 10^{-2}$  min<sup>-1</sup>, T = 56.0 °C and [H<sub>2</sub>SO<sub>4</sub>]<sub>o</sub> =  $8.16 \times 10^{-2}$  M, =  $8.44 \times 10^{-2}$  M and =  $9.0 \times 10^{-2}$  M. Highest sensitivity was found for [H<sub>2</sub>SO<sub>4</sub>]<sub>o</sub> =  $8.44 \times 10^{-2}$  M i.e. in a stable non-equilibrium stationary state that is closest to the bifurcation point found at [H<sub>2</sub>SO<sub>4</sub>]<sub>BP</sub> =  $7.95 \times 10^{-2}$  M. Temporal evolution of the system was recorded by means of a Pt electrode and double junction Ag/AgCl electrode interfaced to a PC-AT 12 MHz compatible computer *via* a PC-Multilab EH4 16–bit ADC. For VB<sub>1</sub> determination in pharmaceutical, the sample solution were prepared by quantitatively transfer the average mass of one tablet in a 25-mL volumetric flask. The intensity of the perturbation corresponded to the total amount (in µmol) of analyte injected in the 50 µL aliquot of standard samples.

#### **Results and Discussion**

The PPT used for quantitative determination of  $VB_1$ , is based on potentiometric monitoring of the response of the non-linear matrix to perturbations induced by different concentrations of standards and analyte (Fig. 1.). The maximal change in potential (in mV), defined as the difference  $\Delta E_m = E_p - E_s$ , where  $E_p$  is the maximal potential value attained after the perturbation is performed, and  $E_s$  is the potential corresponding to the stable stationary state before the perturbation is performed (Fig. 1.); the  $\Delta E_m$  is used as indicator of the perturbation strength. This potential shift is found to vary linearly as a function of the logarithm of  $VB_1$  concentration over the range 0.01  $\mu$ mol  $\leq [VB_1] \leq 1.0$   $\mu$ mol. The regression equation of the standard series calibration curves is  $\Delta E_m = 17.6 + 8.4 \log c$  (r = 0.9986). The detection limit of the method is 0.01  $\mu$ mol.

In order to study the validity of the proposed method, it was applied to the determination of  $VB_1$  in pharmaceutical (Pentovit, Srbolek, Belgrade). The amount of  $VB_1$  obtained by the proposed method is in good agreement with that claimed by the manufactures (RSD is 5.1%). The Table 1 shows the results obtained; it can be seen that the RCV is 102 % indicating that the method developed is free from interference and provides accurate results; it is a useful method for quantitative analysis of  $VB_1$  in pharmaceuticals.

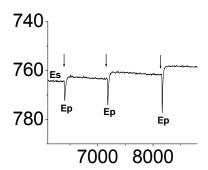


**Fig. 1**. Typical response curves obtained after perturbing the stationary state in the BL reaction found at a mixed inflow concentration of sulfuric acid,  $[H_2SO_4] = 8.44 \times 10^{-2}$  M by addition of different concentrations of  $VB_1$  (from left to right): 0.08 µmol;  $[VB_1] = 0.15$  µmol and  $[VB_1] = 0.75$  µmol. Arrows indicate the moments at which stationary states were perturbed.

**Table 1.** Precision and recovery of VB<sub>1</sub> in pharmaceutical dosage form

Sam	nplea	Claimed (mg)	Concentration found (mean <sup>b</sup> ±	R.S.D. <sup>d</sup>	RCV <sup>e</sup>
			S.D.°)	(%)	(%)
		12.3	$12.7 \pm 0.6$	4.8	103.2

<sup>&</sup>lt;sup>a</sup> Samples containing: thiamin (12.3 mg), pyridoxine (5 mg), B12 (0.05 mg), folic acid (0.4 mg), nicotinamide (20 mg) and excipients; <sup>b</sup>Mean concentration (n=6); <sup>c</sup>average standard deviation; <sup>d</sup>Average relative standard deviation; <sup>e</sup>Performed as accurate addition of 0.16 μmol of VB<sub>1</sub> in the dilute samples (n=3)

#### Conclusion

The proposed method for the determination of  $VB_1$  is fast (30 samples per hour), accurate (RSD is 5.1%), precise (RCV = 102%) and sensitive (LOD = 0.01  $\mu$ mol). It was proved to be very appropriate for routine analysis of pharmaceuticals without any pretreatment of the samples apart from its dissolution; it could be also used for their quality control.

## Acknowledgement

We thank Professor S. Anić for fruitful suggestions during writing the article. The present investigations were partially supported by the Ministry of Sciences of the Republic of Serbia, under Project 142025.

- [1] R. Jimenez-Prieto, M. Silva, D. Perez-Bendito, Anal. Chem., 1995, 67, 729-734.
- [2] V. Vukojević, N. Pejić, D. Stanisavljev, S. Anić, Lj. Kolar-Anić, Analyst, 1999, 124, 147-152.
- [3] N. Pejić, S. Blagojević, S. Anić, V. Vukojević, M. Mijatović, J. Ćirić, Z. Marković, S. Marković, Lj. Kolar-Anić, Anal. Chim. Acta, 2007, **582**, 367-374.
- [4] W.C. Bray, J. Am. Chem. Soc., 1921, 43, 1262-1267.

# BRAY-LIEBHAFSKY REACTION. DYNAMIC STATES WHEN SULFURIC ACID IS THE CONTROL PARAMETER

N. Pejić<sup>1</sup> and J. Maksimović<sup>2</sup>

<sup>1</sup>Faculty of Pharmacy, University of Belgrade, Vojvode Stepe 450, 11000 Belgrade, bimesel@eunet.yu

<sup>3</sup>Faculty of Physical Chemistry, University of Belgrade, Studentski trg 12-16, P.O. Box 137, 11001 Belgrade, Serbia

#### **Abstract**

The experimental results obtained when the Bray-Liebhafsky (BL) reaction is realised in the CSTR (Continuously fed well Stirred Tank Reactor) are presented. The dynamic behavior of the BL reaction is examined by varying inflow concentration of the  $H_2SO_4$  as a control parameter. The experimental evidence for the onset and termination of oscillatory behavior *via* the saddle node infinite period (SNIPER) bifurcation as well as some kind of the Hopf bifurcation is presented. Moreover, the complex dynamic behavior is also found.

#### Introduction

The investigation of the chemical systems, which posses non-linear properties, self-organization and temporal dynamic structures has become one of the most active areas in chemical dynamics. Recently, bifurcation analysis has been attained to obtain dynamic behavior of nonlinear system when driven in the CSTR. We have examined the dynamic behavior of the BL reaction [1] in the CSTR [2] when sulfuric acid is the control parameter, what about there are only few informations [2] We determined the conditions under which transition from a stable stationary state to periodic oscillations can occur. Transition from simple periodic oscillations to complex mixed-mode oscillations and chaos has also been found.

# **Experimental**

We investigated the BL reaction as the reaction where  $H_2O_2$  decomposes into the  $H_2O$  and  $O_2$  in the presence of both  $IO_3^-$  and  $H^+$  ions. The dynamic behavior of the BL reaction is examined in the CSTR when inflow concentration of  $H_2SO_4$  is a control parameter. Under the following experimental conditions:  $[KIO_3]_o = 0.059$  M,  $[H_2O_2]_o = 0.015$  M; the specific flow rate  $j_o = 0.0295$  min<sup>-1</sup>, T = 56°C and the inflow concentration of  $H_2SO_4$  varied from 0.0422 M to 0.09 M. Temporal evolution of the system was recorded by means of a Pt electrode and double junction Ag/AgCl electrode interfaced to a PC-AT 12 MHz compatible computer via a PC-Multilab EH4 16-bit ADC.

#### **Results and Discussion**

In our experiment, concentration of  $H_2SO_4$  varied, while the other parameters (T,  $j_0$  and concentration of both KIO<sub>3</sub> and  $H_2O_2$ ) remained unchanged (Fig. 1 (a)).

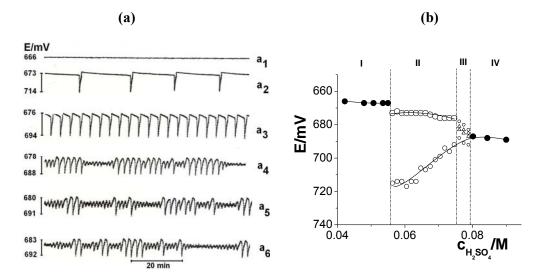


**Fig. 1. (a)** Time series obtained under the given experimental conditions. (a<sub>1</sub>) 0.0422 M (a<sub>2</sub>) 0.0591 M (a<sub>3</sub>) 0.0704 M (a<sub>4</sub>) 0.0761 M (a<sub>5</sub>) 0.0774 M (a<sub>6</sub>) 0.0788 M **b)** Bifurcation diagrams show transition from the stable stationary state (solid circles) to the large-amplitude oscillations (open circles) and small amplitude oscillation (triangle) denoting minimal and maximal potential in an oscillation; dash doted lines show the boundary between different dynamic structures: stable stationary states (I and IV), oscillatory states (II) and aperiodic mixed mode oscillations (III).

For  $H_2SO_4$  concentration in the range from 0.0422 M to 0.055 M, stable stationary states are found. Simple periodic oscillations as well as stable stationary states exist for concentration of  $H_2SO_4$  in the range from 0.0563 M to 0.0746 M as well as 0.0802 M to 0.09 M, respectively. When concentration of  $H_2SO_4$  increases above 0.0761 M, aperiodic mixed mode oscillations with different mixing of the large and small amplitude are detected (Fig.  $1(a_4)$ – $(a_6)$ ). The bifurcation diagram, showing the envelope of the simple periodic oscillations (zone II) and two distinct stable stationary states characterized by lower (zone I) and higher potential values (zone IV) of the stable stationary states are presented in Fig 1b. Also, for  $H_2SO_4$  concentration in the range 0.0761 M  $\leq$  [ $H_2SO_4$ ]  $\leq$  0.0788 M (zone III) a region of aperiodic mixed mode oscillations is entered.

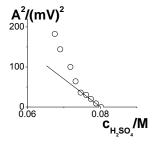


**Fig. 2.** Plot of the square of the large-amplitude oscillations as a function of the mixed flow concentration of  $H_2SO_4$ . The abscissa intercept corresponds to the bifurcation value of the mixed flow concentration of sulfuric acid,  $[H_2SO_4] = 0.0795 \text{ M}$ .

The transition from the stationary state (zone I), into oscillatory goes through losing stability at the lower bifurcation point, ( $[H_2SO_4] = 0.0557 \text{ M}$ ), via SNIPER bifurcation. When the bifurcation point is approached, the period of the simple a periodic oscillation increases whereas their amplitudes remain constant. The bifurcation occurs at the same value of the mixed flow concentration of  $H_2SO_4$ ,  $[H_2SO_4] = 0.0557$  M, when approached from either side. On the other hand, at the higher bifurcation point,  $[H_2SO_4] = 0.0795$  M, the transition from the mixed mode oscillations into a stable stationary state occurs. When this bifurcation point is approached, the period of the large-amplitude oscillations remains constant while the amplitude decreases. This bifurcation point is found by linear extrapolation of a plot of the square of the large-amplitude oscillations observed close to the bifurcation point versus the inflow concentration of H<sub>2</sub>SO<sub>4</sub> (Fig. 2), but this intersection cannot be ascribed easily to Hopf bifurcation point since two kinds of oscillations emerge from it. Moreover, we could have more points between the chaos and the stable steady state where dynamic states with simple sustained oscillations would appear. Then we should probably have the simple Hopf bifurcation point.

# Acknowledgement

The present investigations were partially supported by the Ministry of Sciences of the Republic of Serbia, under Project 142025.

- [1] W.C. Bray, J.Am.Chem.Soc., 1921, 43, 1262-1266.
- [2] V. Vukojević, S. Anić, Lj. Kolar-Anić, J. Phys. Chem. A, 2000, 104, 10731.

# BRAY-LIEBHAFSKY OSCILLATORY REACTION GENERATED IN BATCH REACTOR. INFLUENCE OF PULSE INVOLVING IODIDE AT THE END OF PREOSCILLATORY PERIOD

M. Kragović and S. Anić\*

Faculty of Physical Chemistry, University of Belgrade, P.O.Box 47, 11000 Belgrade, Serbia \*boban@ffh.bg.ac.yu

#### **Abstract**

The oscillatory Bray-Liebhafsky (BL) reaction is generated in the batch reactor at 60  $^{0}$ C. The composition of the BL system was kept constant: ([H<sub>2</sub>O<sub>2</sub>]<sub>0</sub> = 3.00·10<sup>-3</sup>, [H<sub>2</sub>SO<sub>4</sub>]<sub>0</sub> = 5.50·10<sup>-2</sup> and [KIO<sub>3</sub>]<sub>0</sub> = 6.00·10<sup>-2</sup> mol·dm<sup>-3</sup>. The BL reaction characterized by one preoscillatory and one oscillatory period was perturbed with pulse involving different concentration of potassium iodide (1·10<sup>-6</sup> - 1·10<sup>-3</sup> mol·dm<sup>-3</sup>) at the end of preoscillatory period. The significant effect appears for the [KI]<sub>0</sub> > 1·10<sup>-4</sup> mol·dm<sup>-3</sup>; the length of the iodide oscillograms and the number of oscillations decrease when potassium iodide increases. The complex logarithmic function between the length of the iodide oscillograms and initial potassium iodide concentrations was found.

#### Introduction

The Bray-Liebhafsky reaction is the decomposition of hydrogen peroxide into water and oxygen

$$2H_2O_2 \xrightarrow{IO_3^-, H^+} 2H_2O + O_2$$
, D

in the presence of iodate and hydrogen ions.[1] In this reaction appear numerous intermediates such as I-, I2, HOI, HOOI etc.[1-4] The BL reaction can be monotonous or oscillatory in the time [1-5]. The reaction (D) is result of two complex consecutive reactions [1]

$$2IO_3^- + 2H^+ + 5H_2O_2 \rightarrow I_2 + 5O_2 + 6H_2O$$
 R

$$I_2 + 5H_2O_2 \rightarrow 2IO_3^2 + 2H^+ + 4H_2O$$

Influences of different perturbation species on the BL reaction was investigated from its discovery. There are several manners for introducing the perturbation species in the BL system. One of them is pulse perturbation in desired moment during the reaction. The effects of perturbations can be manifested in changing the properties of the BL reaction as the preoscillatory or the oscillatory period, the total number of oscillations etc. [1-5] Attention in present paper is focused on pulse concentration iodide perturbation of BL reaction, which is generated under well stirred isothermal closed reactor (the batch reactor) at the end of the preoscillatory period.

# **Experimental**

The BL oscillator with constant composition ( $[H_2O_2]_0 = 3.00 \cdot 10^{-3}$ ,  $[H_2SO_4]_0 = 5.50 \cdot 10^{-2}$ ,  $[KIO_3]_0 = 6.00 \cdot 10^{-2}$  mol·dm<sup>-3</sup>) and temperature ( $60 \pm 0.2$   $^{0}$ C) is generated in the vessel (Methrom EA 876-20). The BL reaction is recorded by digitalized potenciometric method with  $\Gamma$ -ion sensitive electrode coupled with Ag/AgCl referent electrode. In this

aim is used digital equipment (EH4 pH meter, Merni instrumenti B. MIljkovic, Serbia) connected with PC computer. The electrode is calibrated by the method presented in ref.6.

## **Experimental**

The BL oscillator with constant composition ( $[H_2O_2]_0 = 3.00 \cdot 10^{-3}$ ,  $[H_2SO_4]_0 = 5.50 \cdot 10^{-2}$ ,  $[KIO_3]_0 = 6.00 \cdot 10^{-2}$  mol·dm<sup>-3</sup>) and temperature ( $60 \pm 0.2^{-0}C$ ) is generated in the vessel (Methrom EA876-20). The BL reaction is recorded by digitalized potenciometric method with  $\Gamma$ -ion sensitive electrode coupled with Ag/AgCl referent electrode. In this aim is used digital equipment (EH4 pH meter, Merni instrumenti B. MIljkovic, Serbia) connected with PC computer. The electrode is calibrated by the method presented in ref.6. The BL reaction starts after adding of hydrogen peroxide in the solution of potassium iodide and sulfuric acid at the moment when working electrode gets up potential about 147 mV. Different amount of the potassium iodide (from  $1 \cdot 10^{-6}$  to  $1 \cdot 10^{-3}$  mol·dm<sup>-3</sup>) was added by pulse technique at the beginning of the oscillatory period of BL reaction. All substances are produced by Merck. They are used without aditional purification.

#### **Results and Discussion**

After addition of the potassium iodide, the oscillatory evolution of reaction (D) changes (Figure 1.). Namely, for low concentration of potassium iodide  $(1\cdot10^{-6}-1\cdot10^{-4} \text{ mol·dm}^{-3})$  the length of the iodide oscillograms are changed slowly. In domain from  $3.00\cdot10^{-4} \leq [KI]_0 \leq 3.40\cdot10^{-4} \text{ mol·dm}^{-3}$  the length of oscillograms and the number of oscillations decrease noticeably.

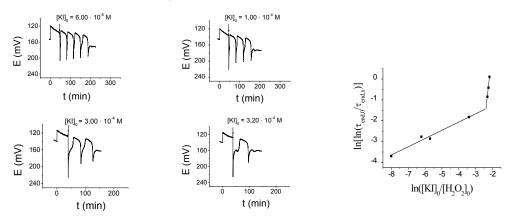


**Fig. 1.** The potential traces of the iodide sensitive electrodes for the BL reaction generated in the batch reactor (see Experimental). The arrows denote the moment of perturbation BL system with solution of potassium iodide.

**Fig. 2.** The graphic presentation of relation between  $\tau_{end} / \tau_{end}^*$  and  $[KI]_0$  in accordance to equation 3.

Figure 2 presents the relation between relative length of oscillograms and initial potassium iodide concentration. It is based on the formal kinetic analysis of the reaction (D). The decomposition of hydrogen peroxide (D) can be described by the equation

$$\tau_{end} = \frac{1}{k_D} \ln \frac{[H_2 O_2]_0}{[H_2 O_2]_{end}}$$
 (1)

where  $\tau_{end}$  is the length of oscillogram, whereas  $[H_2O_2]_0$  and  $[H_2O_2]_{end}$  denote the concentration at the beginning and the end of oscillogram, respectively. [7] If we suppose that the potassium iodide influences on  $k_D$  by the relation

$$k_{KI} = k_D \left( \exp \left( x \left( \frac{[KI]_0}{[H_2 O_2]_0} \right)^y \right) \right)$$
 (2)

where  $k_{KI}$  is the new rate constant, x and y are parameters that are functions of kinetics of BL reaction; and that now the length of oscillograms of the BL perturbed systems can be described by equation (2) but with new constant  $k_{KI}$ , we can obtain relation

$$\ln(\ln \frac{\tau_{end}}{\tau_{end}^*}) = \ln x + y \ln \frac{[KI]_0}{[H_2O_2]_0}$$
(3)

where  $\tau_{end}^*$  is length of oscillograms of perturbed BL system. The constant  $k_{KI}$  reflects the domination of the reaction O after adding potassium iodide in the BL system. This phenomenon was also discussed in ref.4 by G. Schmitz.

#### Conclusion

The influence of potassium iodide on the BL reaction is analyzed and described by classical kinetic considerations. This method can be used as the criterion for the change or the keeping of the kinetic of any investigation process.

# Acknowledgement

This work was partially supported by the Ministry for Science of the Republic of Serbia (Grants no. 142025).

- [1] W. C. J. Bray, Am. Chem. Soc. 1921, 43, 1262.
- [2] I. Matsuzaki, J. H. Woodson, H. A. Liebhafsky, Bull. Chem. Soc. Jpn. 1970, 43, 3317.
- [3] M. G. Peard, C. F. Cullis, *Trans. Farady Soc.* 1951, 47, 616.
- [3] H.Degn, Acta Chem. Scand. 1961, **21**, 1057.
- [4] G. Schmitz, in Special inhomogeneities and transient behaviour in chemical kinetics, P. Gray and al, Manchester University Press, Manchester, 1990, p. 666.
- [5] S. Anić, D. Mitić, Glasnik na hemicariti i tehnolozite na Makedonija, 1989, 7, 303; V. B. Vukojević, N. D. Pejić, D. R. Stanisavljev, S. R. Anić, Lj. Z. Kolar-Anić, *Analyst*, 1999, 124, 147; N. Pejić, S. Blagojević, S. Anić, Lj. Kolar-Anić, *Anal. Bioanal. Chem.* 2007, 389, 2009, and refs. therein.
- [6] G. Horvai, K. Thoth, E. Pungir, Anal. Chim. Acta 1976, 82, 45.
- [7] S. Anić, Lj. Kolar-Anić, Faraday Transaction I 1988, 84, 3413.

### SIMULATION OF TEMPERATURE DEPENDENCE OF THE BELOUSOV-ZHABOTINSKY REACTION

S.M. Blagojević<sup>1</sup> and S.R. Anić<sup>2</sup>

<sup>1</sup>Faculty of Pharmacy, University of Belgrade, Vojvode Stepe 450, Belgrade, Serbia slavica.blagojevic@pharmacy.bg.ac.yu

<sup>2</sup>Faculty of Physical Chemistry, University of Belgrade, Studentski trg 12, POB 551,Belgrade, Serbia

#### **Abstract**

The simulation of the Belousov-Zhabotinsky (BZ) reaction under batch condition was performed and compared with experimental data. With this aim, the reaction scheme with twelve reactions including new ones was used. The experimental and calculated behaviors of the BZ system are in well agreement in the examined temperature range between 30 and 40 °C.

### Introduction

Various kinetic models of the Belousov-Zhabotinsky reaction were proposed [1–2], but they can not simulate our experimental data satisfactory. Therefore, beside other corrections [3], we introduced here the reaction due to evaporation of bromine as was already discussed by Noszticzius and Gaspar [4,5].

### **Experimental**

The Belousov-Zhabotinsky isothermal oscillatory system (the volume of 51 mL) The temporal evolution of the reaction systems was monitored by potentiometric method where a bromide ion–sensitive electrode versus double junction Ag/AgCl as the reference was used. All experiments were carried out under the constant values of the initial concentrations of the following species (in mol dm<sup>-3</sup>):  $[H_2SO_4]_0 = 1.00$ ;  $[CH_2(COOH)_2]_0 = 2.20 \times 10^{-2}$ ;  $[KBrO_3]_0 = 6.20 \times 10^{-2}$ ;  $[KBr]_0 = 1.50 \times 10^{-5}$ ;  $[Ce_2(SO_4)_3]_0 = 2.50 \times 10^{-3}$ . The experiments were performed at 30, 35 and 40 °C.

#### **Results and Discussion**

The typical potentiometric traces of the BZ systems at different temperatures are presented in Figure 1. The obtained time series were simulated by the proposed reaction scheme shown in Table 1. Almost all rate constants were taken from earlier numerical simulations [3]. The rate constants at T=25 °C [6] are recalculated by means of the activation energies to corresponding values at 30, 35 and 40 °C.

The simulations of the BZ reaction (Figure 2) are carried out under the conditions used in the experiments (exp). Most important oscillatory features [preoscillatory period ( $\tau_1$ ), the time elapsed between the start of the reaction and the termination of the oscillatory phase ( $\tau_{end}$ ), period of the oscillations and number oscillations (n)] are well modeled (calc) (Figure 3 and 4). With aim to see the influence of reaction due to evaporation of bromine from the system (R12), in Figure 3 and 4, the simulations of  $\tau_1$  and  $\tau_{end}$  obtained with the model without this reaction are presented.

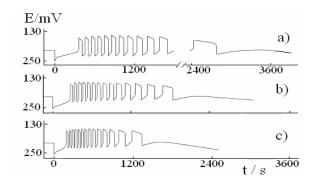


**Fig. 1.** The potentiometric traces of the BZ reaction obtained by the Br<sup>-</sup> - ion sensitive electrode, in order of increasing temperature (in °C): a) 30; b) 35; c) 40.

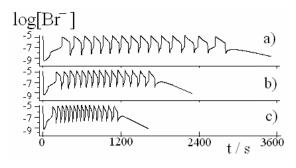
**Table 1.** Reaction and rate constant used in the numerical simulations

	Reaction	<sup>a</sup> Rate constants at 30 ° C		
R1	$Br^- + HOBr + H^+ \rightarrow Br_2 + H_2O$	2.55×10 <sup>9</sup>	$mol^{-2} dm^6 s^{-1}$	
R-1	$Br_2 + H_2O \rightarrow Br^- + HOBr + H^+$	3.18	$s^{-1}$	
R2	$HBrO_2 + Br^- + H^+ \rightarrow Br_2O + H_2O$	c5.93×10 <sup>6</sup>	$mol^{-2} dm^6 s^{-1}$	
R3	$Br_2O + H_2O \rightarrow 2HOBr$	$^{c}3.21\times10^{3}$	$s^{-1}$	
R-3	$2HOBr \rightarrow Br_2O + H_2O$	c3.22×10 <sup>8</sup>	$mol^{-1} dm^3 s^{-1}$	
R4	$Br^- + BrO_3^- + 2H^+ \rightarrow HOBr + HBrO_2$	2.86	$mol^{-3} dm^9 s^{-1}$	
R5	$2HBrO_2 \rightarrow BrO_3^- + HOBr + H^+$	$3.49 \times 10^3$	$mol^{-1} dm^3 s^{-1}$	
R6	$BrO_3^- + HBrO_2 + H^+ \rightarrow 2BrO_2^{\bullet} + H_2O$	44.70	$mol^{-2} dm^6 s^{-1}$	
R-6	$2BrO_2^{\bullet} + H_2O \rightarrow BrO_3^{-} + HBrO_2 + H^{+}$	$6.70 \times 10^7$	$mol^{-1} dm^3 s^{-1}$	
<b>R7</b>	$Ce^{3+} + BrO_2^{\bullet} + H^+ \rightarrow Ce^{4+} + HBrO_2$	b3.20×10 <sup>4</sup>	$mol^{-2} dm^6 s^{-1}$	
R-7	$Ce^{4+} + HBrO_2 \rightarrow Ce^{3+} + BrO_2 + H^+$	$1.12 \times 10^4$	$mol^{-1} dm^3 s^{-1}$	
R8	$MA + Br_2 \rightarrow BrMA + Br^- + H^+$	<sup>b</sup> 4.23	$mol^{-1} dm^3 s^{-1}$	
R9	$MA + Ce^{4+} \rightarrow Ce^{3+} + P_1 + H^+$	0.36	$mol^{-1} dm^3 s^{-1}$	
R10	$BrMA + Ce^{4+} \rightarrow Ce^{3+} + Br^{-} + P_2$	47.17	$mol^{-1} dm^3 s^{-1}$	
R11	$Br_2O + MA \rightarrow BrMA + HOBr$	c4.23×10 <sup>-2</sup>	$mol^{-1} dm^3 s^{-1}$	
R12	$Br_2(sol) \rightarrow Br_2(g)$	<sup>b</sup> 1.10×10 <sup>-2</sup>	$s^{-1}$	

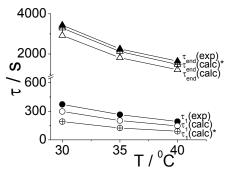
<sup>&</sup>lt;sup>a</sup>The concentration of water  $[H_2O] = 55$  mol dm<sup>-3</sup> is included in the rate constants.

### Conclusion

The proposed model reproduces several experiments performed at different temperatures in closed BZ oscillatory reaction. The numerical results of the dynamics of BZ reaction, which were carried out by the known skeleton model including the Br<sub>2</sub>O species and reaction due to evaporation of bromine, are in a very good agreement with the experimental ones.



**Fig. 2.** Time dependence of  $log[Br^-]$  obtained by the numerical simulation for the different temperatures are as in Figure 1. Simulations of the same system assuming  $[H^+]_0=1.29$  mol dm<sup>-3</sup>[7] and  $[HOBr]_0=1.50\times10^{-8}$  mol dm<sup>-3</sup>



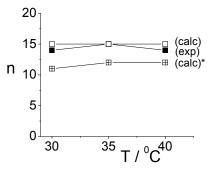


Fig. 3. The dependence of  $\tau_1$  and  $\tau_{end}$  on the temperature. \*denotes the dates calculated with the model without (R12).

**Fig. 4.** The dependence of **n** on the temperature. \*denotes the dates calculated with the model without (R12).

### Acknowledgment

We gratefully acknowledge the partial financial support in grant no. 142025 of the Ministry for Science of the Republic of Serbia.

- [1] R. Field, R. Noyes, J. Chem. Phys., 1974, **60**, 1877–1884.
- [2] L. Györgyi, R. Field, J. Phys. Chem., 1991, 95, 6594-6602.
- [3] S. M. Blagojević, N. Pejić, S. N. Blagojević, Z. Cupić, S. Anić, Lj. Kolar-Anić, Role of Br<sub>2</sub>O species in the model of Belousov-Zhabotinsky reaction, Physical Chemistry 2006, A. Antić-Jovanovic (ed.), SPCS, Belgrade 2006, p. 252
- [4] Z. Noszticzius, P. Stirliling and M. Wittman, J. Phys. Chem., 1985, 89, 4914–4921.
- [5] V. Gáspár, G. Bazsa, and M. T. Beck, J. Phys. Chem., 1985, 89, 5495-5499.
- [6] B. R. Johnson, S. K. Scott and B. W. Thompson, Chaos, 1997, 7, 350-358.
- [7] E. B. Robertson, H. B. Dunford, J. Am. Chem. Soc., 1964, 86, 5080-5089.

## EXPERIMENTAL AND NUMERICAL EVIDENCE OF THE SNIPER BIFURCATION IN THE BELOUSOV-ZHABOTINSKY OSCILLATORY REACTION UNDER BATCH CONDITIONS

S.M. Blagojević<sup>1</sup>, Ž.D. Čupić<sup>2</sup>, N.D. Pejić<sup>1</sup> and Lj.Z. Kolar-Anić<sup>3</sup>

<sup>1</sup>Faculty of Pharmacy, University of Belgrade, Vojvode Stepe 450, Belgrade, Serbia slavica.blagojevic@pharmacy.bg.ac.yu

<sup>2</sup>IChTM – Department of Catalysis and Chemical Engineering,, Njegoševa 12, Belgrade, Serbia <sup>3</sup>Faculty of Physical Chemistry, University of Belgrade, Studentski trg 12, POB 551, Belgrade, Serbia

### **Abstract**

The already found saddle—node infinite period (SNIPER) bifurcation point in transition from stable quasi—steady state to periodic orbits and vice versa is confirmed by both, experimental and numerical investigations of the Belousov-Zhabotinsky (BZ) system, realized under batch conditions.

#### Introduction

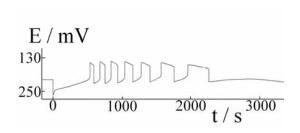
The character of bifurcation points at the beginning and at the end of the oscillatory region is examined by periods, oscillatory amplitudes and excitability of the stable steady state in their vicinity, just as it is already performed in the previous investigations of the Belousov-Zhabotinsky system in closed reactor performed by Noszticzius *et al* [1–2]. In the model applied here for the numerical simulation of the experimentally obtained results, the  $Br_2O$  as intermediate species [3], and the reaction due to evaporation of bromine [4], were included in the existing GF model [5].

### **Experimental**

The Belousov-Zhabotinsky oscillatory reaction was carried out at 30 °C in a thermostated closed reactor with a reaction volume of 51 ml with a magnetic stirrer. Bromide ion-sensitive electrode versus double junction Ag/AgCl as the reference was used for potentiometric monitoring of the temporal evolution of the system. All experiments were carried out under the constant values of the initial concentrations (in mol dm<sup>-3</sup>):  $H_2SO_4=1.00$ ;  $CH_2(COOH)_2=1.60\times10^{-2}$ ;  $KBrO_3=6.20\times10^{-2}$ ;  $KBr=1.50\times10^{-5}$ ;  $Ce_2(SO_4)_3=2.50\times10^{-3}$ . During the preoscillatory and postoscillatory period a small amount  $(8-200~\mu l)$  of 0.1 M KBr solutions was injected repeatedly into the BZ reaction mixture with a micropipettes.

#### **Results and Discussion**

The potentiometric traces of the BZ systems and time evolutions obtained by the numerical simulation according to the kinetic scheme given in Table 1 is presented in Figure 1. The obtained time evolutions have same type and structures as the experimental ones.



### **Experimental results**

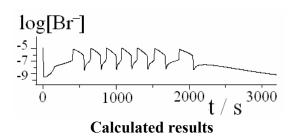
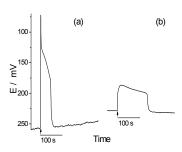


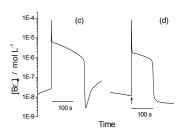
**Fig. 1.** Experimental results: the potentiometric traces of the bromide ion–sensitive electrode at 30.0 °C.

Calculated results: the time dependence of log[Br] obtained by the numerical simulation according to the kinetic scheme given in Table 1.

 $[H^+]_0 = 1.29 \text{ mol dm}^{-3}$ . The concentrations of the other external species are as in experimental results.  $[HOBr]_0=1.50\times 10^{-8} \, \text{mol dm}^{-3}$ .



### **Experimental results**



### Calculated results

**Fig. 2.** One example of excitability of the preoscillatory ((a) and (c)) and postoscillatory ((b) and (d)) stable quasi-steady states in the vicinity of the bifurcation points. The moment of perturbations are denoted by arrows. Perturbations intensity was equal to  $7.84 \times 10^{-5}$  mol dm<sup>-3</sup> KBr.

By analyzing oscillograms obtained experimentally and by simulation of the BZ reaction using the proposed model, the only large-amplitude relaxation oscillations with increasing period between them are found. Moreover, the excitability in the vicinity of the bifurcation points in the preoscillatory (Figure 2a and 2c) and postoscillatory (Figure 2b and 2d) stable quasi–steady states is noted (Figure 2). Thus, we can say that we are dealing with the SNIPER bifurcation points, as it is already obtained under batch conditions in refs [1] and [2]. Besides, we can conclude that such slightly modified model can simulate very good the experimentally obtained results.

	Reaction	<sup>a</sup> Rate constants for 30 ° C		
R1	$Br^- + HOBr + H^+ \rightarrow Br_2 + H_2O$	2.55×10 <sup>9</sup>	$\text{mol}^{-2} \text{dm}^6 \text{s}^{-1}$	
R-1	$Br_2 + H_2O \rightarrow Br^- + HOBr + H^+$	3.18	$s^{-1}$	
R2	$HBrO_2 + Br^- + H^+ \rightarrow Br_2O + H_2O$	c5.93×10 <sup>6</sup>	$mol^{-2} dm^6 s^{-1}$	
R3	$Br_2O + H_2O \rightarrow 2HOBr$	$^{c}3.21\times10^{3}$	$s^{-1}$	
R-3	$2HOBr \rightarrow Br_2O + H_2O$	c3.22×10 <sup>8</sup>	$mol^{-1} dm^3 s^{-1}$	
R4	$Br^- + BrO_3^- + 2H^+ \rightarrow HOBr + HBrO_2$	2.86	$mol^{-3} dm^9 s^{-1}$	
R5	$2HBrO_2 \rightarrow BrO_3^- + HOBr + H^+$	$3.49 \times 10^{3}$	$mol^{-1} dm^3 s^{-1}$	
R6	$BrO_3^- + HBrO_2 + H^+ \rightarrow 2BrO_2^{\bullet} + H_2O$	44.70	$mol^{-2} dm^6 s^{-1}$	
R-6	$2BrO_2^{\bullet} + H_2O \rightarrow BrO_3^- + HBrO_2 + H^+$	$6.70 \times 10^7$	$mol^{-1} dm^3 s^{-1}$	
R7	$Ce^{3+} + BrO_2^{\bullet} + H^+ \rightarrow Ce^{4+} + HBrO_2$	b3.20×10 <sup>4</sup>	$mol^{-2} dm^6 s^{-1}$	
R-7	$Ce^{4+} + HBrO_2 \rightarrow Ce^{3+} + BrO_2 + H^+$	1.12×10 <sup>4</sup>	$mol^{-1} dm^3 s^{-1}$	
R8	$MA + Br_2 \rightarrow BrMA + Br^- + H^+$	<sup>b</sup> 4.24	$mol^{-1} dm^3 s^{-1}$	
R9	$MA + Ce^{4+} \rightarrow Ce^{3+} + P_1 + H^+$	0.36	$mol^{-1} dm^3 s^{-1}$	
R10	$BrMA + Ce^{4+} \rightarrow Ce^{3+} + Br^{-} + P_2$	47.17	$mol^{-1} dm^3 s^{-1}$	
R11	$Br_2O + MA \rightarrow BrMA + HOBr$	c4.23×10 <sup>-2</sup>	$mol^{-1} dm^3 s^{-1}$	
R12	$Br_2(sol) \rightarrow Br_2(g)$	<sup>b</sup> 1.10×10 <sup>-2</sup>	$s^{-1}$	

**Table 1.** Reaction and rate constant used in the numerical simulations

### Conclusion

By the already proposed method for determination of a bifurcation point under batch conditions, the SNIPER bifurcation was obtained, and found that it is in accordance with the previous investigations of the other Belousov-Zhabotinsky system under batch and, also, under CSTR conditions [6].

### Acknowledgment

We thank our colleague, Professor Zoltan Noszticzius, for his important and fruitful suggestions during writing the article. We gratefully acknowledge the partial financial support in grant no. 142025 of the Ministry for Science of the Republic of Serbia.

- [1] Z. Noszticzius, P. Stirliling and M. Wittman, J. Phys. Chem., 1985, **89**, 4914–4921.
- [2] Z. Noszticzius, M. Wittman and P. Stirliling, J. Chem. Phys., 1987, 86, 1922–1926.
- [3] K. Pelle, M. Wittmann, K. Lovrics, Z. Noszticzius, M. L. Turco Liveri and R. Lombardo, J. Phys. Chem. A, 2004, 108, 5377–5385.
- [4] Z. Noszticzius, P. Stirliling and M. Wittman, J. Phys. Chem., 1985, 89, 4914–4921.
- [5] L. Györgyi, R.Field, J. Phys. Chem., 1991, 95, 6594–6602.
- [6] V. Gáspár, P. Galambosi, J. Phys. Chem., 1986, 90, 2222–2226.

<sup>&</sup>lt;sup>a</sup>The concentration of water  $[H_2O] = 55 \text{ mol dm}^{-3}$  is included in the rate constants. <sup>b</sup>The rate constants modified in this work. <sup>c</sup>The rate constants defined in this work.

### BRAY-LIEBHAFSKY REACTION. THE INFLUENCE OF POLYMER SUPPORTED COBALT CATALYST

J. Maksimović<sup>1</sup>, Ž.D. Čupić<sup>2</sup> and D. Lončarević<sup>2</sup>

<sup>1</sup>Faculty of Physical Chemistry, University of Belgrade, Studentski trg 12-16, P.O. Box 137, 11001 Belgrade, Serbia <sup>2</sup> IChTM, Center of Catalysis and Chemical Engineering, Njegoševa 12, 11000 Belgrade, Serbia

### **Abstract**

Poly-4-vinylpyridine-co-divinylbenzene-Co2+ catalyst was analyzed in the Bray-Liebhafsky (BL) oscillatory reaction as the matrix for its characterization. The addition of the catalyst do not change the kinetics of the BL reaction, but the characteristics of its temporal oscillatory evolution as the preoscillatory period  $(\tau_1)$ , the total number of oscillations (n), the duration from the beginning of the reaction to the end of the oscillatory state  $(\tau_{end})$  are changed.

### Introduction

The Bray-Liebhafsky oscillatory reaction is the decomposition of hydrogen peroxide into the water and oxygen in the presence of iodate and hydrogen ions. [1]

$$2H_2O_2 \xrightarrow{IO_3^-, H^+} 2H_2O + O_2$$
, D

The global reaction D is the result of the oxidation O of iodine to iodate

$$I_2 + 5H_2O_2 \rightarrow 2IO_3^* + 2H^+ + 4H_2O$$
 O

and the reduction (R) of iodate to iodine

$$2IO_3^- + 2H^+ + 5H_2O_2 \rightarrow I_2 + 5O_2 + 6H_2O$$
. R

The BL reaction is already used as the matrix for the characterization of the catalysts. [2]

### **Experimental**

Catalyst is prepared by wetness impregnation of cobalt(II)-nitrate on the macroreticular copolymer of poly-4-vinylpyridine with divinylbenzene. The content of octahedral Co<sup>2+</sup> coordination on polymer was 5.72 mas.%. [3]

The experiments were conducted in the thermostated, closed well-stirred reactor. The Pt and  $\Gamma$  as the working electrodes, and  $A_g/A_gCl$  as the reference electrode, were immersed into the stirred (900 rpm) reaction mixture (52 ml).

The chemicals of p.a. cleanliness where used. The composition of the BL system was kept constant:  $[KIO_3]_0 = 7,2\cdot 10^{-2} \text{ mol/dm}^3$ ,  $[H_2SO_4]_0 = 4,8\cdot 10^{-2} \text{ mol/dm}^3$ ,  $[H_2O_2]_0 = 4,6\cdot 10^{-2} \text{ mol/dm}^3$  and  $T = 62^{\circ}C$ .

The catalyst is added in the reaction vessel before other substances. The begins when the hydrogen peroxide is added to the vessel.

### **Results and Discussion**

The iodide oscillograms of the BL matrix and the matrix with 0.07g catalyst are presented in figure 1. The number of oscillations (n) and the duration of the oscillograms ( $\tau_{end}$ ) decrease, whereas the preoscillatory period ( $\tau_{1}$ ) increases, when amount of catalyst increases.

The decomposition of hydrogen peroxide (D) in the matrix can be described by equation

$$\tau_{end} = \frac{1}{k_D} \ln \frac{[H_2 O_2]_0}{[H_2 O_2]_{end}} \tag{1}$$

where  $[H_2O_2]_0$  initial concentration and  $[H_2O_2]_{end}$  the concentration at the end of oscillogram. [4] Similar as in the ref. [5] we can suppose that the catalyst influences on  $k_D$  by the relation

$$k^* = k_D \exp\left(x \left(m_{kat}^*\right)^{\mathcal{Y}}\right) \tag{2}$$

where  $m_{kat}^*$  is dimensionless mass of the catalyst normalized with respect to mass units, x and y are empirical kinetic parameters. If the dynamics of the BL reaction does not change in the presence of catalyst, the equation (1) can be applied on perturbed BL system. In this case according to equations (1) and (2) we obtained following relation. and that now  $\tau_{end}$  of the BL perturbed systems can be described by equation (2), but with new constant  $k^*$ , we can obtain equation

$$\ln\left(\ln\left(\frac{\tau_{end}}{\tau_{end}^*}\right)\right) = \ln x + y \ln m_{kat}^* \tag{3}$$

where  $\tau_{end}^*$  is length of oscillograms of perturbed BL system. The validity of equation (3) is illustrated in Fig. 2.

### Conclusion

Presence of the catalyst under applied conditions did not changed the dynamics of the BL reaction. By the formal kinetic analysis we did evaluate the activity of the tested catalyst.

### Acknowledgment

This work was partially supported by the Ministry for Science of the Republic of Serbia (Grants no. 142025)

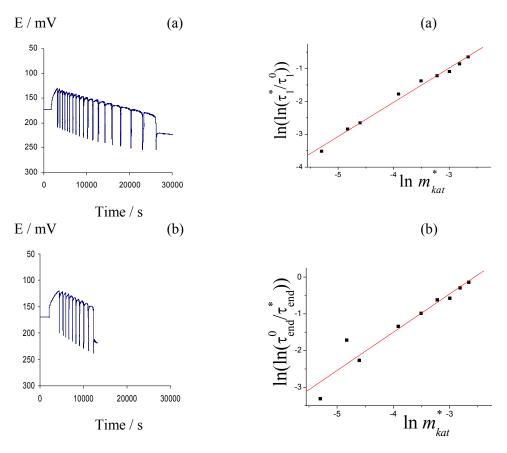


**Fig. 1**. The oscillograms of the (a) matrix and (b) perturbed matrix with 0.070 g of the catalyst.

**Fig. 2.** Dependence of (a)  $\ln(\ln(\tau_1^*/\tau_1))$  and (b)  $\ln(\ln(\tau_{end}/\tau_{end}^*))$  on  $\ln(m_{kat}^*)$ 

- [1] W.C. Bray, J.Am.Chem.Soc., 1921, 43, 1262.
- [2] Lj. Kolar-Anić, S. Anić, Ž. Čupić, Characterization of the catalysts by means of an oscillatory reaction In "Finely Dispersed Particles: Micro-, Nano-, and Atto-Engineering", Eds. A. Spasić and Jyh-Ping Hsu, CRC (earlier: Marcel Dekker), Inc., New York 2005, pp. 191-216 and references therein.
- [3] D. Lončarević, Ž. Čupić, Mater.Sci.Forum, 2005, 494, 363.
- [4] S. Anić, Lj. Kolar-Anić, J.Chem. Faraday Trans. I., 1988, 84, 3413-3421.
- [5] M. Kragović, J. Maksimović an S. Anić, Bray-Liebhafsky oscillatory reaction generated in batch reactor. influence of pulse involving iodide at the end of preoscillatory period, in Physical Chemistry 2008, A. Antić – Jovanović (ed.), SPCS, Belgrade 2008, pp. XX

### AUTO-OSCILLATIONS OF THREE-STAGE REACTIONS IN CONDITIONS OF DEACTIVATION CATALYST

### O.V. Dimitrieva and N.I. Koltsov

Department of Physical Chemistry of Chuvash State University, Moskovskii prospekt 15, 428015 Cheboksary, Russia

### **Abstract**

Outcomes of research and systematization of all possible three-stage schemas of the reactions proceeding on catalyst with changing activity and describing selfoscillations are presented. These schemas used for reproduction of self-oscillations in reaction of catalytic oxidation of carbon monoxide.

### Introduction

In works [1,2] of model three-stage of carbon monoxide oxidation reaction describing self-oscillations are considered at deactivation of the catalyst are considered. In the given report analysis and systematization of all possible three-stage schemas are supplemented by a buffer stage which can be used for the description of self-oscillations.

### Results and discussion

Let's consider in the general view a reaction

$$\sum_{i} d_{i} \sum_{e} v_{ie} A_{e} = \sum_{i} d_{i} \sum_{e} v_{-ie} A_{e},$$
 (1)

proceeding via the following steps

$$\sum_{e} v_{ie} A_{e} + \sum_{j=1}^{4} a_{ij} X_{j} \stackrel{r_{i}}{\Leftrightarrow} \sum_{j=1}^{4} a_{-ij} X_{j} + \sum_{e} v_{-ie} A_{e}, d_{i},$$

$$i = \overline{1, 4}, e = \overline{1, s},$$
(2)

where  $A_e$  and  $X_j$  - the basic and intermediate substances;  $V_{ie}$ ,  $V_{-ie}$  in  $a_{ij}$ ,  $a_{-ij}$  are

stoichiometric coefficients; 
$$(\sum_{j=1}^4 a_{ij} = \sum_{j=1}^4 a_{-ij}, i = \overline{1,4}; a_{i4} = a_{-i4} = 0$$
 at

$$i = \overline{1,3}, \ a_{44} = 0; \ 1 \le \sum_{j=1}^{4} a_{\pm ij} \le 2$$
);  $d_i > 0$  - stoichiometric numbers of stages; ;  $r_i$ ,

 $r_{-i} \ge 0$  – rates of *i* stages in direct and return directions defined by interrelations

$$r_i = \omega_i \prod_j x_j^{a_{ij}^+}, \quad r_{-i} = \omega_{-i} \prod_j x_j^{a_{ij}^-},$$

where  $\omega_{\pm i} = k_{\pm i} \prod_{e} C_{e}^{v_{ie}^{\pm}}$  - frequencies of stages in direct and return directions,  $x_{j}$  -

concentrations intermediate substances ( $j = \overline{1,3}$ ) and buffer substance (j=4),  $C_e$  -concentrations of base substances  $A_e$ ,  $k_{+i}$  - constants of stage rates.

The non-stationary behavior of reaction (1) in conditions of open isothermal system at constancy of concentration of the basic substances is described by system of the ordinary differential equations:

$$\dot{x}_{j} = \sum_{i} \left( a_{ij}^{-} - a_{ij}^{+} \right) (r_{i} - r_{-i}), \ j = \overline{1,4} \ . \tag{3}$$

To kinetic model (3) there corresponds a characteristic polynomial

$$\lambda \left(\lambda^3 + \sigma_1 \lambda^2 + \sigma_2 \lambda + \sigma_3\right) = 0, \tag{4}$$

one of which  $\lambda$  radicals is equal to null in view of justice for heterogeneous catalytic reactions of a conservation law  $\sum_{i} x_{ij} = 1$ .

According to work [3] a condition of occurrence of a self-oscillation regime for a system (3) are negativity of coefficient  $\sigma_2$  and positivity of coefficient  $\sigma_3$ . Analysis of a system (3) and the equations (4) with usage of conditions of the instability [3] has allowed to detail the schema (2) and to systematize of all possible three-stage schemas of the reactions proceeding on catalyst with changing activity and describing self-oscillations. All found schemas have been grouped on number of stages of various molecularities and presence of autocatalytic stages. In total 15 schemas of free of autocatalytic stages, 82 schemas with one autocatalytic stage, 76 schemas with two autocatalytic stages and 18 schemas with three autocatalytic stages have been found. In tab. 1 the elementary schemas are given.

**Table 1.** The elementary four-stage schemas-oscillators\*

№ -	Stoichiometric coefficients of the stages			
	1	2	3	4
1	2000=0200	1000=0010	0110=2000	0100=0001
2	2000=0200	1000=0010	0110=2000	1000=0001
3	2000=0200	1000=0010	0110=2000	0010=0001

<sup>\*</sup>Gangs from four figures at the left and to the right of equal-signs mean stoichiometric factors at loose center  $X_1$ , intermediate substances  $X_2$ ,  $X_3$  and buffer substance  $X_4$  in each of four stages.

The schema of 1 tab. 1 corresponds, for example, to the following mechanism of catalytic oxidation of carbon monoxide

$$2CO + O_2 \rightarrow 2CO_2 \tag{5}$$

on platinum in conditions of its deactivation:

1. 
$$O_2 + 2K \leftrightarrow 2KO$$
  
2.  $CO + K \leftrightarrow KCO$   
3.  $KCO + KO \rightarrow 2K + CO_2$   
4.  $CO + KO \leftrightarrow (KCO_2)$ , (6)

where K are active centres on a catalyst surface;  $KO_2$  and KO - intermediate substances; materials {\*matters\*};  $(KCO_2)$  - buffer substance. On fig. 1 results of numerical calculation of the schema (6) are given.

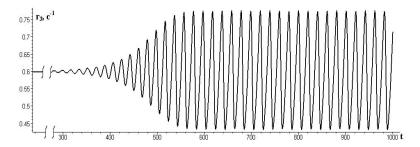


**Fig. 1.** Dependence of rate  $(r_3 = \omega_3 x_2 x_3)$  formations of carbonic gas from time for a reaction (5) weeping under the schema (6) at values of frequencies of stages  $\omega_1 = 12.07730868$ ,  $\omega_2 = 5.991844027$ ,  $\omega_3 = 120.8658151$ ,  $\omega_4 = 0.7380678856$ ,  $\omega_{-1} = 0.1$ ,  $\omega_{-2} = 1$ ,  $\omega_{-3} = 0$ ,  $\omega_{-4} = 0.022$  ( $\omega_{\pm i}$ , s<sup>-1</sup>).

In work [1] the three-stage of catalytic oxidation of carbon monoxide (5) in conditions of deactivation of the catalyst has been investigated:

1. 
$$O_2 + 2K \leftrightarrow 2KO$$
  
2.  $CO + K \leftrightarrow KCO$   
3.  $KCO + KO \rightarrow 2K + CO_2$   
4.  $CO + K \leftrightarrow (KCO)$ . (7)

This mechanism corresponds to the schema of 2 tab. 1. In [1] the numerical accounts confirming a possibility of the description of self-oscillations with the help of the mechanism (7) are given.

Thus we systematize of all possible three-stage schemas describing self-oscillations in conditions of deactivation of the catalyst. These schemas used for reproduction of self-oscillations in reaction of catalytic oxidation of carbon monoxide.

- [1] V.I. Bykov, G.S. Yablonskii, V.F. Kim, Reports of Russian Acad. Sci., 1978, 242, 637-639.
- [2] A.N. Ivanova and etc., Ibid., 1978, 242, 872-875.
- [3] B.V. Alexeev, V.Kh. Fedotov, N.I. Koltsov, Ibid., 1989, 306, 884-888

# Electrochemistry (E)

### PHOTOCATALYTIC INACTIVATION OF PROTEUS MIRABILIS ON IMMOBILIZED TiO<sub>2</sub>

I. Poulios<sup>1</sup>, P. Tsoumparis<sup>2</sup>, A. Grigoriadou<sup>2</sup>, X. Edipidou<sup>2</sup> and K. Delidou<sup>2</sup>

<sup>1</sup>Lab. of Phys. Chemistry, Department of Chemistry,

<sup>2</sup>Lab. of Hygiene, Department of Medicine

University of Thessaloniki, 54124 Thessaloniki, Greece

#### **Abstract**

We report in the present paper a novel photochemical disinfection method for drinking water using *Proteus mirabilis* as model microorganism. The method is based on the bacteria killing by the hydroxyl radicals (OH), which are generated during the irradiation of a semiconductor, like TiO<sub>2</sub>, which is in contact with the infected solution. Photocatalytic inactivation of pathogenic microorganisms is a 'clean' disinfection method, which takes place under mild conditions by using a non toxic and reusable catalyst.

### Introduction

Water is the basic element for growing and maintaining life on earth. Last decades the water quality has significantly worsen due to various organic and inorganic pollutants. Today there is obviously a great need for a more rational use of the water resources and for a more profound research into the methods that will be able to solve the severe pollution problems. The well-known physicochemical methods for water and wastewater treatment, such as sedimentation, adsorption on activated carbon etc, are not any longer sufficient, because they mostly result in the transfer of pollutants from the one phase to the other and not to their complete removal.

The heterogeneous photocatalysis presents in comparison to other methods for water and wastewater treatment some significant advantages [1, 2]. The organic and inorganic compounds that exist in water can be completely oxidized if this is mixed with a chemically and biologically inactive, semiconductive catalyst like TiO<sub>2</sub> and the whole system is exposed to artificial or natural light. The OH· radicals formed on the illuminated semiconductor surface are very strong oxidizing agents with an reduction potential of 2.8 V. According to the literature, OH radicals have also antimicrobial activity, due to the high potential of oxidation and their non-selective reactivity. Furthermore, Matsunaga et al. [3], suggested that the photogenerated holes in the valence band receive electrons from CoA thus forming the dimeric CoA. The dimerisation of CoA inhibits the growth of microorganisms.

In the present paper, some preliminary results of the efficient use of the suggested method are reported. As model microorganism, for the disinfection experiments, *Proteus mirabilis* of the enterobacteriaceae family was used. It was isolated in a drinking water sample by the membran filtration method in m-Enolo agar and was identificated according to the API System 20E by Bio-Merienx.

### **Experimental Methods**

The catalyst used was  $TiO_2$  P-25 Degussa (BET 65 m<sup>2</sup>/g, mean grain size 30 nm, anatase/rutile 65/35). The water samples were artificially infected by *Proteus mirabilis* colonies. The strain of *Proteus mirabilis* was used after being incubated for 24 hours at 37° C in nutrient broth. The experimental setup that was used for the photocatalytic inactivation of the mentioned microorganisms can be seen in Fig. 2.

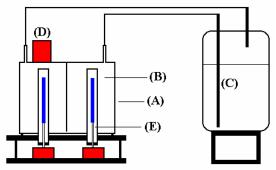
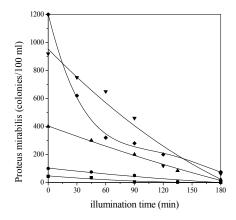


**Fig. 2**: Experimental setup for the photocatalytic inactivation of Proteus mirabilis colonies in a recirculation system: (A) photocatalytic reactor, (B) bed and catalyst, (C) container with the infected solution, (D) pump, (E) glass cylinder with the lamp (OSRAM DULUX 9W / 78).

### **Results and Discussion**

Fig 3 shows the results of the photocatalytic disinfection of contaminated drinking water samples. The concentration of the *Proteus mirabilis* colonies present in the supernatant is plotted as a function of illumination time. The different curves correspond to different initial bacteria concentrations. It is observed that under the given experimental conditions, in the concentration region 100-1200 colonies /100ml a practically complete elimination of the colonies number is achieved after 3 hours of light exposure, while in the absence of illumination noticeable changes in survival were not observed.

The catalyst life time is a significant parameter of the photocatalytic process, especially when the catalyst used is immobilized on a matrix. For this reason the photocatalytic experiment was repeated 25 times with the same catalyst and different initially infected solutions. From Fig. 4 it is clearly seen that the catalyst activity remains constant.



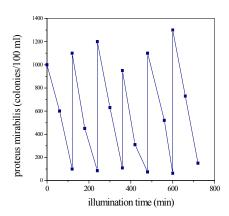


**Fig. 4:** Photocatalytic desinfection of drinking water infected with various initial concentrations of *Proteus mirabilis* colonies.

**Fig. 5**: The photocatalytic inactivation of *Proteus mirabilis* for repeating experiments with the same catalyst.

### **Conclusions**

The first experimental results of the photocatalytic desinfection of drinking water, infected with the model microorganism *Proteus mirabilis*, are presented. The advantages that this method has to offer, in comparison to the existing ones (chlorination ozonation, e.t.c.), are the ability to inactivate any microorganism (due to the very strong oxidizing ability of OH), the absence of organochlorine compounds after the treatment, the synchronous oxidation of many organic pollutants, as well as the extinction of smell and taste without using any chemical additives. The disadvantage of the method, when comparing it to chlorination, is the absence of an oxidising residue, a fact that results in the compulsory addition of chlorine after the photocatalytic disinfection. The combination however of photocatalysis and chlorination for the water disinfection could be preferable to simple chlorination because of the production of smaller amounts of organochlorine compounds.

### Literature

- [1] D. Bahnemann, J. Cunningham, M. Fox, E. Pelizzetti, P. Pichat and N. Serpone, Photocatalytic Treatment of Waters, in Aquatic and Surface Photochemistry, Ed by Helz G, Zepp R and Crosby D, 1994, Lewis Publs., CRC Press, pp. 261-316.
- [2] M. Hoffman, S. Martin, W. Choi, D. Bahnemann, Chem. Rev., 1995, 95, 69.
- [3] T. Matsunaga, R. Tomada, et.al., Appl. Environ. Microbiol., 1988, 54, 1330.

### PHOTOCATALYTIC AND PHOTOELECTROCATALYTIC PROCESSES FOR WATER AND WASTEWATER CLEANING

#### I. Poulios

Laboratory of Physical Chemistry, Department of Chemistry, Aristotle University of Thessaloniki, 54124 Thessaloniki, Greece

### **Abstract**

Advanced oxidation processes (AOPs) are characterized by a common chemical feature: the capability of exploiting the high reactivity of OH radicals in driving oxidation processes, which are suitable for achieving the complete degradation and mineralization of various organic pollutants. Photocatalysis using semiconductors such as TiO<sub>2</sub> in the presence of artificial or solar light, as an advanced oxidation technique, has been a focus of research by a number of groups worldwide during the last two decades. The photocatalytic approach has been adopted successfully to develop an efficient method for purifying water and air. The present article discusses briefly certain directions concerning the ability of heterogeneous photocatalytic oxidation to degrade pollutants such as dyes, pesticides and inactivate pathogenic bacteria.

### Introduction

The elimination of toxic chemicals from water and wastewater is presently one of the most important subjects in pollution control. These pollutants may originate from industrial applications (petroleum refining, textile processing etc.) or from household and personal care areas (pesticides and fertilizers, detergents, etc.). The search for effective means of removing these compounds is of interest to regulating authorities everywhere.

Advances in chemical water and wastewater treatment have led to the development of methods termed advanced oxidation processes (AOPs) or technologies (AOTs). AOPs can be broadly defined as aqueous phase oxidation methods based on the intermediacy of reactive species such as (primarily but not exclusively) hydroxyl radicals in the mechanisms leading to the destruction of the target contaminant. Over the past 30 years, R&D concerning AOPs has been immense particularly for two reasons, namely (i) the diversity of technologies involved and (ii) the areas of potential application. Key AOPs include heterogeneous and homogeneous photocatalysis based on ultraviolet (UV-A) or visible irradiation, electrolysis, ozonation, the Fenton's reagent, ultrasound (US) etc., while less conventional (and consequently less studied) processes include ionizing radiation, microwaves, pulsed plasma and the ferrate reagent [1-3].

Although water and wastewater treatment is by far the most common area for R&D, AOPs have also found applications as diverse as groundwater treatment, soil remediation, municipal wastewater sludge conditioning, water and wastewater disinfection, production of ultrapure water and volatile organic compounds treatment and odor control. The growing interest of academic and industrial

communities in AOPs is reflected in the increasing numbers of (i) publications in several peer-reviewed journals (ii) patents and (iii) international conferences dedicated to the environmental applications of AOPs [4, 5].

Among these methods heterogeneous and homogeneous photocatalytic detoxification methods (TiO<sub>2</sub>/H<sub>2</sub>O<sub>2</sub>, Fe<sup>+3</sup>/H<sub>2</sub>O<sub>2</sub>) have shown recently great promise for the treatment of industrial wastewater, groundwater and contaminated air. The semiconductor mediated photocatalytic process has also shown great potential for disinfection of air and water, thus making possible a number of applications. Additionally, advantages of the photocatalytic processes are their mild operation conditions and the fact that they can be powered by sunlight, thus reducing significantly the electric power required and therefore reducing the operating costs [6, 7].

### **Background of Heterogeneous Photocatalysis**

It has been demonstrated that semiconducting materials mediating photocatalytic oxidation of organic compounds can be an alternative to conventional methods for the removal of organic pollutants from water and air. The illumination of these catalyst particles with light energy greater than the bandgap energy of the semiconductor (hv>E<sub>g</sub>) produces excited high energy states of electron and hole pairs (e'/h<sup>+</sup>) that can migrate to the surface of the particle and initiate a wide range of chemical redox reactions, which can lead to complete mineralization of the organic pollutants. The quantitative formation of  $CO_2$  is of great significance in water treatment, because it provides unequivocal evidence for the total destruction of organic pollutants present in water. The disappearance of these compounds could take place via formation of partially oxidized intermediates that could be even more toxic than the original pollutants. A variety of semiconductor powders (oxides, sulphides, etc.) acting as photocatalysts has been used. Most attention has been given to  $TiO_2$  (anatase) because of its high photocatalytic activity, its resistance to photocorrosion, its biological immunity and low cost.

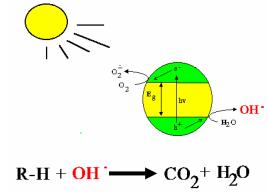


**Fig. 1.** Photocatalytic oxidation of organic compounds in the presence of  $TiO_2$  as a catalyst.

$$TiO_2 + hv (<390 \text{ nm}) \longrightarrow TiO_2 (h^+ + e^-)$$
 (1)

$$O_2 + e^{-} \longrightarrow O_2^{-}$$
 (2)

$$h^+ + H_2O \longrightarrow H^+ + OH$$
 (3)

$$OH + RH \longrightarrow H_2O + R$$
 (4)

$$R^{\cdot} + O_2 \longrightarrow ROO \longrightarrow CO_2 \tag{5}$$

By the illumination of an aqueous  $TiO_2$  suspension with light energy greater than its band gap energy (hv>E<sub>g</sub>=3.2 eV) conduction band electrons (e ) and valence band holes (h ) are generated. The photogenerated electrons, as can be seen in Fig. 1) react with the adsorbed molecular  $O_2$  on the Ti(III)-sites, reducing it to superoxide radical anion, $O_2$ , while the photogenerated holes can oxidize either the organic molecules directly or the OH ions and the  $H_2O$  molecules adsorbed at the  $TiO_2$ surface to OH radicals, which act as strong oxidizing agents (Fig.1 and equations 1-5). These can easily attack the adsorbed organic molecules or those located close to the surface of the catalyst, thus leading finally to their complete mineralization [8-11].

Photocatalysts such as TiO<sub>2</sub> can either be used as powders in a slurry form or as supported films. The latter configuration is advantageous for catalyst separation, but poses surface area and mass transfer limitations. To counterbalance these, the use of a conducting substrate offers the possibility of enhancing the photocatalytic activity of TiO<sub>2</sub> overlayer by applying a positive bias on the catalyst in an appropriate electrochemical cell, thus drawing the photogenerated electrons away from the catalyst interface and minimising recombination with photogenerated holes. As result of the electrochemical enhanced photocatalytic oxidation or photoelectrocatalytic oxidation an improvement of the photocatalytic system to inactivate various organic or inorganic pollutants in water or wastewater is expected [12, 13]. The process occurs in the presence of both artificial or solar light, while at the same time no catalyst removal from the treated solution is needed.

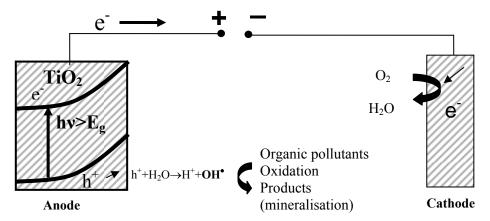
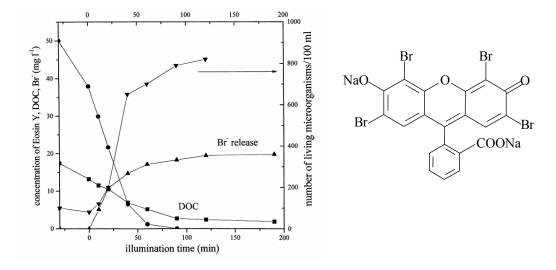


Fig. 2. Photoelectrocatalytic oxidation of organic pollutants.

### **Photocatalytic Degradation of Model Pollutants**

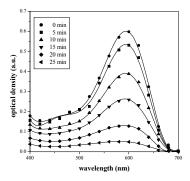
Photocatalytic degradation of organic pollutants in the presence of artificial or solar illumination has become during the last 20 years a growing area of environmental research involving extensive studies on decomposition and deactivation of organic waste materials such as the halogenated hydrocarbons, dyes, pesticides, bacteria, and herbicides [14-21]. Many pollutants, which normally do not undergo any appreciable homogeneous photolysis, have been found photodegradable in the presence of newly developed heterogeneous catalysts. The first complete mineralisation of a compound in water was reported by Ollis et al. [16] in 1983. Using a TiO<sub>2</sub> photocatalyst, the complete destruction of several halogenated hydrocarbons including trichloroethane, methylene chloride, chloroformand carbon tetrachloride was achieved. A detailed kinetic analysis of the destruction was carried and it was found that the simple Langmuir-Hinshelwood (L-H) rate equation represented the destruction of these materials. The use of the L-H model for the photocatalytic destruction of organic compounds has been subsequently applied by a number of researchers.

Halogenated aromatic and aliphatic compounds, as well as pesticides and dyes represent the most comprehensively studied classes of compounds for which photocatalytic water treatment has been applied. In Figures 3-5 some examples of the photocatalytic degradation and mineralization of representative pollutants in the presence of artificial and solar illumination are given.



 $C_{20}H_6O_5Br_4Na + 18.5O_2 \xrightarrow{TiO_2/hv} \longrightarrow 20CO_2 + 2HBr + 2NaBr + 2H_2O_2$ 

**Fig. 3.** Photocatalytic mineralization and toxicity reduction of Eosin Y in the presence of TiO<sub>2</sub> P-25 [22].



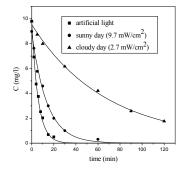
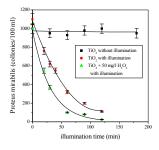


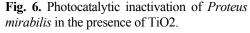
**Fig. 4.** Photocatalytic recolorization of the azo dye Reactive Black 5 in the presence of 1 g L<sup>-1</sup> TiO<sub>2</sub> P-25.

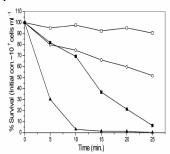
**Fig. 5.** Photocatalytic degradation of the insecticide Triclopyr in the presence of artificial and solar illumination [23].

This process has been implemented successfully, apart from the oxidation of organic and inorganic pollutants, also to the reductive removal of heavy and precious metals (Cr<sup>+6</sup>, Hg<sup>+2</sup>, Pt<sup>+4</sup>, Au<sup>+3</sup>, Ag<sup>+1</sup>) [24]. Additionally the powerful oxidizing ability of the OH<sup>•</sup> radicals in combination with their non-selectiveness allows not only the oxidation of the various organics present in water or wastewater, but also the simultanously destruction and lysis of the cell membrane of various pathogenic microorganisms[25, 26].

The mechanism of the photocatalytic inactivation, as proposed by several authors, contains the attack of the cell wall, followed by the cell membrane and finally the oxidative attack of the cytoplasmic contents. They concluded that alterations in the membrane structure, caused by lipid peroxidation, ultimately lead to conformational changes in membrane- bound proteins and electron mediators with the loss of cell membrane integrity. Once the cell membrane is damaged, cell respiration ceases. The loss of cell energy production mechanisms and subsequent oxidative attack of internal cellular components could ultimately result in cell death. In Figs. 6 and 7 the photocatalytic and the photoelectrocatalytic inactivation of *Proteus Mirabillis* and *E. coli* respectively are presented.

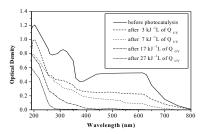






**Fig. 7.** Photoelectrocatalytic inactivation of *E. coli* colonies under various experimental conditions [27].

Solar photocatalytic degradation of water contaminants (a process also known as 'solar detoxification') is an outstanding example of how well solar applications and environmental problems fit together. Solar photocatalytic degradation of organic pollutants in water employing the interaction between ultraviolet radiation from the sun with a semiconductor catalyst has been widely demonstrated and it represents a strong potential method for the industrial destruction of toxic organics in water. Where medium to high solar radiation is available, solar detoxification is useful for treating water containing non-biodegradable contaminants. The process has proven promising for the treatment of contaminated water, air and soil. The use of solar light, combined with the simple technology required for this method, can offer economically reasonable and practical solutions to the processing of wastewater containing non-biodegradable or toxic substances.



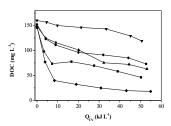


**Fig. 8.** Solar photocatalytic decolorization and DOC reduction of a simulated dyestuff effluent under various experimental conditions [28].

- [1] W. Eckenfelder, A. Bowers, J. Roth, Chemical Oxidation, Technologies for the Nineties, Vol. 1-6, 1994, Technomic Publishing Co., Basel.
- [2] R. Andreozzi, V. Caprio, A. Insola, R. Marotta, Catal. Today, 1999, 53, 51–59.
- [3] S. Parsons, ed., Advanced Oxidation Processes for Water and Wastewater Treatment, 2004, IWA Publishing, London.
- [4] T. Oppenlaender, Photochemical Purification of Water and Air, 2003, Wiley-VCH.
- [5] 1<sup>st</sup> European Conference on Environmental Applications of Advanced Oxidation Processes», 2006, Chania, Greece.
- [6] J. Blanco, S. Malato, Solar Detoxification, 2001, UNESCO, Natural Sciences, WORLD SOLAR PROGRAMME 1996-2005 (http://www.unesco.org/science/wsp).
- [7] D.Y. Goswami, Engineering of the Solar Photocatalytic Detoxification and Disinfection Processes, in K.W. Boer (Ed.), Advances in Solar Energy, Vol. 10, American Solar Energy Society Inc., Boulder, Colorado, 1995.
- [8] N. Serpone and E. Pelizzetti (eds.), Photocatalysis, Fundamentals and Applications, 1989, J. Wiley & Sons, N.Y.
- [9] M.R. Hoffman, S. Martin, W. Choi, D. Bahnemann, Chem. Rev. 1995, 95, 69.
- [10] P. K. J. Robertson, D. W. Bahnemann, J.M. C. Robertson, F. Wood, Hdb Env Chem, 2005, 2, Part M, 367–423.
- [11] J.M. Herrmann, Catal. Today, 1999, 53, 115-29.
- [12] R. Pelegrini, P. Zamora, A. Andrade, et. al., Appl. Catal. B: Environ. 1999, 22, 83.

- [13] P. A. Carneiro, M. E. Osugi, J. J. Sene, M. A. Anderson, M. V. Boldrin Zanoni, Electrochim. Acta, 2004, 49, 3807–3820.
- [14] C. He, Y. Xiong, J. Chen, C. Zha, X. Zhu, J. Photochem. Photobiol. A: Chem., 2003, **157**, 71–79.
- [15] D. Blake, Bibliographic work on the heterogeneous photocatalytic removal of hazardous compounds from water and air, 2001, National Renewable Energy Laboratory, Technical Report, NREL/TP-510-31319.
- [16] C.Y. Hsiao, C.L. Lee, D.F. Ollis, J. Catal., 1983, 82, 418.
- [17] I. Poulios, A. Avranas, A. Zouboulis, E. Rekliti, J. Chem. Technol. Biotechnol., 2005, 75, 205-212.
- [18] A.M. Peiro, J. Ayllon, J. Peral, X. Domenech, Appl. Catal. B: Environ., 2001, 30, 359.
- [19] T.Sauer, G.C. Neto, H.J. Jose, R.F.P.M. Moreira, J. Photochem. Photobiol. A: Chemistry, 2002, 149, 147-154
- [20] I.K.Konstantinou, T.A.Albanis, Appl Catal. B: Environ., 2003, 42, 319-335.
- [21] S. Parra, J. Olivero, C. Pulgarin, Appl. Catal. B: Environ., 2002, 36, 75.
- [22] I. Poulios, E. Micropoulou, R. Panou, E. Kostopoulou, Appl. Catal. B: Environ., 2003, 41, 345–355.
- [23] I. Poulios, M. Kositzi, A. Fouras, J. Photochem. Photobiol. A: Chemistry, 1998, 115, 175-183.
- [24] T. Angelidis, M. Koutlemani, I. Poulios, Appl. Catal. B: Environ., 1998, 16, 347.
- [25] J. R. Peller, R. L. Whitman, S. Griffith, P. Harris, C. Peller, J. Scalzitti, J. Photochem. Photobiol. A: Chem., 2007, **186**, 212–217.
- [26] Vidal, A. Diaz, et.al., Catal. Today, 1999, 54, 283.
- [27] I. Butterfield, P. Christensen, et.al., Wat. Res., 1997, 31, 675.
- [28] M. Kositzi, A. Antoniadis, I. Poulios, I. Kiridis, S. Malato, Solar Energy, 2004, 77, 591–600.

### DETERMINATION OF COPPER AND NICKEL BY ION CHROMATOGRAPHY AND VOLTAMMETRY

K.R. Kumrić, T.M. Trtić-Petrović and J.J. Čomor

Vinča Institute of Nuclear Sciences, Laboratory of Physics (010), P.O. Box 522, 11001 Belgrade, Serbia

### **Abstract**

Simultaneous determination of copper(II) and nickel(II) by ion chromatography (IC) has been optimized and the detection limits of the new method were compared to stripping voltammetry. The best eluent enabling fast end efficient separation of Cu(II) and Ni(II) is a mixture of 8 mM citric and 0.3 mM oxalic acid using a Metrosep C2 (Metrohm) IC column. The detection limits are significantly lower using stripping voltammetry, while IC is considerably faster.

### Introduction

The radionuclide  $^{64}$ Cu combines three types of decay ( $\beta^+$ ,  $\beta^-$  and internal conversion followed by Auger electron emission), making it suitable for applications in positron emission tomography (PET) imaging and targeted radiotherapy of different diseases. The nuclear reaction  $^{64}$ Ni(p,n) $^{64}$ Cu performed with small medical cyclotrons, is the most suitable production route for  $^{64}$ Cu for nuclear medical applications. The most frequently used method for the separation of  $^{64}$ Cu from the enriched nickel target is ion exchange chromatography [1,2].

Our future work will be orientated towards the optimization of separation of Cu(II) and Ni(II) by membrane-based solvent extraction. In order to find adequate separation conditions for Cu(II) and Ni(II), and to investigate the physicochemical parameters of transport of Cu(II) and Ni(II) across the membrane, a suitable analytical method that would enable the determination of low (ppm) and very low (ppb) concentrations of non-radioactive Cu(II) and Ni(II) is needed. Ion chromatography (IC) and stripping voltammetry (anodic, ASV, and cathodic, CSV) are promising techniques for the determination of trace quantities of Cu(II) and Ni(II).

The aim of this study was to find optimum conditions for the determination of Cu(II) and Ni(II), in terms of separation factors, detection limits, linearity and duration.

### **Results and Discussion**

Ion chromatographic separation of transition metals is performed by cation-exchange columns with eluents which contain a complexing agent such as tartaric acid, oxalic acid, citric acid and pyridine-2,6-dicarboxylic acid. Metals form complexes of differing stabilities with the anions and as a result their charge density is reduced. As this occurs in accordance with the kinetics of complex

formation and stability constants of the complexes, differences in selectivity increase and separation becomes possible [3]. Retention of cations is controlled by the concentration of the complexing agent and the pH of the eluent. Ion chromatographic measurements were performed by the 861 Advanced Compact IC system (Metrohm, Switzerland) with conductivity detector and analytical column Metrosep C2 (Metrohm, 150 mm x 4 mm, particle diameter of 7  $\mu$ m). All reagents used were of analytical reagent grade. Working solutions of Cu(II) and Ni(II) were prepared by diluting their stock standard solutions (1000 ppm) with 2 mM HNO<sub>3</sub>.

Considering the stability constants of complexes, the separation of Cu(II) and Ni(II) was tried using eluents which are different mixtures of complexing acids: tartaric and dipicolinic, tartaric and oxalic, tartaric and citric, oxalic and ascorbic, citric and oxalic. By changing the eluent composition and concentrations, the main task was to find a suitable eluent which would enable elution of Cu(II) and Ni(II) in a reasonable period of time.

The best results for the separation of Cu(II) and Ni(II) were obtained using 8 mM citric and 0.3 mM oxalic acid as eluent (Fig. 1). Retention times for the Cu(II) and Ni(II), are 2.6 and 8.1 min, respectively. Duration of the analysis is 11 min, which fulfills the requirements for short and efficient analysis.

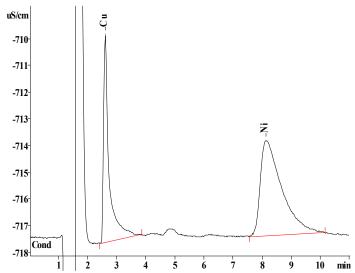


**Fig. 1.** Chromatogram of Cu(II) and Ni(II) obtained using 8 mM citric acid and 0.3 mM oxalic acid (flow rate = 1 ml/min, injection volume = 100 μl)

Concentration ranges of Cu(II) and Ni(II) between 0.1 and 25 ppm were investigated. The obtained conductivity vs. concentration dependences were linear, with correlation coefficients of 0.999 for Cu(II) and 0.998 for Ni(II) determination. Detection limits for the determination of Cu(II) and Ni(II) are 0.2 ppm for both ions.

Voltammetric determinations of Cu(II) and Ni(II) were done according to Metrohm's procedure No. 231/2e using a 797 VA Computrace analyser (Metrohm, Switzerland). The electrolyte used for the determination of Cu(II) and Ni(II) by ASV and CSV, respectively, was 0.05 M ammonium-chloride buffer with pH 9.4. For the determination of Ni(II) addition of 0.1 cm<sup>3</sup> of 0.1 M dimethylglyoxime is necessary.

Cu(II) gives a well developed ASV peak, with peak potential,  $E_p$ , at -0.10 V. Three concentration ranges of Cu(II) were investigated: (0.001 - 0.015) ppm, (0.01 - 0.15) ppm and (0.15 - 1.5) ppm. Depending on the concentration range, Cu(II) was deposited at -1.15 V for a period of 30 to 120 s. The obtained current vs. concentration dependences were linear with correlation coefficients of 0.994, 0.999 and 0.998, respectively. The detection limit of this method is 1.0 ppb.

Ni(II) gives a well developed CSV peak, with a half wave potential,  $E_p$ , at -0.95 V. Two concentration ranges of Ni(II) were investigated: (0.1-1) ppb and (1-10) ppb. Depending on the investigated concentration range, Ni(II) was deposited at -0.7 V for a period of 90 to 120 s. The obtained current vs. concentration dependences were linear with correlation coefficients of -0.998 and -0.999, respectively. The detection limit of this method is 0.1 ppb. Duration of both analysis, ASV and CSV, is at least 30 min.

For the determination of Cu(II) and Ni(II) concentrations higher than 1 ppm and 0.03 ppm, respectively, polarography on static mercury drop electrode (SMDE) can be applied.

### Conclusion

Ion chromatography and stripping voltammetry are complementary methods regarding the determination of low (ppm) and very low (ppb) concentrations of Cu(II) and Ni(II). Detection limits for Cu(II) and Ni(II) by ion chromatography are 0.2 ppm, while ASV and CSV provide significantly lower determination limits of 1.0 ppb and 0.1 ppb, respectively. The main drawback of stripping voltammetry is that Cu(II) and Ni(II) can not be determined during one single run, which implies longer time for the analysis.

IC of Cu(II) and Ni(II) is performed during a single run and provides a fast and efficient method for simultaneous determination of Cu(II) and Ni(II). IC is the method of choice for the determination of Cu(II) and Ni(II) concentrations of 0.2 ppm or higher.

- [1] D. W. McCarthy et al., Nucl. Med. Biol., 1997, 24, 35-43.
- [2] X. Hou et al., Appl. Radiat. Isotopes, 2002, 57, 773-777.
- [3] C. Eith et al., Monograph: Practical Ion Chromatography, Metrohm, 2001.

### ELECTROANALYSIS USING NANOSTRUCTURED METAL OXIDE MATERIALS

G.G. Wildgoose and R.G. Compton

Department of Chemistry, Physical and Theoretical Chemistry Laboratory, University of Oxford, South Parks Road, Oxford, OX1 3QZ, United Kingdom.

### **Abstract**

Several factors affecting the electrochemical and electroanalytical performance of three nanostructured metal oxide materials, namely NiO, MnO<sub>2</sub>, and CuO, formed using hydrothermal and sol-gel methods and supported on graphite electrodes are examined. First, the importance of considering the effect of the substrate electrode upon which such materials are supported is exemplified by the apparent electrocatalytic detection of aspirin and salicylic acid at NiO modified graphite electrodes. By performing the appropriate control experiments, it is possible to demonstrate that the observed electrochemical response towards these analytes is not due to the presence of NiO, but is due to the properties of the underlying graphite electrode. In the absence of these control experiments, one might have, erroneously attributed the enhanced performance of this system as being due to the NiO nanoparticles.[1]

Second, nanorods of  $MnO_2$  were synthesised as two different phases,  $\alpha$ - $MnO_2$  nanorods and  $\beta$ - $MnO_2$  nanorods. The difference in the phase energy of these two materials is estimated using cyclic voltammetry, and found to be of the order of 3 kJ  $mol^{-1}$ . Differences in the electrochemical behaviour of nanometre sized  $MnO_2$  and  $MnO_2$  microparticles, as measured by the potential of the cathodic stripping peak of  $MnO_2$ , are also observed. Finally the electroanalytical performance of the  $\alpha$ - $MnO_2$  nanorods,  $\beta$ - $MnO_2$  nanorods, and  $MnO_2$  microparticles towards the detection of hydrogen peroxide is presented. The  $\alpha$ - $MnO_2$  and  $\beta$ - $MnO_2$  nanorods were found to produce limits of detection of 3-6  $\mu$ M respectively, which was much lower than that obtained at the  $MnO_2$  microparticles (25  $\mu$ M).[2]

Third, the non-enzymatic detection of biologically important analytes, such as hydrogen peroxide, glucose, sucrose and fructose is studied using bundles of CuO nanorod agglomerates. Again, the electroanalytical performance of the nanostructured CuO was compared with CuO microparticles. The CuO nanorods agglomerates were found to produce lower limits of detection for carbohydrates in general than the CuO microparticles, of the order of 1-3  $\mu$ M, and also produced a limit of detection for hydrogen peroxide of 0.22  $\mu$ M.[3]

Finally, the role of CuO nanoparticle impurities in certain types of multiwalled carbon nanotubes (MWCNTs) is presented as the latest, rare, exception to the "edge-plane rule" describing the location of electroactive sites in MWCNTs.[4]

- [1] C. Batchelor-McAuley, G. G. Wildgoose, The influence of substrate effects when investigating new nanoparticle modified electrodes exemplified by the electroanalytical determination of aspirin on NiO nanoparticles supported on graphite, Electrochem. Commun. (2008) 10.1016/j.elecom.2008.1005.1034.
- [2] C. Batchelor-McAuley, Lidong Shao, Gregory G. Wildgoose, Malcolm L. H. Green, Richard G. Compton, An electrochemical comparison of manganese dioxide microparticles versus α- and β-manganese dioxide nanorods: mechanistic and electrocatalytic behaviour, New J. Chem. (2008) DOI: 10.1039/b718862e.
- [3] C. Batchelor-McAuley, Yi Du, G. G. Wildgoose, R. G. Compton, The use of copper(II) oxide nanorod bundles for the non-enzymatic voltammetric sensing of carbohydrates and hydrogen peroxide., Sensors Act. B (2008) submitted.
- [4] C. Batchelor-McAuley, G. G. Wildgoose, R. G. Compton, L. Shao, M. L. H. Green, Copper oxide nanoparticle impurities are responsible for the electroanalytical detection of glucose seen using multiwalled carbon nanotubes, Sensors Act. 2008, **B 132**, 356.

### THE ELECTRODE REDUCTION MECHANISM OF 1-PHENYL-3,3-DIMETHYLTRIAZENE AND ITS 4'-HALOGENO DERIVATIVES

M. Stević<sup>1</sup>, J. Barek<sup>2</sup>, J. Zima<sup>2</sup> and Lj.M. Ignjatović<sup>1</sup>

<sup>1</sup> Faculty of Physical Chemistry, University of Belgrade, Studentski trg 12-16, 11 001 Belgrade, Serbia (milica@ffh.bg.ac.yu)

### **Abstract**

A study was made of the electrode reduction mechanism of the genotoxic substances: 1-phenyl-3,3-dimethyltriazene and its 4'-bromo and 4'-iodo substituted derivatives. It was established that for reduction of the triazene group four electrons and four protons are required resulting in the formation of amino and hydrazo compound. The resulting products were identified, and the reduction pathway was proposed.

### Introduction

1-phenyl-3,3-dimethyltriazene and its *o*-, *m*-, and *p*- substituted derivatives rank among genotoxic substances that also exhibit cancerostatic activity [1,2]. Therefore, there is an increasing demand for sensitive analytical methods for the determination of these substances. Considering the fact that triazene group is polarographically active [3], polarography and more sensitive techniques, such as differential pulse polarography and adsorptive stripping voltammetry could be used for the determination of variously substituted derivatives of 1-phenyl-3,3-dimethyltriazene.

On the basis of voltammetric, coulometric, spectrophotometric and chromatographic measurements, in the present paper, an attempt was made to investigate the mechanism of electrochemical reduction of the studied triazenes and to postulate corresponding reduction scheme.

### **Experimental**

Three substances were investigated: 1-phenyl-3,3-dimethyltriazene (PDMT), 1-(4'-bromophenyl)-3,3-dimethyltriazene (BPDMT) and 1-(4'-iodophenyl)-3,3-dimethyltriazene (IPDMT). Mixed Britton-Robinson buffer – methanol medium was used as supporting electrolyte. All the chemicals used were of *p.a.* grade.

Polarographic and voltammetric measurements were carried out using a PA 4 polarographic analyzer with an SMDE 1 mercury electrode (both from Laboratorní přístroje, Praha, Czech Republic). A saturated calomel reference electrode (SCE) was used along with a platinum wire auxiliary electrode. Constant-potential coulometric (CPC) measurements were performed using a PAR 173 potentiostat with a PAR 179 digital coulometer (both Princeton Applied Research, USA). The mercury pool served

<sup>&</sup>lt;sup>2</sup> Charles University in Prague, Faculty of Science, Department of Analytical Chemistry, UNESCO Laboratory of Environmental Electrochemistry, Hlavova 2030, 128 43 Prague 2, Czech Republic.

as a cathode, with an SCE as reference and platinum gauze as counter electrode. Spectrophotometric measurements were carried out on a Varian Cary 17D UV/Vis spectrophotometer (Varian, USA). HPLC measurements were performed in an isocratic system equipped with a reversed-phase column ProntoSil C18 AQ and UV-Vis spectrophotometric detector (Bischoff Chromatography, Germany). Ion-chromatographic measurements were carried out by 761 Compact IC instrument, equipped with conductivity detector and Metrosep ASupp 1 anion column (Metrohm, Switzerland).

### **Results and Discussion**

Within the investigated range of pH values of the supporting electrolyte, investigated substances yield one polarographic wave, i.e. one differential pulse polarographic peak. Half-wave potential,  $E_{1/2}$ , and the potential of DPP peak,  $E_{\rm p}$ , shift towards negative values with increasing pH of the supporting electrolyte, the resulting  $E_{1/2}$  - pH and  $E_{\rm p}$  - pH dependences having asymptotic character. That fact indicates that protons are involved in the reduction process [4].

The nontypical polarograms obtained in the alkaline pH range of the supporting electrolyte are associated with the presence of methanol and with its influence on the preliminary protonation of electroactive species. That fact indicates [5] that a substance adsorbed on the electrode surface is subjected to protonation prior to the electrode reduction.

Logarithmic analysis of polarograms and cyclovoltammetric measurements lead to the conclusion that the electrode process is irreversible. Voltammetric reduction of PDMT, BFDMT and IFDMT is controlled by the diffusion of electroactive species as the slowest step in the electrochemical process. The diffusion nature of the voltammetric peaks of studied triazenes is confirmed on the basis of linear dependence of CV peak current,  $I_p$ , on the square root of the polarization rate,  $v^{1/2}$ : a linear dependence  $\log I_p = f(\log v)$  with r = (0.9985-0.9945), with the slope of (0.498-0.505) was obtained for the investigated substances.

The number of electrons participating in the tested triazenes reduction on mercury electrode was determined by coulometry at a constant potential of -1.300 V, which corresponds to the limiting current of the polarographic wave of the investigated substances. By coulometric analysis it was established that electrode reduction takes place with the participation of 4 electrons per one molecule of triazene. The obtained UV absorption spectrum of the product of FDMT reduction is similar to the spectra of aniline and phenylhydrazine and it was clear that it is not possible to identify the FDMT electrolysis products with certainty only on the basis of UV absorption spectra. For that reason, additional HPLC measurements were carried out yielding chromatograms of FDMT electrolysis product and the mixture of aniline and phenylhydrazine at various concentrations. UV detector was adjusted to the wavelength 278 nm, so it could detect all the substances of interest. In the chromatogram of the electrolysis product, both aniline and phenylhydrazine

appear. On the basis of calibration curves of aniline and phenylhydrazine, it was found that their relative ratio in the electrolysis product is 55 : 45.

Considering the slopes of the  $E_{1/2}$  – pH dependences and that the total number of exchanged electrons is n = 4, on the basis of the equation

$$dE/dpH = -2.303 \ mRT/\alpha n_aF$$

it is found that the total number of protons participating in the electrochemical reduction amounts to  $m = 3.8\pm0.3$  for all investigated triazenes.

During coulometric electrolysis of BPDMT and IPDMT, small amounts of electrolyzed solutions were taken and analyzed by ion chromatography. No free bromide and iodide ions appeared on the chromatograms, which leads to the conclusion that aromatic ring stayed substituted during electrolysis.

On the basis of the presented results it can be concluded that 1-phenyl-3,3-dimethyltriazene and its 4'-halogeno derivatives are reduced on mercury electrode according to the scheme shown bellow, where substituent X could be H, Br or I:

$$X \longrightarrow N = N - N$$
 $CH_3$ 
 $CH_3$ 

### Conclusion

It was established that electrochemical reduction of FDMT, BFDMT and IFDMT on Hg electrode require 4 electrons and 4 protons. The triazene adsorbed on the electrode surface is subjected to the protonation prior to electrode reduction. Electrode process is irreversible and his rate is controlled by the diffusion of electroactive species as the slowest step. The products of electrochemical reduction of the investigated triazenes are identified as aniline and phenylhydrazine, in the case of PDMT, i.e. *p*-halogenoderivatives of aniline and phenylhydrazine, in the cases of BPDMT and IPDMT.

- [1] J. H. Burchenal, S. K. Carter, Cancer, 1972, **30**, 1639-1646.
- [2] F. A. Schmidt, D. J. Hutchinson, Cancer Res., 1974, **34**, 1917-1925.
- [3] P. E. Iversen in: Encyclopedia of electrochemistry of Elements Organic Section, Vol.13, A. J. Bard, H. Lund (Eds.), Marcel Dekker, New York, 1979.
- [4] R. Greef, R. Pat, L. M. Peter, V. Pletcher, J. Robinson, Instrumental Methods in Electrochemistry, Ellis Horwood, Chichester, 1985.
- [5] S. G. Mairanovskii, Talanta, 1965, 12, 1299-1316.

### KINETICS OF ALUMINUM DISSOLUTION REACTION IN SKELETON NICKEL ELECTRODES PREPARATION

A. Kellenberger\*, N. Vaszilcsin, N. Duteanu and M. Laurentiu Dan

University "Politehnica" of Timisoara, Faculty of Industrial Chemistry and Environmental
Engineering, Piata Victoriei 2, 300006 – Timisoara, Romania
\* andrea.kellenberger@chim.upt.ro

### Abstract

The reaction order of the aluminum dissolution reaction from skeleton nickel electrodes was determined by the complexonometric back-titration method. It was found that the reaction proceeds according to a first order dependence. The reaction order was confirmed by the linear dependence of the logarithm of reactant concentration versus time and by the half lives ratios.

### Introduction

Skeleton nickel electrodes have proved to be efficient electrodes in the hydrogen evolution reaction (HER). An efficient way to improve the electrochemical activity of skeleton electrodes is to increase the real surface area. This can be achieved either by the manufacturing technique, either by removing an active component from the electrode. For the hydrogen electrocatalysts Zn and Al are frequently used as secondary components, which can be easily leached out in order to enhance porosity [1,2]. Although the aluminum dissolution in alkaline solution is a zero-order reaction, literature data suggest that in case of aluminum alloys the dissolution reaction obeys a first-order dependence [3].

The aim of this paper is to establish the reaction order for the aluminum dissolution reaction from NiAl layer and to find out the critical parameters influencing the dissolution reaction which can assure an increased porosity of the electrocatalytic layer in the preparation of skeleton nickel electrodes.

### **Experimental**

Skeleton nickel electrodes were obtained by thermal arc spraying of a nickel wire (97% Ni) together with an aluminum wire (99.5% Al) on a carbon steel substrate. Details about the preparation method are given elsewhere [4]. The thickness of the NiAl coating was about 0.8-0.9 mm.

The aluminum dissolution was performed in 50 cm<sup>3</sup> of 1 mol L<sup>-1</sup> NaOH solution. The temperature of the leaching solution was maintained at  $80 \pm 2^{\circ}$ C using a water jacket. The samples were kept in the sodium hydroxide solution for different leaching times, ranging from 15 to 240 minutes. Prior to each experiment the samples were cleaned for 10 minutes in an ultrasound bath for the advanced removal of reactant traces or metallic powders.

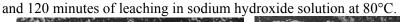
The quantity of dissolved aluminum in the leaching solution was determined by complexonometric back-titration. The leaching solutions were diluted to 100 cm<sup>3</sup> and 10 cm<sup>3</sup> were taken for the titration. The pH of the solution was adjusted to

5.5 by gradually adding 0.1 mol l<sup>-1</sup> acetic acid solution and monitoring the pH value. An excess of ethylene diamine tetraacetic acid (EDTA) was added and the solution was heated to the boiling point to achieve the complexation of aluminum. The solution was afterwards cooled and the EDTA excess was back-titrated with 10<sup>-2</sup> mol L<sup>-1</sup> FeCl<sub>3</sub> in the presence of sulfosalicilic acid. The aluminum content was calculated and reported to the surface of the leached sample.

The composition and morphology of the NiAl coatings was investigated before and after the Al dissolution by scanning electron microscopy (Philips XL ESEM) and energy-dispersive X-ray analysis (EDX).

### **Results and Discussion**

Cross-section SEM micrographs of the NiAl coatings are given in figure 1 for 60 and 120 minutes of leaching in sodium hydroxide solution at 80°C



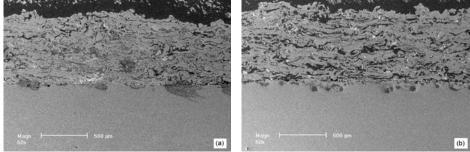


**Fig. 1.** Cross-section micrographs of the NiAl coatings after different leaching times, magnitude 50x. (a) 60 minutes; (b) 120 minutes.

The morphology of the NiAl coating treated for 60 minutes in alkaline solution reveals that the dissolution of Al proceeds from the top of the coating into the depth. In the upper layer, with a thickness of approximately 300  $\mu m$ , the Al is dissolved, while in the depth of the coating un-dissolved Al can be observed. For a leaching time of 120 minutes the aluminum dissolution seems to be complete.

The Al content determined by EDX analysis gave a percentage of 24.9% Al before dissolution and 1.5% Al after 120 minutes of alkaline dissolution.

The dependence of the dissolved Al as a function of leaching time determined by complexonometric back-titration is given in figure 2a. The shape of the curve indicates an exponential increase of the dissolved Al with the increase of the leaching time. Between 120 and 240 min the quantity of dissolved Al changes only to a small extent, so the reaction can be considered to be complete after 2 hours.

The first order kinetic model was applied to our data, described by equation (1):

[Al] / [Al]<sub>0</sub> = exp (
$$-k_{diss} t$$
) (1)

where [Al] is the concentration of the reactant at time t, [Al]<sub>0</sub> is the initial concentration of the reactant and  $k_{\rm diss}$  is the rate constant for the dissolution reaction. The integrated form of the first-order rate law is given by equation (2):

$$ln [Al] = -k_{diss}t + ln[Al]_0$$
 (2)

The plot of ln[Al] vs. t given in figure 2b yielded a straight line, typical for reactions following first-order kinetics.

The rate constant for the Al dissolution was determined from the slope of the ln[Al] vs. t plot. The obtained value is  $k_{diss} = 3.97 \cdot 10^{-2} \text{ min}^{-1}$ .

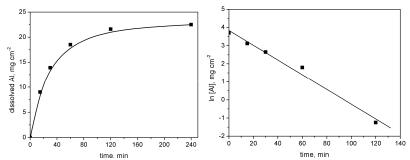


**Figure 2. (a)** Time dependence of the dissolved aluminum; **(b)** logarithm plot of the un-dissolved Al versus time.

The reaction order was verified by the method of half lives ratios. The values of the calculated and theoretical half lives ratios for the Al dissolution reaction from skeleton NiAl coatings are given in Table 1.

**Table 1.** Calculated and theoretical values for the half lives ratios of Al dissolution.

$t_{1/2}$	$t_{1/3}$	$t_{1/4}$	$t_{1/2} / t_{1/3}$		$t_{1/2}/t_{1/4}$		$t_{1/3} / t_{1/4}$	
[min]	[min]	[min]	Calc.	Theor.	Calc.	Theor.	Calc.	Theor.
23.11	13.25	9.45	1.74	1.71	2.44	2.41	1.40	1.41

### **Conclusions**

The obtained data indicate that the Al dissolution reaction from skeleton NiAl coating is a first-order reaction. The kinetics of Al dissolution is therefore strongly influenced by the factors acting on the rate constant, especially the temperature. In case of a first-order reaction, an increase of  $10^{\circ}$ C leads to a 2-3 times increase of the rate constant.

### Acknowledgement

The authors thank Romanian Ministry of Education and Research for financial support offered through PNCDI – II nr. 71-017/2007 and CEEX nr. 758/2006.

- [1] L.Chen, A.Lasia, J.Electrochem.Soc., 1991, 138, 3321-3328.
- [2] Y.Choquette, L.Brossard, A.Lasia, H.Menard, Elchim. Acta, 1991, 35, 1251.
- [3] Y.Choquette, L.Brossard, H.Menard, J.Appl. Electrochem., 1990, 20, 855-863.
- [4] A.Kellenberger, N.Vaszilcsin, W.Brandl, N.Duteanu, *Int.J.Hydrogen Energy*, 2007, **32**, 3258-3265.

# INFLUENCE OF EXTERNAL MAGNETIC FIELD ON THE ELECTROLYTIC HYDROGEN EVOLUTION ON DIFFERENT CATHODE MATERIALS

T.D. Grozdić<sup>1</sup>, D.LJ. Stojić<sup>2</sup> and S.V. Kumrić<sup>2</sup>

<sup>1</sup>Institute for multidisciplinary research, Kneza Višeslava 1a, 11000 Belgrade, Serbia,(gtomisi@cms.bg.ac.yu). <sup>2</sup>Vinča Institute of Nuclear Sciences, Physical Chemistry, P.O. Box 522,11000 Belgrade, Serbia.

### Abstract

The correlation between magnetic properties of cathodic materials on the evolution of hydrogen and the separation factor was found. The cathodes were pure Ni and cathodes with the electrocatalytic coatings of following compositions: Ni-Mo (70-30%), Ni-V (70-30%), Co-Mo (70-30%) and Fe-Mo (60-40%), on Ni substrate. The electrolyte is standard electrolyte (30% KOH) and electrolyte activated with Co-complex [1].

### Introduction

High separation factor was received by using an iron electrode prepared in the magnetic field [2]. Namely, the iron film was electrodeposited in a magnetic field and the obtained separation factor  $\alpha$  was 12.3, that is much higher than of conventional mild steel electrode ( $\alpha = 5$ -9). Further, when new deuterium separation system, using fuel cell, is applied with this new iron electrode the energy requested is significantly reduced [3].

In our previous papers [3-7] water electrolysis in alkaline solutions has been studied as the method for hydrogen production and hydrogen isotopes (D,H) separation. On different kind of cathode materials, single transition metals and/or Brewer hypo-hyper-d-electronic intermetallics of transition metals, significant increase in separation factors were obtained when *in situ* activation with tris-(ethylenediamine)Co(III) chloride complex, tris(en), was applied [3]. Further, ionic activator used have shown significant electrocatalytic effect, that means energy saving per mass unit of evolved hydrogen from alkaline aqueous solutions was reduced (in some cases beyond 10%) [7]. *In situ* activation with the other complex, tris-(trimethylenediamine)Co(III) chloride complex, tris(ten), have given much better result in the case of separation efficiency. It undoubtedly means that all those activated surfaces of the electrodes approved the electrocatalytic effects that, as it is well known, issue from their d-electronic configuration.

The aim of the present work was to find the correlation between magnetic properties of some cathode materials (singly transition metals and/or their intermetallics in standard electrolyte and in activated one) and their efficiency in hydrogen evolution and hydrogen isotopes (H/D) separation processes.

#### **Results and Discussion**

The experimental obtained values of magnetisation, M, at the applied magnetic field of 6000 Oe were compared with previous received values of separation factors,  $\alpha$  It was found that the magnetisation increased on those materials which exhibit the increased values of separation factors. The maximum value of magnetisation and separation factor was achieved by cathode made of nickel (M = 51.14 emu/g and  $\alpha$  = 7.6, respectively) and minimum is for nickel cathode with thermochemically deposited iron and molibdenum, Fe-Mo (60-40%) (M = 45.20 emu/g and  $\alpha$  = 4.0, respectively).

During the electrolysis with addition of following ionic activators: tris(ethylenediammine)Co(III)-chloride, tris(en), and tris(trimethylenediammine) Co(III)-chloride, tris(ten), into the electrolyte, the deposition of fine black powder on cathode surface occured. Therefore, we measured the magnetisation of nickel cathode with deposit and of the same deposit removed from cathode surface. In all cases the separation factors were measured as well. On the basis of the results obtained, when *in situ* activation with tris(en) complex was applied, we concluded that the separation factor and magnetisation of activated nickel cathode is increased compared with non-activated one, magnetisation for about 4% and the attained increase in separation factor was about 32 %.

The best results of separation factor and magnetisation were achieved when activation with tris(ten), as activating complex, was used. During the electrolytic process, black deposit was formed on nickel cathode from complex added into the electrolyte. Pure nickel has magnetisation of 51.14 emu/g and the value of it for deposit sample is 63.02 emu/g. It means that removed deposit from electrode surface has 23 % bigger value of magnetisation then pure nickel, and separation factor increase is 97 %.

The presentation of separation factors as a function of magnetisation for different cathode materials is given in Fig. 1. The linear function of dependence,  $\alpha$  vs. magnetisation, was obtained.

It is important to mention that, in accordance with our previous investigation, the energy consumption was improved, as well. So, for pure nickel the energy requirement was 510.3 kJ mol<sup>-1</sup> and in activated system the decreased value of 487.7 kJ mol<sup>-1</sup>, was obtained [1]. Therefore, in the consideration of the improvement of separation efficiency the decrease in energy requirement in the electrolytic hydrogen evolution process has it's significant contribution.

Emphasizing the role of the hydrogen bonds we do hope to introduce a more suitable approach in understanding and controlling the influence of the deposit on the improvement of hydrogen evolution efficiency. Obtained magnetic properties of deposit, and generally speaking influence of magnetic field, is not well known especially if we take in consideration influence on hydrogen reaction.

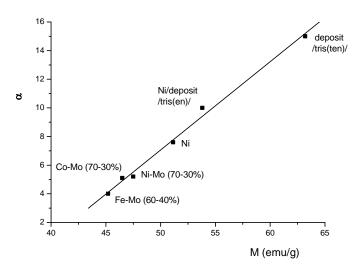


**Fig. 1.** Separation factors as a function of magnetization for different cathode materials singly and/or in the presence of ionic activators.

#### Conclusion

Magnetic properties of cathode materials and cobalt deposit on nickel surface is evident and it has obvious influence and increase on separation factor i.e. increase evolution of hydrogen during electrolyses in water KOH solution. The obtained correlations between magnetic properties and electrocatalytic activity of the investigated cathode materials issue from their d-electronic configuration.

#### Acknowledgement

The present investigations are supported by Ministary of Science of the Republic of Serbia under Projects 142 025 and 141 022.

- [1] Dragica Lj. Stojić, Tomislav D. Grozdić, Vojislav V. Spasojević, Ana B. Umićević and Sofija P. Sovilj, *Influence of magnetic behavior of cathodic surface on deuterium separation factor*, *Electrochemistry Communications*, 2007, **9**, 2408-2411.
- [2] H. Matushima, T. Nohira, Y. Ito, *Improved deuterijum separation factor for the iron electrode prepared in a magnetic field*, Electrochemica Acta, 2004, **49**, 4181-4187.
- [3] H. Matsushima, T. Nohira, T. Kitabata, Y. Ito, *A novel deuterium separation system by the combination of water electrolysis anf fuel cell*, Energy, 2005, **30**, 2413-2423.

## INTERCALATION BEHAVIOR OF ELECTRODE MATERIALS OBTAINED FROM V<sub>2</sub>O<sub>5</sub> + H<sub>2</sub>O<sub>2</sub> SOLUTION

I. Stojković\*1, I. Pašti<sup>1</sup>, N. Cvijetićanin<sup>1</sup>, M. Mitrić<sup>2</sup> and S. Mentus<sup>1</sup>

<sup>1</sup>Faculty of Physical Chemistry, Belgrade University, Studentski trg 12, Belgrade, Serbia <sup>2</sup>The Vinca Institute of Nuclear Sciences, Laboratory for Theoretical and Condensed Matter Physics, Belgrade, Serbia \*ivana@ffh.bg.ac.yu

#### **Abstract**

 $V_2O_5$  was completely dissolved in 30%  $H_2O_2$  aqueous solution, and a powdery solid product remained upon solvent evaporation was dried at 120°C. A part of the dried product was heated at 400°C up to a constant mass. By cyclic voltammetry, comparative study of  $\text{Li}^+$  and  $\text{Mg}^{2^+}$  intercalation into  $V_2O_5$  and into both of its here mentioned derivatives was performed. The dissolution product dried at 120°C displayed the highest intercalation capacity amounting to 100 mAhg<sup>-1</sup> and 120 mAhg<sup>-1</sup>, in  $\text{LiNO}_3$  and  $\text{Mg}(\text{NO}_3)_2$  aqueous solutions, respectively.

#### Introduction

Various vanadium oxides, especially vanadium pentoxide  $(V_2O_5)$  are known electrode materials, applied particularly in electrochemical capacitors, electrochromic devices and Li-ion intercalation processes. Intercalation of Li<sup>+</sup> ions into  $V_2O_5$  was widely investigated in non-aqueous solutions, and quite recently several studies have been published dealing with its electrochemical properties in aqueous solutions [1]. The main disadvantage of  $V_2O_5$ , or generally vanadates, when used as cathode material of a battery, is fast capacity fade during cyclic charging/discharging. The capacity fade was usually attributed to phase transitions during galvanostatic cycling. The way suggested to overcome this problem is either to coat the cathode material with polymer layers, or to modify its chemical composition [2].

In the present work, commercially available  $V_2O_5$  was dissolved in  $H_2O_2$ . According to previously published studies [3], precipitate recovered from such a solution may present nanoparticles or materials with highly developed surface, with improved electrochemical properties. In this work, the characterization of powdery products obtained by evaporation of  $V_2O_5 + H_2O_2$  solutions, was performed by multianalytic approach. Li-intercalation/deintercalation processes of obtained materials in aqueous solutions were investigated by means of cyclic voltammetry.

#### **Experimental**

In the vigorous reaction, commercial  $V_2O_5$  powder (0.5g) was dissolved in 3ml of 30% hydrogen peroxide solution ( $H_2O_2$ ) and after solvent evaporation the powdery precipitate was dried at  $120^{\circ}C$  during 1h. Simultaneous TGA and DTA measurements of such dried sample indicated the further mass and phase changes

up to 350°C. Therefore, a part of the dried sample was annealed additionally at 400°C during 15 minutes.

The X-ray diffractograms (XRPD) were recorded using  $CuK_{\alpha 1,2}$  radiation in  $2\theta$  range  $10\text{--}70^\circ$  with the  $0.05^\circ$  step and 2 seconds exposition time. The scanning electron microscopy (SEM) JEOL JSM-840A was used to observe surface morphology.

Cyclovoltammetric curves were recorded at various scan rates in saturated aqueous solutions of LiNO<sub>3</sub> and Mg(NO<sub>3</sub>)<sub>2</sub>. Three types of powdery materials were used to made working electrode: original  $V_2O_5$  and two powdery precipitates obtained from  $V_2O_5 + H_2O_2$  solution: that dried at  $120^{\circ}C$ , and that annealed at  $400^{\circ}C$ . To each of them, carbon black (Vulcan) and PVDF binder were added in weight ratio 60:30:10. After homogenization in N-methyl 2-pyrrolidone in ultrasonic bath, the mixture was applied on glassy carbon rod and dried under vacuum  $10^{-2}$  mbar at  $140^{\circ}C$  for 12 hours. A platinum foil was used as a counter electrode. The potentials, ranged 1 to -1 V, were measured against the saturated calomel reference electrode (SCE). Faradaic discharge capacity was calculated by coulometric analysis of cyclovoltammetric curves.

#### **Results and Discussion**

XRPD analysis of the oxide product obtained upon V<sub>2</sub>O<sub>5</sub> dissolution in H<sub>2</sub>O<sub>2</sub> and drying at 120°C evidenced that one deals with a multicomponent amorphous

mixture, while SEM images indicated its fibrous structure, Fig 1a. The width of fibers is around 1  $\mu m$ . The sample annealed at 400°C, looks like agglomerates with irregular shapes, Fig 1b.

Among the three electrode material mentioned in Experimental section, the product dried at 120°C enables the highest kinetic of both Li<sup>+</sup> and Mg<sup>2+</sup> intercalation and deintercalation. Generally for all samples. voltammetric the increased during first few cycles and then reached a steady-state regime. commercial V<sub>2</sub>O<sub>5</sub> as electrode material in Li-salt solution, average faradaic capacity was found to be 63 mAhg-1 while the dissolution product dried at displayed faradaic capacity of roughly 100 mAhg<sup>-1</sup>. For Mg-salt solution, faradaic capacity of original V<sub>2</sub>O<sub>5</sub> was 30 mAhg<sup>-1</sup>,

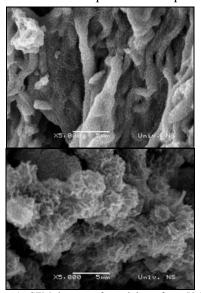


Fig. 1. SEM images of precipitate from  $V_2O_5$ + $H_2O_2$  solution dried at  $120^{\circ}C$  (a), and annealed at  $400^{\circ}$  (b). The magnification was 5000.

while for the dissolution product dried at  $120^{\circ}$ C the corresponding value was 120 mAhg<sup>-1</sup>. Faradaic capacity of the solution product annealed at  $400^{\circ}$ C was even less than that of commercial  $V_2O_5$ , as Fig. 2 shows. This capacity loss may be the

consequence of unfavorable crystallographic ordering and particle growth during annealing procedure.

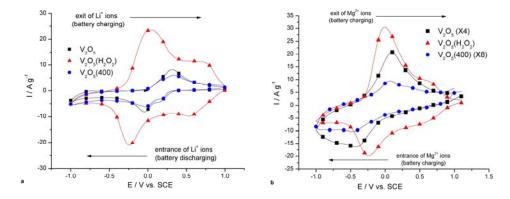


Fig. 2. CV curves for -  $\triangle$  - dissolution product 120°C - $\blacksquare$ - commercial  $V_2O_5$  and - $\blacksquare$ - dissolution product 400°C, in saturated aqueous solution of a) LiNO<sub>3</sub> and b) Mg(NO<sub>3</sub>)<sub>2</sub>. Scan rate was 50 mVs<sup>-1</sup>.

The performances of these materials under galvanostatic charging/discharging cycles been tested between 4.5 and 2.0 V vs Li<sup>+</sup>/Li, at current rate C/3 in organic electrolyte -1M LiClO<sub>4</sub> in propylene carbonate. After 5 cycles, the discharge capacity of the product dried at 120°C (amounting to 337 mAhg<sup>-1</sup>) was increased for 6% of initial discharge capacity (being 319 mAhg<sup>-1</sup>). Commercial V<sub>2</sub>O<sub>5</sub> as well as the annealed dissolution product displayed the capacity fade during cycling.

#### Conclusion

The oxide product recovered from  $V_2O_5+H_2O_2$  solution dried at 120°C displayed most promising properties in the intercalation/deintercalation processes in aqueous electrolyte solutions of Li- and Mg- salts, and thus may be considered as potential electrode material in aqueous Li- and Mg-ion batteries.

#### Acknowledgement

This work was supported by Serbian Ministry of Science, project No. 142047.

- [1] H. Wang, Y. Zeng, K. Huang, S. Liu, L. Chen, *Electrochimica Acta*. 2007, 52, 5102–5107.
- [2] E. Potiron, A. Le Gal La Salle, S. Sarciaux, Y. Piffard, D. Guyomard, *Journal of Power Sources*, 1999, **81–82**, 666–669.
- [3] Z.J. Lao, K. Konstantinov, Y. Tournaire, S.H. Ng, G.X. Wang, H.K. Liu, *Journal of Power Sources*, 2006, **162**, 1451–1454.

## METAL OXIDE GRAPHITE COMPOSITE ELECTRODES: APPLICATION TO ELECTROANALYSIS

B. Šljukić<sup>1</sup>, C.E. Banks<sup>2</sup> and R.G. Compton<sup>3</sup>

<sup>1</sup>Faculty of Physical Chemistry, University of Belgrade, Studentski trg 12, Belgrade, Serbia
<sup>2</sup>School of Biology, Chemistry and Health Science, Manchester Metropolitan University,
Chester St., Manchester, M1 5GDUK
<sup>3</sup>Physical and Theoretical Chemistry Laboratory, University of Oxford,
South Parks Road, Oxford, OX1 3QZ, , UK

#### **Abstract**

A procedure for modification of carbon powder with different metal oxides, namely iron, copper, manganese and lead oxide was developed. Novel composite metal oxide modified carbon powder epoxy electrodes were developed for electrocatalytic sensing of gaseous, inorganic and organic analytes. The composite electrodes showed a high electrocatalytic activity for the detection of various analytes examined in aqueous media, with detection limits comparable or lower than detection limits obtained with other electrochemical sensors.

#### Introduction

Carbon electrodes are characterised with wide potential window, rich surface chemistry, low cost, chemical inertness and suitability for various sensing applications. On the other hand, electron transfer rates observed at carbon electrodes are often slower than those observed at metal surfaces. The usual approach in overcoming the slow kinetics at carbon electrodes is modification of electrode surface. <sup>[25]</sup>. Noble metals are well-known oxidation catalysts: however, due to the high cost of these metals, attention has been given to non-noble metal based catalysts, such as transition metal oxides.

#### Experimental

*Modification of Carbon Powder* - The modification of carbon powder with metal (Fe, Cu, Mn or Pb) oxide was carried out by a wet impregnation procedure. First, carbon powder was impregnated with metal nitrate by stirring carbon powder (1 g) in concentrated aqueous solution of a metal nitrate (25 cm³) at room temperature for 1 hour. The metal nitrate - carbon powder composite was separated from the solution by filtration and left to dry at room temperature. Subsequently, the sample was exposed to temperature of 823 K in the case of Cu and Pb, to 793 K in case of Mn and to 623 K in case of Fe resulting in metal oxide modified carbon powder.

**Preparation of the Working Electrodes** - The working electrodes were made of a composite of metal oxide modified carbon powder and epoxy resin. For the fabrication of the composite electrode, epoxy resin and hardener were first hand mixed in 20:3 weight ratio. This was next blended with a mixture of metal oxide modified carbon powder (10 weight %) and unmodified carbon powder (90 weight

%), with powder to resin ratio of 1:3. The resulting paste was mixed in an ultrasonic bath for 30 min and then placed in a glass tube of 6 mm inner diameter up to 6 mm depth. The electrical contact was completed using a copper wire inserted into the tube up to 3 mm depth. The electrodes were subsequently dried at 40°C for 60 hr.

#### **Results and Discussion**

Carbon powder modified with metal oxide *via* the wet impregnation procedure was first characterised using electrochemical and spectroscopic methods. Results of electrochemical investigations indicated that modified carbon powder containing separately lead (IV) oxide, manganese (IV) oxide and both copper (I) and copper (II) oxides was formed by the wet impregnation procedure. XPS analysis of the modified carbon powder confirmed the results obtained with electrochemical techniques.

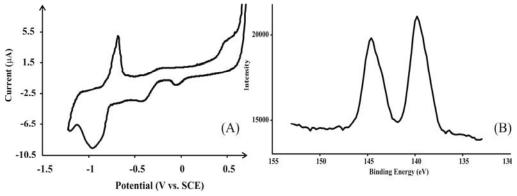


**Fig. 1**. Cyclic voltammogram of BPPG electrode abrasively modified with lead oxide carbon powder in 0.1 M sodium hydroxide solution at a scan rate of 1 mVs<sup>-1</sup> (A) and XPS detail scan of lead oxide modified carbon powder (B)

Next, the effect of several parameters: carbon powder to epoxy resin ratio, length of the electrode and amount of metal oxide modified carbon powder, on the electrode electrochemical behaviour was explored in 1 mM solution of ferrocyanide in 0.1 M KCl. It was found that the electron transfer at the carbon powder epoxy composite electrode becomes faster with decreasing the amount of epoxy resin, the length of the electrode and the amount of metal oxide modified carbon powder. Note that if commercial metal oxide was simply mixed with carbon powder, the composite electrode didn't show satisfactory electroanalytical response. Throughout all further experiments composite electrodes with optimized parameters were made and used.

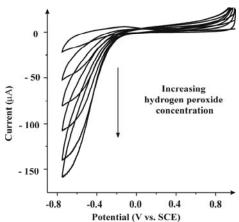


**Fig. 2.** CVs of Fe<sub>2</sub>O<sub>3</sub> – modified graphite composite electrode in pH 7.4 phosphate buffer with increasing hydrogen peroxide concentration in the range 0.5 - 5 mM

Preliminary studies were performed potential for electrocatalytical application of the oxide graphite composite electrodes for detection of different analytes. Iron oxide graphite composite electrodes were examined for the determination of hydrogen peroxide and hydrazine in aqueous solutions using cyclic voltammetry and chronoamperometry and detection limits of 0.13 and 1.2 µM were obtained respectively [1]. Cu, Pb and composite oxide graphite Mn electrodes were applied to detection of nitrite in aqueous solutions with limitis of detection

evaluated to be 1.2, 0.9 and 0.6  $\mu$ M respectively [2, 3, 4]. The electrocatalytic activity of Fe<sub>2</sub>O<sub>3</sub> graphite composite electrode was also studied in respect of sensing of phenol as a model organic contaminant in wastewater and ammonia as model gaseous analyte. MnO<sub>2</sub> graphite composite electrodes were investigated for detection of hydrogen peroxide and ascorbic acid as well. In both cases, the limits of detection were comparable to those obtained with other electrochemical methods.

#### **Conlusions**

A simple wet impregnation method was introduced to modified carbon powder with metal (Fe, Cu, Mn or Pb) oxides. Composite metal (Fe, Cu, Mn or Pb) oxide modified carbon powder epoxy electrode were constructed and their electrocatalytic properties examined in respect to determination of gaseous, inorganic and organic analytes in aqueous solutions demonstrating good electrocatalytic properties and potential application in sensors for monitoring different analytes in water systems.

- B. Šljukić, C. E. Banks, A. Crossley, R. G. Compton, Electroanalysis, 2006, 18(18), 1757-1762.
- [2] B. Šljukić, C. E. Banks, A. Crossley, R. G. Compton, Electroanalysis, 2007, 19(1), 79-84.
- [3] C. E. Langley, B. Šljukić, C. E. Banks, R. G. Compton, Anal. Sci., 2007, 23(2), 165-170.
- [4] B. Šljukić, C. E. Banks, A. Crossley, R. G. Compton, Anal. Chim. Acta, 2007, 587(2), 240-246.

## ELECTROCHEMICAL BEHAVIOUR OF AN Ag/13X ZEOLITE/VULCAN COMPOSITE LAYER IN 0.1 M NaOH AQUEOUS SOLUTION

Z. Mojović<sup>1</sup>, S. Mentus<sup>2</sup> and D.M. Jovanović<sup>1</sup>

<sup>1</sup>IChTM-Center of Catalysis and Chemical Engineering, Njegoševa 12, Belgrade <sup>2</sup>Faculty of Physical Chemistry, Belgrade University, Studentski Trg 12, Belgrade,

#### **Abstract**

The composite Ag/zeolite 13X with 20 wt.% of Ag was synthesized by zeolite impregnation with Ag-acetylacetonate/acetone solution, followed by acetone evaporation and thermal decomposition of organometallic complex. Scannig electron microscopy evidenced that a part of silver, in a form of nanovires and nanodots, appeared outside the zeolite crystals. Ag/13X composite homogenized with 10 wt.% of nanodispersed carbon (Vulcan), pasted on flat glassy carbon suface, was used as an electrode material on which oxygen reduction reaction (ORR) was investigated in an O<sub>2</sub>-saturated aqueous 0.1M NaOH solution. Catalytic activity of the composite electrode was found to be equivalent to that of most active Ag(100) monocrystal surface.

#### Introduction

Oxygen reduction reaction presents main cathodic reaction in fuel cells. Silver displayed good electrocatalytic effectiveness for oxygen reduction in alkaline solutions, comparable to platinum [1]. Increasing the surface area of the catalyst by reducing particle size presents an recognizable way of improving catalytic activity. Zeolites, with their cavities of nanometer dimensions, present a specific support for metal clusters incorporation, limiting the cluster growth to the dimesions of zeolite cavities. The methods available to incorporate metal clusters in the zeolite cavities are either ion exchange followed by reduction, or impregnation by thermodegradable salt solution [2,3], followed by drying and thermal degradation. In this paper, the technique of zeolite impregnation by Agacetylacetonate dissolved in acetone was used to incorporate silver within the zeolite cavities. Ag-modified zeolite, with addition of carbon black (Vulcan) to provide fair electronic conductivity, was investigated as catalyst for oxygen reduction reaction in alkaline solution.

#### **Experimental**

Ag-acetylacetonate was dissolved in acetone. Zeolite 13X was soaked by the solution, dried to evaporate acetone and heated to 350°C in air in order to decompose the complex compounds and desorb the decomposition products. In this way nanodispersed Ag clusters were incorporated into the zeolite cages. Procedure was repeted until Ag/zeolite weight ratio of 0.2 was reached.

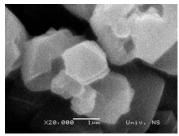
SEM experiments were performed on a JSM-6460LV electron microscope (JEOL, Japan) operating at an accelerating voltage of 25 kV and the samples were sputtered with a thin film of Au

Powdered mixture of the sample and 10 % carbon black, was homogenously dispersed in a solution of Nafion (5 wt.%), at Nafion solution/powder wt. ratio 2.5, and a

droplet of the suspension was applied on glassy carbon disc of rotating electrode. Solvent evaporation resulted in a thin film of modified zeolite bonded, by a Nafion film, to glassy carbon support. The electrochemical performance of this material was investigated in 0.1M NaOH solution using rotating disc technique.

#### **Results and Discussion**

The SEM microphotograph of initial form of zeolite 13X is compared to the one of Agmodified zeolite in Fig. 1. The photographs indicates that modification by Ag does not influence original form of zeolite crystals, and also that at leas a part of silver was accomodated on the outer surface of the zeolite, in the form of nanosferes, 200 - 400 nm in dia, and in the form of nanowires, 100 - 150 nm in dia and about 1  $\mu$ m in length. The XDS analysis confirmed that these forms consisted of silver.



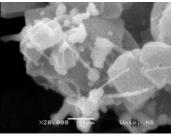
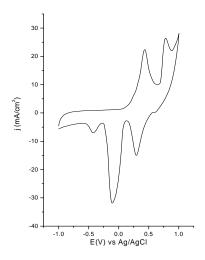
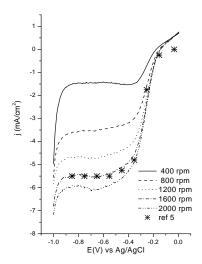


Fig.1: The SEM microphotographs of zeolite13X (left) and Ag/13X composite (right)

The steady state cyclovoltammogram with composite electrode layer, obtained after 20-30 polarization cycles, in nitrogen purged 0.1M NaOH, within the voltage window shorter than that of water splitting, is presented in Fig. 2a. The first anodic peak at +0.42V vs Ag/AgCl is related to the formation of Ag<sub>2</sub>O, and its reverse cathodic peak lies at -0.1V. The second anodic peak at +0.78V is related to the formation of AgO, which is accompanied by corresponding cathodic peak at +0.3V [4]. The polarisation in anodic direction is limited by oxygen evolution reaction at 1.0 V. At catodic plarization direction, at the potential of -0.4V reduction of oxygen remained in the zeolit cages is visible.

The catalytic activity of the composite material toward the oxygen reduction was investigated in oxygen saturated 0.1M NaOH. j-E curves recorded using cathodic sweep and various rotation rates are presented in Fig. 2b. For the sake of comparison, the voltammogram of monocrystalline Ag(100) in the same solution [5] recorded at a rotation rate of 1600 rpm is presented too. It is known already that oxygen reduction reaction on silver surface follows the 4e<sup>-</sup> path in alkaline solutions [6,7]. Y.Yang i Y.Zhou [8] evidenced that oxygen reduction on Ag particles may follow four electron route at crystal face sites and two-electron one at the edge and the corner sites, while the size of the Ag particles affects the different catalytic activity for the four-electron and two electron reduction of oxygen. In view of the last mentioned results, on very developed silver surface like the one formed in this composite material, one might expect a significant role of corner and edge sites, i.e. a remarkable participation of two-electron route of oxygen reduction reaction. Contrary to this, overlapping the j-E for Ag(100) taken from ref. 5 with the here recorded curve for the same rotation rate of 1600 rpm, indicates the predomination of four-electron route in this case





**Fig. 2a:** Voltammogram of composite electrode material (Ag/13X, carbon black, nafion) in nitrogen purged 0.1M NaOH, at a polarization rate of 50mV/s.

**Fig. 2b:** j-E curves for ORR on composite electrode (Ag/13X, carbon black, nafion) in oxygen saturated 0.1M NaOH, at a polarization rate of 5mV/s, and different rotation rates assigned in the legend.

#### **Conclusions**

Composite electrode material based on 13X zeolite and silver dispersed both within and out of zeolite cavities, in  $N_2$  purged 0.1M NaOH solution yielded the cyclic voltammogram corresponding to pure silver of very developed real surface area. The same electrode material in oxygen saturated 0.1M NaOH solution, using rotating dics technique, yielded the voltammograms which indicate four-electron route of oxygen reduction reaction.

**Acknowledgment** This work was supported by the Ministry of Science of the Republic of Serbia, contracts No. TR6712B and 142047 (SM).

- [1] B.B. Blizanac, P.N. Ross, N.M. Markovic, J. Phys. Chem. B, 2006, 110, 4735-4741.
- [2] M.Okumura, K.Tanaka, A.Ueda, M.Haruta, Solid State Ionics, 1997, 95, 143-149.
- [3] S.Mentus, Z.Mojović, N.Cvjetićanin, Z.Tešić, Fuell Cells From Fundamentals to Systems, 2003, **3**, 15-20.
- [4] T.P.Dirkse and D.B. De Vries, J. Phys. Chem., 1959, **63**, 107-110.
- [5] B.Blizanac, Ph.D. Thesis, Faculty of Physical Chemistry, Belgrade University, 2004.
- [6] P.Fisher, J.Heitibam, J.Electroanal. Chem., 1980, 112, 281-293.
- [7] P.K.Adonuvor, R.E.White, J. Electroanal. Chem., 1984, 165, 121-133.
- [8] Y. Yang, Y. Zhou, J. Electroanal. Chem., 1995, **397**, 271-278.

# ELECTROCHEMICAL PROPERTIES OF LiFePO<sub>4</sub>/C COMPOSITES OBTAINED BY ULTRASOUND ASSISTED SYNTHESIS AT DIFFERENT CALCINATION TEMPERATURES

D. Jugović<sup>1</sup>, M. Mitrić<sup>2</sup> and N. Cvjetićanin<sup>3</sup>

<sup>1</sup>Institute of Technical Sciences of the Serbian Academy of Sciences and Arts, Knez Mihailova 35/IV, 11 000 Belgrade, Serbia

<sup>2</sup>The Vinča Institute of Nuclear Sciences, Laboratory for Theoretical and Condensed Matter Physics, P.O. Box 522, 11001 Belgrade, Serbia

<sup>3</sup>Faculty of Physical Chemistry, University of Belgrade, Studentski trg 12-16, P.O. Box 137, Belgrade, Serbia

#### **Abstract**

Olivine structure LiFePO<sub>4</sub>/C composite powders were prepared by combining sonochemical precipitation and calcination at three different temperatures. A polyvinyl alcohol solution was used as the source of an in situ formed carbon. The crystal structures of the powders were revealed by X-ray powder diffraction. Electrochemical properties of the powders calcined at different temperatures were discussed. It was shown that optimal electrochemical performance may be attained by using both slightly reductive atmosphere and moderate temperature of 600 °C.

#### Introduction

Lithium iron phosphate has become of great interest as storage cathode for rechargeable lithium batteries because of its high energy density, low raw materials cost, environmental friendliness and safety. At this time, the main obstacle for reaching the theoretical performances of LiFePO<sub>4</sub> at ambient temperature is its very low electronic conductivity. Possible means to overcome this major problem are the synthesis of a LiFePO<sub>4</sub>/electronic conductor composite compound to increase the extrinsic electronic conductivity, and the achievement of a small and homogeneous particle size distribution [1]. Here is presented novel synthesis route for obtaining composite powders made of olivine-type lithium iron phosphate and carbon combining sonochemical precipitation and calcination. Electrochemical properties of the powders calcined at different temperatures were discussed.

#### **Experimental**

The reaction mixture, consisting of 30 ml of 1wt% polyvinyl alcohol (PVA) aqueous solution, 25 ml of 0.2 M aqueous solution of FeSO<sub>4</sub>\*7H<sub>2</sub>O, and appropriate amount of solid Li<sub>3</sub>PO<sub>4</sub>, was exposed to the ultrasound irradiation. The above mixture was sonicated for one hour by a Vibracell sonicator VCX 750 (Sonics & Materials Inc.) operating at 20 kHz, while reductive gas (75% Ar and 25% H2) was bubbled through it. The reaction product was centrifuged, washed with isopropanol, dried at 120 °C under vacuum and calcined at three temperatures 500, 600 and 700°C, in a slightly reductive atmosphere (95% Ar and 5 % H<sub>2</sub>) for 1.5 hour. A

PVA solution was used as a source of carbon which would enhance the electronic conductivity and suppress particle growth.

X-ray diffraction data were collected on a Philips PW 1050 diffractometer with Cu-K $\alpha_{1,2}$  radiation (Ni filter) at the room temperature. Measurements were done in 20 range of 10-60° with scanning step width of 0.05° and 4 s times per step.

Electrochemical characteristics were evaluated by using galvanostatic charge/discharge tests within 2.7-4.1V versus Li/Li<sup>+</sup> voltage window, and C/3 current density.

Thermal analysis of the sample was performed on SDT 2960 simultaneous DSC-TGA TA Instruments in order to determine carbon content [2].

#### **Results and Discussion**

X-ray powder diffraction patterns (Figure 1) revealed the differences between powders obtained by varying the calcination temperature. In all cases powders of phospholivines were obtained. It was shown that combining 500 or 600 °C with slightly reductive atmosphere resulted in single-phased olivine type LiFePO<sub>4</sub> powders with no detectable Fe(III) impurities. On the other hand, the temperature increase (700°C) caused the formation of another phase Fe<sub>2</sub>P beside olivine type LiFePO<sub>4</sub>.

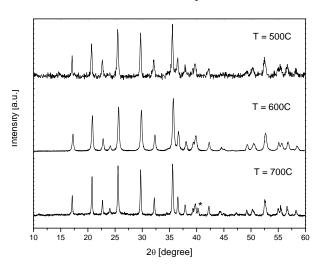


**Fig. 1.** XRD patterns of composites LiFePO<sub>4</sub>/C prepared by using sonochemical reaction with additional thermal treatment at 500, 600, and 700 °C, from the top to the bottom of the picture, respectively. Peak position of Fe<sub>2</sub>P phase is marked with asterisk.

Apparently, reductive atmosphere together with the organic component in the precursor facilitate the reduction of phosphates into phosphides at 700 °C. There is no evidence for the formation of crystalline carbon, so internal carbon in all samples could be treated as a contribution to background. amount of an in situ formed carbon was determined by heating the powder in air, and the estimated value was 5wt%. The in situ formed carbon partly coated LiFePO<sub>4</sub> particles as shown elsewhere [3]. Electrochemical performance of each sample, used as a

cathode of a Li-ion battery, was examined by charge-discharge tests. The cyclings were done between 2.7 and 4.1 V and the

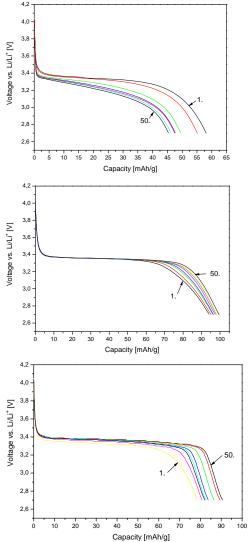


**Fig. 2.** Discharge curves for LiFePO<sub>4</sub>/C samples obtained by the use of sonochemical reaction with calcination at 500, 600, and 700°C from the top to the bottom of the picture, respectively. Current density was C/3.

current density was 59.7 mAh/g which corresponds nearly to C/3 rate. The discharge curves are shown in Figure 2. The best electrochemical performances showed the powder calcined at 600 °C, reaching 100 mAh/g at the end of the fiftieth cycle with excellent capacity retention, while the powder calcined at 700 °C showed slightly lower capacity. which is approximately proportional to the amount of pure LiFePO<sub>4</sub> present in the samples. Powder calcined at 500 °C showed drastically different electrochemical behavior. Such different properties are probably consequences of lower crystallinity of the powder calcined at 500 °C, considering larger full width at half maximum observed in the XRD pattern of the specimen (Figure 1).

#### Conclusion

Olivine structured LiFePO<sub>4</sub>/C composites can be successfully synthesized by combining sonochemical precipitation and calcination. It was found that 600 °C is optimal temperature for obtaining powder of high purity with acceptable electrochemical performances. This method may also be suitable for selective doping with supervalent cations to increase the intrinsic electronic conductivity of LiFePO<sub>4</sub> powder.

- [1] S.-Y. Chung, J.T. Bloking, and Y.-M. Chiang, Nature Mater., 2002, 1, 123-128.
- [2] Sh. Yang, Y. Song, P. Y. Zavalij, M. S. Whittingham, Electrochem. Commun., 2002, 4, 239-244.
- [3] D. Jugović, M. Mitrić, N. Cvjetićanin, B. Jančar, S. Mentus, D. Uskoković, Solid State Ionics, 2008, 179, 415–419.

## FORMIC ACID OXIDATION ON PLATINUM DECORATED WITH COBALT(III) MACROCYCLIC COMPLEXES

S. Stevanović<sup>1</sup>, K. Babić-Samardžija<sup>2</sup>, S.P. Sovilj<sup>3</sup>, A. Tripković<sup>1</sup> and V.M. Jovanović<sup>1</sup>

<sup>1</sup>ICTM, Department of Electrochemistry, Njegoševa 12, P.O. Box 815, 11000 Belgrade, Serbia <sup>2</sup>Baker Petrolite, 12645 West Airport Blvd., Sugar Land, TX 77478, USA <sup>3</sup>Faculty of Chemistry, University of Belgrade, P.O. Box 158, 11001 Belgrade, Serbia

#### **Abstract**

Oxidation of formic acid was studied in acidic solution at Pt electrode decorated with three different mixed-ligand cobalt(III) complexes of the general formula  $[Co(Rdtc)cyclam](ClO_4)_2$ . The preliminar results showed increased catalytic activity of Pt with adsorbed complex ion for this reaction. The increase in catalytic activity depends on the structure of the complex applied and follows the order Morphdtc > Pipdtc > 4-Mepipdtc.

#### Introduction

In effort to improve activity of platinum for the reactions in fuel cells, several kinds of catalysts have been proposed including bi or ternary carbon supported one, platinum-based alloys, platinum dispersed on oxide supports and recently even platinum mixed with organic cobalt complexes. The latest one, enhanced the activity of Pt for methanol oxidation more than several 10-fold times if proper mass ratio of Pt:Co was applied[1]. According to the authors the coexistance of Pt-based sites and sites derived from metal complex is crucial for this increased activity which also dependes on the structure of metal complex precursor.

The aim of this work is to examine possible effect of some mixed-ligand cobalt(III) complexes with tetraazamacrocyclic ligand and heterocyclic dithiocarbamates of the general formula [Co(cyclam)Rdtc](ClO4)2 on formic acid oxidation at Pt polycrystalline electrode.

#### **Experimental**

Three heterocyclic cobalt(III) complexes of the general formula  $[\text{Co(cyclam)Rdtc}](\text{ClO}_4)_2$ ,  $[\text{Rdtc}^- = \text{morpholine- (Morphdtc)}, \text{piperidine- (Pipdtc)},$  and 4-methylpiperidine- (4-Mepipdtc) dithiocarbamates, respectively] were used to modify the surface of Pt polycrystalline electrode. Pt electrode was prepared by mechanical treatment with diamond past and cycling the potential between -0.2 V and 1.0 V vs SCE used in the experiments as referent electrode. Adsorption of each of the examined complex was performed by immersion of Pt electrode in  $10^{-4} \text{ M}$  complex solution during 60 s.

All of the experiments were performed at room temperature in threeelectrode compartment electrochemical cell with a Pt wire as the counter electrode. The electrocatalytic activity of Pt decorated with Co complex was studied in  $0.5 \text{ M H}_2\text{SO}_4 + 0.5 \text{ M HCOOH}$  solution. Formic acid was added in the solution while holding the electrode potential at -0.2 V. The potential was cycled between -0.2 V and 0.9 V with a sweep rate of  $50 \text{ mV s}^{-1}$  and  $1 \text{ mV s}^{-1}$ .

#### **Results and Discussion**

The structure of the applied [Co(cyclam)Rdtc](ClO<sub>4</sub>)<sub>2</sub> complexes is showen in Fig. 1.

**Fig. 1**: The structure of [Co(cyclam)Rdtc](ClO<sub>4</sub>)<sub>2</sub> complexes

We have shown earlier that electrochemical behavior of these mixed-ligand cobalt(III) complexes is influenced by the bidentate heterocyclic S,S'-ligands[2]. Also, these complexes exhibit influence on hydrogen evolution, oxygen reduction as well as iron dissolution, but the effect depends on bidentate dithiocarbamato ligand[3].

Cyclic voltammetry of Pt electrode decorated with Co(III) complex in 0.5 M  $H_2SO_4$  show that coverage of the Pt surface depends on the complex structure i.e. on dithiocarbamato ligand, exhibited by the decreased charge in hydrogen adsorption/desorption region.

Activity of Pt decorated with any of the complexes for the reaction of formic acid oxidation is increased in comparison with pure Pt. The degree of activity inhencement depend also on bidentate heterocyclic S,S' – ligand and is in order of Morphdtc > Pipdtc > 4-Mepipdtc (Fig. 2).

This difference in activity increase could be explained in correlation with earlier results of spectroscopic IR and NMR data of the  $[Co(cyclam)Rdtc](ClO_4)_2$  complexes[4,5]. Those results show shift in frequencies of partially delocalized >C ——N bond in IR spectra of the ligating  $>NCS_2$  group. Due to positive inductive effect of methyl group (in 4-Mepipdtc) v(CN) bond is shifted to lower energies. Heteroatom, on the other side, influences the v(C—N) bond because of the ability to release electrons which than gives higher electron density on the  $>NCS_2$  group and shifts the v(C—N) bond to higher energies (in Morphdtc). Activity of the examined Pt electrodes decorated with Co complexes could be controlled by electrostatic as well as hydrophobic interaction between the surface and the complex ion[8]. The basic characteristics of binding of the Rdtc ligands do not vary dra-

matically from complex to complex, but an important difference being that relatively high symmetry decrease in order of Morphdte > Pipdte > 4-Mepipdte, taking in account IR and NMR data. Accordingly to this order, the complexes are distinctively more mobile, causing chemical interactions occur on the surface with appreciable speed and enhanced selectivity. This approach opens up further intriguing prospects for studies.

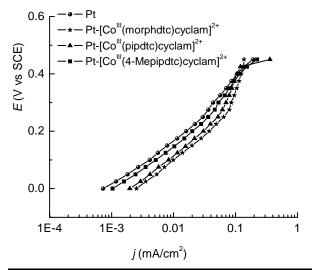


**Fig. 2:** Tafel plots for the oxidation of 0.5 M HCOOH in 0.5 M H<sub>2</sub>SO<sub>4</sub> on Pt and Pt decorated with [Co(cyclam)Rdtc](ClO<sub>4</sub>)<sub>2</sub> complexes

(sweep rate 1 mV/s)

Based on the correlation between spectroscopy results and oxidation of formic acid at the examined Pt electrodes decorated with Co complexes it can be assumed that the effect of the complexes on catalytic activity is in structural changes of Pt surface due to adsorption of complex ion.

- [1] T.Okada, Y.Suzuki, T.Hirose, T.Ozawa, Electrochim. Acta 2004, 49, 385.
- [2] V.M.Jovanović, K.Babić-Samardžija, S.P.Sovilj, Electroanal., 200, 13, 1129.
- [3] K.Babić-Samardžija, V.M.Jovanović, S.P.Sovilj, J.Serb. Chem. Soc. 2008 (accepted).
- [5] S.P.Sovilj, G.Vučković, K.Babić, S.Macura, N.Juranić, J.Coord.Chem., 1997, 41, 19.
- [7] S.P.Sovilj, K.Babić-Samardžija, Synth.React.Inorg.Met-Org.Chem., 1999, 29, 1655.
- [8] N.C. Gianneschi, M.S. Masar III, C.A. Mirkin, Acc. Chem. Res. 2005, 38, 825.

### ELECTROCHEMICAL STUDY OF METAL-CHLOROGENIC ACID COMPLEXES

N.I. Potkonjak<sup>1</sup>, S.Z. Milić<sup>2</sup>, S.Z. Gorjanović<sup>1</sup>, S.D. Veljović-Jovanović<sup>3</sup> and D.Ž. Sužnjević<sup>1</sup>

<sup>1</sup>Institute of General and Physical Chemistry, Studentski trg 12-16, 11000 Belgrade, Serbia
<sup>2</sup>Faculty of Chemistry, Studentski trg 12-16, 11000 Belgrade, Serbia
<sup>3</sup>Institute for Biological Research "Siniša Stanković", Bulevar Despota Stefana 142, 11000 Belgrade,
Serbia

#### **Abstract**

Differential-pulse polarography was applied in study of complexing ability of chlorogenic acid (CGA) with following metal ions: Pb(II), Cu(II), Cd(II), Zn(II) and Hg(II). It was proved complex ability oft CGA toward Pb(II) and Cu(II). Concerning Cd(II), Zn(II) and Hg(II) no complexing of CGA was confirmed. The 1:1 complex formation of CGA with lead and 1:1 and 1:2 with copper was proved by polarographyc titration and Job's method

#### Introduction

It is well known that metal-ion chelates of phenolic acids have shown high reactivity with oxygen species. The suppression of Fenton type reaction in OH radical formation is a result of CGA chelation with iron, so that the free radical reactions induced by iron is protected [1]. From this point of view the interactions of phenolic acids with metal-ions is a very important tool, so the study of their complexing ability with metal-ions is of great interest [2,3]. However, from the disposable literature data, electrochemical methods were not widely included in the mentioned researches. The present authors aimed to give evidence about CGA interaction with several metal ions by applying differential pulse (DP) polarography.

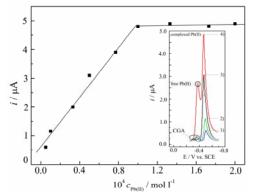
#### **Experimental**

Differential-pulse polarography was applied. The working electrode was dropping mercury electrode, the auxiliary electrode was a Pt-plate and the reference one was a saturated calomel electrode (SCE). Two supporting electrolytes were used: 0.05 mol l<sup>-1</sup> Tris buffer, pH 7.5, and 0.05 mol l<sup>-1</sup> phosphate buffer, pH 7.0. Investigated metal-ion standard solutions were prepared from their analytical grade (p.a.) salts. The chlorogenic acid (CGA) standard solution was freshly prepared from p.a. substance before each set of experiments. The cell temperature was kept at 23 °C.

#### **Results and Discussion**

In order to investigate Pb(II)-CGA system, polarographic titration was performed with Pb(II) addition to the buffered solution of CGA. As Fig. 1 shows, the addition of Pb(II) to CGA produces the increase of the DPP peak approximately at - 0.5 V

which is attributed to the reduction of Pb(II) from complex formed with CGA. When the height of this peak current approaches saturation, the peak current of free metal-ion reduction appears at -0.39 V. Concentration dependence of peak current (at -0.54 V) presented in Fig. 1 indicates that molar ratio of Pb (II)/CGA in the complex formed is 1:1. Aiming to ensure previous statement, Job's method was applied. It was found that the maximum at Job's plot obtained at 0.5 molar fraction of Pb, n, corresponded to 1:1 molar ratio of lead to CGA (insert Fig. 2).



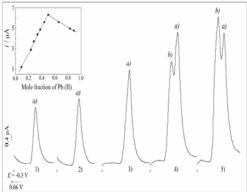


**Fig. 1.** Polarographic titration curve for complexed Pb(II). Insert: DP polarograms of 1  $10^{-4}$  mol  $1^{-1}$  CGA in Tris buffer, titrateted with Pb(II)-ion: 1) 5.0  $10^{-6}$ , 2) 1.0  $10^{-5}$ , 3) 5.0  $10^{-5}$  and 4) 1.0  $10^{-4}$  mol  $1^{-1}$ .

**Fig. 2.** DP polarograms of Pb(II)–CGA complex reduction from Tris buffer solution for n values: 1) 0.24, 2) 0.34, 3) 0.44, 4) 0.50 and 5) 0.66. Insert: Job's plot obtained for Pb(II)–CGA complex.

Concerning Cu(II)-CGA system, the starting solution for polarographic titration was 1 10<sup>-4</sup> mol I<sup>-1</sup> CGA in phosphate buffer. By gradual addition of Cu(II) into the solution of acid, the peak a) (Fig.3), of metal-ion reduction from complex, appears at -0.45 V. After further addition of Cu(II), the peak b) appears at more positive potential (-0.30 V). While peak a) becomes constant in height, peak b) increases by further addition of standard solution. Concentration dependence of peak current (at -0.45 V) presented in Fig. 3 indicates that molar ratio of Cu (II)/CGA is 1:2.

Figure 4 shows series of DP polarograms recorded for series of solution containing different molar fractions of Cu (II) with the respect of CGA. The existence of complex at molar ratio of 1:2 of Cu (II)/CGA was confirmed by analysis of peak current a), presented on plot a) in Fig 4. At higher molar fractions of copper peak current b) could be observed. Furthermore, at slightly positive potential with respect to peak current b) at DP polarogram 6) an inflection becomes visible. This indicated to the existence of two reducible Cu (II) species. The maximum in Job's plot was found at molar fraction of 0.5 when method of continuous variation was conducted, with the respect to peak b), presented on plot b) in Fig 4. The origin of this peak can be assigned to another complex of Cu (II) with CGA where the molar ratio of metal to ligand is 1:1. Therefore, it is reasonable to assume that the origin of noticed inflection corresponds to the reduction of free Cu<sup>2+</sup>. Obtained results

regarding complexing ability of CGA to Cu (II), i.e. the existence of two complexes, 1:1 and 1:2, are in agreement with result reported by Psotová et al. [2]. Regarding Cd(II), Zn(II) and Hg(II) no complexing ability of CGA was proved.

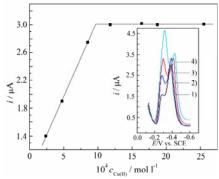


**Fig. 3.** Polarographic titration curve for complexed Cu(II). Insert: DP polarograms of CGA in phosphate buffer in the presence of Cu(II)-ion: 1) 8.5 10<sup>-4</sup>, 2) 1.1 10<sup>-3</sup>, 3) 1.8 10<sup>-3</sup> and 4) 2.5 10<sup>-4</sup> mol 1<sup>-1</sup>.

**Fig. 4.** DP polarograms of Cu(II)–CGA reduction from buffered solution for n values: 1) 0.09, 2) 0.24, 3) 0.33, 4) 0.38, 5) 0.47 and 6) 0.66. Insert: Job's plot obtained for Cu(II)–CGA complex.

#### Conclusion

Complexing ability of CGA with Pb(II), Cu(II), Cd(II), Zn(II) and Hg(II) was tested by applying polarographyc titration and Job's method. It was found that CGA can form complex with Pb (II), 1:1 molar ratio of lead to CGA and with Cu(II), 1:1 and 1:2 molar ratio of copper to CGA. Investigation of chelation of CGA with these metal-ions, but also complexing ability of other phenolic acids will be subject of our further studies.

#### Acknowledgement

The support of this research by the Ministry of Science of the Republic of Serbia through projects No. 142025 and No. 143020 is gratefully acknowledged.

- [1] Y. Kono, S. Kashine, T. Yoneyama, Y. Sakamoto, Y. Matsui, H. Shibata, Biosci. Biotechnol. Biochem., 1998, **62**, 22-27.
- [2] J. Psotová, J. Lasovský, J. Vičar, Biomed. Papers, 2003, 147, 147-153.
- [3] H.S. Mahal, S. Kapoor, A. K. Satpati, T. Mukherjee, J. Phys. Cem. B, 2005, 109, 24197-24202.

#### POLAROGRAPFIC BEHAVIOUR OF CHLOROGENIC ACID

N.I. Potkonjak<sup>1</sup>, S.Z. Milić<sup>2</sup>, S.N. Blagojević<sup>1</sup> and D.Ž. Sužnjević<sup>1</sup>

Institute of General and Physical Chemistry, Studentski trg 12-16, 11000 Belgrade, Serbia

<sup>2</sup>Faculty of Chemistry, Studentski trg 12-16, 11000 Belgrade, Serbia

#### **Abstract**

Direct-current and differential-pulse polarographic behavior of chlorogenic acid (CGA) was studied in Tris buffer, pH 7.5. Nature of anodic waves (peaks) observed at -0.02 V and -0.18 V vs. SCE was determined trough the dependence of limiting current on depolarizer concentration and on drop life time. Both of these diagnostic criteria suggested to the adsorptive behavior of CGA which was followed with catalysed disproportion reaction of mercuric mercury ions in the presence of CGA.

#### Introduction

Chlorogenic acid (3-caffeolyl-D-quinic acid; CGA) is an ester formed between caffeic acid and quinic acid. This polyphenol compound is a powerful natural antioxidant, synthesized in many fruits [1]. Cyclic voltammtery and potentimetric titration are electrochemical methods mostly applied in determination of antioxidant capacity of CGA [2,3]. Despite large number of electroanalytical studies of polyphenol compounds, polarographic behavior of these deficient in literature data. Ferreira et al. have reported possible application of differential-pulse polarography in determination Cinnamic acid in Human urine [4]. Aim of this research is to present polarographic behavior of CGA.

#### **Experimental**

Polarographic methods, i.e. direct current (DC) and differential pulse (DP) polarography were applied. Current-potential (*i-E*) curves were recorded by using a PAR 124 polarographic analyzer. The working electrode was dropping mercury electrode, the auxiliary electrode was a Pt-plate and the reference one was a saturated calomel electrode (SCE). Supporting electrolyte was 0.05 mol l<sup>-1</sup> Tris buffer, pH 7.5. Investigated metal-ion standard solutions of 0.01 mol l<sup>-1</sup> were prepared from analytical grade (p.a.) salts. The CGA standard solution of 0.01 mol l<sup>-1</sup> was freshly prepared from SIGMA p.a. The cell temperature was kept at 23 °C.

#### **Results and Discussion**

Characteristic DC and DP polarografic curves obtained with different CGA concentrations are shown in Fig.1. Existence of two anodic waves (peaks) at -0.02 V (a) and -0.18 V (b) could be observed. As comparative analysis showed, the appearance of wave (b) recorded in DC mode is not followed by peak in DP mode at

low concentrations of CGA. While in the case of DC polarography, wave (b) was noticed at the concentration of  $2.2 ext{ } 10^{-4} ext{ } ext{mol } 1^{-1}$ , (Fig. 1, case 3), corresponding peak (b) becomes noticeable in DP mode when CGA concentration was increased to about  $1.0 ext{ } 10^{-3} ext{ } ext{mol } 1^{-1}$  (Fig. 1, case 4).

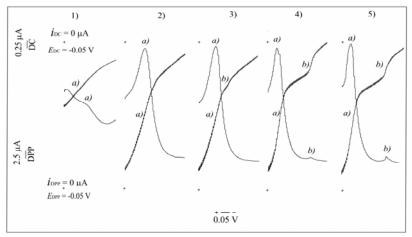


**Fig. 1.** DC and DP polarographic spectrum of different CGA concentrations: 1) 5 10<sup>-6</sup> mol 1<sup>-1</sup>, 2) 1.2 10<sup>-4</sup> mol 1<sup>-1</sup>, 3) 2.2 10<sup>-4</sup> mol 1<sup>-1</sup>, 4) 8.9 10<sup>-4</sup> mol 1<sup>-1</sup>, 5) 1.1 10<sup>-3</sup> mol 1<sup>-1</sup>.

In order to determine the nature of both DC waves, we applied the techniques that permit identification of a particular type of current: the dependence of limiting current on depolarizer concentration and on drop life time [5]. In Fig. 2 curve a) the dependence of limiting anodic current,  $i_1$ , on CGA concentration for wave a), (obtained from Fig. 1), points out to its adsorption nature, and for wave b) to its kinetic-catalytic nature.

In the Fig. 3 DC polarographic

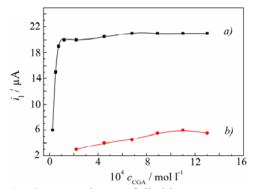


**Fig. 2.** Dependence of limiting current on CGA concentration of waves a) and b) presented at curves a) and b), respectively.

waves are presented as a function of drop life time ( $\tau$ ). According to dependences of  $i_1$  values on  $\tau$ , shown as an insert in the same figure, it is proved that the wave (a) is adsorptive and the wave (b) is kinetic in nature, based on known criteria in polarography [5]. Origin of these two processes could be attributed to adsorptive behavior of CGA with anodically produced meruric ions at the mercury electrode and to catalysed disproportion reaction of Hg (I)-CGA compound.

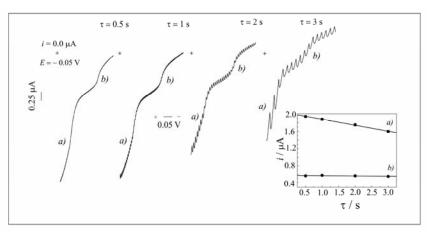


**Fig.3.** DC polarographic spectrum of 1  $10^{-3}$  mol  $1^{-1}$  CGA concentration in 0.05 mol  $1^{-1}$  at different mercury drop life time ( $\tau$ ). Insert: dependence of limiting current of wave a) and b) as a function of  $\tau$ .

#### Conclusion

Chlorogenic acid shows two waves (peaks) on DC/DP polarographic spectrum. Diagnostic analysis of identification of type of polarographic current was applied. Analysis reveal that CGA shows adsorptive behavior toward dropping mercury electrode and catalytic toward disproportion reaction of mercuric mercury ions.

#### Acknowledgements

The authors gratefully acknowledge financial support of the Ministry of Science of the Republic of Serbia provided through the project No. 142025.

- [1] Y. Kono, K. Kobayashi, S. Tagawa, K. Adachi, A. Ueda, Y. Sawa, H. Shibata, Biochim. Biophys. Acta, 1997, 1335, 355-342.
- [2] W.R. Sousa, C. da Rocha, C. L. Cardoso, D. H.S. Silva, M. V. B. Zanoni, J. Food Compos. Analys., 2004, 17, 619-633.
- [3] P. A. Kilmartin, Antioxidants&Redox Signaling, 2001, 3, 941-955.
- [4] V.S. Ferreira, C.B. Melios, M.V.B. Zanoni, N.R. Stradiotto, Analyst, 1996, 121, 263-267.
- [5] J. Heyrovský, P. Zuman, Practical Polarography, Academic Press Inc, London, 1968, Ch. 2.

#### ELECTROREDUCTION OF PUSH-PULL 5-SUBSTITUTED 2-ALKYLIDENE-4-OXO-THIAZOLIDINE DERIVATIVES

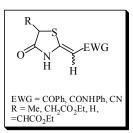
I. Cekić-Lasković<sup>1,2\*</sup>, D. Minić<sup>1,2</sup>, M. Baranac-Stojanović<sup>2,3</sup>, R. Marković<sup>2,3</sup> and E. Volanschi<sup>4</sup>

<sup>1</sup>Faculty of Physical Chemistry, Studentski trg 12, Beograd, University of Belgrade, Serbia, \*isidora@ffh.bg.ac.yu

<sup>2</sup>Center for Chemistry ICTM, P.O. Box 473, 11001 Belgrade, <sup>3</sup>Faculty of Chemistry, University of Belgrade, Studentski trg 16, 11001 Belgrade and <sup>4</sup>Faculty of Chemistry, University of Bucharest, Romania

#### **Abstract**

As a continuation of our investigation on electrochemical activity of *push-pull* 5-substituted 2-alkylidene-4-oxothiazolidines, differing in R at C(5)-position and electron withdrawing group (EWG), we have attempted for the first time to study the electrochemical behaviour of (2*Z*,5*Z*)- and (2*E*,5*Z*)-(5-etoxycarbonylmethylidene-4-oxothiazolidin-2-ylidene)-*N* phenylethana-mides (R: =CHCO<sub>2</sub>Et) by combining cyclic voltammetry with spectral EPR and UV-VIS-absorption techniques in aprotic media (0,1 M TBAHFP in DMSO, ACN and CHCl<sub>3</sub>).



5-substituted 2-alkylidene-4-oxothiazolidines

#### Introduction

Push-pull alkenes are substituted olefins containing one or two electron-donating substituents (D) on one end of a C=C double bond and one or two electron-accepting substituents (A) at the other end. Electronic D-A interactions via the C=C bond result in a polarization of the "push-pull" system [1]. Consequently, an increase of the push-pull character is associated with a decrease of the π-bond character of the polarized C=C bond. In turn, the corresponding π-bond orders of the C-D and C-A bonds are increased. The push-pull effect is of decisive influence on both the dynamic behavior and the chemical reactivity of these compounds.

Stereodefined 2-alkylidene-4-oxothiazolidines 1 exemplify typical *push-pull* compounds which can exist in different configurational and conformational forms and have been previously characterized by <sup>1</sup>H NMR and <sup>13</sup>C NMR, IR, UV, MS spectroscopy and X-ray structural analysis[2,3]. One of the characteristic processes of *push pull* alkenes 1, based on a lowering of the rotational barrier of the C=C bond at the C(2) position, is configurational isomerisation which can be followed by dynamic <sup>1</sup>H NMR spectroscopy under proper experimental conditions.

#### **Experimental**

Cyclic voltammetry (CV) experiments were performed on a VOLTALAB-40 electrochemical device using one-compartment electrolytic cell with stationary and rotating Pt-EDI 101 disc electrode (RDE) of 2 mm diameter as working electrode, Pt counter electrode and Ag/Ag<sup>+</sup> reference electrode. Optical spectra during the chemical and

electrochemical reduction of the selected substrates, i.e., (2*E*,5*Z*)- and (2*Z*,5*Z*)-(5-etoxycarbonylmethylidene-4-oxothiazolidin-2-ylidene)-*N*-phenylethanamides **1a** (EWG: CONHPh; R: =CHCO<sub>2</sub>Et), were recorded on the Unicam Helios-α UV-VIS spectrophotometer and a Radelkis potentiostat. The EPR spectra were recorded on a JEOL FA 100 spectrometer in the X-band frequency. Numerical simulations of the voltammograms were performed with the BAS Digisim simulator 3.03. Semiempirical MO calculations were performed using PM3 hamiltonian and EF (eigen vector following) optimisation algorithm, MOPAC program package and HyperChem release 7 software (Hypercube Inc. Gainesville, Florida), RHF for closed shell and both ROHF and UHF for open shell structures without consideration of the solvent effect (in vacuo calculations).

#### **Results**

CV Measurements were performed in predried solution of the configurational isomers (2E,5Z)-1 and (2Z,5Z)-1 (concentration: 2 ,4, 6 and 8 mM) in 0.1 M TBAHFP in DMSO used without purification at various temperatures and scan rates. The CV data (**Fig. 1**) of both, (2E,5Z)-1 and (2Z,5Z)-1 isomers allow to assign the two peaks to the first reduction step of both isomers, whereas (2E,5Z)-1 is being less susceptible to reduction, than that of the (2Z,5Z)-1 (-0.8V vs-0.6V) due to the intramolecular H-bond stabilization of the (2E,5Z)-1. The complex structure of the second reduction peak and an appearance of the oxidation peak after sweeping the potential in reduction till -1.5V, suggest that the oxidation peak is the result of the prior reduction, after the second wave.

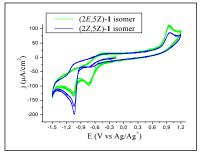


Fig. 1 Cyclic voltammograms of (2E,5Z)-1 and (2Z,5Z)-1 isomers in 0,1M TBAHPF/DMSO, c = 4mM, v=100mV/s, room temperature

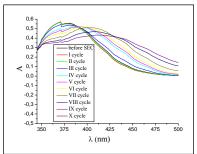


Fig. 2 Spectroelectrochemical evidence of intermediate species and possible products in reduction of (2E,5Z)-1 isomer in 0,1M TBAHFP/DMSO

CV (stationary electrode) and linear voltammetry (RDE) were employed to characterize the electron transfer steps (electron transfer rates  $k_s$ , transfer coefficients  $\alpha$  and diffusion coefficients  $D_0$ ). Based on other electrochemical criteria[4] and RDE results, an ECE mechanism supported by Digisim simulation, can be suggested.

In order to get better insight into the reduction mechanism of compound 1a, optical spectra were recorded during the chemical and electrochemical reduction using *in situ* techniques under different conditions (strong alkaline media:

TBOH in DMSO). The set of curves (**Fig. 2**) obtained at the potential of the first reduction wave at -0.6V suggests the limited reversibility of the process, as indicated by the decrease on the band at 372nm (the (2*E*,5*Z*)-1 isomer), the presence of two intermediate species (bands at 420 and 440nm) and the evolution towards a reduction product (absorption band at 350nm). In CHCl<sub>3</sub> the process is not visible at room temperature even upon prolonged reduction at -0.6V or -1V.

In order to identify the paramagnetic species in the reduction process of 1a, EPR spectrum was obtained during the electrochemical reduction at the first wave potential. The following detectable intermediates were observed: an anion radical (EPR and band at 420nm, appearing first at -0.6V) and anion (band at 440nm, appearing under prolonged electrolysis or higher potentials), formed from a dianion by protonation. The proton source in an aprotic solvent is most likely an acidic lactam NH proton from the substrate 1a. The anion has also been postulated as an intermediate in reduction of various 4-oxothiazolidines 1 (R: CH<sub>2</sub>CO<sub>2</sub>Et) with NaBH<sub>4</sub>[5]. MO Calculations were performed in order to explain the dependence of the redox properties on the electronic structure of the neutral compound 1a and the characteristic follow-up reactions in terms of the electronic features of the electrogenerated species, the anion radical and the dianion.

#### Conclusion

Electrochemical properties of (2*E*,5*Z*)- and (2*Z*,5*Z*)-(5-etoxycarbonylmethylidene-4-oxothiazolidin-2-ylidene)-*N*-phenylethanamides 1 were studied by cyclic voltammetry and UV-VIS spectroelectrochemistry in DMSO, ACN and CHCl<sub>3</sub>. Corroboration of electrochemical and spectral results allows proposition of a possible reaction pathway in electrochemical redox processes.

#### Acknowledgement

We wish to acknowledge financial support by the Ministry of Science of the Republic of Serbia, Grant No. 142007 (to R.M.) and an assistance and expertise of prof. Elena Volanschi from Department of Physical Chemistry, Faculty of Chemistry, University of Bucharest.

- [1] R. G. Giles, N. J. Lewis, J. K. Quick, M.J. Sasse, M. W. J. Urquhart, *Tetrahedron*, 2000, **56**, 4531-4537.
- [2] R. Marković, M. Baranac, Z. Džambaski, M. Stojanović, P. J. Steel, *Tetrahedron*, 2003, **59**, 7803-7810.
- [3] R. Marković, M. Baranac, N. Juranić, S. Macura, I. Cekić, D. Minić, *Journal of Molecular Structure*, 2006, **800**, 85-92.
- [4] D. M. Minić, I. Cekić, F. T. Pastor, V. Jovanović, R. Marković, *Russian Journal of Physical Chemistry A*, 2007, **81(9)**, 1458-1462.
- [5] R. Markovic, M Baranac, M. Stojanovic, Synlett, 2004, 1034-103.

# VOLTAMMETRIC CHARACTERIZATION OF FISETIN AND FISETIN-ALUMINIUM (III) COPLEXES IN AQUEOUS BUFFERED SOLUTIONS: IMPLICATIONS ON IN VITRO ANTIOXIDANT ACTIVITY

J.M. Dimitrić-Marković<sup>1</sup>, Lj.M. Ignjatović<sup>2</sup> and M.S. Petrović

1.2 University of Belgrade, Faculty of Physical Chemistry,
Studentski trg 12-16, 11000 Belgrade
markovich@ffh.bg.ac.yu,

#### **Abstract**

Fisetin and fisetin-aluminium (III) complexes formed in aqueous buffered solutions were characterized by cyclovoltammetry. Fisetin and its complexes show electrochemical activity in a wide range of pH values of the supporting electrolyte, and they undergo the similar mechanism of electrode oxidation. Oxidation potential values indicated rather good antioxidative properties found with these species. The antioxidative ability of fisetin and its aluminium (III) complexes is dependent upon pH value of the medium and the structure, i.e. stoichiometry of the complexes formed.

#### Introduction

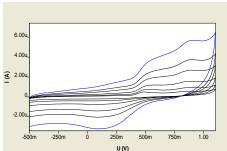
Flavonoids are aromatic secondary plant metabolites found in higher vascular plants particularly in the flower, leaves and bark. Overwhelmingly, biological and physiological activities of flavonoids, including anti-allergic, anti-mutagenic, anti-hypertensive, anti-inflammatory, anti-viral, anti-arthritic and inhibitory activity on some enzymatic systems, are generally related to their pronounced antioxidant activity which arises from their ability to scavenge free radicals [1-3].

Antioxidants are a group of substances which, when present at low concentrations, in relation to oxidizable substrates which have to be repaired and reduced, significantly inhibit or postponed oxidative processes, while often being oxidized themselves. Antioxidants may exert their effect on biological systems by different mechanisms including metal ion chelation, thereby eliminating potential free radicals, or electron donation, as reducing agents. The antioxidative activity of flavonoids besides the direct free radical scavenging, include also trace metal chelation reactions [4-8]. By chelating metal ions flavonoids generally prevent the metal-catalyzed free radical generation and their reactions and accordingly can protect the very important biologically active molecules from oxidative stress [6-8]. Some investigations show that complexed flavonoid molecules exibit more effective radical scavenging action than uncomplexed molecules. The applications of antioxidant flavonoids are numerous and widespread. They are used in preventing natural pigments from discoloration, as additives to cosmetic products, food (especially the one with high fat content), beverages and baking products.

#### **Results and Discussion**

Antioxidative properties of fisetin and its aluminium (III) complexes, formed in a wide range of a pH values (pH 2-9) of acetate buffered solutions, were electrochemically observed by cyclovoltammetry using the values of oxidation potentials as quantitative parameter in determining their oxidation capabilities.

Cyclovoltammograms of fisetin in the pH range investigated show two oxidative peaks at pH values lower than pH 5.0 and only one peak at higher pH values. Figure 1 shows very low intensity reduction CV peak indicating irreversibility of the electrochemical process. The irreversibility of the electrochemical oxidation is also characterized by the dependence of the CV peaks potentials on logarithm of the rate of potential change. Determined  $\alpha n_a$  (irreversibility coefficient) values are presented in Table 1.



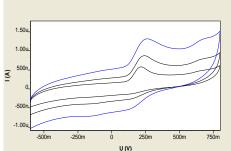


**Fig. 1** CV curves of fisetin (c=1x10<sup>-2</sup> moldm<sup>-3</sup>) at pH 2.0 and pH 7.0, the polarization rate from 25-500 mV/s and 25-100mV/s (from left to the right)

**Table 1.** The *Ep-logy* parameters of the CV oxidation peaks of fisetin

	Peak I		Peak II		
рН	B(mV)	$\alpha n_a$	B(mV)	$\alpha n_{\alpha}$	
2	59.801	0.502	24.900	1.205	
4	24.902	1.205	17.120	1.752	
6	28.701	1.045	19.280	1.556	
7	50.370	0.596	/	/	
9	48.400	0.620	/	/	

(B-the slope of the *Ep-logv* line,  $\alpha N_{\alpha}$ -irreversibility coefficient)

According to our obtained results and previously published results it is possible to presume that oxidation of fisetin proceeds through detachment of two electrons and oxidation of the hydroxyl group at C3 to keto group. Scheme 1 presents oxidation path of fisetin molecule. Fisetin molecule is strong antioxidant agent especially at pH 7.0 (CV oxidation peak is at +0,212 V). Electrochemical

activity of fisetin-aluminium complexes formed at different pH values and at different components mole ratios are not the same. The dependence of the more

Scheme 1. Scheme of electrochemical oxidation of fisetin

positive oxidation peak on the aluminium (III) mole number is not the same for all the pH values investigated indicating at the same time the influence of the medium (pH value) and the structure and stability of the complexes formed .

#### Conclusion

Fisetin molecule exhibits antioxidative activity through the whole interval of the pH values investigated. According to its CV potential values it is possible to conclude that its antioxidative activity is strongest at pH 7.0 which is of the most biological interest. Fisetin-aluminium (III) complexes also show antioxidative activities which follow the complexes stabilities.

- [1] P. Ferriola, V. Cody, E. Middleton, Biochem. Pharm., 1989, **38(10)**, 1647-1624.
- [2] W. F. Hodnick, D.L. Duval, R.S. Perdini, Biochem. Pharm., 1994, 47, 573-580.
- [3] H. Wang, M. G. Nair, G. M. Strasburg, A. M. Chang, J. I. Booren, D. Gray, L. Dewitt, Journal of Natural Products 1999, 62, 294-301.
- [4] G. Cao, E. Sofic, R. Prior, Free Radical Biol. & Med. 1997, 22(5), 749-760.
- [5] A.D Sarma, Y.Sreelakshemi, R. Sharma, Phytochemistry, 1997, 45, 671-677.
- [6] L. Mira, M.T. Fernandez, M. Santos, R. Rocha, M.H. Florenico, K.R. Jennings Free Radic. Res. 2002, 36, 1199-1208.
- [7] M. Fiorani, R. De Sancitis, R. De Bellis, M. Dacha, Free Radical Biol. & Med. 2002, 32, 64-72.
- [8] M.T. Fernandez, M. L. Mira, M. H. Florenco, K. R. Jennings, J. Inorg. Biochem. 2002, 92, 105-111.

## VOLTAMMETRIC BEHAVIOR AND ADSORPTIVE STRIPPING DETERMINATION OF DESACETYLCEFOTAXIME

M.M. Aleksić<sup>1</sup> and V. Kapetanović<sup>2</sup>

Faculty of Pharmacy, University of Belgrade, <sup>1</sup>Institute of Physical Chemistry, <sup>2</sup>Institute of Analytical Chemistry, Vojvode Stepe 450, P.O.Box 146, 11000 Belgrade

#### **Abstract**

The voltammetric behavior of desacetylcefotaxime (DCFX) is investigated by cyclic and differential pulse voltammetry in Britton-Robinson (BR) buffer (pH 2.0 – 10.0). Adsorptive character of the drug on the mercury electrode was observed. Based on the cathodic reduction peak at approximately - 0.3V in BR buffer (pH 2.8), a robust, highly reliable adsorptive stripping differential pulse voltammetric method (AdSDPV) was developed for determination of DCFX. The linearity was achieved in the concentration range  $2\cdot10^{-8}$  M -  $5\cdot10^{-7}$  M with limit detection and limit determination of  $4\cdot10^{-9}$  M and  $1.4\cdot10^{-8}$  M respectively.

#### Introduction

Cephalosporins represent the dominant class of antimicrobial agens, with wide broad spectrum of activity used against most respiratory and urinary infections. In the human organism, DCFX (Fig. 1.) is formed as a cefotaxime (CFX) metabolite after it is metabolized by esterases. DCFX keeps the antibacterial activity and is primarily eliminated by the kidneys [1]. In laboratory conditions DCFX is prepared by alkaline hydrolysis of CFX [2].

Fig. 1. Desacetylcefotaxime

The presence of methoxyimino group in side chain of DCFX molecule is very important for its electrochemical behavior. Our previous studies [3,4] resulted in the mechanistic scheme for the reduction of the Omethyloxime grouping of other third generation cephalosporins. It has been shown that its four-electron reduction occurred in two two-electron steps, corresponding to a reduction to the imine and amine, respectively.

Since both CFX and DCFX possesses metoxyimino group they show the same behavior. However, the absence of the COCH<sub>3</sub> group in C-3 position in DCFX molecule makes the methoxyimino reduction easier and it occurs as one four electron process at about 200 mV positively comparing to CFX.

#### **Experimental**

The voltammetric measurements were performed with an Amel 433-A computerized polarographic analyzer. Three-electrode system was employed: hanging mercury dropping electrode (HMDE), Ag/AgCl reference electrode and a Pt-auxiliary electrode. A Radiometer pH meter, PHM 220, with appropriate standard buffer solutions was used.

An aliquuot of 15ml of supporting electrolyte solution (BR buffer) was introduced into electrochemical cell and de-aerated with pure nitrogen for 10 min. A selected accumulation potential was then applied to a mercury drop, for a selected accumulation period, while the solution was stirred at 300 rpm. The stirring was then stopped, and after a 10 s rest period, an adsorptive stripping differential pulse voltammetry was applied in the negative direction over the range of 0.0 V to - 1.2V vs. Ag/AgCl. The quantification was performed by standard addition method under the optimized conditions. Cyclic voltammetry was performed using scan rate of 100 mVs<sup>-1</sup> and drop size of 40 arbitrary units (a.u.).

#### **Results and Discussion**

The voltammetric behavior of DCFX has been examined in the pH range 2.0 - 10.0 by using CV and DPV. In acid medium, pH<6, one well defined peak at -0.3 V is present. At pH>6 this peak is not well formed anymore, it is dragged out and exhibit small currents. This is probably due to its splitting as in case with CFX, so further DCFX analysis in base medium could not be done.

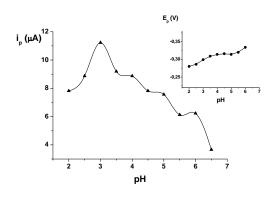


**Fig. 2.** The effect of the pH on the peak current and peak potential of reduction of desacetylcefotaxime on HMDE

The effect of the pH on the peak current and potential is presented in Fig. 2. The dependence of the peak current vs. pH shows maximum at pH = 2.8. The negative shift of the peak potential towards more negative values with increasing the pH indicates that protonation step precedes the electron transfer. The nature of the reduction process was studied by following the effect of the scan rate on the peak current.

Both  $i_p vs. v'^{2}$  and  $i_p vs. v$  dependencies gave non-linear plots, indicating that the diffusion-controlled process is strongly influenced by the adsorption. The irreversibility of the reduction process was confirmed at HMDE, since no anodic peak was observed in whole pH range.

After preconcentratoin of the drug onto the electrode surface, higher peak current was achieved, whereas the second cycle at the same mercury drop showed lower peak intensity due to the desorption of the DCFX from the mercury surface. In order to achieve the high sensitivity for determination of the accumulated drug, the cathodic adsorptive stripping voltammograms of 5·10-7 M DCFX were recorded in BR buffer (pH 2.8). Several experimental parameters were examined in developing a suitable analytical procedure for the determination of DCFX: the scan speed of 20mVs-1, pulse amplitude of -50mV, the potential pulse width of 20ms, and pulse repetition of 100ms were applied. Besides those four parameters, the influence of drop size, stirring rate and rest time on the peak current were also investigated.

In order to achieve best selectivity and sensitivity to determine DCFX a deposition potential of  $E_{acc}$  = -100 mV was selected. The peak current intensity gave a linear relationship with the accumulation time only for short times what means that DCFX is strongly adsorbed, and the adsorptive saturation of the mercury surface is reached in short accumulation period, so the accumulation time of 15s was chosen to evaluate the best conditions for the method proposed.

The linearity was achieved in the concentration range  $2\cdot10^{-8}\,\mathrm{M} - 5\cdot10^{-7}\,\mathrm{M}$  with limit detection and limit determination of  $4\cdot10^{-9}\,\mathrm{M}$  and  $1.4\cdot10^{-8}\,\mathrm{M}$  respectively. The proposed AdSDPV method was validated in terms of specificity, sensitivity, linearity, intra-day and inter-day precision and accuracy short-term and freeze and thaw stability.

#### Conclusion

The AdSDP voltammetry on a Hg drop electrode can be used to determine DCFX at trace levels due to the low detection limit at nano-levels. The sensitivity of the method is increased by effectively accumulated DCFX from aqueous solution samples onto mercury surface. The method proposed is fast, precise and simple to perform.

#### Acknowledgements

This work was supported by the Ministry for Science of the Republic of Serbia, Grant 142071.

- [1] K.B. Patel, D.P. Nicolau, C.H. Nightingale, R. Quintiliani, Pharmacol., 1995, 22, 49-55.
- [2] U.S. Pharmacopoeia 26-NF 2002, pp. 369-370.
- [3] V. Kapetanovic, M. Aleksic, P. Zuman, J. Electroanal. Chem. 2001, 507, 263-269.
- [4] M. Aleksic, V. Kapetanovic, P. Zuman, Collect. Czech. Chem. Commun. 2004, 69, 1429-1442.

## ELECTRONIC SURFACE PROPERTIES OF THE Pt<sub>x</sub>M<sub>1-x</sub>/Pt(111) (M=Sn, Bi) ALLOYS: DFT STUDY

I. Pašti\*, M. Petković and S. Mentus

Faculty of Physical Chemistry, University of Belgrade, Studentski trg 12-16, 11000 Belgrade, \*igor@ffh.bg.ac.yu

#### **Abstract**

Following the intention to correlate electrocatalytic and electronic behaviour of metallic surfaces, work function and d-band centre of  $Pt_xM_{1-x}$  (M=Sn, Bi) monolayers over Pt(111) surface were examined by DFT calculation. The results of two different calculation methods used to estimate work function agree very well with the experimentally obtained data. Centres of d-bands of platinum atoms in the surface layer were found to be compatible with the experimentally determined values of adsorption energies of different adsorbates.

#### Intoduction

Platinum is one of the most important catalysts and electrocatalysts (in fuel cells, electrolysers, etc.), but due to its limited content in earth's shell, much effort is invested nowadays to find effective substitutes either with reduced content, or without platinum at all. In this sense, some platinum alloys have been investigated, and atomic monolayers of  $Pt_xSn_{1-x}$  and  $Pt_xBi_{1-x}$  over Pt(111) surface were found to display promising effectiveness [1,2]. From the point of view of catalysis, two very important properties of the surface are work function and centre of d-band of surface atoms. In many studies, work function was correlated to structural and chemical conditions on the surface. Although calculation of the work function in the framework of density functional theory is well established, some problems connected to quantum size effect may arise [3]. Importance of d-band centre was first recognized by Nørskov and co-workers [4]. They used this parameter to predict catalyst behaviour and select the candidates for further experimental investigations. The aim of this work is to calculate work functions and d-band centres of platinum atoms in  $Pt_xSn_{1-x}/Pt(111)$  and  $Pt_xBi_{1-x}/Pt(111)$  surface alloys by means of DFT.

#### Methodology

DFT calculations were performed using PWscf which is part of Quantum ESPRESSO package for *ab initio* calculations [5]. The Perdew-Burke-Ernzerhof (PBE) functional within general gradient approximation (GGA) was used. As a smearing scheme Marzari-Vanderbilt smearing was used with broadening of 0.05 Ry. Kinetic energy cut off was 20 Ry and for Brillouin-zone integration Monkhorst-Pack set of 9 special k-points was used, as optimal for quality of calculation and calculation costs. Pt(111) surface and PtM(111) surface alloys were constructed using supercell with a thin metal (alloy) slab separated from its periodic

images by a layer of vacuum. In all cases 20 angstroms vacuum layer was separating surfaces. Surface alloy was set on both sides of the slab which allowed us to take the electrostatic potential on the edge of the supercell (in the middle of vacuum layer) as a  $V(+\infty)$ . For work function calculations, the following equation was employed:

$$W = V(+\infty) - E_E \tag{1}$$

where  $V(+\infty)$  was calculated as explained, and  $E_F$  denotes Fermi energy of the slab. In this way all the necessary data were obtained in single calculation. We also applied macroscopic average method [1] in which work function is calculated as:

$$W = \Delta V + V_{bulk} - E_{F\ bulk} \tag{2}$$

where  $\Delta V$ ,  $V_{bulk}$  and  $E_{F,bulk}$  are potential step across the surface, mean electrostatic potential in the bulk and Fermi energy of the bulk metal, respectively. The last two quantities are obtained in separate calculations on clean bulk Pt. Centre of d-bands of Pt atoms in the surface layer was calculated as centre of gravity of projected density of states.

#### Results

For clean Pt, the results of calculations fairly agree with the recently published ones [6]. The calculations performed for alloys show that work function decreases with the rise in mole fraction of solute elements. It was found also that Sn lowers work function of the surface alloy more than Bi. In both cases there is linear relationship between the work function and the mole fraction of solute element. The results are given in Table 1 and Figure 1a.

**Table 1.** The values of work functions, calculated by means of equations (1) and (2), (the later being given in parentheses), and the values of  $E_{d-band}$  centers (*italic*)

	$W / eV$ , $E_{d ext{-}band} / eV$							
Surface	Mole fraction of Me in the $Pt_xMe_{1-x}$ layer							
alloy	x = 1	x = 0.75	x = 0.67	x = 0.5	x = 0.33	x = 0		
	5.83	5.49	5.30	5.01	4.73	4.13		
$Pt_xSn_{1-x}$	(5.88)	(5.48)	(5.32)	(5.01)	(4.74)	(4.12)		
	-2.084	-2.174	-2.290	-2.518	-2.817	-		
	5.83	5.57	5.54	5.29	4.93	4.26		
$Pt_xBi_{1-x}$	(5.88)	(5.61)	(5.59)	(5.32)	(4.96)	(4.27)		
	-2.084	-2.268	-2.302	-2.460	-3.215	-		

The values of W for Pt(111),  $Pt_3Sn/Pt(111)$ ,  $Pt_2Sn/Pt(111)$  and pure Sn monolayer on Pt(111), determined experimentally, amount to 5.8, 5.4, 5.2 and 4.2 eV, respectively [2]. The here calculated values agree obviously very well with the measured ones, reported in ref. [2].

The shift of the band centre toward lower values was observed in both alloys, but it is more prominent in the case of PtBi alloy. In the light of theory of Nørskov,

this is in good agreement with experimental observation that values of binding energies of H, O and CO species on these surfaces are less than on pure Pt(111) surface [2].

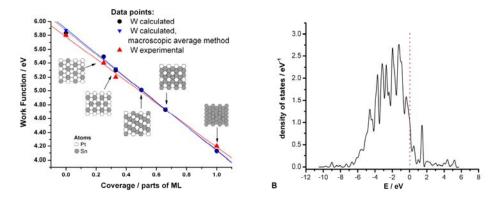


**Fig. 1.** Calculated values of work function (W) for  $Pt_xSn_{1-x}/Pt(111)$  compared with experimental values (A), and projected density of states of  $Pt_3Sn/Pt(111)$  surface alloy; energy is referred to  $E_F$  of the slab (B)

#### Conclusion

The results we obtained for work function of PtSn surface alloy are in excellent agreement with the experiments. The presence of Sn and Bi reduces the value of work function of Pt(111) proportionally to the mole fraction of these metals in surface layer. To our best knowledge no similar behaviour in surface alloys was previously studied theoretically. Results we obtained for d-band centres of surface alloys can be used to explain values of adsorption enthalpy of different adsorbates that were observed experimentally.

#### Acknowledgments

This work was supported by Serbian Ministry of Science within the projects No. 142047 and No. 142055 (M.P.).

- [1] J. Greeley, T.F. Jaramillo, J.Bonde, I. Chorkendorff, J. K. Nørskov, *Nature Materials*, 2006, **5**, 909-913
- [2] M.T. Paffett, S.C. Gebhard, R.G. Windham, B.E. Koel, J. Phys. Chem., 1990, 94, 6831-6839
- [3] C.J. Fall, N. Binggeli, A. Baldereschi, J. Phys.: Condens. Matter 1999, 11, 2689-2696
- [4] B. Hammer, J.K. Nørskov, Surface Science, 1995, 343, 211-220
- [5] S. Baroni, A. et al., Quantum- ESPRESSO, <a href="http://www.pwscf.org">http://www.pwscf.org</a>
- [6] N. E. Singh-Miller, N. Marzari, *Phys. Rev. Lett.* 2008. in press.

#### CHARACTERIZATION OF BORON AND NICKEL DOPED GLASSY CARBON ELECTRODES

A. Stanković, B. Živković and N. Vukelić Faculty of Physical Chemistry, University of Belgrade, Serbia

#### Abstract

Three glassy carbon samples: undoped, doped with boron, and doped with boron and nickel, prepared at 850 °C, were compared using various techniques such as XRD, FT-IR, and cyclic voltammetry. In doped samples boron carbide bonds were confirmed, while cyclic voltammetry measurements indicated high double layer capacity.

#### Introduction

Glassy carbon (GC) has a number of unique properties, including chemical and thermal inertness [1], hardness, high electrical conductivity, mechanical and dimensional stability. Although GC serves well as electrode material in electrochemistry; many attempts have been undertaken to improve its electrochemical properties by chemical modification [2]. Boron has been chosen as dopant because substitutional boron inhibits the desorption of CO and CO<sub>2</sub> and increases the oxidation resistance presumably by formation of a protective oxide coating at the surface.

#### **Experimental**

#### Preparations:

Phenol-formaldehyde resins were used as the starting material for the preparation of glassy carbon electrodes. Catalyst was urotropine. The ratio phenol-formaldehyde resin and urotropine used was 10: 1 (5 g: 0.5 g). These raw materials were mixed and homogenized in mortar, and dissolved in 5 ml of methanol. That is what is called undoped sample. Doped samples were made by addition of either boric acid alone (containing 400 mg of boron) or both boric acid (100 mg of boron) and nickel acetate (400 mg of nickel). Polymerization of samples was carried out up to 150 °C [3], while carbonization was carried out up to 850 °C. Decrement in mass for undoped sample is 39.68%, and for sample doped with boron 43.70% and with boron and nickel 48.65%.

#### The methods of characterization:

The X-ray diffractometry was performed by means of device PHILIPS PW 1710, using  $CuK_{\alpha}$  radiation ( $\lambda$  = 1.54178 nm) in the 2 $\theta$  range 10-80°, step 0.02°. The diffraction lines were assigned by means of computer program PCPDFWIN v. 2.00

For IR measurements FT-IR spectrometar Nikolet 6700 atr [4] (resolution of 2 cm<sup>-1</sup>) was used, with 64 scans.

Cyclic voltammetry (CV) [5] was performed by means of the device Metrohm 757VA Computrace. The commercial Metrohm GC electrode was used throughout this work also. We were deposit our undoped and doped pulverized electrode samples on surface of this GC electrode. The potentials were measured against the Ag/AgCl reference electrode. The counter electrode was a platinum foil electrode. The CV ex-

periments were carried out in the solution  $10^{-3}$  M K<sub>3</sub>[Fe(CN)<sub>6</sub>]. The initial and final potential were -1.0 V and +1.2 V, respectively, and scan rates were 20, 50 and 100 mV/s.

#### **Results and Discussion**

## *X-ray diffractometry:*

For undoped sample the X-ray diffractograms show two wide humps at 23.6° and 43.4°, originating from carbon, corresponding to the Miller indices (002) and (100). For a sample doped with boron, there are maximums from basic glassy carbon material, and several maximums at 14.6° from pure boron, and at 22.6°, 24.4° and 40.3° resulted boron carbid (Fig. 1). Also there is less sharp maximum at 43.4° which indicated that resulted boron carbid affect on reflection from 100 amble of undoped sample. For a sample doped with a boron and nickel, there are three sharp lines at the angles 44.5°, 51.8° and 76.3° belonging to the body centered cubic lattice of nickel.

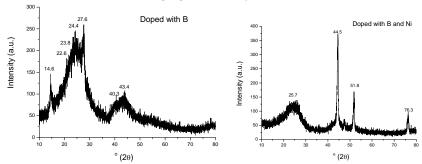


Fig. 1. XRD pattern for sample doped with: a) boron, b) boron and nickel

#### FT-IR:

In the FTIR spectra of the sample doped with boron, two peaks are visible, at 1100 cm<sup>-1</sup> and 1250 cm<sup>-1</sup>, attributed to boron carbide. In the spectra of a sample doped with both boron and nikel, the peak at 1250 cm<sup>-1</sup> is observed.

### Cyclic voltammetry:

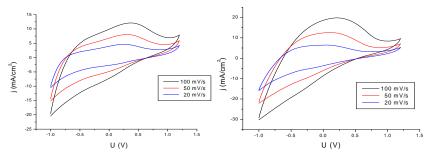
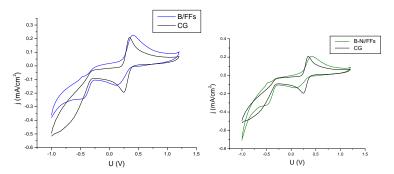


Fig. 2. Cyclovoltammograms of a sample doped with: a) boron, b) boron and nickel in 10<sup>-3</sup> M K<sub>3</sub>[Fe(CN)<sub>6</sub>] solution. Electrodes are made from rods of corresponding doped GC.

In cyclic voltammograms (Fig.2) of the sample doped with boron anodic peaks at -0.397V and 0.333V (100 mV/s), -0.444V and 0.287V (50 mV/s), -0.570V and 0.236V (20 mV/s), and cathodic peaks at -0.215V (100 mV/s), -0.076V (50 mV/s), and -0.078V (20 mV/s).

In the cyclovoltammograms (Fig.2) of the sample doped with both boron and nickel, anodic peaks are at -0.379V and 0.338V (100 mV/s), -0.449V and 0.269V (50 mV/s), -0.536V and 0.189V (20 mV/s), and cathodic peaks are at -0.053V (100 mV/s), 0.012V (50 mV/s), and 0.096V (20 mV/s).

On Fig.3 are voltammograms of commercial GC electrode before and immidiately after removing of pulverized doped electrodes samples bonded on the GC surface with Nafion®.



**Fig. 3.** Cyclic voltammograms (20 mV/s) of commercial undoped CG electrode (black on bouth figure), and for the same electrode after removing of pulverized samples doped with: a) boron (blue), b) boron and nickel (green); (in 10<sup>-3</sup> M K<sub>3</sub>[Fe(CN)<sub>6</sub>])

## **Conclusions**

By means of X-ray diffraction and FT-IR spectroscopy we confirmed that in GC samples doped with boron, boron carbide bond appears. By means of cyclic voltammetry we confirmed that large surface area corresponding with large double layer capacity of all samples. Also (Fig 3), we concluded that there has been some deactivation (widening of the peaks) of commercial GC electrode after removing of Nafion® films. Clearly visible peaks at about – 0.53 V are unexpected.

- S.Marinkovic, Z.Lausevic, M.Polovina, Modern carbon materials, Institute Vinca, Belgrade, 1999
- [2] G.M. Jenkins, K.Kawamura, *Polymeric carbon carbon fibre, glass and char*, Cambrige University Press, Cambrige (1976)
- [3] S. Mondal, A.K. Banthia, *Low-temperature synthetic route for boron carbide*, Journal of the European Ceramic Society 25 (2005) 287-291
- [4] S. Mentus, U. Mioč, *Selected methods of physicalchemistry analyses*, Faculty of physical chemistry, Belgrade, 1993
- [5] S. Mentus, *Electrochemistry*, Faculty of physical chemistry, Belgrade, 2001

# INFLUENCE OF NICKEL AND BORON ON TEXTURAL CHARACTERISTICS OF GLASSY CARBON

B. Živković, A. Stanković, N. Vukelić

Faculty of Physical Chemistry, University of Belgrade, Serbia

#### Abstract

Three glassy carbon samples: undoped, doped with boron one, and doped with boron and nickel one, prepared by carbonization of phenol-formaldehyde resin at 850 °C, were compared from the aspect of texture and density.

#### Introduction

Glassy carbon (GC) possess a unique combination of properties, including chemical and thermal inertness [1], hardness, impermeability to gases and liquids, high electrical conductivity, mechanical stability, and tanks to the widest potential window in aqueous solutions, it was widely used as indicator electrode in electrochemical investigations. Although GC serves well as electrode material, many attempts have been made to improve its electrochemical properties by chemical modification [2-4]. Boron has been chosen as dopant since it inhibits the desorption of CO and CO<sub>2</sub> and increases the oxidation resistance presumably by formation of a protective oxide coating on the GC surface.

# Experimental

# Preparations

The undoped samples were prepared from phenol-formaldehyde resin and urotropine catalyst, mixed in a mass ratio 10:1 (5 g: 0.5 g), homogenized in mortar, then mixed with 5 ml of methanol. To obtain boron doped sample, boric acid (containing 400 mg of boron) was added to the previous mixture. To obtain boron and nickel doped samples, both boric acid (100 mg of boron) and nickel acetate (400 mg of nickel) were added to the starting mixture. The polymerization was carried out up to 150 °C [5], carbonization up to 850 °C. Decrease of mass after carbonization for undoped sample was 39.68%, for sample doped with B 43.70% and for sample doped with B and Ni 48.65%.

#### Characterizations

- Density mesurements: densities of samples were measured by pyknometer (standard volumetric method).
- In order to determine the texture parameters, such as BET surface area, pore size distribution, and total pore volume, nitrogen adsorption-desorption isotherms were recorded at 77.13K using the device Sorptomatic. Prior to the measurment, all the samples were degassed at 110 °C for 8h. The adsorption data were analyzed using the BET equation to determine the BET surface area (using computer program WinADP 2005). The total pore volume was determined by single point method based on the amount of nitrogen adsorbed at the relative pressure. The pore

volumes of micro and mesopores were determined by the Dubinin-Raduskevich method (DR) [7] and by the Barret-Joyner-Halenda (BJH) [6] method.

### **Results and Discussion**

### Density

Density of undoped sample was found to amount to  $1.544 \pm 0.004$  g/cm<sup>3</sup>, for doped with B  $1.625 \pm 0.005$  g/cm<sup>3</sup> and for doped with B and Ni  $1.710 \pm 0.005$  g/cm<sup>3</sup>. For undoped sample the expected value was obtained (which is namely 1.35 - 1.55 g/cm<sup>3</sup>), but for doped samples somewhat enlarged densities were registered. Obviously, boron is responsible for this density increase.

# Specific surface area and pore distribution

Adsorption-desorption isotherm of undoped sample belongs to intermediate class between classes I and II, and hysteresis loop belongs to the class H4. For sample doped with B, isotherm is class IV, and hysteresis loop is class H1, whereas for the third sample isotherm is class IV and hysteresis loop is class H2.

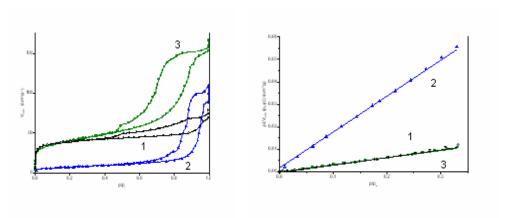


**Fig.1.** a) Nitrogen adsorption-desorption isotherms recorded at 77.13K, and b) BET plot. The samples: undoped (1), doped with B (2) and doped with B and Ni (3)

BET surface area for undoped sample was found to amount  $150 \pm 40 \text{ m}^2/\text{g}$ , for sample doped with B,  $27 \pm 3 \text{ m}^2/\text{g}$  and for B+Ni doped sample  $140 \pm 30 \text{ m}^2/\text{g}$ . In undoped sample approximatelly equal number of micro and mesopores was found while doped samples contained only mesopores. In undoped sample the dominant fraction of free volume and surface area belongs to mesopores with the mean diameter of 4nm. In boron doped sample, most of free volume belong to mesopores with the mean diameter between 10 and 20 nm, while in the sample doped with both B and Ni, most of free volume belongs to mesopores with the mean diameter between 5 and 10 nm.

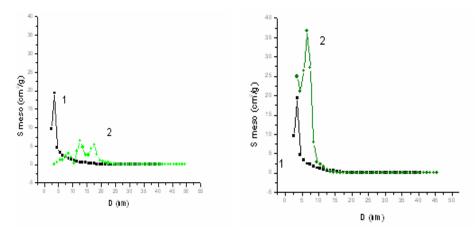


**Fig. 2.** a) Relation between the BET surface area of mesopores and the diameter of mesopores for undoped (1), and boron doped samples (2); b) relation between BET surface area of mesopores and diameter of mesopores for undoped (1) and B+ Ni doped samples (2)

#### **Conclusions**

By density measurements of undoped sample, the density value usual for glassy carbon was confirmed, while doped sample displayed higher densities, indicating the modification in chemical bonding.

The adsorption-desorption isotherms of undoped and doped samples indicate that undoped sample contained equivalent amount of micro and mesopores, while doped sample are exclusively mesoporous. That is confirmed also by BET surface area measurements, namely, doped samples displayed five times lower specific surface area as well as by DR and BJH methods.

- [1] S.Marinkovic, Z.Lausevic, M.Polovina, Modern carbon materials (in Serbian), Institute Vinča, Beograd, 1999.
- [2] G.M. Jenkins, K.Kawamura, Polymeric carbon carbon fibre, glass and char, Cambrige University Press, Cambrige, 1976.
- [3] H. Marsh, P.L. Walker Jr, Chemistry and Physics of Carbon, Marcel Dakker, New York 1971, 7, 106.
- [4] D.B. Fishbach, Chemistry and Physics of Carbon, Marcel Dakker, New York 1971, 7, 107..
- [5] S. Mondal, A.K. Banthia, Low-temperature synthetic route for boron carbide, Journal of the European Ceramic Society, 2005, **25**, 287-291.
- [6] E.P. Barrett, L.G. Joyner, P.P. Halenda, J. Amer. Chem. Soc., 1951, 73, 373.
- [7] A. Gill, P. Grange, Application of the Dubinin-Radushkevich and Dubinin-Astakhov equations in the caracterization of microporus solids, Colloids and surfaces A: Physiochemical and Engineering aspects 1960, **113**, 39-50.

# Biophysical Chemistry Photochemistry Radiation Chemistry

**(F)** 

# COPPER, IRON AND MANGANESE INTERACTION WITH CHLOROPHYLL IN PIGMENT SOLUTIONS AND ISOLATED THYLAKOIDS

J. Zvezdanović<sup>1</sup>, J. Ignjatovic<sup>2</sup> and D. Marković<sup>1</sup>

<sup>1</sup>University of Nish, Faculty of Technology, 16000, Leskovac, Serbia <sup>2</sup>High School "Stanimir Veljković-Zele", 16000 Leskovac

### Abstract

Interactions of copper, iron and manganese with chlorophyll, the major photosynthesis pigment, were studied by VIS spectrophotometry. Copper forms Cu-Chl complexes both in pigment solutions and isolated thylakoids. Iron forms Fe-Chl complexes in pigment solutions only, while manganese interaction with chlorophylls in both systems, was barely observed. In isolated thylakoids, all three metals have weaker interactions, due to a possible interaction with stromal lipo-protein matrix and complex organization of chlorophylls inside the photosynthetic apparatus.

## Introduction

Chlorophyll (Chl), a major photosynthesis pigment, in chemical terms is a porphyrin derivative (a cyclic tetrapyrrole with an isocyclic cyclopentanone ring, fused to a pyrrole ring between the C-13 and C-15 positions), where the central magnesium (Mg) atom coordinates four symmetric pyrrole rings (Fig. 1). Plants easily absorb many toxic heavy

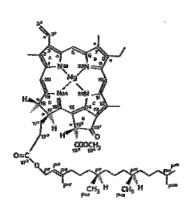


**Fig.1**: Structure of Chla, with numerated C-positions.

metals. Once absorbed, they penetrate the plant tissues (including the leaves) and, in higher concentrations, they may inhibit photosynthesis [1]. Heavy metals can replace the labile bonded central Mg-atom of chlorophyll or they can play a coordinating role between two O-atoms to form a cyclic 6-membered peripheral chelate complex -Chl-HMS "nerinheral" [1]. The Chl-HMS complexes may cause an impairment of the photosynthetic function and this, as a final consequence, may lead to death of the plant. The detailed consequences for higher plants and green algae have been discussed by Küpper [2]. Finally, Chl-HMS show different spectral behavior compared to Chl itself. This work deals with interaction and possible formation of Chl-HMS complexes between

chlorophyll and three chosen heavy metals, copper (Cu), iron (Fe) and manganese (Mn), in pigment solution – in vitro, and in isolated thylakoids – in situ. The interactions were then examined by VIS spectroscopy.

# **Experimental**

Photosynthetic pigments were extracted from spinach leaves (*Spinacia oleracea*  $\underline{L}$ ) by using Swec method [3]. The thylakoids were isolated according to the described procedure

[4]. Chlorophylls content has been determined in acetone as reported [5]. The pigment extracts were evaporated and diluted in ethanol, while isolated thylakoids were dissolved in water. Then, aqueous solutions of  $CuSO_4$ ,  $FeSO_4$  or  $MnSO_4$  (various concentrations) were added. The Chl content in the reaction mixtures ( $c_{Chl}$ ) has adjusted to be 7.60 µg/ml and the ratio of metal ion concentration to chlorophyll concentration ( $c_{M2+}/c_{Chl}$ ) was varied in the range of 1:1 to 1000:1. The time periods following the beginning of the Chl incubation ( $t_{inc}$ ) ranged from 1 to 12 days. The interaction was stopped by dissolving the reaction mixture in cyclohexane and the visible spectra were recorded after different  $t_{inc}$  periods and with different, increasing heavy metal concentrations (on Varian Cary-100 Spectrophotometer).

#### **Results and Discussion**

Chlorophylls have two major absorption regions in visible range (400-800 nm): "red" (Q) band and "blue" (Soret or B) band [5]. Although the changes were detected in incubated systems both with B and Q-bands, the interaction of heavy metals with chlorophylls was followed – both in the pigments mixtures (in vitro) and thylakoids suspensions (in situ) - by using Q-band as sensible indicator, since it belongs to chlorophylls only, and not to carotenoids [5]. In both cases a hypochromic effect related to absorption maximum of Chl Q-band (A<sub>Omax</sub>) is observed. A hypsochromic shift has been observed for Q-band of Cu-incubated pigment solutions and thylakoids, too, while the batochromic shift was detected for Fe-incubated pigment solutions only (Fig.2) - relative to tinc and metal concentration. The changes in Mn-incubated systems were not clearly observed (slight hypsochromic and higher hypochromic effect of the Q band) in the whole period (12 days). With the  $c_{\text{Fe}2+}/c_{\text{Chl}}$  ratio of 1:1 the interaction in pigment solution is barely visible after 8 days, but with the ratio of 100:1 the observed interaction finished in 1 day only after incubation. With the 1000:1 ratio, the results were very similar to the ones observed with the 100:1. Except of strong hypochromic effect, the other changes in VIS spectra of Fe- and Mn-incubated thylakoids were not observed, possible due to metal interaction with the other components in photosynthetic system, in situ. However, the detected VIS spectral changes are not enough to determine which type of interaction took the place. With the Cu<sup>2+</sup>incubated pigment mixtures and the 1:1 ratio (c<sub>Cu2+</sub>/c<sub>Chl</sub>), the interaction was initiated after 1 day only and finished in 7 days; with the ratio of 100:1 and 1000:1 the observed interaction finished after 1 day of incubation. In our earlier experiments with Cu-incubated chlorophylls, the same type of changes was detected, and the formation of Cu-Chl complex was clearly confirmed in vitro and in situ [1,4]. **Table 1** shows the shifts values for the Q-band ( $\Delta\lambda_{Omax}$ ) after 12 days of incubation. The metal interaction with isolated thylakoids can be explained by theoretical analysis of Falk's "stability factor" [6]. According to Falk's equation, the stability of Chl-HMS complexes are ordered as: Mg-Chl ~ Mn-Chl < Fe-Chl < Cu-Chl. Similar reasons stand for unclear and barley visible changes of Mnincubated (in vitro and in situ) systems.

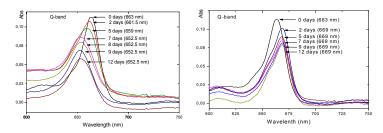


Fig.2: VIS spectra of Cu- (left) and Fe- (right) incubated pigment solutions, for different time periods following beginning of the incubation (t<sub>inc</sub>) in 600-750 nm spectral range (Q-band). c<sub>M2+</sub>/c<sub>Ch1</sub> ratio is 1:1 for Cu-incubated and 100:1 for Fe-incubated pigment solutions.

**Table 1**: The  $A_{max}$  shifts of Q-band  $(\Delta \lambda_{Qmax})$  in VIS spectra of chlorophylls, in pigment solutions and isolated thylakoids.

	M <sup>2+</sup> - Chl interaction in solutions	M <sup>2+</sup> - Chl interaction in isolated thylakoids	c <sub>M2+</sub> /(
	$\Delta\lambda_{\mathrm{Qmax}} (\mathrm{nm})$	$\Delta\lambda_{\mathrm{Qmax}} (\mathrm{nm})$	Сы
Cu-Chl	-10.5	-9	=
Fe-Chl	+6	-	00:
Mn-Chl	-0.5	-	-

#### **Conclusions**

Only copper does form complexes with Chl inside photosynthetic antennas of isolated thylakoids. Iron interactions are little slower with Chl in solutions, while not detected in isolated thylakoids. The manganese interactions with Chl *in vitro* and *in situ* are not clear. Stromal lipo-protein matrix and aggregation of Chl molecules in light-harvesting antennas inside isolated thylakoids may prevent Chl-HMS formation.

# Acknowledgments

Scolar of Ministry of Science of the Republic of Serbia. This work vas supported under the project Development of Technology and Products of Pharmaceutical and Cosmetic Industry, number TR-6708B.

- [1] J. Petrović, G. Nikolić, D. Marković, Journal of the Serbian Chemical Society, 2006, 71(5), 501-512
- [2] H. Kupper, F. Kupper, M. Spiller, J. Exp. Botany, 1996, 47, 259-266
- [3] W. A. Svec, Chlorophylls, CRC Press, Boca Raton, Fl., 1991.
- [4] J. Zvezdanović, D. Marković, G. Nikolić, Journal of the Serbian Chemical Society, 2007, **72**(11), 1053-1062.
- [5] H. K. Lichtenthaler, Methods in Enzymology, 1987, 148, 350-382
- [6] P. H. Hynninen, Chlorophylls, CRC Press, Boca Raton, Fl., 1991.

# CONTRIBUTIONS OF THE SAMPLE GEOMETRY TO THE SHAPE OF AFM FORCE DISTANCE CURVES

S. Kasas<sup>1,2</sup> and G. Dietler<sup>2</sup>

<sup>1</sup>Département de Biologie Cellulaire et de Morphologie, Université de Lausanne, CH-1005 Lausanne, Switzerland, sandor.kasas@epfl.ch <sup>2</sup>Laboratoire de Physique de la Matière Vivante, Ecole Polytechnique Fédérale de Lausanne, EPFL, 1015 Lausanne, Switzerland

#### Abstract

The atomic force microscope is a relatively new tool which permits to measure the mechanical properties of microscopic samples. The measurement itself is trivial, whereas the interpretation of the results is far from being straightforward. In this work we present finite element simulations demonstrating that the shape of the sample strongly influences the force-distance curves, an effect that has to be accounted when calculating the sample's Young's modulus.

#### Introduction

Atomic Force Microscopy (AFM) is a relatively new imaging technique which has been developed in 1986 by Binnig, Quate and Gerber. In addition to its imaging capabilities, the instrument permits to measure the mechanical properties of the observed material. Since 1992, this characteristic of the microscope has been applied to measure the mechanical properties of different types of samples [1.8]. The measurement is accomplished by indenting the AFM tip into the soft sample and by measuring the cantilever deflection during the process. It is assumed that the cantilever behaves accordingly to the Hook law (i.e. the deflection of the cantilever is directly proportional to the vertical component of the force applied onto the tip). The obtained curve, called the force distance (FD) curve, is then subtracted from another FD curve taken onto a hard surface. This operation results in the indentation curve, which indicates the force one needs to apply onto the AFM tip to push it (i.e. to indent it) by a certain distance into the sample. The shape of the FD curve depends on several factors, among which the most interesting for the researchers is the Young modulus of the sample. This modulus, also called elastic modulus defines the stiffness of the sample. Its value is expressed in N/m<sup>2</sup> (or Pa) and varies from 200 GPa for steel to kPa for living cells.

In a typical micro-mechanical study, the Young modulus value of the sample is obtained by fitting the indentation curve (obtained by AFM) with what is known the Hertz model<sup>[9,10]</sup> curve used with or without the Sneddon's modification of the model<sup>[11,12]</sup>. This approach however, requires some knowledge and assumptions about the AFM tip and the sample. The tip geometry has to be known, and the sample is assumed to be flat, homogenous, isotropic with an infinite lateral and vertical size. However, real samples are usually far from this ideal situation and the indentation curves are off a variable amount from the theoretical curves predicted by the Hertz model. In order to estimate this discrepency, analytical solutions are unfortunately of limited help. Complicated geometry and inhomogeneous samples

resist such analysis and can only be approximated by numerical methods. Since the number of publications presenting AFM measurements of the mechanical properties of microscopic samples increases every year, it seemed important to us to draw the attention of the AFM community on the influence of the different geometric parameters upon the shape of the FD curves.

## **Computational Methods**

The simulations were accomplished by using the commercially available finite element software ANSYS<sup>TM</sup> v. 5.7, 7.1. and 9. The tip and the substrate were meshed with plane 42, a 4 node structural solid element. The sample was meshed by using plane 42 or hyper48 hyper-elastic elements. The end of the tip, the upper and the lower parts of the sample as well the upper part of the substrate were meshed with the contac48 contact elements. The stiffness of these elements was set in a way to avoid the overlap of the surfaces and still to permit a convergence during the solution process. The meshing of the model was accomplished by using the mapped mesh option permitting an increased mesh density in the contact and the high stress regions. Setting the boundary conditions consisted in blocking all the degrees of freedom (DOF) of the nodes located at the base of the cantilever. The nodes located at the base of the substrate and the sample, were blocked for all their DOFs except for the vertical displacement. The nonlinear solver was activated for the solution process and the model was solved by successive iterations. During the simulation, the sample was moved upwards unless it came in contact with the tip and induced a deformation of the cantilever. The curve depicting the cantilever deformation versus the vertical position of the sample (or substrate) was recorded by following the z displacement of an arbitrary node on the AFM tip as a function of the position of another arbitrary node located on the substrate. This curve therefore corresponds to the AFM force distance (FD) curve. The slope of this curve reflects the stiffness of the sample: a steep curve indicates a stiff sample whereas a flat curve corresponds to a soft one.

#### Results

## A) Influence of the attack angle

In the first set of simulations we investigated the influence of the tip attack angle (cantilever inclination) on the shape of the FD curves recorded on a soft sample. It corresponds to a measurement in which the sample is mounted onto the substrate with a certain angle or more often, a case where the sample itself is not perfectly horizontal. As depicted on figure 1 the sample looks softer if the attack angle of the cantilever is increased. The importance of this effect is illustrated by the following example: a 30 micrometer long cantilever with an attack angle of 10° indents the same distance in a 150 kPa hard sample as it does in a sample of 240 MPa when its attack angle is increased to 25°. However, it should be emphasized that this effect was dramatically reduced when the cantilever length was increased, i.e. its spring constant decreased: with a 100 micrometer long cantilever the same maximum cantilever deflection was found for a 150 kPa hard sample with a 10° inclination as on a 160 kPa sample with a 25° inclination.

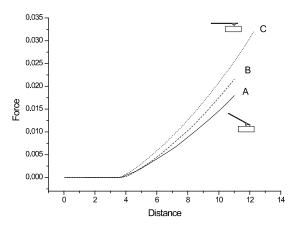


**Fig. 1**. FD curves recorded onto a soft sample at decreasing attack angles (A=30°, B=20° and C=10°).

## B) Influence of the thickness of the sample

The FD curves recorded on a homogenous soft sample follow paths that vary with the thickness of the sample, as depicted on figure 2. The 2D simulation involved a cantilever mounted with an angle of 15° and ended by a spherical tip. The Young modulus of the sample was set to four orders of magnitude lower than that of the tip to mimic a "biological" structure. This simulation demonstrates that thin samples will appear harder to the AFM than the thick ones of the same Young modulus. This phenomenon is an effect of the hard substrate when considering large indentations. The distance at which the effect shows up is a function of the tip shape and the sample's Young modulus. For example, a sample of 3 nm high having a Young modulus of 150 kPa gives the same indentation value as a 5 nm high sample having a Young modulus of 250 kPa, when using a tip with a 2 nm curvature radius.

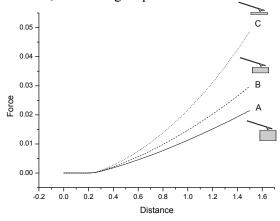


**Fig. 2.** FD curves of a spherical tip indenting 3 different samples having the same Young modulus but an increasing thickness. The curve A was recorded onto the thickest sample whereas curve C onto the thinnest one.

## C) Influence of "small holes"

If during the indentation process the AFM tip penetrates into a hole of the sample, the shape of the FD curve can change dramatically. To illustrate the phenomenon, figure 3 compares FD curves obtained by indenting a tip into a hole with two other FD curves recorded onto flat surfaces. The flat samples had heights corresponding to the largest and the lowest heights of the sample with a hole, respectively. The Young modulus of all the tree samples was the same. The FD curve recorded when the tip was in the hole is the steepest among all the three curves. The phenomenon is induced by the lateral contacts occurring between the tip and the walls of the hole during the indentation process. Here again the apparent increase in the stiffness strongly depends on the geometry of the hole. For illustration, a sample without a hole should have a Young modulus of 340 kPa to give the same cantilever deflection as a sample of 150 kPa with a hole. The hole had a trapezoidal shape with a diameter of 6 nm on the top, 2 nm in the bottom and a depth of 2 nm. The tip radius of curvature was set to 2 nm. The influence of the groove diameter has been studied in more details in the following section D.

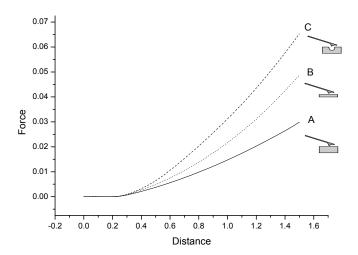


**Fig. 3.** Influence of the presence of a hole in the sample on the shape of FD curves (B). A and C curves have been obtained by indenting the tip into flat samples having a height which corresponds to the largest (A) and the smallest height (C) of the grooved sample.

# D) Influence of "large holes"

As shown in the previous set of simulations, the FD curve adopted the steepest slope if the AFM tip indented into a hole. However this phenomenon strongly depends on the relative size of the groove as compared to the tip. As soon the width of the hole becomes large enough and its lateral walls do not come in contact with the tip any more, this effect disappears (data not shown).

## F) Influence of protrusions

In these simulations we explored how small size protrusions of the sample affect the shape of the indentation curves. It is somehow the geometric "negative" of the previous simulation run. The corresponding FD curves are depicted in figure 4. Here again, the Young modulus of the tree samples was the same. It can be noticed that small lateral size protrusions made the sample appear slightly softer. It was probably due to a primary and "easy" deformation of the protrusion which occurs before indentation into the bulk of the sample starts. Comparing to the previous case it appears that this phenomenon is less important with protrusions than with holes. A homogenous sample with a protrusion of 1 nm above the surface and having a Young modulus of 150 kPa will indent at the same amount as a flat sample with a Young modulus of 100 kPa.

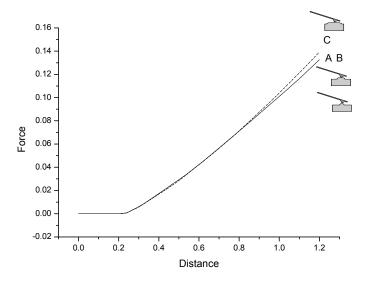
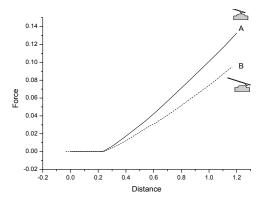


Fig. 4. Small protrusions slightly influence the shape of FD curves.

## G) Influence of the indentation position on a protrusion

In this simulation run we considered soft samples with larger protrusions than those simulated in the section F. The shape of the FD curves was studied as a function of the spot where the indentation occurred. FD curves recorded on the sides of protrusions adopted a flatter path than those recorded on the plateau as depicted in figure 5. It can be explained by the fact that the tip partially slips on the side before starting to indent and therefore gives the illusion of a softer sample. To illustrate the importance of the effect, the curve recorded on the side "looks" 40 kPa softer than the one recorded on the plateau of a 150 kPa hard sample.



**Fig. 5.** FD curves recorded on the side (B) of a sample with a protrusion looks flatter than those recorded onto its plateau (A).

## H) Influence of the size of the sample

The aim of this simulation set was to predict the shape of FD curves recorded on small structures such as single molecules. This case was different from the one we studied in the section C where samples having "infinite" lateral dimensions were simulated. In the present case the sample has lateral dimensions which are in the range of those of the AFM tip. In addition we included a "hard" substrate under the sample to simulate the mica or glass on which AFM samples are usually deposited before observation. Contact elements have therefore been generated between the sample's lower surface and the substrate as well between the tip and the sample's upper surface. Due to the large deformations during the indentation process, an increasing amount of sample's surface comes in contact with the underlying hard substrate modifying the FD curves. This simulation results are depicted in figure 6, and show that small samples appear much harder than large ones. If the smallest sample has a Young modulus of 90 kPa, the biggest one should have 430 kPa to produce the same FD curve.

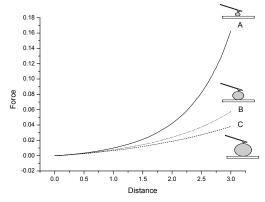


**Fig. 6.** Small samples appear harder than larger ones even if they have the same Young modulus.

## I) Influence of the indentation position onto spherical samples

Similarly to the previous H case, FD curves were recorded on a spherical sample. However, in this set of simulations FD curves obtained above the vertical axis of the sample were compared to FD curves recorded far from the centre of the sample. As depicted in figure 7, the off-axially recorded FD curve are flatter than the one on taken in the centre. The cantilever deflection value of the off-centre sampling corresponds to a 75 kP sample when its "real Young modulus" was 90 kPa.

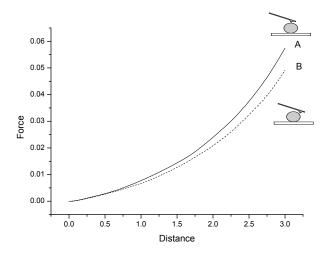


**Fig. 7.** Applying a vertical load in the center (B) of a circular (or spherical) sample makes it appear harder than if the load is applied on the edges.

## **Discussion**

Atomic force microscopy permits to measure the mechanical properties of small sized samples in air, liquid or vacuum. The sample's mechanical properties are deduced from the deformation of the cantilever when the AFM tip is pushed into the sample. The resulting curve, referred to as a force distance curve permits the calculation of the Young's modulus of the sample after a few relatively simple mathematical operations. However, to obtain a Young's modulus value, some basic assumptions have to be made concerning the shape of the tip, the homogeneity of the sample or its infinite lateral and vertical dimensions. In this work we exclusively concentrated our efforts in estimating the importance of the geometry of the sample on the shape of the force distance curves. An analytical approach to estimate the shape of force curves is too complicated to permit a practical use for the AFM community. We therefore developed a finite elements code which permits to calculate FD curves on any type of tip and sample geometry. Because there are an infinite number of possible configurations, we decided to present only some very basic examples in which the geometry of the sample dramatically influences the shape of the FD curves. These simulations point out that the geometry of the

sample plays an important role in the shape of the FD curves, influencing this way the calculated values of the Young modulus. We believe that the studied cases we present here can help to determine if the Young modulus values given by the Hetrz model are over or under estimated.

- [1] N.J. Tao, S. M. Lindsay, S. Lees, Biophys. J. 1992, 63, 1165.
- [2] M. Radmacher, M. Fritz, C. M. Kacher, J. P. Cleveland, P. K. Hansma, *Biophys. J.* 1996, **70**, 556.
- [3] A. L. Weisenhorn, M. Khorsandi, S. Kasas, V. Gotzos, H. J. Butt, *Nanotechnology* 1993, 4, 106.
- [4] C. Rotsch, M. Radmacher, *Biophys J.* 2000, **78**, 520.
- [5] E. A-Hassan, W. Heinz, M. Antonik, N. P. D'Costa, S. Nageswaran, C. A. Schoenenberger, J. H. Hoh, *Biophys. J.* 1998, **74**, 1564.
- [6] Y. Yamane, H. Shiga, H. Haga, K. Kawabata, K. Abe, E. Ito, *J. Electron Microscopy* 2000, **49**, 463.
- [7] R. Matzke, K. Jacobson, M. Radmacher, Nat. Cell. Biol. 2001, 3, 607.
- [8] A. Schäfer and M. Radmacher, Acta Biomaterialia 2005, 1, 273.
- [9] H. Hertz, J. Reine Angew Mathematik 1882, **92**, 156
- [10] M. Radmacher. In: H. Hörber, B. Jena, editors. *Methods in cell biology*. 2002, New York: Academic press.
- [11] IN. Sneddon, Int J Eng Sci. 1965, **3**, 47.
- [12] KL. Johnson, Contact mechanics, 1994, Cambridge University Press.

## UV-INDUCED CHANGES OF CHLOROPHYLLS IN SOLUTIONS, INTACT CHLOROPLASTS AND THYLAKOIDS

J. Zvezdanović<sup>1</sup>, T. Cvetić<sup>2</sup>, S. Veljović-Jovanović<sup>3</sup> and D. Marković<sup>1</sup>

<sup>1</sup>University of Nis, Faculty of Technology, 16000, Leskovac, Serbia
<sup>2</sup> University of Belgrade, Faculty of Biology, 11000, Belgrade, Serbia
<sup>3</sup> University of Belgrade, Institute for Multidisciplinary Research,11030, Belgrade, Serbia

#### **Abstract**

Changes of major photosynthetic pigment, chlorophyll (Chl), induced by UV-irradiation (three ranges: UV-A, -B and-C) have been studied by fluorescence spectroscopy in acetone and *n*-hexane, and in intact chloroplasts and isolated thylakoids. Chlorophyll undergoes bleaching (destruction) accompanied by the fluorescent transient formation following first order kinetics. The mechanism of UV-C induced bleaching of chlorophyll in thylakoids is probably different from the ones induced by UV-A and UV-B.

#### Introduction

Though photosynthetic pigments such are chlorophylls absorb in VIS region, their composure is significantly altered when exposed to UV-light [1-3]. That may cause an impairment of photosynthetic function. The irradiations of chlorophyll solutions, as well as the intact systems such are chloroplasts and thylakoids membranes with strong UV and visible (VIS) light results in irreversible breakdown of chlorophyll, accompanied by the appearance of a number of intermediate and final products [3-5]. The chemical structure of these products is largely unknown because of diversity of the involving pathways and the lability of the primary photoproducts [6]. The fluorescent product(s) are most probably Chlderivatives [7]. Changes and stability of chlorophylls against UV irradiation, has been studied in this work by fluorescence spectroscopy.

# **Experimental**

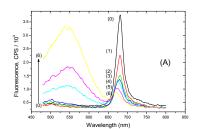
Chlorophylls (containing only Chla with small contributions of Chlb) were extracted from spinach leaves and then separated on a column chromatography, with silica gel as the adsorbent and n-hexane/acetone mixture as the eluent. Intact chloroplasts from spinach were prepared in aqueous suspensions, by using a described procedure [9]; then the thylakoids were prepared by breaking intact chloroplasts in water.

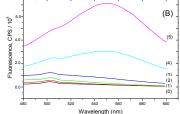
Continuous irradiation was performed in cylindrical photochemical reactor "Rayonnet", with 8 symmetrically placed lamps having emission maxima at 350 nm (UV-A), 300 nm (UV-B) and 254 nm (UV-C). The total measured energy flux (hitting the samples) is about 10.3, 12.0 and 14.3 W/m², respectively. Fluorescence spectra of chlorophylls in solutions, intact chloroplasts and thylakoids were recorded on Fluorolog 3 spectrofluorimeter (Jobin Yvon, France) in 3 cm³ quartz cuvette. The excitation wavelength was 430 nm and the emission spectra were

followed in 450-750 nm range, with both excitation and emission slits set to 1 nm. The transient fluorescence was monitored in 450-600 nm range, with excitation and emission slits set to 2 and 4 nm, respectively. The Chl content has been determined by using VIS spectrophotometry as reported [10]. The Chla content in all investigated systems has adjusted to be  $c_{Chla} = 7.60 \, \mu g/ml$ .

# **Results and Discussion**

Chlorophylls are major fluorescent molecules in intact chloroplasts and thylakoids,. In solutions, fluorescence maximum ( $F_{Chl,max}$ ) of Chla and Chlb are located at 668 nm and 652 nm, respectively [11]. However, in isolated chloroplasts, thylakoids and leaves Chl fluorescence spectrum has a characteristic broad maximum at about 685 nm, and a shoulder near 735 nm in "red" and "far-red" regions, respectively [11]. The "red" fluorescence at 685 nm originates from Chla embedded in the antennas of photosystem II (PSII), and "far-red" fluorescence at 735 nm originates from Chla in antennas of PSI and PSII [11]. The  $F_{Chl,max}$  values at 668-680 nm show decreasing trend during the increasing irradiation time periods,  $t_{irr}$ . (Fig.1A). While fluorescence maximum position ( $\lambda_{F-Chl,max}$ ) barely shows any change for UV-A and UV-B irradiated Chls in the investigated systems, a few nanometers "blue" shift was detected for UV-C irradiation (Fig.1A).





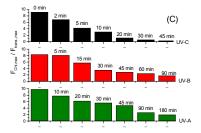


**Fig1:** Fluorescence spectra of UV-C-irradiated aqueous suspensions of thylakoids. **(A)** The fluorescent spectra recorded in spectral region from 450 - 800 nm, **(B)** Emission spectra of the transient recorded in spectral region 450 - 600 nm. The exposure time periods: **(0)** 0 min; **(1)** 2 min; **(2)** 5 min; **(3)** 10 min; **(4)** 20 min; **(5)** 30 min; **(6)** 45 min. **(C)** Fluorescence intensity ratio ( $F_{Chl,max}$  /  $F_{trans,,max}$ ), during the UV- exposure in all three spectral ranges.

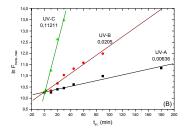


**Fig2**: The kinetic plots of the transient formation in thylakoids, during increasing  $t_{irr.}$  periods of UV-A, UV-B and UV-C. The fluorescence intensity maximum of the transient ( $F_{rans.,lmax}$ ) was followed at 515-550 nm. The corresponding rate constants  $K_{trans.}$  (min<sup>-1</sup>), are displayed for all three UV irradiation ranges.

On the other hand, a rise of fluorescence emission maximum has been clearly detected in a range between 450 and 600 nm during the irradiation regimes, which

directly relates the newly observed phenomenon with UV-induced Chl bleaching (Fig.1A,B). The maximum fluorescence intensity of the transient,  $F_{trans.,max}$  (505-550 nm) increases, with increase of  $t_{irr.}$  (Fig.1B). The appearance of fluorescent

product is already reported, but at slight different experimental conditions and at different  $\lambda_{max}$  positions compared to ours [3]. The ratio of  $F_{Chl max}/F_{trans max}$ decreases proportionally with the increasing irradiation periods (i.e. with UVinduced chlorophyll bleaching) (Fig.1C). The maximum of the transient fluorescence ( $\lambda_{F-trans..max}$ ) is located at 515 nm and 510 nm for all three UV ranges applied, for Chl in acetone and hexane, respectively; on the other hand, the transient maximum is located at 518 nm for UV-A and -B, and at 522 nm for UV-C irradiated intact chloroplasts. Finally, in isolated thylakoids, for UV-A and UV-B the fluorescence peak is located at 515 nm, and at 550 nm for UV-C range. This suggests that different irradiation regimes lead to possibly different fluorescent transients, due to different responding mechanisms of intact chloroplasts and thylakoids toward UV-irradiation. The chlorophylls bleaching kinetics (in vitro and in situ) obeys a first-order law, as already reported [3,5,12]. Kinetics of the fluorescent transient formation seems to obey a first-order law, too. The kinetics of UV-irradiation-induced transient – logarithmic (ln) plots as a result of increasing irradiation intervals for isolated thylakoids and all three UV-ranges have been shown in Fig.2.

#### **Conclusions**

Chlorophylls undergo bleaching (destruction) accompanied by the fluorescent transient formation obeying first order kinetics. The mechanism of UV-C induced bleaching of chlorophylls in thylakoids and intact chloroplasts is probably different from the ones induced by UV-A and UV-B.

## Acknowledgments

Scolar of Ministry of Science of the Republic of Serbia. This work was supported under the projects TR-6708B, 143020B and 143016B by the Ministry of Science of Republic of Serbia.

- [1] Teramura, L. Ziska, Photosynthesiss and the Environment, Kluwer, 1996
- [2] E. Turcsanyi, I. Vass, *Photochemistry and Photobiology*, 2000, **72**, 513-520
- [3] M. Merzlyak, S. Pogosyan, L. Lekhimena, T. Zhigalova, I. Khozina, Z. Cohen, S. Khrushchev, *Russian Journal of Pant Physiology*, 1996, **43**, 160-168
- [4] P. H. Hynninen, *Chlorophylls*, CRC Press, Boca Raton, Fl., 1991
- [5] S. Santabarbara, Archives of Biochemistry and Biophysics, 2006, 455, 77-88
- [6] G. A. F. Hendry, J. D. Houghton, S. B. Brown, New Phytologist, 1987, 107, 255-302
- [7] K. K. Karuktis, *Chlorophylls*, CRC Press, Boca Raton, Fl., 1991
- [8] W. A. Svec, Chlorophylls, CRC Press, Boca Raton, Fl., 1991
- [9] Z. G. Cerović, M. Plesničar, Biochemicaly Journal, 1984, 223, 543-545
- [10] Z. G. Cerović, G. Samson, F. Morales, N. Tremblay, I. Moya, *Agronomy*, 1999, 19, 543-578
- [11] G. C. Papageorgiou, Chlorophyll a fluorescence, Springer, Dordrecht, 2004.
- [12] J. Zvezdanović, D. Marković, *Journal of the Serbian Chemical Society*, 2008, **53**, 271-282.

# NA<sup>+</sup>/K<sup>+</sup>-ATPASE - ACTIVITY AND INHIBITION

#### V. Vasić

Department of Physical Chemistry, Vinča Institute of Nuclear sciences, 11001, Belgrade, Serbia

#### **Abstract**

The aim of the study was to give an overview of the mechanism of inhibition of Na<sup>+</sup>/K<sup>+</sup>-ATPase activity. For this purpose, the effect of ouabain like compounds (digoxin, gitoxin), platinum group complexes ([PdCl<sub>4</sub>]<sup>2-</sup>, [PdCl(dien)]<sup>+</sup> and [PdCl(Me<sub>4</sub>dien)]<sup>+</sup>), transition metal ions (Cu<sup>2+</sup>, Zn2<sup>+</sup>, Fe<sup>2+</sup>, Co<sup>2+</sup>) and heavy metal ions (Hg<sup>2+</sup>, Pb<sup>2+</sup>, Cd<sup>2+</sup>) on the activity of Na<sup>+</sup>/K<sup>+</sup>-ATPase isolated from rat synaptic plasma membranes (SPM), cortex of pig and human erythrocytes and was investigated.

## Introduction

 $Na^+/K^+$ -ATPase (EC 3.6.1.37) is a cell membrane located enzyme, which plays a key role in the active transport of monovalent cations ( $Na^+$  and  $K^+$ ) across the membrane [1, 2]. The enzyme is composed of an  $\alpha$ -subunit, which contains the adenosinetriphosphte (ATP)-, Na,  $K^+$ - and ouabain- binding sites, as well as the site for phosphorylation and a  $\beta$ -subunit, which stabilizes the  $K^+$  binding cage .  $Na^+/K^+$ -ATPase acts as a dimer ( $\alpha\beta$ - $\beta\alpha$ ). The most widely accepted view related to such a dimmer acts is a "flip-flop" model, in which both subunits show complementary conformation:

$$E_1E_2 \leftrightarrow E_2E_1$$

where E is the conformation of each a-subunit. The activity of this enzyme is very sensitive to the presence of some metal ions [3,4] and organic compounds of various structures, especially some drugs and pesticides [5,6]. Besides its transporter function, Na<sup>+</sup>/K<sup>+</sup>-ATPase acts as the receptor for cardiac glycosides such as ouabain. Ouabain binds to the the extracellular part of the protein with very high affinity, leading to the inhibition of enzymatic activity. Furthermore, nephrotoxicity, ototoxicity etc. of platinum anticancer drugs, such as cisplatin and chloroplatinic acid, is related to inhibition of Na<sup>+</sup>/K<sup>+</sup>-ATPase activity. Since Pt(II) complexes have great affinity for binding with –SH containing ligands [7,8], these complexes interact with Na<sup>+</sup>/K<sup>+</sup>-ATPase through enzyme sulfhydril groups. This kind of interaction with Na<sup>+</sup>/K<sup>+</sup>-ATPase was also observed for heavy and transition metal ions [9].

Our study was undertaken with the aim to examine the mechanism of interaction between ouabain-like compounds, platinum group complexes and metal ions with Na $^+$ /K $^+$ -ATPase. The extensive kinetic analysis was done in order to determine kinetic parameters and type of Na $^+$ /K $^+$ -ATPase inhibition. In addition, the ability of sulphur-donor ligands (L-cysteine and glutathione) to prevent metal ions and complexes induced inhibition of Na $^+$ /K $^+$ -ATPase and to recover enzymatic

activity was investigated. Finally, development of highly sensitive and selective analytical tools using the immobilized enzyme is discussed in this paper.

## **Experimental**

Na<sup>+</sup>/K<sup>+</sup>-ATPase was isolated from rat brain, human blood and the commercial enzyme from porcine cortex brain was purchased by Sigma Chemicals Co. was used. Red cell membranes were prepared according to the method of Post et al. [10] with certain modifications. Synaptosomal plasma membranes (SPM) were isolated from the whole rat brain according to the method of Cohen et al. [11], and were stored at -70°C until use.

The enzyme activity was determined in a standard incubation medium (200  $\mu$ l), containing 50 mM Tris – HCl (pH 7.4), 100 mM NaCl, 20 mM KCl, 5 mM MgCl<sub>2</sub>, 2 mM ATP and protein (2 mg/ml) in the presence or absence (control) of the desired concentration of inhibitor. Incubation mixtures were preincubated at 37° C in the presence of inhibitor or distilled water (control). The reaction was started by the addition of ATP, allowed to proceed. The inorganic orthophosphate (P<sub>i</sub>) liberated from the hydrolysis of ATP was measured using modified spectrophotometric procedure based on the stannous chloride method, by reading the absorbance at 690nm.

#### **Results and Discussion**

## Inhibition of Na<sup>+</sup>/K<sup>+</sup>-ATPase activity by digitalis

Some widely used digitalis glycosides (synthetic drugs and medical plants isolates) strongly modulate enzyme activity on a concentration dependent manner. In naturally occurring digitalis glycosides the unsaturated  $\gamma$ - and  $\delta$ -lactones present in 17 $\beta$ -position of the steroidal skeleton are associated with high affinity for the Na $^+$ /K $^+$ -ATPase receptor. Recently, it was confirmed that basicity, i.e. a strong ionic interaction between one of carboxylate residues present in the  $\alpha$ - subunit of the Na $^+$ /K $^+$ -ATPase and the cationic form of some digitalis like derivatives is relevant for interference with enzyme activity [12]. The presence of -OH groups at different positions of the steroidal skeleton reduces, in general, the interaction energy, though it depends on the location and spatial disposition of such –OH groups.

Digitoxin, one of the most frequently used drugs to improve cardiac contractility, undergoes a complex metabolic degradation generating digitoxigenin, digitoxigenin mono-digitoxoside and gitoxin. The structural difference between digoxin and its isomer gitoxin, that usually appears as a result of metabolic degradation of digitoxin, is just the hydroxyl (-OH) group close to the C-17 $\beta$  position, which changes the pharmacokinetics and pharmacodynamics of these substances considerably. It has been recognized that digoxin induced inhibition is not only reversible, but also that the enzyme could be reactivated by the specific antidigoxin antibody. The inhibitory effect depends on the protein preparation [13]. However, human blood erythrocyte Na $^+$ /K $^+$ -ATPase was more sensitive to

exposure to gitoxin, compared to that from porcine cerebral cortex. In addition, biphasic inhibitory curves were obtained in both enzyme preparations, indicating the interference of two distinct inhibitor binding sites (Fig.1). The heterogeneity of digoxin sites has been reported in rat brain and beef heart Na $^+$ /K $^+$ -ATPase and has been related to 2 distinct isoform of the  $\alpha$  subunit. It is well known that the  $\alpha$ 3 isoform is especially abundant in the brain and some other vertebrate tissues. Western blot analysis of the Na $^+$ /K $^+$ -ATPase from mature human erythrocyte, purified by ouabain column chromatography, has shown that erythrocytes contains the  $\alpha$ 1 and  $\alpha$ 3 isoforms of the  $\alpha$  subunit. Our results indicated that the low sensitive  $\alpha$ 1 isoform was also present.

In our study the  $IC_{50}$  values for the high activity isoenzyme in both enzyme preparations were more than two orders of magnitude higher compared to the low affinity isoform. Moreover, the concentration of digoxin that produced 30% inhibition reached the toxic level for gitoxin, displaying the complete inhibition of the high affinity isoenzyme. The high affinity to digoxin and gitoxin can be attributed to the binding to  $\alpha 3$  isoform, which is known to be the most sensitive towards the cardiac glycosides.

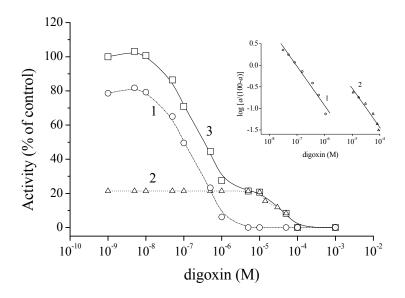


**Fig. 1.** Inhibition of  $Na^+, K^+$ -ATPase activity in human erythrocytes by digoxin. 1 – high activity isoenzyme, 2 – low affinity isoenzyme, 3 - total activity. Inset - Hill analysis of high (1) and low (2) affinity isoenzyme.

Further experiments demonstrated that elevated potassium concentrations were also able to reactivate the enzyme inhibited by digitalis glycosides to a certain extent, and that the reactivation was proportional to the time of exposure to increased  $K^+$  concentration [13]. We have postulated that higher potassium concentrations shift the balance between  $E_1$  and  $E_2$   $Na^+/K^+$ -ATPase conformations

in favor of  $E_1$  and, consequently, enable the continuation of the digoxin impeded enzymatic cycle. Therapeutic effect is achieved with a digoxin concentration that produces a moderate enzyme inhibition (about 30 %), whereas the toxic concentrations inhibit over 60 % of the enzyme activity.

### Inhibition by noble metals complexes

The modification of cysteine residues in proteins due to its ability to strongly coordinate complex metal ions is one of the arguments of critical importance for the design of novel types of pharmacological agents, based on the Pt(II), Au(III) and Pd(II) complexes. Our study was undertaken with the aim to examine the mechanism of interaction of [PdCl<sub>4</sub>]<sup>2-</sup>, [PdCl(dien)]<sup>-</sup> and [PdCl(Me<sub>4</sub>dien)]<sup>-</sup> complexes with Na<sup>+</sup>/K<sup>+</sup>-ATPase [7,8]. All these species induced the concentration-dependent inhibition of Na<sup>+</sup>/K<sup>+</sup>-ATPase activity, and their potency to inhibit Na<sup>+</sup>/K<sup>+</sup>-ATPase depended on the rate of ligand exchange in the coordinative sphere of the metal ion (Fig.2).

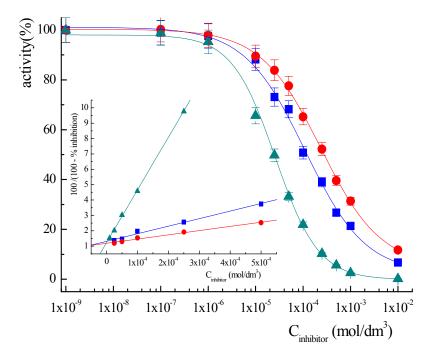


**Fig. 2**. Inhibition of  $Na^+/K^+$ -ATPase activity by  $[PdCl_4]^{2^-}$  (up triangles), [PdCl(dien)]+(squares) and  $[PdCl(Me_4dien)]^+$  (circles). Insert: the Hill plots constructed from the data obtained by inhibition experiments

However, the stability constants of enzyme-Pd(II) complexes were close to the value of the overall binding constant that was reported for the interaction of Na<sup>+</sup>/K<sup>+</sup>-ATPase with cisplatin, but were also two orders of magnitude lower

compared to the aqua complexes of heavy and transition metals. Kinetic analysis indicated a noncompetitive type of inhibition and suggested that Pd(II) complexes did not affect the binding of the substrate. Considering the fact that Pd(II) complexes are model compounds for their Pt(II) analogs, which showed similar inhibitory effects on Na<sup>+</sup>/K<sup>+</sup>-ATPase, the conclusion can be drawn that the same kind of enzyme-inhibitor interaction can be expected for the widely-used platinum anticancer drugs. It was reported that GSH and L-cysteine are potent enzyme reactivators. The reactivation is usually due to the formation of complex between thiols and the metal ion bonded to the –SH groups of the enzyme. More likely, the mechanism of interaction of enzyme, L-cysteine and GSH with Pd(II) complexes was similar, since it involved substitution of the Cl<sup>-</sup> ligand by SH-donor ligands [7,8]. However, the affinity of L-cysteine or GSH for this reaction was much higher compared to the Na<sup>+</sup>/K<sup>+</sup>-ATPase affinity.

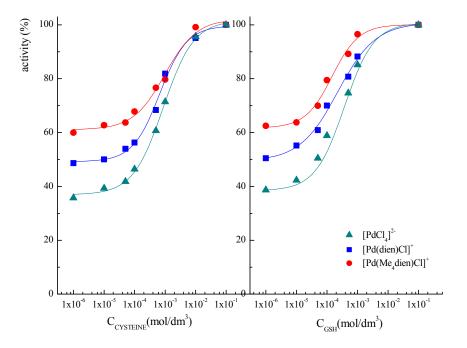


**Fig. 3.** Recovery effect of L-cysteine and GSH on the Na $^+$ /K $^+$ -ATPase activity inhibited in the presence of  $5x10^{-5}M$  [PdCl<sub>4</sub>] $^{2+}$  (up triangles),  $1x10^{-4}M$  [Pd(dien)Cl] $^+$ (squares) and  $1x10^{-4}M$  [Pd(Me<sub>4</sub>dien)Cl] $^+$ (circles).

The inhibitory effects of Pd(II) complexes were prevented and recovered by the addition of L-cysteine or GSH, which showed high potency to extrude and substitute the enzyme from the Pd(II) complex (Fig.3). Is seems that prevention and recovery of Pd(II) complexes-induced  $Na^+/K^+$ -ATPase inhibition were realized due to the competition between the SH functional groups of protein and thiols (L-

cysteine or GSH) for substitution of the Cl<sup>-</sup> ligand in the coordination sphere. These results are consistent with the kinetic analysis, suggesting that these complexes are reversible noncompetitive inhibitors of this enzyme. Since platinum anticancer drugs react in the same manner as their palladium analogs, it was also suggested that L-cysteine or GSH might have the ability for detoxification after chemotherapy.

### Inhibition by an inorganic salts

The highly toxic heavy metals induced inhibition of Na<sup>+</sup>/K<sup>+</sup>-ATPase activity in concentration dependent manner. The influence of Pb<sup>2+</sup>, Cd<sup>2+</sup>, Hg<sup>2+</sup>, Cu<sup>2+</sup>, Fe<sup>2+</sup>, Co<sup>2+</sup> and Zn<sup>2+</sup> on Na<sup>+</sup>/K<sup>+</sup>-ATPase activity was investigated by single exposure to inhibitors in the concentration range from 1-10<sup>-9</sup> M to 1-10<sup>-3</sup> M [3.4]. The IC<sub>50</sub> values (inhibitor concentration that produced the inhibition of 50% of the enzymatic activity) were ranging from  $10^{-7}$ – $10^{-4}$  M. Heavy metal ions, such as Cd<sup>2+</sup> and Hg<sup>2+</sup>, exerted a potent inhibitory effect on Na<sup>+</sup>/K<sup>+</sup>-ATPase isolated from different tissues, like rat brain and rat liver, by binding avidly to sulfhydryl groups with similar affinities. Sensitivity of enzyme toward Cd<sup>2+</sup> and Hg<sup>2+</sup> increased due to its immobilization by adsorption on a nitrocellulose membrane [4,15]. Inhibitory effects of Cu<sup>2+</sup>, Zn<sup>2+</sup> and Fe<sup>2+</sup> on bovine cerebral cortex Na<sup>+</sup>/K<sup>+</sup>-ATPase activity were obtained and the extent of inhibition seems to depend on the presence of chelators. Kinetics analysis showed that the nature of enzyme inhibition by metals was non competitive. The inhibitory effects of Fe<sup>2+</sup>, Co<sup>2+</sup>, Zn<sup>2+</sup> and Cu<sup>2+</sup> could be prevented by addition of 1mM strong metal-ion chelator EDTA, 10 mM L-cystein or 10 mM GSH and the effect was dose dependent [3,9]. Recovery of the Hg<sup>2+</sup>induced inhibition was not achieved, even when the chelators were present at concentration above 0.01 M.

The synergistic effects with binary combinations of heavy metals on the activity of Na,K-ATPase using the mixtures of Cu/Zn, Cu/Fe, Zn/Fe, Pb/Cd, and Cu/Pb/Zn/Cu ions were obtained in all cases [14]. Moreover, all metal ions in the mixture at concentration levels near  $IC_{50}$  values inhibited the enzyme activity completely. The inhibition induced by combination of Pb with Cd was time dependent. Addition of 1mM EDTA in the medium assay recovered 100% of the inhibited enzyme activity.

#### Na<sup>+</sup>/K<sup>+</sup>-ATPase as an analytical tool

In summary, the study of the mechanism of enzyme inhibition by various compounds is of great importance for elucidation of their potential toxicity. Moreover, development of highly sensitive and selective analytical tools using the immobilized enzyme is currently among the topic interest in the bioanalytics. The effect of certain metal ions (Pb<sup>2+</sup>, Cd<sup>2+</sup>, Hg<sup>2+</sup>, Cu<sup>2+</sup>, Fe<sup>2+</sup>, Zn<sup>2+</sup>) and various

organic compounds (cardiotonic drugs, organic solvents, pesticides) on Na<sup>+</sup>/K<sup>+</sup>-ATPase activity, as described in the previous part, offers the possibility to develop a simple qualitative and semi-quantitative test method for selective detection of these analytes in aqueous solutions [14,15]. The method is based on the

spectrophotometric determination of inorganic ortho-phosphate (Pi), liberated from ATP in the Na<sup>+</sup>/K<sup>+</sup>-ATPase-catalysed reaction, that serves as a measure of the enzymatic activity [3,14]. The concentration of Pi liberated in the reaction medium from ATP after exposure of the enzyme to analytes was dose dependent on the analyte concentration. Heavy metals (Pb, Cd, Hg, Cu, Fe, Zn), toxic organic compounds (pyridine, urea) and some pesticides (malathion and the products of its chemical and photochemical transformations, chlorpyrifos, permethrin) showed diverse effects, either the inhibition or stimulation of the enzyme activity. The potency of using ATPase system as a biological component for semi-quantitative and qualitative multi - response sensing system for detection of different compounds is based on the level of change of enzyme activity in the presence of analyte. By varying the medium assay composition, some organic compounds and heavy metal salts can be simultaneously detected using the reaction of ATPases catalysed ATP hydrolysis. However, the test based on the Na<sup>+</sup>/K<sup>+</sup>-ATPase for detection of analytes is simple and useful for quick measurements.

This proposed method was already applied to the quality control of digoxin in Lanoxin injection. The tested sample of Lanoxin injection was added to the standard medium assay (0.2 ml final value), containing 1 mM EDTA. The activity was measured as described, and compared to the control value. The same result  $(0.31\pm0.02)x10^{-3}$  M was obtained as using standard method (HPLC) with the mean standard deviation of 6.45%. This finally confirms applicability of sensing system based on the Na<sup>+</sup>/K<sup>+</sup>-ATPase in the product quality control.

## Acknowledgements

Author would like to thank to the Ministry of Science and Environmental Protection of Serbia for their financial support (Project No. 142051). Also, assistance of the members of the group from the Department of Physical Chemistry from the Institute of Nuclear Sciences "Vinča": Danijela Krstić, Katarina Krinulović, Tatjana Momić, , Jasmina Savić, Mirjana Čolović, and Ana Vujačić is greatly acknowledged.

- [1] L.A. Vasilets, W. Schwarz, Biochem. Biophys. Acta, 1993, 1154, 201-225.
- [2] P.L. Jorgensen, K. O. Hakansson, S. J. D. Karlish, Annual Review of Physiology, 2003, 65, 817-849.
- [3] V.Vasić, D. Jovanović, D.Krstić, G. Nikezić, A.Horvat, Lj. Vujisić, N.Nedeljković, Toxicol.Let., 1999, **110**, 95-104.
- [4] V.Vasić, D.Jovanović, A.Horvat, T.Momić, G.Nikezić, Analyt.Biochem., 2002, 300, 113-120.
- [5] V. Vasić, U. Černigoj, K. Krinulović, G. Joksić, M. Franko, J. Pharm. Biomed. Anal., 2006, 40(2), 404-409.
- [6] D.Krstić, K.Krinulović, V.Spasojević-Tišma, G.Joksić, T. Momić, V.Vasić, J. Enz.Inh.Med.Chem., 2004, **19(5)**, 409-415.

- [7] K. Krinulović, Ž.Bugarčić, M.Vrvić, D. Krstić, V.Vasić, Toxicology in Vitro, 2006, 20, 1292-1299.
- [8] D. Krstić, N. Tomić, K. Krinulović, V. Vasić, J. Enz.Inh.Med.Chem., 2006, 21, 471-475.
- [9] Lj. Vujisić, D. Krstić, K. Krinulović, V. Vasić, J. Serb. Chem. Soc., 2004, 69(7), 541-547.
- [10] R.I. Post, C.R. Merit, C.R. Kosolving, C.D. Albbright, J.Biol.Chem., 1960, 235, 1796-1802.
- [11] R.S. Cohen, F. Blomberg, K. Berzins, P. Siekevitz, J.Cell Biol. 1977, 74, 181
- [12] C. P. Melero, M.Maderade, A.S.Feliciano, Molecules, 2000, 5, 51-81.
- [13] D.Krstić, N. Tomić, K.Krinulović, V. Vasić, J. Enz.Inh.Med.Chem., 2006, 21, 471-475.
- [14] V.Vasić, K.Krinulović, D.Krstić, T.Momić, A.Horvat, Monatshefte fur Chemie, 2004, 135, 605-614.
- [15] T.Momić, Z.Vujčić, V.Vasić, A.Horvat, J.Serb.Chem.Soc., 2002, 67(12), 809-817.

# DIFFERENTIAL ACTIVATION OF JNK IN RAT HIPPOCAMPUS FOLLOWING ACUTE AND/OR CHRONIC STRESSORS

D. Filipović, J. Zlatković and S.B. Pajović

Laboratory of Molecular Biology and Endocrinology, VINČA Institute of Nuclear Sciences, P.O. Box 522, Belgrade, Serbia

#### **Abstract**

c-Jun N-terminal kinase (JNK) is activated by phosporylation in response to cellular stressors and extracellular signals and plays a role in the activation of glucocorticoid receptor (GR) and contributes to the stress-induced apoptosis. Therefore, the expression protein pattern of the active forms of cytosolic phospho-JNK (P-JNK) and inactive JNK in hippocampus of rats exposed to 21daily isolation as chronic stressor, sole and in combination with 2hrs acute stressors of immobilization (IM) or cold (4°C), were followed by Western blot. Concentration of serum corticosterone was monitored. We found significant increase in the levels of P-JNK following acute IM. Decreased levels of P-JNK following chronic isolation and when isolation preceded the application of acute IM were found, compared to its level after acute IM. Data suggest that diminished expression of P-JNK level following chronic isolation in hippocampus, might be involved in deregulation of intracellular GR negative feedback control as well as stress-induced apoptosis.

#### Introduction

c-Jun N-terminal kinase (JNK) phosphorylates glucocorticoid receptor (GR), modulates its subcellular localization and its function [1]. Also, recent evidences have shown a role for JNK signaling in stress-induced apoptosis. Previous study indicated that chronic isolation stress deregulates intracellular GR negative feedback control in limbic-hypothalamo-pituitary adrenal (LHPA) axis [2]. Since phosphorylation and dephosphorylation of intracellular effectors molecules are important regulatory mechanisms in signal transduction a variety of cellular events, including apoptosis, it is supposed that chronic isolation stress may alters JNK phosphorylation status which could be critical for stress-induced apoptosis in rat brain.

# **Experimental**

Adult Wistar male rats, aged three months, were divided at random into two main groups, a control (unstressed) group, where the rats were housed of four individuals *per* cage and chronic isolation stress group *i.e.* rats were individually housed for 21 day (isolates). The control group consisted of three subgroups: unstressed control alone and unstressed controls which were exposed to the 2hrs of acute stressor either immobilization (IM) or cold (4°C). The chronic isolates group also consisted of three subgroups: isolation stress alone, and isolates which were subsequently

exposed to IM or cold for 2hrs representing combined stressors. Separation of hippocampal cytosolic proteins was examined by SDS-PAGE and quantification of levels p-JNK and JNK by Western blot. Concentration of serum corticosterone (CORT) was monitored by ELISA. Data were analyzed by two-way ANOVA followed by Tukey post-hoc test.

#### **Results and Discussion**

Two immunoreactive bands of 46kDa and 54kDa corresponding to the predicted molecular mass of (P) JNK1 and (P) JNK2/3 protein were detected (Fig.1 A and B). A significant increase in the level of cytosolic P-JNK was found following acute IM. At the same time, serum CORT concentration was significantly increased by acute IM (Fig.2, left panel), indicating IM-related activation of adrenocortical system. Since the CORT signaling transduction is regulated by down regulation of cytosolic GR and GR phosphorylation by P-JNK is essential for GR activation, the elevated cytosolic P-JNK protein expression following acute IM (Fig.1A, left panel) represents physiological signal transduction process providing adaptive and protective response for survival [3].

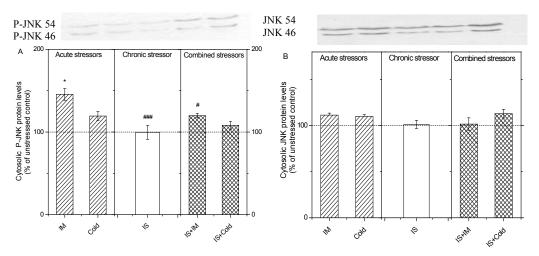


**Fig.1.** Protein content of cytosolic JNKs in the hippocampus of rats exposed to acute stressors immobilization (IM) or Cold, chronic isolation (IS) or their combination. (A) Upper panel: representative P-JNK Western blots for each stressor. Lower panel: cytosolic P-JNK protein expression; (B) Upper panel: representative JNK Western blots for each stressor. Lower panel: cytosolic JNK protein expression; Symbols indicate a significant difference between: the control and acute IM, \*p<0.05; combined stress or IS and acute IM, \*p<0.05, \*##p<0.001.

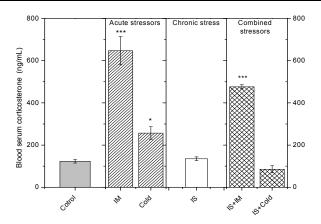


**Fig.2.** Changes in blood serum CORT concentrations (ng/mL) of adult Wistar male rats in control and following acute stressors immobilization (IM) Cold, chronic isolation (IS) or combined stressors, as indicated. Asterisks indicate significant difference between the respective stress group and unstressed control p<0.05, \*\*\*p<0.001.

Cytosolic P-JNK level was significantly decreased following chronic isolation, compared to its level after acute IM, while levels of JNK remained essentially unchanged (Fig.1B). The ratio between cytosolic P-JNK and JNK was decreased. Results indicate that chronic isolation impaired the hippocampal JNK signaling pathway. The two possible explanations are direct or indirect inhibition of cytosolic JNK activation in response to chronic stress and activation of putative phosphatase(s). Since, the chronic isolation compromises intracellular GR regulation [3], decreased protein expressions of cytosolic P-JNK might be included in GR protein modification and its deregulation. Decrease of P-JNK was noticed when isolation preceded the application of acute IM (Fig.1A, right panel), compared to its level after acute IM. Due to deregulated LHPA axis by chronic isolation [3], prolonged elevation of CORT level in combined stress (Fig.2, right panel) and reduction of P-JNK protein expression is most likely start up stress-induced apoptosis in hippocampus (data not shown).

#### Conclusion

Results show that decreased phosphorylation (activation) of JNK by chronic isolation stress in hippocampus might be included in deregulation of intracellular GR feedback system and may have a potential role in stress-induced apoptosis Nevertheless, the precise molecular mechanisms of proapoptotic JNK signaling pathway with other factors acting for apoptosis, such as p53, remains yet to be elucidated

- I. Rogatsky, S. Logan, M, Garabedian, Proc. Natl. Acad. Sci. U.S.A., 1998, 95, 2050-2055.
- [2] D. Filipović, Lj. Gavrilović, S. Dronjak, M. Radojčić, Neuropsychobiology, 2005, 51, 107-114.
- [3] B. Nankova, S. Fuchs, L. Serova, Z. Ronai, D. Wild, E. Sabban, Stress, 1998, 2, 289-298.

# PHYSICO-CHEMICAL STABILITY OF AMYLOID SELF-ASSEMBLIES: IMPLICATIONS FROM DISEASE TO NANOBIOTECHNOLOGY

#### L. Morozova-Roche

Department of Medical Biochemistry and Biophysics, Umeå University, Umeå, Sweden.

#### Abstract

The process of amyloid formation is characterized by general principles applicable to numerous polypeptides, undergoing amyloid self-assembly both *in vivo* and *in vitro*. We have studied *in vitro* the amyloid formation of two abundant proteins – lysozyme and insulin, which also form amyloid deposits in the body. Multiple amyloid species of lysozymes and insulin were characterized by using biophysical and biochemical methods including atomic force microscopy (AFM), thioflavin fluorescence, circular dichroism and gel electrophoresis. The regulatory interaction with amyloids such as calcium binding, pH and temperature were used to govern this process. The application of lysozyme amyloids for the ultrathin silver nanowire formation was demonstrated.

#### Introduction.

Protein aggregation is the most common and problematic manifestation of protein instability, which is encountered during all stages of protein applications in vitro and in a wide range of protein misfolding and amyloid diseases in the body. The formation of protein aggregates effectively decreases the quantity of the functional compounds in the solution. In contrast to amorphous aggregation, the selfassociation of polypeptides can be highly ordered, evolving towards the structurally organized protein polymers characterized by a specific cross-β-sheet core, which are commonly known as amyloids. Over the last decades it has been shown that the amyloids of more than 26 proteins are directly associated with human diseases. Several proteins have been used also as models to study this phenomenon in vitro. It has been suggested that the ability to form the cross-\u03b3sheet containing polymers is a generic property of a polypeptide chain, which implies that any polypeptide can adopt this conformation under amyloid-prone conditions. Compared to functionally active and soluble precursor proteins and their amorphous aggregates the amyloids gain new pathological and potentially highly hazardous properties such as remarkable stability and protease resistance, self-propagation via seeding and cross-seeding, cytotoxicity and induced immunogenicity. These properties need to be taken into account in order to prevent and treat diseases, to insure safer and surer products and also to create new products using amyloid properties for our own benefit [1].

#### **Results and Discussion**

Here we address the problem of amyloid self-assembly and structural properties of naturally occurring and widely used proteins such as lysozymes and insulin. Their monomeric, oligomeric and amyloid states have been characterized in order to provide an insight into the mechanisms of amyloid self-assembly and their practical applications. It is important to note, that due to generic nature of amyloids the principles found for some particular proteins can be applied for understanding of the mechanism of amyloid self-assembly in general.

Equine lysozyme is a naturally destabilized, calcium-binding lysozyme, which belongs to extended family of structurally homologous proteins c-type lysozymes and α-lactalbumins – the most studied model proteins with regard to their structural, folding and amyloidogenic properties. Equine lysozyme is viewed as an evolutionary link between them, as it possesses the structural and folding features of both subfamilies. It contains the active site involved in lysozyme enzymatic activity and the conserved, high-affinity calcium-binding site of α-lactalbumins. Due to equine lysozyme extremely low stability and cooperativity compared to non-calcium-binding c-type lysozymes, it forms equilibrium partially folded states similar to  $\alpha$ -lactalbumins as well as an ensemble of kinetic intermediates during the refolding reaction similar to lysozymes [2]. We have found that equine lysozyme undergoes self-assembly into amyloid protofilaments under the conditions of its molten globule formation at acidic pH [3,4]. We have shown that the morphology of equine lysozyme amyloids depends strongly on solution conditions, such as calcium concentration, pH and temperature. The holo-equine lysozyme assembles into linear protofilaments, while the apo-protein forms ring-shaped amyloids (Fig. 1).

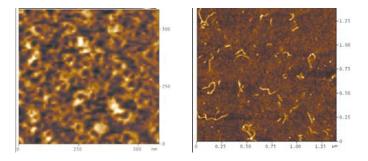


**Fig. 1.** AFM images of equine lysozyme amyloids formed at pH 2.0 and 57 °C (left) and at pH 4.5, 10 mM EDTA and 57 °C (right).

The amyloid-rings are varied in diameters, which equal to 45–50 nm at pH 4.5 and 70–80 nm at pH 2.0, respectively. All amyloid samples are polymorphic, containing a mixture of oligomers and protofilaments. It is important to note that, compared to human lysozyme fibrils, which undergo maturation, lengthening and thickening, the equine lysozyme protofilaments remain single-stranded and never exceed a few hundred nanometers in length. This fact may be attributed to the

presence of the very stable core in its structure, persistent even under amyloid forming conditions. Although the polypeptide sequences contributing to the fibrillar cross- $\beta$ -sheet core are encompassed most likely in the  $\beta$ -domain of equine lysozyme, its stable  $\alpha$ -helical core provides a non-adhesive fibrillar interface and thus prevents significant fibrillar growth [2,4].

These results demonstrate that the factors governing the amyloid formation include not only the propensity to form  $\beta$ -sheet core structure of the fibrils, but also the conformational plasticity of the polypeptide chains involved into the formation of fibrillar interface. Therefore, we suggest that the design of the regions with a high local stability and cooperativity, in addition to the overall stabilization of protein molecules, can be broadly explored as an amyloid-preventing strategy in the various applications involving proteinaceous compounds such as biopharmaceuticals, where the amyloid formation would be highly undesirable.

Another object of our studies is insulin – a 51-residue protein hormone involved in glucose metabolism and universally used in diabetes treatment. The marked tendency of insulin to undergo self-association into soluble dimers and hexamers is a natural process occurring in vivo in the B-cell in pancreases. The association involves the interaction of native insulin monomers and this process is easily reversible by reducing the insulin concentration. As insulin is a widely used therapeutic, the process of its aggregation has received a considerable attention. The formation of insoluble insulin species can lead to the significant reduction of the functionally active substance in the formulations. The regular injections of insulin can also cause long-term effects. Indeed, the amyloid deposits of insulin have been observed in diabetic patients after repeated injections. Under variety of destabilizing conditions in vitro insulin also forms amyloid fibrils. The process of insulin fibrillation occurs via the oligomeric intermediates populated on the pathway between the destabilized monomers and fibrils. This event in amyloid formation is of particular importance, as amyloids conventionally rely on oligomeric structures, which can act as templates for the subsequent depositions of additional protein molecules. The oligomers do not accumulate to the same extent as the fibrils, but they are viewed as a major pathogenic unit in neurodegenerative diseases and they have been shown to induce cytotoxic effect in experiments in vitro. In spite of significant attention to these structures over past decade and attempts to unify them as the entity shearing common conformational epitope, the oligomers of many amyloidogenic proteins remain much more poorly characterized than the final product of proteinaceous assembly - amyloid fibrils. The same refers to insulin fibrillation; the critical stage of its self-assembly involving the initial nuclei formation is still lack of understanding. There is no common view on the nature of oligomeric species formed prior the fibrillar appearance, specifically whether they contain predominantly  $\alpha$ -helical or  $\beta$ -sheet structure, to which extend they are populated and how detrimental they are in the fibrillation process.

Under the conditions used in our studies, i.e. acidic pH and elevated temperature, the fibrillation of insulin is a very cooperative and relatively rapid process, occurring within less then 10 hours. It is preceded by a prolonged lag-

phase, reaching 22 hours. The general consensus is that hexametric insulin requires the dissociation into destabilized monomers in order to undergo fibrillation, which can be achieved under the acidic conditions or by using denaturants. By using AFM, we have shown that the larger with up to 10-15 nm height amyloid-prone oligomers were emerged only at the end of the lag-phase. They exhibited the far UV circular dichroism and fluorescence spectra resembling monomeric insulin and did not bind amyloid specific dye thioflavin T. They were relatively short-lived and consequently transformed into rapidly accumulating amyloid fibrils, the formation of which was manifested in the thioflavin T binding and the development of characteristic cross- $\beta$ -sheet far UV circular dichroism spectrum.

Prior the formation of the large pre-fibrillar oligomers we have found that the smaller oligomers of tetramer range are populated during the early lag-phase. These oligomers contain the secondary structure similar to monomeric insulin. They can be dissociated by addition of sulfur reducing agent mercaptoethanol. By using XPS spectroscopy, we have demonstrated that these oligomers are stabilized by intermolecular bonds formed by oxidative reshuffling of the disulphide bridges of monomeric insulin. They are off-pathway to the amyloid assembly; the covalent bonding within oligomers stabilized their structure and prevented their conversion into the cross-\beta-sheet containing fibrils. As these oligomers effectively "compete" with the amyloids for the monomeric building blocks, their formation decreases the effective concentration of monomeric insulin, thus prolonging the lag-phase of amyloid assembly. These oligomers require further detail characterization with regards to their structural and functional properties. The knowledge of all species populated during insulin self-assembly is of critical importance due to its extensive biopharmaceutical applications in the treatment of diabetes, which rise high requirements to the safety and activity of its formulations.

As the amyloid fibrils are characterized by nanometer-scale dimensions, they have attracted great attention in the rapidly expanding areas of nanobiotechnology and nanobiomedicine. Nanometer-scale ordered complexes, self-assembled from various proteins, provide a renewable source to replicate inorganic composites. Nanoscale biotemplating is a growing field, exploring in particular the polymeric complexes for templating metallic nanowires. The latter are currently in high demand for the construction of conductive circuits in nanoscale electronics and as the active components in electrochemical devices. Apart from their regularity and easy reproduction, the biological templates may have another key advantage as they can grow directly at the required surfaces, thus guiding the assembly of the inorganic nanostructures straight into the nanodevices and eliminating the stage of their positioning and micro-manipulations. Another important feature of the amyloids, which makes them an attractive object in manufacturing procedures, is their remarkable stability, to such an extent that the fibrils composed of insulin were compared with regard to their physical strength to steel and their mechanical stiffness to silk (Smith et al., 2006). The amyloids are also stable towards denaturing treatments within a wide range of conditions, far exceeding the similar properties of other macromolecules such as DNA.

In our study we have selected the amyloid fibrils of highly ubiquitous protein hen egg-white lysozyme and subjected them to the controlled biotemplating of silver nanowire [5]. Initially, we have produced remarkably regular amyloid fibrils of hen egg-white lysozyme of up to 10 µm in length and 2–4 nm in diameter. The fibrils remained in solution for days and months, showing no sign of destruction under examination by AFM. The fibrils showed also a high stability over a broad range of pH from acidic to basic, temperatures and salt concentrations. As the biotemplating scaffolds need to be removed at the end of the production cycle, we subjected the fibrils to proteases and found the requisite conditions which eventually, in spite of their significant resistance, led to their dissolving. That was achieved by incubating the fibrils with an excess of proteinase K at pH 7.0 and 57 °C for 24 h, which resulted in their full digestion.

We have found, that by introducing 2,2,2-trifluoroethanol (TFE) into solution with the fibrils, we have induced their further stabilization and association into longer and thicker amyloid scaffolds up to 9 nm height. Our next step was to demonstrate that, if TFE is incubated with ionic silver, it acts as a mild reducing agent producing colloidal silver. The reaction of silver reduction was corroborated by an increase in the absorption spectra with maximum at 450 nm. AFM analysis also showed the formation of uniform silver nanoparticles. Their dimensions were determined by the reduction time, the particles of ca. 1.2 nm diameter were formed after 2 h and with ca. 35 nm diameter – after 72 h, respectively.

We have succeeded with the production of the silver nanowires by subjecting the amyloid fibrils to TFE in the presence of silver ions. After completing the reaction of silver reduction, monitored by optical absorbance measurements, the proteinaceous moulding scaffolds were removed by proteinase K digestion. This resulted in a drop of the thioflavine T signal to the level of free dye in solution. AFM analysis has confirmed the dissolution of the thick amyloid scaffolds and demonstrated the bulk-deposition on the mica surface of remaining silver wires (Fig. 2a,b).

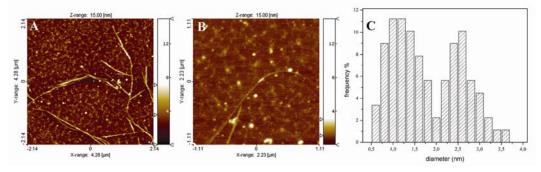


**Fig. 2.** AFM images of silver nanowires. (A) Network of single and winded wires; (B) a single silver wire; (C) the distribution of silver wire diameters measured in the multiple cross-sections.

The dimensions of individual wires were measured by AFM cross-section analysis and the height distribution corresponding to the diameters of the wires is presented in Fig. 2c. Individual wires were characterized by ca. 1 to 1.2 nm diameter and reached up to 2 µm in length (Fig. 2a,b). The wires of ca. 2.5 nm diameter represented a second major population, most likely formed by double silver threads. Thus, two concomitant processes, the amyloid scaffold assembly from individual fibrils and reduction of silver trapped at the fibrillar interfaces within the scaffold resulted in the production of silver nanowires. This indicates that fibrillar lateral assembly and the formation of the structured, hollow interface within the thicker fibrillar bundles is essential for silver moulding, while the individual amyloid fibers with a common diameter of ca. 2–4 nm do not possess such a cavity. Therefore, as the replica reflects the shape of the mold, the process of biotemplating itself has provided a structural insight into the amyloid inner architecture, directly confirming the absence of hollow part within amyloid protofilaments.

#### Conclusions.

The amyloid formation has emerged as a universal phenomenon with very broad implications in the industry and our daily life. While most commonly it is associated with diseases, the amyloids can be spontaneously developed in food during storage and also in biopharmaceuticals and other products containing proteinaceous compounds. Depending on the set up, the amyloids can be used also as valuable resources, providing renewable material for biotechnological applications as demonstrated above.

- [1] L.A. Morozova-Roche, & M.Malisauskas, Curr. Med. Chem., 2007, 14, 1221–1230.
- [2] L.A. Morozova-Roche, FEBS Lett., 2007, 581, 2587–2592.
- [3] M. Mališauskas, V. Zamotin, J. Jass, W. Noppe, C.M. Dobson & L.A. Morozova-Roche, J. Mol. Biol. 2003, **330**, 879–890.
- [4] M. Malisauskas, J. Ostman, A. Darinskas, E. Liutkevicius, E. Lundgren, & L.A. Morozova-Roche, J. Biol. Chem. 2005, 280, 6269–6275.
- [5] M. Malisauskas, R. Meskys & L.A. Morozova-Roche, Biotechnology Progress, in press.

# MODULATION OF CA<sup>2+</sup> ION FLUX THROUGH MITOCHONDRIAL MEMBRANE OF THE RAT BRAIN STEAM SYNAPTOSOMES BY 17β-ESTRADIOL

S. Petrović, M. Milošević and A. Horvat

Laboratory for Molecular Biology and Endocrinology VINČA Institute of Nuclear Sciences, P.O.Box 522, 11001 Belgrade, Serbia

#### **Abstract**

In the present study the modulation of  $Ca^{2+}$  ion flux in the synaptosomal mitochondria isolated from the ovariectyomized rat Brain Steam and the possible roll of membrane bound estradiol was examined. Physiological concentrations of  $17\beta$ -estradiol binds specifically to isolated mitochondria ( $V_{max} 3.37 \pm 0.25$  pmol/mg protein,  $K_m$   $1.85 \pm 0.06$  nmol/l of free estradiol). Addition of  $17\beta$ -estradiol (10 pmol/l - 1 nmol/l) *in vitro* decreased mitochondrial calcium ion efflux significantly (25%) after 10 minutes. Modulation of calcium ion efflux and mitochondrial ion retention may be the way that  $17\beta$ -estradiol (E2) exerts its role in the nerve cell homeostasis.

#### Introduction

The maintaining of Ca<sup>2+</sup> ion homeostasis is of great importance for the normal functioning of neuronal cells. Significant contribution of mitochondria in shaping intracellular calcium ion concentration ([Ca<sup>2+</sup>]<sub>i</sub>) was documented in various neuronal preparations [1]. In mitochondria, Ca<sup>2+</sup> is taken up via ruthenium-red sensitive uniporter driven by the electrochemical gradient, while Ca<sup>2+</sup> ion efflux is mainly mediated by Na<sup>+</sup>/Ca<sup>2+</sup> exchanger activity [1]. Steroid hormones can modulate various processes in mitochondria from nervous tissues [2]. Some of these effects seem to be mediated via the mitochondrial membrane. In our previous work specific binding of E2 to mitochondria isolated from nerve cell endings fom whole rat brain were found [3]. At the concentrations that specifically bind to mitochondrial membrane, estradiol was found to contribute to the modulation of mitochondrial Ca<sup>2+</sup> transport. In that way estradiol regulate mitochondrial homeostasis and cytosolic Ca<sup>2+</sup> concentrations by changing sequestration and release of those ions [3]. In order to examine relations between effects on mitochondrial Ca<sup>2+</sup> flux and binding to mitochondrial membrane in specific brain area, Brain Stem, in the present study we quantified specific binding sites and concentration-dependent modulation of influx and efflux of Ca<sup>2+</sup> in the presence of E2.

# **Experimental**

Synaptosomal mitochondria used for E2 binding and Ca<sup>2+</sup> transport measurements were isolated from the Brain Steam of chronically (3 weeks prior to use)

ovariectomized (OVX) female rats as described previously [4]. For E2 binding and Ca<sup>2+</sup> transport monitoring mitochondria were preincubated at 22 °C for 10 min in medium containing (in mmol/l): 300 mannitol, 10 KCl, 1 maleate, 5 glutamate, 10 Tris-HCl, pH 7.4. In the cease of binding assay, after preincubation without hormone, mitochondria (0.5 mg/ml) were incubated with (3H)estradiol (0.1-100 nmol/l) an additional 10 min, for total hormone binding. Nonspecifically bound estradiol was determined incubating mitochondria with labeled and 100-fold excess of unlabelled estradiol. Specific hormone binding was calculated by subtracting nonspecific bound from total bound estradiol. The influx of Ca<sup>2+</sup> to synaptosomal mitochondria was initiated by adding 0.2 mmol/l CaCl<sub>2</sub> (0.6 µCi <sup>45</sup>CaCl<sub>2</sub>), lasted 5 min and stopped by ruthenium red (17.5 µg/mg protein), a specific inhibitor for Ca<sup>2+</sup> uniporter. For Ca<sup>2+</sup> efflux monitoring, mitochondria were loaded with calcium in the same way and after adding ruthenium red the efflux of Ca<sup>2+</sup> was initiated by adding NaCl (20 mmol/l) and 0.2 mmol/l EDTA and lasted 5 min. The effect of E2 on Na-dependent Ca<sup>2+</sup> efflux was measured by incubating Ca<sup>2+</sup>-preloaded mitochondria with 0.5 pmol/l - 50 nmol/l of E2 for 10 minutes.

#### **Results and Discussion**

As presented in Fig. 1, E2 specifically binds to synaptosomal mitochondria from BS and this binding reaches plateau in the presence 3.25 nmol/l and higher of E2. Michaelis-Menten plot of specific estradiol binding to mitochondria indicates one binding site with estimated  $V_{max}$  of 3.37± 0.25 pmol/mg protein and  $K_m$  of 1.85± 0.06 nmol/l free estradiol. Scatchard plot (fig 1 inset) concave upward indicates the

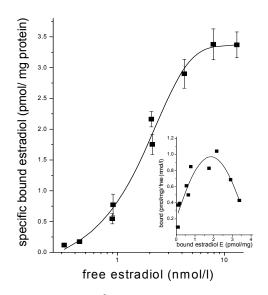


**Fig. 1.** Specific (<sup>3</sup>H)estradiol binding to synaptosomal mitochondria isolated from Brain Stem

existence of positive cooperativity. When compared with our previous results [5], on plasma membranes synaptic from rat BS (capacity of 0.3 pmol/mg and affinity 26 nmol/l estradiol for free high capacity/low affinity site and capacity 0.06 pmol/mg affinity of 4 nmol/l estradiol for low capacity/high affinity site) we found on mitochondria one binding site with different binding properies indicating that different proteins (receptors) are responsible for specific estradiol binding to svnaptosomal membrane and mitochondria of BS.

Ca<sup>2+</sup> influx through the

**Table 1.** Dose-dependent effect of estradiol *in vitro* on mitochondrial Ca<sup>2+</sup> flux (% of inhibition or stimulation of control value)

control value)							
E2 conc.	Ca <sup>2+</sup>	Ca <sup>2+</sup>					
	influx	efflux					
0.5 pmol/l		- 14.9					
1 pmol/l	+ 13	- 13.9					
5 pmol/l	0	- 14.9					
10 pmol/l	+ 1	- 22.4					
50 pmol/l	+ 4	- 27.8					
0.1 nmol/l	- 12.5	- 24.1					
0.5 nmol/l	- 6	- 26.6					
1 nmol/l	+ 12	- 25.9					
5 nmol/l	- 5	- 11.2					
10 nmol/l	+ 10	+ 5.6					
50 nmol/l	- 2	+ 11.1					
0.1 μmol/l	- 11.5	+ 14.8					
1 μmol/l	+ 10	+ 13.2					
10 μmol/l	- 7	+ 15.1					

ruthenium red sensitive uniporter and Nadependent Ca<sup>2+</sup> efflux was measured in <sup>45</sup>Ca<sup>2+</sup> preloaded synaptosomal mitochondria isolated from the BS, in the presence and absence of E2 in vitro. The uniporter, compared to the control values (0.484 nmol Ca<sup>2+</sup>/mg protein) was unaffected by E2. In the case of Ca<sup>2+</sup> efflux (control value in the absence of estradiol 0.54 nmol Ca<sup>2+</sup>/ mg protein), E2 exerts a dosedependent effect (Table 1.). Estradiol concentrations up to 5 pmol/l inhibited Ca<sup>2+</sup> efflux about 15%, while the concentrations between 10 pmol/l and 1 nmol/l decreased Ca<sup>2+</sup> efflux in the BS mitochondria about 25%. This result is in accordance with earlier our synaptosomal mitochondria isolated from rat brain nucleus caudatus and hippocampus [6]. The estradiol concentrations that affect the BS Ca<sup>2+</sup> efflux are between E2 concentrations exerting

effects on two structures mentioned above. The exsistence of multiple populations of mitochondrial binding sites may reflect the diversity of neuronal cell types and their physiological properties within the brain structures.

#### Conclusion

Ca<sup>2+</sup> transport in Brain Steam mitochondria can be modulated by estradiol. While influx of Ca<sup>2+</sup> was unchanged, inhibition of Ca<sup>2+</sup> efflux was detected. The estradiol decrease mitochondrial Na<sup>+</sup>/Ca<sup>2+</sup> exchanger activity, at the same concentrations at which it bound specifically to mitochondria, possibly acting *via* mitochondrial membrane binding sites for estradiol.

# Acknowledgements

This study was supported by the Serbian Ministry of Sciences Project No. 143044.

- [1] P. Gobbi, P. Castaldo, A. Minelli, S. Salucci, S. Magi, E. Corcione, S. Amoroso, Pharmacological Research 2007, **56**, 556-565.
- [2] M.P. Mattson. N. Robinson, Q. Guo, Neuro Rep. 1997, 8, 3918-3821.
- [3] A. Horvat, G. Nikezić, S. Petrović, D.T. Kanazir, Cell. Mol. Life. Sci. 2001, 58, 636-644.
- [4] J.C.K. Lai, J.B. Clark, Methods Enzymol. 1970, 55, 51.
- [5] A. Horvat, G. Nikezić, J.V. Martinović, Experientia 1995, 51, 11-15.
- [6] S. Petrović, M. Demajo, A. Horvat, Ann. N. Y. Acad. Sci. 2005, 1048, 341-343.

# QUANTITATIVE STUDY OF MOLECULAR INTERACTIONS AND MOBILITY IN LIVE CELLS BY FLUORESCENCE CORRELATION SPECTROSCOPY/CONFOCAL LASER SCANNING MICROSCOPY

V. Vukojević<sup>1</sup>, Y. Ming<sup>1</sup>, C. D'Addario<sup>1</sup>, B. Johansson<sup>1</sup>, R. Rigler<sup>2,3</sup> and L. Terenius<sup>1</sup>

<sup>1</sup>Department of Clinical Neuroscience, Karolinska Institutet, 17176 Stockholm, Sweden (Vladana. Vukojevic@ki.se) <sup>2</sup>Department of Medical Biochemistry and Biophysics, Karolinska Institutet, 17177 Stockholm, Sweden <sup>3</sup>Laboratory of Biomedical Optics, Swiss Federal Institute of Technology, CH-1015 Lausanne, Switzerland

#### **Abstract**

Advanced quantitative imaging based on Fluorescence Correlation Spectroscopy (FCS) integrated with Confocal Laser Scanning Microscopy (CLSM) is presented. The potential of this methodology for quantitative investigation of molecular events in real time and with single-molecule sensitivity in live cells is exemplified in the study on  $\mu$ -opioid (MOP) receptor activation.

#### Introduction

Many biological problems are addressed using fluorescence microscopy based approaches and the confocal fluorescence microscope has become a centerpiece in the cell biology laboratory. Fluorescence intensity fluctuation analysis, offering the possibility to study quantitatively molecular interactions in live cells, is still a technique that is overwhelmingly used in laboratories specialized in biophysical analysis and has not yet reached the wider community of researchers in the biomedical field. The introduction of fluorescence intensity fluctuation analysis in imaging offers the possibility to achieve quantitative fluorescence imaging with single-molecule sensitivity, an accomplishment that can considerably advance our understanding of biological processes at the molecular level.

# **Theoretical Background on FCS**

FCS relies on the measurement and analysis of fluorescence intensity fluctuations to characterize quantitatively the investigated system and extract information about the dynamics of processes leading to fluorescence intensity fluctuations [1-6]. To measure fluorescence intensity fluctuations in a diffraction limited volume element, the optical setup of a confocal microscope is used (Fig. 1). Light emitted by fluorescing molecules passing through the observation volume element or undergoing transformations that lead to fluorescence emmision/loss is transmitted to the detector, recorded in real time (Fig. 1 A, B) and analyzed using statistical

methods for fluctuation analysis like temporal autocorrelation analysis (Fig. 1 C, D), but other approaches can also be applied [4].

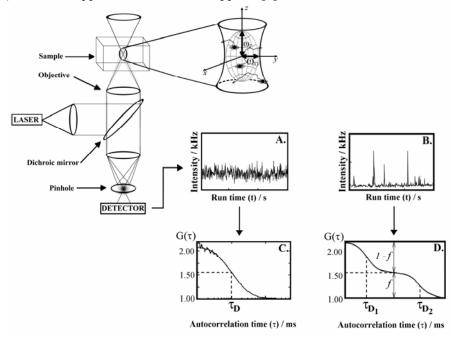


Fig. 1. Schematic presentation of the instrumentation for FCS/CLSM

To induce fluorescence, the sample is illuminated by incident laser light. The irradiating laser beam is reflected by a dichroic mirror and sharply focused by the objective to form a diffraction limited volume element. A confocal aperture is set in the image plane to reject the out-of-focus light and enhance further the signal-tonoise ratio. The pinhole also reduces the volume from which fluorescence is detected, providing an elliptical detection volume element (magnified in the insert) with submicrometer resolution in two lateral directions - the diffraction limited detection volume element is typically smaller than 0.5  $\mu$ m  $\times$  0.5  $\mu$ m  $\times$  2  $\mu$ m. Following the absorption of energy, fluorescent molecules lose energy through photon emission. Light emitted by fluorescing molecules passing through the confocal volume element (magnified in the insert) is separated from the exciting radiation and the scattered light by a dichroic mirror and barrier filter, and transmitted to the detector. A. Fluorescence intensity fluctuations in a system undergoing free three-dimensional diffusion. **B.** Fluorescence intensity fluctuations in a systems undergoing free three-dimensional diffusion with binding to a surface. C. Autocorrelation curve  $G(\tau)$  fitted using equation (2a). The average number of molecules in the observation volume element is determined from the amplitude of the autocorrelation function (1/N = 0.94), and average residence time  $\tau_D$  from the inflection point. **D.** Autocorrelation curve  $G(\tau)$  fitted using equation (2c). The complex shape of the autocorrelation curve indicates that two components with

different diffusion times,  $\tau_{D1}$  and  $\tau_{D2}$ , are present. The average number of particles in the observation volume element is determined from the amplitude of the autocorrelation curve (1/N = 0.8). The ratio of the free fraction versus the bound is given by the ratio of the relative amplitudes (1-f)/f.

In temporal autocorrelation analysis the normalized autocorrelation function  $G(\tau)$  is first derived.  $G(\tau)$  gives the correlation between the deviation of fluorescence intensity, measured at a certain time t,  $\partial I(t) = I(t) - \langle I(t) \rangle$ , and its intensity measured at a later time  $t + \tau$ ,  $\partial I(t + \tau) = I(t + \tau) - \langle I(t) \rangle$ , from the average fluorescence intensity  $\langle I(t) \rangle$ :

$$G(\tau) = 1 + \frac{\langle \partial I(t) \partial I(t+\tau) \rangle}{\langle I(t) \rangle^2}$$
 (1)

The normalized autocorrelation function  $G(\tau)$  is then plotted for different autocorrelation times  $\tau$ , yielding the experimental autocorrelation curve (Fig. 6 C, D). In molecular systems undergoing stochastic fluctuations, one would observe random variations of  $G(\tau)$  around the value  $G(\tau) = 1$ . For processes that are not random, one typically observes a maximal limiting value of  $G(\tau)$  as  $\tau \to 0$ , decreasing to the value of  $G(\tau) = 1$  at long times, indicating that correlation between the initial and the current property value has been lost (Fig. 1 C, D). In a simple system with one component and a single characteristic fluctuation frequency, the autocorrelation curve has a simple sigmoid form (Fig. 1 C). The amplitude of the autocorrelation function  $G(\tau)$  as  $\tau \to 0$ , is inversely proportional to the absolute concentration of the fluorescing molecules, whereas the range of  $\tau$ values over which  $G(\tau)$  changes rapidly as a function of  $\tau$  gives the time scale at which the fluorescence intensity fluctuations occur. In a system with multiple components, for example two components that differ in their diffusion properties, the autocorrelation function assumes a more complex shape (Fig. 1 D). The amplitude of the autocorrelation function as  $\tau \to 0$  is inversely proportional to the average number of all fluorescent particles in the observation volume element, multiple inflection points indicate that fluctuations in the signal occur at two time scales  $(\tau_{D1}$  and  $\tau_{D2})$  and the relative amounts of the two components can be estimated from the amplitudes 1 - f and f.

In real experiments, the autocorrelation curves are fitted numerically using theoretical autocorrelation functions. To derive an appropriate autocorrelation function it is very important to take notice of all processes that may lead to fluctuations in the fluorescence signal, like diffusion, active transport, chemical reactions, structural transformation, photophysical processes *etc.* because all processes leading to statistical fluctuations in the fluorescence signal will induce a characteristic decay time in the autocorrelation curve [4-6]. For example, if the passage of fluorescent particles is governed solely by diffusion, the experimental autocorrelation curve (Fig. 1 C) can be fitted by an autocorrelation function describing free three-dimensional diffusion of one component:

$$G(\tau) = 1 + \frac{1}{N} \cdot \frac{1}{\left(1 + \frac{\tau}{\tau_D}\right) \sqrt{1 + \frac{w_{xy}^2}{w_z^2} \frac{\tau}{\tau_D}}} .$$
 (2a)

In equation (2a), N is the average number of fluorescent molecules in the observation volume element;  $w_{xy}$  and  $w_z$  give the  $1/e^2$  radius of the observation volume element in the radial and axial direction, respectively;  $\tau_D$  is the average time a fluorescent particle stays in the observation volume element. In FCS terminology,  $\tau_D$  is called the lateral diffusion time and is directly related to the size of the observation volume element and the diffusion coefficient (D) of the fluorescent particles:

$$\tau_D = \frac{w_{xy}^2}{4 \cdot D} \tag{2b}$$

If the example given in Fig. 1 D represents ligand binding to plasma membrane associated receptors, the corresponding theoretical autocorrelation function would be:

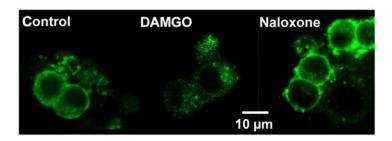
$$G(\tau) = 1 + \frac{1}{N} \cdot \left( \frac{1 - f}{\left(1 + \frac{\tau}{\tau_{D1}}\right) \sqrt{1 + \frac{w_{xy}^2}{w_z^2} \frac{\tau}{\tau_{D1}}}} + \frac{f}{\left(1 + \frac{\tau}{\tau_{D2}}\right)} \right) . \tag{2c}$$

In equation (2c) N is the average number of ligand molecules in the observation volume element; the first term in the parenthesis describes free three-dimensional diffusion of unbound ligand molecules; the second term describes two-dimensional diffusion of the membrane-associated ligand-receptor complexes;  $\tau_{D1}$  and  $\tau_{D2}$  are the lateral diffusion times for the unbound and bound ligand, respectively. The relative amount of unbound *versus* bound ligand molecules is given by the ratio of (1-f) over f.

# μ-Opioid Receptor Activation in Live Cells

The μ-opioid receptor (MOP) belongs to the largest family of cell-surface receptors, the G protein-coupled receptors (GPCRs). Structurally, GPCRs are 7 trans-membrane (7TM) proteins and their biological role is to convey information from the cellular exterior to the internal signaling machinery to regulate cellular physiology. Because of their extremely relevant biological role and implication in disease pathology, GPCRs are most important targets for current and novel drugs and therapeutic approaches [7-9].

Interaction of the  $\mu$ -opioid receptor (MOP) with selected ligands was investigated in live cells [10]. In PC12 cells stably transformed to express the fluorescently labeled MOP-EGFP construct, two pools of MOP were identified that could be discriminated by differences in their lateral mobility in the cell membrane.



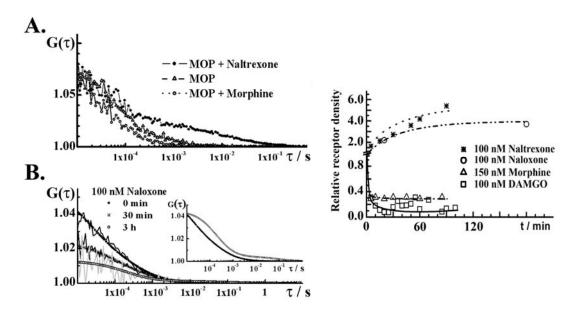


**Fig. 2.** Confocal images showing subcellular localization of MOP-EGFP (green) under control conditions, and upon 3 h treatment with DAMGO (1.0 μM) and naloxone (50.0 μM). **A.** Autocorrelation curves reflecting changes in the lateral mobility of the MOP under stimulation with morphine (open circles) or naltrexone (filled circles). **B.** Autocorrelation curves reflecting increase in the number of plasma membrane associated MOP-EGFP caused by interaction with naloxone (100 nM). The amplitude of the FCS autocorrelation curve is reciprocal to the number of particles in the observation volume (1/N), indicating that during the course of time the MOP gradually accumulated at the plasma membrane. At the same time, the contribution of the slow fraction increased. Insert: Autocorrelation functions corresponding to the autocorrelation curves for 0 min and 3 h, normalized to have the same amplitude at  $\tau = 10$  μs, showing that lateral mobility of the MOP decreased under stimulation with naloxone. **C.** Relative changes in MOP-EGFP surface density under stimulation with selected ligands.

The majority of MOP receptors,  $(80 \pm 10)$  %, was characterized by a diffusion coefficient  $D_{MOP,1} = (4 \pm 2) \times 10^{-11} \text{ m}^2 \text{s}^{-1}$ , as compared to the slowly moving fraction,  $D_{MOP,2} = (4 \pm 2) \times 10^{-12} \text{ m}^2 \text{s}^{-1}$ . Upon stimulation with selected agonists (DAMGO, enkephalin heptatpeptide, morphine and methadone) surface density of the MOP decreased while the lateral mobility increased. In contrast, antagonists (naloxone and naltrexone) "froze" the receptor in the membrane, *i.e.* increased MOP surface density and decreased lateral mobility (Fig. 2).

# **Dynamics of Lipid Constituents in the Plasma Membrane Under Mop Activation**

Quantitative imaging by FCS/CLSM enabled us to study the intricate interplay between the dynamics of MOP receptor and the surrounding lipids [7]. MOP activation with agonists is accompanied by pronounced changes in the dynamics of annular plasma membrane lipids, reflecting the induction of complex cellular processes like ligand-induced receptor internalization or sorting at the plasma membrane (Fig. 3).

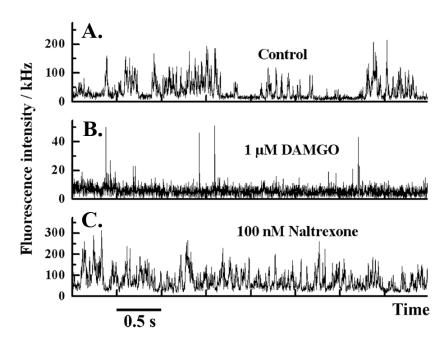


**Fig. 3.** Fluorescence intensity bursts from the lipid probe DiIC18(5) recorded at the plasma membrane of PC12 cells expressing the MOP-EGFP construct, indicating rearrangements in the structural organization/dynamics of lipids upon MOP stimulation. **A.** Constitutive endocytosis. **B.** Upon 30 min stimulation with DAMGO (1.0  $\mu$ M). **C.** Upon 30 min stimulation with naltrexone (100 nM). Lipid dynamics in control PC12 cells was not affected by the ligands.

# **Ligand-Receptor Interactions in Live Cells**

Ligand-receptor interactions could be studied in real time in live cells (Fig. 4). It was found that MOP-hEnk ligand-receptor complexes are characterized with slow lateral mobility,  $\tau_{D2} = (4.0 \pm 2.0)$  ms. The hEnk binding constant at MOP was determined to be  $(5.0 \pm 1.0) \times 10^9$  M<sup>-1</sup> [7].

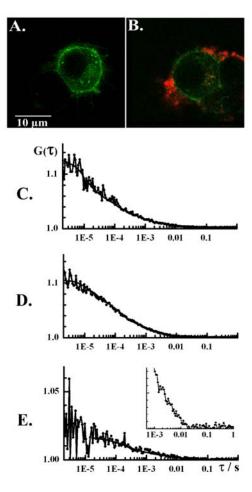


Figure 4. Confocal images showing **MOP-EGFP** expression of undifferentiated PC12 cells before (A) and after 110 min incubation with 50 nM TRITC-labeled hEnk (B). TRITC and EGFP fluorescence were excited using the 488 nm line of the Ar laser. Green and red colors visualize fluorescence emitted in the range 505and above 650 nm respectively. The images were obtained using avalanche photodiode detectors. Detection of ligand-receptor complexes in living cells temporal dual-color cross-correlation analysis. Single-color autocorrelation curves for rMOP-EGFP **(C)** TRITC- labeled hEnk (D), and dualcolor cross-correlation curves obtained in the continuous (E) and the switching mode (magnified in the insert). The two-component model for free 2Ddiffusion (Eq. 2 c) was applied to evaluate the cross-correlation curve, confirming existence of ligand-receptor complexes with lateral mobility  $\tau_{D1}$  =  $(250 \pm 150)$  µs and  $\tau_{D2} = (4.0 \pm 2.0)$  ms, respectively.

#### Conclusion

Imaging approaches are indispensible tools in medical diagnostics, clinical trials and biomedical research. Microscopic fluorescence imaging approaches hold the promise to become essential tools for investigating the mechanisms and ontology of diseases at the molecular level, enable disease detection in early stages of development and may revolutionize our approach to their treatment. In this study, quantitative fluorescence imaging based on FCS/CLSM is presented. This spatially

and temporally resolved imaging approach enabled us to study molecular events in live cells in real time and with single molecule sensitivity.

- [1] M. Ehrenberg, R. Rigler, Chem. Phys. 1974, 4, 390 401.
- [2] D. Magde, W. W. Webb, E. Elson, Phys. Rev. Lett. 1972, 29, 705 708.
- [3] E. L. Elson, D. Magde, Biopolymers, 1974, **13**, 1 27.
- [4] V. Vukojević, A. Pramanik A, T. Yakovleva T, R. Rigler, L. Terenius, G. Bakalkin, Cell. Mol. Life Sci. 2005, 62, 535 550.
- [5] K. Bacia, P. Schwille, Methods Mol. Biol. 2007, **398**, 73 84.
- [6] K. Bacia K, P. Schwille, Nat. Protoc. 2007, 2, 2842 2856.
- [7] R. J. Lefkowitz, *Acta Physiol. (Oxf.)* 2007, **190**, 9 19.
- [8] K. L. Pierce, R. T. Premont, R. J. Lefkowitz, R.J. Nat. Rev. Mol. Cell. Biol. 2002, 3, 639–650
- [9] E. Jacoby, R. Bouhelal, M. Gerspacher, K. Seuwen, ChemMedChem. 2006, 1, 761–782
- [10] V. Vukojević, Y. Ming, C. D'Addario, M. Hansen, Ü. Langel, R. Schulz, B. Johansson, R. Rigler, L. Terenius, FASEB J. 2008, *in press*

# INFLUENCE OF DECAVANADATE ON RAT SYNAPTIC PLASMA MEMBRANE ATPASES ACTIVITY

D. Krstić<sup>1</sup>, M. Čolović<sup>2</sup>, N. Bošnjaković-Pavlović<sup>3</sup>, A. Spasojević-de Bire<sup>4</sup> and V. Vasić<sup>2</sup>

<sup>1</sup>Institute of Medicinal Chemistry, School of Medicine, University of Belgrade, Serbia, e-mail: krsticdana@yahoo.com

<sup>2</sup> Vinča Institute of Nuclear Sciences, P.O.Box 522, 11001 Belgrade, Serbia

<sup>3</sup>Faculty of Physical Chemistry, University of Belgrade, Belgrade, Serbia

<sup>4</sup>Ecole Centrale Paris, Laboratoire SPMS UMR CNRS 8580 1, Grande Voie des Vignes 92295

Châtenay-Malabry, France

#### **Abstract**

The *in vitro* influence of decameric vanadate species on Na<sup>+</sup>/K<sup>+</sup>-ATPase, plasma membrane Ca<sup>2+</sup>-ATPase (PMCA)-calcium pump and ecto-ATPase activity, using rat synaptic plasma membrane (SPM) as a model system was investigated. The concentration-dependent responses to decavanadate of these enzymes were obtained. The half-maximum inhibition (IC<sub>50</sub>) of the enzyme activity was achieved at  $(4.74 \pm 1.15) \times 10^{-7}$ mol/l for Na<sup>+</sup>/K<sup>+</sup>-ATPase and  $(3.13 \pm 1.70) \times 10^{-8}$  mol/l for Ca<sup>2+</sup>-ATPase, while ecto-ATPase is significantly less sensitive toward decavanadate (IC<sub>50</sub>-  $(1.05 \pm 0.10) \times 10^{-4}$  mol/l) than investigated P-type ATPases.

#### Introduction

Interest in the interaction of vanadate oxoanions with biological systems has inceased since it has been demonstrated to have a variety of physiological effects acting either as a phosphate analogue in the monomeric form (H<sub>2</sub>VO<sub>4</sub>) [1] or through oligomeric vanadate species which interact with biomolecules with various and versatile activity (enzymes inhibitor or activator). Several studies report that decavanadate has a stronger effect on various enzymes, when compared to other vanadate oligomers and include the possibility of its use as a tool in the in the understanding of molecular mechanism of muscle contraction as well as inhibition of several ATPases such as P-type ATPases [2,3].

The aim of this work was the investigation of the *in vitro* effect of ammonium decavanadate,  $(NH_4)_6V_{10}O_{28}.5H_2O$  on  $Na^+/K^+$ -ATPase (sodium pump), plasma membrane  $Ca^{2+}$ -ATPase (PMCA)-calcium pump and ecto-ATPase (Mg $^{2+}$ -ATPase) activity, using rat synaptic plasma membrane (SPM) as a model system.

#### **Material and Methods**

Ammonium decavanadate was prepared by dissolving ammonium trioxovanadate(V) NH<sub>4</sub>VO<sub>3</sub> (0.4 g, 3.42 mmol) in distilled water (20 ml) as described in [1] to obtain decavanadate anions. The solution was stirred and heated until complete dissolution of NH<sub>4</sub>VO<sub>3</sub> (about 2h). The pH was adjusted to 5.90 by

dropwise addition of NH<sub>4</sub>OH. Orange crystals were formed within four days from the solution and kept at room temperature.

The SPM were isolated from the whole rat (albino, Vistar) brain according to the standard method [4]. The standard assay medium for investigation of SPM Na<sup>+</sup>/K<sup>+</sup>-ATPase activity contained (in mM) 50 Tris–HCl, pH 7.4; 100 NaCl; 20 KCl; 5 MgCl<sub>2</sub>; 2 ATP; 25 μg SPM proteins, while the rat synaptic PMCA activity was assayed in standard medium containing (in mM): Tris-HCl (pH 7.4), 0.5 EGTA, 0.5 CaCl<sub>2</sub>, 5 MgCl<sub>2</sub>, 2 ATP and 25 μg SPM proteins in a final volume of 200 μl. Incubation mixtures were preincubated for 10 min at 37°C in the presence of investigated compound or distilled water (control). The inorganic orthophosphate (P<sub>i</sub>) liberated from the hidrolysis of ATP, was measured using spectrophotometry at 690 nm. The activity obtained in the presence of Mg<sup>2+</sup> alone was attributed to ecto-ATPase (Mg<sup>2+</sup>-ATPase) activity. SPM Na<sup>+</sup>/K<sup>+</sup> -ATPase as well as SPM Ca<sup>2+</sup>-ATPase activities were calculated by subtracting the Mg<sup>2+</sup>-ATPase activity from the total ATPase activity in the presence of Na<sup>+</sup>, K<sup>+</sup> and Mg<sup>2+</sup> ions (i.e. in the presence of Ca<sup>2+</sup> and Mg<sup>2+</sup> ions).

#### **Results and Discussion**

The influence of decavanadate on SPM ATPases activity was investigated by in *vitro* exposure to enzymes in the concentration range from  $1 \times 10^{-10}$  to  $1 \times 10^{-1}$  mol/L. The results show, that increasing concentrations of decavanadate induced inhibition of enzymatic activity in a concentration-dependent manner in all cases (Fig. 1a). The dependence of enzyme activity, expressed as a percentage of the control value (obtained without inhibitor) on inhibitor concentration fit a sigmoidal function for all enzymes. The half-maximum inhibitory concentrations (IC<sub>50</sub>) of the investigated compound for all ATPases were determined by sigmoidal fitting of the experimental results as well as by Hill analysis (Fig.1b) and are summarized in Table 1. It is obvious that plasma membrane calcium and sodium pumps are more sensitive toward decavanadate anion than ecto - ATPase. At the concentration of 1x10<sup>-5</sup> mol/l decavanadate inhibited Na<sup>+</sup>/K<sup>+</sup>-ATPase as well as Ca<sup>2+</sup>-ATPase up to 80%, while the effect of the same concentration of decayanadate on the ecto-ATPase activity was negligible. The half-maximum inhibition (IC<sub>50</sub>) of the enzyme activity was achieved at  $(4.74 \pm 1.15) \times 10^{-7}$  mol/l for Na<sup>+</sup>/K<sup>+</sup>-ATPase and (3.13) $\pm$  1.70) x 10<sup>-8</sup> mol/l for Ca<sup>2+</sup>-ATPase, while the same effect for ecto-ATPase was observed at a few (several) orders of magnitude higher concentration of decayanadate -  $(1.05 \pm 0.10) \times 10^{-4}$  mol/l. The obtained dose-dependent inhibition of PMCA and sodium pump by decavanadate is in agreement with previously reported findings that decameric vanadate species block the active side of P-type ATPases and consequently prevent formation of the phosphoenzyme intermediary [5]. However, this mechanism could not be responsible for obtained ecto-ATPase inhibition (a member of E-NTPDases) and probably occurs via different mechanism resulting in lower sensitivity toward decayanadate, when compared to P-type ATPases (sodium and calcium pump).

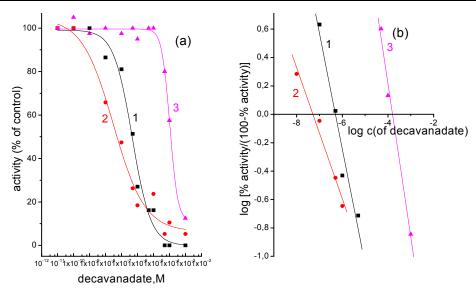


**Fig. 1**. The concentration dependent (a) and Hill analysis (b) inhibition of Na<sup>+</sup>/K<sup>+</sup>-ATPase (1), Ca<sup>2+</sup>-ATPase (2) and Mg<sup>2+</sup>-ATPase (3) by ammonium decayanadate

**Table 1.** IC<sub>50</sub> values of ammonium decavanadate for all ATPases obtained by fit of sigmoidal inhibition curves and by Hill analysis

Enzyme	IC <sub>50</sub> , M Hill	IC <sub>50</sub> , M
Na <sup>+</sup> /K <sup>+</sup> -ATPase	4.79 x 10 <sup>-7</sup>	$(4.74 \pm 1.15) \times 10^{-7}$
Ca <sup>2+</sup> -ATPase	4.68 x 10 <sup>-8</sup>	$(3.13 \pm 1.70) \times 10^{-8}$
Mg <sup>2+</sup> -ATPase	1.58 x 10 <sup>-4</sup>	$(1.05 \pm 0.10) \times 10^{-4}$

#### Conclusion

It could be concluded that the decameric vanadate species induce inhibition of SPM ATPases activity in concentration-dependent manner, probably directly affecting phosphorylation step in the enzyme cycle of P-type ATPases (sodium and calcium pump).

- [1] N.D. Chasteen, Struct. Bonding, 1983, **53**, 105-138.
- [2] M. Aureliano and R.M.C. Gândara, J. Inorg. Biochem., 2005, 99 (5), 979-985.
- [3] M. Aureliano, J. Inorg. Biochem., 2000, 80, 145-147.
- [4] R.S. Kohen, F. Blomberg, K. Berzins, P. Siekevits, J. Cell Biol., 1977, 74, 181-203.
- [5] S. Varga, P. Csermely, A. Martonosi, Eur. J. Biochem., 1985, 148, 119-126.

# STUDY OF VALSARTAN INTERACTION WITH MICELLES AS A MODEL SYSTEM FOR BIOMEMBRANE

O. Čudina<sup>1</sup>, I. Janković<sup>2</sup>, J. Brborić<sup>1</sup>, K. Karljiković-Rajić<sup>1</sup> and S. Vladimirov<sup>1</sup>

<sup>1</sup> Faculty of Pharmacy, Vojvode Stepe 450, P.O. Box 146, Belgrade, Serbia <sup>2</sup> Laboratory for Radiation Chemistry and Physics, Vinča Institute of Nuclear Sciences, P.O. Box 522, Belgrade, Serbia

#### **Abstract**

The interaction of valsartan (VAL), an angiotensin II receptor antagonist, with cationic surfactant cetyltrimethylammonium bromide (CTAB) was investigated. To quantify the degree of VAL/CTAB interactions, two constants were calculated by using mathematical models: micelle/water partition coefficient and drug/micelle binding constant.

#### Introduction

Because of its amphiphilic nature, micelles are known to play a vital role in many processes of interest in both fundamental and applied sciences. The degree of drug/micelle interaction can be evaluated using two descriptors: micelle/water partition coefficient  $(K_x)$  and drug/micelle binding constant  $(K_b)$ , by applying mathematical models [1]. The explanation of these constants is important for the understanding of interactions with biomembranes, QSAR (quantitative structure-activity relationship) studies, as well as the use of surfactants in HPLC in drug quality control. Micelle/water partition coefficient is known as an useful descriptor for hidrophobicity applied in QSAR studies and correlated with log P for a group of cephalosporins [2], barbiturates and steroids [3].

The aim of this work was to investigate the effect of cationic type of micelles on spectroscopic and acid-base properties of valsartan (N-(1-oxopentyl)-N-[[2'-(2H-tetrazol-5-yl)[1,1'-biphenyl]-4-yl]methyl]-L-valine), using UV spectrophotometry at physiological conditions.

# **Experimental**

Absorption spectra were recorded on a Cintra 20 spectrophotometer (GBC Scientific Pty. Ltd., Dandenong, Australia) equipped with 1.0 cm quartz cuvettes thermostated at 25°C and data processing Spectral 1.70 System Software. The optimized operating conditions were: wavelength range 225-335 nm; slit width 1.0 nm; scan speed 100 nm/min; data interval 0.960 nm. Stock solution of 10 mM valsartan (Novartis Pharma AG, Basel, Switzerland) was prepared by dissolving the compound in methanol.

#### **Results and Discussion**

Valsartan is a polyfunctional molecule with generally greater acidity of carboxylic group ( $pKa_1 = 3.9$ ) and with  $pKa_2 = 4.9$  attributed to the deprotonation of tetrazole group. The absorption spectra of VAL, both in aqueous and CTAB micellar solutions were measured at pH 2.8 (VAL molecule) and pH 7.4 (VAL dianion). Upon addition of CTAB into solutions at physiological pH, VAL dianion maximum at 250 nm shifted to 257 nm. A batochromic shift is undoubtedly the consequence of VAL dianion being transferred from highly polar phase (water) to a less polar site [4].

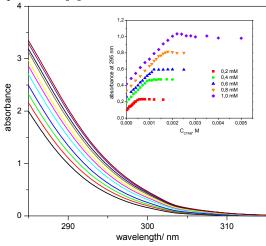


**Fig. 1.** Absorption spectra of 1 mM VAL containing increasing amounts of CTAB ( $C_{CTAB} = 0.2 - 5$  mM). Inset:  $A_{295}$  vs  $C_{CTAB}$ 

The absorption spectra of 1 mM VAL at pH 7.4 in the wavelength spectral range from 285 to 315 nm as a function of various concentrations of CTAB are depicted in Figure 1, with the inset showing the relation between  $A_{295}$  and  $C_{CTAB}$ .  $A_{295}$  asymptotically increases with increasing CTAB concentration, above its critical micelle concentration (CMC = 0.2 mM, determined by SLS), reaching the plateau when all added VAL is solubilized in micelles.  $A_{295}$  can be used for the calculation of  $K_x$ , according to the pseudo-phase model [5].  $K_x$  represents the affinity of a given solubilizate to the micellar phase relative to the aqueous one and can be determined from the equation (1):

$$\frac{1}{\Delta A_{295}} = \frac{1}{\Delta A_{295}^{\infty}} + \frac{n_{w}}{K_{x} \cdot \Delta A_{295}^{\infty} \cdot (C_{VAL} + C_{CTAB} - CMC)}$$
(1)

where  $\Delta A_{295} = A_{295} - A_{295}^{\text{water}}$  and  $\Delta A_{295}^{\infty} = A_{295}^{\infty} - A_{295}^{\text{water}}$ ,  $A_{295}^{\text{water}}$  and  $A_{295}^{\infty}$  being the absorbance of VAL dianions free and completely bound to CTAB, respectively, and  $n_w = 55.5$  M is the molarity of water.

The partition coefficients  $K_x$  were evaluated for series of micellar solutions containing increasing concentrations of CTAB ( $C_{\text{CTAB}} = 0.04-5$  mM) and solubilizing different concentrations of VAL ( $C_{\text{VAL}} = 0.2-1$  mM). The decrease of  $K_x$  with the increase of VAL concentration indicates that solubilization is a

competitive process that becomes progressively more difficult as the amount of drug incorporated into the micelles increases.

Hence, the solubilization of VAL dianion in CTAB micelles may be treated as an adsorption process by fitting the data to a Langmuir adsorption model [6]. The following expression (2) in linearized form is used:

$$C_{VAL} \cdot (1 - f) = -\frac{1}{K_b} + \frac{C_{CTAB} - CMC}{n} \cdot \frac{(1 - f)}{f}$$
 (2)

where  $f = \Delta A_{295}/\Delta A_{295}^{\infty}$  is the fraction of the associated VAL dianions. From the measurements of  $A_{295}$  in 1 mM VAL containing increasing concentrations of CTAB (0.2-5 mM) at pH 7.4, following values of  $K_b = (2.50 \pm 0.49) \cdot 10^4 \, \text{M}^{-1}$  and  $n = 1.24 \pm 0.13$  were obtained. The value of  $K_b$  correlates with the known higher lipophilic properties of VAL and provides support for strong hydrophobic interaction of VAL dianion with CTAB micelles. Since the n value corresponds to the average number of CTAB molecules surrounding each dianion of VAL, the value confirms that one CTAB molecule is forming the site for VAL dianion binding.

#### **Conclusions**

Valsartan dianion is most probably situated in the micelle surface layer, with biphenyl part of the molecule immersed in the micelle and negatively charged carboxilate located at the same level as the positively cherged quaternary ammonium groups of CTAB. In binding valsartan to CTAB micelles both polar and electrostatic effects play an important role. The decrease of  $K_x$  (calculated using pseudo-phase model) with VAL concentrations is consistent with adsorption-like phenomenon.

# Acknowledgment

This work was partially supported by the Ministry of Science of the Republic of Serbia (Project 142072). Novartis Pharma is kindly acknowledged for having supplied valsartan.

- [1] O. Čudina, K. Karljiković-Rajić, I. Ruvarac-Bugarčić, I.Janković, Coll. Surf. A., 2005, **256**, 225-232.
- [2] Y. Mrestani, R. Neubert, J. Chromatogr. A, 2000, 871, 439-448.
- [3] F.A. Alvarez-Núñez, S.H. Yalkowsky, Int. J. Pharm., 2000, 200, 217-222.
- [4] R.S. Sarpal, S.K. Dogra, J. Chem. Soc. Faraday Trans. 1992, 88, 2725-2731.
- [5] H. Kawamura, M. Manabe, Y. Miyamoto, Y. Fujita, J. Tokunaga, J. Phys. Chem., 1989, 93, 5536-5540.
- [6] L. Sepulveda, J. Colloid Interface Sci., 1974, 46, 372-379.

# DELAYED CHLOROPHYLL FLUORESCENCE IN THE THYLACOID: MECHANISMS AND PARAMETERS OF TRANSIENTS AND OSCILLATIONS

Č.N. Radenović<sup>1</sup>, M.V. Beljanski<sup>2</sup>, A. Kalauzi<sup>3</sup> and G.V. Maksimov<sup>4</sup>

<sup>1</sup>Biophysical laboratory, Maize Research Institute, Zemun Polje, Belgrade, Serbia.

<sup>2</sup>Institute of General and Physical Chemistry, Belgrade, Serbia

<sup>3</sup>Institute for Multidisciplinaire Research, Belgrade, Serbia

<sup>4</sup>Lomonosov State University, Moscow, Russia

#### **Abstract**

Induction processes of maize leaf chlorophyll delayed fluorescence, their resolution into several mutually dependent transients, generating of oscillations and rhythms and their correlation are investigated and also, issues on activation energy and critical temperatures within activities of the total induction processes of chlorophyll delayed fluorescence.

#### Introduction

Standard induction process of delayed fluorescence (DF) of chlorophyll (induction signals) occur when an intact leaf segment is kept in the phosporoscope darkroom for more than 15 minutes and then is illuminated with the intermittent white light. The delayed chlorophyll fluorescence phenomenon can be described as an occurrence of luminescence (bioluminescence) within the red range of the visible spectrum. Numerous studies revealed the direct connection between DF and photosynthetic processes, in which DF was considered an unavoidable indicator - a susceptible "probe" for experimental photosynthetic studies. DF becomes an efficient tool in studies of certain, often very complex photoprocesses in the light phase of photosynthesis. Here we report on induction processes of chlorophyll DF, their

**Table 1.** Temporal parameters of transients: A, B, C, D and E of the induction processes of delayed chlorophyll fluorescence in the intact leaf of maize inbreeds and hybrids at 25 °C.

Temporal parameters of transients: A, B, C, D and E	Transients of the induction processes of delayed chlorophyll fluorescence in the intact leaf of maize inbreds and hybrids								
	A: t <sub>A</sub> /	B: t <sub>B</sub> /	C: t <sub>C</sub> /	D: $t_D / s$	E: $t_E / s$				
Time of the beginning of transient generation	2-4	0.8- 1.0	9-11	110-130	180-240				
Longest time of transient duration	75-80	8-9	21-23	480-500	8400				
Average time of transient duration	31±6	5±0.5	15±5	360±20	670±35				

resolution into several mutually dependent transients, generating of oscillations and

rhythms and their correlation and also, issues on activation energy and critical temperatures within activities of the total induction processes of chlorophyll DF in the intact leaf of maize inbreeds and hybrids [1-3].

# **Experimental**

noninvasive photosynthetic fluorescence method was used to measure the intensity chlorophyll DF induction process. Measures included the resolution of induction curve into the transients: A - E, as well as, recording of the generation of oscillations and rhythms. studies were done with the intact leaf of the selected maize hybrids: ZPDC 370, ZPSC 46A, ZPSC 704 and ZPSC 71, and inbred lines: ZPR 70ž and Oh 43. Plants were internodes lengthwise placed in water. Two hours prior to the bioluminescence experiment, they were kept under the black ball glass. A segment of ear intact leaves was taken from such plants and placed into a chamber of the modified Becquerel phosphoro-scope.

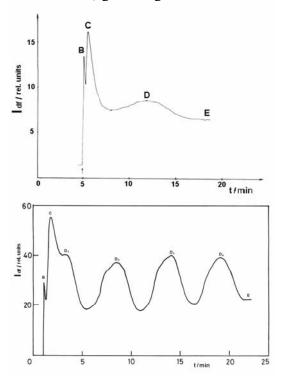


**Fig. 1. (a)** Resolution into transients: B - E of the induction processes of DF for the time interval (30 s  $\leq \tau \leq$  240 s). The arrow indicates the beginning of the measurement. **(b)** Generation of the oscillations of the induction curve of DF with transients B, C, D<sub>1</sub> - D<sub>4</sub> and E in the intact leaf grown under conditions severe air drought and reduced water in the medium.

#### **Results and Discussion**

Standard induction processes of delayed fluorescence (DF) of chlorophyll was measured. Resolved induction processes of DF chlorophyll into transients: A - E occur when the intact leaf segment of maize inbreeds and hybrids is kept in the phosphoroscope darkroom for a significantly shorter period ( $30 \text{ s} \le \tau \le 240 \text{ s}$ ), with the time rate  $\tau$  of 30 s, prior to its illumination with the intermittent white light. Induction transients: A - D and E are characterised with their temporal parameters:  $t_A$ ,  $t_B$ ,  $t_C$ ,  $t_D$  and  $t_E$ , dynamics of changes in transients intensities, and mechanisms of their generation (**Tab. 1**). The induction processes of chlorophyll DF of the intact leaf of maize inbreeds and hybrids resolved into transients: A - D and E are accompanied by

the occurrence and different levels of activation energy (E<sub>a</sub>, kJ mol<sup>-1</sup>) that correspond to different critical temperatures. The generation mechanisms of induction transients: A - D and E are classified into two groups. Transients A and B are of a physical character, while the transients: C, D and E are of a chemical character. Generation of the induction transients: B - D and E simultaneously follows establishing of the oscillations of induction processes of the DF [1-3] chlorophyll (Fig. 1-a). Oscillating of induction processes of DF chlorophyll is explained by the ion (K<sup>+</sup>, Na<sup>+</sup>, H<sup>+</sup>, Cl<sup>-</sup>) transport mechanism across the thylakoid membrane of the intact leaf grown under conditions of air drought, increased temperatures and water deficiency in the medium.

The interdependence of oscillations and induction transients A - D and E occurs in the intact leaves of maize inbreeds and hybrids grown in the glass-house under different conditions of air drought, temperatures and the water deficiency in the medium (Fig. 1-b).

The following properties of the chlorophyll DF induction processes were determined: conditions under which standard induction processes of chlorophyll DF were established in the intact leaf of maize inbreeds and hybrids; conditions under which the induction signal was resolved into transients. The existence of transients A - E was identified. Temporal, physical and chemical parameters for stated transients were shown. Mechanisms of their occurrence were explained.

The following properties of oscillations of the chlorophyll DF induction processes were determined: conditions under which the exited state occurred, fluctuations appeared and oscillations were established in the thylakoid membrane of the intact leaf of maize inbreeds and hybrids; the hypothesis on the mechanism of the generation of oscillations; the interdependence of the generation of oscillations and transients of chlorophyll DF induction processes was explained [4].

#### Conclusion

According to gained and presented results, it may be concluded that the improved photosynthetic-fluorescence method can be successfully applied in the studies on chlorophyll DF induction processes that are resolved into transients in which oscillations can be generated.

# Acknowelagement

This study was supported by Ministry of Science of the Republic of Serbia, Project No. 142025.

- [1] Č. Radenović, Ž. Vučinić, D. Fidler, Studia biophisica, 1981, **86**, 143-147.
- [2] Č. Radenović, M. Jeremić, D. Fidler, D. Marković, Ž. Vučinić, Period. Boil., 1985, 87, 304-306.
- [3] D. Marković, Č. Radenović, L. Rafailović, S. Žeraić, M. Marković, General. Physiol. Biophys., 1999, **18**, 257-267.
- [4] A. Kalauzi, D. Marković, Č. Radenović, Ru. J. Plant. Physiol., 2006, 53, 289-297.

# ORIGIN OF OSCILLATIONS IN MOLECULAR MECHANISM OF RADIORESISTANCE OF PROSTATE CARCINOMA CELLS

#### P.M. Mitrašinović

Institute for Multidisciplinary Research, Kneza Viseslava 1, 11030 Belgrade; Correspondence to: pmitrasinovic@yahoo.ca

#### **Abstract**

Our previous, experimentally verified, systems biology model (ref. 1), elucidating the radioresistance of prostate carcinoma cells, is herein extended by including additional pathways that cause oscillatory signaling. Although the NF-kB signaling pathway within the model consists of 26 species linked by 64 unidirectional reactions, a phase plane interpretation of the model indicated that a much lower-dimensional representation of the system of 64 kinetic equations could narrow down the range of possible instabilities that the oscillatory signaling may exhibit. The broad range of possible instabilities might have undesirable consequences on the development of successful therapies.

#### Introduction

We have developed a systems biology model showing that the adaptation of prostate cancer cells (PC-3) to ionizing radiation (IR) is based on the increasing trend of the effective concentrations of  $H_2O_2$  due to MnSOD induction [1]. As the model was verified experimentally, the radioresistance of PC-3 cells was suggested to be associated with the positive, feed-forward vicious circle established between the  $H_2O_2$ -mediated activation of NF- $\kappa$ B and the elevated MnSOD activity [1]. It was shown that hydroxyl radical (·OH) is primarily responsible for the activation of NF- $\kappa$ B, and that the NF- $\kappa$ B activation is not limited to particular cell types [2]. In this paper, the question, how the ·OH-induced NF- $\kappa$ B activation influences the radioresistance of PC-3 cells, is addressed.

# **Model Description**

The model is based on two main modules: NF- $\kappa$ B and MnSOD modules (Fig. 1a). The kinetic scheme describing the IR-induced expression of MnSOD is given in Fig. 1b. The NF- $\kappa$ B module is a modified version of that previously reported [3,4], which is essentially the I $\kappa$ B-NF- $\kappa$ B signaling pathway of Hoffmann *et al.* [5] modeling experimental data successfully. The MnSOD module is based on a set of 20 unidirectional reactions (67-86) taken form the literature [6]. All kinetic details for the reactions 1-94 are available as the Auxiliary Material of [1]. Two reactions, 95 and 96, are now added to model the NF- $\kappa$ B activation by hydroxyl radical. These reactions are two irreversible, mass action reactions with kinetic constants of 4 and 2 × 10<sup>-3</sup> s<sup>-1</sup>, respectively. The GEPASI 3.3 suite of programs was employed to perform time-course simulations [7].

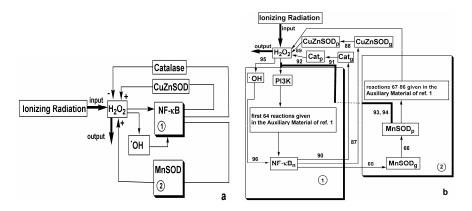
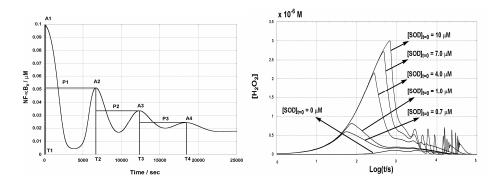


Fig. 1. Main modules (a) and kinetic scheme (b).



**Fig. 2.** Nuclear [NF- $\kappa$ B] vs. time for any initial [MnSOD] (left) and the time-dependent concentration of  $H_2O_2$  for various initial levels of MnSOD (right).

#### Results

According to the IκB-NF-κB signaling model of Hoffmann *et al.* [5], NF-κB is maintained inactive in the cytoplasm of a non-stimulated cell by three IκB isoforms, IκBα, IκBβ, and IκBε. By stimulating a cell and activating IKK complex, phosphorylation and ubiquitination of the IκB proteins are observed. Consequently, activation of genes including IκBα occurs by moving unbound NF-κB into the nucleus. Synthesizing IκBβ and IκBε at a steady rate provides complex temporal control of NF-κB with a local negative feedback [5]. The time course of NF-κB<sub>n</sub> is shown schematically in Fig. 2 (left). This plot is unique for cells that do not contain two isoforms of IκB, IκBβ and IκBε. The IR-induced activation of NF-κB signaling pathway reduces the possibility of having the IκBα-mediated inhibition of NF-κB. Control performances of the biological scenario, which is a part of the overall signaling scheme (Fig. 1b), have been observed by determining the time-dependent [H<sub>2</sub>O<sub>2</sub>] for various [SOD]<sub>[=0</sub> (Fig. 2, right).

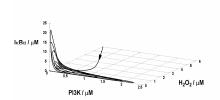


**Figure 3.** Phase plane plot between [PI3K], [I $\kappa$ B $\alpha$ ], and [H<sub>2</sub>O<sub>2</sub>].

An extensive sensitivity analysis [3] of parameters controlling oscillatory signaling has shown that the NF- $\kappa$ B signaling pathway consisting of 26 species linked by 64 unidirectional reactions can be reduced to 9 most important reactions/parameters. Interestingly, these 9 parameters directly affect the concentrations of only 2 reactants other than NF- $\kappa$ B<sub>n</sub>, PI3K and I $\kappa$ B $\alpha$ . To learn more on the involvement of these molecules into the signaling scenario, the phase plane plot of the time-dependent relationship between the concentrations of PI3K, I $\kappa$ B $\alpha$  and H<sub>2</sub>O<sub>2</sub> is shown schematically in Fig. 3. The three stated variables, plotted against each other, reveal an intimate involvement of the mediators in the oscillatory behavior of H<sub>2</sub>O<sub>2</sub>. Even though the reduced representation does not fit the biological scenario formally, it does provide a simplistic picture limiting the range of possible instabilities associated with the oscillation.

### Summary

The present results indicate that the inclusion of some other important pathways, such as 'NO signaling, in the model [1] of the radioresistance of PC-3 cells might be associated with the broad range of possible instabilities having undesirable consequences on the development of successful therapies.

- [1] A. Niciforovic, J. Djordjevic, M. Adzic, V. Vucic, P. M. Mitrasinovic, M. B. Radojcic, Annals of Biomedical Engineering, 2008, **36**, 831-838.
- [2] X. Shi, Z. Dong, C. Huang, W. Ma, K. Liu, J. Ye, F. Chen, S. S. Leonard, M. Ding, V. Castranova, V. Vallyathan, Mol. Cell Biochem., 1999, **194**, 63-70.
- [3] A. E. C. Ihekwaba, D. S. Broomhead, R. L. Grimley, N. Benson, D. B. Kell, Systems Biology, 2004, 1, 93-103.
- [4] P. M. Mitrasinovic, M. L. Mihajlovic, Current Radiopharmaceuticals, 2008, 1, 22-29.
- [5] A. Hoffmann, A. Levchenko, M. L. Scott, D. Baltimore, Science, 2002, 298, 1241-1245.
- [6] G. R. Buettner, F. Ng. Chin, M. Wang, V. G. J. Rodgers, F. Q. Schafer, Free Radic. Biol. Med. 2006, 41, 1338-1350.
- [7] P. Mendes, D. Kell, Bioinformatics, 1998, 14, 869-883.

# BINDING AFFINITY PREDICTION OF DISTINCT INHIBITORS OF GROUP-1 AND GROUP-2 NEURAMINIDASES (NAs): ARGUSLAB4/ASCORE PROTOCOL

M.L. Mihajlović<sup>1,2</sup> and P.M. Mitrašinović<sup>2\*</sup>

<sup>1</sup>Department of Physical Chemistry, University of Belgrade, Akademski Trg 12-16, 11000 Belgrade; <sup>2</sup>Institute for Multidisciplinary Research, Kneza Viseslava 1a, 11030 Belgrade, Serbia; \*Correspondence to: pmitrasinovic@yahoo.ca

#### Abstract

Using the crystal structures of inhibitors bound to either group-2 or group-1 NAs, AScore/ShapeDock-scoring was shown to identify the binding modes in agreement with the experiment for all inhibitors docked in their own NA/inhibitor crystal structures. To investigate the effect of small changes in protein structure on predicted binding modes, in a set of 132 docking experiments (11 inhibitors docked in 12 group-2 NA structures) AScore/ShapeDock identified the correct binding modes of 116 complexes. In a total of 88 docking experiments (8 inhibitors docked in 11 group-1 NA structures) AScore/ShapeDock predicted 80 binding modes correctly. Flexible AScore/ShapeDock docking, as quite reproducible, is suggested to be convenient for designing novel H5N1 inhibitors.

#### Introduction

The first objective of the present study is to explore the ability of ArgusLab 4.0 [1] to reproduce crystallographic binding orientations of various inhibitors bound to group-2 NAs, and to compare its accuracy with that of the QuantumLead program [2]. In the context of a current pandemic threat by the worldwide spread of H5N1 avian influenza [3], the second objective is to estimate the accuracy of the same method to predict the binding modes of known inhibitors of group-1 NAs.

# Methodology

To computationally accomplish the key objectives within a reasonable time, an empirical scoring function (AScore) with the ShapeDock docking engine was developed in ArgusLab 4.0 [1]. The total protein-ligand binding free energy is decomposed into several distinct components:  $\Delta G_{binding} = \Delta G_{vdw} + \Delta G_{hydrophobic} + \Delta G_{H-bond} + \Delta G_{H-bond(chg)} + \Delta G_{deformation} + \Delta G_0$ . The dissected terms account for the van der Waals interaction between the ligand and the protein, the hydrophobic effect, the hydrogen bonding between the ligand and the protein, the hydrogen bonding involving charged donor and/or acceptor groups, the deformation effect, and the effects of the translational and rotational entropy loss in the binding process, respectively [1].

<b>Table 1.</b> RMSDs of overlaid $C\alpha$ and backbone atoms in the binding sites of docked group-
2 NA inhibitors in their highest ranked binding mode. AScore/ShapeDock

PDB ID	inhibitor	$log IC_{50}{}^a$	$RMSD^b$ (Å)	$RMSD^{c}$ (Å)	$RMSD^{d}$ (Å)	$< RMSD > e (\mathring{A})$
1ivd	BANA105	-3.1	0.34	0.49	2.28	4.33
1ivc	BANA106	-1.7	0.26	0.46	1.01	1.72
1ive	BANA108	-1.7	0.32	0.46	1.58	2.47
1 ing	BANA109	-2.4	-	-	0.74	1.49
1 inh	BANA111	-2.3	0.32	0.53	1.81	1.42
1inf	BANA113	-5.0	0.45	0.56	1.04	1.47
2bat	NANA	-2.7	0.31	0.47	1.10	1.40
1ivf	DANA	-4.8	0.31	0.51	1.80	1.84
1nnc	GANA	-9.0	0.40	0.54	1.25	1.57
1inw	aPANA	-2.7	0.31	0.48	2.28	1.79
1 inx	ePANA	-3.7	0.32	0.48	1.89	2.07
1ivg	none	-	0.32	0.49	-	-
average			0.33	0.50	1.53	1.96

<sup>&</sup>lt;sup>a</sup> Experimental values of IC50 for all of group-2 NA inhibitors [4].

#### Results

Table 1 shows RMSDs of overlaid  $C\alpha$  and backbone atoms in the protein active sites relative to 1ing. The RMSD ranges for these superpositions are between 0.26 and 0.45 Å for all  $C\alpha$  atoms, and between 0.47 and 0.56 Å for backbone atoms. Since RMSD of the top-ranked binding mode of each inhibitor docked into its crystal structure is below 2.5 Å (Table 1), all the inhibitors could thus be docked correctly into their crystal structures. 88% (70%) of the docked complexes of group-2 NA is associated with RMSD between the docked and crystallographic binding modes of less than 2.5 (2.0) Å (Table 2). This percentage is higher than that of 82% (64%) previously reported [4]. 80 of the 88 protein/ligand complexes (91%) of group-1 NA have RMSDs below 2.5 Å, while 59 of a total of 88 docked structures (67%) have RMSDs below 2.0 Å (Table 3). Moreover, for 9 NA structures the average RMSD of the docked inhibitors is below or about 2.0 Å.

**Table 2.** RMSDs (in Å) of group-2 NA inhibitors docked in their highest ranked mode

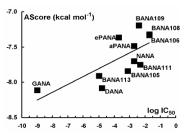
INHIBITOR	2HTY	2HU0	2HU4	2HT5	2HTR	2HT7	2HT8	2HTQ	2HTU	2HTV	2HTW
oseltamivir	1.18	1.66	2.12	2.15	1.57	1.66	1.91	2.47	1.83	1.72	1.83
oseltamivir	2.28	1.57	0.92	1.35	1.46	0.99	1.98	1.56	2.06	2.38	2.03
dana	1.32	2.31	1.76	1.87	1.37	2.07	1.09	1.47	1.61	2.36	2.04
oseltamivir	1.85	1.42	1.60	1.84	1.86	0.73	1.09	1.60	2.08	2.40	2.22
oseltamivir	1.00	1.25	0.93	1.89	1.79	2.40	1.04	1.57	2.19	2.24	2.17
zanamivir	3.18	4.92	1.43	1.14	5.25	1.26	3.17	2.45	1.23	5.39	5.01
peramivir	1.18	2.16	2.48	1.70	1.36	2.40	2.82	2.50	2.38	1.37	2.97
dana	1.64	2.43	1.37	1.87	1.45	2.19	0.98	1.47	1.64	0.69	1.41
average	1.70	2.22	1.58	1.73	2.01	1.71	1.76	1.89	1.88	2.32	2.46

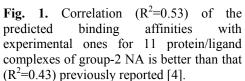
<sup>&</sup>lt;sup>b</sup> RMSD of Cα atoms in the binding site after overlay. The reference structure is 1 ing.

<sup>&</sup>lt;sup>c</sup> RMSD of backbone atoms in the binding site relative to 1ing.

<sup>&</sup>lt;sup>d</sup> RMSD of the highest ranked binding mode of the inhibitor docked into its crystal structure.

<sup>&</sup>lt;sup>e</sup> Average RMSD of the highest ranked binding mode of the inhibitor over all 12 crystal structures.





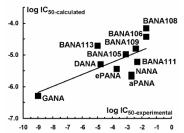


**Fig. 2.** Correlation  $(R^2=0.43)$  of the QuantumLead binding affinities with experimental ones for 11 protein/ligand complexes of group-2 NA.

Table 3. RMSDs (in Å) of group-1 NA inhibitors docked in their highest ranked mode

inhibitor	1ivd	1ivc	1ive	1 ing	1 inh	1inf	2bat	1ivf	1nnc	1inw	1inx	1ivg
BANA105	2.28	2.11	2.49	5.76	5.79	2.22	6.05	6.08	6.12	1.33	6.05	5.70
BANA106	1.11	1.01	2.46	0.57	2.82	2.18	0.47	2.85	1.19	1.47	1.47	2.98
BANA108	2.34	2.74	1.58	2.62	3.72	2.34	2.49	3.08	1.37	2.31	3.75	1.34
BANA109	1.38	1.84	1.96	0.74	1.34	1.52	1.05	1.55	1.88	1.65	1.66	1.26
BANA111	1.24	1.58	1.16	0.89	1.81	1.24	1.25	1.82	1.65	1.38	1.35	1.70
BANA113	1.59	1.89	0.46	1.04	1.69	1.04	1.97	1.16	1.82	1.41	1.99	1.58
NANA	1.47	1.85	1.66	1.34	1.73	1.32	1.10	1.25	0.81	1.31	1.39	1.60
DANA	2.09	2.65	2.15	2.19	2.24	2.28	0.74	1.80	0.97	1.66	2.25	1.12
GANA	1.90	1.84	1.00	1.51	1.27	2.06	1.67	1.55	1.25	1.15	2.22	1.37
aPANA	1.77	2.10	2.27	1.26	2.37	1.96	1.58	1.32	1.28	2.28	2.06	1.18
ePANA	2.25	1.74	1.78	1.85	2.74	2.25	2.15	2.26	2.03	1.84	1.89	2.07
average	1.76	1.94	1.73	1.80	2.50	1.86	1.86	2.25	1.85	1.62	2.37	1.99

# **Summary**

In the context of a current pandemic threat by the worldwide spread of H5N1 avian influenza [3], the flexible ArgusLab4/AScore/ShapeDock docking protocol, as quite reproducible, is suggested to be convenient for the design of novel H5N1 inhibitors.

- [1] M.A. Thompson, ArgusLab 4.0.1, Planaria Software LLC, Seattle, WA, http://www.arguslab.com.
- [2] QuantumLead 3.3.0, Quantum Pharmaceuticals, Moscow, Russia, http://q-pharm.com.
- [3] R. J. Russell, L. F. Haire, D. J. Stevens, P. J.Collins, Y. P.Lin, G. M.Blackburn, A. J. Hay, S. J. Gamblin, J. J. Skehel, Nature, 2006, 443, 45-49.
- [4] I. Muegge, Med. Chem. Res., 1999, 9, 490-500

# EFFECT OF pH ON THE ELASTIC MODULUS OF PLANT CELL WALLS. AN AFM STUDY

K. Radotić<sup>1\*</sup>, S. Kasas<sup>2</sup>, D. Đikanović<sup>1</sup>, J. Bogdanović<sup>1</sup> and G. Dietler<sup>2</sup>

<sup>1</sup>Institute for Multidisciplinary Research, Kneza Višeslava 1, 11000 Beograd, Serbia

<sup>2</sup>Laboratory of Physics of Living Matter, Swiss Federal Institute of Technology,

CH-1015, Lausanne, Switzerland

#### **Abstract**

We studied effect of pH on mechanical properties (Young's modulus of elasticity YM) of the isolated cell walls and constituent lignin from needles of a conifer. We also determined YM of a lignin model polymer (DHP). Both cell walls and lignin showed an increase of their YM with the pH rise, but had different patterns of YM/pH dependence. In the case of DHP, YM/pH ratio depended on the presence of ferulic acid in the polymer.

#### Introduction

Cell wall is a plant cell's compartment lying outside the plasmalemma. Its biological function is to provide mechanical support and to protect the cell from stress. It is also an abundant source of biomaterials used in the new technologies and as biofuels. Cell wall is built mainly from lignin and polysaccharides. The elastic modulus of lignin is of considerable importance in the theoretical modeling of cell wall composite structure and in the understanding its mechanical properties. So far only few AFM studies have been published on the elasticity of cell walls and lignin.

Plant growth is achieved by a combination of cell division and controlled wall extension [1]. Cell wall extension in the short time scale (seconds to hours), may be based on changes in the wall environment that are regulated by the cell via transport across the plasma membrane. It was shown that pH may be one of the factors inducing cell wall expansion or growth secession [1]. In this work we studied effect of pH on the elasticity of isolated cell walls and constituent lignin from needles of a conifer, in order to explore possible role of wall and lignin mechanical properties in the pH induced cell wall extension. We also determined mechanical properties of the lignin model polymer (DHP), the best substitute for the natural lignin. This compound was prepared from coniferyl alcohol (CA) and ferulic acid (FA) mixed in different ratios. As the role of FA is to make interpolymer transversal connections in the cell wall, our aim was to see if these cross links may affect mechanical properties of the polymer, and thus possibly those of the whole wall, in response to pH change.

#### **Materials and Methods**

Lignin model polymer was synthesized from CA or from combination of CA and FA in 1:5 and 1:2 (v/v) ratio, using horseradish peroxidase as an enzymatic catalyst [2].

Extraction of purified cell walls from *P. omorika* needles (obtained from 15-years old trees) and extraction of lignin from purified cell wall material was performed according to the procedure of Chen et al. [3].

The samples for AFM measurements were prepared by depositing onto Petri dishes 5  $\mu$ L of dilluted suspension of the cell walls or polymers in distillated water. After drying on air, the samples were introduced into the AFM and immersed in phosphate buffer (PBS). Imaging and measurements of mechanical properties were accomplished by using Nanoscope III and Bioscope I AFM's operating in the force volume imaging mode. We used silicon nitride cantilevers having a nominal spring constant of 0.06 N/m. The imaging and mechanical measurement experiments were accomplished in PBS adjusted to three different pH values: 5, 7 and 8. The measurements at different pH values were performed at the same place of the sample by exchanging buffer in the order from pH 5 to 8. The extraction of the Young's modulus from the force distance curves was accomplished by software written in our lab in Matlab.

#### **Results and Discussion**

Young's modulus (YM) of the isolated cell walls from *P. omorika* needles rose substantially with changing pH from 5 to 7, while further shift to pH 8 reduced YM slightly. However, isolated lignin from the same cell wall showed a steady increase of YM with rising pH from 5 to 8 (Fig. 1). The cell walls treated with cellulase/pectinase (C/P) demonstrate similar pattern of YM dependence on pH.

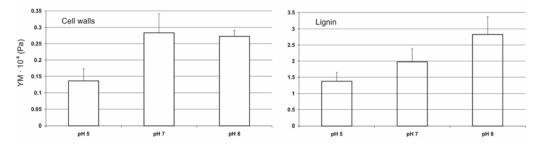


**Fig. 1.** Young's modulus (YM) of the isolated cell walls and lignin from *P. omorika* needles, measured at various pH.

The whole cell walls contain a bulk of transversal connections between polymers. On the other hand, in both (C/P) treated cell walls and isolated lignin, a considerable quantity of cross bonds have been broken. This makes molecular side groups more accessible to protonation/deprotonation during pH change, resulting in gradual increase of YM with pH rise. These results show the role of transversal

connections in reaction of the cell wall to the pH change. It has been shown that FA and its dimmers have a role in making cross connections between cell wall polymers [4]. Young's modulus of a polymer prepared from CA increased gradually with pH change from 5 to 8 (Fig. 2), similarly to isolated lignin. The polymer prepared from 1:5 (w:w) mixture of FA/CA showed a more pronounced rise of YM with changing pH from 5 to 7. The difference between YM value at pH 5 and 7 was even more pronounced for the polymer made from 1:2 (w:w) ratio of FA/CA; at pH 8 YM decreased slightly (Fig. 2). In the latter case the pattern of YM change with pH was similar to that of the cell walls.

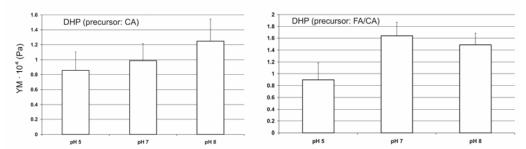


**Fig. 2.** Young's modulus (YM) of lignin model polymer prepared from CA or FA/CA mixture in 1:2 (w:w) ratio, measured at various pH.

The obtained results show that mechanical properties of the cell walls may have a role in pH induced cell wall extension, enabling lower stiffness at low pH. At higher pH, characteristic of normal physiological state of the cell, cell wall stiffness is higher, making its architecture more rigid, which is important for physiological functions of the cell wall. The results also show that FA bridges could play a role in response of the cell wall structure to pH change. This could have implications in enlargement of the cell walls during plant cell growth.

- [1] D.J. Cosgrove, Plant Physiol. Biochem., 2000, 38, 109-124.
- [2] K. Radotić, J. Simić-Krstić, M. Jeremić, M. Trifunović, Biophys. J., 1994, 66, 1763-1767.
- [3] M. Chen, A.J. Sommer, J.W. McClure, Phytochem. Anal., 2000, 11, 153-159.
- [4] K. Iiyama, T.B. Lam, B.A. Stone, Plant Physiol., 1994, 104, 315-320.

# RELATIONSHIPS BETWEEN THE LIPOPHILICITY AND ANTIBACTERIAL ACTIVITY OF SOME 2-AMINO AND 2-METHYLBENZIMIDAZOLE DERIVATIVES

S.O. Podunavac-Kuzmanović<sup>1</sup>, D.D. Cvetković<sup>1</sup> and D.J. Barna<sup>2</sup>

<sup>1</sup>Faculty of Technology, Bulevar Cara Lazara 1, 21000 Novi Sad, Serbia <sup>2</sup>Institute of Public Health, Zmaj Jovina 30, 24000 Subotica, Serbia

#### **Abstract**

In the present paper, a series of 2-amino and 2-methylbenzimidazole derivatives were tested *in vitro* for their antibacterial activity against Gram-negative bacteria *Escherichia coli* and minimum inhibitory concentration (MIC) was determined for all the compounds. Quantitative structure-activity relationship (QSAR) has been used to study the relationships between the antibacterial activity and lipophilicity parameter, log*P*, calculated by using CS Chem-Office Software version 7.0. The stepwise regression method was used to derived the most significant models as a calibration models for predicting the inhibitory activity of these class of molecules. The models were validated by leave one out technique as well as by the calculation of statistical parameters for the established theoretical models. The best QSAR model for prediction of antibacterial activity of the investigated series of benzimidazoles was developed. High agreement between experimental and predicted inhibitory values was obtained.

#### Introduction

Benzimidazoles are a group of molecules which have shown potential for application in a variety of pharmacological targets. They are of wide interest because of their diverse biological activity and clinical applications. Biologically active benzimidazoles have been known for a long time and they can act as bacteriostats or bactericides, as well as fungicides [1-3]. This ring system was proved to be very important as it is involved in numerous antiparasitic, antitumoral and antiviral drugs [4,5].

Octanol-water partition coefficient, referred to as log*P*, is a frequently used parameter in organic synthetic chemistry [6]. It is a quantitative descriptor of lipophilicity, one of the key determinants of pharmacokinetic properties. Log*P* is commonly used in QSAR studies and drug design, since this property is related to drug absorption, metabolism, bioavailability, and toxicity. By knowing exact values for this parameter, it is possible to predict the inhibitory activity of a drug.

In this context, the aim of the present study was to investigate the quantitative effect of lipophilicity on antibacterial activity against bacteria *Escherichia coli*. The main objective was to establish a quantitative lipophilicity-inhibitory activity relationships and derive a high-quality model which would link the lipophilicity of these compounds with their inhibitory activity.

# **Experimental**

All the benzimidazole derivatives were evaluated for their *in vitr*o growth inhibitory activity against Gram-negative bacteria Escherichia coli (ATCC 25922). MIC was performed by the agar dilution method according to guidelines established by the NCCLS standard M7-A5 [7]. The MIC of tested benzimidazoles is defined as the lowest concentration of the compound at which no growth of the strain as observed in a period of time and under specified experimental conditions. CS Chem-Office Software version 7.0 (Cambridge software) [8] have been used for the calculation (prediction) of lipophilicity of chemical compounds, based on their structure. The investigated benzimidazoles are: 2-methylbenzimidazole, 1-benzyl-2-methylbenzimidazole, 1-(4methylbenzyl)-2-methylbenzimidazole, 1-(4-chlorobenzyl)-2-methylbenzimidazole, 1benzoyl-2-methylbenzimidazole, 1-(4-methylbenzoyl)-2-methylbenzimidazole, 1-(4chlorobenzoyl)-2-methylbenzimi-dazole, 2-aminobenzimidazole, aminobenzimidazole, 1-(4-methyl-benzyl)-2-aminobenzimidazole, 1-(4-chlorobenzyl)-2-aminobenzimidazole, 1-benzoyl-2-aminobenzimidazole, 1-(4-methylbenzoyl)-2aminobenzimidazole and 1-(4-chlorobenzoyl)-2-aminobenzimidazole. The complete regression analysis was carried out by PASS 2005, GESS 2006, NCSS Statistical Softwares [9].

#### **Results and Discussion**

In this study, the  $\log 1/c_{\rm MIC}$  values were correlated against  $\log P$  parameters calculated by using CS Chem-Office Software. Usually, the lipophilicity parameters are linearly related to the biological activity (MICs), but in a more general case this relationship is not linear.

Equation	a	b	c	d	r	S
log1/c <sub>MIC</sub> =a logP+b	0.517	2.395	-	-	0.932	0.111
$log1/c_{MIC} = alogP^2 + blogP + c$	-0.255	2.410	-1.048	-	0.959	0.091
$log1/c_{MIC} = a logP^3 + blogP^2 + clogP + d$	12.722	-3.105	0.259	-13.318	0.964	0.091

**Table 1.** Statistical data calculated for relationship between  $log 1/c_{MC}$  and log P values

Therefore, a complete regression analysis resorting to linear, quadratic and cubic relationships (Table 1) was made. It is apparent, from the correlation coefficients (r), that fitting equation improves when resorting to higher order (second or third) polynomials.

#### **Conclusions**

logP values were calculated for 2-amino and 2-methylbenzimidazole derivatives, and three high-quality mathematical models relating the inhibitory activity, log1/c<sub>MIC</sub>, and logP were defined. For the estimation of the predictive ability of these models, the cross-validation statistical technique was applied. Comparison of the linear, quadratic and cubic relationships showed that the quadratic equation was the most appropriate for prediction of antibacterial activity of the investigated class of molecules. It is concluded that the lipophilicity parameter is a convenient quantity for modeling inhibition for the present set of benzimidazole derivatives. The developed QSAR mathematical model is used to predict inhibitory activity of the benzimidazoles investigated, and a high agreement between experimental and predicted values was obtained.

### Acknowledgment

These results are the part of the project No. 142028, supported by the Ministry of Science of the Republic of Serbia.

- [1] S.O. Podunavac-Kuzmanović, S.L. Markov, Centr. Eur. J. Occupat. Environ. Med., 2006, 12, 61-66.
- [2] S.O. Podunavac-Kuzmanović, D. Cvetković, J. Serb. Chem. Soc., 2007, 75, 459-466.
- [3] S. Podunavac-Kuzmanović, S. Markov, D. Barna, J. Theor. Comp. Chem., 2007, 6, 687-698
- [4] J. Valdez, R. Cedillo, A. Hernandez-Campos, L. Yepez, F. Hernandez-Luis, G. Navarrete-Vazquez, A. Tapia, R. Cortes, M. Hernandez, R. Castillo, Bioorg. Med. Chem. Lett., 2002, 12, 2221-2229.
- [5] Z. Kazimierczuk, J.A. Upcroft, P. Upcroft, A. Gorska, B. Starosciak, A. Laudy, Acta Biochim. Polon., 2002, 49, 185-195.
- [6] C. Hansch, A. Leo, D.H. Hoekman, Exploring QSAR, Fundamentals and Application in Chemistry and Biology (American Chemical Society, Washington DC, 1995).
- [7] National Committee for Clinical Laboratory Standards, NCCLS Approval Standard Document M7-A5, Vilanova, Pa, U.S.A, 2000
- [8] CS. Chem. Office, Version 7.0, Cambridge Soft Corporation, 100 Cambridge Park Drive, Cambridge, MA 02140-2317, U.S.A. (2001).
- [9] www.ncss.com.

# THE INVESTIGATIONS OF ANTIBACTERIAL ACTIVITY OF SOME 2-AMINOBENZIMIDAZOLES

S.O. Podunavac-Kuzmanović and D.D. Cvetković

Faculty of Technology, Bulevar Cara Lazara 1, 21000 Novi Sad, Serbia

#### **Abstract**

In this paper, the antibacterial activity of some different substituted benzimidazole derivatives against two Gram negative bacteria (*Pseudomonas aeruginosa* and *Escherichia coli*) was investigated. The tested benzimidazoles displayed *in vitro* inhibitory activity and minimum inhibitory concentration (MIC) was determined for all the compounds. Inhibitory activity was evaluated by the disc-diffusion method under standard conditions, using Mueller-Hinton agar medium. It was found that all tested compounds were more active against *Pseudomonas aeruginosa* than *Escherichia coli*. The effect of molecular structures on the inhibitory activity was discussed.

#### Introduction

Several thousands of benzimidazole analogs have been synthesized and screened for pharmacological activity. They are of wide interest because of their antibacterial and fungicidal activity [1-5]. This ring system were proved to be very important as they are involved in numerous antiparasitic, antitumoral and antiviral drugs. It is also well known that these molecules are present in a variety of antioxidant, antiprotozoal and antiallergic agents. In recent years, benzimidazole derivatives have been attracted particular interest due to their anticancer activity or may act as in vitro anti-HIV agents [6].

In the present paper, different substituted 2-aminobenzimidazoles were tested *in vitro* against two Gram-negative bacterial strains: *Pseudomonas aeruginosa* and *Escherichia coli*. The main objective was to determine MIC for investigated molecules against both the bacteria.

# **Experimental**

In the present paper we evaluated the inhibitory activity of 1-(4-methylbenzyl)-2-aminobenzimidazole (L1), 1-(4-chlorobenzyl)-2-amino benzimidazole (L2), 1-(4-fluorobenzyl)-2-aminobenzimidazole (L3), and 1-(4-methoxybenzyl)-2-aminobenzimidazole (L4) against two Gram-negative bacterial strains (Pseudomonas aeruginosa and Escherichia coli). All the compounds were synthesized according to a procedure described earlier [7]. The antibacterial activity was tested by the disc-diffusion method under standard conditions using Mueller-Hinton agar medium as described by NCCLS [8].

Minimum inhibitory concentration (MIC) was performed by the agar dilution method according to guidelines established by the NCCLS standard M7-

A5 [9]. MIC was described as the lowest concentration of the compound that visibly inhibited colony's growth. Stock solutions of the compounds were prepared in dimethylformamide (DMF). Further dilutions were performed with distilled water. The concentration range of the compounds tested was between 60-750μg/ml in two-fold dilution steps. The inoculated plates were than incubated at 35°C for 16-20h.

## **Results and Discussion**

The inhibitory activity of the 2-aminobenzimidazole derivatives was first tested by the agar disc-diffusion method against two Gram-negative bacteria. The results of antibacterial evluation are summarized in Table 1.

From the data, it can be concluded that all the investigated compounds displayed *in vitro* inhibitory activity against very persistent microorganisms. They were found to be more active against *Pseudomonas aeruginosa* than *Escherichia coli*.

In the next phase, MIC of the tested compounds was performed by the agar dilution method. From the results, it can be concluded that 1-(4-methylbenzyl)-5,6-dimethylbenzimidazole ( $L^1$ ) and 1-(4-chlorobenzyl)-5,6-dimethylbenzimidazole ( $L^2$ ) are the most active molecules against *Pseudomonas aeruginosa* with a MIC value of 62.5µg/ml.

On the other hand, 1-(4-fluorobenzyl)-5,6-dimethylbenzimidazole ( $L^3$ ) and 1-(4-methoxybenzyl)-5,6-dimethylbenzimidazole ( $L^4$ ) are less toxic with a MIC value of 125 µg/ml.

**Table 1.** *In vitro* antibacterial activity of benzimidazoles at a concentration of 1000 µg/ml (mm of inhibition zone)

Compound	Pseudomonas aeruginosa	Escherichia coli
$L^1$	22	14
$L^2$	25	18
$L^3$	21	16
$L^4$	23	13

Against *Escherichia coli*  $L^1$  and  $L^2$  are also the most active molecules with a MIC value of  $125\mu g/ml$ . 2-aminobenzimidazoles with fluoro and methoxy substituents are less toxic against the same bacteria with a MIC value of 250  $\mu g/ml$ .

As can be seen from the results the basic inhibitory activity of the benzimidazoles was produced by the presence of amino substituent at the positions 2 of the benzimidazole ring. If the benzimidazole nucleus was substituted with a 4-chlorobenzyl or 4-methylbenzyl group at the N1 atom, the antibacterial activity was increased.

## **Conclusions**

Some 2-aminobenzimidazole derivatives were evaluated for their *in vitro* antibacterial activity against two Gram-negative bacterial strains (*Pseudomonas aeruginosa* and *Escherichia coli*). Minimum inhibitory concentration (MIC) was performed for all the tested compounds by the agar dilution method. 1-(4-methylbenzyl)-5,6-dimethylbenzimidazole and 1-(4-chlorobenzyl)-5,6-dimethylbenzimidazole are the most active molecules against *Pseudomonas aeruginosa* with a MIC value of 62.5µg/ml, as well as with a MIC value of 125µg/ml against *Escherichia coli*. The basic antibacterial activity of the benzimidazoles tested was produced by the presence of amino substituent at the positions 2 of the benzimidazole ring. 4-chlorobenzyl or 4-methylbenzyl group at the N1 atom of the benzimidazole nucleus increased the inhibitory activity.

# Acknowledgment

These results are the part of the project No. 142028, supported by the Ministry of Science of the Republic of Serbia.

- [1] S. Podunavac-Kuzmanović, S. Markov, D. Barna, J. Theor. Comp. Chem., 2007, 6, 687-698.
- [2] G. Ayhan-Kilcigil, N. Altanlar, Turk. J. Chem., 2006, **30**, 223-228.
- [3] L. Garuti, M. Roberti, C. Cermelli, Bioorg. Medicinal Chem. Letter, 1999, 9, 2525-2530.
- [4] S. Podunavac-Kuzmanović, D. Barna, D. Cvetković, Acta Periodica Technologica, 2007, 38, 139-147.
- [5] S.O. Podunavac-Kuzmanović, D. Cvetković, J. Serb. Chem. Soc., 2007, 75, 459-466.
- [6] A. Akbay, I. Oren, O. Temiz-Arpaci, E. Aki-Sener, I. Yalcin, Arzneim.-Forcsh./Drug Res., 2003, 53, 266-271.
- [7] D. Vlaović, J. Čanadanović-Brunet, J. Balaž, I. Juranić, D. Đoković, K. Mackenzie, Biosci. Biotech. Biochem., 1992, 56, 199-206.
- [8] National Committee for Clinical Laboratory Standards, NCCLS Approval Standard Document M2-A7 (2000) Vilanova, Pa, U.S.A.
- [9] National Committee for Clinical Laboratory Standards, NCCLS Approval Standard Document M7-A5 (2000) Vilanova, Pa, U.S.A

# THE EVALUATION OF INHIBITORY ACTIVITY OF SOME 5,6-DIMETHYLBENZIMIDAZOLE DERIVATIVES

S.O. Podunavac-Kuzmanović and D.D. Cvetković

Faculty of Technology, Bulevar Cara Lazara 1, 21000 Novi Sad, Serbia

# Abstract

Following our previous studies, the present paper reports on the antibacterial activity of some 5,6-dimethylbenzimidazoles against two Gram-positive bacterial strains (*Staphylococcus aureus* and *Sarcina lutea*). Inhibitory activity was tested by the disc-diffusion method under standard conditions, using Mueller-Hinton agar medium. Minimum inhibitory concentration (MIC) was determined for all compounds against bacteria. The effect of molecules structures on the antibacterial activity is discussed.

# Introduction

Benzimidazole and its derivatives are interesting heterocycles because of their diverse biological activity and clinical applications. These heterocycle systems have different activities as they can act as bacteriostats or bactericides, as well as fungicides [1-6]. The success with these group of molecules stimulated the search for new biologically active derivatives. Understanding the role of chemical structure in influencing biological activity is very important.

Following our previous studies [4-6] in view of obtaining some potential biological active compounds, the present paper reports on the antibacterial activity of some 5,6-dimethylbenzimidazoles against two Gram-positive bacterial strains: *Staphylococcus aureus* and *Sarcina lutea*.

# **Experimental**

In the present paper we evaluated the antibacterial activity of 1-(4-methylbenzyl)-5,6-dimethylbenzimidazole ( $L^1$ ), 1-(4-chlorobenzyl)-5,6-dimethylbenzimidazole ( $L^2$ ), 1-(4-fluorobenzyl)-5,6-dimethylbenzimidazole ( $L^3$ ), and 1-(4-methoxybenzyl)-5,6-dimethylbenzimidazole ( $L^4$ ). All the compounds were synthesized according to a procedure described earlier [7].

The inhibitory activity was tested by the disc-diffusion method under standard conditions using Mueller-Hinton agar medium as described by NCCLS [8].

Minimum inhibitory concentration (MIC) was performed by the agar dilution method according to guidelines established by the NCCLS standard M7-A5 [9]. MIC was described as the lowest concentration of the compound that visibly inhibited colony's growth. Stock solutions of the compounds were prepared in dimethylformamide (DMF). Further dilutions were performed with distilled water. The concentration range of the compounds tested was between  $60\text{-}750\mu\text{g/ml}$  in two-fold dilution steps. The inoculated plates were than incubated at  $35^{\circ}\text{C}$  for 16-20h.

## **Results and Discussion**

The antibacterial activity of the 5,6-dimethylbenzimidazole derivatives was first tested by the agar disc-diffusion method against two Gram-positive bacteria. The results of these studies are summarized in Table 1.

As can be seen from the data, all of the investigated compounds displayed *in vitro* inhibitory activity against very persistent microorganisms. They were found to be more active against *Staphylococcus aureus* than *Sarcina lutea*.

In the second phase, MIC of the tested compounds was performed by the agar dilution method. From the results, it can be concluded that 1-(4-methylbenzyl)-5,6-dimethylbenzimidazole ( $L^1$ ) and 1-(4-chlorobenzyl)-5,6-dimethylbenzimidazole ( $L^2$ ) are the most active molecules against *Staphylococcus aureus* with a MIC value of 62.5µg/ml.

On the other hand, 1-(4-fluorobenzyl)-5,6-dimethylbenzimidazole ( $L^3$ ) and 1-(4-methoxybenzyl)-5,6-dimethylbenzimidazole ( $L^4$ ) are less toxic with a MIC value of 125 µg/ml.

**Table 1.** *In vitro* antibacterial activity of benzimidazoles at a concentration of 1000 µg/ml (mm of inhibition zone)

Compound	Staphylococcus aureus	Sarcina lutea
$L^1$	32	15
$L^2$	35	19
$L^3$	31	17
$L^4$	33	14

Also, in the case of <code>Sarcina lutea L^1</code> and  $L^2$  are the most active molecules with a MIC value of 125µg/ml, as well as  $L^3$  and  $L^4$  are less toxic with a MIC value of 250 µg/ml.

It can be concluded that the basic antibacterial activity of the benzimidazoles was produced by the presence of methyl substituents at the positions 5 and 6 of the benzimidazole ring. At the same time, if the benzimidazole nucleus was substituted with a 4-chlorobenzyl or 4-methylbenzyl group at the N1 atom, the inhibitory activity was increased.

#### **Conclusions**

Some 5,6-dimethylbenzimidazole derivatives were evaluated for their *in vitro* antibacterial activity against two Gram-positive bacterial strains (*Staphylococcus aureus* and *Sarcina lutea*). Minimum inhibitory concentration (MIC) was performed for all the tested compounds by the agar dilution method. 1-(4-methylbenzyl)-5,6-dimethylbenzimidazole and 1-(4-chlorobenzyl)-5,6-dimethylbenzimidazole are the most active molecules against *Staphylococcus* 

aureus with a MIC value of 62.5μg/ml, as well as with a MIC value of 125 μg/ml against *Sarcina lutea*. The basic antibacterial activity of the benzimidazoles tested was produced by the presence of methyl substituents at the positions 5 and 6 of the benzimidazole ring, as well as if the benzimidazole nucleus was substituted with a 4-chlorobenzyl or 4-methylbenzyl group at the N1 atom, the inhibitory activity was increased.

# Acknowledgment

These results are the part of the project No. 142028, supported by the Ministry of Science of the Republic of Serbia.

- [1] G. Ayhan-Kilcigil, N. Altanlar, Turk. J. Chem., 2006, **30**, 223-228.
- [2] L. Garuti, M. Roberti, C. Cermelli, Bioorg. Medicinal Chem. Letter, 1999, 9, 2525-2530.
- [3] Z. Kazimierczuk, J.A. Upcroft, P. Upcroft, A. Gorska, A., B. Starosciak, A. Laudy, Acta Biochim. Polon., 2002, 49,185-195.
- [4] S. Podunavac-Kuzmanović, D. Barna, D. Cvetković, Acta Periodica Technologica, 2007, **38**, 139-147.
- [5] S.O. Podunavac-Kuzmanović, D. Cvetković, J. Serb. Chem. Soc., 2007, 75, 459-466.
- [6] S. Podunavac-Kuzmanović, S. Markov, D. Barna, J. Theor. Comp. Chem., 2007, 6, 687-698..
- [7] Đ. Vlaović, J. Čanadanović-Brunet, J, Balaž, I. Juranić, D. Đoković, K. Mackenzie, Biosci. Biotech. Biochem., 1992, **56**, 199-206.
- [8] National Committee for Clinical Laboratory Standards, NCCLS Approval Standard Document M2-A7 (2000) Vilanova, Pa, U.S.A.
- [9] National Committee for Clinical Laboratory Standards, NCCLS Approval Standard Document M7-A5 (2000) Vilanova, Pa, U.S.A.

# CHOCOLATE – A BITTERSWEET ANTIOXIDANT

J. Simonović<sup>1</sup>, A. Ignjatović<sup>1</sup>, I. Spasojević<sup>2</sup>, M. Daković<sup>1</sup> and M. Mojović<sup>1</sup>

<sup>1</sup>University of Belgrade, Faculty of Physical Chemistry, Studentski trg 12-16, 11000 Belgrade, Serbia

<sup>2</sup>Institute for Multidisciplinary Research, POBox 33, 11030 Belgrade, Serbia

# **Abstract**

We studied the positive health effect of different chocolates (antioxidative effects on stable free radicals, reactive oxygen species (ROS) and for prevention of lipid peroxidation). The results show that all chocolates successfully remove 'OH radicals, but only chocolates with high cocoa content are also effective for of ' $O_2$ '. The capabilities for chocolate samples to reduce organic radicals are shown to be positive for hydrophobic DPPH which was not the case for hydrophilic Tempone. Only the chocolate samples with high cocoa content were shown to prevent lipid peroxidation induced by Fenton reaction. Obtained results showed that chocolates have diverse antioxidative effects which are not only dependant on the content of cocoa. The other chocolate constituents like: sugar, polyphenols, cocoa butter, emulsifier and other substances should also be considered for determining the positive health effect of chocolates.

# Introduction

Reactive oxygen species (ROS) have important roles in many biological processes and are regularly produced during normal aerobic metabolism. However, ROS could also damage cell membranes and biological molecules. The ROS include hydroxyl radical (OH), superoxide anion (O<sub>2</sub>), hydrogen peroxide (H<sub>2</sub>O<sub>2</sub>), hypochloric acid (HOCl), singlet oxygen ( ${}^{1}O_{2}$ ) and others. [1], [2] There is a close relationship between antioxidants in diet and immune functions. Antioxidant assays have shown that chocolate have significant antioxidant activities primarily due to the content of polyphenols, in particular catechins and proanthocyanidins. [3], [4] However, the content of cocoa is usually underlined as the main substance responsible for such property. This study had aim to explore the antioxidative capabilities of different chocolates and compare it with their composition. EPR is one of the most efficient techniques for detection of various radical species. EPR spin-trapping technique is based on a reaction in which the transient radical species reacts with specific nitrone or nitroso spin-traps to yield more persistent nitroxide spin adducts. In this study we used spin-trap DEPMPO which can, by forming high yield of distinct and stabile adducts, simultaneously trap different free radicals and trace them to their origin. [5], [6] Spin-probing technique with different types of stable organic free radicals (DPPH and Tempone) have also been used. Reactive oxygen species can induce lipid peroxidation which can break down membrane integrity. Membrane fluidity is in correlation with increased lipid peroxidation, and was measured using the membrane spin probe 7-DS.

# Sample preparation

In this experiment, we used chocolates which had been purchased from local market. Chocolates used for the experiments were: Alpenmilch Chocolate (Milka), White Chocolate (Milka), Dorina (milk chocolate, sugar free with sweeteners), Sensations-Côte d'Or (dark chocolate- 86% of cocoa), Guylian (dark chocolate- 70% of cocoa), Najlepše želje (milk chocolate), Najlepše želje (dark chocolate- 60% of cocoa). Chocolate solution

suitable for EPR measurements was made by scrapping and dissolving 10 mg of chocolates in 1 ml of  $18M\Omega$  bidistillated deionized water (avoiding additional presence of metal ions). Spin-trap DEPMPO (5-diethoxyphosphoryl-5-methyl-1-pyrroline-N-oxide) was purchased from Alexis Biochemical (Lausen, Switzerland), DPPH (1,1- diphenyl- 2- picrylhidrazyl) was purchased from Sigma chemical company (St. Louis, MO, USA). Tempone (4-Oxo-2,2,6,6-tetramethylpiperidine-1-oxyl) was purchased from Alexis biochemicals, Lausen, Switzerland. 7-DS (2-(5-carboxypentyl)-2-undecyl-4,4-dimethyloxazolidine-3-oxyl) was purchased from Molecular Probes, (Junction City, OR, USA). Hydroxyl radicals were reaction and superoxide radicals generated by Fenton system [5] Hypoxanthine/Xanthine-oxidase reaction (XA/XO) [6].

# **EPR** spectroscopy

EPR spectra were recorded at a room temperature using Varian E104-A EPR spectrometer operating at X-band (9.45 GHz) with following settings: modulation amplitude, 2 G; modulation frequency, 100 kHz; microwave power, 10 mW; scan range, 100 or 200 G. Spectra were recorded and analyzed using EW software (Scientific Software).

# **Results and Discussion**

The ability of chocolate samples to remove chosen radicals is presented as antioxidative activity (AA =  $(I_{control} - I_{sample})/I_{control}$ ), performed by comparing the intensities of characteristic EPR peaks (Fig.1) of spin-adducts (or spin-probes) of chocolate and control samples. The ability of chocolate to prevent lipid peroxidation was determined by calculating the order parameter (S). Samples of pure cocoa and sugar were also taken into account.

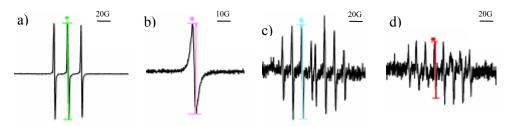


**Fig. 1.** Characteristic EPR spectra obtained using chocolate Guylian: a) Tempone; b) DPPH; c) DEPMPO/OH adducts (Fenton system); d) DEPMPO/OOH adducts (HX/XO) reaction. Measured EPR peaks are marked with filled circles,

Reduction of Tempone and DPPH and removing of 'OH and 'O2 radicals. Results (Table 1) indicate that some chocolates (Sensations > Najlepše želje > Najlepše želje with 60% of cocoa > Guylian) reduce DPPH, but show poor results for reduction of Tempone. Generally, chocolates with higher cocoa content showed to be effective for removing 'OH radicals (in addition, dark chocolates-Guylian and Sensations showed better results than pure cocoa). Only two chocolates, Sensations and Najlepše želje (60% of cocoa) gave good results for removing 'O2 radicals.

Sample	AA (%) Tempone	AA (%) DPPH	AA (%) (OH)	AA (%) ('O <sub>2</sub> ')
Sugar	0.93	4.45	48.56	0
Cocoa	10.04	82.37	91.70	55.93
Alpenmilch chocolate	5.90	23.81	86.42	3.39
Milka white	4.13	13.39	83.09	35.59
Dorina (for diabetics)	7.29	61.47	62.30	20.34
Guylian, 70%	13.24	61.89	92.75	27.12
Côte d'Or- Sensations, 86%	12.46	75.69	91.92	67.80
Najlepše želje	14.19	71.45	88.35	0
Najlepše želje, 60%	7.13	69.48	84.83	54.24

**Table 1:** Antioxidative activities of different chocolate samples.

**Lipid peroxidation preventing capabilities.** The ability of chocolate to prevent lipid peroxidation was tested using Fenton system. Order parameter (S), reciprocally proportional to the membrane fluidity, was measured by inserting EPR spin label 7-DS into liposomes (Fig. 2).

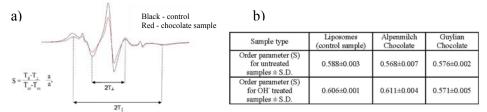


**Fig. 2. a)** EPR spectra of 7-DS (treated and untreated sample) and determination of order parameter S; **b)** Calculated order parameters (S).

Table shows that Guylian chocolate prevent lipid peroxidation which was not the case with Alpenmilch sample.

#### Conclusions

Obtained results show that different chocolates have diverse antioxidative effects. Among cocoa, the amount of sugar, polyphenols, cocoa butter, emulsifier and other substances clearly show to contribute to antioxidative ability of chocolate.

# Acknowledgements

The authors express gratitude to Ministry of Science of Republic of Serbia for the financial support (Project #143016).

- [1] J. M. C. Gutteridge, Clin. Chem., 1995, 41/12, 1819–1828.
- [2] B. N. Ames et al., Proc. Natl. Acad. Sci. USA, 1993, 90, 7915–7922
- [3] J. Wollgast et al., Food Research International, 2000, 33, 423–447
- [4] J. A. Vinson et al., J. Agric. Food Chem., 2006, 54, 8071-8076
- [5] G. Bačić et al., Spectrochim. Acta Part A, 2008, **69**, 1354-1366
- [6] V. Roubaud et al, Anal. Biochem., 1997, 247, 404-411

# NON-ESSENTIAL ACTIVATION OF PEPSIN BY AI3+ "IN VITRO"

V. Pavelkić<sup>1</sup>, K. Gopčević<sup>2</sup>, D. Krstić<sup>2</sup>, M. Ilić<sup>3</sup> and M. Pavelkić<sup>4</sup>

<sup>1</sup>Vinca-Institute of Nuclear Science, Department of Physical Chemistry, POB 522, 11001 Belgrade, Serbia; <sup>2</sup>School of Medicine, University of Belgrade, Visegradska 26, 11000 Belgrade, Serbia; <sup>3</sup>Institute of General and Physical Chemistry, Studentski trg 12-16, 11000 Belgrade, Serbia; <sup>4</sup>Health Center Novi Beograd, Goce Delčeva 30, 11070, Belgrade, Serbia

#### **Abstract**

The *in vitro* effect of  $Al^{3+}$  ions on pepsin activity at pH 2, *via* kinetic parameters was evaluated. Kinetic study showed that  $Al^{3+}$  ions increase the maximal velocity  $(V_{max})$  rather than apparent affinity for substrate  $(K_S)$  implying the non-competitive nature of activation which indicated that aluminium was a non-essential activator of partial non-competitive type.

# Introduction

Porcine pepsin A (EC 3.4.23.1), a prominent member of the aspartic protease, is the principal proteolytic enzyme of gastric juice and as the best understood of this family of proteases it was used as a model enzyme [1]. As the mechanism of Al<sup>3+</sup> ions (known as a moderate toxic element) on pepsin activity is not still clear, the objective of this study is to investigate the *in vitro* influence of different concentrations of Al<sup>3+</sup> ions, physiological and toxic ones, on pepsin activity.

# **Experimental**

Pepsin activity was determined in an incubation medium containing 1 mL of pepsin solution (20 µg/mL in 0.01M HCl, pH 2), 5 mL haemoglobin solution (2% solution of haemoglobin in 0.01M HCl). The working solutions were incubated for 10 minutes at 37°C. The reaction was stopped by addition of 10 mL 5% TCA. Kinetic analysis was carried out according to a slightly modified method of Anson [2], by following the initial velocity of the enzymatic reaction in the absence and presence of Al³+ (1.7·10⁻⁶ – 8.7·10⁻³ M) and rising concentrations of hemoglobin (from 0.025 ·10⁻³ M to 4·10⁻³ M) that used as a specific substrate. All the assays were performed at pH 2.

# **Results and Disscusion**

The dependence of the initial reaction rate *vs.* substrate concentration in the presence and the absence of aluminium exhibited typical Michaelis – Menten kinetics (data not shown). The Lineweaver-Burk plots (Figure 1) show that increase of reaction velocity in a presence of Al<sup>3+</sup> ions resulted in a family of linear plots intersecting at 1/ [Hb] axis. Aluminum was found to stimulate the enzyme activity in dose-dependent manner.

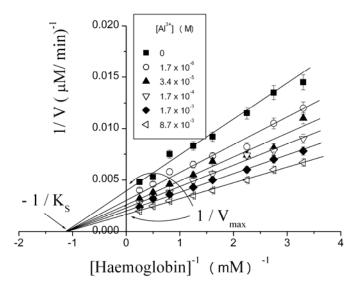


**Fig. 1.** Lineweaver-Burk plot of a series of kinetic measurements in a presence of different Al<sup>3+</sup> ions concentrations at pH 2.

As can be seen, increasing of aluminium concentration increased  $V_{max}$  values from  $254 \pm 7~\mu M~min^{-1}$  to  $599 \pm 17~\mu M~min^{-1}$ , without producing a significant change in the value of apparent enzyme affinity for the substrate  $K_S$ , of  $0.907 \pm 0.072~mM~L^{-1}$ , according the proposed reaction scheme (Scheme 1).

**Scheme 1.** Reaction scheme for nonessential activation; Abbreviations are E-enzyme, S-substrate, A-activator, and P-product.

At equilibrium conditions partially non-competitive activation exists if the following conditions are satisfied, i.e.  $K_S = K_{ms}$ ,  $K_A = K_{mA}$  and k < k' (Scheme 1) [3, 4]. To evaluate the nature of activation secondary Lineweaver-Burk plots were considered. As the secondary plots of the slopes and intersects vs. activator concentrations are not linear (data not shown), the reciprocal of the change in slope and intercept ( $\Delta$ slope and  $\Delta$ intercept) vs. 1/ [Al³+], that are linear [3, 5], were used for calculating equilibrium constants  $K_{mS}$  and  $K_{mA}$  (Figure 2). The calculated values for constants,  $K_{mS}$ ,  $K_{mA}$  and  $K_A$  are 0.904 ± 0.083 mM, 8.56 ± 0.51  $\mu$ M and 8.82 ± 0.90  $\mu$ M respectively, which is consistent with a non-essential partial non-competitive activation system (Scheme 1). Activation constant,  $K_A$ , was determined graphically and by direct measurement of Al³+ binding (data not shown).

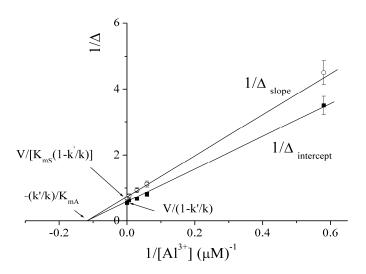


**Fig. 2.** The secondary plots of  $1/\Delta$  against  $1/[Al^{3+}]$ , where  $\Delta$  is defined as slope or intercept in the absence of activator (Al<sup>3+</sup> ions) minus that in its presence.

# Conclusion

In summary, the present kinetic analyses, which classify this phenomenon as a case of non-essential activation, indicate that the activation by Al<sup>3+</sup> ions was of partial non-competitive type.

# Acknowelagement

This study was supported by Ministry of Science of Republic of Serbia, Project No. 142025.

- [1] A.R. Sielecki, A.A. Fedorov, A. Boodho, N.S. Andreeva, M.N.G. James, J. Mol. Biol. 1990; **214**: 43-170.
- [2] M. Anson, J. Gen. Physiol., 1938; 22:79-89.
- [3] M. Dixon, E.C. Webb, Enzymes, 3 th ed. London: Longmans, 1979, p. 339-398.
- [4] R. Fontes, J.M. Ribeir, A. Sillero, Acta Biochim Pol 2000; 47:233-257.
- [5] I.H. Segel, Enzyme kinetics. New York: John Wiley & Sons; 1975. p. 227-272.

# EARLY EFFECTS OF IONIZING IR-RADIATION ON THE ECTO-5'NUCLEOTIDASE ACTIVITY IN RAT BRAIN DURING POSTNATAL DEVELOPMENT

I. Stanojević, D. Drakulić and A. Horvat

Laboratory for Molecular Biology and Endocrinology, "Vinča" Institute of Nuclear Sciences, P.O.Box 522, 11001 Belgrade, Serbia

# **Abstract**

In the present study, early effects of low (50 cGy) and therapeutic dose (2 Gy) of ionizing  $\gamma$ -irradiation on ecto-5'nucleotidase activity in rat brain neuronal cells during postnatal development were studied. Ecto-5'-nucleotidase is the major enzyme that hydrolyzes extracellular AMP and is responsible for the formation of the P1 receptor agonist-adenosine. It was shown that the levels of AMP hydrolyses by the enzyme were not affected by irradiation in the rats during first 4 postnatal weeks. A both low- and therapeutic dose significantly decreased hydrolyses of extracellular AMP in pubertal and adult rats by 10-14%. These findings indicate that low dose exerts the same effects on ecto-5'nucleotidase activity as therapeutic one in first hour after irradiation. Another findings is that in early postnatal development, brain ecto-5'nucleotidase was resistant to irradiation damage.

# Introduction

Adenine nucleotides represent an important class of extracellular molecules that are crucial for normal functioning of the nervous system having special functions during development. The events induced by extracellular adenine nucleotides are controlled by the action of ecto-nucleotidases (NTPDase 1, 2, 3), which play a central role in modulating the extracellular levels of these important signaling (ecto-5'-NT/CD73) Ecto-5'nucleotidase hydrolyses molecules. monophosphates (AMP) to adenosine and is a key enzyme in the nucleotide degradation pathway. Adenosine, the final product of ATP hydrolysis, elicits important physiological responses related to neurotransmission modulation, neuroprotection and cell survival/death, activating specific P1 receptor subtypes. These effects are closely related to extracellular adenosine concentrations, cell surface expression of different adenosine receptor subtypes and signal transduction mechanisms activated following the binding of specific agonists [1].

Effects of ionizing radiation (IR) could not be explained simply by direct damage of the cell DNA molecules. The additional target is the plasma membrane, which is highly sensitive to IR, especially in early period after irradiation. Reactive oxygen species (ROS) formation and oxidative stress that follows are very important in injuries induced by ionizing radiation. IR affects plasma membrane functions mediated through transmembrane proteins by altering their expression or changing the interaction(s) that normally take place between membrane lipids and proteins. ROS, generated in the cell following IR, acts on polyunsaturated fatty

acids of cellular membranes producing lipid peroxides, which may alter functioning of plasma membrane proteins [2].

Thus, the aim of this work was to study the early (1h) effects of low and therapeutic doses of whole body irradiation with gamma-rays on ecto-5'nucleotidase activity during postnatal development by measuring the rate of AMP hydrolysis in young, prepubertal, pubertal and adult rat brain.

# **Experimental procedures**

Female rats of the Wistar strain, 15, 30, 60 and 90 days old, were whole-body irradiated with 50 cGy or 2 Gy (10.7 cGy/min, <sup>60</sup>Co source). During irradiation, the animals were confined in plywood boxes and the second group of animals were treated as the irradiated group but not subjected to irradiation (control group). All groups were sacrificed 1 hour after irradiation. Nerve terminals (synaptic) plasma membranes (SPM) were isolated from whole brains. Activities of ecto-5' nucleotidases were determined under *in vitro* conditions: rate of AMP hydrolysis were measured by colorimetric determination of liberated phosphate in the presence of 80μg SPM proteins, 1mmol/l AMP, 5 mmol/l MgCl<sub>2</sub>, 50 mmol/l Tris-HCl, pH 7,4 and incubations at 37°C for 30 min. The specific enzyme activity was expressed as mean nmolPi/min/mg SPM protein ± S.E.M. from three independent examinations performed in triplicate. Statistical analyses were performed by one-way analysis of variance (ANOVA), followed by a Tukey's test as post-hoc, considering p < 0.05 as significant.

#### **Results and Discussion**

The experimental results of age-dependent effects of low- (50 cGy) and therapeutic- (2 Gy) dose whole body irradiation on the brain ecto-5'nucleotidase hydrolyzing activity are presented in Figure 1. As can be seen, there is significant lower AMP hydrolyzing rate detected in young rats. During postnatal brain development synaptic contacts, dendrite elongation and myelinization, as well physiological apoptosis, are more potent events. Since we measured hydrolyzing activity of ecto-5'nucleotidase in isolated presynaptic plasma membranes in 15and 30-day-old rats with lower number of synapses, the rates of hydrolyses were much lower in respect to the older age rat brains with formed synapses. Also, during early period of development, ecto-5'nucleotidase possess predominantly functions in brain cells communication. The analysis of the developmental profile of ecto-5'nucleotidase hydrolyzing activity revealed that this activity is minor in postnatal animals and reaches the maximum level at adult one [3]. Even though immature neurons are generally more sensitive to IR [4] we could not detect any changes in ecto-5'nucleotidase hydrolyzing activity. One hour after irradiation of 60- and 90-day-old rats with both doses, AMP hydrolysis decreased between 10% and 15% in respect to appropriate controls (Fig.1.). These results indicate that lowdose irradiation is sufficient to modulate ecto-5'nucleotidase activity as early as 1h. Several previous studies have reported that rat brain ecto-ATPase activity,

responsible for hydrolysis of extracellular ATP decreased under conditions that either promote or are associated with increased lipid peroxidation. It was found that 4-hydroxynonenal, the major product of membrane lipid peroxidation inhibits SPM ecto-ATPase activity [5]. Our results suggest that similar mechanisms may induce inhibition of ecto-5`nucleotidases. Inhibition of SPM ecto-5'nucleotidase activity would be expected to decrease formation of adenosine, generally accepted as neuroprotective compound.

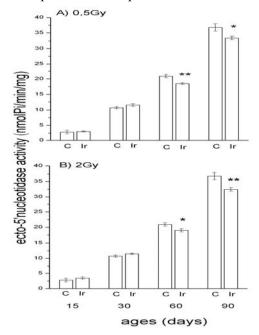


**Fig. 1.** Development-dependent ionizing radiation effects on presynaptic ecto-5'nucleotidase activity. The enzyme activity was measu- red 1h after (A) low-dose and (B) therapeutic-dose irradiation (Ir) and compared with control (C) activity. Results represent mean ±S.E.M from three experiments done in triplicate (\*p<0.05, \*\*p<0.01)

# Conclusion

Whole body irradiation induces modulation of neuronal activity in pubertal and adult rat brain by decreasing extracellular AMP hydrolysis within 1h after irradiation, which may lead to increased cell death. The hydrolyzing activity of ecto-5'nucleotidase in young and prepubertal rats was not affected by irradiation.

# Acknowledgements

The Serbian Ministry of Sciences, Project No. 143044 supported this study.

- [1] N. Strater, Purinergic signaling, 2006, 2, 343-350.
- [2] L.Kh. Eidus, Radiat. Environ. Biophys., 2000, **39**, 189-195.
- [3] H. Zimmermann, Eur. J. Physiol., 2006, 452, 573-588.
- [4] T.D. Foley, Neurochem. Res., 1999, 24, 1241-1248.
- [5] J. Verheyde, M.A. Benotmane, Brain Res.Rev., 2007, 53, 312-320.

# EPR IDENTIFICATION OF CELLULOSE RADICALS IN FOOD INDUCED BY LOW AND HIGH γ-IR-RADIATION DOSES

D. Gojačanin<sup>1</sup>, I. Spasojević<sup>2</sup>, M. Daković<sup>1</sup>, A. Ignjatović<sup>1</sup> and M. Mojović<sup>1</sup>

<sup>1</sup>University of Belgrade, Faculty of Physical Chemistry, Studentski trg 12-16, 11000 Belgrade, Serbia
<sup>2</sup>Institute for Multidisciplinary Research, POBox 33, 11030 Belgrade, Serbia

# Abstract

The objective was to develop the process of detection of high- and low-dose  $\gamma$ -irradiated foodstuffs using EPR technique and to observe the possibility to use them as EPR dosimeters which can be used for both high and low doses [1]. Subject of investigation in this study were seeds of several commonly irradiated foodstuffs. After considering a number of different cellulose-containing foodstuffs, EPR detection of high  $\gamma$ -irradiation doses (used in sterilization process) showed to be confident. On the other hand, the detection of low doses was possible only among two different types of seeds (peach and apricot) which potentially could be used as new universal dosimeters.

#### Introduction

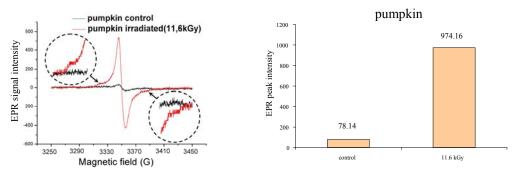
Ionizing radiation is a frequently used for treatment of various foodstuffs in order to improve their hygienic quality and extend their shelf life. However, radiation is known to produce free radicals which are potentially hazardous for human health and can change qualitative characteristics of food. During the interaction of radiation with various foodstuffs to improve their quality and prolongation of best-before date, free radicals are formed and they can be directly detected with EPR method. Detection of irradiated food using Electron Paramagnetic Resonance (EPR) spectroscopy is based on the fact that radiation provokes formation of EPR active species-free radicals, which are relatively stable and long-living in dry foods [2]. The extensive use of ionizing radiation in industry has prompted the development of dosimetric techniques for detection of wide range of doses. Most studies have been focused on Alanine dosimetry which showed to be one of the best solutions for high (above 10 kGy), but also poor solution for detection of low doses (0.2-10 Gy) [3, 4]. Lifetime of radicals produced by irradiation and the kinetics of their decay are limiting factors for the period of time after irradiation during which detection is possible and quantitative, so confident methodological approach should also be developed [2]. Because of their negative influence, the use of radiation in food treatment is limited and European Committee for Normalization led the control of foodstuffs. Except pure detection, to affirm that the food was irradiated, the kinetic of change of EPR signal intensity of free-radical (in dry food it is radical of cellulose) could be observed. This method could be used for detection of food irradiation even after long period of time [2]. Cellulose radicals have triplet spectrum with one central line and two narrow satellite lines. Detection based on these lines is not possible because detected signal is very unstable. Because of thus, it is proposed that detection is based on relative intensity of central peak [5]. On the other hand, there is a need for dosimetric system which could control the amount of radiation that material absorbed. Current EPR dosimeters are not sensitive enough so the attempt was to find new and overrun defects of present dosimeters.

# **Experimental**

Seed samples were prepared at room temperature and left in drying oven at 30°C for several days for humidity removal. Consequently they were grinded, homogenized, and packed in quartz vials and sealed (exposition to humidity or air increases the possible recombination of free radicals). Samples of 100 mg of grinded apricot and peach seeds were irradiated using 60Co  $\gamma$ -irradiation unit with dose of 0.664 Gy/min. Radiation doses were in range of 0.2-10 Gy. Sample of 100 mg of pumpkin was irradiated using 60Co  $\gamma$ -irradiation unit with dose of 13 kGy/min. Radiation dose was 11.6 kGy. EPR measurements were performed using Varian E-104A EPR spectrometer, operating at X-band frequency (9.3 GHz). Measuring conditions in all EPR experiments were: H=3350 G, SW=200 G, MA=2 G, P=10 mW.

#### **Results and Discussion**

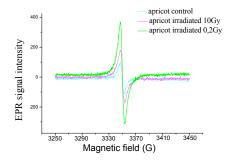
Irradiated pumpkin, apricot and peach showed distinctive EPR signals whose intensities were determined. EPR spectra and intensities of EPR signals are presented on Figures 1, 2 and 3. EPR spectrum of pumpkin has triplet line with one intensive central line and two narrow satellite lines (see Fig. 1). The presence of this line is unequivocal proof that foodstuffs were irradiated. Using this method it could be confirmed that foodstuffs have been irradiated up to 90 days after irradiation [2]. Figures 2 and 3 show EPR spectra and calculated peak intensities of control and irradiated samples of apricot and peach. It could be observed that intensities of EPR signals of irradiated apricot and peach are higher than EPR signals of control samples even for low doses up to 0.2 Gy. Therefore, obtained results indicate that seeds of apricot and peach could be seriously considered as new materials for low-dose EPR dosimetry.

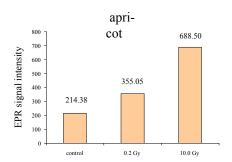


**Fig. 1.** EPR spectra and peak intensities of control and irradiated samples of grinded pumpkin seeds.

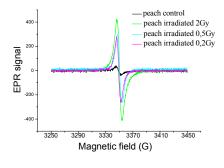
#### **Conclusions**

In conclusion, after considering a number of different cellulose-containing foodstuffs, EPR detection of high  $\gamma$ -irradiation doses (used in sterilization process) were showed to be confident. On the other hand, the detection of low doses was possible only among two different types of seeds (peach and apricot) which potentially could be used as new universal dosimeters.





**Fig. 2.** EPR spectra and peak intensities of control and irradiated samples of grinded apricot seeds.



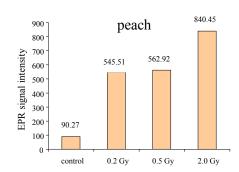


**Fig. 3.** EPR spectra and peak intensities of control and irradiated samples of grinded peach seeds.

# Acknowlegement

The authors express gratitude to the Ministry of Science of Republic of Serbia for the financial support (Project #143016).

- [1] J.Raffi, N.D.Yordanov, S.Chabane, L.Douifi, V.Gancheva, S.Ivanova. Institute of Catalysis, Bulgarian Academy of Sciences, Sofia 1999.
- [2] A.Ignjatović, I.Spasojević, M.Mojović. Zbornik radova 49. Konferencija za ETRAN, Budva, 2005.
- [3] N.D.Yordanov, V.Gancheva. Institute of Catalysis, Bulgarian Academy of Sciences, 1113 Sofia 1999.
- [4] S.K.Olsson, S.Bagherian, E.Lund, G.A.Carlsson, A.Lund Appl. Radiat. Isot. 1999, 50, 955-965
- [5] D.F.Regulla, U.Defner, O.Schindewolf, A.Vogenauer, A.Wieser. IAEATECDOC-321. IAEA, Vienna 1984.

# INVESTIGATION OF LACTULOSE IN DOMESTIC INFANT FORMULA

D. Jakovljević<sup>1</sup>, D. Kanazir<sup>2</sup> and M. Vrvić<sup>1,2</sup>

<sup>1</sup>ICTM - Center for Chemistry, Studentski trg 12-16, Belgrade, Serbia. (djakovlj@chem.bg.ac.yu) <sup>2</sup>Faculty of Chemistry, University of Belgrade, 11001 Belgrade, Studentski trg 16, P.O. Box 158, Serbia

#### **Abstract**

Lactulose is ketose derived from lactose during heating and storage of milk and dairy products. This disaccharide has bifidogenic properties and its recognized as one of prebiotics. A commercial domestic infant formula was investigated by applying *in vitro* experiments on bifidogenic properties. It has been shown that this infant formula have high quality according to bifidogenic effect in relation to other commercial formulas of the same category. Therefore, because lactulose is one of the bifidogenic factor, the aim of this work was to confirm the presence of lactulose in the investigated sample and to determine the concentration of this discenharide

# Introduction

Lactulose (4-*O*-β-D-galactopyranosyl-D-fructofuranose) is a disaccharide consisting of one molecule of galactose and one molecule of fructose which connected by  $\beta$ -(1,4)-glycosidic linkage (Fig. 1). This carbohydrate is a slightly sweeter and more soluble than a lactose, from which is derived by isomerisation, during heating and storage of milk and dairy products [1]. On this occasion two degradation routes were established: 1. lactose isomerization into lactulose (through the Lobry de Bruyn-Alberda van Ekenstein transformation) and subsequent degradation into galactose, formic acid and C5/C6 compounds, and 2. the Maillard reaction in which lactose interacts with protein-bound lysine residues to form protein-bound lactulosyllysine. Also, it was confirmed that lactulose has bifidogenic properties, namely, the presence of this disaccharide in an artificial development of Bifidobacterium infants nutrition initiate the microorganism in the intestinal flora, hence lactulose is recognized as one of prebiotics [2]. Prebiotics have the ability to increase levels of 'health promoting' bacteria in the intestinal tract of humans or animals. This normally involves targeting the activities of bifidobacteria and/or lactobacilli. Non-digestible oligosaccharides such as fructo-oligosaccharides, lactulose and traps-galactooligosaccharides seem to be efficient prebiotics as they cause the selective fermentation of probiotics.

**Fig. 1.** Lactulose (4-*O*-β-D-galactopyranosyl-D-fructofuranose)

In this work we confirmed the presence of the lactulose in a domestic infant formula. It was performed by preparative planar chromatography and using FTIR and HNMR spectroscopy.

# **Experimental**

The precise portion of domestic infant formula sample was deproteinised with Carrez I and II, and the filtrate was subjected to preparative paper descending chromatography using solvent system 1-butanol-etanol-acetic acid-water (10: 10:1:4, v/v) for 12 h at 20 °C. The chromatograms were air-dried and developed with orcinol-trichloroacetic acid made up with 1-butanol saturated with water, at 105 °C for 15 min. The sugars appeared as brown spots on the chromatograms and were identified by reference to standard sugars. The preparatively obtained component was rechromatographied and analysed by FTIR and by <sup>1</sup>H NMR spectroscopy. After that, the concentration of lactulose in investigated sample was determined by spectrophotometric determination [3].

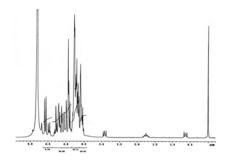


Fig.2. <sup>1</sup>H NMR spectrum of isolated lactulose from domestic infant formula

The  $^1$ H NMR spectrum displayed characteristic signal (*inter alia*) at chemical shift of 4.48 ppm is consistent with anomeric galactopyranosyl protons. This is in accordance with the fact that in an equilibrium mixture in  $D_2O$  of lactulose isomers, 4-O- $\beta$ -D-galactopyranosyl-fructopiranose is dominant. FTIR spectrum displayed bands at 891 cm $^{-1}$   $\pm$  7 cm $^{-1}$ , characteristic for  $\beta$ -D-galactopyranoses which have  $C_1$ -H bond in axial conformation. Also, absorption band at 875 cm $^{-1}$  is

characteristic for D-galactopyranoses, independently of its O-supstituent as well as of its anomeric configuration. It was confirmed that this band arise from deformation of equatorial C-H band at position  $C_4$  of galactopyranoses. Concentration of lactulose in the investigated sample determined by spectrophotometric determination [3], was 398,20 mg/l.

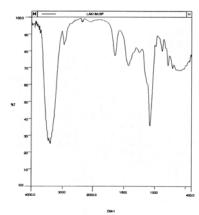


Fig. 3. FTIR spectrum of lactulose isolated from domestic infant formula

# **Results and Discussion**

The sample of domestic infant formula contains lactulose in the value corresponding to UHT milks; i.e. 398,20 mg/l, which is below the limit of 600 mg/l recommended by the International Dairy Federation [4] for UHT milks.

# Conclusion

In this work, the presence of lactulose in a commercial domestic infant formula, as bifidogenic factor and prebiotic was examined, as well as the content of this discapharide. It was concluded that the value of lactulose in investigated domestic infant formula was in recommended limits.

# Acknowledgement

This work was supported by the Serbian Ministry of Science, Projects ON 142018B.

- [1] I. Martinez-Castro and A. Olano, Milchwissenschaft, 1980, 35, 5-8.
- [2] Y. Bouhnik, A. Attar, F.A. Joly, M Riottot, F.Dyard, B. Flourié, Eur J. Clin. Nutr., 2004, **58**, 462–466.
- [3] M. A. Khan, Z. Iqbal, M. R. Jan, J. Shah, W. Ahmad, Z.U. Hag, Obaidulah, Analytical Chem., 2006, 61, 32–36.
- [4] International Dairy Federation, Brussels, 1995.

# MICROWAWE IRRADIATION INFLUENCE ON ENZYME KINETICS

D.R. Stanisavljev<sup>1</sup>, V.M. Pavelkić<sup>2</sup> and M.V. Beljanski<sup>3</sup>

<sup>1</sup>Faculty of Physical Chemistry, Belgrade University, Belgrade, Serbia; <sup>2</sup>Institute of Nuclear Sciences Vinča, Vinča, Belgrade, Serbia; <sup>3</sup>Institute of General and Physical Chemistry, Belgrade, Serbia

# **Abstract**

Kinetic study of microwave (MW) irradiated enzyme pepsin was performed. Decreased enzyme activity was observed, under constant temperature and absorbed MW energy per time unit. In accordance with experimental conditions,  $V_{\text{max}}$  and  $K_{\text{m}}$  were calculated for irradiated pepsin solutions and compared with control reaction with non-irradiated pepsin.

#### Introduction

Microwaves (MWs), now in wide use (i.e. mobile phone, cooking), cause different biological effects depending on applied field strength, frequencies and duration of exposure. Two types of effects are ascribed to MW, i.e. thermal and non-thermal. The thermal effects are related to the fast increase of temperature due to the efficient absorption of MW energy by the irradiated medium and specific thermal effects due to the nonstandard evolution of heat in the reaction media [1]. Knowledge about molecular mechanisms involved in non-thermal effects that could involve energy transfer from the electromagnetic field to the vibration modes of macromolecules, altering their conformation is still obscure [2]. Kinetic properties of the enzyme under MW irradiation are essential for understanding of MW effects on enzyme catalysis. Here we present results of kinetics study of microwave-irradiated pepsin.

# **Experimental**

Porcine pepsin A, Bovine serum albumin (BSA), Brom-phenol blue sodium salt (BPB) were used without further purification. MW irradiation was performed in a single mode focused CEM reactor (Model Discover, CEM Co., Matthew, NC) working at 2.45 GHz. All experiments were done with a same working conditions, *i.e.* the emitted power by the instrument was 30 W, the absorbed MW power,  $P_{abs} = m \cdot C_p \cdot (dT/dt)_i$ , calculated by calorimetric method measuring temperature increase during the initial heating period was  $(2.8 \pm 0.3)$  W, and specific absorbed rate (SAR) of  $(0.47 \pm 0.05)$  W/g. Temperature in the sample was measured by fiber optic temperature sensor preventing interaction with MW and influence on temperature reading. External cooling reaction mixture provided the constant temperature and irradiation power. Enzyme assay was performed in buffer solution at pH 2 and 37° C using BSA-BPB as a substrate [3]. The  $K_m$  and  $V_{max}$  were determined using a linear regression on Lineweaver-Burk double reciprocal plots.

## **Results and Discussion**

Depending on experimental conditions, the degrees of inhibition caused by absorbed MW radiation vary from 39.11% to 45.91% for 5 and 20 min of pepsin MW irradiation respectively (Figure 1).

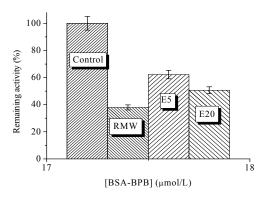


**Fig. 1.** Percentage of remaining activity: Control - without microwave irradiation; RMW-reaction in microwave field; E5 - reaction with irradiated enzyme solution for 5 min; E20- reaction with irradiated enzyme solution for 20 min. Each point represents the mean of three determinations.

The initial velocity  $(V_0)$  of the reactions were calculated and plotted versus BSA-BPB concentrations, generating saturation plots for each monitored reaction. The plots follow Michaelis-Menten kinetics (Fig. 2. - inset) with MW induced decrease of the reaction rates in all cases. A double reciprocal plot of velocity vs. substrate concentration at increasing exposure time (5 and 20 min, due to the discernible changes in enzyme activity) resulted in a linear plots intersecting at different points at 1/[S] axis. From Lineweaver-Burk plots the obtained values of  $V_{max}$  for the control and reactions for the irradiated pepsin were (3.521±0.176) (2.198±0.109) µM/min respectively. The decrease of reaction velocity in a presence of MW irradiated enzyme is not proportional to increased time of irradiation. It is noticeable that for the irradiation times of 5 and 20 min the apparent velocity of enzyme reaction, i.e. the value of  $V_{max}$  is not significantly changed (Figure 2). Compared to the control reaction,  $V_{max}$  of irradiated samples was decreased. However, the apparent Michaelis-Menten constants varied significantly. At exposure time of 5 min of MW irradiation calculated Michaelis-Menten constant was  $K_{mapp} = 17.391 \mu M$ , while at exposure time of 20 min of MW irradiation  $K_{mapp} = 24.938 \mu M$ , (Figure 2). As the temperature of samples were kept constant in all experiments (37°C) the observed inactivation can be ascribed to the non-thermal effects of MW irradiation. The observed inactivation of pepsin can not be explain by numerous models available for mechanism-based inactivation systems. Based on Schnell and Hanson model [4] for quantitative prediction of non-mechanism-based enzyme inactivation, we consider independent proceeding of enzyme inactivation and product formation.

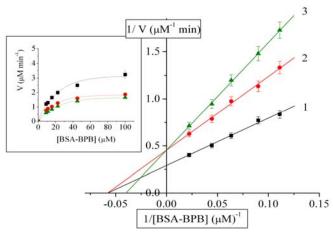


**Fig. 2.** Lineweaver-Burk plot of pepsin inhibition caused by MW radiation. **1-** control reaction under conventional heating in water bath at 37°C; **2-** with 5 min irradiated enzyme; **3-** with 20 min irradiated enzyme. **Inset -** initial velocity versus BSA-BPB concentration with non-irradiated and MW irradiated pepsin at pH 2 and 37°C.

We approximate reaction model which show that the rate of enzyme transformation in the MW field may be described by the reaction of order 0.85 and rate constant  $k_{MW}=(0.38\pm0.02)~(\mu\text{M/dm}^3)^{0.15}~\text{min}^{-1}.$  The same approach give possibility to kinetically characterize MW-modified enzyme with  $V_{max}=(2.194\pm0.110)~\mu\text{M}~\text{min}^{-1}~K_m=~(25.018\pm1.251)~\mu\text{M}$  which is in good agreement with the experimental results.

# Conclusion

The MW irradiation, in controlled experimental conditions (constant absorbed MW energy and temperature) causes a decrease of enzymatic activity, as well as  $V_{\text{max}}$ . Although MW quanta have no energy to break peptide bonds, decreased enzyme activity can be ascribed to relaxing protein structure, assuming excessive breaking and reforming hydrogen bonds. Accordingly, kinetic behavior of pepsin was described with approximate, "non-mechanism based inactivation", reaction model that is in good agreement with obtained results.

# Acknowelagement

This study was supported by Ministry of Science of the Republic of Serbia, Project No. 142025.

- [1] J.L Kirschvink, Bioelectromagnetics, 1996, 17, 187-194.
- [2] L.S. Taylor Bioelectromagnetics, 1981, 2, 259-267.
- [3] S.P. Gray, J.A. Billings, Clin. Chem, 1983, 29, 447-451.
- [4] S. Schnell, S.M. Hanson, Biophysical Chemistry, 2007, 125, 269-274.

# DEPENDENCE OF STARTING WHEAT GROWTH ON DYNAMICS OF HYDROLYSIS, BIOSYNTHESIS AND FREE ENERGY

V. Dragičević\*, S. Sredojević and M. Milivojević

Maize Research Institute, Slobodana Bajića 1, 11185 Zemun Polje, Serbia \*E-mail: vdragicevic@mrizp.co.rs

# **Abstract**

The object of investigation was germinating dynamics of two wheat subspecies, by measuring of hydrolysis, biosynthesis and fresh mass growth. It was find that free energy of two-phase water shifting had crucial importance for biological balance, compared to energetic potential of hydrolysis and biosynthesis, during the primary growth of wheat seedlings, so as, the energy inputted by water and total energy of reactions have to be in stable equilibrium.

## Introduction

Seed germination is characterized by water absorption, what increase free energy level, shifting of biological system from anhydrobiosis. This activate endothermic hydrolysis [1], leading to a range of exothermic and endothermic reactions [2]. The next phase is characterized by water and substance distribution, denoting as the plant growth, biosynthesis. Unequal distribution in seedlings [3], could affect lather growth and yielding.

The aim of experiment was to examine growth of two wheat subspecies, with different growth rates, in function of substance and water distribution, connected with thermodynamical parameter of free energy.

# Material and Methods

The seeds of two wheat subspecies: common (*Triticum aestivum*) and durum wheat (*Triticum durum*) were settled to germination according to the ISTA Rules [4], during 13 days. The uniformly grown seedlings were fractioned to the plant (root+shoot) and the seed rest, then weight (fresh mass determination, FW), dried at  $60^{\circ}$ C (dry weight determination, DW) to calculate the water content (W<sub>c</sub>), hydrolysis ( $\Sigma$ Hy) and biosynthesis ( $\Sigma$ Bs):

$$\Sigma$$
Hy = DWseed – DWseed rest  
 $\Sigma$ Bs = DWroot + DWshoot

The measurements were used to calculate: free energy, based on water volume  $(G_{Wc})$  according to Clausius-Clapeyron equation for heat of vaporization, as well as, free energy of hydrolysis  $(G_{Hy})$  and biosynthesis  $(G_{Bs})$ , based on reactional constants:

$$G_{Wc} = -RT \ln (W_c)$$

$$G_{Hv. Bs} = -RT \ln (k)$$

where R is gas constant and T is germination temperature (293.16 K), rendered as sum of average day temperatures.

# **Results and Discussion**

The common wheat at 12<sup>th</sup> day reached maximal fresh mass of 178 mg plant<sup>-1</sup> (Tab. 1), while the durum wheat gained it at 7<sup>th</sup> day: 152 mg plant<sup>-1</sup>. Thought, both subspecies produced the same, maximal biosynthesis of 17 mg at 11<sup>th</sup> day. After minimum obtained at 5<sup>th</sup> and 3<sup>rd</sup> day for common and durum wheat, the hydrolysis, as forerunner of biosynthesis [3] increased up to 13<sup>th</sup> day in both. Meanwhile, a conversion of hydrolysis to biosynthesis, with two minimums, at 5<sup>th</sup> and 11<sup>th</sup> in common and 5<sup>th</sup> and 9<sup>th</sup> days in durum wheat indicated that biosynthesis hasn't follow hydrolysis, what is similar to results find on wheat genotypes with lower yield potential [5]. The maximums of FW accumulation in 11<sup>th</sup> and 9<sup>th</sup> day, for common and durum wheat, indicates that biosynthates produced in durum wasn't able to span water, decreasing FW, continually to 13<sup>th</sup> day.

**Table 1.** Dynamics of fresh weight, hydrolysis, biosynthesis in mg per seedling of common wheat (C. wh.) and durum wheat (D. wh.), during 13 days of germination

	(		- ,				(	,,		<i></i>		0		
	Days	1	2	3	4	5	6	7	8	9	10	11	12	13
_:	Fresh weight	0	0	47	71	78	114	126	128	128	135	175	178	168
wb	Hydrolysis	22	21	17	16	13	17	20	23	25	28	30	30	33
C.	Biosynthesis	0	0	5	7	9	12	12	13	13	14	17	16	15
	Fresh weight	0	0	12	10	02	144	152	137	13/	120	90	74	71
w.	Fresh weight Hydrolysis	17	16			12	20	26	28	29	31	35	36	39
	Biosynthesis	0	0	9	10	12	14	15	15	16	16	17	16	16

The  $G_{Wc}$  bring in with water was linearly increased (Fig. 1), but more intensive in common, than in durum wheat. It is important to underline that high corresponding of  $G_{Wc}$  and  $G_{Hy}$  was occurred in common wheat seedlings. Then again, durum wheat seedlings characterise higher values of  $G_{Hy}$  and  $G_{Bs}$ , compared to common wheat. The observed situation could signify higher energetic potential of hydrolysis and biosynthesis in durum wheat seedlings. In common wheat was present opposite trend, i.e. higher values of free energy, based on water volume. Owing to two-phase water shifting [2] and unbalanced hydrolysis and biosynthesis velocity, the consequence is expressed in continual drop of  $_{Hy}\Delta_{Wc}G$  and  $_{Bs}\Delta_{Wc}G$  ratios (0.6 to 0.3 and 0.5 to 0.2) in common wheat; unchanged  $_{Hy}\Delta_{Wc}G$  ratio (0.6) and steep drop of  $_{Bs}\Delta_{Wc}G$  ratio (1 to 0.4) in durum wheat.

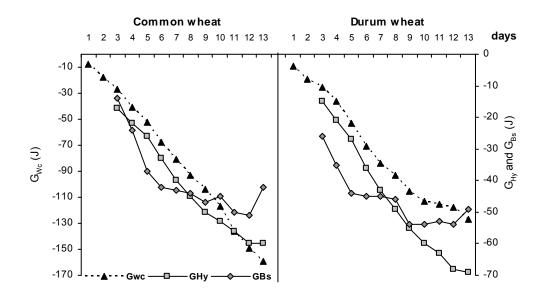


**Fig. 1.** Dynamics of free energy, based on water volume  $(G_{Wc})$ , hydrolysis  $(G_{Hy})$  and biosynthesis  $(G_{Bs})$ , during 13 days of germination

# Conclusion

Obtained results pointed out significance of energetic potential entered by water (two-phase shifting) to energetic potential of hydrolysis and biosynthesis, during the primary growth of wheat seedlings. In living, as highly hydrated systems, energy inputted by water and total energy of reactions have to be in stable equilibrium.

- [1] A.L. Lehninger, Biochemistry, second edition. The John Hopkins University School of Medicine. Worth Publishers. INC.,1976
- [2] W.Q. Sun, Desiccation and survival in plants: drying without dying. Black M. and Pritchard H. W. (Eds), CABI Publishing, 2002
- [3] S. A. Ajayi, M. A. B. Fakorede, Seed Sci. Technol., 2000 28, 301-319
- [4] ISTA, International rules for seed testing, 2007, Chapter 5, Tab. 5A
- [5] M. Lj. Mihailović, M. Antić, D. Hadžijev, Plant Soil, 1965 XXIII, 117-128

# RADIATION-MEDIATED INDUCTION OF P53 PATHWAY IN THE RAT HIPPOCAMPUS

N. Veličković and S. Petrović

Laboratory for Molecular Biology and Endocrinology, "Vinča" Institute of Nuclear Sciences, P.O. Box 522, 11001 Belgrade, Serbia

# **Abstract**

Ionizing radiation (IR) is commonly used in the treatment of brain tumors but it can cause significant damage to surrounding normal brain tissue. In this study, heads of young Wistar rats (18 days old) were subjected to a single dose of gamma irradiation (10 Gy) similar to that used in prophylactic brain irradiation of children with acute lymphoblastic leukemia. The kinetics of apoptosis associated proteins (p53 and Bax) were examined by Western blotting and RT-PCR. We observed that p53 mRNA expression was unchanged after irradiation, while induction of p53 protein was rapid, leading to the accumulation of p53 protein in the cytoplasm. In addition, Bax mRNA and protein levels were also increased following cranial irradiation. These results indicate that cranial irradiation, used in terms of prophylactic therapy, is associated with activation of the p53 system, alongside with induction of positive apoptosis regulator Bax.

#### Introduction

Under normal conditions the tumor suppressor protein p53 is a short-lived protein that is maintained at low level in the cell. In many tissues, irradiation results in the upregulation of p53 protein by a post-translational stabilization mechanism, presumably not followed with change in the mRNA level [1]. Active p53 protein induces the transcription of several downstream genes that, in turn, can trigger a variety of biological processes such as cell cycle arrest, apoptosis and DNA repair. The overall consensus is made that Bcl-2 family members are crucial in p53-mediated apoptosis. This family includes two categories of proteins: those functioning as suppressors of apoptosis (Bcl-2, Bcl-x<sub>L</sub>, Bcl-w) and those that promote apoptosis (Bax, Bcl-x<sub>S</sub>, Bak, Bad, Bik and Noxa). Pro-apoptotic members like *bax*, *bak* and *noxa* are transcriptionally upregulated by p53, while expression of anti-apoptotic *bcl-2* is suppressed by p53 [2]. The relative ratios of these various pro- and anti-apoptotic members of the Bcl-2 family have been shown to determine the ultimate sensitivity or resistance of cells in response to ionizing irradiation.

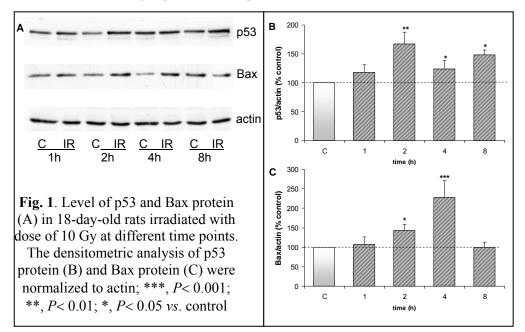
The aim of the present study was to investigate the expression of p53, in the hippocampus of head-irradiated rats, both at the level of mRNA and protein. Simultaneously, expression of positive apoptosis regulator Bax, as downstream p53-target gene, was explored in the same animal model of CNS prophylactic brain irradiation.

# **Experimental**

The experiments were performed using previously established animal model for CNS prophylactic therapy of childhood acute lymphoblastic leukemia (ALL) [3]. Animals at the age of 18 days were divided into two groups: sham-irradiated controls (C) and irradiated animals (IR). IR animals had to be immobilized during irradiation procedure, so the sham-irradiated controls (C) were treated equally, except for being exposed to the source of radiation. The heads of the IR rats were exposed to a single 10 Gy dose of  $\gamma$ -rays using Co<sup>60</sup>-source (Institute of Nuclear Sciences "Vinča"). The hippocampus was isolated at the following post-irradiation times: 1 h, 2 h, 4 h and 8 h. The levels of p53 and bax mRNA were assessed by semi quantitative RT-PCR using as the internal standard mRNA for actin. The levels of p53 and Bax proteins in cytosolic fractions were detected by Western blot using mouse anti-p53 (StressGene) and rabbit anti-Bax antibody (Cell Signaling), respectively.  $\beta$ -Actin (Santa Cruz Biotechnologies) was used as an equal loading control. Analysis of variance (one-way ANOVA) followed by *post hoc* Tukey test was used to estimate statistically significant differences (P < 0.05).

# Results and discussion

It was well known that the tumor suppressor p53 protein is induced in response to irradiation and genotoxic drugs in order to produce either cell cycle arrest or apoptosis, depending on the cell type and the microenviroment [1]. Both of these events can be viewed as ways of protecting cells from DNA damaging agents. In this study, cranial irradiation rapidly stimulated p53 protein expression in a time-dependent manner (Figure 1A, B), whereas the level of *p53* mRNA expression showed no statistically significant changes (data not shown).



These results are in agreement with a previous report, demonstrating that gamma-irradiation induces apoptosis as well as the induction of p53 protein in fetal rat brain, without a major up-regulation of p53 mRNA [4].

It is known that p53 transcriptionally activates Bax in some types of cells after treatment with ionizing radiation, chemotherapeutic drugs and other forms of genotoxic stress [4]. We found that the level of cytosolic Bax protein was higher in irradiated rats that in the control ones; the maximum level was attained at 4 h, then subsequently reduced again to low level (Figure 1C). This induction temporally coincides with the elevation of p53 protein (Figure 1B), as expected for a cause-and-effect relationship. Moreover, cranial irradiation moderately increases the level of *bax* mRNA, as revealed by RT-PCR (Figure 2).

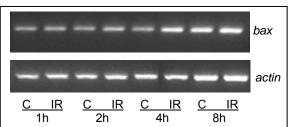


**Fig. 2**. Level of hippocampal *bax* mRNA expression in rats irradiated with 10 Gy at different time points.

Bax promotes apoptosis by facilitating release of apoptosis inducing factor and cytochrome-*c* from the mitochondria, thus triggering a cascade of caspase activation. It should be noted, however, that not all types of radiation-induced apoptosis involve p53 induction [5]. In irradiated p53-/- lymphoblasts overexpression of Bcl-2 protein leads to apoptosis, hence p53 is

not the only mediator of apoptosis provoked by DNA damage [5].

# Conclusion

Our result exemplifies the activation of p53-dependent genes by irradiation in this animal model system. Ionizing irradiation leads to rapid induction of p53 protein in the cytoplasm of rat hippocampal cells, without change in its mRNA level. This is followed by induction of positive apoptosis regulator Bax, both at the level of protein and mRNA.

# Acknowledgement

This study was supported by the Serbian Ministry of Science, Project No. 143044.

- [1] L. Donehower and A. Bradley. Biochem. Biophys. Acta, 1993, 1155, 181-205.
- [2] L. J. Ko and C. Prives, Genes Dev., 1996, 10 (9), 1054-1072.
- [3] P. J. Mullenix, W. J. Kernan, M. S. Tassinari, A. Schunior, D. P. Waber, A. Howes, N. J. Tarbell, Cancer Res., 1990, 50, 6461-6465.
- [4] A. E. Borovitskaya, V. I. Evtushenko, S. L. Sabol, Brain Res. Mol. Brain Res., 1996, **35** (1-2), 19-30.
- [5] A. Strasser, A. W. Harris, T. Jacks, S. Cory, Cell, 1994, 79, 329-339.

# OXIDATIVE STABILITY OF COLD-PRESSED HIGHOLEIC SUNFLOWER OILS IN BULK OILS AND EMULSIONS

M. Pavlović<sup>1</sup>, S. Ostojić<sup>1</sup>, S. Jocić<sup>2</sup>, M. Kićanović<sup>1</sup>, S. Zlatanović<sup>1</sup>, Z. Sakač<sup>2</sup>, M. Živić<sup>1</sup> and V. Mićović<sup>1</sup>

<sup>1</sup>Institute of General and Physical Chemistry, Belgrade, Studentski trg 12-16, <sup>2</sup>Institute of Field Vegetables and Crops, Novi Sad, Maksima Gorkog 30

# **Abstract**

Oxidative stability of cold-pressed sunflower oils with enhanced oleic acid and  $\beta$  tocopherol content, was analysed in bulk oils and emulsions, using differential scanning calorimetry method, lipid hydroperoxide and free fatty acid determination. Oleic:linoleic acid ratio influenced oxidative stability of both bulk oils and emulsions, although bulk oils appear to be more stable.

# Introduction

Degree of unsaturation of fatty acids and tocopherol content are the most important factors affecting oxidation of oils. Differential scanning calorimetry (DSC) has been applied, as an oil oxidative stability method, based on thermal release, by several authors and has shown good correlation with other accelerated methods, such as oil stability index (OSI) method, commonly known as Rancimat (AOCS Meth. Cd12-92) $^1$ . The phenomenon that the oxidation is, generally, faster in bulk oils than in emulsions may be attributed to the large interfacial area in emulsions, compared to the relatively small interface between the air and oil in bulk oil. In the present study we explored the oxidative stability of sunflower oils with enhanced concentration of oleic acid and  $\beta$  tocopherol, in bulk oils and whey-based emulsions, using DSC method compared to peroxide value.

# Experimental

Fatty acid composition of oils was determined by gas-chromatography (Conik HRGC 4000b, Spain) after methylation. Tocopherol content was analysed by HPLC (Sycam, Germany). Whey-based emulsions with 40% sunflower oil (similar to mayonnaise) were produced as previously described<sup>2</sup>. After the desired period of time, emulsions were frozen at -80°C until determination of peroxide value (PV),(AOCS Cd 8-53, 1996), free fatty acid content (AOCS Cd 18-90, 1996) and differential scanning calorimetry analysis (DSC) of separated oil phase. Accelerated oxidative stability of oils was determined by DSC method under isothermal conditions with oxigen flow, as previously described<sup>1</sup> on Q 1000, TA instruments, (Delaware, USA). pH was analysed on pH-meter (Consort, C 830, USA) with the electrode for emulsions with enhanced viscosity.

## **Results and Discusion**

Oxidative stability of cold-pressed oils, obtained from six sunflower hybrides of "Oliva" type, produced in the "Institute for Field Vegetables and Crops", with presumed high oleic acid and  $\beta$  tocopherol content, correlates with unsaturated higher fatty acid content. The ratio between  $\alpha$  and  $\beta$  tocopherol is similar in all hybrides, while  $\beta$  tocopherol content was enhanced, Tabl. 1, compred to standard, linoleic type of oil.  $\beta$  tocopherol is a stronger antioxidant *in vitro* than  $\alpha$  tocopherol. The initial peroxide value, PV was 0 mmol/l  $O_2$  in all analysed oils, while the AV (free fatty acid content) was 1.3 - 3.88. Some of these oils are potentially unstable, because of high free fatty acid content which could promote oxidation.

**Table 1.** Oleic (18:1) and linoleic (18:2) acid content,  $\alpha$  and  $\beta$  tocopherol content and oxidative characteristics of cold-pressed higholeic sunflower oils

NS hybrid —		18:1 and 18:2 content (%)		rol content	t (mg/kg)	<sup>a</sup> AV, 0 day	<sup>b</sup> OIT 105°C	°OIT 120°C
	18:1	18:2	α	β total		0 day	103 C	120 C
NSH- OL1	88.2	5.3	311.67	250.67	564.33	1.52	216.8	104.1
NSH- OL2	89.4	5.0	205.33	206.67	412.33	2.38	262.2	65.3
NSH- 2073	46.3	44.8	244.67	237.33	482.00	1.46	96.3	37.4
NSH- 2034	74.8	17.3	174.33	241.33	482.00	3,88	83.0	18.4
NSH- 2075	40.3	50.6	338.00	217.33	556.67	2.99	41.7	7,5
NSH- 2076	67.0	25.30	311.67	250.67	562.33	3.15	111.3	58.3

<sup>&</sup>lt;sup>a</sup>AV Acid value, (free fatty acid conten).

Oleic acid content(>88%) of oils obtained from two hybrides: NSH-OL1 and NSH-OL2 correlates with the long OIT, oxidation induction time, obtained by DSC method at 105°C and 120 °C, which was taken as a time where a rapid exotermic reaction between oil and oxigen occured<sup>1</sup>. We have noticed that NSH-OL1 oil is more stable than NSH-OL2 at 120 °C, probably due to higher tocopherol content. NSH-OL5 oil, with medium oleic acid content, has extremly short OIT on both temperatures and is presumed to be of low oxidative stability.

The analysis of oxidative stability of bulk oils and emulsions revealed high stability of both NSH-OL2 and NSH-2075 on 4°C in two month period. Accelerated oxidation at room temperature revealed that PV of NSH-OL2 (both in bulk oil and emulsion) changed minimally, while PV of NSH-2075 was 2.50 in

<sup>&</sup>lt;sup>b</sup>OIT at 105°C, <sup>c</sup>OIT at 120°C. Oxidation induction time (min), determined by (DSC) at 105°C and 120°C, respectively.

bulk oil and 9.06 in separated oil phase of emulsion, after two months storage at room temperature, Tabl. 2. The enhancement of free fatty acids (acid number) was noticed in separated oil phase of emulsions of both oil type: 11.75%, for NSH-OL2 and 8%, for NSH-2075, connected with a decrease of pH from 4.55 to 4.35, which is normal for the products of unbleached cild-pressed oil.

**Table 2.** Oxidative stability of higholeic sunflower oils in bulk oils and emulsions (mayonnaise), based on whey, during storage on 4°C and room temperature (R.T.), determined by PV and DSC method in separated oil phase.

determined by 1 v and BBC method in separated on phase.										
NS hybrid	OIT	PB	OIT	PB	OIT	PB				
	105°C	(mmol	105°C	(mmol	105°C	(mmol				
	0 day	O2/kg)	60 days	O2/kg)	60 day	O2/kg)				
		0 day	4°C	60 days	R. T.	60 days				
				4°C		R. T.				
NSH-OL2	262.20	0	255.10	0	190.55	0.20				
bulk oil										
NSH-OL2	141.55	0	186.55	0	117.55	0.37				
emulsion										
NSH-2075	41.70	0	40.20	0.40	31.25	2.50				
bulk oil										
NSH-2075	20.07	0	18.81	1.52	12.85	9.06				
emulsion										

DSC analysis of separate oil phase of emulsions revealed lower oxidative stability, compared to bulk oils, in both type of oils. NSH-OL2 has shown higher durability than NSH-2075 in separated oil phase of mayonnaise (OIT, 117.6 versus 12.85, Tabl.2.) after accelerated oxidation at room temperature.

# Conclusion

Oxidative stability of cold-pressed higholeic sunflower oils with enhanced  $\beta$  tocopherol content, determined by DSC method and hydroperoxide analysis in bulk oil and emulsions, correlates with monounsaturated (oleic) acid content. Emulsion (mayonnaise) were less stable than bulk oils.

- [1] J. Velasco, M. L. Andersen, L.H. Skibsted, Food Chemistry, 2004, 85 623-625.
- [2] S. Ostojić, M. Pavlović, M. Živić, Z. Filipović, S. Gorjanović, S. Hranisavljević, M. Dojčinović, Env. Chem. Lett., 2005, **3**, 29-32
- [3] C. Jacobsen, A.S. Meyer, J. Adler-Nissen., J. Food Lipids, 1998, 5, 87-101

# <sup>238</sup>U, <sup>226</sup>Ra, <sup>232</sup>Th AND <sup>40</sup>K DISTRIBUTION WITH SOIL DEPTH IN AGRICULTURAL SOIL *RIGOSOL* TYPE AND ITS RELATION WITH MAIN SOIL PROPERTIES

M.B. Rajković<sup>1</sup>, I. Vukašinović<sup>1</sup>, A.R. Đorđević<sup>1</sup>, D. Todorović<sup>2</sup> and V. Pavlović<sup>1</sup>

<sup>1</sup> Faculty of Agriculture, Zemun, University of Belgrade, Serbia

<sup>2</sup> "Vinča", Institute of Nuclear Science, Belgrade, Serbia

# **Abstract**

Distributions of natural gamma emitting radionuclides <sup>238</sup>U, <sup>226</sup>Ra, <sup>232</sup>Th and <sup>40</sup>K were determined in two soil profiles *rigosol* type under the peach-tree field: one from and second out of the peach-tree root zone. Radioisotope activities (Bq/kg) lie in the range of normal terrestrial gamma-radiation in soil [1]. It is found that variation in natural radionuclides activities along a soil depth of 0-80 cm is due to differences in main soil properties: pH-reaction, carbonates, humus, clay and sand contents confirmed by high correlation between them.

# Introduction

Naturally occurring radionuclides of terrestrial origin are members of <sup>238</sup>U and <sup>232</sup>Th series together with <sup>40</sup>K and their concentrations in soil are related to the nature of parent rock during soil genesis. Artificial fertilizers application on agricultural soil may change the natural level of terrestrial gamma-radiation since they are product of phosphate rock containing elevated level of natural radionuclides, especially <sup>238</sup>U [2,3]. In soils, radionuclides occur in minerals or are adsorbed onto soil components and main influence to their concentration and behavior in soil has soil parameters such as pH, organic matter, clay or carbonates contents [2,4]. The paper aims to investigate contents of natural isotopes <sup>238</sup>U, <sup>226</sup>Ra, <sup>232</sup>Th and <sup>40</sup>K in agricultural soil and its relation with main soil properties that affects their distribution with soil depth.

# **Materials and Methods**

From the area of school estate good "Radmilovac" of Faculty of Agriculture, under the peach-trees field two soil profiles *rigosol* type has been taken. In 1992, *rigosol* type soil is derived from natural soil type *chernozem* by special anthropogenic treatment that changed natural structure and build of original soil. Peach-trees field has been treated with fertilizers about 10-12 years when fertilization stopped and tree years after that was the moment of collection of our samples. Soil samples collected from Ap-horizon of 80 cm depth within soil layers 0-20 cm, 20-40 cm, 40-60 cm and 60-80 cm. First soil profile (**P1**) were taken from the peach-tree root zone and second one (**C1**) from the soil area covered with grass but of the same, previously fertilized, field.

To prepare 8 soil samples for measurement, soil were air-dried and sieved through 2 mm sieve and their physical and chemical properties were analyzed by

standard methods. Soil samples were packed in 500 cm³ Marinelli beakers and kept sealed for 4 weeks to attain radioactive equilibrium. Gamma-spectrometry method applied using HPGe detector (Canberra type) in order to determine natural radionuclides activity concentration. Activity of <sup>238</sup>U was determined by <sup>234</sup>Th (63 keV) or by <sup>234</sup>Pa (1000 keV). The activities of <sup>226</sup>Ra and <sup>232</sup>Th were determined by their decay products: <sup>214</sup>Bi (609 keV), <sup>214</sup>Pb (352 keV) and <sup>228</sup>Ac (911 keV), respectively and <sup>40</sup>K from its 1460 keV *y*-line. Analytical precision of measurements was approximately 10%.

## **Results and Discussion**

The distribution of natural radionuclides in the 20 cm depth intervals, in two soil profiles (P1 and C1) is presented in Table1. together with values of their main soil properties pH (KCl) reaction, humus, carbonates, clay and send contents.

**Table 1.** Depth distribution of natural radionuclides and values of pH, humus, carbonate, clay and sand contents in the studied profiles **P1** and **C1** 

	<sup>238</sup> U (Bq/kg)	<sup>226</sup> Ra (Bq/kg)	<sup>232</sup> Th (Bq/kg)	<sup>40</sup> K (Bq/kg)	рН	Humus (%)	CaCO <sub>3</sub> (%)	Clay (%)	Sand (%)	
Profile 1 (P1)										
0-20 cm	90	59	58	683	6.61	2.12	0.25	43.02	2.18	
20-40 cm	79	44	49	615	6.50	1.36	0.29	41.63	6.62	
40-60 cm	52	53	56	689	6.43	1.19	0.38	41.62	6.01	
60-80 cm	81	55	62	755	6.26	0.92	0.24	43.33	4.54	
Control 1	(C1)									
0-20 cm	84	49	56	692	6.71	2.80	1.05	38.75	5.33	
20-40 cm	69	45	52	623	6.76	1.97	0.98	37.79	9.61	
40-60 cm	72	54	55	627	6.69	1.64	0.63	38.32	5.97	
60-80 cm	54	53	60	673	6.70	1.05	0.46	35.48	8.22	

Radioisotope activities (Bq/kg) lie in the range of 52-90 for <sup>238</sup>U, 44-59 for <sup>226</sup>Ra, 49-62 for <sup>232</sup>Th and 615-755 for <sup>40</sup>K. These values agree with recommended values for background gamma-radiation reported for soils worldwide [1]: 16-110 for <sup>238</sup>U, 17-60 for <sup>226</sup>Ra, 16-64 for <sup>232</sup>Th and 140-850 for <sup>40</sup>K. Total uranium enhancement above natural level is estimated to be less than 0,5%, amount so small that radioactive impact of fertilizer is considered negligible [5].

Activity concentration variation of <sup>238</sup>U with soil depth is higher (18-22 %) with respect to <sup>226</sup>Ra, <sup>232</sup>Th and <sup>40</sup>K that exhibit more homogeneous depth distribution. Their variation with depth (approximately 10%) is comparable with experimental uncertainty of activity determination. All radionuclides incline to accumulate in the upper (0-20 cm) and the deepest layer (60-80 cm), except <sup>238</sup>U in C1. In order to investigate is there any relation along a soil profile depth between radionuclides activity concentration and main soil properties, linear correlation coefficients were found.

For  $^{238}$ U, in **P1**, highest correlation found with carbonates contents (r = -0.95). Since there is absence of large amounts of humus uranium is considered mobile, occurring as a uranyl ion  $(^{UO_2^{2+}})$  and in neutral solutions transported as a  $^{UO_2(CO_3)_2^{2-}}$  complex [3]. In **P1**, it becomes available for uptake in the plant root zone (40-60 cm). In **C1**, out of the root zone, uranium is decreasing with depth gradually where high correlation with clay is found (r = 0.95). Natural radioisotopes are adsorbed onto clay surface or fixed within the lattice structure [2,4] that is connected with reduced downward movement of  $^{238}$ U in **C1**.

Group of  $^{226}$ Ra,  $^{232}$ Th and  $^{40}$ K in **P1** exhibits similar behavior as their main correlations are with clay (r = 0.73, r = 0.83 and r = 0.74 for  $^{226}$ Ra,  $^{232}$ Th and  $^{40}$ K respectively) and sand (r = 0.87, r = 0.61 and r = 0.40). In general, increased sand content in soil enables radioisotopes to move along soil layers [2]. In **P1**, as sand content is low,  $^{226}$ Ra,  $^{232}$ Th and  $^{40}$ K stayed fixed within clay minerals and accumulated in the upper or the deepest soil layer being in the form unavailable for plant root uptake. In the **C1** profile, behavior of  $^{226}$ Ra and  $^{232}$ Th is connected with pH, that is more constant down the **C1**. However, for  $^{40}$ K in **C1** important correlation with soil properties is not found.

# Conclusion

Soil properties differently affects <sup>238</sup>U, <sup>226</sup>Ra, <sup>232</sup>Th and <sup>40</sup>K radionuclides mobility: accumulation of all radionuclides to the deepest soil layer and restricted mobility of <sup>226</sup>Ra, <sup>232</sup>Th and <sup>40</sup>K in soil is influenced by clay and sand content while carbonate content is the main predictor for <sup>238</sup>U mobility. In the root zone, anthropogenicaly introduced uranium, being in the migrative phisico-chemical form was partially transferred to the deeper soil layers and partially absorbed by the root system of the peach-trees. Low mobility and constant depth distribution of <sup>226</sup>Ra, <sup>232</sup>Th and <sup>40</sup>K indicates that their distribution in soil is related to the mineral composition of parent materials.

- [1] UNSCEAR, Report to the General Assembly with Scientific Annexes, New York, USA, 2000, 111-125,.
- [2] M. Stojanović, Utvrđivanje zavisnosti između sadržaja urana i fosfora u različitim zemljištima Srbije, Doktorska disertacija, Polj. fakultet, Zemun, 2000.
- [3] J.J. Mortvedt, Environ. Qual., 1994, 23, 643-650.
- [4] A. Navas, J. Soto, J. Lopez-Martinez, App. Radiat. Isot., 2005, 62, 809-816,.
- [5] A. Takeda, H. Tsukada, Y. Takaku, S. Hisamatsu, M. Nanzyo, Sci. Tot. Env., 2006, 367(2-3), 924-931.

# CHANGES IN THE FATTY ACID COMPOSITION AND OXIDATIVE STABILITY OF HIGHOLEIC SUNFLOWER OILS INDUCED BY HEAT TREATMENT

M. Pavlović<sup>1</sup>, J. Krstić<sup>2</sup>, Z. Sakač<sup>3</sup>, M. Živić<sup>1</sup> and V. Mićović<sup>1</sup>

Institute of General and Physical Chemistry, Belgrade, Studentski trg 12-16

Institute of Chemistry Technology and Metalurgy, Belgrade, Njegoševa 12

Institute of Field Vegetables and Crops, Novi Sad, Maksima Gorkog 30

## **Abstract**

Cold-pressed sunflower oil, with high oleic acid and  $\beta$  tocopherol content, incubated for 48 h at 180°C, had enhanced oxidative stability compared to medium oleic and refined oil. Prolongued heating induced *cis* to *trans* isomerisation of oleic and linoleic acids in both types of cold-pressed oleic oils, while refined sunflower oil contained *trans* and conjugated isomers of linoleic acid before heating.

# Introduction

Cold-pressed higholeic sunflower oils are good alternatives to standard refined linoleic type of sunflower oil, regarding oxidative stability<sup>1</sup>. However, unrefined oils may contain trace of prooxidative metals, free fatty acids and other compounds which stimulate autooxidation of oil and formation of potentially harmful decomosition products. The interest in the trans-fatty acids has increased because of the relation between fatty acid intake and the risk of cardiovascular disease<sup>2</sup>. Trans-fatty acids of unsaturated lipids are not natural lipid isomers and can be induced from cis isomers in several ways: on high temperatures, by some bacteria or during partial hydrogenation of oil. Refined edible vegetable oils contain low quantities of *trans*-fatty acids, however heat treatments, such as the frying process (180-190 °C) have produced diverse amounts of trans fatty acids, depending of the oils used. Tocopherols are supposed to prevent, not only lipid oxidation. but also isomerisation in unsaturated fatty acids<sup>3</sup>. As β tocopherol is an intrinsic natural antioxidants in oils, several times more potent than α tocopherol, the aim of this study was to explore fatty acid composition and oxidative stability of oils from two sunflower hybrides, with enhanced concentration of oleic acid and β tocopherol, compared to comercially available refined oil, during heating at 180 °C.

# **Experimental**

Cold-pressed oils, obtained from two sunflower hybrides of "Oliva" type, designated NSH-OL2 and NSH-OL5 were produced in the "Institute of Field Vegetables and Crops", (Novi Sad, Serbia) Heating procedure was performed by incubating 120 ml of oil at 180 °C in air atmosphere. Fatty acid compositions of the oils were determined by capillary gas-chromatography (GC) with a (Shimadzy GC-9A, Japan) equiped with splitter system, an HP-88 capillary column and flame ionization detector, after methylation. Tocopherol isomers contained in oils were

analysed by HPLC (Sycam, Germany). Oxidative stability of oils was analysed by determination of peroxide value (PV),(AOCS Cd 8-53, 1996), free fatty acid content (AOCS Cd 18-90, 1996) and differential scanning calorimetry (DSC). DSC method of accelerated oil oxidation was performed under isothermal conditions with oxigen flow, as previously described<sup>4</sup> on Q 1000, TA instruments, (Delaware, USA).

### **Results and Discusion**

Oleic acid (18:1c) contents of cold-pressed oils, obtained from two sunflower hybrides, were enhanced, (Tabl. 1). compred to standard refined, linoleic type of oil. α and β tocopherol contents were 205.33 and 206.67 mg/kg in NSH-OL2 oil, respectively, and 338,00 and 217. 33 mg/kg in NSH-2075 oil, while refined oil contained \( \alpha \) to coherol, only (620.00 mg/kg). The initial peroxide values, PV were 0 mmol/l O<sub>2</sub> in both type of oleic oils, while the acid values (free fatty acid content) were 2.38, 2.99 and 0.00 in NSH-OL2, NSH-2075 and refined oil, respectively. These oils are potentially unstable, because of high free fatty acid content which could promote oxidation. DSC method has been applied, as a measure of advanced oxidation, comparable to Rancimat method (AOCS Meth. Cd12-92)<sup>4</sup>. Oleic acid content of NSH-OL2 oil, obtained by GC, (86.87%) correlates with the long OIT, oxidation induction time, obtained by DSC on 105°C (141.7') and 120 °C (65.3'). OIT of NSH-OL5 oil, with medium oleic acid content (39.35%), is very short (47.0') and (7.50'), on respective temperatures and is presumed to be of low oxidative stability. Heat treatment of oils at 180 °C revealed enhancement in oxidative parameters. PV (primary oxidation product) enhanced during first hour of heating and then decreased after 4 h, in all oils tested. Further enhancement in PV was observed after 24 and 48 h. NSH-OL2, with the lowest content of linoleic acid (18:2cc), was the most stable, Fig.1A.. Hydrolysis of cold-pressed oils, started after 1 h of heating, while refined oil, with 0.00 initial acid value, was stable for 4h, Fig.1B.

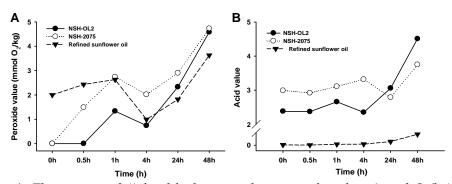


**Fig. 1.** The amount of A) lipid hydroperoxides, peroxide value, (mmol  $O_2$ /kg) and B) free fatty acids, acid value, produced when cold-pressed higholeic oils: NSH-OL2 and NSN-OL5 and refined sunflower oil were incubated at  $180^{\circ}$ C.

GC analysis of oils, heated at 180°C, revealed changes in fatty acid composition, due to oxidation and degradation of 18:2cc and formation of volatile products and, consequently, relative increase in saturated fatty acids and 18:1c. Heating induced *cis* to *trans* isomerisation of 18:1c and 18:2cc in both types of cold-pressed oils, and 18:1c to 18:1t in refined oil, while *trans* and conjugated 18:2 already existed in refined oil, before heating, as previously desribed<sup>3</sup>.

**Table 1.** Fatty acid composition (%) of cold pressed and refined sunflower oils

incubated at 180°C. Abreviations: c, cis; t, trans; cc, con., cis/trans

Time	16:0	18:0	18:1 t	18:1 c	18:2 tt	18:2 cc	18:3 ccc	18:2 con.
NCH OL 2 cold grossed highestein growflower oil								
NSH-OL2 cold-pressed higholeic sunflower oil								
0 h	3.28	3.26	0.00	86.87	0.00	6.02	0.00	0.00
0.5 h	3.24	3.33	0.00	86.80	0.00	6.11	0.00	0.00
1 h	3.26	3.17	0.00	86.18	0.00	6.36	0.00	0.00
4 h	3.27	3.27	0.00	86.90	0.09	5.94	0.00	0.00
24 h	4.14	4.04	0.00	87.77	0.35	2.93	0.00	0.00
48 h	5.90	5.80	1.69	84.28	0.53	0.72	0.00	0.00
		N	SH-2075 c	old-presse	d higholeic	sunflower	oil	
0 h	5.33	3.68	0.00	39.35	0.00	51.15	0.27	0.00
0.5 h	5.44	3.78	0.00	39.30	0.00	51.13	0.35	0.00
1 h	5.28	3.79	0.00	39.38	0.00	50.97	0.23	0.11
4 h	5.38	3.84	0.00	39.84	0.13	50.20	0.27	0.12
24 h	7.41	5.12	0.19	46.88	0.20	39.62	0.33	0.11
48 h	10.63	7.23	0.50	55.61	0.42	24.63	0.69	0.05
Refined sunflower oil								
0 h	6.81	3.90	0.00	24.26	0.32	63.94	0.26	0.13
0.5 h	6.78	3.87	0.00	24.18	0.33	64.31	0.26	0.09
1 h	6.81	3.88	0.00	24.42	0.41	63.99	0.23	0.09
4 h	6.97	3.89	0.00	24.49	0.35	63.79	0.24	0.08
24 h	7.23	4.22	0.10	25.75	0.48	61.55	0.27	0.07
48 h	8.90	4.84	0.26	28.16	0.80	56.20	0.32	0.20

## Conclusion

Cold-pressed sunflower oil, with high oleic to linoleic acid ratio, after 48 h incubation at 180°C, revaled enhanced oxidative stability compared to medium oleic and refined linoleic type of oil. Heating induced *cis* to *trans* isomerisation of oleic and linoleic acids in both types of cold-pressed higholeic oils, while *trans* and conjugated isomers of oleic acid preexisted in refined sunflower oil.

- [1] J. P. Hazebroek, Progress in Lipid Research, 2004, 39, 477-506.
- [2] G.V., Mann, The Lancet, 1994, 343, 1268-1271.
- [3] W.Tsuzuki, R. Nagata, R.Yunoki, M. Nakajima, T. Nagata, Food Chemistry, 2008, 108, 75-80
- [4] J., Velasco, M. L., Andersen, L.H., Skibsted, Food Chemistry, 2004, 85 623-625.

## HPLC ANALYSIS OF ANTHRAQUINONE COMPOUNDS IN SOME LICHENS

N. Manojlović<sup>1</sup> and Z. Marković<sup>2</sup>

<sup>1</sup>Department of Pharmacy, Medical Faculty, University of Kragujevac, S. Markovića 69, 34000 Kragujevac, Serbia, e-mail: ntm@kg.ac.yu

<sup>2</sup>Faculty of Agronomy, University of Kragujevac, Čačak 32000, Serbia

#### **Abstract**

A High-performance liquid chromatographic (HPLC) method has been developed for the characterization of some anthraquinone metabolites in extracts of the lichens *Xanthoria parietina* and *Laurera benguelensis*. With this method four anthraquinones 1,8-dihydroxy-3-methoxy-6-methylanthraquinone, 1,8-dihydroxy-3-formyl-6-methoxyanthraquinone 1,8-dihydroxy-3-hydroxymethyl-6-methoxyanthraquinone and 1,3,8-trihyroxy-6-methylanthraquinone can be analyzed. These derivatives could be used as new antioxidants and food additives because natural antioxidants are mainly not danger for healt humans and animals. Components of lichen were detected by characteristic ultraviolet spectra and relative retention times for the first time. Importance of this research is in recognizing some new source (lichen and its extacts) as a natural emplacement of antioxidants because oxidation with free radicals or autooxidation is big problem for preservation of food products.

#### Introduction

Oxidation with free radicals or auto oxidation is a big problem for preservation of food products [1]. Presence of natural antioxidants in food products is very important for their stable duration, because they are natural additives. The natural antioxidants as food additives are mainly not dangerous for health of humans and animals. They are also used in pharmacy, agriculture and plant protection. Importance of this research is in recognizing of some plants (their extracts) as natural emplacement of antioxidants.

The secondary lichen metabolites show a wide range of potentially useful biological activities [2-3]. Most lichen substances with antibiotic activity are phenolic metabolites (e.g. usnic acid and the anthraquinone, endocrocin) [4].

Anthraquinones are ingredient in many medicines of plant origin since they possess anti-bacterial, anti-inflammatory, anti-tumor, purgative, astringent, anti-viral [5] and antifungal properties [6-7].

Lichens produce some characteristic anthraquinone derivatives, which have yet to be found in higher plants [8-11]. Anthraquinones are widely distributed in lichens of the genera *Xanthoria*, *Teloschistes* and *Caloplaca* of the family Teloschistaceae [12-13]. Until now, only 1,5,8-trihydroxy-6-methoxy-3-methyl-anthraquinone, has been found in the other species of the genus *Laurera* [14] Emodin and parietin have also been reported from some other lichens (Teloschistaceae) [15] and high plant families [16-17].

## **Materials and Methods**

## Lichen species studied

*Xanthoria parietina* belongs to the family *Teloschistaceae* and could be found in Serbia. This lichen was collected near Kragujevac during September 2007 and identified by Prof. Dr. Nedeljko Manojlovic. *Laurera benguelensis* (Mull. Arg.) Zahlbr. belongs to the family *Trypetheliaceae* which is distributed in tropical region [18]. Lichen material was collected from Ratchaburi province, Thailand during July 2006 and identified by Prof. Dr. Boonpagob, Faculty

of Science, Ramkhamhaeng University, Bangkok, Thailand. A voucher specimen (No RU-22120) has been maintained at the Lichen herbarium of the Ramkhamhaeng University, Thailand.

## Identification of anthraquinones by High-performance liquid chromatography

The lichens *Xanthoria parietina* and *Laurera benguelensis* were extracted in benzene by Soxhlet extractor. High-performance liquid chromatography (HPLC) analysis carried out on WATERS HPLC instrument with: WATERS 717 Plus Autosampler, C18 column, 1525 Binary HPLC Pump, 2478 Dual  $\lambda$  Absorbance UV Spectophotometric detector with solvent methanol—water—phosphoric acid 80:20:0.9, v/v/v). Anthraquinones analysed in this research are: 1,8-dihydroxy-3-methoxy-6-methylanthraquinone, 1,8-dihydroxy-3-hydroxymethyl-6-methoxyanthraquinone 1,8-dihydroxy-3-formyl-6-methoxyanthraquinone and 1,3,8-trihyroxy-6-methylanthraquinone. Anthraquinones were identified by their UV-VIS spectra and retention time, by comparison with authentic substances made to standard concentration.

#### **Results and Discussion**

In our present study, 1,8-dihydroxy-3-methoxy-6-methylanthraquinone, 1,8-dihydroxy-3-hydroxymethyl-6-methoxyanthraquinone, 1,8-dihydroxy-3-formyl-6-methoxyanthraquinone and 1,3,8-trihyroxy-6-methylanthraquinone were identified in the lichens *Xanthoria parietina* and *Laurera benguelensis*. Phytochemistry of *Laurera benguelensis* was worked for the first time. Physcion (retention time = 3.224 min) was dominant anthraquinone in both extracts examined. In addition quantitative analysis were also determined. Content of the physcion in *Xanthoria parietina* and *Laurera benguelensis* was 357.8 and 463.2 μg per 1g of extract, respectively. Other anthraquinones were present in a smaller amount (from 3.4 to 44.6 μg per 1g of extract for *Laurera benguelensis* and from 2.3 to 33.6 μg per 1g of extract for *Xanthoria parietina*).

Figure 1 and Figure 2 are shown structures of anthraquinone analysed and HPLC chromatogram of benzene extract investigated, respectively. 1,8-dihydroxy-3-methoxy-6-methyl-anthraquinone (physcion) is orange crystal substance with good solubility in chloroform. It is used in medicine and phytopharmacy. It possess some biological activity including antifungal properties. In the nature it can be found in plants belong to *Rhamnus* and *Rheum*, some lichen belong to the family *Teloschistaceae*. For standard solution of physcion we used 0.15 mg crystal physcion and 3 ml methanol and recorded chromatogram compared with the chromatogram of extract. 1,3,8-trihydroxy-6-methylanthraquinone (emodin) is light-orange crystal substance with good solubility in methanol. Emodin is biological active substance and ingredient of some pharmaceutical drugs. Emodin can be found in nature in plants: *Rheum*, *Rhamnus*, some fungi and some lichens belong to the family *Teloschistaceae*. For standard

**Fig. 1.** The structures of the detected anthraquinone derivatives

solution of emodin we used 0.6 mg crystal emodin and 3 ml of methanol and obtained chromatogram compared with chromatogram of the extract. 1,8-

dihydroxy-3-formyl-6-methoxyanthraquinone (fallacinal) is orange needles which has been found mainly in some lichen which belong to the family *Teloschistaceae* (*Caloplaca, Xanthoria* and *Teloschistes*). For standard solution of this antioxidant we used 1.7 mg crystal fallacinal and 3 ml methanol.

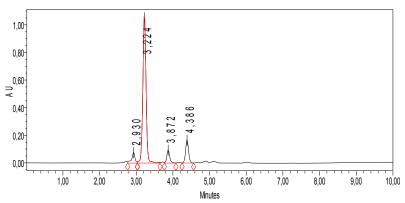


Fig. 2. High-performance liquid chromatogram of Xanthoria parietina extract

#### Conclusion

Lichens produce a number of secondary metabolites many of which are phenolic compounds. The role of phenolic compounds as scavengers of free radical is emphasized in several reports. On the basis of the results it is suggested that the extracts of the lichens *Xanthoria parietina* and *Laurera benguelensis* could be of use as an accessible source of natural anthraquinones for the possible food supplement and in the pharmaceutical industry. Further work could be done on the isolation and purification of the active component from the crude extracts of the lichen described. Importance of this research is in recognizing some new source (lichen and its extacts) as a natural emplacement of antioxidants because oxidation with free radicals or autooxidation is big problem for preservation of food products.

**Acknowledgements** The authors acknowledge financial support by the Ministry of Science of the Republic of Serbia (Grant No. 142025) and Medical Faculty University of Kragujevac, Serbia (Grant No. 01-1362).

- [1] Ames, B.N., Shigenaga, M.K., Hagen, T.M. Proceedings of the National Academy of Sciences of the Unit. 1993. 90, 7915.
- [2] Yamamoto, Y., Kinoshita, Y., Matsubara, H., Kinoshita, K., Koyama, K., Takahashi, K., Kurokawa, T., Yoshimura, I., Rec. Res. Phytochem. 1998, 2, 23.
- [3] Shahi, S.K., Shukla, A.C., Dikshit, A., Uperti, D.K., Lichenologist 2001, 33, 177.
- [4] Hale, M.E., The Biology of Lichens, 4th ed. Edward Arnold, London (1983).
- [5] Muzychkina, R.A., Natural anthraquinones, Biological and Physicochemical Properties. House Phasis, Moscow. (1998).
- [6] Agarwal, K.S., Sudhik, S., Singh, Verma, S., Kumar, S., J. Ethnoph. 2000, 72, 43.
- [7] Manojlovic, T.N., Solujic, S., Sukdolak, S., Lichenologist 2002, 34, 83.
- [8] Santesson, J., Phytochem. 1970, 9, 2149.
- [9] Nakano, H., Komiya, T., Shibata, S., Phytochem. 1972, 11, 3505.
- [10] SØchting, U., Bibl. Lichen. 1997, 68, 135.
- [11] SØchting, U., Bibl. Lichen. 2001, 78, 395.
- [12] Manojlovic N.T., Solujic, S., Sukdolak, S., Krstic, LJ., J Serb Chem Soc 1998, 63, 7.
- [13] Manojlovic T.N., Solujic, S., Sukdolak, S., Milošev, M., Fitoterapia 2005, 76, 244.
- [14] Stensio, K.E., Wachtmeister, C.A., Acta Chem Scand 1968, 23, 144.
- [15] Elix, J.A., 1996. Biochemistry and secondary metabolites. In: Nash III, T.H. (Ed.),
- [16] Barbosa, G.F., Maria da Conceição F. de Oliveira, Braz-Filho, R., S. R. Edilberto, 2004,
- [17] França C.V., M. de Fátima Agra, Barbosa-Filho, M. J., da-Cunha E. V. L., da-Silva S. M. Biochem Sys Ecol, 2003, 31, 1341
- [18] Vongkolsuk, K., McCarthy, P.M., Mongkolsuk, P., Boonpagob, K., Mycotaxon 1999, 70, 227.

## BIOINFORMATICS ANALYSUS OF SARS CoV S PROTEIN

S. Ranisavljević<sup>1</sup>, S. Tadić<sup>1</sup>, N. Tošić<sup>1</sup>, G. Pavlović-Lažetić<sup>1</sup>, N. Mitić<sup>1</sup>, M. Pavlović<sup>2</sup> and S.Ž. Gorjanović<sup>2</sup>

<sup>1</sup>Faculty of Mathematics, University of Belgrade, Belgrade, Serbia <sup>2</sup>Institute of General and Physical Chemistry, Belgrade, Serbia

## **Abstract**

Bioinformatic study of SARS-CoV S protein for 148 fully sequenced isolates was performed, including different aspects of genome polymorphism (i.e. single nucleotide polymorphisms - SNP), amino acids properties changes.

### Introduction

Severe acute respiratory syndrome (SARS) is a respiratory disease in humans caused by the SARS coronavirus (CoV). The SARS CoV genome is approximately 30 Kb positive single strand RNA that corresponds to polycistronic mRNA, consisting of 5- and 3- untranslated regions, up to 15 open reading frames (ORFs) and about 10 intergenic regions. Spike (S) protein is of special interest because of its role in viral attachment and host range determination. It is coded by ORF 2 and consists of 1255 amino acids (aa), with at least three domains: external (aa 1-1196), that includes signal peptide (aa 1-14), receptor binding domain (RBD, aa 270-625) and several experimentally determined epitope sites, transmembrane (aa 1196-1218), and internal (aa1218-1255) domains (Fig. 1. B.) [1, 2].

In this work we performed bioinformatics study (i.e. single nucleotide polymorphisms - SNPs, amino acids properties changes etc.) of SARS-CoV S protein for 148 fully sequenced isolates.

## **Experimental**

Nucleotide sequences of 148 SARS-CoVs and S proteins were taken from PubMed NCBI Entrez [3] database in GenBank and Fasta format. We located start and end of S protein in sequences in which it has not been annotated with ORF finder tool [4]. With use of Extracseq and Transseq programs from EMBOSS [5] package we extracted S protein nucleotide sequences and translated them to aa sequences. All 148 nucleotide and aa sequences have been aligned with ClustalW program [6]. Statistic was generated using Biom [7], software which we originally developed using Java programming language, which determines all statistics represented in this paper.

## **Results and Discussion**

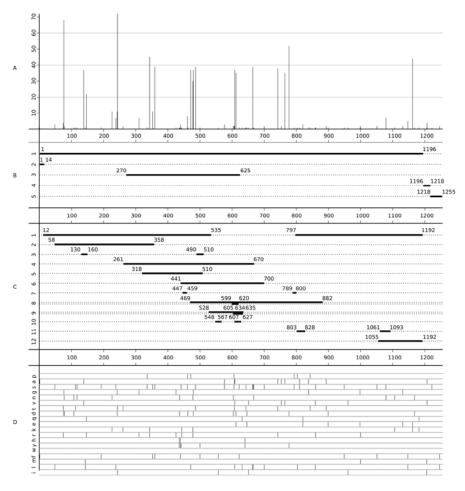


Fig. 1.

Position of aa changes and their number relatively to average "profile" isolate S protein (for all of 148 SARS CoV isolates) are shown in Fig. 1. A. S protein domains (Fig 1. B) and experimentally determinated epitopes from ref. [1] are shown on Fig. 1. C, while positions of all determinate aa changes relatively to each other are revealed at Fig 1. D.

**Coding sequence analysis.** In all of 148 S protein gene sequences, there is 119 SNPs positions. There is totally 1146 SNPs, 856 and 290 of which are transitions and transversions, respectively. Most common nucleotide substitution is  $T \rightarrow C$  which happened 284 times favoured by the preceding T (125 times) and the followed by T (151 times). A $\rightarrow$ G nucleotide substitution happened 271 times favoured by the preceding A and following A (124 times and 145 times, respectively). Nucleotide substitution A $\rightarrow$ T happened only 2 times favoured by the pre-

ceding T (one time) and following A (one time). Nucleotide substitution  $C \rightarrow A$  happened 6 times favoured by the preceding A and following A (4 times and 5 times, respectively). SNPs are found on first, second and third place in codon 36, 44 and 39 times respectively. Consequently, number of silent mutations (without aa changes) is 32, number of mutations without aa properties changes is 2, and there are 85 mutations with amino acid properties changes.

**Protein sequence analysis.** Changes in S protein external domain are of specific importance, since it correlates with altered pathogenesis, virulence and may be important for vaccine design [1, 2]. Total number of an substitutions in external domain is 83, where 82 substitutions have an properties changed in respect to profile sequence and may led to different structural forms of S protein. There are 26 an substitutions in RBD (all having change of an properties) in 65 isolates. These changes may lead to wider range of cellular receptors for viral binding. Since experimentally determined epitopes overlap almost whole external domain, (including RBD), all of these changes are significant for future vaccine development [1, 2].

## Conclusion

There are 83 as changes in 148 fully (up to now) sequenced isolates. Most of them (82) have changed as properties that may lead to wider range of cellular receptors for viral binding and also may be important in production of protective agents against SARS CoV.

## Acknowelagement

This study is undergraduate students exercise in Bioinformatics, under guidance of Dr M. V. Beljanski and is supported by Ministry of Science, Republic of Serbia, Project No. 144030.

- [1] G. M. Pavlović-Lažetić, N. S. Mitić, A. M. Tomović, M. D. Pavlović, M. V. Beljanski, Geno. Prot. Bioinfo., 2005, **3**, 18-34.
- [2] C. R. Astell, R. A. Holt, S. J. M. Jones, M. A. Marra, in: Coronaviruses with Special Emphasis on First Insights Concerning SARS, A. Schmidt, M.H. Wolff and O. Weber (Eds.), Birkhäuser Verlag, Basel, 2005
- [3] http://www.ncbi.nlm.nih.gov/entrez
- [4] http://www.ncbi.nlm.nih.gov/gorf/gorf.html
- [5] http://emboss.sourceforge.net/
- [6] http://www.ebi.ac.uk/clustalw
- [7] http://biom.sourceforge.net/

## BIOINFORMATIC ANALYSIS OF SARS CORONAVIRUS M-PROTEIN

LJ. Nikolić\*<sup>1</sup>, LJ. Martać<sup>1</sup>, M. Stanić<sup>2</sup>, D. Bataveljić<sup>2</sup> and S. Gorjanović<sup>3</sup>

<sup>1</sup>Institute for biological research "Siniša Stanković", University of Belgrade, Belgrade, Serbia

<sup>2</sup>Faculty of Biology, University of Belgrade, Belgrade, Serbia

<sup>3</sup>Institute of General and Physical Chemistry, Belgrade, Belgrade, Serbia.

\*Corresponding author: LJ. Nikolic, ljnikolic@ibiss.bg.ac.yu

#### **Abstract**

Bioinformatic study of SARS-CoV M protein amino acid properties changes was performed for 140 fully sequenced isolates. Changes which could have influence on viral gene expression and be of importance in immune response reactions were noted and further analyzed.

#### Introduction

SARS coronavirus is known as an etiological agent in patients with acute respiratory syndrome. SARS coronavirus is a large enveloped, RNA virus. The SARS coronavirus genome consists of approximately 30 Kb positive single strand RNA with 13-15 open reading frames and about 10 intragenic regions. The structural glycoproteins are S-surface spike, M-matrix, E-envelope and N-nucleocapsid. M-protein is a transmembrane protein probably involved in virus assembly, and there is evidence that it also might have a role in immunity induction [1]. Therefore it is target for anti-SARS coronavirus drug research. M-protein is determined by 663 nucleotides coding for 221 amino acids (aa), which form outer N terminus, 3 transmembrane domains, one inner and one outer loop and long inner C terminus. The aim of this study was to investigate amino acid sequences of SARS coronavirus M-protein.

## **Experimental**

Amino acid sequences of 140 isolates of SARS coronavirus M protein were taken from the PubMed NCBI Entrez database [2]. As sequences have been aligned with CLUSTAL W program [3]. Evaluation of as properties was made using Venn diagram and Kyte and Doolittle hidropathy index [4]. Disprot program [5] was used for prediction of protein disorder domains. Peptide binding afinity was assessed by Multipred program and Kyte-Doolittle hydropathy plot for evaluation of changes in hydropathy score between most common isolates and mutant isolates [6, 7].

#### **Results and Discussion**

Compared to most common isolates ("profile") we found 13 different as substitutions in 140 isolates: 6 in transmembrane domain, and 7 in extramembrane domain (Table 1.). 13 isolates had substitutions on position 5 ( $G\rightarrow S$ ), 2 on position 11 ( $E\rightarrow K$ ), 28 on position 27 ( $F\rightarrow C$ ), 2 on position 38 ( $Y\rightarrow H$ ), 6 on position 67

 $(A \rightarrow V)$ , 1 on position 72  $(N \rightarrow T)$ , 1 on position 81  $(I \rightarrow T)$ , 1 on position 92  $(W \rightarrow R)$ , 1 on position 99  $(F \rightarrow L)$ , 1 on position 113  $(P \rightarrow S)$ , 2 on position 119  $(L \rightarrow P)$ , 1 on position 154  $(S \rightarrow P)$  and 1 on position 210  $(A \rightarrow V)$ . There were no overlapping substitutions except for isolate AY613947 where we found two substitutions on positions 81 and 92. In 7 substitutions, as properties were changed (as positions 5, 11, 27, 72, 92, 113 and 154) which could lead to changes in molecular structure of the protein.

Table 1. Amino acid changes and hydropathy index; hphob-hydrophobic,	hphyl-
hydrophylic, p-polar, s-small, t-tiny, ar-aromatic, al-aliphatic	

Domain	Position	Change	Туре		hydropathy Kyte Doolitle/Charge			tle/Charge	
ext N term	5	G→S	hphob, p, t	$\rightarrow$	hphyl, p, t	-0.4	neutral	-0.8	neutral
ext N term	11	E→K	hphyl, p	$\rightarrow$	hphob, p	-3.5	negative	-3.9	positive
l transm	27	F→C	hphob, ar	$\rightarrow$	hphob, s	2.8	neutral	2.5	neutral
I transm C term	38	Y→H	hphob, p, ar	$\rightarrow$	hphob, p, ar	-3.1	neutral	-3.2	positive
II transm	67	$A \rightarrow V$	hphob, t	$\rightarrow$	hphob, s, al	1.8	neutral	4.2	neutral
ext N term	72	N→T	hphyl, p, s	$\rightarrow$	hphob, s	-3.5	neutral	-0.7	neutral
III transm	81	l→T	hphob, al	$\rightarrow$	hphob, s	4.5	neutral	-0.7	neutral
III transm	92	W→R	hphob, p, ar	$\rightarrow$	hphyl, p	-0.9	neutral	-4.5	positive
III transm C term	99	F→L	hphob, ar	$\rightarrow$	hphob, al	2.8	neutral	3.8	neutral
int C term	113	P→S	hphob, s	$\rightarrow$	hphyl, p, t	-1.6	neutral	-0.8	neutral
int C term	119	L→P	hphob, al	$\rightarrow$	hphob, s	3.8	neutral	-1.6	neutral
int C term	154	S→P	hphyl, p, t	$\rightarrow$	hphob, s	-0.8	neutral	-1.6	neutral
int C term	210	$A \rightarrow V$	hphob, t	$\rightarrow$	hphob, s, al	1.8	neutral	4.2	neutral

Analysis of aa substitutions and their properties shows that some of them might have effect on protein structure and stability. Kyte-Doolittle Hydropathy plot [4] was used to identify the posible position of transmembrane domains. In all isolates 3 transmembrane domains were found, except in isolate AY613950 which has two mutations in third transmembrane region on positions  $81(I \rightarrow T)$  and  $92(W \rightarrow R)$ . These mutations led to change in amino acid charge which might cause loss of transmembrane region stability. Changes in  $1^{st}$  (aa 27 and 38) and  $2^{nd}$  (aa 67) transmembrane regions acording to Kyte-Doolittle Hydropathy plot have no significant effect on M protein structure.

Changes in C terminus show the least change in hydropathy index and this region is conservative. Changes in C terminus,  $119(L\rightarrow P)$  and  $154(S\rightarrow P)$ , because of P rigide form, destabilize any possible formation of  $\alpha$ -helix.

Many disordered proteins have binding properties. It was proposed that disordered regions flexibility facilitates different conformational requirements for binding [8]. Disprot analysis shows that regions between aa 1-7 and 211-221 might be disordered. Isolate AY559096 has substitution on position 210 ( $A\rightarrow V$ ) due to which disordered region is shorter (216-221). This might have effect on protein function. Hydropathy plot analysis indicated that one region (aa 150–210) on the cytoplasmic domain is fairly hydrophilic, suggesting its involvement in antigenicity. Based on the fact that cytoplasmic domain of the M protein of some

other coronavirus could induce protective activities against virus infection, this region might be one potential target for SARS vaccine development [9].

External N terminus is responsible for immune response of M protein [1]. Using Multipred program for prediction of peptide binding affinity, several antigen regions from  $1^{st}$  to  $16^{th}$  aa were tested and identified as putative immunological hotspots. Multipred analysis of 13 isolates with substitutions on position 5 (G $\rightarrow$ S) and 2 isolates on position 11 (E $\rightarrow$ K) reveals that these substitutions do not have significant effect on immunoreactivity of this region.

#### Conclusion

Variability of SARS coronavirus M protein was analyzed. Amino acid variability may have different effects on M protein stability. Substitutions at positions  $5(G \rightarrow S)$  and  $11(E \rightarrow K)$  reveal changes in an properties (Tab.1), suggesting their involvement in immunoreactivity. Even tough  $F \rightarrow C$  substitution does not change significantly hidropathy index , its effect on transmembrane region stability cannot be excluded. These findings could be of importance in predicting immune response modifications and might be helpful in producing a protective agent against SARS coronavirus.

## Acknowelagement

This study is PhD students exercise in Bioinformatics under guidance of Dr M. V. Beljanski and is supported by Ministry of Science of Republic of Serbia, Project No. 144030.

- [1] C. Qian, D. Qin, Q. Tang, Y. Zeng, G. Tang, C.Lu. Identification of B-cell antigenic epitope at the N-terminus of SARS-CoV M protein and characterization of monoclonal antibody against the protein. *Virus Genes*, 2006, **33**, 147-156.
- [2] http://www.ncbi.nlm.nih.gov/entrez
- [3] www.ebi.ac.uk/clustalw
- [4] J.Kyte, R.F. Dootlittle, A simple method for displaying the hydropathic character of a protein. *J.Mol Biol.*, 1982, **157** (1), 105-32.
- [5] http://www.ist.temple.edu/disprot
- [6] <a href="http://antigen.i2r.a-star.edu.sg/multipred">http://antigen.i2r.a-star.edu.sg/multipred</a>
- [7] http://gcat.davidson.ed/rakarnik/kd.cgi
- [8] H.J. Dyson and P.E. Wright, Intrinsically unstructured proteins and their functions. *Nature Reviews Molecular Cell Biology*, 2005, **6**, 197-208.
- [9] W. Liu, Y. Lu, Y. Chen, Bioinformatics analysis of SARS-Cov M protein provides information for vaccine development. *Progress in Natural Science*, 2003, 13, 844-847.

## PRODUCTION OF FREE RADICALS IN AQUEOUS SOLUTIONS BY PHOTO-EXCITED URANYL ION

M. Daković, M. Mojović, D. Milosavljević and G. Bačić

Faculty of Physical Chemistry. University of Belgrade,, Studentski trg 12-16, Belgrade, Serbia

## Abstract

Photo-excited uranyl ion is extremely reactive specie and it participates in various chemical reactions. Reactions which include free radical production were investigated using EPR spin trap methods. Production of OH radicals in reactions with excited uranyl ion showed complex dependence on uranyl concentration and speciation in aqueous solutions. The intensity of EPR signal of DEPMPO/OH adducts decreases upon addition of strong complex agents, which can be explained by involvement of OH ions from coordination sphere of uranyl.

## Introduction

In its excited state uranyl ion is extremely reactive specie. It participates in various reactions with both organic [1] and inorganic [2] compounds. However, little attention has been paid on the processes of free radicals production in aqueous solutions by excited UO<sub>2</sub><sup>2+</sup> ion. Uranyl ion in aqueous media forms several complexes with hydroxyl ions, which is strongly affected by pH of the solution [3]. Under such conditions, one can expect alteration of energy and structure of uranyl ions excited electronic states. These changes could influence kinetics and yield of reactions with water molecules. The purpose of this work is to investigate, using EPR spin trap methods, the influence of pH variation and presence of complexing agents on processes of free radical forming in reactions with excited uranyl ion.

#### **Matherials and Methods**

Solutions of  $UO_2(CH_3COOH)_2 \cdot 2H_2O$  and  $UO_2(NO3)_2 \cdot 6H_2O$  were prepared by dissolving of analytical grade chemicals (Merck, Germany) in deionized water (MiliQ). pH values of solutions were adjusted by adding of 0.1 M HCl and 0.1 M NaOH and controlled by pH-meter. Spin trapping agent was DEPMPO (5-(Diethoxyphosphoryl)-5-methyl-1-pyrroline-N-oxide) (Alexis, USA). Solutions together with spin trap were placed in quartz quivetes and irradiated in home-made UV reactor at the wavelength of  $300 \pm 30$  nm. Following irradiation solutions were transferred in teflon tubes and trapped radicals were measured using VARIAN E104-A X-band EPR spectrometer (modulation amplitude 2 G, power 10 mW). Processing of spectra was performed by Origin<sup>TM</sup> v 7.5 software using window average smoothing. Intensity of DEPMPO/OH peak in adduct spectra was measured as peak to peak height. Dependence of uranium speciation on pH in water solutions was calculated by Phreege v 2.13 software (USGSC).

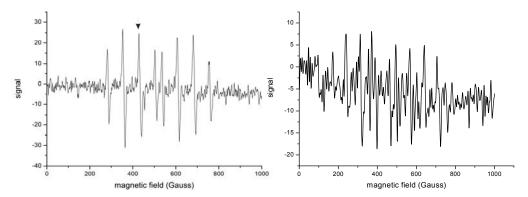


**Fig. 1.** EPR spectra of DEPMPO/OH adduct after UV irradiation of 30 ppm uranium solution at pH = 2. The arrow shows the peak used to measure the amount of OH radicals

**Fig. 2.** EPR spectra of DEPMPO/OH adduct after UV irradiation of solution of uranyl acetate in 0.01 M sodium citrate

## **Results and Disscusion**

Figure 1 represents the typical EPR spectrum of DEPMPO/OH adducts used for determining the amount of radicals obtained in the system. The pH dependence of EPR signal intensity of DEPMPO spectra is shown in Fig. 3. At values bellow pH = 6 signal intensity diagram follows contour of UO<sub>2</sub><sup>2+</sup>in speciation graph (figure 4),

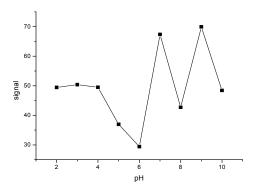


**Fig. 3.** EPR signal height of DEP-MPO/OH adduct (see Fig. 1) at different pH values.

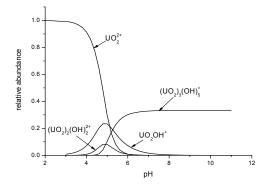


**Fig. 4.** Uranyl species distribution in aqueous solution of uranyl acetate at different pH values.

which implies that the main contribution in OH radicals forming comes from excited  $UO_2^{2+}$  and perhaps other uranyl species. Situation becomes more complicated as pH rises since more species appear in solution, which should have different

characteristics of excited state (energies and lifetimes). As speciation diagram shows prevailing specie in region beyond pH = 6 becomes  $(UO_2)_3(OH)_5^+$ ; however, pH profile of EPR signal intensity of adduct does not follow such trend, which could indicate more complex structure of excited uranyl states.

Figure 2 shows the EPR spectra of adduct in solution which, besides of uranium, contains 0.01 M of sodium citrate. Citrate is a strong tridentate complexing agent and its complex with uranyl ion has a high stability constant ( $10^{12}$  [5]). Signal of /OH adduct is significantly lower than that of pure uranyl acetate solution. Changes in ligand field of  $UO_2^{2+}$  ion should affect energy and lifetime of its excited state and have impact on reaction with molecules of solvent. Uranium concentration dependence of DEPMPO/OH adduct signal (measured at pH = 7), for both uranyl acetate and uranyl nitrate, was found quite complex (data not shown). This is probably because uranyl in different excited states participates in reactions with water molecules.

## **Conclusions**

Production of OH radicals in reactions with excited uranyl ion showed dependence on uranyl speciation in aqueous solutions. Complex behavior of signal under variation of pH can be explained by variety of uranyl excited states in different forms of  $UO_2^{2+}$  complexes with hydroxyl ions.

- [1] M. Sarakha et al, J. Photochem. Photobiol. A, 1997, 107 (1-3), 101-106.
- [2] J.Wheeler, J. K. Thomas, J. Phys. Chem. 1984, 88, 750-754
- [3] G. Meinrath et al, J. Radioanal. Nucl. Chem. 1993, 74, 299
- [4] C. Moulin and P. Decambox, Anal. Chem. 1995, 67, 348-353
- [5] CRC Handbook of Chemistry and Physics, CRC Press, 2006.

# CORTICOSTERONE LEVEL ALTERS OPTIMAL HEAT SHOCK PROTEIN 90/GLUCOCORTICOID RECEPTOR RATIO IN HIPPOCAMPUS OF STRESSED RATS

A. Đorđević, M. Adžić, J. Đorđević and M.B. Radojčić VINCA Institute of Nuclear Sciences P.O. Box 522, 11001 Belgrade, Serbia

## **Abstract**

Hippocampus (HIPPO) is one of the key brain structures, rich in glucocorticoid receptor (GR), a transcriptional factor involved in negative feedback of hypothalamic-pituitary-adrenal (HPA) axis in response to stress. Heat shock proteins accompany GR maintaining its optimal conformation, ligand binding ability and translocation to the nucleus. In order to evaluate the expression of GR, Hsp90 and their ratio we exploited three diverse types of stress (acute immobilization, chronic isolation and combination of the two). Our results indicated the same pattern of expression and compartmental distribution for both proteins, as well as for their ratio, under acute and combined stress when the level of corticosterone (CORT) was high. On the contrary, when CORT was low, such as in chronic stress, Hsp90/GR ratio exhibited opposite pattern of expression and GR was not translocated to the nucleus.

#### Introduction

The hypothalamic-pituitary-adrenal (HPA) axis plays a primary physiological role in response to stress. One of the key brain structures that regulates HPA axis is the hippocampus (HIPPO), a part of the brain "limbic system", abundant with glucocorticoid receptor (GR) [1]. GR is a hormone dependent transcriptional factor which mediates final effects of glucocorticoids. Under no stress conditions, GR is primarily located in the cytoplasm where it is associated with different heat shock proteins (HSPs) including Hsp90 [2]. Hsp90 predominantly resides in cytoplasm maintaining optimal GR conformation for ligand binding. After hormone binding, Hsp90 dissociates from the receptor, enabling its translocation to the nucleus. Nuclear GR regulates stress responsive genes and activity of HPA axis [3]. Moreover, Hsp90 is also found in the nucleus, alone, or in association with GR, where it may be involved in negative regulation of GR activity through removing receptor from its responsive elements [4]. Considering that fact, disrupted nuclear Hsp90/GR ratio or elevated nuclear Hsp90 level may be implicated in GR inactivation. Given the essential role of Hsp90 in GR translocation the aim of this work was to obtain information about GR and HSPs co-expression levels in the cytoplasm and nucleus of animals subjected to diverse types of stress.

## **Experimental**

All experiments were performed on adult Wistar male rats kept according to the standards of the Ethical Committee for the Use of Laboratory Animals of the VINCA Institute. The experimental groups were: (I) control group; (II) acute immobilization, 30 min; (III) chronic isolation, 21 day; (IV) combined stress-chronic isolation for 21 day followed by 30 min immobilization. After sacrifice, blood serum was prepared and used for corticosterone determination by OCTEIA Corticosterone kit. Cytoplasmic and nuclear extracts from HIPPO were obtained by differential centrifugation. Proteins were subjected to electrophoresis and detected by Western Blot. GR M-20 antibody was used to detect GR, Hsp90 (F-8) antibodies (Santa Cruz Biotechnology) were used for detection of Hsp90. β-actin was used as a loading control.

## **Results and Discussion**

**Glucocorticoid receptor:** High corticosterone (CORT) levels found upon acute immobilization (626.94±107.08 ng/ml) or in combined stress (601.24±89.69 ng/ml) resulted in significantly reduced level of cytoplasmic and increased level of nuclear GR in hippocampus (HIPPO) (p<0.001, Figure 1a), implicating CORT dependent GR nuclear translocation. However, after chronic stress, both the cytoplasmic and nuclear levels of GR were reduced (p<0.001, Figure 1a), indicating decrease in GR expression and/or stability under low CORT conditions (64.73±28.29 ng/ml) found in prolonged isolation.

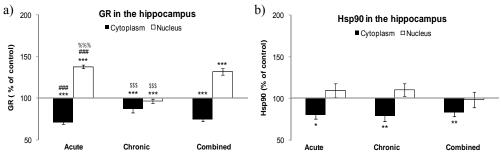
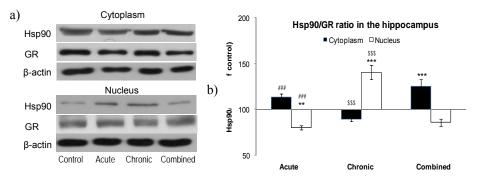


Fig. 1 Hippocampal GR (a) and Hsp90 (b) expression in cytoplasm and nucleus of rats subjected to acute, chronic and combined stress (data presented as mean± SEM, n=6)

**Heat shock protein 90:** The analysis of Hsp90 protein indicated that its pattern of expression in the cytoplasmic compartment was similar to the expression level of GR. Namely, in all three types of stress the cytoplasmic Hsp90 protein levels were decreased (p<0.05, p<0.01, respectively, Figure 1b). As it may be observed in Figure 1b, upon acute and chronic stress, Hsp90 was translocated to the nuclear compartment, judged by its nuclear increase. In case of combined stress nuclear level of Hsp90 remained unchanged.

**Hsp90/GR ratio:** Under the high serum CORT conditions Hsp90/GR ratio was elevated in cytoplasm and decreased in the nuclear compartment. Although both GR and Hsp90 were translocated to the nucleus under these conditions, it seemed that GR translocation exceeded the one of Hsp90 (Figure 2b). On the contrary, when the CORT level was low, i.e. under the chronic stress, the Hsp90/GR ratio

was changed in the opposite direction, with significant elevation in the nuclear compartment, and decrease in the cytoplasm.



**Fig. 2** Hippocampal Hsp90/GR ratio in cytoplasm and nucleus of stressed rats; (a) representative Western blots; (b) densitometric scans (data presented as mean± SEM, n=6)

#### Conclusion

The results indicated that acute and combined stress induced hippocampal GR translocation to the nucleus, whereas chronic stress resulted in altered localization of GR in this brain structure. In case of Hsp90, acute and chronic stress induced nuclear translocation and decreased its level in cytoplasmic compartment. As the optimal Hsp90/GR ratio is necessary for modulation of steroid dependent response, in case when this ratio is altered (either enhanced or diminished) steroid dependent responses may be disturbed [4]. Therefore, the pattern of changes in Hsp90/GR ratio seemed to be related to CORT level. Namely, when CORT was high the ratio of Hsp90/GR was elevated in the cytoplasm, and decreased in nucleus, while when CORT was low, the opposite pattern was found.

## Acknowledgements

The work was supported by MN project 143042B.

- [1] R.M. Sapolsky, L.C. Krey, B.S. McEwen, Endocr. Rev., 1986, 7, 284–301
- [2] W.B. Pratt, J. Biol. Chem., 1993, 268, 21455-21458
- [3] P.J. Barnes, Clin. Sci., 1998, **94**, 557-572
- [4] K.I. Kang et al., Proc. Natl. Acad. Sci. USA, 1999, 96, 1439-1444

## STRESS EFFECTS ON THE PHOSPHORYLATION OF C-JUN-N-TERMINAL KINASES AND ON NUCLEAR TRANSLOCATION OF HSP70 IN RAT HIPPOCAMPUS

M. Adžić<sup>1</sup>, A. Đorđević<sup>1</sup>, J. Đorđević<sup>1</sup>, M. Krstić-Demonacos<sup>2</sup> and M.B. Radojčić<sup>1</sup>

<sup>1</sup> VINCA Institute of Nuclear Sciences P.O. Box 522, 11001 Belgrade, Serbia <sup>2</sup> Faculty of Life Sciences, University of Manchester, Manchester, M13 9PT, England, U.K.

## Abstract

Glucocorticoids have diverse effects in cellular processes in hippocampus (HIPPO) under stress. Beside genomic pathways, their effects are also mediated by direct activation of subfamily of mitogen-activated protein kinases termed, c-Jun-N-terminal kinases (JNKs). We analysed the phosphorylation status of cytoplasmic and nuclear JNK isoforms, and expression of its inhibitor Hsp70 protein in HIPPO of rats exposed to diverse types of stress. Activity of JNK1 in cytoplasm and nucleus was decreased in all types of stress, while the activity of cytoplasmic JNK2/3 was markedly higher in acute stress, and unaltered or lowered in chronic and combined stress. Hsp70 was significantly decreased in cytoplasm and increased in nucleus under all stress conditions indicating its cytoplasmic-nuclear translocation.

## Introduction

Hippocampus (HIPPO), part of limbic brain system, has a crucial role in response to stress by mediating inhibition of the hypothalamic-pituitary-adrenal (HPA) axis [1]. Stress hormones modulate brain functions by changing the structure of neurons and thus influencing neuronal damage or suppressing neurogenesis and cell survival [2]. Except for glucocortiocoid receptors, which are the main molecular regulators of stress response, MAPKs are also sensitive to stress and activated by it [3]. The JNK family belongs to the MAPKs and it is comprised of three isoforms (JNK1, 2 and 3) which have been mainly considered as degenerative signal transducers and efficient activators of apoptosis in nervous system [4]. To prevent cellular damage, cells activate the transcription of heat shock proteins. Hsp70 mediates neuroprotection and its overexpression was shown to protect HIPPO neurons from cytotoxic effects of stress [5]. We studied how different stress types (acute, chronic or combined) alter JNKs activity, expression level of Hsp70 protein and cytoplasm-nuclear translocation of both proteins in the HIPPO of Wistar rat brain.

## **Experimental**

The adult Wistar male rats used in experiment were divided into four groups: (I) unstressed animals (controls); (II) acute immobilization, 30 min; (III) chronic isolation stress for 21 day; (IV) chronic isolation followed by 30 min immobilization. HIPPO samples were prepared by differential centrifugation and separated by SDS-electrophoresis. Western blot was performed using: anti-human JNK1/JNK2

monoclonal antibody, phospho-SAPK/JNK antibody, Hsp70 antibody and rabbit polyclonal anti- $\beta$ -actin, for detection of Hsp70 and  $\beta$ -actin, respectively.

#### **Results and Discussion**

Effect of stress on JNKs activity: We estimated JNK1 (46kDa) and JNK2/3 (54kDa) activities in the cytoplasm and nucleus of HIPPO under stress conditions by following its phosphorylation at Thr183 and Tyr185 that are crucial for their activation (Figure 1a and b). The ratio of pJNK1 to total (tJNK1) *i.e.* pJNK1/tJNK1 indicated that cytoplasmic and nuclear JNK1 phosphorylation was low in all types of stress in respect to control. Only in the case of acute stress the phosphorylation of nuclear JNK1 was not significantly changed (Figure 1b and d). In contrast, the activation of cytoplasmic JNK2/3 was markedly higher in acute stress, while it was unaltered or lowered in other types of stress (Figure 1a and c).

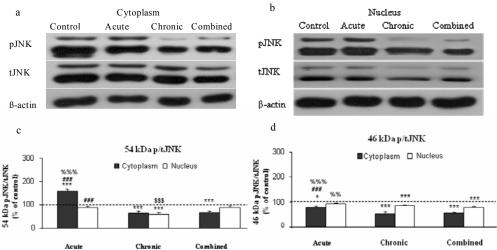
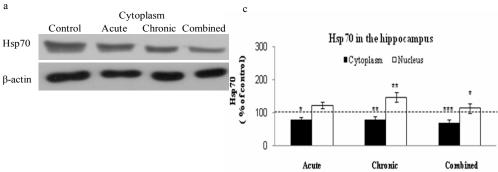


Figure 1. Western blot demonstrating the effects of acute immobilization, chronic isolation or the combined stress on the levels of JNKs (JNK1 at 46kDa and JNK2/3 at 54kDa) and their phospoisoforms in cytoplasm (a) and nucleus (b) of hippocampus. Phospo JNK immunoreactivities represented as ratio of 54kDa pJNK/tJNK (c) or 46kDa pJNK/tJNK(d). Results are presented as mean $\pm$ S.E.M (n=8) \*p<0.05, \*\*p<0.01, \*\*\*p<0.01.

**Effect of stress on the Hsp70:** In parallel with JNKs activity we investigated cytoplasmic and nuclear levels of Hsp70 in acute, chronic and combined stress. The cytoplasmic level of Hsp70 was significantly decreased under all stress conditions (Figure 2a and c). Increase in nuclear Hsp70 indicated its cytoplasmic-nuclear translocation in all types of stress, with most prominent elevation under chronic stress (Figure 2b and c).



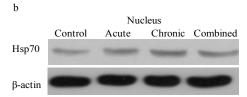


Figure 2. Western blot demonstrating the effects of acute immobilization, chronic isolation or the combined stress on the level of Hsp70 in cytoplasm (a) and nucleus (b) of hippocampus. Hsp70 immunoreactivities (c) are represented as mean $\pm$ S.E.M (n=8, \*p<0.05, \*\*p<0.01, \*\*\*p<0.001.

Overall, the decreased activity of all JNK isoforms in both cell compartments under all stress conditions could led to interruption of JNKs signaling, which may influence neurodegeneration or neural cell remodeling (neural plasticity). Nuclear translocation of Hsp70 on the other side may represent an adaptive mechanism to stress conditions by diminishing JNKs action.

## Conclusion

Since both JNK isoforms (46kDa and 54kDa) are downregulated in both cytoplasmic and nuclear compartments, and Hsp70 is simultaneously translocated to the nucleus under most of the stress conditions, the degenerative JNKs function may be influenced by Hsp70 enabling cell adaptation or remodelling particularly under severe stress conditions.

## Acknowledgements

The work was supported by MN project 143042B.

- [1] R.M. Sapolsky, L.C. Krey, B.S. McEwen, Endocr. Rev., 1986, 7, 284–301.
- [2] B. Czeh, T. Michaelis, T. Watanabe, et al. Proc Natl Acad Sci USA., 2001, 98, 12796-12801.
- [3] E. Meller, C. Shen, A. N. Talia, C. Jensen, Y. Tsimberg, J. Chen, R. J. Gruen, Brain Research, 2003, 979, 57–64
- [4] V. Waetzig, T. Herdegen, Neuroscience Letters, 2004, 361, 64–67.
- [5] N. Beaucamp, T. C. Harding, B. J. Geddes, J. Williams, and J. B. Uney, FEBS Lett. 1998, **441**, 215–219.

## ANTIOXIDANT ENZYMES EXPRESSION IN LIVER OF STRESSED WISTAR RAT

J. Đorđević, M. Adžic, A. Đorđević, A. Nićiforović and M.B. Radojčić VINČA Institute of Nuclear Science, P.O. Box 522, 11001 Belgrade, Serbia

## Abstract

The antioxidant enzymes (AOEs) expression was studied in Wistar rat liver under two types of stress: acute (immobilization) and chronic (isolation). The acute stress induced increase in blood corticosterone (CORT) and glucose (GLU), but decreased AOEs expression, and such conditions may result in oxidative stress. In contrast to acute stress, in chronic stress conditions, when both CORT and GLU were low, the AOEs expression was markedly induced. This increase in MnSOD, CuZnSOD, and catalase exhibited similar trend implying efficient detoxification of O<sub>2</sub>- and H<sub>2</sub>O<sub>2</sub>.

## Introduction

Adaptation to neuroendocrine stress involves action of glucocorticoids (GCs), the hormones of hypothalamo-pituitary-adrenal (HPA) axis, which mediate central and peripheral recovery of organism's homeostasis. The main peripheral GCs target is liver, in which GCs stimulate metabolic processes serving to increase and/or maintain normal concentrations of blood glucose, thus providing other organs with energy necessary for successful adaptation [1]. Although beneficial, the increased energy requirements are also followed by the enhanced production of potentially toxic reactive oxygen species (ROS) [2]. The cellular regulatory pathways activated by ROS involve action of antioxidant defence enzymes (AOE) that may efficiently detoxify cells from transiently elevated ROS. However, prolonged stress and constantly high (mM) concentration of ROS may compromise AOE detoxifying capacity of cells, and thus influence energy/glucose production necessary for successful cell/organism adaptation. The aim of the presented study was to characterize AOEs protein expression in Wistar rat liver under different types of stress: acute (immobilization) and chronic (social isolation). Liver enzymes: CuZnsuperoxide dismutase (CuZnSOD), Mn-superoxide dismutase (MnSOD), and catalase (CAT), were measured and their expression was correlated with the input signal of blood GCs and the resulting glucose level.

## Experimental

Wistar male rats were kept according to the standards of the Ethical Committee for the Use of Laboratory Animals of the VINCA Institute. The experimental groups were: (a) control; (b) acute immobilization, 30 min; (c) chronic isolation, 21 day. After sacrifice, blood serum was prepared by 15 min centrifugation at 3000 rpm and used for corticosterone determination by OCTEIA Corticosterone EIA kit, and

control acute chronic

glucose determination by Accutrend strips. Livers were perfused, homogenized, and lysed by ice-cold 1% Triton X-100 in 10mM TrisHCl pH 7.4, containing 0.32M sucrose and 5mM MgCl<sub>2</sub>, centrifuged at 12,000rpm for 15 min and protein concentration was determined by method of Lowry. Cell extracts were denatured in sodium dodecyl-sulphate (SDS) buffer, separated by 7.5% SDS-polyacrylamide gel electrophoresis, transferred to PVDF membranes, and probed with specific primary antibodies: anti-MnSOD, anti-CuZnSOD, anti-catalase or anti-β-actin, and secondary goat anti-rabbit IgG-HRP conjugate. Quantification of protein bands on X-ray film was performed by Image J analysis PC software. Statistical significance was determined by one-way ANOVA and Tukey's posthoc test.

## **Results and Discussion**

a)

MnSOD

Since stress-induced gluconeogenesis in liver is controlled by the level of corticosterone (CORT) and since it is reflected in the serum level of glucose (GLU), we determined these parameters in Wistar rats subjected to different stress

**Table 1** Stress effects on serum corticosterone and glucose level Results are presented as mean  $\pm$  SD (n=4), \*p<0.05, \*\*p<0.01, \*\*\*p<0.001.

Stress Parameters	Control	Acute	Chronic
Corticosterone (ng/ml)	136,80±44,51	626,94±107,08***	64,73±28,29**
Glucose (mmol/l)	5,67±0,80	8,08±0,66 ***	3,40±0,71***

chronic

control acute

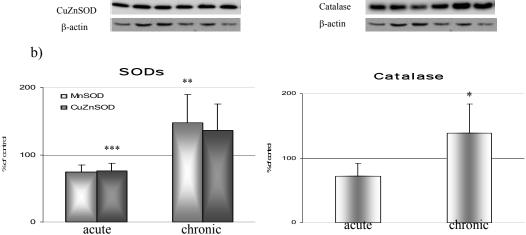


**Fig. 1** Stress effects on antioxidant enzymes expression measured by Western blot (a) and quantified by Image J analysis PC software (b). Results are presented as mean± SEM (n=4), \*p<0.05, \*\*p<0.01, \*\*\*p<0.001.

conditions. The results indicated that in acute stress when the serum CORT was high the concentration of blood GLU was also increased (Table 1). Under the chronic stress both CORT and GLU concentration were below the control level (Table 1). Quantification of protein expression of the antioxidant enzymes (AOEs): Mn-and CuZn-superoxide dismutases (MnSOD and CuZnSOD), and catalase (CAT) indicated that all three enzymes were increased in chronic stress, but unaltered or lowered in acute stress (Figure 1). It is known that CORT triggeres increase in the metabolic rate (respiration, syntesis of ATP) required for gluconeogenesis which would result in the equal increase in ROS. Discrepancy between ROS generation due to increased metabolism and decreased antioxidant capacities may result in the state of oxidative stress. Since the increased expression of AOEs is well known indicator of elevated ROS our data suggest that state of oxidative stress may also exist under low CORT conditions. The observed increase in MnSOD, CuZnSOD, and CAT in chronic stress exhibited similar trend which may imply efficient detoxification of O<sub>2</sub> and H<sub>2</sub>O<sub>2</sub> under these conditions. The apparent discrepancy between the stress intensity defined by CORT level, and oxidative stress, defined by AOEs expression, may be due to downregulation of AOEs by glucocorticoid receptor [3] or to altered activity of AOEs due to inhibitors, such as NO [4].

## Conclusion

The increase in blood glucose (GLU) due to stress-induced elevation of CORT (*i.e.* increased rate of gluconeogenesis) in rat liver is not followed by the respective increase in antioxidant enzymes (AOEs) expression. AOEs expression is markedly elevated in chronic stress, when both CORT and GLU are low. This increase in MnSOD, CuZnSOD, and catalase exhibited similar trend implying efficient detoxification of  $O_2$  and  $O_2$  and  $O_2$  and  $O_2$ .

## Acknowledgements

The work was supported by MN project 143042B.

- [1] H. DeWulf, H.G. Hers, European J. Biochem., 1967, 2, 57-60.
- [2] N.Lane, J.Theoretical Biol., 2003, 225, 531-540.
- [3] H.T. Kim, Y.H. Kim, J.W. Nam, H.J. Lee, H.M. Rho, G. Jung, Biochem. Biophys. Res. Commun. 1994, **201**, 1526–1533.
- [4] Y.S.Kim, S.Han, Biol.Chem., 2000, 381, 1269-1271.

## PROTECTION OF COPPER IONS INDUCED INHIBITION OF RAT MYOMETRIAL ecto-ATPase ACTIVITY BY EDTA

M. Milošević, S. Petrović and A. Horvat

Laboratory for Molecular Biology and Endocrinology, "Vinča" Institute of Nuclear Sciences, P.O. Box 522, 11001 Belgrade, Serbia

## Abstract

The potential protective effects of ethylenediamine tetraacetic acid (EDTA) on the CuSO<sub>4</sub> cell toxicity was examined on rat myometrial plasma membranes. Activity of plasma membrane ecto-ATPase, as modulator of purinergic signaling in the presence of increasing concentrations of copper salt and in the presence or absence of EDTA was studied. Our results show that 1mmol/l EDTA may exert protective effects on Cu<sup>2+</sup>-induced toxicity by increasing half-maximum inhibitory activities of this ion.

## Introduction

Copper is one of 26 essential trace elements, but its toxicity is also an important contributor to at least one hundred different symptoms and disease conditions. The literature data classify copper as a reproductive toxicant [1]. Effects of Cu<sup>2+</sup> ions on rat synaptic and uterine plasma membrane ecto-ATPase activity were reported previously [2, 3]. Ecto-adenosine triphosphatase (ecto-ATPase) is an integral plasma membrane glycoprotein, with large extracellular domain containing the active site. This enzyme, as a member of E-NTPDases (EC 3.6.1.5) family, hydrolyzes terminal phosphoanhydride bonds of extracellular nucleoside tri- and diphosphates in the presence of divalent cations (Ca<sup>2+</sup> or Mg<sup>2+</sup>). The reproductive organs are innervated by several groups of autonomic and sensory nerves. ATP is coreleased from nerves with neurotransmitters, but is also released from non-nerve cells. Extracellular ATP and the products of its hydrolysis (ADP, AMP, and adenosine) are involved in signaling processes by activating of P2 receptors in the myometrium [4]. High ecto-ATPase activity in myometrial tissue indicates its role in a signal termination mechanism for purinergic transmission.

The aim of this work was to investigate in *in vitro* conditions the ability of EDTA to prevent Cu<sup>2+</sup>-induced inhibition of ecto-ATPase activity.

## Experimental

Experiments were performed on 3-months-old female Wistar albino rats obtained from the local colony. Myometrial plasma membranes (MPM) were isolated as described previously [3]. Incubation medium contained (in mmol/l): 50 Tris-HCl (pH 7.4), 1 MgCl<sub>2</sub>, increasing concentration of CuSO<sub>4</sub> in absence or presence of 1 EDTA and 7µg MPM protein. The enzyme reaction was started by addition of 1mmol/l ATP, allowed to proceed for additional 10 min and stopped by the addition 22µl of the ice cold 3mol/l perchloric acid. The inorganic phosphate (Pi) liber-

ated from the hydrolysis of ATP was determined by the spectrophotometric method. All measurements were performed in triplicate.

## **Results and Discussion**

Copper sulphate was added to the reaction mixture in concentration ranges from  $1\times10^{-7}$  to  $5\times10^{-2}$  mol/l. The effects of increasing concentrations of Cu<sup>2+</sup> were measured in the absence and in the presence of 1mmol/l EDTA. In the absence of EDTA, ecto-ATPase activity shows total inhibition, relative to the control sample in the presence of  $1\times10^{-3}$  mol/l of added CuSO<sub>4</sub>, but the same metal concentration in the presence of EDTA has an inhibition of about 30% (Fig 1.). The half-maximum inhibitory activities (IC<sub>50</sub>) determined by Hill analysis of experimental curves (Fig.1 inset) were  $1.15\times10^{-4}$  and  $1.71\times10^{-3}$  mol/l in the absence or presence of EDTA, respectively.

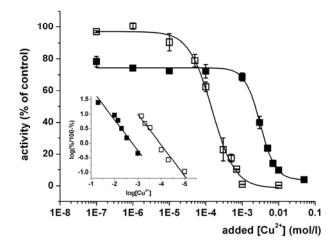


**Fig. 1.** Inhibition of ecto-ATPase activity by CuSO<sub>4</sub> in the absence (open symbol) and in the presence (solid symbols) of  $1\times10^{-3}$  mol/l EDTA. The values given are the mean of at least three experiments  $\pm$ S.E.M

The concentrations of ionic species were calculated, taking into account equilibrium reactions involving  $Mg^{2+}$ , ATP, EDTA and  $Cu^{2+}$  (Tab.1). The stability constants were found in the literature [5].

Toxic mechanisms of Cu<sup>2+</sup> on the enzyme activity are based on competition with Mg<sup>2+</sup> in the MgATP<sup>2-</sup> complex and in that way decreasing substrate concentration [2], membrane lipid peroxidation [1], and interaction with -SH, -NH<sub>2</sub>, -COOH, -OH groups of the enzyme protein. Chelating copper ions, EDTA decreases free ion concentrations, which may interact with the enzyme protein or with ATP. EDTA has been used for years as a drug of choice for metal overload, but also as additive to food and cosmetics. Some resent data suggests that EDTA cause membrane destabilization, by chelating of divalent cations on lipid surface

(Mg<sup>2+</sup>, Ca<sup>2+</sup>) and direct insertion in membrane [6]. Our results suggest that effects of the EDTA on enzyme activity inhibition could not be excluded [7], since initial enzyme activity is maximum 80% of control activity, measured in the absence of EDTA.

**Table 1.** The values of free Cu<sup>2+</sup>, CuATP<sup>2-</sup> and CuEDTA<sup>2-</sup> calculated in the medium assay containing various Cu<sup>2+</sup> concentrations in the presence and absence of 1mmol/1 EDTA.

	without EDT.	A	with 1mmol/l EDTA				
addedCu <sup>2+</sup>	free Cu <sup>2+</sup> CuATP <sup>2-</sup>		addedCu <sup>2+</sup>	free Cu <sup>2+</sup>	CuATP <sup>2-</sup>	CuEDTA <sup>2-</sup>	
1x10 <sup>-7</sup>	1.1x10 <sup>-8</sup>	9.9 x10 <sup>-8</sup>	1x10 <sup>-7</sup>	1.9x10 <sup>-21</sup>	1.1x10 <sup>-18</sup>	$0.9 \times 10^{-7}$	
$1x10^{-6}$	1.1 x10 <sup>-8</sup>	$9.9 \times 10^{-7}$	$1x10^{-6}$	$2.0 \times 10^{-20}$	$1.2 \times 10^{-17}$	$0.9 \times 10^{-6}$	
$1x10^{-5}$	$1.1 \times 10^{-7}$	$9.9 \times 10^{-6}$	$1x10^{-5}$	$3.4 \times 10^{-19}$	$1.9 \times 10^{-16}$	$0.9 \times 10^{-5}$	
$5x10^{-5}$	$6.4 \times 10^{-7}$	$4.9 \times 10^{-5}$	$1x10^{-4}$	$2.7 \times 10^{-17}$	1.5x10 <sup>-14</sup>	9.9 x10 <sup>-5</sup>	
$1x10^{-4}$	$1.5 \times 10^{-6}$	$9.8 \times 10^{-5}$	$1x10^{-3}$	$1.2 \times 10^{-12}$	$1.1 \times 10^{-10}$	9.9 x10 <sup>-4</sup>	
$3x10^{-4}$	$9.1 \times 10^{-5}$	$2.9 \times 10^{-4}$	$3x10^{-3}$	$1.1 \times 10^{-10}$	$9.5 \times 10^{-4}$	$9.9 \times 10^{-4}$	
$5x10^{-4}$	$2.8 \times 10^{-5}$	$4.7 \times 10^{-4}$	$5x10^{-3}$	$3.1 \times 10^{-3}$	$9.8 \times 10^{-4}$	$9.9 \times 10^{-4}$	
$7x10^{-4}$	$6.8 \times 10^{-5}$	$6.3 \times 10^{-4}$	$7x10^{-3}$	$5.1 \times 10^{-3}$	$9.9x10^{-4}$	$9.9 \times 10^{-4}$	
$1x10^{-3}$	$1.9 \times 10^{-5}$	$8.0 \times 10^{-4}$	$1x10^{-2}$	$8.0 \times 10^{-3}$	$9.9x10^{-4}$	9.9 x10 <sup>-4</sup>	
1x10 <sup>-2</sup>	$9.0 \times 10^{-3}$	9.9 x10 <sup>-4</sup>	$5x10^{-2}$	$4.8 \times 10^{-3}$	9.9x10 <sup>-4</sup>	$9.9 \times 10^{-4}$	

## Conclusion

EDTA having high affinity for  $Cu^{2+}$  may prevent or decrease the toxic effects of this metal ion. According to the results presented in this work, 1 mmol/l EDTA increase by one order of magnitude  $CuSO_4$  concentration for half-maximal inhibition (IC<sub>50</sub>), by decreasing  $Cu^{2+}$  concentrations, available to form inactive complex  $CuATP^{2-}$ .

## Acknowledgements

This study was supported by the Serbian Ministry of Sciences, Project No. 143044.

- [1] P. Kovačić, J. D. Jacintho, Curr. Med. Chem., 2001, 8, 863-892.
- [2] V. Vasić, D. Jovanović, A. Horvat, T. Momić, G. Nikezić, Anal. Biochem., 2002, 300, 113-120.
- [3] M. Milošević, S. Petrović, M. Demajo, A. Horvat, Ann.N.Y.Acad. Sci., 2005, 1048, 445-448.
- [4] M. Bardini, H.Y. Lee, G. Burnstock, Cell Tissue Res., 2000, 299, 105–113.
- [5] L.G.Silen, A.E Martell, Stability Constants of Metal-Ion Complexes. The chemical Society, London Special Publication No. 25, 1971.
- [6] V. Prachayasittikul, C. Isaramkura-Na-Ayudhya, T. Tantimongcolwat, C. Nanatasena-mat, H.J.Galla, Acta Bioch Bioph Sinica, 2007, 39 (11), 901-913
- [7] M. Milosević, M. Demajo, A. Horvat, Physical Chemistry Proceedings, 2006, I, 395-397.

## TIME – DEPENDENT INHIBITION OF ELECTRIC EEL AChE INDUCED BY CHLORPYRIFOS

M. Čolović<sup>1</sup> and D. Krstić<sup>2</sup>

<sup>1</sup>Vinča Institute of Nuclear Sciences, P.O.Box 522, 11001 Belgrade, Serbia, e-mail: colovicm@vin.bg.ac.yu <sup>2</sup>Institute of Medicinal Chemistry, School of Medicine, University of Belgrade, Serbia,

## **Abstract**

The aim of the work was to investigate the influence of contact time between acetylcholinesterase (AChE) and chlorpyrifos, on the sensitivity of earlier developed AChE based bioanalytical method for detection and determination of organophosphates in water samples. The IC<sub>50</sub> values were obtained from the concentration-dependent responses of AChE activity to chlorpyrifos and they decreased with the increasing the contact time. The results indicated that the sensitivity of AChE based bioassay can be improved by increasing the time of incubation, but this comes at the expense of additional analysis time. In addition, the inhibition parameters of chlorpyrifos induced inhibition of AChE were determined.

## Introduction

Organophosphorus compounds (OP), such as chlorpyrifos, malathion, parathion, have been commonly used as insecticides for over 50 years. These compounds are specific irreversible inhibitors of acetylcholinesterase (AChE, EC 3.1.1.7), the enzyme involved in the hydrolysis of the neurotransmitter acetylcholine (ACh) at cholinergic synapses in the central and peripheral nervous systems (cholinergic syndrome) [1].

Organophosphates are preferred in agriculture because of their relatively low persistence in the environment. In recent years various bioanalytical methods and biosensors, based on specific inhibition of AChE by organophosphorus compounds, have been widely developed for the fast screening organophosphates in the environment [2, 3]. The aim of this work was to investigate chlorpyrifos-induced inhibition of AChE activity as a function of the contact time between enzyme and inhibitor, in order to improve sensitivity of the recently developed bioanalytical method for detection and determination of OPs [2]. In addition, inhibition parametres,  $K_I$  and  $k_3$ , of chlorpyrifos-induced AChE inhibition were determined.

## **Material and Methods**

Acetylcholinesterase (AChE, specific activity 288 IU/mg solid) from electric eel, acetylthiocholine iodide (ASChI) and 5,5'-dithio-bis-(2-nitrobenzoic acid) (DTNB) were purchased from Sigma Chemicals Co. Chlorpyrifos (98% purity) was purchased from Galenika (Zemun, Serbia). The inhibition of enzyme was measured using the Ellman's method [2]. Experiments were performed by *in vitro* exposure of 0.174 μg enzyme to inhibitors in a final volume of 0.650 ml.

## **Results and Discussion**

The influence of chlorpyrifos on AChE activity, was investigated by *in vitro* exposure of the enzyme to the inhibitor in the concentration range from 1 x  $10^{-8}$  to 5 x  $10^{-4}$  M in several incubation times (enzyme-inhibitor contact time): 14, 17, 20, 25 min (Fig.1). The IC<sub>50</sub> values (inhibitor concentration that produced 50% of enzyme inhibition), determined by sigmoidal fitting of the experimental inhibition curves, are presented in Fig. 1. It is obvious that IC<sub>50</sub> value decreased for almost one order of magnitude due to the prolonged incubation time. Consequently, the percent of inhibition in the presence of the particular inhibitor concentration decreased as a function of exposure time.

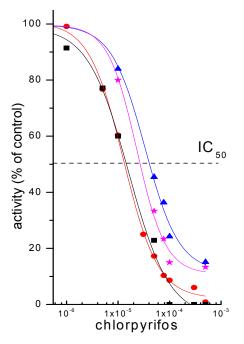


**Fig. 1.** (a) The concentration dependent irreversible inhibition of AChE activity by chlorpyrifos after 14 min (triangle), 17 min (asterisk), 20min (circle), and 25 min (square) of contact time.

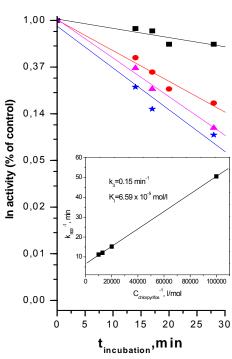


**Fig 2.** Progressive development of AChE inhibition by different chlorpyrifos concentrations (M):

 $1 \times 10^{-5}$  (square),  $5\times 10^{-5}$  (circle),  $7.7\times 10^{-5}$  (triangle) and  $1\times 10^{-4}$  (asterisk). The dependence of  $1/k_{app}$  upon  $1/C_{inhibitor}$  (inset).

Moreover, the chlorpyrifos concentration which induced 10% inhibition of enzyme activity, the statistically significant value to indicate the presence of inhibitor using AChE based bioanalytical method [2,3], decreased from  $1x10^{-5}M$  to  $1x10^{-6}$  M by prolonged incubation under the experimental conditions.

These results are in accordance with the previously reported for malathion and its degradation and oxidation products [2]. However, it can be noticed, based

on IC<sub>50</sub> values obtained in this work, that chlorpyrifos is more potent AChE inhibitor compared to malathion, but weaker compared to the malathion degradation products (malaoxon and isomalathion). Besides, the reaction between chlorpyrifos and AChE is much slower compared to malathion group of compounds, since a significant improvement in inhibitory power of these compounds, about one order of magnitude, was observed after 5 min incubations of the enzyme with inhibitors.

Inhibition parametres,  $K_I$  (the dissociation constant for the initial reversible enzyme inhibitor complex) and  $k_3$  (the first order rate constant for the conversion of the reversible complex to the irreversibly inhibited enzyme) were calculated, according to the method reported by Kitz et.al [4]. Fig. 2 represents the progressive development of inhibition produced by reaction of AChE,  $lnE / E_o vs. t$ , with different concentrations of chlorpyrifos.  $E/E_o$  represents here the percent of the remining activity. From the slope and intercept of the dependence of  $1/k_{app} vs. 1/C_{inhibitor}$  (Fig. 2, (inset)).  $k_{app}$  was obtained from the slope of the dependence of  $lnE / E_o vs. t$  (Figure 2), where  $E/E_o$  represents the percent of the remaining enzyme activity in relation to the initial activity,  $E_o$ , and t is incubation time [4]. The inhibition parameters are given in Fig.2(inset)

## Conclusion

The dependence of AChE inhibition on the time of exposure to the chlorpyrifos is in agreement with results reported earlier [2, 3]. This finding is important from the analytical point of view and shows that the sensitivity of used bioassay towards the investigated compound can be improved by increasing the contact time between the enzyme and organophosphate, but this comes at the expense of additional analysis time. The inhibition parametres for chlorpyrifos induced inhibition of AChE obtained in this work show that chlorpyrifos, although structurally different, inhibits the activity *via* the same mechanism as previously investigated irreversible organophosphorous AChE inhibitors, malathion and its related compounds [3].

- [1] M. O'Malley, Lancet, 1997, **349**, 1161-1166.
- [2] D. Krstie, M. Colovie, M.B. Kralj, M. Franko, K. Krinulovie, P. Trebse, V. Vasie, J. Enz. Inh. Med. Chem., 2008, DOI: 10.1080/1475360701632031.
- [3] L. Pogacnik, M. Franko, Talanta, 2001, **54**, 631-641.
- [4] R. Kitz, I. Wilson, J. Biol. Chem., 1962, 237 (10), 3245-3249.

# IONIZING IRRADIATION AFFECT EXTRACELLULAR NUCLEOTIDE HYDROLYSIS IN BRAIN OF RATS IN DIFFERENT STAGES OF DEVELOPMENT: I 15-DAY-OLD RATS

I. Stanojević, D. Drakulić and N. Veličković

Laboratory for Molecular Biology and Endocrinology, "Vinča" Institute of Nuclear Sciences, P.O.Box 522, 11001 Belgrade, Serbia

## **Abstract**

Ionizing radiation affects plasma membrane functions mediated through transmembrane proteins including enzymes. Plasma membrane surface-located enzyme chain of ecto-nucleotide triphospho diphosphohydrolases (NTPDases) are involved in termination of cell purinergic signalization by hydrolysing extracellular adenosine tri- and di-phosphate (ATP and ADP). In the present study, effects of low (50 cGy) and therapeutic (2 Gy) dose of ionizing  $\gamma$ -irradiation on NTPDase activity in early postnatal rat brain neuronal cells were studied. Both low- and therapeutic doses significantly decreased hydrolyze of extracellular ATP (by 11% and 30%) and ADP (18% and 46%) in postnatal rats. These findings indicate that gammaradiation inhibits the enzyme activity in dose-dependent manner. This decreasing NTPDase activity 24h after whole body irradiation may lead to neuronal cell function disturbance, even cell death.

### Introduction

The high sensitivity of cellular membranes to the action of great variety of chemical and physical agents including ionizing radiation (IR) is well known. Reactive oxygen species (ROS), generated following IR in the cell, act on polyunsaturated fatty acids of cellular membranes producing lipid peroxides, which may alter plasma membrane proteins function. Although, ionizing radiation may affects the expression of membrane proteins or change the interaction(s) that normally take place between membrane lipids and proteins [1].

Adenosine triphosphate (ATP) functions as a fast excitatory neurotransmitter and neuromodulator, activating various purino-receptors in the central nervous system. ATP released in the synaptic cleft can be hydrolyzed to adenosine by the conjugated action of synaptic plasma membrane (SPM)-bound, surface-located enzyme chain of NTPDases and ecto-5'nucleotidase. Thus, ectonucleotidase pathway has a double function of removing the one signal (ATP) and generating second one (adenosine), consequently controlling the levels of adenine nucleotides in the extracellular environment and the duration and extent of their receptor activation. Inhibition of SPM ecto-ATPase activity would be expected to potentiate excitatory synaptic transmission by supporting synaptic efficacy of ATP and inhibiting the formation of adenosine [2].

The aim of this work was to study the effects of low and therapeutic doses one day after whole body gamma-ray irradiating on ATP and ADP hydrolysis by

NTPDase of postnatal rats brain SPM.

## **Experimental procedures**

Female rats of the Wistar strain, 15 and 90 days old, were whole-body irradiated with 50 cGy or 2 Gy (10.7cGy/min, <sup>60</sup>Co source). During irradiation animals were confined in plywood boxes and the second group of animals were treated as the irradiated group but not subjected to irradiation (control group). All groups were sacrificed 24 hour after irradiation. Nerve terminals (synaptic) plasma membranes (SPM) were isolated from whole brains. Activities of NTPDases were determined under *in vitro* conditions: rate of ATP and ADP hydrolysis were measured by colorimetric determination of liberated phosphate in the presence of 40μg SPM proteins, 1mmol/l ATP or ADP, 5 mmol/l MgCl<sub>2</sub>, 50 mmol/l Tris-HCl, pH 7,8 and incubations at 37°C for 15 min. The specific enzyme activity was expressed as mean nmolPi/min/mg SPM protein ± S.E.M. from three independent examinations performed in triplicate. Statistical analyses were performed by one-way analysis of variance (ANOVA), followed by a Tukey's test as post-hoc, considering p < 0.05 as significant.

## **Results and Discussion**

The results of low- (50 cGy) and therapeutic- (2 Gy) dose radiation on the brain NTPDase activity 24h after irradiation are presented in Figure 1. In 15-day-old rats both doses decrease ATP hydrolysis in dose-dependent manner by 11% and 30% compared to non-irradiated control (Fig. 1.A). Changes in ADP hydrolysis go along ATP hydrolysis, and are decreased by 18% and 46% in respect to control (Fig. 1.B). The results indicate that even a low dose is enough for induce inhibition of NTPDase activity 24h after irradiation. In the nerve terminals of adult rat brain, 24h after irradiation, ATP hydrolysis is increased by 30% compared to nonirradiated control only with low dose (Fig. 1.A), while no change was observed with the rapeutic dose. The ADP hydrolysis was unchanged irrespective of radiation dose (Fig. 1.B). It was assumed that low doses initiate activation of enzymatic reaction because of disturbed plasma membrane permeability [1]. Several previous studies have reported that rat brain ecto-ATPase activity decreased under conditions that either promote or are associated with increased lipid peroxidation. The results demonstrate that low-pathologically relevance of 4-hydroxynonenal, the major product of membrane lipid peroxidation, selectively inhibits SPM NTPDase [3]. Lack of changes in ADP hydrolyses in adult rats indicate presence of two NTPDases with different sensitivity to membrane disturbance. Increased ATP hydrolysis indicates increased adenosine formation, possessing neuroprotective effects. Another finding from the results was that infant brain NTPDase(s) was differently vulnerable on ionizing radiation or cellular events induced by radiation. It is well known that immature neurons are more sensitive to ionizing irradiation. By decreased NTPDase activity in infant rats and consequently decreased adenosine production, neuronal cells in that stage of development were susceptible to apoptosis. Certain cells of the CNS have been reported to undergo p53-dependent apoptosis after 2 Gy irradiation and its inhibition of NTPDase activity may have implication in cell death of immature brain. Whole-brain irradiation with large-scale doses (2-10 Gy) also caused a decrease in number of cells and their progenitor cells in young rodent brain in the dose-dependent fashion a few hours after irradiation [4].

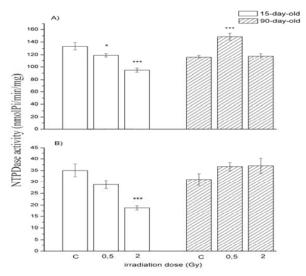


**Fig. 1.** The ATP (A) and ADP (B) hydrolysis in 15- and 90-old-rats 24h after 50 cGy and 2 Gy irradiation. Results represent mean  $\pm$ S.E.M from three experiments done in triplicate. Significance in respect to non-irradiated controls (C) (\*p<0.05, \*\*\*p<0.001).

#### Conclusion

In young rat brain, 24h after low and therapeutic doses of gamma-irradiation induce decreasing in NTPDase activity that may lead to disturbance in neuronal cells function and increased cell death.

## Acknowledgements

The Serbian Ministry of Sciences, Project No. 143044 supported this study.

- [1] L.Kh. Eidus, Radiat. Environ. Biophys., 2000, 39, 189-195.
- [2] S.C. Robson, J. Sevigny and H. Zimmermann, Pur. Signal., 2006, 2, 409-430
- [3] T.D. Foley, Neurochem. Res., 1999, 24, 1241-1248.
- [4] J. Verheyde, M.A. Benotmane, Brain Res.Rev., 2007, 53, 312-320.

## IONIZING IRRADIATION AFFECT EXTRACELLULAR NUCLEOTIDE HYDROLYSIS IN BRAIN OF RATS IN DIFFERENT STAGES OF DEVELOPMENT: II 30-DAY-OLD RATS

D. Drakulić, I. Stanojević, M. Milošević and N. Veličković

Laboratory for Molecular Biology and Endocrinology, "Vinča" Institute of Nuclear Science, P.O.Box 522, 11001 Belgrade, Serbia

## **Abstract**

The effect of acute gamma irradiation (IR) on enzyme activity of rat brain Ecto-Nucleotide Diphosphohydrolase (E-NTPDase), in presence of adenosine triand diphophashates (ATP and ADP) and divalent cations (Ca<sup>2+</sup> and Mg<sup>2+</sup>), has been investigated. The aim of research was to study the influence of low (50 cGy) and therapeutic (2Gy) doses of whole-body irradiation on rat brain E-NTPDase enzyme activity 24h after treatment in prepubertal and adult rats. Our results suggest that whole-body irradiation could induce modulation of neural activity in rat brain, especially in young rats.

## Introduction

E-NTPDase1, 2, 3 are glycoproteins, expressed on of brain cell's plasma membranes. These proteins contain transmembrane domain; N- and C-terminus, located in intracellular and large highly conserved active domain, located in extracellular space. Substrate-active site enables hydrolysis of extracellular nucleotides to nucleosides and induces purinergic signalling modulation and termination. E-NTPDases1, 2, 3 hydrolyze ATP and ADP with different affinities. E-NTPDase1 hydrolysis ATP equally as ADP, other two E-NTPDases (E-NTPDase2 and E-NTPDase3) prefer ATP [1]. In central nervous system, ATP acts as universal signal and fast excitatory neurotransmitter and co-transmitter, as well as neuromodulator. Binding of extracellular ATP and products of its hydrolysis (ADP, AMP and adenosine) to specific surface located purinergic receptors, triggers signalling cascade and regulates many physiological processes. Changes in E-NTPDase activity causes disruption in synaptic transmission and adenosine formation, leading to cell dysfunction, apoptosis and cognitive disorders [2].

Ionizing radiation, that is commonly used in every day life, for instance in diagnostic protocols and therapeutic purposes, is able to induce plasma membrane structure alterations, metabolic process inhibitions, ion transport changes as well as DNA damages [3]. Through arising of reactive oxygen species (ROS), IR modulates permeability and fluidity of plasma membrane by altering expression and interaction of transmembrane proteins and protein-lipid connections.

It is supposed that low and therapeutic doses alter brain's E-NTPDase enzyme activity through the rate of ATP and ADP hydrolysis 24h after whole-body

irradiation and this hypothesis was tested in the present study. Also, susceptibility of young brain to IR was studied.

## **Experimental procedures**

Experiments were performed on 30 (prepubertal) and 90 (adult) days old female Wistar albino rats obtained from the local colony. Animals were divided into three groups: the control group non-irradiated (C); second and third group whole-body irradiated with 50 cGy or 2 Gy (10.7 cGy/min, <sup>60</sup>Co source INN Vinča). Animals from all three groups were confined in plywood boxes, and sacrificed 24h after treatments. Synaptic plasma membranes (SPM) were isolated from whole brains. Activities of E-NTPDase were determined under *in vitro* conditions: rate of ATP and ADP hydrolysis were measured by colorimetric determination of liberated inorganic phosphate in the presence of 40μg SPM proteins, 1mmol/l ATP or ADP, 5 mmol/l MgCl<sub>2</sub>, 50 mmol/l Tris-HCl pH 7.8, and incubations at 37°C for 15 min. The specific enzyme activity was expressed from 3 independent experiments performed in triplicate as mean nmolPi/min/mg SPM protein ± S.E.M. The data were analyzed using one-way ANOVA followed by post-hoc Tukey's test and p<0.05 values were considered significant.

## **Results and Discussion**

In attempt to reveal if whole-body irradiation alters the E-NTPDase enzyme

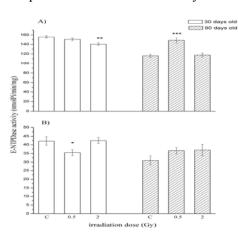


**Fig. 1.** E-NTPDase activity presented as a mean  $\pm$  S.E.M. from 3 experiments done in triplicate. A) ATP and B) ADP hydrolysis in imobilized control (C) group and groups irradiated with 50 cGy (0,5) and 2 Gy (2). \*\*\* p<0,001, \*\*\*p<0,01, \* p<0,05 vs. control.

the production activity, inorganic phosphate, as result of ATP and ADP hydrolysis, was monitored. Analyses showed that in prepubertal rat brain, compared to control (C), 24h after irradiation with 50 cGy, ADP hydrolysis was decreased by 20% and irradiation with therapeutic dose caused decrease of ATP hydrolysis by 10%. Low dosage whole-body irradiation of adult (90-day-old) animals leaded to **ATP** hydrolysis augmentation by 28%.

Results suggest that more than one E-NTPDases is present on the neural cell surface and all of them are differently sensitive to whole-body irradiation. In 90

days old rat's brain, ATPase part of these enzymes was more sensitive to low dose

irradiation then ADPase component, while in young rat ADPase component was more sensitive.

In developing central nervous system cells are highly sensitive to certain chemical and physical agents such as IR [4]. Few previous studies demonstrated that all three E-NTPDase enzymes play an important role in neural development. Decreased hydrolitic activity of these enzymes in prepubertal rats could be a consequence of reactive oxygen and nitrogen species formation and plasma membrane disturbance, lipide peroxidation, as well as inhibition of enzyme activity [3]. Futher, inhibition of the enzyme activity could cause augmentation of excitatory nucleotides amount in synaptic cleft and apoptosis inducement by activation of P2 receptor, that results in appearence of motoric and cognitive disfunctions.

Ionizing irradiation could alter signal transduction and gene expression. Cells are supplied with defense mechanisms and 24 h after irradiation is enough time for the adaptive response. According to our results, 24h after whole-body irradiation with 2 Gy, defence cells mechanisms in adult rats, were induced. Apparantly, increased ATP hydrolysis after 50 cGy treatment is protective because IR *per se* could induce augmentation of extracellular ATP and cause cytotoxity. Observed increased enzyme activities may reduce the amount of these nucleotides in synaptic cleft. In prepubertal rat brain ADPase part of the enzymes was more sensitive to low dose irradiation, while ATPase component was sensitive to 2 Gy. Perhaps young rats were not able to induce defence mechanisms. Futher, ADPase part of the E-NTPDases was more senzitive to IR with 50 cGy then ATPase component.

## Conclusion

Our results showed that whole-body irradiation with low- and therapeutic doses affects neuronal activity in prepubertal rat brain by decreasing extracellular ATP and ADP hydrolysis 24h after irradiation. In this way, concentrations of excitatory ATP and ADP were increased, while concentration of neuroprotective adenosine was decreased. Low dose irradiation modulates neuronal activity in adult brain by increasing ATP hydrolysis and it enables neuroprotective effect.

## Acknowledgements

The Serbian Ministry of Sciences, Project No. 143044 supported this study.

- [1] H. Zimmermann, Eur J Physiology, 2006, **452**, 573-588.
- [2] J. Verheyde, M.A. Benotmane, Brain Research Reviews 2007, 53, 312-320.
- [3] T.D. Foley, Neurochemical Research, 1999, **24**(10), 1241-1248.
- [4] L.E. Feinendegen, M. Pollycove, R.D. Neumann, Experimental Hematology 2007, 35, 27-46.
- [5] Y. Dimberg, M. Vazqeez, S. Sodestrom, T. Ebendal, Toxicology Letters 1997, 90, 35-43.

CIP - Каталогизација у публикацији Народна библиотека Србије, Београд

544(082) 621.35(082) 543.42(082)

MEĐUNARODNA konferencija iz fundamentalne i primenjene fizičke hemije (9; 2008; Beograd)

Physical Chemistry 2008: proceedings of the 9th International Conference on Fundamental and Applied Aspects of Physical Chemistry, [September 24-26, 2008, Belgrade, Serbia]. Vol. 1 / [organized by The Society of Physical Chemists of Serbia; editor A.[Ankica] Antić-Jovanović]. - Belgrade: The Society of Physical Chemists of Serbia, 2008 (Belgrade: Jovan). - XI, 468 str.: ilustr.; 24 cm

Tiraž 250. - Str. VII: [Preface] / editor. - Bibliografija uz svaki rad. - Abstracts.

ISBN 978-86-82475-16-3
1. Antić-Jovanović, Ankica [уредник] [аутор додатног текста] 2. Društvo fizikohemičara Srbije (Beograd)
а) Физичка хемија - Зборници b)
Електрохемијско инжењерство - Зборници с)
Спектроскопија - Зборници
COBISS.SR-ID 150991372



# PHYSICAL CHEMISTRY 2008

### **Proceedings**

of the 9th International Conference on Fundamental and Applied Aspects of Physical Chemistry

#### Volume II

The Conference is dedicated to the 200th Anniversary of the University in Belgrade



September 24-26, 2008, Belgrade, Serbia



# PHYSICAL CHEMISTRY 2008

### **Proceedings**

of the 9<sup>th</sup> International Conference on Fundamental and Applied Aspects of Physical Chemistry

Volume II

ISBN 978-86-82475-13-2

Title: Physical Chemistry 2008. (Proceedings)

Editor: Prof. dr A. Antić-Jovanović

Published by: The Society of Physical Chemists of Serbia, Student-

ski trg 12-16, P.O.Box 137, 11001 Belgrade, Serbia

Publisher: Society of Physical Chemists of Serbia

For publisher: Prof. dr S. Anić, president of the Society of Physical

Chemists of Serbia

Printed by: "Jovan" Printing and Published Comp;

250 Copies; Number of Pages: x + 301 (469-770);

Format B5; Printing finished in September 2008.

Text and Layout: Aleksandar Nikolić

250 – copy printing

## The Conference is organized by the Society of Physical Chemists of Serbia

in cooperation with Institute of Catalysis, Bulgarian Academy of Sciences

Boreskov Institute of Catalysis, Siberian Branch of the Russian Academy of Sciences

Faculty of Physical Chemistry, University of Belgrade

Institute of Chemistry, Technology and Metallurgy, Belgrade

Institute of General and Physical Chemistry, Belgrade

#### **International Organizing Committee**

Chairman: S. Anić (Serbia) Vice-chairman: A. Elias (Bulgaria)

> I. V. Koptyug (Russia) B. Adnadjević (Serbia)

#### Members:

M. Gabrovska (Bulgaria), T. Grozdić (Serbia), D. Jovanović (Serbia), P. M. Lalic (BiH),

Manojlović (Serbia), D. Marković (Serbia), B. Milosavljević (USA),

N. Miljević (Serbia), T. Nenadović (Serbia), N. Ostrovski (Serbia), C. Pona (Italy),

B. Simonović (Serbia), A. G. Stepanov (Russiaia), N. Vukelić (Serbia),

V. Vukojević (Sweden)

#### International Scientific Committee

Chairman: A. Antić-Jovanović (Serbia) V. N. Parmon (Russia) Vice-chairmans:

Ž. Čupić (Serbia)

S. Rakovsky (Bulgaria)

#### Members:

G. Bacic (Serbia), R. Cervellati (Italy), B. Cretin (France), V. Dondur (Serbia), V. Gaspar (Hungary), M. Jeremić (Serbia), A. L. Kawczyński (Poland), Lj. Kolar-Anić (Serbia), I. V. Koptyug (Russia),

S. Mentus (Serbia), S. Miloniić (Serbia), B. Minceva-Sukarova (R.Macedonia).

Lj. Morozova-Roche (Sweden), Z. Noszticzius (Hungary), M. Perić (Serbia), V. Petruševski (R.Macedonija), M. Plavšić (Serbia), I. Poulios (Greece), G. Schmitz (Belgium), I. Schreiber (Czech), P. Sevcik (Slovakia), N. Stepanov (Russia), M. Trtica (Serbia), D. Veselinović (Serbia),

#### **Local Executive Committee**

Chairman: B. Adnadjević Vice-chairmans: S. Blagojević

#### Members:

N. Begović, S. N. Blagojević, I. Cekić, N. Cvjetičanin, M. Daković,

Lj. Damjanović, A. Đerić, A. Ignjatović, Lj. Ignjatović, A. Ivanović, A. Jović, D. Lončarević, M. Mojović,

I. Pašti, N. Pejić, N. Potkonjak, D. Ranković, D. Stanisavljev, B. Šljukić

#### **Honorary Committee**

Nikola Hajdin, President of Serbian Academy of Sciences and Arts

Branko Kovačević, Rector, University of Belgrade

Paula Putanov, Member of Serbian Academy of Sciences and Arts

Momčilo Ristić, Member of Serbian Academy of Sciences and Arts

Ivan Draganić, Honorary Member of Society of Physical Chemists of Serbia

Bratislav Đorđević, Ambassador, Ministry of Foreign Affairs of Republic of Serbia

#### **SPONSORS**

Ministry of Science of the Republic of Serbia

The Faculty of Physical Chemistry, University of Belgrade

Institute for Chemistry, Technology and Metalurgy, University of Belgrade

NovoLab, Belgrade

Organisation for the Prohibition of Chemical Weapons

MOL, Belgrade

ENOLOŠKA STANICA dp, Society Company for Agricultural Products and Foodstuffs Control, Vršac

Gradski zavod za zaštitu zdravlja, Beograd

Following the tradition of the preceding Conferences on Fundamental and Applied Aspects of Physical Chemistry, the aim of the present Conference is again to allow researchers from different countries to enhance contacts and exchange information and experiences.

The program of the Conference includes invited plenary lectures, invited section lectures, oral contributions and poster sessions of 480 authors from twenty three countries.

Beside six Plenary Lectures, given by internationally recognized scientists, this book contains twenty two Invited Lectures and 184 contributions, given as ether oral or poster presentations, arranged in sessions corresponding to their scientific topics. All accepted papers are reviewed but without language revision, for which authors bear responsibility.

Organizers of the Conference "Physical Chemistry 2008" thank to all authors for the effort to provide us with their paper and take part in the Conference, our sponsors, as well as to the Ministry of Sciences of the Republic of Serbia for contribution to the success of Conference.

Belgrade, 2008

Editor

#### **Contents**

Va	lume	i
Vυ	uume	_

Plenary Lectures (PL)	1
General Physical Chemistry (A)	31
Spectroscopy, Molecular Structures (B)	63
Kinetics, Catalysis (C)	123
Nonlinear Dynamics (D)	199
Electrochemistry (E)	253
Biophysical Chemistry, Photochemistry, Radiation Chemistry (F)	319
Volume II	
Radiochemistry, Nuclear Chemistry (G)	457
Material Science (H)	469
Phase Boundaries (I)	539
Macromolecular Physical Chemistry (J)	553
Environmental Protection, Forensic Science (K)	607
Complex Compounds (L)	689
Education (M)	719
Supplement	727
Autor Index	738
Participating Institutions	747
Supplement 2	757

# Radiochemistry, Nuclear Chemistry

(G)

#### THE RADIOLOGICAL RISK ASSESMENT METHODOLOGY AP-PLIED ON SANDS FROM PUBLIC BEACHES

M.B. Radenković<sup>1</sup>, A.M. Saeed<sup>2</sup> and Š.S. Miljanić<sup>2</sup>

<sup>1</sup>Vinča Institute of Nuclear Sciences, Radiation and Environmental Protection Department, P.O.B. 522, 11001 Belgrade, Serbia

<sup>2</sup>Faculty of Physical Chemistry, University of Belgrade, P.O.B. 276, 11001 Belgrade Serbia

#### **Abstract**

The radiological risk of public exposure to terrestrial radiation in the sand beaches is assessed through the total absorbed gamma dose rate in air and annual effective dose outdoors determination according to international recommendations. Corresponding hazards due to sand use as a building material has been estimated by gamma irradiation hazard indices, based on the data of natural radionuclides contents in sands from public seaside and riverbank beaches (Ulcinj, Belgrade-Danube) obtained in this study, using spectrometry of gamma radiation.

#### Introduction

Sand deposits originate either igneous or metamorphic rocks, changed during the weathering and erosion processes, but still with some constituent minerals bearing natural radionuclides from U and Th series and <sup>40</sup>K. The assessment of their radiological implications due to the gamma ray exposure of the body and irradiation of lung tissue from inhalation of radon and its daughters as well as possible radiation hazards arising due to the use of particular sand in the constructions and dwellings is of a special concern. The objective of our investigation was to identify natural radionuclides contents in sand samples from seaside (Ulcinj, Montenegro) and riverbank (Danube-Belgrade, Serbia) public beaches and to estimate corresponding radiation hazards and dose rates relevant for humans.

#### **Materials and Methods**

Superficial beach sand samples were collected from Ulcinj, Montenegro (Ulcinj City Beach, Ulcinj Great Beach) and the river sediment island (Lido Beach) on the Danube, near the Belgrade, Serbia. Samples are homogenized, dried at 110 °C, weighed and sealed into Marinelli beakers for 40 days until the secular radioactive equilibrium was reached. The activities were obtained by standard gamma spectrometry, using HP Ge detector (Canberra) with 23% relative efficiency and resolution 1.8 keV for 1332.5 keV <sup>60</sup>Co gamma line.

Two different hazard indices were calculated: radium equivalent activity  $Ra_{eq}$  [1] and representative level index  $I_r$  [2]. The absorbed dose rate D in air was estimated [3] based on the average activity concentrations (Bq kg<sup>-1</sup>) of <sup>238</sup>U, <sup>232</sup>Th and <sup>40</sup>K, obtained in this work. Annual effective dose E (mSv y<sup>-1</sup>) outdoors was

than calculated according to ICRP (International Commission on Radiological Protection) recommendations.

#### **Results and Discussion**

The activity concentrations (Bq kg $^{-1}$ ) of natural radionuclides:  $^{226}$ Ra,  $^{232}$ Th and  $^{40}$ K in sand samples analyzed in this study are presented in Figure 1.

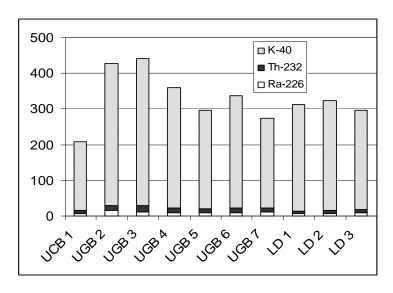


**Fig. 1.** The activity concentrations C (Bq kg<sup>-1</sup>) of  $^{226}$ Ra,  $^{232}$ Th and  $^{40}$ K in sand samples from Ulcinj (UCB, UGB1-UGB6) and Lido-Danube Beach (LD1-LD3)

The most of activity was due to the naturally occurring <sup>40</sup>K and much lower concentrations of <sup>226</sup>Ra and <sup>232</sup>Th were noticeable. There was no significant difference between the seaside and riverbank sand samples, The activity concentrations values are in accordance with some previous results [4] and the world quoted intervals: 7-50 Bq kg<sup>-1</sup>, 10-50 Bq kg<sup>-1</sup> and 100-700 (mean 370) Bq kg<sup>-1</sup> for <sup>226</sup>Ra, <sup>232</sup>Th and <sup>40</sup>K in send minerals, respectively [3].

The gamma-ray radiation hazards indices: the radium equivalent activity  $(Ra_{eq})$  and representative level index  $(I_r)$  values and corresponding dose values are shown in Table 2. The values of  $Ra_{eq}$  index for analyzed sands are in the same range as the population-weighted average value of global primordial radiation of 59 nGy h<sup>-1</sup> [3]. This index is related to the external gamma dose and internal dose due to radon and its daughters and allows comparison of the activities and radiological effects of sediment samples containing different radionuclides concentrations.

Sample No	$Ra_{eq}$ (Bq kg <sup>-1</sup> )	$I_r$ (Bq kg <sup>-1</sup> )	D (nGy h <sup>-1</sup> )	E (mSv y <sup>-1</sup> )
1	35.1	0.27	17.4	0.041
2	67.4	0.52	33.7	0.021
3	67.5	0.52	33.9	0.041
4	54.1	0.42	27.3	0.033
5	47.7	0.37	23.8	0.029
6	51.9	0.40	26.1	0.032
7	47.7	0.36	23.6	0.029
Mean 1-7	50.5	0.43	28.1	0.033
8	40.0	0.32	20.6	0.025
9	43.7	0.34	22.3	0.027
10	43.7	0.34	22.0	0.027
Mean 8-10	42.5	0.33	21.6	0.026

**Table 2.** Gamma radiation hazard indices and corresponding dose values

The  $I_r$  values obtained for samples from Ulcinj and Belgrade Danube beaches are 33-43% of the 1 Bq kg<sup>-1</sup> limit value. Both mean gamma-ray absorbed dose rates values are less than the world average: 55 nGy h<sup>-1</sup> [3]. Finally, to make an estimate for the annual effective dose outdoors, E, we have used 0.7 Sv Gy<sup>-1</sup> as the conversion coefficient from the absorbed dose in air to effective dose received by adults, and 0.2 for the outdoor occupancy factor.[3] Obtained values for all analyzed sands are lower than the worldwide outdoors annual effective dose average 0.07 mSv y<sup>-1</sup> and below the value of 1.0 mSv y<sup>-1</sup>, recommended by the ICRP as the maximum allowed annual dose for public.

#### References

- [1] J. Beretka, P. Mathew, Natural Radioactivitz of Australian building materials, industrial wastes and by-products. Health Physics, 1985, 48, 87-95.
- [2] NEA-OECD., (1979). Exposure to Radiation from Natural Radioactivity in Building Materials. OECD Report, Paris.
- [3] UNSCEAR. (1988, 1993, 1998 and 2000). United Nations Scientific Committee on the effects of atomic radiation. Sources, Effects and Risks of Ionizing Radiation. New York, United Nations.
- [4] Vukotić, P., Borisov, G.I., Kuzmič, at al. Radioactivity on the Montenegrin Coast, Yugoslavia. Journal of Radioanalitycal and Nuclear Chemistry, 1998, **235**, 151-157.

## PHYSICO-CHEMICAL CHARACTERIZATION OF <sup>90</sup>Y-LABELED ANTIMONY TRISULFIDE COLLOID AND COMPARISON WITH <sup>99m</sup>Tc-LABELED ONE

D. Janković, D. Đokić and N. Nikolić

Vinča Institute of Nuclear Sciences, 11000 Belgrade, Serbia

#### **Abstract**

In radionuclide therapy, the importance of  $^{90}\mathrm{Y}$  as a beta-emitting radionuclide is increasing rapidly. The properties of the  $^{90}\mathrm{Y}$ -labeled antimony trisulfide colloid (Sb<sub>2</sub>S<sub>3</sub>) were compared with the  $^{99\mathrm{m}}\mathrm{Tc}$ -labeled one. Labeling efficiencies reached >96% and >97% for  $^{90}\mathrm{Y}$ - and  $^{99\mathrm{m}}\mathrm{Tc}$ -labeled colloids respectively. Both preparations were stable for 72 h in saline and 1% albumin solution. Filtration analysis showed that more than 94% of total  $^{90}\mathrm{Y}$  radioactivity is associated with the colloidal particles smaller than 20 nm, while more than 90% of  $^{99\mathrm{m}}\mathrm{Tc}$  radioactivity is associated with the particles retained on the filter with a 20 nm pore size.  $^{90}\mathrm{Y}$ -labeled colloids showed high labeling efficiency, stability and potency for clinical use.

#### Introduction

During the last decade there has been an increased interest in the application of radiopharmaceuticals in the direct management of serious illnesses, especially various forms of cancer and rheumatism. Yttrium-90 ( $^{90}$ Y) is a clinically acceptable  $\beta$ -emitting radionuclide, useful for therapy. It is a pure beta emitter, with a half-life of 64.4 hours,  $E_{max\beta}$  of 2.27 MeV and also has a lack of gamma radiation, and these characteristics of  $^{90}$ Y make it a good choice for safe patient treatments.  $^{90}$ Y is obtained from  $^{90}$ Sr as a high yielded fission product [1].

Radiocolloids play an important role as diagnostic and therapeutic agents in nuclear medicine. The properties of radiocolloid dispersion, characterized by particle size, shape, charge and stability, are significant parameters which determinate its organ distribution *in vivo*.

<sup>99m</sup>Tc-antimony trisulfide colloid has been used for bone marrow imaging, lymphedema assessment, and more recently, for scintigraphic mapping of lymphatic channels and sentinel nodes in melanoma and breast cancer [2, 3]. Its particles have been reported to range from 3 to 30 nm, which is an optimum size for imaging lymphatic channels in lymphoscintigraphy. The aim of this study was to investigate the labeling and stability of <sup>90</sup>Y-antimony trisulfide colloid particles.

#### **Experimental**

<sup>90</sup>YCl<sub>3</sub> was purchased from Polatom, Poland. <sup>99m</sup>Tc-pertechnetate was obtained from a <sup>99</sup>Mo/<sup>99m</sup>Tc radionuclide generator (INS Vinca, Belgrade). *Antimony sulfide colloid* was prepared by saturating 100 ml of boiled water for injection with hydrogen sulfide gas for 1 h. Twenty milliliters of 1% aqueous solution of antimony potassium tartrate (Merck,) were added and after the mixing an orange

liquid was obtained. In the next step 10 ml of a 4.0% aqueous solution of polyvinylpyrrolidone (povidone, PVP, average  $M_w$  ca. 44,000, Fluka) were added and an excess of hydrogen sulfide was removed by purging with nitrogen gas for 30 min. Absence of hydrogen sulfide was confirmed with lead acetate paper. The preparation was then divided into aliquots of 2 ml and sterilized by membrane filtration (220 nm) into sterile reaction vials and storage in a refrigerator. Right before the adding of  $^{90}\rm YCl_3$ , pH of the colloid solutions was adjusted to a desired value (1.5, 3.0 and 5.0).  $^{90}\rm Y$ -antimony sulfide was then prepared by adding 5-10  $\mu$ l of  $^{90}\rm YCl_3$  stock solution (~185 MBq). The mixture was kept at room temperature for different times or heated in a boiling-water bath for 30 min and then left to cool at room temperature. The  $^{99\rm m}\rm Tc$ -labelled colloid was prepared in the same manner as reported for the  $^{90}\rm Y$ -labelled one.

Radiochemical purity of the <sup>90</sup>Y-labeled colloid was evaluated by using Whatman-3 paper strips and developed in a solvents mixture of pyridine, ethanol and water with a volume ratio of 1:2:4 respectively. Labeling efficiency of the <sup>99m</sup>Tc-labeled colloid was checked by the ITLC-SG/ acetone system.

To check the stability, the particles of <sup>90</sup>Y and <sup>99m</sup>Tc-labeled colloids were incubated in a saline and 1% albumin solution and the mixture was agitated at 37 °C for 72 hours. At different points in time, the particles were centrifuged, separated from the liquid phase and counted to estimate the extent of leaching of the activity from them.

Filtration analysis. Sterile filters: Whatman (20-100 nm) and Millipore (220 nm) were used for particle size analysis.

#### **Results and Discussion**

The radiolabeling yield of the  $^{90}$ Y-antimony trisulfide colloid was dependant on the reaction temperature as well as the pH value. The results of labeling studies with this colloid at various pH values and temperatures are given in Fig. 1 as mean value of 3 radiolabeling probes (n=3). Studies on the effect of temperature showed that the labeling was low at room temperature (RT), with the yield being < 50% for a reaction time of 2 h at a pH value of 1.5. The maximum labeling yield of  $96.8\% \pm 1.2\%$  could be obtained when the labeling was carried out at a pH value of approximately 1.5 and at a reaction temperature of 95  $^{\circ}$ C for 30 min. Since the highest labeling yield was observed at these conditions, the following stages of the study were carried out with this formulation. The radiochemical purity of  $^{99\text{m}}$ Tc-antimony trisulfide prepared in these conditions was found to be higher than 97%.

The stability of  $^{90}$ Y- and  $^{99m}$ Tc-labeled Sb<sub>2</sub>S<sub>3</sub> colloid in a saline and 1% albumin solution was assessed by measuring the release of  $^{90}$ Y and  $^{99m}$ Tc from the particles at 37 °C up to 72 hours. The  $^{90}$ Y-antimony trisulfide colloid was quite stable, confirming that the metal remained bound to the colloid. During 72 h of incubation in saline and 1% albumin solution approximately <1.0% and <1.5% of  $^{90}$ Y were released respectively. The  $^{99m}$ Tc-antimony trisulfide colloid was also stable in vitro, showing >2% and >3.0% releases of the radionuclide during 72 h of incubation in saline and 1% albumin solution, respectively.

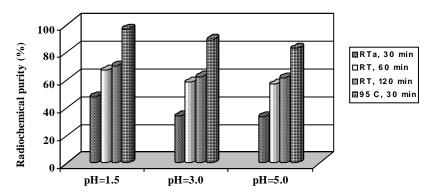


**Fig 1.** The labeling yield of  $^{90}$ Y-antimony trisulfide in different reaction conditions (mean, n=3)

The results of filtration analysis showed that more than 94% of the total <sup>90</sup>Y radioactivity is associated with the antimony trisulfide colloid particles smaller than 20 nm, while more than 90% of <sup>99m</sup>Tc radioactivity is associated with the particles retained on the filter with pore size of 20 nm (Table 1).

**Table 1.** Radioactive particle size distribution

Filter pore size	% Activity retained (mean $\pm$ SD)				
Colloids	0.22 μm	0.1 μm	0.05 μm	0.02 μm	
$^{90}$ Y- Sb <sub>2</sub> S <sub>3</sub>	-	1	-	5.9±2.1	
<sup>99m</sup> Tc- Sb <sub>2</sub> S <sub>3</sub>	-	-	5.3±0.8	90.7±2.2	

#### Conclusion

The antimony trisulfide colloid particles used in this study appear to be very well suited for labeling with beta emitting radionuclides. This colloid can be prepared from common chemicals and can be formed into particles of a desired size range using a controlled process. Radiolabeling of this colloid with <sup>90</sup>Y is simple to perform and provides a very high yield. The <sup>90</sup>Y-antimony trisulfide colloid demonstrates high *in vitro* stability in either saline or 1% albumin solution at 37 °C up to 72 h.

#### Acknowledgments

The research work has been financially supported by the Ministry of Sciences of the Republic of Serbia, Grant No. 142051.

#### Reference

- [1] M. Chinol, J.D. Hnatowich. J Nucl Med, 1987, **28**, 1465–1470.
- [2] L. Gang, W-J. Shih, C. Chou. Clin Nucl Med, 1995, **20**, 706 –708.
- [3] G. Trifirò, G. Viale, O. Gentilini, L.L. Travaini, G. Paganelli. Eur J Nucl Med Mol Imaging, 2004, **31** (Suppl.1), S46–S55.

#### RADIOCAESIUM IN SURFACE SOILS OF STARA PLANINA MOUNTAIN AND ITS CORRELATION WITH SOIL CHARACTERISTICS

M.Z. Momčilović<sup>1</sup>, B. Gajić<sup>2</sup>, N. Mihailović<sup>1</sup> and S. Dragović<sup>1</sup>

Institute for the Application of Nuclear Energy - INEP, Banatska 31b, Belgrade, Serbia, mmomcilovic@inep.co.yu

<sup>2</sup>Faculty of Agriculture, University of Belgrade, Nemanjina 6, Belgrade, Serbia

#### Abstract

Correlations between radiocaesium activities in surface soils of Stara Planina Mountain and soil characteristics were investigated in this study. Radiocaesium activity is significantly correlated with organic matter content and cation exchange capacity. The correlation with clay was not found probably due to the absence of clay structures with high capacity of radiocaesium adsorption.

#### Introduction

In the radioecological context, radiocaesium (<sup>137</sup>Cs) derived from Chernobyl accident is one of the most hazardous radionuclides because of its long half-life of 30.2 years, high bioavailability and physiological behavior similar to potassium. The specific activity of <sup>137</sup>Cs and its bioavailability vary depending on soil characteristics [1, 2]. Stara Planina Mt. received a high amount of radioactive fallouts derived from Chernobyl accident. In 1988, activity deposition on the ground was found to be up to 71 Bq/m<sup>2</sup> [3].

#### **Materials and Methods**

Soil samples were collected from 37 uncultivated locations in the northern part of Stara Planina Mt. The specific activities of <sup>137</sup>Cs were measured using HPGe gamma-ray spectrometer ORTEC-AMETEK (34% relative efficiency and 1.65 keV FWHM for <sup>60</sup>Co at 1.33 MeV). Soil pH was determined in distilled water and in 1 M KCl solution, in a solid-liquid (S/L) ratio of 1:2.5 mL g<sup>-1</sup>. Organic matter (OM) content was determined by dichromate digestion based on Walkley-Black method [4]. The total cation exchange capacity of the sorptive complex (CEC) was calculated as the sum of the hydrolytic acidity and total exchange bases, both measured according to Kappen [5]. The traditional pipette method was used for particle size analysis [6]. Once the organic matter had been removed, the remaining mineral sample was weighed and subjected to particle size analysis to determine the following fractions: coarse sand (0.2–2 mm), fine sand (0.05-0.2 mm), silt (0.002-0.05 mm) and clay (<0.002 mm).

#### **Results and Discussion**

Basic statistics of <sup>137</sup>Cs specific activities and soil characteristics is summarized in Table 1.

**Table 1.** Basic statistics of <sup>137</sup>Cs activities and soil characteristics

Parameter	Me	ean	S	D	M	in	M	ax
Depth (cm)	0-10	10-20	0-10	10-20	0-10	10-20	0-10	10-20
<sup>137</sup> Cs (Bq/kg)	22.4	12.6	11.9	12.9	3.90	1.69	58.7	72.1
$pH_{H2O}$	6.41	6.41	0.98	1.07	4.70	4.48	7.97	7.92
$pH_{KCl}$	5.22	5.10	1.18	1.27	3.34	3.25	7.02	7.09
CEC (cmol/ kg)	26.7	25.6	19.3	22.2	5.10	5.40	76.3	80.8
OM (%)	6.83	5.43	3.36	3.52	1.98	1.60	14.8	14.0
Coarse sand (%)	24.2	23.2	13.4	13.7	1.30	0.10	46.3	45.5
Fine sand (%)	13.1	12.8	7.80	6.88	2.00	0.80	34.8	32.1
Silt (%)	48.6	47.1	14.7	14.2	23.7	12.6	78.0	71.7
Clay (%)	14.1	16.6	6.40	12.6	6.20	5.80	28.8	75.5

The correlation between analyzed parameters are presented in Table 2.

**Table 2.** The Pearson correlation matrix for <sup>137</sup>Cs and soil characteristics

	<sup>137</sup> Cs	$pH_{\rm H2O}$	$pH_{KCl}$	CEC	OM	Coarse sand	Fine sand	Silt	Clay
<sup>137</sup> Cs	1.00	-0.17	0.00	$0.40^{*}$	0.61**	-0.15	-0.19	0.22	0.04
$pH_{H2O}$	$0.01^{\#}$	1.00	0.91**	0.59**	0.16	-0.51**	-0.48**	0.59**	0.30
$pH_{KCl}$	0.16	0.93**	1.00	0.71**	0.34	-0.56**	-0.36*	0.60**	0.24
CEC	$0.36^{*}$	0.56**	0.72**	1.00	0.63**	-0.54**	-0.56**	0.76**	0.07
OM	0.61**	0.15	0.33*	0.59**	1.00	-0.13	-0.38*	0.39*	-0.15
Coarse sand	0.10	-0.52**	-0.47**	-0.44**	-0.15	1.00	0.50	-0.85**	-0.74**
Fine sand	-0.19	-0.51**	-0.48**	-0.58**	-0.40*	0.61**	1.00	-0.80**	-0.41*
Silt	0.21	0.44*	0.50**	0.68**	0.46**	-0.67**	-0.70**	1.00	0.46**
Clay	-0.27	0.33*	0.18	-0.01	-0.21	-0.65**	-0.39*	-0.05	1.00

<sup>#</sup>Values above the diagonal (correlation coefficients of 1.00) are for depth of 0-10 cm and those under the diagonal for the depth of 10-20 cm.

Radiocaesium showed a wide range of specific activities as a consequence of many parameters such as physicochemical properties of soil, the rainfall, and the biological and physicochemical processes in the natural environment. The specific activities of <sup>137</sup>Cs were decreased with increasing depth in the soil and these results mean that <sup>137</sup>Cs moves slowly into deeper soil. Numerous studies conducted worlwide have shown that there is a clear vertical gradient of radiocaesium distribution in most natural soils [7].

<sup>\*\*</sup>Correlation is significant at 0.01 level, \*Correlation is significant at 0.05 level

Correlations between  $^{137}$ Cs and the main soil properties were established, but few were significant. In these soils,  $^{137}$ Cs was positively correlated with CEC (r = 0.40) and with organic matter content (r = 0.61). The high CEC and organic matter contents of soil affect the retention of the fallout radionuclides [2, 8].

Clay minerals are known to absorb <sup>137</sup>Cs very strongly [9-11]. High clay content generally implies a slow migration of <sup>137</sup>Cs. In this study, no significant correlation between <sup>137</sup>Cs and the clay percentage was found. Clays can be constituated of many minerals like caolinite, montmorillonite, illite, vermiculite, nontronite, hydrous mica etc. Some of these minerals have lower sorption capacities (montmorillonite, and especially caolinite). An piossible explanation would be that soils from Stara Planina Mt. do not contain enough clay, particulary illites, to immobilise caesium. Before definite conclusions are drawn, more systematic data and further analyses of the clay structure are required.

#### References

- [1] M.M. Rahman, G. Voigt, J. Environ. Radioactivity, 2004, 71, 127-138.
- [2] M.H. Lee, C.W. Lee, J. Environ. Radioactivity, 2000, 47, 253-262
- [3] Environmental Radioactivity in Yugoslavia. Federal Commission for Work, Health and Social Politics, Belgrade, 1990.
- [4] L.P. van Reeuwijk, Procedures for soil analysis. Technical paper 9 of the international Soil Reference and Information Centre (ISRIC), Wageningen, The Netherlands, 1986, pp. 106.
- [5] H. Kappen, Die Bodenazidität, Springer Verlag, Berlin, 1929.
- [6] D.L. Rowell, Bodenkunde. Untersuchungsmethoden und ihre Anwendungen, Springer, Berlin, 1997.
- [7] P.L. Nimis, Stud. Geobot., 1996, **15**, 3-49.
- [8] S. Staunton, C. Dumat, A. Zsolnay, J. Environ. Radioactivity, 2002, 58, 163-173.
- [9] B.L. Sawhney, Clay. Clay Miner., 1972, 20, 93-100.
- [10] D.D. Eberl, Clay. Clay Miner., 1980, 28, 161-172.
- [11] R.M. Cornell, J. Radioanal. Nucl. Chem., 1993, **171**, 483-500.

# Material Science (H)

### ESR STUDY OF VARIABLE PRESSURE DEPOSITED PHOTO-CVD SILICON NITRIDE THIN FILMS

#### G.M. Nikolić

Department of Chemistry, Faculty of Medicine, Bulevar dr Zorana Đinđića 81, 18000 Niš, Serbia, e-mail: goranhem@yahoo.com

#### **Abstract**

Silicon nitride thin films were deposited at 250°C by the mercury-sensitized photo-CVD method using pure SiH<sub>4</sub> and NH<sub>3</sub> gases. The structural properties of the films deposited at different reaction chamber pressures, other deposition conditions being the same, were evaluated by ESR spectroscopy. ESR results for samples obtained in this study indicate that increase of reaction chamber pressure favored the formation of nonstoichiometric Si-rich silicon nitride thin films.

#### Introduction

Low temperature deposited silicon nitride thin films have numerous applications in fabrication of various solid state electronic devices [1]. At present, low temperature silicon nitride film deposition for semiconductor device fabrication is mainly achieved by plasma-enhanced chemical vapor deposition (PECVD). However, damage produced by ionic and electronic bombardment of the deposited film and/or underlying substrate could be a serious disadvantage of the PECVD process in some applications. As a good alternative for damage-free low temperature silicon nitride deposition the mercury-sensitized photochemical vapor deposition (photo-CVD) process has been suggested [1,2].

In this paper the results of electron spin resonance (ESR) study are presented for mercury-sensitized photo-CVD silicon nitride films deposited at different total pressures of reactant gases.

#### **Experimental**

A modified Samco PD-10 PECVD reactor was used in this study for silicon nitride film deposition. Reaction design was basically the same as for photo-CVD reactors described in the literature [2,3]. Pure SiH<sub>4</sub> and NH<sub>3</sub> with flow rates of 3 sccm and 12 sccm, respectively, were used for silicon nitride deposition on fused silica glass substrates at the temperature of 250°C. Deposition time was 120 minutes for all the samples and total reaction chamber pressure was varied from 25 to 200 Pa by adjusting the pumping speed of diffusion pump.

An X-band Varian E 109 system was used for the ESR measurements at room temperature.

#### **Results and Discussion**

Figure 1 shows the dependence of photo-CVD silicon nitride film thickness as a function of reaction chamber pressure. Similar dependence of the film deposition rate on the reaction chamber pressure was already described in the literature and explained by considering the rate constants of most significant secondary reactions occurring in the gas phase during the deposition process [4].

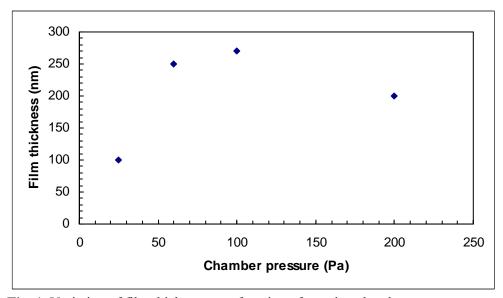
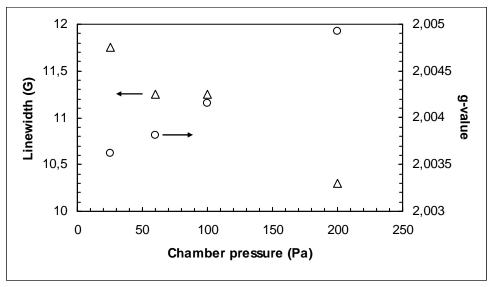


Fig. 1. Variation of film thickness as a function of reaction chamber pressure.

ESR signals recorded at room temperature for photo-CVD silicon nitride films obtained in this study consisted of one broad slightly asymmetric absorption band and therefore they could be attributed to Si dangling bonds [5,6]. Fig. 2 presents the dependence of ESR signal *g*-value and linewidth on the reaction chamber pressure.

With increasing reaction chamber pressure *g*-value of ESR signal increased and linewidth decreased. Such changes of *g*-value and linewidth of ESR signals were usually observed when SiH<sub>4</sub>/NH<sub>3</sub> gas flow ratio was increased both for PECVD [5] and photo-CVD [7] silicon nitride thin films resulting in the formation of nonstoichiometric Si-rich films. The conclusion that increase of the reaction chamber pressure favored the Si-rich silicon nitride films formation is also in accordance with the data showing that photo-CVD silicon nitride films resistivity decreased when the reaction chamber pressure was increased [8].

Spin density of photo-CVD silicon nitride films obtained in this study was higher in comparison with the high quality PECVD silicon nitride [5] but showed no regular dependence on the reaction chamber pressure.



**Fig. 2.** Dependence of ESR signal *g*-value (circles) and linewidth (triangles) on the reaction chamber pressure.

#### Acknowledgement

The author is indebted to Prof. Tatsuo Shimizu and the staff of his laboratory at Kanazawa University (Japan), where the main part of this work has been done, for continuous encouragement and support. The Japanese government (Monbusho) provided a scholarship for the author's research stay in Japan.

#### References

- [1] O.P. Agnihotri, S.C. Jain, J. Poortmans, J. Szlufcik, G. Beaucarne, J. Nijs, R. Mertens, Semicond. Sci. Technol., 2000, 15, R29-R40.
- [2] K. Hamano, Y. Numazawa, K. Yamazaki, Jpn. J. Appl. Phys., 1984, 23, 1209-1215.
- [3] E. Fourmond, G. Dennler, R. Monna, M. Lemiti, A. Fave, A. Laugier, Sol. Energy Mater. Sol. Cells, 2001, 65, 297-301.
- [4] V.K. Rathi, M. Gupta, R. Thagaraj, K.S. Chari, O.P. Agnihotri, Thin Solid Films, 1995, **266**, 219-223.
- [5] A. Morimoto, Y. Tsujimura, M. Kumeda, T. Shimizu, Jpn. J. Appl. Phys., 1985, 24, 1394-1398.
- [6] W.L. Warren, J. Kanicki, F.C. Rong, E.H. Poindexter, J. Electrochem. Soc., 1992, 139, 880-889.
- [7] G.M. Nikolić, Vacuum, 1990, 40, 144-145.
- [8] S. Yamamoto, M. Migitaka, Jpn. J. Appl. Phys. Pt.1, 1994, 33, 5005-5011.

#### STRUCTURE AND MAGNETIC PROPERTIES OF Nd-Fe-B ALLOYS WITH NONSTOICHIOMETRIC Nd CONTENT

N. Talijan and V. Ćosović

Institute of Chemistry, Technology and Metallurgy, Njegoševa 12, 11000 Belgrade, Serbia

#### Abstract

Two nonstoichiometric rapid quenched Nd-Fe-B alloys in the optimized magnetic state were compared using the X-ray diffractometry (XRD, <sup>57</sup>Fe Mössbauer spectroscopic phase analysis (MS), Transmission electron microscopy (TEM) and SQUID magnetometer. The obtained experimental results suggest that the Nd-Fe-B alloy with the reduced Nd content (Nd<sub>4.5</sub>Fe<sub>77</sub>B<sub>18.5</sub>) in the optimized magnetic state has the nanocomposite structure of Fe<sub>3</sub>B/Nd<sub>2</sub>Fe<sub>14</sub>B and partly α-Fe with mean grain size below 30 nm. The overstoichiometric Nd<sub>14</sub>Fe<sub>79</sub>B<sub>7</sub> alloy, in the optimized magnetic state, has almost monophase structure with the dominant content of the hard magnetic phase Nd<sub>2</sub>Fe<sub>14</sub>B (up to 95 wt. %), with a mean crystallite size about 60 nm, as determined by XRD and TEM analysis. The SQUID magnetic measurements have confirmed the nanocomposite structure of the Nd-low alloy and nanocrystalline decoupled structure of the Nd-rich alloy after the optimal heat treatment.

#### Introduction

Current investigations of permanent magnetic materials based on Nd-Fe-B alloys are focused on three major topics: increase of magnetic energy, improvement of corrosion resistance and reduction of rare-earth content as a way of decreasing prices of final permanent magnets with still significant magnetic energy. A special emphasis is put on the research and development of high-energy permanent Nd-Fe-B magnetic materials and their influence on miniaturization and increase of effectiveness of a wide spectrum of devices, as well as on entirely new constructive solutions in various technical and technological domains. In the optimized magnetic state Nd-rich Nd-Fe-B alloys consist predominantly of the main hard magnetic phase Nd<sub>2</sub>Fe<sub>14</sub>B with minor quantities of soft magnetic phases situated on the grain boundaries of the main magnetic phase. Consequently, the magnetic properties of Nd rich Nd-Fe-B alloys are under dominant influence of the magnetically isolated grains of hard magnetic Nd<sub>2</sub>Fe<sub>14</sub>B phase [1].

The new nanocomposite permanent magnetic materials based on Nd-Fe-B alloys with reduced amount of Nd are very attractive because of their suitability for production of bonded magnets. The microstructure of this nanocomposite permanent magnet is composed of a mixture of magnetically hard and soft phases. Depending on the alloy composition, the nanocomposite structure in optimized magnetic state can be  $Fe_3B/Nd_2Fe_{14}B \text{ and/or } \alpha\text{-Fe/Nd}_2Fe_{14}B. \text{ Nanocomposite magnets have large saturation magnetic polarization due to the soft magnetic phase, and also have high coercivity$ 

because of the hard magnetic phase. The exchange coupling between soft and hard magnetic phases explains the total hard magnetic property [1-4].

It was found out that the intergranular interactions which have significant influence on the magnetic properties become more pronounced on nanoscale, hence the significant efforts are put into optimization of the microstructure. The main condition for obtaining nanocomposite structure is uniform distribution of soft and hard phase in magnetic matrix where size of grains should be less than 40 nm [1-3]. The key for obtaining optimal microstructure is heat treatment since the phase composition and grain sizes can be controlled by application of appropriate heat treatment.

The paper covers part of the results of comparative study of two characteristic Nd-Fe-B alloys with Nd-low and Nd-rich neodymium content after the applied optimal heat treatment. On the basis of obtained experimental results magnetic properties of investigated magnetic materials were discussed.

#### **Experimental**

For the realization of proposed investigations two types of rapid-quenched Nd-Fe-B alloys were selected, Nd-low Nd $_{4.5}$ Fe $_{77}$ B $_{18.5}$  (12 wt.% Nd) alloy and Nd-rich Nd $_{14}$ Fe $_{79}$ B $_{7}$  (32 wt.% Nd) alloy. Magnetic characteristics of the investigated alloys after subsequent annealing to the optimized magnetic state were measured on a vibrating sample magnetometer. The applied heat treatment regimes were optimized in previous investigations [4-8]. Basic data concerning both powder samples of the investigated alloys are summarized in Table 1.

O	2			C	
Alloy	Preparation met-	Heat	$_{\mathrm{i}}H_{\mathrm{c}}$	$B_r$	(BH) <sub>max</sub>
Anoy	hod	tretment	(kOe)	(kG)	(MGOe)
$Nd_{4.5}Fe_{77}B_{18.5}$	Centrifugal	660°C/	2.8	10 9	10.7
(12 wt.% Nd)	atomization	5 min.	2.0	.6 10.7	10.7
$Nd_{14}Fe_{79}B_7$	Centrifugal	630°C/	16.2	7 4	10.6
(32 wt.% Nd)	atomization	3min	10.2	/ . <del>4</del>	10.0

Table 1. Origin and basic magnetic characteristics of investigated Nd-Fe-B alloys

Phase composition of the investigated alloys after applied heat treatment regimes was determined by the X-ray diffractometry (XRD) and  $^{57}\text{Fe}$  Mössbauer spectroscopic phase analysis. X-ray diffraction measurements were performed on an X'Pert PRO MPD multi-purpose X-ray diffraction system from PANanalytical using Co K $\alpha$  radiation. Mössbauer spectra were taken in the standard transmission geometry using a  $^{57}\text{Co}(Rh)$  source at room temperature. For the spectra fitting and decomposition, the "CONFIT" program package was used [9]. Mean grain (crystallite) size, micro strain and quantitative composition of the identified phases were calculated from XRD data by the FullProf computer program [10]. The X-Ray line broadenings were analyzed through refinement of the TCH-pV function parame-

ters. The microstructure of the investigated alloys in optimized magnetic state was analyzed using transmission electron microscopy (TEM). Magnetic properties of the samples of Nd-Fe-B alloys in optimized magnetic state were measured on the temperature of the ambient, on vibrating sample magnetometer (VSM) with magnetic field strength of 50 kOe and on the Superconducting Quantum Interference Device magnetometer (SQUID) with magnetic field strength  $\mu_0$ H from -5 T up to 5 T was used.

#### **Results and Discussion**

The results of XRD analysis of both investigated raped quenched Nd-Fe-B alloys in optimized magnetic state are presented in table 2.

<b>Table 2.</b> Phase composition and crystallite size of the investigated Nd-Fe-B alloys
with Nd-low and Nd- rich Nd content in the optimized magnetic state

		e <sub>76.2</sub> B <sub>19.5</sub> -low)	<b>Nd<sub>14</sub>Fe<sub>79</sub>B<sub>7</sub></b> (Nd–rich)		
Phases	Content [wt.%]	Crystallite size [nm]	Content [wt.%]	Crystallite size [nm]	
Nd <sub>2</sub> Fe <sub>14</sub> B	43.63	12.4	95	57	
α - Fe	16.54	5	5	59	
$Fe_3B$	39.83	24	-	-	
FeB	identified	-	-	-	
$Nd_{1.1}Fe_4B_4$	-	-	identified	-	
Fe-Nd, Fe-B	-	-	identified	-	

Results of XRD phase analysis of the investigated Nd<sub>4.5</sub>Fe<sub>77</sub>B<sub>18.5</sub> (Nd-low) alloy after optimal heat treatment at 660°C for 5 min show presence hard magnetic phase Nd<sub>2</sub>Fe<sub>14</sub>B, soft magnetic phases with high saturation magnetization, predominantly Fe<sub>3</sub>B and partially α-Fe as well as minor quantities of soft magnetic phases of FeB type. Since the intensities of obtained diffraction peaks of FeB phases are very low it can be assumed that these phases are present in minor quantities and therefore their content was not determined. The contents and mean crystallite sizes of main magnetic phases, determined using FullProf software, are presented in table 2. The calculated mean crystallite size of analysed phases confirms the nanocrystalline structure of the investigated alloy in the optimized magnetic state, with crystallites sizes below 30nm. Together with the obtained phase composition this nanocrystalline structure enables more effective interaction of ferromagnetic exchange coupling, giving the raise to the remanence enhancement. Based on the XRD analysis of the investigated Nd-rich Nd-Fe-B alloy (Nd<sub>14</sub>Fe<sub>79</sub>B<sub>7</sub>) in the optimized magnetic state, the hard magnetic phase Nd<sub>2</sub>Fe<sub>14</sub>B is identified as the primary phase (up to 95 wt.%) with a mean crystallite size about 57 nm and soft magnetic α-Fe phase (5 wt.%) with mean crystallite size of 59 nm.

The MS phase analysis of both investigated rapid quenched Nd-Fe-B alloys corroborates the phase compositions determined by XRD. The obtained MS spectra of both investigated alloys are presented on Fig. 1 and corresponding phase compositions are given in table 3.

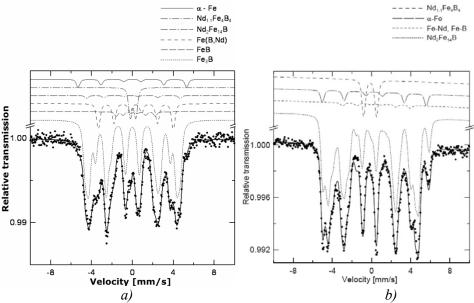


**Fig 1.** Mössbauer spectra of the investigated Nd-Fe-B allys in optimized magnetic state: a) Nd<sub>4.5</sub>Fe<sub>77</sub>B<sub>18.5</sub> alloy, b) Nd<sub>14</sub>Fe<sub>79</sub>B<sub>7</sub> alloy

**Table 3.** Tentative content of identified phases determined by MS phase analysis

Nd <sub>4.5</sub> Fe <sub>7</sub>	B <sub>18.5</sub>	$Nd_{14}Fe_{79}B_7$			
Phase Content		Phase	Content		
Nd <sub>2</sub> Fe <sub>14</sub> B	0.02				
Fe-(B,Nd)/Fe(B)	0.24	$Nd_2Fe_{14}B$	0.87		
Fe <sub>3</sub> B	0.67	Fe-Nd, Fe-B	0.05		
FeB	0.01	α-Fe	0.01		
α-Fe	0.02	$Nd_{1.1}Fe_4B_4$	0.07		
$Nd_{1.1}Fe_4B_4$	0.04				

Given that MS analysis provides more detailed identification of phases containing Fe, apart from main magnetic phases, the presence of other soft and paramagnetic phases was also determined. Although the determined content of Nd<sub>2</sub>Fe<sub>14</sub>B phase is much smaller compared to XRD results, its presence can be assumed as the part of the identified phases of Fe-(B,Nd)/Fe(B) type with overall content estimated to 24 wt.%.

The TEM micrographs (Fig. 2 and Fig. 3), showing the average grain size of both analysed alloys in the optimized magnetic state, confirm the mean crystallite size determined by XRD analysis. The average grain size of Nd-low alloy in the optimized magnetic state determined by TEM analysis is below 30 nm.

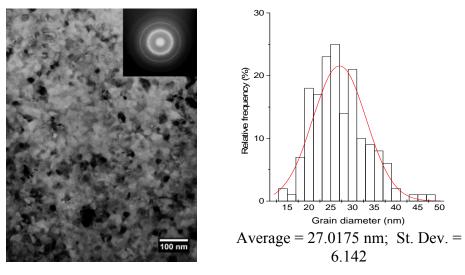


**Fig 2.** Bright field TEM micrograph of Nd<sub>4.5</sub>Fe<sub>77</sub>B<sub>18.5</sub> alloy in optimal magnetic state with grain size distribution

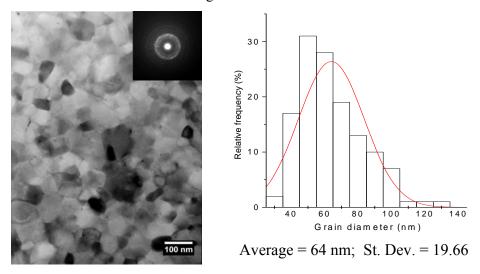


**Fig 3.** Bright field TEM micrograph of Nd<sub>14</sub>Fe<sub>79</sub>B<sub>7</sub> alloy in optimal magnetic state with grain size distribution

The presented grain size distribution indicates that the majority of grains have sizes in the range 20-30 nm. A microdiffraction analysis gave evidence for the mixing of the nano-crystalline phases. This implies that the alloy has a nanocomposite struc-

a)

ture of  $Fe_3B/Nd_2Fe_{14}B$  and partly  $\alpha$ -Fe. TEM analysis of the Nd-rich Nd-Fe-B alloy in the optimized magnetic state has revealed the average grain size on nanoscale ( $\approx$  64 nm). The better agreement between the results of XRD and TEM analysis for Nd-rich alloy can be explained by higher degree of crystallinity of the analysed phases and the fact that the investigated alloy has almost monophase structure, involving less complex calculations. The obtained electron diffraction patterns show very high density of diffraction rings, due to which the reliable identification of present phases was not possible [11].

The shapes of the hysteresis loops obtained by magnetic measurements on SQUID magnetometer are in correspondence with magnetic microstructure of the investigated alloys in the optimized magnetic state.

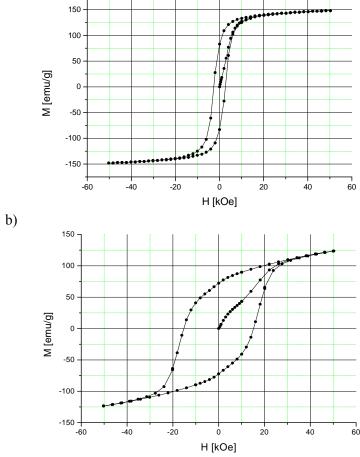


**Fig. 4** Hysteresis loops of the investigated rapid quenched Nd-Fe-B alloys in the optimized magnetic state: a) Nd<sub>4.5</sub>Fe<sub>77</sub>B<sub>18.5</sub> alloy, b) Nd<sub>14</sub>Fe<sub>79</sub>B<sub>7</sub> alloy

The hysteresis loop of the Nd-low alloy presented on Fig. 4a indicates the presence of the interaction of ferromagnetic exchange coupling between the grains

of soft and hard magnetic phases, suggesting the nanocomposite structure of the investigated alloy in the optimized magnetic state. This assumption is supported by the obtained high value of remanence ( $B_r = 10.9 \ kG$ ) and calculated remanence ratio (Jr/Js = 0.6) higher than the theoretical limit for the noninteracting magnetic structures [12]. The shape of the SQUID hysteresis loop of the Nd-rich Nd-Fe-B alloy (Fig. 4b) in the optimized magnetic state implies the presence of the magnetically decoupled nanocrystalline structure. The obtained high value of coercivity ( $_{\rm j}H_c = 16.2 \ kOe$ ) supports this and indicates almost monophase structure of the alloy with dominant content of main hard magnetic phase Nd<sub>2</sub>Fe<sub>14</sub>B.

#### Conclusion

Both the mean crystallite size and grain size of the investigated alloy with reduced Nd content (Nd<sub>4.5</sub>Fe<sub>77</sub>B<sub>18.5</sub>) in optimal magnetic state determined by XRD and TEM analysis were below 30 nm, indicating that in average one grain is composed of one crystallite i.e. all crystalline phases were well crystallized. The value of the remanence ratio Jr/Js>0.5, calculated from the SQUID hysteresis loops, suggests that exchange coupling interactions between grains of the soft and hard magnetic phase exist. This assumption is supported by the higher value of the remanence and (BH)<sub>max</sub>, which are typical for nanocomposite structures of Nd-Fe-B alloys. Correlation of determined phase composition of the investigated Nd-low alloy in the optimized magnetic state (Nd<sub>2</sub>Fe<sub>14</sub>B, Fe<sub>3</sub>B and α-Fe phase), the results of microstructural analysis and measured magnetic properties, implies that the alloy has a Fe<sub>3</sub>B/Nd<sub>2</sub>Fe<sub>14</sub>B and partly α-Fe nanocomposite structure. On the other side obtained experimental results suggest the nanocrystalline magnetically decoupled structure of the Nd-rich (Nd<sub>14</sub>Fe<sub>79</sub>B<sub>7</sub>) alloy in the optimized magnetic state. Determined, almost monophase composition of the alloy, with the dominant content of the hard magnetic Nd<sub>2</sub>Fe<sub>14</sub>B phase, mean grain size on nano scale and measured high value of coercive force confirm this assumption and the hard magnetic quality of this alloy. The presented experimental results clearly illustrate the influence of the Nd content on the structure, phase composition and corresponding magnetic properties of the investigated rapid quenched Nd-Fe-B alloys with nonstoichiometric Nd content.

#### Acknowledgement

The presented work has been supported by the Ministry of Science of the Republic of Serbia under Project OI 142035B. The authors acknowledge support of the National Center for Electron Microscopy, Lawrence Berkeley Lab, which is supported by the U.S. Department of Energy under Contract # DE-AC02-05CH11231.

#### References

- [1] O. Gutfleisch, J.Phys.D:Appl.Phys., 2000, 33, R157.
- [2] A. Manaf, R.A. Buckley, H.A. Davies, J. Magn. Magn. Mater. 1993, 128, 302.
- [3] H.A. Davies, J. Magn. Magn. Mater. 1996, 157–158, 11.

- [4] N. Talijan, Proc. 1st International Workshop on Nanoscience & Nanotechnology IWON, Belgrade, Serbia, 2005, p. 64.
- [5] N. Talijan, T. Žák, J.Stajić-Trošić, V. Menushenkov, J. Magn. Magn. Mater. 2003, 258-259, 577.
- [6] N. Talijan, V. Ćosović, J. Stajić-Trošić, T. Žák, J. Magn. Magn. Mat. 2004, 272–276, e1911.
- [7] .A. Grujić, N. Talijan, A. Maričić, J. Stajić-Trošić, V. Ćosović, V. Radojević, Sci. Sint. 2005, 37, 139.
- [8] V. Ćosović, T. Žák, N. Talijan, A. Grujić, J. Stajić-Trošić, J. Alloys Comp, 2008, 456, 251.
- [9] T. Žák, Mössbauer spectroscopy in material science, in: M. Miglierini, D. Petridis (Eds.), NATO Science Series, Kluwer, Dordrecht, 1999, p. 385.
- [10] Rodriguez-Carvajal, J. 1998 FullProf computer program; ftp://charybde.saclay.cea.fr/pub/divers/fullprof.98/windows/winfp98.zip
- [11] E.F. Kneller, R. Hawig, IEEE Trans. Magn., 1991, 27, 3589.
- [12] V. Ćosović, PhD thesis, The Influence of the Heat Tretment Regime on the Structure and Magnetic Properties of nanocrystalline Nd-Fe-B Alloys With Nonstoichiometric Neodymium Content, TMF University of Belgrade, 2008.

### NON-ISOTHERMAL DEHYDRATION OF EQUILIBRIUM SWOLLEN RADIOLYTICALLY SINTHESIZED Fe<sub>3</sub>O<sub>4</sub> – PVA FERROGEL NANOCOMPOSITE

M.T. Marinović-Cincović, A. Krklješ, N. Bibić and Z.M. Kačarević-Popović Vinča Institute of Nuclear Sciences, 11001 Belgrade, PO Box 522, Serbia (zkacar@vin.bg.ac.yu)

#### **Abstract**

In this study, the Fe<sub>3</sub>O<sub>4</sub> - PVA ferrogel nanocomposite was synthesized by gamma irradiation. Obtained ferrogel had greater swelling capacity and activation energy of dehydratation as measured by thermogravimetric analysis under non-isothermal conditions

#### Introduction

New promising class of materials are ferrogels, a magnetic field sensitive gels, in which magnetic particles of colloidal size are dispersed and incorporated into the gels [1]. When the gels were placed into a spatially non-uniform magnetic field, forces act on the magnetic particles and as result of strong interaction between magnetic particles and polymer chains, they all move together as a single unit. The coupling of hydrogels and magnetic particles has potential application in soft actuators such as artificial muscles [2]. On the other hand, the polymer networks have properties which make the hydrogels suitable for applications in controlled drug delivery systems, while the magnetic particles, with ferromagnetic or superparamagnetic properties are used for magnetic hyperthermia [3].

The purpose of this work was to develop magnetically responsive polymer network based on composites of magnetic particles and hydrogels using gamma irradiation as a crosslinking agent, and to investigate the kinetics of dehydration of equilibrium swollen ferrogel.

The feasibility of this idea was explored by using poly (vinil alcohol) (PVA-Fe<sub>3</sub>O<sub>4</sub>) ferrogel system. PVA and Fe<sub>3</sub>O<sub>4</sub> were chosen because of their well-established biocompatibility and history of clinical usage. Iron oxide is chemically stable, non-toxic and non-carcinogenic with mild magnetic properties and the Curie point near desired heating temperature range [3]. Moreover PVA as a matrix component is selected because it is radiation crosslinking type polymer. Radiation chemistry has proven to be a very effective method to construct three-dimensional polymer networks [4] offering advantages over conventional physical or chemical methods of network formation: mild reaction conditions, negligible formation of by-products, fast gelation, no need for catalysts and finally sterilization.

# Experimental

Iron oxide dispersion was prepared using the method already described, based on the coprecipitation of FeCl<sub>2</sub> and FeCl<sub>3</sub> by adding a concentrated solution of base into the mixture of iron salts [1]. In order to counterbalance the Van der Waals at-

traction and the attractive part of magnetic dipole interactions, additional repulsion between the grains was achieved by electrostatic repulsion due to peptization (with HClO<sub>4</sub>). The deareated solution of PVA (MERCK, molecular weight 72000, degree of hydrolysis 99%) dissolved in distilled water and mixed with ferroflud was irradiated by gamma rays in Co<sup>60</sup> radiation facility at room temperature, at dose rate of 0.5 kGy/h to the total radiation doses of 25 kGy.

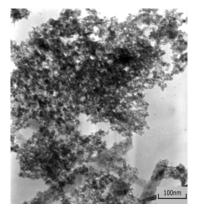
The morphology of the as prepared magnetic particles was exemined by transmission electron microscopy (TEM), Philips EM 400 microscope.

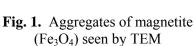
Swelling properties of dried PVA hydrogel (xerogel) and dried ferrogel were investigated at the temperature of 37 °C. At the predetermined time intervals a swollen gel vas removed from the water, gently dried by paper tissue and weighted until constant mass was reached.

Dehydratation was analyzed by thermogavimetric method. Thermogravimetric curves were recorded by a Setaram thermogravimetric analyzer Setsys Evolution 16/18. These analyses were performed with equilibrium swollen hydrogel in platinum pans under Ar atmosphere at a gas flow rate of 16 mLmin<sup>-1</sup>. Experiments were performed at heating rates of 2.5, 5, 10 and 20Kmin<sup>-1</sup> from ambient temperature to 623 K.

#### **Results and Discussion**

The TEM image of a typical sample is shown in Fig.1. It can be seen that Fe<sub>3</sub>O<sub>4</sub> nanoparticles consist of spherical particles several nanometers in diameter.





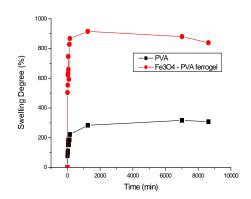


**Fig. 2.** Swelling isotherms of PVA xerogels and dried ferrogel

Figure 2. shows the swelling isotherms of dried ferrogel compared to the PVA xerogel. As can be seen from the presented results the swelling isotherm curves are similar in shape but the overall swelling degree is larger for the Fe<sub>3</sub>O<sub>4</sub>-PVA ferrogel.

Beside the swelling capacity another important factor of hydrogels (and ferrogels) which may affect its usability in various applications is dehydratation. Although the swelling kinetics and swelling behavior of various types of hydrogels are extensively studied, according to our knowledge there are not available investigations concerning the kinetics of the Fe<sub>3</sub>O<sub>4</sub> - PVA ferrogel dehydratation. According to obtained dehydratation curves, activation energy of dehydratation (calculated using Flyn-Wall method) is greater for the ferrogel system, as shown in Fig 3.

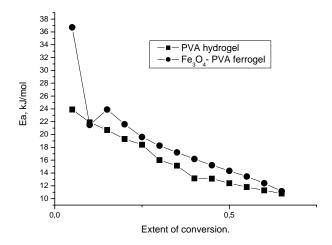


**Fig. 3.** The activation energy plotted as a function of the extent of conversion under non-isothermal conditions

#### **Conclusion**

The Fe<sub>3</sub>O<sub>4</sub> - PVA ferrogel nanocomposite system was successfully synthesized by gamma irradiation. Fe<sub>3</sub>O<sub>4</sub> - PVA ferrogel had greater swelling capacity and activation energy of dehydratation compared to pure PVA hydrogel, as measured by thermogravimetric analysis under non-isothermal conditions.

- [1] M.Zrinyi, L. Barsi, Buki, Polym. Gels Netw. 1997, 5, 415-427.
- [2] R.V. Ramanujan, L.L. Lao, Smart Mater. Struct., 2006, 15, 952-956.
- [3] L.L. Lao, R.V. Ramanujan, J. Mater. Sci. Mater. Med., 2004, 15, 1061-1064.
- [4] A. Krkljes, J. Nedeljkovic, Z. Kacarevic-Popovic, Polym. Bulletin, 2007, 58, 271-279.

# SORPTION OF Cu<sup>2+</sup> IONS ON GEOSYNTHETIC CLAY LINERS

J. Dostanić, A. Milutinović-Nikolić, P. Banković, N. Jović-Jovičić and D.M. Jovanović

IChTM-Department of Catalysis and Chemical Engineering, Njegoševa 12, Beograd, Serbia

#### **Abstract**

The sorption of Cu<sup>2+</sup> ions from aqueous solution by a new type of bentonite-clay-textile synthesized composite was studied. Batch kinetics and isotherm studies were carried out to evaluate the effect of contact time and initial concentration. The Langmuir model was found to be excellent in describing the sorption process.

#### Introduction

Properly designed municipal solid waste landfills (MSWLs) attempt to mitigate transport of different contaminants from MSWLs into the underlying groundwater by incorporating engineered and natural barriers. The ability of barrier systems, such as compacted clay liners (CCLs) and geosynthetic clay liners (GCLs), to sorb or attenuate contaminants through MSWL liner system is an important mechanism to consider when designing such systems. In most of modern landfills composite liners consisting of a geomembrane overlying CCL or GCL are used [1-3].

Although there are a great number of investigations that consider the sorption of heavy metals by natural clay minerals [4-7], there is a lack of references related to the sorption of heavy metals by GCLs.

The aim of this paper was to synthesize a new type of GCL composite based on polyester (PES) nonwoven (NW) and domestic bentonite clay and to evaluate the sorption of Cu<sup>2+</sup> ions from aqueous solution by synthesized composite.

#### **Materials and Methods**

The GCL was synthesized from commercial needlepunched polyester nonwoven ("INTEX", Mladenovac, Serbia,  $m_A$ =300 g/m²) and bentonite clays ("Bogovina", Serbia with particle size < 74  $\mu$ m). Bentonite was applied on NW in the form of the suspension in aqueous solution of adhesive based on modified cellulose soluble in water (Aero Balkan, Serbia). After heat treatment and drying to the constant mass the obtained composite GCL contained 50 mass % of bentonite.

The adsorption of  $Cu^{2+}$  ions from aqueous solution by synthesized GCL was studied according to a batch equilibration procedure. The sorption test was performed on cut-out composite samples each having the same mass (0.5 g) with 50 ml of  $Cu(NO_3)_2x3H_2O$  (Merck) solution in the concentration range from 2.5-10.0 mM. The samples were shaken at  $20\pm 2^{\circ}C$  in a temperature-controlled water bath shaker for 24 h (Memmert WNE 14 and SV 1422). After predetermined periods of time (0.25, 0.5, 1, 2, 4 and 24h), the solutions were filtered using Millipore filters (NY filters with PP housing; pore size  $\leq 0.20 \ \mu m$ ). The concentrations of  $Cu^{2+}$  ions before and after the sorption test were analyzed using Thermo Electron Nicolet

Evolution 500 UV-VIS spectrophotometer in the wavelength range from 550-850 nm. The ion absorption peak at 806 nm was chosen for the estimation of the Cu<sup>2+</sup> concentration, since it had previously been shown that the absorbance in the concentration range from 0.5-200 mM at the chosen wavelength was linear (correlation coefficient is 0.999).

#### **Results and Discussion**

The adsorption data for the relative uptake of Cu<sup>2+</sup> ions on the composite versus contact time at different initial concentrations is presented in Fig. 1.

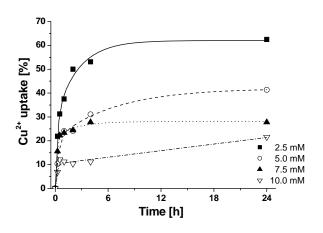


Fig. 1. The influence of contact time and initial  $Cu^{2+}$  concentration on the GCL's uptake of  $Cu^{2+}$ 

The results indicate that the sorption process can be regarded as very fast, since the major uptake of Cu<sup>2+</sup> ions occurs within the first 15 minutes. With the increase of the initial Cu<sup>2+</sup> concentration the percentage of the uptaken Cu<sup>2+</sup> ions decreases. For better evaluation of the investigated process the Langmuir (eq. 1) and Freundlich isotherm (eg. 2) models were applied to the experimental data.

$$\frac{C_e}{q_e} = \frac{1}{q_{\text{max}} K_L} + \frac{C_e}{q_{\text{max}}}$$
 (1)  $\ln q_e = \ln K_F + \frac{1}{n} \ln C_e$  (2)

Where:  $C_e$  is the equilibrium  $Cu^{2+}$  concentration in the solution (mg/dm<sup>3</sup>),  $q_e$  is the amount of adsorbed  $Cu^{2+}$  at equilibrium (mg/g),  $q_{max}$  is the maximum adsorption capacity of the sorbent (mg/g),  $K_L$  is the energy of adsorption (dm<sup>3</sup>/mg),  $K_F$  (dm<sup>3</sup>/g) and n are the Freundlich adsorption constants characteristic for the system and describe the adsorption capacity and adsorption intensity, respectively.

The Freundlich equation is employed to describe heterogeneous systems and reversible adsorption and is not restricted to the formation of monolayers. The Langmuir adsorption isotherm assumes that the adsorption takes place at specific homogeneous sites within the adsorbent and is the most appropriate for monolayer adsorption [8].

Parameters of Langmuir and Freundlich isotherm models are given in. Table 1.

Langmuir constants			Freundlich constants			
q <sub>max</sub> (mg/g)	$K_L(dm^3/mg)$	R	$K_F (dm^3/g)$	1/n	R	
13.09	0.050	0 9999	5 931	0.125	0.9560	

Table 1. Parameters of Langmuir and Freundlich isotherms

According to the results presented in Table 1, both models can be applied to the experimental data, but the correlation coefficient (R) in Langmuir model is closer to unity and therefore is more appropriate.

#### Conclusion

New type of composite with embedded bentonite particles within textile layer was synthesized from domestic raw materials (needlepunched polyester nonwoven and bentonite clay). The adsorption of Cu<sup>2+</sup> ions from aqueous solutions (initial concentrations in the range from 2.5-10.0 mM) by synthesized composite GCL was studied. The batch equilibration procedure using cut-out samples of equal mass at 20± 2°C was performed. The sorption process was found to be very fast. The isotherm data was best fitted by the Langmuir model indicating homogeneous distribution of active sites within the composite and monolayer adsorption. This work has proved that sorption of Cu<sup>2+</sup> ions by GCLs is as good as by bentonite.

#### Acknowledgements

This work was supported by the Ministry of Science of R. Serbia (Projects TR 6712B)

- [1] S.F. Thornton, J.H. Tellam, D.N. Lerner. Waste Manage. Res., 2001, 19, 70-88
- [2] T. Urase, M.Salequzzaman, S.Kobayashi, T.Matsuo, K.Yamamoto, N.Suzuki, Water Sci. Technol., 1997, 36, 349-356
- [3] T.B.Edil, Waste Manage., 2003, 23, 561-571
- [4] H. B. Bradl, J. Colloid Interface Sci., 2004, 277, 1-18
- [5] M.H.Al-Qunaibit, W.K. Mekhemer, A.A. Zaghloul, J. Colloid Interface Sci., 2005, 283, 316-321
- [6] K.G.Bhattacharyya, S. S. Gupta, Chem. Eng. J., 2008, 136, 1-13
- [7] O. Abollino, M.Aceto, M.Malandrino, C.Sarzanini, E.Mentasti, Water Res., 2003, 37, 1619-1627
- [8] N.Jović-Jovičić, A. Milutinović-Nikolić, I.Gržetić, D.Jovanović, Chem.Eng.Technol., 2008, **31**, 567-574.

# FREE AND PHOTOTHERMALLY FORCED ELASTIC VIBRATION SPECTRA OF CANTILEVERS

D.M. Todorović<sup>1</sup>, Y. Song<sup>2,3</sup>, B. Cretin<sup>2</sup> and P. Vairac<sup>2</sup>

<sup>1</sup>Institute for Multidisciplinary Researchs, Beograde, Serbia <sup>2</sup>FEMTO-ST, Université de Franche-Comté, CNRS, ENSMM, UTBM, 32,Avenue de l'Observatoire, 25044, Besançon Cedex, France <sup>3</sup>MOE Key Laboratory for Strength and Vibration, School of Aerospace, Xi'an Jiaotong University, PR China

#### **Abstract**

Dynamic free (spontaneous) and forced (optically excited) elastic vibrations spectra of the cantilever were studied. The experimental amplitude of elastic displacements of cantilevers were measured and analyzed as a function of the frequency. Two obvious peaks were observed in the vibration spectrum (the amplitude signal versus frequency) amplitude. The first peak represents the forced vibrations at the same frequency as the modulation of laser excitation (3 kHz). The second peak at the frequency close to frequency ~ 3.8-4.1 kHz is the first natural resonance of the CL (free vibrations; spontaneous vibrations).

#### Introduction

The photoacoustic (PA) and photothermal (PT) science and technology extensively developed new methods in investigation of semiconductors and microelectronic structures during the last ten years. The PA and PT effects can be important as driven mechanisms for micromechanical structures, especially for cantilevers (CLs) [1]. A new approach for producing compact, lightweight, a highly sensitive micromechanical detector is provided by CL technology, which functions based on the bending of a CL upon absorption of optical energy. When a CL is exposed to optical radiation, the temperature of the CL increases due to absorption of this optical energy. The electronic deformation (ED) and thermoelastic (TE) effects will cause the CL to bend in response to this carrier-density and temperature variations. In previously published papers, the TE and ED effects micromechanically structures were theoretically and experimentally analyzed by Todorović et al. [2,3]. In this work for the first time, dynamic free (spontaneous) and forced (optically excited) elastic vibrations spectra of the cantilever were experimentally studied by photothermal elastic vibration method.

# **Experiment Results**

Silicon CLs with different lengths and thicknesses used in this paper were fabricated using chemical etching process. The small photothermal elastic vibrations of CLs were measured with a laser probe [4,5]. The laser probe is an optical interferometer designed to measure the low amplitude vibration of the micromechanical structures, whose sensitivity is very close to the physical barrier. The small deflec-

tion can be detected below 10 pm magnitude in accurate adjustment conditions. This nondestructive apparatus mainly include optical excitation (doubled Nd:YAG laser, 532 nm), and optical probe detection (the interferometric heterodyne HeNe laser probe). The excitation laser beam is modulated with an acousto-optic modulator (AOM), and the response signal was measured with a FFT spectrum analyzer (the detection range is 0~100 kHz). The measurement results used in this paper are the mean values of at least three measurements at the same conditions. The results have showed that the measurement has good reproducibility.

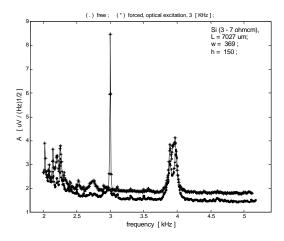
The dynamic elastic vibrations (the spontaneous; without the optical excitation) and (forced; with focused laser beam located at the clamped end) of the Si cantilevers were studied. Figure 2 shows the experimental amplitude elastic vibration spectra for a typical CL (Si, n-type, 3-7  $\Omega$ cm), with dimensions: length  $L = 7027 \mu m$ ; width  $w = 369 \mu m$  and thickness  $h = 150 \mu m$ . The amplitude of vibration is given in  $\mu V/(Hz)^{1/2}$  (the units typical for noise signals), which correspond to an equivalent displacements of 0.8 pm/(Hz)<sup>1/2</sup>. One curve represents the amplitude displacements for CL without the optical excitation (the noise measurement); the second curve is the spectrum with excitation. The modulation frequency of optical excitation is 3 kHz, while the optical probe is located at 5/8 of the CL length (x = 5/8L). Fig.3 shows the experimental spectra of spontaneous vibrations (the noise) for the same CL for two different position of optical probe (the optical probe at x = 0 and x = 3/4L).

# **Analyze of Dynamic Elastic Vibration Spectra**

In Figure 2 two obvious peaks can be observed in the vibration spectrum (the amplitude signal versus frequency) amplitude. The first peak represents the forced vibrations at the same frequency as the modulation of laser excitation (3 kHz). The second peak at the frequency close to frequency ~ 3.8-4.1 kHz is the first natural resonance of the CL (free vibrations; spontaneous vibrations).

There are at least three sources of noise (spontanous) vibrations of CL: (1) thermal vibrations of the CL, (2) noise in the CL mechanical support and (3) noise generated in the interaction of CL with surrounding medium (air). In our case, thermal vibrations of the CL are the dominant noise source under most conditions. As it is possible to see in Fig.2 and 3, in the low frequency range the noise signal increases with the decreasing of the frequency as a consequence of acoustic noise (measurements in air).

Absorption of the optical energy in a semiconductor CL causes the various TD and ED effects. The TE and ED effects are the main driven mechanisms for semiconducting micromechanical structures, especially for CLs. Then, the elastic displacement u(r,t) can be given as the sum of two components: thermoelastic  $u^{TE}(r,t)$  and electronic deformation  $u^{ED}(r,t)$ . The vibration spectrum in Fig.2 (the curves labeled with -\*-) represents the sum of free (thermomechanical) and forced (optically excited) thermal and electronic elastic vibrations.



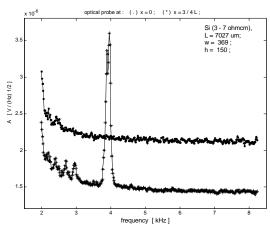


**Fig.2** Experimental amplitude elastic vibration spectra: (.) without the optical excitation; (\*) with excitation.

**Fig.3** Experimental spectra for spontaneous vibrations (noise) of a typical Si cantilever for two different position of optical probe: (-) x = 0; (-\*-) x = 3 / 4 L.

#### Conclusion

The experimental amplitude of elastic bending of cantilevers were measured and analyzed as a function of the frequency. Experimental spectra show peaks: one corresponds to the free (spontaneous, self-excited, thermomechanically excited) vibrations at the first natural resonant frequency and the second peak which corresponds to the forced vibrations at frequency of modulated optical excitation. The optically excited elastic vibrations are the consequence of thermal and electronic elastic effects in Si cantilever. These investigations are in progress.

- [1] D.M.Todorovic, P.M.Nikolic, Ch. 9 in *Semiconductors and Electronic Materials* (A.Mandelis and P.Hess, Eds., SPIE Opt.Eng . Press, Belingham, Washington, 2000, p. 273-318.
- [2] D.M.Todorovic, P.M.Nikolic, A.I.Bojicic, K.T.Radulovic, Phys. Rev. B, 1997., 55(23), 15631-15642.
- [3] D. M. Todorović, Rev. Sci. Instrum., 2003, 74 (1), 578-581.
- [4] B. Cretin and P. Vairac, Appl. Phys. Lett., 1997, **71**(15), 2083-2088.
- [5] P. Vairac, B. Cretin, and A.J. Kulik, Appl. Phys. Lett. ,2003, 83(18), 3824.

### MAGNETIC PROPERTIES OF MAGNETITE NANOPARTICLES BY MONTE CARLO CALCULATIONS

G. Munteanu<sup>1</sup>, C. Miclea<sup>2</sup> and N. Stanica<sup>1</sup>

<sup>1</sup>Ilie Murgulescu, Institute of Physical Chemistry of the Romanian Academy Bucharest, Romania <sup>2</sup>Institute of Res. & Dev. Material Physics, Bucharest, Magurele, Romania

#### **Abstract**

Considering magnetite cubes which have the edges of various lengths and computing their magnetic properties by Monte Carlo method one showed that both Curie point and saturation magnetization depends on the dimension of the nanoparticles. When the length of the cube edge is arround 10-11 lattice constants the magnetic properties are practically identical to those of the bulk magnetite. All the calculations where performed consedering that only the antiferromagnetic exchange interraction between the tethraedral and octahedral sub-lattices exists.

#### Introduction

It is known that magnetite is a ferrimagnetic material consisting of two ferromagnetic sub-lattices coupled by a strong antiferromagnetic interaction. According to these we performed Monte Carlo Metropolis [1] calculations showing that [2] the bulk magnetic properties can be simulated considering that the two ferromagnetic spin exchange interaction integrals are of only 17.15 and 12.25 cm<sup>-1</sup> and the antiferromagnetic interaction is of -24.50 cm<sup>-1</sup>.

We have to stress that these results suggest that the antiferromagnetic interaction is determinant for the magnetic behaviour of this material.

This phenomenon seems to be natural if we take into account the fact that every iron ion from the tetrahedral lattice has twelve octahedral and only four tetrahedral neighbours and, in the same time, the octahedral iron ions have equal numbers of neighbours, six, in both sub-lattices. These observations suggest that the two ferromagnetic arrangements could be determined by the antifferomagnetic interaction between the two sub-lattices.

Consequently, we tried – in a first stage – to simulate the bulk magnetic properties considering only the antiferromagnetic interaction. After that we computed the properties of several nano-magnetite cubes. We did these performing Monte Carlo calculations. In such a procedure it is necessary to consider an enough large structure that has statistically a significant large number of states. This structure has not necessarily to be very large, but the continuity condition must be imposed (to assure that a border ion is equivalent to one from the bulk). In this way, in spite of the fact that the structure has finite dimensions, one simulates the fact that the crystal has an infinite extension.

Suppressing the above condition the ions from the border of the structure are not any more equivalent to those from the bulk. Such an ion interacts with less

neighbours and this fact has to reflected into the magnetic properties. The higher is the ratio between the number of ions which exists at the border and number of the ions from the bulk the higher would have to be the effects on the magnetic properties. We tested this fact considering different cubic particles having the edge from only 3 up to 11 lattice constants.

#### **Results and Discussions**

Naturally, we simulated firstly the magnetic properties of the bulk magnetite. We considered for this – taking into account the above mentioned continuity condition – cubic structures with the edge of only 5 lattice constants. As one may seen in Table 1 the number of the ions is enough large, statistically significant.

Denoting by A the tetrahedral sub-lattice and with B the other, the octahedral one, the energy of one ion from first sub-lattice is

$$E_A = -2J_{AA} \sum_{i=1}^{4} S_A S_i - 2J_{AB} \sum_{i=1}^{12} S_A S_j$$

the energy of one ion from the second being

$$E_{B} = -2J_{BB} \sum_{i=1}^{6} S_{B} S_{i} - 2J_{BA} \sum_{i=1}^{6} S_{B} S_{j}$$

Consequently, the energy of the lattice is

the magnetic specific heat.

$$E = \sum_{i=1}^{N_A} E_{A_i} + \sum_{j=1}^{N_B} E_{B_j}$$

Proceeding in this way we succeeded to fit the computed magnetization curve to the experimental one considering that  $J_{AA} = J_{BB} = 0$  and  $J_{AB} = J_{BA} = -32.7$  cm<sup>-1</sup>. Using these values of the exchange integrals we performed Monte Carlo calculations for nine types of nano-magnetites having the characteristics mentioned in Table 1. There were computed the magnetization, the magnetic susceptibily as well as

**Table 1.** The main characteristics of the Fe<sub>3</sub>O<sub>4</sub> crystallites considered in calculations

		Į.	0115.			
Edge	Edge length	Volume	Total	O <sub>h</sub> ions	O <sub>h</sub> Fe <sup>3+</sup>	T <sub>d</sub> ions
length (l.c.)	(nm)	$(nm^3)$	nr. ions		ions	$(Fe^{3+})$
3	2.424	14	648	432	216	216
4	3.232	34	1536	1024	512	512
5	4.040	66	3000	2000	1000	1000
6	4.848	114	5184	3456	1728	1728
7	5.656	181	8232	5488	2744	2744
8	6.464	270	12288	8192	4096	4096
9	7.272	384	17476	11644	5832	5832
10	8.080	527	24000	16000	8000	8000
11	8.888	702	31944	21296	10648	10648

In Figure 1 we present the saturation magnetization as function of temperature for all the nine structures. One may note that at very low temperatures the magnetization almost does not depends on the dimension of the magnetite crystallite. The dimension of the crystallite has an influence at high temperature: the lower is the crystallite size the lower is the magnetization. As one may be seen in Figure 1 the strongest effect of the crystallite dimension is on the transition temperature. Again the lower is the crystallite size the lower is Curie temperature.

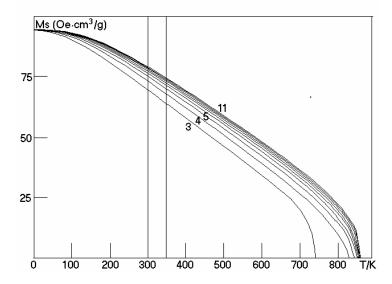


**Fig. 1.** The saturation magnetization as function of temperature for  $Fe_3O_4$  crystallites listed in Table 1.

This size effect is general. It can be noted in the calculations in case of any magnetic material. In case of any magnetic material the spins which exist near the border (on the surfaces, on the edges or in corners) have a lower number of neighbours than any spin from the bulk. Because this effect has not been reported yet as an experimental result we have to ask why? In connection to this problem we may discuss if the models like Ising or Heisenberg are or not appropriate to discribe/explain the magnetic properties of the meterials. But we are afraid that the reason is more deep.

- [1] N. Metropolis, A.W. RosenBluth, M.N. RosenBluth, A.H. Teller, E. Teller, *J. Chem. Phys.*, 1953, **21**, 1087.
- [2] N. Stanica, F. Cimpoesu, G. Dobrescu, V. Chihaia, L. Patron, G. Munteanu, C. G. Bostan, J. Theo. Comput. Chem., 2004, **3**, 179-187.

# THREE-DIMENSIONAL COMPUTER STUDY OF SKELETAL SETTLING DURING LIQUID PHASE SINTERING

#### Z.S. Nikolić

Faculty of Electronic Engineering, Department of Microelectronics University of Nish, 18000 Nish, P. O. Box 73, Serbia.

#### **Abstract**

In this paper we have defined three-dimensional method for computer study of gravity induced skeletal settling and formation of large solid skeleton during liquid phase sintering. Computed microstructures for tungsten heavy alloy substantiated previous observations that the settled solid-volume fraction can be directly related to the solid-liquid density difference but dictated by the formation of a solid skeleton.

#### Introduction

The influence of gravitational effects on grain coarsening during liquid-phase sintering (LPS) is of both fundamental and practical interest in materials science. Settling of solid grains in a two-phase liquid-solid is a phenomenon common to several metallurgical processes including LPS, where solid-liquid segregation in liquid-phase sintered structures is related to the density difference between the solid and liquid phases.

Niemi and Courtney [1] were the first to document quantitatively this solid-liquid segregation phenomenon. They investigated skeletal settling phenomenon and concluded that a solid skeleton formation prevents further settling when a critical solid-volume fraction is reached. As it was proposed by Courtney [2], the formation of solid skeleton is the result of interparticle collisions caused by Brownian motion and/or density difference between solid and liquid.

In this paper we will concern with definition of three-dimensional (3-D) numerical method for simulation of microstructural evolution due to gravity induced skeletal settling during LPS. The method will be based on domain topology (no shape restriction) and skeletal settling based on a settling procedure.

# **Model Topology**

For simulation of LPS we will use 3-D generalization of previously defined 2-D methodology [3]. It can be obtained with setting up a discretized, 3-D simulation domain, defined as a set of identical cubic elements  $CV_{ijk}$  stacked along three orthogonal x, y and z directions, i.e.  $D = \{CV(x_i, y_j, z_k)\}$ , where  $(x_i, y_j, z_k)$  is the center of  $CV_{ijk}$ . A microstructure consisting of S solid-phase domains immersed in liquid matrix can be now completely described by an integer matrix  $\|e_{ijk}\|$ , where the value of the element  $e_{ijk}$  indicates a phase present at  $CV_{ijk}$ , so that  $e_{ijk} > 0$ 

when  $CV_{ijk}$  belongs to the solid phase (i.e. 1,2,...,S), and  $e_{ijk} = 0$  when  $CV_{ijk}$  belongs to the liquid phase.

During LPS domains will be settled due to gravity. As the domains arrive the already settled domains they make contacts with each other and necks between them form. Neck growth will be ended when the equilibrium dihedral angle between the domain boundaries and the liquid is established. Thus a solid skeleton forms.

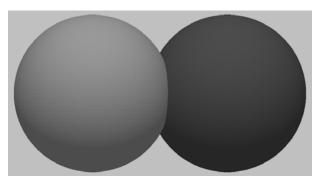


**Figure 1.** Two contacting domains with the neck between them.

Let  $D^a$  and  $D^b$  are two contacting domains due to settling. If the discrete neck surface  $(S_N)$  fulfills the inequality  $S_N \ge S$ , where S is the minimal neck surface, then the domains  $D^a$  and  $D^b$  will form a solid skeleton unit consisting of two domains with a neck between them (Fig. 1). The critical surface S is an empirical parameter.

Generally speaking gravity induced settling can be roughly separated into two stages [4]: free settling of isolated domains and skeletal settling of a connected solid structure. The settling procedure in 3-D can be modeled by domain translation along the gravitational (z) direction.  $D(x_c, y_c, z_c) \mapsto (x_c, y_c, z_c - q(t))$ , where  $(x_c, y_c, z_c)$  is the center of mass of domain D, and q(t) is the average distance that domain should travel within time interval  $\Delta t$  [3]. Combined translations in horizontal (x and y) directions (domain sliding over already settled domains) and in gravitational (z) directions modeled can now  $D(x_c,y_c,z_c)\mapsto D(x_c\pm q(t),y_c\pm q(t),z_c-q(t))$  , where the signs "+" or "-" can be taken at random. It should be noted that this translation is very similar to assumed scenario of Courtney [2].

In LPS domain coarsening occurs by mass transport through the liquid surrounding domains, with a corresponding driving force determined by the solubility of solid-phase domains. In that sense, 3-D flux for the element  $CV_{i,j,k}$  can be computed as  $J_{ijk} = J^x_{ijk} + J^y_{ijk} + J^z_{ijk}$ , where the flux components can be modeled on similar way as in [3]. Starting from the time dependent domain topology  $D = \{(x_c(t), y_c(t), z_c(t)), \langle r(t) \rangle \}$ , time dependent domain evolution can be now modeled on similar way as in 2-D [3].

#### **Results and Discussion**

For the simulation of gravity induced skeletal settling during LPS of tungsten heavy alloy we will use numerical models defined above. In this calculation the same data [3] will be used. For simulation we will apply an initial randomly generated model containing non-uniformly distributed domains of different radii (Fig. 2a). Figure 2b shows microstructural evolution of liquid phase sintered W-Ni after 110 min. It was observed that after a very short time pure settling of isolated domains was almost finished with formed necks between contacting domains. Due to combined translation some domains have formed bonds with neighboring domains prior finishing complete settling and producing chain-like clusters. It means that densification inside these regions was stopped, although further densification through solid-skeleton densification was possible, too. The computed microstructures obtained have shown that the settled solid-volume fraction is dictated by the formation of a solid skeleton and can be directly related to the solid-liquid density difference.

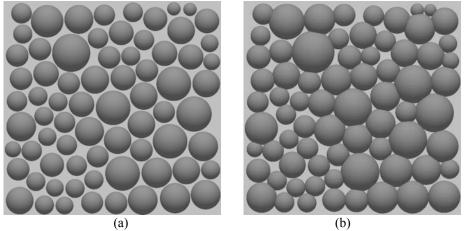


**Fig. 2**. (a) Initial model. (b) Computed microstructures for LPS of W-Ni after 110 min. Domains are dark-gray colored and liquid is light-gray colored.

# Acknowledgements

The present work was performed under the project (No. 142011) supported financially by the Ministry of Science of Serbia.

- [1] N. Niemi and T. H. Courtney, Acta metall. 1983, **31**[9], 1393-1401.
- [2] T. H. Courtney, Metall. Trans. 1977, **8A**, 679-684.
- [3] Z. S. Nikolic, Numerical simulation of gravity induced skeletal settling during liquid phase sintering, Submitted to Computers and Mathematics with Applications, 2007.
- [4] T. H. Courtney, Scripta Mater., 1996, 35 [5], 567-571.

#### BIOCOMPATIBLE NANOSTRUCTURE MATERIALS

M. Nenadović, M. Novaković, M. Popović, Z. Rakočević and T. Nenadović *Institute of Nuclear Sciences "Vinča"*, Laboratory for Atomic Physics, 11001 Belgrade, Serbia

#### Abstract

Materials suitable for medical systems have always been the product of interdisciplinary collaboration between material and biological science. As well as different area of physics and chemistry. For medical application materials must not damage blood cells or bones and must be resistant. Some implant materials for chemical bonds can be stabilized by implantation of different elements or deposition of very thin films. In this work we presented some results for replacement of damaged human tissues.

#### Introduction

Material scientists and engineers are now developing new processing methods that require little or no reliance on imported materials and yield more efficient and cost effective products. No single synthetic materials has satisfied all biocompatibility requirements but several substances have provided to be usable. Progress has been great .New polymers , ceramics, glasses and composites are among the many materials now enabling medical engineers to design innovative , and increasingly biocompatible, replacements for damaged human tissues. A rapid development in recent years has been derived from the large number of grain bounderies compared to large fraction of atoms at the surface on nanocrystaline materials.[1]

One of the most important characteristics of nanoparticles is their high surface to volume ratio and consequently large fraction of surface atoms. Because of large fractions of surface atoms nanoparticles exhibit distinctly different properties comparing to the bulk of the same chemical composition. When the concentration of atoms or ions in solids became sufficiently high they aggregate in to small clusters. This clusters coalesce and grow to form larger cluster assembly. Thus, the nanoparticles are often built-up from a full-shell cluster of atoms having cubic or hexagonal closed-packed structure. Such a structure can be constructed from a central atom surrounded by a first shell of 12, a second of 42, at third of 92 atoms, etc.[2]

Materials suitable for medical application have always been the results of interdisciplinary collaborations among investigators in materials science, bioengineering, biological science and clinical medicine. The success application of new biocompatible materials depends especially on progress in discovering properties of materials particularly the properties of the surface. The progress in vacuum science and techniques of characterization will help us in development of new biocompatible materials. At present biomaterials are important for application from intraocular lens replacement to artificial hearts. The progress has been so great that we can not describe promising systems and materials on the market or under stud-

ies. We shall therefore limit ourselves to several examples of medical system developed in Laboratory of Atomic Physics in Vinca Institute of Nuclear Sciences. To be acceptable as a biomaterial a substance must pas chemical and mechanical studies and has to be biocompatible. It means that it must interact with human tissue in a nontoxic, controlled and predictable way. In our laboratory we have made a lot of experiments with osseous, or bones, dental implants and stents used in cardio surgery.

#### Results

Significant progress has been made in understanding of different aspects of synthesis of nanomaterials, nanoparticles and the commercial products. New technology includes a wide range of vapor liquid and solid state processing roads.

Materials for osseous or bone implants must be rigid and stress resistant. Bone implant should ideally reside in the bone without interfering with bone remineralization and must have the surface without changes and damaged zone. Because of that the bone surface must be prepared by electrochemical polishing or CVD preparation, ion beam preparation of bone surface and PVD preparation technique and by implantation. Metallic prostheses are usually used for orthopedic and as dental implants. On the figure 1 artificial hip joint is presented. The surface of the bone is prepared by mechanical polishing and because of that patient has problem with two surface layers (destroyed surface layers and deformed surface layer).

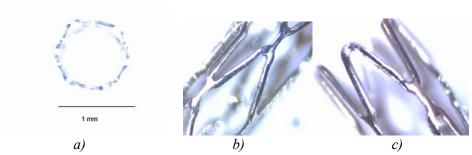


Fig. 1. Artificial hip joint prepared only by mechanical polishing of the surface.

They are made from chrome or cobalt alloys (steels) or titanium alloys. Bio material infection can be a serious problem for clinical application of implanted biomedical material. In contact with living materials at the surface it is an easy channel for bacterial proliferation. To prevent adhesion and colonization of biomaterials some experiments are focused on modification of implant surface by ion implantation.[3]

Some good results are obtained for dental implants. Implants are made from nanostructure titanium alloys (Ti,Al,V). Because of the infection and rejection risk metallic dental implants do sometimes inflammatory reaction at the implant side.

For cardiovascular systems materials have to be elastic and blood compatible. The earliest medical heart valve were made from stainless steel and silicon rubber. These material were durable but anticoagulant treatment was necessary to prevent blood clot formation. On figure 2 cardiovascular stent is presented.



**Fig.2.** (a-c) Cardiovascular stent: a- stent diameter 1 mm( top view) , b and c – length structure (magnification 20 x).

There is a great interest for the human skin and musculoskeletal system. The replacement of this parts of human body have particular importance in material science. [4]

#### Conclusion

Decision of choosing one material rather than another can be made in quantitative terms. In these work we are presented only the results obtained in our laboratory concerning hip joints, dental implants and cardiovascular stent.

## Acknowledgements

This research was financially supported by the Ministry of Science Republic of Serbia, project No. 141001.

- [1] S.C.Tjong and H.Chen, Mat. Sci. and Engineering, 2004, 45, 1-356.
- [2] T.Nenadović, Oplemenjeni Materijali, BIGZ, Beograd 2001.
- [3] J.X.Li, J.Wang, L.R.Shen, Surf. and Coat. Technology, 2007, 201, 8155-8159.
- [4] N.R.James, A.Jayakrishnan, *Biomaterials*, 2003, 24, 2205-2211.

# ENCAPSULATION OF HORSERADISH PEROXIDASE INTO POLY(D,L-LACTIDE) BY THE MODIFIED PRECIPITATION METHOD

I. Jovanović<sup>1</sup>, B. Nedeljković<sup>2</sup> and N. Ignjatović<sup>1</sup>

<sup>1</sup>Institute of Technical Sciences SASA, Belgrade, Serbia <sup>2</sup>Faculty of Technical Sciences, University of Čačak, Serbia

#### **Abstract**

Biodegradable microspheres such as those made of poly-D,L-lactide (PDLLA) are widely investigated delivery systems for drugs or antigens. The aim of this study was to examine experimental conditions in order to produce PDLLA microspheres with the best properties for controlled and sustained delivery of proteins. Horseradish peroxidase (HRP), as an example of hydrophilic drug, was encapsulated within the particles as model protein. The size of microspheres ranged between 460 and 1130 nm, according to the preparation conditions.

#### Introduction

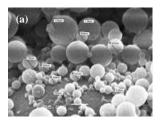
Injectable PDLLA microspheres containing proteins or peptides as controlled release devices have been widely used for the treatment of human diseases and animal health. Fundamental understanding of the relationship among the size of microspheres, encapsulation efficiency and protein release capacity are essential for the design of microsphere delivery systems [1,2]. The modified precipitation method [3,4] is amethod of encapsulating hydrophilic drugs, especially protein and peptide ones, into microspheres. Since the release profiles of proteins dominantly depend on the nature and morphology of the polymer, drug distribution within microspheres and release temperature, the fabrication of microspheres with specific morphology and drug distribution is a challenge for chemical engineers [5]. PDLLA microspheres can protect proteins against biological inactivation and can ensure their release for long time frames, and at specified time. Finally, the size of the particles can be used to passively target the delivery vehicles for uptake by specific types of cells, such as professional antigen-presenting cells, or to target specific tissues [6].

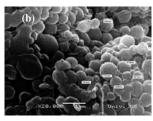
#### **Materials and Methods**

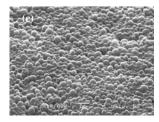
Poly-D,L-lactide with an average molecular weight of 50,000 g/m was purchased from Sigma (Sigma-Aldrich, Germany). Horseradish peroxidase with molecular weight of 45 kDa was used as model protein. Microspheres were prepared by modified precipitation method. The following parameters were varied: co-solvent was methanol or ethanol and the surfactant concentration was 1% w/v or 5% w/v. Individual preparations were repeated at least three times.

#### **Results and Discussion**

The aim of this study was to examine experimental conditions in order to produce PDLLA microspheres with the best properties for controlled and sustained delivery of HRP. The ability to control the size of spheres should facilitate the investigation of their applicability in drug delivery [7]. The sphere preparation technique is so complex that it is very difficult to predict optimum conditions for a specific polymer. In practice, optimal conditions have to be empirically found for each polymer–drug system to be formulated. In this study, the applicability of the modified-precipitation method for obtaining PDLLA-HRP particles was further tested using various types of co-solvents and PVA concentrations.

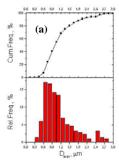


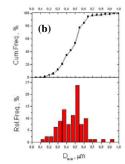




**Fig. 1:** SEM images of PDLLA-HRP microspheres. (a) the first series: co-solvent: ethanol, 1% w/v PVA, (b) the second series: co-solvent methanol, 5%w/v PVA, the third series: (c) co-solvent: ethanol, 5% w/v PVA. Scale bar  $1\mu$ m.

Figure 1. shows SEM images of prepared microspheres. The microspheres are found to be spherical with smooth surfaces. From the results obtained through the stereological examination we can see that particles from the first series are larger, having a size distribution with mean diameter of 1.13 µm (Fig. 2.(a)). The particles from the second and third series are smaller, with mean diameter of 460 nm and 530 nm (Fig. 2.(b) and (c)), respectively. These microspheres are stable for months and, being slightly smaller than erythrocytes, can be intravenously injected to pass unimpeded through circulatory system.





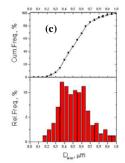


**Fig. 2:** Stereological analysis of PDLLA-HRP microspheres prepared by the precipitation method. (a) co-solvent-ethanol, 1% w/v PVA, (b) co-solvent methanol, 5% w/v PVA, (c) co-solvent ethanol, 5% w/v PVA.

When used in process, the surfactant acts as a chemical barrier preventing the agglomeration of composite particles. A high concentration of emulsifier results in size reduction of produced microspheres (Fig. 1. and Fig. 2.). These results might be due to the effect of PVA in the water phase increasing hydrophilicity of the environment. PVA stabilizes the emulsion droplets, inducing a decrease in particle size and loading efficiency. When PVA concentration in the external water phase increased from 1-5% w/v, there was a decrease in granulometric distribution (series 2. and 3., Figs. 2. and 3.). When alcohol was used as co-solvent in the precipitation method, it diffused to the external aqueous phase due to its hydrophilicity, thus resulting in a faster formation of the solid polymeric shell. The motivation for replacing MeOH with EtOH in pharmaceutical applications is explained by less harmful nature of EtOH. Ethanol is a less polar solvent than methanol, but its viscosity is much higher than that of methanol. The particles obtained with ethanol mostly have perfectly spherical shape, whereas those prepared with methanol are smaller compared to the particles prepared with ethanol (Figs. 1. and 2.).

#### Conclusion

The main advantage of this method is that it does not require an increase in temperature and, therefore, may be useful when heat-sensitive drugs, like proteins, are used. HRP-loaded PDLLA microspheres were successfully obtained by the precipitation method. In addition, the optimal particles were obtained with ethanol and 5% PVA. The mean diameter of the particles was 530 nm, whereas encapsulation efficiency was 46 %.

- [1] Y. Ataman-Önal, S. Munier, A. Ganée, C. Terrat, P.-Y. Durand, N. Battail, F. Martinon, R. Le Grand, M.-H. Charles, T. Delair, B. Verrier, J. Control. Release 2006, 112, 175-185.
- [2] Y.-Y. Yang, T.-S. Chung, X.-L. Bai, W.-K. Chan, Chem. Eng. Sci. 2000, 55, 2223-2236
- [3] M. Stevanović, J. Savić, B. Jordović, D. Uskoković, Colloids Surf., 2007, B 59, 215-223.
- [4] I. Jovanović, B. Jordović, M. Petković, N. Ignjatović, D. Uskoković, Microsc. Res. and Tech. 2008, 71, 86-92.
- [5] F. Mollica, M. Biondi, S. Muzzi, F. Ungaro, F. Quaglia, M. I. La Rotonda, P. A. Netti, J. Mater Sci: Mater Med 2008, 19, 1587-1593.
- [6] M. Liu, Z. Zhou, X. Wang, J. Xu, K. Yang, Q. Cui, X. Chen, M. Cao, J. Weng, Q. Zhang, Polymer 2007, 48, 5767-5779.
- [7] N. Rizkalla, C. Range, F.-X. Lacasse, P. Hildgen, J. Microencapsul. 2006, 23, 39-57.

# APPLICATION OF THE MASTER SINTERING CURVE THEORY TO SINTERING OF BTS FGMS

S.B. Marković and D. Uskoković

Institute of Technical Sciences of the Serbian Academy of Sciences and Arts, Knez Mihailova 35/IV, Belgrade 11001, Serbia (smilja@ffh.bg.ac.yu)

#### Abstract

The master sintering curves (MSCs) were constructed for two different BTS layer (BTS2.5 and BTS15) in functionally graded materials (FGMs). The MSCs were constructed for data obtained during non-isothermal sintering of BTS FGMs using a heating microscope at two constant heating rates (2 and 10 °/min) up to 1420 °C. The concept of MSC was used for calculation of the activation energy. Values of 65.4 and 95.2 kJ/mol were obtained for layers BTS2.5 and BTS15, respectively. Knowing these values it can be possible to control and plan the sintering process of FGMs, which is important for preparation of high-quality FGMs.

#### Introduction

Functionally graded materials (FGMs) belong to an attractive class of materials, with a gradient of properties which cannot be obtained in any monophase materials. Continuous changes in the properties of these materials, for instance: composition, grain size, porosity, etc., result in the gradient of their features such as mechanical strength and thermal conductivity. During the years, FGMs have found applications as various functional materials, for example as piezoelectric ceramics.

 $BaTi_{1-x}Sn_xO_3$  (BTS) FGMs are very useful because they have a high dielectric constant in a wide temperature range. Width of transition temperature range for BTS FGMs depends on number of the layers, as well as on gradient of tin content.

Fabrication of FGMs by powder technology brings significant problems due to deformations of the components. At the same thermal conditions, BTS powders with different tin content show different extents of shrinkage during sintering, as well as different final density. This phenomenon can lead to excessive shape distortion, warping, delamination, developments of cracks and microstructural damage in the sintered FGMs consist of those powders. Therefore, it is desirable to predict the sintering process for different layer in FGMs and design sintering strategies to achieve high quality FGMs without any form of deformation.

Bi-layered FGMs consist of BTS2.5 and BTS15 layers were prepared. Shrinkage of each BTS layer in FGMs was studied as a function of tin contents and sintering heating rates. MSCs were constructed for BTS2.5 and BTS15 layers in FGMs.

# **Experimental**

BaTi<sub>1-x</sub>Sn<sub>x</sub>O<sub>3</sub> powders (x=0.025 and 0.15, denoted as BTS2.5 and BTS15, respectively) were prepared by a solid state reaction between BaCO<sub>3</sub>, TiO<sub>2</sub> and SnO<sub>2</sub>. Theoretical density ( $\rho_T$ ) of BTS2.5 and BTS15 powders was 6.08 g/cm<sup>3</sup> and 6.23 g/cm<sup>3</sup>, respectively. The BTS powders were stacked sequentially in die with gradi-

ent changes in composition; they were uni-axial pressed into cylindrical compacts ( $\varnothing$  4 mm and  $h \approx 2$  mm) at 300 MPa. The average green density of the layer was 63.5 %  $\rho_T$  for BTS2.5 and 65 %  $\rho_T$  for BTS15. The samples were sintered in a heating microscope (E. Leitz, Wetzlar, Germany) in order to determine the sintering shrinkage. The experiments were performed in air up to 1420 °C, using a heating rate of 2 and 10 °C/min.

#### **Results and Discussion**

One of the objectives for sintering studies is to predict densification results under different thermal histories. Using a concept of master sintering curve [1,2], it is possible to make quantitative predictions of the densification behavior of powders under arbitrary temperature-time excursions due to a minimal set of preliminary experiments. These predictions can be used in planning sintering strategies, and to achieve high-quality products. For the development of master sintering curves, the parameters in sintering rate equations are separated into those related to the microstructure and those related to time and temperature terms, on the opposite sides of the equation; then the two sides of the equation are related to each other experimentally. The time and temperature dependent side of the equation, for a constant heating rate, can be represented as  $\Theta$  parameter [1,2],

$$\Theta(t, T(t)) = \frac{1}{c} \int_{T}^{T} \frac{1}{T} \exp(-\frac{E_a}{RT}) dT$$
 (1)

where *c* is the heating rate and  $T_0$  is the temperature below no sintering take place.  $\Phi(\rho) = \Theta(t, T(t))$ (2)

The relationship between the density  $(\rho)$  and  $\Theta$  (Eq. (2)) is defined as the master sintering curve [1]. For the construction of MSC, the integral of Eq. (1) and the experimental density should be known. A series of runs at different temperatures (isothermal) or constant heating rate over a range of heating rates are required. Fig. 1 shows

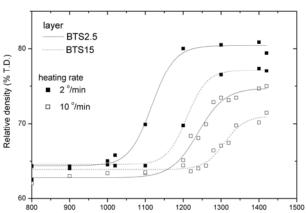


**Fig. 1** Relative density (% TD) *vs* temperature for: layer BTS2.5 (full line) and layer BTS15 (dash line), in BTS2.5-BTS 15 FGM.

the relative density *vs* temperature for BTS2.5-BTS15 FGMs sintered at the heating rate of 2 and 10 °C/min up to 1420 °C. Obviously, the relative density at a low heating rate is higher than at a higher heating rate for the same temperature.

Different shrinkage behavior of the layers with different Sn content can be explained by their different theoretical density, consequently they need different activation energy for sintering, which can lead to different shrinkage i.e. densifi-

cation of layeres BTS2.5 and BTS15. The density curves have the similar shapes and generally shifted to higher temperatures with increasing heating rate (Fig. 1). It can be noted that the sintered densities obtained at any temperature showed a modest but systematic dependence on the heating rate. Furthermore, the density data for BTS2.5 and BTS15 layers, and values calculated from equation (2) were used for calculations of  $E_a$ . A  $\rho$ - $\Theta$  curves were constructed for BTS2.5 layer, for a both heating profiles (2 and 10 °/min), for a chosen values of activation energy. The same procedure was repeated for layer BTS15.

Fig. 2 presents the mean residual squares for the various values of activation energy. After fitting values of 65.4 and 95.2 kJ/mol E<sub>a min</sub> for layer BTS15 is 95.2 kJ/mol were obtained as the  $E_a$ 0.15 minimums for BTS2.5 and Mean residua square BTS15, respectively. The estimated results for acti-0.10 vation energy for layers BTS2.5 and BTS15 BTS2.5-BTS15 FGM are 0.05 similar. indicates that delamination or distortion of FGM are not expected 0.00 during sintering. 100 Ea (kJ/mol)

**Fig. 2** Mean residual square vs  $E_a$  for BTS2.5 and BTS15 layers in FGMs.

#### Conclusion

BTS FGMs show different sintering behavior during different thermal history. Percents of shrinkage increase with decreasing of heating rate during sintering. The concept of MSC was used to calculate the activation energy of sintering for BTS2.5 and BTS 15 layers in FGMs, values of 65.4 and 95.2 kJ/mol were obtained, respectively. Knowing these values it can be possible to control and plan the sintering process of FGMs, which is very important for preparation of high-quality FGMs, without delamination, distortion or other forms of defects.

### Acknowledgments

The Ministry of Science of the Republic of Serbia provided financial support under grant no. 142006.

- [1] H. Su, D.L. Johnson, J. Am. Ceram. Soc. 1996, 79, 3211-17.
- [2] D. Li, S.O. Chen, X.Q. Sun, W.Q. Shao, Y.C. Zhang, S.S. Zhang, Advanc. Appl. Cer. 2008, 107(1), 52-56.

### SURFACE MODIFICATIONS OF TIN COATING BY PULSED IR LASERS: TEA CO<sub>2</sub> AND HF LASER

M. Trtica<sup>1\*</sup>, V. Tarasenko<sup>2</sup>, B. Gaković<sup>1</sup>, A. Panchenko<sup>2</sup> and B. Radak<sup>1</sup>

\*VINCA Institute of Nuclear Sciences, P.O. BOX 522, 11001 Belgrade, Serbia

\*etrtica@vin.bg.ac.yu\*

\*High Current Electronics Institute SB of RAS, Tomsk, 634055, Russia\*

#### **Abstract**

Interactions of a pulsed Transversely Excited Atmospheric (TEA) CO<sub>2</sub> and chemical HF laser with polycrystalline titanium nitride (TiN) coating deposited on high quality steel AISI 316, were studied. It was shown that both lasers, at energy densities of 43 J/cm<sup>2</sup> and 38.6 J/cm<sup>2</sup>, induce morphological changes on the target. The HF laser produces more pronounced damage than the TEA CO<sub>2</sub> laser. The energy absorbed from either of these lasers is mainly converted into thermal energy.

#### Introduction

Surface modification studies of titanium-based ceramic coatings, especially titanium nitride deposited on steel substrates, by various types of energetic beams including the laser beam are of great fundamental and technological interest. There are not many papers in literature dealing with interactions of the TEA CO<sub>2</sub> [1] or HF [2] laser with TiN. The TiN coating has extraordinary properties, applied in industry, microelectronics, bio-medicine, etc.

The present paper deals with morphological effects of pulsed IR lasers emitting at  ${\sim}10~\mu m$  (TEA  $CO_2$  laser) and  ${\sim}2.8~\mu m$  (HF laser) on polycrystalline TiN coatings deposited on high quality steel AISI 316.

# **Experimental**

TiN coatings (typical thickness 1  $\mu$ m) were deposited on a steel substrate by: (i) reactive d.c. magnetron sputtering or (ii) vacuum arc deposition. The steel substrate was in the form of a plate.

Irradiations were performed with laser beams focused by KBr ( $\rm CO_2$  laser) and NaCl (HF laser) lenses of focal lengths 6.0 cm and 13.0 cm respectively. The angle of incidence of the laser beams with respect to the surface plane was 90°. The irradiation was carried out in air, at a pressure of 1013 mbar. Both TEA  $\rm CO_2$  and HF lasers were typically operated in the TEM<sub>00</sub> mode. Conventional  $\rm CO_2/N_2/He$  gas mixtures were used for the TEA  $\rm CO_2$  laser [3] yielding pulses with a gain switched peak followed by a slowly decaying tail. The HF laser operated with typical  $\rm H_2/SF_6$  mixtures [4].

Various analytical techniques were used for characterization of the samples, like X-ray diffraction (XRD); optical microscopy (OM); scanning electron microscopy (SEM) and atomic force microscopy (AFM). The SEM was coupled to an

Energy Dispersive Analyzer (EDX). A profilometer was used to characterize to-pographic changes of the irradiated area.

#### **Results and Discussion**

X-ray analysis of the TiN coating prior to laser irradiation confirmed its polycrystalline structure. Laser induced TiN morphological changes showed dependence on beam characteristics: primarily on the energy density, peak power density, pulse duration, number of pulses, wavelength, etc.

Morphological changes of TiN resulting from 500 and 100 accumulated pulses for TEA  $CO_2$  and HF laser are presented in Figure 1 and 2, respectively. The regime of high *l*aser *r*adiation *e*nergy *d*ensities (LRED) was applied. The induced modifications can be presented as follows:

#### The TEA CO<sub>2</sub> laser

After 500 pulses at 43 J/cm<sup>2</sup> (Figs. 1B1,B2) the morphology features at the surface were: (i) complete removal of the TiN coating, in the central zone, and appearance of relatively rough bottom; (ii) appearance of hydrodynamic effects at the periphery, in the form of resolidified droplets (Fig. 1B1); almost three outer damage zones can be observable at the periphery.

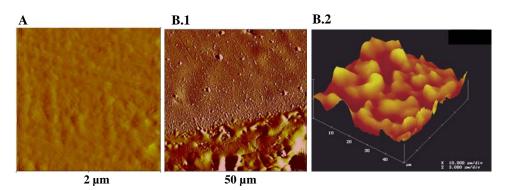


**Fig. 1.** TEA CO<sub>2</sub> laser-induced morphological changes of the TiN coating/steel, AFM analysis. Pulse width 120 ns (initial spike, FWHM). (A), (B)- Views of the TiN prior to and after 500 laser pulses, respectively.

#### The HF laser

The HF laser radiation at 38.6 J/cm<sup>2</sup> modified the TiN coating, Figure 2. Changes on the surface were: (i) ablation of the TiN coating in the central zone accompanied with partial material "lifting", Fig. 2B1; (ii) appearance of the accumulated material in the peripheral direction (crown-like form), Fig. 2B1; and (iii) appearance of roughly three concentric damaged zones on the periphery.

Generally, the energy absorbed from the TEA  $\rm CO_2/HF$  laser beam is assumed to be converted to thermal energy which causes melting, vaporization of the molten material, shock waves, etc. Calculation showed that target surface tempera-

ture reached quite high values, i.e. about 3300 and 4000-6000 K for TEA  $\rm CO_2$  and HF lasers, respectively. These temperatures practically exceed the temperatures for TiN decomposition.

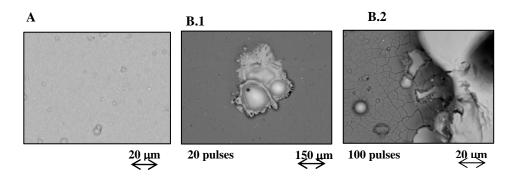


**Fig. 2.** HF laser-induced morphological changes of the TiN coating/steel, SEM analysis. Pulse width 230 ns (FWHM). (A), (B) - Views of the TiN coating prior to and after 100 laser pulses, respectively.

#### Conclusion

A study of morphological changes of TiN coating deposited on steel AISI 316, induced either by a TEA  $CO_2$  or a HF laser is presented. It was shown that both lasers induce morphological changes on the target. The HF laser action at a wavelength of 2.8  $\mu$ m exhibits more pronounced damage than the TEA  $CO_2$  laser at 10.6  $\mu$ m. This is in correlation with a higher TiN absorptivity at the wavelength of 2.8  $\mu$ m. Under the present experimental conditions, it is clear that the IR laser wavelength used has an important role in producing different morphological effects on the TiN coated steel.

# Acknowledgements

This research was sponsored by the Ministry of Science of the Republic Serbia, Contract No. 142065.

- [1] M.S. Trtica, V.F. Tarasenko, B.M. Gakovic, A.V. Fedenev, Lj.T. Petkovska, B.B. Radak, E.I. Lipatov, M.A. Shulepov, Appl. Surf. Sci., 2005, **252**, 474-482.
- [2] B.M. Gakovic, et al., "Surface modif. of ceramic films by TEA CO<sub>2</sub> and HF laser", Conf.: NASM, Septem. 2005, Chester, UK. Abstr. Book, pp. 22-23.
- [3] M.S. Trtica, B.M. Gakovic, B.B. Radak, S.S. Miljanic, Proc. SPIE, 2002, 4747, 44-49.
- [4] A.V. Fedenev, I.M. Goncharenko, N.N. Koval, V.M. Orlovski, V.F. Tarasenko, A.N. Pachenko, E.I. Lipatov, Appl. Surf. Sci., 2002, **197-198**, 45-49.

# SURFACE MODIFICATION OF TiO<sub>2</sub> NANOPARTICLES WITH CATECHOL

I.A. Janković<sup>1</sup>, Z.V. Šaponjić<sup>1</sup>, E. Džunuzović<sup>2</sup> and J.M. Nedeljković<sup>1</sup>

<sup>1</sup>Vinča Institute of Nuclear Sciences, P. O. Box 522, 11001 Belgrade, Serbia

<sup>2</sup>Faculty of Technology and Metallurgy, Department of Physical Chemistry and Electrochemistry,

University of Belgrade, Karnegijeva 4, 11120 Belgrade, Serbia

#### **Abstract**

Surface modification of nanocrystalline  ${\rm TiO_2}$  particles with catechol was found to result in a red shift of the semiconductor absorption compared to unmodified nanocrystallites. The undercoordinated defect sites at  ${\rm TiO_2}$  surface are the source of novel enhanced and selective reactivity of the nanoparticle toward bidentate ligand binding. Catechol, an enediol ligand, have the optimal geometry for chelating surface  ${\rm Ti}$  atoms, resulting in a five-membered ring coordination complex and restoration of six-coordinated octahedral geometry of surface  ${\rm Ti}$  atoms.

#### Introduction

Semiconductor nanoparticles exhibit unique properties being different from those of bulk crystals. The electronic, optical, structural and photoredox properties can be greatly varied by changing the particle size without changing the chemical composition [1]. Controlling the nanoparticle size distribution and surface properties opened up the possibility for their application in microelectronics and photocatalysis.

Titanium dioxide is the photocatalytic material being studied extensively because of its inexpensiveness, nontoxicity, and photostability. Unfortunately, the use of  $TiO_2$  for photocatalytic applications driven by solar light is limited by its wide band gap (E = 3.2 eV) leading to the absorption of less than 5 % of the available solar spectrum photons. There has been tremendous interest in recent years in developing the way for sensitization of  $TiO_2$  for photoexcitation in the visible region [2]. Optical properties of nanocrystalline  $TiO_2$  can be improved by surface modification with electron-donating bidentate ligands. In this work we report optical characterization of  $TiO_2$  nanoparticles, with average diameter of 4.5 nm, modified with catechol

# **Experimental**

All chemicals used were of the highest purity available. All solutions were prepared with triply distilled water. The TiO<sub>2</sub> nanoparticles with mean particle diameter of 4.5 nm were prepared by controlled hydrolysis of titanium (IV) chloride (Fluka), as described elsewhere [3]. Surface modification of TiO<sub>2</sub> nanoparticles was accomplished by dissolution of catechol in TiO<sub>2</sub> colloidal dispersion (pH=2). Spectrophotometric measurements were carried out on a Thermo Evolution 600

UV-vis spectrophotometer and on Thermo Nicolet 380 FTIR (Smart Orbit ATR accessory).

#### **Results and Discussion**

The absorption spectra of TiO<sub>2</sub> nanoparticles and surface modified TiO<sub>2</sub> with increasing concentrations of catechol are presented in Figure 1. It can be seen that the optical properties of TiO<sub>2</sub> nanoparticles change and the onset of absorption shifts by 1.4 eV to the red, compared to unmodified nanoparticles. This can be explained with the complex formation between catechol and Ti atoms on the surface of 4.5 nm TiO<sub>2</sub> nanoparticles. Similar results were obtained when TiO<sub>2</sub> nanoparticles have been modified with various enediol ligands.[4] It was reported that the coordination of Ti surface atoms changes from six coordinate (octahedral) in bulk to pentacoordinate (square-pyramidal) in small particle colloids. Distortion of bond length accounts for the large curvature of small particles and converts surface into more reactive "corner defects". Upon binding with enediol ligands to the surface sites, the asymmetry of these sites is removed, and the bulk structure of the conduction bands is restored.

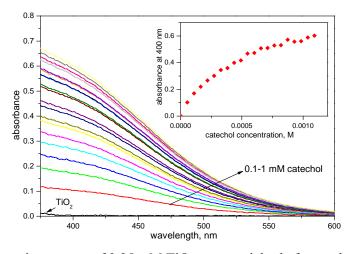


Fig. 1. Absorption spectra of  $3.25 \text{ mM TiO}_2$  nanoparticles before and after surface modification with catechol. Inset:  $A_{400}$  vs catechol concentration

The binding of catechol ligand follows the Langmuir-type adsorption isotherm (Inset of Figure 1) and from the linear dependence

$$\frac{1}{A_{400}} = \frac{1}{KA_{400}^{max}} \frac{1}{\left[cat\right]} + \frac{1}{A_{400}^{max}}$$

binding constant K= (2460±120) mol<sup>-1</sup>dm<sup>3</sup> was obtained.

Using FTIR spectroscopy, we have confirmed bidentate binding of catechol (Figure 2). It is obvious that upon formation of catechol- $Ti_{surf}$  complex infrared spectra different from catechol [5] is obtained. The intensities and the position of the bands corresponding to stretching aromatic ring vibrations  $\nu(C=C)$  are

changed. The bands assigned to phenol OH in-plane bending ( $\delta_{inpl}$  (PhOH), 1100-1200 cm<sup>-1</sup> region) and stretching vibrations (v(PhOh), 1200-1300 cm<sup>-1</sup> region) loose their fine structure while the band assigned to bending in-plane OH vibrations at 1365 cm<sup>-1</sup> disappears completely.

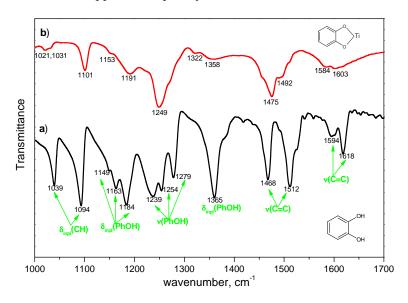


**Fig. 2.** FTIR spectra of dried samples: a) catechol and b) 0.05M catechol-modified 0.18M TiO<sub>2</sub> at pH 2

#### **Conclusions**

Specific binding of catechol modifier to surface "corner defects" on 4.5 nm TiO<sub>2</sub> nanoparticles induces red shift of 1.4 eV in the onset of absorption, compared to unmodified nanoparticles. Formation of bidentate chelating complex is the consequence of an adjustment in the coordination geometry of the Ti atoms near the TiO<sub>2</sub> nanoparticle surface, from octahedral to square-pyramidal in order to accommodate the large surface curvature. Surface modification is alternative method for light sensitisation of large band gap semiconductors.

- [1] O.I. Mićić, T. Rajh, J.M. Nedeljković, M.I. Čomor, Israel J. Chem, 1993, 33, 59-65.
- M.R. Hoffman, S.T. Martin, W. Choi, D.W. Bahnemann, Chem. Rev., 1995, 95, 69-98.
   A. Hagfeldt, M. Grätzel, Chem Rev., 1995, 95, 49-68.
- [3] T. Rajh, Z.V. Šaponjić, O.I. Mićić, Langmuir, 1992, **8**, 1265-1269.
- [4] T.Rajh, L.X. Chen, K. Lukas, T. Liu, M.C. Thurnauer, D. M. Tiede, J. Phys. Chem. B, 2002, **106**, 10543-10552.
- [5] P. Z. Araujo, P. J. Morando, M. A. Blesa, Langmuir, 2205, 21, 3470-3474.

### STRUCTURAL TRANSFORMATIONS OF Fe<sub>75</sub>Ni<sub>2</sub>Si<sub>8</sub>B<sub>13</sub>C<sub>2</sub> AMOR-PHOUS ALLOY INDUCED BY HEATING

D.M. Minić<sup>1\*</sup>, A. Gavrilović<sup>2</sup> and P. Angerer<sup>2</sup>

<sup>1</sup>Faculty of Physical Chemistry, University of Belgrade, Beograd, Serbia,\*dminic@ffh.bg.ac.yu

<sup>2</sup>ECHEM Kompetenzzentrum für angewandte Elektrochemie GmbH,

A-2700 Wiener Neustadt, Austria

#### Abstract

The structural transformations of amorphous  $Fe_{75}Ni_2Si_8B_{13}C_2$  alloy induced by heating in the temperature range  $350\text{-}1000^{\circ}C$  were investigated by using differential scanning calorimetric (DSC) and X-ray (XRD) analyses. During the exothermal stepwise crystallization the formation of solid  $\alpha\text{-Fe}$ ,  $Fe_2B$  and  $Fe_3Si$  phases was established

#### Introduction

The magnetic amorphous alloys possessing excellent soft magnetic properties such as high saturation magnetization, high permeability, low coercivity and loss can be used in power devices, information handling technologies and magnetic sensors [1]. It is well known that the magnetic properties of soft magnetic materials depend on their structure, the structure of domain walls and the domain wall stability. By modifying the structure of ferromagnets, one can control their magnetic properties [2]. This modification can be done by heating as was reported for Fe-Co amorphous materials [3]. Therefore, the investigation of the structural transformations of these materials can contribute to improve their magnetic properties, i.e. the study and control of the amount of crystalline phases formed in these materials is a key of success of their technological applications.

The aim of the present paper is the study of structural transformations occurring in amorphous  $Fe_{75}Ni_2Si_8B_{13}C_2$  alloy during heating.

# **Experimental Methods**

The DSC curves in nitrogen atmosphere for different heating rates were obtained by using SHIMADZU DSC50 analyzer. The amorphous structure prepared by rapid quenching of the melt alloy was proved by X-ray diffraction method. To study the transformation of structure, the samples of alloy were heated at different temperatures in the range 350-1000°C. In order to avoid oxidation problems during heating, each sample was first introduced to a quartz tube, sealed under a vacuum and heated during 30 minutes at a desired temperature. The devitrified crystal samples were then characterized by XRD using CuKα radiation in Bragg-Brentano geometry on an X-Pert powder diffractometer device (PANalytical, Netherlands) at 40kV and 30mA.

#### Results

The DSC curves corresponding to samples of as-prepared ribbon during heating at two heating rates are displayed in Fig. 1. In both cases one observes the existence of two overlapping exothermic peaks in the temperature range 540-580°C associated with crystallization processes occurring during heating.

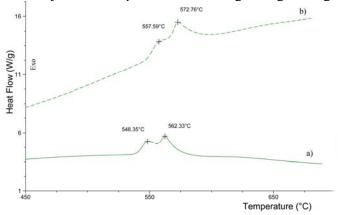


**Fig.1.** DSC curves obtained at heating rates: a) 20 and b)  $40^{\circ}$ C/min

**Table 1.** Phase composition of crystallized alloy

Phase name	Formula	Space group	System	Lattice parameters [nm]				
				a	c			
Iron Boron	Fe <sub>2</sub> B	I-42m	Tetragonal	5.099	4.240			
Iron Silicon	Fe <sub>3</sub> Si	Fm-3m	Cubic	5.670	-			
α-Fe	Fe	Im-3m	Cubic	2.867	=			

Fig. 2 displays XRD patterns of alloy as-prepared and after different heat treatments at temperatures 350, 450, 550, 650, 750 and 850°C. The amorphous state of as-prepared ribbon is confirmed by the broad diffusion halo visible on the related pattern. After a thermal treatment at 450°C, distinct diffraction peaks appear on the XRD pattern indicating the start of crystallization. With increasing temperature, the crystallization rate raises and more peaks are clearly visible on corresponding diffraction patterns pointing the crystallization of alloy. The structures are identified according to peak positions of formed phases (Table 1). The first crystallization stage occurs at 450°C with the appearance of α-Fe and a small contribution of iron-silicon (Gupeiite) phase. After heating up to 650°C, the first peaks of iron-boron phase became visible. It is clear that in the final stage of crystallization at 850°C all three phases are present, α-Fe, Fe<sub>2</sub>B and Fe<sub>3</sub>Si. Despite overlapping effects of the iron-silicon and  $\alpha$ -iron peaks, the existence of specific Gupeiite peaks at small angles (21.2° and 37.6° in 2θ) confirms the presence of this phase. Semi-quantitative grain size X-ray diffraction measurements show that the crystallization process starts with nanosized crystallites and their growth is temperature dependent (Table 2).

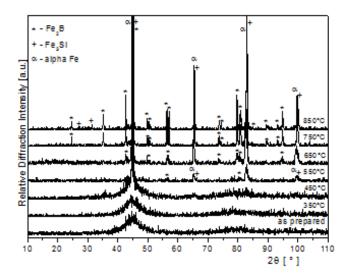


**Fig.2.** X-ray diffraction patterns of Fe<sub>75</sub>Ni<sub>2</sub>Si<sub>8</sub>B<sub>13</sub>C<sub>2</sub> samples as prepared and after thermal treatment at given temperatures.

**Table 2.** Crystallite size, dislocation density and microstrain of alloys heated at different temperatures

	Boı	ron-iron	α−Fe		Iron-silicon		
Temp.	$D_{hkl}$	$ ho_{ m hkl}$	$D_{hkl}$	$ ho_{ m hkl}$	$D_{hkl}$	$ ho_{hkl}$	$\epsilon_{ m hkl}$
[°C]	[nm]	$[m^{-2}]$	[nm]	$[m^{-2}]$	[nm]	$[m^{-2}]$	[%]
550	3.04	$3.25 \cdot 10^{17}$	43.45	$1.59 \cdot 10^{15}$	14.52	$1.43 \cdot 10^{16}$	7.35
650	40.19	$1.86 \cdot 10^{15}$	44.88	$1.49 \cdot 10^{15}$	66.06	$6.87 \cdot 10^{14}$	2.74
750	77.22	$5.03 \cdot 10^{14}$	72.89	$5.65 \cdot 10^{14}$	27.18	$4.06 \cdot 10^{15}$	1.15
850	88.94	$3.79 \cdot 10^{14}$	61.11	$8.03 \cdot 10^{14}$	20.91	$6.86 \cdot 10^{15}$	0.46
1000	97.28	$3.17 \cdot 10^{14}$	72.75	$5.67 \cdot 10^{14}$	-	-	1.32

# Acknowledgements

The investigation was partially supported by the Ministry of Science and Environmental Protection of Serbia, Project 142025 and the K plus programme by the Austrian Research Promotion Agency (Österreichische Forschungförderungsgesellschaft, FFG) and the government of Lower Austria.

- [1] T.Gloriant, S. Surinach, M.D. Baro, J. of Non-crystalline Solids, 2004, 333, 320.
- [2] N.I. Noskova, V.V. Shulika, A.G. Lavrent'ev, A.P. Patapov, G.S. Korzunin, Solid-State Electronics, 2005, 75, 61.
- [3] E.Nunes, J.C.C. Frietas, R.D. Pereira, A.Y. Takeuchi, C. Larica, E.C. Passamani, J. Alloys and Compounds, 2004, **369**, 131.

# AN IMPROVED MODEL FOR SIMULATION OF RAPID SOLIDIFICATION FROM UNDERCOOLED MELT

Z.S. Nikolic<sup>1</sup> and M. Yoshimura<sup>2</sup>

<sup>1</sup>Faculty of Electronic Engineering, Department of Microelectronics University of Nis, 18000 Nis, PO Box 73, Serbia <sup>2</sup>Tokyo Institute of Technology, Yokohama 226-8503, Japan

#### **Abstract**

Complex rapid solidification process kinetics can be solved only by using numerical techniques. In this paper a finite difference method based on control volume methodology and interface-tracking technique for computer simulation of rapid solidification from undercooled melt will be described.

#### Introduction

Rapid solidification (RS) from undercooled melt has attracted much attention because of the large potential for new material properties originating in the refinement of the cast structure, extended solid solubility, metastable crystalline phases and amorphous alloys [1]. However, RS is not easily accessible experimentally due to the simultaneously short time and spatial scales. Therefore, attempts have been made to calculate the operating conditions for the formation of crystalline and amorphous alloys from heat transfer models. In this paper we will describe an improved numerical method based on control volume methodology and interface-tracking technique for simulation of RS from undercooled melt.

#### **Numerical Model**

We will define two-dimensional heat transfer model by considering RS of a solid spherical sample on a solid substrate cooled by water [2]. The governing heat conduction equations, assuming constant conductivity, can be written as:

$$\partial^{2} T_{p}(x, y) / \partial x^{2} + \partial^{2} T_{p}(x, y) / \partial y^{2} = (\rho_{p} c_{p} / \lambda_{p}) \partial T_{p}(x, y) / \partial t$$
 (1)

where T is temperature,  $\rho$  is the density, c is the specific heat capacity,  $\lambda$  is the thermal conductivity, t is time, and the subscript p=1,2 or 3 represents melt, solid and substrate, respectively. For numerical solution of equation (1) we will assume rectangular experimental region replaced by finite difference mesh and defined by grid spacings  $\Delta x$  and  $\Delta y$  for Cartesian coordinates x and y, respectively. Using control-volume methodology [3], the domain (the sample, the substrate) will be a region that is equitably divided into definite number of interconected control volumes,  $CV(x_k, y_k)$ , halfway between neighboring grid points  $(x_k, y_k)$ .

Let we assume that the interface substrate-sample is stable through the entire solidification process and that RS starts at time  $t_{\rm n}$  on the sample bottom surface across the contact interface with the substrate at the nucleation temperature

 $T_{\rm n}$ . Since there is no heat source inside the sample, its surface temperature starts to decrease due to the heat transfer from the sample to the colder substrate and to the ambient. During this process interface starts to change from an initial liquid-solid contact to a solid-solid contact. Afterwards the liquid-solid interface position will be defined by the local equilibrium condition at the solid-liquid interface, i.e.  $\rho_{\rm S} v_{\rm I} L = \lambda_{\rm S} \left. \partial T_{\rm S}(x,y) / \partial y \right|_{\rm I} - \lambda_{\ell} \left. \partial T_{\ell}(x,y) / \partial y \right|_{\rm I}$ , where  $T_{\ell}$  and  $T_{\rm S}$  are the temperatures of the melt and solid phase, respectively, L is the latent heat of solidification, and  $v_{\rm I} = dw/dt$  is the velocity of the solid-liquid interface, where w is the thickness of the solidified layer. Since the interface solid-liquid positions are dictated by the undercooling, for small to moderate undercooling the interface velocity can be related to the interface undercooling  $\Delta T = T_{\rm m} - T_{I(k)}^n$  by the linear kinetics relationship  $v_{I(k)}^n = \mu_{\rm m} \Delta T$ , where  $T_{\rm m}$  is the melting point,  $\mu_{\rm m}$  is the linear kinetic coefficient and  $T_{I(k)}^n$  is the interface temperature in direction k at previous time step. The new interface position in direction k will be now:

$$w_k^{n+1} = w_k^n + v_{I(k)}^n \Delta t . \tag{2}$$

If  $T_{i,j}^n = T^n(x_i, y_j)$  is the temperature of  $CV(x_i, y_j)$  at previous time step, new temperature  $T_{i,j}^{n+1}$  in the sample will be now computed by solving the full system consisting of implicit schemes for numerical solution of equation (1), i.e.:

$$\left[\lambda_{\rm s}/a\Delta x+\lambda_{\ell}/b\Delta x\right]T_{{\rm I}(i)}^{n+1}-\lambda_{\rm s}\,T_{i,j}^{{\rm s},n+1}\Big/a\Delta x-\lambda_{\ell}\,T_{i,j+1}^{\ell,n+1}\Big/b\Delta x=\rho_{\rm s}v_{{\rm I}(i)}^{n}L\,,$$

where  $a\Delta x$  and  $b\Delta x$  ( $\Delta x = \Delta y$ ) are the distances between the interface position ( $w_i^n$ ) and the centers of solidified  $CV_{i,j}$  and liquid  $CV_{i,j+1}$ , respectively, and will be determined by equation (2) for k = i. Similar equation will be written for the interface between solidified  $CV_{i-1,j}$  and liquid  $CV_{i,j}$  and between  $CV_{i+1,j}$  and liquid  $CV_{i,j}$ , as well as for solidification of the sample top before all interior  $CV_i$  have solidified. At time  $t_i$  all  $CV_i$  in the sample will be solidified.

#### **Results and Discussion**

Our model-experiment will be alumina sample of the diameter 0.003 m placed onto Cu substrate of the diameter 0.05 m with assumed substrate-sample circular contact surface of the diameter 0.001 m during RS. For the initial temperature of the sample we will assume melt to be superheated uniformly by 2545 K ( $T_{\rm m}$  + 218 K), and for the substrate and the ambient uniform temperatures 308 K and 300 K, respectively. The thermophysical data used in simulation will be taken from [4]. The developed digital pyrometry system with a silicon photocell for an arc-image furnace [5] will be used for recording temperature data.

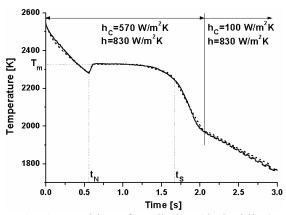


**Fig. 1**. Matching of prediction (dashed line) with experimental data (solid line).

Figure 1 shows typical temperature measurement (solid line) and matching prediction (dashed line) for RS of alumina sample on copper substrate. The specimen was initially liquid and at a temperature above the melting point. When cooling was initiated (by rapidly moving the copper substrate from the focal point), the temperature decreased to the nucleation temperature.

Crystallization released the heat of fusion and reheated the specimen to the recalescence temperature. As one can see, a good match between the prediction and measurement is achieved using  $\Delta T = 50 K$ ,  $h = 830 \, \text{W/m}^2 \text{K}$  (the interfacial heat transfer coefficient),  $h_c = 570 \, \text{W/m}^2 \text{K}$  (the convective heat transfer coefficient). Solidification started at  $t_n = 0.559 \, \text{s}$  when the sample bottom surface reached the nucleation temperature  $T_n = T_m - \Delta T$ . After that the solidification front moved into a supercooled melt, where the melt itself absorbed most of the latent heat and the recalescence took place ( $\Delta t_R = 51 \, \text{ms}$ ). After recalescence, the sample should be cooled down slowly. However, due to convection and radiation, solidification of lateral sample surfaces also occurred. At the same time the sample interior was still at temperature above or very close to  $T_m$ . The total solidification time ( $\Delta t = t_s - t_n$ ) was  $1.105 \, \text{s}$ . After that solidified alumina sample continued to cool down.

# Acknowledgements

The first author performed present work under the project (No. 142011) supported financially by the Ministry of Science of the Repubic of Serbia.

- [1] T. R. Anantharaman and C. Suryanarayana, J. Mater. Sci., 1971, 6, 1111-1135.
- [2] Z. S. Nikolic and M. Yoshimura, Physical Chemistry 2006, 492-494.
- [3] Handbook of Numerical Heat Transfer, edited by W.J. Minkowycz, E.M. Sparrow, G.E. Schneider and R.H. Pletcher, Wiley, New York, 1988, p. 68.
- [4] Z. S. Nikolic, M. Yoshimura, S. Araki and T. Fujiwara, Science of Sintering, 2007, 36, 111-116.
- [5] T. Yamada, M. Yoshimura and S. Somiya, High Temp.-High Press., 1986, 18, 377-388.

# THE EFFECT OF THE VISCOSITY ON NUCLEATION OF GERMANATE GLASS

M.B. Tošić<sup>1</sup>, S.R. Grujić<sup>2</sup>, N.S. Blagojević<sup>2</sup>, V.D. Živanović<sup>1</sup> and J.D. Nikolić<sup>1</sup>

<sup>1</sup>Institute for Technology of Nuclear and other Mineral Raw Materials,

86 Franchet d' Esperey St, 1100 Belgrade, Serbia

<sup>2</sup>Faculty of Technology and Metallurgy, 4 Karnegijeva St.,11000 Belgrade, Serbia

#### Abstract

This paper presents the effect of the viscosity on nucleation behaviour of germanate glass. It was shown that the viscosity of this glass considerably influences the temperature and the time dependence of nucleation rate. The temperature of the maximum nucleation rate,  $T_n^{\text{max}}$ , occurs in the higher temperature range of  $T_{\text{gr}} > 0.6$ .

#### Introduction

Nucleation is the process of formation of the precursors of the crystalline phases, which can be formed by different mechanisms. Commonly, these mechanisms are considered as homogeneous and heterogeneous nucleation. Generally, for analysis of these processes the classical nucleation theory was used [1]. Accordingly, the steady-state homogeneous nucleation rate (I) was described by an exponential dependence of two terms: the thermodynamic barrier ( $W^*$ ) and the kinetic barrier ( $\Delta G_D$ ) for nucleation. The thermodynamic barrier  $W^*$  designates an increase in the free energy of a system due to the formation of a nucleus with critical size [2]. The kinetic barrier ( $\Delta G_D$ ) is the activation free energy for an atom/molecule transfer from melt to nucleus [3]. The kinetic barrier for glass-forming liquids is replaced by an activation free energy for viscous flow,  $\Delta G_{\eta}$ , because the effect of viscosity on nucleation behaviour of glass is very important. In the present work the influence of temperature dependence of viscosity on the nucleation of 19  $K_2O\cdot22TiO_2\cdot58GeO_2$  (mol%) was investigated.

# **Experimental**

The starting materials used are reagent grade  $GeO_2$ ,  $K_2CO_3$ , and  $TiO_2$ . The appropriate batch composition was melted at  $1200^{\circ}C$  for 1 h in a Pt crucible. The melts were cast on a steel plate and cooled in air. The obtained glass samples were transparent, without visible residual gas bubbles. The peak temperature of crystallization  $T_p$  and liquidus temperature  $T_m$  were determined by DTA run of glass powder with Netzch STA 409 EP instrument and  $Al_2O_3$  powder as the reference material. Dilatometry measurements were performed using a BÄHR 8025 instrument on samples 3 mm in diameter and 40 mm long. The dilatometric testing procedure was performed in accordance with ISO 7884-8.

For studying the structure and phase compositions, the bulk glass samples were isothermally treated at selected temperatures for different times. Identification of the phase crystallized and its morphology was performed with the Powder X-ray

diffraction analysis (XRD)( Philips PW-1710) and SEM measurements(Jeol JSM 6460)

### **Results and Discussion**

The results of the chemical analysis shows that a glass composition:  $19.27 ext{ } 19 ext{ } ext{K}_2 ext{O} \cdot 22 ext{TiO}_2 \cdot 58 ext{GeO}_2$  was obtained. This composition is close to stoichiometric one of  $ext{K}_2 ext{O} \cdot ext{TiO}_2 \cdot 3 ext{GeO}_2$  [4].

For a supercooled liquid the steady state crystal nucleation rate is given [2]

$$I = [A_c T/\eta] \exp(-W^*/kT)$$
 (1)

were  $A_c$  = 4.75·10<sup>31</sup> J·m<sup>-6</sup>·K<sup>-1</sup>, T is temperature,  $\eta$  is the viscosity and k is the Boltzmann constant. The thermodynamic barrier ( $W^*$ ) can be estimated from the experimental values of the nucleation data (I) at different temperatures. The experimental nucleation rate, I, at the treatment temperature, T, was determined from the time dependence of the number of particles per unit volume (SEM measurements). To analyze of the effect viscosity on the nucleation rate is need to know the viscosity temperature dependence of this glass. As a good approximation of the viscosity dependence on temperature for most glasses, the empirical Vogel-Fulcher-Tamann equation (VFT) is used. Based on the glass transformation temperature,  $T_g$  = 953.15 K, the dilatometric softening temperature,  $T_{om}$  = 848.15 K and the melting temperature,  $T_m$  = 1308.15 K, determined by dilatometric and DTA measurements, following VFT equation was fitted:

$$\log (\eta, \text{Pa·s}) = -0.286 + 1739/(\text{T-684}) \tag{2}$$

Using equations (1) and (2), the theoretical nucleation rate was calculated and compared with the experimental nucleation rates, Fig. 1.

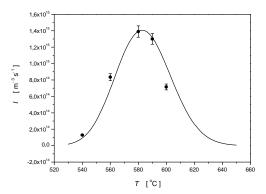


**Fig. 1.** Experimental (•) and calculated nucleation rate( — ) as a function of temperature.

To obtain a more exact insight into the effect of viscosity on nucleation behaviour of this glass, its parameters were compared with the silicate glass  $Na_2O-2CaO-3SiO_2$  ( $NC_2S_3$ ). The nucleation rate of the  $NC_2S_3$  glass was determined

of  $\sim 10^{11}$  m<sup>-3</sup>s<sup>-1</sup> [3]. Both glasses were crystallized by homogenous mechanism of nucleation

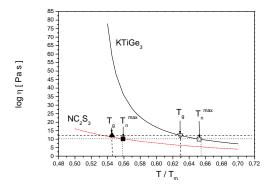


**Fig. 2.** Viscosity curves for KTG<sub>3</sub>, and NC<sub>2</sub>S<sub>3</sub> glasses in the range  $T_r = 0.5$ -0.7. The points denote viscosity at the reduced temperatures of maximum nucleation rates  $(T_n^{\text{max}})$  and glass transition temperature  $(T_g)$ .

From Fig. 2 can be seen that the viscosity of KTG<sub>3</sub> glass in the temperature range of  $T_r(T_{\rm gr}=T_{\rm g}/T_{\rm m})=0.5$ -0.7 differs considerably from those of silicate NC<sub>2</sub>S<sub>3</sub> glass. Its viscosity is higher and temperature dependence is strongly expressed. Also, considerable viscosity change with temperature occurs at  $T_r > 0.55$ . Consequently,  $T_{\rm g}$ ,  $T_{\rm n}^{\rm max}$  and nucleation interval are shifted to higher  $T_{\rm r}$ . Based on experimental nucleation data for several silicate glasses [1], it has been observed that glasses which exhibit homogeneous nucleation have a reduced glass transition temperature  $T_{\rm gr}$  ( $T_{\rm gr}=T_{\rm g}/T_{\rm m}$ ) < 0.60. As can be seen the glass NC<sub>2</sub>S<sub>3</sub> have  $T_{\rm gr} < 0.6(0.56)$  while the KTG<sub>3</sub> glass has  $T_{\rm gr} > 0.6$  (0.63). This indicates that the viscosity of this glass considerably influences the temperature and the time dependence of nucleation rate, as well as the shifting of  $T_{\rm n}^{\rm max}$  toward higher  $T_{\rm r}$  values. The temperatures of the maximum nucleation rate,  $T_{\rm n}^{\rm max}$ , of these glasses appeared at a viscosity of  $\eta \approx 10^{10}$  Pa s.

#### Conclusion

The results presented in the study showed that the viscosity of the germanate glass considerably influenced the temperature and the time dependence of nucleation rate, as well as the shifting of  $T_{\rm n}^{\rm max}$  toward higher  $T_{\rm r}$  values.

- [1] V.M.Fokin, E.D.Zanotto, N.Y.Yuritsyn, J.W.P.Schmelzer, J.Non-Cryst.Solids, 2006, 352 2681-2714
- [2] P.F.James J.Non-Cryst.Solids, 1985,73, 517-540
- [3] C.J.R.Gonzales Oliver, D.O.Russo, P.F.James, Phys. Chem. Glasses, 2004, 45, 100-106
- [4] S.Grujić, N.Blagojević, M.Tošić, V.Živanović, Ceramics-Silikàty, 2005, 49,278-282

## SYNTHESIS OF APATITE-TYPE Ce<sub>4.67</sub>(SiO<sub>4</sub>)<sub>3</sub>O VIA GLYCINE-NITRATE COMBUSTION

S. Zec<sup>1</sup>, S. Bošković<sup>1</sup> and R. Petrović<sup>2</sup>

<sup>1</sup>Institute of Nuclear Sciences Vinča, Serbia, Belgrade, POB 522 <sup>2</sup>Faculty of Technology and Metallurgy, Belgrade, Serbia, Karnegijeva 4

#### **Abstract**

The pure  $Ce_{4.67}(SiO_4)_3O$  with the apatite-type of structure was obtained for the first time from cerium nitrate, glycine and tetraethyl orthosilicate (TEOS) through the self-combustion of the gel. The solution of the reactants with the molar ratio of TEOS to water 1: 42 and glycine to  $NO_3$  1: 3 was transformed into gel. During combustion of the gel the ash containing nanostructured  $CeO_2$  and noncrystalline  $SiO_2$  was formed. The phase identification and the measurement of the crystallite size was done by XRD diffraction.  $Ce_{4.67}(SiO_4)_3O$  was synthesized from the ash subsequently fired in argon at 1200 °C.

#### Introduction

Rare earth silicates with the apatite-type structure can be used as electrolytes for solid oxide fuel cells (SOFCs) because of their high ion conductivities. Beside the solid-state reaction between oxides [1], and the sol-gel synthesis using metal alcoxides [2], combustion procedure is applied to prepare some silicates [3] recently. Combustion synthesis involves a highly exothermic redox reaction between metal nitrates and an organic fuel to produce a fine solid powder of metal oxide. Properties of the as-synthesized powders are dependent on the fuel-to-oxidizer ratio, which also determines the reaction temperature [4]. The second component SiO<sub>2</sub> is mostly obtained from alkoxide, TEOS during its hydrolysis [5]. The hydrolysis of TEOS is a sol-gel process and proceeds via series of condensation reactions forming Si-O-Si linkages as well as the ethanol as a side product. Owing to that, the products of combustion synthesis are strongly affected by the ratio TEOS: H<sub>2</sub>O: ethanol.

In this study the self-combustion of the gel obtained from solution of cerium nitrate, glicine and TEOS, was performed that produced nanostructured CeO<sub>2</sub> and noncrystalline SiO<sub>2</sub>, which have formed Ce<sub>4.67</sub>(SiO<sub>4</sub>)<sub>3</sub>O during firing. This is according to our knowledge, the first experiment described in the literature for production of nanosized Ce-apatite by glycine-nitrate method using TEOS as starting chemical.

# **Experimental**

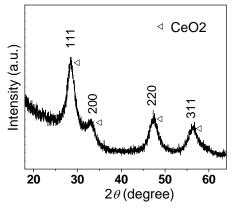
The starting materials were  $Ce(NO_3)_3 \cdot 6H_2O$ , TEOS  $(Si(OC_2H_5)_4)$ , glycine (2-aminoacetic acid,  $NH_2CH_2COOH$ ) and ethanol  $(C_2H_5OH)$ .  $Ce(NO_3)_3 \cdot 6H_2O$  (10.769 g) was first dissolved in 20 ml of ethanol. Then, stoichiometric amount of TEOS (Ce:Si = 4.67:3), distilled water and, finally, glycine were added into solution. The

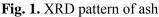
molar ratio of TEOS to added water was 1: 42, while the molar ratio of glycine to  $NO_3$  was 1: 3. At every stage of this procedure, reactants were stirred at room temperature with a magnetic stirrer for appropriate time, until clear solution was obtained. During heating at 60 °C the solution got transformed into transparent gel which was then dried. Afterwards, the dried gel was heated on the hot plate when the spontaneous ignition occurred and self-propagating combustion continued producing yellow-white and voluminous ash and large amounts of gases. Ash was calcined at 600 °C for 3 h to remove the organic contents, then uniaxially pressed into pellets and sintered in flowing argon at 1200 °C for 5 h.

X-ray diffraction (XRD) analyses performed by  $CuK\alpha$  radiation was used for phase identification and crystallite size determination.

#### **Results and Discussion**

In the performed combustion process, glycine acts as an organic fuel while the cerium nitrate is an oxidizer. For stoichiometric redox reaction between a fuel and an oxidizer, the net oxidizing valency of metal nitrate should be equalized to the net reducing valency of the fuel [4]. With the aim to obtain nanostructured oxides by combustion process fuel-deficient ratio was chosen (glycine:  $NO_3 = 1$ : 3). This ratio is only something above the lowest ratio (0.3) needed for autoignition to occur, but provides the low flame temperature and the minimum evolved gaseous products. As a consequence, the crystallites growth is suppressed as well as the loss of the ashes out of the reaction bottle that are released along with gaseous products.  $N_2$ ,  $CO_2$  and  $H_2O$  are primarily evolved during combustion. The unstable  $Ce^{3+}$ -ions of cerium nitrate produce  $CeO_2$  during combustion in air.





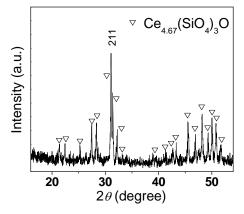


Fig. 2. XRD pattern of fired ash

On the XRD pattern (Fig. 1) of the powder produced by self-combustion only the broad peaks of  $CeO_2$  (JCPDS 34-0394) are visible, indicating that  $SiO_2$  is noncrystalline. The crystallite size of  $CeO_2$  was calculated from the full width at half maximum (FWHM = 1.909 °2 $\theta$ ) of the 111 peak using Scherrer equation. The

obtained value of 4 nm confiermed the nanostructure of  $CeO_2$ . Only the  $Ce_{4.67}(SiO_4)_3O$  phase was identified (JCPDS 43-0441) on the diffraction pattern (Fig. 2) of the sample fired in argon 5 h at 1200 °C, that is considerably lower temperature in comparison with the 1550 °C at which this compound was obtained by solid-state reaction [6]. The temperature decrease resulted in the 43 nm crystallite size of  $Ce_{4.67}(SiO_4)_3O$  calculated from 211 peak (FWHM = 0.224 °2 $\theta$ ). This crystal structure of  $Ce_{4.67}(SiO_4)_3O$  will likely enable to get dense sintered product, also at a lower temperature. The formation of solely  $Ce_{4.67}(SiO_4)_3O$  phase is mostly influenced by chemical homogeneity of the solution and the gel in which the constituents are mixed at the molecular level. In the solution, glycine molecules with two complexing groups, amino and carboxylic acid make the complex ions of cerium, which prevent precipitation and maintain homogeneity among the constituents.

#### Conclusion

The Ce<sub>4.67</sub>(SiO<sub>4</sub>)<sub>3</sub>O with the apatite-type structure was synthesized at 1200 °C in argon from nanostructured CeO<sub>2</sub> and noncrystalline SiO<sub>2</sub> obtained through the glycine-nitrate combustion procedure. The homogenous solution of cerium nitrate dissolved in ethanol, glycine, TEOS and water was prepared at room temperature by stirring. The molar ratio of TEOS to water was 1: 42, while the molar ratio of glycine to NO<sub>3</sub> was 1: 3. The heated solution was transformed into gel. The thermaly induced autoignition of the gel and its self-propagated combustion gave the mixture of CeO<sub>2</sub> and SiO<sub>2</sub> powders. The crystallites size of CeO<sub>2</sub>, determined by XRD diffraction, was 4 nm, while Ce<sub>4.67</sub>(SiO<sub>4</sub>)<sub>3</sub>O contained crystallites of 43 nm.

# Acknowledgment

The authors gratefully acknowledge support of the Ministry of Science of the Republic of Serbia under the Project No. 142003.

- [1] P. Panteix, I. Julien, D. Bernache-Assollant, P. Abelard, Mat. Chem. Phys. 2006, 95, 313-320.
- [2] S. Tao, J. Irvine, Mater. Res. Bull. 2001, 36, 1245-1258.
- [3] C. Tian, J. Liu, J. Cai, Y. Zeng, J. Alloys Compd. 2008, 458, 378-382.
- [4] R. Purohit, B. Sharma, K. Pillai, A. Tyagi, Mater. Res. Bull. 2001, 36, 2711-2721.
- [5] S. Celerier, C. Laberty, F. Ansart, P. Lenormand, P. Stevens, Ceram. Int. 2006, 32, 271-276.
- [6] S. Zec, S. Bošković, J. Mater. Sci. 2004, 39, 5283-5286.

# OPTICAL PROPERTIES OF CdSe AND CdSe/ZnS QUANTUM DOTS

N.D. Abazović and M.I. Čomor

Vinča Institute of Nuclear Sciences, 11001 Belgrade, PO Box 522, Serbia (mirjanac@yin.bg.ac.yu)

#### **Abstract**

Original organic capping TOPO/TOP groups of CdSe and CdSe/ZnS quantum dots, from mother solution were replaced with 2-mercaptoethanol, which was chosen as model compound, in order to achieve water solubility. Obtained water dispersions of CdSe and CdSe/ZnS QDs were characterized by UV/Vis absorption and luminescence techniques. Luminescence measurements revealed that bare cores are very sensitive to surface capping, transfer to water diminished emission intensity. Core/shell, CdSe/ZnS, QDs are much more resistant to changes of the capping and solvent, and significant part of emission intensity was preserved in water.

#### Introduction

The organic ligand bound to the surface of colloidal quantum dots (QDs) plays a important role in determining their electronic and optical properties. A mixture of trioctylphosphine and trioctylphosphine oxide (TOP/TOPO) is the prototypical ligand system for most II-VI semiconductor systems, such as CdSe. These ligands provide colloidal stability in common organic solvents such as hexane and toluene.

Overcoating QDs with higher band gap inorganic materials has been shown to improve the photoluminescence quantum yields by passivating surface nonradiative recombination sites. Particles passivated with inorganic shell structures are more robust than organically passivated dots and have greater tolerance to processing conditions necessary for incorporation into solid state structures, transfer to water and further conjugation. Water solubility is increasingly recognized as a desirable characteristic as QDs are becoming the system of choice for PL biolabelling applications, and in many cases their greater stability is seeing as an important advantage in comparison to of their molecular counterparts (organic dyes) [1].

In this article, we report a study of the optical properties of CdSe and CdSe/ZnS QDs, that have been synthesized in noncoordinating organic solvent (TOPO/TOP) at high temperature, dispersed in nonpolar solvent and water. We show that capping of QDs with 2-mecraptoethanol readily produces stable water dispersions.

# **Experimental**

All reagents were used without further purification.

**Synthesis of CdSe QDs.** Highly crystalline CdSe QDs were synthesized by method previously described by Peng and Peng [2]. Briefly, CdO, TOPO and HPA were loaded in 25 ml flask. The mixture was heated to 300 – 320 °C under Ar flow.

Selenium stock solution was injected in the mixture at 270 °C and left nanocrystals to grow for 4 minutes.

**Synthesis of CdSe/ZnS core/shell QDs.** Roughly, 0.1µmol of CdSe QDs dispersed in hexane was transferred into reaction flask with dry TOPO and solvent was pumped out. Then, temperature of the solution was raised at 160°C, and precursors of Zn and S dissolved in TOP were added dropwise over a period of 5 minutes. The overcoated particles were stored in their mother solution during the night to ensure that the surface of the dots remained passivated with TOPO [3].

Extraction of QDs in water: Equal aliquots of CdSe or CdSe/ZnS QDS dispersed in hexane and 0.01 M aqueous solution of 2-mercaptoethanol (pH = 8-9) were mixed. Two separated layers were formed, hexane (colored) layer was at the top. After slight shaking, QDs were transferred in aqueous (bottom) layer, and it was used as is for optical measurements.

**Optical characterization:** Measurements of the absorption spectra were carried out on an Evolution 600 UV–Vis spectrophotometer (Thermo Scientific). The photoluminescence spectra were recorded on Perkin-Elmer LS-45 spectro-fluorimeter. Quantum yields of emission were calculated using Tris[2,2'-bipyridyl]Ruthenium(II)chloride as standard.

#### **Results and Discussion**

The absorption and emission spectra of CdSe (triangles) and CdSe/ZnS (cycles) QDs are presented in Fig 1A and Fig 1B, respectivelly. As can be concluded from the position of the absorption peak, CdSe cores were from 3-4 nm in diameter. Exchange of capping agent and extraction in water didn't affect shape of absorption spectrum (Fig 1 A); CdSe QDs retain their original size. Unfortunately, extraction in water led to disappearance of characteristic emission peak at 560 nm (QY in chloroform was  $\sim 0.42$  %).

Overcoating of CdSe QDs with shell of ZnS led to changes in shape and position of peak in absorption spectrum (Fig 1 A, cycles). Absorption peak moved from 543 nm to 553 nm and its FWHM increased, what indicated that particle sizes increased and their size distribution is wider in comparison to bare CdSe ODs. Changes in emission spectra (Fig. 1B, cycles) are more prominent. Emission intensity increased 10 times (OY= 4.2%) compared to bare CdSe and emission peak moved to 580 nm. Exchange of capping agent and extraction in water didn't affect shape of emission spectrum just its intensity. CdSe/ZnS QDs in water retain a measurable part of their original emission (QY= 0.55%). Once the QDs are dispersed in the water they can be used to detect different analytes as sensors, as a passive fluorescent labels (through conjugation with selective receptor molecules, antibodies) and design of simple multiplexed immunoassays, for FRET (fluorescence resonance energy transfer) and for labeling biological cells. Obtained results showed that 2-mercaptoethanol is suitable for transfer of core/shell ODs in water. Its functional groups allow excellent capping of the OD surface (SH group and ZnS) from one side, and polarity (OH) of its other side gives good water solubility.

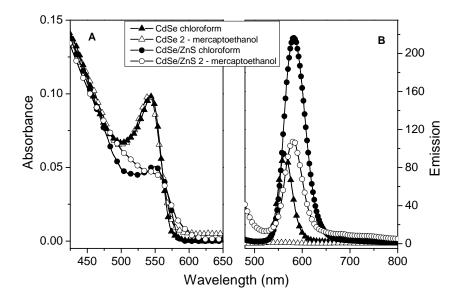


**Fig. 1.** Absorption (A) and emission (B) spectra of CdSe and CdSe/ZnS QDs dispersed in chloroform and water.  $\lambda_{exc}$ = 450nm.

#### Conclusion

The proposed synthetic method resulted in formation of CdSe QDs cores with diameters in the range from 3-4 nm. Addition of shell of ZnS over CdSe core didn't affect dimensions of core. CdSe/ZnS QDs have 10 times increased QY of emission in comparison to bare CdSe QDs. Extraction of QDs in water by exchange of capping agents, led to decrease of QY of emission of both bare CdSe and CdSe/ZnS QDs. Core/shell QDs dispersed in water sustained QY of emission large enough to be used for different bio-applications.

## Acknowledgement

This work was supported by the FP6- NANOMYC (LSHB-CT-2007, contract number 036812) and by Serbian Ministry of Science (Project number 142066).

- [1] X. Ai, Q. Xu, M. Jones, Q. Song, S. Ding, R.J. Ellingson, M. Himmel, G. Rumbles, Photochem. Photobiol. Sci., 2007, 6, 1027–1033.
- [2] Z.A. Peng, X. Peng, J. Am. Chem. Soc, 2001, **123**, 183–184.
- [3] B.O. Dabbousi, J. Rodriguez-Viejo, F.V. Mikulec, J.R. Heine, H. Mattoussi, R. Ober, K.F. Jensen, M.G. Bawendi, J. Phys. Chem. B, 1997, **101**, 9463–9475.

# SYNTHESIS AND CHARACTERIZATION OF Co<sup>2+</sup> DOPED TiO<sub>2</sub> NANOPARTICLES

J. Kuljanin-Jakovljević<sup>1</sup>, Z. Šaponjić<sup>1</sup>, T. Radetić<sup>2</sup> and M. Radoičić<sup>1</sup>

<sup>1</sup>Vinča Institute of Nuclear Sciences, P.O. Box 522, 11001 Belgrade, Serbia <sup>2</sup>Lawrence Berkeley National Laboratory, Berkeley, CA 94720, USA

#### **Abstract**

Scrolled titania nanotubes were synthesized by a hydrothermal method using commercial  $TiO_2$  powder in proton-deficient aqueous systems. In presence of  $CoCl_2$  extended hydrothermal treatment of  $TiO_2$  nanotubes lead to formation  $Co^{2+}$  doped  $TiO_2$  nanoparticles. TEM and HRTEM measurement were used for determining the shape, dimension and structure of doped nanoaprticles. XRD confirmed anatase crystalline structure od  $Co^{2+}$  doped  $TiO_2$ . The presence of  $Co^{2+}$  ions did not induce distortions of the overall anatase crystal structure of  $TiO_2$  matrix. The concentration of  $Co^{2+}$  ions was 1.5% compared with the amount of  $Ti^{4+}$  ions.

#### Introduction

Doping of wide band gap metal oxide semiconductors such as TiO2 and ZnO with transition metal ions will influence the electronic, optical, catalytic, and magnetic properties of metal oxides. Semiconductor containing magnetic ions has been studied for several decades and has come to be known as diluted magnetic semiconductors (DMSs). More recently, interest in DMSs has turned toward their applications in spin-based electronics technologies or "spintronics"[1]. Another major category of usage dopants in semiconductor nanocrystals is that of luminescence activators. The manipulation of the luminescence properties of pure semiconductor nanocrystals by doping with ions such as Mn<sup>2+</sup> or Eu<sup>2+</sup> has the potential to broaden the range of useful spectroscopic properties of this class of materials. Nanostructured titanium dioxide is very well known as an ideal photocatalyst due to its photostability and high reactivity. Excitation of TiO<sub>2</sub> with light energy greater than its band gap (3.2 eV) generates electron-hole (e'/h<sup>+</sup>) pairs that can be exploited in various processes at the particle interface. Doping of TiO<sub>2</sub> nanocrystals with paramagnetic atoms is predicted to lead to interesting magnetic and magnetooptical behavior of nanocrystals resulting in room-temperature ferromagnetism [2]. In this work we report the synthesis and characterization of Co doped anatase nanoparticles using titania scrolled nanotubes as the starting materials.

## **Experimental**

Titania nanotubes were synthesized by using TiO<sub>2</sub> (Fluka) powder as a precursor in a chemical process described elsewhere [3]. Co<sup>2+</sup> doped TiO<sub>2</sub>

nanoparticles were synthesized using hydrothermal treatment of a suspension containing 3x10<sup>-2</sup>M titania nanotubes at pH=3 as the starting material in the presence of 6.4x10<sup>-4</sup> M CoCl<sub>2</sub>. The suspension was stirred for 3h followed by 90 min hydrothermal treatment at 250°C. Nanoparticles were efficiently redispersed in water using a titanium ultrasonic bath, giving transparent colloidal dispersion of Co<sup>2+</sup>doped TiO<sub>2</sub> nanocrystals. The sample was filtrated to remove excess Co<sup>2+</sup> ions, washed and redispersed in water pH=3 or dialyzed against water pH=3 at 4°C for 3 days. The X-ray diffraction (XRD) measurements were carried out on a Philips PW-1050 (Eindhoven, the Netherlands) automatic diffractometer using CuKa radiation. Spectrophotometric measurements were carried out on a Thermo Evolution 600 UV-vis spectrophotometer. Conventional transmission electron microscopy using Philips EM-400 at 100kV was used for determining the overall shape and appearance of the particles. Atomic-resolution transmission electron microscopy investigation of doped nanoparticles was performed using HRTEM Philips CM200 (with FEG) operating at an accelerating voltage of 200kV. The percentage ratio of Co<sup>2+</sup> and Ti<sup>4+</sup> ions in doped nanoparticles was determined using ICP technique.

#### **Results and Discussion**

Co<sup>2+</sup> were incorporated into TiO<sub>2</sub> nanocrystals using hydrothermal treatment of scrolled anatase nanotubes in the presence of CoCl<sub>2</sub>. Titania nanotubes as axially anisotropic nano-objects, had the diameter of 12 nm. It is known that scrolled titania nanotubes, presented in Figure 1a, contain large amounts of surface Ti atoms in highly reactive undercoordinated sites that can be exploited for adsorption of Co ions.



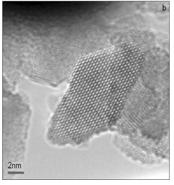


**Fig. 1.** a) TEM image of scrolled TiO<sub>2</sub> nanotubes obtained from dispersion of TiO<sub>2</sub> powder; b) HRTEM image of Co<sup>2+</sup> doped TiO<sub>2</sub> nanoparticles.

Hydrothermal treatment of this composite structure results in the formation of Co<sup>2+</sup> doped anatase TiO<sub>2</sub> nanoparticles having rhombic shape and average dimensions of 8-10 nm, Figure 1b. Particles appear to be almost defect free single

crystal. The concentration of  $\mathrm{Co^{2+}}$  ions, determined using ICP technique, was 1.5% compared with the amount of  $\mathrm{Ti^{4+}}$  ions in dialyzed sample. Dialysis process we used for removing of weakly bound  $\mathrm{Co^{2+}}$  ions.

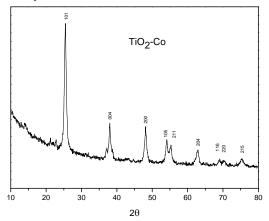


Fig. 2. XRD pattern of Co<sup>2+</sup> doped TiO<sub>2</sub> nanocrystals

X-ray diffraction measurement of  $Co^{2^+}$  doped  $TiO_2$  nanocrystals confirmed the existence of homogeneous anatase crystal structure. The presence of  $Co^{2^+}$  ions does not induced distortions of overall crystal structure. There is no indication of cobalt oxide formation. Optical properties of  $Co^{2^+}$  doped  $TiO_2$  nanoparticles are slightly changed in comparison with bare  $TiO_2$ , red-shifting the onset of absorption spectra. Doping of the core of  $TiO_2$  nanoparticles with  $Co^{2^+}$  ions, make possible synthesis of optically transparent films for the measurement of the magnetic properties.

#### **Conclusions**

We have shown that hydrothermal synthesis of  $\mathrm{Co}^{2^+}$  doped anatase  $\mathrm{TiO}_2$  nanoparticles using titania scrolled nanotubes as a precursor results in thermodynamically stable incorporation of  $\mathrm{Co}^{2^+}$  dopants within anatase lattice that is resistant to a "self-purification" mechanism. HRTEM analysis revealed almost defect free rhombic nanoparticles (d~8-10nm). XRD measurements of doped nanoparticles confirmed absence of any disturbance of the overall anatase crystal lattice.

- [1] J.K. Furdyna, J. Appl. Phys., 1988, 64, R29.
- [2] M.S. Park, S.K. Kwon, B.I. Min, Phys. Rev. B, 2002, 65, 161209-(R).
- [3] Z. V. Saponjic, N. M. Dimitrijevic, D. M. Tiede, A. Goshe, X. Zuo, L. X. Chen, A. S. Barnard, P. Zapol, L. Curtiss, T. Rajh, Advanced Materials, 2005, **17**, 965-971.

#### INFLUENCE OF ALUM ON FOCAL LENGTH OF MICROLENSES

B. Murić, D. Pantelić, D. Vasiljević and B. Panić *Institute of Physics, Pregrevica 118, Belgrade, Serbia* 

#### **Abstract**

Influence of alum on the focal length of microlenses, formed on the tot'hema and eosin sensitized gelatin layer, was investigated. The focal lengths from 400  $\mu m$  to 1200  $\mu m$  were obtained for alum concentrations from 0 to 10%.

#### Introduction

Microlenses (individual or array) are increasingly used in different optical and biomedical applications: such as cameras in cell phones, medical devices, optical data storage, fiber optics, confocal microscopy, wave-front sensing, imaging sensors, and so on [1-5]. Aspheric, colorless and transparent, concave microlenses (individual or array) are formed on the tot'hema and eosin sensitized gelatin layer (TESG) thickness of 100  $\mu$ m. The details of the preparation procedure of TESG layer, were described in [6]. Microlenses formed rapidly with low power of unfocused, 532 nm, Nd:YAG laser beam.

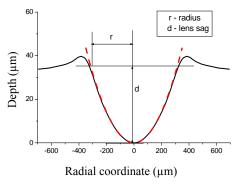


**Fig. 1.** TESG microlens profile and parabolic fit (dashed curve)

An experimental setup for the TESG microlenses fabrication was described in [7]. The surface profile of microlens was parabolic in the central part, 80% of the aperture (Fig.1.), as verified by stylus profilometry (Talystep TM surface profiler, Taylor-Hobson Ltd.). At the edge of microlens, a convex, ring-shaped area was formed [7, 8]. The influence of chemical processing on the focal length of TESG microlenses was presented. We denote the process as fixing.

# **Experiments and Results**

In our previous experiments, it was noticed that, due to crystallization, TESG layer becomes opaque after a few days (Fig.2a, 2b). Because of that, the TESG layer must be chemically processed (Fig. 2c). In our initial experiments, layer was soaked in isopropyl alcohol. However, few more days were needed for water to fully evaporate. We have found that, by using a solution of 1% alum (instead of isopropyl alcohol), the drying of TESG layer can be accelerated. In addition, treatment of TESG microlenses with alum decreases the height of the ring shaped area around the lens. Also, alum bleaches TESG layer. We investigate influence of con-

centration of alum on the profiles TESG microlenses. At the constant experimental conditions five TESG microlenses were formed, on the 100  $\mu$ m thickness of layer, with unfocused Nd:YAG laser beam operating at 532 nm. The power of laser was 70 mW, and exposure time was 10s.

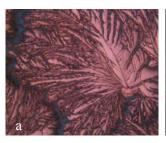
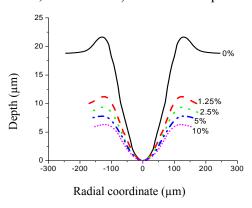






**Fig. 2.** Photograph's of the TESG layer: a) crystallized; b) crystallized microlens; c) chemically processed TESG microlenses (each producing an image of a text**-phy** placed behind the lenses)

The first microlens was soaked in isopropyl alcohol, while remaining four microlenses were soaked in solution of alum with various concentrations (1.25%, 2.5%, 5% and 10%). The times of processing was the same in all cases (5 minutes).



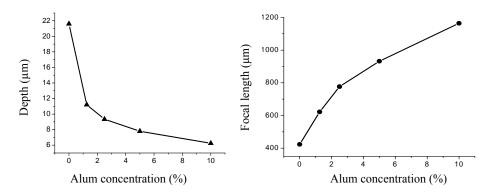
**Fig. 3.** Influence of alum concetration on the focal length of microlens

Figure 3. shows surface profiles of TESG microlenses treated with solution of alum with different concentraons. Namely, microlens fixed by isopropyl alcohol is denoted as 0% of alum. We can see in Fig.3. that application of a solution of alum with different concentrations changes surface profiles of microlenses and influences on their radii of curvature.

Also, depth of microlenses was changed. As can be seen in Fig. 4. depth of TESG microlenses exponentially decreased from 22  $\mu$ m to 6  $\mu$ m, with increasing concentration of alum.

Variable radii of microlenses curvature influences their focal lengths. The focal length-f of the microlens was calculated from the following thin lens formula: f = R/(n-1), where R is radius of curvature and n is refractive index. The refractive index of TESG layer (n=1.537) is determined by using immersion technique [8]. Calculated microlenses focal lengths have values from 400  $\mu$ m to 1200  $\mu$ m. Focal length variation with concentration of alum is shown in Figure 5. As can be

seen in Fig. 5. the focal lengths increased with increasing concentrations of alum. Also, it was demonstrated that alum solution bleached TESG layer and that its colour was changed with concentration alum.



**Fig. 4.** Influence of alum concentration on the depth of microlenses

**Fig. 5.** Focal length variation of microlenses with alum concentration

#### **Conclusions**

Experimental results show that application of solution alum with different concentrations varies surface profiles of TESG microlenses and results in a change theirs focal lengths. We demonstrate a range of focal lengths from 400  $\mu$ m to 1200  $\mu$ m for concentrations of alum from 0 to 10 % applied.

#### Acknoledgments

This work is realized with the support of the Serbian Ministry of Science, through contract No. 141003. We thank Radomir S. Petrović for help with scanning of microlenses profiles.

- [1] W. Wang, J. Fang, IEEE Sensors J., 2007, 7, 11-18.
- [2] S. Kuiper, B. H. W. Hendriks, Appl. Phys. Lett., 2004, 85, 1128-1130.
- [3] L. Seifert, H.J. Tiziani, W. Osten, Opt. Comm., 2005, 245, 255-269.
- [4] J. Kim, S. Nayak, L. A. Lyon, J. Am. Chem. Soc., 2005, 127, 9588-9592.
- [5] T. Tanaami, S. Otsuki, N. Tomosada, Y. Kosugi, M. Shimizu, H. Ishida, Appl. Opt., 2005, 41, 4704-4708.
- [6] B. Murić, D. Pantelić, D. Vasiljević, B. Panić, Opt. Mat., 2008, 30, 1217-1220.
- [7] B. Murić, D. Pantelić, D. Vasiljević, B. Panić, Appl. Opt., 2007, 46, 8527-8532.
- [8] D. Vasiljević, D. Pantelić, B. Murić, Proc. SPIE, 2007, **6604**, (66040Q-1)-(66040Q-5).

# INFLUENCE OF CHEMICAL PROCESSING ON BAND GAPS IN DICHROMATED PULLULAN PHOTONIC CRYSTALS

S. Savić-Šević, D. Pantelić and B. Jelenković Institut of Physics, Pregrevica 118, Zemun, Serbia

#### Abstract

This paper describes the influence of the chemical processing on the band gaps position. One- dimensional photonic crystals are fabricated as volume reflection holograms in dichromated pullulan (DCP). The spectral measurements show that the band gap centre shifts towards the short wave region with decreasing water concentration.

#### Introduction

Photonic crystals are dielectric materials that exhibit band gaps (BG) in which electromagnetic wave propagation is forbidden [1]. Here we report the fabrication of photonic crystals using the optical holography. One-dimensional photonic crystals were fabricated as volume reflection holograms.

Several photonic band-gap materials such as dichromated gelatin [2], polymers with  $TiO_2$  [3], photoresists [4,5] and sol-gel materials [6] have recently been used for the fabrication of photonic structures using holographic techniques.

In this study we present one-dimensional photonic crystals recorded in pullulan (biopolymer with linear polysaccharide structure) sensitized with ammonium dichromate (DCP) [8-11].

We have investigated the effect of the chemical processing on the band gap position. We have shown that chemical processing influences the position of band gap (as found through spectral measurements).

# **Experiments and Results**

Holographic photosensitive material was prepared by mixing 8% aqueous solution of pullulan (Sigma) and 10% ammonium dichromate by weight of pullulan. Using magnetic stirrer DCP solution was stirred and warmed to 50°C to achieve homogeneity. The solution was then coated onto clean glass slides in a horizontal position. Film was dried overnight under normal laboratory conditions. The thickness of the dried layer was approximately 10 μm.

A single-frequency, diode pumped Nd-YAG laser, at 532 nm, was used to expose the material. The laser beam was expanded and exposed pullulan layer at normal incidence. The energy density of the incident beam was 24 J/cm<sup>2</sup>. After going through the emulsion, beam was reflected back from a mirror behind the holographic plate. The hologram was obtained by interference of two oppositely directed beams inside the emulsion. The interference pattern consists of planes parallel to the substrate surface with spacing  $d = \lambda/2n$ , where  $\lambda$  is the wavelength of

the laser source and n is the refractive index of the DCP (n=1.44). The space between the two adjacent constructive planes was 184 nm.

After exposure, plates were chemically processed. Processing involves washing the plates in mixture of water and isopropyl alcohol for 120 seconds, and drying for 60 seconds in pure isopropyl alcohol. The ratio of water and alcohol in the bath was varied while the duration of chemical treatment was the same all the time. The four different ratios of water and isopropyl alcohol were used: 2:3, 1:1, 3:2 and 3:1, respectively.

To verify the existence of band gaps in volume holograms, diffraction spectra were measured. Light from a halogen lamp was collimated and directed onto the sample. Transmittance spectra of the sample were measured with spectrometer. Fig. 1 (a) shows the transmission spectra and (b) band gap versus the ratio of water and isopropyl alcohol, corresponding to the sample developed with four bath treatments, with different concentration of water and isopropyl alcohol.

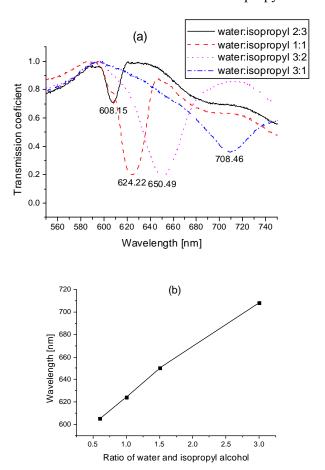


**Fig. 1**. (a) Transmission spectra, (b) band gap versus ratio of water and isopropyl alcohol

Results show that the band gap centres were shifted towards the short wave region with decreasing the concentration of water in the mixture. Position of the band gap center ranges from 608 nm to 708 nm.

#### Conclusion

This paper describes the influence of the chemical processing on band gaps in DCP. One–dimensional photonic crystals are fabricated as volume reflection holograms in dichromated pullulan. The spectral measurements show that the band gap centre shifts towards the short wave region with decreasing water concentration. We have shown that it is possible to shift band gaps by controlling chemical processing.

#### Acknowledgments

Research was performed under the contract 141003 funded by the Ministry of Science of the Republic of Serbia.

- [1] J. D. Joannopoulos, R. D. Meade and J. N. Winn, Photonic crystals, Princeton 1995.
- [2] R. Ma, J. Xu, and W. Y. Tam, App. Phys. Lett. 2006, 89, (081116-1)-(08116-3).
- [3] Z. Ye, J. Zheng, D. Liu, S. Pei, Phys. Lett. 2002, A 299, 313-317.
- [4] D. T. Sharp, M. Campbell, E. Dedman, M. Harrison, D. R.G, and A. J. Tuberfield, Opt. and Quan. Elect. 2002, 34, 3-12.
- [5] T. Ohira, T. Segawa, K. Nagai, K. Utaka, and M. Nakao, Jpn. J. Appl. Phys. 2002, 41, 1085-1089.
- [6] Y. Miklyaev, D. Meisel, A. Blanco, and G. Freymann, Appl. Phys.Lett. 2003, 82, 1284-1286
- [7] K. Saravanamuttu, C. Blanford, D. Sharp, E. Dedman, A. Tuberfield, and R. Denning, Chem. Mater. 2003, **15**, 2301-2304.
- [8] D. Pantelić, S. Savić, D. Jakovljević, Opt. Lett. 1998, 23, 807-809.
- [9] S. Savić, D. Pantelić, D. Jakovljević, Appl. Opt. 2002, 41, 4484-4488.
- [10] S. Savić Šević, D. Pantelić, Opt. Exp. 2005, 13, 2747-2754.
- [11] S. S. Šević and D. Pantelić, Appl. Opt. 2007, 46, 287-291.

#### CRYSTAL NUCLEATION IN GERMANATE GLASS

S.R. Grujić<sup>1</sup>, N.S. Blagojević<sup>1</sup>, M.B. Tošić<sup>2</sup>, V.D. Živanović<sup>2</sup> and J.D. Nikolić<sup>2</sup>

<sup>1</sup>Faculty of Technology and Metallurgy, 4 Karnegijeva St.,11000 Belgrade, Serbia

<sup>2</sup>Institute for Technology of Nuclear and other Mineral Raw Materials,

86 Franchet d' Esperey St, 11000 Belgrade, Serbia

#### **Abstract**

The crystal nucleation in  $K_2TiGe_3O_9$  glass was studied by scanning electron microscopy (SEM). Volume nucleation with spherical morphology of the growing crystals was determined. The nucleation range is in the temperature interval 540-630  $^{\bullet}C$  with high nucleation rates.

#### Introduction

Crystallization occurs by a combination of nucleation and growth. Crystal nucleation is a subject scientific and technology importance since it governs the crystallization kinetics and glassforming ability of undercooled melt. For the investigation of nucleation by commonly used isothermal method, it is necessary to count the number of nuclei in the glass that is thermally treated at different temperatures for different time making this method time consuming and laborious. Nucleation measurements are usually performed via two-stage heat treatments. This method consists of heating the glass to low temperature to produce nuclei, followed by high temperature heat treatment to grow nuclei to an observable size. This procedure is applicable when there is no overlap between nucleation and grow of nuclei. However, if the grow rate at the nucleation temperature is significant, the single-stage heat treatment is used. In this work the results of determination of the nucleation rates in germanate glass by single-stage heat treatment are presented.

# **Experimental**

The melting of appropriate glass batch for  $K_2TiGe_3O_9$  glass was performed in an electric furnace with a temperature control of  $\pm$  1 °C at T=1300 °C during t=2 h. The glass was obtained by quenching the melt on a steel plate. Powder X-ray diffraction analysis (XRD) confirmed the quenched melts to be vitreous. The glass samples were transparent, without visible residual gas bubbles.

The experiments under isothermal conditions were performed on bulk samples. On the basis of the results of previous investigations [1, 2] a single-stage heating schedule was chosen. The glass samples were heated at a heating rate  $\beta$  = 10 °C/min up to the temperature of the heat treatment (540-640 °C) and maintained at the chosen temperature for different times (10-360 min). After the selected heat treatment, the samples were taken out of the furnace. Sections fractures through the samples were gold sputtered and examined by SEM using a Jeol JSM 6460 microscope. From the SEM micrographs, the number of particles per unit area,  $N_A$ , and the diameters, d, of the circular intersections of the particles were de-

termined. The number of particles per unit volume,  $N_V$ , was determined from ratio of  $N_A$  and the largest circular cross-section diameter, d [3. 4]. The nucleation rate, I, at the treatment temperature, T, was determined from the time dependence of the number of particles (spherulites) per unit volume,  $N_V$ , in the heat treated glass samples.

#### **Results and Discussion**

In previous investigations of the crystallization of this glass, it was shown that during heat treatment a  $K_2TiGe_3O_9$  crystalline phase was formed [1, 2]. Selected SEM micrographs are presented in Fig. 1. It is obvious that the nucleation process commences within the bulk of the heat treated glasses and that the morphology of the growing crystals is spherical.

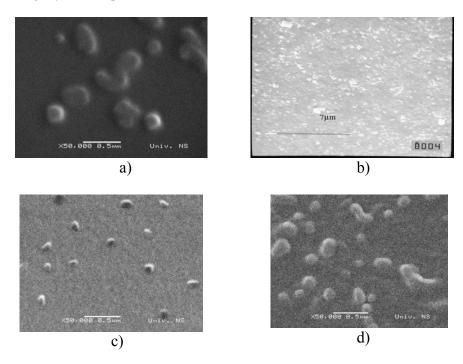


**Fig. 1.** SEM micrographs of heat treated glass after heat treatment at: a) T = 560 °C for t = 90 min; b) T = 560 °C for t = 150 min; c) T = 580 °C for t = 38 min and d) T = 580 °C for t = 48 min.

The number of crystal and their size continuously increase with heat treatment time, indicating simultaneous crystal nucleation and growth.

The time dependence of  $N_V$  measured from SEM micrographs of samples heat treated at 540, 560, 580, 590 and 600 °C are shown in Fig. 2. The slopes of these dependences correspond to the nucleation rate at the heat treatment temperature.

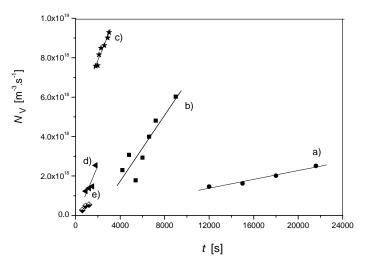


**Fig. 2** The number of particles per unit volume,  $N_V$ , as a function of time at the heat treatment temperature: a) 540 °C; b) 560 °C; c) 580 °C; d) 590 °C and e) 600 °C. Obtained crystal nucleation rates are summarized in Table 1.

**Table 1.** Crystal nucleation rates, *I*, in K<sub>2</sub>TiGe<sub>3</sub>O<sub>9</sub> glass.

···	
<i>T</i> [°C]	$I\left[\mathrm{m}^{-3}\cdot\mathrm{s}^{-1}\right]$
540	$1.29 \cdot 10^{14}$
560	$8.34 \cdot 10^{14}$
580	$1.39 \cdot 10^{15}$
590	$1.30 \cdot 10^{15}$
600	$4.0910^{14}$

#### Conclusion

The crystal nucleation rates in K<sub>2</sub>TiGe<sub>3</sub>O<sub>9</sub> glass were studied by scanning electron microscopy in the temperature interval 540-640 °C. The crystal nucleation takes place at randomly distributed nuclei in the volume of glass with spherical morphology of growing crystal. The determined nucleation rates in K<sub>2</sub>TiGe<sub>3</sub>O<sub>9</sub> glass are among the highest so far measured in inorganic glass.

- [1] S. Grujić, N. Blagojević, M. Tošić, V. Živanović, B. Božović, J. Therm. Anal. Calor., 2006, 83, 463-466.
- [2] S. Grujić, N. Blagojević, M. Tošić, V. Živanović, Cermics-Silikaty, 2005, 49, 278-282.
- [3] C. J. R. Gonzales Oliver, P. F. James, Thermochim. Acta, 1996, 280/281, 223-236.
- [4] P. F James, Phys. Chem. Glasses, 1974, 15, 95-105

# Phase Boundaries (I)

# PHASE TRANSFORMATIONS OF IRON MINERALS IN PROCESS OF COAL FIRING AT ELECTRIC POWER STATI-ONS

A. Dangić<sup>1</sup>, B.R. Simonović<sup>2</sup>, D. Dimitrijević, Lj. Cvetković<sup>1</sup> and S. Gajinov<sup>2</sup>

<sup>1</sup>University of Belgrade, Faculty of Mining & Geology, Djušina 7, 11000 Beograd, Serbia <sup>2</sup>Holding Institute of General and Physical Chemistry, Stud. Trg 16, 11000 Beograd, Serbia

#### **Abstract**

Coals, especially lignite, are worldwide using for operation of large electric power staitons (EPS). In the process of coal firing in EPS, coal organic matter is firing but its mineral matter is transforming into high-temperature mineral phases which form coal ash. Based on studies of coal and EPS's ash in the Kostolac lignite basin in Serbia, we studied phase transformations of iron minerals in process of coal firing in EPS. It was found that pyrite as main Fe-mineral in coal may be during coal firing transformed in diverse iron phases: Fe-metal, wüstite, magnetite, hematite and maghemite, depending on redox features in EPS's oven.

#### Introduction

Coals, especially lignites, are worldwide very important raw materials for operation of electro power staitons (EPS). Lignites, as low rank coals, contain beside comustable organic coal matter a lot of mineral matter. The lignite-operating EPSs fire enormous large coal masses and produce enormous large masses of coal ash and slag (in further text: ash). In the process of coal firing in EPS, mineral matter appears to be subject of several phase transformations [1-4]. The paper presents phase transformations of iron minerals in this process, based on studies of coal and EPS' ash in the Kostolac coal basin in Serbia.

#### Material and Methods

In the Kostolac basin in Serbia, the Drmno open pit produces as much as 6 million tons of lignite which is firing in the EPS Kostolac. In the Drmno coal deposit, the lignite coal seam at the open pit is as thick as around 18 m. Lignite have been studied and sampled in the coal seam profile at the open pit. Coal ash from EPS is transfering by a hydraulic transport (as a water suspension) to the ash deposit and it have been sampled from the ash deposit. In the geochemical studies of coal and ash samples the following methos of analyses have been applied: coal petrographic microscopy, ore microscopy, XRF and AAS analyses.

#### **Results and Discussion**

The lignite consists in general of organic (coal) matter and mineral matter (mineral impurities). In the studied Drmno lignite, the average contents of organic matter and mineral matter («ash») are (on dry basis) 62 % and 38 %, respectively. The

coal matter consists of several coal microlithotypes: detrite, textite (xylite), gelite, fusite, etc., and related minerals (macerals). Mineral matter mostly consists of clayey minerals but some pyrite (FeS<sub>2</sub>) is also present. Pyrite is main Fe mineral, is as abundant as 2.17 % (contains about 60 % of total iron) and forms thin grains (mainly up to 100  $\mu$ m in size) which are dispersed mostly in coal matter (Fig. 1).

The studied coal ash/slag mostly consists of diverse silicate minerals and glass but contain also some metallic minerals and thiny particles of unfired coal. Almost all metallic minerals are iron minerals. The following iron minerals are determinated: iron (metal), wüstite, magnetite, hematite, maghemite and goethite. The metal iron and anhydrous iron oxides have been formed in the process of coal combustion in EPS, by pyrite oxidation at diverse oxygen regimes, i.e. redox conditions. They appear in small grains in silicate matrix and may have preserved forms of the former mother pyrite grains, as in Fig. 2. Goethite has been formed during the hydraulic transport from the EPS, by hydration of hematite/maghemite.

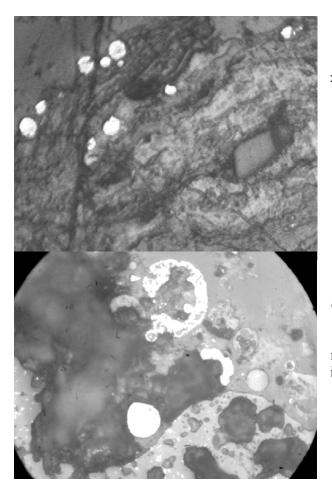


Fig. 1. Microphotograph of coal from KB: the gelled xylithic ground mass containing coal macerals (gelinite, cutinite, microspores), impregnation of clayey matter and dispersed pyrite (bright grains).

Magnification: 40 X.

Fig. 2. Microphotograph of coal ash from EPS: magnetite and wüstite (bright) pseudomorph after former spheroid and worm-like gel pyrite in silicate ground mass. Magnification: 100 X.

The iron mineral phases formed by coal firing in EPS (Table 1) indicate that the firing process in the EPS's oven is rather complex and is characterized by variable thermodynamic/redox conditions. The oxygen regime in the diverse sectors/spots in the oven varies from reduced to oxidized conditions. At rather reduced conditions, pyrite firing produces iron metal and SO<sub>2</sub> (reaction 1).

**Table 1.** Iron minerals in coal ash/slag.

Mineral	Composition
Iron	Fe
Wüstite	FeO
Magnetite	Fe <sub>3</sub> O <sub>4</sub>
Hematite	Fe <sub>2</sub> O <sub>3</sub>
Maghemite	Fe <sub>2</sub> O <sub>3</sub>
Goethite	FeOOH

FeS<sub>2</sub> + 2O<sub>2</sub> = Fe + 2 SO<sub>2</sub> ......(1)  
pyrite iron  
FeS<sub>2</sub> + 
$$2\frac{1}{2}$$
 O<sub>2</sub> = FeO + 2 SO<sub>2</sub> ......(2)  
pyrite wüstite  
3FeS<sub>2</sub> + 8O<sub>2</sub> = FeO·Fe<sub>2</sub>O<sub>3</sub> + 6SO<sub>2</sub> ...(3)  
pyrite magnetite  
2FeS<sub>2</sub> +  $5\frac{1}{2}$  O<sub>2</sub> = Fe<sub>2</sub>O<sub>3</sub> + 4SO<sub>2</sub>....(4)  
pyrite hematite

At mild and higher oxidized conditions pyrite fires to form wüstite and magnetite, respectively, along with SO<sub>2</sub> (reactions 2 and 3). At highly oxidized conditions, pyrite fires to form hematite/maghemite (reaction 4). For the best effects of coal usage in EPS it is necessary to enable oxidizing conditions in the EPS's oven for an efficient firing of all coal organic matter. The presence of iron mineral phases formed in reactions 1-3 indicates that in the oven partly existed diverse stages of oxygen deficiency which may decrease efficiency of the coal matter firing.

The presented results show that studies of phase transformation of iron minerals in coal firing process in EPS may enable very important information on the thermodynamic features of the process and may be used for its optimization. These optimizations of coal firing process may have important economic effects.

#### **Conclusions**

In the Kostolac basin coal is typical lignite with common high content of mineral matter and pyrite as main iron mineral. It was found that during coal firing in EPS, pyrite appear to be transformed in diverse iron phases: Fe-metal, wüstite, magnetite, hematite and maghemite, depending on redox features in EPS's oven. This indicates that studies of phase transformation of iron minerals in coal firing process in EPS may enable very important information on the thermodynamic features of the process and may be used for its optimization.

- [1] Dangić, A., Prelević, D., Dangić, J., Petrović, I., II Symp. Chem. Env. Protection, V.Banja, S.Ch.S., 191-192.
- [2] Dangić, A., Prelević, D., Petrović, I., Comptes Rend. Soc. Serbe Geol., 1998, 1992-1997, 107-114.
- [3] Mardon, S.M., Hower, J. Coal Geol., 2004, **59**, 169-214.
- [4] Ward, C.R., Int. J. Coal Geol., 2002, **50**, 135-168.

# **β – CAROTENE REMOVAL FROM SOYBEAN OIL WITH SMECTITE CLAY USING FULL FACTORIAL DESIGN**

Lj. Rožić, S.P. Petrović and T. Novaković

IchTM-Department of Catalysis and Chemcal Engineering, Njegoševa 12, Belgrade, Serbia

#### Abstract

In this study removal of  $\beta$ -carotene from soybean oil by adsorption was investigated and experimental design was applied. Acid activated smectite clay from Serbia was used as adsorbent. The effects of relevant factors, such as temperature, solid-to-liquid ratio and time, on removal of  $\beta$ -carotene were investigated. Process conditions for maximum removal of  $\beta$ -carotene were: 60 °C, 1800 s and 1: 50 solid to liquid ratio.

#### Introduction

Acid-activated bentonites are mainly used for the purification, decolorization and stabilization of vegetable oils. They remove phospo-lipids, soaps, trace metals, carotenoides, xanthophylls, chlorophyll, tocopherols, gossypol and their degradation products which impart undesirable colors to the edible oils [1, 2]. The mechanism of retention of the pigments, including carotene and carotenoids, at the surface of an activated clay is not clear. Most of the previous studies which focused on the removal of  $\beta$ -carotene by activated bentonites suggest that the adsorbent consist of smectite [3, 4].

In this study removal of  $\beta$ -carotene from soybean oil by acid activated smectite clay was investigated using statistical design of experiments. Two level factorial designs were applied to investigate the effects of the parameters and their interactions on removal of  $\beta$ -carotene from soybean oil.

# **Experimental**

#### Materials and methods

Smectite clay from Serbia was used as the raw material. Chemical activation of smectite was carried out in glass reactor at 80 °C, during 2.8 h with solid-liquid ratio 1:4.5, with HCl concentration of 4.8 M. Adsorption efficiency of acid activated smectite clay was evaluated by means of removal of  $\beta$ –carotene from soybean oil. The color changes in the treated oils were determined by using UV-visible spectrophotometer, Thermo Electron Corporation, Evolution 500, at the wavelength corresponding to the maximum absorbance of  $\beta$ -carotene, 455 nm.

#### Statistical design of experiments

The use of statistical design of experiments is advantageous as it allows one to obtain conditions through a relatively small number of systematic experiments. Using a proper design matrix one can obtain a regression equation, which highlights the effect of individual parameters and their relative importance in given operation

process. The interaction effects of two or more variables can also be known, which is not possible in a classical experiment.

The principal steps of statistically designed experiments are: determination of response variables, factors and factor levels, choice of the experiment design and statistical analysis of the data. Today, the most widely used experimental design to estimate main effects, as well as interaction effects, is the  $2^n$  factorial design, where each variable is investigated at two levels. So,  $2^3$  factorial design was selected in this study. The number of experiments (N) required for understanding all the effects is given by  $a^k = 2^3 = 8$  where a is the number of levels and k is the number of factors. The regression equation developed from different sets of experiments shows the dependence of yield on individual parameters as well as interactions for simultaneous variations of parameters.

#### **Result and Discussion**

In order to examine the main factors and their interaction for  $\beta$ -carotene removal from soybean oil by adsorption  $2^3$  full factorial design was applied. Temperature  $(X_1)$ , contact time  $(X_2)$  and solid to liquid ratio  $(X_3)$  were chosen as independent variables to model. Variables and levels for the study are given in Table 1.

**Table 1.** Variables and experimental design levels

Independent variable	Level			
	-1	0	+1	
Temperature $(X_{I_2} \circ \mathbb{C})$	60	72.5	85	
Time $(X_2, s)$	500	1150	1800	
Solid/liquid ratio $(X_3)$	1:50	1:33	1:25	

The experimental design matrix in coded form for three parameters  $X_1$ ,  $X_2$ ,  $X_3$  based on full factorial design and measured and predicted corresponding results (adsorption efficiency) are shown in Table 2.

**Table 2.** Matrix of experimental design.

Run	X1	X2	Х3	Measured value (%)	Predicted value (%)
1	_	_	_	87.13	86.01
2	+	_	_	94.22	94.13
3	_	+	_	96.67	97.79
4	+	+	_	96.64	96.73
5	_	_	+	65.10	66.22
6	+	_	+	79.03	79.12
7	_	+	+	79.13	78.01
8	+	+	+	81.80	81.71

The mathematical model representing the  $\beta$ -carotene removal from soybean oil as a function of the independent variables within the region under investigation was expressed by the following equation:

$$Y = 84.97 + 2.96X_1 + 3.60X_2 - 8.70X_3 - 2.23X_1X_2 + 1.19X_1X_3$$
 (1)

were Y is response (adsorption efficiency), and  $X_1$ ,  $X_2$  and  $X_3$  are the coded variables for temperature, contact time and solid to liquid ratio, respectively. By analysis of variance, the  $r^2$  value of this model was determined to be 0.994 which showed that the regression model defined well the true behavior of the system. The model (Eq. 1) indicated that positive coefficients of  $X_1$ ,  $X_2$ ,  $X_1X_3$  have a linear effect to increase Y, while, linear terms  $X_3$ ,  $X_1X_2$  had negative effects that decreases Y. As, a consequence, the best adsorption conditions for  $\beta$ -carotene were obtained: 60 °C, 1800 s and 1: 50 solid to liquid ratio.

#### Conclusion

From the statistical analysis, temperature and contact time have positive effects, whereas solid to liquid ratio have negative effects on  $\beta$ -carotene removal. On the other hand, the interaction between temperature and solid to liquid ratio has positive effect on  $\beta$ -carotene removal from soybean oil. These obtained results were important before detailed kinetics, mechanisms and optimization.

## Acknowledgments

This work was supported by the Ministry of Science of the Republic of Serbia (Projects number ON 142019)

- [1] S.C. Kheok, and E.E. Lim, J. Am. Oil Chem. Soc., (1982) 59 129-131.
- [2] W. Zschau, Eur. J. Lipid Sci. Technol., (2001) 103 505-551.
- [3] K. Boki, M. Kubo, N. Kawasaki, H. Mori, J. Am. Oil Chem. Soc., (1992b) 69 372-378.
- [4] G.E. Christidis, P.W. Scott and A.C. Dunham, Appl. Clay Sci., (1997) 12 329-347.

# THE ROLE OF INTRAPARTICLE DIFFUSION IN THE SORPTION OF $Cu^{2+}$ IONS ONTO HYDROXYAPATITE

M. Šljivić<sup>1</sup>, I. Smičiklas<sup>1</sup>, S. Pejanović<sup>2</sup> and I. Plećaš<sup>1</sup>

<sup>1</sup>The "Vinča" Institute of Nuclear Sciences, P.O.Box 522, 11001 Belgrade, Serbia <sup>2</sup>Faculty of Technology and Metallurgy, Karnegijeva 4, 11000 Belgrade, Serbia

#### **Abstract**

The  $Cu^{2^+}$  sorption onto HAP was investigated as a function of time, in the concentration range  $5\cdot 10^{-4}$  -  $5\cdot 10^{-3}$  mol/dm<sup>3</sup>. The experimentally obtained kinetic data were fitted with the intraparticle diffusion model. The correlation coefficients were low considering the overall reaction period. However, q versus  $t^{0.5}$  plots could be divided into three segments, out of which the second linear segment can be attributed to the intraparticle diffusion. Intraparticle diffusion rate constants ( $k_i$ ) increased from  $3.57\cdot 10^{-3}$  to  $7.80\cdot 10^{-3}$  mmol/g min<sup>0.5</sup> with the increase of the initial  $Cu^{2^+}$  concentration. As the lines did not pass through the origin it was concluded that intrapaticle diffusion is not the only rate-controlling step.

#### Introduction

It is generally accepted that the sorption dynamics consists of three consecutive steps: (1) transport of sorbate particles from the bulk solution to the external surface of the sorbent by diffusion through the liquid boundary layer, (2) diffusion of the sorbate from the external surface into the pores of the sorbent and (3) sorption of the sorbate on the active sites on the internal surface of the pores [1]. The overall rate of sorption may be controlled by each process or by their combination. It has been noticed in many studies that boundary layer diffusion is dominant during the initial sorbate uptake, and then gradually, after the sorbent's external surface is loaded, the sorption rate becomes controlled by intraparticle diffusion.

In this paper, the role of intraparticle diffusion in the kinetics of  $Cu^{2+}$  sorption from the aqueous solution by hydroxyapatite  $(Ca_{10}(PO_4)_6(OH)_2, HAP)$  was studied.

#### **Materials and Methods**

As a sorbent, synthetic HAP, prepared by neutralization of  $Ca(OH)_2$  with  $H_3PO_4$ , was used [2]. The sorbent was shaken (120 rpm) with  $Cu(NO_3)_2$  solutions (solid to liquid ratio 1:200), at room temperature ( $20\pm1^{\circ}C$ ). The contact times were varied in the range 5 min. - 48 h. The initial concentrations of  $Cu^{2+}$  were  $5\cdot10^{-4}$ ,  $1\cdot10^{-3}$  and  $5\cdot10^{-3}$  mol/dm<sup>3</sup>, while initial pH values were adjusted to 5. After filtration, the  $Cu^{2+}$  concentrations were measured by a Perkin Elmer Analyst 200 Atomic Absorption Spectrometer.

#### **Results and Discussion**

The intraparticle diffusion model, proposed by Weber and Morris [3], can be expressed by following equation:

$$\underline{q} = k_i t^{0.5} + \underline{c} \tag{1}$$

where q is the amount of  $Cu^{2+}$  sorbed (mmol/g) at time t,  $k_i$  is intraparticle diffusion rate constant (mmol/g min<sup>0.5</sup>), and c is constant related to the boundary layer thickness. According to this model, the plot of uptake, q versus the square root of time, should be linear if intraparticle diffusion is involved in the adsorption process. Furthermore, if these lines pass through the origin then the intraparticle diffusion is the rate controlling step.

The plots of the amounts of Cu<sup>2+</sup> sorbed by HAP against the square root of time, for various initial sorbate concentrations, are presented in Fig.1.

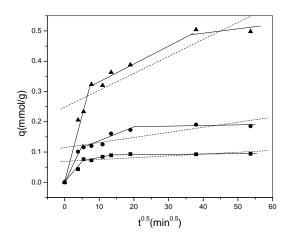


**Fig. 1.** Dependency between the amount of  $Cu^{2+}$  sorbed by HAP and square root of time.  $Cu^{2+}$  concentrations (mol/dm<sup>3</sup>):  $5\cdot10^{-4}$  ( $\blacksquare$ ),  $1\cdot10^{-3}$  ( $\bullet$ ) and  $5\cdot10^{-3}$  ( $\blacktriangle$ ). Linear data fitting for overall process (--) and different process stages (—).

Considering the overall reaction period, the intraparticle diffusion model has shown low correlation with experimental data (Table 1). Owing to the varying extent of sorption in the initial and final stages, plots of q versus  $t^{0.5}$  often demonstrate multilinearity, signifying that different types of mechanisms are operating in the various stages of the sorption [4].

In the case of Cu<sup>2+</sup> sorption by HAP (Fig. 1). at the beginning of sorption there is a region representing more rapid diffusion through the boundary layer, followed by the second stage representing diffusion of the sorbate molecules by a pore dif-

fusion process through the liquid filled pores or by a solid surface diffusion mechanism [5]. The third segment corresponds to equilibrium [5]. The rates of the first two stages increase with initial concentration increase, since the driving force for the mass transfer increase in the same way. The equilibrium was achieved faster (about 6 h) in the systems with lower metal concentrations, while approximately 24 h was needed in the case of the highest studied Cu<sup>2+</sup> concentration. The intraparticle diffusion step (Stage 2) approximately takes place in the time ranges 25 min-3

h, 25 min-6 h and 60 min-22 h for initial concentrations  $5\cdot10^{-4}$ ,  $1\cdot10^{-3}$  and  $5\cdot10^{-3}$  mol/dm<sup>3</sup>, respectively.

The correlation coefficients for the second linear segments (Table 1) are relatively high, while the calculated intraparticle diffusion rate  $(k_i)$  increases from  $3.57\cdot 10^{-3}$  to  $7.80\cdot 10^{-3}$  mmol/g min $^{0.5}$  with the initial concentration increase. The increased initial  $Cu^{2+}$  concentration create a lower intraparticle diffusion resistance and accordingly give higher internal diffusion coefficient. However, the plots indicated that the intraparticle diffusion is not the only rate controlling step because the lines did not pass through the origin.

**Table 1.** Linear regression coefficients for the overall sorption process and the stage involving intraparticle diffusion, and calculated intraparticle diffusion rate constants.

Initial Cu <sup>2+</sup>	Overall	Stage 2		
concentration	process	R	$k_i \cdot 10^3$	
(mol/dm <sup>3</sup> )	R	K	$(\text{mmolg}^{-1}\text{min}^{-0.5})$	
5.10-4	0.63	1.00	3.57	
1.10-3	0.85	0.93	5.10	
5.10-3	0.91	0.93	7.80	

#### Conclusion

The intraparticle diffusion model was found to be inappropriate for the description of the overall process of  $Cu^{2+}$  sorption by HAP. However, intraparticle diffusion which can be attributed to the second linear segment of the q vs,  $t^{1/2}$  plots, takes place in the time ranges 60 min-22 h for  $Cu^{2+}$  concentration  $5\cdot 10^{-3}$  mol/dm<sup>3</sup>, 25 min-6 h for  $1\cdot 10^{-3}$  mol/dm<sup>3</sup> and 25 min-3h for  $5\cdot 10^{-4}$  mol/dm<sup>3</sup> solution. The calculated  $k_i$  values were found to increase with the increase of initial  $Cu^{2+}$  concentration. The results imply that both boundary layer and intraparticle diffusion might be involved in this removal process.

- [1] M. Trgo, J. Perić, N. Vukojević Medvidović, J. Environ. Manage., 2006, 79, 298-304.
- [2] I. Smičiklas, A. Onjia, S. Raičević, Sep. Purif. Technol., 2005, 44, 97-102.
- [3] W.J. Weber, J.C. Morris, J. Sanit. Eng. Div. Am. Soc. Civ. Eng. 1963, 89, 31-60.
- [4] W.H. Cheung, Y.S. Szeto, G. McKay, Biores. Technol., 2007, 98, 2897–2904.
- [5] B.H. Hameed, M.I. El-Khaiary, J. Hazard. Mater., 2008, Article in Press.

# THE EVALUATION OF RADIONUCLIDES REMOVAL USING CLINOPTILOLITE, HYDROXYAPATITE AND THEIR MIXTURES

I. Smičiklas, S. Dimović, M. Šljivić and I. Plećaš

The Vinča Institute of Nuclear Sciences, P.O.Box 522, 11001 Belgrade, Serbia

#### **Abstract**

The sorption properties of clinoptilolite and hydroxyapatite towards  $Cs^{1+}$ ,  $Co^{2+}$ , and  $Sr^{2+}$  ions were compared, under the same experimental conditions.  $Cs^{1+}$  was preferably sorbed by natural clinoptilolite. Conversely, synthetic hydroxyapatite exhibited higher sorption capacities for  $Co^{2+}$  and  $Sr^{2+}$ , while the sorption of  $Cs^{1+}$  was negligible. It was shown that, as a consequence of different affinity towards investigated cations, application of mixed clinoptilolite/hydroxyapatite sorbent represents a good strategy for the purification of effluents containing a mixture of  $Cs^{1+}$ ,  $Co^{2+}$  and  $Sr^{2+}$ .

#### Introduction

Sorption technologies in liquid radioactive waste management, based on the use of selective sorbents, have been developed rapidly due to simplicity of the technology and necessary equipment and possibility of obtaining good liquid/solid radioactive waste ratio [1].

The sorption studies are generally focused on an individual sorbent, and single metal solution, while little effort has been done to perform the studies with the combinations of different sorbents and/or sorbates. The objective of the present work was to compare the effectiveness of local clinoptilolite (Serbia), synthetic hydroxyapatite (HAP) and their mixtures in decontamination of mixed metal solutions ( $^{60}\text{Co}^{2+}$ ,  $^{90}\text{Sr}^{2+}$  and  $^{137}\text{Cs}^{1+}$ ).

#### **Materials and Methods**

Zeolite sample was obtained from the Zlatokop mine near Vranjska Banja, Serbia. XRD analysis of the sample have shown that it consists mainly of clinoptilolite (>90%), with quartz and albite as impurities [2]. A fraction of particles 200 - 250 µm in size was used. Low-crystalline hydroxyapatite (HAP) sample was synthesized at room temperature, by neutralization method [3].

Sorption experiments were conducted using inactive forms of metal cations. As most real wastes consist of mixtures of various contaminants, a solution containing  $100 \text{ mg/dm}^3$  of each contaminant ( $\text{Co}^{2+}$ ,  $\text{Cs}^{1+}$  and  $\text{Sr}^{2+}$ ) was prepared. This solution was shaken with HAP, clinoptilolite or their mixtures prepared at different HAP/clinoptilolite ratios, at initial pH 5, solid to solution ratio of 1: 200, for 24 hours, at room temperature ( $20\pm1^{\circ}\text{C}$ ). The suspensions were filtrated, and the metal concentrations were determined using Perkin Elmer Analyst 200 Atomic Absorption Spectrometer.

#### **Experimental Results**

Table 1. presents the mass ratios of sorbents, as well as the percentages of metal cations removed and final solution pH values.

<b>Table 1.</b> Mass ratio of HAP and clinoptilolite and the amounts of metal ions re-
moved from the mixed metal solution.

HAP/Clin.	Cation sorbed (%)			
ratio	Cs <sup>1+</sup>	$\mathrm{Sr}^{2+}$	Co <sup>2+</sup>	Total
1:0	0.0	53.6	51.3	35.9
5:1	31.9	49.1	43.2	41.6
3:1	47.3	48.0	43.5	46.2
2:1	65.9	45.8	41.8	50.8
1:1	78.5	41.7	35.1	51.0
1:2	89.6	35.8	25.8	49.2
1:3	91.9	33.3	16.7	45.9
1:5	93.6	31.0	18.0	46.1
0:1	95.6	20.8	5.6	39.0

Synthetic HAP powder, applied as an individual sorbent, retained 53.6 and 51.3 % of Sr<sup>2+</sup> and Co<sup>2+</sup>, whereas the sorption of Cs<sup>1+</sup> was in the range of experimental error. The previously determined HAP selectivity towards Sr<sup>2+</sup> and Co<sup>2+</sup> from their single metal solutions was the same, while the calculated maximum sorption capacities were 26 mg/g and 20 mg/g, respectively [3, 4]. HAP selectivity towards divalent metal cations is a result of the ion-exchange process with Ca<sup>2+</sup> ions [5]. Crystal radii of strontium (1.13 Å) and cobalt (0.72 Å) slightly differ from Ca<sup>2+</sup> crystal radius (0.99Å); therefore these cations can substitute Ca<sup>2+</sup> in the HAP crystal lattice. On the other hand, the crystal radius of Cs<sup>1+</sup> (1.69 Å) is much larger, which explains why it cannot be effectively sorbed. Similar results were reported by Krajzler and Narbutt [6], for biogenic apatite. This sorbent was efficient for the removal of radionuclides of strontium, as well as europium and trivalent actinides, but not of cesium due to its large ionic radius and low charge.

In the case of clinoptilolite, although various cations are available for ion exchange ( $Ca^{2+}$ ,  $Mg^{2+}$ ,  $Na^+$ ,  $K^+$ ), the hydrated ionic radii of sorbates were found to be the most influential concerning removal efficiency. Monovalent cations, contrary to divalent ones, have larger ionic but smaller hydrated ionic radii, and with fewer and weakly bonded water molecules they move more freely into and out of the clinoptilolite channels [7]. The sequence of hydrated ionic radii of  $Cs^{1+}$ ,  $Sr^{2+}$  and  $Co^{2+}$  (3.29, 4.12, 4.23 Å, respectively) follows the sequence of experimentally determined clinoptilolite capacities:  $Cs^{1+}$  (48.4 mg/g)  $>Sr^{2+}$  (9.8 mg/g)  $>Co^{2+}$  (2.8 mg/g) [2]. From the results of this study, it can be concluded that clinoptilotite selectivity towards examined cations from their mixture, followed the same trend (95.6 % of  $Cs^{1+}$ , 20.8 % of  $Sr^{2+}$  and 5.6 % of  $Co^{2+}$ ).

HAP sorption capacity towards Co<sup>2+</sup> ions from mixed metal solution is ten times higher that the value obtained for clinoptilolite. Furthermore, although among various investigated divalent cations (Pb, Cd, Zn, Sr) HAP exhibit lowest sorption capacity for Sr<sup>2+</sup> [3], it is still about three times better sorbent of Sr<sup>2+</sup> than clinoptilolite

Considering removal efficiency of various HAP/clinoptilolite mixtures, as the fraction of clinoptilolite phase increased, the sorption of Cs<sup>1+</sup> increased, while the sorption of divalent cations decreased. The highest total percentage of metal ions removed from the solution (51%) was obtained at a HAP/clinoptilolite mass ratio of 1:1.

#### Conclusion

HAP is more selective towards divalent Sr and Co ions, while clinoptilolite towards monovalent Cs. Sorption of Cs<sup>+</sup> on hydroxyapatite is negligible. If the mixed wastes, containing all tree metal cations, have to be treated, the mixture of HAP and clinoptilolite will give better results than each of the sorbents alone. For the wastes containing equivalent concentrations of Cs<sup>1+</sup>, Co<sup>2+</sup> and Sr<sup>2+</sup>, the best total removal efficiency was achieved at HAP/ clinoptilolite =1:1 ratio.

- [1] N. V. Elizondo, E. Ballesteros, B. I. Kharisov, Appl. Radiat. Isotopes, 2000, 52, 27-30.
- [2] I. Smičiklas, S. Dimović, I. Plećaš, Appl. Clay Sci., 2007, 35, 139-144.
- [3] I. Smičiklas, A. Onjia, S. Raičević, Đ. Janaćković, M. Mitrić, J. Hazard. Mater., 2008, 152, 876-884.
- [4] I. Smičiklas, S. Dimović, I. Plećaš, M. Mitrić, Watr. Res., 2006, 40, 2267 2274.
- [5] F. Monteil-Rivera, M. Fedoroff, in: Encyclopedia of Surface and Colloid Science, Marcel Dekker. Inc., New York, 2002, p.1-26.
- [6] J. Krejzler, J. Narbutt, Nukleonika 2003, 48, 171-175.
- [7] R. M. Woods, M. E. Gunter, Am. Mineral. 2001, 86, 424–430.

# Macromolecular Physical Chemistry (J)

### SYNTHESIS AND CHARACTERIZATION OF CONDUCTING POLYANILINE NANOTUBES IN THE PRESENCE OF COLLOIDAL TIO<sub>2</sub> NANOPARTICLES

M. Radoičić<sup>1</sup>, Z. Šaponjić<sup>1</sup>, J. Nedeljković<sup>1</sup>, J. Stejskal<sup>2</sup> and G. Ćirić-Marjanović<sup>3</sup>

<sup>1</sup>Vinča Institute of Nuclear Sciences, P.O. Box 522, 11001 Belgrade, Serbia

<sup>2</sup>Institute of Macromolecular Chemistry, Academy of Sciences of the Czech Republic,

162 06 Prague 6, Czech Republic

<sup>3</sup>Faculty of Physical Chemistry, University of Belgrade, Studentski Trg 12-16,

11158, Belgrade, Serbia (gordana@ffh.bg.ac.yu)

#### **Abstract**

Conducting polyaniline nanotubes were synthesized by the oxidative polymerization of aniline with ammonium peroxydisulfate in water, in the presence of colloidal  ${\rm TiO_2}$  nanoparticles of an average diameter ~5 nm. Polyaniline- ${\rm TiO_2}$  nanocomposite has been characterized by the electrical conductivity measurements, thermogravimetric analysis, FTIR spectroscopy, scanning and transmission electron microscopies. The electrical conductivity of synthesized nanocomposite was  $1.1 \times 10^{-3} \, {\rm S \ cm^{-1}}$ , slightly higher than that of pure polyaniline prepared under the same conditions. Polyaniline nanotubes have an outer diameter of 45–230 nm nm, an inner diameter of 15–130 nm, and a length extending from 0.5 to 2.0  $\mu$ m.

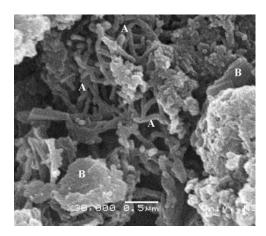
#### Introduction

It has recently been shown that the dispersibility and processability of nanostructured conducting polymers, as well as their performance in numerous applications, are significantly improved in comparison with conducting polymers having granular morphology [1]. The preparation of self-assembled PANI nanotubes and nanorods has received a growing attention during the last years [2– 4]. Oxidative polymerization of aniline with ammonium peroxydisulfate (APS) as an oxidant in aqueous solutions (the initial pH  $\geq$  3.5) represents an efficient synthetic route to PANI nanostructures, without the use of an external template [2– 4]. In recent years, synthesis of conducting polymer/inorganic particles composites with improved mechanical properties, processability and heat resistance, in comparison to corresponding pure conducting polymer, constitutes an important scientific challenge. TiO<sub>2</sub> nanoparticles are especially interesting because of their unique electrical and optical properties, as well as extensive industrial applications [5]. The hybrid PANI-TiO<sub>2</sub> nanomaterials, which combine the electrical conductivity of PANI and UV-sensitivity of TiO<sub>2</sub>, look as a promising candidate for application in electrochromic devices, nonlinear optical systems, and photo electrochemical devices [6]. Although many papers on PANI-TiO<sub>2</sub> nanocomposites have been published [7], only one work was devoted to the preparation of PANI-TiO<sub>2</sub> nanotubes, in the presence of β-naphthalenesulfonic acid [8]. The purpose of this work is the synthesis of conducting PANI nanotubes by the oxidative polymerization of aniline with APS in the presence of colloidal TiO<sub>2</sub> nanoparticles

of an average diameter  $\sim$ 5 nm, in aqueous solution without added acid, and characterization of prepared nanocomposite by scanning (SEM) and transmission (TEM) electron microscopies, FTIR spectroscopy, and thermogravimetric (TGA) and electrical conductivity measurements.

#### **Results and Discussion**

Colloidal  $TiO_2$  solution, containing nanoparticles of an average diameter ~5 nm, was prepared according to the procedure described by Rajh et al. [9]. In a typical procedure for preparing PANI nanotubes in the presence of  $TiO_2$  nanoparticles, the aqueous solutions of aniline (0.32 M, 25 ml), oxidant (0.4 M APS, 25 ml), and colloidal  $TiO_2$  (0.016 M, 50 ml) were mixed at room temperature. The reaction mixture was stirred for 180 min, and then the precipitated PANI- $TiO_2$  composite was collected on a filter, rinsed with ethanol acidified with sulfuric acid (5 × 10<sup>-3</sup> M), and dried in vacuum at 60  $^{\circ}$ C for 3 h. As a reference, the pure PANI sample was prepared by the same procedure, without  $TiO_2$  addition.



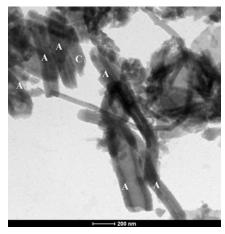


**Fig. 1**. SEM (left) and TEM (right) images of the PANI-TiO<sub>2</sub> nanocomposite: A-nanotube, B-nanosheet, C-nanorod.

The presence of PANI nanotubes was revealed by SEM and TEM microcopies (Fig. 1, A). Nanotubes have an outer diameter of 45–230 nm, an inner diameter of 15–130 nm, and a length extending from 0.5 to 2.0 µm. The nanotubes are accompanied by nanosheets (Fig. 1, B) and nanorods (Fig. 1, C).

The conductivity of obtained PANI-TiO<sub>2</sub> nanocomposite was  $1.1 \times 10^{-3} \ \mathrm{S}$  cm<sup>-1</sup>, slightly higher than the conductivity of pure PANI which was synthesized under the same conditions without added TiO<sub>2</sub>,  $9.1 \times 10^{-4} \ \mathrm{S}$  cm<sup>-1</sup>. Figure 2 shows the TGA curves of pure PANI and PANI–TiO<sub>2</sub> nanocomposite, recorded in air stream.

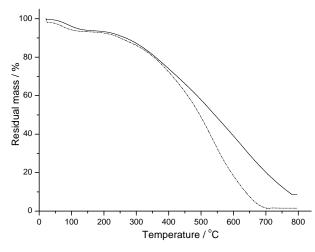


**Fig. 2.** TGA curves for PANI-TiO<sub>2</sub> nanocomposite (—) and pure PANI  $(- \cdot -)$ , recorded in air.

In the temperature range 300-780  $^{\circ}C$ the weight loss of the PANI-TiO<sub>2</sub> occurred, attributed to degradation combustion of **PANI** backbone. Pure **PANI** sample was completely decomposed at ca. 700 °C. From the TGA curve obtained during complete combustion organic matter present in the nanocomposite, the content of TiO<sub>2</sub> in PANI-TiO<sub>2</sub> was determined to amount 8.5 wt. %.

In the FTIR spectrum of PANI-TiO<sub>2</sub> nanocomposite, characteristic bands of PANI were observed at wavenumbers 1569, 1495, 1307, 1246, 1146 and 825 cm<sup>-1</sup>, as well as the bands of counterions (sulfate and hydrogensulfate) at 617 and 588 cm<sup>-1</sup>, indicating the presence of PANI chains in its protonated form in PANI-TiO<sub>2</sub>.

#### Conclusion

Conducting PANI nanotubes have been synthesized in the presence of colloidal TiO<sub>2</sub> nanoparticles by the oxidative polymerization of aniline with APS in aqueous solution without added acid. Novel PANI-TiO<sub>2</sub> nanocomposite was characterized by scanning and transmission electron microscopies, FTIR spectroscopy, and thermogravimetric and electrical conductivity measurements.

- [1] S.Virji, J. Huang, R.B. Kaner and B.H. Weiller, Nano Lett., 2004, 4, 491–496.
- [2] M.Trchová, E.N. Konyushenko, J. Stejskal, I. Šeděnková, P.Holler and G. Ćirić-Marjanović, J. Phys. Chem. B. 2006, 110, 9461–9468.
- [3] J. Stejskal, I. Sapurina, M. Trchová, E.N. Konyushenko and P. Holler, *Polymer* 2006, 47, 8253–8262.
- [4] A. Janošević, G. Ćirić-Marjanović, B. Marjanović, P. Holler, M. Trchová and J. Stejskal, Nanotechnology 2008, **19**, 135606.
- [5] T. Matsumoto, Y. Murakami, Y. Takasu, J. Phys. Chem. B, 2000, 104, 1916.
- [6] M. K. Ram, Ö. Yavuz, V. Lahsangah, M. Aldissi, Sens. Actuators B, 2005, 106, 750.
- [7] H. Tai, Y. Jiang, G. Xie, J. Yu, X. Chen, Sens. Actuators B, 2007, 125, 644.
- [8] L. Zhang, M. Wan, J. Phys. Chem B, 2003, **107**, 6748.
- [9] T. Rajh, D. Tiede, M. Thurnauer, J. Non-Cryst. Solids, 1996, 207, 815.

#### EXPRESSION OF FUSION PROTEINS FOR DETECTION OF TNT-DERIVATIVES IN ONE OR TWO COMPONENT SYSTEM

M. Simonović<sup>1</sup>, S. Milošević-Zlatanović<sup>2</sup>, M.M. Vrvić<sup>3</sup>, N. Milosavić<sup>4</sup> and B.R. Simonović<sup>1</sup>

<sup>1</sup> Institute of General and Physical Chemistry, Studentski Trg 12-16, Belgrade, Serbia (mladen@iofh.bg.ac.yu),

#### Introduction

The aim of this work was to construct and examine different fusion proteins of type antibody-enzyme, which would carry the TNT-specific scFv-fragments on its N-terminus coupled with multiple marker-enzymes. The fusion resulted in a bifunctionality of such immunoreagents. As a model enzyme the beta-lactamase was used, because it offers optimal conditions for construction of fusion proteins due to its low molecular weight (263 aminoacids, 29 kDa) and only one protein chain with a single disulfide bond in the structure. Regarding the binding properties and affinity the most sensitive immunoreagent should be used in the assay for detection of TNT-derivatives. As a testing molecule a TNT-derivative TNP was chosen, which was coupled to the protein carrier BSA forming a conjugate TNP-BSA.

#### **Material and Methods**

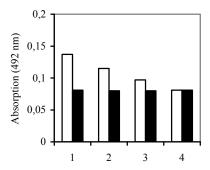
- 1. Cell lines/Bacterial species. The different bacterial strains from *E. coli* K12 were used.
- 2. Vectors. For cloning the phagemid-vector pHEN2 was used. *E. coli*-expression vector pET26b(+) was commercially purchased from Novagen (Schwalbach).
- 3. Standard molecular biology and protein biochemistry techniques were done according to the standard protocols [1].
- 4. IMAC (Immobilized Metalion Affinity Chromatography) was performed with dialysates of a periplasmatic extract on Ni-NTA-agaorse. The elution was done with imidazol in a final concentration of 300 mmol/l. The fractions were examined in 10-15% PAGE-gels for the presence of proteins, then pooled, dialyzed in PBS pH 7.4 over night at 4 °C and again analyzed in SDS-PAGE.
- 5. ELISA. The 96-wells plate was covered over night at 4° C with a strong diluted TNP-BSA conjugate (50  $\mu$ g/ml). As negative control in each assay the wells were covered with BSA. After the washing procedure the wells were blocked with BSA for 45 min at room temperature. The fusion protein scFv-beta-lactamase in the concentration of 10-60  $\mu$ g/ml was incubated for 1 h at the room temperature and nitrocephin was added for detection. After 5 minutes the signal was measured in the ELISA-reader at 492 nm.

<sup>&</sup>lt;sup>2</sup> Faculty of Mathematics and Natural Sciences, University of Kragujevac, Radoja Domanovica 12, Kragujevac, Serbia,

<sup>&</sup>lt;sup>3</sup> Faculty of Chemistry, University of Belgrade, Studentski Trg 12-16, Belgrade, Serbia, <sup>4</sup>Institute of Chemistry, Technology and Metallurgy, Studentski trg 12, Belgrade, Serbia

#### Results

- 1. Fusion protein 11B3-scFv-beta-lactamase. The gene for 11B3-scFv was available and contained  $V_{\rm H}$  and  $V_{\rm L}$  regions developed by immunization of mice. The scFv-gene had to be placed on 5' terminus and the gene for beta-lactamase on 3' terminus. The clone examination using PCR confirmed the presence of both genes. The expression of the fusion protein 11B3-scFv-beta-lactamase was done in *E. coli* strain BL21 DE3. After expression at 25 °C the cells were separated from the expression supernatant and the periplasmatic extract was separated. The confirmation of the beta-lactamase activity was done visually using the substrate nitrocephin. The fusion protein was then used for the assay on the microtiter plate as a bifunctional reagent in order to evaluate its binding properties and detection capability (figure 1).
- 2. Fusion protein 3.5-scFv-beta-lactamase. 3.5-scFv is a selected scFv from a synthetic library of human scFvs. The gene for 3.5-scFv was inserted behind the signal sequence. Beta-lactamase had to be located behind scFv, but in front of stop-codon. The periplasmatic expression of the fusion protein 3.5-scFv-beta-lactamase were done in the *E. coli* strain DH5 $\alpha$  at 30 °C. The presence of the protein was verified in the periplasma and cell extract using immunoblot and the protein was purified on the Ni-NTA-agarose. The confirmation of the beta-lactamase activity was done visually just as for its analog 11B3-scFv-beta-lactamase (figure 1).



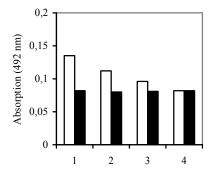


**Fig. 1.** ELISA for detection of TNP using fusion protein 11B3-scFv-beta-lactamase (left) and 3.5-scFv-beta-lactamase (right) in the concentration 60  $\mu$ g/ml (1), 40  $\mu$ g/ml (2), 20  $\mu$ g/ml (3) and 10  $\mu$ g/ml (4) respectively. Dark lines are negative controls.

#### **Discussion**

The future works in detection of TNT-derivatives should concern the sensitivity enhancement. The monoclonal antibodies fused with enzymes such as alkali phosphatase with a large turnover number could potentially serve as high sensitive

one-component detection systems. An alternative usage of beta-lactamase concerning higher sensitivity could be achieved with the fluorescent substrate [2]. Further, on the solid phase covered with streptavidin the previously biotinilated scFv molecules can be immobilized. Using fluorescently marked TNP molecules a competitive assay would be established.

The sensitivity enhancement for 2-3 orders of magnitude could be achieved with noncompetitive ELISA [3], [4]. Thereby fluorescent detection should be regarded.

With change from optical to electrochemical detection, a recombinant fusion protein should be cloned and expressed with a suitable enzyme (alkaline phosphatase, beta-galactosidase), for which already exist the substrates for changeable redox potentials [5], [6]. Electrochemical detection will not enhance assay sensitivity, but will allow the rapid detection of TNT-derivatives also in turbid solutions.

- [1] Ausubel, F.M., Current protocols in molecular biology. Wiley interscience, New York, 1996.
- [2] Zlokarnik, G., Negulescu, P.A., Knapp, T.E., Mere, L., Burres, N., Feng, L., Whitney, M., Roemer, K., Tsein, R.Y.: Quantitation of transcription and clonal selection of single living cells with β-lactamase as reporter. Science, 1998, **279**, 84-88.
- [3] Suzuki, C., Ueda, H., Mahoney, W., Nagamune, T.: Open sandwich enzyme-linked immunosorbent assay for the quantitation of small haptens. Analytical biochemistry, 2000, **286**, 238-246.
- [4] Yokozeki, T., Ueda, H., Arai, R., Mahoney, W., Nagamune, T.: A homogeneous non-competitive immunoassay for the detection of small haptens. Anal. Chem., 2002, **74**, 2500-2504.
- [5] Thomas, J.H., Kim, S.K., Hesketh, P.J., Halsall, H.B., Heineman, W.R.: Bead-based electrochemical immunoassay for bacteriophage MS2. Anal Chem., 2004, 76(10), 2700-2707.
- [6] Yu, Z., Xu, Y., Ip, M.P.: An ultra-sensitive electrochemical enzyme immunoassay for thyroid stimulating hormone in human serum. J Pharm Biomed Anal., 1994, 12(6), 787-793.

### POLYMERISATION OF DIBUTILITACONATE IN THE MICROWAVE FIELD

J. Jovanović<sup>1</sup>, B. Adnađević<sup>1</sup>, I. Popovic<sup>2</sup> and M. Babić<sup>2</sup>

<sup>1</sup>Faculty of Physical Chemistry, Studentski trg 12-16, 11001 Belgrade <sup>2</sup>Faculty of Technology and Metalurgy, Karnegijeva 4, 11001 Belgrade

#### **Astract**

Poly(dibutilitaconate) (PDBI) was successfully synthesized for first time by radical polymerization in bulk in microwave field using 2,2'-azobisisobutironitril (AIBN) as an initiator. Effects of temperature and of imitator concentration on reaction rate and molar mass of the obtained polymers were investigated. It was established that the rate of polymerization of dibutilitaconate (DBI) in the microwave field was 2-4 times higher than under the conventional conditions, but molar mass of the polymerization products were decreased.

#### Introduction

Microwave synthesis represents a major break-through in synthetic chemistry methodology, a dramatic change in the way chemical synthesis is performed and in the way it is perceived in the scientific community [1]. Microwave-assisted heating could accelerate the rates of polymerization reaction and improve the properties of the products and due to that microwave-assisted chemical synthesis has attracted wide attention. Previously, the conventional and microwaves kinetics of methyl methacrylate (MMA) polymerization was compared and discussed. [2]. The structural similarity of poly(di-itaconate)s and poly(methacrylate)s make polymers based on itaconic acid potentially very useful materials [3]. To the best of our knowledge, there are not any data about poly(dibutilitaconate) (PDBI) synthesis under the influence of microwave field...

#### **Experimental**

Poly(dibutilitaconate) (PDBI) was synthesized via free-radical polymerization in bulk (without solvents) under conventional and microwave isothermal heating. Monomer, DBI, was synthesised in laboratory [4]. 2,2'-azobisisobutironitril (AIBN) was used as an initiator. Polymerization were carried out in nitrogen atmosphere at temperatures: 40°, 50°, 60° and 70°C. Reaction times were from 10 min to 60 min. Concentration of initiator was varied from 0.4-1.2 mol%.

Conventional polymerizations were carried out in thermostated four-necked reaction vessel supplied with nitrogen in-and-outlet; reflux condensate and thermometer. In the case of microwave-assisted synthesis, the prepared reaction mixture was placed in a focused microwave reactor (Discover, CEM Corporation, Matthews, North Carolina, US). All the reactions were carried out in the microwave field of 2.45 GHz with different input powers from 3-50 W required to maintain the desired temperatures. Yield (%) of the synthesized polymer was determined by gravimetry, by precipitation polymer in isopropanol. Molar mass of

the synthesized polymer were determined by GPC method, using Waters instrument, supplied with four columns. Tetrahydrophyrane was used as mobile phase and polystyrene standards for calibration. Reaction rate was calculated as: Rp= dM/dt, where M is monomer concentration and t is reaction time.

#### **Results and Discussion**

Figure 1 presents effect of reaction time on the yield of PDBI for conventional and microwave polymerization process, obtained at constant temperature t=60°C and initiator concentration c(AIBN)=0.6mol%.

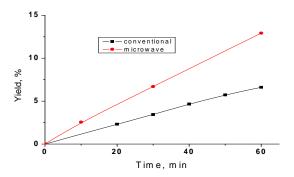
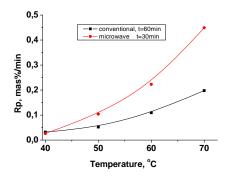


Fig. 1. Effect of reaction time on PDBI yield

As can be clearly seen, yield of PDBI linearly increases with reaction time increase, but more significantly in the case of microwave assisted polymerization. Yield of PDBI was about twice higher in the polymerization reaction under microwave field then in conventional one.

Figure 2 presents temperature influence on

reaction rate under the constant initiator concentration (c(AIBN)=0.6mol%) and Figure 3 shows effects of initiator concentration on reaction rate.



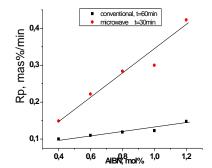


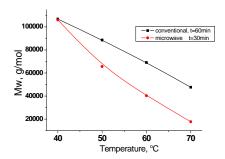
**Fig. 2.** Temperature influence on reaction rate influence on influence of reaction Fig. 3

**Fig. 3.** Initiator concentration influence on reaction rate

As expected, temperature increrse speeds up both conventional polymerization and under microwave field. Polymerization rate increase exponentially with temperature increase, but more dramatically when polymerization was carried out in the microwave field. Initiator concentration was varied from 0.4 to 1.2 mol%, when temperature was kept const. (60°C). Within the investigated range of AIBN concentration, reaction rate increase linearly with

initiator concentration increase both for conventional and microwave process, but more dramatically for microwave process. Reaction rate for DBI polymerization with 0.6 mol% AIBN was found to be increased about 2 times (100%) but the same process with twice more initiator concentration (1.2mol%) was increased up to 3.5 times in microwave field.

Figure 4. presents temperature influence on the average molar mass (Mw) of the synthesized PDBI. Temperature increase leads to the lower average molar mass of the PDBI synthesized both under the conventional procedure and under microwave field. Temperature increase in the microwave field exhibit stronger effect on molar mass decrease than in conventionally process. Figure 5 present changes of molar masses (Mw) with initiator concentration. Molar mass of polymer obtained in microwave process decreased linearly with initiator concentration increase, on the contrary to the conventional process where initiator concentration actually has not influence on molar mass.



70000
60000

Conventional, t=60min
microwave t=30min

0,4 0,6 0,8 1,0 1,2

AIBN. mol%

Fig. 4. Temperature influence on molar mass

**Fig. 5.** Initiator concentration influence on reaction rate

#### **Conclusions**

Rate of polymerization of DBI was 2-4 times higher in the microwave heated process while molar mass of PDBI were decreased under compared to the conventional process.

#### Acknowledgements

The investigation was supported by the Ministry of Science of the Republic of Serbia, through project G 142025.

- [1] Collins, M.J. "Microwave Synthesis- Chemistry at the Speed of Light," Hayes, B.L., CEM Publishing, Matthews, 2002, p 11.
- [2] J. Jovanovic, B. Adnadjevic, J.Appl. Polym. Sci., 2007, **104(3)**, 1775–1782.
- [3] I.G.Popović, L. Katsikas, J.S. Veličković, Pol. Deg. \$ Stab. 2005, 89, 165-174.
- [4] M.V. Babic, BSc, Faculty of Technology and Metalurgy, 2007.

#### CHITOSAN COUPLING ON MACROPOROUS COPOLYMER

D. Jakovljević<sup>1</sup>, A. Nastasović<sup>1</sup> and M. Vrvić<sup>1,2</sup>

<sup>1</sup>ICTM - Center for Chemistry, Studentski trg 12-16, Belgrade, Serbia.(djakovlj@chem.bg.ac.yu)
<sup>2</sup>Faculty of Chemistry, University of Belgrade, Belgrade, Studentski trg 16, P.O. Box 158, Serbia

#### **Abstract**

In this study, chitosan and synthetic macroporous crosslinked poly(glycidyl methacrylate-*co*-ethylene glycol dimethacrylate), poly(GMA-*co*-EGDMA), modified with ethylene diamine, were combined by reagent glutaraldehyde to produce a hybrid synthetic-natural material. The chemical structure of the resulting material was analyzed by FTIR and elemental analysis.

#### Introduction

Chitosan is a linear polysaccharide comprising variable proportions of 2-amino-2-deoxy-D-glucopyranose (GlcNAc) and 2-acetamido-2-deoxy- $\beta$ -D-glucopyranose (GlcN) through  $\beta$ -(1–4) linkages (Fig. 1). Although naturally present in some microorganisms and fungi, commercial chitosan is industrially produced by partial deacetylation of chitin, the most abundant natural polysaccharide on the earth after cellulose [1]. Due to its advantageous properties (nontoxicity, antimicrobial activity, solubility, biocompatibility and biodegradability) chitosan is widely used in medicine, pharmacy, biotechnology, food and cosmetic industry, etc. Chitosan or deacylated chitin contains repeating units of amine groups, capable of coordination with toxic transition metals. The formation of a hybrid synthetic-natural material by attaching chitosan onto macroporous crosslinked poly(glycidyl methacrylate-co-ethylene glycol dimethacrylate), poly(GMA-co-EGDMA) modified with ethylene diamine (Fig. 2) would lessen the solubility of chitosan in acidic aqueous solutions and enhance the metals chelation ability of such a product [2].

In this work we reported a route to produce natural–synthetic polymer through covalent coupling of chitosan and macroporous poly(GMA-co-EGDMA) modified with ethylene diamine, poly(GMA-co-EGDMA), by means of reagent glutaraldehyde.

Fig. 1. Chemical structure of hybrid synthetic-natural material

#### **Experimental**

All reagents and solvents were purchased from commercial sources and used as supplied. The copolymer samples were analyzed for their carbon, hydrogen and nitrogen content using the Vario EL III device (GmbH Hanau Instruments, Germany). Poly(GMA-co-EGDMA) was synthesized as described elsewhere [3] and modified modified with ethylene diamine at 70 °C for 12 h at pH 10. The modified copolymer was incubated with 2% (w/v) glutaraldehyde in sodium phosphate buffer at pH 8 for 24 h and washed thoroughly with the same buffer. The reaction of chitosan and poly(GMA-co-EGDMA) with glutaraldehyde was carried out in a screw cap culture tubes, equipped with a magnetic stirring, at room temperature. Chitosan was dissolved in 1% acetic acid over 2 h at 30 °C with constant stirring. Polymer was then incubated with chitosan in sodium phosphate buffer pH 7 at room temperature for 12 h. The preparation was centrifuged at 3000g for 10 min at 25 °C and washed with acetate buffer until washings were free of this polysaccharide. The ATR-IR spectra of samples were obtained using Thermo Nicolet 6700 FT-IR Spectrophotometer with Smart Orbit Diamond ATR (attenuated total reflectance) accessory.

#### **Results and Discussion**

The coupling of poly(GMA-co-EGDMA) with glutaraldehyde was confirmed by FTIR (Fig. 3). The characteristic bands for chitosan are present in hybrid synthetic-natural material. The inherent functional groups of pure chitosan were determined in broad ranges of 3360 (-OH, -NH, and -NH<sub>2</sub>), 1150, and 1082 cm<sup>-1</sup> (C-O-C stretching vibration in glucosamine ring), while amides I (C=O in O=C-NH, at 1647 cm<sup>-1</sup>) and II (-NH in O=C-NH, at 1570 cm<sup>-1</sup>) and amine (-NH<sub>2</sub>, at 1252 cm<sup>-1</sup>) were also observed. The respective glucosamine ring from the coupled chitosan was also found at 1150 cm<sup>-1</sup>.

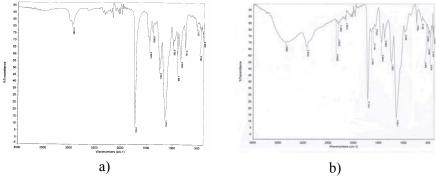


**Fig. 3.** FTIR spectra of a) poly(GMA-co-EGDMA) and b) novel material obtained by covalent coupling of chitosan with poly(GMA-co-EGDMA) with glutaraldehyde

Additional evidence that chitosan was coupled with poly(GMA-co-EGDMA)-en by glutaraldehyde was found in the results of elemental analysis of chitosan, untreated polymer and obtained hybrid synthetic-natural material (Table 1). The content of coupled polysaccharide is reflected by the increase in nitrogen content after the reaction of the chitosan with poly(GMA-co-EGDMA)-en.

Table 1. The results of elemental analysis

	% N	%C	%Н
chitosan	7,64	40,09	6,94
untreated polymer	/	57,91	7,96
hybrid polymer	5,65	53,55	7,77

#### Conclusion

The results presented in this study show a route to produce natural–synthetic polymers for potentially useful applications. The hybrid synthetic–natural material was obtained through covalent coupling of chitosan and macroporous poly(GMA-co-EGDMA) modified with ethylene diamine, poly(GMA-co-EGDMA), by means of reagent glutaraldehyde.

#### Acknowledgement

This work was supported by the Serbian Ministry of Science, Projects ON 142018B and ON 142039.

- [1] M. G. Peter in: Biopolymers., 2002, Vol. **6,** E. J. Vandamme, S. De Baets, A. Steinbuchel Eds. Wiley-Vch, 522–532.
- [2] R. R. Navaro, K. Tatsumi, Water. Sc. Technol., 2001, 43, 9-16.
- [3] A. Nastasović, D. Jakovljević, Z. Sandić, D. Đorđević, Lj. Malović, S. Kljajević, J. Marković, A. Onjia, in: M. I. Barroso Ed. Reactive and Functional Polymers Research Advances, Nova Science Publishers, New York, 2007, Chapter 2, 79-112.
- [4] Y. M. Dong, Z. Y. Xu, J. W. Wang, Science in China, Series B, 31, 2001, 53–160.

### THE INFLUENCE OF BENTONITE ON THE POROUS STRUCTURE OF GLYCIDYL METHACRYLATE BASED COPOLYMER

Z. Vuković<sup>1</sup>, A. Milutinović-Nikolić<sup>1</sup> and A. Nastasović<sup>2</sup>

<sup>1</sup>IChTM-Department of Catalysis and Chemical Engineering, Njegoševa 12, Beograd, Serbia
<sup>2</sup> IChTM-Department of Chemistry, Njegoševa 12, Beograd, Serbia

#### **Abstract**

Macroporous crosslinked copolymer of glycidyl methacrylate, GMA, and ethylene glycol dimethacrylate, EGDMA, poly(glycidyl methacrylate-co-ethylene glycol dimethacrylate), was synthesized by suspension copolymerization. The copolymer modification was performed by introducing 5 mass % of bentonite into reaction system. Grafting of organic groups on the bentonite surface in polymer-clay synthesized composite was confirmed by IR analysis. The synthesized composite has smaller pore volume and specific surface area than corresponding copolymer, while maximum pore diameter increases in comparison with pure copolymer.

#### Introduction

Macroporous copolymers are widely used for preparation of various types of ion exchange resins, as adsorbents, supports for conventional catalysts or enzymes, in biosynthesis, etc [1]. In recent years, polymer-clay composites gain in importance since they modify different properties of polymers i.e. thermal and mechanical endurance with minimal loss of ductility; flame, abrasion and chemical resistance, alter electrical, electronic and optical properties [2].

The hydrophilic nature of the clay surface provides homogeneous dispersion in the polymer phase, giving inorganic-organic composite remarkable properties. Since clay minerals and polymers in composite materials represent solid/solid distribution, the type of aggregation of the clay mineral particles or layers and the resulting porosity at different scales must be clearly defined. In clay an assembly of layers is called a "particle" and an assembly of particles forms an "aggregate". Interlayer, interparticle and interaggregate spaces form pores of different sizes and shapes [3]. In this paper the influence of bentonite clay on the parameters of porous structure of glycidyl methacrylate based copolymer is investigated.

#### **Experimental**

Macroporous crosslinked copolymer of glycidyl methacrylate, GMA, and ethylene glycol dimethacrylate, EGDMA, poly(glycidyl methacrylate-*co*-ethylene glycol dimethacrylate), was synthesized by suspension copolymerization [4]. The monomer phase containing reaction mixture (20.8 g of GMA and 13.8 g EGDMA), AIBN as an initiator (0.35 g), 45.4 g of inert components (36.3 g cyclohexanol and 9.1 g of tetradecanol) was suspended in the aqueous phase which consisted of 240 g of water and 2.4 g of polyvinilpyrrolidone (Sigma-Aldrich). The copolymerization

was carried out at 70 °C for 2h and at 80 °C for 6 h with stirring rate of 300 rpm. After reaction, the copolymer particles were washed with distilled water and vacuum dried at 40° C and denoted as SGE-20/14. The copolymer modification was performed by introducing 5 mass % (1.73 g) of bentonite into reaction system and SGE-20/14-5B was obtained. The previously characterized [5, 6] fraction (< 74  $\mu$ m) of bentonite clay from "Bogovina", Serbia, having smectite as dominant phase, was used in synthesis.

In order to confirm composite formation, the samples were characterized by infrared spectroscopy. The ATR-IR spectra of samples were obtained using Thermo Nicolet 6700 FT-IR Spectrophotometer with Smart Orbit Diamond ATR (attenuated total reflectance) accessory.

The porous structure of samples was determined using Carlo Erba Porosimeter 2000 with Milestone 100 Software System. The specific surface area of samples ( $S_{Hg}$ ), total specific pore volume ( $V_s$ ) were determined from cumulative pore size distribution curves. The most common pore diameter ( $D_{max}$ ) was obtained from derivative of this curve [7].

#### **Results and Discussion**

The composite SGE-20/14-5B IR spectrum has all bands observed in IR spectrum of copolymer SGE-20/14. In IR spectrum of composite the shoulder on approx. 1620 cm<sup>-1</sup> was assigned to OH in stretching band in water within smectite as well as the sharp absorption bands at 2923 cm<sup>-1</sup> and 2852 cm<sup>-1</sup> assigned to the symmetric and asymmetric stretching vibrations of methyl and methylene groups [8]. The later indicate grafting of organic groups on the bentonite surface as in organobentonites [9]. The results for porous copolymer SGE-20/14 and composite SGE-20/14-5B obtained by mercury intrusion porosimetry are given in Fig. 1 and Table 1.

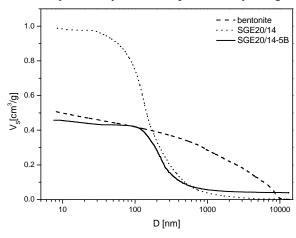


**Fig. 1.** Cumulative pore size distribution curves of SGE-20/14, bentonite and composite SGE-20/14-5B

**Table 1.** Porosity parameters of bentonite,

The forming of copolymerbentonite composite results in decrease of pore volume and specific surface area, while D<sub>max</sub> increases in comparison with pure copolymer. The monodisperse pore distribution remains in composite as in polymer, while in bentonite the wide pore distribution in entire investigated interval (7.5-10000 nm) is obtained as well as in microporous region [6].

This is in accondance to bentonite is structure as

Sample	$S_{Hg}$ $(m^2/g)$	V <sub>S</sub> (cm <sup>3</sup> /g)	D <sub>max</sub> (nm)
Bentonite	20	0.51	-
SGE-20/14	41	1.02	123
SGE-20/14-5B	13	0.46	214

natural material with aggregates of plate-like particles. On the other hand, the shape of both cumulative pore size distribution curves of copolymer and composite indicate that no micropores are expected.

#### Conclusion

The composite of macroporous crosslinked poly(glycidyl methacrylate-co-ethylene glycol dimethacrylate) and bentonite was synthesized by suspension copolymerization. The synthesized composite has smaller pore volume and specific surface area than copolymer, while maximum pore diameter increases in comparison with pure copolymer. Due to monodisperse pore distribution and increased  $D_{\text{max}}$ , the application of composite is possible in enzyme immobilization and for the removal of bacterial cells and large molecules from waste waters.

#### Acknowledgements

This work was supported by the Ministry of Science of R. Serbia (Projects TR 6712B and ON 142039)

- [1] M. Alexandre, P. Dubois, Mater. Sci. Eng. 2000, 28, 1-63.
- [2] M. Celik, M. Onal, J. Appl. Polym. Sci., 2004, 94, 1532-1538
- [3] F. Bergaya, G. Lagaly in Clay-based polymer nano-composites (CPN) Clay Minerals Society, Chantily, USA, 2007, **15**, 62-97.
- [4] S. M. Jovanović, A. Nastasović, N. N. Jovanović, K. Jeremić, Z. Savić, Angew. Makromol. Chem., 1994, 219 161-168 (Nr.3833)
- [5] Z. Vuković, A. Milutinović-Nikolić, Lj. Rožić, A. Rosić, Z. Nedić, D. Jovanović, Clays Clay Miner., 2006, 54, 699-704
- [6] Z. Vuković, A. Milutinović-Nikolić, J. Krstić, A. Abu-Rabi, T. Novaković, D. Jovanović, Mater. Sci. Forum, 2005, 494, 339-344
- [7] P. A. Webb, C. Orr, Analytical methods in fine particle technology, Micrometrics Instrument Corporation, Norcross, GA USA, 1997
- [8] J. C. Dai, J. T. Huang, Appl. Clay. Sci., 1999, 15, 51-65.
- [9] A.S.Özcan, B. Erdem, A. Özcan, J. Colloid Interf. Sci, 2004, 280, 44-54.

# THE INFLUENCE OF DUAL ACTIVE FILLERS ON CURING CHARACTERISTICS OF ELASTOMERS BASED ON NATURAL RUBBER AND CHLOROSULPHONATED POLYETHYLENE RUBBER

G. Marković<sup>1</sup>, B. Radovanović<sup>2</sup>, M. Marinović-Cincović<sup>3</sup> and J. Budinski-Simendić<sup>4</sup>

<sup>1</sup> Tigar, Pirot, (agmarkov@tigar.com)

<sup>2</sup> Faculty of Science, Niš,

<sup>3</sup>Institute of Nuclear Science VINČA, Belgrade,

<sup>4</sup>Faculty of Technology, Novi Sad, Serbia

#### Abstract

The effects of two type active filler (carbon black and silica) on the characteristics of elastomers based on natural rubber and chlorosulphonated polyethylene rubber blend blend (NR/CSM) were investigated. For cure studies, torque-time curves were registered at different temperatures (150, 160 and 170°C). It was estimated that higher curing temperature cause decreas of the cure plateau torque and lead to higher crosslinking rate constant.

#### Introduction

Physical properties of rubber vulcanisates are improved by reinforcing with active fillers such as carbon black and silica [1]. Silica has been used as an important reinforcing agent in a rubber compound together with carbon black [2-4]. Silica has a number of hydroxyl groups on the surface, which results in strong filler-filler interaction and adsorption of polar material by hydrogen bonding and it can aggregate tightly [3-4]. Since intermolecular hydrogen bonds between hydroxyl groups on the surface of silica are very strong and it can form a tight aggregate. Carbon black filled vulcanisates has good polymer- filler interaction, even better than silica [5]. Its property can cause a poor dispersion of silica in a rubber compounds than carbon black and its acidity is responsible for cure retardation, and aditional ingredients like ethylene glycol [6]. The aim of this work was to study the influence of carbon black and silica on curing NR/CSM rubber blend at different temperatures and to calculate the crosslinking rate constant.

#### **Experimental**

Natural rubber, type SMR CV 60 was supplied by Malaysia. Chlorosulfonated polyethylene rubber type, Hypalon 40S, was supplied by Du Pont, USA. Carbon black with nominal particle size 26-30nm (N-330) and precipitated silica with nominal particle size 15nm (Ultrasil WN3) were used as active fillers. Other ingredients such as zinc oxide, stearic acid, sulfur and poly (ethylene glycol) were of reagent grade. Mixing was carried out on a two-roll mill at 50°C and speed

ratios 1:1.25 (according to ASTM D 3182). For cure studies, torque-time curves were registered at temperatures of 150, 160 and 170 °C by Monsanto rheometer 100S. The expression for the crosslinking rate constant can be written in terms of torque as [5]

$$kt = \ln \left( \frac{M_h - M_l}{M_h - M_t} \right) \dots 1$$

Where  $M_t$  is the torque at a given time t.  $M_l$  and  $M_h$  are the minimal and maximal torque, respectively. k is the crosslinking rate constant, since the rate in the early stages reflects the character of the main forward reaction [6]. The compounds were prepared by using a plasticorder (model PLE-330; Brabender OHG, Duisburg, Germany) at 80C and a rotor speed of 60 rpm. Rubber sheets were prepared by molding the compounds according to the respective optimum cure times.

#### **Result and Discussion**

In the Table I are summarized all estimated curing chracteristics at different temperatures. It is observed that the addition of carbon black to rubber blend tends to increase torque more rapidly than silica.

<b>Table I</b> Vulcanization characteristics of NR/CSM rubber blend compounds
filled with silica and carbon black

	Cure temperature (°C)	Minimum torque M (dNm)	Maximum torque $M_h$ (dNm)	$\Delta M$ $(M_h - M_l)$ $(dNm)$	Scorch time t s2 (min)	Optimum cure time t 90 (min)
1	150	9.0	50.2	41.2	7.6	14.7
	160	8.7	49.3	40.6	4.1	8.2
	170	8.6	48.6	40	2.4	5.0
2	150	8.7	48.8	40.1	7.0	14.6
	160	8.3	47.9	39.6	4.8	7.9
	170	8.3	47.2	38.9	2.8	4.9
3	150	7.2	48.1	40.9	2.1	3.4
	160	6.6	45.1	38.5	1.5	2.3
	170	6.3	43.0	36.7	0.9	1.2

The variation of rate constant (k) for carbon black and silica-filled NR/CSM compounds are represented in the figure 1. The optimum and scorch rheometer cure time  $t_{c90}$  and  $t_{s2}$  values, which are a measure of the rate of crossslinking, decrease as the curing temperature increases for all formulation of NR/CSM rubber blends. The initial decrease in torque is due to the softening of the matrix. Torque then increases due to the formation cross-links between the macromolecular chains and cross-links between active filler and macromolecular chains.

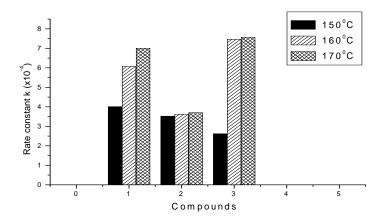


**Fig. 1**. Variation of rate constant for carbon black and silica filled NR/CSM compounds at different temperatures

#### Conclusion

The optimum and scorch rheometer cure time  $t_{c90}$  and  $t_{s2}$  values decrease as the curing temperature increases for all formulation of NR/CSM rubber blends. Higher temperature influenced the decreas of the cure plateau torque and lead to higher crosslinking rate constant.

- [1] H. Ismail and T.A.Ruhaizat, Polym.-Plast. Technol. Eng 1998, 37, 483.
- [2] A.Y. Coran, in: F.R. Eirich (Ed.), Science and Technology of Rubber, Chap. 7, Academic Press, Inc, London, 1978.
- [3] B.B.Boonstra, in: C.M. Blow (Ed.), Rubber Technology and Manufacture, Chap. 7, Newnes-Butterworth, London, 1971.
- [4] N.J. Morrinson and M. Porter, Rubber Chem. Technol 1964, 37, 650.
- [5] S. H. Chough and D.H. Chang, Polym. Sci. 1996, **61**, 449.
- [6] M.P. Wagner, Rubber Chem. Technol. 1976, 49, 703.

## ULTRASOUND-INDUCED STABLE PLANAR SPATIAL ORGANIZATION OF POLY (D,L-LACTIDE-CO-GLYCOLIDE)/HYDROXYAPATITE SPHERE-LIKE PARTICLES

M. Jevtić<sup>1</sup>, S. Škapin<sup>2</sup>, K. Krnel<sup>2</sup>, N. Ignjatović<sup>1</sup> and D. Uskoković<sup>1</sup>

\*Institute of Technical Sciences SASA, Belgrade, Serbia

2 "Jozef Štefan" Institute, Ljubljana, Slovenia

#### **Abstract**

Self-assembled, plate-like planar spatial organization of PLGA/HAp spherical particles, preceded by the formation of linear, tetragonal and pentagonal structures, was analysed. Planar organization of particles stabilized by PVP with lower average molecular mass was more regular due to smaller and more uniform particle sizes. These structures were stable, the main reason of their stability being the physical nature of their connections.

#### Introduction

"Self-assembly" has been paid much attention as the next generation micro-/ nano-fabrication process.[1] From a tissue engineering standpoint, self-assembly could be used to engineer different types of surface topography on the nano- and micro-scale. They can influence cell adhesion, migration, function, and tissue integration. It can establish a controlled local microenvironment (protein and other macromolecular patterning) via surface functionalization of biomaterials to generate micro- and nanoscale mechanical stresses affecting cell-biomaterials interactions, and to position cells precisely on scaffold surface in order to control cell interactions.[2] Self-assembly can be used to produce a variety of structures, such as films, bilayer, membranes, nanoparticles, fibers, micelles, capsule, tubes, coils, mesophases, or unilamellar and multilamellar vesicles [3]. These structures can further self-organize into superstructures, such as lamellar, hexagonal, and cubic structures. However, these structures are not very stable, due to noncovalent interactions, such as hydrogen bonds, ionic bonds, hydrophobic interactions, and van der Waals interactions among the assembled molecules.[4]

The aim of this work was to give an explanation for the formation of stable planar spatial organization of PLGA/HAp biocomposite spheres, to analyze their stability and to show influence of poly(vinyl-pyrrolidone) with different average molecular mass on its shape and size.

#### **Materials and Methods**

The formation of poly(d,l-lactide-co-glycolyde)/hydroxyapatite (PLGA/HAp) composite material was performed in the following way: HAp was synthesized by homogeneous precipitation method with urea as homogeneous precipitation agent [5]; the obtained apatite crystals were deagglomerated by high-intensity ultrasonic field in a small volume of ethanol as inert medium and coated with PLGA by the

use of ultrasonic field. The as-obtained dispersion was stabilized by water solution of poly(vinyl-pyrrolidone) (PVP) with different molecular masses (25 and 650 kDa). After the stabilization, some parts of dispersions were separated and filtered on polycarbonate membranes for SEM and granulometric analyses.

#### **Results and Discussion**

During the process of self-assembly of particles, several stages in their organization, very important for the formation of the final morphology of the material can be observed. The formation of PLGA/HAp composite material in the field of ultrasound is marked by self-assembly of its sphere-like particles which make the final morphology of this material. Figure 1 represents various stages of organization of PLGA/HAp spheres obtained after the ultrasonic processing. The presence of individual particles, linear, tetragonal, pentagonal structures and germs of the final plate-like arrangement of PLGA/HAp sphere-like particles in Figs. 1a, 1b, 1c and 1d, respectively, enables us to grasp the mechanism of the formation of the final plate-like spatial organization of spheres represented in Fig. 1e. It is well-known that ultrasonic field induces collision of solid particles driven by shock wave formed after the bubble collapse in the cavitation process.[6] In the moment of the impact of these sphere-like particles induced by ultrasonic field they remain connected due to the increase in the plasticity of the surface, polymeric part, of the PLGA/HAp spheres.

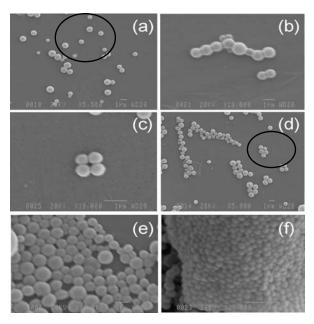


**Fig. 1:** SEM micrographs of PLGA/HAp sphere-like particles: (a) individual, (b) linear, (c) tetragonal (d) pentagonal and part of the planar spatial arrangement of spheres. Morphology of composite spheres stabilized by PVP with (e) higher (650 kDa) and (f) lower (25 kDa) average molecular mass.

Figs. 1e and 1f represent planar spatial organization of PLGA/HAp sphere-like particles stabilized with PVP with (e) higher (650 kDa) and (f) lower (25 kDa) average molecular masses. Having in mind that particles stabilized with PVP with lower average molecular mass are smaller and more uniform in size, planar spatial organization represented in Fig. 1f is more regular than those stabilized by PVP with higher average molecular mass represented in Fig. 1e. Figure 2 represents particle size distributions of samples stabilized by PVP with (a) higher and (b) lower average molecular mass. These distributions show significantly larger particle sizes than those measured according to SEM micrographs. These larger sizes correspond to connected sphere-like particles, which indicate the stability of their connections within self assembly planar spatial organization.

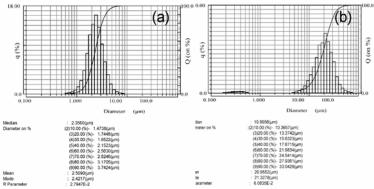


**Fig. 2.** Particle size distributions of PLGA/HAp composite stabilized by PVP with: (a) higher (650 kDa) and (b) lower (25 kDa) average molecular mass.

#### Conclusion

In this work, the formation of plate-like spatial organization of sphere-like PLGA/HAp particles was analyzed. Results indicated the formation of linear, tetragonal and pentagonal interparticle connections as lower levels of organization important for the final self assembly planar plate-like morphology. These organized structures obtained in the field of ultrasound were more regular when PLGA/HAp composite was stabilized with PVP with lower average molecular mass due to smaller and more uniform sphere-like particles. Particles were physically connected and it was the main reason of their stability.

- [1] Y. Masuda, J. Soc. Powder Tech., 2006, 43, 362-371.
- [2] X. Wen, D. Shi, N. Zhang, Am. Sci. Pub., 2005, 1, 1-23.
- [3] J. M. Schnur, Science, 1993, 262, 1669-1676.
- [4] I. W. Hamley, Nanotechnology, 2003, 14, 39-54.
- [5] M. Jevtć, D. Uskoković, Mat. Sci. Forum, 2007, 555, 285-290.
- [6] S. J. Doktycz, K. S. Suslick, Science, 1990, **247**, 1067-1069.

#### ON MINIMUM ENERGY STRUCTURE OF POLYALANINE

M.L. Mihajlović<sup>1,2</sup> and P.M. Mitrašinović<sup>2,\*</sup>

<sup>1</sup>Faculty of Physical Chemistry, University of Belgrade, Studentski Trg 12-16, 11000 Belgrade; <sup>2</sup>Institute for Multidisciplinary Research, Kneza Viseslava 1, 11030 Belgrade, Serbia; \*Correspondence to: pmitrasinovic@yahoo.ca

#### Abstract

Because of the insolubility of homo-oligopeptides (HOPs) in water, experimental investigations of polyalanine (PA) structure are somewhat limited. Herein, various computational strategies for generating the minimum energy structure of polyalanine are contrasted, and several structure-function standpoints are elucidated.

#### Introduction

Because of homo-oligopeptides insolubility and their aggregation in water, experimental investigations of HOPs are a challenging task [1]. Since alanine is well-known to have a high propensity to form helical structures, especially  $\alpha$ -helix, various structures of poly-(Ala) peptides have been previously proposed [2]. Because the size of a specific crystal structure does not allow applying the most sophisticated quantum-mechanical methods including the correlation effects of all electrons being responsible for bonding, making some reasonable approximations during the computational process of generating the minimum energy structure is quite conceivable [3,4]. Herein, it is shown that both full and rigid-body optimizations, based on molecular mechanics neglecting the behavior of electrons, may provide some useful insights into the structure-function relationship of poly-(Ala) dimmer consisting of two  $\alpha$ -helices.

#### **Methods**

All of the calculations were done using the TINKER suite of programs known as the Software Tools for Molecular Design running under the Windows operating system [5]. Running the modeling tools was facilitated by the Force Field Explorer 4.2, a graphical user interface to TINKER [6]. The complete OPLS-UA force field with united-atom parameters for proteins and many classes of organic molecules was employed, including explicit hydrogens on polar atoms and aromatic carbons [7-9]. The initial geometry of PA was the subject to two types of the optimization procedures: (1) full optimization without imposing any geometric constraints and (2) rigid-body optimization taking into account only Van der Waals contacts within two helices making the PA crystal. The full optimization procedure was done using a truncated Newton minimization method which requires potential energy, gradient and Hessian information. The rigid-body optimization of initial structure having 120 atoms was done using the OPTRIGID subroutine. The SPACEFILL program within TINKER was employed to compute the volume and surface areas.

Energy (kcal mol <sup>-1</sup> )	Initial Poly-(Ala) Structure	Fully Optimized Poly-(Ala)	Rigid-Body-Optimized Poly-(Ala)
Total Potential Energy	-654.21	-711.06	-663.36
Bond Stretching	4.68	0.84	4.68
Angle Bending	16.82	3.05	16.82
Improper Torsion	0.18	2.37	0.18
Torsional Angle	0.74	5.15	0.74
Van der Waals	-19.36	-40.34	-29.04
Charge-Charge	-657.28	-682.13	-656.75
	Van der Waals A	Area and Volume	
Area (Å <sup>2</sup> )	1419.53	1421.46	1416.50
Volume (Å <sup>3</sup> )	1311.20	1315.19	1311.09

**Table 1.** Energy and its components of initial and optimized poly-Ala structures

#### Results

The fully optimized structure is below the initial geometry by 56.85 kcal/mol (Table 1). The Van der Waals and Charge-Charge energy components are below those in the initial geometry by 20.98 and 24.85 kcal/mol, respectively. Hence, the stabilization energy of about 11 kcal/mol of a total of 56.85 kcal/mol comes from all the other energy contributions, such as the Bond Stretching, Angle Bending, Improper Torsion, and Torsional Angle components.

The cost of having the Van der Waals contacts within two groups (helices) of atoms optimized was estimated to be -9.68 kcal/mol (Table 1). If the numerical value is compared with those obtained previously by full optimization, it is interesting to note that all potential energy components other than electrostatic ones have a total stabilization contribution of about 11 kcal/mol, which is almost equal to this of 9.68 kcal/mol. In other words, the stabilization energy cost for only Van der Waals contacts appears to be quite similar to that for all energetic components, other than electrostatic, produced by a full optimization.

A careful inspection of the total potential energy values for the initial, rigid-body-optimized and fully-optimized structures of PA (-654.21, -663.36 and -711.06 kcal/mol) shows a trend that is quite conceivable: a rigid-body-optimized structure with having only Van der Waals contacts inside of two helices stabilized is below the initial geometry by about 9 kcal/mol, while the fully-optimized structure is substantially below the initial geometry by 57 kcal/mol. To rationalize the standpoint, Van der Waals volumes and molecular surfaces were computed and examined (Table 1). Interestingly, the optimization of only intra-helical Van der Waals contacts results in both smaller total area by about 3 Å<sup>2</sup> and unchanged molecular volume. In contrast, the full optimization of the initial structure results in larger total area and molecular volume by about 2 Å<sup>2</sup> and 4 Å<sup>3</sup>, respectively.

#### **Conclusions**

Taking into account electrostatic nature of Van der Waals contacts being primarily responsible for function of a crystal structure, a decrease of total molecular surface and unchanged volume due to optimization of these particular contacts have a more functional character. In contrast, an increase both of total molecular surface and of molecular volume associated with a substantial stabilization of an initial geometry by a full optimization has a more energetic and structural character.

- [1] B. Leitgeb, A. Kerenyi, F. Bogar, G. Paragi, B. Penke, G. Rakhely, J. Mol. Model., 2007, 13, 1141-1150.
- [2] S. M. Miick, G. V. Martinez, W. R. Fiori, A. P. Todd, G. L. Millhauser, Nature, 1992, 359, 653-655.
- [3] M. L. Mihajlovic, P. M. Mitrasinovic, Tehnika-Novi Materijali, 2006, 15(6), 1-6.
- [4] M. L. Mihajlovic, Master thesis, Department of Physical Chemistry, University of Belgrade, October 29, 2007.
- [5] J. W. Ponder, *TINKER Molecular Modeling Package*, http://dasher.wustl.edu/tinker.
- [6] J. W. Ponder, Force Field Explorer 4.2: a graphical user interface to TINKER, http://dasher.wustl.edu/tinker.
- [7] W. L. Jorgensen, D. S. Maxwell, J. Tirado-Rives, J. Am. Chem. Soc., 1996, 117, 11225-11236.
- [8] W. L. Jorgensen, J. Tirado-Rives, J. Am. Chem. Soc., 1988, 110, 1657-1666.
- [9] J. Aqvist, J. Phys. Chem., 1990, 94, 8021-8024.

### THERMAL AGEING AND γ-RADIATION RESISTANCE OF POLYISOPRENE /CHLOROSULPHONATED POLYETHYLENE RUBBER BLENDS

G. Marković<sup>1</sup>, B. Radovanović<sup>2</sup>, M. Marinović-Cincović<sup>3</sup> and J. Budinski-Simendić<sup>4</sup>

<sup>1</sup> Tigar, Pirot, gmarkov@tigar.com <sup>2</sup> Faculty of Science, Niš, <sup>3</sup>Institute of Nuclear Science VINČA, Belgrade, <sup>4</sup>Faculty of Technology, Novi Sad, Serbia

#### **Abstract**

The effect of carbon black (average particle size 26nm) and wood flour (particle size from 300 to 400  $\mu$ m) on thermal ageing and  $\gamma$ -radiation resistance of polyisoprene /chlorosulphonated polyethylene rubber blend (NR/CSM) was studied. The tensile strength of the aged samples was determined, after conditioning at 70°C during 72h. The radiation exposure of samples was performed at two doses: 212 and 400 kGy.

#### Introduction

Rubber compound are composed of fillers, curing agents, and other chemical additives to improve processing behavior and ageing properties of final crosslinked material [1]. Degradation of rubber is accelerated mainly by heat, humidity, light, radiation etc. The aim of these work was to study the influence of carbon black and wood flour on curing characteristics and thermal aging and high-energy radiation resistance of polyisoprene/chlorosulphonated polyethylene rubber blend (NR/CSM).

#### **Experimental**

Natural rubber, type SMR CV 60 was supplied by Malaysia; Chlorosulfonated polyethylene rubber type, Hypalon 40S, was supplied by Du Pont, USA; Carbon black (CB) HAF-HS (DBP 120ml/100g (average particle size 26nm); Wood flour (WF) was obtained from M/s Kosla Metal Powder Co. Pvt. Ltd, Pune, India, (particle size from 300 to 400 µm). Phenolformaldehyde resin (PF), type VULKADUR A was used to achieve better adhesion between rubber macromolecules and wood particles. Other ingredients such as zinc oxide, stearic acid and sulfur. Mixing was carried out on a two-roll mill at 40°C and 1:1.25 speed ratios according to ASTM D 3182. For thermal ageing study the specimens for tensile measurements were kept in an air oven, maintained at 70 °C for 72 h. Irradiations have been performed in air in the Co-60 radiation sterilization unit with the dose rate of 212 and 400 kGyh<sup>-1</sup>.

#### **Result and Discussion**

In the table I are summarized data obtained by Monsanto rheometer (scorch time  $t_{s2}$ , cure time  $t_{c90}$ , cure rate index (CRI) and MU(1+4) at 373K for componds with different ratio of filler. It is obvious that compounds with carbon black CB have higher Ml, Mh, CRI and MU (1+4) at 373K values than those with WF.

**Table I** Curing characteristics of NR/CSM rubber blend compounds (80:20) filled with different coratio of carbon black and wood flour (CB/WF)

	Curing characteristics							
Filler content CB/WF (phr)	MU(1+4) at 373K	Scorch time (min)	Ml (dNm)	Mh (dNm)	Cure time (min)	CRI $(100/t_{c90}-t_{s2})$ min <sup>-1</sup>		
0/0	28	2.5	3.9	27	6.4	26		
10/0	25	2.5	3.5	30	7.4	20		
20/0	30	2.5	4.5	36	7.9	19		
30/0	36	2.2	5.8	43	8.5	16		
40/0	47	2.1	8	51	9.4	14		
50/0	55	2.0	9.8	55	5.8	26		
30/10	28	2.2	4.9	47	7.3	20		
30/20	28	2.2	5.2	50	5.6	29		
30/30	29	2.1	5.3	55	5.7	28		
30/40	32	2.2	5.7	59	5.6	29		
30/50	33	2.1	6	61	5.4	30		

It is estimated that the scorch time  $(t_{s2})$  and cure rate  $(t_{c90})$  are reduced substantially by addinfg fillers. Wood flour particles are non-reinforcing filler[2]. With the presence of resin, the interaction between the filler and rubber matrix is increased while the carbon black content increases could be due to the agglomeration of particles in the rubber matrix. The effects of thermal aging and two different radiation doses (212 and 400 kGy) of WF and CB filled NR/CSM compounds with FP resin on the tensile strength are shown on fig. 1. The incorporation of CB and WF with resin has influenced the chemical bonds between both: carboxyl group of CB and rubber matrix, and hydroxyl groups of the WF and the rubber matrix via hydroxymethyl group of resin [3]. Thus the polymer-filler interaction are improved and imparted better tensile strength. Ageing for 3 days at 70°C results in

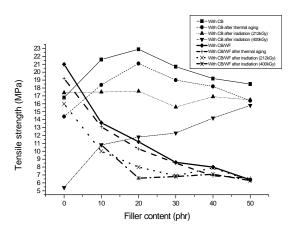


**Fig. 1**. Variation in tensile strength of CB and WF filled NR/CSM rubber blends before and after thermal and radiation aging

a decrease of tensile strength at all filler loadings. During thermal ageing the composite gradually loses their tensile strength due to degradation. At a radiation dose of 212 kGy, the variation of tensile strength are lower, due to the covalent bonds formed at the interface (through the reactive sites created by the radiation). When the radiation dose is increased to 400 kGy, the variation in properties is greather, and decreases continuously with CB and WF loading.

#### Conclusion

Compared to CB filled NR/CSM rubber blend, WF filled rubber blends have smaller changes of mechanical properties after thermal ageing. Ageing of elastomeric composites slightly increased the tensile strength due to the continued crosslinking reaction. The radiation degradation is predominates in the case of 400kGy radiation dose.

- [1] R. Baker, Natural rubber technology, 1998, 19, 28.
- [2] S. Varghese, Polym. Degrad. Stab. 1994, 44, 55.
- [3] J. Leblanc, Progress in Polymer Science, 2002, 27, 627.

### CHELATING COPOLYMERS: METAL SORPTION KINETICS AND REUSABILITY

A. Nastasović<sup>1</sup>, D. Jakovljević<sup>1</sup>, Z. Sandić<sup>2</sup>, D. Đorđević<sup>1</sup>, Lj. Suručić<sup>3</sup> and L. Slavković-Beškoski<sup>4</sup>

<sup>1</sup>ICTM - Center for Chemistry, Studentski trg 12-16, Belgrade, Serbia. (anastaso@chem.bg.ac.yu)

<sup>2</sup>Faculty of Science, Mladena Stojanovića 2, Banja Luka, BIH.

<sup>3</sup>Faculty of Forestry, Kneza Višeslava 1, Belgrade, Serbia.

<sup>4</sup>Vinča Institute of Nuclear Sciences, P.O. Box 522, Belgrade, Serbia

#### **Abstract**

Macroporous crosslinked poly(glycidyl methacrylate-co-ethylene glycol dimethacrylate), PGME, was synthesized by suspension copolymerization and functionalized with diethylene triamine, PGME-deta. Kinetics for Au(III), Ag(I) and Cu(II) sorption, as well as the possibility of repeated recovery of Cu(II) ions was investigated.

#### Introduction

The most important properties of chelating copolymers are high capacity and selectivity, fast kinetics and possibility of the repeated application. In this study, macroporous PGME synthesized by suspension copolymerization and functionalized with diethylene triamine (PGME-deta) was used for metal ions sorption. Kinetic data for Au(III), Ag(I) and Cu(II) were analysed with the pseudo-first and pseudo-second order kinetic models. The potential reusability of PGME-deta for Cu(II) sorption was tested in several sorption/desorption cycles.

#### **Experimental**

Macroporous PGME (surface area 50 m<sup>2</sup>g<sup>-1</sup>, pore diameter 53 nm, particle size 150-500 µm) was prepared by suspension copolymerization [1]. PGME-deta was obtained by heating the mixture of 3.6 g of PGME, 15.7 g of diethylene triamine and 100 ml of toluene at 80 °C for 6 h. Modified sample (surface area 70 m<sup>2</sup>g<sup>-1</sup>, pore diameter 42 nm, particle size 150-500 µm) was filtered, washed with ethanol and dried. For determination of Au(III), Ag(I) and Cu(II) sorption rate, 0.5 g of copolymer was contacted with 50 cm3 of metal salt solution (0.05 M). The experimental data were treated with pseudo-first and pseudo-second-order equations [2]. For regeneration experiments, PGME-deta (0.1 g) was contacted with 10 cm<sup>3</sup> of 0.05 M CuCl<sub>2</sub> (sorption time 120 min). The loaded samples were stripped with 0.1 and 1 M H<sub>2</sub>SO<sub>4</sub> (20 cm<sup>3</sup>, desorption time 30 min), filtered, dried and treated with metal salt solution. For neutralization, samples were treated with 0.1 or 1 M NaOH, before next sorption cycle. The Ag(I) and Au(III) concentration was determined by Inductively Coupled Plasma (ICP-OES, Perkin Elmer, Model ICP\6500), while the concentration of Cu(II) was determined by atomic absorption spectrometry (AAS, SpektrAA Varian Instruments).

#### **Results and Discussion**

For practical use, the rapid sorption of metal ions by amino-functionalized PGME is beneficial, providing a short solution-sorbent contact time in the actual process. The sorption of Cu(II), Ag(I) and Au(III) for PGME-deta was rapid (Fig. 1), with  $t_{1/2}$  values (time required to reach 50% of the total sorption capacity) of 1, 2 and 5 minutes, respectively. The correlation coefficients,  $R^2$ , as well as theoretical and  $q_{eq}$  values calculated for two kinetic models (Table 1) suggest that Au(III), Ag(I) and Cu(II) sorption on PGME-deta proceeds according to pseudo-second order kinetics and depends both on metal concentration and the properties of chelating copolymer.

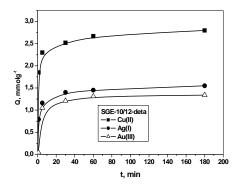
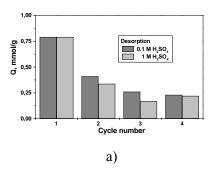


**Fig. 1.** Sorption of Cu(II), Ag(I) and Au(III) ions vs. time, on PGME-deta [metal ions initial concentration 0.05 M, pH=4 for Cu(II); pH=5.5 for Ag(I) and pH=0.3 for Au(III)].

		Pseudo-firs	st order kinet	ics	Pseudo-second order kinetics			
Sample	$q_{e,\exp}$ ,	k <sub>1</sub> , min <sup>-1</sup>	$q_{\it eq}$ ,	$R^2$	k <sub>2</sub> , gmmol <sup>-1</sup>	$q_{\it eq}$ ,	$R^2$	
	mmolg <sup>-1</sup>		mmolg <sup>-1</sup>		min <sup>-1</sup>	mmolg <sup>-1</sup>		
SGE-10/12	SGE-10/12-deta, 0.05 M Me solution							
Au(III)	1.30	0.0296	0.32	0.961	0.252	1.32	0.999	
Ag(I)	1.45	0.0494	0.64	0.792	3.33	1.45	0.999	
Cu(II)	2.80	0.0451	1.12	0.781	0.681	2.80	0.999	

**Table 1.** Kinetic data for Au(III), Ag(I) and Cu(II) sorption on PGME-deta.

The stripping of Cu(II) with H<sub>2</sub>SO<sub>4</sub> leads to an initial capacity loss of 50 % in first sorption/desorption cycle (Fig. 2a) and decrease of capacity in the following cycles. After additional treatment with NaOH, amino groups become active again and capacity of poly(GMA-co-EGDMA)-deta for Cu(II) ions increases (Fig. 2a).



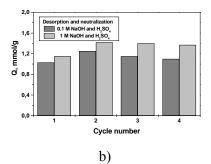


**Fig. 2.** Sorption/desorption and repeated use of PGME-deta with H<sub>2</sub>SO<sub>4</sub> a) without and b) with neutralization [34].

#### Conclusion

The sorption of Cu(II), Ag(I) and Au(III) by PGME-deta is rapid and proceeds according to pseudo-second order kinetics. Additional treatment with NaOH after stripping of Cu(II) with acid enhances the regeneration and reusability of PGME-deta.

#### Acknowledgement

This work was supported by the Serbian Ministry of Science, Project ON 142039.

- S. Jovanović, A. Nastasović, N. Jovanović, K. Jeremić, Mater. Sci. Forum, 1996, 214, 155-162.
- [2] P. K. Malik, J. Hazard. Mater. B, 2004, 113, 81-88.
- [3] Z. Sandić, S. Kljajević, Lj. Malović, I. Mrkić, D. Đorđević, A. Nastasović, The Sixth European Meeting on Environmental Chemistry, Belgrade, Book of Abstracts, 2005, 225.

#### RHEOLOGICAL AND THERMOGRAVIMETRIC ANALYSIS OF UNMODIFIED AND MODIFIED ALIPHATIC HYPERBRANCHED POLYESTER

J. Vuković<sup>1</sup>, S. Jovanović<sup>2</sup>, M.D. Lechner<sup>3</sup> and V. Vodnik<sup>4</sup>

<sup>1</sup> IHTM-Center of Chemistry, Studentski trg 12-16, 11000 Belgrade, Serbia
<sup>2</sup> Faculty of Technology and Metallurgy, University of Belgrade,
Karnegijeva 4, 11120 Belgrade, Serbia
<sup>3</sup> Institute for Chemistry, University of Osnabrück, Barbarastraße 7, 49069 Osnabrück, Germany
<sup>4</sup> Institute of Nuclear Science "Vinča", P. O. Box 522, 11001 Belgrade, Serbia

#### Abstract

The influence of the type of end groups on the rheological and thermal properties of aliphatic hyperbranched polyesters (AHBP) was investigated in this work. Unmodified, hydroxy-functional AHBP sample of third pseudo generation (AHBP-3) and the same sample whose end –OH groups were modified with stearic acid (AHBP-3SA) were examined. The presence of the long alkyl chain ends, instead of the polar –OH groups, has reduced the possibility for H-bonding and value of the glass transition temperature. On the other side, by modification of the end –OH groups with stearic acid, thermal stability of AHBP has been improved.

#### Introduction

The specific and unique features of hyperbranched polymers (HBP) have generated increasing scientific attention over the last years [1,2]. Their compact structure and presence of a large number of functional end groups enable a spectrum of unusual properties in comparison with analogue linear polymers.

Unmodified, hydroxy-functional aliphatic hyperbranched polyester (AHBP) of third pseudo generation (AHBP-3) and the same sample whose end –OH groups were modified with stearic acid (AHBP-3SA) were investigated in this work. The influence of the nature of end groups on the rheological and thermal properties of these AHBP was examined.

#### **Experimental**

The sample AHBP-3 was synthesized starting from 2,2-bis(hydroxy-methyl)propionic acid (AB<sub>2</sub> monomer) and di-trimethylolpropane (B<sub>4</sub> core molecule), using acid-catalyzed polyesterification reaction and pseudo one-step procedure. A detailed description of the procedure for the synthesis of AHBP-3, as well as, modification of end –OH groups with stearic acid are presented elsewhere [3].

 $^{13}$ C NMR spectra of AHBP samples were recorded on Bruker (250 MHz) NMR spectrometer in DMSO- $d_6$ . The degree of branching, DB, was calculated using equations developed by Fréchet [4]. Rheological properties of AHBP were determined by Carri-Med CSL-100 stress controlled cone and plate rheometer (TA

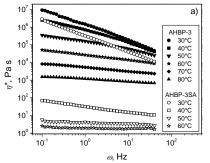
Instruments), fitted with a 2 cm diameter cone of 2° cone angle. The thermal stability of HB polyesters was determined by nonisothermic thermogravimetric (TG) analysis, using a NETZSCH TG 209 instrument in nitrogen atmosphere, at heating rate of 5 °C/min (flow rate of N<sub>2</sub> was 25 cm<sup>3</sup>/min).

#### **Results and Discussion**

Some important properties of investigated AHBP samples are listed in Table 1. From these results and results presented in Fig. 1 it can be seen that value of the glass transition temperature,  $T_{\rm g}$ , (determined from the maximum of loss modulus temperature dependence) and complex viscosity,  $\eta^*$ , are lower for the sample AHBP-3SA than for AHBP-3. This indicates that the presence of such long terminal alkyl chains (C18) instead of polar –OH groups, reduces to a certain amount the possibility for the H-bonding, but at the same time can induce crystallinity in the AHBP sample [5]. The sudden decrease of the  $\eta^*$  values at around 37 °C for the AHBP-3SA is ascribed to the melting of this sample, while non-Newtonian behaviour up to the 40 °C is probably due to the interpenetration of end alkyl groups from the surrounding molecules.

**Table 1.**The theoretically expected values of the molar mass,  $M_{\text{theor}}$ , values of degree of branching, DB, glass transition temperature,  $T_{\text{g}}$ , and characteristic temperatures of thermal degradation for the investigated AHBP samples

Sample	$M_{ m theor}, \  m g/mol$	DB	$T_{\rm g}$ , °C	<i>T</i> <sub>5</sub> , °C	<i>T</i> <sub>20</sub> , °C	<i>T</i> <sub>50</sub> , °C	<i>T</i> <sub>80</sub> , °C
AHBP-3	3498	0.45	38	240	274	297	328
AHBP-3SA	29482	0.45	29	246	285	334	388



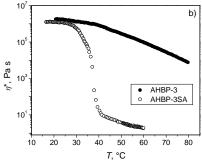


**Fig. 1.** (a) Frequency and (b) temperature dependences of the complex viscosity,  $\eta^*$ , of investigated AHBP

From the TG curves presented in Fig. 2 it can be observed that under the given experimental conditions a measurable mass loss of investigated AHBP is detected at around 220 °C. Beside that, obtained results show that the thermal stability of the AHBP increases significantly by modification of the end –OH

groups with stearic acid. This can also be seen from the results listed in Table 1, where temperatures obtained for mass losses of 5, 20, 50 and 80 wt. % ( $T_5$ ,  $T_{20}$ ,  $T_{50}$  and  $T_{80}$ , respectively) are listed.

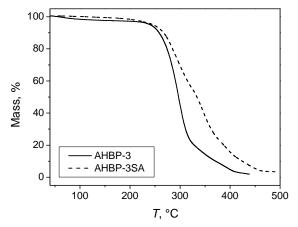


**Fig. 2.** TG curves of investigated AHBP, determined in nitrogen atmosphere at heating rate of 5 °C/min

#### **Conclusions**

According to the results presented in this work it may be concluded that the nature of end groups have marked influence on the rheological and thermal properties of AHBP samples. By modification of the end –OH groups with stearic acid, the values of the complex viscosity and glass transition temperature has been reduced, while thermal stability has been improved.

- [1] Hult, M. Johansson, E. Malmström, Adv. Polym. Sci., 1999, 143, 1-34.
- [2] E. Žagar, M. Huskić, M. Žigon, Macromol. Chem. Phys., 2007, 208, 1379-1387.
- [3] J. Vuković, J., Synthesis and characterization of aliphatic hyperbranched polyesters, PhD Thesis, University of Osnabrück, Germany, September 2006.
- [4] J. Hawker, R. Lee, J. M. J. Fréchet, J. Am. Chem. Soc., 1991, 113, 4583-4588.
- [5] E. Malmström, M. Johansson, A. Hult, Macromol. Chem. Phys. 1996, 197, 3199-3207.

### EFFECT OF SYNTHESIS PARAMETERS ON POLY(METHACRYLIC ACID) XEROGEL STRUCTURES AND EQUILIBRIUM SWELLING

V. Pavlović<sup>1</sup>, J. Jovanović<sup>2</sup>, B. Adnađević<sup>2</sup> and S. Veličković<sup>1</sup>

<sup>1</sup>Faculty of Technology and Metallurgy, Karnegijeva 4, 11001 Belgrade

<sup>2</sup>Faculty of Physical Chemistry, Studentski Trg 12-16,11001Belgrade

#### **Abstract**

Three series of hydrogels based on crosslinked poly(methacrylic acid) (PMAA) were synthesized. The influence of such reaction variables as the neutralization degree (ND) of methacrylic acid (MAA), the initial monomer concentration, and the amounts of crosslinker on the basic structural properties of xerogels and on the equilibrium swelling degree ( $SD_{eq}$ ) were investigated and discussed. It was found that the mentioned reaction variables significantly influence the structural properties of xerogels and therefore their ability to take in different amounts of water

#### Introduction

Methacrylic acid was used in synthesis of many copolymers and special attention is given to their swelling behavior and factors that have an effect on it. S.K.Bajpai investigated network and swelling parameters of poly(methacrylamide-comethacrylic acid) hydrogels and fortified that there were considerable effects of synthesis conditions, such as reaction temperature, initiator content, etc. on water absorbency [1]. In this work, poly(methacrylic acid) hydrogels were synthesized and effects of synthesis parameters on xerogel structures and equilibrium swelling were investigated.

#### **Experimental**

Materials: Methacrylic acid (MAA) was used as monomer, N,N'-methylene bisacrylamide (MBA) and 2,2-Azobis-[2-(2-imidazolin-2-il)-propane dihydrochloride (AIPD) were used as a crosslinker and an initiator, respectively, and NaOH was used for neutralization. Synthesis: Series of poly(methacrylic acid) xerogels with different neutralization degree (ND) of MAA, the initial monomer concentration, and the amount of crosslinker, were synthesized via simultaneous free-radical polymerization and cross-linking in an aqueous solution, by the procedure based on the process described in our previous works for poly(acrylic acid) hydrogel synthesis[2]. Structural properties: of PMAA xerogels were determined and calculated: xerogel density,  $ρ_{xg}$ , average molar mass between the network crosslinks,  $M_c$ , crosslinking density,  $ρ_c$ , polymer volume fraction in the equilibrium swollen state,  $υ_{2,s}$ , and distance between macromolecular chains (pore size), ξ, by using equations proposed by Peppas and Wright [3]. Swelling experiments: xerogel sample was immersed in an excess of water at 25°C and

measured until equilibrium was achieved. <u>Equilibrium swelling degree:</u> ( $SD_{eq}$ ) was calculated using the following equation:  $SD_{eq} = (m_{eq} - m_0) / m_0$ , where  $m_{eq}$  and  $m_0$  are weights of the hydrogel sample in the equilibrium swollen state and in dry state, respectively.

#### **Results and Discussion**

The effect of synthetic parameters: neutralization degree (ND) of MAA, crosslinking density and the initial MAA concentration, on the equilibrium swelling degree of PMAA hydrogels, in distilled water at 25°C, are shown in Figure 1.

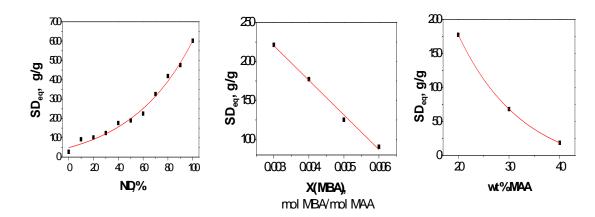


**Fig. 1.** The effects of synthetic parameters on the equilibrium swelling degree of PMAA hydrogels

As it can be clearly seen from Figure 1, the equilibrium swelling degree ( $SD_{eq}$ ) increases exponentially with the increase in the neutralization degree of MAA, while  $SD_{eq}$  linearly decreases from 221 g/g to 90.6 g/g with the increase in nominal crosslinker ratio. The increase in the crosslinker content increases generation of more crosslinking points on the polymeric chains and decreases free space between them. Therefore, the space left for water to enter is smaller and  $SD_{eq}$  decreases. Initial MAA content increase from 20 wt% to 40 wt% leads to decrease in the equilibrium swelling degree from 177.4 g/g to 18.6 g/g. This behavior can be attributed to an increase in the viscosity of the reaction medium, which made the movement of free radicals and monomer molecules in reaction mixture difficult, which contributes to creation of the network that absorbs less amount of water. Table 1 presents influence of synthesis parameters on the structural properties of PMAA xerogels.

**Table 1.** Influence of the synthesis parameters on the structural properties of PMAA xerogels

	2	Structural properties			
	$\rho_{xg}$ , $g/cm^3$	$v_{2,s}$	M <sub>c</sub> , g/mol	$\rho_c \times 10^4$ , $mol/cm^3$	ξ, nm
ND, %					
0	1.33	0.0367	10750	1.23	28.0
20	1.29	0.0099	11300	1.17	43.4
40	1.35	0.0057	11850	1.14	52.2
60	1.38	0.0045	12400	1.11	56.6
80	1.42	0.0024	12950	1.09	69.6
100	1.45	0.0017	13500	1.07	78.5
MAA, wt%					
20	1.35	0.0057	11850	1.14	52.18
30	1.40	0.0147	11850	1.18	38.00
40	1.44	0.0539	11850	1.21	24.63
MBA, mol%					
0.3	1.26	0.0045	15800	0.795	64.99
0.4	1.35	0.0057	11850	1.14	52.18
0.5	1.40	0.0080	9480	1.48	41.64
0.6	1.46	0.0110	7900	1.85	34.12

As it can be seen, changes of structural parameters comply with experimental data for  $SD_{eq.}$  The increase in MAA neutralization degree (ND) leads to increase in xerogel density ( $\rho_{xg}$ ) as well as in  $M_c$  and  $\xi$ , while  $\upsilon_{2,s}$  and  $\rho_c$  decrease. As MAA concentration in the initial reaction mixture increases, the values of the xerogel density increase as well as the values of crosslinking density and polymer volume fraction in the equilibrium swollen state, while  $SD_{eq}$  and  $\xi$  decrease. Presented results also show that  $\rho_c$ ,  $\upsilon_{2,s}$ , and  $\rho_{xg}$  increase with the increase in MBA concentration, while  $\xi$  and  $M_c$  decrease.

# Acknowledgement

The investigation was supported by the Ministry of Science and Environmental Protection of Serbia, through project G 142025.

- [1] S.K. Bajpai, S. Singh, Reactive & Functional Polymers 2006, 66, 431–440.
- [2] B. Adnadjevic, J. Jovanovic, J Appl Sci 2008, **107(6)**, 3579-3587.
- [3] N.A. Peppas, S.L. Wright, Eur J Pharm & Biopharm 1998, 46, 15–29.

# SYNTHESIS AND USE MALEIMIDES AS MODIFIERS POLYURETHANES

V.A. Danilov, O.A. Kolyamshin and N.I. Koltsov

Department of Physical Chemistry of Chuvash State University, Moskovskii prospekt 15, 428015 Cheboksary, Russia

#### **Abstract**

The properties of maleimides have been synthesized and investigated on the basis of ethers 4-N-maleimidebenzoic acid. The obtained maleimides have been used for modification of polyurethane composition on the basis of isocyanate-containing prepolymer. According to the investigation, polyurethanes on the basis of maleimides posses high physical-mechanical and chemical resistance to the aggressive organic and inorganic solvents.

#### Introduction

The imides of maleic acids and their derivatives represent a perspective class of organic compounds for chemistry of polymers. The presence of highly active double bond, maleimides are easily polymerized and copolymerized with various classes of compounds, forming strong and heat-resistant materials. Inturn, polyurethanes, having unique combination of high durability and elasticity, are widely found in industry. One of the perspective methods of applied polyurethanes obtaining is the synthesis of oligomers with various reactive groups. The main advantage of this method is that of safety technology and great opportunity to regulate polyurethanes properties by means of changing the nature and the building of oligomers and the application of modifiers, increasing different properties of polymer. One of such perspective compounds are maleimides. That is why the aim of the given work is synthesis and investigation of properties of new maleimides. The study of these maleimides usage as modifiers of polyurethane compositions on the basis of isocyanate-containing prepolymer.

#### **Results and Discussion**

The properties of four maleimides have been synthesized and investigated: N-phenilmaleimide (N-PhM), ethyl ether of 4-N-maleimidebenzoic acid (I), pentyl ether of 4-N-maleimidebenzoic acid (II), octyl ether of 4-N-maleimidebenzoic acid (III) in the given work.

The synthesis of maleimides was carried out in 2 stages. The maleimides have the following structure

were  $R = I - C_2H_5$ ,  $II - C_5H_{11}$ ,  $III - C_8H_{17}$ .

The synthesis urethane oligomer with trailer methacrylic groups on the basis of isocyanate-containing prepolymer with molecular weight 1400 and monomethacrylic ether ethyleneglycol (MEG) was carried out, changing a ratio of initial components according to a ratio of functional groups NCO:OH from 1:1,0 up to 1:1,2. On the basis of the received data the optimum mode of synthesis oligomer with methacrylic groups (OM) has been established: ratio NCO:OH=1:1,05; temperature 60°C.

Researches have shown, that the best properties compositions OM+MEG received by polymerization have polyurethane. Composition OM: MEG at a ratio 50:50 on weight of making components is optimum from the point of view of high values of durability and elasticity.

The researches have shown that maleimides additives result in increase strengthening properties of polymers. The maximal values of durability at break for modified polyurethane have been achieved at: 3 %-s' contents N-PhM and I, accordingly, 25,2 and 23,5 MIIa; 1 %-s' contents II and III - 30 and 45 MIIa accordingly. Thus high sizes of gel - fraction have been observed also, that testifies to spatial mesh structure of the received polymers. As the increasing of the maleimides contents there is a reduction in strength at break modified polyurethane and their relative lengthening changes insignificantly. It is probably said that maleimides at their optimum contents in the investigated systems promote formation of the spatial mesh structure raising strengthening properties of polymers. High values of relative lengthening for the received polymers points at presence OE which contains in the structure various groups. The forming flexible blocks promoting increase of elasticity of polymers.

Further the investigations have shoen that polymers have high chemical resistance action to water, water solutions HCl and NaOH enough. This confirms the presence of spatial mesh structure in these polymers. Higher degree of swelling polymers in organic solvents is due to that they contain a part of not reacted rests monomers and OM (which are washed away by these solvents) and also presence of polar groups in macromolecules of the received polymers. It is established that the polymers containing additives II have the greater resistance action to organic solvents than polyurethanes received with application of additives of other investigated maleimides. Modified polyurethanes contain polar groups in the structure which promote increase in interaction of polymer with polar solvents. Thus, the received results allow to estimate operational opportunities of use

modified polyurethanes in various environments - they can be applied as polymeric coverings, steady against action of the water, the diluted solutions of acids and alkalis. Results of research of dielectric properties have shown, that increase of the contents maleimides results in reduction of specific superficial and volumetric resistance and increase in dielectric permeability polyurethanes and consequently to increase electroconductivity, that shows the presence maleimides polar groups in structure. It is possible to judge it comparing these properties for the polymers received without additives maleimides and with the smaller contents maleimides. Thermo stability of polymers containing maleimides grows up to 20 - 22 °C.

Thus we have synthesized and investigated new maleimides. The properties polyurethanes have obtained, modified by these maleimides. The results have shown that researches in this area are perspective.

# SYNTHESIS AND CHARACTERIZATION OF CROSSLINKED POLYURETHANES

M. Vučković<sup>1</sup>, J. Vuković<sup>1</sup>, S. Jovanović<sup>2</sup> and V. Vodnik<sup>3</sup>

IHTM-Center of Chemistry, Studentski trg 12-16, 11000 Belgrade, Serbia
 Faculty of Technology and Metallurgy, University of Belgrade, Karnegijeva 4, 11120 Belgrade, Serbia

<sup>3</sup> Institute of Nuclear Science "Vinča", P. O. Box 522, 11001 Belgrade, Serbia

#### **Abstract**

Two polyurethane samples, crosslinked with aliphatic hyperbranched polyester, were synthesized and examined in this work. The sample PUPDMS-EO was prepared using ethylene oxide-poly(dimethylsiloxane)-ethylene oxide as macrodiol, while the synthesis of PUPTMO was performed using poly(tetramethyleneoxide). The obtained results show that thermal stability of these networks can be improved by introducing the siloxane sequences. However, the sample PUPDMS-EO has at the same time much lower crosslinking density than PUPTMO.

#### Introduction

Crosslinked polyurethanes (PUs) are important class of PU family, due to their interesting physical and chemical properties and extensive applications in the manufacture of coatings, elastomers, foams, etc. Two types of network are usually present in crosslinked PUs: physical (created by the H-bonds) and chemical. The nature of the chemical network and properties of crosslinked PUs strongly depend on the type of crosslinking agent. The use of hyperbranched (HB) polymers as crosslinker of PUs has attracted large scientific attention over the last years, because of their unique structure and properties and simple synthetic procedure [1,2].

In this work, the influence of the nature of macrodiol on swelling and thermal properties of two crosslinked PUs, PUPDMS-EO and PUPTMO, based on ethylene oxide-poly(dimethylsiloxane)-ethylene oxide and poly(tetramethyleneoxide), respectively, was investigated. Both samples were crosslinked by the hydroxy-functonal aliphatic HB polyester of the second pseudo generation (BH-2, Boltorn®).

# **Experimental**

The PU networks were synthesized in bulk using PDMS-EO ( $M_{\rm n}$  = 1200 g/mol) or PTMO ( $M_{\rm n}$  = 1000 g/mol) and 4,4'-diisocyanatodiphenylmethane (MDI) as monomers and BH-2 ( $M_{\rm n}$  = 1340 g/mol, functionality  $f_{\rm n}$  = 12 [3]) as crosslinking agent. The NCO/OH ratio was 0.8 for both samples. The crosslinked samples were obtained as yellow films.

IR spectra of the crosslinked PUs were recorded on ATR NICOLET 6700 IR spectrometer. Swelling behavior of square samples was investigated in N-methyl-2-pyrrolidinon (NMP) at room temperature. The thermal stability of samples was

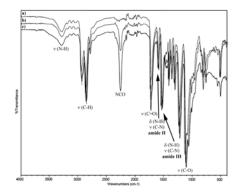
determined by thermogravimetric (TG) analysis, using Setaram Setsys Evolution 16/18 instrument in argon atmosphere, at heating rate of 10 °C/min.

#### **Results and Discussion**

Some important properties of the synthesized PU networks are listed in Table 1. The soft segments content, SSC, calculated according to the feed mass ratio (SSC% =  $[W_{\text{Macrodiol}}/W_{\text{MDI}}+W_{\text{BH-2}}+W_{\text{Macrodiol}}]\times 100$ ), is similar for both samples. The course and the end of the reaction, as well as the chemical structure of both samples were determined by IR spectroscopy. As an illustration, in Fig. 1 is presented IR spectra of PUPTMO sample, determined at different times during the synthesis. In the IR spectra of final PU samples the diisocyanate -N=C=O band (2250-2275 cm<sup>-1</sup>) was not detected.

**Table 1.** The soft segments content, SSC, swelling degree, q, and characteristic temperatures of thermal degradation of synthesized crosslinked PUs

Sample	SSC, wt.%	q	$T_{20}$ , °C	<i>T</i> <sub>50</sub> , °C	<i>T</i> <sub>70</sub> , °C	<i>T</i> <sub>80</sub> , °C
PUPDMS-EO	59	4.8	351	400	438	457
PUPTMO	56	2.7	352	406	424	433



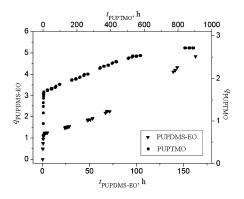


**Fig. 1.** IR spectra of PUPTMO sample determined at a) 26 h, b) 19 h and c) 0 h during the synthesis

**Fig. 2.** The change of the swelling degree, q, with time for crosslinked PUs

The results obtained by investigation of swelling behavior of the synthesized crosslinked PUs in NMP at room temperature are presented in Table 1 and Fig. 2. Values of the swelling degree, q, were calculated using conventional gravimetric method, equation  $q = (m-m_0)/m_0$  and values of the sample masses before,  $m_0$ , and after swelling, m. The equilibrium swelling of the sample PUPTMO was accomplished after 35 days with q value of 2.7, while sample PUPDMS-EO broke up after 163 h of swelling, having q of 4.8. The reason of such big differences in swelling behavior in NMP between PUPTMO and PUPDMS-EO is the heterogene-

ity of the network composition of PUPDMS-EO, containing relatively low number of chemical cross-links and consequently much lower crosslinking density than the network of PUPTMO sample.

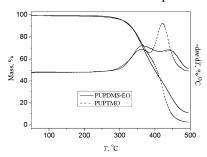


**Fig. 3.** TG and DTG curves of investigated crosslinked PUs, determined in argon atmosphere, at heating rate of 10 °C/min

From the results presented in Fig. 3 it can be observed that the thermal degradation of these crosslinked PUs is a two-step process in argon. This is clearly demonstrated from the thermogram derivative curves (Fig. 3). The thermal degradation of polyurethanes first goes via decomposition of urethane bonds, followed by breakage of the soft segment phase [4]. A measurable mass loss of investigated samples is detected between 250 and 270 °C. In Table 1 are listed temperatures obtained for mass losses of 20, 50, 70 and 80 wt. % ( $T_{20}$ ,  $T_{50}$ ,  $T_{70}$  and  $T_{80}$ , respectively). Up to the temperature corresponding to the mass loss of 60 wt. %, the thermal stability of PUPTMO and PUPDMS-EO is almost the same, while at higher mass loss temperatures PUPDMS-EO is more thermally stable than PUPTMO.

#### **Conclusions**

The results presented in this work show that the nature of monomer can have significant influence on the properties of PU networks. Crosslinked PU synthesized using PDMS-EO as macrodiol has much lower crosslinking density than PUPTMO sample. However, by introducing the siloxane sequences in these crosslinked PUs, thermal stability increased.

- [1] S. Nasar, M. Jikei, M. Kakimoto, E. Polym. J., 2003, 39, 1201-1208.
- [2] L. Okrasa, P. Czech, G. Boiteux, F. Mechin, J. Ulanski, Polymer, 2008, 49, 2662-2668.
- [3] J. Vuković, M. D. Lechner, S. Jovanović, Macromol. Chem. Phys., 2007, 208, 2321-2330.
- [4] Z. S. Petrovic, Z. Zavargo, J. H. Flynn, W. J. Macknight, J. Appl. Polym. Sci., 1994, 51, 1087-1095.

# THERMAL STUDIES OF SILVER-POLY(METHYLMETHACRYLATE) NANOCOMPOSITES

V. Vodnik<sup>1</sup>, J. Vuković<sup>2</sup> and J. Nedeljković<sup>1</sup>

<sup>1</sup> Institute of Nuclear Science "Vinča", P.O. Box 522, 11001 Belgrade, Serbia <sup>2</sup> IHTM-Center of Chemistry, Studentski trg 12-16, 11000 Belgrade, Serbia

#### **Abstract**

The novel nanocomposite material based on surface-modified silver nanoparticles (Np) with average diameter of 6 nm and poly(methylmethacrylate) (PMMA) matrix was synthesized. The effect of silver loading on the thermal properties of PMMA was studied. The obtained transparent nanocomposites Ag/PMMA films were characterized by IR spectroscopy and thermal techniques (TGA, DSC). The chemical composition of the PMMA matrix is not changed in the presence of the metal nanoparticles, but the thermal stability of the nanocomposites was found to be better than thermal stability of the pure polymer. Also, Ag nanoparticles have pronounced effect on a glass transition temperature (Tg) of PMMA.

#### Introduction

Polymer composites containing metal Np have being investigated for a broad variety of applications such as microelectronics, optical filters, magnetic or optical data storage, etc. [1,2] Because of their high surface to bulk ratio, nanoparticles significantly affect the matrix leading to some new properties which are not present in either of the pure materials. These nanocomposite systems require particles with uniform size, controlled dimension and regular shape. A disturbing factor in such filled polymer system is non-uniformity of composite properties owing to poor dispersion of the nanoparticles. Surface modification of the filler with suitable coupling agent is often recommended to enhance filler dispersion, as well as aid in processing. Thermal properties of the nanocomposites are affected by the filler content, the chemical composition of the filler surface and different synthetic routes. As no evidence of the influences of silver Np on thermal properties of Ag/PMMA nanocomposite and glass transition temperature of PMMA were found in the literature, we were focused in the present paper to explain these effects.

# **Experimental**

Silver hydrosols were prepared using NaBH<sub>4</sub> as a reducing agent, as described elsewhere [3]. Silver nanoparticles were transferred into chloroform using oleylamine as transfer agent. In order to prepare Ag/PMMA nanocomposites, silver nanoparticles (0.5-2 wt %) dispersed in chloroform were mixed in an appropriate ratio with PMMA (Diakon<sup>TM</sup> CMG 314V), dissolved in chloroform. After evaporation of the solvent in vacuum oven at room temperature, yellow coloured transparent films with thickness of about 25 μm were obtained.

IR measurements of pure PMMA and Ag/PMMA nanocomposites were carried out on a Bruker Vector 22 Spectrometer (Opus 2.2 Software). Thermogravimetric analyses (TGA) were carried out on a Perkin Elmer TGS-2 instrument either in air or under nitrogen atmosphere (flow rate 25 cm³/min) with heating rate of 10  $^{0}$ C/min. Differential scanning calorimetry (DSC) measurements were performed using Perkin Elmer DSC-2 instrument in the temperature range from 50 to 170  $^{0}$ C under nitrogen atmosphere (heating rate was 20  $^{0}$ C/min).

#### **Results and Discussion**

According to the IR measurements, no difference between the IR spectra of the pure PMMA and Ag/PMMA nanocomposites were found, indicating that Ag/PMMA nanocomposites resemble solid solution with weak interaction between the polymer matrix and nanofiller particles. The thermal stability of the synthesized samples was examined by non isothermal thermogravimetry both in nitrogen and air atmosphere, Fig. 1. The obtained results showed, that the presence of the silver Np increased the thermal stability of polymer probably because of inhibiting effects of the Ag Np on some degradation stages of the thermal and thermo-oxidative degradation of PMMA. For example, the thermal degradation of the filled polymer with 2 wt% of the Ag Np is shifted towards higher temperature for about 26°C in the nitrogen and about 27°C in the air atmosphere.

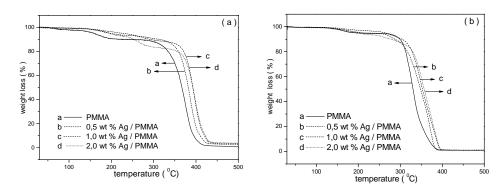


**Fig. 1** TG curves of pure PMMA and Ag/PMMA nanocomposites with different content of the Ag Np obtained in nitrogen (a) and air (b).

It is generally considered that PMMA thermally degrade through depolymerisation [4]. The improvement of the thermal stability in PMMA nanocomposites may be associated with reactivity of metal with polymeric radicals and the different thermal stability of the resulting complexes or coordinates [5]. In the presents of oxygen, PMMA decomposition was explained by the dual function of oxygen. At lower temperatures, oxygen inhibits PMMA decomposition by reacting with a polymeric radical and forming a more stabile peroxy radical which degrades at higher temperature and releases a more reactive radical, resulting in the acceleration of

PMMA decomposition [6]. The inhibiting effects of the Ag Np on thermooxidative degradation of PMMA could be explained by the reaction of Ag Np with oxygen, which led to the slower degradation of the PMMA matrix [7].

**Table 1.** Glass transition temperature (T<sub>g</sub>) of Ag/PMMA nanocomposites

content of Ag Np (wt %) in				
Ag/PMMA nanocomposites	0	0.5	1.0	2.0
$T_g$ , $(^0C)$	97	96	92	91

The influence of silver nanoparticles on the glass transition behavior of polymer matrix was studied with DSC technique and the results are listed in Table 1. It can be seen the tendency of slight decrease of  $T_g$  values by increasing silver content for Ag/PMMA nanocomposites. Ash et al. [8] explained the decrease of  $T_g$  values in terms of thin film model. When the inter-particles distance is small enough, then the polymer between two particles can be considered as a thin film. Assuming that little or no interfacial interaction between the filler and matrix exists, the  $T_g$  decreases as the film thickness, i.e. inter-particles distance decreases.

#### **Conclusions**

The obtained results showed that the presence of silver Np increased the thermal stability of polymer probably because of inhibiting effects of the Ag Np on some degradation stages of the thermal and thermo-oxidative degradation of PMMA. On the other hand, it was shown that small inter-particles distance have pronounced effect on glass transition temperature of PMMA matrix.

- [1] D.Y. Godovski, Advan. Polym. Sci., 2000, **165**, 153.
- [2] Biswas, O.C. Aktas, U. Schurmann, U. Saeed, V. Zaporjtchenko, F. Faupel, Appl. Phys. Lett., 2004, **84**, 2655.
- [3] V. Vuković, J. Nedeljković, Langmuir, 1993, 9, 980.
- [4] I. C. McNeill, Eur. Polym. J., 1968, 4, 21.
- [5] H. Wang, P. Xu, W. Zhong, L. Shen, Q. Du, Polym. Degrad. Stabil., 2005, 87, 319.
- [6] D. J. Peterson, S. Vyazovkin, A. C. Wight, J. Phys. Chem. B, 1999, 103, 8087.
- [7] Z. Kai, F. Qiang, F. Jinghui, Z. Dehui, Matter. Lett., 2005, **59**, 3682.
- [8] B.J. Ash, L.S. Schadler, R.W. Siegel, Mater. Lett., 2002, 55, 83.

# EFFECT OF POROUS SUPPORT AND NONSOLVENT ADDITIVE ON MORPHOLOGY OF PESF COMPOSITE MEMBRANES

#### V. Laninović

IMS Institute, Bulevar vojvode Misica 43, Belgrade, Serbia e-mail: verica.laninovic@imsinstitute.co.yu

#### **Abstract**

Polyethersulfone (PESf) composite membranes were prepared from polymer solutions containing PESf, nonsolvent additive and N,N-dimethylacetamide as solvent. Water was used as nonsolvent in the coagulation bath. The effects of the NSA and the support type on the membrane morphology were studied via scanning electron microscopy. It was observed that the porous non-woven support significantly changes mechanical properties of the prepared composite membranes compared to the integral asymmetric PESf membranes.

#### Introduction

Efforts to eliminate mechanical integrity problems associated with structural defects in the sublayer of integrally skinned membranes led to development of the composite technique. The composite technique permits a combination of properties that are not available in a single material: good permeability and separation of the solute, excellent resistance to mechanical stress. According to the literature data composite polymer membranes can be prepared using different methods [1,2,3].

### **Experimental**

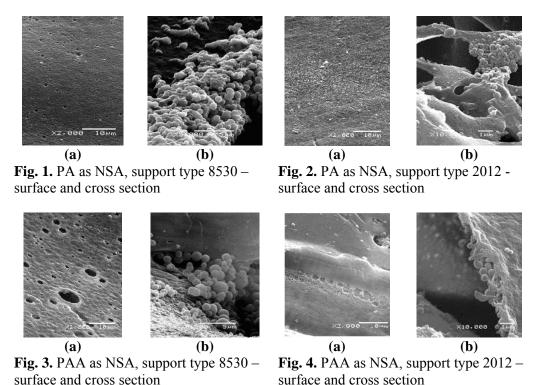
Polymer solutions (15 wt % polymer) were prepared using polyethersulfone, PESf (Ultrasone E 6020) and N,N-dimethylacetamide, DMAc (Merck) as solvent. Propionic acid, PA (Fluka) and propionic acid anhydride, PAA (Merck) were used as nonsolvent additive in the polymer solution. Pure water was used as nonsolvent in the coagulation bath ( $t=23^{\circ}$ C). Two types of the glass non-woven glass fabric sheets were used: type 2012 and type 8530 available from Scandatex. This versatile material is widely used due to its good and desirable properties. Namely, most chemicals have little or no effect on this material, it doesn't stretch or shrink, and it is also a no adsorb material. Furthermore glass fibers have high tensile strength and excellent thermal stability.

The morphology of prepared composite PESf membranes was examined with JEOL JSM-6460 LV Scanning Electron Microscope. Breaking strength was measured with a Zwick tensile tester at testing speed of 5 mm/min.

#### **Results and Discussion**

SEM micrograph of the obtained composite membranes shows a more or less developed nodular structure. Smolders et al. and Boom assume that spinodal decom-

position of the polymer solution is responsible for formation of the nodules [4,5]. Namely, according to them in the case of rapid exchange processes, the relaxation time of the polymer is to long to obtain a thermodynamic equilibrium at the interface. The highly entangled polymer molecules clustering and forms the spherical morphology known as nodules.



Obtained results shows that the membranes prepared with the support type 2012, has dense non-porous skin layer. On the other hand, in composite membranes with support type 8530 the degree of surface porosity is very high and the pore size are quite heterogeneous. It could be assumed that dense fiber structure of the support type 2012 induces coalescence of the polymer aggregates at the air – solution – support interface due to capillary force and higher polymer concentration in the surface layer. Capillary forces promoting the elimination of intersticial surface voids, hense reducing the surface porosity and resulting in dense membrane skin.

Porous non-woven support makes prepared composite membranes mechanically strong. The obtained results [Fig. 5] shows an increase of the tensile strength at break compared to the integrally skinned asymmetric PESf membranes [6].

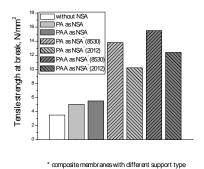


**Fig. 5.** Mechanical properties of the integral asymmetric and composite PESf membranes.

#### **Conclusions**

If the polymer solution was spread onto dense support type (2012), the formed composite membrane have almost non-porous surface layer. On the other hand, in composite membranes with more porous support type (8530) surface porosity is very high. The developed nodular structure in all prepared composite membranes is more probably the result of liquid-liquid demixing by nucleation and growth of polymer poor phase. The mechanical properties of the obtained composite membranes are improved, compared to the integrally skinned membranes.

### Acknowledgements

The financial support by the Ministry of Science of the Republic of Serbia in the form of the research project No 142034 G is gratefully acknowledged.

- [1] "Ullmann's Encyclopedia of Industrial Chemistry", ed. VCH Verlagsgesellschaft GmbH, Weinheim Germany, 1996, A 16, 187-263.
- [2] R.C.Ruaan, T.Chang, D.Wang, J.Polym.Sci. part: B Polymer Physics, 1999, 37, 1495-1502.
- [3] G.Rusch, J.A.Kolde, US Pat 6130175 (2000).
- [4] C.A.Smolders et al., J.Membr.Sci., 73 (1992).
- [5] R.Boom, PhD Thesis, University Twente, Netherlands (1992).
- [6] V. Laninovic, Desalination, 2005, **186**, 39-46.

### INFLUENCE OF DIFFERENT DEGRADATION MEDIUM ON RELEASE OF ASCORBIC ACID FROM PLGA NANO AND MICROSPHERES

M. Stevanović<sup>1</sup> and D. Uskoković<sup>1</sup>

Institute of Technical Sciences of the Serbian Academy of Sciences and Arts, Belgrade; Serbia

#### **Abstract**

The major goals of the present study were to examine the effects of the type of release medium on the resulting drug release kinetics and to get further insight into the underlying drug release mechanisms. Spherical micro and nanoparticles were prepared by a physicochemical solvent/non-solvent method with polyvinyl pyrrolidone as a surfactant and characterized with ultraviolet (UV) spectroscopy and scanning electron microscopy (SEM) before and upon exposure to various release media.

#### Introduction

Biodegradable nano/microparticles of poly(D,L-lactide-co-glycolide) (PLGA) and PLGA-based polymers are widely explored as carriers for controlled delivery of therapeutics such as proteins, peptides, vaccines, genes, antigens, growth factors, vitamins, etc [1-3]. Polymer degradation plays a key role in medicament release from sustained release polyester systems, therefore in order to elucidate the mechanism governing release, it appears essential to analyze the in vitro degradation behavior of these devices [4]. The selection of an appropriate release medium for *in vitro* tests simulating *in vivo* conditions can be very important for getting rapid feedback on the release characteristics of a specific batch.

# **Experimental**

In the experiment we used poly(DL-lactide-co-glycolide) (PLGA) which was obtained from Durect, Lactel and had a lactide-to-glycolide ratio of 50:50. Molecular weight of the polymer was 40000-50000g/mol. Molecular weight of ascorbic acid is 176.13 g/mol (Microvit<sup>TM</sup>, Adisseo). Polyvinyl pyrrolidone (povidone, PVP) was obtained from Merck Chemicals Ltd (k-25, Merck, Germany). All other chemicals and solvents were of reagent grade. Poly(DL-lactide-co-glycolide) micro and nanoparticles without and with encapsulated ascorbic acid were prepared using a physicochemical solvent/non-solvent method as we reported in our previously work [3, 4]

The degradation of the PLGA/ascorbic acid nanoparticles and release rate of the ascorbic acid were studied for more than fifty days in a physiological solution (0.9% sodium chloride in water) or in phosphate buffered saline (PBS, one tablet dissolved in 200mL of deionized water yields 0.137 M sodium chloride, 0.01 M phosphate buffer and 0.0027 M potassium chloride) with sodium azide (0.1M solution natriumazid  $NaN_3$ ) as a degradation medium. In the PBS was added 110 (il

sodium azide because sodium azide acts as a bacteriostatic. The UV measurements were performed on Perkin-Elmer Lambda 35 UV-vis Spectrophotometer in the frequency interval of 200-400 nm. The pH of the physiological solution or PBS has been measured using pH indicator strips obtained from Merck (KGaA, Germany) at various time periods to follow the acidity of the degrading medium with time. The morphology of PLGA/ascorbic acid 85/15% nanoparticles after 17 and 28 days of the degradation in phosphate buffered saline has been examined by scanning electron microscope JEOL JSM-6490LV.

#### **Results And Discussion**

PLGA completely degrades within period of 8 weeks in physiological solution as a degradation medium as well as in phosphate buffered saline, fully releasing all the encapsulated ascorbic acid (Figure 1).

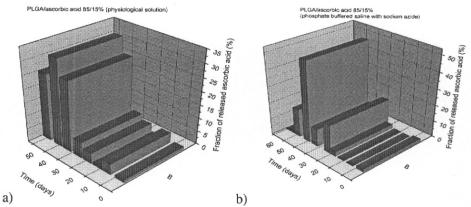


**Fig. 1.** Release of the ascorbic acid in percentages over the period of time of the degradation in the case of a) physiological solution and b) phosphate buffered saline as a degradation medium (relative review)

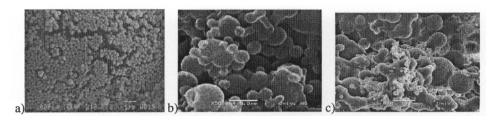
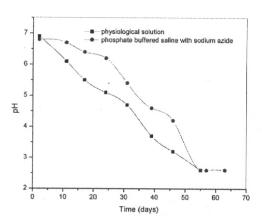


**Fig. 2.** SEM images of PLGA/ascorbic acid 85/15% nanospheres before (a) and after 17 (b) and 28 days (c) of the degradation in phosphate buffered saline

From the image 2, we can see that during the degradation the particles were first agglomerated, then forming the film. By the end of the experiment the particles have fully degraded and there were no more traces of them in the solution. From the figure 3 it can be noted that during the time of the degradation pH of the solution decreases as a result of the accumulation of PLGA degradation products

and ascorbic acid. It could be expected that the faster degradation of the lower molar mass fraction, present in copolymer, increase the local acidity, thereby, accelerating the hydrolysis of higher molar mass species. In other words, when acid accumulation creates a local pH drop, catalytic degradation of the polymer itself occurs.

**Fig. 3.** Changes in the pH of the degradation medium with immersion time for the PLGA/ascorbic acid 85/15% nanoparticles in the case of a) physiological solution and b) phosphate buffered saline



#### Conclusion

The release dynamics of the ascorbic acid from the polymer matrix is different when PLGA particles degrade in PBS and when they degrade in physiological solution, as a degradation medium. The ascorbic acid is released slower from the PLGA particles at the beginning, when PBS is used. This is explained with the slower change of pH solution as well as with the presence of sodium azide.

### Acknowledgements

Authors would like to thank Milos Bokorov for his help in SEM analysis. The Ministry of Science of the Republic of Serbia supports this work through the project No. 142006.

- [1] M. Stevanovic, N. Ignjatovic, B. Jordovic, D. Uskokovic, Journal of Materials Science: Materials in Medicine, 2007, **18**, 1339-1344.
- [2] M. Stevanovic, A. Radulovic, B. Jordovic, D. Uskokovic, Journal of Biomedical Nanotechnology, 2008, accepted.
- [3] M. Stevanovic, B. Jordovic, D. Uskokovic, Journal of Biomedicine and Biotechnology, 2007, article id 84965.
- [4] M. Stevanovic, J. Savic, B. Jordovic, D. Uskokovic, Colloids and Surfaces B: Biointer-faces, 2007, 59, 215-223.

# **Environmental Protection, Forensic Science**

(K)

# GAS CHROMATOGRAPHY DETECTION OF AIR POLLUTED GRAPHIC INDOOR

D. Adamović, Ž. Pavlović, I. Karlović, J. Kiurski and M. Vojinović-Miloradov Faculty of Technical Sciences, Trg D. Obradovića, Novi Sad

#### **Abstract**

The presences of VOCs indoor of printing house have been analyzed. Air samples have been collected in three different locations inside of the printing house – prepress department including CtP device, offset press department including 4 colors aggregate plus one varnish aggregate sheet feed offset machine and post pres department. While this printing house uses vegetable oil based printing inks, low concentration of VOCs have been detected. Most of the detected organic solvents come from cleaning agents used on the offset printing machine. Many cleaners for offset printing forms and printing machine are based on petroleum distillates and methyl ethyl ketone. The concentration of benzene, toluene, and xylene showed levels below the recommended maximum level set by EPA.

#### Introduction

Graphic industry as one of the biggest industrial polluter generates many toxic, harmful dangerous substances with organic compounds especially volatile organic compounds (VOCs) such as benzene, toluene, xylene and other. Compounds from VOC group are in composition of basic solvent used in graphic industry, printing inks, varnishes, adhesives, grease removers and glues [1]. Insidious toxicity which may include carcinogenicity of solvents has been intensively investigate in recent years, and efforts have been made to reduce solvent exposure, not only occupationally but in the general population as well trough measures such as the use of water and vegetable oil based printing inks [2].

Monitoring and the right time detection of VOC and the adequate conduction criteria of protection are an imperative of any technological process.

The aim of the right time detection of VOC in graphic industry is the optimal method using in situ mobile gas chromatograph device Voyager. Beside BTEX gases, this device can be used for detection for about 40 primary aero pollutants from the group of the volatile organic compounds. Mobile device GC – Voyager dissociates and detect components of specimen based on the gas chromatography principle.

The goal of the present study was to investigate the concentration of VOCs in a printing house pinpointing their sources and suggesting remediation measures to improve the air quality.

#### **Results and Discussion**

Lithographic printing is often referred to as offset printing and it is based on the fact that oil and water do not mix. The ink is offset from the plate to a rubber blanket on an intermediate cylinder and from the blanket to the substrate, which could be paper, plastic, or metal, on an impression cylinder. On the plate, the printing areas are oil or

ink receptive and water repellent and the non-printing areas are water receptive and ink repellent. When the plate, mounted on a cylinder, rotates, it contacts rollers that have been wet by water or dampening solution and rollers wet by ink. The dampening solution wets the non-printing areas of the plate, which prevents the ink from wetting these areas. The ink wets the image areas and these are transferred to the blanket cylinder, as the converting to the alternatives. The factors that could affect the cost include long-term performance and compatibility testing. IRTA (The Institute for Research and Technical Assistance) is conducting extended testing in the ongoing SCAQMD (The South Coast Air Quality Management District) project to determine the impact of these variables. SCAQMD rule is one of the categories of cleaning regulated in lithographic printing operations. This is an important category because VOC emissions of cleanup solvents amount to about four tons per day [1]. Table 1 shows the VOC limits specified in the rule for this category.

 Table 1 VOC Limits for Cleanup Solvents Used in Lithographic Printing [1]

Cleaning Activity	Current VOC Limit (g/l)
Lithographic or Letterpress Printing	
Roller Wash – step 1	600
Roller Wash – step 2, Blanket	800
Wash and On-Press Components	
Removable Press Components	25

The values of Table 1 show that the VOC limit of the cleanup solvent used today for cleaning rollers and blankets in on-press cleaning range from 600 to 800 g/l. The alternative low-VOC, low toxicity cleanup materials IRTA recommended [2]. The alternative low-VOC can be classified into three categories: water-based cleaners, solvent that are exempt from VOC regulations and methyl esters which have a very low VOC content.

Measurements in this study have been conducted by mobile Gas Chromatograph-Voyager Photovac. The Voyager uses the principle of Gas Chromatography (GC) to identify volatile organic compounds. The Voyager portable GC employs a unique set of analytical columns and preprogrammed temperatures and flow rates to optimize the separation of complex VOC mixtures found in specific industries.

Using mobile GC Voyager three series of measurements have been conducted in three different locations of printing house: prepress department including CtP device, offset press department and post pres department. The aim of our measurements was detection and quantification concentration levels of BTEX compounds indoor of printing house. The following results have been presented in Table 2. Table 2 summarizes the results of BTEX detection and quantification in printing house in Novi Sad, Vojvodina region. Obtained results indicate low concentration levels of BTEX compounds in printing house as a result of using vegetable – based process inks and solvents in printing process. Benzene and isomers of xylene haven't been detected. Enhanced levels of toluene have been detected in post press department, as a result of using VOC containing adhesives in this part of printing procedure.

Measuring place	Benzene [mg/m³]	Toluene [mg/m <sup>3</sup>	Ethyl benzene [mg/m <sup>3</sup> ]	m, p- xylene [mg/m <sup>3</sup> ]	o- xylene [mg/m <sup>3</sup> ]
Offset press	0	0	3.64	0	0
	0	0	0	0	0
department	0	0	0	0	0
Prepress	0	0	0	0	0
department	0	0	0	0	0
(CtP)	0	0	0	0	0
D4	0	0.281	0	0	0
Post pres	0	0.566	0	0	0
department	0	0	0	0	0

**Table 2** Concentration Levels of BTEX Compounds in Printing House

#### **Conclusions**

Printing inks and coatings used in the commercial graphic printing industry contain VOC in varying amounts, depending on the type of ink, the drying and printing processes, substrates and end-use application requirements. Changes in printing ink and solvents technology and formulations are being driven by the desire to lower the levels of air pollution caused by the printing industry. The extent of the conversion from petroleum distillate to vegetable oils is limited by both chemistry and customer applications. Many of the petroleum derived components of printing ink such as pigments and additives have no equivalent in vegetable derived products and, therefore, cannot be substituted. In addition, requests by printers for low costs, higher gloss, better rub resistance, faster setting and other production demands limit the use of vegetable derived products in ink. The best option for printers is to compare inks of equivalent run ability and end product characteristics. The vegetable-based process inks and solvents will minimize environmental harm through reduced VOC emission, reduced toxic emissions upon disposal, and increased non-renewable resource conservation. That will be the more environmentally responsible choice. Results in this study represent environmentally responsible choice is printing house in Novi Sad with minimal impact of BTEX compounds to workers and global environment.

### Acknowledgment

The authors acknowledge the financial support of the Ministry of Science of the Republic of Serbia, in the frame of projects applied under No.21014.

- [1] Bartlett IW, Dalton AJP, McGuiness A, Palmer H: Substitution of organic solvent cleaning agents in the lithographic printing industry. Ann occup Hyg 1999, **43**, 83-90.
- [2] Adrina G., Francisco R.: Neto Exposure to high Levels of VOC and Other Pollutants in a Printing Facility in Rio de Janeiro, Brazil. Indoor and Built Environment 2002, 11, 302-311.
- [3] Adamović, D., Kiurski J., Milovanovic D, Otpadne vode, komunalni čvrsti otpad i opasan otpad, Vršac, Serbia, 14-17 april, 2008, str. 59- 63, ISBN 13 978-86-82931-24-9

# DETERMINATION OF METALLOTHIONEINES BY MEANS OF HPLC-NAM SPECTROFLUORIMETRY

V. Ermakov<sup>1</sup> and V. Khabarov<sup>2</sup>

<sup>1</sup>V.I.Vernadsky Institute of geochemistry and analytical chemistry of the Russian Academy of Science, Moscow

<sup>2</sup>A.N.Frumkin Institute of physical chemistry and electrochemistry of the Russian Academy of Science, Moscow

#### **Abstract**

In order to assess the environmental status, metallothioneins (MT) as biomarkers are determined in blood plasma of mammals in the form of fluorescent complexes after SH-groups react with N-(9-acrydinyl)maleimide (NAM) by high-performance liquid chromatography (HPLC) on columns with polymer packing materials: polystyrene-divinylbenzene (PS-DVB) and polydivinylbenzene (P-DVB). On columns with PS-DVB and P-DVB, 2-3 chromatographic peaks corresponding to MT after its derivation are overlapped with glutathione. The last was separated from MT on Jupiter column.

#### Introduction

Among physical and chemical methods of studying of substance the brightest application have a spectroscopy and chromatography. At present development by last is connected to wide introduction of the highly effective liquid chromatography (HPLC), allowing to solve complex aims, combining advantages as chromatography, and spectroscopy. Special value the HPLC has got now in connection with the decision of some environmental problems and development of new technologies. This article is an example application of HPLC for determination of biologically active compounds.

#### Methods

It was used a liquid chromatograph with an injector (20-µl loop) and RF-530 fluorescent detector (excitation 277.2 and 360 nm, fluorescence 435 nm), two Knauer pump, a 150 x 4.6-mm metallic column packed with TSK gel Octadecyl 4PW with a particle size 7 µm and a 150 x 3-mm glass column packed with 10-µm P-DVB monospherical grain and Jupiter column 150 x 4,6 mm (5 mcm C18 300A). The feed rate of eluent (35 % ethanol in 0.05 M phosphate buffer, pH 6.5) through the column with TSK gel Octadecyl 4PW was 0.8-1.0 ml/min, with P-DVB – 0.4 ml/min. The columns were recovered with water solution of NaOH with pH 12 as eluent at a rate of 0.5 ml/min. The degree of recovery was evaluated based on the background signal quality of the fluorescent detector. Besides the clear methanol and mixture of water and ethanol were used as eluent with a flow 0.5-1 ml/min. Metallothioneins (MT) were determined in MT standard from rabbit liver; animal blood plasma; extracts from plasma, serum and whole blood of cattle and sheep. Derivatization method was one proposed by Japan scientists [2].

#### Results

Due to the use of the polymer packing materials, chromatographic analysis of MT can be conducted in 13 to 25 minutes. NAM chromatography ("idle" test) with the fluorescent detector at 360-nm excitation and 435-nm fluorescence indicates the presence of two small peaks, which are much higher at 277.2-nm excitation and 435-nm fluorescence. The fluorescent complexes of MT and glutathione with NAM at 277.2 nm excitation produce the highest fluorescence at 435 nm, whereas at 360-nm excitation their fluorescence at 435 nm reduces.

The fluorescent complexes of glutathione with NAM at the fluorescent detector (277.2-nm excitation, 435-nm fluorescence) at a feed rate of eluent (35 % ethanol in 0.05 M phosphate buffer (pH=6.5) up to 0.8 ml/min, produce the strongest signal, and at a feed rate in excess of 0.8 ml/min. its strength reduces. This is because the quartz cell smaller (3  $\mu$ l) than required. At an eluent rate of 1.0 ml/min and more, the cells need to be as large as 5-10  $\mu$ l.

The investigations show that the variation of the background signal strength at the fluorescent detector is related not only to the biomolecule sorption by chromatographic columns with polymer packings PS-DVB S-18 and P-DVB, but also to the sorption of NAM dissociation products. It takes longer to remove these products (4-10 hours) than biomolecules at column recovery with a water solution of NaOH with pH 12 at a rate of 0.5 ml/min.

Figs. 1 shows chromatograms of standard MT determination (2 mcg in the form of fluorescent complexes with NAM) using the procedure [2], obtained on the metal column (150 x 4.6 mm) with the TSK gel Octadecyl 4PW packing. Eluent -35% ethanol in 0.05 M phosphate buffer (pH=6.5), a flow rate - 1 ml/min.

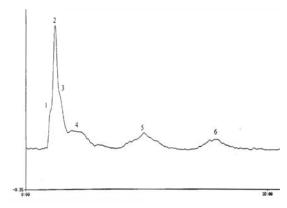


**Fig. 1.** Chromatogram of fluorescent complexes of MT (2 mcg) with NAM obtained using the metallic Toson Bioscience (150 x 4.6 mm) column with the TSK gel octadecyl 4PW packing material. Detector: fluorescent, RF-350 (Shimatzu), excitation 360 nm, fluorescence 435 nm.

Fig. 2. shows a chromatogram of glutathione and MT in the form of fluorescent complexes with NAM in acetonitrile cattle whole blood plasma ( $10~\mu$ l) of Tyrnyauz field cattle. The chromatogram was obtained using the 150~x 3-mm glass column with the P-DVB polymeric packing. The feed rate of eluent (35~% ethanol in 0.05~M phosphate buffer with pH 6.5) was 0.4~ml/min. The chromatogram shows 8 chromatographic peaks in the acetonitrile extract of blood plasma: 1-3, 6-8

- MT in the form of fluorescent complexes with NAM with retention times 2.14, 2.31, 2.56, 5.22, 6.06, 8.02 min and 4-5 – fluorescent complexes of glutathione + MT with NAM with retention times 3.32, 4.14 min.

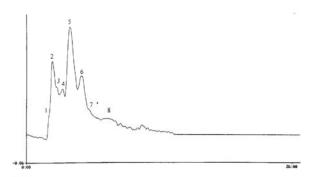
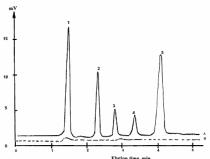


Fig. 2. Chromatogram of fluorescent complexes of glutathione and metallothionein with NAM in the acetonitrile extract of Tyrnyauz cattle blood plasma (10 μl).

It follows that in order to provide more accurate determination of glutathione and MT in the form of fluorescent complexes with NAM, they need to be separated. It was achived by means of resolution of this substances on column Jupiter. Fig. 3 shows clear resolution of glutathione and MT peaks.



**Fig. 3.** Chromatograms of mixture of reduced glutathione and MT after treatment by NAM (A), blank (B). HPLC. Fluorimetric detector. Excitation light – 340 nm, emission– 436 nm. A flow rate – 0.75 ml/min. 1 – reduced glutathione, 10 HΓ. 2-4 – MT, 160 ng.

At analyzing the rabbit liver MT preparation available (100-400 ng/10 µI), one can observe a reproducible quantitative dependence between the amount of protein and the area of peaks in the chromatograms recorded by the fluorescent detector. For reduced glutathione having a pronounced peak in the chromatograms, linear dependence in maintained in the range of 10 to 40 ng. Quantitative determination of MT depends on the parameters of blood plasma derivation. In order to increase the sensitivity of MT determination in biological liquids, MT need to be pretreated with acetonitrile, acetone or alcohol [1].

- [1] V. Ermakov, V. Khabarov, A. Soboleeva. Metallothioneins as a bioindicator of the environmental geochemical situation// Trace Elements in Human: New Perspectives, Athens, 2005, 509-516.
- [2] T. Kamata, M. Yamaguchi, H. Meguro. Sensitive Assay of Metallothionein by HPLC-NAM Fluorometry //Problems of Geochemical Ecology, Diagnostic of Microelementhoses and their Correction. M.: Nauka, 2005, 214-225.

# MONITORING OF PCBs IN THE AMBIENT AIR OF VOJVODINA REGION APPLAYING PASSIVE SAMPLERS

M. Turk-Sekulić, J. Radonić, M. Vojinović-Miloradov and J. Kiurski Faculty of Technical Sciences, Trg Dositeja Obradovića 6, Novi Sad

#### Introduction

Caused by the physical, chemical and biological stability, low hydrophilicity and high lipophilicity potential, extreme toxicity, and high resistance to environmental degradation processes, PCBs are distributed throughout the globe and could be detected in remote regions where they never have been used [1]. As the result of the air/soil sampling campaign conducted in 2006, the concentration levels of seven PCB congeners were measured in air and soil samples from different locations to determine the spatial variation and air-soil partitioning over the Voivodina, agriculture and industrial region. In addition, PCB congeners were also determined in samples of early human milk collected at the Clinic of Obstetrics and Gynaecology, Novi Sad. Atmospheric concentrations were determined using passive air sampling method (PAS) by samplers containing polyurethane foam filters. Samples were collected continuously during the 5 cycles of 28 days, simultaneously at the two selected localities in Vojvodina (NIS Refinery Novi Sad and mountain Fruska Gora - background site). GC coupled with MS analysis was carried out in laboratories of RECETOX, Masaryk University in Brno, CZ [2]. PCBs pattern was used to illustrate the spatial differences and type of distribution for selected POPs after the bombing of the industrial and military targets accompanied by incomplete combustion during the NATO operation (March -June, 1999). Significant quantities of PCB congeners were released into the environment due to complete or incomplete destruction of the transformers containing pyralene oil [3].

#### **Results and Discussion**

PCB concentrations in soil showed a large variation between sampling areas with median total concentrations ranging between 0.3 and 27.3 ng/g (Fig. 1). The highest concentrations were found at two industrial sites (NIS Refinery Novi Sad – surface and ground), one with sandy soils, and other with extremely high organic carbon content

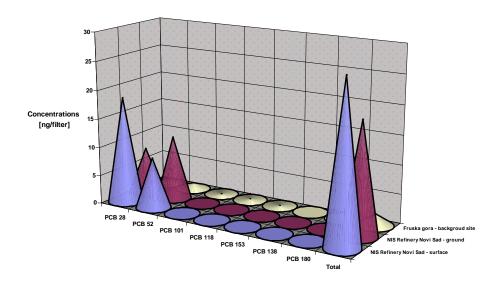


Fig. 1. PCBs concentrations in soil (ng/g) at the sampling sites in Vojvodina

Concentration levels of PCB congeners in air ranged from 12.5 ng/filter to 60.5 ng/filter (Fig. 2, Fig. 3). The higher concentrations were detected at oil refinery (up to 60.6 ng/filter). In the samples of human milk, total concentration of PCB congeners was unchanged compared with level measured ten years ago [4].

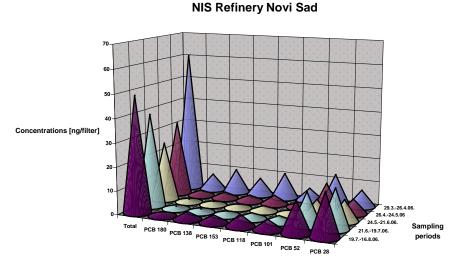
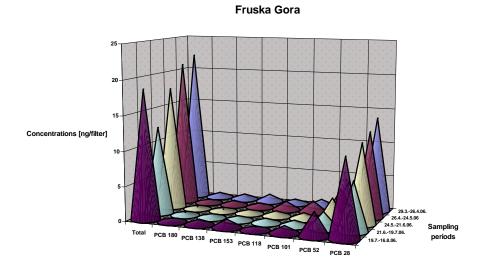


Fig. 2. Temporal variations of PCBs concentrations in the ambient air [ng/filter]



**Fig. 3.** Temporal variations of PCB concentrations in the ambient air [ng/filter]

#### Conclusion

Results of air/soil samples analysis confirmed correlation between both types of data, compatibility of the concentration in the atmosphere and surface soil layers, as well as equivalent distribution of congeners in the air-soil [5]. The results obtained by sampling of human milk suggests the continuous inlet of PCBs into the environment – water, air and especially in soil of Vojvodina region. Comparsion of measured concentration levels of PCBs congeners by PAS in ambient air with detected level in soil and human milk indicates very good application of PAS method for monitoring of selected POPs in ambient air, due to its simple usage, low costs and technically feasibility.

# Acknowledgment

The authors acknowledge the financial support of the Ministry of Science of the Republic of Serbia, in the frame of projects applied under No.21014.

- [1] K.C. Jones, P. de Voogt, Environ Poll, 1999, 100, 209-221.
- [2] J. Klanova, et al., REC. TOC. REP. No 319, 2007, ISBN 978-80-210-4393-0.
- [3] M. Turk, et al., Environ Chem Lett (ECL) Journal, 2007, 5, 109-113.
- [4] T. Vukavic, et al., Environ Toxicol Pharmacol, 2008, 25, 176-178.
- [5] S. Kaisarevic, et al., Bull Environ Contam and Toxicol, 2007, 79, 422-426.

# DISTRIBUTION OF POLYCYCLIC AROMATIC HYDROCARBONS IN THE ENVIRONMENT

B. Škrbić, N. Đurišić-Mladenović and J. Cvejanov

Faculty of Technology, University of Novi Sad, Bulevar cara Lazara 1, 21000 Novi Sad, Serbia

#### **Abstract**

In order to investigate the distribution pattern of individual polycyclic aromatic hydrocarbons (PAHs) in soil and air samples worldwide, principal component analysis (PCA) was performed on the sets compiled of the relevant literature data. PCA detected few outliers and quite uniform PAH levels in soils and air.

#### Introduction

Polycyclic aromatic hydrocarbons (PAHs) are ubiquitous pollutants and wellknown to be carcinogenic and mutagenic. They are products of incomplete combustion and pyrolisis of fossil fuels and other organic materials. PAHs belong to the semi-volatile organic contaminant class, occurring in the atmosphere under gaseous and particulate phases, and could be transported over long distances before the deposition [1,2]. They are accumulated mainly in the humus layer of soil. The high variability of the concentrations of PAHs in soil and ambient air obtained at various sampling sites requires a careful evaluation and interpretation. Multivariate statistical approaches, such as principal component analysis (PCA), seem to enable more information on links among sampling sites, pollutant concentrations, correlation patterns and latent factors responsible for the data set structure [3,4]. In this work, PCA was performed on data matrices consisting of information gathering from relevant published data to find out which soil characteristics had influence on the presence of PAHs in soil; to clarify the soil- and air-distribution patterns of the investigated compounds; and to evaluate their spatial distribution throughout the world and investigate their regional variability.

#### Materials and Methods

#### Data

Multivariate characterization was performed using data for PAHs in atmosphere and in soils previously reported in the literature (Table 1). Half of the limit of detection (LOD) was accepted as content of investigated PAH compounds in the case where their values were below the reported LOD. Four sets of data were analyzed by PCA to: a) investigate the correlation between the PAHs-soil loads and soil characteristics, b) analyze the PAH-soil-, and c) PAH-air-patterns worldwide, as well as d) to simultaneously compare the soil and air patterns.

a) The most comprehensive data set on PAHs in soil and the soil characteristics available in literature was analyzed in order to reveal the correlation between them. This set consisted of contents of 11 PAHs and 4 soil parameters (percentage of clay

and humus, soil density and the acidity), referring to 18 soil samples from unpolluted and polluted areas of Germany and Russia [40].

- b) To analyze the PAH-soil pattern worldwide, the input matrix was consisted of the levels of 9 PAHs in 210 soil samples worldwide (see Table 1).
- c) The general PAH-air pattern was investigated by applying PCA on the matrix formed of the contents of the same 9 PAHs as it was under b), which was found in 100 samples around the world (see Table 1).
- d) Simultaneous comparison of the PAH distribution in soil and air sampled in different parts of the world was performed by PCA of the set 9 x 308 (variables x cases) compiled of the b) and c) matrices.

Table 1. Data investigated in this study by PCA to obtain PAH air and soil pattern worldwide

Sample of	No of	Sample type	Reference (year	
location	samples		of sampling <sup>b</sup> )	
AIR				
Canadian and	6	Remote	[5] ('93-'94)	
Russian				
Arctic				
America				
USA	10	Industrial location, suburban, background	[6] ('97-'98)	
	3	Urban	[7] ('97)	
	1	Bayside	[8] ('02)	
Argentina	3	Urban, industrial	[9] ('99/'02)	
Brazil	1	Suburban area-industrial	[10] ('05)	
Chile	4	Urban, suburban	[11] ('00)	
Asia				
China	3	Urban, residental	[12] ('05)	
	1	Urban-residental, commercial area	[13] ('93)	
Indonesia	1	Urban-residental, commercial area	[13] ('92-'93)	
Philippines	24	Urban-residental, rural-residental	[14] ('05)	
South Korea	1	Urban-residental, commercial area	[13] ('93)	
Taiwan	4	Urban-residental, traffic intersection	[15]	
	3	Industrial, urban, rural	[16] ('02)	
Thailand	1	Urban-residental, commercial area	[13] ('93-'94)	
Turkey	1	Institutional, residential area	[17] ('04/'05)	
-	2	Industrial region	[18] ('04/'05)	
Australia				
	1	Suburb, residental	[13] ('93)	
	4	Urban	[19] ('02)	
Europe				
Czech	2	Urban	[20] ('01)	
Republic				
Germany	2	Urban	[9] ('99-'02)	
Italy	1	Urban park	[21] ('02-'03)	
France	3	Urban, sub-urban, rural	[22] ('04)	
Spain	5	Urban-traffic	[23] ('00-'01)	

UK	4	Urban	[24] ('92)
	4	Urban, industrial	[25] ('91-'92)
		SOIL	
America			
Costa Rica	1	Rural	[26] ('04-'05)
USA	3	Oil-contaminated soil	[27]
Brazil	8	Forest, savanna	[28] ('98)
Asia			
China	10	Park, rural, arable, industrial	[29] ('03)
	3	Urban, rural	[30] ('00)
	4	Urban suburban rural	[31] ('05)
	10	Paddy, wastewater irrigated	[32]
	43	Vegetable soil	[33] ('99,'02)
India	4	Airport, remote	[34] ('05-'06)
Japan	4	Paddy	[35] ('59-'02)
South Korea	2	Agricultural (paddy, upland)	[36]
Turkey	2	Industrial region	[18] ('04-'05)
Australia			
	1	Roadside	[37] ('88)
Europe			
Estonia	8	Urban, rural	[38] ('96)
France	7	Urban, suburban industrial, remote	[39]
Germany	11	Unpolluted, polluted, recreational,	[40] ('92-'92)
		agricultural, forestland, grassland, forest	
		bedding, park	
Greece	29	Industrial	[41] ('95)
Italy	1	Industrial	[42] ('01)
Poland	5	Railway junction, control	[43] ('95)
Russia	11	Unpolluted, polluted, recreational,	[40] ('92-'92)
		agricultural, forestland, grassland, forest	
		bedding, park	
Serbia	1	Urban/rural	[44] ('03/'04)
	5	Urban, agricultural	[45] ('01)
Slovakia	8	Agricultural, forest	[46] ('92/'96)
Spain	4	Urban/residental	[47] ('02)
Switzerland	23	Arable, grassland, forest, urban	[48] ('02)
UK	4	Agricultural soil	[49]
			(1846,1881,'56,'80)

<sup>&</sup>lt;sup>a</sup> Numerical identifier given to the samples from the particular reference and further used for representing the input cases (samples) in the PCA score plots.

#### Principal component analysis

Data submitted for the analysis were arranged in the matrix with the PAH contents (and soil characteristics) taken as variables (column of the input matrix), and soil or air samples as mathematical – statistical cases (rows of the matrix). Data were analyzed using the correlation matrix. Varimax orthogonal rotation and Kaiser's

<sup>&</sup>lt;sup>b</sup> Year of sampling is given if it was stated in the article

rule were applied [50]. Only those loadings (coefficients) whose absolute value was greater than 60% of the maximum coefficient in absolute value in each PC were considered [51]. Relationships between samples and between variables were evaluated in score and loading plots, respectively. Throughout the study the software package STATISTICA 6.0 was used.

### **Results and Discussion**

PCA used on the matrix with data from the study of Franzle et al. [40] reduced large number of the original variables (15) into small number of principal components (3) explaining ~ 92% of the total variance in data. PC1 accounted for ~ 68% of the variance and it was significantly loaded with the contents of all analyzed (11) PAHs; PC2 (~14% of the variance) was positively correlated with the content of humus and negatively with the soil density, while PC3 (~10%) was negatively loaded with both pH and the clay content. Hence, PCA did not revealed any significant links between the PAH-soil contents and the soil characteristics, contrary to some previous findings on positive correlations between soil organic matter and some other classes of the persistent organic pollutants [4]. It might be speculated that the observed absence of any associations could be the consequence of the constant input of these pollutants to the soils and their thorough environmental mixing such that differences between different sample types could no longer be seen.

The preliminary application of PCA to the set of data for the PAHs presence in soils around the world (9×210) showed that 2 underlying components explaining ~94% of the original data variance governed the distribution of PAHs in the investigated soils: PC1, accounting for the highest share of the variance, i.e. ~73\%, was significantly loaded as follows pyrene (PYR) > anthracene (ANT) > fluoranthene (FLU) > benzofluoranthenes (BFLU) > phenanthrene (PHE) > benzo(ghi)perylene (BghiP), while loadings along PC2 ordered PAHs in the (benzo(a)anthracene) > CHR (chrysene) > following way BaA (benzo(a)pyrene) > PHE > BghiP. The most of the soil sample sites located near the origin of the PCA score plot (not shown here) reflecting uniform concentrations of PAHs in soils from various parts of the world. Six outlying samples highly polluted were observed (3 from oil-contaminated site in Texas [27], 1 from soot waste site in Italy [42], 1 from the industrial area in Estonia [38], and 1 from the park in polluted zone in Germany [40]); the total PAH contents in them ranged from about 9 to 138 mg/kg. Knowing that outliers can mask the data structure, they were eliminated before the subsequent PCA was carried out. Only 1 PC was retained according to the Kaiser's rule, accounting for 78% of the variance and it was significantly correlated with all 9 PAHs, thus reflecting the total PAH levels. The score plots did not reveal neither regional differences nor differences between urban, industrial and remote sites (Figure 1a).

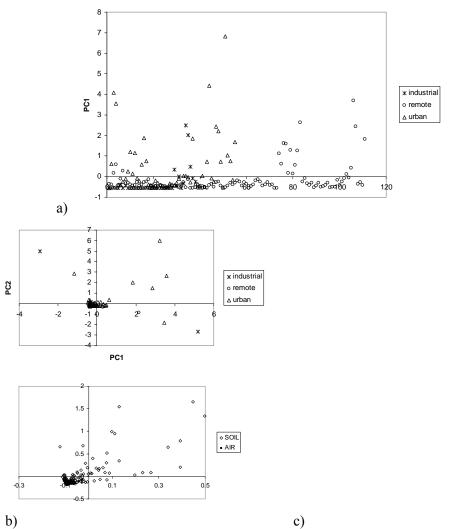


**Fig. 1.** The score plots PC1-PC2 for PCA on matrices consisted of 9 PAH contents in: a) 204 soil samples; b) 98 air samples; c) 310 air and soil samples (close-up to the majority, excluding the outlying samples)

Concerning the PAHs patterns in air, after eliminating two samples representing stack flue gases, PCA of the  $9\times98$ -matrix revealed two underlying PCs explaining 79% of the variance: PC1 accounting for  $\sim68\%$  was significantly loaded with CHR > ANT > PYR > FLU > PHE > BaP, whereas PC2 ( $\sim11\%$  of the variance) with BghiP > BaP > BFLU. Nine outliers emerged on the score plot and the rest of the samples situated very closely around the plot zero. There were no major differences between samples from industrial, urban and remote areas (Figure 1b) and between different countries.

The PCA of the matrix complied of the soil and air samples showed that 2 PCs explained ~94% of the variance. PAH compounds loaded PC1.: PC1 (73% of the variance) and PC2 (11%) in the same way as it was previously shown for PCA of the soil matrix. On the score plot (Figure 1c) it could be seen that the cluster of the air samples coincided with the lowest PAH levels in soils. Additionally, more dispersion of the soil PAH pollution levels than the one for air could be observed worldwide.

#### Conclusion

Principal component analysis of the data on the PAHs occurrence in the soils and air sampled across the world revealed quite uniform distribution without geographical differences. Much more dispersion of soil pollution levels than those in air was found, as distribution of PAHs in soils is a complex function of the accumulation rates and numerous factors influencing the weathering processes.

#### Acknowledgement

This work is a part of the project 152001 funded by the Serbian Ministry of Science.

- [1] B. Škrbić, N. Miljević, J. Environ. Sci. Health A, 2002, 37, 1029-1039.
- [2] B. Škrbić, Refinery Fires: Environmental Issues. In: Speight J. G. (Ed.) Encyclopedia of Petroleum Science and Engineering. Marcel Dekker Ltd, ISBN-10: 82470942X, ISBN-13: 978-0824709426, 2008.
- [3] D. Golobočanin, B. Škrbić, B., N. Miljević, Chemom. Intell. Lab. Syst., 2004, 72, 219-223.
- [4] B. Škrbić, N. Đurišić-Mladenović, Chemosphere, 2007, 68, 2144-2152.
- [5] C. J. Halsall, L. A. Barrie, P. Fellin, D. C. G. Muir, B. N. Billeck, L. Lockhart, F. YA. Rovinsky, E. YA. Kononov, B. Pastukhov, Environ. Sci. Technol., 1997, 31, 3593-3599.
- [6] M. P. Fraser, Z. W. Yue, R. J. Tropp, S. D. Kohl, J. C. Chow, Atmos. Environ., 2002, 36, 5751-5758.
- [7] J. Dachs, T. R. Glenn IV, C. L. Gigliotti, P. Brunciak, L. A. Totten, E. D. Nelson, T. P. Franz, S. J. Eisenreich, Atmos. Environ., 2002, 36, 2281-2295.
- [8] N. Poor, R. Tremblay, H. Kay, V. Bhethananabotla, E. Swartz, M. Luther, S. Campbell, Atmos. Environ., 2004, 38, 6005-6015.
- [9] M. Rehwagen, A. Muller, L. Massalo, O. Herbarth, A. Ronco, Sci. Total Environ., 2005, 348, 199-210.
- [10] S. L. Quiterio, G. Arbilla, G. F. Bauerfeldt, J. C. Moreira, Water Air Soil Pollut., 2007, 179, 79-92.
- [11] M. del R. Sienra, N. G. Rosazza, M. Prendez, Atmos. Res., 2005, 75, 267-281.
- [12] Y. Liu, S. Tao, Y. Yang, H. Dou, Y. Yang, R. M. Coveney, Sci. Total Environ., 2007, 383, 98-105.
- [13] B. C. Panther, M. A. Hooper, N. J. Tapper, Atmos. Environ., 1999, 33, 4087-4099.
- [14] E.C.Santiago, M.G.Cayetano, Atmos. Environ., 41, 4138-4147, 2007.

- [15] W-J. Lee, M-C. Liow, L-T. Hsieh, T. J-H. Chen, P-J. Tsai, J. Air Waste Manage. Assoc., 2003, 53, 1149-1157.
- [16] G-C. Fang, K-F. Chang, C. Lu, H. Bai, Chemosphere, 2004, 55, 787-796.
- [17] Y. Tasdemir, F. Esen, Atmos. Res., 2007, 84, 1-12.
- [18] A. Bozlaker, A. Muezzinoglu, M. Odabasi, J. Hazard. Mater., 2008, 153, 1093-1102.
- [19] M. C. H. Lim, G. A. Ayoko, L. Morawska, Atmos. Environ., 2005, 39, 463-476.
- [20] M. Ciganek, J. Neca, V. Adamec, J. Janosek, M. Machala, Sci. Total Environ., 2004, 334, 141-148.
- [21] M. Possanzini, V. di Palo, P. Gigliucci, M. C. T. Sciano, A. Cecinato, Atmos. Environ., 2004, 38, 1727-1734.
- [22] A. Albinet, E. Leoz-Garziandia, H. Budzinski, E. Villenave, Sci. Total Environ., 2007, 384, 280-292.
- [23] A. Gutierrez-Daban, A. J. Fernandez-Espinosa, M. Ternero-Rodriguez, F. Fernandez-Alvarez, Anal. Bioanal. Chem., 2005, **381**, 721-736.
- [24] D. J. T. Smith, R. M. Harrison, Atmos. Environ., 1996, 30, 2513-2525.
- [25] C. J. Halsall, P. J. Coleman, B. J. Davis, V. Burnett, K. S. Waterhouse, P. Harding-Jones, K. C. Jones, 1994, 28, 2380-2386.
- [26] G. L. Daly, Y. D. Lei, L. E. Castillo, D. C. G.Muir, F. Wania, Atmos. Environ., 2007, 41, 7339-7350.
- [27] H. K. Bojes, P. G. Pope, Regular. Toxicol. Pharmacol., 2007, 47, 288-295.
- [28] W. Wilcke, W.Amelung, M. Kraus, C. Martius, A. Bandeira, M. Garcia, Organic Geochem., 2003, 34, 1405-1417.
- [29] M. K. Chung, R. Hu, K. C. Cheng, M. H. Wong, Chemosphere, 2007, 67, 464-473.
- [30] H. B. Zhang, Y. M. Luo, M. H. Wong, Q. G. Zhao, G. L. Zhang, Environ. Poll., 2006, 141, 107-114.
- [31] Z. Wang, J. Chen, X. Qiao, P. Yang, F. Tian, L. Huang, Chemosphere, 2007, 68, 965-971.
- [32] Y. F. Song, B.-M. Wilke, X. Y. Song, P. Gong, Q. X. Zhou, G. F. Yang, Chemosphere, 2007, 65, 1859-1868.
- [33] L. Chen, Y. Ran, B. Xing, B. Mai, J. He, X. Wei, J. Fu, G. Sheng, Chemosphere, 2005, 60, 879-890.
- [34] S. Ray, P. S. Khillare, T. Agarwal, V. Shridhar, J. Hazard. Mater., 2008 (in press)
- [35] K. Honda, M. Mizukami, Y. Ueda, N. Hamada, N. Seike, Chemosphere, 2007, 68, 1763-1771.
- [36] J. J. Nam, B. H. Song, K. C. Eom, S. H. Lee, A. Smith, Chemosphere, 2003, 50, 1281-1289
- [37] S. Pathirana, D. W. Connell, P. D. Vowles, Ecotoxic. Environ. Safety, 1994, 28, 256-269.
- [38] M. Trapido, Environ. Poll., 1999, 105, 67-74.
- [39] A. Motelay-Massei, D. Ollivon, B. Garban, M. J. Teil, M. Blanchard, M. Chevreuil, Chemosphere, 2004, 55, 555-565.
- [40] O. Franzle, J. Krinitz, W. Schmotz, T. Delschen, J.Leisner-Saaber, Harmonization of investigation methods and evaluation for risk assessment in soil protection with the Russian Federation, Report. UBA-FB 95-048, Terytze, K. (Ed.). Umweltbundesamt, Berlin, 1996
- [41] C. D. Stalikas, C. I. Chaidou, G. A. Pilidis, Sci. Total Environ., 1997, 204, 135-146.
- [42] L. M. Moretto, S. Silvestri, P. Ugo, G. Zorzi, F. Abbondanzi, C. Baicchi, A. Iacondini, J. Hazard. Mater., 2005, 126, 141-148.
- [43] M. Malawska, B. Wilkomirski, Water Air Soil Pollut., 2001, 127, 339-349.

- [44] D. Crnković, M. Ristić, A. Jovanović, D. Antonović, Environ. Monit. Assess., 2007, 125, 75-83.
- [45] B. Škrbić, J. Cvejanov, N. Đurišić-Mladenović, J. Environ. Sci. Health A, 2005, 40, 29-43.
- [46] V.Linkeš, J.Kobza, M.Švec, P.Ilka, P.Pavlenda, G.Barančikova, L.Matuškova, Soil monitoring of Slovak Republic, Present state of monitored soil properties. The Results of Partial Monitoring System-Soil as a part of Environment Monitoring of Slovak Republic for the Period 1992/96., Bratislava, 1997.
- [47] M. Nadal, M. Schuhmacher, J. L. Domingo, Environ. Poll., 2004, 132, 1-11.
- [48] T. D. Bucheli, F. Blum, A. Desaules, O. Gustafsson, Chemosphere, 2004, 56, 1061-1076.
- [49] K.C.Jones, J.A.Stratford, K.S.Waterhouse, E.T.Furlong, W.Giger, R.A.Hites, C.Schaffner, A.E.Johnston, Environ. Sci. Technol., 23, 95-101, 1989.
- [50] B. Škrbić, N. Đurišić-Mladenović, J. Cvejanov, J. Agric. Food Chem., 2005, 53, 2171-2175.
- [51] B. Škrbić, N. Đurišić-Mladenović, Arch. Environ. Contam. Toxicol., 2007, 52, 466-474.

# SINUSOIDAL CODED MODEL

D. Golobočanin and N. Miljević Vinča Institute of Nuclear Sciences, POB 522, 11001 Belgrade, Serbia

#### **Abstract**

This article discusses a usage of modified periodic harmonic analysis to prove the periodicity of experimental data for seasonal stable isotope variations in precipitation and stream water. A proof for sinusoidal coded model is based on a hypothesis concerning the importance of the first harmonic. The utility of proposed model was demonstrated on experimental data for oxygen isotope stream water content of the Velika Morava catchment over the period 2004-2007. This study suggests an applicability of sinusoidal coded model for more accurate estimation of mean residence time without a loss of theoretical or physical significance.

# Introduction

The residence time of water draining a catchment has important implications for flow pathways and storage, as well as water quality, since many biogeochemical reactions are time-dependent periodical functions. Seasonal stable isotopic variations ( $^{18}\text{O}/^{16}\text{O}$  and  $^2\text{H}/^1\text{H}$ ) in surface and groundwater have been used for the estimation of mean residence times (MRTs) of less than 5 years using regression models with annual sinusoidal components [1]. Generally, the stream  $\delta^{18}\text{O}$  composition reflects the temporal pattern of the precipitation  $\delta^{18}\text{O}$  composition with the signals that are significantly damped. Any claim that natural meteorological phenomena are in general periodic and could be characterized by the generalized sine-function equation produces limitations of the seasonal amplitude-attenuation (convolution integral) approach for estimating MRTs due to (1) multiyear isotopic data for surface water and groundwater; (2) accurate and representative isotopic values of basin precipitation over several years; (3) high-precision, unbiased isotopic analyses over the period of interest; and (4) sufficient time of travel for attenuation of the isotope precipitation amplitude [2].

A shape of continual and limited function should not affect to its basic periodicity. The starting point is an application of harmonic analysis [3] to a periodic function significantly different from sinusoidal shape that frequently leads to rejection of hypothesis concerning the importance of the first harmonic. In the case that raw data previously have been coded near to a sinusoidal wave shape, this problem would be overcome. The main hypothesis being tested in this paper is that variations of isotopic composition in precipitation and stream water are periodical appearances of a seasonal cycle over a 12 month period which could be fitted to a coded sine function.

# **Results and Discussion**

Weighted mean monthly isotopic data (concerning amount of precipitation or discharge for precipitation and stream water, respectively) were transformed using Equation 1 to be varied in the interior of the interval (—1, 1)

$$\delta_{N}(i) = 2 \cdot \frac{\overline{\delta}_{W}(i) - \overline{\delta}_{WMin}}{\overline{\delta}_{WMax} - \overline{\delta}_{WMin}} - 1 \tag{1}$$

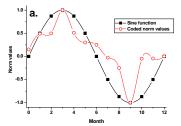
where  $\overline{\delta}_W$  is weighted mean monthly value of the feature of interest in the *i-th* month and subscripts Min and Max are refereeing to minimal and maximal values, respectively. Then, transformed data were coded in a sinusoidal shape function using permutation function along a time axis (Equation 2).

$$\delta_N^{Cod}(i) = \delta_N(P_k^{12}(i)) \qquad i = 1, 2, ... 12$$
 (2)

 $P_k^{12}(i)$  is a permutation function of the k-th lexical order. By suitably choosing the constants k, the coded function should resemble to a sinusoidal form of the resulting curve. Superscript Cod stands for a coded value. In order to get the most representative calculated periodic function, the process of decoding was performed on the fitted sinusoidal function  $\delta_{Cal}$  using Equation (3).

$$\delta_{Cal}^{Decod}(i) = \delta_{Cal}(P_k^{12}(i)^{-1}) \qquad i = 1, 2, ... 12$$
 (3)

Superscript (-1) designates the inverse of permutation function  $P_k^{12}(i)$ . Superscript Decod and subscript Cal stand for decoded and calculated fitted sinusoidal function, respectively. The other notation used is the same as previously mentioned in Equation (2).



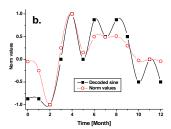


Fig. 1. Coded and decoded data for a sine function with white noise ( $\sigma^2 = 1$ )

Figure 1a shows one original sinusoidal function (solid symbol) and derived function using proposed coded model (open symbol). Figure 1b compares the sine function returned by our coded model (solid symbol) and raw norm values (open symbol).

If the condition written in Equation 4 is satisfied, it has made considerable use of a zero hypothesis [3] concerning the periodicity of the coded model statistically significant at the 95% level

$$\frac{\sigma^2 - \overline{\sigma}_m^2}{\sigma^2} \ge 0.638\tag{4}$$

where  $\sigma^2$  is the variance for all considered data and  $\overline{\sigma}_m^2$  presents average monthly variance.

The isotopic measurements of bimonthly steam water samples (solid symbol) sequentially collected at the last profile (Ljubicevski most) on the Velika Morava before confluence with the Danube span a large but variable annual range that does not accurately resemble a sine wave (Figure 2). Under the conditions of Equation 4, coded model was used to fit actual isotopic records (open symbol).

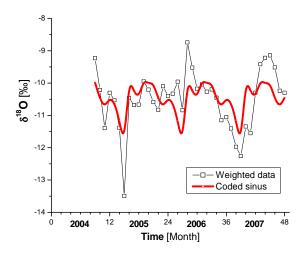


**Fig. 2.** Measured and simulated oxygen-18 content for stream water of the Velika Morava catchment using sinusoidal coded model over the period 2004-2007

#### Conclusion

In conclusion, the seasonal stable isotope signal in precipitation and stream water exhibit a periodicity of 12 months with 95% confidence limits. The proposed model provides superior fit to actual isotopic records for the Velika Morava catchment. Sinusoidal coded model can be applicable as an alternative method in order to refine our understanding of flow paths and residence times, and to help structure and validate more accurate hydrological models.

- K. J. McGuire, J. J. McDonnell, M. Weiler, C. Kendall, B. L. McGlynn, J. M. Welker, J. Seibert, Water Resour. Res. 2005, 41, W05002, doi:10.1029/2004WR003657, 2005.
- [2] M.M. Reddy, P. Schuster, C. Kendall, M. B. Reddy, Hydrol. Process., 2006, 20, 1753–1772.
- [3] R. Fisher, Tests of significance in harmonic analysis, Contribution to mathematical statistics, J. Wiley and Sons, New York, 1950.

# SOLVENT-REAGENT EFFECT IN CHEMICAL DETECTION OF ENERGETIC MATERIALS TYPE CONTAMINANTS

E. Dimitriu<sup>1</sup>, S.C. Moldoveanu<sup>2</sup> and E.E. Iorgulescu<sup>3</sup>

<sup>1</sup>REGO COM, Calea 13 Septembrie 115, Bl.111, Bucharest - 5, Romania
<sup>2</sup>R.J. Reynolds. Co., 950 Reynolds Blvd,. Winston-Salem NC, USA
<sup>3</sup>University of Bucharest, Faculty of Chemistry, Department of Analytical Chemistry, Sos. Panduri, no.90. Bucharest-5, Romania

#### Abstract

Present study extended the list of solvent and reagents appropriate to use for the colorimetric detection and semi quantitative analysis of various energetic compounds. The new reagents used in this study include DMSO as solvent/reagent, and tetramethylammonium hydroxide and tetrabutylammonium hydroxide for the generation of a basic medium. The advantages of these reagents vs. older procedures are discussed in this paper. Also, a standardized procedure for the analysis of several classes of energetic compounds has been developed, allowing an excellent practical application of the recommended method. The influence of different solvents on the changes in the UV/VIS spectra were evaluated and an attempt to interpret the resulting absorption UV spectra based on quantum chemical calculations has been done

#### Introduction

Detection and identification of energetic compounds is a vital problem, due to the direct risks posed of these substances towards the people life and material damages during explosion (detonation). The environmental contamination with post-blasting reaction products, and with wastes resulted from the reaction products of explosive compounds and munitions or from unexploded ordnance, represents another potential risk. [1] Energetic materials, such as military explosives, propellants and pyrotechnics are classified according to their explosive properties (primary and secondary explosives) and chemical composition (nitroderivates, nitramines, esters nitrates, inorganic salts, peroxide –based explosives). A huge number of studies are dedicated to the synthesis, characterization, detection and identification, degradation and removal of energetic compounds, and identification of their environmental transformation products. [2-10] Experimental results were correlated with theoretical studies for monitoring the environmental contamination risk. [11] An energetic compound is rendered soluble with a suitable solvent. Protic solvents (as ethanol, iso-propanol), amphiprotic solvents (as water, methanol) and dipolar aprotic solvents (as acetone, dimethyl sulfoxide - DMSO, dimethyl formamide, acetonitrile) are used for the solvation or extraction of energetic compounds. Usually, the hydrogen atoms in dipolar aprotic solvents are not ionisable and do not form hydrogen bridges. If the hydrogen atoms are bonded to oxygen, or other more electronegative atom than carbon, hydrogen bridges could occur in the presence of proton-acceptors compounds. The dipolar aprotic solvents are polarized and interact with polarizable ions. These properties, together with values of dielectric constant ( $\varepsilon > 15$ ) higher than in non-polar aprotic solvents, recommend the dipolar aprotic solvents as the best medium for reactions with a nucleophile substitution mechanism and for increase the ratio of energetic materials solvation. For instance, the exhaustive extraction time of secondary explosives (TNT, and RDX) from soil, with acetone is 1 min, while with methanol (a protic solvent) is 3 min. [10] The resulted extract is subjected to chemical identifications. Two types of tests are used for chemical identification of functional groups: a) direct tests, in which they form coloured reaction products, in the presence of certain reagents, and b) indirect tests, in which an intermediary reaction product is formed and this one is identified with a specific reagent. [1, 3, 8]

This study is focused on colorimetric identification of post-explosion debris with simple operations, good selectivity, and sensitivity of the order from nanograms to milligrams. The method is extended to prevent or to manage the environmental pollution with energetic compounds. Mixtures of solvents and reagents are tested for colorimetric identification of energetic compounds. Solute-solvent interactions are evidenced by changes in the UV/VIS spectra. Theoretical aspects using a computational method to obtain Highest Occupied Molecular Orbitals (HOMO) and Lowest Unoccupied Molecular Orbitals (LUMO), are presented in an attempt to calculate the expected wavelength of absorption spectra. For this purpose, the energy levels of HOMO and LUMO orbitals were calculated for some explosives and their coloured anions. The stability in time of reagents is discussed, and finally, a procedure for on-site identification of organic energetic compounds is proposed.

# Experimental

In this study, an in-situ colorimetric method for identification of organic energetic materials was evaluated. The following energetic materials were investigated: polynitroaromatics [2, 4, 6- trinitrotoluene (TNT), trinitrobenzene (TNB), tetranitroaniline (TNA), 2,4,6-trinitro - 1,3,5-triazine (TNTA),], nitrates esters [explosive blends with nitroglycerine content (dynamite, astralite, AGP explosive), pentraeritrol tetranitrate (PETN or pentrite)], nitramines [2,4,6-trinitrophenyl-N-methylnitramine (Tetryl), RDX (cyclotrimetilen trinitramine, or Hexogene or Cyclonite). Mixtures of amphiprotic solvent (methanol) and dipolar aprotic solvents (acetone, DMSO) have been used. Three types of reagents were prepared:

Reagent 1: any of the alkaline reagents for polynitroaromatics identification were aqueous solutions of sodium hydroxide and potassium hydroxide, and solutions of tetramethylammonium hydroxide (TMAM) and tetrabutylammonium hydroxide (TBAH) in methanol.

Reagent 2: a) solution containing sulphanilamide 1 wt%, and hydrazine sulphate 1 wt% (10/1 V/V); b) solution containing sulphanilamide 2.5 wt%, and hydrazine sulphate 1 wt% (10/1 V/V)

Reagent 3: a) N-(1-Naphtyl) ethylenediamine dichloride 1wt%, and b) N-(1-naphtyl) ethylenediamine dichloride 1 wt% +  $H_3PO_4$ .

# Procedure for energetic materials identification

Amount of energetic materials less than 10<sup>-3</sup> g were collected on filter paper [1], and solvated with several groups of solvents, presented in Table 1. On the same filter paper reagent 1 is dropped. The presence of TNT or explosives with TNT content is shown by the formation of a pink, or red or red-brown colour, function of the increasing TNT concentration. If no colour appears, on the same filter paper, one drops, successively, the reagents 2 and 3 for the identification of nitrates esters, nitramines and nitrites. A pink or violet colour formed in less than 30 minutes indicates the presence of the above compounds, for any of the solvents mixtures have been used. The tested compounds and the colour formed were: nitrocellulose/pink, Rovex, pentrite, and EPH88/pinkish violet, AGP/violet.

	1 ~ .	<u> </u>	
Test	Solvent + reagent /	Explosive compound tested	Colour test with
no	proportion by volume	/colour	reagents stocked during
			10 months
1-1	Acetone+ DMSO+ KOH	TNT/ Red-brown	TNT/ Red-brown
	9 wt% soln. (1:1:1.3)		
1-2	Acetone + methanol +	TNT/ Red-brown	TNT/ Red-brown
	DMSO+ KOH 9 wt%		Astralita /red-violet
	soln. (4:1:1.3:3)		
1-3	Acetone + metanol +	TNT/ Red-brown	TNT/violet
	DMSO+ TMAH	Dynamite/ yellow-green	Dynamite/ green-
	(2:1:1.5:0.5)	with violet on the boundary	brown
		of the spot	Astralite /red-violet
		Astralite / Red-brown -violet	
1-4	Methanol + DMSO+	TNT/Red- violet	TNT / Red-brown
	TMAH (1.5:8:5)		Dynamite/ green-
	, ,		brown
			Astralita/red-brown
1-5	Methanol +DMSO	TNT/violet	-
	+NaOH soln		
1-6	DMSO + TBAH	TNT/ red-violet	-

**Table 1.** Solvents and reagents used for polynitroaromatics identification

The differences observed in the coloured anions used for energetic compounds identification were further investigated by computational methods. The calculated maximum wavelength obtained from the differences between the energy levels of HOMO and LUMO orbitals are compared with those resulted from experimental UV-VIS records data, indicated in other studies. The calculations were performed with MOPAC-7, and AM1 parameters. [12-14] The geometries were initially obtained using structures in Alchemy 2000 (Tripos Assoc.) and an original program [14] and further optimized in MOPAC-7 program.

UV-VIS absorption spectra of Janowsky-type anion of TNT in protic and dipolar aprotic solvents were measured on a Jasco (V-530) double beam spectrophotometer. The measurements were done using 1 cm path quartz cells, on

the spectral domain 300-600 nm. The scanning speed for spectra recording was 100 nm/min.

# **Results and Discussions**

The new reagents/solvents utilized in the present study are in the line of previous work that uses acetone and a strong inorganic base (KOH, NaOH) to generate a colour reaction from nitroaromatic compounds. Similarly to acetone, which in the presence of a base forms a Janowsky anion with nitroaromatic compounds, DMSO also forms a coloured compound. The strong base is likely to form with DMSO an anion of the form CH<sub>3</sub>(SO)CH<sub>2</sub>. This anion reacts with nitroaromatic compounds forming a Janowsky-type anion [10], as shown in the following reaction for TNT:

$$O_2N$$
 $O_2N$ 
 $O_2N$ 

Since DMSO can be a better solvent than acetone, this reagent is preferred. Also, the base KOH or NaOH previously used to form either Meisenheimer ions or (in the presence of acetone) a Janowsky ion, can be replaced with an organic base such as tetramethylammonium hydroxide (TMAH) or tetrabutylammonium hydroxide (TBAH). The advantages of these bases are their solubility in organic solvents and lower propensity to deteriorate the matrix and form interfering colours

The use of various mixtures of solvents and/or of TMAH and TBAH showed that the addition or absence of a specific solvent or base may induce considerable variation in the UV/VIS spectra of the Janowsky type anion generated from nitroaromatic compounds. This is exemplified below in Figures 1, where are given the absorption spectra for TNT/DMSO Janowsky anion in different solvent mixtures.

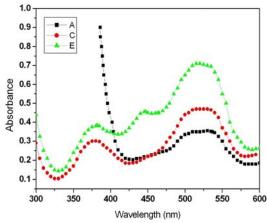


Fig. 1. Absorption spectra of Janowsky TNT anion in methanol and DMSO with NaOH (A), a mixture of methanol and DMSO with NaOH and TBAH (C), a mixture of DMSO with TBAH (E)

The variability in the maximum intensity and shift in the wavelength with the addition of various solvents/reagents can be caused by both solvent interaction effects, and also by the formation of different molecular coloured species. In an attempt to determine the 'theoretical" value for the wavelength of the absorption spectra, a quantum chemical calculation was performed with the determination of the energy levels of HOMO and LUMO orbitals, following the calculation of the maximum absorption wavelength,  $\lambda$ , for the molecule in ideal gas form. The calculation was done using the expression:

$$\lambda = \frac{1240.27}{\Delta E(eV)} (nm)$$

The results of the calculations for the theoretical expected absorption wavelength are given in Table 2. The calculations were performed for the free compound, expected Meisenheimer ion, Janowsky ion, and DMSO adduct. In addition, for TNA and TNDA it was attempted to calculate the energy levels for a Schiff base formed with acetone by these amines. (Heats of formation and dipole moments are also shown). As seen from Table 2, good agreement of experimental results with the theoretical values for the absorption spectra is observed for many compounds, such as TNB-Meisenheimer anion, TNB-Janowsky anion, TNT-Meisenheimer anion, TNT-Janowsky anion, Tetryl-Meisenheimer anion, and Tetryl-Janowsky anion. However, for the compounds involving DMSO, the results are not in agreement with the experiment, and much longer absorption wavelengths were predicted.

Performing an Unrestricted Hartree-Fock (UHF) calculation and considering a different transition than HOMO-LUMO allowed to predict absorption wavelength values much closer to those found in experimental spectra for TNB-DMSO, TNT-DMSO and Tetryl-DMSO compounds. These results are shown in Table 3. The theoretical results from Table 2 and Table 3, and the disagreement with the experimental wavelength of absorption would indicate that TNA, and TNDA do not form either Meisenheimer or Janowsky products.

**Table 2.** Theoretical results for the HOMO, and LUMO energy levels, and the calculated absorption wavelength for several compounds, used for the analysis of energetic compounds (Heats of formation and dipole moments are also shown)

Compound	НОМО	LUMO	ΔΕ	λ	Heat of	Dipole
	(eV)	(eV)	(eV)	(nm)	formation	(Debye)
					(kcal/mol)	
TNB	-12.24	-2.53	9.72	127.60	44.88	0.02
TNB-Meisenheimer anion	-7.82	-5.51	2.31	536.76	-91.94	1.13
TNB-Janowsky anion	-7.85	-5.55	2.30	539.02	-89.43	2.72
TNB DMSO	-6.18	-5.57	0.61	2020.43	-28.05	3.30
TNT	-11.70	-2.44	9.26	133.94	41.29	1.44
TNT-Meisenheimer anion	-7.52	-5.43	2.08	595.54	-92.82	1.53
TNT-Janowsky anion	-7.83	-5.56	2.26	547.75	-89.29	2.73
TNT DMSO	-6.21	-5.58	0.63	1974.40	-27.88	3.43
TNA	-12.45	-0.16	12.30	100.85	34.16	3.46
TNA-Meisenheimer anion	-6.41	-5.50	0.91	1356.56	-96.69	2.04
TNA-Janowsky anion	-6.44	-5.59	0.85	1455.19	-95.59	1.32
TNA DMSO	-6.11	-5.60	0.52	2404.13	-34.48	2.07
TNA Schiff	-10.82	-2.29	8.53	145.42	61.97	4.53
TNDA	-10.28	-1.81	8.47	146.33	25.39	3.24
TNDA-Meisenheimer	-6.15	-5.61	0.54	2315.12	-101.21	3.79
anion						
TNDA-Janowsky anion	-6.22	-5.65	0.57	2186.52	-101.64	2.46
TNDA DMSO	-5.99	-5.65	0.34	3687.40	-40.55	1.70
TNDA Schiff	-10.28	-1.94	8.34	148.65	51.82	4.87
TNDA two Schiff	-10.43	-1.89	8.54	145.26	70.33	5.40
TNTA	-10.19	-1.37	8.82	140.65	20.65	0.15
Tetryl	-11.71	-2.96	8.75	141.66	90.80	3.35
Tetryl-Meisenheimer	-8.03	-5.82	2.20	563.11	-53.29	2.75
anion						
Tetryl-Janowsky anion	-8.07	-5.85	2.22	558.59	-48.71	3.59
Tetryl DMSO	-6.30	-5.86	0.44	2827.11	12.70	3.35
Griess	-8.26	-1.09	7.17	173.03	52.85	5.88

Their colour may be generated by the formation of other reaction products. The results also show that more than one transition can possibly explain the spectra of the compounds generated in the analytical identification of nitroaromatic compounds in reactions of Meisenheimer/Janowsky type.

**Table 3.** Theoretical results using UHF calculations and different transition than HOMO-LUMO for the energy levels, and calculated absorption wavelength for several compounds between DMSO and nitroaromatic compounds (Heats of formation and dipole moments are also shown).

Compound	Level 1 (eV)	Level 2 (eV)	ΔE (eV)	λ (nm)	Heat of Formation (kcal/mol)	Dipole (Debye)
TNB DMSO	-7.89	-5.56	0.61	532.30	-27.95	3.22
TNT DMSO	-7.84	-5.57	2.28	543.94	-27.35	3.35
TNA DMSO	-6.46	-5.58	0.88	1409.40	-34.44	2.02
TNDA DMSO	-5.99	-5.63	0.60	2067.12	-40.51	1.66
Tetryl DMSO	-8.06	-5.84	2.22	558.68	+12.66	3.30

These theoretical values are not identical but close (for most compounds) with those measured in solutions, which are influenced by various additives used for practical purposes during the analytical determination (see Figure 1 and Table 4).

**Table 4.** Visible absorption maxima,  $\lambda_{max}$ , of some polynitroaromatics explosives

Compound	Solvent/reagent	$\lambda_{max}(nm)$	Reference
1, 3, 5-TNB	1% EDA in DMSO	455	Glover and
	(ethylenediamine)	540	Kayser (1968)[1]
2, 4, 6-TNT	50% EDA in	465	
	DMSO	540	
2, 4, 6-TNA	Ethanol+NaOH	488-491	Schroeder et all
		411-412	(1951) [1]
	2% EDA in DMSO	418	Selig (1978) [1]
1, 3-diamino-2, 4, 6-TNB (DATB)	DMSO	417	
	2% EDA in DMSO	412	
1, 3, 5-triamino-2, 4, 6-TNB	2% EDA in DMSO	418	
(TATB)			
2,4,6-TNT	Methanol / NaOH	516	[10]
	Acetone /KOH	540	

Among the solvent/reagents pairs, a special role is played by DMSO. If in the identification of TNT and some of polynitroaromatics, the DMSO is reagent, for all other compounds, DMSO is a very good solvent, with high stability in time, and no effect on the operator health. The solutions of tetramethylammonium hydroxide and tetrabutylammonium hydroxide in methanol presented a higher stability in time compared to NaOH or KOH. The highest stability in time is observed for the reagents 1-4 and 1-6 from Table 1, with the content of DMSO and TMAH

#### **Conclusions**

Solvent / reagent mixtures were used for colorimetric identification of energetic compounds. In the proposed colorimetric procedure, the mixture of methanol with DMSO and TMAH or TBAH is the most suitable for solvation and identification of the polynitroaromatics and for dissolvation of nitrates esters and nitramines. The measured absorption wavelenghts in UV-VIS of coloured products developed during reactions for TNT, TND and Tetryl in DMSO, are in good agreement with those calculated using a computational method to obtain the energy levels of HOMO and LUMO orbitals.

- [1] J.Yinon, S. Zitrin, The analysis of Explosives. Pergamon Series in Analytical Chemistry, Vol.3, Pergamon Press, New York, 1981
- [2] A. Beveridge, Journal of Energetic Materials, 1986, 4, 29-75
- [3] T.Urbanski, T. Chemistry and Technology of Explosives, Vol. 3; Pergamon Press: Oxford, 1965
- [4] B. Glattstein, European Patent Application, 1988, **0 264 252 A2**, Int. Cl. G 01 N 31/22
- [5] D. S. Moore, Sens. Imaging (2007) 8:9-38 DOI 10.1007/s11220-007-0029-8.
- [6] A. Hilmi, J. H.T. Luong, An-Lac Nguyen, Journal of Chromatography A, 1999, 844 (1-2), 97-110
- [7] A.B. Crockett, H.D. Craig, and F.F. Jenkins. EPA /600/S-99/002, May 19, 1999.
- [8] Fritz Feigl, Spot Tests, Vol. II. Organic Applications, Fourth, completely revised English Edition, Elsevier Publishing Co, Amsterdam, Houston, London, New York, 1954
- [9] D. De Tata, P. Collins, N. Campbell, Journal of Forensic Sciences, 2006, **51** (2), 303–307 doi:10.1111/j.1556-4029.2006.00075.x
- [10] T. F. Jenkins, P.W. Schumacher, J. G. Mason, P. G. Thorne, 1996, **Special report 96-10**. US Army Corps of Engineers. Cold Regions Research & Eng. Lab.
- [11] M.M. Quasim, B. Moore, L. Taylor, P. Honea, L. Gorb, J. Leszcznsky, Int. J. Mol. Sci. 2007, 8, 1234-1264
- [12] J. J. P. Stewart, J. Comp.-Aided Mol. Design, (1990) 4, 1-105, Special Issue
- [13] J. J. P. Stewart, MOPAC-7, QCPE 113, Indiana Univ. Bloomington, 1994
- [14] S. C. Moldoveanu. Unpublished results

# EXTERNAL GAMMA EXPOSURE FROM SURFACE SOILS IN BELGRADE AND ITS SURROUNDINGS

Lj. Janković-Mandić<sup>1</sup> and S. Dragović<sup>2</sup>

<sup>1</sup>Military Medical Academy, Crnotravska 17, 11000 Belgrade, Serbia <sup>2</sup>Institute for the Application of Nuclear Energy - INEP, Banatska 31b, 11080 Belgrade, Serbia

# **Abstract**

External gamma exposure due to terrestrial radionuclides ( $^{226}$ Ra,  $^{232}$ Th and  $^{40}$ K) was assessed based on specific activities of these radionuclides in soils from different location in Belgrade and its surroundings. External hazard indexes obtained in this study (mean  $H_{\rm ex}=0.30$ ) pointed out insignificant radiation hazard for the population of investigated areas. The differences in radiation exposure among sampling locations reflect variety of geological background formations of soil parent material.

# Introduction

In order to estimate the effects of chronic exposure to varying levels of ionizing radiation in the past decades considerable attention has been paid to low-level doses arising from natural radionuclides present in soils [1]. Belgrade is expected to change from city to city conurbation by the end of the next decade and baseline data on natural radionuclides in soil will be of importance in making estimations of population exposure. In the present study the specific activities of primordial radionuclides <sup>226</sup>Ra, <sup>232</sup>Th and <sup>40</sup>K in surface soil samples were determined and used to calculate external radiation exposure.

## Materials and methods

Surface soil samples (n=62) were taken from 31 regions in Belgrade and its surroundings during 2006-2008. The samples of undisturbed soil were collected down to the depth of 5 cm from each location. Samples were dried at 105 °C to constant weight and then powdered and passed through a 2 mm mesh sieve to homogenize them. The specific activities of  $^{232}$ Th and  $^{40}$ K were measured on a HPGe gamma ray spectrometer [2]. From these results total gamma dose rates due to terrestrial gamma rays at 1 m above the ground, the outdoor annual effective doses and external hazard indexes (H<sub>x</sub>) were calculated according to the internationally accepted activity-to-dose rate conversion equations [1, 3].

#### **Results and Discussion**

Total gamma dose rates, annual effective doses and external hazard indexes due to gamma exposure are presented in Table 1.

**Table 1.** Total gamma dose rates, annual effective doses and external hazard indexes due gamma exposure in Belgrade and its surroundings

Region	Total gamma dose rate (nGy h <sup>-1</sup> )	Annual effective dose (10 <sup>-5</sup> Sv)	H <sub>ex</sub>
Ada Ciganlija	50.8	6.24	0.29
Avala	58.3	7.15	0.34
Banjica	60.8	7.46	0.35
Banovo brdo	38.0	4.66	0.22
Beli potok	69.5	8.52	0.40
Cerak	44.7	5.48	0.26
City centre	53.6	6.57	0.30
Čukarica	49.2	6.05	0.28
Dedinje	58.2	7.14	0.33
Grocka	52.2	6.40	0.30
Karaburma	38.8	4.75	0.23
Konjarnik	76.6	9.40	0.44
Kosmaj	62.7	7.69	0.36
Krnjaca	24.8	3.04	0.14
Lipovička šuma	21.2	2.59	0.12
Mali Mokri Lug	61.2	7.51	0.35
Mali Požarevac	70.4	8.64	0.41
Miljakovac	61.9	7.60	0.35
Mirijevo	53.0	6.50	0.30
Mladenovac	58.8	7.21	0.34
Novi Beograd	38.3	4.69	0.22
PetlovoBrdo	63.4	7.78	0.37
Rakovica	63.3	7.76	0.36
Ralja	53.3	6.54	0.30
Resnik	59.0	7.23	0.34
Ripanj	60.7	7.44	0.35
Senjak	38.2	4.68	0.22
Sopot	52.8	6.48	0.30
Vinča	47.5	5.83	0.27
Vrčin	26.0	3.19	0.14
Zemun	58.3	7.15	0.34

The total dose rates from terrestrial exposure obtained in this study varied from 21.2 nGy h<sup>-1</sup> to 76.6 nGy h<sup>-1</sup>, with the mean value of 52.4 nGy h<sup>-1</sup>. The outdoor annual effective dose ranges from  $2.59 \times 10^{-5}$  to  $9.39 \times 10^{-5}$  Sv, with the mean value of  $6.43 \times 10^{-5}$  Sv. The average annual effective dose obtained in this study is close to the world wide average value of  $7.5 \times 10^{-5}$  Sv [1]. The values calculated for external hazard indexes  $H_x$  for the soil samples investigated in this work range from 0.12 to 0.44 (Table 1) pointing out the insignificant radiation hazard arising from terrestrial naturally occurring radionuclides. None of external

hazard indexes exceeds the safety limits for the public recommended by International Commission on Radiological Protection (ICRP) [4].

The annual effective doses for the population of Belgrade are comparable with those of  $6.6 \times 10^{-5}$  Sv obtained in similar study in Manisa, Turkey [5]. Lower values are obtained for the population of Tripoli, Lybia [6] and cities of Zacatecas and Guadalupe, Mexico [7], i.e.  $2.3 \times 10^{-5}$  Sv and  $4.1 \times 10^{-5}$  Sv, respectively. The differences in annual effective doses are influenced by the differences in types of rock from which soils originate and depend on geological and geographical conditions of the investigated area.

#### Conclusions

Exposure due to natural radionuclides in soil for the population of Belgrade and its surroundings was assessed in this study. Mean values of total gamma dose rates due to terrestrial exposure at 1 m above ground of 52.4 nGy h<sup>-1</sup>, annual effective dose of  $6.43 \times 10^{-5}$  Sv and external hazard index of 0.30, calculated based on specific activities of <sup>226</sup>Ra, <sup>232</sup>Th and <sup>40</sup>K determined by gamma-ray spectrometry were found to be close to world average values. Results obtained indicate the acceptable level of background exposure for the population of Belgrade and its surroundings.

- [1] UNSCEAR. Sources and Effects of Ionizing Radiation. Report to General Assembly, with Scientific Annexes, 2000, United Nations, New York.
- [2] S. Dragović et al., Radiat. Meas., 2006, 41, 611-616.
- [3] J. Beretka, P.J. Mathew, Health Phys., 1995, 48, 87-95.
- [4] ICRP. 1990 Recommendations of the International Commission on Radiological Protection, ICRP Publication 60, 1991, Pergamon Press, Oxford.
- [5] F.S. Ereeş et al., Radiat. Meas., 2006, 41, 598-601.
- [6] M.A. Shenber, Appl. Radiat. Isot., 1997, 48, 147-148.
- [7] F. Mireles et al., Health Phys., 2003, **84**, 368-372.

# **FOOD QUALITY AND SAFETY:** SENSORY EVALUATION OF FOODS, HYGIENE AND HACCP

C. Tzia

Lab. of Food Chemistry and Technology, School of Chemical Engineering, NTUA, Greece

# Abstract

Ouality of foods includes the characteristics that are significant for the selection and acceptability of products by the consumers. Nutritive value is fundamental quality characteristic of foods, sensory properties are determinative for food acceptance, while safety is of major importance for human health. The quality characteristics of foods should be controlled by objective measurements and analyses. Specific methods are used for the sensory evaluation of foods, as well as for the control of the safety factors (pathogens, contaminants etc.) according to HACCP procedure.

# 1. Quality - Sensory Quality - Quality Control of Foods

Quality of foods may be defined as the composite of those characteristics that have significance in determining the degree of the consumer acceptability. Although the 1.

acceptability is perceived by the senses, however a number of factors contributes to the perceived quality of a product in addition to its sensory properties. Microbiological integrity, other safety factors, and nutritional content are all important. Brand image, price, and competitive positioning all affect a consumer's perception of quality. The sensory characteristics can be easily evaluated by the humman senses, while the hidden characteristics have health and economic importance. The quality attributes of foods are classified as it is shown in the Table

Attributes of food quality SENSORY HIDDEN Smell and taste – Flavor Touch - Kinesthetic (texture) Sight - Appearance - Nutritive value - Hand or finger feel - Odor - Toxicity - Color - Defects - Shelf-life - Gloss - Viscosity Mouth feel - Taste - Size and shape

**Table 1.** Classification of food quality attributes

Quality of foods depends on the quality of raw materials and process technology. The quality may be considered as the sum of the partial qualities that are respective to quality factors which affect it:  $Q = Q_1 + Q_2 + \dots + Q_i$ 

Sensory quality is a most important factor of food quality which is in relationship to its sensory properties such as colour, appearance, shape, size, odour, taste, flavour, texture, kinesthetic, body, etc. Sensory or organoleptic attributes of foods

are evaluated by sensory analysis. Sensory testing has been developed as a formalised, structured and codified methodology.

Quality Control of foods intends to be produced a constant designed quality level. For this purpose predictive analyses must be conducted in the raw materials, during the processing and in the final product in order to result foods of desirable quality level. Physical, physicochemical, chemical and microbiological measurements as well as sensory analyses are conducted for the needs of quality control. Sensory techniques are used in quality control and product research and development.

# 1.1 Sensory Evaluation - Perception - Acceptance of Foods

<u>Sensory evaluation</u> has been defined as "a scientific discipline used to evoke, measure, analyse and interpret reactions to those characteristics of foods and materials as they are perceived by the senses of sight, smell, taste, touch and hearing".

<u>Sensory perception</u> is a three step process:

The stimulus hits the sense organ and it is converted to a nerve signal which travels to the brain; the brain then organises and integrates the incoming sensations into perceptions; lastly a response is formulated based on the subject's perceptions. Humans often yield varied responses to the same stimulus. Sensation is not under control of the mind, and differences in sensation by the subjects cannot be influenced but must be treated as a component of the internal error in any experiment or test. By contrast, perception and response are open to the analyst's influence. Through training and the use of references subjects can attempt so that show the same response to a given stimulus.

Sensory evaluation principles have their origin in physiology and psychology. It is of interest to be related the response to the stimulus. Since sensation cannot be measured directly, it is necessary to measure sensitivity by means of differential changes. By determining the detectable amount of difference between two stimuli (the just-noticeable difference, or jnd), one can establish a unit of sensation. The jnd has found widespread application in the sensory evaluation of food products.

Fechner considers that each jnd is equivalent to a unit of sensation and the jnds are equal:

 $S = k \log R$  (Weber's or Weber-Fechner or Psychophysical Law),

where *S*: magnitude of sensation, *k*: constant, and *R*: magnitude of stimulus.

Stevens proposed that equal stimulus ratios result in equal sensation ratios rather than equal sensation differences:

 $\log R = k \log S^n$  (Psychophysical Power Law),

where *R*: response, *k*: constant, *S*: stimulus concentration and n: function slope. Weber noted that the perception of the difference between two products was a constant, related to the ratio of the difference:

$$K = \frac{\Delta R}{R}$$
,

where *R*: magnitude of the stimulus and *K*: constant of the jnd.

Mathematical relationships can be used to model the connection between <u>acceptance</u> and <u>perceived sensory properties</u>. A simple polynomial expression by which food acceptance is predicted by a weighted function of the perceived intensities of various sensory attributes is:

where  $S_n$  = perceived intensity of attribute n

Intensity,  $S_n$  can also be predicted by equations such as:  $S_n = K_n$   $I^b_n$  where b: the characteristic of the power function exponent and I: the stimulus intensity in physical units

Weighting coefficients are positive for desirable attributes, while negative coefficients are for product defects, in which the more intense the sensory attribute, the more or less acceptable the product respectively. Higher order terms may be added to describe continua with optima which is reached most desirable level. This is achieved with a small negative coefficient for a squared term. Interaction terms may take into account the simultaneous balancing of two or more attributes. Perceived intensity, in turn, can be modelled on the basis of ingredient concentrations, by relationships such as Steven's power law or alternative functions.

Understanding sensory thresholds (minimum perceivable levels), psychophysical functions (dose-response curves), and sensory interactions, as well the weighting coefficients for sensory contributions to overall acceptance, can help the product formulator in engineering acceptable products. The relationship of acceptance to the intensity of various sensory characteristics emphasises the value of understanding and quantifying sensory attributes of products in determining eventual success.

Sensory evaluation tests are divided into: i) affective (or subjective), its purpose is to evaluate preference and/or acceptance of products and ii) analytical (or objective) that evaluate differences or similarities, quality, and/or quantity of sensory characteristics of products. In affective tests the spontaneous, personal reaction of the panelist is evoked in order to determine preference or acceptance. These are subjective tests designed to capture the original and spontaneous impressions of the panelists. In analytical tests, some aspect of sensory quality of the product itself is of interest and not the personal reaction of the panelist. The

panel is the analytical tool. In any type of analytical work there is an obvious need for control and standardization. This is especially in sensory evaluation, since it is based on the psychological evaluation of physiological sensations.

The International Organisation for Standardisation (ISO) defines an objective method as "a method in which the effects of personal influence are minimised". For analytical sensory tests, procedures have been developed in an effort to control or minimise the effect that psychological and physical conditions can have on the panelists' reactions. When these procedures are followed, analytical sensory tests meet the requirements to be called "objective".

# 1.2 Sensory Control of Foods - Methodology

The sensory evaluation of foods in order to provide reliable results should satisfy certain prerequisites, such as: sensory laboratory, trained assessors (panelists), sensory methods and standard sensory tests, presentation of results and evaluation after statistical processing.

Fundamental to the successful conduct of any sensory evaluation test is a clear understanding and statement of the objective of the study.

<u>Sensory laboratory</u> is special for sensory analyses of foods and general specifications for the installation of a test room with the booths and the additional premises are described by the Standard ISO 8589: 1988 "Sensory analysis; general guidance for the design of test rooms".

The test room is designed to provide the panel participating in the sensory tests with a suitable, comfortable, standardised environment which facilitates work and helps to improve the repeatability and reproducibility of the results. The sensory analysis booths shall be sufficiently large and comfortable. Each booth shall contain one table and one seat for the taster, one shelf for placing various accessories, and it shall be provided with individual lighting and sink with running, drinking water. The booths shall be placed alongside each other in the premises. They shall be separated by partitions which must be sufficiently high and wide as to isolate the tasters when seated. The booths and premises shall be pleasant and meet specifications and appropriate conditions (construction material, light color, easy-cleaned, lighting, noise, odors, communication, environmental conditions: 20-22°C, 60-70% RH) in order to can not affect the results of the sensory analysis. Additional premises for preparing the samples, shelves for containers or discussions rooms should also be provided.

<u>Assessors - Panelists - Training</u>: The panel is the analytical tool in sensory evaluation. The value of this tool depends on the objectivity, precision, and reproducibility of the judgements of the panelists. Before a panel can be used with confidence, the ability of the panelists to reproduce judgements must be determined. The number of the panelists used will influence the statistical significance of the results obtained. The reliability and validity of the results will vary according to the selection, training, and instructions that the panelists are given. The rules which are essential for the panel supervisor to select, train and

monitor the tasters are described by the Standards: ISO 8586-1: 1993 "Sensory analysis; general guidance for the selection, training and monitoring of assessors; part 1: selected assessors" and ISO 8586-2: 1994 "Sensory analysis - General guidance for the selection, training and monitoring of assessors - Part 2: Experts". The purpose of training is to develop familiarity with the product and its characteristics, to develop a common language to describe these characteristics, and to improve the panel's ability to make consistent judgements. General terms and physiological terms of sensory analysis are described in the Standard ISO 5492: 1992 "Sensory analysis - Vocabulary" and General guidance for the methodology in the Standard ISO 6658: 1985 "Sensory analysis; Methodology; General guidance". Standards special for the individual sensory characteristics (color, flavour, taste, odor etc.) useful for the assessors training are:

ISO 3972: 1991	Sensory analysis; methodology; method of investigating sensitivity of taste
ISO 5496: 1992	Sensory analysis; methodology; initiation and training of assessors in the detection and recognition of odors
ISO 6564: 1985	Sensory analysis; Methodology; Flavor profile methods
ISO 11035: 1994	Sensory analysis - Identification and selection of descriptors for establishing a sensory profile by a multidimensional approach
ISO 11037: 1996	Sensory analysis - General guidance and test method for assessment of the color of foods
ISO 11056: 1995	Sensory analysis – Methodology - Magnitude estimation
ISO 13299: 1995	Sensory analysis – Methodology - General guidance for establishing a sensory profile
ISO 13301: 1995	Sensory analysis - Methodology - General guidance for defining and calculating individual and group sensory thresholds from three alternative forced-choice data sets

During training the panelist learns to disregard personal preferences, making the evaluations more objective. Panelist who have been selected for their ability to discriminate are more likely to give the same results on another replication of the test. They will be able to detect smaller differences than randomly selected panelists.

Instructions and recommendations are given to the tasters which should be applied to before and during sensory analysis i.e. not smoke at least 30 min before the test, not use any perfume, cosmetic before the test, fast at least 1 h before the tasting, feel physically well, not under any psychological effect that prevents their work etc.

<u>Samples</u>: Many factors related to the samples which affect sensory analysis depend on the products being testing: sample preparation in respect to the product, dilution or mixing with carriers, serving temperature at which they are normally eaten, containers serving (masked for color, covered for odor), quantity of samples, coding (with random numbers) and order of presentation of samples, rinsing with water, crackers, apples, celery or bread between samples.

<u>Sensory methods</u>: Several sensory methods can be used as analytical tests, the best can be selected after considering the test objective. The following tests are used in sensory analysis:

ISO 4120: 1983 - Triangle Test	ISO 8587: 1988 – Ranking
ISO 10399: 1991 - Duo-Trio Test	ISO 4121: 1987 - Scaling Methods
ISO 5495: 1983 - Paired Comparison Test	Ratio Scaling
ISO 8588: 1987 – Test 'A' no 'A'	Descriptive Sensory Analysis

Presentation of sensory analyses results - Correlation to objective analyses: The tasters after the tasting complete their records in suitable sheets according to the sensory test i.e. using symbols  $(+, \sqrt{})$  or numbering scale (1-5, 1-10). The sensory sheets should be easy for the tasters to complete and for the supervisor to select and evaluate the results. The sensory data may be presented using net-work diagrams etc. and they are processed with proper statistical methods such as Analysis of Variance (ANOVA). The method of data analysing influences the accuracy of the results. In most instances the objective of the study can be stated in the form of a null hypothesis which will be accepted or rejected depending on the results of the statistical analysis of the data collected. A type I error consists of rejecting the null hypothesis when it is true and a type II error consists of accepting the null hypothesis when the alternative is true. Type II errors are minimised by using acute reliable judges and/or by increasing the number of observations in which the conclusion is based. The probability of type I error is the level of significance selected (5, 1 or 0.1 %,) by the experimenter before the test. The sensory results can be correlated to the objective results (i.e. results from chemical analyses for flavor compounds, instrumental measurements of texture) using Principal Component Analysis (PCA) method.

# 2. Food Safety - HACCP - Legislation

Although foods are consumed for their nutritional and sensorial characteristics, they must be safe for the consumers without introducing risks in human health. Food processing reduces or eliminates food hazards, but it can introduce new hazards. In order to assure food safety, special care must be taken from harvesting through the production to the retailing of the end product. Nowadays the production of healthy foods, as well as foods with improved sensory characteristics is very important. A food must be safe, not contain levels of pathogens, toxins, chemicals or foreign materials likely to cause illness when the food is consumed. A food must be acceptable, not contain levels of microorganisms sufficient to render it organoleptically spoiled in an unacceptable short time.

The current technological food protection rationale, HACCP, has been rapidly evolved and is being addressed by a number of organizations (EEC, FDA, USDA, etc.). HACCP (Hazard Analysis and Critical Control Points) is a highly specialized predictive system for safety assurance of foods designed in a systematic way for protecting public health. HACCP has been evolved by the International Commission on Microbiological Specifications for Foods (ICMSF) (1988) and the

National Advisory Committee on Microbiological Criteria for Foods (NACMCF) (1992). Codex Alimentarius Commission (FAO/WHO) published "Guidelines for HACCP application" (1993, 1997) and "General Principles of Food Hygiene" (1994).

Because of an intense requirement for food safety, national organizations (FDA, USDA) have stated legislation in order to protect health and hygiene of foods. According the above, the protection of human health constitutes an objective of fundamental importance. This agrees with the internationally acceptable approach recommended by Codex Alimentarius for food hygiene. In Europe the requirements for food hygiene were firstly determined in the Directive 93/43 EEC where the concept of HACCP was adopted. Food safety may be assured by the detailed application of hygiene throughout the food chain and a traceability system inside the food industry according to Regulation E.C. 178/2002. The implementation of appropriate hygienic practices according to the Regulation E.C. 852/2004 requirements is mandatory to all food establishments in Europe (food industry, food service). Nowadays food safety is appeared as necessity by the national scientific community, the consumers, the food producers and manufacturers, the food industries and the states. Due to the intense requirement for food safety Regulatory bodies and food industry are actively interested in determining and controlling the safety of food products. The regulatory authorities must do so to fulfill their statutory responsibility to protect the public from hazardous or inferior goods.

## 2.1 Food Hazards

Food hazards occurred in food throughout the food chain are categorized as: i) microbiological (pathogenic bacteria, viruses, parasites), ii) chemical (heavy metals, pesticides residues, hormones, toxic substances from environment or the packaging materials etc.), and iii) physical (foreign materials: metal pieces, stones etc.). Hazard is a potential source of danger and risk is a measure of the probability and severity of harm to human health, while safety is a judgment of risk acceptability. The nature and size of risk in a process called risk assessment. Raw materials are processed in order to be converted to acceptable food products with pleasant sensory characteristics. Processing includes receiving of raw materials, handling, pretreatment, main processes, packaging to storage and distribution of final products. Processing operations reduce or eliminate food hazards, but in the same time can introduce new hazards (cleaning agents, lubricants, refrigerants, pest control chemicals, plasticizers, additives from packaging, metallic pieces and foreign materials, microbiological hazards introduced by handling, contact with contaminated surfaces or by cross-contamination).

Food microbiology dealing with pathogens and food toxicology with doseresponse studies of hazardous substances have provided valuable results to evaluate risk and severity of each hazard. ICMSF has published data for all pathogens and for every food product. Microbiological criterion (ICMSF) is:

- (1) <u>Microbiological standard</u> is a criterion specified in a law or regulation. It is a legal requirement that foods must meet and is enforceable by the appropriate regulatory agency.
- (2) <u>Microbiological specification</u> is a criterion applied in commerce. It is a contractual condition of acceptance that is applied by a purchaser attempting to define the microbiological quality of a product or ingredient.
- (3) <u>Microbiological guideline</u> is used to monitor the microbiological acceptability of a product or process. It is more often advisory than mandatory.

Maximum allowable levels of toxic substances in food products have been defined by national and international legislation (i.e. MRLs for pesticide residues, NOEL for additives). Physical hazards are mainly related to the food processing plant and can be only evaluated by in the specific establishment; GMPs-GHPs provide the requirements to avoid these hazards.

# 2.2 - HACCP Principles - Application of HACCP - PRPS

Various microorganisms (bacteria, viruses, parasites) may be naturally present or introduced during food processing. Microorganisms, chemicals and foreign materials may be found in foodstuffs due to contamination (environment, equipment, workers, processing techniques, packaging). Hazard analysis includes the identification of the potential risks throughout food process and the Critical Control Points (CCPs) that must be controlled to assure food safety. HACCP approaches food safety focusing to the critical control points (CCPs) of food processing and is considered to be the most effective method of maximizing product safety. It is a cost-effective system and therefore reduces the risk of manufacturing and selling unsafe products. The HACCP system was introduced to the food processing industry in the early 1970's. It is a systematic approach to be used in food production as a means to assure food safety. It consists of seven basic principles:

PRINCIPLE 1: Hazard analysis and preventative measures

PRINCIPLE 2: Identification of CCPs

PRINCIPLE 3: Establishment of critical limits

PRINCIPLE 4: Establishment of monitoring procedures

PRINCIPLE 5: Establishment of corrective actions to be taken, when there is a deviation from a critical limit

PRINCIPLE 6: Establishment of effective record-keeping procedures

PRINCIPLE 7: Establishment of verification procedure.

HACCP necessitates the performance of an analytical study on microbiological, chemical and physical risks. The most significant part of the HACCP study is the I. Hazard analysis and the II. Determination of CCPs.

Based on the first principle, the HACCP team -which is responsible for implementing the whole program- must evaluate the raw materials and the products and identify the potential hazards associated with food production at all stages, from growing, harvesting, processing, manufacturing, distribution, sale, until the final consumption of the product. The team must also estimate the severity and the

likelihood of occurrence of the hazards and identify the preventative measures of their control. Before conducting a hazard analysis the members of the HACCP team must describe the food, its raw materials and the method of its distribution and they must identify the intended use and consumers of the product. Furthermore, they have to develop and verify a process flow diagram that describes all steps in the process and not only those activities that are under the direct control of the food manufacturer. The next step is to perform a detailed hazard assessment.

<u>I. Hazard analysis (Principle 1)</u> consists of: Hazard Analysis of raw materials and products and b) Hazard Analysis of manufacturing process.

<u>a) Hazard Analysis of raw materials and products</u>: Each food and its raw materials or ingredients must be ranked according to six hazard characteristics (A-F).

HAZARD A	Nonsterile foods intended for consumption by high-risk population (e.g. infants, the aged, pregnant
	women etc.). This hazard characteristic is extremely important to foodservice operations, especially
	in hospitals.
HAZARD B	<u>Product contains "sensitive" ingredients.</u> A "sensitive" ingredient is any ingredient historically
	associated with a known microbiological hazard (e.g. meat and poultry, fish and shellfish, milk and
	dairy products, mushrooms etc.) or is known to be potential source of toxic chemicals or dangerous
	physical hazards.
HAZARD C	No process step to eliminate (prevent, destroy or remove) a microbiological, chemical or physical
	hazard. A typical example is lack of a heat treatment to destroy bacterial pathogens and other
	harmful microorganisms.
HAZARD D	Potential recontamination after manufacturing and before packaging. This point is added in response
	to the proligeration of specialty chilled foods.
HAZARD E	Potential for product abuse. This hazard characteristic considers the potential for abusive handling in
	distribution, retailing or at home that could result in an increased hazard.
HAZARD F	No terminal heat process or no way for the consumer to detect, remove or destroy a toxic chemical
	or a dangerous physical hazard. This hazard characteristic considers the absence of a terminal heat
	process or any other kill-step after packaging of the product or when it is cooked at home.

The six characteristic ranking system is applied for microbiological, chemical and physical hazards. A food is scored by using a plus (+) if the food has the characteristic and a zero (0) if it does not exhibit the characteristic. Based on the results of ranking by hazard characteristics each food and raw material is assigned to a product hazard category, depending on the number and type of hazard characteristics present. Foods with no hazard characteristics are designated "0", whereas foods which exhibit hazard characteristic A are automatically assigned category VI, the highest risk category. Foods and raw materials possessing 1-5 of hazard characteristics B-F are assigned to risk categories I-V respectively. These hazard categories are helpful in determining CCPs, in developing appropriate sampling plans during monitoring and verification and in finding out if a raw material must be managed as a CCP.

b) Hazard Analysis of manufacturing process: After completion of the hazard analysis for the product, the raw materials and the ingredients and their classification in one of the six hazard categories for each type of hazard, the next step for the members of the HACCP team is to conduct a hazard analysis of the manufacturing process. This procedure includes:

- i. Identification of all potential microbiological, chemical and physical hazards: The HACCP team initially lists all perceived microbiological, chemical and physical hazards and indicates their location on the process flow diagram. At each process step, point or procedure in the flow diagram the potential for any introduction, increase or survival of the hazards must be considered, taking into account the process equipments, the environment and the personnel practices.
- <u>ii.</u> Assessment of each identified hazard: The next step is to assess the potential significance of each identified hazard by considering two factors, namely risk and severity, in order to build in appropriate control mechanisms. This procedure is known as risk assessment. The hazards must be of such degree that their prevention, elimination or reduction to acceptable levels is essential to the safety of the product. Therefore, potential hazards of low risk and low severity are not significant and must not be considered in the HACCP plan. There is little point in setting up a HACCP system to control a potential hazard which will never occur. The quantitative aspect of hazard analysis is important and the evaluation of the hazards requires considerable technical expertise.
- <u>iii.</u> Determination of preventative measures for each hazard: When all potential hazards have been identified and analyzed, the HACCP team must then consider what preventative measures exist which can be applied for each hazard. Preventative measures are those actions and activities that can be used to eliminate or reduce the occurrence of hazards to an acceptable level.

<u>Determination of CCPs (Principle 2)</u>: The information which is obtained during the hazard analysis of both the product and the manufacturing process will enable the HACCP team to identify which steps in the process are CCPs using the HACCP Decision Tree.

III. Application of the rest five HACCP principles: The establishment of critical limits (CLs) for identified CCPs (Principle 3), by obtaining information from scientific literature and regulatory guidelines, the monitoring procedures of critical limits (Principle 4), which include all modern methods of analysis and measurements with required accuracy and reliability and are completed with monitoring of hygienic practices and GMP for equipment, area and personnel, the establishment of corrective actions (Principle 5), which should be developed by experienced members of the HACCP team and should be specified for every possible deviation that may occur in each CCP, the establishment of effective record-keeping procedures (Principle 6), and the verification of the HACCP Plan (Principle 7).

IV. HACCP implementation: After development of the HACCP system, its implementation follows, thus all important controls and procedures should be organized. HACCP, as a system that assures the safety of food products, may be incorporated to the Quality Control system ISO 9001; the combined system ISO 9001-HACCP can then work as a uniform system that assures both quality and safety of food products. HACCP may be certified by ISO 22000. The system must

be inspected, re-evaluated and improved. The inspection of HACCP systems must be carried out by state agencies.

Prerequisites Programmes (PRPs): For the efficient implementation of HACCP, food industries should satisfy general rules of "hygiene". All these meters are prerequisites which are of decisive for the safe food production and are categorized to: i) Construction Prerequisites: are related to hygiene practices in the plant design (GHPs) and hygienically designed facilities for the place and the personnel and ii) Operational Prerequisites: are related to manufactiring or hygienic practices (GMPs, GHPs) for food handling or for personnel hygiene. The required actions are organized by Sanitation Standard Operating Procedures (SSOPs) and «Prerequisites Programs» (PRPs) (cleaning/ sanitation, preventive maintenace of equipment/ machines, pest-control, wastes management).

# 2.3 Monitoring and Control Methods

For the needs of HACCP, monitoring of the critical limits of CCPs should be performed. Different types of monitoring can be used: i) On-line monitoring: parameter is measured *in* the process line and may be continuous: allows rapid detection of drift (early intervention) e.g. T, pH, metal detection or discontinuous e.g. pH, T etc. ii) Off-line monitoring: sample is taken and analysed in the laboratory e.g. microbiological analysis, residue analysis etc. All analytical measurements have a certain level of error, thus sufficient number of measurements and frequency of monitoring is necessary to carry out.

Many food microbiologists consider that the traditional enumeration methods are not only too slow but lead to an overdependence on the significance of numbers of colony-forming units. Food manufacturers require information about the microbiological quality of commodities and raw materials rapidly and it could be argued that an assessment of microbial activity is so important as a knowledge of numbers. A number of methods has been developed that aim to give answers more quickly and hence are often referred to as Rapid Methods: Dye-reduction tests, electrical methods, ATP determination, and for detection of specific organisms and toxins by immunological methods and DNA/RNA methodology (ELISA, PCR).

# 2.4 Food Safety Management - Food Safety Objectives (FSOs)

The continuously increasing of food safety is attained by means of HACCP and of FSOs (Food Safety Objectives). HACCP is logical approach for achievement of safer food processes. Controlling the CCPs by accurate/reliable measurements and recording guarantee safe foods for producers, authorities and consumers. FSOs provide the targets for the control of the food hazards focusing on public health. FSOs, combining HACCP with Pathogen Reduction Programs develop food safety programs for public health. The establishment of Food Safety Performance Standards (FSPS) and of Sanitation Standard Operating Procedures (SSOPs) in the food industrial processes is necessary.

In order hazard control to be more efficient, a Quantitative Risk Assessment must be carried out, particularly for microbiological hazards (Microbiological Risk Assessment - MRA). The procedure for the Risk Assessment includes Hazard identification, Risk Assessment and Risk Quantification by means of Dose/Exposure and Exposure Assessment, Risk Characterization and Risk Management- Risk Communication. Monitoring of identified CCPs requires responsibilities, procedures, determination of specifications, documentation etc. Necessarily, for the achievement of HACCP and food safety purposes the PRPs associated with hygienic design and operation of the food industries (layout, personnel, environment, equipment etc.) should be implemented. Efforts to manage food safety and protect public health and industrial practices for food hazards control should be continuously detected.

- [1] Munoz A.M., (2002). Sensory evaluation in quality control: an overview, new developments and future opportunities, Food Quality and Preference, 13, 329-339.
- [2] King S., Gillette M., Titman D., Adams J., Ridgely M., (2002), The Sensory Quality System: a global quality control solution, Food Quality and Preference, 13, 385-395.
- [3] Gacula M.C.Jr., (1993). Design and analysis of sensory optimization, Food & Nutrition Press, Trumbull, CT, ÚSA.
- [4] Tzia, C., Tsiapouris, A. 1995. HACCP in food industries, Papasotiriou, Athens, Greece.
- [5] Ropkins, K., Beck, A.J. 2000. Evaluation of worldwide approaches to the use of HACCP to control food safety, Trends in Food Science & Technology, 11: 10-21.
- [6] Billy, T.J. 2002. HACCP a work in progress, Food Control, 13: 359-362. [7] Walker, E., Pritchard, C., Forsythe, S. 2003. Hazard Analysis Critical Control Point and Prerequisite Programme Implementation in small and medium size food businesses, Food Control, 14: 169-174.

# TRITIUM CONTENT IN PRECIPITATION AND ATMOSPHERIC WATER VAPOUR OF THE REACTOR HALL IN THE VINČA INSTITUTE OF NUCLEAR SCIENCES

M. Janković and N. Miljević Institute Vinča, P.O. Box 522, 11001 Belgrade, Serbia

## **Abstract**

Tritium activity was determined in precipitation samples collected at two locations in Belgrade over the period 1998-2007: meteorological station Belgrade (Zeleno Brdo 44°47′ N, 20°32′ E, altitude 243.2m asl) and the station at the Vinča Institute of Nuclear Sciences. Tritium concentrations in precipitation ranged from 0.4 to 4.41 Bq l<sup>-1</sup> (samples collected at Zeleno Brdo) and from 2.31 to 41.30 Bq l<sup>-1</sup> (samples collected at VINS). Tritium content in atmospheric water vapour of the indoor reactor hall and inside of the reactor during the regular inspection of the fuel channels in the Vinča Institute of Nuclear Sciences in March and May 2006 was measured. The obtained results showed that the tritium content in HTO form varied from 1.56x10<sup>2</sup> Bq m<sup>-3</sup> to 4.05x10<sup>2</sup> Bq m<sup>-3</sup>.

# Introduction

Tritium released from man-made source to the environment could be in the form of tritiated hydrogen gas (HT) and gaseous compounds, tritiated water (HTO) and aerosols of solid compounds. Transfer of tritiated water from the atmosphere to the surface of the earth occurs mainly by precipitation, but also by vapor exchange. Precipitation samples are of special interest because their tritium concentration govern the tritium activity fed into the soil and, consequently, have an impact on all the other media [1].

The research reactor RA in the Vinča Institute of Nuclear Sciences worked from 1959 to 1986 at a nominal power level of 6.5 MW. Heavy water ( $D_2O$ ) of the reactor moderator and coolant, with a concentration of some TBq  $I^{-1}$  of tritium produced by neutron reaction during reactor operation, was drained and placed in a storage tank in October 1987 [2]. The RA reactor was placed in the "long term shutdown" condition in April 1986 in order to reconstruct and improve practically all the vital reactor systems. Since then, during the regular inspection of the fuel channels, tritium in HTO form can be released to the environment. From that reason, tritium content in precipitation in VINS and in Belgrade (meteorological station Zeleno Brdo) has to be measured.

# **Experimental**

Composite monthly precipitation samples were collected at two locations: meteorological station Belgrade (Zeleno Brdo 44°47' N, 20°32' E, altitude 243.2 m asl) and the Vinča Institute of Nuclear Sciences (95 m asl).

Sampling of atmospheric water vapour was performed using the differential moisture sampler HT/HTO, produced by the Institute for Isotopes, Hungarian

Academy of Sciences. Sampling is based on the absorption technique [3]. Atmospheric water vapour in reactor hall was collected during 24 h over the period 30/03 – 03/04/2006, and inside of the reactor during 17/05 (1.1 h), 18/05 (0.41 h) and 19/5/2006 (0.66 h). In this period regular inspection of the fuel channels was performed.

Tritium activity measurements were carried out by a liquid scintillation spectrometer LKB-Wallac 1219 RackBeta, and expressed in Bq I<sup>-1</sup> or Bq m<sup>-3</sup>. The activity of tritium in precipitation samples was measured after electrolytic enrichment, while tritium activity in atmospheric water vapour was measured without electrolytic enrichment.

# **Results and Discussion**

The obtained yearly mean tritium concentrations in precipitation samples collected at Zeleno Brdo (ZB) and Vinča Institute of Nuclear Sciences (VINS) are presented at Fig. 1. The activity concentration of tritium for samples at ZB ranged from the limit of detection (0.4 Bq l<sup>-1</sup>) to 4.41 Bq l<sup>-1</sup> and for samples collected at VINS ranged from 2.31 Bq l<sup>-1</sup> to 41.30 Bq l<sup>-1</sup>. Generally, tritium activity in precipitation increase in spring and summer months and decrease in the other part of a year. This pattern corresponds to tritium stratospheric origin. The obtained values for precipitation samples from VINS are higher then samples from ZB, which is attributed to the influence of local contamination by heavy water nuclear reactor.

Previous measurements showed that the tritium concentration in precipitation collected at Zeleno Brdo ranged from 1.1 to 18.3 Bq l<sup>-1</sup> for period 1976-1990 [4]. Concentration of tritium observed at this location show the tendency of current global levels found at the other towns (Vienna, Budapest, Zagreb) [5]. For period 1988-1997, tritium concentration in precipitation ranged from 0.9 to 11.5 Bq l<sup>-1</sup> (precipitation collected at ZB) and from 4.2 to 74.6 Bq l<sup>-1</sup> (precipitation collected at VINS) [2].

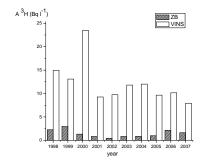


Fig. 1. Tritium concentration in the precipitation at ZB and VINS

Content of tritium in atmospheric water vapour is presented in Table 1. Activity of tritium measured in the reactor hall during the working days 30/03/2006 - 31/03/2006, was  $3.37\times10^2$  Bq m<sup>-3</sup>, while during the weekend 31/03/2006 - 03/04/2006, activity of tritium was  $4.05\times10^2$  Bq m<sup>-3</sup>. The obtained value of tritium content for weekend is higher because for weekend ventilation does not work,

which means that tritium in HTO form released to the environment during the working days. Tritium content measured in atmospheric water vapour inside of the reactor is the same order of magnitude as water vapour in the hall. All obtained values for tritium activity in atmospheric water vapour are below  $80 \times 10^4$  Bq m<sup>-3</sup>, which is acceptable for working environment [6].

TO 11 1 TO '.'	4 4.	• 4 1	• ,
<b>Table 1.</b> Tritium cond	centration	in atmosph	eric water vanour
I dole It I I I I I I I I I I I	centiation	III atiliospii	cric water vapour

date	RA HTO $\times 10^2$ (Bq m <sup>-3</sup> )
30.03. 31.03.	3.37
01.04.	
02.04. 03.04.	4.05
17.05.	3.87
18.05. 19.05.	1.56

The obtained values for tritium activity in atmospheric water vapour in reactor hall (reactor RA) in this paper are in agreement with the results obtained in 1996  $(0.40 \times 10^3 \text{ Bq m}^{-3} \text{ to } 112 \times 10^3 \text{ Bq m}^{-3})$  [7]. These values are one order of magnitude higher than values obtained in 2006, which is a consequence of tritium half-life.

# Conclusion

Tritium content of samples collected at VINS appears to be one order of magnitude higher than that of samples from Zeleno Brdo, that is attributed to the influence of local contamination by heavy water nuclear reactor. The obtained values for tritium activity in atmospheric water vapour of the indoor reactor hall and inside of the reactor RA are below  $80\times10^4$  Bq m<sup>-3</sup>, which is acceptable for working environment.

- [1] N. Miljević, V. Šipka, Environmental aspects of tritium around the Vinča Institute of Nuclear Sciences, I Regional Symposium "Chemistry and Environment", Vrnjačka Banja, September 25-29, 1995, 967-970.
- [2] N. Miljević, V. Šipka, A. Žujić, D. Golobočanin, Tritium around the Vinča Institute of Nuclear Sciences, J. Environ. Radioact., 2000, 48, 303-315.
- [3] H. G. Ostlund, A. S. Mason, Atmospheric HT and HTO, Tellus, 1974, 26, 91-101.
- [4] M. Hadžišehović, N. Miljević, V. Šipka, D. Golobočanin, Environmental tritium of the Danube basin in Yugoslavia, Environ. Poll., 1992, 77, 23-30.
- [5] IAEA/WHO, Environmental isotope data no. 10: World survey of isotope concentration in precipitation (1988-1991). Technical Report Series No. 371, IAEA, Vienna, 1994.
- [6] "Regulations for the maximum limits of radioactive contamination of the human environment and decontamination procedures", Official Journal of the Socialist Federal Republic of Yugoslavia (in Serbian), 1987, **8**, 226-246.
- [7] V. Šipka, N. Miljević, Z. Gršić, D. Todorović, M. Radenković, Tritium release during inspection of reactor "RA" at "Vinča" Institute, Proc. of XIX Conference of JDZZ, Golubac, 1997, 193-196.

# <sup>137</sup>Cs DESORPTION FROM *CETRARIA ISLANDICA* LICHEN USING ACID SOLUTIONS

A. Čučulović, D. Veselinović<sup>1</sup> and Š.S. Miljanić<sup>1</sup>

INEP-Institute for the Application of Nuclear Energy, Banatska 31b, Zemun, Serbia, anas@inep.co.yu,

<sup>1</sup>Faculty of Physical Chemistry, University of Belgrade, P.O.Box 137, Belgrade, Serbia

# **Abstract**

Desoprtion of <sup>137</sup>Cs in samples of *Cetraria islandica* lichen using HCl (**A**) and HNO<sub>3</sub> (**B**) acid solutions with pH values from 2.00 to 3.75 was investigated. After five consecutive desorptions lasting 24 hours it was shown that between 52.2% (solution (**B**) pH 3.28) and 72.2% (solution (**A**) pH 2.00) of <sup>137</sup>Cs was desorbed from the lichen and the first desorptions were the most successful. The pH value influenced <sup>137</sup>Cs desorption from lichen if desorption was performed using solution (**A**). Lichen desorbed with the stated solutions did not undergo any visually noticeable structural changes. The amount of absorbed water from solutions (**A**) and (**B**) when they are used for desorption from lichen in relation to the starting volume (expressed in %) showed that solution concentration did not take place. Lichen act as neutralizing agents as the pH of the lichen thallus is higher than the pH value of the solution used.

# Introduction

Lichen can adopt and accumulate polluting substances (radionuclides, heavy metals, pesticides) in tissue or on the thallus surface [1]. After the Chernobyl accident (Soviet Union, 1986) it was shown that in lichen sorption of radionuclides from air was dominant, tolerance to radionuclides was passive and hyperaccumulation of radionuclides in lichen was the consequence of genetically independent organism properties and that lichen tissue reflects the environment composition [2]. Radionuclides entering the lichen body become sources of internal radiation and also radiation sources for other linked organisms. Lichen are natural reservoirs of matter that can be periodically released [3,4].

#### **Material and Methods**

200 mL of solutions (**A**) HCl and (**B**) HNO<sub>3</sub> was poured over 10 g of dry *C. islandica* lichen. Solutions (**A**), i.e. (**B**) were made by adding concentrated HCl or HNO<sub>3</sub> to 200 mL of water until a desired pH value of 2.00; 2.58; 2.87; 3.28 and 3.75 was reached. Samples were consecutively desorbed with solutions 5 times and desorption series were repeated twice. Desorptions were performed at room temperature lasting 24 hours. After each desorption, following filtration, lichen samples were dried at room temperature until a constant mass. Activity levels of <sup>137</sup>Cs were measured in samples before and after each desorption on an ORTEC-AMETEK gamma spectrometer with 8192 channels, resolution of 1.65 keV and

efficiency of 34% at 1.33 MeV <sup>60</sup>Co with a measurement error below 5%. Based on measurements the specific activities (Bq/kg) were calculated. The sorbent absorbed a certain volume of water from the added desorption solution after each of the five desorptions. The remaining desorption solution was strained through filter paper and its volume was measured. Knowing the starting and measured solution volume obtained after each desorption the absorption percentage of desorption liquid by the lichen was calculated. The pH of the lichen thallus was determined by destructing 100 g of lichen thallus with liquid nitrogen and mixing it with 4 mL of de-ionized water (pH 5.77) followed by centrifuging in a centrifuge at 100xg 10 minutes. The solution pH value was measured on a pH meter [5,6].

# **Results and Discussion**

Activity levels of <sup>137</sup>Cs in samples of *C. islandica* lichen before desorption were from 1786 Bq/kg to 2994 Bq/kg. After five consecutive desorptions lasting 24 hours at room temperature from 52.2% (solution (**B**) pH 3.28) to 72.2% (solution (**A**) pH 2.00) of the starting value of <sup>137</sup>Cs was desorbed (table 1). Between 59.3 and 74.2% is desorbed with the first desorption in relation to the total amount of desorbed <sup>137</sup>Cs. The pH value has an influence on <sup>137</sup>Cs desorption from lichen if desorption is performed using solution (**A**).

**Table 1**. Activity of <sup>137</sup>Cs in lichen before desorption (Bq/kg), the total amount of absorbed <sup>137</sup>Cs from lichen using HCl (**A**) and HNO<sub>3</sub> (**B**) solutions and the amount of <sup>137</sup>Cs after the first desorption in relation to the total amount of desorbed <sup>137</sup>Cs (%)

	<sup>137</sup> Cs act	<sup>137</sup> Cs activity in Total amo			Amount of <sup>137</sup> Cs after th	
Solution	lichen b	efore	desorbed <sup>137</sup> Cs from		first desorption in relation	
pН	desorp	otion	lichen (%) using		to the total amount of	
	(Bq/	kg)	solutions		desorbed <sup>137</sup> Cs (%)	
	(A)	<b>(B)</b>	<b>(A)</b>	<b>(B)</b>	$(\mathbf{A})$	<b>(B)</b>
2.00	1810	2618	72.2	58.1	74.2	68.3
2.57	1912	2994	64.8	56.6	70.8	67.7
2.87	2299	2664	60.6	53.1	72.3	65.9
3.28	1786	2353	58.0	52.2	59.3	73.4
3.75	2034	2129	56.4	53.7	72.5	64.6

Table 2 shows the amount of absorbed water from solutions (**A**) and (**B**) used for desorption of *C. islandica* lichen in relation to the starting volume (expressed in %). The results show that the solution concentration effect is not present and all noted changes are within the margin of error. The same table gives measured pH values of the thallus before treatment with desorption solutions (**A**) and (**B**). These results show that lichen act as neutralizing agents as in all cases the thallus pH is higher than the pH value of the solution used. Processes leading to this could be neutralization with inorganic or organic bases, but also possible utilization of acid

from desorption solutions on decomposition processes of organic compounds in the lichen tissue.

**Table 2**. Amounts of absorbed water from solutions used for desorption from *C. islandica* lichen in relation to the starting volume (%) and changes in pH of lichen thallus after treatment with desoption HCl (**A**) and HNO<sub>3</sub> (**B**) solutions

	Amount of al	sorbed water	Change of thallus pH after		
Solution	from solutions	used for lichen	treatment with desorption		
	desorption in	relation to the	solutions		
pН	starting vo	olume (%)			
	( <b>A</b> )	<b>(B)</b>	<b>(A)</b>	<b>(B)</b>	
2.00	19.3	20.0	2.54	2.66	
2.57	18.3	19.3	3.17	3.28	
2.87	21.3 20.1		3.59	3.75	
3.28	19.0 21.4		4.18	4.26	
3.75	20.6	21.6	4.74	4.72	

# Conclusion

HCl (**A**) and HNO<sub>3</sub> (**B**) solutions with pH 2.00-3.75 were used for desorption of  $^{137}$ Cs from *C. islandica* lichen. The pH value has an influence on  $^{137}$ Cs desorption from lichen if it is performed using solution (**A**).

- [1] J.E. Sloof, B. Walterbeek, J. Environ. Radioact., 1992, 16, 229-242.
- [2] M.E. Conti, G. Cecchetti, Environ. Pollut., 2001, 114, 309-371.
- [3] Čučulović, D. Veselinović, Š.S. Miljanić, J. Serb. Chem. Soc., 2007, 72(7), 673-678
- [4] Čučulović, M.S. Pavlović, D. Veselinović, Š.S. Miljanić, J. Serb. Chem. Soc., 2008, 73(4), 405-413.
- [5] Y. Gauslaa, Lichenologist, 1985, 17, 117-140.
- [6] O.L. Gilbert, Environ. Pollut., 1986, (Ser A) 40, 227-231.

# AIR POLLUTION INFLUENCE ON CARDIOVASCULAR DISEASES IN BELGRADE DURING 2001 – 2006 YEAR

I.T. Grozdić and T.D. Grozdić

Institute for multidisciplinary research, Kneza Višeslava 1a, 11000 Belgrade, Serbia,(gtomisi@cms.bg.ac.yu).

#### **Abstract**

All data were used as officially data published for period 2001-2006. year [1, 2]. Air quality data are presented as certain parameters in period 2001-2006. year. Other data for maximal year concentration of air pollution criteria are presented, as well. Thematic studies about air pollution show that human life can be shorter for a year if one is exposed in urban air pollution to high concentrations PM10 (compared with others exposed to air pollution with lower concentration) [1]. In paper is shown data of number of nonhospitalized and hospitalized persons with cardiovascular diseases, as angina pectoris, insuff. cordis and myocardiopathia in period 1997- 2005. Long-term exposure to fine-particulate-matter air pollution may accelerate the development and progression of coronary atherosclerosis and increase the risk of dying from cardiopulmonary causes. Comparison is done with other countries and cities in world.

#### Introduction

Technology revolutions is one of basic reasons for increase air pollution, which is detected in last three centuries. Before 1980. year the greatest part of pollution is occurred as a consequence of heating by coal in steam power plant. Under certain conditions, smog and SO<sub>2</sub> can be united with fog making industrial smog (winter smog). High concentration of industrial smog can be toxic for people and other living organism. Today, other fossil fuel, nuclear energy and energy comes from hydropower plants, considerably can decrease concentration of industrial smog. However, liquid fossil fuel, as gasoline and diesel, can be produced other airpollutant, which can cause photosmog (white smog). It occurs as a primary pollutant (nitrogen-oxide and organic compounds-hydrocarbon), react under soon light, which product are mixture of very toxic chemical compounds known as secondary pollutant. Traffic is main well of primary pollutant and photosmog occurs as a rule in places with high traffic.

Urban air pollution is primarily derived from fossil fuel combustion and consists of both gaseous and particulate matter(PM). The particles believed to be most deleterious to health are those with an aerodynamic diameter of less than  $10\mu m$  (PM10) although increasingly attention has focused on the ultrafine component. Although effect sizes vary greatly between studies, meta-analyses suggest that an increase in fine particulate pollution of  $10\mu g/m^3$  is associated with an increase in total mortality of 1.8% and cardiovascular mortality of about 1.4%. The highest risk appears to be in people with pre-existing cardiac disease.

Several hypotheses have been proposed to show connection between air pollution and cardiovascular effects. Inhalation of fine particles may provoke an inflammatory response and release of prothrombotic and inflammatory cytokines. A systemic acute phase response of this nature would put people with coronary atheroma at increased risk of plaque rupture and thrombosis. Secondly, exposure to PM may have an adverse effect on cardiac autonomic control, leading to an increased risk of arrhythmia in susceptible patients. An increase in resting heart rate suggests either reduced vagal or increased sympathetic cardiac controls an independent risk factor for total cardiovascular mortality and sudden death.

Numerous study of different town in America and Europe show as on a risk of respiratory diseases as a consequence of air pollutant. Study of Bronx (New York) [3] show as that people, which are living near big traffic crossings or highway has 66% greater chance for asthma diseases. Studies about Austria, France, Switzerland [4 and 5] show as that air pollution (traffic pollution) can cause increase mortality people older then 30 years from cardiovascular diseases.

# **Results and Discusion**

Data presented in this part are authentic data from the City public-health Institute in Belgrade. Firstly, there will be shown data about air pollution and than health statistic (epidemiological data) for period of 2001-2006.year in Belgrade. Air quality on Belgrade territory is measured in 66 measuring points. In the city center there are 16 measuring points where is major air pollution. In all measuring points are measured concentration of  $SO_2$ , soot and  $NO_2$ . On the basis of those data for the period of 2001-2006. here is shown average annual concentration of  $SO_2$ , soot and  $SO_2$  (in  $SO_2$ ), see Table 1. Increase of average annual concentration of those pollutants in Belgrade is obvious. In 2003, there is significant increase of concentration of  $SO_2$ .

**Table 1.** Average year concentration  $SO_2$ , soot and  $NO_2$ , shown in  $\mu g / m^3$  for city Belgrade [1, 2, 5].

Year	2001	2002	2003	2004	2005	2006
$SO_2$	11	13	30	16	24	20.9
Soot	32	30	32	29	33	33.6
$NO_2$	21	30	32	16	31	31.6

According to data from City public-health Institute in Belgrade the most common morbidity cause of people 19-60 years old in time period 1997-2005. are respiratory diseases and cardiovascular diseases. In population elder then 60 year, who were hospitalized the most common cause of death are: cardiomyopathy, acute myocardial infarction and insufficiencio cordis. Similar results are found in many international studies. Findings from a London time series analysis were consistent with 1 in 50 myocardial infarctions treated at London hospitals being triggered by

outdoor air pollution. By extrapolation, across the UK high levels of ambient pollution may be responsible for at least 6000 cardiovascular events per year.

Age group	199	97	2005		
	% in total morbidity	morbidity rate per 100 000	% in total morbidity	morbidity rate per 100 000	
20- 59	19,5	172,5	18,5	181,5	

**Table 2.** Patients with cardiovascular diseases non hospital treatment [2].

Studies in Germany and Netherlands show that deaths from heart failure, myocardial infarction and stroke were all increased significantly in polluted compared with the control areas. Also, a 50% reduction in sulfur dioxide concentrations following legal restrictions on fuel oil sulfur in Hong Kong was immediately followed by a 2,4% reduction in cardiovascular deaths.[X]

# Conclusion

On the presented data one can conclude that in Belgrade urban region and down town are very air pollute. Traffic and heating by fossil fuel make air pollution. All town citizen are exposed to air pollutant.

Air pollution influence on increase of cardio-vascular diseases is evident, as is it is shown for Belgrade (1997-2006.) [2, 5] and other town in world [4, 6]. Air is important for people, and this is main reason why we have to protect air from all pollutants. This prevention is necessity for healthy and quality life.

- [1] T. D. Grozdić, I. T.Grozdić, Uticaj zagadjenja vazduha na bolesti respiratornih organa u Beogradu u periodu 2001-2006. godine, Ecologica, 2007, **14**, 55-57.
- [2] Kvalitet životne sredine grada Beograda u 2005. godini, izdavač Sekretarijat za zaštitu životne sredine Beograd, Gradski zavod za zaštitu zdravlja Beograd i Regionalni centar za životnu sredinu za Centralnu i Istočnu Evropu (REC), 2005.
- [3] V.Dragićević, Z. Dimitrijević, "Analiza zdravstvenog stanja stanovništva Beograda u periodu od 1997-2005,, Dani gradskog zavoda 2006, Izazovi novog javnog zdravlja, ed. GZZZB, Beograd, 2005.
- [4] N Künzli at all., Public-health impact of outdoor and traffic-related air pollution: a European assessment Climate change the new bioterrorism, *The Lancet*, 358, 9294, 2001, 1657.
- [5] www.zdravlje.org.yu, www.beoeko.com/sr/vazduh01.htm
- [6] J.Heinrich, H.E. Wichmann, Traffic related pollutants in Europe and their effect on allergic disease, Current Opinion in Allergy and Clinical Immunology, 2004, 4,5, 341-348.

## POSSIBILITY ANALYSIS OF VEGETATION PROCESSING SATELLITE IMAGES OF INFRARED SPECTRUM

M. Milanovic<sup>1</sup>, M. Ljesevic<sup>1</sup>, S. Bakrac<sup>2</sup> and I. Novkovic<sup>1</sup>

<sup>1</sup>Faculty of Geography, University of Belgrade, Studentski trg 3/III, 11000 Belgrade, Serbia <sup>2</sup>Military –Geography Institute, Mije Kovacevica 5, 11000 Belgrade, Serbia

#### **Abstract**

This is study describe a possibility analysis of changes at vegetation using process satellite images of infrared spectral wave. Procedure of practice is coordinated with programme of CORINE (Coordination of Information on the Environment), programme, which is; create European Union for researche of environmenta using remote sensing products. Processing infrared satellite images afford of possibility at surveillance, observation and control. Images of infrared spectral wave conduce at control and observation nagative feature action of people, drought of vegetation and forest fire. Combination are methods of follow for all elements of environment. Results from processing satellite image of infrared spectral wave, showed that a possibly for control practise for artificial areas, agriculture areas, forest areas, humidity marsh areas, and water areas.

#### Introduction

Generated pseudo color composite of short infrared spectral wave band can be determinate old age forest, type of vegetation, damaged forest (partial or complement), etc. Based on restful data and information at terrain created frame of systematically planning and management at forest. That is frame to vegetation protection, too. Data about torrid vegetation comprehend data of water in leafs and branches, plant volume per unit of surface, statistical data of relation between topography terrain and hydrological conditions [4]. Data got in processing images indicated to more or less water at bushes, grass areas and pasture, indicated to volume of water in soil, etc.

Infrared images are optimum for analysis vegetation, especially for contaminant and pollution materials [2]. Themselves use for create pseudo color composite for every three wave areas, near IR  $(0,7-1,5~\mu m)$ , short or middle IR  $(1,5-5,6~\mu m)$  and thermal IR  $(5,6-1000~\mu m)$ . Herein is used pseudo color composite attained for short infrared spectral areas  $(1,5-2,6~\mu m)$ . Images were bought for necessaries production PhD thesis. Processing images comprehend analysis of urban areas, zone of industrial, as all people activity as, which observed at images (artificial areas). At images are analysed agriculture areas, forest areas, humidity marsh areas, and water areas [5].

#### **Experimental**

Vegetation at images is showed red color [3]. For analysis vegetation on next figure, used pseudo color composite attained for short infrared spectral areas  $(1,5-2,6 \mu m)$ . Result of research indicate that urban area and zone of industrial most contaminant [1]. Dark shade of red color present well vegetation, shade of bright red color present unwell vegetation, while shade rose red color indicated to contaminant and pollution material in vegetation.

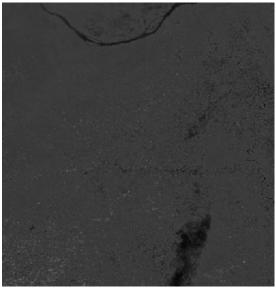


**Fig. 1.** Composite with central point between Mladenovac and Smederevska Palanka, Serbia (short IR – 546; satellite ASTER)

The studied indicate that bigger cities on images (Smederevo, Arandjelovac, Mladenovac, ) present potential contaminant for vegetation in theirs environment.

#### Results

On parts of image in the figure 1 for color composite short IR 546, observed shade bright red which most occur percents. There are near the bigger cities, but most bright of red color are around Smederevo. Bright red color indicate that has less water at leafs, grass, bushes, tree, etc. Dark shades of red color on image are less, often at boundary between rural and urban areas [1]. Those shades indicate to well vegetation (less percents). Dark shades of red color observed on South part of images (mountain Bukulja and North section of Rudnik). The shades of rose red color are often at agriculture areas near rivers (Velika Morava, Jasenica). It is for used divers class of agriculture compost.

#### Conclusion

Possibility analysis of vegetation using processing satellite images of infrared spectral wave are comprehensives. Processing of color composite images are important, so and base instrument for control and management environment [4]. Area of research is the great, himself propagate at 60 x 60 km. Terrain work has relieved and possibility of laboratories work has more. The primary aim of this study is detection and control all of elements at environment. Images which were bought for necessaries production PhD thesis were relative old, but images of new date are with new-laid data of environment for showed areas of Serbia (I am not at possibility that buy images of new date, because really costly).

- [1] Artiola at al., 2004 F. Artiola, I. Pepper and M.Brusseau, *Environmental Monitoring and Charakterization, Elsevier Academic Press, San Diego, California* (2004).
- [2] Goldschleger at al., 2002 N. Goldschleger, E. Ben Dor, Y. Benyamini, D. Blumberg and M. Agassi, *Spectral properties and hydraulic conductance of soil crusts formed by raindrop impact*, *International Journal of Remote Sensing*, 2002, **23(19)**, 3909-3920.
- [3] Kušan, 1996 V. Kušan, Kartiranje šuma pomoću Landsat TM satelitskih snimaka, Šumarski fakultet, Sveučilište u Zagrebu, Zagreb, (1996).
- [4] Lješević, 2005 M. Lješević, Životna sredina teorija i metodologija istraživanja, Geografski fakultet Univerziteta u Beogradu, Beograd, (2005).
- [5] Salisbury at al., 1992 W. Salisbury, S. Walter, N. Vergo and M. D'Aria, Infrared Spectra of Minerals and Soil, The John Hopkins University Press, Baltimore, Maryland, USA, (1992).

### IMPACT OF THE GEOGRAPHIC FACTORS ON THE TRANSPORT OF LEAD AND CADMIUM IN THE AIR

S. Milovanović<sup>1</sup>, J. Stasić<sup>1</sup>, Lj. Matovic<sup>1</sup>, J. Grbović-Novaković<sup>1</sup>, B. Matović<sup>1</sup> and M. Ljesević<sup>2</sup>

<sup>1</sup>Institute for Nuclear Sciences Vinča, Laboratory of Material Science, P.O.box 522, 11000 Belgrade, Serbia

#### **Abstract**

The aim of this study is to describe the effect of geographical varieties on the transport of lead and cadmium in the air. During period between 1997-2006, the concentrations of lead in suspended in the air at 5 measuring sites in Serbia were measured. The minimal measured daily concentrations of lead ranged from 0,42  $\mu$ g/m³ (2002.) in Kraljevo. The maximal measured daily concentrations of lead to 251,8  $\mu$ g/m³ (2004.) in Belgrade. During the period between 1997-2006., the concentrations of cadmium in suspended in the air at 5 measuring sites in Serbia were measured. The minimal measured daily concentrations of cadmium ranged from 0,1  $\mu$ g/m³ (1999) in Kraljevo. The maximal measured daily concentrations of lead to 42,0  $\mu$ g/m³ (2000) in Belgrade. Results from our experiments demonstrated that when rapid infiltration conditions or a rainstorm exist, particle-facilitated transport of contaminants is likely to the dominant metal transport pathway influenced by acid rain.

#### Introduction

To make an accurate assessment of the ecological risk of contaminants in soil, it is necessary to be able to quantitatively estimate the mobility of contaminants. However, attempts to describe and predict contaminant transport cannot succeed if major pathways and mechanisms for transport are not defined [1]. Most predictions of contaminant transport have been based on a two-phase system in which contaminants partition between the immobile solid constituents and the mobile aqueous phase [2]. It is generally assumed that metals are adsorbed by the soil solid phase with low mobility in soil. Some particles in the soil solid phase, however, also may be mobile in soil, and these particles are relatively reactive with respect to sorption of chemical species due to their large specific surface area and high number of functional surface groups [3]. Once mobilized, these particles may bind contaminants and enhance contaminant transport in soil [1-4].

Urban aerosol is a mix of a background aerosol resulting from long distance transport and "fresh" locally emitted particles. The latter ones are mainly composed of organic compounds, elemental carbon, water, metal oxides and salts containing ammonium, sulphate or nitrate species depending on the source of emission [5]. In fact, transport sector can be considered as an important source of diffuse pollution to the environment.

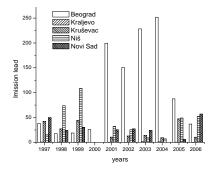
<sup>&</sup>lt;sup>2</sup>Faculty of Geography, University of Belgrade, Studentski trg 3/III, 11000 Belgrade, Serbia

#### **Experimental**

The studied sites are located in five measuring points (Belgrade, Kraljevo, Krusevac, Nis and Novi Sad). Over the past 10 years, four of the five measuring points for monitoring air quality indicated sizeable differences in pollution. The main factor which defines weather and climate of measuring points is a geographic location etc. "geografical width and length, the height above sea level, surrounding by mountains and distance from the rivers

#### Results

In the Fig.1 the changes in imission of lead in Serbia between 1997 and 2006 has been presented. The biggest emission of sedimental substances from 251,8  $\mu g/m^2/day$  was found to be in 2000 in Belgrade, which is located on 44°49'14" geografical width and 20°27'44" geografical length and AT 116,75 m height above sea level



Beograd

Kraljevo

Kruševac

Novi Sad

Niš

20

1997 1998 1999 2000 2001 2002 2003 2004 2005 2006

years

**Fig.1.** Changes in imission of lead between 1997 and 2006

Sources: Institute of public health of Serbia "Dr Milan Jovanovic Batut"

**Fig 2.** Changes in imission of cadmium between 1997 and 2006.

Sources: Institute of public health of Serbia "Dr Milan Jovanovic Batut"

The lowest emission has been found in 2002. in Kraljevo, which is located on  $43^{0}34'26''$  geografical width and  $21^{0}41'49''$  geografical length and on 246 m height above sea level as shown in Figure 1. As it is shown in Fig. 2 the biggest emission of sedimental substances from 42  $\mu g/m^2/day$  was found in 2000 while the lowest emission has been found in 1999. in Kraljevo.

#### Conclusion

The inflence of geografical factors on diffusion of pollution substances in the air is showed. During period from 1997 to 2006 the research was done on the diffrent industrial localities in Serbia: Belgrade, Kraljevo, Kruševac, Niš i Novi Sad. It was showen that there is connection between geo-systems and geographical environment from one side and physical-chemical processes from other side. As

the relief of select localities, the location of the cities, the industrial development of the cities are different the influence of meteorological parameters and diffusion of pollution substances is different too. Some characteristic shapeof topography have a clear and expressive influence to meteorological parameters and so on space distribution of concentration of pollution substances.

#### Acknowledgement

This work is supported by Serbian Ministry of science under project 142016.

- [1] McCarthy and Zachara, 1989 J.F. McCarthy and J.M. Zachara, Environ. Sci. Technol., 1989, 23, 496–502.
- [2] Puls and Powell, 1992 R.W. Puls and R.M. Powell, Environ. Sci. Technol., 1992, 26, 614–621.
- [3] Grolimund et al., 1996 D. Grolimund, M. Borkovec, K. Barmettler and H. Sticher, *Environ. Sci. Technol.*, 1996, **30**, 3118–3123.
- [4] Lagdsmand et al., 1999 M. Lagdsmand, K.G. Villholth, M. Ullum and K.H. Jensen, Geoderma., 1999, 93, 33–59.
- [5] Ryan and Elimelech, 1996 J.N. Ryan and M. Elimelech, *Colloids Surface A*, 1996, **107**, 1–56.

# DETERMINATION OF Pb AND Mn IN TREE-RINGS AND BARK OF LINDEN (Tilia platyphyllos Scop.) BY U-SHAPED DC-ARC

D.M. Marković<sup>1</sup>, I. Novović<sup>1</sup>, D. Vilotić<sup>2</sup> and V. Srećković<sup>1</sup>

<sup>1</sup>Institute of Physics, Pregrevica 118, Belgrade, Serbia
<sup>2</sup> Faculty of Forestry, University of Belgrade, Kneza Viseslava 1, Belgrade, Serbia,
<sup>3</sup> Faculty of Physical Chemistry, University of Belgrade, Studentski trg 12-16, Belgrade, Serbia

#### **Abstract**

As an indicator of environmental pollution we collected tree-rings and bark of *Tilia platyphyllos* Scop. from urban area of Zemun. An argon-stabilized U-shaped DC arc with a system for aerosol introduction was used for determination of Pb and Mn. The mean concentrations of Pb and Mn in tree-rings and bark are higher than corresponding concentration of Mn.

#### Introduction

Heavy metals are natural components in the environment, but are of concern lately because they are being added to soil, water, and air in increasing amounts. Heavy metals that get into plants, animals, are not degraded, pointing to their accumulation. Increasing urbanisation results in the production of a wide range of different pollutants that can have an adverse effect on the surrounding environment. The primary sources of anthropogenic emission of most trace metals are the combustion of fossil fuels and automobile exhaust emission in certain areas and they now exceed or equal their natural emission [1].

Dendroanalysis, the method of analyzing tree-rings for trace metal pollution is based on the assumption that element concentrations in the tree represent element availability in the environment in which the tree was grown [2]. Some authors have successfully shown a correlation between environmental pollution and the concentration of heavy metals in the growth rings [2, 3, 4, 5]. Tree-bark, has been found to be useful bioindicator for monitoring airborne pollution [6, 7].

The knowledge of the elemental content of wood, bark and other plant related materials could be of great interest for industrial and environmental authorities, since monitoring with plants supplies low-cost information on the environmental quality and quantity [8]. Considering the increasingly stricter demands for environmental control, the development of very sensitive methods for the detection of trace elements in natural samples and complex matrices is of great significance. The spectrochemical method applied in the study is a simple method for determination of low concentrations.

*Apparatus*. The experimental operational conditions of our spectrochemical method are presented in Table I.

Excitation source	U-shaped DC arc
Spectrograph	PGS-2, Carl Zeiss, Jena
Grating	Carl Zeiss, 2100 gr./mm
Photomultiplier	Hamammatsu, R-3788
AD conversion card	ED-300
Arc current	7.5 A
Argon flow	3dm³/min
Wavelength for Pb	405.78 nm
Wavelength for Mn	403.08 nm

**Table I.** Experimental operating conditions of our spectrochemical method

**Solutions.** A series of Pb and Mn reference solutions in the range from 10 to 1000 ng/mL was prepared by appropriate dilution of the stock solution (1 mg/mL, Merck). Each solution contained 0.5 % potassium chlorate as a spectroscopic buffer.

*Sampling location.* Tree-ring and bark samples were collected in March 2007 from location Zemun (urban area 10 km NW from the center of the Belgrade). Each *Tilia platyphyllos* Scop. core was divided into 3 year segments between 1971 and 2006.

Sampling preparation. Tree-ring samples (3 year segments) were placed in prewashed ( $15\% \ H_2SO_4$ ) 50mL borosilicate glass tubes dried at  $70^{\circ}C$  for 48h and weighed. Samples were suspended in 10 mL of 70 % HNO<sub>3</sub> at 80°C for 24h. The cold solution was filtered through acid washed ( $10\% \ HNO_3$ ) Whatman No. 42 filter paper and diluted to 50 mL with bidistilled water [9].

#### **Results and Discussion**

The mean concentrations of Pb and Mn found in *Tilia platyphyllos* Scop. tree-rings from the location Zemun between 1971 and 2006, in bark and soils are shown in Table II.

**Table II.** The mean concentrations of Pb and Mn in *Tilia platyphyllos* Scop. treerings from the location Zemun between 1971 and 2006, in bark and soils.

	Mean values of tree-rings between 1971 and 2006	bark	Soil total	Soil available
$C_{Pb} (\mu g/g)$	4.09	63.53	126.57	19.99
$C_{Mn} (\mu g/g)$	1.17	14.44	483.97	96.87

In Table III are shown relations and differences in the mean Pb and Mn concentrations in tree-ring in *Tilia platyphyllos* Scop., bark and soils from the location Zemun.

**Table III.** Ratios and differences in the mean Pb and Mn concentrations in treerings in *Tilia platyphyllos* Scop. between 1971 and 2006, bark and soils from the location Zemun.

Element	C <sub>bark</sub> / C <sub>wood</sub>	$C_{bark}/C_{soil\ total}$	$C_{bark} / C_{soil \ available}$	$\Delta C = C_{\text{bark}} - C_{\text{wood}}$ $(\mu g/g)$
Pb	15.53	0.5	3.18	59.44
Mn	12.34	0.03	0.15	13.27

The results presented in this paper indicate that the values for Pb are higher than values for Mn in all cases except in cases soils (total and availables). Concentrations of Pb in soils are lower than concentrations of Mn. However, mean concentrations of Pb in tree-rings and in bark are higher than corresponding concentrations of Mn.

#### Conclusion

In this study Pb and Mn contents in *Tilia platyphyllos* Scop. tree-rings and soils from the location Zemun were monitored and compared. The mean concentrations of Pb in *Tilia platyphyllos* Scop. tree-rings and bark are higher than concentrations of Mn in tree-rings and bark. This is mainly consequence automobiles traffic and combustions of fossil fuels.

- [1] O. Odukoya, T.A. Arowolo, O. Bamgbose, Environ. Internat., 2000, 26, 11-16.
- [2] K.L. Padilla, K.A. Anderson, Chemosphere, 2002, 49, 575-585.
- [3] Jonsson, M.Eklund, K. Håkansson, J. Environ, Oual., 1997, 26, 1638-1643.
- [4] B.E. Cutter, R.P. Guyette, J. Environ. Qual., 1993, 22, 611-619.
- [5] G.Liu, Y. Zhang, Y. Qi, L. Zheng, Y. Chen, Z. Peng, Environ. Monit. Assess., 2007, 133, 99-103.
- [6] H. Schulz, P. Popp, G. Huhn, H.J. Stark, G. Schurmann, Science Total Environ., 1999, 232, 49-58.
- [7] L. Harju, K.E. Saarela, J., Rajander, J.O. Lill, A. Lindroos, S.J. Heselius, Nuclear Instrum.Methods B, 2002, **189**, 163-167.
- [8] S. Rossini Oliva, M. D. Mingorance, Chemosphere, 2006, 65, 177-182.
- [9] M. Orlandi, M. Pelfini, M. Pavan, M. Santilli, M. P. Colombini, Microchem. J., 2002, 73, 237-244.

# DETERMINATION OF Fe, Mn AND Pb IN TREE-RINGS AND BARK OF LINDEN (*Tilia platyphyllos* Scop.) FROM LOCATIONS ZEMUN AND OBRENOVAC

I. Novović<sup>1</sup>, D.M. Marković<sup>1</sup>, D. Vilotić<sup>2</sup>, Lj. Ignjatović<sup>3</sup> and V. Srećković<sup>1</sup>

<sup>1</sup>Institute of Physics, Pregrevica 118, Belgrade, Serbia

<sup>2</sup> Faculty of Forestry, University of Belgrade, Kneza Viseslava 1, Belgrade, Serbia,

<sup>3</sup> Faculty of Physical Chemistry, University of Belgrade, Studentski trg 12-16, Belgrade, Serbia

#### **Abstract**

The U-shaped DC arc with aerosol supply was applied for the determination of Fe, Mn and Pb in *Tilia platyphyllos* Scop. tree-rings and bark from the locations Zemun and Obrenovac. The mean concentrations of Mn and Pb in bark in *Tilia platyphyllos* Scop. are higher than corresponding concentrations in tree-rings.

#### Introduction

Heavy metals are present in the atmosphere in ever increasing levels as a result of anthropogenic and natural emissions. Heavy metals are long-term contaminants with the ability to accumulate in soils and plants and have no natural way to be removed. Increasing urbanization results in the production of a wide range of different pollutants that can have an adverse effect on the surrounding environment. The primary sources of anthropogenic emission of most trace metals are the combustion of fossil fuels and automobile exhaust emission in certain areas and they now exceed or equal their natural emission [1].

Dendroanalysis, the method of analyzing tree-rings for trace metal pollution is based on the assumption that element concentrations in the tree represent element availability in the environment in wich the tree was grown [2]. The presence of distinct annual rings in the wood of trees growing in temperate climates gives them a unique potential as indicators of pollution histories and numerous studies have delt with the use of tree-rings as historical monitors of heavy metal pollution [2, 3, 4, 5]. Tree-bark, has been found to be useful bioindicator for monitoring airborne pollution [6, 7].

Considering the increasingly stricter demands for environmental control, the development of very sensitive methods for the detection of trace elements in natural samples and complex matrices is of great significance. The spectrochemical method applied in the study is a simple method for determination of low concentrations

#### **Experimental**

The experimental operational conditions of our spectrochemical method are presented in Table I.

Excitation source	U-shaped DC arc
Spectrograph	PGS-2, Carl Zeiss, Jena
Grating	Carl Zeiss, 2100 gr./mm
Photomultiplier	Hamammatsu, R-3788
AD conversion card	ED-300
Arc current	7.5 A
Argon flow	3dm³/min
Wavelength for Fe	371.99nm
Wavelength for Mn	403.08 nm
Wavelength for Pb	405.78 nm

Table I. Experimental operating conditions of our spectrochemical method

In this study, Fe, Mn and Pb concentrations were measured in annual tree rings in linden growing in Obrenovac. Tree-ring and bark samples were collected in March 2007 from location Zemun and Obrenovac. The first measuring site was in urban area 10 km NW from the center of Belgrade, the second one was in Obrenovac 42 km upstream from the Serbian capital, Belgrade. Each *Tilia platyphyllos* Scop., core was divided into 3 year segments. Tree-ring samples (3 year segments) were placed in pre-washed (15% H<sub>2</sub>SO<sub>4</sub>) 50mL borosilicate glass tubes dried at 70°C for 48h and weighed. Samples were suspended in 10 mL of 70 % HNO<sub>3</sub> at 80°C for 24h. The cold solution was filtered through acid washed (10 % HNO<sub>3</sub>) Whatman No. 42 filter paper and diluted to 50 mL with bidistilled water [8]. A series of reference solutions ( Fe, Mn and Pb) were prepared in the range from 5 to 5000 ng/mL, by appropriate dilution of the stock solution (1 mg/mL, Merck). Each solution contained 0.5 % potassium chlorate as a spectroscopic buffer.

#### **Results and Discussion**

The mean concentrations of Fe, Mn and Pb in *Tilia platyphyllos* Scop. in tree-rings and bark from the locations Zemun and Obrenovac are shown in Table II.

**Table II.** The mean concentrations of Fe, Mn and Pb in *Tilia platyphyllos* Scop. in tree-rings and bark from the locations Zemun and Obrenovac between 1971 and 2006 and bark.

	Zemun		Obrenovac		
C	Mean values of tree-		Mean values of tree-		
$(\mu g/g)$	rings befween 1971	bark	rings befween 1971	bark	
	and 2006		and 2006		
Fe	83.94	67.84	22.31	162.53	
Mn	1.17	14.44	2.09	11.07	
Pb	4.09	63.54	3.87	29.85	

In Table III are shown differences and ratios in the mean Fe, Mn and Pb concentrations in tree-rings and bark in *Tilia platyphyllos* Scop. from the locations Zemun and Obrenovac.

**Table III** Differences and ratios in the mean Fe, Mn and Pb concentrations in treerings and bark in *Tilia platyphyllos* Scop. from the locations Zemun and Obrenovac between 1971 and 2006 and bark.

	Zemun		Obrenovac	
	$\Delta C = C_{\text{bark}} - C_{\text{tree-rings}}$ $(\mu g/g)$	$C_{bark}/C_{tree\text{-rings}}$	$\Delta C = C_{\text{bark}} - C_{\text{tree-rings}}$ $(\mu g/g)$	$C_{bark}/C_{tree-rings}$
Fe	-16.10	0.81	140.22	7.29
Mn	13.28	12.34	8.98	5.30
Pb	59.45	15.53	25.98	7.71

In almost all cases the average values concentrations of Fe, Mn and Pb in bark were higher than in tree-rings except in case of Fe from the location Zemun. The heist ratio of  $C_{\text{bark}}/C_{\text{tree-rings}}$  is for Pb from the location Zemun. The results presented in this paper indicate that the value ratio for Pb from Zemun was 15.53 and from Obrenovac 7.71.

#### **Conclusions**

In this study Fe, Mn and Pb contents in *Tilia platyphyllos* Scop. tree-rings and bark from the locations Zemun and Obrenovac were compared. The mean concentrations of Mn and Pb in *Tilia platyphyllos* Scop. bark are higher than corresponding concentrations in tree-rings.

- [1] O. Odukoya, T.A. Arowolo, O. Bamgbose, Environ. Internat., 2000, 26, 11-16.
- [2] K.L. Padilla, K.A. Anderson, Chemosphere, 2002, 49, 575-585.
- [3] Jonsson, M.Eklund, K. Håkansson, J. Environ. Qual., 1997, 26, 1638-1643.
- [4] B.E. Cutter, R.P. Guyette, J. Environ. Qual., 1993, 22, 611-619.
- [5] G.Liu, Y. Zhang, Y. Qi, L. Zheng, Y. Chen, Z. Peng, Environ. Monit. Assess., 2007, 133, 99-103.
- [6] H. Schulz, P. Popp, G. Huhn, H.J. Stark, G. Schurmann, Science Total Environ., 1999, 232, 49-58.
- [7] L. Harju, K.E. Saarela, J., Rajander, J.O. Lill, A. Lindroos, S.J. Heselius, Nuclear Instrum.Methods B, 2002, **189**, 163-167.
- [8] M. Orlandi, M. Pelfini, M. Pavan, M. Santilli, M. P. Colombini, Microchem. J., 2002, 73, 237-244.

# INFLUENCE OF ALGAE ON QUALITY OF WATER IN RESERVOIR "GARAŠ" AND "BUKULJA"

T.D. Grozdić, A. Hegediš and D. Mutavdžić

Institute for multidisciplinary research, Kneza Višeslava 1a, 11000 Belgrade, Serbia, (gtomisi@cms.bg.ac.yu).

#### **Abstract**

Primary function of reservoir "Garaši, is storage space for raw water which can be use in production of drinking water for town Arandjelovac. Total quantity of algae is measured in period of September 2005. to October 2006. in reservoir "Garaši" and "Bukulja". Quantity of algae is also measured vs. depth of reservoir. Natural production of algae is maximal during summer seasons and when its decay occurs, as well. All this cause a degradation of water quality.

#### Introduction

Water quality directly is connected with biomass quantity of phytoplankton (e.g. cyanobacteria) and increase of chlorophyll a, decrease of water clearness and/or increase turbidity. All this facts is connected with natural production of algae and show as quantity of it's primary production, and day-night oxygen regime, shortage of oxygen in layer of water near the bottom of reservoir, increase of quantity of nutrients (phosphorus, nitrogen), increase of value for COD and BODs

The raw water, from reservoir, ought to have optimal quality characteristics (as chemical and/or biochemical properties) in case to be exploited for drinking water [1]. The main problem is tropic index of raw water, which is dependent of eutrofication. Process of eutrofication can occur slowly or can be accelerated by increase concentration of nutrients (P, N) in water. Nutrients accelerate process of production phytoplankton and improve quantity of algae.

#### **Results and Discussion**

In both reservoir is detected 145 takson from six type of algae: ciyanophyta, pyrophyita, cryophyte, bacillariophyta, chlorophyta and euglenophyta [2]. In "Garaši" and "Bukulja" reservoir are detected 116 and 110, respectively. Variety of taksons is detected in November 2005. year (see Fig 1.)

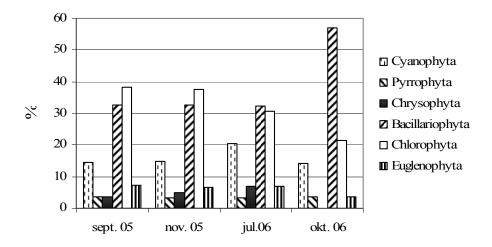
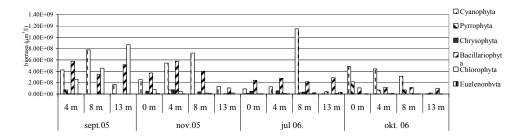


Fig. 1. Cenotic composition of phytoplanetons in reservior ,, Garaš,,[4].

Total number phytoplankton in reservoir "Garaši"( see Fig.2) is detected in region from minimum  $2.9x10^5$  cell./dm³ in October 2006, on the 13m depth, to maximum  $2.14x10^7$  cell./dm³ in Jull 2006. year on 8m depth.

In reservoir "Bukulja,, total number phytoplankton is detected in region from minimum  $1.9x10^6$  cell./ dm³ in November 2005. year on 8m depth, and maximum  $1.3x10^7$  cell./ dm³ in Jull 2006. on 8m depth.



**Figure 2.** Vertical distribution of biomass phytoplankton in reservoir "Garaši, [4]

Overproduction algae occurs parallel with overproduction of fish, especially young fish (sprout). Young fish is mainly feed by zooplankton, which directly lead to disturbance in plankton community and disturbance in ratio of phyto and zooplankton and overproduction (blooms) variety of algae, especially cianobactery, blue-green. The optimal conditions for decrease algae overproduction can be reach

by decreasing concentration of nutrients. Total amount of  $PO_4$  is 0.02 mg/ dm<sup>3</sup>,  $NH_4^+$  is 0.17 mg/ dm<sup>3</sup>,  $NO_2^-$  is 0.021 mg/ dm<sup>3</sup>,  $NO_3^-$  is 2.2 mg/ dm<sup>3</sup>, measured at 07.07.2005. year.

#### Conclusion

Natural overproductions and quantity of algae it turn out that ecosystem is close to collapse. Ratio of phyto and zooplankton and overproduction (blooms) algae is disturbed. The great number of cyanobacteria (blue-green) is produced [3, 4]. Improvement overproduction of algae is helped by increase concentrations of nutrients (nitrogen and phosphorus substances). Higher concentration of nutrients make optimal conditions for production algae. The facts are high density and biomass of phytoplankton, and high concentration hydrophilic a. All these facts point out that occurs an intensive process of eutrophication of both reservoir [5]. Saprobic analyze show that water quality in reservoir are between II and III class, i.e., from  $\beta$ -mezzo to  $\alpha$ -mezosaprobna [6].

- [1] A.Hegediš, T.Grozdić, V.Karadžić, Problem ribarstvenog gazdovanja na akumulacijama za vodosnabdevanje, Ecologica, 2007, **14**, 103-106.
- [2] H. Utermohl, Zur vervolkmmung der quantitativen phytoplankton methodik. Mitt. int. Ver. Limnol., 1958, **9**, 1-38R.
- [3] ISO 10260 Water quality: Measurement of biochemical parameters Spectrometric determination of the chlorophyll a concentration, 1992.
- [4] E.F.Round, The Biology of the Algae, ed. Edward Arnold., London, 1970, 269.
- [5] J.J.Elser, The pathway to noxious cyanobacteria blooms in lakes: the food web as the final turn. Freshwater Biology, 1999, **42**, 537-543.
- [6] E.R.Carlson, A trophic state index for lakes. Limnol. Oceanogr., 1977, 22, 361-368.

#### ADSORPTION OF AFLATOXIN B<sub>1</sub> BY COPPER AND ZINC MODI-FIED MONTMORILLONITES

A. Daković<sup>1</sup>, Ž. Sekulić<sup>1</sup>, G.E. Rottinghaus<sup>2</sup>, D.R. Ledoux<sup>3</sup>, S. Milićević<sup>1</sup> and P. Butkeraitis<sup>3</sup>

<sup>1</sup>Institute for Technology of Nuclear and Other Mineral Raw Materials, P. O. Box 390, 11 000 Belgrade, Serbia <sup>2</sup>Vet. Med. Diag. Lab., College of Veterinary Medicine, University of Missouri, Columbia, MO 65211, USA <sup>3</sup>Animal Science Center, University of Missouri, Columbia, MO 65211-5300, USA

#### **Abstract**

Results of *in vitro* aflatoxin  $B_1$  adsorption by natural montmorillonite (MONT) and montmorillonites modified with copper (Cu-MONT) and zinc ions (Zn-MONT) are presented in this paper. The Cu-MONT and Zn-MONT were obtained via ion exchange of inorganic cations in montmorillonite with copper and zinc ions. Investigation of AFB $_1$  adsorption by MONT, Cu-MONT and Zn-MONT at different amounts of solid phase in suspension and at different pH values showed that adsorption of aflatoxin  $B_1$  by all MONTs was high (over 93%). No differences in AFB adsorption by MONTs at pH 3, 7 and 9, were observed.

#### Introduction

Aflatoxins comprise a diverse group of pervasive, naturally occurring, fungal elaborated toxins that have been strongly implicated in animal deseases. *Aspergillus* fungi frequently produce aflatoxin  $B_1$ ,  $B_2$ ,  $G_1$  and  $G_2$ . Aflatoxin  $B_1$  (AFB<sub>1</sub>) is the most toxic and carcinogenic of the aflatoxins [1]. The chemical structure of AFB<sub>1</sub> is presented in Figure 1.

Fig. 1. Chemical structure of AFB<sub>1</sub>

The most promising and practical approach for reducing aflatoxicosis has been the addition of nonnutritive adsorptive materials to contaminated feed. Aluminosilicates – natural zeolites, and natural bentonites – montmorillonite are the most commonly used adsorbents. Montmorillonite (MONT), a smectite clay with a 2:1 layer structure, has the ability to effectively reduce AFB<sub>1</sub> toxicity to animals. On the other hand, Xia et al. reported that copper carried on MONT has antibacte-

rial activity against E. Coli and Clostridium [2]. It is possible that modifying MONT with copper or zinc ions may affect its ability to bind AFB<sub>1</sub>.

In this study, the *in vitro* adsorption of AFB<sub>1</sub> by MONT, Cu-MONT and Zn-MONT was investigated, at different pHs. The main objective of this study was to compare the adsorption of AFB<sub>1</sub> by these materials..

#### **Experimental**

The starting material was a natural bentonite from the Šipovo deposit (Bosnia). Its composition was approximately 90% montmorillonite with small amounts of quartz and calcite based on X-ray powder diffraction analysis. From the raw material, particles larger than 5  $\mu$ m were separated in a centrifuge. The <5  $\mu$ m fraction – concentrate of montmorillonite (MONT) was dried at 80°, and then milled to less than 63  $\mu$ m. The total cation exchange capacity of MONT was 92.2 meq/100g.

Copper and zinc modified MONTs were prepared by stirring the MONT (2 g) for 6 h in the the copper or zinc solution (100 mL of 0.02 M CuSO<sub>4</sub> ·  $5H_2O$  or  $ZnSO_4 \cdot 7H_2O$ ) at  $60^{\circ}C$ . The products were centrifuged at 10,000 rpm for 10 min, washed with distilled water until Cu<sup>2+</sup> or  $Zn^{2+}$  ions were not detected, dried at  $80^{\circ}C$  to a constant mass, and ground to a size less than 63 µm. The total cation exchange capacities of the Cu-MONT and Zn-MONT were 90.7 meq/100g and 91.6 meg/100g, respectively

In order to investigate  $AFB_1$  adsorption by MONT, Cu-MONT, and Zn-MONT, 10 or 5 mg of each adsorbent was added to centrifuge tubes and 10 mL of  $AFB_1$  buffer solution (pH 3, 7 or 9) were added at a concentration of 4 ppm.  $AFB_1$  concentrations in buffer solutions with and without mineral adsorbents were determined by HPLC.

#### **Results and Discussion**

Copper and zinc modified montmorillonites were obtained by ion exchange of inorganic cations in MONT with copper and zinc ions. The copper content in Cu-MONT was 2.35%, while the zinc content in Zn-MONT was 2.45% based on atomic absorption spectrophotometry.

AFB<sub>1</sub>, a fairly nonpolar molecule, is a member of the dihydrodifurano-coumarin group and contains a  $\beta$ -keto-lactone functional group [1]. The results of AFB<sub>1</sub> adsorption by MONT, as well as Cu-MONT and Zn-MONT, at different pHs are presented in Table 1. Percent of AFB<sub>1</sub> bound was calculated from the difference between the initial and final concentration of AFB<sub>1</sub> in the aqueous supernatant. As can be seen from Table 1, AFB<sub>1</sub> adsorption by all three MONTs was high (over 93%). Since AFB<sub>1</sub> is not ionizable (Figure 1), no differences in adsorption, at pH 3, 7 and 9, were expected, and none were observed. Similar results were obtained by Ledoux et al. [3] for *in vitro* adsorption of AFB<sub>1</sub> by Improved Milbond TX<sup>®</sup> (IMTX) – hydrated sodium calcium aluminosilicate (MONT). They reported that IMTX was able to bind 100% of AFB<sub>1</sub> at pH 3, and the binding ability of IMTX for AFB<sub>1</sub> did not change as the pH increased from 3 to 9.

**Table 1.** Adsorption of AFB<sub>1</sub> by MONT, Cu-MONT, and Zn-MONT, at pH 3, 7 and 9

	AF	B <sub>1</sub> adsorption indexes	s, %
	pH 3	pH 7	pH 9
MONT (mg/mL)			
1	100	98	96
0.5	100	96	94
Cu-MONT			
(mg/mL)			
1	98	98	96
0.5	98	97	93
Zn-MONT			
(mg/mL)			
1	99	98	96
0.5	100	94	93

#### **Conclusions**

Results presented in this paper demonstated that the effectiveness of MONT to bind  $AFB_1$  was not altered by ion exchange of inorganic cations in MONT with copper and zinc ions. The known antibacterial activity of Cu-MONT and Zn-MONT and their high affinity for binding  $AFB_1$  as well as the simple ion exchange of inorganic cations in MONT with copper and zinc make these materials suitable for potential practical application.

- [1] IARC Monographs On Evaluation Of Carcinogenic Risks To Humans, Some naturally occurring substances: Food items and constituents, heterocyclic aromatic amines and mycotoxins, IARC, Lyon, France, 1993, **56**, 445.
- [2] M. S. Xia, C. H. Hu, Z. R. Xu, Poultry Science 2004, 83, 1868.
- [3] D. R. Ledoux, G. E. Rottinghaus, A. J. Bermudez, M. Alonso-Debolt, Poultry Science 1999, **78**, 204.

#### PESTICIDE-ORGANOCLAY INTERACTIONS

D. Kovacevic<sup>1</sup>, J. Lemic<sup>2</sup>, S. Zildzovic<sup>1</sup> and D. Iles<sup>1</sup>

<sup>1</sup>Institute for Technology of Nuclear and Other Raw Materials, Belgrade, 86 Franchet d' Esperey St, Serbia, 

<sup>2</sup>LAD Group, Belgrade, 7/I Milesevska St, Serbia

#### **Abstract**

Replacement of natural inorganic cations of clay minerals with organic cations has been proposed as a strategy to improve the adsorptive capacity of clay minerals for organic compounds, including pesticides. The organic cations most commonly used for this purpose have been quaternary ammonium ions containing alkyl or aryl chains without specific functional groups. The objectives of this work were to assess the adsorption capacity of organoclay minerals for pesticide fenitrothion (0,0-dimethyl 0-40 nitro-m-tolyl phosphorothiate) as related to amount of stearyl dimethyl benzyl ammonium cation (SDBA) on mineral surface.

#### Introduction

Adsorption of hydrophobic organic pesticides on a hydrophilic clay minerals and zeolites is suppressed in the presence of water because relatively hydrophobic pesticides can not effectively compete with highly polar water with hydrophilic adsorption site on clay surfaces. Organoclays and zeolites, i.e. natural clay minerals with their orginal inorganic exchangeable cations replaced with organic cations, have been shown to be excellent sorbents for different kinds of pesticides, and accordingly have been proposed for decontamination purposes [1, 2] and also as carriers for controlled release of pesticides [3, 4].

The objectives of this work were to assess the adsorption capacity of organoclay minerals for pesticide fenitrothion (0,0-dimethyl 0-40 nitro-m-tolyl phosphorothiate) as related to amount of stearyl dimethyl benzyl ammonium cation (SDBA) on mineral surface.

Bentonite from the Sipovo deposit in Bosnia was used as the starting material for the sorption experiments. The surfactant SDBAC was purchased from Hoest, Germany, with the specification of technical purity. The report presented by the manufacturer indicates that the surfactant, besides the active ingredient, also contained propan-2-ol ( $\sim$ 20%) and water ( $\sim$ 1%), which was considered in calculating the concentration of the surfactant in solution. The adsorbates used in this study were technical grade pesticides (95% active substance) obtained from the Sumitomo Chemical Company LTD, Japan.

Preparation of organo-minerals: The bentonite was modified using SDBAC solutions of five initial concentrations: 200, 500, 800, 1200 and 1600 mmol /dm³. The ratios CEC/SDBAC were 1:0.25, 1:0.62, 1:1, 1:1.5 and 1:2. The prepared organo-bentonites were denoted as: B20, B50, B80, B120 and B160 where the Arabian numerals denote loading mmol SDBAC /100 g minerals.

Adsorption of fenitrothione on the different loaded surfactant: The organomineral samples of different SDBAC loading was added to 100 cm<sup>3</sup> of fenithrothione solution in 25% ethanol having a concentration of 10mg/dm<sup>3</sup>. The adsorption index is defined as percent of the initial amount of fenitrothione adsorbed on the mineral surface.

Adsorption isoterms: The adsorption of pesticide onto the organo-minerals was investigated by batch experiments. Pesticides were dissolved in 25% (v/v) ethanol solution with concentrations up to its solubility limit in water. In these experiments, 1.0g of the organo- mineral samples with highest adsorption index (B80) was shaken with  $100~\rm cm^3$  of fenitrothion solution (25% ethanol) with a concentration ranging from 18 to  $1299.6 \mu mol/dm^3$ .

#### **Results and Discussion**

Adsorption of fenitrothione on the organo-minerals: The amount of fenitrothione adsorbed on the organomineral surface increased with SDBAC loading up to cation exchange capacity of the minerals. The adsorption indexes of the organo-bentonite were in the range of 90-99%. The maximal adsorption for pesticide, at a given concentration of solution, was achieved at monolayer surface coverage, which can be ascribed to an intensification of the hydrophobic properties of the mineral surface. The adsorption indexes of samples B80, at an given concentration of solution, were 99%.

Adsorption experiments: The equilibrium relationships between a sorbent and a sorbate are described by sorption isotherms, which represent the ratio between the amount adsorbed and that remaining in the solution at a fixed temperature under equilibrium conditions. Over the examined range, the experimental results were fitted to the isotherm equations:

Langmuir: n=K C M / (1+K C)

Freundlich:  $n=(K C)^{\beta}$ 

Langmuir - Freundlich:  $n=(K C)^{\beta} M / (1+(K C)^{\beta}),$ 

where n is the amount adsorbed per kilogram of organo-mineral (mmol/kg); K the surface adsorption equilibrium constant (mmol/dm³)  $^{-1}$ ; M the maximum amount adsorbed per kilogram of organomineral (mmol/kg); C the equilibrium solution concentration (mmol/dm³); and  $\beta$  the heterogeneity factor which is related to the affinity of surface.

On the basis of the correlation coefficients,  $R^2$ , the applicabilities of different isotherm equations were compared. The best fits of the experimental data were obtained using the Freundlich model ( $R^2$ =0.999) (Tabla 1).

3	*			
Parameters	$R^2$	K ( $\mu$ mol <sup>-1</sup> dm <sup>3</sup> ) ( $\beta$ =1)	$M (\mu mol g^{-1})$	β
Langmuir	0.9800	0.170044	109.378	
Freundlich	0.9999	27.125		0.367
Langmuir - Freundlich	0.9995	0.00177	431.143	0.434

**Table 1.** Adjustable parameters and correlation coefficients for various isotherms

#### **Conclusions**

Adsorption of fenitrothion by clay and organoclay were studied. Organoclays were prepared by the exchange of quaternary ammonium type surfactants such as stearyl dimethyl benzyl ammonium cation (SDBA) for inorganic cations like Ca<sup>2+</sup> on internal and external surface of the clays. This modification produces a change of surface property of clay from hydrophilic to hydrophobic. The adsorption equilibrium data points were fitted to Freundlich isotherm equations.

- [1] M.S. Andrades, M.S. Rodríguez-Cruz, M.J. Sánchez-Martin, M. Sánchez-Camazano, International Journal of Environmental Analytical Chemistry, 2004, **84**, 133-141
- [2] M.J. Carrizosa, M.C. Hermosín, W.C. Koskinen, J. Cornejo, Applied Clay Science, 2001, 18, 223-231
- [3] R. Celis, G. Facenda, M.C. Hermosín, J. Cornejo, International Journal of Environmental Analytical Chemistry, 2005, **85**, 1153-1164
- [4] Nennemann, Y. Mishael, S. Nir, B. Rubin, T. Polubesova, F. Bergaya, H. van Damme, G. Lagaly, Applied Clay Science, 2001, **18**, 265-275

#### REMOVAL OF COPPER BY NATURAL ZEOLITE

S. Milićević, A. Daković, V. Milošević, T. Stanić and S. Matijašević

Institute for Technology of Nuclear and Other Mineral Raw Materials,

P. O. Box 390, 11 000 Belgrade, Serbia

#### **Abstract**

Heavy metals are prior toxic pollutants in industrial wastewaters and they represent serious threat to human health, living resources and ecological systems. In this paper the ability of natural zeolite to remove copper from aqueous solution in batch reactors has been studied. In batch reactor the effect of the particle size and temperature was investigated. The adsorption of copper by clinoptilolite fractions -0,4+0,0 mm; -0,8+0,4 mm and -1,5+1,0 mm was 27,7, 26,0 and 21,9 %, respectively. It was, also determined, that temperature had no influence on adsorption of copper by two fractions (-0,4+0,0 mm; -0,8+0,4 mm) of clinoptilolite.

#### Introduction

The increasing levels of toxic metals that are discharged to the environment as industrial wastes, represent a serious threat to soil and water pollution [1]. Heavy metals (copper, zinc, etc.) are not biodegradable and tend to accumulate in living organisms, causing various diseases and disorders [2]. Although there are many sources of heavy metals, specific industrial sectors, at present time, mostly contribute to environmental pollution with these toxic metals.

Treatment processes for metals contaminated waste streams include chemical precipitation, membrane filtration, ion exchange, electrodialisys, etc. Because of the enourmous amount of these wastewaters, cost effective technologies or sorbents for the treatment should be neccessarily applied. Natural materials (zeolites, bentonites, etc.) that are available in large quantities may have potential as inexpensive sorbents [3, 4].

Zeolites are hydrated aluminosilicates of alkali and alkaline earth elements with unique crystal structures consisting of a three-dimensional framework of  ${\rm SiO_4}$  and  ${\rm AlO_4}$  tetrahedral. The negative charge of the zeolites surface is balansed by the presence of monovalent and divalent cations. In contrast to clays, zeolites occur as millimeter or larger sized particles and are free of shrink-swell behavior. As a result, zeolites exibit superiorhydraulic characteristics and are suitable for use in filtration systems.

In this paper, the adsorption of copper by clinoptilolite rich zeolitic tuff was investigated. The objective was to determine the influence of particle size and temperature on adsorption process.

#### **Experimental**

The starting material was the raw natural zeolitic tuff from Baia Mare deposit, Romania. The mineralogical composition of the starting zeolitic tuff was primarily clinoptilolite, with the smaller amounts of feldspar, calcite and quartz, as measured by X-ray powder diffraction (XRPD) analysis. The starting material had the following chemical composition: SiO<sub>2</sub>-66.87, Al<sub>2</sub>O<sub>3</sub> -13.46, Fe<sub>2</sub>O<sub>3</sub>-0.98, CaO-3.85, MgO-0.69, Na<sub>2</sub>O-0.37, K<sub>2</sub>O-2.23, loss of ignition-11,45. The cation exchange capacity (CEC) of the natural zeolitic tuff was 166 meq/100g measured with 1M NH<sub>4</sub>Cl After crushing and grinding the sample was wet sieved to obtain different fractions: -0.4+0 mm. -0.8+0.4mm and -1.5+1.0 mm.

For kinetics of copper adsorption by different fractions of natural zeolite, 1 g of each fraction was mixed with 100 mL of copper solution (C  $_{\text{Cu2+}}$ =300 mg /L) in the time interval between 1-120 min, at temperatures 25°C, 40°C and 60°C. After the reaction time, the suspensions were centrifuged at 10.000 rpm, and in supernatant, the concentration of unadsorbed copper was determined. The initial and final concentrations of copper were determined by atomic absorption spectophotometry. Percent of adsorbed copper was calculated from the difference between the initial and final concentration of copper in the aqueous supernatant.

#### **Results and Discussion**

The results of copper adsorption by different fractions of the zeolitic tuff are presented at Figure 1.

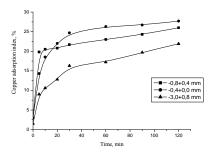
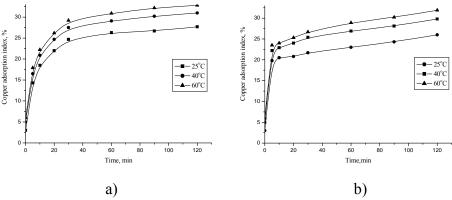


Fig. 1. Copper adsorption by different fractions of clinoptilolite vs. particle size

As can be seen from Figure 1, the decrease in copper adsorption with increasing the particle size of material is observed. This is probably associated with the reduction of the specific surface of the zeolitic tuff with increasing the particle size. After the 2 hours, the copper adsorption index by -0.4+0 mm. -0.8+0.4 mm and -1.5+1.0 mm fractions was 27,7; 26,0; 21,9%, respectively.

To study the effect of temperature on adsorption of copper by clinoptilolite, fractions -0.4+0 mm, and -0.8+0.4mm were used. The obtained results are presented in Figure 2. From Figure 2, no significant differences in copper adsorption from the aqueous solution with increasing the temperature were noticed. The copper adsorption by -0.4+0.0 mm fraction was 31.5% at 40°C and 32.8% at 60°C. Similarly,

the copper adsorption by 0.8+0.4mm fraction of clinoptilolite at 40°C and 60°C was 29.8 and 31.9 %, respectively.



**Fig. 2.** Copper adsorption by (a) -0,4+0,0 and (b) -0,8+0,4 fractions of clinoptilolite vs. temperature

#### **Conclusions**

The results reported in this paper indicated that particle size of clinoptilolite material had the influence on copper adsorption from aqueous solution. It was shown that the smallest cliniptilolite fractions (-0.4+0 mm) was more efficient than larger fractions, which was associated with the higher specific surface area and availability of the exchangeable cations at the surface. No significant differences in copper adsorption from the aqueous solution by -0.4+0 mm, and -0.8+0.4 mm fractions of clinoptilolite, with increasing the temperature were noticed.

- [1] M.A. Stylianou, V.J. Inglezakis, K.G. Moustakas, S.Ph. Malamis, M.D. Loizidou, Desalination, 2007, 215, 133-142.
- [2] M. Trgo, J. Perić, N. Vukojević Medvidović, Journal of Environmental Menagement 2006, **79**, 1893-1899.
- [3] Susan E. Bailey, Trudy J. Olin, R. Mark Bricka, D. Dean Adrian, Water Research 1999, 33, 2469-2479.
- [4] Ali Hakan Oren, Abidin Kaya, Journal of Hazardous Materials, 2006, **B131**, 59-65.

### IMMOBILIZATION OF PRINTING PLANT WASTEWATER AND CONTAMINATED SEDIMENT IN CEMENT MATRIX

M. Prica, J. Kiurski and J. Fišl

Faculty of Technical Sciences, Trg Dositeja Obradovića 6, Novi Sad

#### Abstract

Cement based stabilization/solidification process was used to immobilize zinc from contaminated sediment and printing plant wastewater. Cement based stabilization/solidification (S/S) effectiveness was evaluated by performing semi-dynamic leaching tests. The S/S effectiveness was evaluated by measuring effective diffusion coefficients (De) and leachability indices (LX). Treatment was most effective in samples treated with 40% of cement. Upon treatment LX values were higher than 9, suggesting that S/S treated samples are acceptable for "controlled utilization".

#### Introduction

The raw wastewater from printing plant can be, potentially, very polluting, depending on technology used, with increased concentrations of some metals. Thus, wastewater from the industry needs to be treated to reduce any possible impacts on the aquatic environment, but this is still not in the case in our country. Pollution by heavy metals is a serious problem because of their toxicity and ability to accumulate in biota. One of the most crucial properties of these metals, which differentiates them from other toxic pollutants, is that they are not biodegradable in the environment. In the ecosystem, sediments are the main sink for these elements, but when environmental conditions change, sediments can act as a source of metals [1].

In this study, a stabilization/solidification (S/S) process was used in order to remediate sediment contamination, because S/S techniques have been widely applied in order to treat soils with heavy metal contamination [2]. Optimum water content was achieved with waste water printing plant addittion with the aim of association of two types of waste. During S/S treatment, the hazardous waste potential of waste materials can be minimized by converting the contaminant into forms which are less-soluble, less mobile or less toxic and encapsulating the waste within a monolithic solid of high structural integrity [3, 4].

The objectives of this study were to determine the leaching behavior of zinc from cement remediated sediment and wastewater printing plant by performing semi-dynamic leaching tests, evaluate the effectiveness treatment by measuring the effective diffusion coefficient (*De*) and leachability index (LX).

#### **Results and Discussion**

Zn sediment content was 1250 mg kg<sup>-1</sup>. In accordance with Dutch regulation standards [5] sediment is severely polluted with zinc (class 4) and needs dredging, dis-

posal in special reservoirs and if possible, sediment clean-up measures. Zn content in waste water from printing plant was 110 mg l<sup>-1</sup> which is far above MDL for municipal waste waters [6]. Sediment possessing an average initial moisture content of 65% was dried at 105°C to the constant mass. Cement addition was 5, 10, 15, 20, 30 and 40% by wt. (samples S1, S2, S3, S4, S5, S6 respectively). The optimum water content was achieved with the addition of wastewater from printing plant. Following compaction, all specimens were cured for 28 days in sealed sample bags at 20 °C. The effectiveness of cement immobilization was assessed using the American Nuclear Society (ANS) 16.1 test [3, 7]. ANS 16.1 is a semi-dynamic leaching test that evaluates the release of metals in a diffusion-controlled environment. Specifically, the cumulative fraction of zinc leached over time can be determined using this method. Using ANS 16.1 model [3, 4], we can calculate the effective diffusion coefficients (D<sub>c</sub>). This model employs Fick's diffusion theory and provides diffusion rates that can be applied to evaluate the effectiveness of the S/S treatment. Once the De values are determined the leachability index (LX) could be obtained as the negative logarithm of the effective diffusivity. In accordance with Waste Technology Centre [7], LX values can be considered performance criteria for the utilization and disposal of S/S treated wastes. For LX values above 9, treatment is considered effective and S/S treated wastes are appropriate for "controlled utilization". For LX values between 8 and 9, S/S treated wastes can be disposed of in segregated or sanitary landfills. S/S waste with an LX value below 8 is not considered appropriate for disposal. Prior to the ANS 16.1 leaching experiment, any loose particles from the specimens' surface were removed by immersion in distilled water for 30 s. Each specimen was then suspended near the centre of the leachant in a polyethylene container with a nylon mesh harness. The leachate was collected and entirely replaced at designated intervals (2, 7, 24, 48, 72, 96, 120, 456, 1128 and 2160 h). A 0.45 µm pore-size membrane filter was used to separate the sampled leachate. Zn content was analyzed on atomic absorption spectrometer (AAS). All materials in contact with the leachant were pre-cleaned with HNO<sub>3</sub> and subsequently rinsed with de-ionised water.

The *De* values were between  $2.8 \times 10^{-13}$  and  $2.0 \times 10^{-8}$  cm<sup>2</sup> s<sup>-1</sup> (Table 1). *De* values generally range from  $10^{-7}$  (mobile, S1-S3) to  $10^{-13}$  cm<sup>2</sup> s<sup>-1</sup> (immobile, S4-S6). Therefore, the mobility of Zn in this study was reduced upon cement addition. The LX values for samples were between 6.7 and 12.55 (Table 1). Overall, cement treatment resulted in a mean LX value above 9, except for samples S1, S2 and S3. Such high mean LX values suggest that zinc retentions were significantly improved with these treatments. Based on the protocol proposed by Environment Canada's Wastewater Technology Centre [7], samples S3, S4, S5 were acceptable for "controlled utilization".

**Table 1.** Diffusion coefficients (De) and leachability indices (LX)

	S1	S2	S3	S4	S5	S6
De (cm2 s-1)	2.0 x 10 <sup>-7</sup>	5.0 x 10 <sup>-8</sup>	1.5 x 10 <sup>-8</sup>	6.3 x 10 <sup>-11</sup>	3.7 x 10 <sup>-12</sup>	2.8 x 10 <sup>-13</sup>
LX	6.70	7.32	7.81	10.20	11.43	12.55

#### **Conclusions**

The release of zinc from cement based S/S-treated samples was evaluated in this study with semi-dynamic leaching tests. Overall, cement treatment was effective in reducing zinc release upon 20-40% cement addition. All S/S treated samples with at least 20% of cement were acceptable for "controlled utilization" based on the protocol proposed by the Environment Canada Wastewater Technology Centre.

#### Acknowledgment

The authors acknowledge the financial support of the Ministry of Science of the Republic of Serbia, in the frame of projects applied under No.21014.

- [1] Wilson DJ and Chang E. Bioturbation and oxidation of sulfide in sediments. Journal of the Tennessee Academy of Sciences, 2000, **75**(3-4), 76–85.
- [2] Yukselen, M.A., Alpaslan, B.J. Leaching of metals from soil contaminated by mining activities. J. Hazard. Mater. 2001, **B87**, 289–300.
- [3] ANS, American national standard measurements of the leachability of solidified low-level radioactive wastes by a short-term test procedure, ANSI/ANS, 16.1, in: American Nuclear Society (Eds.), La Grange Park, Illinois, 1986.
- [4] G.J. de Groot, H.A. van der Sloot, in: T.M. Gilliam, C.C. Wiles (Eds.), Stabilization and Solidification of Hazardous, Radioactive, and Mixed Wastes, vol. 2, ASTM STP 1123, ASTM, PA, 1992, p. 149
- [5] Ministry of Housing, Spatial Planning and Environment Directorate-General for Environmental Protection. Circular on target values and intervention values for soil remediation, Netherlands Government Gazette, 2000; **39**.
- [6] Wastewater resolution for the city of Novi Sad, Official City Novi Sad Gazette, 1993.
- [7] Environment Canada. Proposed evaluation protocol for cementbased solidified wastes, environmental protection series. Rep. No. EPS 3/HA/9, 1991.

# Complex Compounds (L)

#### PALLADIUM(II) COMPLEXES WITH R<sub>2</sub>EDDIP LIGANDS: SYNTHESIS, CHARACTERIZATION AND ANTITUMORAL ACTIVITY

B.B. Zmejkovski<sup>1</sup>, G.N. Kaluđerović<sup>1,2</sup>, Ž. Žižak<sup>3</sup>, D. Steinborn<sup>2</sup>, H. Schmidt<sup>2</sup>, Z.D. Juranić<sup>3</sup>, S.R. Trifunović<sup>4</sup> and T.J. Sabo<sup>5</sup>

<sup>1</sup>Department of Chemistry, Institute of Chemistry, Technology and Methallurgy, Studentski Trg 14, 11000 Belgrade, Serbia; <sup>2</sup>Institut für Chemie, Martin-Luther-Universität Halle-Wittenberg, Kurt-Mothes-Straße 2, D-06120 Halle, Germany; <sup>3</sup>Institute of Oncology and Radiology of Serbia, 11000 Belgrade, Serbia; <sup>4</sup>Department of Chemistry, Faculty of Science, University of Kragujevac, 34000 Kragujevac, Serbia; <sup>5</sup>Faculty of Chemistry, University of Belgrade, P.O. Box 158, 11001 Belgrade, Serbia

#### Abstract

Two R<sub>2</sub>eddip-type O,O'-dicyclopentyl-, novel ligand precursors  $[(S,S)-H_2cp_2eddip]Cl_2\cdot 1.5H_2O$  (L3) and O,O'-dicyclohexyl-(S,S)-ethylenediamine-N,N'-di-2-propanoate dihydrochloride, [(S,S)-H<sub>2</sub>Cy<sub>2</sub>eddip]Cl<sub>2</sub>·H<sub>2</sub>O (**L4**) and correpalladium(II) complexes  $[PdCl_2\{(S,S)\text{-cp}_2\text{eddip}\}]$ sponding  $[PdCl_2\{(S,S)-Cy_2eddip\}]\cdot H_2O$  (4), as well as  $[PdCl_2\{(S,S)-iBu_2eddip\}]$  (2), were synthesized and characterized by IR, <sup>1</sup>H and <sup>13</sup>C NMR spectroscopy and elemental analysis. In adition, antitumoral invertigations were performed including previously obtained complex compound  $[PdCl_2\{(S,S)-iPr_2eddip\}]$  (1). In vitro antiproliferative activity was determined against several tumor cell lines HeLa, Fem-x, K562 and normal PBMC.

#### Introduction

Many platinum complexes have been screened for antitumoral activity and some are used as anticancer drugs [1,2]. Because of the similar coordination modes and chemical properties of palladium(II) and platinum(II), it was convenient to study complexes of palladium(II) as well. Recently, in a reaction of K<sub>2</sub>[PdCl<sub>4</sub>] with *O*,*O*'-diisopropyl-(*S*,*S*)-ethylenediamine-*N*,*N*'-di-2-propanoate dihydrochloride monohydrate two products were prepared [3]. Herein, we report synthesis, characterization and antiproliferative activity of two novel R<sub>2</sub>eddip-type ligands precursors **L3** and **L4**, their corresponding palladium(II) complexes **3** and **4**, as well as complex **2**. In adition, antitumoral invertigations were performed including previously obtained complex compound **1**.

#### **Experimental**

The ligands were prepared by using the esterification reaction previously described [4], on room temperature at first step. **L3**: Yeild 52%. Anal.calcd. (%) C, 49.09; H, 8.47; N, 6.36. Found (%): C, 48.88; H, 7.87; N, 6.12. **L4**: Yeild: 56%. Anal.calcd. (%): C, 52.28; H, 8.78; N, 6.10. Found (%): C, 51.78; H, 8.74; N, 5.70.

Complexes were prepared in a reaction of two  $10 \text{ cm}^3$  water solutions of  $K_2[PdCl_4]$  (0.158 g, 0.512 mmol) and **L2** (0.194 g, 0.512 mmol) or **L3** (0.225 g, 0.512 mmol) or **L4** (0.235 g, 0.512 mmol). During two hours of stirring  $10 \text{ cm}^3$  of 0.1M LiOH (0.040 g, 1.024 mmol) was added in small portions to the reaction solution. Yellow precipitates were obtained. **2**: Yeild 92%. Anal.calcd. (%): C, 38.92; H, 6.53; N, 5.67. Found (%): C, 38.98; H, 6.78; N, 5.74. **3**: Yeild 68%. Anal.calcd. (%): C, 41.75; H, 6.23; N, 5.41. Found (%): C, 41.36; H, 6.55; N, 5.21. **4**: Yeild 42%. Anal.calcd. (%): C, 42.60; H, 6.79; N,4.97. Found (%): C, 42.42; H, 6.69; N, 4.71.

#### **Results and Discussion**

IR spectra of **2**, **3** and **4** all show specific absorption bands: v(C=O) at 1740, 1734 and 1734 cm<sup>-1</sup>, v(C=O) at 1212, 1223 and 1223 cm<sup>-1</sup> and  $v(CH_3)$  at 2960, 2965 and 2940 cm<sup>-1</sup>. All data is given respectively and similar to free lignads (**L2–L4**). Indication of nitrogen coordination may be found by existence of bands for secondary amino groups (3113, 3115 and 3125 cm<sup>-1</sup>), and neither one of the complexes has a band for secondary ammonium groups (as in spectra of ligands **L2–L4**).

In  $^{1}$ H and  $^{13}$ C NMR spectra expected signals were found. In  $^{1}$ H NMR spectra the broad singnal of hydrogen atoms belonging to secondary amino groups appears in range of 5.8 - 6.6 ppm (comparing with **L2–L4**: 9.5 - 10.5 ppm). The signals of protons between two nitrogen donor atoms show coordination induced shifts (0.1 - 0.9 ppm) in comparasion with spectra of ligands.

**Scheme 1.** Investigated Pd(II) complexes

The ligands and complexes were tested for cytotoxic activity on tumor cell lines human adenocarcinoma HeLa, human myelogenous leukemia K562, human malignant melanoma Fem-x and normal immunocompetent cells, i.e. human peripheral blood mononuclear PBMC cells. Analysed agents showed a dosedependent antiproliferative effect toward all cell lines and on human PBMC and stimulated PBMC. Antitumoral tests were performed as described for corresponding platinum complexes [4].

It can be seen that **L3** is showing low to mild activity against the selected cell lines, but in the case of **L4** the activity against the cell line K562 is considerably higher (IC<sub>50</sub>  $29.83 \pm 3.15$ ). When cyclopentyl group is substituted with cyclohexyl, antiproliferative activity on all target cells increased. This is also a fact in case of **3** and **4**. Complex **2** is slightely more active than **1**, so when isobutyl group is substituted with isopropyl, the cytotoxic action decreases (Table 1). All com-

pounds show medium activity and not very significant in comparasion with platinum complexes.

**Table 1.**  $IC_{50}(\mu M)^a$  for the 72 h of action of investigated compounds on HeLa, K562, Fem-x cells, on PBMC and PBMC stimulated with PHA determined by KBR test

No., Compound	HeLa	Fem-x	K-562	PBMC*	PBMC+PHA*
1, $[PdCl_2\{(S,S)-iPr_2eddip\}]$	>200	$193.3 \pm 1.7$	>200	>200	>200
2, $[PdCl_2\{(S,S)-iBu_2eddip\}]$	>200	$139.5\pm4.6$	$169.3 \pm 3.5$	>200	180.5
$3, [PdCl2{(S,S)-cp2eddip}]$	$186.6 \pm 1.9$	$94.7 \pm 2.2$	$92.0 \pm 2.8$	177.4	145.8
$4, [PdCl2{(S,S)-Cy2eddip}]$	$127.0 \pm 7.9$	$68.0 \pm 4.9$	$61.8 \pm 4.4$	157.2	124.5
L3, [(S,S)-H <sub>2</sub> cp <sub>2</sub> eddip]Cl <sub>2</sub>	$171.5 \pm 6.8$	$89.5 \pm 2.9$	$82.8 \pm 1.3$	>200	143.5
L4, [(S,S)-H <sub>2</sub> Cy <sub>2</sub> eddip]Cl <sub>2</sub>	$89.0 \pm 3.6$	$69.9 \pm 1.9$	$29.8 \pm 3.1$	142.8	95.1

<sup>\*</sup>Results from one experiment

#### **Conclusions**

Two novel  $R_2$ eddip-type ligand precursors and three palladium(II) complexes were synthesized and characterized. All of the coumpounds including previously synthesized  $[PdCl_2\{(S,S)-iPr_2eddip\}]$  were tested for antitumoral activity on four cell lines. The compounds show moderate cytotoxic action against used cell lines, but not comparable with the very high activity of similar platinum complexes.

- [1] L. Kelland, Nature Reviews Cancer, 2007, 7, 573–584.
- [2] G. N. Kaluđerović, H. Schmidt, D. Steinborn and T. J. Sabo, Review article, Inorganic Biochemistry: Research Progress, Nova Science Publishers, Inc. Hauppauge, NY, in press (2008).
- [3] B. B. Krajčinović, G. N. Kaluđerović, D. Steinborn, H. Schmidt, Ch. Wagner, K. Merzweiler, S. R. Trifunović, T. J. Sabo, Z. Anorg. Allg. Chem. submited.
- [4] B. B. Krajčinović, G. N. Kaluđerović, D. Steinborn, H. Schmidt, Ch. Wagner Ž. Žižak, Z. D. Juranić, S.R. Trifunović, T. J. Sabo, J. Inorg. Biochem., 2008, 102, 892-900.

# CHALLENGING INTERMETALLIC INTERACTIONS IN ORGANOMETALLIC COMPOUNDS, A CASE STUDY: NON-COVALENT "BINDING" IN SYN-FACIAL [TRICARBONYL( $\eta^6, \eta^1$ -BENZYL)CHROMIUM]MANGANESETRICARBONYL COMPLEXES

I. Hyla-Kryspin<sup>1</sup>, S. Grimme<sup>1</sup> and <u>J.-P. Djukic<sup>2</sup></u>

<sup>1</sup>Organisch-Chemisches Institut, Westfälische Wilhelms Universität, Corrensstrasse 40, 48149 Münster, Germany <sup>2</sup>Institut de Chimie, UMR 7177 CNRS, Université Louis Pasteur, 4 rue Blaise Pascal, 67000 Strasbourg, France.

#### **Abstract**

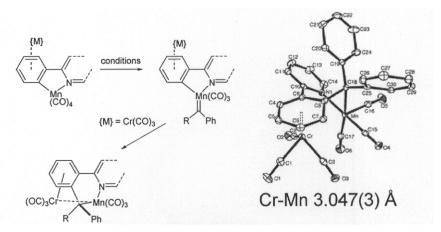
So-called metallophilic interactions are considered an efficient mean to organize supramolecular networks of inorganic molecules. However, the intimate nature of such weak interactions, is a matter of intense theoretical and experimental investigation and their "non-covalent" or "covalent" nature still unsettled in many cases. In the present contribution we present the theoretical study of a typical case of bimetallic complex displaying a new intermetallic interaction between an electron saturated Cr centre and a formally unsaturated Mn centre that outlines unusual attractive and binding interactions between first row transition metals and that points the methodological challenges faced by experimentalists interested in elucidating the nature of such weak interactions

#### Introduction

A few years ago, a peculiar class of air-stable *syn*-facial heterobimetallic compounds accounted for as *syn*-facial Cr,Mn benzyl complexes were synthesized by the sequential reaction of organolithium reagents and methyltriflate with cyclomanganated ( $\eta^6$ -arene)Cr(CO)<sub>3</sub> complexes [1,2] (scheme 1). In the mean time, new Cr,Mn benzyl complexes bearing a variety of different substituents were synthesized, [3] thus confirming that similar *syn*-facial arrangements could be reproduced by an alternative synthetic route.[4]

Syn-facial heterobimetallic Cr,Mn benzyl complexes raise the issues of electron-book keeping and bond formalism in electron-deficient dinuclear species. This was historically first raised by Hock and Mills for a di-iron organometallic species [5] and only sparsely investigated in the following years [6,7].

Syn-facial Cr,Mn benzyl complexes do possess structural similarities with other benzyl-bridged Cr-Pd complexes reported by Kalinin and co-workers in the early 90's. However, the nature of the latter's Cr-Pd interaction was never studied in detail. Several experimental data support the hypothesis of a "dynamic" donor-acceptor Cr→Mn interaction [8] (Chart 1, form B), which resembles, all things considered, the non-bridged cases of dative metal→metal adducts reported by Pomeroy et al.[9]



**Scheme 1.** Left, the general synthetic route for Cr,Mn *syn*-facial complexes; Right, x-ray diffraction structure of a typical Cr,Mn *syn*-facial benzyl complex.

Chart 1 presents three limit forms that were put forward to describe *syn*-facial heterobimetallic Cr,Mn benzyl complexes. Each form A, B and C entails different consequences over the bonding modes of the organic ligand, oxidation state of the metals and over molecular geometry.

$$(OC)_3Cr \longrightarrow Mn(CO)_3$$

$$R' \qquad R \qquad R' \qquad R \qquad R' \qquad R \qquad R' \qquad R \qquad R'$$

$$A \qquad B \qquad C$$

$$no metal-metal bond$$

**Fig. 1.** Test valence bond formulation for *syn*-facial Cr,Mn benzyl complexes.

The nature of Cr-Mn interaction was pursued with the support of computational methods including the density functional theory, in the light of the structural features of 13 X-ray structures deposited with the CSDB.

The methodology chosen to address the nature of the intermetallic interaction entailed a broad scrutiny of theoretical method first in their ability to reproduce the geometries of prototype compounds, whose X-ray structure has been determined.

Typical methods were HF, MP2, hybrid DFT and pure DFT methods[10] for which in several cases correction for dispersion interactions [11] (also known as the "D" or van der Waals correction) was applied to probe the relevance of dispersion forces. The best geometry fits were obtained with pure DFT functionals (BP86[12], PBE[13]) that reproduced consistently all experimental test-geometries. In addition, the "D" correction applied to hybrid functionals such as B3LYP[14]

produced better geometry fits than without correction. Note, that the commonly used in organometallic chemistry B3LYP/LANL2DZ approach was not able to reproduce the Cr-Mn distance with an acceptable accuracy. Also the dependency on the size of the basis set was probed and our results show that there is only little dependency when hybrid or pure DFT functionals are used. As an example, Figure 2 shows the deviations of the optimized at several method/basis set levels Cr-Mn distances of the complex *syn*-<sup>1</sup>1.

Overall, NBO analysis[15] of the best fitted geometries indicates that the Wiberg bond index for the Cr-Mn segment falls within the 0.10-0.11 range, which clearly indicates that the inter-metallic interaction is not covalent in such *syn*-facial Cr,Mn complexes. This is however ponderated with the fact that in triplet state geometries a significant increase of the Cr-Mn distance is noticed, suggesting that contribution of covalence although weak is not to be neglected (Figure 3). Study of the orbital interaction diagram between non-optimized fragments of the title compounds suggests that the intermetallic interaction possesses some degree of donor-acceptor character and that it can be best defined as a 3 orbitals-4 electrons interaction.

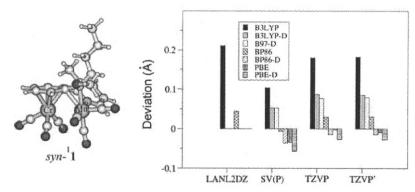


**Fig. 2.** Deviations at several method/basis set levels of the optimized Cr-Mn distances of the complex  $syn^{-1}1$  with respect to its experimental values (3.035 A, Ref. 2).

Intrinsic interaction energy determination between non-optimized fragments of several models, i.e. *syn*-facial and fictitious *anti*-facial Cr,Mn benzyl complexes, points towards a value of ca. 10 kcal/mol for the Cr-Mn interaction energy, a value lower than the barrier to rotation of the Cr(CO)<sub>3</sub> moiety determined by variable temperature <sup>13</sup>C NMR with a <sup>13</sup>CO labelled sample[16].

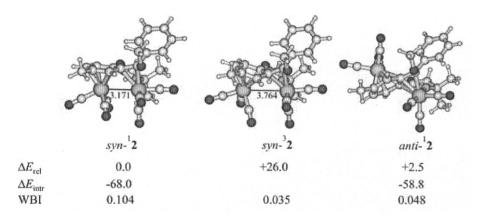


**Fig. 3.** Relative energies ( $\Box E_{rel}$ ), intrinsic interaction energies of the Cr(CO)<sub>3</sub> moiety ( $\Box E_{intr}$ ), and the Wiberg bond index (WBI) of the Cr-Mn interaction determined at the BP86/TZVP' level for  $syn^{-1}\mathbf{2}$ ,  $syn^{-3}\mathbf{2}$  and  $anti^{-1}\mathbf{2}$ . The energy values are given in kcal mol<sup>-1</sup>.

#### **Conclusions**

In conclusion, this study shows that the theoretical treatment and characterization of weak inter-metallic interactions between closed-shell centres requires the deployment of a large array of methods and a careful comparative analysis. In the case studied here there is clear evidence for the relevance of van der Waals interactions, however the interaction between what could be considered an electron-deficient Mn(I) center and a saturated Cr(0) centre possesses some donor-acceptor character that is evident from fragment interaction analysis.

#### Acknowledgements

J.P. D. gratefully thanks the CNRS and the Alexander von Humboldt Foundation for their support. Drs A. Maisse-Francois, A. Dedieu, C. Michon, M. Robitzer and M. Pfeffer from the CNRS and the University of Strasbourg as well as S. D. Zaric (University of Belgrade) and K.H. Doetz (University of Bonn) are gratefully acknowledged for their past contributions to this work. I. H.-K. and S. G. thank for the support from the Deutsche Forschungsgemeinschaft in the framework of the SFB 424 ("Molekulare Orientierung als Funktionskriterium in chemischen Systemem")

#### References and Notes.

- [1] J. P. Djukic, A. Maisse, M. Pfeffer, K.H. Dotz, M. Nieger, *Eur. J. Inorg. Chem.* 1998, 1781-1790.
- [2] J. P. Djukic, A. Maisse-Fran£ois, M.Pfeffer, K.H. Dotz, A. De Cian, J. Fischer, *Organometallics* 2000, **19**, 5484-5499.
- [3] J. P. Djukic, C. Michon, A. Berger, M. Pfeffer, A. de Cian, N. Kyritsakas-Gruber, *J. Organomet. Chem.*, 2006, **691**, 846-858.

- [4] J. P. Djukic, K. H. Dotz, M. Pfeffer, A. De Cian, J. Fischer, Organometallics, 1997, 76, 5171-5182.
- [5] A. A. Hock, O. S. Mills, Acta Cryst. 1961, 14, 139-148.
- [6] a) R. M. Bullock, C.P. Casey, Ace. Chem. Res. 1987, 20, 167-173. b) S. Tofke, U. Behrens, J. Organomet. Chem. 1988, 338, 29-45.
- [7] a) V. N. Kalinin, I. A. Cherepanov, S. K. Moiseev, A. S. Batsanov, Yu. T. Struchkov, Mendeleev Commun. 1991, 77-78. b) V. N. Kalinin, I. A. Cherepanov, S. K. Moiseev, F. M. Dolgushin, A. I. Yanovski, Yu. T. Struchkov, Acta Cryst. 1993, C49, 805-808. c) S. K. Moiseev, I. A. Cherepanov, P. V. Petrovskii, M. G. Ezernitzkaya, H. Butenschon, M. Strotmann, V. N. Kalinin, Inorg. Chim. Acta, 1998, 250, 71-74.
- [8] H. Nakatsuji, M. Hada, A. Kawashima, Inorg. Chem. 1992, 31, 1740-1744.
- [9] a) F. W. B. Einstein, R. K. Pomeroy, P. Rushman, A. C. Willis, Organometallics, 1985, 4, 250-255. b) L. W. Arndt, M. Y. Darensbourg, T. Delord, B. Trzcinska Bancroft, J. Am. Chem. Soc. 1986, 108, 2617-2627. c) F. W. B. Einstein, M. C. Jennings, R. Krentz, R. K. Pomeroy, P. Rushman, A. C. Willis, Inorg. Chem. 1987, 26, 1341-1344. d) H. B. Davis, F. W. B. Einstein, P. G. Glavina, T. Jones, R. K. Pomeroy, P. Rushman, Organometallics 1989, 8, 1030-1039. e) R. J. Batchelor, H. B. Davis, F. W. B. Einstein, R. K. Pomeroy, J. Am. Chem. Soc. 1990, 112, 2036-2037.
- [10] a) F. Jensen, Introduction to Computational Chemistry, Wiley-VCH, Weinheim, 1999.
  b) W. Koch, M. C. Holthausen, A Chemist's Guide to Density, Wiley-VCH, Weinheim, 2000.
  c) R. G. Parr, W. Yang, Density Functional Theory of Atoms and Molecules, Oxford University Press, New York, 1989.
- [11] a) M. Allen, D. J. Tozer, J. Chem. Phys. 2002, 117, 11113-11120. b) U. Zimmerli, M. Parinello, P. Koumoutsakos, J. Chem. Phys. 2004, 120, 2693-2699, c) S. Grimme, J. Comput. Chem. 2004, 25, 1463-1473. d) S. Grimme, J. Comput. Chem. 2006, 27, 1787-1799 and references cited.
- [12] a) A. D. Becke, Phys. Rev. A. 1988, 38, 3098-3100. b) J. P. Perdew, Phys. Rev. B 1986, 33, 8822-8824.
- [13] J. P. Perdew, K. Burke, M. Ernzerhof, Phys. Rev. Lett. 1996, 77, 3865-3868.
- [14] a) A. D. Becke, J. Chem. Phys. 1993, 95, 5648-5652. b) S. H. Vosko, L. Wilk, M. Nusair, Can. J. Phys. 1980, 58, 1200-1211. c) C. Lee, W. Yang, R. G. Parr, Phys. Rev. B. 1988, 37, 785-789.
- [15] A. E. Reed, R. B. Weinstock, F. Weinhold, Chem. Rev. 1988, 88, 899.
- [16] J. P. Djukic, M. Pfeffer, K. H. Dotz, CR. Acad. Set Paris, T.2, Serie He 1999, 403-408.

## HYDROPHOBIC INTERACTIONS IN THE STABILITY OF PORPHYRIN-CONTAINING PROTEINS

S. Stojanović<sup>1</sup> and S.D. Zarić<sup>2</sup>

 IHTM - Department of Chemistry, University of Belgrade, Njegoševa 12, P.O.Box.815, 11001 Belgrade, Serbia
 Faculty of Chemistry, University of Belgrade, Studentski trg 16, P.O.Box.158, 11001 Belgrade, Serbia

#### **Abstract**

This study aims to systematically characterize hydrophobic interactions of porphyrins in porphyrin containing proteins. Structures of porphyrin containing proteins from the Protein Data Bank (PDB) Select January 2007, the list of non-redundant protein chains (25% threshold), were searched in order to find out hydrophobic interactions of porphyrins in proteins. The study has revealed that hydrophobic interactions are commonly found in porphyrin containing proteins and are widely present in different regions of the protein chain, such as the backbone or side chain. Examination of the highly cross-linked hydrophobic network points to a core of several residues with multiple contacts. These contacts cross-link the porphyrin ring in the proteins, essentially tying them together. Side-chains hydrophobic interactions are more frequent than those with backbone. Besides, amino acids involving in these interactions shows significant conservation score.

#### Introduction

Hydrophobic interactions are considered to be essential in many systems; micelles, vesicles, colloids, membranes and transport; self-organization, polymer interactions, protein folding and ligand binding, nucleic acids, drug action, water-mediated organic reaction. Hydrophobic interactions belong to the most often cited intermolecular forces [1].

Porphyrin-containing proteins include molecules with quite distinct activities, ranging from electron transfer, catalysis, oxygen transport and storage, ligand binding, signal transduction to the control of gene expression. This diversity of functions originates from the versatility of the porphyrin group and the variety of interactions with protein scaffolds that generate different porphyrin environments [2]. Noncovalent interactions of porphyrin in porphyrin containing proteins are very important since in the majority of different types of porphyrin containing proteins, porphyrin is noncovalently bound [3,4].

In our previous work it was shown that porphyrin in metal complexes and in proteins can be involved in specific noncovalent interactions. Searching structures of porphyrin containing proteins from the Protein Data Bank revealed that  $\pi$ -system of every porphyrin ring is involved in CH/ $\pi$  and NH/ $\pi$  interactions, most of the porphyrins are making several interactions [4,5].

Here we used a non-redundant data base of the Protein Data Bank (PDB) to examine systematically the occurrence and the role of hydrophobic interactions in porphyrin-protein structures.

#### **Results and Discussion**

For this study we used the Protein Data Bank (PDB) Select January 2007 list of non-redundant protein chains (25% threshold version, 3,398 protein chains). The following criteria were employed to assemble the set: (1) no theoretical model structures and no NMR structures, were accepted, (2) only crystal structures with a resolution of 3.0 Å or better and a crystallographic R-factor of 25.0% or lower were accepted, (3) crystal structures containing porphyrine were accepted. Hydrophobic contacts between porphyrin rings and surrounding amino acids involved were calculated by program LIGPLOT v.4.4.2. The criteria used for the current study are: All atoms not involved in hydrogen bonds but separated by <3.9 Å were considered to be interacting through hydrophobic contacts. Minimum covalent separation 3 covalent bonds. We used the Bayesian method for calculating rates of amino acid conservation scores.

In the dataset obtained from PDB Select described above we found 57 proteins with porphyrin. We found out that all of the porphyrins are involved in the hydrophobic interactions.

The number of hydrophobic interactions, based on data in the non-redundant data base of the PDB, for different types of amino acids are shown in Figure 1A.

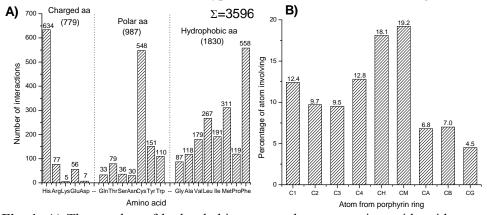


**Fig. 1.** A) The number of hydrophobic contacts between amino acid residues and porphyrin rings, B) The percentage of atom from porphyrin ring involvilng in hydrophobic contacts.

The results presented in Fig. 1A indicate a high number of hydrophobic interactions are found in the hydrophobic environment of the protein. Both the charged and the polar amino acid residues making hydrophobic interactions are considerably less, with the hydrophobic side chain environment being relatively higher. A significant number of these residues are essential for protein function.

The backbone groups are the least frequently involved (data not shown), because their atoms are not as accessible as the side-chain atoms.

We find that peptide interactions with the hydrophobic face of the porphyrin play an important role in the stabilization of porphyrin-peptide complexes (Fig. 1B). The most prominent porphyrin atoms involving in hydrophobic interactions are CH and CM from vinyl and methyl groups respectively because they are closer to the protein chain. The other atoms from porphyrin face (C1, C2, C3 and C4) also significant participate in hydrophobic interactions. Atoms from acetyl and propionate groups of porphyrin (CA, CB and CG) provides a less significant contribution of hydrophobic interactions. Noncovalent interactions between the acetyl and propionate groups of porphyrin and basic residues of the protein, as well as hydrophobic interactions between the periphery of the porphyrin and the active site pocket, are also important in porphyrin binding to protein chain.

Bayesian method for calculating rates of amino acid conservation scores showed that amino acids involved in hydrophobic interactions with porphyrin have significant conservation score  $(7.3 \pm 2.0)$ .

#### Conclusion

The results show that large number of hydrophobic interactions with porphyrin exists in crystal structures of proteins and are widely present in different regions of the protein chain, such as the backbone or side chain. Side-chains hydrophobic interactions are more frequent than those with backbone. Hydrophobic interactions of the periphery of the porphyrin are exist only. Hydrophobic interactions between the porphyrin face and hydrophobic amino acids residues can be a major component in the formation and stability of porphyrin-peptide complexes and porphyrin proteins. The number of interactions and significant conservation score of amino acids that are involved in these interactions are strong argument for their importance.

#### References

- J. L. Atwood, J. W. Steed, Encyclopedia of supramolecular chemistry, CRC Press, Boca Raton, 2004.
- [2] K. M. Kadish, K. M. Smith, R. Guilard, The porphyrin handbook, Academic Press, San Diego, 2000.
- [3] S. D. Zarić, D. M. Popović, E. W. Knapp, Biochemistry, 2001, 40, 7914-7928.
- [4] S. Đ. Stojanović, V. B. Medaković, G. Predović, M. Beljanski, S. D. Zarić,  $XH/\pi$  interactions with the  $\pi$  system of porphyrin ring in porphyrin-containing proteins, J. Biol. Inorg. Chem., 2007, **12**, 1063-1071.
- [5] V. B. Medaković, M. K. Milčić, G. A. Bogdanović, S. D. Zarić, Journal of Inorganic Biochemistry, 2004, **98**,1867–1873.

#### PLATINUM(II/IV) COMPLEXES WITH H<sub>2</sub>EDDA-TYPE LIGANDS AND THEIR DERIVATIVES: ON THE SYNTHESIS, CHARACTERIZATION AND *IN VITRO* ACTIVITY

G.N. Kaluđerović<sup>1,2</sup>, H. Schmidt<sup>1</sup>, D. Steinborn<sup>1</sup> and T.J. Sabo<sup>3</sup>

<sup>1</sup>Institut für Chemie, Martin-Luther-Universität Halle-Wittenberg, Kurt-Mothes-Straße 2, 06120 Halle, Deutschland; <sup>2</sup>Department of Chemistry, Institute of Chemistry, Technology and Metallurgy, Studentski trg 14, 11000 Belgrade, Serbia; <sup>3</sup>Faculty of Chemistry, University of Belgrade, Studentski trg 16, P.O. Box 158, 11000 Belgrade, Serbia

#### **Abstract**

Platinum(II) and platinum(IV) complexes with  $H_2$ edda-type ligands ( $H_2$ edda = ethylenediamine-N,N'-diacetic acid) and its derivatives are main focus of research in our group. Many complexes, including new  $H_2$ edda-type analogues and their derivates, have been synthesized and characterized by spectroscopic (NMR and IR) and single crystal X-ray diffraction. Coordination of these ligands can be in a bidentate ( $\kappa^2 N$ ,N') or tetradentate ( $\kappa^2 N$ ,N', $\kappa^2 O$ ,O') fashion. Tetradentate coordination with platinum(IV) leads to the formation of various isomers which, interestingly, display varying cytotoxic activity. The in vitro antitumoral cytotoxicity of the synthesized complexes and some general conclusions regarding the relationship between the structure and antitumoral activity of the complexes with  $H_2$ edda-type ligands are drawn.

#### Introduction

Coordination ability of edda-type ligands (H<sub>2</sub>edda-type: ethylenediamine-*N*,*N*'-diacetic acid – H<sub>2</sub>edda; ethylenediamine-*N*,*N*'-di-3-propionic acid – H<sub>2</sub>eddp; ethylenediamine-*N*,*N*'-di-2-propionic acid – (*S*,*S*)-H<sub>2</sub>eddip; propylenediamine-*N*,*N*'-diacetic acid – H<sub>2</sub>pdda) with various metal ions has been investigated (Fig. 1) [1]. All of the ligands are of the

**Fig. 1**. H<sub>n</sub>edda-type ligands (n = 0, 1, 2), shown are the dianionic doubly deprotonated ligands (n = 0)

 ${}^{-}\text{O}_2\text{C}(\text{CH}_2)_n\text{NH}(\text{CH}_2)_m\text{NH}(\text{CH}_2)_n\text{CO}_2^-$  type ligands (n = 1, 2; m = 2, 3) and belong to a family of acyclic flexidentate ligands (up to tetradentate) with two nitrogen

and two oxygen donor atoms (Fig. 1).

In octahedrally configured complexes with two monodentate ligands the edda unit is expected to form three geometric isomers: *sym-cis*, *unsym-cis* and *trans* (X = Cl, Br; configuration index: *OC*-6-32, *OC*-6-32 and *OC*-6-13, respectively, Fig. 2).

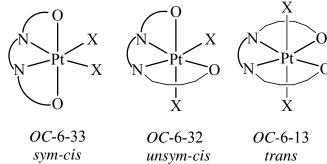


**Fig. 2.** Possible geometrical isomers of [PtX<sub>2</sub>(edda-type)] complexes (X = Cl, Br).

There is growing interest in platinum(IV) compounds because of their inertness relative to platinum(II) complexes [2]. This property lends itself favourably to oral administration of platinum(IV) drugs and reduced toxicity during platinum based chemotherapy due to a decrease in the amount of the drug lost or deactivated through side reactions before reaching the target site [2].

The H<sub>2</sub>edda-type ligand has the ability to coordinate to platinum(IV) in a mode that maintains the  $[Cl_2N_2O_2]$ ligating present in JM-216. environment discussed herein, although complexes with edda-type carboxylate ligands do not offer a viable alternative to JM-216, the ester derivatives these ligands of show enormous promise for the expansion of platinum(IV) anticancer drug development.

#### **Results and Discussion**

#### Synthesis and characterization

Platinum(II) and platinum(IV) compexes with edda ligands were synthesized for the first time by Liu in 1963 [3]. Fourty years later, the first crystal structure was determined by X-ray crystallography (Fig. 3) by Jolley et *al.* [4]. Following this,

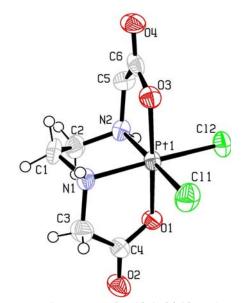


**Fig. 3.**  $Sym\text{-}cis\text{-}[PtCl_2(edda)]\cdot H_2O$ 

complexes of platinum(IV) and platinum(II) with eddp and pdda ligands were synthesized according to the procedure described by Liu [3] for platinum-edda complexes [5-9]. Only the *trans* isomer (configuration index *OC*-6-13, two nitrogen and two oxygen atoms of eddp bound in the equatorial plane, Fig. 2) is formed in

reactions of hexahaloplatinate(IV) with the eddp and pdda ligands, respectively, while a similar reaction performed with edda affords exclusively the *sym-cis* isomer (configuration index *OC*-6-33, equatorial nitrogen and axial oxygen atoms of edda). Synthesis and characterization of (*S,S*)-ethylenediamine-*N,N'*-di-2-propionate, (*S,S*)-ethylenediamine-*N,N'*-(4,4-dimethyl)-2,2-di-pentanoate and the corresponding platinum(IV) complexes was recently communicated [10,11].

Bidentate (R = Me, Et, n-Pr, i-Pr, n-Bu, i-Bu, n-Pe, Cy and cp; O, O-dialkyl-ethylenediamine-N, N'-di-3-propanoate) ligand precursors can be obtained from the reaction between  $H_2$ edda-type acid, the corresponding absolute alcohol and thionyl chloride [13,14]. More recently, these esters with  $\kappa^2 N$ , N' ligating mode, have been used in platinum chemistry [15-18]. X-ray structural analysis has been performed for several platinum(IV) complexes containing different  $R_2$ edda-type ligands, as well as for uncoordianted ester molecules [17-19].

#### Antitumoral activity of platinum complexes

Antitumoral activity against a panel of various cell lines (HeLa – human adenocarcinoma, K562 – human myelogenous leukemia, Fem-x – human malignant melanoma, PBMC – , L929 – fibrosarcoma, U251 – actrocitoma, 1411HP and H12.1 – testicular germ cell tumors, DLD-1 – colon carcinoma, 518A2 – melanoma, A549 – lung carcinoma, and others) illustrates how the activity can depend on the type of derivative (acid/esters), oxidation state of the platinum, mode of coordination of the ligand and the halogeno ligands [16-18,20,21]. While searching for more potent antitumor agents some important structure–activity relationships have emerged.

Platinum(II) and platinum(IV) complexes with  $H_2$ edda-type ligands of the types [PtX<sub>n</sub>(H<sub>n</sub>edda-type)] and [PtX<sub>n+2</sub>(H<sub>n</sub>edda-type)] (n = 0, 1, 2; X = Cl, Br, I), respectively, have similar effects on cytotoxicity but in general the activity is less than cisplatin.

Platinum(IV) complexes with R<sub>2</sub>edda-type ligands posses greater antitumoral activity than corresponding platinum(II) complexes. In some cases the *in vitro* activity of theses Pt(IV) complexes is higher than that of cisplatin and the kinetics of the tumor cell death process induced by these complexes is

considerably faster in comparison to that induced by cisplatin.

The platinum(IV) complexes of the R<sub>2</sub>eddatype ligands with the greatest activity are those with chloro ligands, e.g. [PtCl<sub>4</sub>(R<sub>2</sub>eddatype)]. The most promising compounds

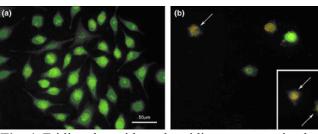


**Fig. 4.** Etidium bromide and acridine orange stained pretreated with platinum complexes for 24 h, HeLa cells: (a) control; after the action of (b) [PtCl<sub>4</sub>(Bu<sub>2</sub>eddp)]

to emerge thus far from these findings are  $[PtCl_4(Bu_2eddp)]$  (Fig. 4) and  $[PtCl_4(Pe_2eddp)]$ .

The future development of this area of platinum antineoplastic drugs will undoubtedly expand on the current structure-activity guidelines thus far established. In particular, despite extreme positive results found so far for complexes with  $R_2$ edda-type ligands, there is still relatively little known on their exact role in tumor cells or indeed what effect can have manipulation of the ligand structure on the overall activity. In addition, sophisticated drug delivery systems, such as encapulation of the drugs in macromolecules and combinatorial treatment regimes are largely unexplored within the scope of  $R_2$ edda-type complexes, although intial findings are promising.

#### Acknowledgements

The author G. N. Kaluđerović gratefully acknowledges financial support from the Alexander von Humboldt Foundation. We would like to thank the Ministry of Science of the Republic of Serbia (Grant no. 145010).

#### References

- T. J. Sabo, S. R. Grguric-Sipka, S. R. Trifunovic, Synth. React. Inorg. Met.-Org. Chem., 2002, 32, 1661–1717.
- [2] L. Kelland, Nat. Rev. Cancer 2007, 7, 573-584.
- [3] C. F. Liu, Inorg. Chem., 1964, 3, 680–684.
- [4] J. N. Jolley, A. I. Yanovsky, L. R. Kelland, K. B. Nolan, J. Inorg. Biochem., 2001, 83, 91–100
- [5] G. N. Kaluđerović, G. A. Bogdanović, T. J. Sabo, J. Coord. Chem., 2002, 55, 817–822.
- [6] V. M. Đinović, G. A. Bogdanović, S. Novaković, T. J. Sabo, J. Coord. Chem., 2004, 57, 535–541.
- [7] T. J. Sabo, G. N. Kaluđerović, D. Poleti, Lj. Karanović, A. Boccarelli, F. Cannito, G. Natile, J. Inorg. Biochem., 2004, 98, 1378–1384.
- [8] V. M. Đinović, L. T.Mančić, G. A. Bogdanović, P. J. Vulić, G. del Rosario, T. J. Sabo, O. B. Milosevic, J. Mater. Res., 2005, 20, 102–113.
- [9] G. N. Kaluđerović, V. M. Đinovic, Z. Juranić, T. Stanojković, T. J. Sabo, J. Coord. Chem., 2006, 59, 815–819.
- [10] V. V. Glodjović, G. Vasić, V. M. Djinović, S. R. Trifunović, ICOSECS 5 -International Conference of the Chemical Societies of the South-East European Countries in Ohrid, FYR Macedonia, September 2006, Vol. ICH-13, 313.
- [11] G. Vasić, V. V. Glodjović, V. M. Djinović, S. R. Trifunović, ICOSECS 5 International Conference of the Chemical Societies of the South-East European Countries in Ohrid, FYR Macedonia, September 2006, Vol. OCH-64, 488.
- [13] D. B. Haydock, T. P. C. Mulholland, J. Chem. Soc., 1971, C, 2389–2395.
- [14] G. N. Kaluđerović, T. J. Sabo, Polyhedron, 2002, 21, 2277–2282.
- [15] T. J. Sabo, G. N. Kaluđerović, S. R. Grgurić-Šipka, F. W. Heinemann, S. R. Trifunović, Inorg. Chem. Comm., 2004, 7, 241–244.
- [16] G. N. Kaluđerović, V. M. Đinović, Z. D. Juranić, T. P. Stanojković, T. J. Sabo, J. Inorg. Biochem., 2005, 99, 488–498.

- [17] G. N. Kaluđerović, H. Schmidt, S. Schwieger, Ch. Wagner, R. Paschke, A. Dietrich, T. Mueller, D. Steinborn, Inorg. Chim. Acta., 2008, **361**, 1395–1404.
- [18] B. B. Krajčinović, G. N. Kaluđerović, D. Steinborn, H. Schmidt, Ch. Wagner, Ž. Žižak, Z. D. Juranić, S. R. Trifunović and T. J. Sabo, J. Inorg. Biochem., 2008, 102, 892–900.
- [19] G. N. Kaluđerović, H. Schmidt, Ch. Wagner, D. Steinborn, Acta Cryst. E 2007, 63, m1985.
- [20] G. N. Kaluđerović, Dj. Miljković, M. Momčilović, V. M. Đinović, M. Mostarica Stojković, T. J. Sabo, V. Trajković, Int. J. Cancer., 2005, 116, 479–486.
- [21] S. Mijatović, D. Maksimović-Ivanović, J. Radović, Dj. Miljković, G. N. Kaluđerović, T. J. Sabo, V. Trajković, Cell. Mol. Life Sci., 2005, **62**, 1275–1282.

## PREPARATION AND STUDY OF C<sub>0</sub> (II) COMPLEXES WITH OCTAAZAMACROCYCLE AND MONO/DI *N*-SUBSTITUTED GLYCINE

G. Vučković<sup>1</sup>, S.B. Tanasković<sup>2</sup> and M. Antonijević-Nikolić<sup>3</sup>

<sup>1</sup>Faculty of Chemistry, University of Belgrade, Studentski trg 16, 11001 Belgrade, Serbia (gordanav@chem.bg.ac.yu)

#### **Abstract**

A two new binuclear mixed-ligand complexes Co(II) of general formula  $[Co_2(Y)tpmc]$   $(BF_4)_3 \cdot xH_2O$ , (HY = N-methylglycine, N,N-dimethylglycine and x = 4 or 3) (tpmc = N,N',N'',N'''- tetrakis(2-pyridylmethyl)-1,4,8,11-tetraazacyclotetradecane) are isolated. Analytical data composition of the complexes, some of the physico-chemical properties and tentative geometries were evaluated based on elemental analysis (C,H,N), conductometric and magnetic measurements, spectroscopic data (UV/VIS, IR), and comparison with previously described analogous glycinato and other aminocarboxylato complexes. Both complexes were also tested against some microorganisms, and certain antibacterial activity is detected in both cases.

#### Introduction

Aminocarboxylato ligands with transition metals could coordinate on variety modes depending on the reaction conditions, central metal ion, experimental conditions, pH etc. In most of up to now described complexes, they are bonded either as N,O-bidentate chelate or O,O'-bridged, but rarely as monodentate. In addition, for such complexes are expected or found some biological activity. A series of binuclear Co (II) complexes with octaazamacrocycle tpmc and aminocarboxylates are prepared and studied previously [1, 2, and 3]. Their general formula was  $[Co_2(Z)tpmc](ClO_4)_3$ , where HZ = glycine, L-alanine, L-aminobutiric, aminoisobutiric acid,  $\alpha$ - or  $\beta$ -aminobutiric/isobutiric acid, L-nor or L-valine. Different amount of crystal solvents as  $H_2O$ ,  $CH_3CN$ , were present in some of them. In these complexes tpmc adopted a boat conformation with an *exo* coordination mode. Besides,  $\mu$ -O,O'-coordination of aminocarboxylato ligands was proposed (Scheme 1a). All attempts to prepare Co (II) tpmc complexes of *N*-methyl/*N*,*N*-dimethylglycinato ligands as perchlorate salts failed due to their rapid decomposition. Therefore, we prepared analogous complexes as tetrafluoroborates and compared with previous data.

#### **Results and Discussion**

#### Preparation

Ligand tpmc was prepared and purified according to the literature procedure [4] and other chemical were used as *p.a.* commercial products.

 $[Co_2(Y)tpmc](BF_4)_3 \cdot xH_2O (YH = N-methylglycine, N,N-dimethylglycine, abbreviated below as N-mgly /N,N-dmgly; <math>x = 4,3$ )

<sup>&</sup>lt;sup>2</sup> Faculty of Pharmacy, University of Belgrade, Vojvode Stepe 450, 11000 Belgrade, Serbia <sup>3</sup>Higher Technological School of Professional Studies 15000 Šabac, Serbia

General procedure.  $Co(BF_4)_2 \cdot 6H_2O$  (0.5 mmol) and N-methyglycine / N,N-dimethylglycine (0.375 mmol) (neutralized previously to pH $\sim$  6,0 with NaOH, c=0,1mol/dm³) were dissolved in minimum amount of CH<sub>3</sub>OH and refluxed on water bath (80° C) for 30 min with stirring. After that, a suspension of tpmc (0,25 mmol) in CH<sub>3</sub>OH (molar ratio of reactants was 2 : 1.5 : 1) was added. Reaction mixture was continuously stirred and heated for the next 2 h, concentrated to ½ of initial volume and left in refrigerator overnight. Microcrystalline purple-violet product was separated by suction, dried at room temperture, powdered, washed properly with cold water, and the procedure of is repeated until pure product is obtained.

[Co<sub>2</sub>(*N*-mgly) tpmc](BF<sub>4</sub>)<sub>3</sub> · 4H<sub>2</sub>O. Yield (78%). *Anal*. Calc. for  $C_{37}H_{59}O_6N_9Co_2B_3F_{12}$  (FW = 1103): C, 40.28; H, 5.30; N, 11.42. Found: C, 39.94; H, 5.33; N, 11.41. Solubility: well soluble in CH<sub>3</sub>CN, sparingly in DMSO and DMF, insoluble in water,  $C_2H_5OH$  and CH<sub>3</sub>OH.  $Λ_M^{25^\circ C}$  (in CH<sub>3</sub>CN) = 360 Scm<sup>2</sup>mol<sup>-1</sup> (electrolyte type 1 : 3);  $μ_{eff}$ /Co (room temperature) = 4.75  $μ_B$ .

[Co<sub>2</sub>(*N*,*N*-dmgly) tpmc](BF<sub>4</sub>)<sub>3</sub> · 3H<sub>2</sub>O. Yield (75%). *Anal*. Calc. for  $C_{38}H_{59}O_5N_9Co_2B_3F_{12}$  (FW = 1099): C, 41.52; H, 5.31; N, 11.46. Found: C, 41.30; H, 5.25; N, 11.50. Solubility: well soluble in CH<sub>3</sub>CN, sparingly in DMSO and DMF, insoluble in water,  $C_2H_5OH$  and CH<sub>3</sub>OH.  $Λ_M^{25^\circ C}$  (in CH<sub>3</sub>CN) = 366 Scm<sup>2</sup>mol<sup>-1</sup> (electrolyte type 1 : 3);  $μ_{eff}$ /Co (room temperature) = 4.70  $μ_B$ .

**Table I.** VIS spectral data (in CH<sub>3</sub>CN)

Complex	$\lambda_{\text{max}} [\text{nm}], (\epsilon) [\text{dm}^3 \text{mol}^{-1} \text{cm}^{-1}]$			
[Co <sub>2</sub> (gly)tpmc](ClO <sub>4</sub> ) <sub>3</sub> *	458(80)	511(96)	548(79)sh	
[Co <sub>2</sub> (N-mgly)tpmc](BF <sub>4</sub> ) <sub>3</sub> · 4H <sub>2</sub> O	455(30)	508(53)	544(35)sh	
$[\text{Co}_2(N,N-\text{dmgly})\text{tpmc}](\text{BF}_4)_3 \cdot 3\text{H}_2\text{O}$	487(38)	510(42)	546(28)sh	

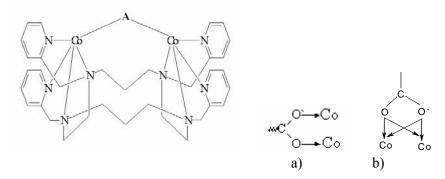
<sup>\*</sup> data taken from ref. [2]

VIS electronic spectral data are compared with earlier described Co(II) glycinato complex (Table I). Electronic spectra corresponded to high-spin Co(II) complexes. Glycinato and N-methylglycinato Co(II) complexes exhibited very similar spectra. There is a slight batochromic shift in the case of N-methylglycinato complex related to glycinato one. However, in the case of N,N-dimethylglycinato ligand a hipsochromic shift is found. In both compexes lower intensities due to lower asymmetry is obvious. In IR spectra (KBr technique) of both complexes the following bands were found (in cm<sup>-1</sup>): at 3560-3240 for the v(O-H) from crystal water (medium), ~1600 skeletal vibrations of pyridine (strong, sharp) and ~1100 from  $v(BF_4)$ , weak bands at 485 from v(Co-N) and at ~ 420 ascribed to v (Co-O), respectively. The absence of the band in the region ~1700 might indicate that there are no free C=O groups, or that both oxygens participate in coordination. Another possibility is its participation in H-bonds formation. However, in the range 1582-1301 several bands of medium intensities were found from the asymmetrical  $(v_s)$  or symmetrical  $(v_s)$ stretching valence vibration of COO group (Table II). The shifting and positions of these bands, as well as  $\Delta v$  values ( $\Delta v = v_a - v_s$ ) is useful tool for the coordination mode and the strength of Co-O bonds prediction when compared mutually and with the same data for free ligands, although not always unambiguously. Based on IR spectra only in both cases could be supposed combined chelate-bridged coordination (Scheme 1b). However, from all other data and using models the more probable geometry for N-mgly is O,O'-bridged (Scheme 1a) and coordination number 5. The other coordination modes (for example asymmetrical in which one O is common), are also not excluded. Co(II)-O bond is the strongest in glycinato complex and the weakest in *N*,*N*-dmgly which is expected due to the enhanced steric repulsion of methyl group(s).

**Table II** Characteristic  $v_a$ ,  $v_s$  and  $\Delta v$  values of free aminocarboxylates and derivatives and in their corresponding complexes in cm<sup>-1</sup>

Compound	$v_a$	$\nu_{\mathrm{s}}$	Δν
Na-glycinate	1595 s	1399 s	196
$[Co_2(gly)tpmc](ClO_4)_3*$	1580 m	1365 m	215
Na- N-mglycinate	1581 s	1391 m	190
$[\text{Co}_2(N\text{-mgly})\text{tpmc}](\text{BF}_4)_3 \cdot 4\text{H}_2\text{O}$	1479 m	1302 m	177
Na- N,N-dmglycinate	1620 s	1410 m	210
$[\text{Co}_2(N, N\text{-dmgly})\text{tpmc}](\text{BF}_4)_3 \cdot 3\text{H}_2\text{O}$	1460m	1301m	159

taken from reference [2], s = strong, m=medium



**Scheme 1.** Proposed geometries in the complex cation: A= aminocarboxylato (or methyl derivatives) ligand; a) O,O'-bridged b) combined chelate-bridge

#### Conclusion

Two Co (II) complexes with macrocyclic ligand (tpmc) and mono or dimethyl *N*- substituted glycine were isolated in good yield in pure state. Some of their physico-chemical characteristics and tentative the most probable way of coordination are discuses and proposed. Both complexes, all ligands and solvents were preliminary also tested against some microorganisms, in DMSO//H<sub>2</sub> O and certain bacteriostatic activity is detected in both cases.

#### References

- [1] G. Vučković, D. Opsenica, S.P. Sovilj, D. Poleti, M. Avramov-Ivić, *J.Coord.Chem.*, 1997, **42**, 241
- [2] G. Vučković, D. Opsenica, S.P. Sovilj, D. Poleti, J. Coord. Chem., 1999, 47, 331
- [3] S.B.Tanasković, G.N.Vučković, oral presentation announced on XLI Conference of the Serbian Chemical Society, Belgade, Book of Abstracts, 2003,75
- [4] S. Chandrasekhar, W.L. Waltz, L. Prasad, J.W. Quail, Can.J.Chem., 1997, 75, 1363.

#### ORGANOMETALLIC PLATINUM(IV) METALLACROWN ETHERS – SYNTHESIS, HOST PROPERTIES AND ANTI-CANCER EVALUATION [1]

H. Schmidt<sup>1</sup>, M.E. Kelly<sup>1</sup> and G.N. Kaluđerović<sup>1,2</sup>

<sup>1</sup>Institut für Chemie, Martin-Luther-Universität Halle-Wittenberg, 06120 Halle, Germany. <sup>2</sup>Department of Chemistry, Institute of Chemistry, Technology and Metallurgy, Studentski trg 14, 11000 Belgrade, Serbia.

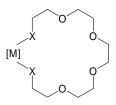
#### Abstract

Via the reaction of appropriate  $\alpha, \omega$ -bis(imidazolyl) substituted polyether ligands, (im)(CH<sub>2</sub>CH<sub>2</sub>O)<sub>x</sub>CH<sub>2</sub>CH<sub>2</sub>(im); im = imidazol-1-yl; x = 2–5, 7, with [(PtBr<sub>2</sub>Me<sub>2</sub>)<sub>n</sub>] octahedral configured platinum(IV) metallacrown ethers (MCE) [PtBr<sub>2</sub>Me<sub>2</sub>{(im)(CH<sub>2</sub>CH<sub>2</sub>O)<sub>x</sub>CH<sub>2</sub>CH<sub>2</sub>(im)}] (**A**) were synthesized. Reaction of [(PtBr<sub>2</sub>Me<sub>2</sub>)<sub>n</sub>] with (im)CH<sub>2</sub>CH<sub>2</sub>(im) or 2,2'-bis(im)ethyl ether yielded dinuclear [(PtBr<sub>2</sub>Me<sub>2</sub>)<sub>2</sub>{ $\mu$ -(im)(CH<sub>2</sub>CH<sub>2</sub>O)<sub>x</sub>CH<sub>2</sub>CH<sub>2</sub>(im)}<sub>2</sub>] (x = 0, 1) (**B**). Full characterization of these complexes by microanalysis, NMR, ESI- and EI-MS as well as X-ray structure determination is discussed.

The ability of the larger MCEs to act as hosts to  $[R_2NH_2]^+$  guests is investigated in solution (NOE, ESI-MS). Finally, several of these MCEs were found to possess *in vitro* antitumor activity on human tumor cell lines. [2]

#### Introduction

Metallacrown ethers (MCE) are a class of metallomacrocycles that can be prepared through a ring closing reaction between a ditopic ligand with donor functionalities X (here X = imidazol-1-yl moiety) at the extremities of a polyether chain and a transition metal fragment [M]. Both the size of the ring cavity in the MCEs and the orientation of the oxygen atoms indicate its potential to bind cations in the metallacrown ether ring cavity.



Nowadays, the development of organometallic complexes, particularly of Ru and Fe, with anticancer properties provides alternatives to the more traditional cisplatin–like derivatives. [2] The imidazole moiety, prevalent in biological systems, is known to form part of the coordination environment in a large number of metalloenzymes. The inclusion of polyether chains in transition metal complexes may be expected to lend these complexes better to hydrophilic environments. With these features in mind, we were interested in synthesis and properties of a series of organometallic MCEs of platinum(IV) with polyether bis(imidazol-1-yl) type ligands.

#### **Results and Discussion**

#### Synthesis and Characterization

Mononuclear (type **A**) and dinuclear (type **B**) MCEs were obtained as yellowish microcrystalline solids in high yields (72–100%) by reaction of different (im)(CH<sub>2</sub>CH<sub>2</sub>O)<sub>x</sub>CH<sub>2</sub>CH<sub>2</sub>(im) ligands (im = imidazol-1-yl; x = 0-5, 7) with the precursor complex [(PtBr<sub>2</sub>Me<sub>2</sub>)<sub>n</sub>]:

These MCEs were characterized in solution by  $^{1}$ H,  $^{13}$ C and  $^{195}$ Pt NMR spectroscopy. NMR data prove the presence of octahedrally coordinated Pt(IV) complexes with mutual *trans* coordination of the nitrogen donor ligands to the methyl ligands (configuration index: OC–6–13). This structural information is confirmed by X-ray crystallographic measurements. Fig. 1 shows examples for the molecular structures of both types of MCEs. All structures show a roughly octahedral arrangement of ligator atoms [Br<sub>2</sub>C<sub>2</sub>N<sub>2</sub>] around the platinum center.

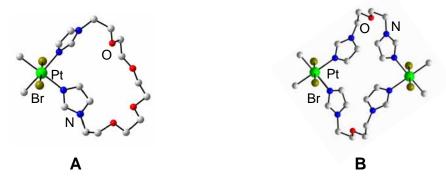


Fig. 1: Molecular structures of mononuclear (A) and dinuclear (B) MCEs

Bond lengths and angles of molecular structures in larger mono- and dinuclear MCEs show no unusual deviations from the norm. The size of the ring cavity in structures of larger mononuclear MCEs and the orientation of the oxygen atoms in the polyether bridge indicate their potential to bind cations in the MCE ring cavity.

#### **Binding Studies**

Similar to crown ethers, larger MCEs of type **A** may behave as host molecules to dialkylammonium guests in solution. Whereas in polar solvents (acetonitrile, acetone) dialkylammonium salts are freely soluble and no evidence of interaction with the MCEs was found, in CD<sub>2</sub>Cl<sub>2</sub> solution coordination induced shift on the guest is found in the respective <sup>1</sup>H and <sup>13</sup>C NMR spectra. Nuclear Ovenhauser enhancement (NOE) experiments were undertaken for [R<sub>2</sub>NH<sub>2</sub>]<sup>+</sup>/MCE combinations. Whereas

for larger MCEs (x > 3) intensity enhancement of the N-C $H_2$  resonance of the  $[R_2NH_2]^+$  guest was found by irradiating into CH<sub>2</sub> resonances of ethereal backbone, similar enhancement with smaller MCEs was not observed. Evidence of complexation was also obtained using high resolution ESI mass spectrometry. Spectra of the respective  $[R_2NH_2]^+$ / MCE combinations resulted in the observation of intense peaks for the respective  $[MCE + R_2NH_2]^+$  adduct.

#### Anticancer Properties

In vitro anticancer activity of selected MCEs of the types **A** and **B** was tested on the three human tumor cell lines. The  $IC_{50}$  data of these compounds are compared with those of cisplatin and two of the (im)( $CH_2CH_2O$ )<sub>x</sub> $CH_2CH_2$ (im) ligands.

Drug uptake was determined by atomic absorption spectroscopy, but analysis of results demonstrates anticancer activity of MCEs tested cannot be correlated to the platinum uptake of the complexes in the three cell lines.

A study investigating the mode of cell death showed that apoptosis (programmed cell death) is induced preferentially in all cell lines, as determined by a trypan blue staining test.

#### Conclusion

The preparation of new types of MCEs afforded in high yields via the reaction of  $\alpha, \omega$ -bis(imidazol-1-yl) polyether type ligands with a platinum(IV) precursor. Investigations in weak donor solvents revealed dialkylammonium/MCE host/guest interactions. Furthermore MCEs possess significant *in vitro* antitumor activity.

#### Literature

- [1] Part of the Ph.D. thesis of M. E. K., planned for 2008 at Martin-Luther-Univer-sität Halle
- [2] M. E. Kelly, A. Dietrich, S. Gómez-Ruiz, B. Kalinowski, G. N. Kaluđerović, Th. Müller, R. Paschke, J. Schmidt, D. Steinborn, Ch. Wagner and H. Schmidt, Organometallics, submitted

#### SPECTRAL ANALYSIS OF Pd(II) COMPLEX WITH ISATIN-3-THIOSEMICARBAZONE

S.S. Konstantinović<sup>1</sup> and R.S. Nikolić<sup>2</sup>

<sup>1</sup>Faculty of Technology, Bulevar oslobodjenja 124, 16000 Leskovac, Serbia <sup>2</sup>Faculty of Science and Mathematics, Višegradska 33, 18000 Niš, Serbia

#### **Abstract**

Coordination compound of Pd(II) with isatin-3-thiosemicarbazone (L) was prepared. Its structure was established to be PdLCl<sub>2</sub> by using elemental analysis, as well as FTIR and UV/VIS spectroscopic methods. The results indicate coordination through the nitrogen and sulfur of ligand.

#### Introduction

A different thiosemicarbazones have wide application in medicine and veterine as active physiological preparations, due their anti-inflammatory, antituberculosis, anticancer, activity, etc [1]. The heterocyclic thiosemicarbazones and their metal complexes are among the most widely studied compounds, when its about their biological activity and applications[1,2].

#### **Experimental**

All chemicals used for the preparation of complex were of AR grade. Microanalysis for carbon, hydrogen and nitrogen was carried with a Carlo Erba 1106 microanalyser. The chloride content was determined potentiometric. The metal contents were determined using a Virial AA-457 Double beam spectrometer. The melting points were determined by using Thomas-Hoover melting point apparatus and are uncorrected. The molar conductivity of the complex was measured with Iskra Conductivity Meter 0.67 using 10<sup>-3</sup> mol·dm<sup>-3</sup> solutions in DMF. FTIR spectra were recorded using a Michaelson Bomen MB-series spectrophotometer, using KBr pellet (1 mg/100 mg) technique. The electronic spectra were recorded on Perkin/Elmer Lambda 15 UV/VIS spectrophotometer using 10<sup>-3</sup> mol·dm<sup>-3</sup> solutions in DMF.

#### Synthesis of isatin-3-thiosemicarbazone and Pd(II) complex

An equimolar amount of isatin and thiosemicarbazide were dissolved in 95% ethanol. The solution was heated under reflux for 1 hour. The yellow product was filtered, washed with ethanol and dried *in vacuo* over CaCl<sub>2</sub> [3,4]. The complex was synthesized in ethanol, using equimolar amounts of PdCl<sub>2</sub> and ligand. The solution was heated under reflux for 5 hours. The orange product was filtered, washed with ethanol and dried *in vacuo* over CaCl<sub>2</sub> [3,4].

#### **Results and Discussion**

The complex of Pd(II) with isatin-3-thiosemicarbazone was synthesized by the direct reaction in ethanol, using 1:1 molar ratio of all reactants.

*Isatin-3-thiosemicarbazone* **IR** (KBr, cm<sup>-1</sup>): 3470, 3304  $\nu$ (NH<sub>2</sub>), 3239, 3132  $\nu$ (NH), 1710  $\nu$ (C=O), 1585  $\nu$ (C=N), 1250  $\nu$ (C=S). **UV/VIS** (DMF, ν cm<sup>-1</sup>/εmol<sup>-1</sup>dm<sup>3</sup>cm): 28.6/0.946 ( $\pi$ - $\pi$ \*), 27.3/1.325 (n- $\pi$ \*). *Analysis:* **Found:** 48.95%C, 3.75%H, 25.30%N, 14.61%S; **Calculated:** 49.08%C, 3.70%H, 25.32%N, 14.56%S. **Yield** 91.1%, **m.p.** 239-241°C.

*PdLCl*<sub>2</sub> IR (KBr, cm<sup>-1</sup>): 3460, 3413  $\nu$ (NH<sub>2</sub>), 3233, 3124  $\nu$ (NH), 1705  $\nu$ (C=O), 1575  $\nu$ (C=N), 1231  $\nu$ (C=S). **UV/VIS** (DMF, ν cm<sup>-1</sup>/εmol<sup>-1</sup>dm<sup>3</sup>cm): 27.2/3.195 ( $\pi$ - $\pi$ \*), 34.1/3.589 (n- $\pi$ \*), 19.5/0.817 *CT-transfer*, 16.7/0.01 d—d\*. Analysis: Found: 28.75%C, 2.03%H, 13.45%N, 18.56%Cl.; Calculated: 28.71%C, 2.09%H, 13.39%N, 18.54%Cl. Yield 59.69%, Color orange, m.p. 286°C.

The complex was isolated in high yield and is air-stable both in the solid-state and in solution. The result of elemental analysis is consistent with a proposed structure of the obtained complex. Molar conductance of  $10^{-3}$  mol dm<sup>-3</sup> solution of the complex in DMF are in correlation with its structure. It indicates that Pd(II) complex behaves as non-electrolytes [4]. This suggests that the chloride ion be involved in the coordination by its presence in the inner space of the complex (Fig. 1).

Fig. 1. Reaction scheme of complex formation

The electronic spectra of isatin-3-thiosemicarbazone shows primer absorption band of aromatic ring and thiosemicarbazone moiety due to transition of  $\pi$ - $\pi$ \* type and an n- $\pi$ \*. These transitions are found also in the spectra of the complex, but they are shifted towards lower and higher frequencies, confirming the coordination of the ligand by the metallic ion. The electronic spectrum of palladium (II) complex, exhibits bands at 16.700 and 19.500 cm<sup>-1</sup>, assigned to charge transfer and  $d \rightarrow d^*$  transition, respectively [5]. The comparation of similar palladium (II) compounds with this one suggests a square-planar stereochemistry around the central ion. As all thiosemicarbazones, isatin-3-thiosemicarbazone can exhibit thione-thiol tautomerism, since it contains a thioamide –NH-C=S functional group. There is no IR band at 2500-2600 cm<sup>-1</sup> in the spectrum of the free ligand as well as complex

and this indicates the absence of S-H grouping in the ligand [2]. At 1700 cm<sup>-1</sup>, band assigned to v(C=O) mode was observed at similar position in the ligand and complex spectra, suggesting the noninvolvement of carbonyl oxygen in complex formation. The absorption band v(C=N) is shifted to lower frequency in the spectrum of the complex, indicates that this group is the coordinated site of the ligand. It also can be seen that absorption bands of v(C=S) stretching vibration in the spectrum of coordination compound is shifted to the lower frequency upon coordination, too. Taking into account the assignments of the vibrational absorptions, an N, S bidentate ligand behavior can be proposed in the Pd(II) complex with square-planar geometry around the metal atom [4,6].

#### Reference

- [1] J. F. M. da Silva, S. J. Garden, A. C. Pinto, J. Braz. Chem. Soc., 2001, 12 273-280.
- [2] E. M. Jouad, G. Larcher. M. Allain. A. Riou, G. M. Bouet, M. A. Khan, X. Do Thanh, J. Inorg. Biochem., 2001, 86, 565-571.
- [3] S. S. Konstantinović, B. C. Radovanović, S. P. Sovilj, S. Stanojević, J. Serb. Chem. Soc., 2008, 73, 7-13.
- [4] S. S. Konstantinović, B. C. Radovanović, A. Krklješ, J. Therm. Anal. Calorim., 2007, 90, 525-531.
- [5] A. B. P. Lever, Inorganic Electronic Spectroscopy, Elsevier, Amsterdam, 1984.
- [6] M. B. Ferrari, C. Pelizzi, G. Pelosi, M. C. Rodrigey-Arguelles, Polyhedron, 2001, 21 (2002) 2593-2599.

## SPECTRAL ANALYSIS AND ANTIFUNGAL ACTIVITY OF Co(II) COMPLEX WITH ISATIN-3-THIOSEMICARBAZONE

S.S. Konstantinović<sup>1</sup>, B.C. Radovanović<sup>2</sup> and R.S. Nikolić<sup>2</sup>

<sup>1</sup>Faculty of Technology, Bulevar oslobodjenja 124, 16000 Leskovac, Serbia <sup>2</sup>Faculty of Science and Mathematics, Višegradska 33, 18000 Niš, Serbia

#### **Abstract**

Isatin-3-thiosemicarbazone complex with Co(II) was synthesized. It's chemical structure have been proposed using elemental analysis, as well as, molar conductivity, magnetic susceptibility measurements IR, UV/VIS and <sup>1</sup>H NMR methods. The complex was evaluated for it's antimifungal activity against 4 fungi using microdilution method. The complex have an enhanced activity compared to the ligand due to transition metal involved in coordination

#### Introduction

The synthetic versatility of isatin has led to an extensive use of this compound in organic synthesis [1]. It has stemmed from the interest in the biological and pharmacological properties of its derivatives. Also, thiosemicarbazone derivatives are of considerable interest because of their chemistry and potentially beneficial biological activities, such as antitumor, antibacterial, antiviral and antimalarial activities [1,2]. Many coordination compounds of transition metals with isatin derivativess show greater activity than the ligands alone.

#### Experimental

Microanalysis for carbon, hydrogen and nitrogen was carried with a Carlo Erba 1106 microanalyser. The chloride content was determined potentiometric. The metal contents were determined using a Virial AA-457 Double beam spectrometer. The melting points were determined by using Thomas-Hoover melting point apparatus and are uncorrected. The molar conductivity of the complex was measured with Iskra Conductivity Meter 0.67 using 10<sup>-3</sup> mol·dm<sup>-3</sup> solutions in DMF. FTIR spectra were recorded using a Michaelson Bomen MB-series spectrophotometer, using KBr pellet (1 mg/100 mg) technique. The electronic spectra were recorded on Perkin/Elmer Lambda 15 UV/VIS spectrophotometer using 10<sup>-3</sup> mol·dm<sup>-3</sup> solutions in DMF. The compounds were evaluated for their in vitro antifungal activity against Microsporum gypsum, Epidermophyton floccosum, Histoplasma capsulatum, Candida albicans and Aspergillus niger following the guidelines in NCCLS document M27-A using the mi-crodilution broth method [6]. The minimum inhibitory concentrations (MIC) of the chemical compounds were recorded as the lowest concentration of each chemical compound in the tubes with no growth (i.e. no turbidity) of inoculated yeast.

Synthesis of isatin-3-thiosemicarbazone (L) and Co(II) complex

Isatin-3-thiosemicarbazone was synthesized using conventional method [3,4]. The complex was synthesized in ethanol, using equimolar amounts of CoCl<sub>2</sub> and ligand. The solution was heated under reflux for 4 hours. The dark red product was filtered, washed with ethanol and dried *in vacuo* over CaCl<sub>2</sub>[3,4].

#### **Results and Discussion**

The complex of Co(II) with isatin-3-thiosemicarbazone was synthesized by the direct reaction in ethanol, since ligand is soluble in ethanol, methanol, DMF and DMSO.

*Isatin-3-thiosemicarbazone* **IR** (KBr, cm<sup>-1</sup>): 3470, 3304  $\nu$ (NH<sub>2</sub>), 3239, 3132  $\nu$ (NH), 1710  $\nu$ (C=O), 1585  $\nu$ (C=N), 1250  $\nu$ (C=S). **UV/VIS** (DMF, v cm<sup>-1</sup>/εmol<sup>-1</sup>dm<sup>3</sup>cm): 28.6/0.946 ( $\pi$ - $\pi$ \*), 27.3/1.325 (n- $\pi$ \*). <sup>1</sup>**H NMR** (DMSO, δ, ppm) 6.9-7.7 (m, 4H, Ar), 8.69, 9.05 (s, 2H, NH<sub>2</sub>), 11.21 (2, 1H, NH), 12.47 (s, 1H, NH). *Analysis:* **Found:** 48.95%C, 3.75%H, 25.30%N, 14.61%S; **Calculated:** 49.08%C, 3.70%H, 25.32%N, 14.56%S. **Yield** 91.1%, **m.p.** 239-241°C.

*CoL*<sub>2</sub>*Cl*<sub>2</sub> **IR** (KBr, cm<sup>-1</sup>): ): 3418, 3306, 3221, 3137  $\nu$ (NH)+ $\nu$ (NH<sub>2</sub>), 1651  $\nu$ (C=O), 1551  $\nu$ (C=N), 838  $\nu$ (C=S). **UV/VIS** (DMF, ν cm<sup>-1</sup>/εmol<sup>-1</sup>dm<sup>3</sup>cm ): 28.9/3.195  $\pi \rightarrow \pi^*$ , 27.1/3.580  $n \rightarrow \pi^*$ , 19.5/0.817  $^4T_{1g} \rightarrow ^4T_{1g}$  (P), 16.7/0.013  $^4T_{1g} \rightarrow ^4A_{2g}$  (F), 14.7/0.005  $^4T_{1g} \rightarrow ^4A_{2g}$ . Analysis: Found: : 42.71%C, 2.15%H, 22.13%N, 12.42%Cl, 10.43%Co; Calculated: 42.70%C, 3.20%H, 22.10%N, 12.46%Cl, 10.34%Co Yield 49.12%, Color dark red, m.p. 264°C.

The complex was isolated in high yield and is air-stable both in the solid-state and in solution (Fig. 1). The result of elemental analysis is consistent with a proposed structure of the obtained complex. Molar conductance of  $10^{-3}$  mol dm<sup>-3</sup> solution of the complex in DMF are in correlation with its structure. It indicates that Co(II) complex behaves as electrolyte since chloride ions are present in outer space of compound. [4].

Fig. 1. Reaction scheme of complex formation

The transitions of  $\pi$ - $\pi^*$  type and an n- $\pi^*$  are found in the electronic spectra of ligand and complex in which they are shifted towards lower and higher frequencies, confirming the coordination of the ligand by the metallic ion. The electronic absorption spectra of the cobalt (II) complex contain two distinct d-d bands located at  ${}^4T_{1g} \rightarrow {}^4T_{2g}(F)$ , and  ${}^4T_{1g} \rightarrow {}^4T_{1g}(P)$  transitions corresponding to a hexacoordinated Co(II). The third band corresponds to the forbidden two-electron transition  ${}^4T_{1g} \rightarrow {}^4A_{2g}$ , which is weaker with the majority of Co(II) complexes, and usually appears as a shoulder. [5]. As all thiosemicarbazones, isatin-3-thiosemicarbazone can exhibit thione-thiol tautomerism, since it contains a thioamide –NH-C=S functional group. There is no IR band at 2500-2600 cm<sup>-1</sup> in the spectrum of the free ligand as well as complex and this indicates the absence of S-H grouping in the ligand [2]. In the Co(II) complex the  $\nu$ (C=O),  $\nu$ (C=N) and  $\nu$ (C=S) values undergoe a negative shift upon coordination Taking into account the assignments of the vibrational absorption, an N,O, S tridentate ligand behavior can be proposed in the Co(II) complex with octahedral geometry around the metal atom [4,7].

The antifungal activity of the complex was studied with four pathogenic fungi, using dilicione method. The results are summarized in Table 1.

**Table 1.** MIC values  $(\mu g \cdot cm^{-3})$  of the investigated compounds against tested fungi.

	M.gypsum	E. floccosum	H.capsulatum	C.albicans	A.niger
Com.					
ITS	39.06	39.06	156.25	78.12	78.12
Co(ITS) <sub>2</sub> Cl <sub>2</sub>	9.76	19.53	39.06	9.76	2.44

Compare to ligand, the complex exhibit better activity against all tested fingi. The best activity is achievied in case of fungi *Aspergillus niger*.

#### Reference

- [1] J. F. M. da Silva, S. J. Garden, A. C. Pinto, J. Braz. Chem. Soc., 2001, 12 273-280.
- [2] E. M. Jouad, G. Larcher. M. Allain. A. Riou, G. M. Bouet, M. A. Khan, X. Do Thanh, J. Inorg. Biochem., 2001, 86, 565-571.
- [3] S. S. Konstantinović, B. C. Radovanović, S. P. Sovilj, S. Stanojević, J. Serb. Chem. Soc., 2008, 73, 7-13.
- [4] S. S. Konstantinović, B. C. Radovanović, A. Krklješ, J. Therm. Anal. Calorim., 2007, 90, 525-531.
- [5] A. B. P. Lever, Inorganic Electronic Spectroscopy, Elsevier, Amsterdam, 1984.
- [6] National Committee for Clinical Laboratory Standards, Reference meth-od for broth dilution antifungal susceptibility testing for yeasts; approved standard Document M27-A, Villanova, National Committee for Clinical Laboratory Standards 17 (1997) 1–29.
- [7] M. B. Ferrari, C. Pelizzi, G. Pelosi, M. C. Rodrigey-Arguelles, Polyhedron, 2001, 21 (2002) 2593-2599.

# Education (M)

#### **SVANTE AUGUST ARRHENIUS**

#### T. Halasi

Department for Chemistry, Faculty of Sciences, Novi Sad, Trg Dositeja Obradovica 3 halasi@ih.ns.ac.yu

#### **Abstract**

Svante August Arrhenius was an excelent scientist, originally a physicist, and pioneer physical chemist. Ha was in childhood typical Wunderkind, afterwards very ambitious student at University of Uppsala. In 1881, he went to Stockholm to work with professor Erik Edlund. His dissertation appeared in 1884, and it consisted from 56 thesis. Arrhenius' explanation was that in forming a solution, the salt dissociates into charged particles. His dissertation was noted as non sine laudate, but deffende of thesis with cum laudate and so Arrhenius bekam Ph.D. In 1903, the Nobel Prize in Chemistry was awarded to Svante August Arrhenius "for his electrolytic theory of dissociation". Arrhenius' best friends was two physical chemists, Wilhelm Ostwald (1853—1933) [1] and Jacobus Henricus van't Hoff (1852-1911), both awarded with Nobel Prize in chemistry [2].

#### Introduction

Arrhenius is the third best known Swedish chemist, after Tolbern Bergman, 1735-1784) and Jöns Jacob Berzelius, 1779-1848). Arrhenius was professor of Astrophysics and author of Textbook of Cosmic physics and book of cosmogy *Worlds in the making* (1908). Arrhenius's theory of origin of world is much more Science fiction than science hypothesys. He studied the "Greenhouse effects" and role of carbon-dioxide in atmosphere [3].

Name of one lunar impact crater located just on the far side of the Moon Svante Arrhenius. The Crater characteristics are: Coordinates 55.6° N, 91.3° E; Diameter 40 km; Depth Unknown; Colongitude 269° at sunrise [6].

#### **Arrhenius' 56 Thesis**

Svante Arrhenius suprised the Oponents with 56 thesis in his doctoral dissertation. Oponets of Arrhenius's Doctoral dissertatin evaluated the Work with with *Non sine laudate*, or on english, not praiseworthy. But, the Arrhenius' 56 thesis were developed the theory of electrolyte dissociation, and most also accepted today anchanged or with minor modificatin. The titel of Arrhenius' Doctoral dissertation on original french was: *Recherches sur la conductebilité galvanique des électrolytes* (Investigation on the galvanic conductivity of electolytes), published in 1884. in Uppsala. At the age of 24, Arrhenius had determined the conductivity of many electrolytes. His data may have taken the following format:

	Conductivity ( $\Omega^{-1}$ cm <sup>2</sup> mol <sup>-1</sup> )					
Electrolyte	0.001 M	0.005	0.01	0.05	0.1	0.5
CH₃COOH	41	20	14	6.5	4.6	2.0
HCl	377	373	370	360	351	327
CH <sub>3</sub> COONa	75	72	70	64	61	49

Table 1. Conductivity of electrolytes into Arrhenius Disertation

Arrhenius from this datas of conductivity concluded:

- In the first these: The resistance of an electrolyte is increased when the dilution is doubled.
- In very dilute solutions the conductivity is nearly proportional to the concentration.
- The conductivity of a solution is equal to the sum of conductivities of the salt and the solvent,
- In the theses 7, 8 and 9: The electrical resistance rises with increasing viscosity, complexity of the ion, and the molecular mass of the solvent, (incorrect)
- In the these 15: If these laws are not observed, it must be due to a chemical reaction between the substances including the solvent [4].

Arrhenius concluded from the above statements that the "molecule" breaks apart into a positive fragment and negative fragment, called ions, by its interaction with the solvent. This was a great leap in thinking. The concept of dissociation did not come at first accepted but developed as time allowed Arrhenius to talk with other chemists. The review committee at University of Uppsala was very reluctant to award the doctorate degree to Arrhenius but finally gave a fourth rank (barely passing) for the dissertation. The disgrace would be prevent Arrhenius for aspiring to any professorship.

#### Arrhenius' shortly biography

Svante August Arrhenius was born on February 19, 1859 at Wik, near Uppsala and died on October2, 1927. The father Svante Gustav Arrhenius (1813-1885) was a Questor employed by the Uppsala University (chief of penalty council). His mother was Carolina Thumberg (1820-1906) and in four boys were born in the family Arrhenius. Svante August was the second son. In 1876 he entered the University of Uppsala, studying matematics, chemistry and physics. In 1881. he went to Stockholm to work at Professor Erik Edlund at the Academy of Sciences. Here, Arrhenius began his thesis where he concluded that alaectrolytes, dissolved in water, become to different degrees split or dissociated into electrically opposite positive and negative ions. The dissertation was not acceptable in Uppsala, for example by professor Tobias Robert Thalen (1827-1905). On the other hand, professor Sven Otto Peterson (1848-1908), professor of Chemistry at Stockholms Högskola, emphasized the originality of the dissertation. A new difficulty arose in Arrhenius career by election for the Swedish Academy of Sciences in 1901. In 1903 he become the first Swede to be awarded the Nobel Prize in chemistry, and he bacame a

Fellow of the Royal Society in 1910. In 1905. upon the founding of the Nobel Institute for Physical Research at Stockholm, he was appointed as a rector of the institute. In the position where remained until retirement in 1927. He was twice married. In 1894, he married Sofia Rudbeck, and in this marriage they had son Olof, excellent Biologist. Svante Arrhenius and in 1905., he married his former student, Maria Johansson by whom he had one son, Swen (was born 1909) and twoo daughters Ester(1913.) nad Anna-Lisa (1914). Arrhenius in November 7., 1924., he fell in serious illness, died in October 2, 1927, and was burried in Uppsala in October 8, 1927[5].

#### Acknoledgement

The authors wish to thank Ministry Sciences of the Republic of Serbia for financial support this work with Project *European Dimension of Change of the Education System in Serbia* No.149009 (2006-210)

#### Literature

- G. Ostwald, (1953). Wilhelm Ostwald Mein Vater, Berliner Union, Stuttgart, p.171-180.
- [2] E. Cohen, (1912). Jacobus Henricus van't Hoff, Sein leban und Wirken, Akademische Verlasgeselscaft m.b.H, Leibzig, 219-254.
- [3] E.H. Riesenfeld, (1931). Svante Arrhenius, Akademische Verlagsgeselschaft B.M.H, Leipzig,
- [4] Yu.I. Solovjev, N.A. Figurovskij, (1959). Svante Arrenius 1859-1959, Izdatelstvo Akademii nauk SSSR, Moskva, p.3-118.
- [5] Eucken, (1922). Grundniss der physikalische Chemie, Akademische Verlagsgeselschaft, Leipzig, 217-240.
- [6] L.E. Andersson, E. A. Whitaker, (1982). NASA Catalogue of Lunar Nomenclature. Nasa RP-1097

#### GRAVIMETRIC MEASUREMENT OF THE SECOND VIRIAL CO-EFFICIENT OF CO<sub>2</sub>

Ph.J. Wantuck and B.H. Milosavljevic\*

Pennsylvania State University, Department of Chemistry, 104 Chemistry Building, University Park, PA 16802, USA \*corresponding author: bhm11@psu.edu

#### **Abstract**

The development of a new simple experimental technique for determination of the second virial coefficient of carbon dioxide at room temperature is under way. It will be used in an undergraduate physical chemistry laboratory setting. The preliminary experiment was performed with an aluminum vessel (V = 565.8 mL) in the pressure interval from 0 to 10 bar thus avoiding the  $CO_2$  condensation problem. By measuring the mass of  $CO_2$  with a 1 mg accuracy, the relative error of the second virial coefficient of  $CO_2$  can be as low as 0.2%.

#### **Theory**

The Ideal Gas Law,  $pV_{\rm m}=RT$ , where p is the pressure,  $V_{\rm m}$  is the molar volume of the gas, R is the universal gas constant, T is the temperature expressed in Kelvin degrees, is one of the most ubiquitous relationships throughout the field of chemistry. Its numerous applications and easily measurable variables make it attractive for use in countless applications. However, the conditions under which the equation gives accurate results are limited over certain ranges, notably low pressures and high temperatures. Deviation from these conditions results in differences in calculated results versus measured results. The virial equation of state, Equation 1,

$$pV_m = RT\left(1 + \frac{B}{V_m} + \frac{C}{V_m^2} + \cdots\right) \tag{1}$$

where B is the second virial coefficient and C is the third virial coefficient, is needed to account for the real properties, i.e. finite molecular volume, intermolecular forces, etc., of gasses. Substituting the compression factor Z, Equation 2,

$$pV_m = RTZ \tag{2}$$

into Equation 1 and rearranging, Equation 3 is obtained.

$$Z - 1 = \frac{B}{V_m} \tag{3}$$

where Z is compression factor, B is the second virial coefficient and  $V_m$  is the molar volume of the gas. The third virial coefficient C can be neglected

since at low pressures  $\frac{C}{V_m} \ll \frac{B}{V_m}$ . [1] Thus by plotting equation 3 one can de-

termine the second virial coefficient with relative ease, unlike the currently used methods [2].

#### **Experimental**

An aluminum pressure vessel with a 0.5658L volume was fabricated to meet pressure constraints of an upper limit of 20 bar. Commercially available (Sigma-Aldrich) bone dry carbon dioxide was used. The low pressures, below 1 torr, were measured using a McLeod gauge. The high pressure measurements were done using an Ashcroft 2089 Digital Gauge with an accuracy of 0.05% total error band. Temperature measurements were preformed using a mercury thermometer with a precision of 0.01 °C in the range of 19 – 35 °C resulting in a 0.03% error in the temperature interval applied. A FLUKE 52II digital thermometer with a 0.1 °C precision was used also. Mass measurements were done using Mettler Toledo PB 503-S FACT balance with 0.001g readability over a range of 0g to 510g.

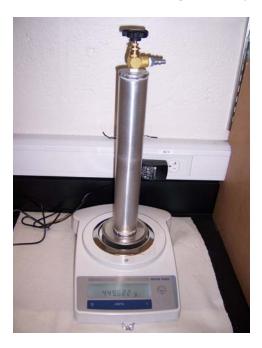




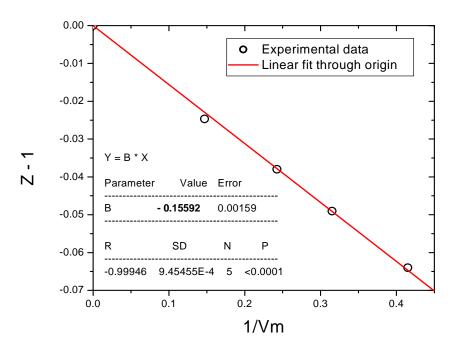
**Fig. 1.** (above) The experimental set-up for the pressure measurement.

**Fig. 2.** (left) The aluminum pressure vessel placed on a Mettler Toledo PB 503-S FACT balance for the CO<sub>2</sub> mass measurement.

#### **Performing the Experiment**

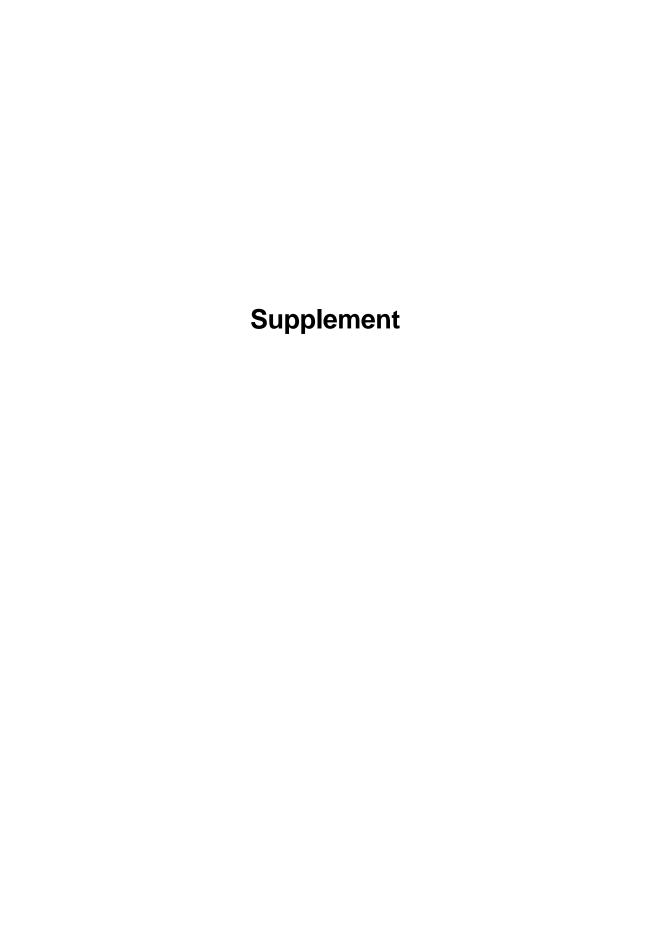
The pressure vessel exterior was cleaned with ethanol and dried using Kimwipes. The vessel was evacuated to a final pressure of 0.02 torr. This pressure is below 0.33 torr which, according to the ideal gas law corresponds to a mass of 0.5mg of  $CO_2$  confined in a 0.6 L vessel. Thus the pressure difference below 0.33 torr is not measurable by the balance. The evacuated vessel was massed and the value recorded. The vessel was then attached to the  $CO_2$  supply tank / pressure gauge assembly with standard regulator (see Figure 1).  $CO_2$  was introduced to the vessel

until the pressure reached approximately 10 bar. The digital thermocouple was placed between the housing cylinder and the pressure vessel. After approximately 10 minutes the pressure vessel and water bath reached equilibrium. The pressure vessel valve was closed and the pressure was noted. The bleed off valve was then opened and the line pressure was allowed to reach between 1-2 bar before closing. The line was kept at higher than atmospheric pressure to ensure no  $N_2$  or  $O_2$  entered the system. The pressure vessel was disengaged from  $CO_2$  supply tank / pressure gauge assembly and then it was weighed. The vessel was reattached to the  $CO_2$  supply tank / pressure gauge assembly. The pressure vessel valve was opened. The typical amount of  $CO_2$  allowed to escape from the pressure vessel to the line was ~2.5 bar. The system was allowed to reach thermal equilibrium. The pressure vessel valve was closed and the process above was repeated until a final pressure of ~2.5 bar was reached. The graph below shows the Z-1 vs. reciprocal volume data. The slope (-0.156 cm³ mol⁻¹) is equal the second virial coefficient of  $CO_2$  which is in good agreement with the literature value [3].



#### Literature cited

- [1] P. Atkins and J. De Paula, Physical Chemistry, 8th Ed, Freeman, 2006
- [2] Arthur Halpern and George McBane, Experimental Physical Chemistry *A Laboratory Textbook*, First Edition, © 2006, W.H. Freeman and Company, Chapter 2, Experiment 4, Real Gases Part 2: The second virial coefficient.
- [3] R. S. Dadson, E. J. Evans and J. H. King, Proc. Phys. Soc., 1967, 92, 1115.



## DEVELOPMENT AND VALIDATION OF A NEW RP-HPLC METHOD FOR THE LOPERAMID HYDROCHLORIDE DETERMINATION IN DRUGS

G.S. Nikolić, I. Savić and V. Marinković

<sup>1</sup> Faculty of Technology, University of Nis, Bulevar oslobodjenja 124, Leskovac16000, Serbia; (goranchem yu@yahoo.com)

#### **Abstract**

A selective, precise and new high-performance liquid chromatographic method for the analysis of loperamid hydrochloride in pharmaceutical formulations was developed and validated. The mobile phase consisting buffer (sodium-octansulphonate, triethylamine and ammonium hydroxide) in water:acetonitrile (45:55 v/v) (pH 3.2). The absorbance was monitored with a DAD detector at 226 nm. The flow rate was 1.5 cm<sup>3</sup>min<sup>-1</sup>. The linearity (r = 0.9947) and the recovery (98.58-100.42 %) were found to be satisfactory. The detection and quantitation limits were found to be 0.95 and 3.12 µgcm<sup>-3</sup>. The results demonstrated that the procedure was accurate, precise and reproducible. It can be suitably applied for the estimation of loperamid hydrochloride in pharmaceutical formulations.

#### Introduction

Loperamid (4-(p-chlorophenyl)-4-hydroxy-N,N,-dimethyl-,-diphenyl-1-piperidine butyramide hydrochloride is an opiate agonist widely used as an effective drug for the control and symptomatic relief of the acute non-specific diarrhea [1]. Loperamid is orally administered and is moderately absorbed (~ 40%) from the gastrointestinal tract to undergo the first-pass metabolism in the liver and the excretion in the faces via the bile as inactive conjugates (sulfo- and glucurono combination). For the routine analysis, a simple and rapid analytical HPLC method is suggested in the paper. The objective of the present study was to develop simple, precise, accurate and validated, economic analytical methods for estimating loperamid hydrochloride in a pure form and in pharmaceutical formulations. The developed analytical method was validated as per ICH guidelines [2] and Serbian requirements [3]. Statistical tests were performed on validation data [4].

#### **Experimental**

The method development was performed with an Agilent 1100-Series HPLC system. The repeatability was performed with another LC system consisting of an Agilent 1200-Series binary pump and the UV detector. The separation was carried out at ambient temperature using a ZORBAX Eclipse XDB-C18 column,  $(4.6 \text{ x} 250 \text{ mm}, 5 \mu\text{m})$ . RP-HPLC analysis was performed by isocratic elution with a flow rate of 1.5 cm<sup>3</sup>min<sup>-1</sup>. The mobile phase cosisted of 0.1% sodium-octansulphonate, 0.05% triethylamine, 0.1% ammonium hydroxide in water:acetonitrile (45:55 v/v).

<sup>&</sup>lt;sup>2</sup> Pharmaceutical and chemical industry Zdravlje-Actavis, Vlajkova 199, Leskovac, Serbia.

pH value at 3.2 adjusted with phosphoric acid. All solvents were filtered through a 0.45  $\mu$ m millipore filter. The volumes of 50  $\mu$ L of the solutions and samples were injected into the column. The quantification was effected by measuring at 226 nm.

#### **Results and Discussion**

The mobile phase consisting buffer in water:acetonitrile (45:55 v/v) was selected to achieve the maximum separation and sensitivity. A flow rate of 1.5 cm³min⁻¹ gave an optimal signal to the noise ratio with a reasonable separation time. The maximum absorption of loperamid hydrochloride was detected at 226 nm and this wavelength was chosen for the analysis. Using a reversed-phase C18 column, the retention times for the standard solution of loperamid hydrochloride (c = 0.1 mgcm⁻³) and loperamid hydrochloride in preparation were observed to be 5.54 min and 5.58 min, respectively. The chromatographic parameters such as the efficiency column and the peak asymmetry were reconsidered for the loperamid hydrochloride standard. According to the Number of Theoretical Plato (N=9133), the conclusion was that the efficiency column was satisfactory (HETP=0.027).

The excellent linearity was obtained between the peak areas and the concentrations. The linear regression equation obtained with a regression coefficient (r) of 0.9947 and standard deviation (SD) of 56.0222 was:

$$A_{226} = [20523.028 \times C \text{ (mgcm}^{-3}) + 117.65]$$

Beer's law was obeyed in the range of 10-100 µgcm<sup>-3</sup>. The chromatogram of loperamid hydrochloride was not changed in the presence of common excipients used in the pharmaceutical preparations. The chromatogram of the pure drug sample was matched with the formulation samples in the mobile phase. The calculated t-values of 1.96 were found to be less than that of the tabulated t-values (2.225). Therefore, the proposed analytical method is specific and selective for the drug. The linearity range for loperamid hydrochloride estimation was found to be  $10-100 \text{ µgcm}^{-3}$  (r = 0.9947). The goodness of the fit of the regression equations was supported by high regression coefficient values. The accuracy ranged from 20 to 60 ugcm<sup>-3</sup>. The excellent mean % recovery values, close to 100 %, and their low standard deviation values (SD < 1.0) represent high accuracy of the analytical methods. The validity and reliability of the proposed methods were assessed by the recovery studies. The mean % recoveries (% RSD) for lower, intermediate and higher concentrations were found to be 99.25 (20 µgcm<sup>-3</sup>), 100.42 (40 µgcm<sup>-3</sup>) and 98.58 (60 µgcm<sup>-3</sup>), respectively. The validity and reliability of the proposed methods were further assessed by the recovery studies via a standard addition method. The mean % recoveries (% RSD) for the concentration from 20 µgcm<sup>-3</sup> were found to be 99.73 (0.58), 100.87 (0.64) and 99.74 (0.53), respectively. These results revealed that any small change in the drug concentration in the solutions could be accurately determined by the proposed analytical methods. The precision was determined by studying the repeatability and the intermediate precision. The repeatability (% RSD) ranged from 20 to 60 µgcm<sup>-3</sup>. The repeatability results

indicated the precision under the same operating conditions over a short interval of time and the inter-assay precision. The intermediate precision expresses within-laboratory variations in different days and in different instruments. In the intermediate precision study, RSD values were not higher than 2.0 % in all the cases. RSD values found for the proposed analytical method were well within the acceptable range indicating that the method has excellent repeatability and the intermediate precision. RSD values for the precision studies with real samples of nasal drops were found to be less than 2 %. LOD and LOQ for loperamid hydrochloride were found to be 0.95 and 3.12 µg·cm<sup>-3</sup>.

The assay value of loperamid hydrochloride in preparations was found to be 98.20 % with the standard deviation not more than 0.0091 %. The assay values of formulations were the same as mentioned in the label claim indicating that the interference of the excipient matrix is insignificant in estimation of loperamid hydrochloride by the proposed analytical methods. The estimated drug content with low values of the standard deviation established the precision of the proposed method. The calculated Student's t-values (1.98) did not exceed the tabulated values (theoretical values at 95% confidence limits is t = 2.225).

#### Conclusion

The proposed RP-HPLC method was developed for loperamid hydrochloride. The analytical method is simple, sensitive, rapid and specific and it can be conveniently employed for the routine analysis and the quality control of loperamid hydrochloride in pharmaceutical dosage forms. The method was suitable to determine concentrations in the range 0.01 to  $0.1 \text{ mgcm}^{-3}$ , precisely and accurately. The limits of detection and quantitation for loperamid hydrochloride with a lower concentration were 0.95 and  $3.12 \, \mu \text{g} \cdot \text{cm}^{-3}$ , respectively, the values which are under the lowest expected concentrations in the sample. The sample recovery from the formulation was in good agreement with its respective label claim, which suggested non-interference of formulation excipients in the estimation.

#### References

- [1] K. Lavrijsen, D. Van Dyck, J. Van Houdt, J. Hendrickx, J. Monbaliu, R. Woestenborghs, W. Meuldermans, J. Heykants, J. Pharmacol. Exp. Ther., 1995, 23, 354.
- [2] The European Agency for the Evaluation of Medicinal Products. ICH Topic Q2B Note for Guideline on Validation of Analytical Procedures: Methodology GPMP/ICH/281/95, 1996.
- [3] Jugoslovenska Pharmacopoeia, V ed., Savremena administracija, Beograd, 2000.
- [4] S. Bolton, Pharmaceutical Statistics: practical and clinical application, III ed., Marcel Dekker, New York, 1997, pp. 216–264.

# IDENTIFICATION AND COMPATIBILITY OF THE MAJOR ACTIVE PRINCIPLES IN SOME NEW NATURAL ORIGIN ANTISEPTICS

S. Zlatković, G.S. Nikolić and N. Nikolić

<sup>1</sup>Actavis Trading Ltd., Đorđa Stanojevića 12, Beograd 11070, Serbia <sup>2</sup>Faculty of Technology, Bulevar Oslobođenja 124, 16000 Leskovac, Serbia (goranchem yu@yahoo.com)

#### Abstract

The newly established instrumentation of HPLC/DAD, FTIR, and NMR techniques have been applied for simultaneous identification and physicochemical compatibility determination of the potential major antiseptic constituents (*Hypericum perforatum* L. and *Usnea barbata* extracts) which can be present in some new origin pharmaceutical preparation. Based on the obtained results the conclusion is that a simultaneous use of the analyzed constituents in production of some new preparations with antiseptic properties is possible. The chromatographic separation of antiseptic mixture was performed on a RP-HPLC C18 column. For the NMR detection, the analytes eluted from LC column were trapped and hereafter transported into the NMR flow-cell. The NMR and FTIR techniques allowed the characterization of the major constituent of *Hypericum perforatum* L., mainly hypericin, as well as of *Usnea barbata*, mainly usnic acid.

#### Introduction

A number of effective oral antiseptic compounds administered either topically or systemically is available for the treatment of throat diseases (pharyngitis, laryngitis and tonsillitis). This work is an attempt to provide a simultaneously application of some bioactive natural origin components in new oral antiseptic preparations. A specific mechanism of the influence and new technological solution of manufacturing gives bigger stability and efficiency of natural origin oral antiseptic at an oral tissue. Usnic acid, a yellow crystal substance of natural origin, is one of the most important components from the standpoint of pharmacological activity of domestic oral antiseptic. Usnic acid, isolated from the lichen Usnea barbata, having significant antibacterial activity [1]. It is the fact that if not complied to directions of oral antiseptic consumption they may cause a serious damage lip cavity mucous membrane by usnic acid. Conversely, Hypericum perforatum L. extract, besides antiseptic, shows regenerative abilities to the mucous membrane. The advantage of the new oral antiseptic, including Hypericum perforatum L. extract, is the inhibition of the negative influence from other present ingredients of oral antiseptics to the lip cavity mucous membrane. Hypericine is one of the most important components from the standpoint of pharmacological activity of Hypericum perforatum L. [2]. The study of usnic acid and hypericine is of particular importance due to its practical application in the production of the antiseptic pharmaceutical preparations. Therefore, the compatibility of hypericine and usnic acid in pharmaceutical antiseptics mixture, directly or combined with other excipients, were analyzed by certain instrumentation.

# **Experimental**

The liquid extract of St. John's wort was obtained by maceration with 70% methanol, ratio 1:10, during 48 h. The dry extract of St. John's wort was separated by drying the liquid extract in hot air stream. Usnic acid, freshly isolated from *Usnea barbata*, and its sodium salt was obtained according literature data [3]. The quality of hypericin contained in liquid and dry extracts from the locality of southeast Serbia was determined by HPLC method (Hewlett Packard 1100 Agilent, Lichrosorb RP-C18 column (5  $\mu$ m, 250 x 4 mm), methanol-ethyl acetate-NaH<sub>2</sub>PO<sub>4</sub> mobile phase (pH = 2.1), 0.8 cm<sup>3</sup>min<sup>-1</sup> flow rate, 590 nm detection, 20  $\mu$ l injection volume). The identification and compatibility of hypericine and usnic acid were analyzed by spectrophotometric FTIR and NMR methods. The quality of pharmaceutical product was determined by FTIR method (Bomem MB-100, 40 scans in the range 4000-400 cm<sup>-1</sup>, with resolution of 2 cm<sup>-1</sup>). The identification of usnic acid was performed by <sup>1</sup>H-NMR (400 MHz) spectrum was run in CDCl<sub>3</sub> on a Bruker-Spectrospin Avance DPX 400 with TMS as internal standard.

# **Results and Discussion**

The HPLC chromatography method was developed to profile the major constituents of St. John's wort extract. The objective was to simultaneously separate, identify and quantify hypericin and usnic acid using HPLC (Fig. 1). Quantification was performed using an external standardization method with reference standards. The method consisted of two protocols: one for the analysis of flavonoids and the other for the analysis of the usnic acid. Both protocols used a reverse phase C18 column. The separation of the flavonoids and the usnic acid was achieved within 10 min. The linear response range was established for each compound and all had linear regression coefficient values greater than 0.97. Both protocols proved to be very specific for the constituents analysed.

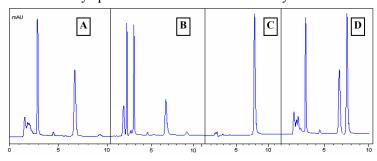


**Fig 1.** Typical HPLC chromatograms of St. John's wort liquid extract (A), St. John's wort dry extract (B), usnic acid (C), pharmaceutical product (mixture of St. John's wort extract and usnic acid) (D)

The FTIR analysis showed no other signals within the analyte peaks (Fig. 2). The method was applied to evaluate the quality of St. John's wort phytopharmaceutical preparation in order to test the method and investigate if they contain at least the main constituents and at what concentrations. The adequate proton NMR spectrum of usnic acid is shown in Fig. 3.

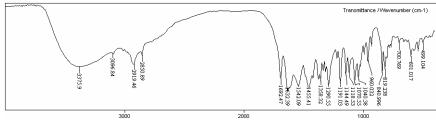


**Fig. 2.** Typical FTIR spectrum of St. John's wort pharmaceutical preparation (mixture of hypericin and usnic acid in mass ratio of 1:1)

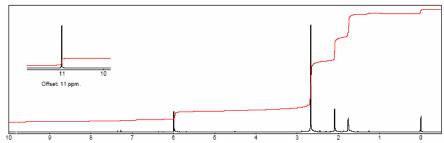


Fig. 3. Typical NMR spectrum of usnic acid isolated from *Usnea barbata*,

# **Conclusion**

The analysis and compatibility studies of the major natural origin active principles were performed for the some new antiseptic products based of St. John's wort and lichen *Usnea barbata*. The identification and compatibility of St. John's wort extracts with active solid state substance from lichen *Usnea barbata*, in various quantitative ratios, was confirmed by use of HPLC, FTIR and NMR spectroscopy. By correlation of spectroscopic data of initial reference compounds (usnic acid and hypericine) and their mixture, it was found that tested pharmaceutical product (mixture) retained physicochemical properties qualitatively and quantitatively.

### References

- [1]. M. Cocchietto, N. Skert, P. Nimis, G. Sava, A review on usnic acid, an interesting natural compound, *Naturwissenchaften* 89 (2002) 137-146.
- [2]. S. Glišić, S. Popadić, D. Skala, St. John's Wort *Hypericum perforatum* L. Supercritical extraction, antimicrobial and antidepressant activity of extract and some component, Chem. Ind. (Serb), 60(3-4) (2006) 61-71.
- [3]. M. Stankovic, S. Stankovic, Z. Djordjevic, S. Djordjevic, Patent YU-43978 (1989).

# DETERMINATION OF CRYSTALLINE STRUCTURE OF CALCIUM CARBONATE OBTAINED FROM DRINKING WATER

M.B. Rajković, T.M. Rajković, U.Č. Lačnjevac, Z. Baščarević D.V. Tošković, D.D. Stanojević and Č.M. Lačnjevac

<sup>1</sup>Faculty of Agriculture, Belgrade-Zemun, <sup>2</sup>Center for Multidisciplinary Studies of University of Belgrade, Belgrade, Serbia, and <sup>3</sup>Faculty of Technology, Zvornik, University of East Saraevo, Bosna&Herzegovina

# Introduction

In this research work the analysis of water quality, regarding the content of metals, especially heavy and radioactive ones, has been carried out in an indirect way, by testing scale formed in a hot-water heater, using water from the water-supply network of the city of Belgrade – the district of New Belgrade.

The determination of the composition and the structure of the scale has resulted in its complete identification, and its crystallochemical formula has been defined.

# **Experimental**

A sample of scale formed by precipitation on a water-heater surface during a time period of 6 months has been used in this research work. The sample of scale originated from water present in water-supply system of the town of Belgrade - the district of New Belgrade. The content of all solids, which actually represents scale, has been determined by heating 1.0 dm<sup>3</sup> of drinking water to boiling and evaporating point to obtain the dry residue.

Composition of a sample of scale was determined on atomic absorption spectrophotometer AAS Perkin Elmer 703, according to methods DM 10–0/4, 0/6, 0/7, 0/8, 0/9, 0/10, 0/11, 0/12, 0/13 and 0/17.

The X-ray diffraction analysis of the preground scale sample has been made, and a fraction of fine scale powder (6.3-2  $\mu$ m) has been studied. The X-ray analysis has been conducted on a Phillips PW 1009 diffractometer, with CuK $\alpha$  rays  $\lambda$  = 1.54178, under the operating conditions of the tube U = 36 kV, I = 18 mA, at a goniometer velocity Vg = 1°2θ/min and under the conditions R/C = 8/2. In the obtained diffractogram the position of reflection has been determined and  $\underline{d}$  value of the measured area i.e. the integral intensities of certain reflections have been calculated with the aid of the program DRX Win 1.4 designed by V.P.Martin [2]. The scale sample has also been analysed by the Scanning Electron Microscopy (SEM), using an SEM (VEGA TS 5130MM, Tescan Brno, Czech republic), with the possibility of magnification of 10x 1 000 000x and the resolution (in high vacuum mode (SE)) of 3 nm at 30 kV.

# **Results and Discussion**

Evaporation of 1.0 dm<sup>3</sup> of water to the dry matter has resulted in 0.3 g of the scale. The results of the scale sample analysis, in accordance with the standard JUS B.B8.070, are: Ca (as CaO 48,90%), Mg (as MgO 5,43%), Na (as Na<sub>2</sub>O 0,034%),

K (as  $K_2O$  0,0072%), Fe (as  $Fe_2O_3O_0084\%$ ), Mn (as MnO 20 ppm), Si (as  $SiO_21,14\%$ ), Al (as  $Al_2O_3O_0070\%$ ), Pb (0,0033%), Zn (0,023%), Cu (0,134%), U (2,03 ppm), Cd (6 ppm), Cr (10 ppm), S (0,14%) [3].

The X-ray diffractogram of the scale powder is shown in Fig. 1.

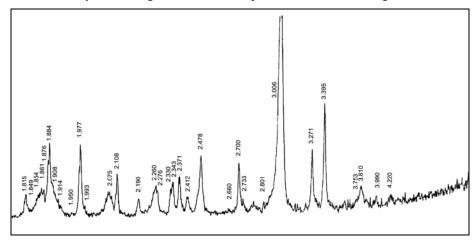


Fig. 1. X-ray diffraction analysis of household water scale

The composition of the scale sample, which represents the carbonate mixture composed of Mg calcite and aragonite, has been determined based on the X-ray diffraction of the scale powder applying the qualitative and semiquantitative method. Miller indexes ( $\mathbf{h}$   $\mathbf{k}$   $\mathbf{i}$   $\mathbf{l}$ ) have been determined on the basis of the obtained angular values ( $\mathbf{\theta}$ ) and interplate distances ( $\mathbf{d}$ ). Dimensions of elementary cells have been calculated on the basis of hexagonal and rhombic grating, by means of the LSUCRI program.

Based on the qualitative and semiquantitave X-ray analysis, the carbonate mixture has been found to consist of 66.92 % of *calcite* and 33.07 % of *aragonite*. *Calcite* and *aragonite* are two polymorphic modifications of the CaCO<sub>3</sub> composition. Aragonite belongs to the rhombic and calcite to the widespread rhombohedral carbonates.

The interplate distances as of calcite so too of aragonite have revealed minor deviations in relation to the standard values (JCPDS 47-1743; 41-1475). The interplate distance  $d_{(10^{-14})}$  of the main calcite reflection has shifted towards higher angular values  $\theta$ , indicating the partial substitution of  $Ca^{2+}$  ion for ions of a smaller ionic radius, among which the commonest are  $Mg^{2+}$ ,  $Ni^{2+}$ ,  $Fe^{2+}$ ,  $Mn^{2+}$  and etc. The parameters of the calcite elementary cell are very close to the standard values. Moreover, the decrease in the value of parameters  $a_0$  and  $c_0$  has confirmed the substitution of  $Ca^{2+}$  ion for the ions of the smaller ionic radius as also testified by the interplate distances [3].

The SEM photography of the water-heater scale samples is shown in Fig. 2.

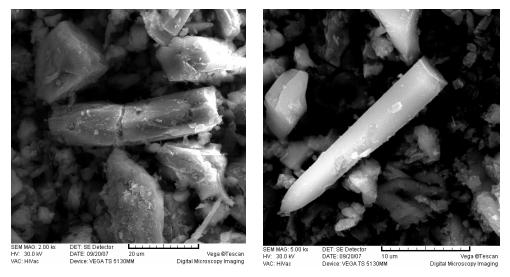


Fig. 2. Obtained SEM photographs under different magnification

# Conclusion

The subject of this research work has been the scale developed by heating the drinking water from the water-supply system of the city of Belgrade – the district of New Belgrade. The studies of the scale have shown that its main ingredient is calcium carbonate, proved not only by the SEM screening but also by the X-ray diffractional analysis, and also that it contains different chemical substances in different parts of the city. On the strength of the crystallographic parameters and the obtained composition, 66.92% *calcite* and 33.07% *aragonite*.

# Acknowledgements

The work was supported by the Ministry of Science and Environmental Protection of the Republic of Serbia (Grant ON 142039).

## **References:**

- [1] M.B.Rajković, M.D.Stojanović, G.K.Pantelić, D.Tošković, *Acta Periodica Technologica*, 2004, **35**, 131-140.
- [2] V.P.Martin. DRXW in 1.4 a computer program: A Graphical and Analytical Tool for Powder XDR Patterns. University of Valence, Faculty of Chemistry, 1994, Valenca, Spain.
- [3] M.B.Rajković, M.Stojanović, G.Pantelić, Određivanje radioaktivnih elemenata u vodi za piće metodom indirektne analize na osnovu ispitivanja sastava kamenca, XXIV simpozijum Društva za zaštitu od zračenja Srbije i Crne Gore, Zlatibor, 03.-05.10.2007.god., Sekcija 2.: Radioekologija, Zbornik radova, s. 37-41.

# IMPROVED BIOCATALYSTS FOR POLYMERIZATIONS VIA IMMOBILIZATION

# K. Loos

Department of Polymer Chemistry & Zernike Institute for Advanced Materials University of Groningen, Nijenborgh 4, 9747AG Groningen, The Netherlands K.U.Loos@rug.nl

Enzymes have excellent features (activity, selectivity, specificity) for designing synthetic processes to obtain a wide range of products under mild and environmentally friendly conditions.[1] However, enzymes have been optimized via natural evolution, to fulfill their biological function: catalyzing reactions in complex metabolic pathways exposed to many levels of regulation. Therefore, natural enzymes seldom have the features adequate to be used as industrial catalysts in organic synthesis. The operational conditions of chemical processes are far from the biological environment in which enzymes flourish in nature. Enzymes can denature due to solvent effects and mechanical shear. Recovery of enzymes from reaction solutions and separation of the enzymes from substrates and products are generally difficult. The productivity (space, time, and yield) of enzymatic processes is often low due to substrate and/or product inhibition.

An important route to improving enzyme performance in non-natural environments is to immobilize them by either adsorption, covalent attachment or by incorporation in hydrophobic organic-inorganic hybrid materials by a sol-gel process. [2] These immobilization procedures have resulted in remarkable improvements in enzyme activity (up to a factor of 100), long-term stability, increased enantioselectivity, and more. The increased stability is due to the fact that enzyme activity will change as a function of its local environment (e.g., solvent polarity, surface chemistry). However, it is important to move beyond general correlations to a better understanding on a molecular level of how immobilization on surfaces can stabilize and activate protein catalysts.

For this purpose, molecularly engineered surfaces are necessary, and one method to produce these can be provided by self-assembled monolayers (SAMs). [3]These systems give a powerful tool to study biological processes on a variety of well-defined substrates. The formation of such monolayer systems is extremely versatile and can provide a method for the *in vitro* development of biosurfaces that mimic naturally occurring molecular recognition processes. [4]

The most frequently employed enzymes in chemical synthesis, especially for transesterifications in organic media, are lipases. Lipases are triacylglycerol-hydrolases (EC 3.1.1.3) produced in intra- and extra-cellular compartments that function in organism metabolism and they possess a broad range of catalytic activities for chemical synthesis. [5] *Candida antarctica lipase B* (CAL-B) was selected for this investigation of surface interactions because of its extensive use in organic synthesis and polymerizations.

Considering that a variety of different surfaces should be probed, which can be time-consuming, we used a novel combinatorial approach to explore, in a single experiment, enzyme interactions with multiple surface chemistries. This approach is based on studies of the immobilization behavior of Lipase on surfaces having a gradient in surface energy. [6] Gradient surfaces are well suited to interrogate the behavior of polymers[7], proteins[8], cells[9] etc. Surface gradients were prepared by the gradual exposure of an octadecyltrimethoxysilane (ODTS) SAM on commercial glass slides to UV/O<sub>3</sub>. The surface energy gradient along the glass slide was assessed by contact angle measurements. A fluorescence activity assay based on the lipase-catalyzed transesterification of 6,8-difluoro-4-methylumbelliferyl octanoate (DIFMU octanoate) in acetonitrile to 6,8-difluoro-7-hydroxy-4-methylcoumarin (DIFMU) was developed to assess the enzyme activity on the gradient surface. With this at hand it has become possible to spatially resolve the enzyme kinetic information from different positions along the gradient surface simultaneously and in real time.

With the help of well defined macroporous poly(glycidyl methacrylate-coethylene glycol dimethacrylate)s resins it becomes possible to transfer the results obtained in the surface-enzyme interaction experiments into resin structures. [10]

In this talk an introduction on enzymatic polymerizations will be given and our recent results on enzyme immobilization systems will be reviewed.

### References

- [1] (a) Drauz, K.; Waldmann, H.; Editors. *Enzyme catalysis in organic synthesis: A comprehensive handbook, Volume I*, 2002; (b) Silverman, R. B. *The Chemistry of Enzyme-Catalyzed Reactions*, 2000, Academic Press, San Diego; (c) Faber, K. *Biotransformations in Organic Chemistry*, 4<sup>th</sup> edition, 2000, Springer, Berlin.
- [2] (a) Reetz, M. T.; Tielmann, P.; Wiesenhofer, W.; Konen, W.; Zonta, A. Advanced Synthesis & Catalysis 2003, 345, 717; (b) Dumitriu, E.; Secundo, F.; Patarin, J.; Fechete, L. J. Molec. Catal. B 2003, 22, 119; (c) Chan, C. M.; Ko, T. M.; Hiraoka, H. Surf. Sci. Rep. 1996, 24, 3; (d) Goldstein, L. Meth. Enzym. 1987, 135, 90; (e) Dyal, A.; Loos, K.; Noto, M.; Chang, S.; Spagnoli, C.; Shafi, K.; Ulman, A.; Cowman, M.; Gross, R. J. Am. Chem. Soc., 2003, 125, 1684-1685.
- [3] (a) Ulman, A. Chem. Rev. 1996, 96, 1533; (b) Ulman, A. Acc. Chem. Res. 2001, 34, 855.
- [4] (a) Ostuni, E.; Grzybowski, B. A.; Mrksich, M.; Roberts, C. S.; Whitesides, G. M. Langmuir 2003, 19, 1861; (b) Kada, G.; Riener, C. K.; Hinterdorfer, P.; Kienberger, F.; Stoh, C. M.; Gruber, H. J. Single Molecules 2002, 3, 119-125; (c) Petrash, S.; Cregger, T.; Zhao, B.; Pokidysheva, E.; Foster, M. D.; Brittain, W. J.; Sevastianov, V.; Majkrzak, C. F. Langmuir 2001, 17, 7645; (d) Ostuni, E.; Yan, L.; Whitesides, G. M. Colloids Surf. B 1999, 15, 3.
- [5] (a) Gross, R. A.; Kalra, B.; Kumar, A. Appl. Microbiol. Biotech. 2001, 55, 655; (b)
   Matsumura, S. Macromolecular Bioscience 2002, 2, 105; (c) Reetz, M. T.
   Tetrahedron 2002, 58, 6595; (d) Secundo, F.; Carrea, G. J. Molec. Catal. B 2002, 19,

- 93; (e) Uyama, H.; Kobayashi, S. J. Molec. Catal. B 2002, 19, 117; (f) Krishna, S. Hari; Karanth, N. G. Catalysis Reviews Science and Engineering 2002, 44, 499.
- [6] Loos, K.; Kennedy, S. B.; Eidelman, N.; Tai, Y.; Zharnikov, M.; Amis, E. J.; Ulman, A.; Gross, R. A. *Langmuir* 2005, 21, 5237.
- [7] Smith, A. P.; Sehgal, A.; Douglas, J. F.; Karim, A.; Amis, E. J. Macromol. Rapid Comm. 2003, 24, 131.
- [8] (a) Elwing, H.; Welin, S.; Askendal, A.; Nilsson, U.; Lundström, I. J. Coll. Interf. Sci. 1987, 119, 203; (b) Gölander, C.-G., Lin, Y.-S.; Hlady, V.; Andrade, J. D. Coll. Surf. 1990, 49, 289; (c) Warkentin, P.; Wälivaara, B.; Lundström, I.; Tengvall, P. Biomaterials 1994, 15, 786; (d) Spijker, H.T.; Bos, R.; van Oeveren, W.; de Vries, J.; Busscher, H.J. Coll. Surf. B 1990, 15, 89.
- [9] (a) Ruardy, T. G.; Schakenraas, J. M.; van der Mei, H. C.; Busscher, H. J. Surf. Sci. Rep. 1997, 29, 1; (b) Spijker, H. T.; Busscher, H. J.; van Oeveren, W. Thrombosis Research 2003, 108, 57; (c) Meredith, J. C.; Sormana, J. L.; Keselowsky, B. G.; Garcia, A. J.; Tona, A.; Karim, A.; Amis, E.J. J. Biomed. Mater. Res. A 2003, 66A, 483; (d) Lee S. J., Khang G., Lee Y. M., Lee H.B. J. Coll. Interf. Sci. 2003, 259, 228.
- [10] Miletić, N.; Vuković, Z.; Nastasović, A.; Loos, K. *Journal of Molecular Catalysis. B, Enzymatic,* in pr



		¥	
Abazović, N.D.	524	Čolović, M.	364, 448
Adamović, D.	641	Čomor, J.J.	267
Adnađević, B.	145, 561, 588	Čomor, M.I.	524
Adžic, M.	436, 439, 442	Čučulović, A.	656
Aleksić, M.M.	306	Čudina, O.	367
Angerer, P.	512	Čupić, Ž.D.	223, 244, 247
Anić, S.R.	223, 238, 241	Ćirić-Marjanović, G.	555
Antić-Jovanović, A.	105	Ćosović, V.	471
Antonijević-Nikolić, M.	710	D'Addario, C.	344
Arsenijević, Z.	157	Daković, M.	391, 400, 433
Avgouropoulos, G.	160	Daković, A.	677, 683
Babić, M.	561	Damjanović, Lj.	59
Babić-Samardžija, K.	291	Dangić, J.	51
Bačić, G.	433	Dangić, A.	51, 541
Bakeš, D.	229	Danilov, V.A.	591
Bakrac, S.	662	Danilova, V.	39
Banković, P.	148, 485	Delidou, K.	264
Banks, C.E.	282	Despotović, A.	33
Baranac-Stojanović, M.	300	Dietler, G.	321, 379
Barek, J.	270	Dimitrić-Marković, J.M.	108, 303
Barna, D.J.	382	Dimitrieva, O.V.	250
Baščarević, Z.	729	Dimitrijević, D.	541
Bataveljić, D.	430	Dimitriu, E.	621
Beljanski, M.V.	166, 370, 406	Dimitrov, D.	136, 151
Bibić, N.	482	Dimović, S.	550
Blagojević, N.S.	518, 536	Dinovic, S. Dostanić, J.	148, 485
Blagojević, N.S. Blagojević, S.M.	241, 244	· · · · · · · · · · · · · · · · · · ·	409
		Dragičević, V.	
Blagojević, S.N.	297 379	Dragović, S.	465, 650
Bogdanović, J.		Drakulić, D.	397, 451, 454
Bojović, V.	105	Duteanu, N.	273
Bošković, S.	521	Đikanović, D.	111, 379
Bošković-Vragolović, N.	42	Đukic, JP.	691
Bošnjaković-Pavlović, N.	364	Đokić, D.	462
Brankov, J.	217, 220	Đorđević, A.	436, 439, 442
Brborić, J.	367	Đorđević, A.R.	418
Budinski-Simendić, J.	570, 579	Đorđević, J.	436, 439, 442
Butkeraitis, P.	677	Đorđević, D.	582
Cajka, T.	10	Đurišić-Mladenović, N.	613
Cakić, M.	117	Đurović, I.	33, 181
Cekić-Lasković, I.	300	Džunuzović, E.	509
Cherkezova-Zheleva, Z.	136, 151	Edipidou, X.	264
Compton, R.G.	7, 262, 282	Edreva-Kardjieva, R.	163, 175, 178
Cretin, B.	24, 488	Endo, M.	85
Cvejanov, J.	613	Ermakov, V.	39, 609
Cvetić, T.	355	Filipović, D.	358
Cvetković, D.D.	382, 385, 388	Fišl, J.	686
Cvetković, Lj.	541	Gabrovska, M.	142, 175, 178
Cvijetićanin, N.	279, 288	Gajić, B.	465
Čolović, M.	36	Gajinov, S.	541

Calarrit D	50(	T ('', N.	572
Gaković, B.	506	Jevtić, M.	573
Garić-Grulovic, R.	42, 157	Jocić, S.	415
Gavrilović, A.	512	Johansson, B.	344
Gibbons, S.	73	Jovanović, D.M.	178, 285, 485
Gojačanin, D.	400	Jovanović, V.M.	291
Golobočanin, D.	647	Jovanović, D.	33
Gopčević, K.R.	166, 394	Jovanović, J.	145, 561, 588
Gorjanović, S.Ž.	294, 427, 430	Jovanović, I.	500
Grahovac, Z.M.	139	Jovanović, S.	585, 594
Grbavčić, Ž.	42, 157	Jović-Jovičić, N.	148, 485
Grbić, B. Grbović-Novaković, J.	157	Jugović, D.	288 704
	665	Juranić, Z.D.	
Grdanović, T.	217, 220	Juranić, N.	8 482
Grigoriadou, A.	264 691	Kačarević-Popović, Z.M.	
Grimme, S.		Kalauzi, A.	111, 114, 370
Grozdić, T.D. Grozdić, I.T.	276, 659, 674	Kaluđerović, G.N.	696, 701, 704
	659 163	Kanazir, D.	403
Grozeva, T. Grujić, S.R.	518, 536	Kapetanović, V.	306
	65	Karadžić, I.	169
Grupče, O.	226	Karljiković-Rajić, K.	367 641
Hadač, O. Hajslova, J.	10	Karlović, I.	
Halasi, T.	721	Kasas, S.	321, 379 273
Hegediš, A.	674	Kellenberger, A. Kelly, M.E.	701
	59	Khabarov, V.	609
Holclajtner-Antunović, I. Horvat, A.	361, 397, 445	Khushvakhtova, S.	39
Hyla-Kryspin, I.	691	Kiicanović, M.	190, 193, 415
Idakiev, V.	160	Kiurski, J.	641, 644, 686
Ignjatović, Lj.M.	270, 303, 671	Kohout, M.	226
Ignjatovic, J.	352	Kollout, W. Kolar-Anić, Lj.Z.	223, 232, 244
Ignjatović, A.	391, 400	Kolar-Allie, LJ.Z. Kolev, H.	136, 151
Ignjatović, N.	500, 573	Koltsov, N.I.	250, 591
Iles, D.	680	Kolyamshin, O.A.	591
Ilić, B.S.	54, 117	Konstantinović, S.S.	713, 716
Ilić, M.	394	Kovacevic, D.	680
Ioannides, T.	160	Kragović, M.	238
Iorgulescu, E.E.	621	Krinulović, K.	36
Ivanov, K.	136, 151	Krklješ, A.	482
Ivanović, A.Z.	223	Krnel, K.	573
Ivanovski, V.	77	Krstić, D.	448
Izrael-Živković, L.	169	Krstić, D.	364, 394
Jakovljević, D.	403, 564, 582	Krstić, J.B.	151, 178, 421
Janjić, G.V.	96	Krstić, N.S.	54
Janković, D.	462	Krstić-Demonacos, M.	439
Janković, I.A.	367, 509	Kuchanov, S.I.	16
Janković, M.	653	Kuljanin-Jakovljević, J.	527
Janković-Mandić, Lj.	650	Kumrić, S.V.	276
Jelenković, B.	533	Kumrić, K.R.	267
Jeremić, M.	111, 114	Kuzmanović, M.M.	99, 105
*	*	,	,

Lačnjevac, Č.M.	729	Milošević, V.	683
Lačnjevac, U.Č.	729	Milošević-Zlatanović, S.	558
Laninović, V.	600	Milovanović, D.	145
Laurentiu Dan, M.	273	Milovanović, S.	665
Leblanc, R.M.	3, 114	Milutinović-Nikolić, A.	148, 485, 567
Lechner, M.D.	585	Minčeva-Šukarova, B.	65
Ledoux, D.R.	677	Ming, Y.	344
Lemic, J.	680	Minić, D.M.	300, 512
Ljesević, M.	665, 662	Mioč, U.B.	59
Lončarević, D.	142, 247	Mitić, N.	427
Macura, S.	8	Mitić, S.S.	139, 184
Maksimov, G.V.	370	Mitić, Ž.	117
Maksimović, J.	232, 235, 247	Mitov, I.	136, 151
Manojlović, N.	120, 424	Mitrašinović, P.M.	373, 376, 576
Marek, M.	226	Mitrić, M.	279, 288
Marinković, A.	45	Mojović, M.	391, 400, 433
Marinković, V.	732	Mojović, Z.	285
Marinović-Cincović, M.T.	482, 570, 579	Moldoveanu, S.C.	621
Marković, D.	352, 355	Momčilović, M.Z.	102, 465
Marković, D.M.	671, 668	Momić, T.	36, 172
Marković, G.	570, 579	Morozova-Roche, L.	338
Marković, R.	300	Munteanu, G.	491
Marković, S.	33, 181, 187	Murić, B.	530
Marković, S.B.	503	Mutavdžić, D.	114, 674
Marković, Z.	120, 181, 424	Nakamura, T.	85
Marković, Z.S.	108	Nastasović, A.	564, 567, 582
Martać, LJ.	430	Nedeljković, J.M.	509, 555, 597
Masuda, T.	85	Nedeljković, B.	500
Matijašević, S.	683	Nedić, B.	8
Matovic, Lj.	665	Nedić, Z.P.	108
Matović, B.	665	Nenadović, M.	497
Mentus, S.	279, 285, 309	Nenadović, T.	497
Miclea, C.	491	Nevoral, V.	226
Mićović, V.	415, 421	Nićiforović, A.	442
Mihailović, N.	465	Nikolić, G.M.	479
Mihajlović, M.L.	376, 576	Nikolić, G.S.	117, 732,735
Miladinović, J.	48	Nikolić, J.D.	518, 536
Miladinović, Z.	196	Nikolić, LJ.	430
Milanovic, M.	662	Nikolić, N.	462, 735
Milenković, A.	172	Nikolić, R.S.	713, 716
Milić, S.Z.	294, 297	Nikolić, Z.S.	494, 515
Milićević, S.	677, 683	Nikolova, D.	163, 175
Milivojević, M.	409	Ninković, R.	48
Miljanić, Š.S.	459, 656	Novaković, M.	497
Miljević, N.	647, 653	Novaković, T.	544
Milosavić, N.	558	Novkovic, I.	662
Milosavljevic, B.H.	724	Novović, I.	
2	433	Ostojić, B.D.	668, 671
Milosavljević, D.		3 -	96
Milošević, M.	361, 445, 454	Ostojić, S.	190, 193, 415

Ostrovelsii NIM	128	Doloo Xarrida 7	407
Ostrovskii, N.M.	358	Rakočević, Z.	497 427
Pajović, S.B.	506	Ranisavljević, S.	99
Panchenko, A.	136, 151	Ranković, D.P.	232
Paneva, D.	530	Ribič, D. Rigler, R.	344
Panić, B.			
Pantelić, D.	530, 533 160	Rosić, A.	148
Papavasiliou, J.	59, 279, 309	Rottinghaus, G.E. Rožić, Lj.	677 544
Pašti, I.	39, 279, 309		
Pavelkić, M. Pavelkić, V.M.	166, 394, 406	Sabo, T.J. Saeed, A.M.	696, 704 459
Pavlović, M.D.	415, 421, 427	Sakač, Z.	415, 421
Pavlović, M.S.	54, 102	Sandić, Z.	582
Pavlović, V.	418, 588	Saridic, Z. Savić, I.	732
Pavlović, Ž.	641	Savić, J.	36, 172
Pavlović-Lažetić, G.	427	Savić, J. Savić-Šević, S.	533
Pecev, E.T.	139	Savic-Sevic, S. Savović, J.J.	99, 102
Pecev, T.G.	139	Schmidt, H.	696, 701, 704
Pejanović, S.	547	Schmitz, G.	201
Pejić, N.D.	232, 235, 244	Schreiber, I.	209, 229, 226
Pešek, O.	209	Schreiberová, L.	209, 229, 229
Petković, M.	309	Sekulić, Ž.	677
Petrović, M.S.	108, 303	Serwicka, E.	163
Petrović, R.	521	Shtereva, I.	178
Petrović, S.	361, 412, 445	Simić, S.	175
Petrović, S.P	544	Simijonović, D.	187
Petrović, V.	187	Simonović, B.R.	193, 541, 558
Petrović, Z.D.	187	Simonović, J.	391
Pjanović, R.	42	Simonović, M.	558
Plećaš, I.	547, 550	Slavković-Beškoski, L.	582
Podunavac-Kuzmanović, S.		Smičiklas, I.	547, 550
Popovic, I.	561	Solujić, S.	56
Popović, M.	497	Song, Y.	488
Potkonjak, N.I.	294, 297	Sovilj, S.P.	291
Poulios, I.	255, 264	Spasić, A.M.	214
Premović, P.I.	54, 117	Spasojević, I.	391, 400
Prendergast, F.G.	8	Spasojević-de Bire, A.	364
Prica, M.	686	Srećković, V.	668, 671
Radak, B.	506	Sredojević, S.	409
Radenković, M.B.	459	Stanić, M.	430
Radenović, Č.N.	370	Stanić, T.	683
Radetić, T.	527	Stanica, N.	491
Radić, N.	157	Stanisavljev, D.R.	217, 166, 406
Radoičić, M.	555, 527	Stanković, M.	142, 175, 178
Radojčić, M.B.	436, 439, 442,	Stanković, A.	312, 315
Radonić, J.	644	Stanojević, D.	45, 729
Radotić, K.	111, 114, 379	Stanojević, I.	397, 451, 454
Radovanović, B.C.	570, 579, 716	Stasić, J.	665
Rajković, M.B.	45, 418, 729	Stefanov, Pl.	175
Rajković, T.M.	729	Steinborn, D.	696, 704
J	, = >	, •	,

Stejskal, J.	555	Vasić, V.	172, 330, 364
Stepanov, A.G.	125	Vasiljević, D.	530
Stevanović, S.	291	Vaszilcsin, N.	273
Stevanović, M.	603	Veber, T.	229
Stević, M.	270	Veličković, N.	412, 451, 454
Stoiljković, M.M.	99, 102	Veličković, S.	588
Stojanović, S.	707	Veljović-Jovanović, S.D.	294, 355
Stojić, D.LJ.	276	Veselinović, D.	656
Stojković, I.	279	Vilotić, D.	668, 671
Sukdolak, S.	56	Vladimirov, S.	367
Sunarić, S.M.	184	Vodnik, V.	585, 594, 597
Suručić, Lj.	582	Vojinović-Miloradov, M.	641, 644
Sužnjević, D.Ž.	294, 297	Volanschi, E.	300
Šaponjić, Z.V.	509, 527, 555	Vrvić, M.M.	403, 564, 558
Škapin, S.	573	Vučković, G.	710
Škrbić, B.	613	Vučković, M.	594
Šljivić, M.	547, 550	Vujačić, A.	36, 172
Šljukić, B.	282	Vukašinović, I.	418
Tabakova, T.	160	Vukelić, N.	312, 315
Tadić, S.	427	Vukojević, V.	344
Talijan, N.	471	Vuković, J.	585, 594, 597
Tanasković, S.B.	710	Vuković, N.	56
Tančić, A.R.	93	Vuković, Z.	567
Tanevska, V.	65	Wantuck, Ph.J.	724
Tarasenko, V.	506	Wildgoose, G.G.	262
Terenius, L.	344	Xu, J.	114
Todorović, D.	418	Yoshimura, M.	515
Todorović, D.M.	488	Zakrzewska, J.	196
Todorović, M.	48	Zarić, S.D.	96, 707
Tošić, N.	427	Zec, S.	521
Tošić, M.B.	518, 536	Zildzovic, S.	680
Tošković, D.	45, 729	Zima, J.	270
Trifunović, S.R.	704	Zlatanović, D.	154
Tripković, A.	291	Zlatanović, S.	190, 193, 415
Trtica, M.	506	Zlatković, J.	358
Trtić-Petrović, T.M.	267	Zlatković, S.	735
Tsoumparis, P.	264	Zloh, M.	73
Turk-Sekulić, M.	644	Zmejkovski, B.B.	704
Tzia, C.	629	Zvezdanović, J.	352, 355
Tzvetkov, P.	142	Živanović, V.D.	518, 536
Uchiyama, T.	85	Živić, M.	415, 421
Uskoković, D.	503, 573, 603	Živković, B.	, 315
	488		704
Vairac, P.	408	Žižak, Ž.	/04

# **Participating Institutions**

Actavis Trading Ltd., Đorđa Stanojevića 12, Beograd 11070, Serbia	735
A.N.Frumkin - Institute of Physical Chemistry and Electrochemistry of the Russian Academy of Science, Moscow, Russia	609
Agricultural University, 4000 Plovdiv, Bulgaria	136, 151
Animal Science Center, University of Missouri, Columbia, MO 65211-5300, U.S.A.	677
Baker Petrolite, 12645 West Airport Blvd., Sugar Land, TX 77478, U.S.A.	291
Boreskov Institute of Catalysis, Siberian Branch of Russian Academy of Sciences, Prospekt Akademika Lavrentieva 5, Novosibirsk 630090, Russia.	125
Charles University in Prague, Faculty of Science, Department of Analytical Chemistry, UNESCO Laboratory of Environmental Electrochemistry, Hlavova 2030, 128 43 Prague 2, Czech Republic.	270
Chuvash State University, Department of Physical Chemistry, Moskovskii prospekt 15, 428015 Cheboksary, Russia	250, 591
ECHEM Kompetenzzentrum für angewandte Elektrochemie GmbH, A-2700 Wiener Neustadt, Austria	512
Ecole Centrale Paris, Laboratoire SPMS UMR CNRS 8580 1, Grande Voie des Vignes 92295 Châtenay-Malabry, France	364
Ecole Polytechnique Fédérale de Lausanne, Laboratoire de Physique de la Matière Vivante, EPFL, 1015 Lausanne, Switzerland	321
Faculty of Agriculture, University of Belgrade, Nemanjina 6, Belgrade, Zemun, Serbia	45, 418, 465, 729
Faculty of Agronomy, University of Čačak, Cara Dušana 34, 32000 Čačak, Serbia,	108
Faculty of Agronomy, University of Kragujevac, Čačak 32000, Serbia,	120, 181, 424
Faculty of Biology, University of Belgrade, 11000, Belgrade, Serbia	355, 430
Faculty of Chemistry, University of Belgrade, Studentski trg 16, P.O. Box 158, 11000 Belgrade, Serbia	96, 291, 294, 297, 300, 403, 558, 564, 696, 704, 707, 710
Faculty of Chemistry, University of Bucharest, Romania	300
Faculty of Electronic Engineering, Department of Microelectronics, University of Nish, 18000 Nish, P. O. Box 73, Serbia.	494, 515
Faculty of Forestry, University of Belgrade, Kneza Viseslava 1, Belgrade, Serbia	582, 668, 671

Faculty of Geography, University of Belgrade, Studentski trg 3/III, 11000 Belgrade, Serbia	662, 665
Faculty of Life Sciences, University of Manchester, Manchester, M13 9PT, England, U.K.	439
Faculty of Mathematics and Natural Science, University of Priština, Serbia	154
Faculty of Mathematics and Natural Sciences, University of Kragujevac, Radoja Domanovica 12, Kragujevac, Serbia,	558
Faculty of Mathematics, University of Belgrade, Belgrade, Serbia	427
Faculty of Medicine, Department of Chemistry, Bulevar dr Zorana Đinđića 81, 18000 Niš, Serbia	479
Faculty of Medicine, Department of Pharmacy, Bul. dr Zorana Đinđića 81, 18000 Niš, Serbia	117, 184
Faculty of Mining and Geology, University of Belgrade, Đušina 7, Belgrade, Serbia	51, 148, 541
Faculty of Pharmacy, University of Belgrade, Institute of Analytical Chemistry, Vojvode Stepe 450, P.O.Box 146, 11000 Belgrade	306
Faculty of Pharmacy, University of Belgrade, Institute of Physical Chemistry, Vojvode Stepe 450, P.O.Box 146, 11000 Belgrade	306
Faculty of Pharmacy, University of Belgrade, Vojvode Stepe 450, Belgrade, Serbia	244, 232, 235, 710, 241, 367
Faculty of Physical Chemistry, University of Belgrade, Studentski trg 12-16, 11158 Belgrade 118, Serbia	51, 59, 99, 102, 105, 108, 111, 145, 166, 217, 220, 223, 232, 235, 238, 241, 244, 247, 270, 279, 282, 285, 288, 300, 303, 309, 312, 315, 364, 376, 391, 400, 406, 433, 459, 512, 555, 561, 576, 588, 656, 668, 671
Faculty of Science and Mathematics, University of Niš, Višegradska 33, 18000 Niš, Serbia	139, 184, 570, 579, 713, 716
Faculty of Science, Mladena Stojanovića 2, Banja Luka, BIH.	582
Faculty of Science, University of Kragujevac, 34000 Kragujevac, Serbia	33, 181, 187

Faculty of Science, University of Kragujevac, Department of Chemistry, P.O.Box 12, Kragujevac, Serbia	56, 704
Faculty of Sciences, Department for Chemistry, Novi Sad, Trg Dositeja Obradovica 3, Serbia	721
Faculty of Technical Sciences, Trg D.Obradovića , Novi Sad, Serbia	641, 644, 686
Faculty of Technical Sciences, University of Čačak, Serbia	500
Faculty of Technology and Metallurgy, 4 Karnegijeva St., 11000 Belgrade, Serbia	42, 45, 48, 157, 518, 521, 536, 547, 561, 585, 588, 509, 594
Faculty of Technology, Bulevar Oslobođenja 124, 16000 Leskovac, Serbia	117, 713, 716, 732, 735
Faculty of Technology, University of Novi Sad, Bulevar Cara Lazara 1, 21000 Novi Sad, Serbia	382, 385, 388, 570, 579, 613
Faculty of Technology, Zvornik, University of East Saraevo, Bosna & Herzegovina	45, 729
Foundation for Research and Technology-Hellas (FORTH), Institute of Chemical Engineering and High Temperature Chemical Processes (ICE-HT), P.O. Box 1414, Patras, Greece	160
Health Center Novi Beograd, Goce Delčeva 30, 11070, Belgrade, Serbia	394
High Current Electronics Institute SB of RAS, Tomsk, 634055, Russia	506
High School "Stanimir Veljković-Zele", 16000 Leskovac, Serbia	352
Higher Technological School of Professional Studies, 15000 Šabac, Serbia	710
HIPOL a.d., 25250 Odžaci, Serbia	128
Holding Institute of General and Physical Chemistry Studentski trg 12/V P.O. Box 551 11000 Belgrade, Serbia	166, 190, 193, 196, 294, 297, 370, 394, 406, 415, 421, 427, 430, 541, 558
Ilie Murgulescu, Institute of Physical Chemistry of the Romanian Academy Bucharest, Romania	491
IMS Institute, Bulevar vojvode Misica 43, Belgrade, Serbia	600
Institute for Biological Research "Siniša Stanković", University of Belgrade, Bulevar Despota Stefana 142, 11000 Belgrade, Serbia	294, 430
Institute for Chemistry, University of Osnabrück, Barbarastraße 7, 49069 Osnabrück, Germany	585

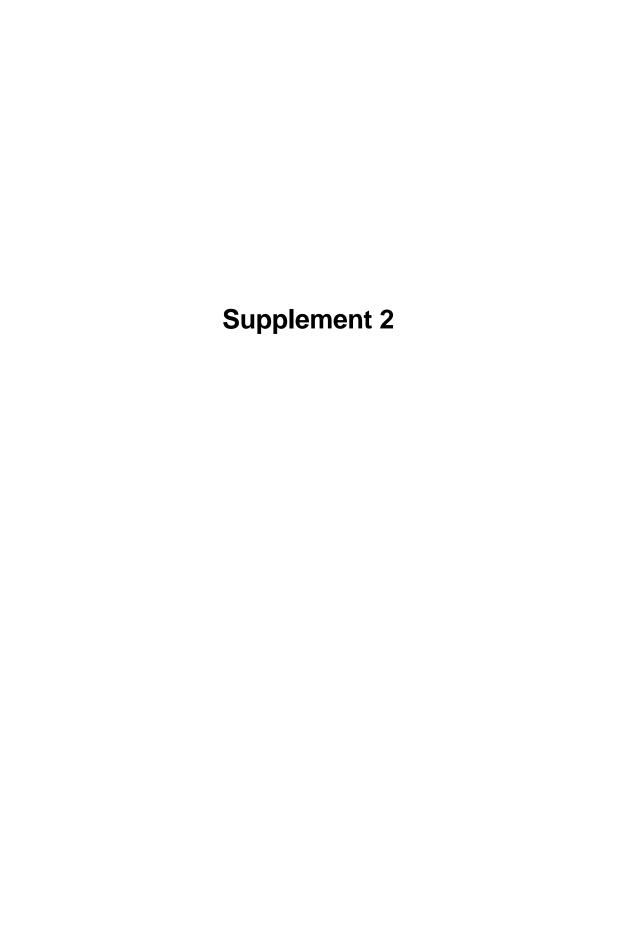
	•
Institute for Multidisciplinary Research, Kneza Višeslava 1, 11000 Beograd, Serbia	111, 114, 276, 355, 370, 373, 376, 379, 391, 400, 488, 576, 659, 674, 729
Institute for Technology of Nuclear and Other Mineral Raw Materials 86 F. d'Esperey St. 11000 Belgrade, Serbia	214, 518, 536, 677, 680, 683
Institute for the Application of Nuclear Energy - INEP, Banatska 31b, Belgrade, Serbia	465, 650, 656
Institute of Catalysis and Surface Chemistry, Polish Academy of Sciences, Krakow30-239, Poland	163
Institute of Catalysis, Bulgarian Academy of Sciences, 1113 Sofia, Bulgaria	136, 142, 151, 160, 163, 175, 178
Institute of Chemical Technology Prague, Department of Chemical Engineering and Center for Nonlinear Dynamics of Chemical and Biological Systems, Technická 5,166 28 Praha 6, Czech Republic	209, 226, 229
Institute of Chemical Technology, Prague, Department of Food Chemistry and Analysis, Technicka 3, 16628 Prague 6, Czech Republic	10
Institute of Chemistry, Technology and Metallurgy, Center of Chemistry, Studentski trg 12-16, 11000 Belgrade, Serbia	300, 403, 564, 582, 585, 594, 597, 696, 701, 704
Institute of Chemistry, Technology and Metallurgy, Department of Electrochemistry, Njegoševa 12, P.O. Box 815, 11000 Belgrade, Serbia	291
Institute of Chemistry, Technology and Metallurgy, Department of Chemistry, University of Belgrade, Njegoševa 12, P.O.Box.815, 11001 Belgrade, Serbia	567, 707
Institute of Chemistry, Technology and Metallurgy, Department of Catalysis and Chemical Engineering, Njegoševa 12, Belgrade, Serbia	108, 142, 148, 151, 157, 175, 178, 223, 244, 247, 285, 485, 544, 567
Institute of Chemistry, Technology and Metallurgy, Njegoševa 12, 11000 Belgrade, Serbia	471
Institute of Chemistry, Technology and Metallurgy, Studentski trg 12, Belgrade, Serbia	558
Institute of Chemistry, Technology and Metallurgy, University of Belgrade, Belgrade, Serbia	42, 96, 421

Institute of Field Vegetables and Crops, Maksima Gorkog 30, Novi Sad, Serbia	415, 421
Institute of General and Inorganic Chemistry, Bulgarian Academy of Sciences, Acad. G. Bonchev str., bl. 11, 1113 Sofia, Bulgaria	142, 175
Institute of Macromolecular Chemistry, Academy of Sciences of the Czech Republic, 162 06 Prague 6, Czech Republic	555
Institute of Nuclear Science "Vinča", P. O. Box 522, 11001 Belgrade, Serbia	54, 93, 166, 364, 406, 418, 436, 439, 442, 448, 462, 482, 506, 509, 521, 524, 527, 547, 550, 555, 570, 579, 582, 585, 594, 597, 647, 653
Institute of Nuclear Sciences "Vinča", Laboratory for Atomic Physics, 11001 Belgrade, Serbia	497
Institute of Nuclear Sciences Vinča, Department of Physical Chemistry, P.O.Box 522, 11001 Belgrade, Serbia	36, 99, 102, 172, 276, 330, 394
Institute of Nuclear Sciences Vinča, Laboratory for Molecular Biology and Endocrinology P.O.Box 522, 11001 Belgrade, Serbia	358, 361, 397, 412, 445, 451, 454
Institute of Nuclear Sciences Vinča, Laboratory for Theoretical and Condensed Matter Physics, P.O. Box 522, 11001 Belgrade, Serbia	279, 288
Institute of Nuclear Sciences Vinča, Laboratory of Material Science, P.O.box 522, 11000 Belgrade, Serbia	665
Institute of Nuclear Sciences Vinča, Laboratory of Physics (010), P.O. Box 522, 11001 Belgrade, Serbia	267
Institute of Nuclear Sciences Vinča, Radiation and Environmental Protection Department, P.O.B. 522, 11001 Belgrade, Serbia	459
Institute of Nuclear Sciences, Vinča, Laboratory for Radiation Chemistry and Physics, P.O. Box 522, Belgrade, Serbia	367
Institute of Oncology and Radiology of Serbia, 11000 Belgrade, Serbia	704
Institute of Physics, Pregrevica 118, Belgrade, Zemun, Serbia	530, 533, 668, 671
Institute of Public Health, Zmaj Jovina 30, 24000 Subotica, Serbia	382
Institute of Res. & Dev. Material Physics, Bucharest, Magurele, Romania	491

Institute of Technical Sciences of the Serbian Academy of Sciences and Arts, Knez Mihailova 35/IV, 11 000 Belgrade, Serbia	288, 503, 603, 500, 573
Jozef Štefan - Institute, Ljubljana, Slovenia	573
Karolinska Institutet, Department of Clinical Neuroscience, 17176 Stockholm, Sweden	344
Karolinska Institutet, Department of Medical Biochemistry and Biophysics, 17177 Stockholm, Sweden	344
Keio University, Department of System Design Engineering, Faculty of Science and Engineering, 3-14-1 Hiyoshi, Kohokuku, Yokohama 223-8522, Japan	85
Lab. of Food Chemistry and Technology, School of Chemical Engineering, NTUA, Greece	629
Laboratory for Geochemistry, Cosmochemistry and Astrochemistry, University of Niš, P.O. Box 224, 18000 Niš, Serbia	54, 117
Laboratory of Biomedical Optics, Swiss Federal Institute of Technology, CH-1015 Lausanne, Switzerland	344
LAD Group, Belgrade, 7/I Milesevska St, Serbia	680
Lawrence Berkeley National Laboratory, Berkeley, CA 94720, U.S.A.	527
Lomonosov Moscow State University, Chair of Physics of Polymers & Crystals, Vorobjevi Gory, 119992 Moscow, Russia	16
Lomonosov State University, Moscow, Russia	370
Macura adresa	8
Maize Research Institute, Biophysical laboratory, Zemun Polje, Belgrade, Serbia.	370
Maize Research Institute, Slobodana Bajića 1, 11185 Zemun Polje, Serbia	409
Manchester Metropolitan University, School of Biology, Chemistry and Health Science, Chester St., Manchester, M1 5GD U.K.	282
Martin-Luther-Universität Halle-Wittenberg, Institut für Chemie, Kurt-Mothes-Straße 2, 06120 Halle, Germany	696, 701, 704
Mayo Clinic, Department of Biochemistry, Mayo Graduate School, Rochester, Minnesota, 55905, USA	8
Medical Faculty, Department of Pharmacy, University of Kragujevac, S. Markovića 69, 34000 Kragujevac, Serbia	120, 424
Military Medical Academy, Crnotravska 17, 11000 Belgrade, Serbia	650
Military-geography Institute, Mije Kovacevica 5, 11000 Belgrade, Serbia	662

Pharmaceutical and chemical industry Zdravlje-Actavis, Vlajkova 199, Leskovac, Serbia.	732
Pennsylvania State University, Department of Chemistry, 104 Chemistry Building, University Park, PA 16802, U.S.A.	724
R.J. Reynolds. Co., 950 Reynolds Blvd,. Winston-Salem NC, U.S.A.	621
REGO COM, Calea 13 Septembrie 115, Bl.111, Bucharest - 5, Romania	621
School of Medicine, University of Belgrade, Department of Chemistry, Visegradska 26, 11000 Belgrade, Serbia	166, 169, 394
School of Medicine, University of Belgrade, Institute of Medicinal Chemistry, Serbia	364, 448
School of Pharmacy, 29-39 Brunswick Square, London, WC1N 1AX, United Kingdom.	73
Swiss Federal Institute of Technology, Laboratory of Physics of Living Matter, CH-1015, Lausanne, Switzerland	379
Tigar, Pirot, Serbia	570, 579
Tokai University, Department of Physics, School of Science, 1117 Kitakaname, Hiratsuka 259-1292, Japan.	85
Tokyo Institute of Technology, Yokohama 226-8503, Japan	515
Umeå University, Department of Medical Biochemistry and Biophysics, Umeå, Sweden.	338
Université de Franche-Comté, FEMTO-ST Institute, department MN2S CNRS, ENSMM, UTBM 32, avenue de l'observatoire, 25044 Besançon cedex, France	24, 488
Université de Lausanne, Département de Biologie Cellulaire et de Morphologie, CH-1005 Lausanne, Switzerland	321
Université Libre de Bruxelles, Faculté des Sciences Appliquées, CP165, Av.F.Roosevelt 50, 1050 Bruxelles, Belgium	201
Université Louis Pasteur, Institut de Chimie, UMR 7177 CNRS, 4 rue Blaise Pascal, 67000 Strasbourg, France.	691
University "Politehnica" of Timisoara, Faculty of Industrial Chemistry and Environmental Engineering, Piata Victoriei 2, 300006 – Timisoara, Romania	273
University of Bucharest, Faculty of Chemistry, Department of Analytical Chemistry, Sos. Panduri, no.90, Bucharest-5, Romania	621
University of Miami, Department of Chemistry, 1301 Memorial Drive, Cox Science Center, Coral Gables, FL. 33146. U.S.A.	3, 114

University of Missouri, College of Veterinary Medicine, Vet. Med. Diag. Lab., Columbia, MO 65211, U.S.A.	677
University of Nis, Faculty of Technology, 16000, Leskovac, Serbia	355
University of Nish, Faculty of Technology, 16000, Leskovac, Serbia	352
University of Oxford, Department of Chemistry, Physical and Theoretical Chemistry Laboratory, South Parks Road, Oxford, OX1 3QZ, United Kingdom.	7, 262, 282
University of Sts. Cyril and Methodius, Institute of Chemistry, Faculty of Natural Sciences and Mathematics, Arhimedova 5, 1000 Skopje, Republic of Macedonia	65, 77
University of Thessaloniki - Aristotle, Laboratory of Physical Chemistry, Department of Chemistry, 54124 Thessaloniki, Greece	255
University of Thessaloniki, ,Lab. of Hygiene, Department of Medicine, 54124 Thessaloniki, Greece	264
University of Thessaloniki, 54124 Lab. of Phys. Chemistry, Department of Chemistry, Thessaloniki, Greece	264
V. I. Vernadsky Institute of Geochemistry and Analytical Chemistry of the Russian Academy of Science, Moscow, Russia	39, 609
Westfälische Wilhelms Universität, Organisch-Chemisches Institut, Corrensstrasse 40, 48149 Münster, Germany	691
Xi'an Jiaotong University, MOE Key Laboratory for Strength and Vibration, School of Aerospace, PR China	488



# DEGRADATION MECHANISMS IN ORGANIC LIGHT EMITTING DIODES (OLEDS)

# Z. Popović

Department of Materials Science and Engineering, McMaster University, Hamilton, Ontario, Canada ZP Technology Solutions Inc., 3349 Sawmill Valley Dr., Mississauga, Ontario L5L 2Z8, Canada Serbian Academy of Sciences and Arts, foreign member

# **Abstract**

Organic Light Emitting Diodes (OLEDs) are thin film devices based on organic materials, which are capable of producing light of different colours and can be integrated into large areas. This makes them suitable for new generation of highly efficient, thin, and inexpensive flat panel displays. After more than two decades of extensive research at many academic and industrial institutions the first products are appearing on the market but the main problem for the wide application of this technology still remains device life. In this paper our current knowledge of degradation mechanisms in hydroxyquinoline aluminum (AlQ<sub>3</sub>) based OLED devices will be reviewed.

# Introduction

The electroluminescence (EL) in organic materials has been known for a long time. In 1960's it was discovered that anthracene single crystals emit light when provided with proper electrodes and external bias [1]. Anthracene devices based on evaporated amorphous films were demonstrated [2], but their light output decayed catastrophically in a few minutes. Electroluminescence in a polymer was first observed in polyvinylcarbazole (PVK), but light emission also decayed very quickly [3]. In 1987 Tang and Van Slyke described a two layer vacuum evaporated organic thin film structure, based on tris(8-hydroxyquinoline)aluminum (AlQ<sub>3</sub>), an emitter and electron transport material, and a hole transport material (tertiary amine) [4]. The half-life (time of operation elapsed before luminance decreases to 50% of its initial level) of these devices was measured in hundreds of hours, many orders of magnitude larger then any organic thin film devices reported previously. Soon after in 1990 Buroughs *et al.* reported observation of EL in a single layer device made of a polymer polyphenylenevinilene (PPV), made by a spin coating process [5]. These two developments were seeds of a new technology of organic light emitting diodes (OLEDs).

A basic requirement for any emissive technology is providing adequate device stability for intended applications. In case of displays, it is generally assumed that a half-life of at least 10,000 hours, at initial display brightness (luminance) of 100 cd/m<sup>2</sup>, is needed. For some specialized applications where the usage duty cycle is low, a shorter device half-life may be adequate. In this paper, device half-life is sometimes also referred to as device lifetime or simply device life.

Figure 1 shows a schematic diagram of a typical OLED structure. Often ITO (indium thin oxide) anode is first covered by a buffer layer (sometimes also referred to as a hole injection layer or HIL), followed by a hole transport layer

(HTL), emitter layer (EML), electron transport layer (ETL), optional electron injection layer (EIL), and finally a cathode. Specific device designs may be lacking some of these layers or may have additional layers to further improve device performance.

Many different materials are used in small molecule based OLEDs. The molecular structures of some frequently used materials, which will be referred to often in this paper, are shown in Figure 2.

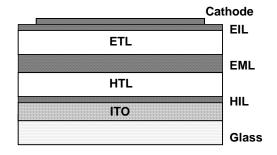


**Fig. 1.** A typical OLED device structure. The function of different layers and the meaning of acronyms is given in the text.

**Fig. 2.** Chemical structures of some of the materials commonly used in small molecule based OLEDs.

Hydroxyquinoline aluminum (AlQ3, Fig. 2a) is the most frequently used emitter and electron transport molecule (ETM). Copper phthalocyanine (CuPc, Fig. 2b) is commonly used in a buffer layer contacting the hole injecting anode. N,N'-diphenyl-N,N'-bis(3-methylphenyl)-1,1-biphenyl-4,4'-diamine) (TPD) and N,N'-di(naphthalene-1-yl)-N,N'-diphenyl-benzidine (NPB) (Figs. 2c,d) have been the most frequently used hole transport materials (HTMs). For control of emission color, various dopants have been identified. Two typical dopants are dimethyl quinacridone (DMQ), and 5,6,11,12-tetraphenyl naphthacene (rubrene), which produce green and

yellow emission, respectively (Fig. 2 e,f). ITO is almost exclusively used as a hole injecting anode. A Mg:Ag alloy (9:1 by volume) is usually utilized as an electron injecting cathode, because of its efficient electron injection into AlQ3. However, other cathode materials (Ca, Al:Li alloy, etc.) are also used.

In this paper, the discussion of stability and degradation in OLEDs will be limited to small molecule based devices. In general, degradation in OLEDs, which appears in the form of a decrease in device luminance, proceeds through two independent and visually distinct degradation modes. The first, associated primarily with degradation at the device electrodes, occurs through the formation of non-emissive regions, usually referred to as dark spots, that lead to a decrease in device luminance as a result of losses in the emissive area of a device due to electrode corrosion in atmosphere containing oxygen and water vapour [6],[7]. The second degradation mode is reflected in a long-term "intrinsic" decrease in the electroluminescence efficiency of the emissive area of a device [7]. Our focus will be on the intrinsic degradation, in which device brightness, at constant current bias, decreases in time without any obvious change in device appearance.

# **Empirical Approaches for Improving OLED Stability**

The initial thin film OLED device described by Tang and Van Slyke [4] had a half-life of only about few hundred hours at an initial luminance of about 100 cd/m². The first substantial increase in OLED device life was reported in 1995 by Hamada *et al.* [8]. They found that doping of the TPD transport layer with rubrene significantly improved device half-life, compared to devices where the electron transport layer was doped with the same material. The half-life of the best devices exceeded 3500 hours at 500 Cd/m² initial luminance. It was concluded that the change of emission site from the electron transport to the hole transport material was responsible for improved device performance.

In 1996, Van Slyke *et al.* [9] introduced a thin (15 nm) copper phthalocyanine (CuPc) buffer layer between ITO and a new hole transport molecule NPB. Using a 60 nm NPB hole transport layer and a 75 nm AlQ<sub>3</sub> electron transport and emitter layer, half-life of about 4000 hours was obtained, at an average current density of 20 mA/cm<sup>2</sup> and initial luminance of 510 cd/m<sup>2</sup>. This work also established a scaling law for accelerated OLED testing. As light output is proportional to device current this scaling law can be expressed by the simple formula:

$$L_{\text{(initial)}} T_{1/2} = \text{constant}, \tag{1}$$

stating that the product of initial luminance  $L_{(initial)}$  and device half-life,  $T_{1/2}$ , is constant. The law enabled the use of accelerated half-life measurements where testing at high current (resulting in a high luminance) can be used to predict expected half-life at typical currents and luminance needed for display applications. According to this scaling law, at typical display brightness level of  $100 \text{ cd/m}^2$  their device half-life would exceed  $20{,}000$  hours. Applied to the rubrene doped TPD device described in the previous paragraph, the scaling law would predict half-life in excess of  $16{,}000$  hours. The remarkable stability of devices based on NPB HTM and CuPc buffer layer was attributed to the higher glass

transition temperature of NPB (95°C) compared to TPD (65°C), and to the presence of CuPc buffer layer, whose role was not quite clear.

In 1998, Popovic *et. al.* investigated in depth the influence of mixing of NPB hole and AlQ<sub>3</sub> electron transport materials on device performance [10]. The study was motivated by the suggestion that interlayer diffusion could be causing device degradation [11]. The device structure containing mixed emitter layer between electron and hole transport layers showed a half-life that was at least an order of magnitude longer than that of conventional bilayer devices.

In summary, a number of different, seemingly unrelated, approaches were found to increase OLED stability. These approaches were: (i) doping of the hole transport layer, (ii) introducing a CuPc buffer layer in-between the ITO and the HTL, and (iii) using mixed emitter layers composed of hole and electron transport materials. However, the explanations offered for the underlying degradation mechanisms were essentially speculative in nature and often contradictory. The use of dopants to modify device emission color and increase efficiency also influenced device life when used in conjunction with these three methods.

# **Degradation Mechanism Based on Unstable AlQ<sub>3</sub> Cation**

Our studies on understanding the mechanism of degradation of OLEDs during prolonged operation was motivated by the existence of the seemingly unrelated approaches, described in the previous section, which all led to substantial improvements in device stability. In this section, we will closely follow the argument of Aziz et al. [12] to explain the origin of long-term degradation of OLEDs based on AlO<sub>3</sub> electron transport and emitter material. To investigate the mechanism for the enhanced stability Aziz et al. studied OLEDs of various structures, including ones with a CuPc buffer layer at the ITO contact, or rubrenedoped HTLs [20]. The J-V and L-J characteristics of these devices showed that, compared to standard bilayer devices, longer lived devices had higher efficiencies and also higher operating voltages for the same device current. Based on these results, a common feature in the role of different approaches to improve OLEDs stability was found to be the slowing down of hole transport to the HTL/AlQ<sub>3</sub> interface where they get injected into the AlQ<sub>3</sub> layer. Therefore, the injection of holes into the AlO<sub>3</sub> layer appeared to be the main factor responsible for the longterm degradation in OLEDs, leading to the hypothesis that AlQ<sub>3</sub> cations are unstable.

To investigate this hypothesis photoluminescence (PL) measurements were employed to monitor changes in the PL quantum efficiency of a 5 nm thick AlQ<sub>3</sub> sandwiched between two thick NPB layers and equipped with ITO anode and Mg:Ag cathode. Under positive ITO bias, charges driven through the AlQ<sub>3</sub> layer would be only holes (hole-only device). On prolonged current flow a gradual decrease of the AlQ<sub>3</sub> PL was observed, revealing a continuous decrease in the PL quantum efficiency of the AlQ<sub>3</sub> [12]. This indicates that cationic AlQ<sub>3</sub> species were unstable and that their degradation products were fluorescence quenchers.

It is important to point out that the transport of electrons through AlQ<sub>3</sub>, being itself an excellent electron transport material [13], should not be expected to cause degradation. In order to prove the validity of this assumption, devices containing 5 nm thick AlQ<sub>3</sub> layers sandwiched between two BTB (4,4'-Bis-[2-(4,6-diphenyl-1,3,5triazinyl)]1-1,1-biphenyl, insert in Fig. 3) electron transport layers were also studied. Like NPB, BTB has the absorption cutoff around 400 nm and therefore allowed unobstructed photo-excitation of photoluminescence measurements. The devices where only electron transport was allowed (electron-only device), did not

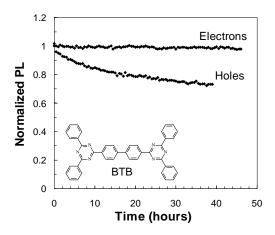


**Figure 3.** Integrated PL as a function of time from AlQ<sub>3</sub> sandwiched between two hole or electron transport layers.

show any decrease in the photoluminescence of  $AlQ_3$  under similar testing conditions [14]. The results of photoluminescence measurements on samples where  $AlQ_3$  was subjected to predominantly hole or electron flow are shown in Fig. 3. While significant photoluminescence decrease is observed in the case of transporting holes, the photoluminescence stays remarkable constant in case of transporting electrons. These results therefore provided strong evidence that injection of holes into the  $AlQ_3$  layers of the OLEDs was a main factor in device degradation.

Further insights into the nature of electroluminescence aging were obtained by measuring simultaneously PL and EL in devices containing 5 nm thick AlQ<sub>3</sub> layer sandwiched between NPB hole transport and BTB electron transport layer [15]. These studies showed that EL degradation is always larger than PL degradation, leading to the conclusion that AlQ<sub>3</sub> degradation leads to production of both fluorescence quenchers and recombination centers. Increase of operating voltage on aging at constant device current also indicates accumulation of trapped space charge. Kondakov *et al.* were able to establish a linear correlation of device light output reduction with measured accumulated space charge indicating that degradation products also act as charge traps [16].

# **Indium Migration Degradation Model**

According to this model, which was proposed by Lee *et al.*, OLED intrinsic degradation is attributed to penetration of indium ionic species released from the ITO anode into the organic layers, which results in luminescence quenching [17]. The experiments described in the previous section cannot distinguish if unstable

AlQ<sub>3</sub> or indium migration is responsible for device degradation. In order to differentiate between these two possible degradation mechanisms Luo et al. compared PL decrease in devices similar to the ones described in the previous section but also equipped with a buffer layers, which are known to dramatically increase device life [18].

The results of these experiments are shown in Figures 4. Figure 4a shows the influence on device life of three different buffer layers, CuPc, Pt:Au, and Mg on top of ITO. They all lead to significant device life extension. On the other hand the same buffer layers in devices that transport only holes lead to similar degrees of PL quenching as the current is passed through the device. If indium migration was responsible for device degradation we would expect that PL quenching will also be significantly reduced as buffer layers are used. As this is not the case we conclude that indium migration is not an important factor in device aging.

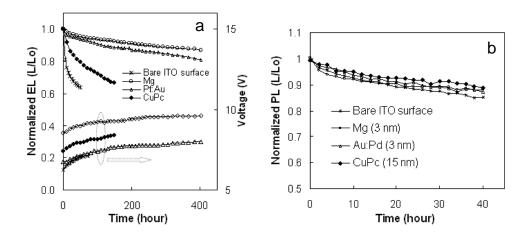


**Fig. 4.** (a) shows degradation of standard AlQ<sub>3</sub>/NPB devices without and with different buffer layers. (b) shows PL decrease in devices transporting only holes with the same buffer layers driven at 50 mA/cm<sup>2</sup>.

# **Electron Induced Degradation**

Electron-only device experiments do not show any degradation of  $AlQ_3$  (Fig. 3). The question is if negative  $AlQ_3$  ions are really so stable or there are other factors influencing degradation. Important difference for electron and hole transport in  $AlQ_3$  is mobility ( $\mu_e >> \mu_h$ ). Actually in  $AlQ_3$  hole mobility is about 100 times smaller than electron mobility [19,20]. Therefore, for the same current density, J,

$$J_e = en_e\mu_e E = J_h = en_h\mu_h E, \qquad (2)$$

where E is the electric field, there must be a large difference in concentration of electrons and holes,  $n_h \gg n_e$ , which could be the reason for apparent stability of AlQ<sub>3</sub> negative ions in electron-only device experiments (Fig. 3).

This idea was tested by investigating PL aging in electron-only devices containing a specially designed layer, which reduces mobility of electrons to different degrees [21]. The structure of the device used for these studies is shown in Fig. 5a. On top or ITO a thin Mg layer is deposited first, which serves as a hole blocking layer. 50 nm of BTB electron transport molecule is followed by 10 nm of a buffer layer consisting of BTB/NPM mixed layer with different amounts of NPB, which represents a layer with reduced electron mobility. 5 nm AlQ<sub>3</sub> emiiter layer is deposited next followed by 50 nm of BTB and electron injecting Mg:Ag cathode.

As these different cells are subjected to 50 mA/cm<sup>2</sup> electron current a marked difference in the change of photoluminescence in time is observed. While PL in the device with 0% NPB in the buffer layer stays essentially constant, as the amount of NPB is increased more pronounced PL decrease is observed. This can be interpreted as electron induced AlQ<sub>3</sub> degradation. Increased amounts of NPB in the mixed buffer layer lead to electron mobility decrease and increased negative charge accumulation in AlQ<sub>3</sub>, which, in turn leads to increased AlQ<sub>3</sub> degradation.

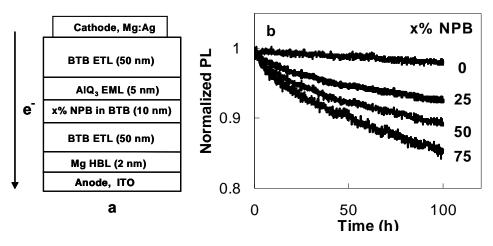


**Fig. 5.** (a) shows the structure of an electron-only device used to establish the existence of electron induced degradation in AlQ<sub>3</sub> emitter. (b) shows PL decrease in a series of devices with different amounts of NPB in NPB/BTB reduced electron mobility layer. The devices are operated at 50 mA/cm<sup>2</sup>.

There is also a possibility that mixed BTB/NPB buffer layer is degrading due to electron flow. To investigate this possibility we constructed devices where BTB/NPB buffer layer and AlQ<sub>3</sub> layer order was reversed. As in this case electrons pass first through the buffer layer and then through AlQ<sub>3</sub>, no charge accumulation in AlQ<sub>3</sub> occurs. In these structures no decrease in AlQ<sub>3</sub> PL is observed for all levels of NPB concentration demonstrating that indeed the degradation happens in AlQ<sub>3</sub> layer rather than in BTB/NPB mixed buffer layer.

### **Conclusions**

In conclusion, intrinsic degradation in AlQ<sub>3</sub>-based OLEDs is primarily caused by excessive hole injection into the AlQ<sub>3</sub> emissive layer and subsequent degradation of AlQ<sub>3</sub> cations, which leads to production of fluorescence quenchers and charge traps. However, excessive electron density also induces significant degradation of the AlQ<sub>3</sub> layer. Therefore the main message of these investigations for increased OLED stability is establishment of good charge balance in supply of electrons and holes to the charge recombination and emission zone.

# Acknowledgements

I would like to thank my long-time collaborators Prof. Hany Aziz, Prof. Gu Xu and Dr. Yichun Luo for their contributions in elucidating degradation mechanism of OLED devices based on AlO<sub>3</sub>.

### References

- [1] W. Helfrich and G. Schneider, Phys. Rev. Lett., 1965, 14, 229.
- [2] P. S. Vincett, W. A. Barlow, R. A. Hann, and C. G. Roberts, Thin Solid Films, 1982, 94, 171.
- [3] R. H. Partridge, Polymer, 1983, 24, 733.
- [4] C. W. Tang, S. A. Van Slyke, and C. H. Chen, J. Appl. Phys., 1989, 65, 3610.
- [5] J. H. Burroughes, D. D. C. Bradley, A. R. Brown, R. N. Marks, K. D. Mackay, R. H. Friend, P. L. Burn, and A. B. Holmes, Nature, 1990, 347, 539.
- [6] P. E. Burrows, V. Bulovic, S. R. Forrest, L. S. Sapochak, D. M. McCarty and M. E. Thompson, Appl. Phys. Lett, 1994, 65, 2922.
- [7] J. McElvain, H. Antoniadis, M. R. Hueschen, J. N. Miller, D. M. Roitman, J. R. Sheets and R. L. Moon, J. Appl. Phys., 1996, **80**, 6002.
- [8] Y. Hamada, T. Sano, K. Shibata and K. Kuroki, Jpn. J. Appl. Phys., 1995, 34, L824.
- [9] S.A. Van Slyke, C.H. Chen and C.W. Tang, Appl. Phys. Lett., 1996, **69**, 2160.
- [10]Z. D. Popovic, H. Aziz, C. P. Tripp, N. X. Hu, A. M.. Hor and G. Xu., Proceedings of the SPIE, Organic Light-Emitting Materials and Devices II, 1999, **3476**, 68.
- [11]E. Han, L. Do, N. Yamamoto and M. Fujihira, Chemistry Lett., 1995, n 1, 57.
- [12]H. Aziz, Z. D. Popovic, N. X. Hu, A. M. Hor and G. Xu, Science, 1999, 283, 1900.
- [13]L. B. Bin, S. A. Jenekhe, R. H. Young, P. M. Borsenberger, Appl. Phys. Lett., 1997, **70**, 2052.
- [14]H. Aziz, Z. Popovic, N.Hu, P. Dos Anjos and A. Ioannidis, Proceedings of SPIE Conference on Organic Light Emitting Materials and Devices IV, 2001, **4105**, 251.
- [15]Z. Popovic, H. Aziz, N. Hu, A. Ioannidis, and P.N.M. dos Anjos, J. Appl. Phys., 2001, **90**, 4673.
- [16] D. Y. Kondakov, J. R. Sandifer, C. W. Tang, R. H. Young, J. Appl. Phys. 2003, 93, 1108.
- [17]S.T. Lee, Z.Q. Gao and L.S. Hung, Appl. Phys. Lett., 1999, 75, 1404.
- [18]Y.C. Luo, H. Aziz, Z.D. Popovic and G. Xu, J. Appl. Phys., 2007, **101**, 34510.
- [19]B. Lin, C. Cheng, Z. You, C. Hsu, J. Am. Chem, Soc., 2005, 127, 66.
- [20] A. Moliton, W. Rammal, B. Lucas, Eur. Phys. J. Appl. Phys. 33, 175 (2006).
- [21]Y.C. Luo, H. Aziz, G. Xu, and Z.D. Popovic, Chem. Mater., 2007, 19, 2079.



PRIMORSKA 17A 11000 BEOGRAD nola@EUnet.yu www.novolab.com Tel: (011) 3293 534 3293 758 2763 683 Fax: (011) 764 026

Ovlašćeni zastupnik:



analiza ulja, goriva i maziva ...



pH metri, konduktometri, plameni fotometri, spektrofotometri ...



instrumenti za ispitivanje uslova radne i životne sredine i meteorologije ...



instrumenti za merenje debljine prevlaka u industriji boja i lakova ...



Adam Equipment Co. Ltd

laboratorijske vage ...



laboratorijske žarne peći, inkubatori i sušnice ...

# **Spectrolab**

atomska absorbcija, FT-IT spektrometri, hromatografi, plameni fotometri ...



referentni standardi za naftne proizvode ...



PHARMA

oprema za ispitivanje u farmaceutskim laboratorijama ...

# CIP - Каталогизација у публикацији Народна библиотека Србије, Београд

544(082) 66.017/.018(082) 502/504(082)

MEĐUNARODNA konferencija iz fundamentalne i primenjene fizičke hemije (9; 2008; Beograd)

Physical Chemistry 2008: proceedings of the 9th International Conference on Fundamental and Applied Aspects of Physical Chemistry, [September 24-26, 2008, Belgrade, Serbia]. Vol. 2 / [organized by The Society of Physical Chemists of Serbia; editor A.[Ankica] Antić-Jovanović]. - Belgrade: The Society of Physical Chemists of Serbia, 2008 (Belgrade: Jovan). - X str., str. 469-770: ilustr.; 24 cm

Tiraž 250. - Str. VII: [Preface] / editor. - Bibliografija uz svaki rad. - Abstracts. -Registri.

# ISBN 978-86-82475-13-2

1. Antić-Jovanović, Ankica [уредник] 2. Društvo fizikohemičara Srbije (Beograd) а) Физичка хемија - Зборници b) Наука о материјалима - Зборници c) Животна средина - Заштита - Зборници COBISS SR-ID 150993676